SAE TRANSACTIONS

TL
1
S6
Vol. 69

21 June 72

Society of Automotive Engineers, Inc.
485 Lexington Avenue New York 17, N. Y.

A. A. Kucher
President

Joseph Gilbert
Secretary and General Manager

G. A. Delaney
Treasurer

Kathleen Napier
Editor

All articles appearing in SAE Transactions are indexed by Engineering Index, Inc.

Copyright 1961, Society of Automotive Engineers, Inc.

Price: $3 to members, $7 to public and college libraries and U. S. Government Agencies, $10 to nonmembers. Foreign: $3 to members, $8 to public and college libraries, $11 to nonmembers.

Photolithographed reproductions are available of any article published in SAE Transactions. Prices, on quantities of 100 copies or more, varying with number of pages and illustrations, can be obtained upon request from SAE General Publications Department, 485 Lexington Avenue, New York 17, N. Y.

Contents

Vol. 69

1961

The Antiknock Behavior of the Alkyl Lead Compounds—H. E. Hesselberg and J. R. Howard 5

A New Tool for Combustion Research—Fred W. Bowditch 17

Corrosion Resistance of Aluminum Automobile Engine Components—Allen M. Montgomery 24

Automatic Highway and Driver Aid Developments—H. M. Morrison, A. F. Welch, and E. A. Hanysz 31

Applications of the Army-Navy Instrumentation Program to Transport Aircraft—A M. Mayo, and H. L. Wolbers 54

A Nitrosyl Chloride Solar Regenerative Fuel Cell System—W. E. McKee, J. D. Margerum, E. Findl, and W. B. Lee 64

Fatigue, Impact, and Tensile Properties of High Strength Leaded and Nonleaded SAE 4140 Steel—William Simon 69

Cures for Powerplant Bending Noise Problems—R. H. Bollinger and J. H. Ruhl 77

A Radioactive Tracer Study of Lubricating Oil Consumption—E. S. Starkman 86

U. S. Lunar Travel Program—Donald H. Heaton 101

Analysis and Simulation of Automobile Ride—Robert H. Kohr 110

Fuel Injection and Positive Ignition, A Basis for Improved Efficiency and Economy—C. W. Davis, E. M. Barber and Edward Mitchell 120

Crank-Piston Gas-Generator Locomotives—L. H. Tengner 135

Mating Materials in Unlubricated, High Load, Low Speed, Wear Tests at High Temperature in Air—L. E. Fuller 148

Cord Fatigue in Fleet Tested Tires—W. G. Klein, M. M. Platt and W. J. Hamburger 158

Mach 3 Wing Structures Stiffened Skin Versus Sandwich—Jack C. Joanides, Stanley C. Mellin and Leslie M. Lackman 167

The NSU-Wankel Rotating Combustion Engine—Dr. Walter G. Froede 179

Curtiss-Wright's Development on Rotating Combustion Engines—M. Bentele 194

Metallic Tracer Method for Determining Lubricant in Engine Exhaust —F. R. Bryan, J. C. Neerman and J. E. Hinsch 204

Stress Analysis of Aluminum V-8 Diesel Cylinder Block—H. W. Van Camp 212

An Advanced Automotive Gas Turbine Engine Concept—I. M. Swatman and D. A. Malohn 219

Vibration and Noise Control of Outboard Motors and Other Products—James W. Mohr 228

From Four Plies to a Single Ply in Steel-Cord Casing Tires—M. P. Baumont 238

Practical Application of High Temperature Gas Carburizing—Orville E. Cullen 250

Vehicle Steering Fundamentals—William H. Baier 256

Scientific Highway Design for Safer Motoring—K. A. Stonex 269

Piston Rings for Transportation Diesels—Glenn F. Hyde, Fred A. Robbins, and Paul R. Shepler 283

By-Pass Engine Noise—F. B. Greatrex 312

The Performance of Springs at Temperatures Above 900 F—William R. Johnson and Ronald D. Crooks 325

Secondary Power Systems for Space Vehicles—D. B. Mackay 331

Plasma Propulsion—S. W. Kash 346

Computer Predicts Car Acceleration—Henry L. Setz 351

Production Application of High Energy Rate—E. W. Feddersen 361

"Case Crushing" of Carburized and Hardened Gears—R. Pedersen and S. L. Rice 370

Handling Requirements—O. J. Winkelmann 381

Snap 2—A Reactor Powered Turboelectric Generator for Space Vehicles—Guveren M. Anderson 390

Aircooling Versus Water-Cooling in Agricultural and Construction Equipment—H. H. Haas 402

An Engine Test for Predicting the Performance of Engine Lubricants in Most Severe Passenger Car Service—P. A. Bennett, G. K. Malone and C. K. Murphy 416

A Consideration of the Deposit Ignition Mechanism—F. W. Bowditch and T. C. Yu 435

Concurrent Pyrolytic and Oxidative Reaction Mechanisms in Precombustion of Hydrocarbons—C. E. Welling, G. C. Hall and J. S. Stepanski 448

Unsteady Heat Transfer in Engines—Vern D. Overbye, James E. Bennethum, O. A. Uyehara and P. S. Myers 461

End-Gas Temperature Measurement by a Two-Wavelength Infrared Radiation Method—W. G. Agnew 495

The Measurement of Unburned-Gas Temperatures in an Engine by an Infrared Radiation Pyrometer—M. C. Burrows, S. Shimizu, P. S. Myers and O. A. Uyehara 514

End-Gas Temperature-Pressure Histories and Their Relation to Knock —M. E. Gluckstein and C. Walcutt 529

The Effect of Material and Processing Variables on Residual Stresses in Carburized and Induction-Hardened Gears—E. T. Bergquist and S. M. Lenhoff 554

The Film Vaporization Combustor—A. W. Hussmann and G. W. Maybach 563

Radioisotopes Broaden the Approach to Machining Studies—Marko Paliobagis and E. J. Krabacher 575

Recent Developments in Cam Design—J. H. Nou se, R. C. Dennis and W. M. Wood 585

Theoretical Prediction of the Effect of Traction on Cornering Force—Walter Bergman 614

Rotating Combustion Engine—Roy T. Hurley and M. Bentele 641

Strength Prediction After Severe and Complex Thermal Histories—D. M. Badger and C. D. Brownfield 650

Ride Requirements—R. Schilling 658

Case Hardenability of SAE 4028, 8620, 4620 and 4815 Steels—J. A. Halgren, and E. A. Solecki 662

Index 677

Other SAE Publications

SP-14 Cooperative Testing of Torsiographs and Calibrators

SP-37 Highway Safety — Review and Forecast — 1947 Beecroft Memorial Lecture by Paul G. Hoffman

SP-71 Highway Safety through Eyes of Motor Vehicle Administrator—1951 Beecroft Memorial Lecture by Rudolph King

SP-72 Traffic Law Enforcement—1952 Beecroft Memorial Lecture by Franklin M. Kreml

SP-73 Role of Public Information in Safety Cause—1953 Beecroft Memorial Lecture by W. Earl Hall

SP-74 Driver Education—Key to Safe Operation of Motor Vehicles—1954 Beecroft Memorial Lecture by Amos E. Neyhart

SP-75 Traffic Engineering, Its Role in Safe and Efficient Operation of Streets and Highways—1955 Beecroft Memorial Lecture by D. Grant Mickle

SP-76 Skill and Will To Drive Safely—1956 Beecroft Memorial Lecture by O. E. Hurt

SP-119 Engineering Know-How in Engine Design, Part 1 (1953)—fundamentals of engine design

SP-122 Engineering Know-How in Engine Design, Part 2 (1954)—theory, test data, and empirical formulas of engine design

SP-130 Design, Evaluation, and Selection of Heavy-Duty Rear Axles—first L. Ray Buckendale Lecture by K. W. Gordon

SP-132 New Drive Lines for New Engines—third L. Ray Buckendale Lecture by W. P. Mitchell

SP-133 Bearing Applications for Heavy-Duty Axles—fourth L. Ray Buckendale Lecture by R. M. Riblet and C. M. Kitson

SP-134 Design of Planetary Gear Trains—fifth L. Ray Buckendale Lecture by O. K. Kelley

SP-136 The SAE Story—history of SAE 1905-1955

SP-137 Engineering Know-How in Engine Design, Part 3 (1955)—reciprocating engine dynamics, fuel applications, two-stroke engines, opposed piston diesel

SP-139 Symposium of Fuels and Lubricants—detergency activity tests, lubrication of hydraulic valve lifters, air pollution (1955)

SP-140 Symposium on Fuel Injection—8 papers on passenger-car application

SP-142A Human Body Size and Passenger Vehicle Design—"general driving population" as related to passenger car design

SP-143 Engineering Know-How in Engine Design, Part 4 (1956)—gear design and manufacture, supercharging, development of small engines, automotive gasoline injection, diesel fuel injection

SP-148 Engineering Know-How in Engine Design, Part 5 (1957)—engine crankshafts and connecting rods, bearings and bearing lubrication, pistons and rings

SP-152 Engineering Know-How in Engine Design, Part 6 (1958)—valve train engineering, two-stroke engines, fuel injection, liquid cooling systems, and aircooled engine design criteria

SP-154 Better Truck Ride for Driver and Cargo—ride as affected by suspension system and configuration of vehicle, recommendations of SAE Committee on Ride, report by R. N. Janeway

SP-155 Better Braking—How? (1958)

SP-157 Engine Noise Symposium—combustion-chamber noises in high compression ratio engines, 11 papers (1958)

SP-159 Aluminum Engine Symposium (Part 1)—5 papers and discussion on manufacturing techniques for automotive aluminum engines (1958)

SP-162 Make Slides Worth While

SP-163 Engineering Know-How in Engine Design, Part 7 (1959)—engine roughness, viscous torsional vibration damper, vibration engine mounting, air cleaners, silencers

SP-165 Safety The Motorist Gets—insuring safety in motor cars: design factors, material selection, testing, quality control, reduction of driver fatigue, durability of structural parts (1959)

SP-166 Engine and Speed Governors (1959)

SP-168 Anti-Friction Bearings Seminar—design, materials, lubrication, service

SP-171 Tire and Wheel Runout and Balance Problems

SP-172 Computer-Based Selection of Balanced-Life Automotive Gears—sixth L. Ray Buckendale Lecture by G. J. Huebner

SP-173 Applications and Limitations of New Developments in Metals Joining Processes, by P. J. Rieppel (1960)

SP-174 Automobile Side-Impact Collisions, by D. M. Severy, J. H. Mathewson, and A. W. Siegel (1960)

SP-175 What's New in Engineering Materials for 1960—technological developments in steel, plastics, rubber, plating, and aluminum

SP-178 Engineering Know-How in Engine Design, Part 8 (1960)—valve train dynamics, dynamometers, radioisotopes, instrumentation for testing, field testing diesels

SP-180 Automobile Aerodynamics—fundamentals and techniques of testing (1960)

SP-181 Surface Rolling Symposium—techniques and mechanical prestressing (1960)

SP-183 B-58 Reliability Program (1960)

SP-184 Designing with Plastics for automotive applications—Six articles by members of Plastics Subcommittee of Engineering Materials Activity Committee

SP-185 Auto Air Conditioning Forum

SP-186 The Design of Single-Stage, Three-Element Torque Converter—7th L. Ray Buckendale Lecture by V. J. Jandasek

SP-188 Truck Electrical System Reliability

SP-189 How to Write Reports That Get Read—report by Tyler G. Hicks

SP-192 Engineering Know-How in Engine Design—Part 9—(1961) small engine hydraulic governor design, disc clutch design, hydrostatic transmissions, mechanical transmissions

SP-193 Engineering Know-How in Engine Design—Contains SP-119, SP-122, SP-137, SP-143, SP-148, SP-152, SP-163, SP-178, SP-192

SP-194 Coolant Temperature Effects on Engine Life and Performance

SP-195 Hurricane Road (Wind Tunnel Testing)—wind tunnel testing techniques for automotive vehicles

SP-197 Vistas in Astronautics—1960—Symposium jointly sponsored by AFOSR and SAE, October 1960, Astronautic Vehicle Utilization, Astronautic Propulsion, Bioastronautics, Planetary and Space Environment, Astronautic Communications, Astronautic Guidance

SP-216 Looking Ahead in Fuels for Automotive Transportation—1957 Horning Memorial Lecture by J. M. Campbell

SP-218 Single-Cylinder Engine Fuel Research—1958 Horning Memorial Lecture by A. W. Pope, Jr.

SP-222 Instincts in Action—"For Sake of Argument" pieces from SAE Journal, 1948-1961

TPS-1 Fuel Filter Test Methods

TPS-2 Selecting the Right Vehicle for the Job

Antiknock Behavior of Alkyl Lead Compounds

H. E. Hesselberg, and J. R. Howard

Ethyl Corp.

WHEN THE antiknock effectiveness of TEL was discovered by Midgley and his co-workers in 1921, it was felt certain that other alkyl lead compounds would also possess antiknock properties. In fact, a number of other lead alkyls were covered in the original patent applications on TEL. Early in the 1930's, it was believed that other alkyls might be superior to TEL in certain fuels under certain engine conditions. Since that time Ethyl has evaluated 30 individual lead alkyls and 10 mixtures of these alkyls under a wide range of operating conditions and engine environments.

It became apparent very early in this work that there was no simple solution to the problem of which alkyl or alkyl mixture was the most effective as an antiknock. It was found that the relative effectiveness of the alkyls was influenced to a major extent by base fuel composition, alkyl concentration, sulfur concentration, and the engine in which the evaluation was made as well as its method of operation. The marked effect of alkyl volatility under operating conditions where fuel segregation occurred was established as early as 1936.

Just prior to World War II an extensive cooperative road test program of a lighter alkyl mixture showed insufficient advantage as compared with TEL to warrant further consideration at that time.

In 1948, however, several lighter alkyl compositions were found to have significant advantages over TEL in several base fuels. Studies since that time have indicated that the trends in fuel composition have continued to increase the antiknock effectiveness of the lighter alkyls. Our most recent studies are in agreement with those of others and particularly in regard to tetramethyl lead (TML), indicate definite road antiknock behavior advantages as well as intrinsic advantage by the laboratory knock test methods. Because TML is much more volatile, its advantage over TEL in fuels of low-octane number front end in vehicles knocking at low engine speeds is most pronounced.

Early History

The original Midgley patent, which was issued in 1926, taught the use of TML as well as TEL as antiknock compounds. Our records indicate that TML was compared with TEL in 1928 and found to be only 3/4 as effective. In 1933, TML was again compared with TEL in an Ethyl Series "30" knock rating engine under conditions similar to those of the present Research method. The comparison showed that TML was considerably less effective than TEL in two commercial 75 octane gasolines and in secondary reference fuels.

From time to time during the early 1930's, changes in gasolines, engines, and knock testing methods occasioned further testing of TML and other lead alkyls. In all of this work, TEL was found to be either equal to or better than the other lead alkyls tested. It is interesting to note that since these early years, 30 individual lead alkyls and 10 selected mixtures of these alkyls have been evaluated under a wide range of operating conditions, engine environments, and fuel types.

Due to the relatively high boiling point of TEL (390 F)

it was reasoned that some of the TEL would tend to lag in the intake manifold with the heavier portions of the fuel. This would cause unequal distribution of antiknock quality among the engine cylinders and severe depreciation of the fuel relative to its laboratory knock test engine rating. (1)*

Accordingly, it was decided to investigate the most volatile lead alkyl, TML, which boils at 230 F, in addition to the mixed methyl-ethyl alkyls of intermediate volatility to see whether these lighter materials would improve the road ratings of 1936 type gasolines.

Before discussing the results of this investigation, it is advisable to briefly describe these lead alkyls.

Description of Lead Alkyls

There are three possible methyl-ethyl lead alkyls with boiling points between that of TML and that of TEL:

1. Trimethyl ethyl lead.
2. Dimethyl diethyl lead.
3. Methyl triethyl lead.

Table 1 shows their formulae and boiling points.

In preparing adequate amounts of these materials for test purposes, it was found that equilibrium mixtures of the required alkyls could be produced by a redistribution reaction (2). Such a reaction occurs when sodium-lead alloy is reacted with methyl and ethyl chlorides in the presence of an aluminum catalyst. An equilibrium mixture of lead alkyls results. Depending on the proportions of the methyl and ethyl chloride used, the resulting mixture is composed of various proportions of the C_4 to C_8 alkyls shown in Table 1.

Hence, by varying the proportions of the starting materials, a wide range of mixture volatilities was obtainable. Modifications in the mixtures were also obtainable by stripping out one or more alkyl components by distillation. Lead alkyls less volatile than TEL were also made and tested. These included compounds made with propyl, butyl, and amyl groups both normal and isomeric, such as trimethyl isopropyl lead, triethyl butyl lead, and trimethyl amyl lead.

*Numbers in parentheses designate References at end of paper.

Table 1 - Methyl and Ethyl Lead Alkyls

Name	Chemical Formula	No. of Carbon Atoms	Boiling Point, F
Tetraethyl lead	$(C_2H_5)_4Pb$	8	390
Methyl triethyl lead	$CH_3(C_2H_5)_3Pb$	7	355
Dimethyl diethyl lead	$(CH_3)_2(C_2H_5)_2Pb$	6	319
Trimethyl ethyl lead	$(CH_3)_3(C_2H_5Pb$	5	279
Tetramethyl lead	$(CH_3)_4Pb$	4	230

Evaluation from 1935 to 1940

Many road tests were conducted as the alkyls and their mixtures became available in 1936. The antiknock effectiveness of the various mixtures showed sufficient promise in a variety of gasolines and cars, as compared with TEL. An extensive research program was planned and executed during the next three years.

Wide variations in effectiveness from car to car and fuel to fuel were found. In fact, during the early test work, for any given car, merely opening or closing the radiator shutters made TML, for instance, either much more or much less effective than TEL. This was traced to the operation of the automatic heat control valves which in their "hot" position greatly depreciated TML, and in their "cold" position showed TML to advantage.

Road tests indicated that alkyls less volatile than TEL were of little interest, since more rather than less volatility might be required for best performance in the fuels and engines then in use.

In the thermally-cracked and straightrun naptha blends which were commercial during these years the various mixed alkyls on the road seemed to respond best in highly-volatile straightrun gasolines. However, no improvements in intrinsic antiknock effects were noted in laboratory engines by the L-3, research, or motor methods.

Fig. 1 typifies the single-cylinder laboratory engine data obtained during this period. Here, TML, TEL, and the intermediate alkyls are compared in two representative commercial fuels by the L-3 rating method which was intended to yield ratings representing the mean of the research and motor ratings. The results shown are averages for the two fuels which were tested in 16 CFR engines in five Ethyl Corp. gasoline testing laboratories. One fuel was a blend of 80% cracked and 20% vapor recovery components and the other contained 44% cracked, 42% straightrun, and 14% natural gasolines.

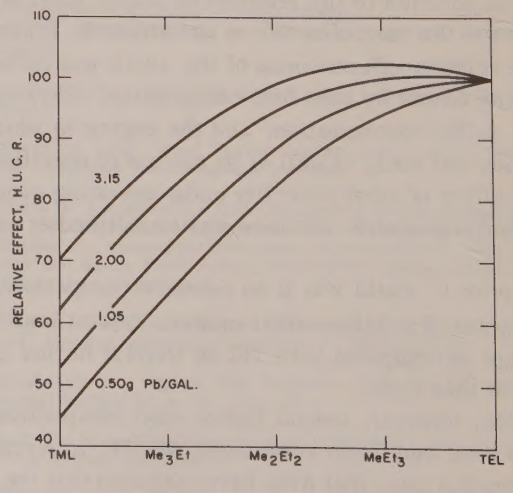

Fig. 1 — Intrinsic effectiveness, average data, 2 fuels, L-3 method

Both fuels rated at about 80 research octane number with 3.0 ml of TEL. Results are shown in terms of the highest useful compression ratio (HUCR) relative to TEL at a given lead level, rather than relative increase in octane number.

Fig. 1 shows that, except for methyl triethyl lead at 3.15 gr of lead, all of the alkyls tested were less effective than TEL. Their relative effectiveness also decreased with decreasing lead concentration. In the light of our present knowledge on the importance of fuel composition factors and research-octane level in considering lead alkyl response, these results are not at all surprising.

Despite the wide variation in road effectiveness displayed by the ethyl and methyl alkyls and their mixtures during the years 1936 to 1938, their potential possibilities are indicated by the extent of the test program. During this period, 12 major road test projects were conducted in Detroit, Michigan, San Bernardino, California, and Tulsa, Oklahoma. Each project involved 5 to 22 different cars, 3 to 10 different fuels, 2 to 5 lead alkyls and/or mixtures, and several lead concentrations.

Final results of this extensive program showed that, at the higher lead concentration (3.0 gr of lead), the road antiknock superiority of some of the alkyl mixtures over TEL would produce a 10-14% saving in the amount of lead necessary to achieve the same road antiknock quality. At the lower lead concentrations (1.0-1.5 gr of lead), the alkyl mixtures were less effective than TEL. (To keep our arithmetic straight, 1.0 gr of metallic lead is equivalent to 0.95 ml of TEL and to 0.65 ml of TML.)

On the basis of these results, it was decided to select the optimum alkyl mixture from the cost-effectiveness standpoint, and to invite several oil companies to test the mixture in their own fuels by their own test methods. The alkyl mixture selected was designated MA-350 and, on a mole basis, contained 1.3% tetramethyl, 11.7% trimethyl ethyl, 33.4% dimethyl diethyl, 38.2% methyl triethyl, and 15.4% tetraethyl. Six major oil companies agreed to conduct this evaluation.

The results of the oil company evaluations of MA-350 are shown in Table 2. The maximum gains shown at the 2.10 gr and 3.15 gr lead concentrations were 2.8 and 2.4 road octane numbers respectively. However, these gains were obtained in only a minor fraction of the fuels tested. With these results, it was concluded that the substitution of the MA-350 mixture for TEL would not be economically attractive to a large enough segment of the oil industry to justify commercialization.

Bled Manifold

During the years in which Ethyl's work on the lead alkyls was going on, the extensive cooperative oil and automotive industry program was being conducted to develop satisfactory laboratory and road methods of knock rating. In addition to cooperating in this program, Ethyl started investigating, in 1937, the possibility of modifying the CFR knock rating engine so that it could be made to simulate the fuel segregation effects that result in madldistribution of antiknock quality among the cylinders of automobile engines.

Several special "bled" intake manifolds were developed for the CFR engine to provide fuel segregation effects. Fig. 2 shows one of the later versions of these bled manifolds on which a large amount of data (3) has been obtained. The water-jacketed separating chamber has a cross-sectional area over four times as great as that of the remainder of the manifold, and thus reduces the velocity of flow to a point that ensures good separation of liquid fuel from the stream of air and vaporized fuel.

In a later version of this device and in representative present-day fuels, octane gains for TML over TEL of the same magnitude as those now measured on the road were obtained. This modification provides a method for indicating the CFR engine the advantage of TML attributable to its high volatility.

The bled manifold offers a promising field for further investigation in industry's approach to laboratory knock-rating

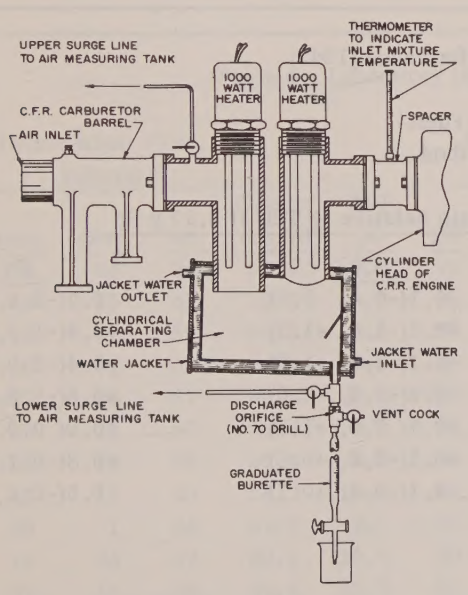

Fig. 2 — Bled manifold for CFR engine

Table 2 - Oil Co. Tests of MA-350 (1940)

Gram Pb/Gal	No. of Fuels	Gain Due to MA-350, O.N. Res.	Motor	Road Avg.	Range
1.05	26	-1.2	-0.6	-0.1	-0.4 to +0.7
2.10	11	-0.1	0.0	+0.6	-0.5 to +2.8
3.15	28	-0.6	-0.5	+0.3	-0.5 to +2.4

methods which more nearly predict road behavior than the research and motor methods.

Road Evaluations Following World War II

The marked trend in 1949 towards increasing compression ratios as well as the corresponding increases in premium-fuel antiknock quality which this change required prompted a re-evaluation of the lighter alkyls on the road. Ten commercial premium base stocks were evaluated by the Modified Uniontown method in three 1949 premium-requirement cars plus one 1949 car equipped with the General Motors Research engine at compression ratios of 8:1 and 10:1. All cars were equipped with automatic transmissions. The alkyls investigated were dimethyl diethyl, methyl triethyl, tetraethyl, and MA-250 at 0.53 and 3.17 gr of lead per gal. (MA-250 is an equilibrium alkyl mixture containing 25% methyl radicals. The lead in the mixture, on a weight percent basis, is present as 1% of the C_4, 4% of the C_5, 21% of the C_6, 42% of the C_7, and 32% of the C_8 alkyls.)

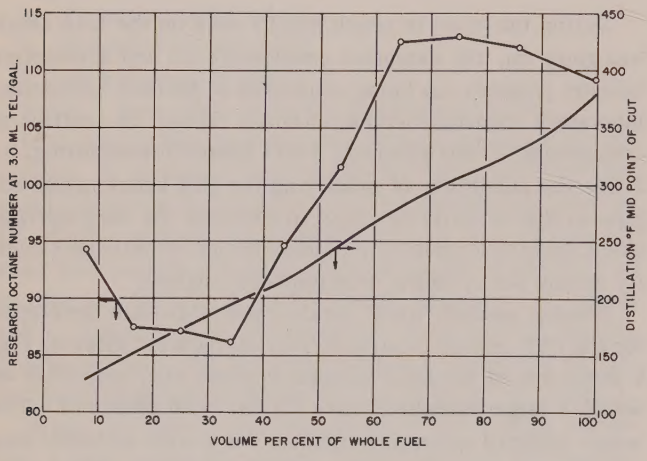

Fig. 3 — Octane-temperature profile of test fuel

At 0.53 gr of lead, the lighter alkyls showed no advantage over TEL in the cars on the road or by the research and motor methods. The results obtained at the 3.17 gr of lead level are shown in Table 3. Here, despite fairly wide ranges in relative effectiveness in the ten fuels, the average road results indicate a slight advantage for the lighter alkyls. Of interest are the gains in the General Motors Research engine at the 8:1 and 10:1 compression ratios.

By the research and motor methods, only small average differences were found between the various alkyls. A study of the available inspection data on these fuels reveals no correlation between hydrocarbon composition and alkyl effectiveness. In the cars, the least-volatile fuel, which contained 46% straightrun stock, showed the more volatile alkyls to the greatest advantage, while the most-volatile fuel consistently showed all the lighter alkyls to disadvantage.

The antiknock performance of several of the alkyls was investigated again at a later date in a fuel in which the octane number profile was such that the octane number of the more volatile portion was considerably lower than that of the heavier fractions. This fuel was a blend of 25% light straightrun, 55% heavy reformate, and 20% debutanized straightrun. The octane number profile as well as the distillation are shown in Fig. 3.

The TML (C_4), C_6, and MA-250 alkyls were compared with TEL at 1.58 gr of lead, as shown in Fig. 4. The same alkyls plus a 50-50 mixture of TML and TEL also were rated

Table 3 - Alkyl Lead Antiknock Performance (1949)

10 Commercial Premium Fuels
Modified Uniontown Method

1949 Car	C. R.	Road O. N. Gain Relative to TEL at 3.17 g Pb		
		MA-250	C_6	C_7
E	6.9	-0.3(-0.5, +0.5)	-0.1(-0.5, 0.0)	0.0(-0.5, +0.5)
Q	7.25	0.0(-1.0, +1.5)	+0.2(-1.0, +1.5)	+0.4(-1.0, +1.5)
M	7.5	-0.1(-1.5, +1.0)	-0.1(-1.5, +1.0)	-0.4(-3.0, +1.0)
Q*	8.0	+0.6(0.0, +2.5)	+0.6(-0.5, +2.0)	+0.6(-1.0, +3.0)
Q*	10.0	+0.7(0.0, +2.0)	+0.8(0.0, +1.5)	+0.9(0.0, +2.0)
Research		+0.2(-0.2, +0.6)	+0.1(-0.5, +0.8)	+0.3(-0.1, +0.7)
Motor		0.0(-0.2, +0.4)	-0.1(-0.4, +0.1)	0.0(-0.2, +0.3)

*Equipped with General Motors Research engine.
Note: Values in parentheses indicate ranges.

at 3.17 gr of lead, as shown in Fig. 5. Modified Borderline as well as Modified Uniontown ratings were made in a 1958 Car M equipped with a 10.7:1 compression ratio engine, and in a 1958 Car R equipped with a 10.3:1 compression ratio engine and three 2-barrel carburetors. The test fuel containing 3.17 gr of lead per gal had a research rating of 100.1 and a motor rating of 89.1, and was close to satisfying the octane requirements of the two cars. The road results for the alkyls are plotted in Fig. 4 and 5 relative to the antiknock gain obtained with TEL. The large advantage shown for the more volatile lead alkyls in Car R at both lead concentrations, and in particular at the lower engine speeds, indicates marked fuel segregation and manifold lag in this vehicle. The exact magnitude of the extreme gains shown by modified borderline ratings at 1650 rpm is subject to some question since the vehicle was difficult to rate at this speed, and variability from run to run was quite high. In Car M, the more volatile alkyls showed mostly a loss in antiknock quality at both lead concentrations. At the higher lead concentration in Car R, the 50-50 mixture of TML and TEL appeared to be equal to TML in road performance.

There is little correlation between gains by the research

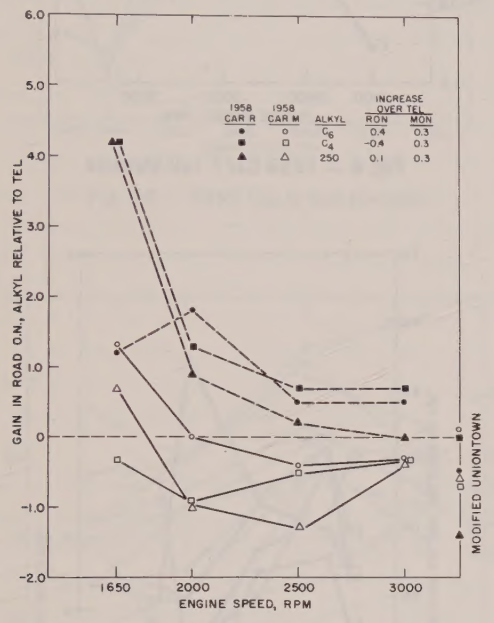

Fig. 4 — Alkyl lead antiknock performance in profile fuel, 1.58g Pb per gal

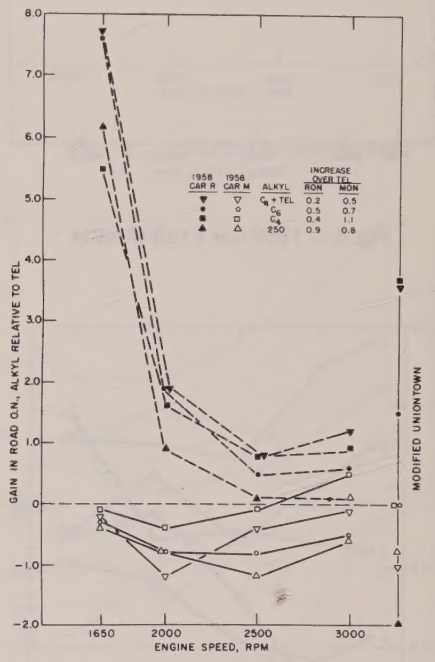

Fig. 5 — Alkyl lead antiknock performance in profile fuel, 3.17g Pb per gal

Table 4 - Laboratory Inspection Data on Fuels Used in Road Tests

Fuel No.	Hydrocarbon Type, volume %			Gravity, deg API	RVP, psi	ASTM Distillation, F at % Evaporated					Sulfur, wt %	TEL 3.17 g Pb		Gain Due to TML 3.17 g Pb	
	Arom.	Olef.	Sat.			IBP	10	50	90	EP		Res.	Motor	Res.	Motor
A	35	26	39	57.6	9.8	94	121	216	323	393	0.045	99.2	87.7	0.0	0.7
B	44	15	41	52.3	8.9	95	122	238	374	425	0.064	99.0	87.8	0.5	0.9
C	47	1	52	54.3	8.8	98	126	226	275	282	0.002	104.6	95.8	0.5	1.9
D	46	1	53	54.9	9.0	96	116	221	331	398	0.001	103.6	95.5	0.7	1.8
E	39	24	37	55.8	8.7	104	125	209	322	405	0.100	100.3	88.1	0.2	1.1
F	36	11	53	58.8	9.2	93	117	198	323	422	0.056	100.6	90.8	0.4	1.0
G	29	15	56	60.4	9.4	92	120	206	304	398	0.013	99.0	89.8	0.2	0.7
H	42	12	46	54.7	10.2	87	127	241	328	398	0.044	99.5	89.7	0.0	0.6
I	35	1	64	59.7	9.7	89	124	201	282	355	0.030	99.7	91.2	0.1	0.9
J	19	34	47	63.8	10.7	89	113	187	309	386	0.022	98.3	86.4	-0.2	0.4
K	37	15	48	59.4	12.7	82	106	200	333	418	0.063	99.1	88.6	-0.1	1.7

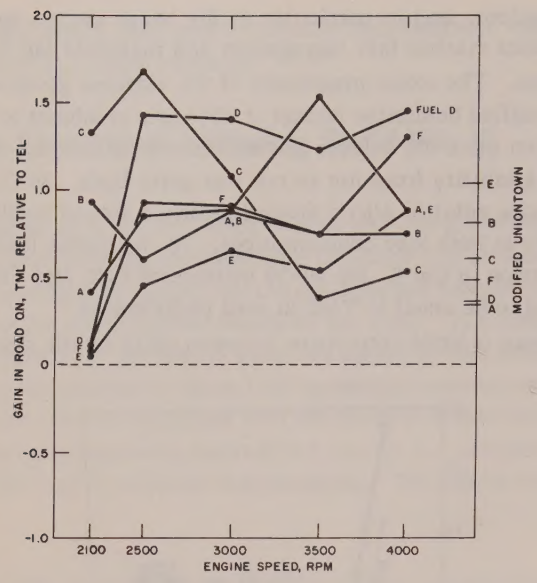

Fig. 6 — 1959 Car E full-throttle

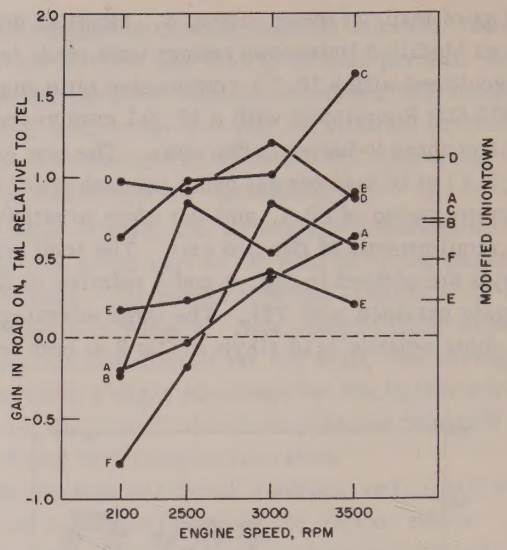

Fig. 8 — 1959 Car F full-throttle

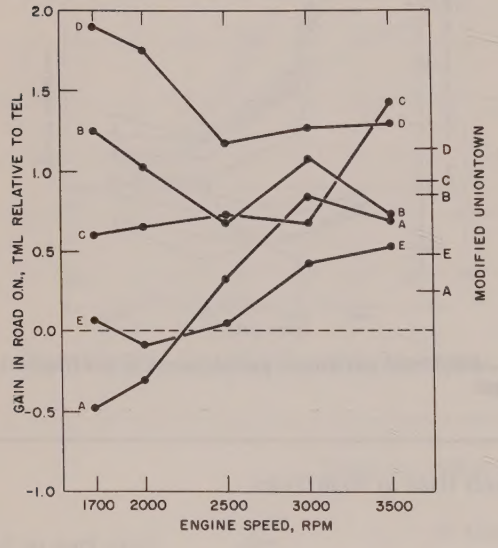

Fig. 7 — 1959 Car M full-throttle

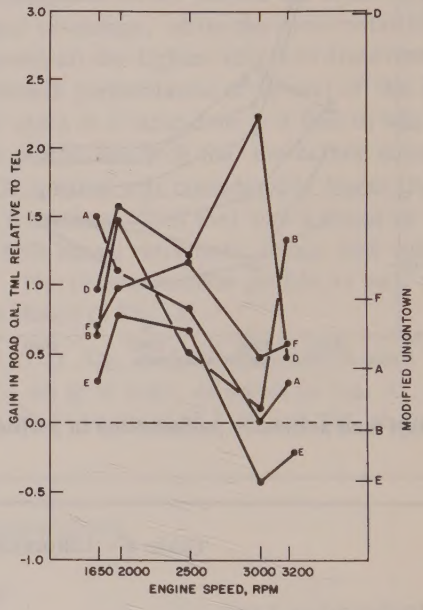

Fig. 9 — 1959 Car P full-throttle

and motor methods for these various alkyls relative to TEL and their performance in the two vehicles. These data indicate the definite influence of engine design and operating characteristics upon the performance of the alkyls more volatile than TEL. The data also indicate the ability of the lighter alkyls to give superior road antiknock performance under conditions where fuel segregation and manifold lag are combined with a fuel having low antiknock components in the more volatile fractions.

TML was also compared with TEL in the 1958 Car R, this time equipped with a 12.2:1 compression ratio engine, in two fuels of similar octane number profile. One was a blend of 25% light straightrun and 75% heavy reformate having a research octane number of 100.5 and a motor octane number of 90.3. The other was a blend of 40% light straightrun, 30% aromatic extract, and 30% heavy reformate having a research rating of 100.0 and a motor rating of 89.9. The superior road antiknock performance of TML in these two fuels of low front-end octane number was again clearly evident.

Recent TML Evaluation

The pronounced volatility advantage of TML plus its advantage by the research and motor methods in certain fuel

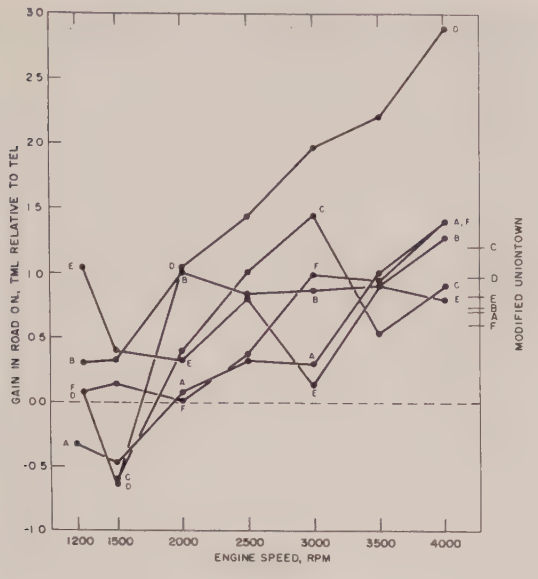

Fig. 10 — 1959 Car Q full-throttle

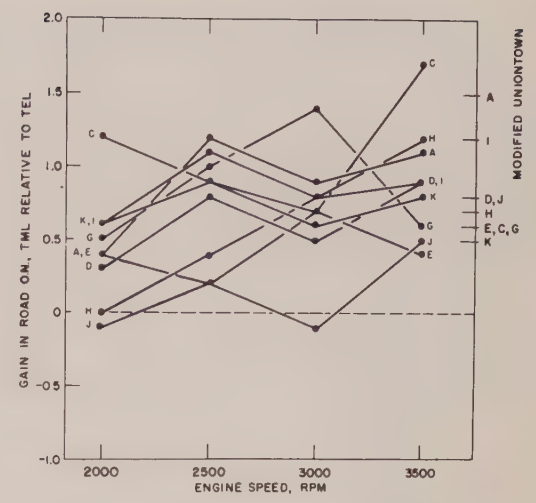

Fig. 12 — 1960 Car M full-throttle

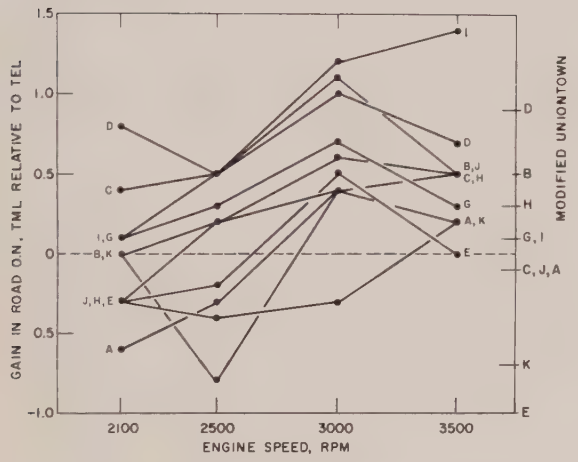

Fig. 11 — 1960 Car E full-throttle

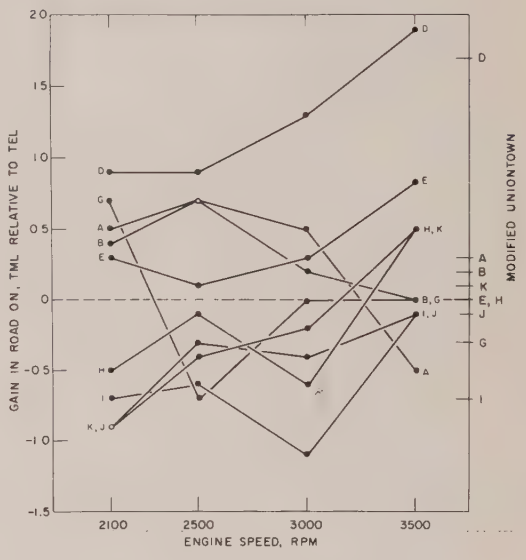

Fig. 13 — 1960 Car F full-throttle

compositions led to a recent major investigation of its vehicle antiknock performance relative to TEL. Eleven commercial premium-fuel base stocks were included in the program. Laboratory inspection data on these fuels as well as the changes in research and motor ratings due to the substitution of TML at the 3.17 gr lead level are shown in Table 4. In all eleven fuels, TML was more effective by the motor method, with gains ranging from 0.4 to 1.9 O.N. By the research method TML was equal to or better than TEL in nine of the fuels, and only insignificantly less effective in the other two.

The program included: two cars equipped with experimental 12:1 compression ratio engines, five 1959 premium-requirement cars, three 1960 premium-requirement cars, and two 1960 compact cars equipped with manual transmissions. All of the road ratings were carried out on a controlled-weather chassis dynamometer with air temperature held at 70 ±5 F and relative humidity held at 40 ±5%. In all cases, the data are based upon at least triplicate ratings by both the Modified Uniontown and Modified Borderline techniques. The accelerations were made at the manifold vacuum producing maximum knock rather than at wide-open throttle. Since the manifold vacuum for maximum knock was always less than 3 in. of mercury, these ratings are referred to as full-throttle ratings.

To illustrate the wide range in the performance of TML relative to TEL, depending not only upon the fuel being rated but upon characteristics of the vehicle in which the comparison is being made, the road results obtained in each of the vehicles equipped with automatic transmission are shown in Figs. 6-15.

In each figure, the change in Modified Borderline and

Modified Uniontown octane ratings of each fuel is shown when when substituting TML for TEL at 3.17 gr of lead. It is immediately apparent that any statements regarding the road behavior of TML relative to TEL must be well qualified. For example, in 1960 Car M (Fig. 12) engine speed did not appear to have much effect on the relative performance of TML and TEL. On the other hand, in 1959 Car Q (Fig. 10) the TML advantage definitely increased with engine speed. And in 1957 Car E (Fig. 14), with a 12:1 compression ratio engine, TML showed to greatest advantage at the lowest engine speed.

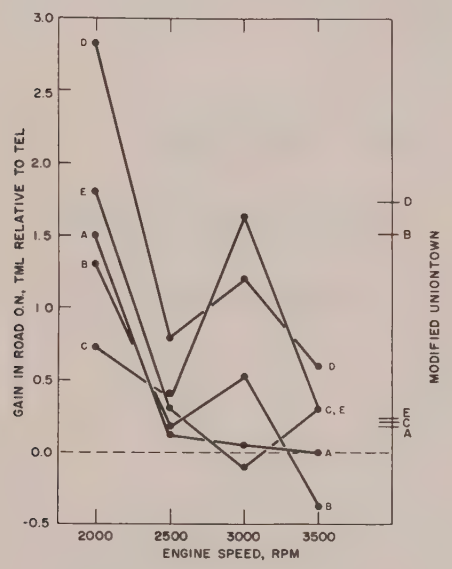

Fig. 14 — 1957 Car E, 12 CR, full-throttle

On the whole, however, these data indicate that, in these fuels, TML has a marked advantage by both the Modified Borderline and Modified Uniontown methods. Across the board, Fuels C and D show TML to the best advantage both in the cars and also by the research and motor ratings. These fuels also are the most highly aromatic of the group (47 and 46% aromatics). The consistently poor vehicle performance of TML in Fuel J correlates with low laboratory response of this fuel to TML as well as its low (19%) aromatic content.

The vehicle ratings obtained in the two compact cars equipped with manual transmissions are shown in Fig. 16 and 17. At the low speeds, where these cars have their highest octane requirement, the advantage of TML is consistently large. This is undoubtedly due to the higher volatility of TML as compared with TEL, which tends to provide more antiknock quality in individual cylinders under conditions which promote fuel segregation. Judging from these comparisons in the compact cars, it is entirely possible that standard-sized cars with manual transmissions will also show significant advantages for TML in these fuels. Foreign cars equipped with manual transmissions which are prone to knock at low speeds will show definite advantage for the more volatile alkyls, particularly in fuels having low octane number front ends.

Part-throttle road ratings of TML versus TEL were made in two cars, and the results are shown in Figs. 18 and 19. In establishing part-throttle operating conditions, the manifold vacuum producing the greatest octane requirement on sensitive reference fuels was used in these two cars. It was found to be 12 in. of mercury. Consistent ratings were most

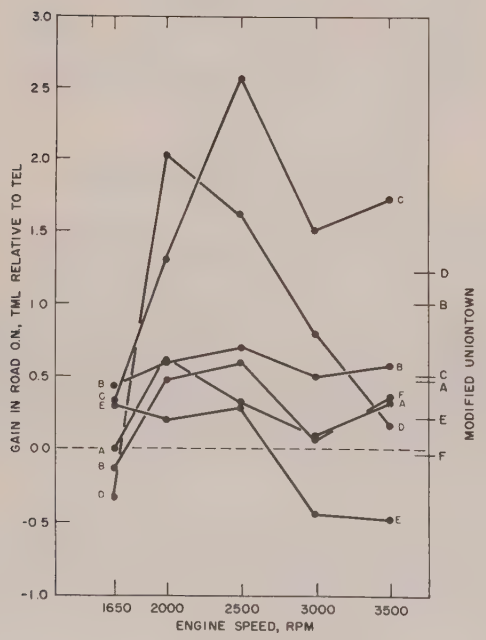

Fig. 15 — 1958 Car R, 12 CR, full-throttle

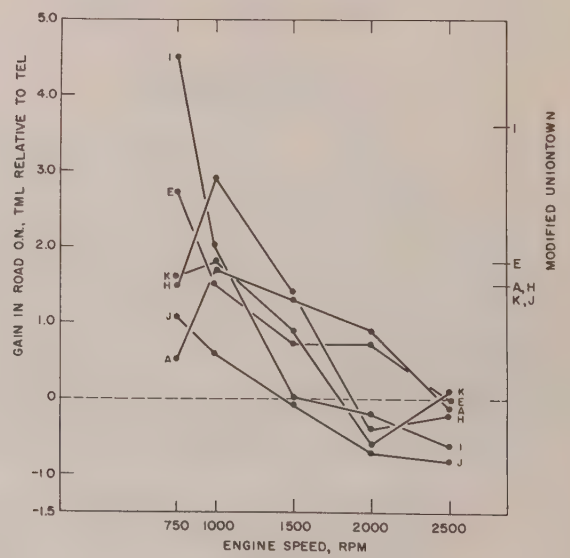

Fig. 16 — 1960 Compact car AY full-throttle

difficult to obtain at part-throttle. The noise intensity was not as sharp, nor as reproducible, as under full-throttle conditions. It will be noted that, except at the lowest rating speed (1000 rpm in one car and 1500 rpm in the other), TML gains are appreciable in all fuels rated. They are, in fact, about double those shown for the same fuels at full throttle in the same two cars.

Fuel Distribution Studies - A factor of major importance in the road performance of the lighter alkyls relative to TEL is their vapor pressure. At 65 F the vapor pressure of TML is 100 times that of TEL. In addition to increasing the lead concentrations in the cylinders under conditions where the heavier fuel components are retarded in the intake manifold, the increased volatility of the lighter alkyls also promotes more even distribution of the antiknock compound under most operating conditions.

Using radioactive-tagged hydrocarbons and additives, fuel distribution studies were made in a multicylinder engine(4). It was shown that a closer approach to a constant concentration of hydrocarbon or additive in the fuel in each cylinder was obtained when the boiling point of the hydrocarbon or additive in the fuel in each cylinder was obtained when the boiling point of the hydrocarbon or additive is near the mid-distillation range of the whole fuel. These results are presented in Fig. 20, and are expressed as the percent average deviation among the cylinders based on the component con-

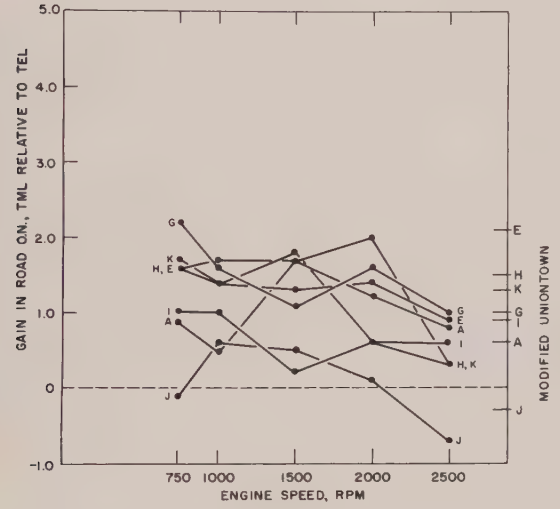

Fig. 17 — 1960 Compact car AX full-throttle

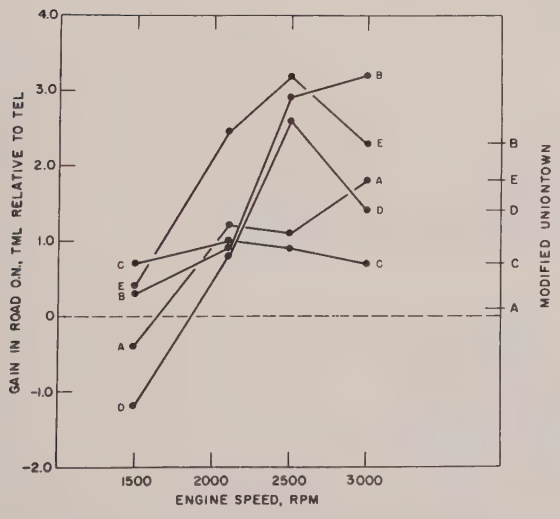

Fig. 18 — 1959 Car F part-throttle, 12 in. Hg manifold vacuum

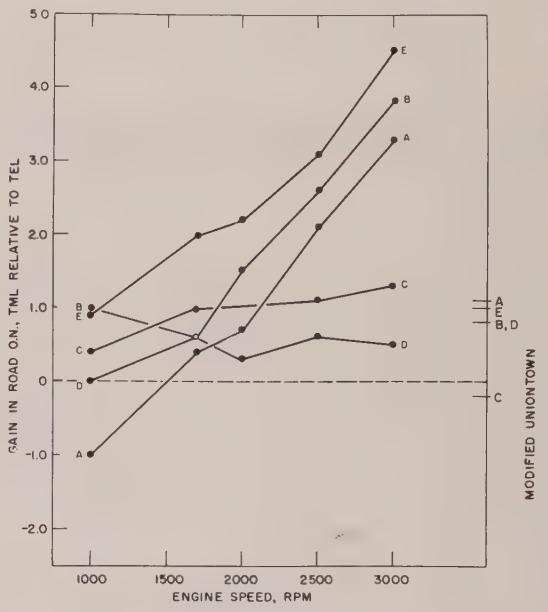

Fig. 19 — 1959 Car M part-throttle, 12 in. Hg manifold vacuum

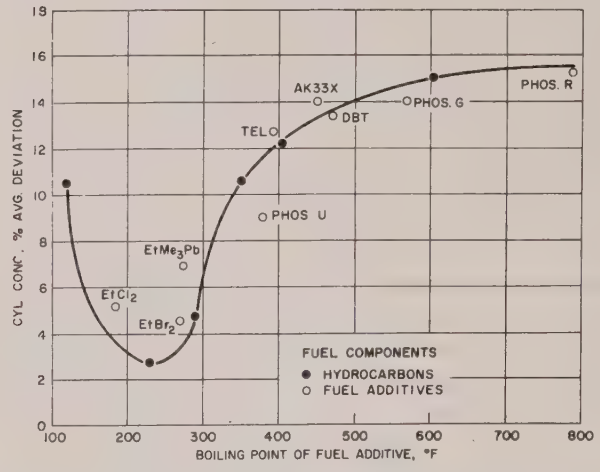

Fig. 20 — Average cylinder diviation for concentration of various fuel additives blended in typical fuel, engine D, 2400 rpm, 40 deg throttle

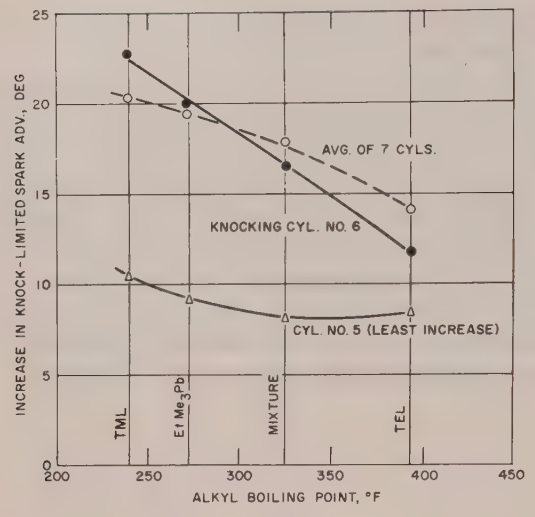

Fig. 21 — Effect of lead-alkyl volatility on knock-limited spark advance due to antiknock addition to base fuel, engine D, 2400 rpm, 40 deg throttle, fuel — 90.0 ron (with antiknock)

centrations in the cylinders. The solid curve was based on individual hydrocarbons, and various fuel additives are also shown. Although TML was not actually run as a radioactive-tagged component, its relative distribution can be predicted from this curve, since we know it has a boiling pont of 230 F. Its predicted average deviation among the cylinders would be approximately 3%, the lowest shown for any of the fuel components under these engine conditions. It will be noted that trimethyl ethyl lead, which has a boiling point of 274 F, shows a deviation of about 7%.

Another set of data showing the beneficial effects of the more even distribution of TML is presented in Fig. 21. Individual cylinders were knock rated using a base fuel without lead and then with sufficient lead alkyl to provide a research octane number of 90. The increase in knock-limited spark advance allowed by various lead alkyls is plotted against their boiling points. The lower the boiling point of the lead alkyl, the greater the knock-limited spark advance. The greatest difference was noted in the knock-limiting cylinder No. 6.

Single-Cylinder Antiknock Performance - Many investigations to determine the fuel composition factors of greatest importance in predicting the antiknock performance of the various lead alkyls have been conducted. Programs with designed composition variables have been conducted, as well as analyses of composition data on a great number of commerical fuel compositions. While it has been possible to arrive at generalizations which hold for many fuels, there have always been a large number of exceptions. This is not too surprising since even the vast amount of data relating TEL effectiveness to fuel composition has not permitted the development of relationships that apply in all cases.

The majority of our recent work has been on relating the anticknock effectiveness of TML to TEL. Data investigated included the laboratory ratings of 20 finished gasolines specially blended from refinery components to represent a wide range of antiknock levels and fuel compositions, and ratings of a group of 56 commercially available gasolines. Analysis of these data has led to a number of generalizations. These are that the antiknock effectiveness of TML relative to TEL at equal metallic lead concentration increases with the following (not necessarily listed in order of their importance).

1. Increasing aromatic content.
2. Increasing leaded octane number.
3. Increasing lead content
4. Decreasing fuel sulfur content.
5. Decreasing TEL susceptibility.

And, that the advantage for TML is almost without exception greater by the motor method than by the research method.

Table 5 - TML versus TEL in Aromatic Blends

60% Aromatic + 40% 40 O.N. PRF

Aromatic Component	TML Rating minus TEL Rating 1.05 g Pb Research	1.05 g Pb Motor	3.17 g Pb Research	3.17 g Pb Motor
Benzene	-2.2	-0.6	-1.3	-0.6
Toluene	-1.0	0.2	0.1	0.7
Ethyl benzene	-1.6	-2.0	-.05	-0.7
0-Xylene	-0.8	0.0	1.0	1.9
m-Xylene	-0.2	0.9	0.4	1.5
Isopropyl benzene (Cumene)	-2.0	-2.0	-1.0	-1.3
1,2,4-Trimethyl benzene	-0.9	0.5	0.7	2.8
n-Butyl benzene	-4.0	-3.0	-3.2	-2.2
sec-Butyl benzene	-1.6	-0.8	-0.5	0.0
tert-Butyl benzene	-2.0	-0.9	-0.8	-2.3

The relative stability of the alkyls in the engine is undoubtedly a major factor in their antiknock behavior. It has been established that any lead alkyl must decompose during the combustion process to exert its antiknock effect (5). It has also been established that the varying thermal stabilities of the alkyls in the combustion chamber result in significant changes in the degree of alkyl decomposition at a given time during the combustion process (6). Since the reactions leading to knock differ widely depending upon fuel composition (7), it is natural to assume that a major factor in the relative effectiveness of the alkyls is their degree of decomposition at the critical time in the combustion process when the reactions leading to knock can be inhibited.

Fuel Composition Factors - The poor performance of TML in the saturated hydrocarbons has been well established. Limited data by the research and motor methods and some obtained under supercharged conditions in a 17.6 engine indicate that TML will be less effective than TEL in the olefins. The marked beneficial influence of fuel aromatic content

Table 6 - Relative Sulfur Effect

Sulfur Type	Loss in Octane Number*			
	Research Method		Motor Method	
	TML	TEL	TML	TEL
Disulfide Oil				
0.1 wt % S	4.0	2.2	4.7	3.6
0.2 wt % S	5.2	3.0	6.4	5.0
Thiophene				
0.1 wt % S	0.3	0.3	0.5	0.9
0.2 wt % S	1.0	0.7	1.5	1.5

*Based on octane number of sulfur-free fuel.

Table 7 - Relative Phosphorus Effect

Phosphorus Compound	Loss in Octane Number*			
	Research Method		Motor Method	
	TML	TEL	TML	TEL
A				
0.2 Theory	0.4	0.2	0.6	0.5
0.5 Theory	1.2	0.5	1.4	1.1
B				
0.2 Theory	0.1 (Gain)	0.0	0.1	0.3(Gain)
0.5 Theory	0.2 (Gain)	0.1 (Gain)	0.3	0.1
C				
0.2 Theory	0.1	0.1	0.2	0.2
0.5 Theory	0.0	0.0	0.1	0.4

*Based on octane of phosphorus-free fuel.

on TML effectiveness has led to a more detailed investigation of this class of hydrocarbons. Because of the extremely high antiknock quality of the aromatics and the questionable nature of knock ratings that would be obtained at these levels, the ratings were made on blends of 60% aromatics with 40% of a 40 O.N. primary reference fuel blend. The blends were rated with TML and TEL by the research and motor methods. at 1.05 and 3.17 gr of lead per gal. The results of these ratings are shown in Table 5.

The significant effect of aromatic structure on the relative performance of TML is clearly shown. In the four aromatics from this group showing an advantage for TML (toluene, the two xylenes, and 1,2,4-trimethyl benzene), the gain is always the greatest by the motor method and at the highest lead concentration. The data are also quite consistent in that only the aromatics having methyl groups attached to the benzene ring show TML to advantage, and the advantage increases with the number of methyl groups present in the compound.

Sulfur Effects - The reduction in antiknock quality of leaded fuels due to the presence of sulfur compounds is a function of both amount and type of sulfur present. The relative antiknock losses due to added sulfur when comparing TML and TEL appear to be markedly influenced by sulfur type. With high concentrations of a highly destructive sulfur compound, such as a disulfide oil, the loss of octane number is much greater in the case of TML. With a less-destructive sulfur compound, thiophene, destruction is about the same for the two alkyls.

These conclusions are based on the data shown in Table 6. At least two direct-comparison ratings were made of blends of pure hydrocarbons, without sulfur and with sulfur in the types and amounts shown. For these tests, the lead concentration was 3.17 gr for both TML and TEL.

Removal of the naturally occurring sulfur present in a gasoline component also increased the relative attractiveness of TML to TEL. In a cooperative program with the Paulsboro Research Laboratories of Socony-Mobil Oil Co., Inc., a full-boiling catalytically-cracked gasoline was desulfurized by a sodium treatment process. The untreated-fuel sulfur content of 0.07 wt% was reduced to 0.002 wt % by the treatment. The treatment did not affect the unleaded research and motor method ratings of the stock. Duplicate Research and motor method ratings of the treated and untreated fuel at the 3.17 gr of lead level showed that while TEL was improved by 0.9 and 1.7 octane numbers by the research and motor methods, respectively, the corresponding gains with TML were 2.2 and 2.8 octane numbers. In the desulfurized gasoline, TML rated higher than TEL by 0.6 and 1.2 octane numbers by the research and motor methods respectively.

Phosphorus Effects - With all phosphorus compounds, slight losses in antiknock quality of leaded fuels may occur, the magnitude depending on the particular compound, its concentration fuel composition, and the rating method. To secure data on the effects of phosphorus compounds and concentration, at least two direct-comparison ratings were made of fuels, without phosphorus and with phosphorus compounds in the types and amounts shown. The results at 3.17 gr of lead are shown in Table 7.

The data in Table 7 show that, with one possible exception, antiknock destruction due to the presence of phosphorus is the same for both TML and TEL. The possible exception is in the case of Compound A at the 0.5 T level; in a pure-hydrocarbon blend which magnifies destruction, the loss is greater with TML under research method conditions.

Halogen Effects - The halogens present in commercial antiknock fluids containing TEL have no significant influence on antiknock performance. Direct-comparison ratings of a commercial prototype fuel have established that this also is the case with TML. At 3.17 gr of lead, the addition of Motor Mix halogens (0.5 T of ethylene dibromide and 1.0 T of ethylene dichloride) resulted in an indicated increase

of 0.2 octane number with both TML and TEL by the research method, and no change with either by the motor method.

Antiknock Promotion Effects - The ability of relatively small quantities of AK-33X, methylcyclopentadienyl manganese tricarbonyl, to increase the antiknock quality of leaded fuels is closely related to fuel composition. This promotion of antiknock quality by AK-33X is influenced to a much greater extent by fuel composition than by the nature of the lead alkyl. In general, the range of promotion by AK-33X when used with TML may be expected to be as great as when used with TEL, and to be at its highest levels in the same general fuel compositions. The definite influence of fuel composition on both the relative antiknock performance of TML and TEL and the antiknock promotion of AK-33X makes it impossible, at present, to generalize as to the composition factors resulting in optimum performance.

The ability of organic supplements, such as tertiary butyl acetate, to increase the antiknock quality of highly leaded, high-octane-level stocks is currently under investigation in many laboratories. Tests by Ethyl on a large number of promoters in several commercial fuels indicate that the beneficial effects of organic supplements are consistently less with TML by the Research method, and in some fuel-supplement combinations are less by the motor method.

Conclusions

The antiknock behavior of lead alkyls and various mixtures of lead alkyls has been investigated in the laboratory and on the road since shortly after the discovery of the remarkable antiknock ability of TEL. It was established early in these investigations that two factors of major importance must be considered when evaluating the relative effectiveness of the various alkyls. One is the ability of the lead alkyl to control knock, and the other is to have the proper amount of lead present in the various cylinders of the engine at the time it is needed.

The relationships between lead alkyl antiknock effectiveness and fuel composition are complex. However, some generalizations can be made on the relative effectiveness of TML to TEL. Relative TML effectiveness increases with increasing aromatic content, increasing leaded octane number level, increasing lead content, decreasing fuel sulfur content, and decreasing TEL susceptibility, and is always greater by the motor method than by the research method. In the presence of high concentrations of compounds which cause loss in antiknock quality of leaded fuels, the loss is greater with TML than with TEL. The antiknock promoter effect of AK-33X is as great with TML as with TEL, but TML does not respond as well to organic supplements as does TEL.

Vehicle ratings have established that the greater volatility of TML enables it to reach the cylinders of an engine more readily than TEL under conditions where manifold lag occurs. This is of particular importance when the light fuel components reaching the cylinders under these conditions are of low antiknock quality. In addition, TML's increased volatility promotes more even distribution to the cylinders under all engine operating conditions.

References

1. J. M. Campbell, W. G. Lovell, and T. A. Boyd, "Relative Knocking Characteristics of Motor Fuels in Service," SAE Trans., Vol. 32, (1937), 144-150.

2. H. A. Beatty, G. Calingaert, et al,, series of eleven papers entitled "The Redistribution Reaction," J. A. C. S., (1939-1945).

3. E. Bartholomew, B. Brewster and H. Chalk, "Carburetion, Manifolding, and Fuel Antiknock Value," SAE Trans. Vol. 33, (1938), 141-156.

4. D. E. Cooper, R. L. Courtney, and C. A. Hall, "Radioactive Tracers Cast New Light on Fuel Distribution," SAE Trans. Vol. 67, (1959), 619-639.

5. E. B. Rifkin and C. Walcutt, "A Basis for Understanding Antiknock Action," SAE Trans. Vol. 65, (1957), 552-566.

6. E. B. Rifkin, 'The Role of Physical Factors in Knock," 23rd A. P. I. Div. of Ref., Midyear Meeting, Los Angeles. (1938).

7. C. Walcutt and E. B. Rifkin, "Precombustion Reactions in an Engine, "Ind. Eng. Chem. Vol. 43, (1951), 2844-2849.

A New Tool for Combustion Research
A Quartz Piston Engine

Fred W. Bowditch
General Motors Research Laboratories

QUARTZ WINDOW engines have been used to observe combustion processes occurring in combustion chambers of operating engines at General Motors Research Laboratories since 1930. In the first such engine a long narrow window was mounted in the head of an "ell" head single-cylinder engine and drum camera photographs were taken of the combustion process occurring in the engine. It was with this engine that Withrow and Boyd[1]* were able to show that there was a flame front during a gasoline engine explosion and that it traversed the combustion chamber.

A subsequent window engine design permitted unrestricted views of the entire combustion chamber so that the first high-speed motion pictures of the combustion process could be taken. In this engine, for instance, Rassweiler and Withrow[2] showed the relationship between the mass rate of burning of the fuel-air mixture and the resulting pressure records. Ensuing changes in the window engine design, mainly in the method of holding the quartz in the head, permitted other combustion experiments in which Withrow and Bowditch[3] were able to define the character of the deposit ignition phenomenon.

The most recent model quartz window engine, used by Bowditch and Stebar[4] to identify the combustion phenomena occurring under hot starting conditions, has a compression ratio of 6.75:1 and is of "ell" head design. Since today's modern automotive engine is of overhead-valve design and has a compression ratio of around 9.5:1, it appeared appropriate that a new engine be considered for combustion research. Such an engine is described in the following sections.

Engine Design

Basic Engine Features - The basic idea for a window engine of high compression ratio and overhead-valve design is shown schematically in Fig. 1. As shown in the figure, the engine has a normal overhead-valve construction, an elongated piston, and a quartz piston crown. By providing a slot in the side of the piston and holding a canted mirror stationary inside the piston, it is then possible to view the combustion process by looking at the reflection of the combustion process in the mirror.

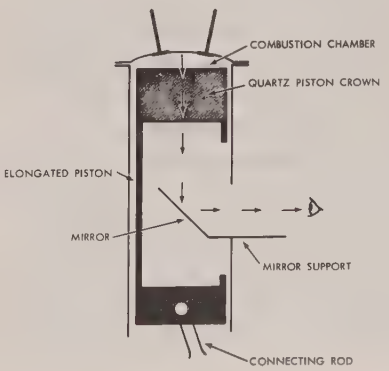

Fig. 1—Schematic view of engine operating principles

* Numbers in parentheses denote References at end of paper.

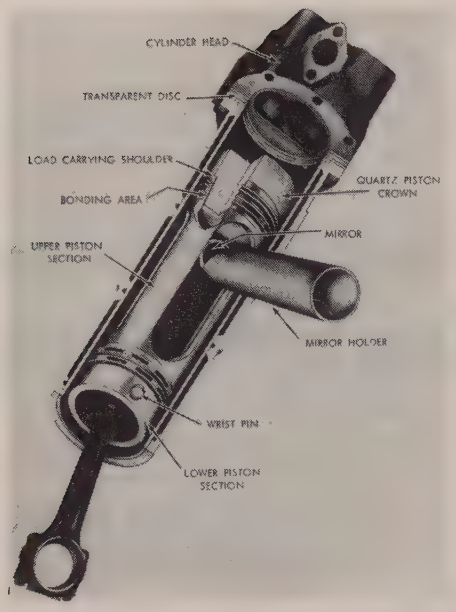

Fig. 2—Cutaway illustration of cylinder, piston, and head assembly

Two major problems involved in constructing an engine incorporating these ideas were: (1) finding a satisfactory means of attaching the quartz to the piston, and (2) finding or designing an engine to which the basic idea could be adapted. The problem of attaching the quartz to the piston appeared to be at least partially solved by previous experience with a quartz head engine which had shown that some epoxy resin adhesives adhered strongly to both quartz and metal even at moderately elevated temperatures.

Recently, a single-cylinder engine became available which appeared to offer the necessary features for the installation of an elongated, heavy piston. The engine was equipped with an overhead camshaft so that only lengthening of the vertical drive for the camshaft and the head support members was required to provide for a long cylinder liner. Also, the engine had two pistons for balancing purposes so that the additional weight of the elongated piston was readily taken care of by the addition of weight to the balance pistons. It was thus necessary to design only the piston assembly, cylinder, and mirror support,

A cutaway illustration of the final cylinder, piston, and head assembly is shown in Fig. 2. The unique feature of the engine is the construction of the piston. It is composed of three parts: a quartz crown, an upper piston section and a lower piston section.

The crown of the piston is made of clear fused quartz. Top and bottom surfaces of the quartz are flat and are polished to provide a transparent piston crown. The final dimensions of the quartz were determined by simultaneous consideration of optical limitations, bonding area requirements, requisite metal wall thickness, and quartz weight--all of which will be considered in appropriate succeeding sections.

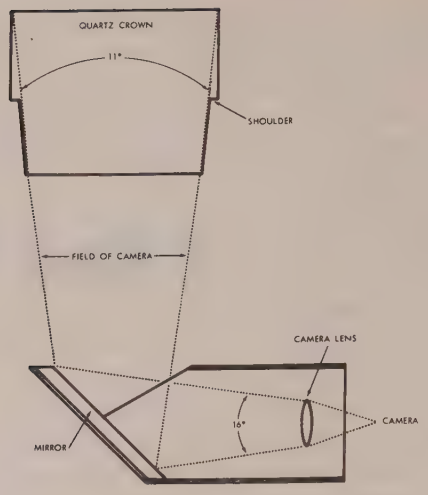

Fig. 3—Schematic view of optical system

The upper piston section serves three functions: (1) It provides support for the quartz crown; (2) it seals the combustion chamber from the mirror region by providing two compression rings and one oil control ring; (3) it provides the necessary room to permit the stationary mirror to be mounted inside the piston.

The third function is accomplished by making the upper piston section hollow with a slot in one side to permit the mirror to be held stationary while the piston reciprocates about it. The additional two slots in the upper piston section were made to decrease the weight of the piston assembly.

The lower piston section serves two functions: First, it supplies support for the wrist pin; second, it provides an oil seal between the mirror region and the crankcase by supplying oil control rings.

The transparent disc, shown in Fig. 2, sandwiched between the cylinder and the head was furnished so that external light could be admitted into the combustion chamber. This is often desirable when photographs of the combustion process are taken since proper external illumination will light up various portions of the combustion chamber providing location references for interpretation of the photographs. The construction of the disc will be discussed later.

The cylinder head is of standard overhead-valve design. Since a flat top is furnished on the quartz piston crown, the combustion chamber formed by the piston and cylinder head can be of standard automotive design and, therefore, compression ratio is limited only by the usual problems of valve and spark plug location. Various cylinder heads are available providing combustion chambers of from 4. 9:1 to 10. 7:1 compression ratios.

Design Factors -- Mechanical - The most difficult problem associated with the piston construction was centered around the quartz-to-metal seal region of the piston. This consisted of supplying sufficient compressive and tensile strength to the region and yet not obscuring the view of the combustion chamber.

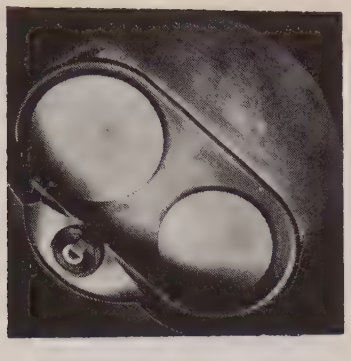

Fig. 4—Camera view of combustion chamber

Providing a means of transferring the gas load on the quartz to the upper piston section was reasonably simple because of the high compressive strength of fused quartz. Assuming a compressive strength of 190,000 psi for the quartz, a maximum gas pressure of 1000 psi, and a cylinder bore of 3.75 in., a surface of about 0.070 sq in. is required to carry the load. In the final design, a shoulder on the quartz 0.120 in. wide was supplied giving about 20 times the required area. This large an area was used because of the method used to cool the quartz and will be discussed in a subsequent section.

Providing the necessary tensile strength in the quartz-to-metal seal was a more difficult problem. Assuming an engine speed of 2000 rpm, a stroke of 3.44 in., a connecting rod length of 6.625, and a quartz weight of 2.5 lb, the maximum tensile force on the seal due to the momentum of the quartz crown is about 750 lb. Solution to this problem lay in finding a bonding material of sufficient tensile properties under moderately high temperatures.

From past experience, it had been found that Shell Chemical Co. Epon 828 provided the best properties for quartz-to-metal bonds. It was therefore chosen to bond the quartz crown to the upper piston section. This adhesive has tensile and shear strengths of 1000 psi at 300 F and about 100 psi at 400 F. For design purposes, it was assumed that the temperature of the bonding region would not exceed 400 F.

It had been found previously that it was advisable to separate the compressive and tensile load-carrying regions. This was true because when an adhesive was placed in the compressive load region, the adhesive apparently furnished an uneven load-carrying surface. This could be caused by the adhesive becoming pliable as temperatures increase. The uneven surface redistributes the compressive and tensile forces on the quartz, increases the tensile forces in a material which is quite weak in tensile strength, and quite often causes the quartz to break.

In order to separate the compressive and tensile load-car carrying regions as well as to furnish sufficient bonding area, a tapered portion was designed on the bottom of the quartz piston crown as shown in Fig. 2. As finally designed, the tapered section of the quartz provided 14.5 sq in of bonding surface and, therefore, a tensile strength of 1450 lb at 400 F to the quartz-to-metal bond, about a 100% safety factor.

The one oil and two compression rings on the upper piston section served not only to seal the combustion chamber from the mirror region but also to cool the bonding area. In order to furnish sufficient metal wall thickness to accommodate the rings in the bonding area, it was necessary either to supply a shoulder on the quartz equivalent to the metal wall thickness required (Fig. 2) or to use a smaller shoulder, taper the wall, and place the rings part way down the taper. As will be discussed later, the latter provision is the better one from optical considerations. Even with the tapered wall, however, the shoulder required to provide the requisite wall thickness was about 20 times greater than that required to accommodate the compressive load.

Design Factors--Optical - To be sure that the entire combustion chamber would be visible when flame photographs were to be taken, it was necessary to consider the optical angle of the field of view of the camera. The camera to be used for this purpose was an Eastman High-Speed Camera, Model II, equipped with an f 1.9, 25 mm focal length lens. This lens has a 16 deg optical angle of field of view. Due to the differences in the indexes of refraction of quartz and air, this angle becomes 11 deg in the quartz.

As shown in Fig. 3, this 11 deg angle then marks the maximum taper of the bottom section of the quartz which can be tolerated. If the taper were greater than 11 deg, the bottom edge of the tapered section would restrict the field of view of the camera.

The field of view of the camera also affects the height of the quartz above the shoulder. The minimum height is determined when the optical conditions shown schematically in Fig. 3 are fulfilled with the camera as close to the mirror as the field will permit and the piston is at top dead center. As shown, the inside diameter of the shoulder of the quartz must be the same as the diameter of the field of camera at the shoulder. Then, the minimum height is the distance above the shoulder where the diameters of the field of view and of the piston coincide.

In order to minimize the height of the quartz above the shoulder, the shoulder should be as small as possible. Hence, the reason why a smaller shoulder and tapered bonding region was preferred to a larger shoulder and cylindrical region.

Provision was made in the original design to admit external light into the combustion chamber. This was accomplished by making a Pyrex disc the same dimensions as the head gasket, but 1/4 in. thick, and including it as a sandwich between the cylinder and head. By directing four 110 volt photo spotlights at the disc, sufficient illumination could be obtained to light up the major features of the combustion chamber for photographic purposes.

Fig. 4 shows the camera view of the combustion chamber. The intake valve is in the upper left, the exhaust in the lower right, the spark plug in the lower left, and the squish, or close clearance area, in the upper right. The head shown forms a 10.7:1 compression ratio combustion chamber.

An exploded view of the actual piston, cylinder, and head assembly as originally designed is shown in Fig. 5. The mirror is supported in a 2 in. diameter tube which is held in position by the bracket shown on the cylinder. The piston assembly less connecting rod is about 10-3/4 in. long, and the bore of the cylinder is 3.75 in. in diameter.

Operational Difficulties--Oil Control - One of the greatest problems which developed after the engine was placed in operation was that of oil control in the cylinder. It was found that an excessive amount of oil reached the mirror region from around the valve guides, through the combustion chamber and past the rings on the upper piston section and from the crankcase around the oil ring on the lower piston section. The valve guide contribution was corrected by adding neoprene-teflon valve stem seals to both the intake and exhaust valves and guides.

The oil coming up from the crankcase by the oil ring on the lower piston section proved to be a more difficult problem. Apparently, the requirement that a bare minimum of oil enter the mirror region so that the mirror would not become coated with oil and the lack of blowby past the ring toward the crankcase intensified the problem. A second ring was added to the lower piston section and, after trying three piece chrome oil rings with little success, cast iron rings with expanders were tried and found to be reasonably successful in controlling the problem.

Operational Difficulties--Transparent Disc - While the Pyrex disc sandwiched between the cylinder and head provided adequate means for the admission of external light into the engine, it invariably fractured if the engine was run for more than a few minutes. Either the metallic faces of the head and cylinder distorted somewhat as engine temperatures increased or the thermal coefficient of expansion of the Pyrex was too great. Lapping the surfaces of the head and block and using both soft and hard gaskets did not alleviate the problem.

An attempt was made to improve the thermal properties of the disc material by using Vycor rather than Pyrex. Since the thermal coefficient of expansion is lower for Vycor than for Pyrex, it was anticipated that a disc made of Vycor might solve the problem. Such was not the case.

High temperature plastics were also used. However, discs made of these materials melted on the inner surface after a few minutes of engine operation and were, therefore, unsatisfactory even though they did not break.

A reasonably satisfactory solution to the problem has been a water-cooled, laminated quartz-metal disc illustrated in Fig. 6. The disc is so constructed that eight rectangular quartz plates about 1-1/2 in. wide and 3/16 in. thick are cemented in a water-cooled metallic matrix. This provides eight individual paths for the light to reach the combustion chamber. Because so much of the external illumination was cut off by the metallic portion of the laminated disc when photo spots were used, eight Sylvania DFA T-12 prefocused projection lamps were substituted for the photo spots to provide the external illumination.

Operation Difficulties--Viewing Combustion Process - The quartz piston crown has performed very well except that it has been difficult to prevent a few chips of quartz from being broken from the edge of the quartz. These chipped sections appear in the flame photographs as unreacted regions in the combustion chamber. Placing a small chamfer on the top edge of the quartz piston crown has partially alleviated the problem.

It was found that taking flame photographs was not always a convenient way of studying the combustion process

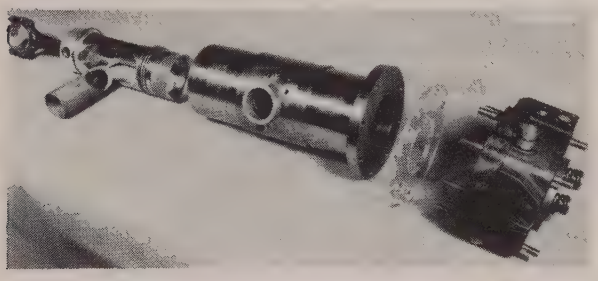

Fig. 5—Exploded view of first piston, cylinder, and head assembly

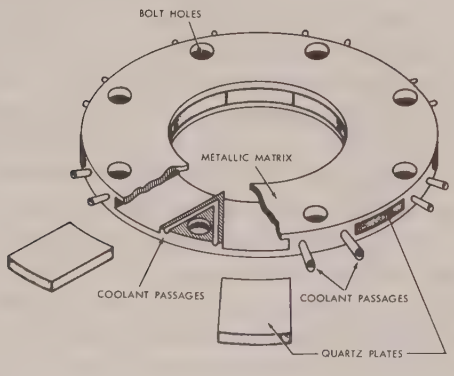

Fig. 6—Cutaway illustration of laminated quartz-metal disc

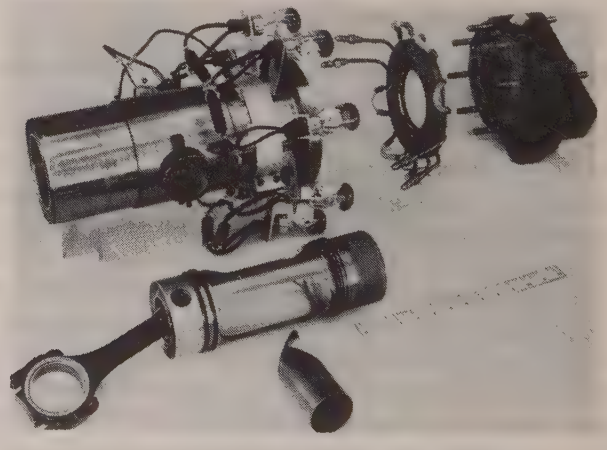

Fig. 7—Exploded view of present engine assembly

occurring in the engine and that a mechanical stroboscope would be a more appropriate means of accumulating data in some instances. Such an application of a mechanical stroboscope allows a viewer to see into the combustion chamber of the engine for a few crank angle degrees at the same preset time in every explosion. For instance, an average time of completion of combustion can be determined by noting the crank angle time at which the viewing time of the stroboscope is set in order that, on the average, the combustion process appears to have just been completed.

The stroboscope built for this purpose utilized two selsyn motors. One motor was attached to an extension of the camshaft of the engine and, therefore, rotated at camshaft speed. Provision was also made so that the housing of the motor could be rotated concentrically with the camshaft and clamped in any angular position.

The second selsyn motor, driven electrically by the first, rotated a 12 in. diameter disc in phase with the camshaft. The disc contained a narrow radial slot. By placing a cover around the disc and putting a 3/4 in. diameter hole in the cover which registered with the slot in the disc, it was possible to see through the rotating disc for about 3 crank angle deg of disc, hence the camshaft rotation.

When the stroboscope is to be used, the motor, disc, and cover assembly are mounted in place of the camera in such a position that the mirror in the engine is visible during the three degrees it is possible to see through the disc. By adjusting the angular position of the housing of the first selsyn motor, the time of viewing through the disc is changed. Thus, it is possible to view the combustion chamber repeatedly at any preset time in the engine cycle for three degrees of camshaft rotation.

Current Engine - An exploded view of the present piston, cylinder, and head assembly is shown in Fig. 7. The changes in construction shown include the laminated disc, the pre-focused projection lamps shown in position around the cylinder, and the additional oil ring on the lower piston section.

Fig. 8 shows an external view of the engine with the high-high-speed camera in position. The additional housing on top of the head contains the overhead camshaft and rocker arm assemblies. The jack screw above the camshaft housing provided a variable compression ratio feature to the original engine which is no longer available in the present engine because of the construction of the piston and mirror assembly.

Typical Problems for Study

To illustrate the nature of the combustion phenomena which may be studied using the quartz piston engine, a number of movies of normal explosions occurring under various engine operating conditions were taken as well as movies of explosions involving abnormal phenomena. The examples shown are not intended to be a complete list of the possible uses of the engine but rather are intended to show the general types of problems the engine is best suited for and the kinds of information which may be obtained.

Normal Explosions - Photographs from high-speed movies of a normal, full-throttle engine explosion which occurred at a compression ratio of 8.8:1 is shown in Fig. 9. The time in terms of crank angle degrees is shown under each photograph. Negative numbers denote crank angles before top center; positive numbers, degrees after top center.

The spark discharge is just visible in the second photograph at 14 deg btc in the lower left corner. The combustion process propagated from this source of ignition and entered the squish area at about 19 deg atc. Combustion was complete for the explosion shown by 37 deg atc. The darkened areas around the periphery of the combustion chamber in which combustion does not appear to occur are actually caused by chips in the quartz piston crown.

Since combustion was initiated at 15 deg btc and is com-

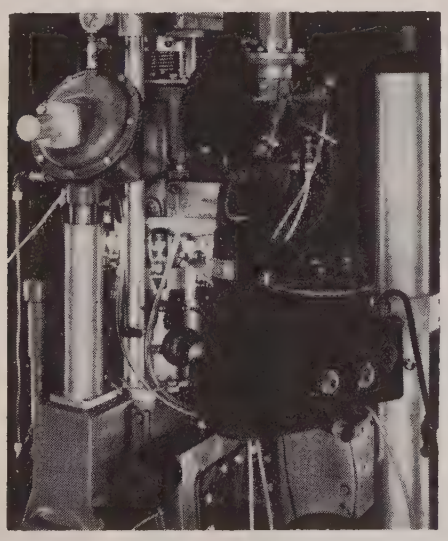

Fig. 8—External view of quartz piston engine

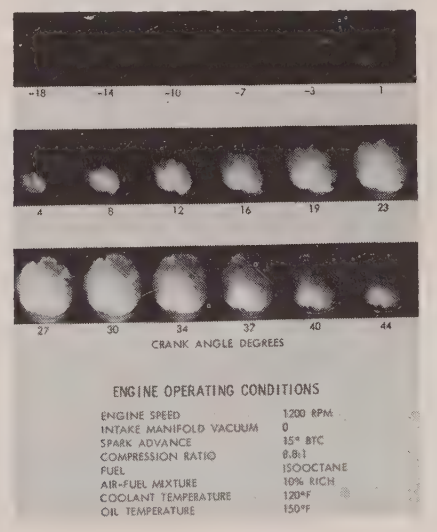

Fig. 9—Flame photographs of a normal, full throttle, average compression ratio, engine explosion

pleted by 37 deg atc, the entire combustion process required about 52 crank angle deg for completion. The apparent rate of flame travel was almost constant throughout the entire combustion process at approximately 75 ft/sec. By the time the combustion process entered the squish area, the piston had moved down about 0.13 in. and this added to the gasket thickness of 0.040 in. made a squish area thickness of about 0.17 in.

In an effort to show the effect of intake manifold vacuum on combustion, photographs of the combustion process occurring under approximately 30 mph road load conditions were attempted. Fig. 10 shows the result. So far as is known, these are the first photographs ever shown of an untreated explosion which occurred under road load engine conditions.

A comparison of the full-throttle (Fig. 9) and road load (Fig. 10) explosions shows two obvious differences. First, the road load explosion appears less intense than the full-throttle explosion. This difference is even greater than appears in the photographs since twice the lens opening was used in obtaining the photographs in Fig. 10 than was used in Fig. 9.

The second difference between the road load and full-throttle explosions is the length of time required to complete combustion. For the full-throttle condition, about 52 crank angle deg were required, whereas for the road load condition about 68 crank angle deg were required--about 30% more than the full-throttle condition. As was true for the full-throttle condition, the rate of flame travel for the road load condition appears nearly constant for the entire combustion process, amounting to approximately 55 ft/sec.

The effect of intake manifold vacuum on the time required for combustion is summarized by the curve in Fig. 11. Data for this curve were obtained using the mechanical stroboscope described previously. Engine operating conditions for the data were quite similar to those used when the combustion photographs shown previously were taken except that an engine speed of 1000 rpm, rather than 1200 rpm, was used.

In order to show some of the effects of compression ratio on the combustion process, flame photographs were taken of explosions occurring at a compression ratio of 10.7:1 and the same road load conditions used previously. Fig. 12 shows a characteristic explosion which occurred under these conditions. The major apparent difference between the lower (Fig. 10) and higher (Fig. 12) compression ratio explosions is that the explosion occurring at the lower compression ratio required about 10 crank angle deg longer to complete than did high ratio explosion.

Obviously, a comparison of a single explosion at each of two compression ratios provides meager data for illustrating the effect of compression ratio on the time required for combustion. A summary of this effect for propane at 16 in. of Hg intake manifold vacuum is shown by the curve in Fig. 13. Each point represents an average determination of time to complete combustion from flame photographs of at least 15 explosions at each compression ratio.

The curve shows that, under the stated conditions, doubling the compression ratio approximately halves the time required for combustion. Isooctane and ethylene react sim-

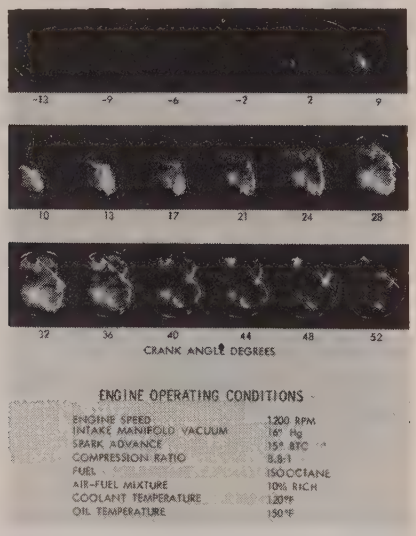

Fig. 10—Flame photographs of a normal, road load, average compression ratio, engine explosion

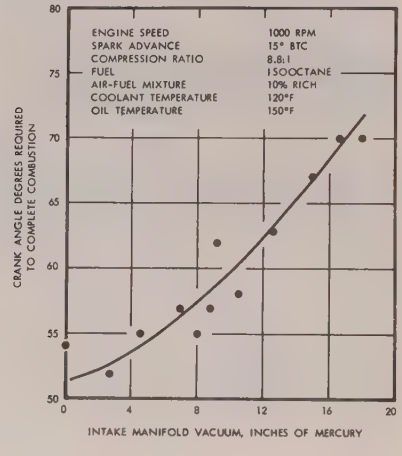

Fig. 11—The effect of intake manifold vacuum on the time required to complete combustion

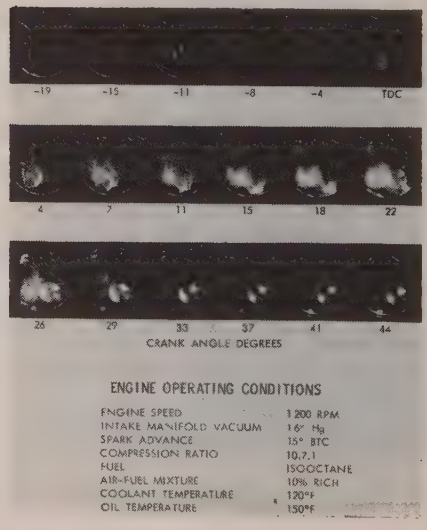

Fig. 12—Flame photographs of a normal, road load, high compression ratio, engine explosion

ilarly in this regard with ethylene showing a greater effect and isooctane a lesser effect than propane.

Abnormal Explosions - Thus far, only examples of the application of the quartz piston engine to studies of the characteristics of normal gasoline engine combustion processes have been shown. However, this equipment is also of great use in studies of abnormal combustion processes. An example of one abnormal combustion phenomenon, spark knock, is shown in Fig. 14.

Knock apparently occurred sometime between 20 and 23 deg atc preceded by an end gas autoignition phenomenon shown at 20 deg atc. This phenomenon appeared in about one-quarter of the photographs of knocking explosions occurring under these engine conditions. Because the "shutter" of the high-speed camera used to take these photographs is closed about 75% of the time, it is not possible to determine whether or not the end gas autoignition phenomenon always precedes knock under these operating conditions.

Fig. 15 illustrates hot spot ignition, another type of abnormal combustion process. Actually, the explosion shown in the figure shows a combination of hot spot ignition and knock. The sources of the two extraneous ignitions at 12 and 16 deg atc are not known. Since the engine had very little opportunity to collect deposits before these photographs were taken, it is likely that the ignitions were due to hot combustion chamber surfaces.

Concluding Remarks

An attempt has been made to show the new possibilities of a quartz piston engine as a means of investigating the gasoline engine combustion phenomena. This engine is an improvement over past window engines for such studies since they can now be carried out in an engine of current combustion chamber design and at high compression ratios. For the first time it is possible to study the combustion phenomena occurring under road load as well as full-throttle engine operating conditions. It is anticipated that this new engine will open a new avenue to gasoline engine combustion research.

Acknowledgments

The author would like to thank Dr. L. L. Withrow for his work in the development of a quartz piston engine, Messrs. Hacala and Leonard of the power development section, Engineering Staff, for assistance in the design of the engine, and the members of the fuels section of the fuels and lubricants department for assistance in preparation of the manuscript.

References

1. L. L. Withrow and T. A. Boyd, "Photographic Flame Studies in the Gasoline Engine," Ind. Eng. Chem., Vol. 23 (1939), 539.

2. G. M. Rassweiler and L. L. Withrow, "Motion Pictures of Engine Flames Correlated with Pressure Cards," SAE Trans., Vol. 42 (1938), 185.

3. L. L. Withrow and F. W. Bowditch, "Flame Photographs of Autoignition Induced by Combustion Chamber Deposits," SAE Trans., Vol. 6 (1952), 724.

4. F. W. Bowditch and R. F. Stebar, "Autoignition Associated with Hot Starting," SAE Trans., Vol. 66 (1958), 179.

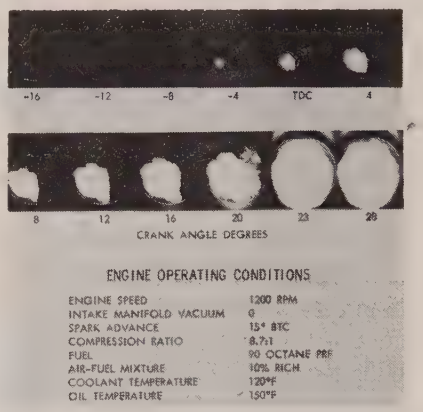

Fig. 14 — Flame photographs of a knocking engine explosion with standard spark plug location

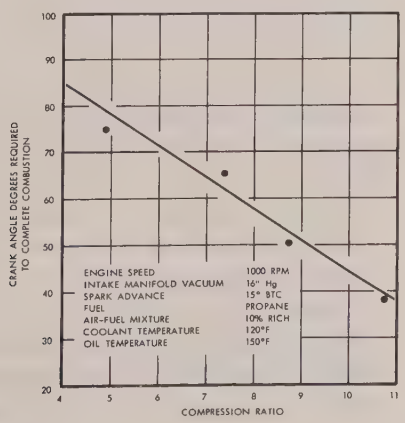

Fig. 13—The effect of compression ratio on the time required to complete combustion

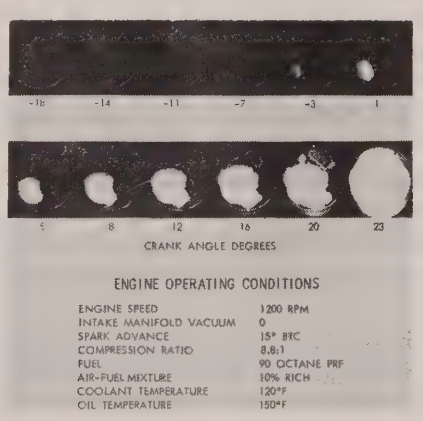

Fig. 15—Flame photographs of a hot spot ignited, knocking engine explosion

Table 1 - Solution Potential Differences Between Cast Iron and Several Aluminum Casting Alloys*

Alloy	Potential Difference, v
319-F	0.060
333-F	0.060
380-F	0.070
319-T71	0.110
319-T5	0.130
356-T6	0.170
C612	0.300

*Determined in solution of two volumes of high chloride (273 ppm C_1) tap water plus one volume of ethylene glycol at 165 F.

Corrosion Resistance of Aluminum

A. M. Montgomery
Aluminum Company of America

ALUMINUM CASTING alloys possess certain inherent characteristics which make them excellent materials of construction for the automotive engine. Probably the most important of these is a high strength-to-weight ratio. An aluminum engine component will weigh 50-60% of the same part in iron. It is frequently found that an even greater weight saving can be effected because of the ease of die casting aluminum with thin walls. Because weight saving in one part reduces the load in others, the weight of nonaluminum parts accordingly may be reduced. Aluminum alloys exhibit a thermal conductivity that is about twice that of cast iron. This excellent conductivity provides better heat dissipation which can result in longer valve life and lower octane number requirements. Aluminum alloys generally are more readily cast, machined, and fabricated than iron alloys. The use of aluminum can reduce shipping charges and investment in fabricating tools.

One characteristic of the aluminum casting alloys that is of special interest is good resistance to corrosion. Aluminum and aluminum alloys develop, on exposure to air, an inert oxide film that is responsible for this resistance to corrosion. The continuity and degree of protection afforded by this film will vary with the aluminum alloy involved and with the method of fabrication of a specific part. Pure aluminum has a more continuous and protective film than the alloys. Nevertheless, the resistance to corrosion of the least resistant aluminum casting alloy is generally better than that of competitive ferrous parts. An additional reason for this is the self-stopping nature of aluminum corrosion. Once corrosion has begun, corrosion product films develop that interfere with further attack so that the rate of corrosion decreases with time.

Corrosion Problems in Aluminum Engines

This paper is concerned with the liquid cooled engine and with cast aluminum alloy parts that are in direct contact with the coolant. Serious corrosion of components other than these has not been reported and is not anticipated. The information presented is the result of over 200 cyclic engine or road tests performed on aluminum cylinder heads mounted mostly on V-8 engines with cast iron blocks and with split radiators to compare two separate coolant solutions. In the earliest experiments it was determined that beaker tests were of little or no value in predicting service characteristics. Even continuous engine tests were abandoned in favor of cy-

Automobile Engine Components

clic tests to reproduce service conditions. The automotive engine is such a complex of corrosion factors including alloys, areas, temperatures, coolant composition, coolant flow, and vibration that the simplest, most reliable corrosion test is a service test of an engine.

The composite engine, combining aluminum and cast iron components in the same cooling system, presents more of a corrosion problem than either an all aluminum or an all cast iron engine. The composite engine provides the possibility of galvanic corrosion between adjacent aluminum and cast iron components of the cooling system. If excessive coolant flow or abnormal hydraulic conditions are present in a cooling system, erosion or cavitation of the aluminum may occur. In certain instances, improper gaskets may cause crevice corrosion. Stuck head studs have been encountered in the past. Improper cleaners, unsuitable corrosion inhibitors and unsafe antifreeze solutions can cause corrosion of aluminum. Finally, certain local waters are more corrosive than others to aluminum components. Each of these will be dealt with in detail.

Galvanic Corrosion

Present-day corrosion theory is based on an electrochemical explanation in which a cathode, an anode, and an electrolyte are essentials. All metals or alloys display characteristic solution potentials when immersed in an electrolyte, and in the cast of an aluminum-cast iron composite engine, the aluminum component is the more electronegative of the two. This relationship makes the aluminum the anode which is the element that is sacrificed during the corrosion process, and the case iron becomes the cathode. The farther apart the solution potentials of the anode and cathode, the greater the driving force causing galvanic corrosion between the two. The solution potential differences between cast iron and several aluminum casting alloys in a hot antifreeze solution are shown in Table 1.

Of the alloys listed, 319-F and 333-F are most compatible with cast iron because of the low solution potential difference. Alloy C612 on the other hand is the least compatible. These laboratory observations were confirmed by engine and road tests of cylinder heads of these alloys mounted on cast iron blocks. Fig. 1 shows the appearance of a coolant port in cylinder heads of 319, 356, and C612 alloys after two years of road service using a high chloride water-proprietary ethylene glycol antifreeze solution coolant. The respective depths of corrosion were 0.020, 0.034, and 0.120 in. reflecting the differences in solution potential. In the case of the 319 alloy, the copper content (Table 2) of the alloy is responsible for the more positive solution potential while the zinc content of C612 renders this alloy more negative. The copper must be in solid solution in order to be

effective in rendering the solution potential more positive. Thus, the as-cast (-F) condition is more desirable than the aged (-T5) condition in which the copper is largely precipitated from solid solution. Alloy 319 is a sand casting alloy, while 333 and 380 are used in permanent mold castings and die castings, respectively. All these alloys have suitable solution potentials and are recommended for composite engines.

The most severe corrosion encountered with aluminum cylinder heads mounted on cast iron blocks has been at the coolant ports where close proximity to cast iron has resulted in galvanic corrosion. This location has also been influenced by the sweeping action of coolant flow, particularly since the coolant ports in the cast iron block have frequently been of larger diameter than the corresponding ports in the cylinder heads. In this case, the coolant impinges on the aluminum surface, erodes any protective films and thus accelerates corrosion. The use of a gasket with metering ports at the interface can prevent direct impingement of the coolant stream. An alternative is the use of larger ports in the aluminum than in the iron. This, combined with an aluminum casting alloy containing copper, such as 319, 333, or 380, can effectively reduce corrosion at this point. These recommendations also hold for coolant system components other than cylinder heads that are attached to cast iron components, such as water pumps, elbows, and thermostat housings.

In considering galvanic corrosion, one naturally examines the possibility of heavy metal components other than the cast iron block as contributing to attack of aluminum. Brass temperature wells, copper or steel gaskets, brass ther-

Table 2 - Nominal Composition of Some Aluminum Casting Alloys

	Cu	Si	Mg	Zn
319	3.5	6.3		
333	3.8	9.0		
356		7.0	0.3	
380	3.5	9.0		
C612	0.5		0.35	6.5

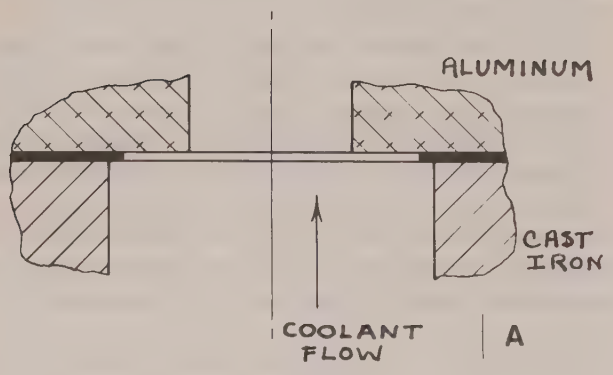

Fig. 1a — Cross-section sketch of aluminum cylinder head-cast iron block cooling port junction, magnified 3 times.

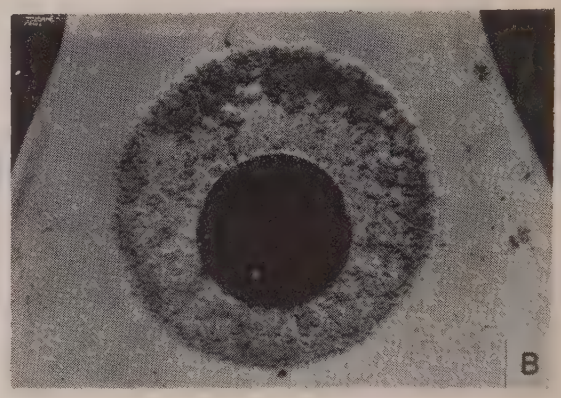

b — 319 alloy cylinder head port with 0.020 in. deep pitting

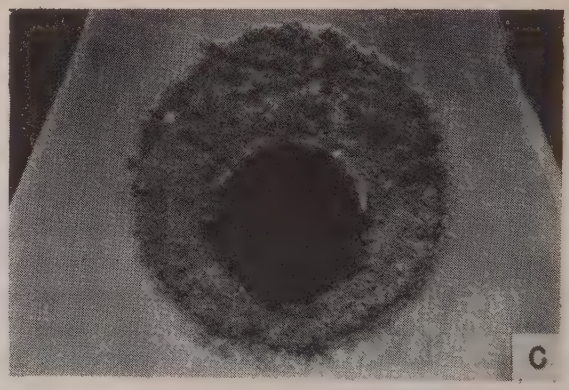

c — 356 alloy cylinder head port with 0.034 in. deep pitting

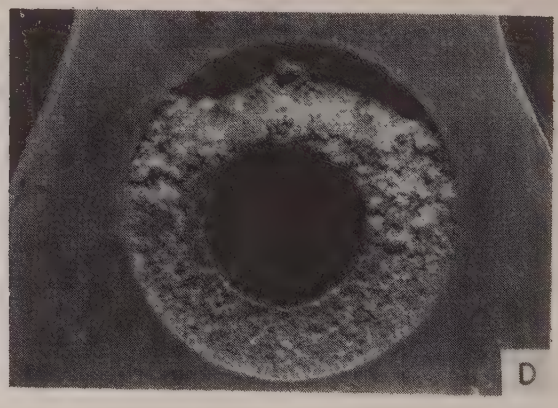

d — C612 alloy cylinder head port with 0.120 in. deep pitting

Fig. 1b-d — Galvanic corrosion of aluminum cylinder head ports adjacent to cast iron blocks after 2 years of service with 2:1 synthetic Royal Oak water-proprietary ethylene glycol coolant

mostats, and brass radiators could conceivably act as cathodic elements. However, solution potential difference is not the sole controlling factor in galvanic corrosion. In the case of the first three possibilities mentioned, the anode area to cathode area ratio is the controlling factor. Because the aluminum area is much larger than the heavy metal area, the latter is polarized to the same potential as the aluminum and relatively little corrosion current flows. In the case of the brass radiator, the indications are that it does not contribute directly to galvanic corrosion of the aluminum, probably because of the long path in the electrolyte over which the solution potential differences would have to operate.

EROSION AND CAVITATION

The aluminum casting alloys have adequate resistance to coolant erosion under normal circumstances. However, direct impingement of a high velocity stream on an aluminum surface should be prevented since suspended solids can scour away the normally protective oxide and corrosion product films and cause damage. Flow should be streamlined with a minimum of abrupt turns. Where such changes in flow cannot be eliminated, hard metal inserts have been used in some nonautomotive applications to minimize erosion. Figs 2-3 show the microstructural difference between

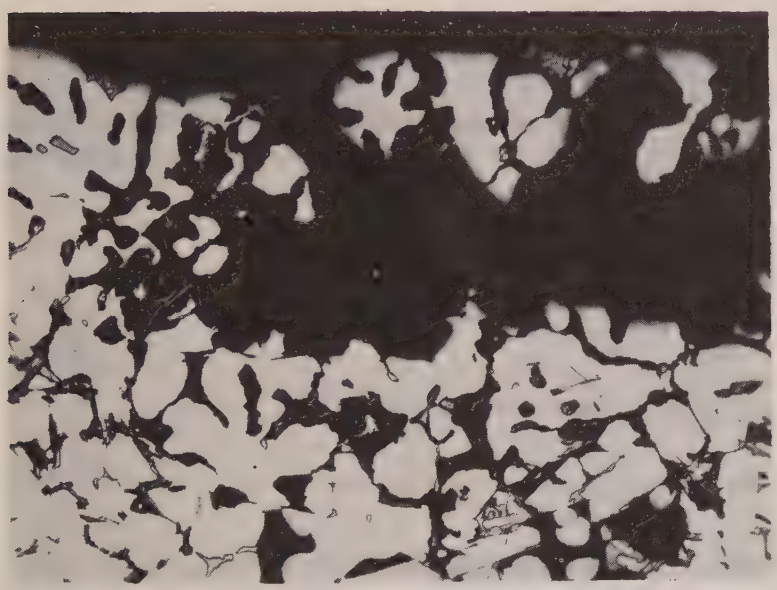

Fig. 2 — Cross-section of general corrosion in an aluminum-copper-silicon alloy coolant manifold. Note interdendrite nature of corrosion. Magnified 250 times, unetched

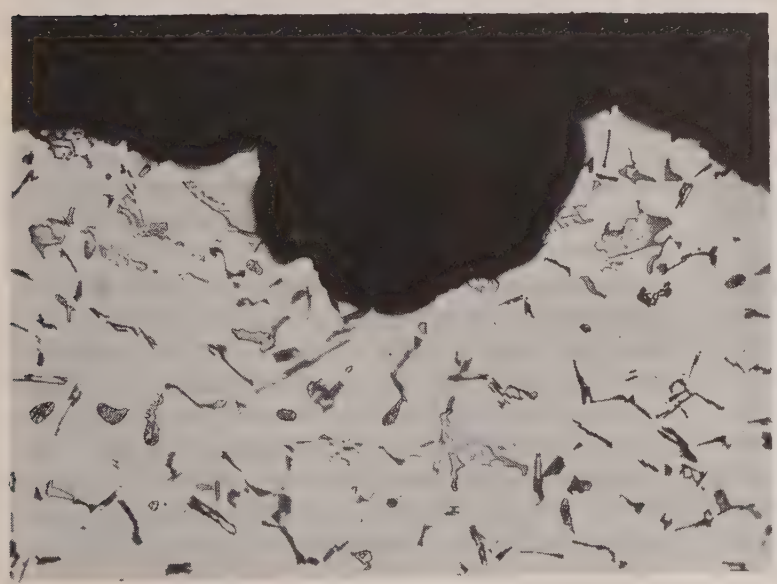

Fig. 3 — Cross-section of erosion pit in an aluminum-copper-silicon alloy coolant manifold. Note clean, open nature of pit. Magnified 250 times, unetched

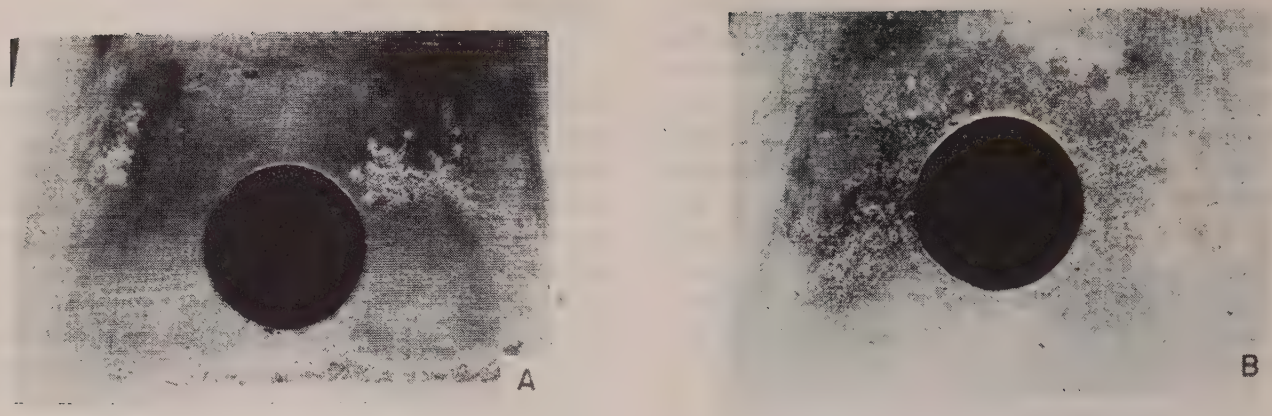

a — distilled water, 0.005 in. deep pitting

b — Lubbock, Texas water, 0.002 in. deep pitting

Fig. 4 — Galvanic corrosion of alloy 319-F aluminum cylinder cyclic (144 cycles) engine test with

general corrosion and erosion in an aluminum-copper-silicon alloy coolant manifold. It is doubtful that among the aluminum alloys, with the possible exception of the hypereutectic aluminum-silicon alloys, there is sufficient difference in resistance to erosion to warrant consideration of an alloy change to overcome this condition.

Cavitation has been encountered in several instances in aluminum diesel engine components. This phenomenon is said to be the result of the hammer-like collapse of voids in the coolant generated by mechanical vibration of the coolant passages. The exciting energy in one case was attributed to piston slap resulting from excessive piston clearance. Cast iron and hard chrome plate as well as aluminum were attacked. When the clearance was reduced the serious cavitation attack disappeared. Cavitation was also observed in some early experimental aluminum water pump housings which had a large impeller clearance. Reducing this clearance eliminated the cavitation. The point of this discussion is that cavitation can be a serious problem and that it can be encountered with other materials beside aluminum. The only really effective method of combatting cavitation is by design to eliminate the source of vibration responsible for the cavitation.

Coolant Composition

Using road tests of composite engines, consisting of aluminum cylinder heads and cast iron blocks, a wide variety of coolant compositions was investigated to determine their effect on the galvanic corrosion expected at the coolant ports previously mentioned. Distilled water produced a superficial attack, in the form of pits only 0.005 in. deep. Water from Lubbock, Texas, reported to be corrosive to aluminum, and synthetic Royal Oak, Michigan water, which was high in chloride content, were relatively harmless to aluminum in this test, producing light attack of only 0.002 and 0.012 in. depth, respectively.

However, when the synthetic Royal Oak water was combined with proprietary glycol or methanol antifreeze solutions, the attack became appreciable - 0.040 and 0.060 in., respectively (Fig. 4). It is believed that the increased attack in these cases was a result of the presence of inhibitors of iron corrosion in the antifreeze solutions. These changed the polarization characteristics of the system so that the difference in solution potential between aluminum and cast iron became more effective in promoting galvanic corrosion.

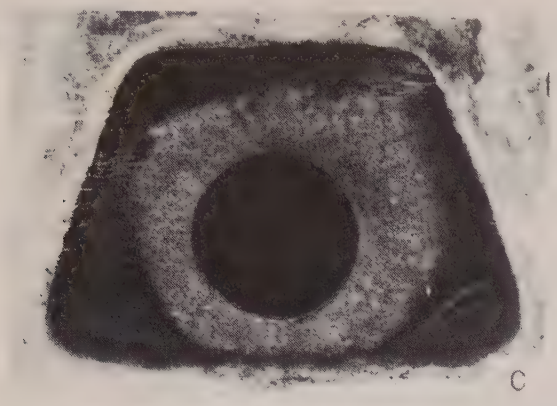

c — synthetic Royal Oak, Mich. water, 0.012 in. deep pitting

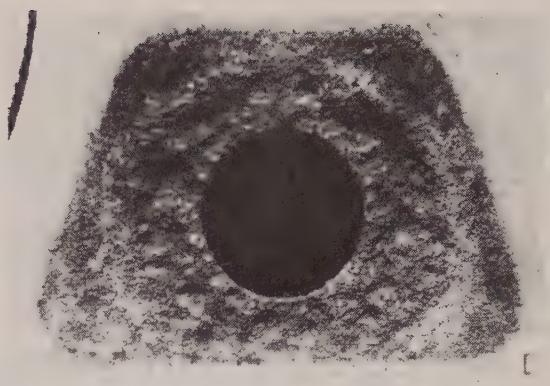

d — synthetic Royal Oak water, proprietary ethylene glycol 2:1 solution, 0.040 in. deep pitting

head coolant ports adjacent to cast iron blocks after 12 weeks various coolants. Magnified 3 times

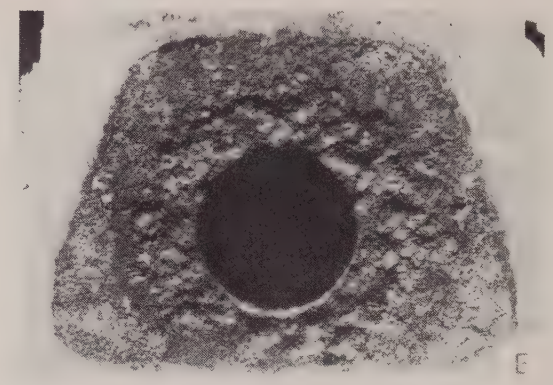

e — synthetic Royal Oak water, proprietary methanol 2:1 solution, 0.060 in. deep pitting

At present, the major antifreeze manufacturers are working diligently to develop inhibitor systems compatible with aluminum and iron and have had very encouraging results.

It should be emphasized that the adoption of an all-aluminum engine would greatly simplify the corrosion inhibitor problem because it would no longer be necessary to select an inhibitor compatible with dissimilar metals.

Gaskets

It is important that gasket materials be used that do not absorb water since poultice type corrosion may otherwise occur. Under these circumstances, aluminum in contact with absorbed water in the gasket reacts with oxygen dissolved in the water and locally depletes the oxygen. At an adjacent free surface, the water in the gasket is saturated with oxygen. This variation in oxygen produces a difference in solution potential which can cause corrosion.

Steel asbestos and even copper have been used successfully as head gaskets. Intimate contact with these heavy metals has been without serious consequence because of the large anode to cathode area ratios involved in the portions wetted by the coolant.

Studs

At one time, considerable difficulty was encountered in the removal of aluminum cylinder heads from cast iron blocks because of the buildup of galvanic corrosion products between steel head studs and the aluminum head. This difficulty is essentially eliminated by the provision of 1/16 in. clearance on the diameter of stud holes in the head over the diameter of the studs and by the present common use of cap bolts.

Cleaners, Inhibitors, and Anti-Freeze Solutions

Cleaning compounds used in cooling systems should be thoroughly flushed out after each use. After the cleaning operation is finished, the cooling system should be completely drained, refilled with fresh water, the engine run for 5 min and drained. This should be repeated again to insure the removal of the cleaning compounds which would be particularly corrosive to aluminum in a composite engine.

In the composite engine most of the inhibitors of iron corrosion used commercially will actively promote corrosion of an aluminum-iron couple. Engine tests of 14 commercial

soluble oils indicated that a satisfactorily inhibited coolant was provided by the introduction of 1% of a naphthenic base soluble oil. Chromates, dichromates, and nitrites should never be used in composite engines as they promote severe galvanic corrosion of aluminum.

As previously indicated, the leading antifreeze manufacturers have made considerable advances in improving their formulae in recent months so that it is to be expected that antifreeze solutions no longer will contribute to corrosion in composite engines. The virtual elimination of calcium chloride antifreeze solutions from the market has removed a serious corrosion hazard to iron as well as aluminum.

The use of high conductivity water, and particularly high chloride water, should be avoided in a composite engine since it tends to promote galvanic corrosion, particularly in the presence of antifreeze solutions. However, if the alloy and gasket designs outlined above are followed even the presence of corrosive coolant solutions should not cause corrosion problems. This was demonstrated by a service test of 12 vehicles at various locations throughout the country for periods up to 4-1/2 yrs. No control was exercised over the coolant solutions, but 319-F alloy cylinder heads and metering gaskets were used. Even though high chloride waters were employed in two instances, over 4 yr of service produced no appreciable corrosion.

All Aluminum Engine

In the interior passages of aluminum coolant system components, away from junctions with cast iron and the attendant possibility of galvanic corrosion, only superficial and inconsequential corrosion has been encountered. Thus, an aluminum-copper-silicon alloy cylinder head that had been in service for 29,000 miles showed an average depth of corrosion of 0.014 in. This has been true also of the all aluminum engines that have been examined, in spite of the fact that the majority of the components and engines have been cast from alloys with an appreciable copper content. It is general knowledge that copper is an alloying element that usually reduces the resistance to corrosion of the cast aluminum alloys. However, in automotive cooling system applications, alloys containing appreciable amounts of copper exhibit a uniform type of corrosion, free from isolated pits while copper free alloys may develop isolated attack. Despite this observation the copper free alloys should be entirely suitable for the all aluminum engine. In fact, thousands of all aluminum diesel engines of copper free 356 alloy have given years of service without corrosion difficulties.

A visit made recently to 18 European automotive engine manufacturing companies disclosed practically complete freedom from corrosion problems even though a variety of aluminum alloys including copper containing and copper free alloys have been used in the production of these engine components.

The automotive engine of the future will have one of the following combinations:

1. An iron cylinder block and an aluminum head.
2. An aluminum block and an iron head.
3. An aluminum block and head with wet iron sleeves.
4. An aluminum block and head with dry sleeves or wet aluminum sleeves.

In the case of (1) the recommendations for mixed systems should be observed and should provide protection.

The (2) construction should also be served by the same recommendations but would generally not be expected to be as severe as (1), since coolant flow is usually from the block to the head and impingement of aluminum surfaces should not be a problem.

The (3) combination might be expected to afford the greatest possibility for corrosion since the elements for both galvanic and crevice corrosion are present at the seat of the sleeve. In this case an aluminum alloy containing appreciable copper would be desirable to minimize potential differences. A sprayed or hot dipped aluminum coating of the cast iron or possibly galvanizing should eliminate corrosion of the cast iron as well as the possibility of galvanic corrosion.

As indicated previously, the (4) construction would be free of potential galvanic corrosion and essentially free from corrosion in general.

Summary

Aluminum automotive cooling system components may be expected to provide excellent resistance to corrosion even in mixed aluminum-iron systems provided that the described precautions are taken in alloy choice and design.

The all aluminum engine will be free of the corrosion problems caused by galvanic attack associated with the composite engine. Further, the use of the all aluminum engine should provide a system more resistant to general corrosion than present, all-iron or mixed systems. It is anticipated that any difficulties which may arise, as frequently happens in the case of new materials, can be overcome by design techniques.

Reference

M. W. Daugherty and R. F. Koenig, "Service Tests Solve Aluminum Cylinder Head Corrosion Problems." Paper presented at SAE Summer Meeting, June, 1949.

Automatic Highway and Driver Aid Developments

Harold M. Morrison, Albert F. Welch, and Eugene A. Hanysz
General Motors Corp.

DURING the past few years many investigators have proposed utilizing electronic aids, and completely automatically controlled vehicles as a means of improving safety and highway transportation efficiency. The discussion in this paper is centered about a completely automatic system, called Auto-Control, and two driver aids, called Electro-Lane and Hy-Com. Auto-Control is applicable to limited access highways and is presently embodied in a 1/40 scale model. Electro-Lane is a path error detector and Hy-Com is a low frequency induction radio communications system. Each of the latter aims to provide an aid to car drivers and with further development might be made generally applicable for use in the relatively near future. Fortunately, both of these systems would be complementary to a completely automatic system.

Auto-Control

General Design Concepts and Considerations - It is unnecessary here to discuss in great detail the reasons for devising automatic vehicle control systems. Briefly, these are based on

1. Reduced driver effort and improved comfort.
2. Potential safety improvement through elimination of driver error.
3. Increase in highway capacity by eliminating driver lags which influence the spacing of vehicles on our present roads.

In the development of the GMR Auto-Control System it was decided to concern ourselves only with operation of vehicles on a limited access highway in order to reduce the complexity of the control system. Even such a limited application could prove very practical and useful, when it is recognized that some 90% of inter-city passenger travel is accomplished in private cars. The transition problem is recognized in this design, and, therefore, the road model was built to accommodate both automatically controlled vehicles and conventional manual cars. Before discussing the details of operation of this highway model, its general physical arrangement will be reviewed.

GMR 1/40 Scale Model - Essential features of the Auto-Control System are embodied in a scale model oval track, approximately 20 x 30 ft over-all, representing a 4-lane divided highway. Distances and speeds are 1/40 scale. The tract has been arbitrarily divided into 16 5 ft blocks, simulating a stretch of highway 6/10 of a mile long. At 1/40 scale, each block represents 200 ft on an actual highway. Suitable wiring is embedded in the blocks to accomplish the various control functions. The general layout of the track is shown in Fig. 1. Only the two counterclockwise lanes

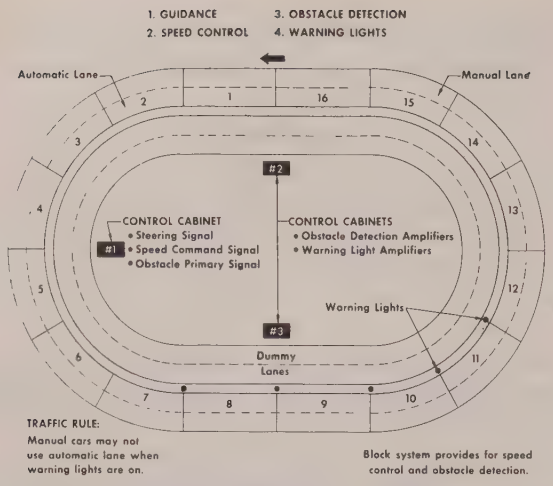

Fig. 1 — Auto-Control system features — 1/40 scale model

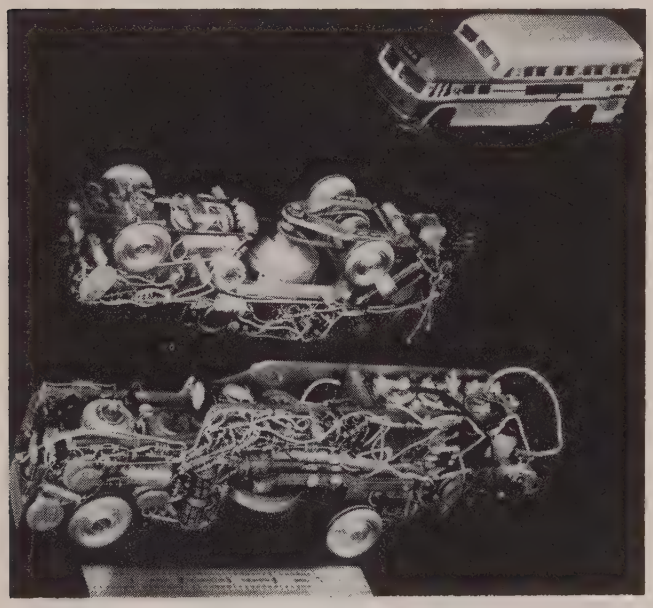

Fig. 2 — Model buses

are equipped for vehicle operation. The right hand lane has been designated as a manual lane, and the left hand lane is equipped with sensing and control wiring to provide completely automatic operation of scale model buses. The functions performed automatically consist of:

1. Providing guidance to maintain the proper vehicle path.
2. Detecting obstacles in the automatic control lane.
3. Regulating vehicle speed to prevent collision with other vehicles or obstacles in the automatic control lane.
4. Providing warning signal lights to control use of the automatic lane as a passing lane for manual cars.

There is clearly a wide variety of means of accomplishing the several functions just outlined. The particular means adopted for this automatic highway system are considered to be desirable compromises. From the standpoint of ease of transition from manual to automatic control, it would be desirable to have all of the special equipment contained in the car. If neither active nor inactive control equipment were required in the road, vehicles could operate under automatic control on our present road system. On the other hand, there appears to be many shortcomings in such an arrangement, particularly with respect to sensing all of the information required to regulate speed and direction from the vehicle itself. For this reason the control equipment has been divided between the car and the road. In addition, we have elected to utilize a block system for detection of obstacles and speed control rather than a continuous spacing control system for reasons of simplicity and reliability. In fact, a number of design choices involving compromises between reliability and operating efficiency were made in favor of reliability.

Model Vehicles - In order to provide space for the batteries and electric motors required to drive the vehicles, model buses, shown in Fig. 2, have been used. All of the transistorized electronics sufficient to sense the input signals and provide controls for the power systems of a full scale car are mounted on two insulating boards which also serve as a frame for the mechanism. An electric torque motor turns the front wheels to provide steering corrections. A silver-zinc battery mounted near the rear supplies power for both the electronics and the drive and steering motors. Additional description of the vehicle details accompanies discussion of the several functions.

Steering Control - Providing steering control signals from the road is relatively simple. Since the desired path of the car is the same as that of the road, only the position error of the car on the road must be sensed for guidance. The

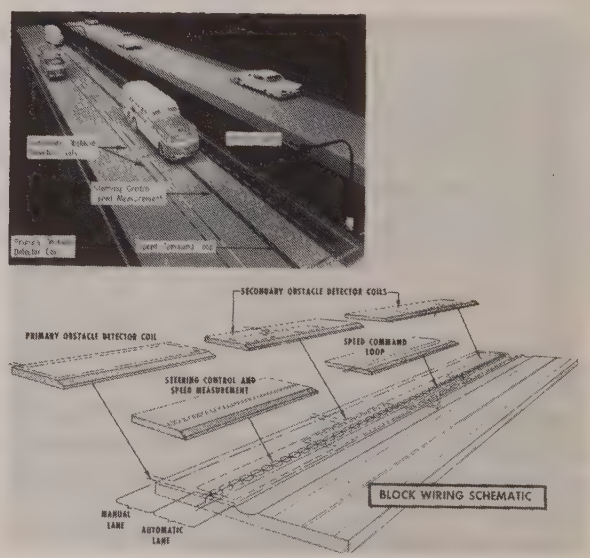

Fig. 3 — Layout of control wires in one block of automatic highway

required steering correction can then be determined and system stability assured by taking car response characteristics into account.

The steering control element in the model highway is in the form of a criss crossed wire that essentially forms two parallel wires embedded in pavement down the center of the lane. Alternating current of about 50 kc in the wire generates a magnetic field along its entire path. As pointed out in the following section, this same wire is used for speed sensing. The arrangement of all the control wiring in one block is shown in Fig. 3.

Two pickup coils mounted on the underside of the model car straddle the criss crossed wire. Changes in voltage between the two coils, as determined by their position relative to the cable, automatically adjust the steering mechanism to keep the car on course. Fig. 4 shows the various signal pickup coils mounted on the underside of the small model.

This technique is similar to the electromagnetic system demonstrated on a full-size car by GM Research Laboratories in February 1958. In that system, changes in voltage between the two pickup coils were fed into a small electronic analog computer which directed a servo system controlling the car's steering gear. Similar components within the car are envisioned in any future full scale version of the Auto-Control System.

Speed Control - Rather than permit each vehicle to select its own speed, it was decided that all cars under automatic control should operate at the road speed limit. This eliminates the many passing situations which otherwise develop, simplifies the automatic equipment, and also prevents delays in the automatic lane due to slow vehicles. Such expeditious handling of automatic traffic is one of the greatest potential virtues of automatic car control.

A scaled top speed of 60 mph was arbitrarily established for the scale vehicles running on the model road. At 1/40 scale, however, their actual top speed is only 1-1/2 mph. Provision is also made to automatically impose a 30 mph speed limit or to stop the cars completely under circumstances when 60 mph is unsafe. In a full scale application, any maximum speed could be selected and varied automatically to compensate for changes in vehicle performance depending on driving conditions, such as wet pavement, ice, or darkness.

Two basic requirements must be met to provide automatic speed control.

1. Precise measurement of the car's actual speed.
2. A speed command signal telling the car how fast it should be going.

Any differential between these two quantities can be used to initiate automatic adjustment of the car's speed through control of accelerator and brakes.

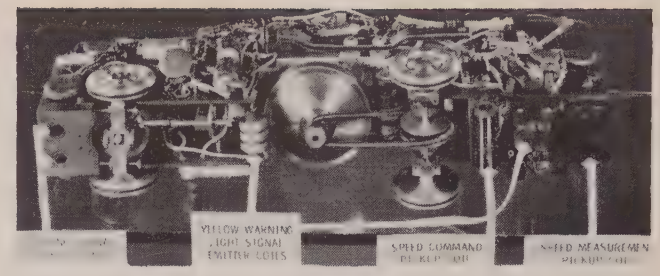

Fig. 4 — Signal pickup coils mounted on underside of model

The criss crossed wire is so installed that its two branches cross at equally spaced intervals. The voltage induced in the speed measurement pickup coil on the car (see Fig. 3) becomes zero midway between each crossing of the wire, thus providing a definite marker that can be sensed by a pickup coil and counted. The car measures its own speed precisely by a count of the number of voltage nulls passed per second. The cross spacing is selected so that 1 cycle/sec = 1 mile/hr both in the model and full scale road.

Another wire, parallel with and centered in the criss crossed wire, provides a speed command signal that is picked up by another coil on the car. This wire carries a signal of about 90 kc modulated by either of two low frequencies to provide the 60 mph and 30 mph speed command signals. For zero command speed, or "stop", the signal is interrupted. The command speed is determined by the obstacle detectors in adjacent blocks.

If the car's speed is over or under the command speed, an error signal is created proportional to the difference between the frequency of the command speed modulating signal and the number of voltage nulls per second from the criss crossed wire. The error signal regulates the current to a small electric motor in the model, causing the car's speed to become equal to the road command speed. In a full-size vehicle, this error signal could be used to control the accelerator and brake pedal combination.

The signal frequencies used in the model track are more or less arbitrary values for this particular small scale application. In a full scale highway, the actual frequencies used would be dependent upon the details of the electronic techniques used.

Obstacle Detection - The speed and acceleration of individual cars on an automatic highway must be dependent on the position and speed of other vehicles or obstacles on the same road. Therefore, some kind of sensing means is required for determining the relative position and/or speed of other vehicles and objects. It appears that the obstacle detection function must necessarily be part of the road equipment because of certain fundamental limitations in such car-based sensing apparatus as radar, ultrasonics, or infrared. (1)* The Auto-Control System provides for the electromag-

*Numbers in parentheses designate References at end of paper.

netic detection of vehicles and other metallic objects in the automatic lane only.

Embedded below the surface of each 5 ft block (representing 200 ft on an actual highway) are four obstacle detector coils (secondary) and a larger coil (primary) which encloses the secondary coils (see Fig. 3). The four secondary coils are connected in pairs. The two coils in each pair are connected in opposition and are alternately spaced with the two coils of the other pair. Metal objects located in an obstacle detector section have eddy currents induced by the alternating magnetic field produced by the obstacle detector primary coil which is energized with alternating current. This results in a disturbance of the magnetic field through the secondary coil over which the obstacle is located and the resulting unbalance in induced voltage provides a reliable indication of the obstacle whether stationary or moving. The time interval between detection at successive secondaries is also used to give an approximate indication of the speed of the vehicle. Its presence and speed regulate the command speed in following blocks in accord with the following rules.

A car traveling over 30 mph causes a 30 mph (half speed) speed command signal to exist in the first block to the rear and a 60 mph signal in the second block to the rear. A car traveling at 30 mph or below causes a zero speed command signal to exist in the first block to the rear and a 30 mph signal in the second block to the rear. Thus, if a car unexpectedly stopped in block 9, for example, the following car would be stopped in block 8, and the next car would be stopped in block 7. If another car were coming up from behind at 60 mph, its speed would be cut to 30 mph in block 5, and it would be stopped in block 6.

To avoid the need for a great deal of road intelligence (with resulting complication) it is proposed that the driver utilize manual control when fixed obstacles are encountered. The manual lane can be used for getting around the obstacles before resuming automatic operation. In fact, if an automatic vehicle is stopped for an obstacle, the automatic vehicle becomes an obstacle for itself, and is not allowed to continue automatically, even though the obstacle is removed. To return to automatic control, the driver must manually accelerate the car over 30 mph, and then flip the Auto-Control switch.

Manual Car Operation - In general, drivers of manually controlled cars would drive as usual keeping in the right hand lane. Their use of the left lane for passing is regulated in our model road by traffic signals which indicate the presence of an automatic car in the immediate vicinity. The warning lights are turned on by a 2 kc signal from a coil on the automatic car to the speed command coil in the road. These lights "travel" along with the car to warn manual cars in the vicinity that the automatic lane is in use. For example, when an automatic car enters block 8, it turns on the lights in blocks 7, 8, 9, and 10. When it enters block 9, light 7 goes off and light 11 comes on. In an actual installation, one light would be installed for each 200-ft block. The signal lights are used to provide smooth operation in the automatic lane but if a manual car entered against a signal it would be detected as an obstacle and cause following automatic cars to stop.

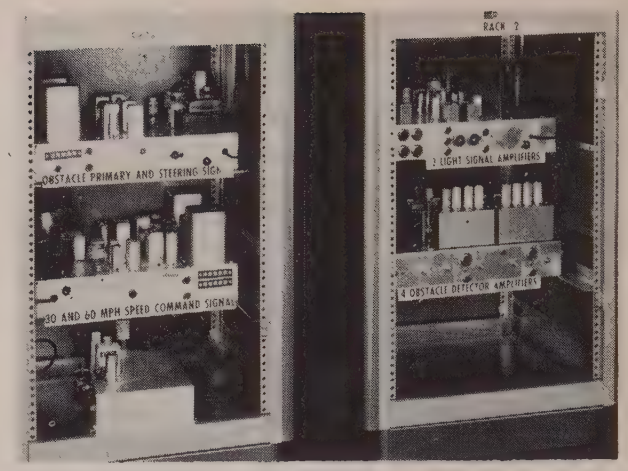
RACK 2
OBSTACLE PRIMARY AND STEERING SIGN
30 AND 60 MPH SPEED COMMAND SIGNALS
2 LIGHT SIGNAL AMPLIFIERS
4 OBSTACLE DETECTOR AMPLIFIERS

Fig. 5 — Electronic equipment racks

Road Electronics - The electronic equipment racks used with the road model are shown in Fig. 5. These are actually representive of functional full scale road equipment. No particular attention has been paid to reducing size in this prototype. The two cabinets shown provide all of the road electronics needed for 400 ft (2 blocks) of controlled road with the exception of the primary guidance signal. This signal can be supplied to many blocks by a single simple oscillator. In a full scale installation this equipment could be installed below grade and operated from batteries floated on a charger to increase reliability.

Reliability - Practical application of automatic vehicle control depends largely on the ability of engineers to produce both mechanical and electronic equipment with adequate reliability. Unless this is accomplished, attainment of improved safety will not be possible.

Redundancy has been used in the Auto-Control model to increase the steering signal reliability. In addition to the crossed guidance wire signal, the speed command wire may be used for this purpose. In a full scale installation, automatic switchover could occur in the event of loss of primary system signal. Protection has also been provided in event of speed command signal failure. Loss of command speed is equivalent to commanding zero speed and vehicles in the affected area stop until manual control is assumed by the driver.

Automatic Spacing and Road Capacity - The spacing control in the Auto-Control Model has been previously described in a general way. A more technical discussion of spacing control will demonstrate the importance of auto-

matic spacing in highway carrying capacity. In fact, an important motivation for automatic highway research is the increased highway capacity and accompanying economy of transportation that automation can theoretically afford. In a previous SAE Paper (2), Bidwell showed that with automatic control there exists a potential increase of approximately 100% in vehicle capacity for the speed range above 10 mph. Bidwell assumed the following in his computations:

1. A lead car travelling at velocity V_1, can decelerate at a maximum rate of 1 g.

2. A following car travelling at velocity, V_2, can decelerate at a maximum rate of 2/3 g.

3. The relative velocity and spacing between the two vehicles are know continuously by the rear car.

4. The response time in the following car is zero.

From practical considerations it appears that an automatic highway must be divided into blocks for determining the position of vehicles on the road. As a result, the following car must assume that a vehicle in a block ahead is at the near end of the block, and must be spaced from this block accordingly. To detect a velocity change in the lead car, the Auto-Control road measures the time required to cover the length of one secondary obstacle detector coil. Therefore, to the spacing (less the car length) computed by Bidwell in his Eq. 5 (2), one must add the length of the obstacle detector, L_B, which measures the lead car's velocity. To the above spacing one must add the length of the number of blocks the vehicle can at most occupy. The resultant spacing is that spacing need for computing the capacity of an automatic road using the Auto-Control spacing technique (Eq. 1). Since an automatic road cannot space vehicles as close as the ideal minimums described by Bidwell's paper, it is of interest to know just how close the vehicles can be spaced on an automatic road when the practical limitations of a block system are considered. To illustrate the influence of discrete blocks on spacing and vehicle capacity, the results of making the blocks 5, 20 or 80 ft long shall be explained. Eq. 1 shows the ideal minimum spacing from the rear of the block of the lead car to the rear of the block occupied by the following car as a continuous function of steady-state velocity. Eq. 2 gives the stepwise spacing of vehicles required by the block system. Eqs. 3 and 4 give the capacity resulting from the spacings given in Eqs. 1 and 2 respectively.

$$\Delta S = L_{OD} + N L_B + \frac{V_2^2}{2a_2}\left[1 - \frac{K_1}{K_2}\right] \qquad (1)$$

$$\lfloor S = ML_B \qquad (2)$$

$$C_{\Delta S} = \frac{V}{\Delta S} \qquad (3)$$

$$C_{\lfloor S} = \frac{V}{\lfloor S} \qquad (4)$$

where:

ΔS = Spacing from the rear of the car ahead to the rear of the following car (ft)

L_{OD} = Length of the obstacle detector coil (ft)

N = Next largest integer greater than the fraction $\frac{\text{Vehicle Length}}{L_B}$

L_B = Block length (ft)

V_2 = Velocity of the following car (ft/sec)

$K_1 = \frac{V_1^2}{V_2^2}$

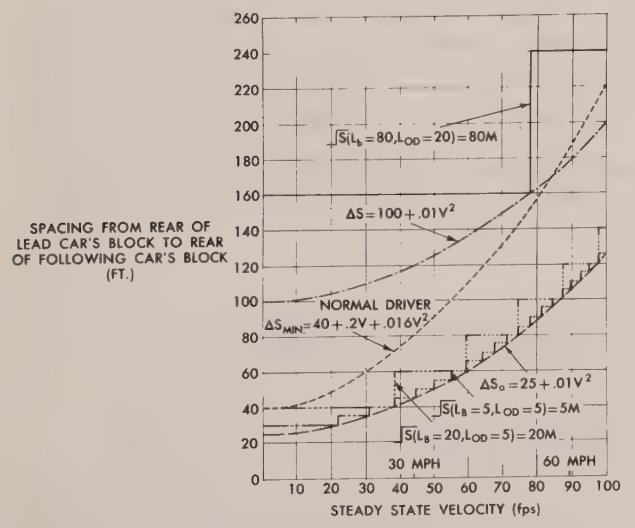

Fig. 6 — Plot of car spacing versus steady-state vehicle velocity for automatic block of 5, 20 and 80 ft

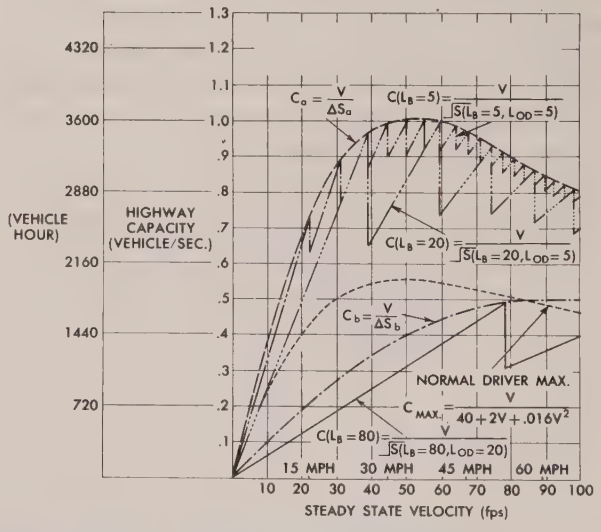

Fig. 7 — Plot of automatic road capacity versus steady-state vehicle velocity for blocks of 5, 20 and 80 ft

$K_2 = \frac{a_1}{a_2}$

$\lfloor\overline{S}$ = Stepwise spacing from the rear of the lead car's block to the rear of the following car's block (ft)

M = Next larger integer in the fraction $\frac{\Delta S}{L_B}$

$C_{\Delta S}$ = Capacity of the road for spacing as a continuous function of the steady-state velocity (car/sec)

C_S = Capacity of the road for spacing as a stepwise function of velocity (cars/sec)

V = Steady-state velocity of the two cars (ft/sec)

It is also assumed here that the response time of the vehicle's speed control system is zero. Thus, the spacing given by Eq. 2 yields the ideal minimum spacing obtained by any real speed control system of the Auto-Control type. It is also assumed that as soon as the lead vehicle decreases its speed by some small percentage, say 0.3% of the road full speed, the rear car is warned. The additional spacing caused by this small speed error for the first car shall be neglected.

Letting $K_1 = 1.0$, $K_2 = 1.6$, $a_2 = 18.2$ ft/sec^2 and a vehicle length just less than 20 ft, Figs. 6 and 7 are drawn using Eqs. (1, 3) and (2, 4) respectively. Notice that in Fig. 6 the continuous curve ΔS_a is approximated by $\lfloor\overline{S}(L_B = 5, L_{OD} = 5)$ and $\lfloor\overline{S}(L_B = 20, L_{OD} = 5)$, but on the high side. Also $\lfloor\overline{S}(L_B = 80, L_{OD} = 20)$ is a high side staircase approximation of ΔS_b. As the block length increases the spacing of the steps becomes larger.

For reference purposes the minimum spacing of the normal driver has been included from the previously mentioned SAE paper by Bidwell. Referring to the capacity curve (Fig. 7) the curves [$C(L_B = 5)$, $C(L_B = 20)$] and $C(L_B = 80)$ are low side, saw-toothed approximations to the curves C_a and C_b, respectively. As block length increases, the saw-toothed approximations deviate further from the continuous capacity curve, and the capacity of the road decreases. Although it is not quite apparent from the curves, Eqs. 1, 2, and 4 show that the capacity will also suffer somewhat from an increased obstacle detector coil length. The bright side of the picture comes when one compares the curves $C(L_B=5)$ and $C(L_B = 20)$ with the best capacity the normal driver can attain. Although these curves are lower than the continuous capacity curve, they still demonstrate that an automatic road can carry on the average 70% and 50% more traffic, respectively, than the normal driver.

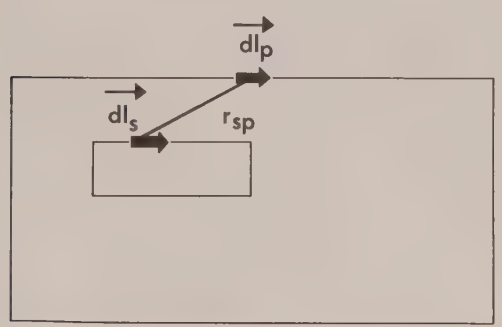

Fig. 8 — Schematic of voltage induced in secondary coil inside primary coil

Another important consideration in the construction cost of an automatic road is the amount of rear warning distance needed for automatic vehicles. The worst situation that would be encountered is that of an automatic vehicle that must stop for a stopped vehicle. The distance at which the car must be given its first warning is given by Eq. 5.

$$L_T = IL_B \tag{5}$$

where:

L_T = Length of the warning tail (ft)

I = Next higher integer above the fraction $\left\{\frac{(V^2max/2a\ min) + L_{OD}}{L_B}\right\}$

V_{max} = Maximum velocity for automatic vehicle operation (ft/sec)

a_{min} = Minimum allowable deceleration for automatic vehicles (ft/sec) (If a vehicle cannot decelerate at at least a_{min}, then the vehicle is not allowed on the automatic road)

L_B, L_T, L_{OD}, V_{max}, a_{min} then become the design parameters for the construction of an automatic highway and for the vehicles that travel the highway.

Table 1 relates construction costs, vehicle costs, and highway capacity to the automatic highway design parameters.

Notice that although construction costs decrease with increasing block lengths and obstacle detector coil length, there is a corresponding decrease in highway capacity. Also, although an increase in minimum deceleration will increase the capacity of the road, it may well cost the automatic car owner more. A compromise between the parameters involved can best be made when the particular application of the system is known.

Basic Theory of Obstacle Dectors - In general, the voltage induced in a secondary coil inside a primary coil may be given by Eq. 6 (3), with schematic representation in Fig. 8.

$$e_s = L_m \frac{di_p}{dt} = \frac{Mo}{4\pi} \oint\oint \frac{\overrightarrow{dl_p} \cdot \overrightarrow{dl_s}}{r_{ps}} \tag{6}$$

where:

e_s = Instantaneous voltage in secondary coil

$\frac{di_p}{dt}$ = First derivative of primary current with respect to time

L_M = Mutual inductance of the two coils

Mo = Permeability of free space

Table 1 - Inter-relationships of Construction Costs, Vehicle Costs, and Highway Capacity With The Automatic Highway Design Parameters

Dependent Variable	Dependent Variable Increase as These Parameters Increase	Dependent Variable Decrease as These Parameters Increase
Construction Costs	L_T, V_{max}	L_{OD}, L_B, a_{min}
Vehicle Costs		a_{min}, V_{max}
Highway Capacity	a_{min}	L_B, L_{OD}

dl_s = An infinitesimal direction vector on the secondary coil

dl_p = An infinitesimal direction vector on the primary coil

r_{ps} = Distance between the vectors $\overrightarrow{dl_s}$ and $\overrightarrow{dl_p}$

From the mathematical expressions the following simple conclusions may be drawn. The voltage induced in a single rectangular secondary coil, when placed so that its sides are parallel to a larger rectangular primary coil will increase as follows:

1. In direct proportion to
   a. the ratio of secondary to primary turns.
   b. the primary current amplitude.
   c. the frequency of the primary energy
   d. the permeability of the material surrounding the coils.
2. In nearly direct proportion to the factor by which all dimensions of both primary and secondary coils are increased.
3. When the area of the inside of the secondary coil encloses more of the area of the primary coil.

Also, it is basic to understand that the eddy currents induced in a flat sheet parallel to the plane of the secondary coil will attenuates the voltage pick-up by that coil. The attenuation is greater as:

1. Conductivity of the metal increases
2. Thickness of the metal increases
3. Area of the secondary coil covered by the metal increases
4. Distance between the metal and the coil decreases

Thus, when a pair of detector secondary coils become unbalanced, it is because the secondary in which the metal resides has less, rather than greater, voltage output. Moreover, the greatest possible unbalance voltage that may occur is the pickup voltage of one of the secondary coils. Indeed, there should be a voltage increase when a ferromagnetic material is placed in the secondary coils, but this effect has not been detectable in comparison to the much stronger eddy current effect for frequencies between 1 kc to 100 kc.

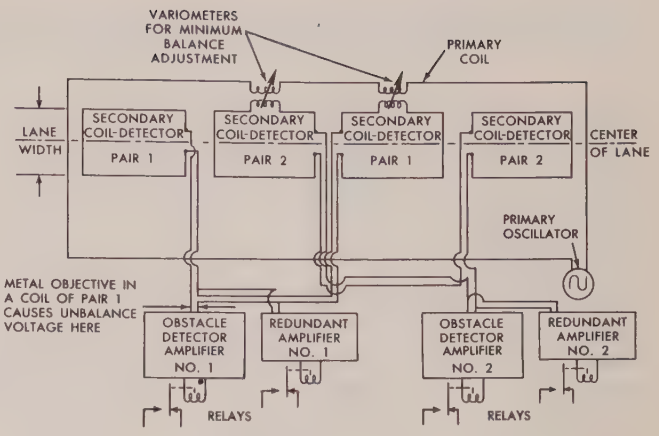

Fig. 9 — Obstacle detection system

Actual Design of Obstacle Detection System - Using the following basic knowledge, one can better design an obstacle detection system. The system contains five main components:

1. A primary oscillator, which feeds
2. A primary coil, which energizes
3. 2 secondary coils, the unbalance of which feeds
4. A high gain amplifier which actuates
5. A relay.

The system arrangement is shown in Fig. 9. The opposed secondary coils are balanced in output voltage by adjusting the variometer for a minimum. Although a multiple-turn secondary would allow one to decrease the primary power needed to obtain a given signal voltage in the secondary, the single turn of low resistance wire affords a simpler, more rugged installation. If the coils are made smaller in dimension, a multiturn coil may be prewound, and installation would be more practical. However, the smaller size would increase the number of detector components needed to cover a given area.

Part of the obstacle detector wire goes in the shoulder of the road. For a large coil, as is used in the model, a groove would have to be diamond cut in the concrete for the wire. The wire could then be covered with an epoxy resin or tar. If a road is to be black topped the wire could be laid on the concrete surface before the road is covered.

Since neither the primary coil nor the secondary coils are tuned, small changes in the circuit parameters will not affect the performance of the system. If the primary and secondary wires have been laid together where possible, a small separation of the two wires at one point would cause a detectable change in the balance of a pair of secondary coils. Thus, a finite separation of the primary and secondary wires improves the reliability of secondary balance.

Fail-Safe Features of Obstacle Detection System - Table

Table 2 - Obstacle Detector Failures and Results

Failure	Result
Loss of signal to primary coil (broken primary coil, bad oscillator, Edison power failure in one block).	Secondary coils in adjacent blocks become unbalanced.
Loss of secondary pickup (cut secondary).	Sufficient noise to trip high gain amplifier.
Amplifier No. 1 fails	Redundant amplifier No. 1 works
Redundant amplifier No. 1 fails	Amplifier No. 1 works
Amplifier No. 1 and Redundant amplifier No. 1 fail	System fails
Power failure to whole road	Speed command = 0 in all blocks

2 indicates the possible failures that might occur in the obstacle detection system and the accompanying results. Since the only unsafe failure that could occur would be that of a defective amplifier, two amplifiers in parallel are used with each pair of secondary coils to increase system reliability.

Obstacle Detection Experiments - Several experiments will be described to indicate how the obstacle detection equipment used in the model road may be improved in geometrical configuration. Although the experiments have been conducted on a 1/40 scale basis, the initial investigation leads the authors to believe that all dimensions of the model road coils may be scaled up by a constant factor and still obtain at least as high an unbalance signal from the secondaries. This could be accomplished with the same primary impedance, the same current in the primary, and an equivalent obstacle (one with all dimensions multiplied by the scale factor). In a test in which the scale of the coils was increased by a factor of four, the minimum unbalance voltages, for frequencies of 1, 10 and 40 kc also increased by roughly four. With the three constraints previously mentioned and the frequency at 10 kc, the unbalanced voltages were equal for the two different scales.

When tested with the primary at 3 milliwatts of power, the model obstacle detection system demonstrated the road coverage shown in Fig. 10. Notice the unbalance voltage read on an oscilloscope is quite low as the bus straddles the coils in the positions marked b, c, & d. However, as the bus enters the block at a or as the bus leaves the block at e the unbalance voltage is still appreciable. The poor coverage of the positions, b, c, and d may be rectified by overlapping the coils as is shown in Fig. 11. Thus, complete coverage of the road is accomplished.

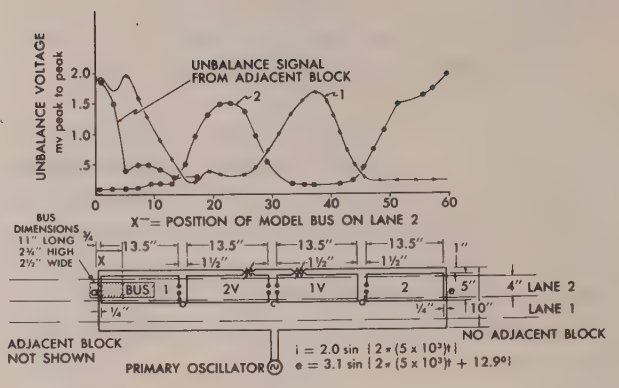
UNBALANCE VOLTAGE mv peak to peak
UNBALANCE SIGNAL FROM ADJACENT BLOCK
X = POSITION OF MODEL BUS ON LANE 2
BUS DIMENSIONS 1" LONG 2¾" HIGH 2½" WIDE
BUS
LANE 2
LANE 1
NO ADJACENT BLOCK
ADJACENT BLOCK NOT SHOWN
PRIMARY OSCILLATOR
i = 2.0 sin {2π (5 x 10³)t}
e = 3.1 sin {2π (5 x 10³)t + 12.9°}

Fig. 10 — Plot of unbalance signal voltage versus position of model bus for overlapped coils

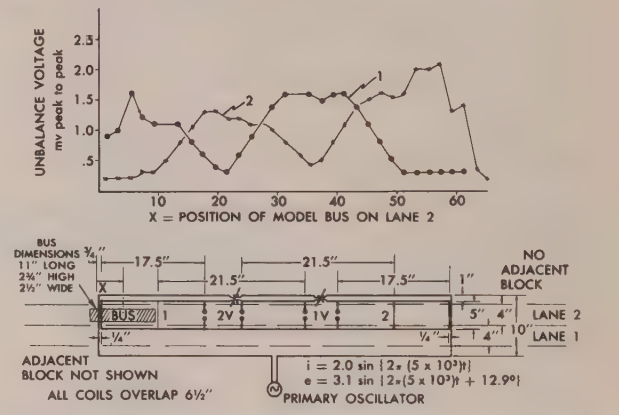
UNBALANCE VOLTAGE mv peak to peak
X = POSITION OF MODEL BUS ON LANE 2
BUS DIMENSIONS ¾" 1" LONG 2¾" HIGH 2½" WIDE
NO ADJACENT BLOCK
LANE 2
LANE 1
ADJACENT BLOCK NOT SHOWN
ALL COILS OVERLAP 6½"
PRIMARY OSCILLATOR
i = 2.0 sin {2π (5 x 10³)t}
e = 3.1 sin {2π (5 x 10³)t + 12.9°}

Fig. 11 — Plot of unbalance signal voltage versus position of model bus for model road coils

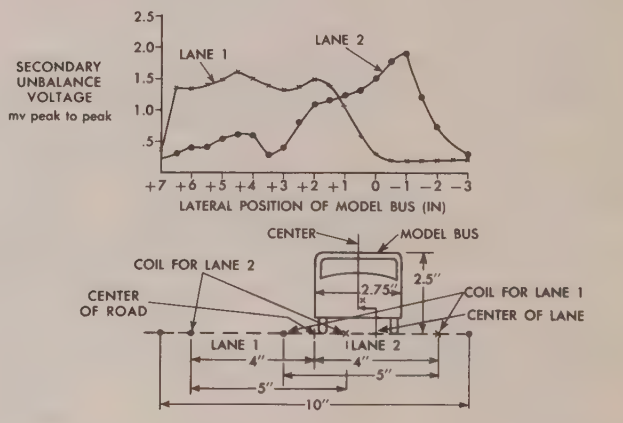

Fig. 12 — Plot of unbalanced voltage versus lateral position of bus

The balanced secondary method of metal detection also provides excellent lane definition. Fig. 12 shows the unbalance voltage as a function of the lateral position of the center of the model bus from the center of its own lane. Notice that, if the bus stays in its own lane, the input to the obstacle detector amplifier is only the minimum unbalance voltage. However, if the bus heads toward the adjacent lane, the voltage unbalance sharply increases. It is this unbalance that is amplified and then used to trip a relay for slowing a vehicle down in preceeding blocks. Fig. 11 shows a near optimum arrangement of coils, and Fig. 12 demonstrates that the adjacent manual lane might some day be automated as well, by just adding extra secondaries in the manual lane. There has been no interaction difficulties encountered between the overlapping secondaries.

Reliability Analysis - Since reliability of an automatic system is important, the following analysis was undertaken to develop a greater understanding of the problem. The automatic vehicle and road system that the reliability engineer would construct is different from the ordinary system in that it contains redundant components where the system might be weak. Thus, as an exercise, the reliability of the hypothetical vehicle and road system shown in Fig. 13 shall be computed. The individual reliability for each component or assembly in the road-car system is defined in Appendix A.

Reliability Algebra (4) - Let the reliability of component 1, 2, 3 . . . . n be given by R_1, R_2, R_3, ..., R_n, respectively. Let R_R be the resultant reliability of the components when combined together. The reliability of the components working in series is given by Eq. 7 and in parallel by Eq. 8.

$$R_{R_{series}} = (R_1)(R_2)(R_3) \ldots\ldots, R_n \qquad (7)$$

$$R_{R_{parallel}} = [1-(1-R_1)(1-R_2)(1-R_3) \ldots\ldots, (1-R_n)] \qquad (8)$$

Let components 1 and 2 now be connected through a switching mechanism of reliability $R_{(S1)}$ such that, when component 1 fails, 2 works. With such a switching arrangement, the minimum resultant reliability obtainable for the system $R_{R_{switch}}$ is given by Eq. 9.

$$\left[R_{R_{switch}} = 1 - (1-R_1)(1-R_{(S1)}\ R_2)\right] \qquad (9)$$

Great use has been made of this switching method in the design of a possible automatic system, shown in Fig. 13. Fig. 13 shows that almost all main line components have been paralleled with a redundant component that may be switched in to perform the component task. At the same time the switch commands the car to stop. Thus, whenever any one of the first line set of components has failed, the car is commanded to stop through a switching arrangement. The reliability of the switch may include the reliability of the device that detects the failure. Since the automatic system is a long series system of components, the first author felt the redundancy necessary.

The total reliability of safety of a system of μ cars trav-

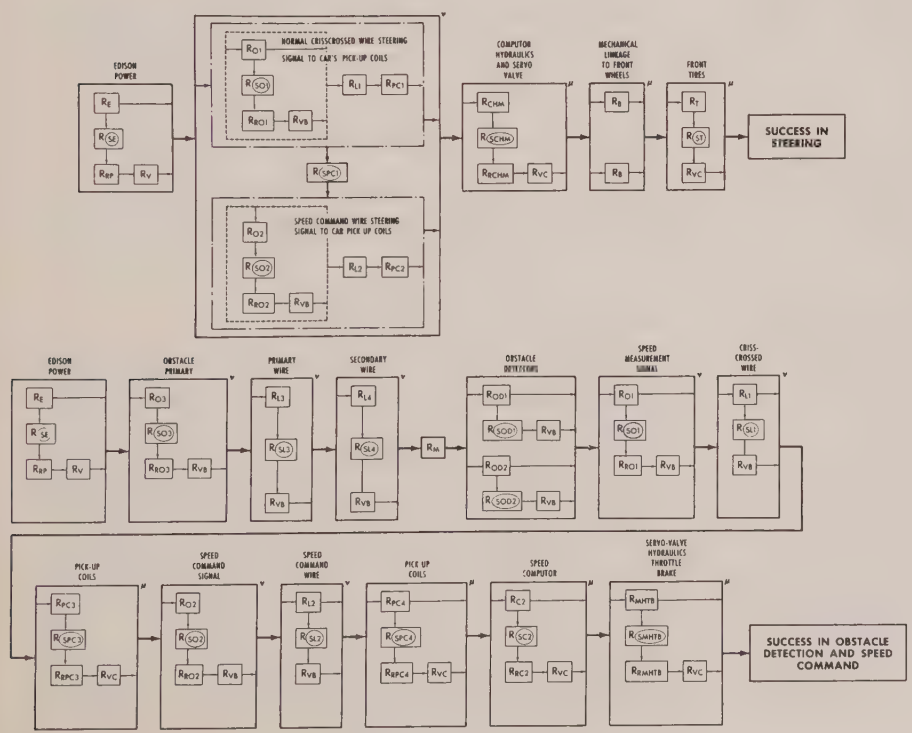

Fig. 13 — Hypothetical vehicle and road system

elling over ν blocks of road, without independently considering the influence of time, is given in Eq. 10.

$$R_{Safety} = R_{\substack{Safety \\ in\ Steering}} \; R_{\substack{Safety \\ in\ Obstacle\ Detection \\ and\ Speed\ Command}} \tag{10}$$

$$R_{\substack{Safety \\ in\ Steering}} = 1 - (1-R_E)(1-R_{(SE)} R_{RP} R_V)^{\nu} \times \tag{11}$$

$$\left\{1-\left[1-\left\{\left[1-(1-R_O)(1-R_{(SO1)} R_{RO1} R_V)\right] R_{L1} R_{PC1}^{\mu/\nu}\right\}\right]\times$$

$$\left[1 - R_{(SPC1)}\left\{\left[1 - (1-R_{O2})(1-R_{(SO2)} R_{RO2} R_V)\right] R_{L2} R_{PC2}^{\mu/\nu}\right\}\right]^{\nu}$$

$$\left\{1 - (1-R_{CHM})(1-R_{(SCHM)} R_{RCHM} R_V)\right\}^{\mu} \times$$

$$\left\{1 - (1-R_B)^2\right\}^{\mu} \times \left\{1 - (1-R_T)(1-R_{(ST)} R_V)\right\}^{\mu}$$

$$R_{\substack{Safety\ in \\ Obstable\ Detection \\ and\ Speed\ Command}} = \left\{1 - (1-R_E)(1-R_{(SE)} R_V R_{RP})\right\} \times$$

$$\left\{1 - [1-R_{O3}][1-R_{(SO3)} R_{RO3} R_V]\right\}^{\nu} \times \left\{1 - [1-R_{L3}][1-R_V]\right\}^{\nu} \times$$

$$\left\{1 - [1-R_{L4}][1-R_V]\right\} \times \left\{1 - [1-(1-[1-R_{OD1} R_V])]^{2Z}\right\}^{\nu}$$

$$\left\{1 - [1-R_{O1}][1-R_{(SO1)} R_{RO1} R_V]\right\}^{\nu} \times \left\{1 - [1-R_{L1}][1-R_{(SL1)} R_V]\right\}^{\nu} \times$$

$$\left\{1 - [1-R_{PC3}][1-R_{(SPC3)} R_{RPC3} R_V]\right\}^{\mu} \times \tag{12}$$

$$\left\{1 - [1-R_{O2}][1-R_{(SO2)} R_{RO2} R_V]\right\}^{\nu} \times$$

$$\left\{1 - [1-R_{L2}][1-R_{(SL2)} R_V]\right\}^{\nu} \times$$

$$\left\{1 - [1-R_{PC4}][1-R_{(SPC4)} R_{RPC4} R_V]\right\}^{\mu} \times$$

$$\left\{1 - [1-R_{C2}][1-R_{(SC2)} R_V]\right\}^{\mu} \times$$

$$\left\{1 - [1-R_{MHTB}][1-R_{(SMHTB)} R_{RMHTB} R_V]\right\}^{\mu}$$

The component reliabilities are, in general, functions of μ, ν, t the number of cars, the number of blocks, and time, respectively. To process μ cars over ν blocks (without any failures) involves a total elapsed time for the road components and car components $T_{Road}(\mu, \nu)$ and $T_{Per\ Car}(\nu)$, respectively. Each particular component i will be subjected to some average stress, $\bar{S}_i$, at some average rate of stressing, $\bar{P}_i$, for as many stress cycles $N_i(\mu, \nu)$ as can be completed in the elapsed time, $T_{Road}(\mu, \nu)$, for the road components, and $T_{Per\ Car}(\nu)$ for road the car components. Thus, when we say that components of type i has reliability $1-10^{\alpha}$, it is assumed that, if 10^{α} such components of types i are each tested for $N_i(\mu, \nu)$ cycles at $\bar{S}_i$ stress, there will be one failure. $N_i(\mu, \nu)$ is the success number.

The reliability distributions for components are not known. Thus, a considerable amount of data must be collected, as described above, before true evaluation of system reliability can be made. However, as an indication of trend, it would be instructive to make the crude assumption that the reliabilities of all components are equal to $(1-\epsilon)$. ϵ is a small number, say between 0.1 and 0.0. Thus, the smaller ϵ, the higher is the reliability. Eq. 10 simplifies to Eq. 13. Also, since non-metal objects cannot be detected by the system, assume the reliability of an obstacle being metal to be 1.0.

$$R_{\substack{Safety \\ Total\ System}} = 1 - \epsilon^2\left[7 + 51\mu + 16\nu + \nu\left(\frac{\mu}{\nu}\right)^2\right] \tag{13}$$

It is also of interest to know how reliable travel will be on such an automatic road system. Since a driver will be stopped every time one of the first line set of components fails, the reliability of travel across the length of the automatic road is just the reliability of the first line set of components. The reliability of travel is given in Eq. 14 and in simplified form in Eq. 15.

$$R_{\substack{Travel \\ Cars\ Over \\ Blocks}} = R_{\substack{Travel \\ Steering}}(\nu, \mu) \; R_{\substack{Travel \\ Obstacle\ Detection \\ and\ Speed\ Command}}(\nu, \mu) \tag{14}$$

$$\left\{R_E R_{CHM}^{\mu} R_T^{\mu} R_{O1}^{\nu} R_{L1}^{\nu} R_{PC1}^{\mu/\nu} [1-(1-R_B)^2]^{\mu}\right\} \times$$

$$\left\{R_E R_{O3}^{\nu} R_{L3}^{\nu} R_M R_{L4}^{\nu}\left[1-(1-R_{OD1})^{2Z}\right]\right.$$

$$\left. R_{O1}^{\nu} R_{L1}^{\nu} R_{PC3}^{\mu} R_{O2}^{\nu} R_{L2}^{\nu} R_{PC4}^{\mu} R_e^{\mu} R_{MHTB}^{\mu}\right\}$$

$$R_{\substack{Travel \\ (\mu, \nu)}} = 1 - \left[2+11\mu+8\nu\right]\epsilon \tag{15}$$

The important difference between Eq. 13 and 15 is the power of the epsilon. The increased reliability caused by the additional ϵ factor in Eq. 13 is apparent in Table 3.

Eq. 16 gives the reliability of travel with no steps of one car over ν blocks of road, if all component reliabilities are assumed equal:

$$R_{\substack{Travel \\ (\mu=1,\ \nu) \\ No\ Stops}} = R^{T\nu} \tag{16}$$

Table 3 - Table of Reliabilities of Travel and Safety

ν = 25,000 Blocks, 20 ft in Length, $\cong$ 100 miles

(All Reliabilities at 50% Confidence Level)

Component Reliability	$1-10^{-4}$	$1-10^{-6}$	$1-10^{-7}$	$1-10^{-9}$
ϵ of Components	10^{-4}	10^{-6}	10^{-7}	10^{-9}
Reliability of travel with no stops per $16.X10^5$ cars ($16X10^6$ vehicle miles) Eq. 14	Near Zero*	Low*	$1-1.95X10^{-1}$	$1.195X10^{-3}$
Reliability of travel with no stops/car (100 vehicle miles) (τ = 10) Eq. 18	Low*	.7788	$1-2.5X10^{-2}$	$1-2.5X10^{-4}$
Reliability of travel with at most 1 stop/car (100 vehicle miles) (τ = 10) Eq. 19	Low*	$1-3.12X10^{-2}$	$1-3.12X10^{-4}$	$1-3.12X10^{-8}$
Reliability of Safety ($16.X10^6$ vehicle miles) Eq. 13	$1-1.02X10^{-1}$	$1-1.02X10^{-5}$	$1-1.02X10^{-7}$	$1-1.02X10^{-11}$
Average No. of stops/car (100 vehicle miles) (τ = 10) Eq. 21	25	$25X10^{-2}$	$25X10^{-3}$	$25X10^{-5}$

*These reliabilities have not been computed, since the simplified expressions break down.

where:

τ = number of components that may fail in a given block.

Eq. 17 gives the reliability of travel with at most one stop of one car over ν blocks of road if all component reliabilities are assumed equal.

$$R_{\substack{\text{Travel}\\ \text{at Most one}\\ \text{stop}}}(\mu=1,\ \nu) = R^{\tau\nu} + \tau\nu R^{\nu\tau-1}(1-R) \qquad (17)$$

Eqs. 16 and 17 become Eqs. 18 and 19, respectively, when simplified

$$R_{\substack{\text{Travel}\\ \text{no Stops}}}(\mu=1,\ \nu) = 1 - \tau\nu\epsilon \qquad (18)$$

$$R_{\substack{\text{Travel}\\ \text{at Most One Stop}}}(\mu=1,\ \nu) = 1 - \frac{\tau\nu}{2}(\tau\nu-1)\epsilon^2 \qquad (19)$$

Again the important difference to be observed between Eq. 18 and 19 is the power of epsilon. Notice this difference in Table 3. Lastly, the average number of stops per car is given by Eq. 20, which simplifies to Eq. 21 when the R_s' equal $(1-\epsilon)$

$$\text{Average No. of Stops/Car} = \sum_{i}^{\tau v} (1-R_i) \qquad (20)$$

$$\text{Average No. of Stops/Car} = \tau v \epsilon \qquad (21)$$

Thus, it becomes apparent that for component reliabilities as low as one failure in 10,000 the reliability of safety for the 16,000,000 vehicle miles is high, but the reliability of travel is low by comparison. If the component reliability is increased, the reliability of travel is increased, and the reliability of safety goes up much faster. Although the following table is only intended as a rough treatment of the reliability problem, an interesting comparison statistic to the reliability figures in Table 3 is the current reliability of 0.5 (at the 50% confidence level) that a driver will stay alive after approximately 16,000,000 vehicle miles. (5) To be sure, the reliability listed on line 6 of the table does not imply that the entire 16,000,000 vehicle miles were travelled. However, on the other hand, neither does it imply that when the system fails, the driver is killed. The reliability of safety is the reliability that all 160,000 vehicles will be safe regardless of the distance any individual car travels without interruption on a possible 100 mile trip.

The following statements can be made concerning reliability:

1. A high reliability of safety can be achieved by using enough redundant components.
2. If the system imposes a stop because one of the first line set of components has failed, a major difficulty will be the fairly frequent automatic stops the system causes.
3. The obstacle detection system cannot at present detect nonmetallic objects. This deficiency may prove the most severe reliability limitation.

Transition Problems - One of the most difficult problems with regard to automatic vehicle control is that associated with the transition from our present day manual system. This is a particularly difficult problem, as it is necessary to provide some of the control equipment in both the highway and the vehicle. It is clearly not practical to either produce vehicles with automatic control systems or to provide roads equipped for this type of operation unless the other is also available. For this reason, it is necessary for us to consider the steps which might be taken to finally arrive at a completely automatic system. Consideration of this problem has led to some fairly immediate possible steps in this direction. The following discussion will be concerned with two possible immediate uses for the guidance wire necessary in a completely automatic system.

Electro-Lane

It is likely that electronic highways will evolve gradually, and that many features of a fully automatic road will appear first as driver-aids. Electro-Lane is one such device that is immediately applicable to present day roads. This driver aid is a warning device that informs the driver that his vehicle is within a predetermined distance from the edge of the lane or of the road on which he is driving. The presentation to the driver is visual and/or aural and is intended to cause proper instinctive response. For example, a buzzer located on the left side in the passenger compartment would be actuated if the vehicle were too near the left edge of the road or lane. A buzzer on the right side would warn against straying toward the right. Or, a single 2-tone buzzer could be used for left-right discrimination. Electro-Lane appears to have the capability to reduce accidents caused by vehicles that drift out of their proper lanes or off the road because of driver inattention resulting from drowsiness, or distractions. In addition, the driver of a vehicle could use Electro-Lane as an aid in driving near the edge of the road at very low speeds during times of poor visibility. The device as discussed here is intended to be purely a driver aid and would not be necessary for the safe and normal operation of the vehicle.

Electro-Lane works this way (see Fig. 14): A straight wire is installed along each edge of the road when it is desired to warn against straying toward either road edge. If it is desired to sense the edges of a lane rather than the edges of a road on a multi-lane road, it is necessary to install a wire in the center of the lane. In the former case a wire can simply be buried in shallow earth at each road edge; in the latter case the wire must be installed in the concrete. This can be done during the construction of new roads or, in the case of an existing road, by cutting a narrow slot with a standard diamond-blade power saw. Also possible is a 3-wire system for a 2-lane road: one at each edge and one between lanes. The system operation is identical for all of these configurations.

The road wire carries a low frequency alternating current supplied by small oscillators buried at intervals along the road edge. The vehicle is equipped with a pair of electromagnetic, ferrite-cored sensing coils mounted on the front bumper. Each coil has a voltage induced in it that is directly proportional to the vehicle's deviation from the cen-

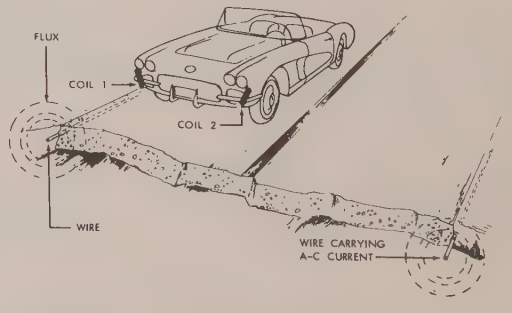

Fig. 14 — Schematic of Electro-Lane

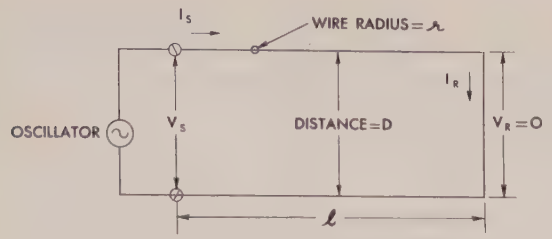

Fig. 15 — Single phase transmission line

ter of the road or lane. For the case in which a pair of road wires are used, one at each edge, the coil on either side is virtually unaffected by the opposite road wire, and the two sensing coils provide independent signals, one for each road edge. Operation in the case of a single road wire is similar in that the two sensing coils are mounted on the vehicle so that they straddle the lane-center road wire, and the signal in one increases while the signal in the other decreases for lateral vehicle motions. Hence, independent signals are again provided for each direction of deviation.

The sensing coils are wired as respective inputs of a 2-channel transistorized amplifier located in the passenger compartment. The output of each channel is rectified and compared with a mercury-cell reference voltage. When this voltage overrides the reference voltage (corresponding to a certain input level and hence a certain lateral position on the road) an alarm is actuated through a transistor switch to indicate approach to the respective road or lane edge.

Electro-Lane is attractive for present day usage because it is simple, rugged, reliable, inexpensive, and easy to install. The device could be offered as hang-on rental equipment on tollways and turnpikes. In a study extending from May 1953 to December 1958 on the Will Rogers and Turner Turnpikes of Oklahoma in which 759 accidents were reported, the sleepy driver accidents were severe, accounting for 42% of the fatal accidents. The high number of accidents attributed to vehicles wandering out of their proper road lanes is evidence that Electro-Lane has great potential as a safety device.

In addition, Electro-Lane would be useful in alerting a driver to any situation requiring special attention such as: an exit, toll gate, or very sharp curve. This would be accomplished by crisscrossing the road wire across the lane resulting in simultaneous actuation of both edge-indicators. While not providing specific information like Hy-Com (to be discussed), this may be a relatively inexpensive way to provide such warning and to increase the usefulness of Electro-Lane.

Electro Lane System Requirements - Road Equipment - The Electro-Lane road equipment consists of a road wire and low frequency oscillators buried at intervals along the roadside. Use of an audio-frequency (2000 cps in GM prototype) lessens the transmission line problem (discussed in detail below) if it is desired to control a rather long section of road with each oscillator. A transistorized oscillator with good frequency stability and relatively low power output is all that is required. For example, the road wire installed in the Check Road of GM Technical Center for automobile guidance is suitable for Electro-Lane usage. This wire is approximately 2.6 miles long, or 1.3 miles on a loop basis: the wire and its return in the two adjacent lanes. This line is supplied by a single oscillator with a total power dissipation in the wire of less than 3 w. Even lower power requirements are possible by using a larger road wire or by increasing the sensitivity of the vehicle receiving equipment. In an actual installation the roadside oscillators could operate from batteries floated on an ac power line.

The incompatible requirements of relatively high frequencies for high induced voltage in the sensing coils, and relatively low frequencies to avoid attenuation along the road wire requires the use of transmission line theory for a good compromise. Also involved is the selection of road length to be driven by each oscillator. Longer lengths provide efficient use of oscillators on the one hand, and the loss of larger parts of the system in the event of failure on the other. The goal is a flat line from a current standpoint; that is, it is desired to have the same rms value of ac current flowing in the line at every point along the road to provide a constant system sensitivity. The considerations in this regard for Electro-Lane are applicable to the design of a guidance wire for automatic car control. Fig. 15 shows a single phase ac transmission line with a shorted receiving end.

Where V_S and I_S are the phasor voltage and current at the sending end and V_R and I_R are the phasor voltage and current at the receiving end, the length of the line is ℓ and the distance between the two parallel conductors is D. The following is standard nomenclature:

z = Series impedance per unit length
y = Shunt admittance per unit length
$Z = z\ell$ Total series impedance (22)
$Y = y\ell$ Total shunt admittance
$Z_C = \sqrt{z/y}$ = Characteristic impedance
$r = \sqrt{yz}$ = Propagation constant

$$V_S = V_R \cosh \gamma\ell + I_R Z_C \sinh \gamma\ell \quad (23)$$

$$I_S = I_R \cosh \gamma\ell + V_R/Z_C \sinh \gamma\ell \quad (24)$$

For $V_R = 0$

$$I_S = I_R \cosh \gamma\ell \quad (25)$$

Eq. 25 shows that the sending current and receiving current ratio is the hyperbolic cosine of the complex argument $\gamma\ell$.

$\gamma\ell = \sqrt{yz}\ \ell$

If R, L, C are respectively the resistance, inductance, and capacitance per unit length of the line, then

$$\gamma\ell = \ell\sqrt{(R + jwL)\, jwC} \qquad \gamma\ell = w\ell\left(\sqrt{(LC)}\right)\sqrt{-1 + j\frac{R}{wL}} \tag{26}$$

The inductance and capacitance of a single phase line are given by

$$L = 1.482 \log \frac{D}{0.7788r} \quad \frac{mh}{\text{loop mile}} \tag{27}$$

$$C = \frac{0.0194}{\log \frac{D}{r}} \quad \frac{\mu f}{\text{mile}} \tag{28}$$

Therefore

$$LC = \sqrt{(1.482)\,10^{-3}\left(\log \frac{D}{r} + \log \frac{1}{0.7788}\right)\left(\frac{0.0194 \times 10^{-6}}{\log \frac{D}{r}}\right)}$$

$$= 10^{-6}\sqrt{28.8\left(1 + \frac{0.108}{\log \frac{D}{r}}\right)}$$

Since D>>r in usual cases, the second term under the radical contributes little and

$$\sqrt{LC} = 5.36 \times 10^{-6}$$

then Eq. 26 becomes

$$\gamma\ell = (33.7 \times 10^{-6})\, f\ell\sqrt{-1 + j\frac{R}{wL}} \tag{29}$$

Then for the case being considered

$$I_S = I_R \cosh\left(33.7 \times 10^{-6}\, f\ell\, \sqrt{-1 + j\frac{R}{wL}}\right) \tag{30}$$

Charts have been prepared (7) for the cosh $r\ell$. Since cosh $r\ell$ is a complex quantity, the charts present the real and imaginary parts separately. Frequency is set at 60 cps and the two values are plotted against line length with R/wL as a parameter. Inspection of Eq. 30 shows that since $f\ell$ occurs as a product, these charts can be used at other frequencies by simple rescaling. The charts show that for $f\ell$ = 6000 cycles/miles, and R/wL ≅ 0.4, Real [cosh $\gamma\ell$] = 0.98, imaginary Imag [cosh r] = 0.01.
Hence

$$\text{Cosh } \gamma\ell \cong 0.98 + j\,0.01 \tag{31}$$

Eq. 25 shows that the line would be flat within 2% for f = 2000 cps, $\ell \leq 3$ miles, and shorted end. This is the design

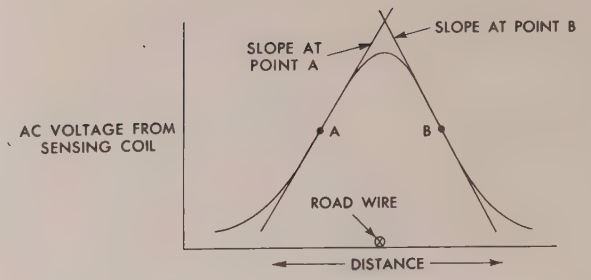

Fig. 16 — Sensing coil discriminator curve

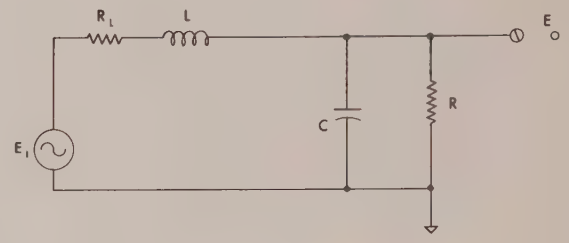

Fig. 17 — Sensing coil schematic

of the Prototype Electro-Lane.

If it were desired to use a single oscillator for more than 3 miles of road and to maintain a line flat within 2%, the frequency would have to be proportionately lowered to keep the $f\ell$ product essentially constant since R/wL is not a sensitive parameter. Hence, wire size can be determined as a compromise between power dissipation on the one hand and ease of installation and initial cost on the other, without primary regard for the value of R/wL.

The variation of resistance with frequency by skin effect has not been mentioned. Skin effect depends on frequency, conductor size, and permeability. For the cases discussed here, its value has been measured empirically.

Automobile Equipment Design - The vehicle portion of Electro-Lane is made up of three parts:

1. Sensing coils.
2. Amplifier.
3. Warning lights and/or buzzers.

The electromagnetic pickup coil-sensing coil, considered here, is rather straightforward. High-Q ferrite material is used as a core to obtain a high voltage output. Layer winding is permissible because of the low frequencies involved. The coil is tuned to the frequency of the road-wire current. Fig. 16 shows the general shape of the voltage versus position curve for such a coil.

The sensing coil is mounted on the vehicle relative to the wire so that the operation of interest occurs in the linear region near point A or point B.

Discussion of the dynamics of the pickup coil as a transducer is more important for automatic guidance work than for the Electro-Lane application. Nevertheless, a short dis-

cussion here is appropriate.

Fig. 17 is a schematic diagram of the pickup coil together with the input impedance R of the following device.

E_1 = induced emf

R_L = coil resistance

L = coil inductance

C = total capacity consisting of the tuning capacitor, stray capacity, and any input capacity of the following device.

The transfer function is

$$\frac{E_0}{E_1} = \frac{\frac{R}{R + R_L}}{\frac{RLC}{R + R_L} S^2 + \left(\frac{RRLC + L}{R + L_L}\right) S + 1} \tag{32}$$

The direct inverse of which is, of course, the impulse response of the coil. It is a good approximation that $R >> R_L$; hence, Eq. 32 becomes

$$\frac{E_0}{E_1} = \frac{1}{LCS^2 + \left(\frac{RR_LC + L}{R}\right) S + 1} \tag{33}$$

Hence, for this transducer

$$\text{Natural Frequency} = w_N = \sqrt{\frac{1}{LC}} \tag{34}$$

$$\text{Damping Ratio} = \xi = \frac{RR_LC + L}{2R \quad LC} \tag{35}$$

From which the time constant of the complex root pair is

$$\tau = \frac{2LCR}{RR_LC + L} \tag{36}$$

$$\text{Band Width} = \frac{\xi w_N}{\pi} \text{ for } \xi^2 << 1.0 \tag{37}$$

The relations given in Eqs. 33-37 describe the dynamics of a particular sensing coil when values are inserted for the parameters. Hence, the determination of the type of wire and the number of turns used is dependent in part on these considerations as well as on the output voltage desired for a certain road field strength.

Since Electro-Lane is an amplitude system, system drifts must be avoided. Also, the sensing coils are tuned and, therefore, have high output impedances. Hence, each amplifier channel must meet these requirements:

1. High input impedance.
2. Stable gain value.
3. Small size and ruggedness.

Transistors are chosen on the basis of item (3), and items (1) and (2) must be taken care of with proper circuitry design. One solution is as follows: A 2-stage transistorized buffer amplifier can be designed to have a gain value dependent only on resistor values in the circuitry and a high input impedance through use of positive feedback. The output is fed to an emitter follower then to a transformer for isolation. The transformer output is rectified and the filtered dc is compared with a mercury-cell reference level. When the signal level exceeds that of the reference by a small amount, the difference drives a 2-stage transistor switch into saturation, operating a relay which energizes a light and/or buzzer alarm as previously described. Thus, each channel of the 2-channel amplifier has five low power transistors, one reference cell, a small relay and associated components. It is possible to eliminate the need for a reference cell by utilizing a regulated portion of the 12 vdc system voltage as reference. The total amplifier package is quite small, and, in fact, could be made in miniature for large-scale production. It operates from vehicle system voltage (usually 12 vdc).

The lights and/or buzzers are standard components operating on vehicle system voltage.

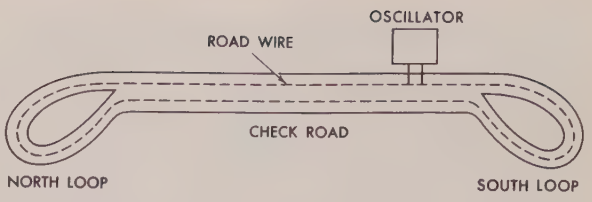

Fig. 18 — Wire installation in check road

Prototype Electro-Lane - A prototype Electro-Lane has been designed, built, and tested by GM Research Laboratories with full success. GM Technical Center Check Road is a 2-way test track over a mile in length as shown in Fig. 18.

A single wire loop has been installed in this track, one wire in the center of each of the adjacent lanes. This wire can be utilized for both automatic car control and for Electro-Lane. The approximate parameters of this line are

$$R_{2KC} = 67.0 \text{ ohms}$$

$$L = 7.94 \text{ mh.} \tag{38}$$

These are total values for the whole line and are empirical. Conductance is neglected and calculation shows that

$$C \cong 0.001 \text{ mfd./1000 ft} \tag{39}$$

in the parallel section of the line if a dielectric constant of unity is assumed. Hence, series tuning the line with

$$C_{Tune} = 0.085 \text{ mfd.} \tag{40}$$

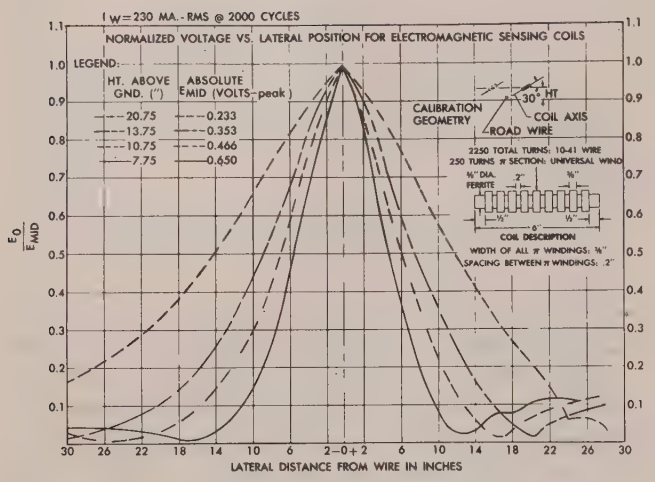

Fig. 19 — Sensing calibration curves

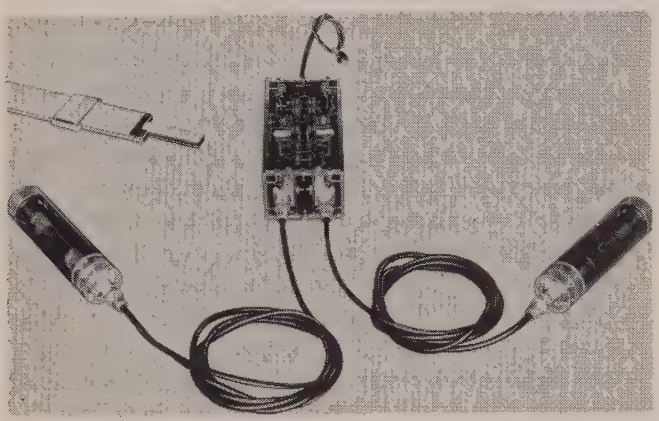

Fig. 20 — Sensing coils and dual-channel amplifier package

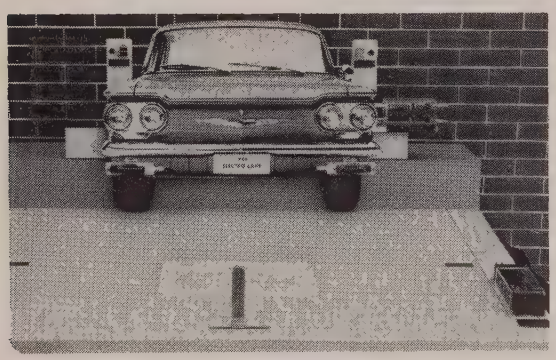

Fig. 21 — Table-top display of Electro-Lane

makes the line appear as a pure resistance of 67.1 Ω value at 2 kc. For Electro-Lane, approximately 200 ma of wire current is sufficient. Therefore

$$P_D = (0.200)^2 (67.0) = 2.68 \text{ watts} \qquad (41)$$

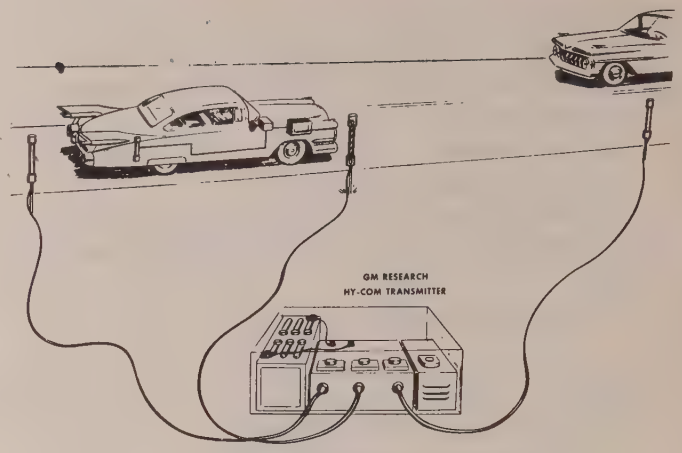

Fig. 22 — Basic elements of Hy-Com

The requirements for automatic car control are approximately the same.

The vehicle equipment of Electro-Lane is designed to fit the requirements as outlined above. Fig. 19 is a set of sensing calibration curves. Fig. 20 is a photograph of the sensing coils and the dual-channel amplifier package. It is important to note that this is a prototype model; no particular attention has been paid to size. A great reduction in size is surely possible. A table-top display of Electro-Lane is shown in Fig. 21.

Hy-Com

Another recent development, this one directed toward increasing the safety and comfort of automobile travel on the highway today, is Hy-Com. (8, 9) It is a system which brings into the vehicle a voice message concerning the road conditions ahead. Hy-Com ushers in a new concept in roadside-to-vehicle communications, offering great advantages over other means of disseminating information, particularly under conditions of darkness and inclement weather. It is complementary to road signs and other visual aids, and should supplement rather than replace them.

The basic elements of Hy-Com, Fig. 22, consist of a low powered transmitter driving a suitable antenna system which establishes an amplitude modulated magnetic induction field across the adjacent road, and a special receiver in each vehicle to detect the signal and convert it into an audible message. This system is proposed to operate in the 10-14 kc band which is a region conducive to induction transmission and virtually free of any other activity.

For emergency installations ferrite rod-type transmitting antennas such as illustrated are most suitable because they can be set up quickly. Portable transistorized transmitters can be powered by storage batteries since less than 25 w of power is required. They can be placed alongside the road. The message can be either taped on a message repeater, or

a patrolman can direct traffic using a live microphone. For a permanent installation, such as to announce a freeway exit distance, a single wire loop antenna would be more suitable. This type of antenna not only provides a more uniform message field but can be conveniently buried a foot beneath the shoulder surface. The electronics can be placed in a concrete bunker and can also be buried alongside the road. Power could be brought in from nearby power lines and modulation again effected by a tape repeater. Or, it can originate at a remote location and be brought in via existing telephone lines.

A block diagram of the transmitter developed by our laboratory is shown in Fig. 23. Other than the unusually low carrier frequency, it does not differ from transmitters used in other services. Modulation is effected at the lowest carrier level, the 9 kc oscillator delivering 8.5 microwatts of power to the modulator. The signal undergoes an additional 65 db amplification in the subsequent amplifier, driver, and output stages to provide the necessary power for the message field. Thermisters in the base biasing networks enable the all-germanium transistorized transmitter to be stabilized over the temperature range from -20 to +120 F.

Operation of the receiver is automatic once the ignition is turned on. Normally it would operate in conjunction with the standard car radio, sharing the transistorized power output circuit and speaker. If the standard broadcast radio is on it will be heard until such time as the vehicle enters a message field. Immediately the standard broadcast is muted and the Hy-Com message is heard. If the standard broadcast receiver is not on, then the Hy-Com receiver powers the output circuit so that the safety message can be heard. Upon passing out of the message field both receivers revert back to their initial conditions.

The design of the experimental Hy-Com receiver departs considerably from that of standard receiver design practice, as can be seen from the block diagram of Fig. 23. Selectivity is effected only at the antenna, and this is necessarily slight due to the low carrier frequency. A 15 kc low-pass amplifier with a maximum gain of 66 db follows, the gain being controlled over a dynamic range of 30 db by the AVC circuit. Hy-Com message audio is separated from the carrier by the 1.5 kc low-pass amplifier. The automatic muting and signal selection functions are attributed to the message control circuit. Stability of operation over the temperature range from -30 to +140 F is assured through the use of thermistors in the base circuits of the all transistor receiver.

The outstanding feature of Hy-Com, and what makes it so attractive and practical, is the use of a magnetic induction link between the transmitter and receiver, rather than radiation as in standard radio broadcasts. An induction field is easily contained and the extent of coverage can be defined with almost the same precision as painting the limits on the pavement. The obvious advantage is that the appropriate messages only are heard by passing motorists. Also, interference to other services, as well as between adjacent Hy-Com transmitters, is avoided. It is thus possible to operate all Hy-Coms on one and the same frequency channel. Reliability is thereby improved and greater economy achieved since only fixed tuned transmitters and receivers are necessary. The greatest advantage of single frequency operation, however, is that the receivers are always ready to deliver a Hy-Com message without the need to tune in.

Two examples of the application of Hy-Com are illustrated in Figs. 24 and 25. Although the weather and darkness renders the local speed limit sign practically illegible in the first of these figures the Hy-Com version of the identical message is received with instant clarity. The second figure illustrates a condition that prevails frequently on our highways: the driver's vision is obscured by the vehicle of a passing motorist or by one being passed. A Hy-Com installation would deliver the information in spite of the visual obstruction.

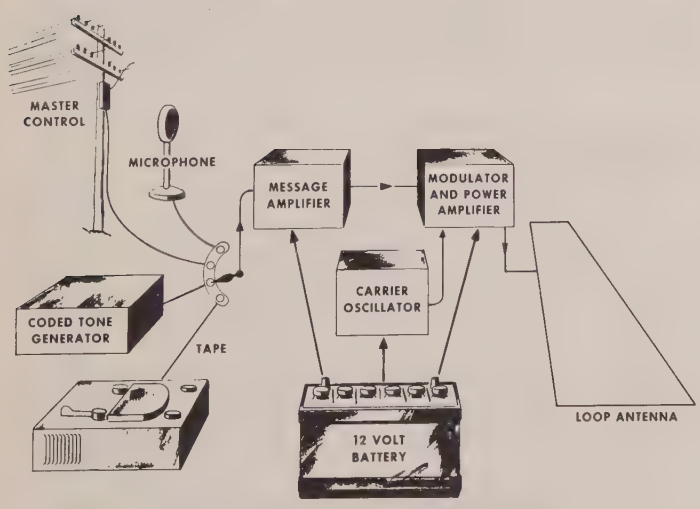

Fig. 23a — Hy-Com transmitter

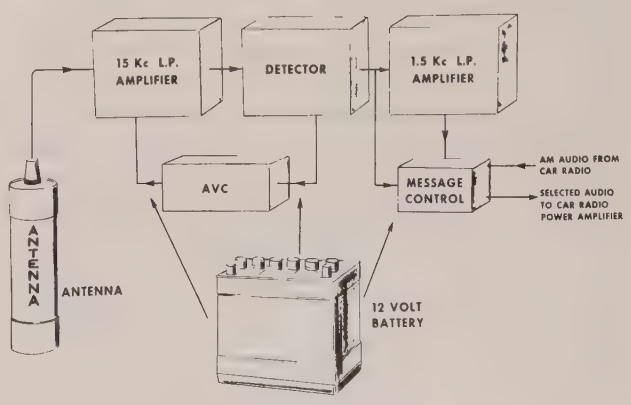

Fig. 23b — Hy-Com receiver

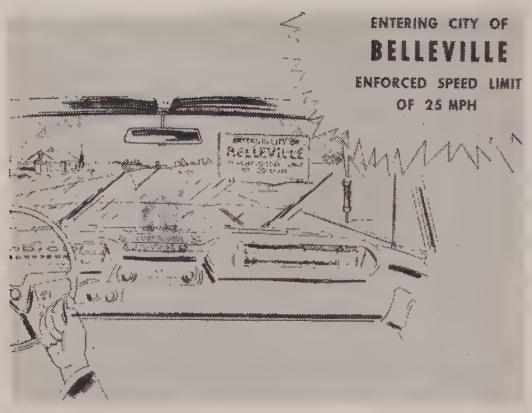

Fig. 24 — Application of Hy-Com

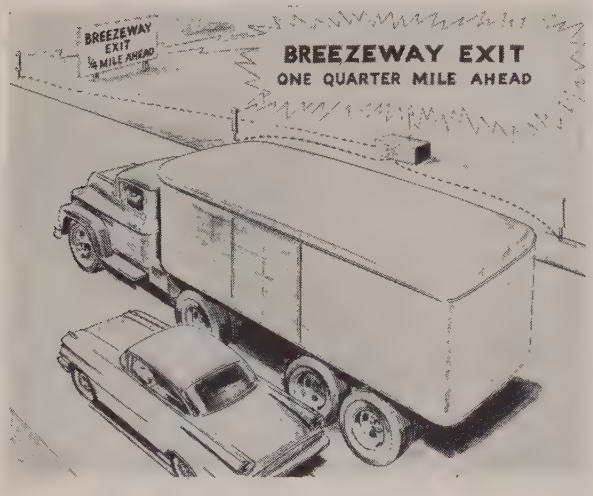

Fig. 25 — Application of Hy-Com

Conclusion

Although many problems, both technical and nontechnical, must be solved before reliable automatic highways can come into general use, the Auto-Control System does illustrate one potentially useable concept. The division of equipment between car and road seems most practical and limitation to operation on controlled access roads permits retention of reasonable simplicity.

For the immediate future it is possible to utilize a wire in the center of each lane, both for communication to moving cars and in connection with a path error warning system. While retaining driver control, Electro-Lane can provide a warning to the inattentive operator and help prevent some of the large number of single car accidents. Hy-Com can make driving simpler and safer by providing audible speed, traffic, and emergency messages to the driver. This system has been further developed by GM Delco Radio Division. Its practicality is attested to by the fact that one complete installation has been in use since September of 1959. The city of Flint, Michigan has installed Hy-Com in a city-operated driver training grounds for effecting communications between the instructor and students in 20 automobiles used in training. Two additional test installations are being used in training. Two additional test installations are being considered by highway authorities. One on a three mile section of the John Lodge-Edsel Ford Expressway in Detroit and the other on a research highway operated by the Ohio State Highway Department.

Both Hy-Com and Electro-Lane are particularly appealing for use by toll facilities since they could be readily attached to vehicles using this facility, and can provide road information and path error warning with only a modest amount of road installed equipment.

References

1. J. B. Bidwell, "Vehicles and Drivers - 1980". SAE Annual Meeting, Detroit, Michigan, January 13, 1959.

2. J. B. Bidwell, and R. S. Cataldo, "How Will Future Motor Cars Affect Highway Construction", SAE Summer Meeting, Atlantic City, N. J., 1958.

3. G. P. Harnwell, "Principles of Electricity and Electromagnetism", McGraw Hill Book Co. Inc., 1949, 322.

4. L. G. Johnson, "GMR Reliability Manual", Data Processing Group, GM Research Laboratories, started June, 1959, unpublished.

5. House Document 93 entitled "Federal Role in Highway Safety" 86th Congress, 1st Session, March 3, 1959, 17.

6. W. B. Hoback, "Accidents on Oklahoma Turnpikes", Traffic Quarterly, Vol. 13, No. 4, October 1959, 547.

7. W. D. Stevenson, Jr., "Elements of Power Systems Analysis", McGraw-Hill Book Co., Inc., 1955.

8. C. E. Quinn, "New Voice System Alerts Drivers", Traffic Engineer, July, 1959.

9. C. E. Quinn, "The General Motors Highway Information System" Electronics Committee, American Association of State Highway Officers, Boston Meeting, October 15-16, 1959

Appendix A

A set of definitions of the reliability terms follows:

R_E = reliability of Edison power.

R_{SE} = reliability of switching to reserve power.

R_{RP} = reliability of reserve power.

R_V = reliability of obtaining speed command zero.

R_{01} = reliability per block of steering signal oscillator.

$R_{(S01)}$ = reliability per block of switching to reserve steering signal oscillator.

R_{R01} = reliability per block of reserve steering signal oscillator.

R_{VB} = reliability per block of obtaining speed command zero.
R_{L1} = reliability per block of steering wire (criss-crossed wire).
R_{PC1} = reliability per car pick-up coils for steering.
$R_{(SPC1)}$ = reliability per car of switching to a secondary steering signal.
R_{02} = reliability per block of speed command signal oscillator.
$R_{(S02)}$ = reliability per block of switching to the reserve speed command signal oscillator.
R_{R0Z} = reliability per block of reserve speed command signal oscillator.
R_{CHM} = reliability per car of the steering computer, hydraulics system and servo valve.
$R_{(SCHM)}$ = reliability per car of switching to reserve steering computer, hydraulics and servo valve.
R_{RCHM} = reliability per car of reserve steering computer, hydraulics and servo valve.
R_B = reliability per car of steering bar linkage to front wheels.
R_T = reliability per car of front tires.
R_{03} = reliability per block of the obstacle primary oscillator.
$R_{(S03)}$ = reliability per block of switching to the reserve obstacle primary oscillator.
R_{R03} = reliability per block of the reserve obstacle primary oscillator.
R_{L3} = reliability per block of the obstacle loop of wire.
$R_{(SL3)}$ = reliability per block of switching to speed command zero.
R_{PC2} = reliability per car of pickup coils for speed command.
R_{L2} = reliability per block of speed command wire.
R_{VC} = reliability per car of obtaining speed command zero.
$R_{(SL2)}$ = reliability block of switching to speed command zero.
R_{L4} = reliability per block of secondary loops of wire.
$R_{(SL4)}$ = reliability per block of switching to speed command zero.
R_M = reliability per block of the obstacle being metal.
R_{OD1} = reliability per block of obstacle detector.
$R_{(SOD1)}$ = reliability per block of switching to speed command zero.
R_{OD2} = reliability per block of obstacle detector in parallel with OD1.
$R_{(SOD2)}$ = reliability per block of switching to speed command zero.
R_{PC3} = reliability per car of speed measurement pick-up coil.
$R_{(SPC3)}$ = reliability per car of switching to speed command zero.
R_{RPC3} = reliability per car of the reserve speed measurement pick-up coils.
R_{PC4} = reliability per car of speed command pick-up coils.
$R_{(SPC4)}$ = reliability per car of switching to speed command zero.
R_{RPC4} = reliability per car of the reserve pick-up coils for speed command.
R_{C2} = reliability per car of speed computer.
$R_{(SC2)}$ = reliability per car of switch to the reserve speed computer.
R_{RC2} = reliability per car of reserve speed computer.
R_{MHTB} = reliability per car of servo valve, hydraulics throttle and brakes assembly.
$R_{(SMHTB)}$ = reliability per car of switching to the speed command zero.
R_{RMHTB} = reliability per car of the reserve servo valve, hydraulics, throttle and braking assembly.
$R_{(SL1)}$ = reliability per car of switching to speed command zero.
ν = number of blocks
μ = number of cars
Z = next higher integer in the fraction

$$\frac{\text{Vehicle Length} = Lv}{\text{Obstacle Detector Length}}$$

for individual obstacle detection in the length, L_{OD}, not obstacle detection with paired secondaries both in road.

Discussion

Practical Application of Driver Aids

Alger F. Malo
Department of Street & Traffic, Detroit

RESEARCH concerning automatic highway systems cannot help but eventually lead to better and safer transportation facilities. My comments will be restricted to the practical application of these systems or devices on existing or future highways. I appreciate the fact, as stated in the conclusion, that many problems need be solved before reliable automatic highways can be obtained but am confident that someday such facilities will become a reality.

There is little doubt that if these systems were in use today our highways would be carrying larger volumes of traffic with less accidents and loss of life. Some of our traffic engineers would realize the solution to some of their problems. Typical of these are the ones encountered on facilities such as the New Jersey Turnpike where they point to their major problem as maintenance of capacity, rear-end collisions, low visibility, and snow conditions. They stress the need for devices to detect impending congestion, and the need for warning devices as a means of reducing if not eliminating rear-end collisions. The Auto-Control System with its features of guidance, speed control, obstacle detection, and

warning lights would solve most of these problems.

In recent years, there has been an increasing number of single car accidents which are reported as "running off road" or "hitting fixed object". Electro-Lane could minimize this type of accident besides making driving more convenient and safer for the average driver. This system could easily be installed on any new or existing highway. It appears also that the car equipment would be an inexpensive accessory that could easily be installed. This system has possibilities for immediate application. Some Highway departments have adopted a policy of painting the edge of pavements; other departments have refrained from adding this safety device because of the expense involved. Paint is a continuous item of expense, and possibly the initial installation of the wire used in the Electro-Lane system may be cheaper and eventually more effective. Certainly dirt and snow would not obliterate its effect as it does the painted line, and it would not have to be replaced every year as does paint.

Hy-Com has all manner of interesting possibilities. The applications suggested by the authors are all possible and would add to the safety and convenience of present day driving. This device may eventually be the answer to one of the problems encountered in the operation of Detroit's expressways, namely, the warning of drivers approaching a stoppage of some kind. The lack of warning has resulted quite often in chain-reaction accidents.

Many miles of highway have been completed and many more are under construction. Unfortunately, many of the operational problems of today's highways will be encountered in those completed tomorrow. The traffic engineer is looking for any type of device that will increase capacity and create greater safety on streets and highways. I believe that any immediate help must come from hardware added to the vehicle which will operate independently of any highway installation, or, devices added to the highway which will operate independent of the vehicle; unless, of course, the automobile manufacturer and the highway and traffic engineers can team up and integrate the highway and the vehicle which uses it into a single transportation facility. The start could be made by such a system as Electro-Lane which if installed in the highway would be of aid to those who installed the device in the vehicle and would not affect the operation of the unequipped vehicle. It would simply be a driver aid as is power brakes or power steering, but would represent an example of closer coordination between the vehicle and the highway.

Traffic authorities have recognized the fact that the highway itself is lacking in control devices which may provide greater capacity and safety. The proposed research project planned for a 3-1/2 mile section of John Lodge Expressway is an effort to discover better methods of operating such a facility. Daily volumes of 130,000 to 140,000 vehicles a day for six lanes with peak-hour volumes as high as 2000 vehicles per hr. per lane have posed operating problems difficult to solve. Such high volumes result in slowdowns and stoppages. Means of locating immediately these slowdowns or stoppages are needed, and means are needed to warn drivers so that they may adjust their driving to conditions ahead. It may be necessary to close lanes, divert traffic from the facility or close access ramps. The project will employ a 14 camera television system as a means of surveillance and will include signals over the expressway lanes and on the access and egress ramps for traffic control. Information regarding conditions would be fed to the local radio stations who would relay it to the driver of the vehicle over standard broadcast facilities. (At present the police dispatcher is connected to all local radio stations by a Conference line.) This additional warning or information might eventually be incorporated in the system by means of Hy-Com or similar device.

I am confident, in spite of the pessimism expressed by many regarding the future of highway transportation, especially in our urban areas, that our highways will always be capable of satisfying the demands of traffic. However, in closing this brief discussion, I would like to stress the fact there is need for closer cooperation between the automobile manufacturer and the highway and traffic engineer. Such cooperation would result in attaining better and safer highways more rapidly. Perhaps an Illinois Test Road is needed for highway design and traffic operation. We are hopeful that our television research project will point the way to improve operating conditions on urban expressways.

Author's Closure to Discussion by Malo

IT HAD NOT occurred to us that it might be cheaper to install a wire in the middle of the road or at the edge of the road, than it would be to continually paint the white line. As a matter of interest, however, we have had highway people interested in laying a wire in the road which could be used for guidance of a high speed paint truck for painting the white lines. Their assumption was that the savings due to the increased speed of the paint truck would shortly pay for the guidance installation.

We agree that the driver needs more and better information than he now has. With this additional information, we can expect greater safety and higher human driver road capacities.

We also feel the need of closer cooperation between the automotive manufacturers and the traffic and highway engineers. Without this cooperation many good highway improvements may die in the initial hardware stages for lack of a driver testing. Hy-Com, for instance, presents a particularly difficult problem, since road administrators will not buy one transmitter for highway installation until there are receivers in the cars, and vice versa. Thus, one faces the old problem of which comes first the "chicken or the egg". Certainly an Illinois Test Road type facility would be ideal for controlled testing of new ideas. On the other hand, we

feel that the creation of the experimental test section on the John Lodge, in which people are invited to bring new ideas for testing, will answer more of the immediate problems.

Should Automatic Aids be Utilized?

John Versace
Chrysler Corp.

THE AUTHORS should be congratulated for at least three areas of accomplishment: First

1. The great emphasis placed on the systems approach to the man-car-highway complex. Certain systems requirements or criteria were shown, and then an automatic system was derived to meet the objectives. This procedure has become conventional in the design of military systems, but is not commonly seen elsewhere. There is, however, a major reservation to this approach if it does not allow for evolution as technology grows.

2. The thorough reliability analysis described in the paper.

3. The compactness and minimum system cost achieved by the appropriate distribution of equipment between car and highway, which was done by introducing a highway block system for obstacle and speed control thus eliminating apparatus, such as radar, which would be needed in the car itself to perform these functions continuously rather than discretely.

There are a number of questions that must be faced in considering a system like this. A method for building one kind of automatic highway has been described. Why should such a system be built? Ordinarily, this would be a matter for sociologists, economists, lawyers, political scientists, and legislators, but since the matter is pertinent, a few comments should be made on it.

In the introduction to the paper it was stated that we want to reduce driver effort and improve comfort, reduce driver error and hence increase safety, and increase highway capacity by eliminating driver lags. These goals can be summarized as: convenience, safety, efficiency -- and to these should be added cost economy. This latter is a most pertinent consideration, and the other goals can ultimately be related, at least in principle, to what one wants to pay for them.

Let us consider transportation systems: The train is more convenient en route but takes longer, and local transportation will be needed which is available on whim, and adequate to carry all the cargo. Airplane travel has its advantages, but one must ask if the time saving and travel convenience is worth the extra cost. Thus, one decides to drive, if he wanted more safety and convenience, he would have it by paying for it. He would fly or take a train and then rent a car at the other end.

He would have to pay for automatic highways, too. The general public might be willing to pay $500 to equip each car. But if 2/3 of all cars were so equipped, it would be possible to build some 21,000 miles of super highway at $1,000,000 per mile with this money alone, which would pay taxes for highway installation and, especially, maintenance.

The number of people killed in a recent year on 400 miles of New York Throughway was just 33. A hundred such highways, with completely automatic provisions and perfect reliability thus would save about 3300 lives a year, or about 8% of the total traffic deaths, as the result of the automatic feature. The rural average toll is 8.5 deaths per 10^8 miles, but the New York Throughway has a rate of only 1.9 deaths. Thus, the the superhighway feature can be expected to account for about 75% of the total improvement that would be obtained by going to automatic superhighways of 100% effectiveness. It would seem that with a finite money resource available, one should consider carefully its allocation.

There are other improvements that can increase safety and comfort. These, I believe, are principally those that will make the driving task simpler, and less uncertain, by providing the driver with more unambiguous information, such as anticipatory information about other drivers' intentions. Tremendous improvement can still be made in highway signing and geometry to improve perception of the road ahead.

This is not to denigrate the efforts described by the authors for progress requires that there be constant imaginative, exploratory development and test of such ideas. Of course, recognition has been given the issues posed here, for transitional, evolutionary compromises, like Electro-Lane and Hy-Com have been developed and are obviously showing some promise within their own limited area of performance.

Author's Closure to Discussion by Versace

THE FOURTH goal for an automatic highway, cost economy, added by Mr. Versace, is, indeed, required before one could actually decide to build an automatic highway. By making several assumptions, Mr. Versace does make an important point; namely, that it is possible that a large proportion of the potential savings in lives that could occur through the installation of limited access automatic highways can be obtained by just installing limited-access highways alone.

However, we believe that there are certain features in addition to safety that might accrue to the drviers of an automatic highway. These are increased capacity of the highway and the convenience of being driven automatically. It is quite true that the value of the service received (improved safety, increased road usage, and automatic operation) would have to more than equal the cost of these services in order to make an automatic highway appear attractive.

Additional Points Concerning the Method of Approach

H. S. Mika
Ford Motor Co.

IT HAS BEEN rather conclusively shown that the state of development in the electronics and control field is such that sucessful hardware can be built. True, there is some question of reliability, economic feasibility, and driver acceptance, but the important thing is to start somewhere and this the authors have done very capably.

I think it is picayune to discuss the details of the hardware and nothing would be gained. I would rather confine my comments to the philosophy of approach. If time had permitted the author's might have brought up the following points.

1. Any automatic system whether it is a process or a missile or an automobile is primarily dependent on the dynamic characteristics of each component in this system. In the case of a vehicle this is usually called the handling and stability and depends on such things as tire characteristics, suspension, weight distribution, and many other variables. Any automatic control of the vehicle must be matched into the handling and stability characteristics of the vehicle or else the net result is either a sluggish system or one that will hunt continuously. At 60 mph an optimum match is necessary. This has the implication that the electro-hydraulic controller must have fairly wide limits of adjustment to permit tuning in to any vehicle. This tuning would have to be done by control experts and once it was done for a given vehicle there is no reason to expect this optimum match would last indefinitely. For instance, if for some reason the tire pressure changed by a few psi, a rather large change in vehicle steering response would ensue. In other words an adaptive controller is indicated, and this is a somewhat nebulous thing in present control theory application. A somewhat less desirable approach would be to standardize the vehicle dynamic characteristics.

2. The author points out the need for throttle and brake control. This may very well imply the additional cost of a full power hydraulic system for braking and the development of disc brakes.

3. Another system parameter is the minimum allowable deceleration limit on vehicles. This implies very close inspection and enforcement. The difficulties that this might cause are well known. The burden would be on the police and the driver to a much greater degree than at present.

4. The paper discusses primarily the steady-state condition on a highway. Vehicles have to enter and leave lanes such as are proposed and this raises the very considerable problem of entrance acceleration and exit deceleration space. An entirely new ramp design approach would be necessary. Certainly, either left or right exits, but not both, would have to be used. Interchanges such as are common at present would not be readily adapted to automatic control lanes. The reason for this is that manual vehicles would have to use the same exits and interchanges. The result would be the entrance of a manual vehicle on an automatic lane at the driver's discretion. Mere signal lights will not deter the eager driver as is well known. The least that could happen in this case is an automatic stopping of all vehicles on the automatic lane and in most cases, needlessly. I think the answer lies in the two traffic systems being entirely independent with no possibility of mutual usage.

5. As far as Figs. 6 and 7 are concerned, I would like to point out that actual experimental data exist on driver spacing and highway capacity. In some work that was done on the Ford-Lodge Expressway, it was determined that the spacings for the normal driver are considerably lower than shown. For instance, at a speed of about 40 mph (58.7 ft/sec) the modal, most frequent, spacing between drivers was 82 ft as contrasted to the 109 ft in the figure. Further, it was found that about 8.5% of drivers used a spacing of 41 ft or less and about 1% used a spacing of about 29 ft. All this adds up to a higher real capacity than indicated in Fig. 7. For the highest capacity measured, 2200 vehicles per hr, a 14% higher capacity existed than indicated on the figure.

In conclusion, I would like to repeat that the important thing is that something has been started and actually hardwarized. The answers to the points I have raised will be answered eventually through trial and error. This is a complex problem and progress will be slow. The authors should be congratulated on getting the ball rolling.

Author's Closure to Discussion by Mika

SEVERAL of Mr. Mika's points shall be discussed. It is true that changing the tire pressure, suspension, tire characteristics or weight distribution will change vehicle handling characteristics. However, small changes in these parameters would probably induce small changes in vehicle's handling characteristics not large changes. Take the example to which Mr. Mika referred, namely, the small change in tire pressure. If one increased the tire pressure from 24 psi to 29 psi, that is 21% increase, about a 15% increase in cornering stiffness would result. Take the worse case in which only the front wheels had undergone this 5 psi change in tire pressure. For a typical car at 30 mph at most a 12% increase in the steady-state yaw rate would result. The transient respone would be slightly over damped, the settling time (the time required for the yaw rate to reach and stay within 5% of its final value) having increased 7.5%. If all four tires had their pressure increased, the resulting increase in steady-state yaw rate for the 30 mph typical car would be less than 1.2%. Again the transient response would stay nearly critically damped, the settling time having decreased by 7.5%. Certainly in this case the changes in vehicle response are small, not large.

Furthermore, a feedback servo-system, which is what is

used in the automatic guidance system, does tend to wash out the influence of small changes in the car parameters so that these changes do not make an appreciable difference in the car steering performance.

There is a fairly large, known change in car handling response possible with car velocity. This change in response can be compensated for in the servo-controller. The full scale steering system seems reasonable to us, and it is not felt that a constant check on the system is necessary.

One would use an adaptive system when the dynamics of the variable being controlled are unknown or the variations in the variable being controlled are large. The adaptive servo concept might come into play for the blow-out condition. Although the response of our present steering system to a blow out has not yet been tested, it may prove to the adequate. The natural frequency of our present steering system is above 7 cps. This is undoubtedly a better response than that of the human. Furthermore, our steering system is always alert for a rapid change. It is not distracted by say, the blonde in the front seat. On the other hand, the driver has more steering information in the case of a blow-out than does the servo guidance system. We do feel that it is within the realm of present technology to provide additional information to the steering system, if this information is needed to handle the blow-out condition.

The information used for the maximum capacity versus velocity that the normal driver can attain was admittedly old, having been taken from the "Highway Capacity Manual", published in 1950. It was the high caliber of Mr. Mika's recent study of car spacing on the Detroit Expressways that induced me to ask him for criticism. It appears that normal driver capacity is about 14% low. Mika has found that on the Ford and Lodge Expressways 1% of the drivers use a spacing of about 29 ft at 40 mph. It would seem to me that this "riding your rear bumper" driver might well be the driver most apt to be involved in a rear collision.

Fig. 1 — Early aircraft

Applications of Army-Navy

A. M. Mayo* and H. L. Wolbers
Douglas Aircraft Co., Inc.

AS RECENTLY as 1938 only 29,000 planes were operating within the available United States air space. Today more than 109,000 aircraft move about in this same area. From pre-World War II speeds of 180 mph, commercial aircraft have moved to an operational regime of 600 mph. The safety problems these conditions generate are legion.

What can be done to achieve the precise control of flight which these conditions demand? Any proposed solution must satisfy the needs of four rather divergent groups.

The first group is the airline carriers. The primary interest of the airline operator is an efficient and profitable operation. A flight operation must show improvement in economy of operation. This would include, among other objectives, the reduction of maintenance, and better equipment reliability and economy.

The second group is the government. The government agencies regulating the airlines have a slightly different orientation in their requirements. Of paramount importance in this case are the requirements for safer and better utilization of air space, particularly over highly congested terminal areas.

The third group includes the pilots themselves and their cooperative organizations. From the standpoint of the pilot, an effective system should keep him constantly aware of what is happening, even during the times that the aircraft is on automatic control. He, in the final analysis, is the one man in whose hands the success or failure of the operation lies.

Last but not least is the passenger, who is the chief reason for the existence of the airlines. Thought and consideration must be given to his convenience, his time, and his pocketbook.

A system to meet all of these needs, must simultaneously improve the economy of operation and the safety and air space utilization, and provide the pilot with not only improved automatic functions but also with continuously available indications of what is happening.

The problem is being approached from two points of view; that of the ground controller, and that of the pilot and crew in the aircraft. Recognizing the need to modernize and improve data handling methods for the nation's air traffic control, the Federal Aviation Agency is sponsoring considerable effort in the study and introduction of automation to the processing and display of air traffic control data. However, improving the ground monitoring procedures for controlling air traffic solves only a part of the problem. The remainder of this problem rests with the human pilot who controls and monitors his own aircraft, and at whose fingertips lies the responsibility for the comfort and safety of passengers and crew. It is to this area of flight control that the following remarks apply. Specifically, we will discuss the approach taken by the United States Navy in unburdening the pilot through the development of an integrated instrumentation program and some of the applications of this instrumentation program to transport aircraft operation.

Consideration of Pilot

Let us start with the human operator, the pilot. Man has consistently demonstrated his intellectual powers by creating tools and machines to extend his capabilities and his senses. As the machines have become more complex, the requirements on the human operator to control them precisely have become more exacting.

The Army-Navy Instrumentation Program was based on the principle of using man's earth evolved capabilities to the maximum extent, on the basis that changes in any man-

*Now with Office of Life Science Programs, National Aeronautics and Space Administration.

Instrumentation Program to Transport Aircraft

made machine could be quicker and more certain in results than changes in the man.

If you will recall the early days of commercial aviation and the equipment available then (Fig. 1), and contrast those early aircraft with today's sleek jet transports (Fig. 2), it should be readily apparent that considerably greater changes have occurred in aircraft in 35 years than have occurred in man in 35,000,000 years (Fig. 3).

The strength and limitations of the human brain are the foundations on which the requirements for integrated control systems are derived.

Dr. Finagle has given us the definition of a "constant variable" which when added, subtracted, multiplied, or divided into a wrong answer will turn it into a right answer. The only known source of this "constant variable" is the human brain. Give a computer wrong or incomplete data and it returns a wrong answer or none at all. The human brain characteristically operates with such data and surprisingly often, by a creative leap, comes up with the right answer in defiance of logic.

Human beings are unique in this capability to arrive at reasonable decisions based on considerations of may complex and highly inter-related, but often poorly defined, factors. The ability to apply memory data, stored from a lifetime gathering of knowledge, and to arrive at a decision, has never been approached by a man-made computer.

In spite of its evident huge capacity, some of the brain's limitations are of critical importance in the design of man-

Fig. 2 — Modern transport

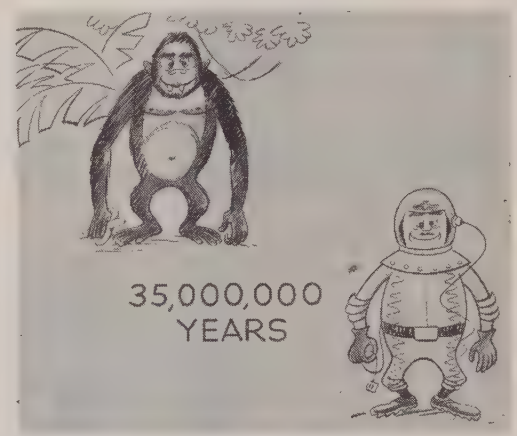

Fig. 3 — Development of man

$$\frac{4x^2}{25} + \frac{y^2}{4} = 1 \; ; \; 0 < z \; \frac{3}{4}$$

$$z = \frac{3}{4} \; ; \; \frac{4x^2}{25} + \frac{y^2}{4} < 1$$

$$\left(x+\frac{3}{2}\right)^2 + y^2 = \left(\frac{43}{32}\right)^2 \; ; \; \frac{3}{4} < z < \frac{9}{4}$$

$$z = \frac{167}{32} \; ; \; \left(x+\frac{3}{2}\right)^2 + y^2 < \left(\frac{3}{16}\right)^2$$

$$\frac{(x-z)^2}{2} + y^2 = \left(\frac{3}{16}\right)^2 \; ; \; \frac{3}{4} < z < \frac{167}{32\sqrt{2}}$$

Fig. 4 — Equations describing common object

machine systems. The time constant is long, compared to those of many kinds of mechanisms and circuits; the brain tires quickly and is easily distracted. Also, certain configurations of information are accepted much more readily than others. This point is illustrated by the difficulty of the average person in visualizing a simple everyday article from simplified mathematical formulae (Fig. 4), or even by a three-view drawing (Fig. 5); and his ease in recognizing a picture of the article (Fig. 6). The point is that information can be conveyed in various ways. The job of the system designer is to provide information to the system operator in the form which he can interpret most readily and understand.

The pilots of today's high performance aircraft are faced with a very similar type of problem. One of the fundamental things the pilot needs is an answer to the question, "Where am I?" But, how does he obtain an answer? (Fig. 7) In conventional instrument panels he must read his indicated altitude and airspeed in numeric terms, correct them for the outside air temperature, estimate the wind direction and velocity, compute his ground speed, and finally end up with an approximation of the actual aircraft position. If what the pilot really needs to know is his present location, one will have to admit that this is quite a complicated procedure to go through to establish this bit of information. Furthermore, in spite of the increasing demands being placed upon the pilots of our modern transport systems, the ways in which the necessary information is provided to him have not really changed at all in the last 35 years. Witness a cockpit panel circa 1927 (Fig. 8) and the panel of our latest jet transport (Fig. 9). The same round dials and moving pointers are being used today that were used three decades ago. In today's cockpit the pilot is still faced with the job of mentally interpreting, integrating, computing, and somehow eventually determining his exact location. How well he does can be inferred by the current great concern expressed by the Federal Aviation Agency on the gross inaccuracies made by airline pilots in reporting their positions over check points and marker beacons.

The disjointed addition of radio aids, computers, and other electronic equipment to the aircraft has not improved matters. As the number of electronic systems increase, the number of tubes, capacitors, and resistors increases geometrically. Furthermore, the greater the number of electronic components, the higher the probability of partial or complete system failure.

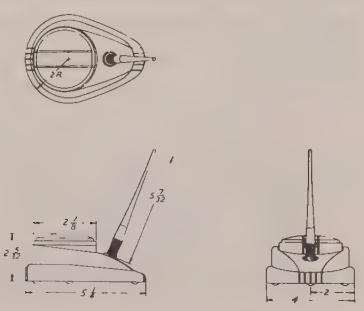

Fig. 5 — Three-view drawing of common object

Fig. 6 — Photograph of common object

Development of Army-Navy Instrumentation Program

This, then, was the problem faced by the United States Navy when, in 1953, it was decided that if air superiority was to be maintained, a broad program to improve the all-

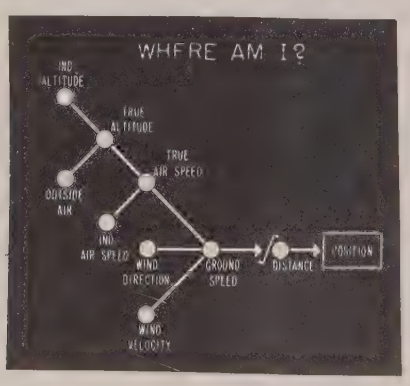

Fig. 7 — Position computation

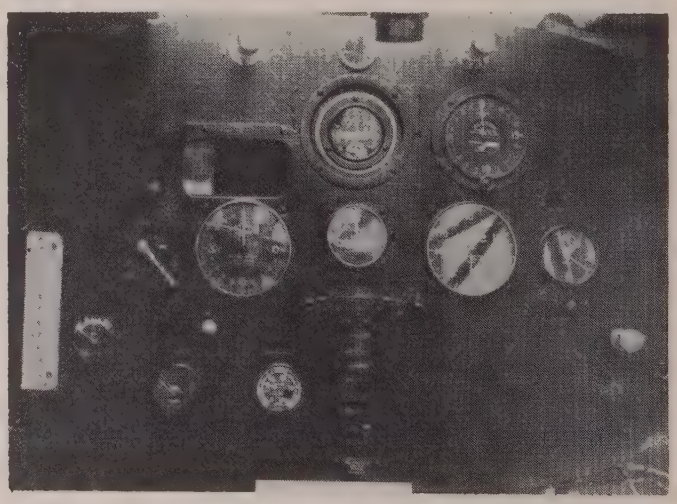

Fig. 8 — Aircraft instrument panel — 1927

weather operation of aircraft by research in instrument systems was mandatory.

One of the early decisions concerning such a broad program was that the overall effort should be coordinated by a major aircraft concern in order that full consideration would be given to a complete man-aircraft system, and that proper recognition of system integration and size and weight problems would be assured. A number of major companies were asked to bid on the program, and Douglas Aircraft Co. 's El Segundo Division was selected as the prime contractor for the industry-wide effort.

In 1953 a meeting was called by the Navy to explain the program. Representatives of all military services and the industry in general were invited. Following the promising start, the Army joined the program with emphasis on helicopter and light aircraft problems. The Bell Helicpter Corp. was chosen as a prime contractor to consider the problems of the helicopter, to adapt research from the original program to helicopter needs, and to provide added research as required by special problems. At the present time, two other prime contractors are engaged on other phases of the program; Electric Boat in the field of submarine operation, and Sperry Gyroscope in the field of surface ship control.

The expressed goal of the program was to first define the problem and secondly, to take as large a step toward the solution of the problem as present knowledge and immediately definable research projects would allow.

It was found early in the program that a most effective way to describe the total system function was in terms of a man-machine diagram (Fig. 10). It can be seen from this diagram that the "black box" called man is linked to the rest of the system by his displays (his inputs) and his controls (his outputs). Accordingly, a system was set up to determine, in an effective order, the requirements for the man-aircraft system. As an example, (Fig. 11) information requirements established display requirements, and the display requirements in turn determined the hardware requirements by which the desired display could be generated.

The initial program emphasis was placed upon the human factors area since improvements in technological areas of equipment design would, by themselves, not necessarily insure maximal system efficiency. In all man-machine systems, the effectiveness of the operator (even if he only initiates action) is a product function in the equation for system efficiency (Fig. 12). The overall effectiveness of the system cannot exceed that of its least effective factor.

In following the requirements approach, a study was made of the way in which a man visualizes data from the real world. Based upon this study, four teams of human factors

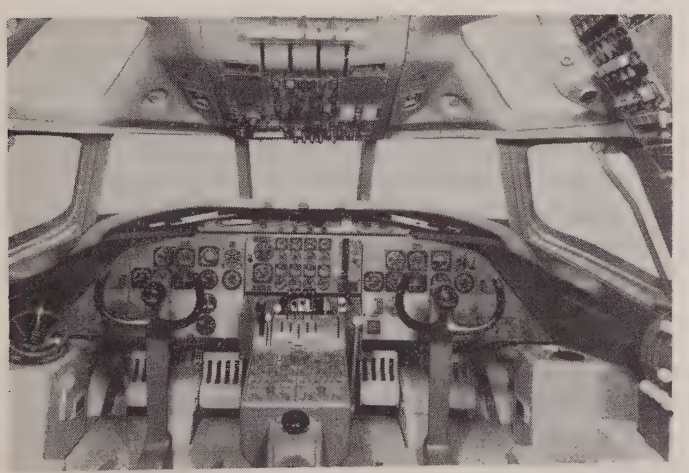

Fig. 9—Aircraft instrument panel— 1960

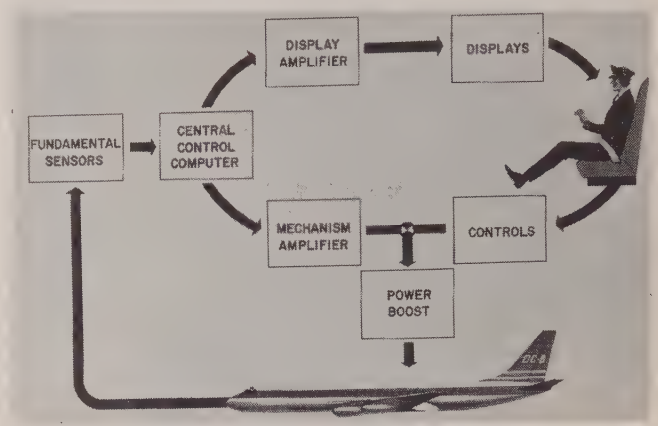

Fig. 10 — Man-machine system

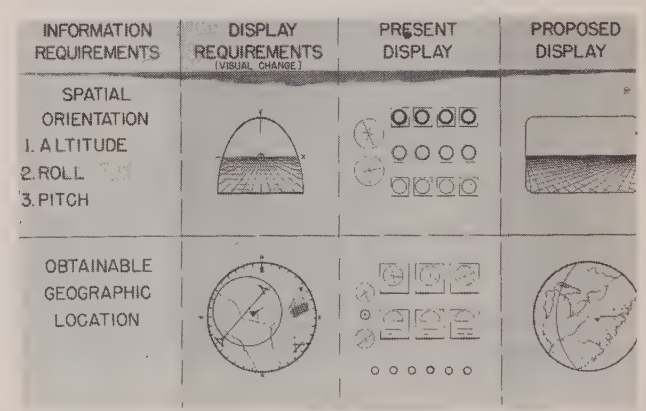

Fig. 11 — Display requirements

$$= f_1 \left[\text{EFFICIENCY OF MAN} \right] \times f_2 \left[\text{EFFICIENCY OF MACHINE} \right]$$

Fig. 12 — System efficiency

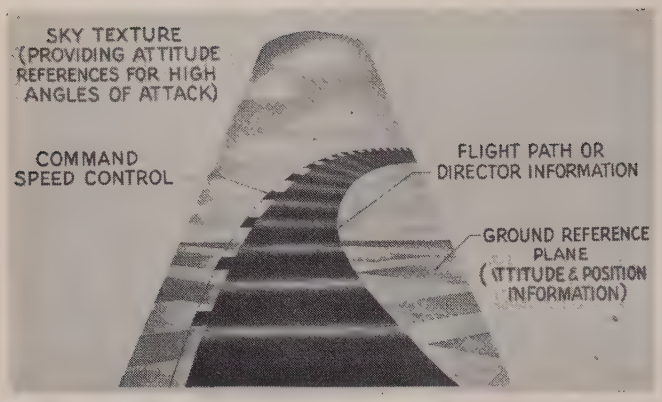

Fig. 13 — Vertical reference display

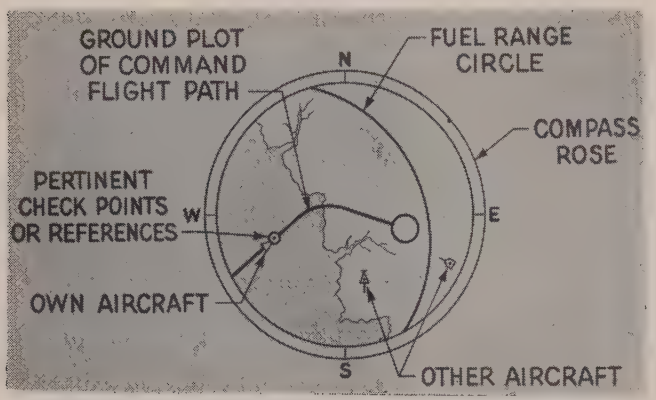

Fig. 14 — Pictorial, navigation display

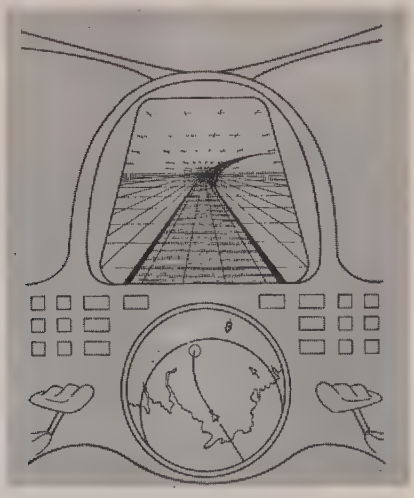

Fig. 15 — Advanced display configuration

specialists translated these requirements into a single pair of displays. One of these displays (Fig. 13), shown in the vertical plane, provided an operator with immediate time scale information in pictorial form. It answered for him these questions with respect to all of the immediate time information requirements. These are:

1. What am I doing?
2. What should I be doing?
3. How am I doing?

A tactical or navigation information display (Fig. 14) was

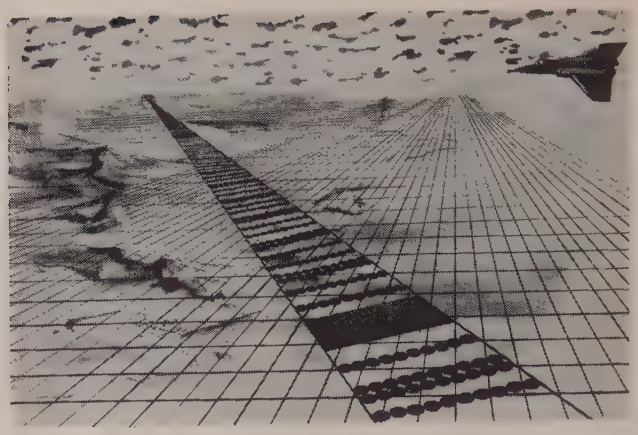

Fig. 16 — Situation model — navigation

Fig. 17 — Standard display — navigation

provided in the horizontal plane to enable the pilot to visualize himself in a situation encompassing a longer period of time. This display performed the functions of a map. In addition to showing the aircraft position with respect to geographic reatures, the tactical situation, and possible hazards, it is also capable of displaying fuel availability in terms of where the aircraft can go. Together (Fig. 15) these two displays comprise the basic sources of information to the pilot.

To illustrate how these two displays might be used, let us consider a simple navigation problem. Fig. 16 is a situation model showing an aircraft relative to a command path. Fig. 17 shows how the same information is presented on existing instruments, and Fig. 18 shows the presentation in the form of a contact analog and situation display. It can be seen that Fig. 18 is much easier to understand and interpret. It is emphasized that the dynamic motions of both displays are also first order variables in giving operational information to the man in a form directly useful with minumum mental interpretation and time lost.

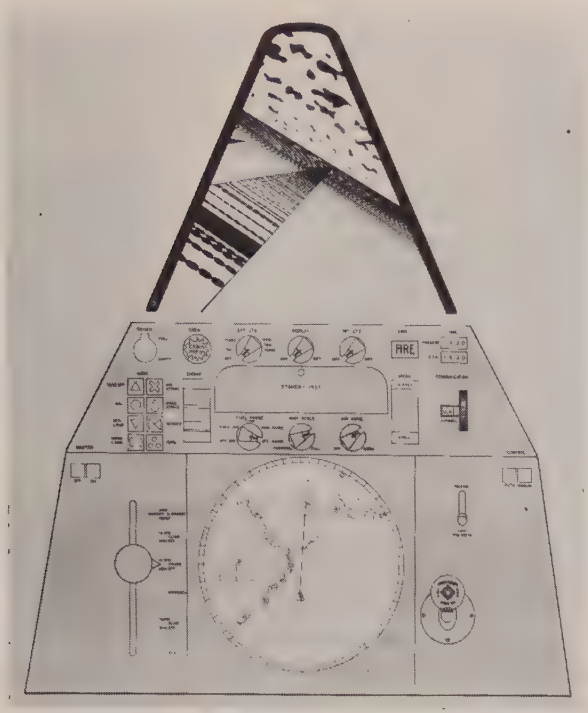

Fig. 18 — Advanced display — navigation

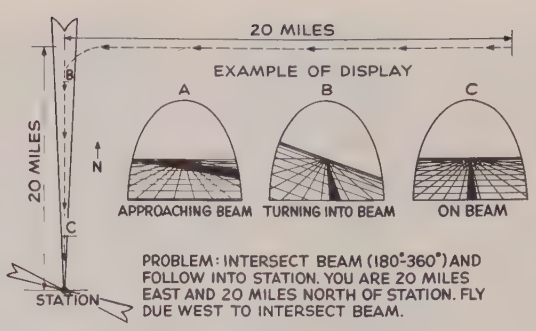

Fig. 19 — Navigation problems

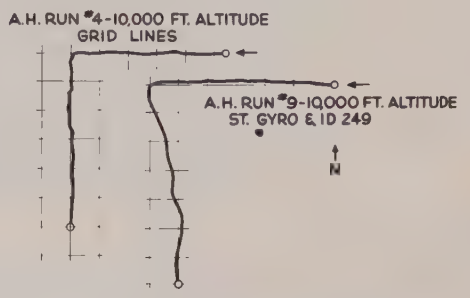

Fig. 20 — ID249-ANIP performance comparisons

The display concept, of course, has been validated in simulation studies. Fig. 19 indicates, for example, a hypothetical problem given to pilots in a laboratory situation. The pilot is placed 20 miles north and east of a VOR station. He is told to fly a heading of 270 deg until intercepting the north-south radial and then to fly due south over the station. Fig. 20 indicates a typical ground plot showing the actual variation using conventional instruments (ID 249 cross pointer, gyro horizon, et al), and performance using the advanced display. In both cases the same computer is used, only the form of information display is different. The differences in performance and the implications for cruise control, fuel management, and precise navigation are readily apparent.

The program has involved far more than the display of information. It became evident that a radically different approach of overall system engineering and completely new methods of implementation would be required to provide the defined displays. Let us refer to the man-machine diagram, (Fig. 11). In addition to the man, the other demands of a basic system include display devices, computers, controls, and sensors.

Specifications were written covering research effort and feasibility studies in each of the broad areas of the man-machine system. Not all possible approaches were taken, however, since limitations in available money limited the depths to which each of these areas could be explored.

Because considerable progress had already been made in radar and navigation sensing systems, relatively little of the early money was expended in these areas. Nonetheless, several notable results were achieved. Fig. 21 illustrates a tiny

Fig. 21 — Miniature integrating gyro

gyro developed for the program by Minneapolis-Honeywell. This gyro has been used extensively not only in missiles, but it is the prime component in at least three major inertial navigation platform systems. Fig. 22 illustrates a vacuum-deposited resistance temperature unit developed by Servomechanisms, useful in environments ranging from those of liquid gases to jet exhaust temperatures. Further clarification of the sensor requirements has indicated the potential of allowing direct values of the various phenomena to be sensed by a device which itself is able to configure information to forms directly useful in the computer or, in some cases, by the operator. New work in this area is currently showing important progress.

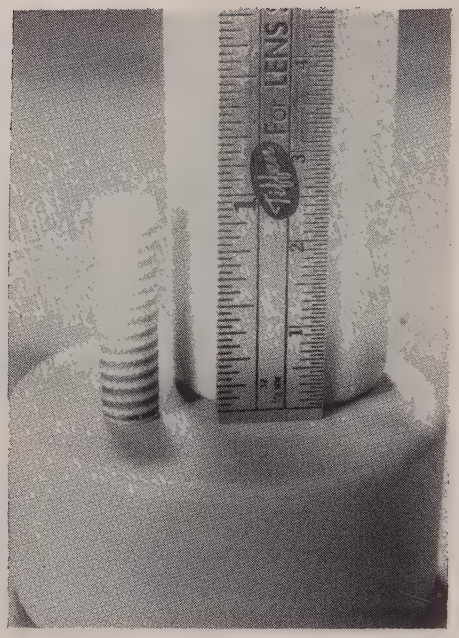

Fig. 22 — Temperature sensing element

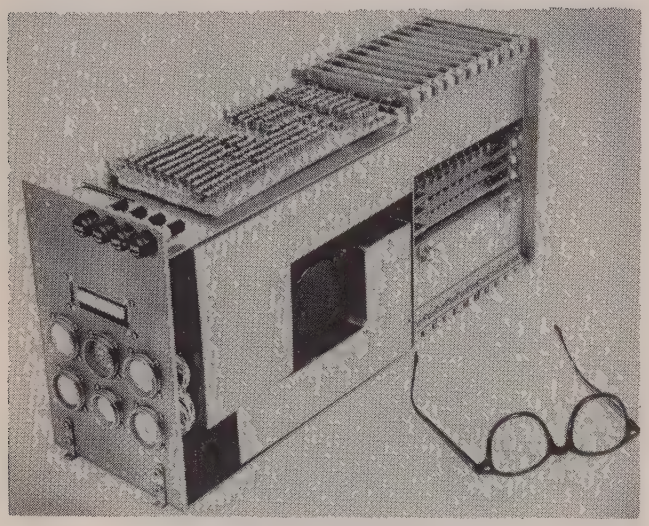

Fig. 23 — T2V — computing

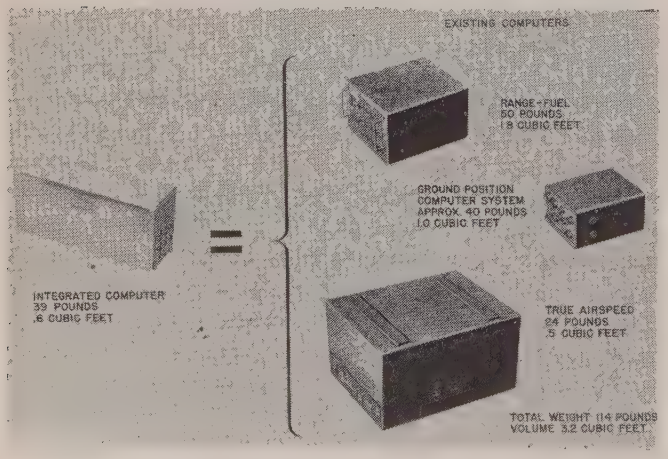

Fig. 24 — T2V — computer size and weight reduction

It was recognized in the very earliest efforts of the ANIP program that the success of implementing the desired displays and controls would be a first order function of how effective the central computer could be made. Litton Industries was given the first computer subcontract, and the brilliant conceptual thinking of George Floyd Steele, coupled with excellent implementation by the Litton team, resulted in the interim control computer. (Fig. 23) This unit weighed less than 40 lb, occupied only 0.6 cu ft, and did the work of previous units weighing hundreds of pounds. (Fig. 24). It was the first of its type to be flown. Large numbers of successful production computer systems for a wide variety of purposes, including aircraft and missile control and tactical data analysis applications, have been based on this pioneering unit.

It was recognized, however, that much greater gains were required, and that the 250,000 bits-per-sec of information capable of being processed in the ICCC computer were but a fraction of the desirable capacity. Promising results in the depositing of thin films of active electronic and magnetic materials indicated the potential of eliminating the mechanical drum storage and of greatly increasing the capacity of the computer. A team of companies including Litton, Varo, Servomechanisms, Bell Helicopter Corp., and Laboratory for Electronics, was set up under the direction of Douglas Aircraft Co. to simultaneously push efforts in advanced electronics and new computers. The RV-2 computer concept (Fig. 25) was conceived and shows promise of providing the capability of handling millions of bits of information per second by utilizing magnetic film data storage and handling. Data input and amplification functions utilize advanced microcircuitry made of thin films of materials in active contact with each other. This method of construction essentially eliminates components and potentially greatly increases reliability.

Further computer advances are indicated from studies showing the possibility of combining the advantages of digital and analog computers by means of direct manipulation of electromagnetic and sound waves.

Limitations in the number of bits of information capable of being configured by available computer equipment made it necessary to assign some added display requirements to the initial display amplifier systems. Kaiser Aircraft and Electronics designed a mechanical analog unit for presenting the contact analog display in the first research vehicle. They have also provided a simple electronic contact analog and pathway generator which is being utilized in ground test and production vehicles. General Electric and Avion Inc. have configured more advanced, all electronic, display generators for use in the second research aircraft.

In the display field, Kaiser Aircraft and Electronics was the first successful bidder. They developed a flat cathode ray tube which was tested first in the RV-1 vehicle (Fig. 26).

A transparent phosphor developed for this display by the

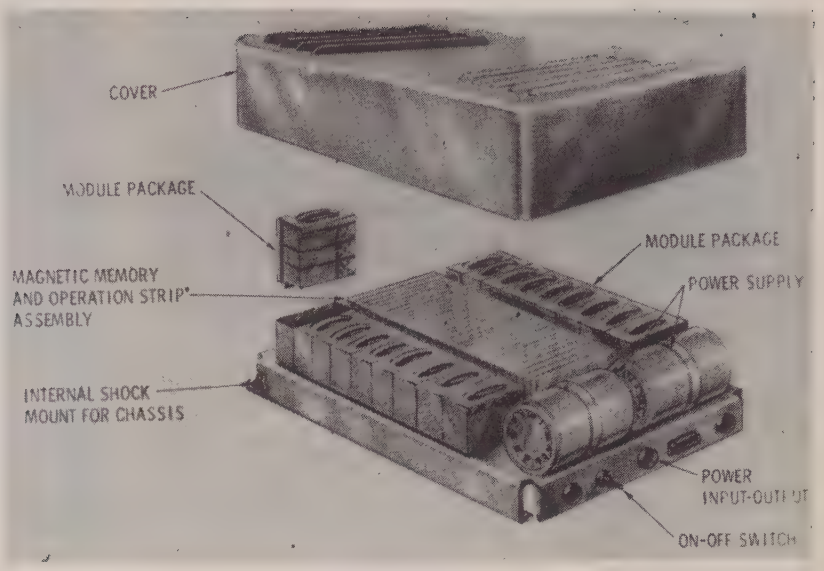

Fig. 25 — Advanced computer (RV2-1)

Naval Research Laboratories has made practical large gains in the daylight viewing efficiency of standard types of cathode ray tubes and is being utilized extensively in present development programs.

Fig. 27 illustrates the excellent optical properties of the new transparent cathode ray tubes now ready for development and application from the Kaiser effort. The requirements for still lighter weight display devices offering further gains in reliability and more extensive pictures have led to new requirements for solid-state display screens. Research to date has indicated that these new systems are feasible, but much detailed research will be necessary before they are ready for production use. The advent of these new display devices will give almost unlimited flexibility to the designer of space craft and remotely controlled vehicles.

Very early in the program it was recognized that radically improved electronic equipment implementation techniques would be needed and contracts were let to Varo Mfg. Co. to study the potentials of some microcircuitry concepts of Austin Stanton. These studies have, of course, broadened into a multiple company effort and are now being generally exploited by the industry as a whole. (Fig. 28) The promise of these techniques in greatly simplifying the manufacture of complex equipment can hardly be overemphasized and can be exploited to provide the basis for radically new industrial concepts.

Where formerly circuit components were composed of many resistors, capacitors, and vacuum tubes (Fig. 29), the techniques of solid state circuitry can be used to achieve radical improvements in circuit component size. In lieu of vacuum tubes we can now talk literally in terms of microcircuits, fabricated by deforming the basic molecular structure of matter. Instead of dimensions in inches, we now talk in terms of angstrom units. By properly designing these microcircuits to achieve functional outputs, we no longer

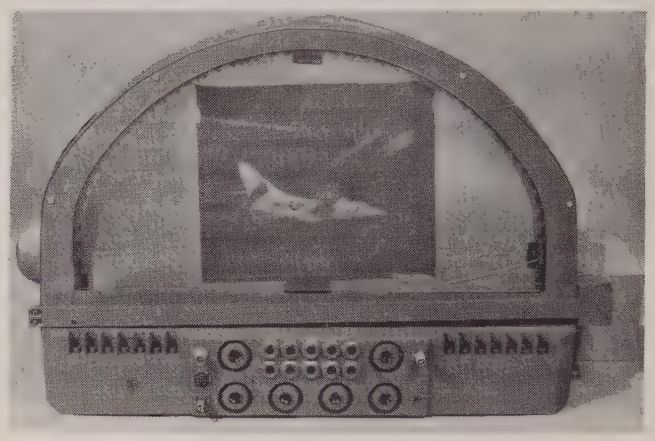

Fig. 26 — T2V — flat plate cathode ray tube

Fig. 27 — Advanced flat plate, cathode ray tube

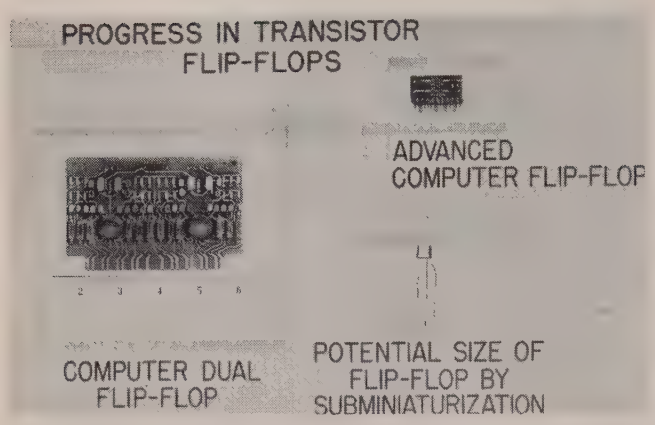
PROGRESS IN TRANSISTOR FLIP-FLOPS
ADVANCED COMPUTER FLIP-FLOP
COMPUTER DUAL FLIP-FLOP
POTENTIAL SIZE OF FLIP-FLOP BY SUBMINIATURIZATION

Fig. 28 — Progress in transistor flip flops

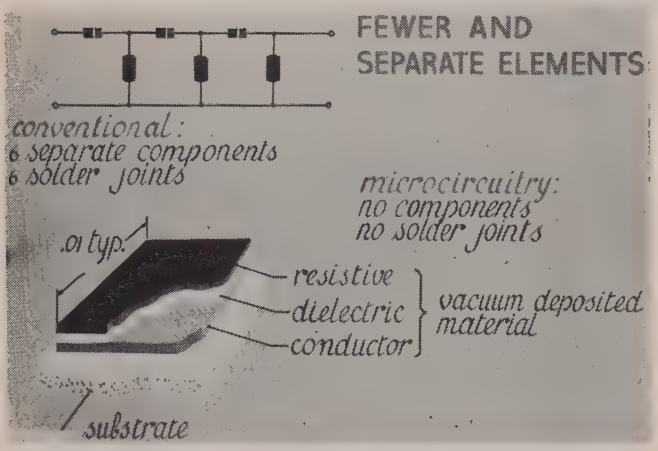

Fig. 29 — Microcircuit reliability

need separate resistors and capacitors in the conventional sense. Furthermore, with the possibility open of depositing entire circuit functions as a block, the number of unique components needed is radically reduced. The reduction of the sheer numbers of individual components leads to an increase in the reliability of systems, and with the increase of reliability comes an increase in system capability.

As work on components and techniques proceeded,a series of test vehicles and cockpits were designed at Douglas Aircraft Co. to solidify the gains. Fig. 30 is the first flight vehicle, a Lockheed T2V aircraft, configured with early laboratory versions of equipment from the program. Limited flight tests in this vehicle indicated that flight operations with the system showed even greater gains that were evident in the simulated ground tests.

Fig. 31 illustrates a cockpit utilizing the ANIP principles, but applying only techniques for which the research program has completely defined the necessary developments. Fig. 32 shows the application of the concept to a jet transport type aircraft.

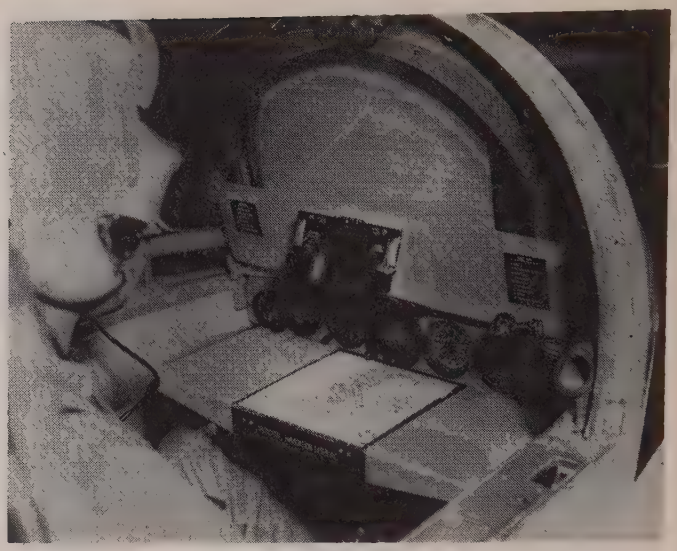

Fig. 30 — T2V cockpit

Fig. 31 — Interim cockpit

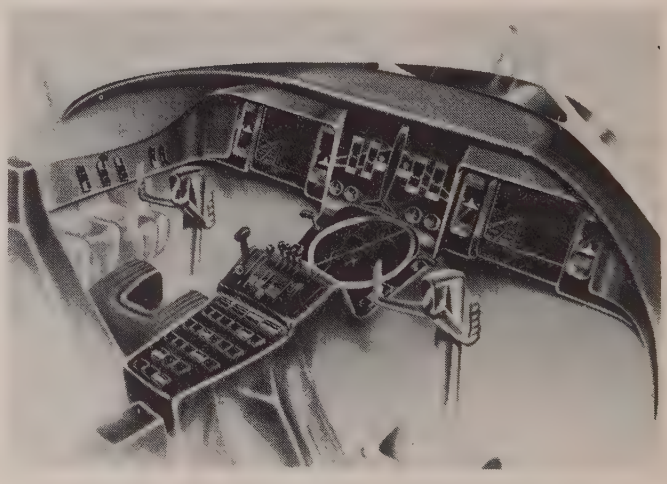

Fig. 32 — Jet transport cockpit

Summary

A relatively few million dollars spent in broad systems and equipment research has resulted in the useful output of hundreds of millions of dollars of advanced equipment production programs already under way. A system has been developed which is applicable to space vehicles, unmanned missiles, aircraft, submarines, surface vessels, and tanks. It is significant that the first full aircraft application of the system was called out in 1958.- the original target year for useful design data. Other major objectives of this overall program, still in the future, promise a much greater total return. The microcircuitry approach toward advanced equipment configuration promises in itself to be the basis for a whole new industry.

Most scheduled airline flights today move under Instrument Flight Rules (IFR) even in good weather with unlimited visibility. The voluntary decision in July 1958 by scheduled commercial airlines to fly IFR on all flights above 10,000 ft, while increasing precision of control, has contributed to the burden on pilots (and aircrew) and has also added to the traffic control burdens of the ground-based traffic control personnel. The central figures in the total system are still the pilot in the aircraft and the human controller on the ground. To help promote a safe, orderly, expeditious flow of aircraft flying IFR, these central figures must be unburdened from the tedious, repetitive, clerical functions now handled manually. Through the use of integrated displays and controls. they must be given more time for vital decision making functions.

It is believed that data now available from the ANIP Program are sufficient that serious consideration should be given to the application of these data for civil aircraft. The results of such applications should simultaneously benefit the passenger, the airlines operators, the government control agencies, and the pilots.

A Nitrosyl Chloride Solar

W. E. McKee, E. Findl, J. D. Margerum, and W. B. Lee
Sundstrand Corp.

ABOUT A YEAR and a half ago, Sundstrand Corp. became interested in the possible use of solar regenerative fuel cells as a source of power for space and remote terrestial applications. It was felt that this type of power source offered a number of possible advantages over solid state devices.

This paper presents: (1) a brief discussion of some of the problems and theoretical aspects of a photochemical type of solar regenerative system, and (2) a status report on the regenerative nitrosyl chloride fuel cell system which Sundstrand is developing under contract to the Wright Air Development Division, Aeronautical Accessories Laboratory, Power Branch. In this system, Chlorine (Cl_2) and nitric oxide (NO) are combined in a fuel cell to produce electricity, the nitrosyl chloride (NOCl) formed in the process is subsequently photodissociated into chlorine and nitric oxide. These fuels can be stored for future use or fed back into the fuel cell.

General Discussion

There are very few chemical reactions which can be incorporated into a solar regenerative fuel cell system. The requirements for fuel cell operation and photochemical regeneration are quite severe and somewhat contradictory. Some of the criteria used as a guide in the choice of our system were as follows:

1. The reactants should be gases or liquids to facilitate circulation.
2. The reaction must take place readily on electrodes at convenient temperatures.
3. The reactants should be easy to handle.
4. The product of the fuel cell reaction should be an ionizing liquid which could be used to make the electrolyte solution. Thus, both electrodes would use a common electrolyte and the need for semi-permeable membrane to separate the electrode compartments would be eliminated.
5. The fuel cell reaction should have a large loss in free energy, in order to produce a high cell voltage.
6. The product of the fuel cell reaction should be amenable to dissociation by photolysis. Consequently, there would be a limit on how high the cell voltage could be. Otherwise, it could not be photodissociated by an appreciable part of the available light energy.
7. The tendency of the photodissociated products to recombine, except in the fuel cell, should be negligible.
8. The dissociated products should be separable in relatively pure form.
9. From a volume standpoint, it would be better for both reactants to be liquid, but from a separation standpoint, a gas and a liquid would be preferred.
10. The fuel cell product should absorb light over a broad spectral range, but the fuels formed by dissociation should not absorb.
11. The photochemical reaction should have a high quantum yield. This is the efficiency with which photons can cause the dissociation to take place. In general, one photon causes a maximum of one dissociation.
12. The fuel cell reaction and photochemical regeneration should be 100% reversible. No side reactions should occur which would eventually destroy the reactants.

Theoretical Efficiency

It is important to note that not all light energy which is absorbed in a photochemical reaction can be converted into electrical energy. Calvert (1a)* has defined a useful ap-

* Numbers in parenthesis designate References at end of paper.

Regenerative Fuel Cell System

proximate equation which expresses the percentage efficiency for conversion of light into chemical energy suitable for use in a fuel cell.

$$\Omega = \frac{100(\Delta F_{298})(\phi_A)}{E_\lambda} \quad (1)$$

ΔF = Standard free energy for the overall reaction in terms of Kcal/mole of product A

ϕA = Quantum uield of product A

E_λ = Energy of light in Kcal/mole of quanta at wavelength

Maximum power available from a photylysis fuel cell combination can be calculated from the equation:

$$\text{Power } \frac{\text{watts}}{\text{cm}^2} = \phi \, Ia \, \frac{1}{6{:}02\text{x}10^{23}} (96,500) \, V(\underline{N}) \quad (2)$$

ϕ = Quantum yield

Ia = Light intensity in quanta absorbed/sec x cm^2

$6.02\text{x}10^{23}$ = Avogadro's number

V = Voltage of chemical cell

$\underline{N}$ = Number of equivalents/mole

or

$$\frac{\text{Power in microwatts}}{\text{cm}^2} = (1.6 \times 10^{-13}) \phi \, Ia \, \underline{N} \, V \quad (3)$$

From this it can be seen that to obtain high power, one should have a high quantum yield, high light intensity, high voltage per/cell, and a large number of equivalents per mole of the fuel.

Usable Solar Energy

The spectral band of photochemically useful solar energy extends from about 1500 to 8000 A. Below 1500 A, photons cause ionization; above 8000 A, the energy of the quanta is too weak to break chemical bonds and it merely heats up the system. This usable band represents about 58% of the total solar energy. The object then is to choose a photolysis reaction which will absorb and use as much of this light as possible.

Choice of Chemical System

Survey of the many endothermic photochemical reactions which had been reported in the literature (Calvert's (1b) list of reactions is excellent), showed few which showed promise as fuel cells or met enough of the above requirements. The regeneration process was considered to be the most important limiting factor. Emphasis was, therefore, placed on choosing a promising photochemical reaction which might be adapted to a fuel cell system.

Of all the photochemical reactions considered, the decomposition of nitrosyl chloride appeared to be the most promising. Kistiakowsky (2) had reported a quantum yield of two at wavelengths extending from the ultraviolet up to about 6370 A. This means that for every quantum absorbed, two molecules of nitric oxide are produced. It can be calculated from Friedman's data (3), as indicated in Fig. 1, that this spectral region contains about 43% of the total solar energy and about 75% of the photochemically active light (i.e. 8000 A).

Fig. 1 shows the absorption spectrum of nitrosyl chloride gas, in arbitrary units, in relation to an approximate representation of solar energy distribution versus wavelength. Depending on the thickness of the absorbing layer, gaseous nitrosyl chloride absorbs up to 6500 A. Theoretically, light of wavelengths up to 7500 A has sufficient energy to break the Cl-NO bond, and by use of sensitizers this band may someday be utilized.

There is evidence to show that the quantum yield of two is obtained through a two step free radical process (2, 4, 5, 6).

Primary process:

$$NOCl + h\nu \longrightarrow NO + Cl.$$

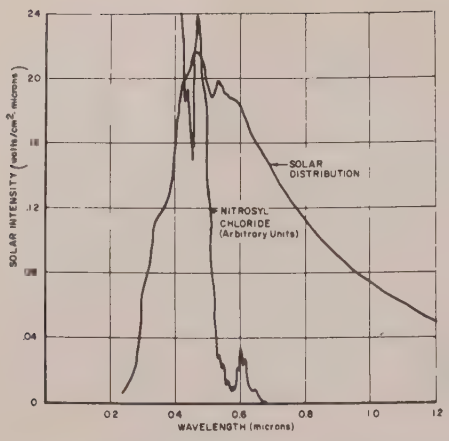

Fig. 1—Solar energy distribution and light absorption of nitrosyl chloride

Secondary reaction:

$$Cl\cdot + NOCl \longrightarrow NO + Cl_2$$

Overall reaction:

$$2\ NOCl + h\nu \longrightarrow 2\ NO + Cl_2$$

The increase in free energy, ΔF, of this reaction amounts to +4.9 Kcal/mole. The two products have thus stored part of the energy absorbed from the photon.

Fuel Cell Reaction - The photolysis products can be made to give up this energy as electrical energy if they can be recombined in the reverse reaction by way of an electrode reaction in a fuel cell.

$$2\ NO + Cl_2 \longrightarrow 2\ NOCl$$

$$\Delta F = -4.9\ Kcal/mole$$

As ΔF is negative, the reaction should proceed spontaneously giving a cell voltage which can be calculated by the well-known equation relating the Faraday, equivalents per mole, and free energy of the reaction.

$$\Delta F = -NEF$$

where: $E = 0.21$

Theoretical Efficiency of the NOCl Reaction - From Eq. 1 previously discussed, it is possible, by using the free energy increase in the products, to determine the theoretical maximum efficiency of converting radiant energy at various wavelength into electrical energy. Some of these values are shown in Table 1.

At the ultraviolet end of the spectrum, the efficiency of conversion is much lower. The quanta absorbed have far more energy than is required for the dissociation of nitrosyl chloride. The excess energy is, therefore, wasted as heat.

Maximum Power Obtainable - It is possible to calculate the maximum power available from a nitrosyl chloride fuel cell which is being regenerated by one square meter of absorber surface. However, a number of assumptions, which may not be completely correct, must be made.

1. All the light up to 6300 A is absorbed only by NOCl, not the Cl_2 or NO. This amounts to an Ia value of 14×10^{15} quanta/cm^2 sec.

Table 1 - Theoretical Conversion Efficiency

Wavelength, A	Efficiency, Ω, %
Wavelength, A	Efficiency, Ω, %
6500	22.3
3000	10.3
2000	6.9

2. Quantum yield, ϕ, is two over the range.
3. No back reaction occurs.
4. The theoretical voltage is 0.21 v.

By use of Eq. 3,

$P = 9500$ microwatts/cm^2 or 95 watts/$meter^2$

Overall Theoretical Efficiency - The overall maximum efficiency of conversion solar energy into electrical energy can be calculated from the above value as follows:

$$\%\ Efficiency = \frac{\text{chemical power available from conversion power from incident solar radiation}}{} \times 100$$

For the range 2150-6300 A the incident power is about 560 watts/m^2. The efficiency of nitrosyl chloride is, therefore:

$$\%\ E = \frac{95}{560} \times 100 = 17\%$$

Considering the entire solar spectrum, 1400 watts/m^2, the efficiency is about 7%. The rest of the energy is lost as heat.

Practical Application — Regeneration Process

The photodissociation of nitrosyl chloride can be carried out in either the gaseous state, liquid state, or as a solution in an inert solvent (7).

Photolysis of liquid nitrosyl chloride presented several important advantages. It was more compact than the other systems. Only a 1/4 in. absorbing layer was needed, compared to several inches for gas. It also had a built in separation device. Nitric oxide produced during irradiation was insoluble, and thus would bubble off as a gas leaving the chlorine behind in the liquid.

However, it was found that irradiation of the pure liquid, or liquid dissolved in inert solvents, was impractical because of the rapid rate at which the decomposition products recombined.

The rate of recombination, after irradiation of gaseous nitrosyl chloride, was found to be much slower. Fig. 2 shows Cary spectrophotometer curves indicating the rate of formation of nitrosyl chloride from photochemically produced nitric oxide and chlorine. These rates mean that there will

be a practical period of time in which to separate the products. We have actually separated nitric oxide amounting to 10% of the nitrosyl chloride present, but this is not considered a max. We have decomposed as much as 80% after a brief illumination with sunlight, but we did not attempt separation in this case.

Separation of Products - Separation of vapor phase products will be a little more cumbersome than from a liquid irradiation. However, several methods are available, including: Compression and condensation, absorption by an inert solvent, or absorption of chlorine by a reactive solvent from which it can be later separated. Some recombination will probably occur in all these processes.

Production of Power from Photolysis Products - Previous investigators who have considered using nitrosyl chloride as a means of producing storable chemical energy from sunlight, proposed to combine chlorine and nitric oxide thermally to drive a heat engine. A relatively low heat reaction and a high rate of thermal dissociation would cause the available temperatures to be quite low, probably much less than 400 C.

The present study has undertaken a new approach, namely, the direct conversion of chlorine and nitric oxide on the electrodes of a fuel cell. This removes the Carnot efficiency limitation and makes possible the use of a low energy reaction which might otherwise be impractical.

To the best of our knowledge, a fuel cell operating on these fuels has not been attempted before. It may be that the low cell voltage looked too unpromising or that a suitable electrolyte was lacking.

Actually, however, liquid nitrosyl chloride is rather unique in its ability to act as an ionizing solvent for the fuel cell electrolyte. Its action is somewhat like that of water in the hydrogen-oxygen fuel cell.

Fig. 3 is a simplified schematic of a one cell fuel cell operating on gaseous chlorine and nitric oxide. The electrolyte is aluminum chloride which reacts with nitrosyl chloride to form conducting ions as follows (8):

$$NOCl + AlCl_3 \longrightarrow NO^+ + AlCl_4^-$$

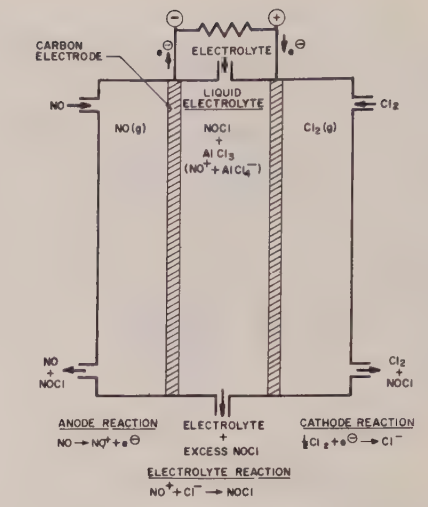

Fig. 3—Nitrosyl chloride fuel cell

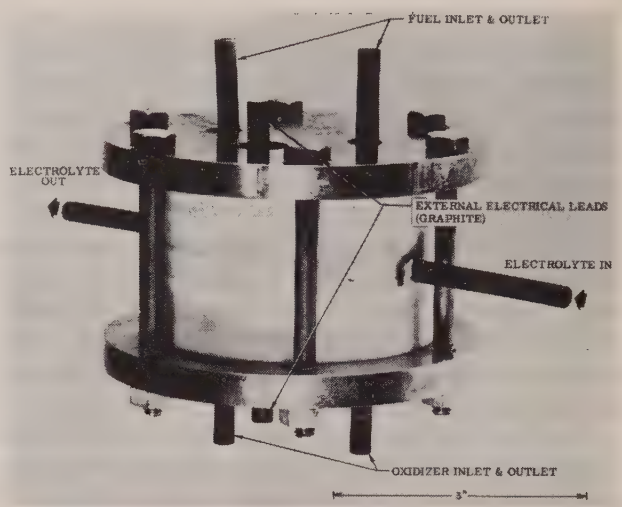

Fig. 4—Nitrosyl chloride fuel cell—Model No. 3, Teflon

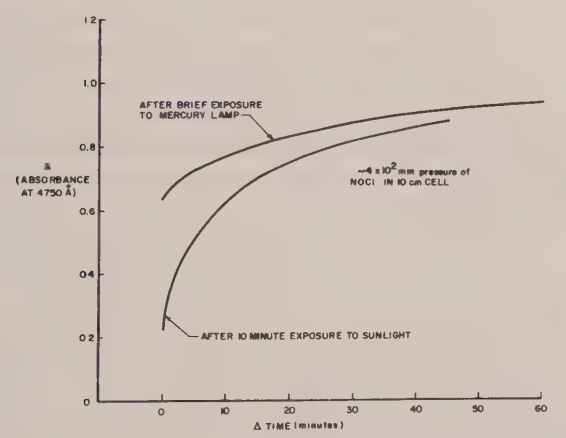

Fig. 2—Back reaction from NOCl photolysis, $2NO(g)+Cl_2=2NOC(g)$. (Absorbance of sample before exposure and after long period in dark $=A_\infty=1.186$)

In brief, the fuel cell reactions are as follows: nitric oxide ionizes at one electrode by giving up an electron and becoming NO^+; chlorine picks up an electron at the other electrode and becomes Cl^-. The chloride ion immediately reacts with the excess NO^+ ions to form the solvent, unionized NOCl.

Because of the low boiling point of the electrolyte, less than 0 C, the early work on these fuel cells was carried out at -10 C to -20 C. Thus, it was possible to maintain a liquid electrolyte at atmospheric pressure. We were able to obtain the theoretically predicted cell voltage of 0.21 v per cell and to establish to our satisfaction that we really had a fuel cell reaction. However, at these temperatures, currents were vanishingly low.

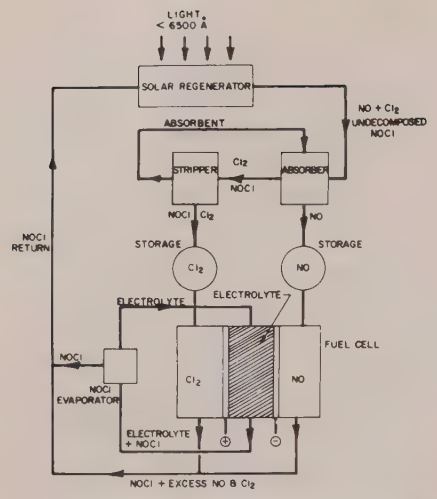

Fig. 5—Solar regenerative fuel cell system

In order to operate at room temperature and pressures up to 100 psig, the rather massive cell shown in Fig. 4 was constructed. The internal construction is quite similar to the schematic (Fig. 3). The high vapor pressure of electrolyte, in addition to its corrosiveness, caused some substantial operating difficulties. It had to be pressurized to at least 30 psig to remain liquid at room temperatures. As nothing was available commercially, there was quite a problem in devising a regulating system which would sense the pressure over the electrolyte and supply nitric oxide and chlorine at an approximately equivalent pressure. Wide variations in pressure would burst the rather fragile carbon electrodes.

As in most fuel cell work, electrode flooding has been a problem in our case also. Although the pressure regulation helps prevent flooding, we do not rely on it entirely.

As this paper was being written, we finally ran some tests on this high pressure, room temperature fuel cell. We were able to produce the theoretical 0.21 v per cell, and were able to get a very encouraging current output. At short circuit, a current density of 7.5 amp/ft^2 was obtained, for a short time, before polarization reduced it, and at 0.1 v, approximately 1.5 amp/ft^2.

We are now in a position to concentrate on the problem of increasing our current output through various improvements in electrode catalysis and conductivity.

System Development

Our next efforts will be directed toward the incorporation of the two separate phases of the study, the solar regeneration and the fuel cell, into a single unit. This will allow actual utilization of nitric oxide and chlorine produced by solar regeneration.

A functional schematic of such a system is shown in Fig. 5. Light is absorbed in the regenerator where part of the gaseous nitrosyl chloride is decomposed into chlorine and nitric oxide. The gases then pass into the scrubber where chlorine and unreacted nitrosyl chloride are absorbed in a nonvolatile solvent. Nitric oxide passes through to storage or the fuel cell. In the stripper, heat is applied to drive chlorine and nitrosyl chloride out of the solvent. These gases then also pass to storage or to the fuel cell. In the fuel cell, nitrosyl chloride is produced as previously discussed. Excess nitrosyl chloride, which dissolves in the electrolyte, is removed in the evaporator and sent to the regenerator. The concentrated electrolyte passes back to the fuel cell.

Summary and Conclusions

This paper has presented a brief background of the theoretical aspects of a solar regenerative fuel cell system which is based on the photochemical decomposition of nitrosyl chloride. Some of the experimental results have been described. Although the work is still in the laboratory stages, it is felt that the system shows great promise. The production and separation of significant amounts of nitrosyl photolysis products, and the demonstration of a new type of fuel cell which can operate on these products, makes further research and development both interesting and worthwhile.

References

1a. J. G. Calvert, "Photochemical Processes for Utilization of Solar Energy," Ohio J. Sci., Vol. 53 (1953), 293.

1b. J. G. Calvert, chapter in "Introduction to Solar Energy," A. M. Zaerm, editor, New York: McGraw Hill Publishing Co.

2. G. B. Kistiakowsky, "Photochemical Decomposition of Nitrosyl Chloride," J. Amer. Chem. Soc., Vol. 52 (1930), 102.

3. Daniel Friedman, NRL Memorandum Report 1005, December, 1959.

4. C. R. Bailey and A. B. D. Cassie, "Investigations in the Infrared Region of the Spectrum X. The Asymmetric Molecule Nitrosyl Chloride, NOCl," Proc. Roy. Soc., London, Vol. A 145 (1934), 336-344.

5. C. F. Goodeve and S. Katz, "The Absorption Spectrum of Nitrosyl Chloride," Proc. Roy. Soc., London, Vol. A 172 (1939), 432.

6. G. L. Natanson, "On the Mechanism of Photodecomposition of NOCl," Acta Physiocochimica URSS, Vol. 11 (1939), 521-536.

7. Otto S. Neuwirth, "The Photolysis of Nitrosyl Chloride and the Storage of Solar Energy," J. Phys. Chem., Vol. 63 (1959), 17.

8a. A. B. Burg and G. W. Campbell, Jr., "Liquid Nitrosyl Chloride as an Ionizing Solvent," J. Amer. Chem. Soc., Vol. 70, 1964-1965.

8b. A. B. Burg and D. E. McKenzie, "Further Studies of Nitrosyl Chloride as an Ionizing Solvent," J. Amer. Chem. Soc., Vol. 74 (1952), 3143-3147.

Fatigue, Impact, and Tensile Properties of High Strength Leaded and Nonleaded SAE 4140 Steel

William Simon
Westinghouse Electric Co.

USE OF LEADED, free-machining steels has expanded considerably in the last decade. Practically any of the standard SAE alloy steels can now be obtained as leaded, free-machining grades.

Since most service failures are the result of metal fatigue, it follows that the fatigue strength of these leaded grades is of particular interest, especially for applications which involve high magnitude stresses of a cyclic, repetitive nature. In this paper, the fatigue strength, or endurance limit, is defined as the limiting stress, psi, at or below which a metal will withstand an indefinitely large number of stress cycles without failure.

The impact properties of a steel grade are of interest for applications such as gears which require that a part have the ability to absorb, without failure, a definite amount of impact energy. Also, the propensity of the steel grade to fail in a brittle manner can be determined by impact testing.

Very little quantitative data have been published to date regarding the fatigue strengths and impact properties of leaded alloy steels at high strength levels. A meager amount of published work has dealt with the fatigue properties of SAE 4140 steel at ultimate strength levels up to 170,000 psi. Ordinarily, steels are considered to have a constant fatigue strength ratio which is defined as the ratio of fatigue strength to ultimate strength, expressed as per cent, and which varies from 35-55%, depending upon the steel grade. However, the fatigue strength ratio decreases with increasing ultimate strengths regardless of the type or grade of steel tested, although the rate of decrease will vary for different grades.

Westinghouse uses a considerable amount of SAE 4140 steel at high strength levels for gears and pinions for various applications. The substitution of a free-machining leaded alloy steel for these applications would be highly desirable from an economic viewpoint, but stringency of the application requires that any material which is used as a substitute have transverse fatigue and impact properties comparable to those of high strength conventional SAE 4140 steel. The investigation discussed in this paper was conducted to ascertain the practicality of substituting a leaded free-machining SAE 4140 steel for the conventional grades for such applications.

The investigation consisted of:

1. Fatigue testing leaded and non-leaded SAE 4140 steel at hardness levels of 55 and 47 RC to determine endurance limits.
2. Charpy V-notch impact testing the same materials at a hardness level of 47 RC to determine impact properties within a range of temperatures between -200 F and +250 F.
3. Additional Charpy V-notch impact tests on the two steel grades to determine the relationship of room temperature impact strength and tempering temperature between 425 F and 775 F.
4. Tensile tests of leaded and non-leaded specimens at two hardness levels, 55 and 47 RC.

These hardness levels, 55 and 47 RC, imply an ultimate strength of 285,000 and 220,000 psi, respectively, as derived from the relationship between hardness and ultimate strength of steel. All of the tests, except where noted, were made using specimens whose lengths were transverse to the rolling direction.

The following conclusions were made as a result of the investigation.

1. The differences in the transverse fatigue, impact, and tensile properties between leaded and non-leaded SAE 4140 alloy steel at hardness levels of 55 and 47 RC are insignificant for normal applications.
2. The transverse fatigue, impact, and tensile strength properties of high strength leaded and non-leaded SAE 4140

alloy steel are considerably lower than the corresponding longitudinal properties.

3. The low transverse properties are caused by inclusions which are commonly found in commercial grades of SAE 4140 alloy steel. These inclusions act as stress-raiser notches and have their major effect in the transverse direction.

As a result of the conclusions noted above, the following recommendations were made.

1. Gears, pinions, and other similar parts which are loaded in the transverse direction should be designed on the basis of transverse properties such as those which are reported in the text of this investigation.

2. A grade of steel which is less notch sensitive than SAE 4140 steel, possibly SAE 4340 steel, or a cleaner grade of steel such as vacuum melted SAE 4140 or 4340 steel, should be used for gear and pinion applications which are heavily loaded in the transverse direction.

Details of Investigation

The two bars used for the investigation were obtained as 1 ft lengths of 6 in. diameter, hot rolled and annealed, leaded and non-leaded SAE 4140 steel. The chemical composition of the two bars were reported by the supplier to be within normal limits for the two grades. (See Table 1.)

Table 1 - Composition of Test Bars

	Leaded Ht. No. 45204 (%)	Non-Leaded Ht. No. 29678 (%)	Specified by SAE 4140 (%)
Carbon	0.45	0.43	0.38/0.43
Manganese	0.83	0.93	0.75/1.00
Phosphorus	0.019	0.018	0.04 max
Sulphur	0.026	0.032	0.04 max
Silicon	0.28	0.30	0.20/0.35
Chromium	0.85	1.04	0.80/1.10
Molybdenum	0.17	0.21	0.15/0.25
Lead	0.15/0.35	--	---
Iron	Remainder	Remainder	Remainder

The McQuaid-Ehn grain size of both heats was ASTM No. 6 to No. 8; the Westinghouse specification specifies that the grain size shall be ASTM No. 5 or finer.

Slices 3/4 in. thick were sawed from the 6 in. diameter bars. Fatigue, impact, and tensile specimens were rough blanked transversely from the various slices, as shown in Fig. 1, which also describes the method of identifying the various specimens.

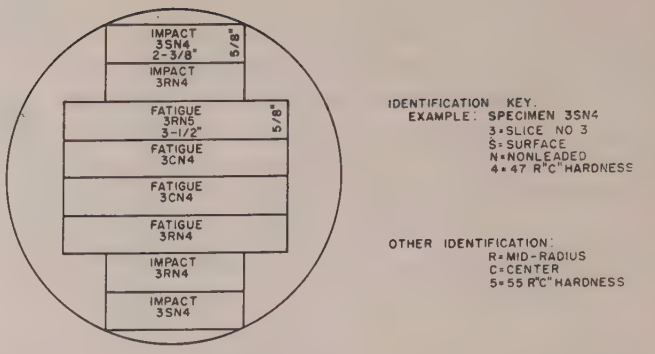

Fig. 1 — Manner of rough blanking and method of identifying fatigue and impact specimens from slices ¾ in. thick and 6 in. in dia

The impact and tensile specimen blanks were finish-machined or ground (except where noted) after which they were heat treated in an inert atmosphere. The fatigue specimen blanks were rough-machined, heat-treated, then finish ground as smooth-bar R.R. Moore rotating beam fatigue specimens. All specimens were subjected to fluorescent magnetic particle inspection prior to testing to ensure that none were cracked before testing.

The specimens from each heat intended for fatigue tests were heat treated to two hardness levels, 47 and 55 Rc. Table 2 lists the hardness, after finish grinding, of each heat-treat-

Table 2 - Hardness of Leaded and Non-Leaded SAE 4140 Steel Fatigue Specimens After Heat Treatment

Leaded Hardness		Non-Leaded Hardness	
R 45N	RC	R 45N	RC
50	46	51	47
51	47	52	48
51	47	51	47
51	47	50	46
51	47	51	47
51	47	50	46
51	47	52	48
52	48	50	46
59	54	58	53
61	55	61	55
61	55	61	55
61	55	62	56
61	55	60	54
62	56	60	54
62	56	61	55
62	56		

ed fatigue specimen as determined with a Rockwell Superficial Hardness Tester using the 45N scale. The conversions from 45 N to RC are also listed for convenient reference. After finish grinding, the four series of leaded and non-leaded steels were fatigue tested at various stress levels to determine the endurance limit of each. The endurance limit criterion was set at 100,000,000 cycles. This criterion is not uncommon for high strength steels and is practical for Westinghous applications. Table 3 lists the fatigue test results for each specimen. Endurance limit curves for each series are plotted conventionally in Figs. 2 and 3 on semi-log paper as stress versus cycles to failure. Specimens which endure 100,000,000 stress-cycles without failure are assumed to be capable of operating indefinitely at the specified load.

Table 3 - Transverse Fatigue Test Results for Leaded and Non-Leaded SAE 4140 Steel at Two Hardness Levels

Stress psi	Cycles	Stress psi	Cycles
Leaded		Non-Leaded	
		47 RC	
154,000	5,000	154,000	9,000
90,475	21,000	88,000	32,000
88,000	29,000	90,426	65,000
66,000	114,000	66,000	272,000
53,000	115,000	60,000	730,000
55,000	427,000	44,000	103,200,000
44,000	107,200,000	57,000	109,179,000
50,000	110,000,000	55,000	119,578,000
		55 RC	
151,000	3,000	160,000	5,000
80,000	45,000	130,000	10,000
50,000	187,000	110,000	34,000
54,000	2,919,000	80,000	295,000
50,000	10,646,000	54,000	7,956,000
43,000	14,084,000	52,000	101,076,000
46,000	52,954,000	50,000	105,945,000
38,000	132,260,000		

Fig. 2 shows that the non-leaded SAE 4140 steel, at a hardness of 47 RC, has an endurance limit of 58,500 psi in the transverse direction. The same graph shows that the comparable leaded steel has a lower endurance strength of 51,500 psi. Similarly, the curves in Fig. 3 show that the non-leaded SAE 4140 steel, at a hardness of 55 RC, has an endurance limit of 53,000 psi in the transverse direction as compared to 44,000 psi for the leaded steel.

Fig. 4 contains photomicrographs which show the relative

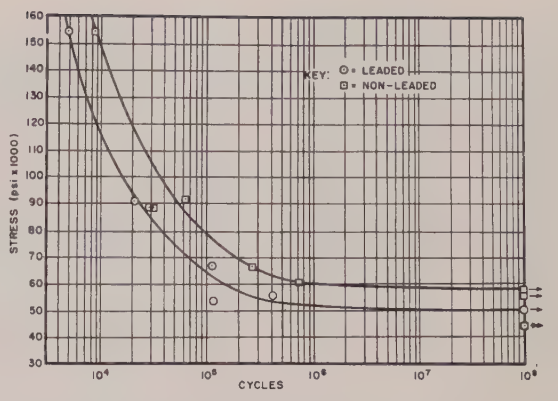

Fig. 2 — Endurance limit curves as determined from transverse tests for leaded and non-leaded SAE 4140 steel heat treated to 47 RC hardness

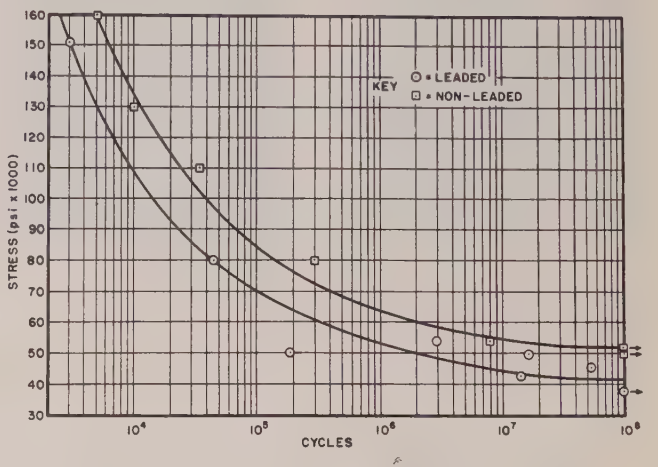

Fig. 3 — Endurance limit curves as determined from transverse tests for leaded and non-leaded SAE 4140 steel heat treated to 55 RC hardness

cleanliness of the leaded and non-leaded steels used in this investigation, and the microstructures of each after heat treating to a hardness of 55 RC. Both steels are relatively "dirty," mainly because of silicate inclusions. The microstructure of both samples is tempered martensite.

The impact specimens intended for testing at various temperatures were heat treated to a hardness of 47 RC. The results of the impact tests are shown in Table 4. Since both steels showed extremely poor impact strength at even relatively high temperatures (4 to 5 ft-lb at +250 F), it was not considered worthwhile to plot the data. The average difference in impact strength between the leaded and non-leaded steel is very slight: only about 1/2 ft-lb, at each temperature, in favor of the non-leaded steel.

All of the impact specimen fracture faces were examined fractographically at magnifications up to 500 times. Surprisingly, everyone was found to be practically 100% shear. Shear fractures are usually ductile but not so in this case. In every instance, the lack of ductility and the inability to plastically deform, even at +250 F, was substantiated by little

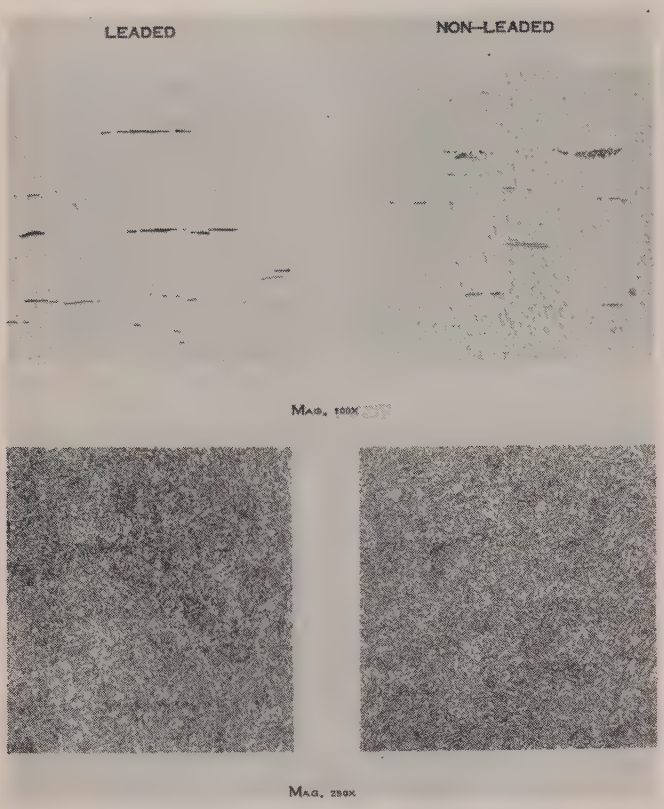

Fig. 4 — Composite photomicrograph showing cleanliness and microstructure at 55 RC

Table 4 - Charpy V-Notch Impact Test Results on Leaded and Non-Leaded SAE 4140 Steel at 47 RC Hardness

Testing Temp. F	Impact Strength (Ft-Lb) Leaded	Non-Leaded
-200	2.0, 2.5	1.5, 2.0
-60	2.0, 2.0	2.0, 2.5
80	3.5, 3.5	4.0, 4.5
150	3.0, 4.0	3.5, 5.0
250	4.5, 6.0	4.0, 4.0

or no visible lateral contraction in the notch areas of the impact specimens (see Fig. 5).

The impact specimens intended for room temperature tests after tempering at various temperatures were heated for hardening in a salt bath, oil quenched, and tempered in a protective atmosphere. Three specimens of each steel were tempered at each temperature. Table 5 lists the hardness and room temperature (89 F) impact strength of each specimen after tempering at each temperature. The data show that the two steels are equal in their response to tempering. The drop in hardness with increasing tempering temperature is

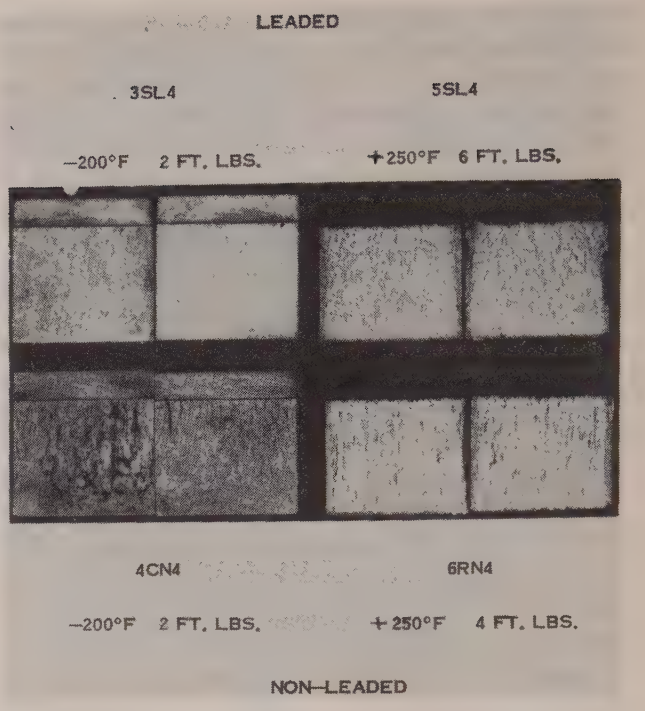

Fig. 5 — Fracture faces of charpy V-notch specimens

very gradual and amounts to 7 RC points over a range of 300 F (475 to 775 F). The table also shows that the maximum average difference in the ability to absorb energy for specimens tempered at the same temperature is less than 1 ft-lb. The maximum increase in absorbed impact energy obtained by tempering at 775 F as compared to 475 F was about 2 ft-lb for each steel. Visual examination of the impact specimen fracture faces again showed the anomaly of essentially 100% shear fractures with very little visible lateral contraction.

Two 0.505 in. diameter tensile specimens were rough machined from each material in the transverse direction and then heat treated so that one specimen from each steel was 47 RC and the other was 55 RC. After heat treatment, the specimens were finish ground in the conventional manner and tensile tested. The results are shown in Table 6. Note that none of the specimens developed the ultimate strength which the hardness of these steels imply, according to conversion tables. There was little or no ductility as measured by the elongation and reduction of area results.

The four fractured tensile specimens were examined visually and metallographically to determine the characteristics which caused such poor results. The specimens had all fractured in an unacceptable manner: the two leaded specimens showed quarter breaks, and the two non-leaded specimens fractured in the fillet. All four fractures were flat, striated, and pithy in appearance. There were no indications of any flaws in the specimens. Metallographically, the tensile specimens appeared normal with respect to structure

Table 5 - Hardness and Impact Strength at 89 F of Leaded and Non-Leaded SAE 4140 Steel Charpy V-Notch Impact Specimens after Tempering

Tempering Temp. F	Impact Strength (Ft-Lb)	Hardness RC	Impact Strength (Ft-Lb)	Hardness RC
475	4.5	48	3.5	50
475	3.0	50	3.5	49
475	3.0	50	3.5	50
525			3.5	50
525			3.5	48
525			4.0	49
575			3.5	48
575			4.0	49
575			4.5	49
625	5.5	46	4.0	47
625	3.5	46	5.0	46
625	3.5	46	4.5	46
675	4.0	47	2.5	46
675	4.0	48	5.0	46
675	4.0	47	4.0	47
725	5.5	43	5.0	43
725	5.0	44	4.5	43
725	6.0	44	4.5	47
775	4.5	43	6.0	44
775	6.0	44	5.5	43
775	4.0	44	5.5	43

Table 6 - Transverse Tensile Test Results of Conventionally Machined and Ground Specimens

Specimen	Hardness RC	Ultimate Strength psi	Yield Strength psi	Elongation, %	Reduction of Area %
Leaded	47	135,500	--	--	--
Non-Leaded	47	174,750	--	0.6	0.4
Leaded	55	183,000	--	1.2	0.8
Non-Leaded	55	211,450	209,700	1.0	0.4

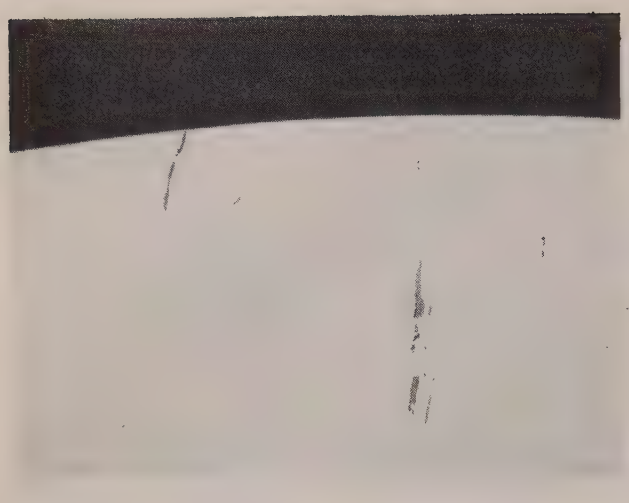

Fig. 6 — Inclusion at surface of transverse fatigue specimen

Two additional transverse and two longitudinal specimens were machined from the same two steels previously described. After rough machining and heat treating the specimens to the same hardness levels previously investigated, the eight specimens were very carefully finish ground as button head tensile specimens and then hand polished to remove any trace of surface marks or scratches. The specimens were tested in an FGT SR-4 Universal Testing Machine. Two SR-4 strain gages were mounted diametrically opposite on each specimen during testing so that the amount of misalignment could be measured from the difference between loads on each side of the specimen at any measured strain. The maximum deviation on any specimen was 6% of the measured strain, a very low value. The results are tabulated in Table 7.

Note that the very carefully prepared and tested longitudinal tensile specimens did reach the ultimate strength levels expected from the conversion of hardness data. Note also

Table 7 - Tensile Test Results of Specially Finished and Carefully Aligned Longitudinal and Transverse Specimens

Specimen	Hardness RC	Ultimate Strength psi	Yield Strength psi	Elongation, %	Reduction of Area %
Longitudinal Leaded	47	222,000	210,000	7.6	46.4
Longitudinal Non-Leaded	47	220,000	206,000	6.8	47.7
Transverse Leaded	47	169,150	126,100	2.8	6.5
Transverse Non-Leaded	47	166,100	125,850	3.5	3.3
Longitudinal Leaded	55	272,500	245,500	5.8	36.6
Longitudinal Non-Leaded	55	269,000	228,000	7.9	45.2
Transverse Leaded	55	180,450	117,400	2.8	8.9
Transverse Non-Leaded	55	169,150	115,200	3.5	6.5

(tempered martensite) and absence of decarburization; but in the "as polished" condition, both specimens contained inclusions, some at the specimen surface extending into the specimen for a depth of 0.0025 in. (see Fig. 6).

It is well known that conventional tensile specimens of steel at very high strength levels are so susceptible to machining marks and slight misalignment during testing that, unless extreme precautions are taken during machining and testing, the specimens will usually fail prematurely during testing. This prevents accurate evaluation of the strength and ductility properties.

The inability of the transverse tensile specimens to achieve any significant ductility or the theoretical ultimate strength made the above a possibility in this case. In order to determine the validity of the data and, also, to obtain more information, a new series of tensile specimens was prepared. that the transverse specimens which were prepared and aligned with equal care are still very much lower in ultimate strength than is indicated by their hardness.

The test results confirm that ductility in the transverse direction at comparable strength levels is quite low and insignificantly different for both the leaded and non-leaded AISI 4140 steel even under the best of laboratory testing conditions. The longitudinal elongation results are about twice as high as the transverse results: 7% in 2 in. as compared to 3%. The longitudinal ductilities of the leaded and non-leaded steels show no significant difference.

Discussion of Results

The fatigue ratio of any steel is usually expressed as the ratio of endurance limit to ultimate strength of the steel.

Quite often, especially for ultra high strength steels, the value for ultimate strength is obtained from a hardness conversion because tensile testing is costly due to the extreme care required in testing steel at high strength levels. This use of the hardness relationship to determine the fatigue ratio of certain steels at ultra high strength levels is not valid if tests are made in the transverse direction because, as shown by this investigation, the conventional relationship between hardness and ultimate strength does not always apply to tensile tests oriented in the transverse direction. For instance, both the leaded and non-leaded SAE 4140 steels of this investigation, at a hardness of 55 RC, had ultimate strengths of about 270,000 psi when tensile tested longitudinally but only about 170,000 psi when tested transversely. Any fatigue ratios expressed for transverse test results can be very misleading unless tensile tests have established that the longitudinal and transverse tensile properties for the steel tested are essentially the same. A sample calculation will illustrate this point. The longitudinal tensile test results in Table 7 show that leaded steel at a hardness of 55 RC had an ultimate strength of 272,500 psi while the transverse test result was only 180,450 psi. The transverse fatigue strength of the leaded steel at 55 RC is shown in Fig. 3 as 44,000 psi. The transverse fatigue ratio is, therefore,

$$44,000/180,450 \times 100 = 24.5\% \quad (1)$$

Some investigators cite the transverse fatigue strength not percentage ratio of transverse fatigue strength to longitudinal fatigue strength.

The inability of the steels used in this investigation to develop their theoretical strength during transverse tensile tests is probably the result of inclusions elongated in the rolling direction so that they act as stress-raising notches when transverse specimens are tested. The same stress-raiser notch effect is, no doubt, responsible for the low fatigue strength values obtained and the extremely poor impact test results. This conclusion concerning the effect of inclusions in the transverse direction is validated by the data obtained during tensile testing of longitudinal and transverse specimens with misalignment and surface flaws eliminated as factors.

In the past, transverse tensile tests made by the author on SAE 4140 steel, leaded and non-leaded, at a tensile strength of 120,000 psi resulted in elongation and reduction of area values of 5-7% and 10-14%, respectively. Normal longitudinal values at this strength level are 16 and 50% minimum, respectively.

Fatigue tests conducted by Prof. A. P. Taber of Syracuse University Research Institute on longitudinal and transverse specimens of SAE 4340 steel (essentially SAE 4140 with 2% nickel added), heat treated to a hardness of 55 RC, showed that longitudinal fatigue strength was 101,000 psi but only 74,000 psi in the transverse direction. It is evident that normal heats of conventionally produced alloy steel are extremely sensitive to the effects of inclusions when tested in the transverse direction after being heat treated to high strength levels.

The conclusions drawn are of great practical significance for applications where high strength parts are loaded transversely and are subjected to fatigue or impact loading. Namely, all the design calculations for transversely loaded pinions and gears should be made on the basis of transverse properties unless it has been experimentally demonstrated that the transverse properties of the material being used do not differ significantly from the longitudinal values.

Since the effect of inclusions is the controlling factor on the transverse properties of SAE 4140 steel, it is obvious that improvement can only be attained by the use of steel which has a minimum number of harmful inclusions. Steel suppliers will not make this grade of steel on an inclusion count basis. It would appear that the best possibility for improvement lies in the use of a steel which has inherently better transverse properties. The previously quoted results of A. P. Taber indicate that significant improvement could be obtained by the use of SAE 4340 steel. A test program similar to this one would have to be conducted to determine if the improvement applied also to leaded SAE 4340 steel. Another alternative for obtaining better and more consistent transverse mechanical properties would be to use vacuum melted alloy steels of the SAE 4140 or SAE 4340 grades which are now commercially available. It has been reported in the literature that vacuum remelting of an SAE 4340 steel resulted in an improvement in the ratio of transverse to longitudinal fatigue strength from an original value of 61 to 81% at a hardness of 41 RC.

It has been stated in the literature of leaded steel producers that leaded steel with an ultimate strength of 165,000 psi suffers a reduction of 5-10% in fatigue ratio as compared to the same steel non-leaded. Similarly, the reduction at an ultimate strength level of 260,000 psi has been reported to be as high as 20%. The data of this work and other work by myself and other investigators show that the drop in fatigue ratio due to the addition of lead is zero at 110,000 psi ultimate strength, 5% at 165,000 psi ultimate strength, 10.7% at 47 RC hardness, and 16% at 55 RC hardness. Although this 16% difference appears to be a considerable variance, in actuality, it amounts to a stress level difference of about 9000 psi. This amount of difference could be significant only in applications in which the material is stressed almost to the endurance limit, or in applications involving very high operating stresses for a lesser number of cycles.

The transverse impact tests showed that neither the leaded nor the non-leaded SAE 4140 are subject to brittle cleavage failure even at testing temperatures of -200 F. However, both steels will fail by brittle shear fracture even at +250 F if the principal stresses are in the transverse direction. The mode of failure (cleavage or shear) makes little difference

as long as both are completely brittle. The unusual feature of a 100% shear fracture without any ductility or deformation occurring during fracture was previously mentioned. It is obvious that service temperature and transition temperature are not important factors for either the leaded or nonleaded steel. The important consideration for gearing applications is that when transverse properties are critical, the design stresses, regardless of whether they are torsional, impact, or tensile, must be calculated with the low limits of the transverse properties as a basis for safe design.

Difficulties of Applying Research Studies to Engineering Practice

Dr. H. E. Merritt
Consulting Engineer

GEAR ENGINEERING, for new design work, is based largely upon analysis of past and current practice, and is essentially empirical. For example, gear engineers avoid making highly stressed pinions from bar stock, recognizing by experience and intuition the lower transverse properties to be expected.

In striving to put gear design upon a more absolute basis, one seeks to make use of test data such as those presented by the author. The most important aspect is that of fatigue, and it is unfortunate that, out of the mass of literature on the subject, fatigue data directly applicable to gear design are meager in the extreme. The properties of case-hardened and machineable steels used in the industrial field have been less studied.

It is generally recognized that comparable values of the fatigue strengths of different materials when used for a particular component, can be obtained only by using test pieces of substantially similar form and stress-pattern to the component in question. To the gear engineer, the wide-spread use of the rotating-beam fatigue test has been most unfortunate. Gear-teeth operate in plane bending, usually nondirectional, and in the writer's experience the results obtained from rotating beam tests differ so markedly from those obtained under plane bending tests on gear-tooth specimens that they must be rejected as a basis for design. This does not invalidate the author's comparative data on leaded and nonleaded forms of the same basic steel, but it limits somewhat their use as design criteria.

Another regrettable circumstance in the literature is the varied practice in plotting fatigue data by S-N curves. Some use a semi-log plot, as the author does; others use a log-log plot. Several practical advantages attend the latter. For steels in general, a log-log plot gives a closer approximation to a straight line, and its equation can be written down; its slope is a very significant factor in design, although just what it signifies still remains in doubt. In designing short-life gear sets, stressed with variable cyclic amplitude above the endurance limit, a log-log plot can be used very conveniently in association with Miner's law of cumulative fatigue damage.

Another comment is that it is quite rare to encounter gear applications which will be subjected to true impact loading, as distinct from suddenly-applied loading. Consequently, impact values can generally be ignored except, in particular cases which indicate abnormality in the steel.

A growing problem, in a world of ever-increasing application, is to bridge the gap between research studies and engineering practice. It is from this point of view that the foregoing observations are offered.

Cures for Powerplant Bending Noise Problems

R. H. Bollinger, and J. H. Ruhl
Ford Motor Co.

IN THE PAST YEARS, a number of vehicle noise and vibration problems have been encountered at Ford Motor Co. which have been classified as powerplant bending. Contacts with vibration engineers from other automotive companies have indicated that all vehicles equipped with conventional Hotchkiss or torque tube drivelines are prone to this malady. Powerplant bending is the vibratory bending or beaming of the structure formed by the engine block, clutch housing, transmission, and transmission-extension. The bending occurs primarily in the vertical plane as described by Fig. 1. It may be difficult to conceive that this structure, which appears so rigid, could bend; but when these rigid structures vibrate at their resonant frequencies in the vicinity of 100 cps, amplitudes of vibration approaching a maximum value of 25/1000 in. are attained. Structural fatigue problems attributable to this phenomenon have never been experienced but it can produce one or more critical speeds at which the car is disagreeably noisy.

This problem was noticed originally in 1949 on the first postwar Ford to use a Hotchkiss drive. Following this early experience with powerplant bending, major model changes have sometimes produced new versions of the same problem.

After first encountering powerplant bending, it was observed that the vibration response of the powerplant alone is altered when combined with the driveshaft. Driveshaft whip speed (critical speed) studies made concurrently revealed that whip speed was influenced by the vibration response of both the powerplant and rear axle carrier. The obvious conclusion was that both powerplant bending and whip speed were manifestations of bending vibrations of the complete drivetrain or powertrain (see Fig. 2).

Since the greatest potential for structural changes is possible in the powerplant assembly and since changes to the powerplant usually strongly influence the response of the complete drivetrain, this presentation will concentrate on the structural group of the engine block, clutch housing, transmission and transmission extension.

An extensive survey of past literature has disclosed no solutions to the problem of powerplant bending, although this subject is mentioned by several authors. Therefore, the major objective of this presentation is to describe known methods of identifying and curing noise problems arising from powerplant bending.

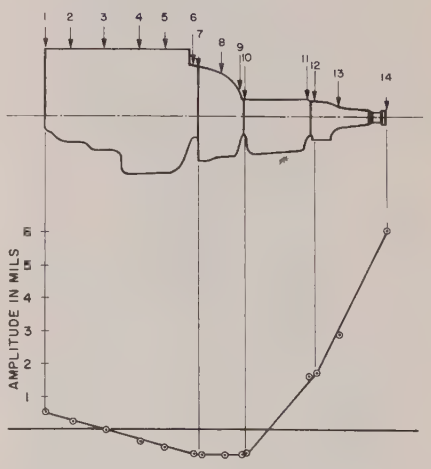

Fig. 1 — Powerplant bending

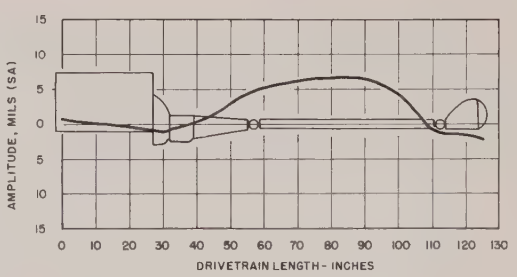

Fig. 2 — Drivetrain bending

Identification of Powerplant Bending

In the development of a passenger car it is necessary to build and test many experimental prototypes. These prototype vehicles are usually subject to much more noise and vibration than the final design. When the car is accelerated at wide-open-throttle up through its speed range, its interior total noise level will generally increase as the car speed increases as shown by Fig. 3. This graph also shows that the noise level will peak at certain speeds. For the

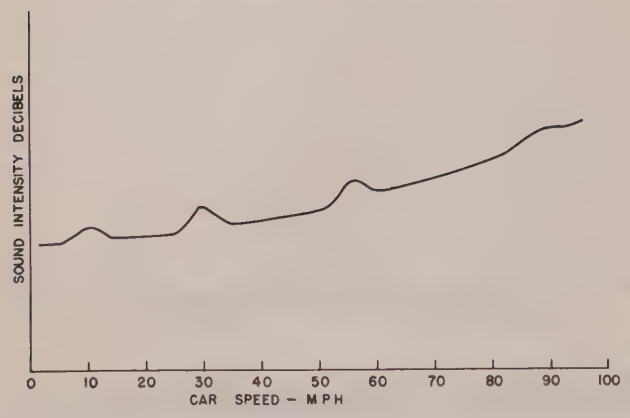

Fig. 3 — Car interior noise, wide open throttle acceleration

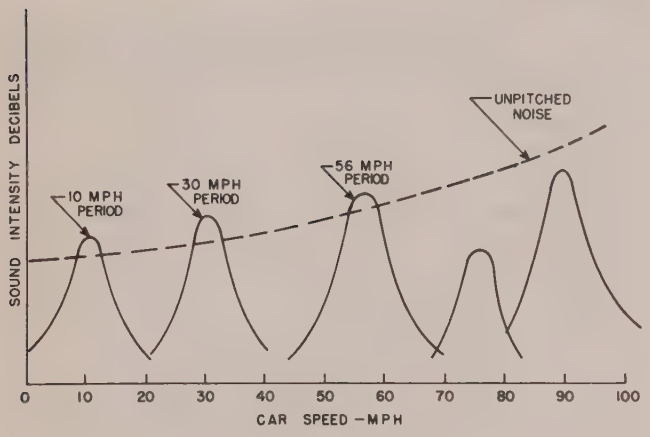
SOUND INTENSITY DECIBELS
10 MPH PERIOD
30 MPH PERIOD
56 MPH PERIOD
UNPITCHED NOISE
0 10 20 30 40 50 60 70 80 90 100
CAR SPEED – MPH

Fig. 4 — Period noise

purpose of analysis, the components of the total noise are divided into two categories (see Fig. 4):

1. Background noise, comprised of wind, road and machinery noises, which gradually increases with car speed.

2. Pure Tone noise, due to a component resonance, which peaks at certain car speeds.

Automotive engineers refer to the car speeds at which such pure tone noises occur as period speeds and define the tonal sounds as periods. Noise caused by powerplant bending is a period type of noise.

When the vibration engineer receives the prototype vehicle, his first task is to identify the component or component group that is contributing to or influencing each noise. There are four major types of tests or criteria that he can apply to relate the noise to its component group.

1. The frequency (or frequencies) of the noise or vibration.

2. The torque sensitivity of the noise or vibration.

3. The effect of a change to the suspected components.

4. Vibration measurements of the suspected components while the period is being produced.

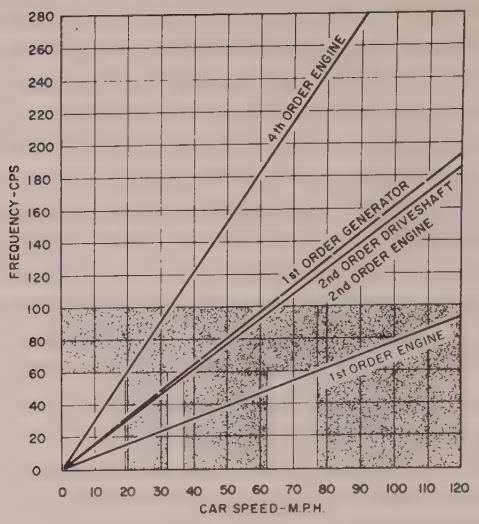
FREQUENCY-CPS
280 260 240 220 200 180 160 140 120 100 80 60 40 20 0
4th ORDER ENGINE
1st ORDER GENERATOR
2nd ORDER DRIVESHAFT
2nd ORDER ENGINE
1st ORDER ENGINE
0 10 20 30 40 50 60 70 80 90 100 110 120
CAR SPEED-M.P.H.

Fig. 5 — Alignment chart

A useful tool for the frequency test is the Alignment Chart shown by Fig. 5. This is a graph of Frequency versus Car Speed for the various possible sources of excitation. Frequencies for 1st, 2nd and 4th order engine, plust 1st and 2nd order driveshaft have been plotted against car speed. These excitation frequencies respectively correspond to engine unbalance, torque variations, firing impulses, driveshaft unbalance and universal joint couples. The generator 1st order has also been plotted, corresponding to generator unbalance, to emphasize that accessories are also possible sources of excitation.

The bending natural frequencies of most drivetrains lie between 60 and 100 cps. A horizontal band has been drawn between these frequencies across the Alignment Chart. From the regions that the excitation frequencies cross through the 60 to 100 cps band, it can be seen that powerplant bending could occur at almost any speed.

The frequency of a noise or vibration can be obtained by analysis of a tape recording of the car interior. For on the spot analysis, however, a battery-operated frequency graduated oscillator and headset may be all that is needed. If the period noise is loud enough, its frequency can be determined by adjusting the oscillator signal to the period frequency. When the two tones are 2 or 3 cps apart, an easily recognizable beat occurs.

The torque sensitivity of a noise or vibration period is the increase or decrease of the period intensity with an increase or decrease of engine torque as the car and engine speed remain essentially unchanged. This can be described graphically using a version of the original graph of noise level versus car speed. (See Fig. 6). When the torque is reduced, the 12 and 30 mph noise peaks disappear and these lower speed periods are defined as torque sensitive. Since the 56 mph noise peak remains at road load and coast, the high speed period is not torque sensitive.

For powerplant bending, torque sensitive forces could

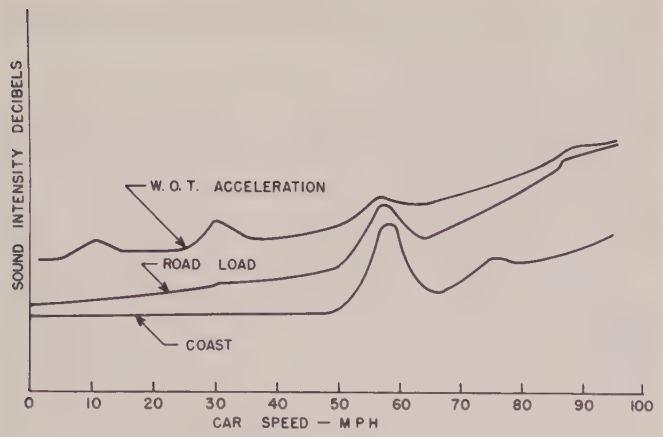

Fig. 6 — Car interior noise

originate from firing impulses, variations of firing impulses (torque variations) and universal joints. The periods caused by unbalance seldom vary with torque.

If a structure change in the drivetrain system produces a change in the intensity of the period or the speed at which it occurs, powerplant bending should be suspected. A routine test is to loosen the lower bolts between the transmission and clutch housing or the clutch housing and engine block. If this influences the period intensity to any extent, powerplant bending is suspected.

With the bump rig facilities shown in Fig. 7, it is possible to measure the vibration of various components on the car at each of the period speeds. For this component vibration identification test, two other criteria must be satisfied:

1. The component vibration must be the same frequency as the period noise.
2. The component vibration must appear and disappear with the period noise (for example, by slightly increasing or decreasing car speed).

For powerplant bending the mode of vibration of the complete drivetrain can be used to define the problem. This is usually the final test for identification. The nonrotating components such as the engine block, clutch housing, transmission, transmission-extension and the rear axle housing can be probed with conventional vibration pickups. Probing along the rotating driveshaft is accomplished by means of the Optron shown in Fig. 8. This device employs a servo-driven beam of light to follow the displacement along the driveshaft, making it possible to measure the driveshaft's deflection while it is rotating.

Vibration Analysis

In general, powerplant noise or vibration is reduced by one or more of the following methods:

1. Reducing the system's response by changing its resonant frequency or increasing its damping.
2. Reducing the input excitation.
3. Isolating the vibration from the body.

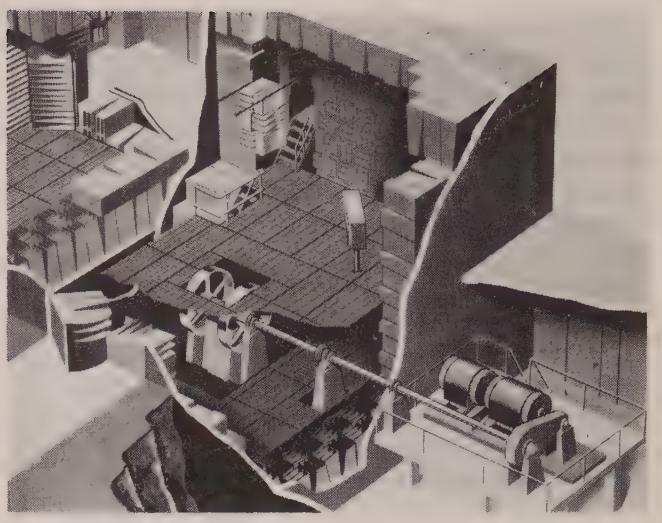

Fig. 7 — Cutaway of bump rig facility

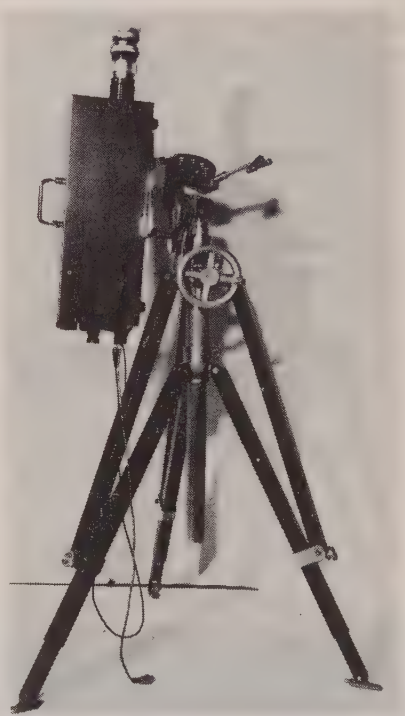

Fig. 8 — Optron for measuring vibratory displacement by servo-driven light beam

The details of these reduction methods are discussed in later sections of this paper. The purpose of this section is to outline the analytical techniques available to study the vibration response of the drivetrain structure.

When analyzing the drivetrain it is convenient to break it down into subsystems of the powerplant, driveshaft and rear axle carrier, as shown in Fig. 9. Analysis of these subsystems and their interaction permits the drivetrain designer to redesign the components to obtain the best drivetrain natural frequencies.

The theoretical techniques available to perform this analysis are beam theory and mobility (or impedance) concepts. These techniques are augmented by digital computors, electro-mechanical shakers, and noise and vibration instrumentation. The effect of driveshaft rotation does not invalidate the beam equations, and the drivetrain structure is generally considered to behave as a beam of irregular cross section.

Mr. Staffeld (6)* demonstrated how to successfully combine beam theory with the digital computer to give the drivetrain modes and bending natural frequencies based only on design information. It is recommended that engineers concerned with the structural design of drivetrain components should make use of the concepts presented or suggested in this excellent paper.

If experimental components are available, an electro-mechanical shaker can be used to obtain their individual, or assembled, vibration responses (see Fig. 10). Care must be taken to closely simulate the conditions of the drivetrain when it is running in the car. For example, with a standard transmission, the axle is normally locked and air pressure is applied to one of the engine cylinders to take the backlash out of the splines and gears.

The subsystems can be vibrated separately to determine their individual junction mobilities. Fig. 11 gives Mobility versus Frequency for a typical powerplant and driveshaft at the front universal joint junction. (For reasons apparent later, the driveshaft values have been multiplied by minus one).

Mobility is defined as the ratio of the vibratory velocity of a system response to an imposed vibratory force. Thus, it is the reciprocal of mechanical impedance and is used to define the response of a mechanical circuit analogous to electrical impedance concepts used for electrical circuits.

From this graph it is found that the bending natural frequencies are 90 cps for the powerplant structure and 130 cps for the driveshaft. The 130 cps driveshaft mode corresponds to a Hinged-Free beam, whose frequency is approximately 55% above the Hinged-Hinged assumptions conventionally used to determine the driveshaft critical frequency. This 55% is constant, however, and the variations of diameter, length and so forth that influence the critical speed vary the Hinged-Free frequency response by the same percent.

Resonance of the complete system occurs when the junction mobility of one subsystem equals the negative of the other. Since, in Fig. 11 this occurs at 82 and 111 cps, drivetrain resonances are expected to occur at these frequencies. With the drivetrain actually assembled, the resonant frequencies were 78 and 108 cps, or within 5% of the predicted frequencies.

Closer examination of Fig. 11 indicates that raising the driveshaft frequency would increase the first drivetrain natural frequency only slightly. That is, to obtain a sizable increase in this particular drivetrain's natural frequency, it would be necessary to first raise the powerplant bending frequency.

*Numbers in parenthesis designate References at end of paper.

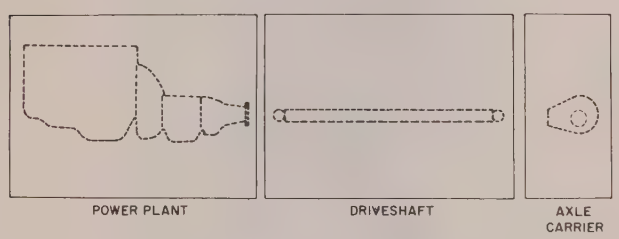

Fig. 9 — Subsystems of a drivetrain

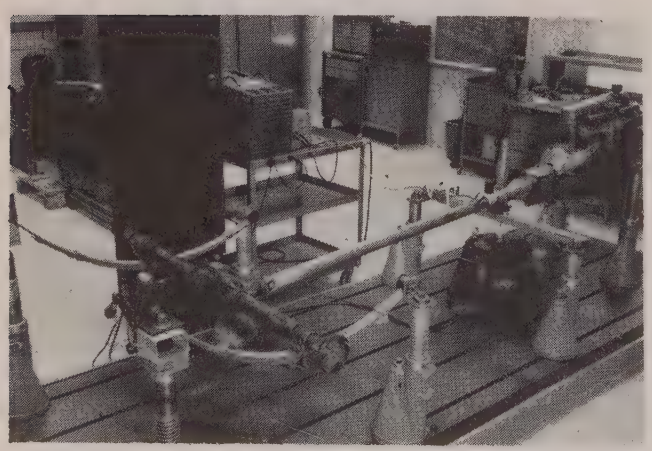

Fig. 10 — Bed plate test set-up to obtain drivetrain vibration response

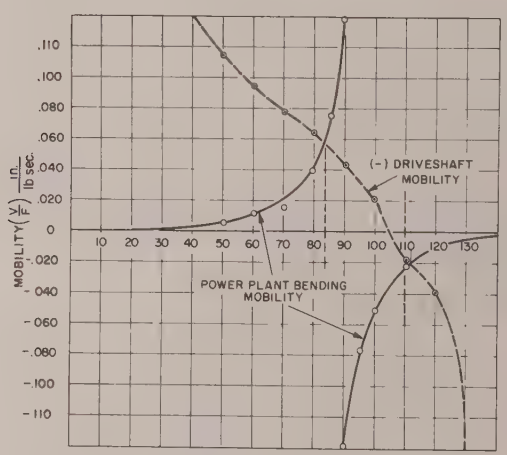

Fig. 11 — Mobility of powerplant and driveshaft at front universal joint

Structural Modifications

One cure for bending would be to increase the drivetrain natural frequency above 320 cps so that the 3rd order engine excitation would not excite this system in the engine speed range. Close examination of the dynamic bending curve (Fig. 1) shows that certain drivetrain components, such as the engine, clutch, and transmission have very small deflections over their lengths and, furthermore, that the joints between these components act somewhat as hinges. Thus, large increases in natural frequencies should be obtained by reducing or eliminating these joint deflections by such means as the gusset used to reinforce the clutch housing to engine block joint shown in Fig. 12. Additional stiffening of individual structural components has little effect on increasing the powerplant bending natural frequency as long as no joint change is made.

It is believed that the following three basic design parameters should be part of future conventional powerplant designs when an increased natural frequency is desired.

1. The slope of the structural bending curves should not change abruptly at the joints.
2. The structural material of the powerplant should be kept as far from the neutral axis and have as few changes as possible in load path direction.
3. Joints should be eliminated when possible by combining adjacent component housings.

These parameters are currently being incorporated into a combined clutch housing, transmission and transmission-extension structure to determine the maximum limitations for this concept. A mockup of this design is shown in Fig. 13.

In rare instances lowering the drivetrain natural bending frequency may be necessary to obtain the desired results. In this case the three design parameters should be ignored or their opposites applied.

Generally, however, the natural bending frequency is made as high as possible. A prime goal is a frequency high enough to keep the first order driveshaft unbalance frequency from exciting the drivetrain in the car's speed range.

Car chassis and bodies are also vibrating systems, responding to powerplant bending vibrations transmitted through the mounts and other connecting members. In some instances car bodies were found to be extra sensitive to powerplant bending vibrations. This extra sensitivity stems from body structure resonances which, because of their proximity to powerplant bending frequencies, reinforce the transmitted vibrations.

To reduce this sensitivity it is necessary to modify the body. Increased rigidity may be achieved by adding new body structural members or strengthening existing members. The mount attachment areas are particularly critical. Moving the mount bracket to a different transverse location has on occasion produced measurable improvements.

Panel deadening may also provide some slight help, but this treatment should be left as the final touch.

Excitation Reduction

As pointed out earlier, the output vibration magnitude can be reduced by reducing the input forces. The following discussion concerns several typical inputs and (where possible) suggests methods to reduce them.

Engine Unbalance, (1st Order Engine) - The unbalance forces in inherently balanced engines can be reduced by improved quality control. This may mean modifying a balancing method, that is, balancing the engine in the vertical plane instead of the horizontal plane. Inherently unbalanced engines may require counterweighted shafts or gear sets.

Torque Variation (1/2, 1st, 1-1/2, 2nd, etc. Order Engine) - These torque variations are the result of one or more cylinders firing more strongly or weakly than the average of all cylinders. Reduction is achieved by improved induction or ignition systems.

Engine Firing Impulses (4-cyl. - 2nd order engine; 6-cyl. - 3rd order engine; 8-cyl. - 4th order engine) - The mechanism of how these always-present vibratory forces cause the powerplant to bend is not completely understood. Measurements of instantaneous bearing cap loads, as shown in Fig. 14, have revealed that impact forces exceed 1500 lb. One hypothesis is that the shock waves generated from these im-

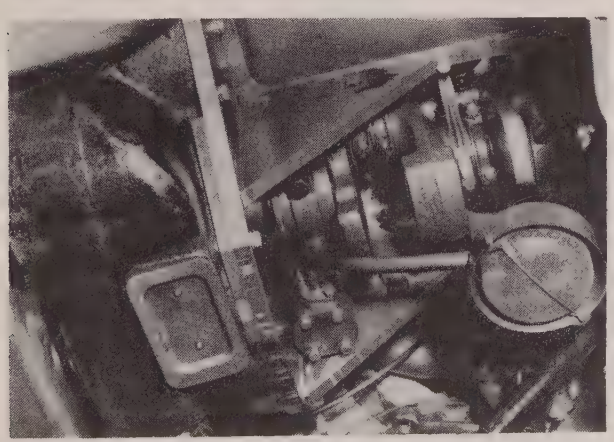

Fig. 12 — Experimental gusset to stiffen joint between clutch housing and engine block

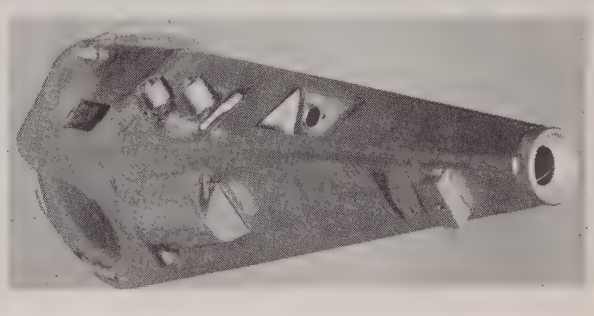

Fig. 13 — Experimental mock-up of structurally combined clutch housing, transmission, and transmission extension

pacts are transformed into structural bending, particularly when the impacts occur at the structure's natural bending frequency. A different hypothesis includes the flexibility of the crankshaft in bending as an important coupling of the firing impulses to structural bending. Some improvement may be obtained by decreasing the main bearing clearances and/or stiffening the crankshaft.

Driveshaft Unbalance (1st Order Driveshaft) - Whipspeed is strongly influenced by moments generated by internal unbalances which lie dormant until the speed range is reached at which the driveshaft no longer behaves as a rigid body. Nodal point balancing (that is, locating the counterweights at the free-bending nodes) will help avoid introducing these additional internal moments and reduce the tendency of the driveshaft to bow.

Universal Joints (2nd Order Driveshaft) -Bending inputs arising from universal joint side couples can be reduced by altering the angle of either the first or second joint behind the transmission-extension. It is the arrangement of the joint angles during high torque that is important to the forces generated, not the configuration with the car at rest. Improved joint angles may be determined experimentally or analytically. If these cannot be changed sufficiently, a carefully positioned snubber above the pinion nose may be necessary to provide joint angle control. Installation of a constant velocity universal joint at one or both ends will also reduce the universal joint couples.

Accessories - Inputs from accessories should be considered on an individual basis. There is no general approach except to assure that good design practice and quality control has been applied to items such as the generator, power steering pump, and air conditioning pump.

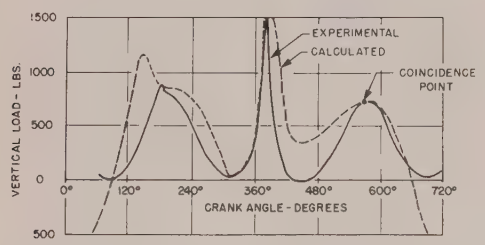

Fig. 14 — Rear main bearing impact loads

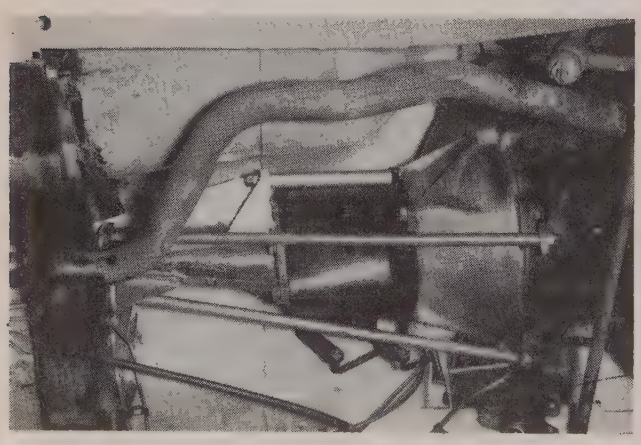

Fig. 15 — Experimental reinforcement rods added to powerplant structures to increase bending natural frequency

Isolation of Powerplant Bending Vibration from Vehicle

At times it is impractical to eliminate the drivetrain exciting forces or modify the system to change the resonant bending frequency. Under these conditions it becomes necessary to isolate the vibration from the vehicle. Since engine mounts are the primary vibration paths from the drivetrain to the vehicle, they are usually the first component investigated.

Powerplant bending implies that at least two bending nodes exist on the powerplant. These nodes are points of relatively small amplitude and are, therefore, optimum transverse locations for engine mounts. Since it is not always possible to position the mounts directly in the transverse plane of the nodes (which are usually experimentally determined), they should be located as close as other factors will permit.

Another approach is to reduce the amplitude of the vibratory forces transmitted through the engine mount. Powerplant bending amplitude at resonance is a function of the input force and the internal system damping. Changes in the conventional engine mount dynamic spring rates will not appreciably change the bending amplitude. Thus, it is reasonable to conclude that reductions in spring mount rate for a given bending deflection will reduce the transmitted forces, since:

Transmitted Force = Engine Displacement x Mount Dynamic Spring Rate (Approximately)

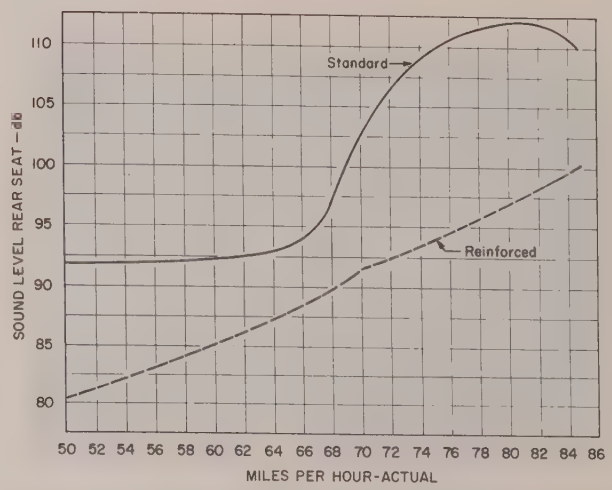

Fig. 16 — Noise reduction achieved by reinforcing powerplant

One limitation to both approaches is that the engine mounts must satisfy other conditions. The rates needed to reduce car shake do not always give sufficient isolation to bending vibrations.

Undoubtedly, there will be times when perfect engine mounts will not eliminate the objectionable powerplant vibrations from reaching the passenger. In these cases, the vibration will enter the body by some other vibration path. It then becomes necessary to provide further isolation for these other paths between the drivetrain and body. Low rate spring connections may not be practical for rear spring and shock absorbers, and it may be necessary to use a subframe or increase the body mass at the attachment areas.

Specific Cures for Powerplant Bending

The noise and vibration due to power plant bending in the 1949 Ford was later eliminated by substituting a ferrous casting clutch housing for the stamped clutch housing. This change improved the car by accomplishing the four following functions:

1. It increased the speed of the high speed (driveshaft unbalance) period above the driving range.
2. It moved the lower speed periods firing impulses and universal joints) away from critical body resonances.
3. It reduced the amplitude of bending.
4. It moved the node closer to the mount position.

Powerplant bending was later encountered on one of the first unitized constructed vehicles. Prototype models of this car were found to have several severe noise periods ranging from 600 to 1100 engine rpm. An additional period occurred on the road at the speed of 60 to 70 mph. An investigation revealed that the lower speed periods were the results of several of the accessories exciting powerplant bending. The 60 to 70 mph period was also powerplant bending excited by 2nd order driveshaft. Thus, it was decided to work on the system rather than the individual inputs. The response of the system was detuned by the addition of a dynamic absorber tuned to the frequency of the drivetrain (60 cps). This produced a marked improvement in the passenger compartment noise without introducing additional noise peaks at other speeds.

In a recent prototype, powerplant bending was found to cause an objectionable interior noise at 80 mph. This was traced to drivetrain bending, excited by unbalances of both the crankshaft and driveshaft.

Since the period occurred just below the top speed one suggestion was to increase the powerplant rigidity, increasing the resonant frequency so that the period would occur above the speed range. To simulate this rigidity, the reinforcing structure shown in Fig. 15 was superimposed on the production powerplant. This raised the critical speed from 80 to 93 mph. Fig. 16 compares the Interior Sound Level versus Miles Per Hour. Although this approach was successful it was too close to production time to incorporate the needed changes and further methods of improvement were sought.

Since this period was excited by unbalances from both the engine and propeller shaft, both components were balanced at the speed of the period. This was accomplished by running the components in the car and balancing them to within less than 1/10 of an oz-in. Fig. 17 compares the interior sound levels before and after the period balancing operation. Although this treatment was also successful, the balancing speed and accuracy required to eliminate the noise were not practical for production.

An experimental rear engine mount and bracket located at the nodal point as shown in Fig. 18 was designed and installed. The noise reduction results, shown by Fig. 19, were highly encouraging. This experimental mount design was later modified slightly and incorporated into the final production design.

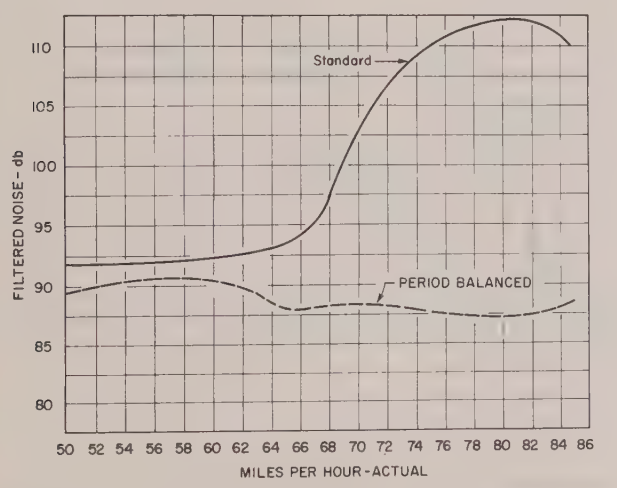

Fig. 17 — Noise reduction achieved by period balancing driveshaft and crankshaft

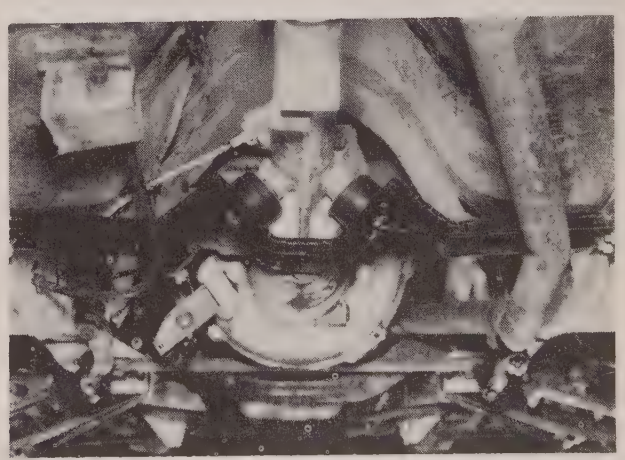

Fig. 18 — New mounts and bracket relocated at rear nodal plane

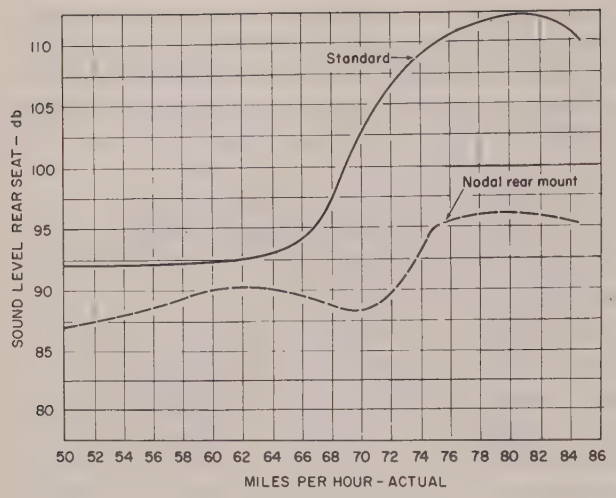

Fig. 19 — Noise reduction achieved by nodal mount

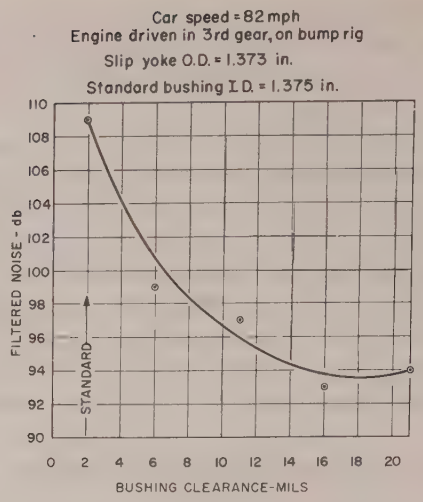

Fig. 20 — Noise level versus extension bushing clearance

An interesting phenomenon encountered during these tests was the effect on the period of an oversized transmission-extension bearing. A small increase in the bearing clearance apparently permitted the propeller shaft to revolve with a slight eccentricity without disturbing the powerplant. Subsequent tests with this discovery showed that the interior noise level decreased with increasing bearing clearance as shown by Fig. 20. In combination with the nodal mount described earlier, a 10/1000 in. oversized extension bearing virtually removed all trace of the high speed vibration, (see Fig. 21).

A specific case of body structure revision affecting the powerplant bending noise was also encountered on this same car. Road tests indicated that floor panels were contributing to the high speed noise peak so that floor reinforcing rails, which originally terminated at the front seat, were extended to the rear axle kickup. These reinforcing members (which decreased the span of the rear floor panels by approximately 1/2) decreased the total rear seat noise by several decibels.

Summary

It has been shown that, once it is properly identified, powerplant bending noise problems can be cured by modifying one or more of the following:

1. Vibration input.
2. Drivetrain structure.
3. Drivetrain mounting.
4. Body (or chassis).

Other factors remaining equal, experience indicates that it it generally better to alter the system rather than attempt to reduce inputs. This is true particularly when the system is responding to several inputs. In one case a system modification eliminated several periods.

Generally, individual improvements will be additive. Thus, a sizeable reduction of powerplant bending noise could be obtained by combining several lesser individual reductions. For example, imagine that four individual modifications resulted in a 3 db reduction apiece. Since a 3 db change is difficult to detect by ear, personal observations of each modification could indicate that no improvement has occurred. If made simultaneously, however, these four modifications would reduce the noise by 12 db which could make the car completely acceptable.

Thus, these small, sometimes unnoticed improvements emphasize the need for accurate sound measuring instrumentation and facilities for controllable test conditions.

References

1. F. J. Hooven, "Dimensional Effects on Noise and Vibration in Unitized Construction", SAE Preprint No. 143B, March, 1960.

2. F. R. Kishline, and E. M. Lawler, "Suspension Design for Single Unit Construction", SAE Preprint No. 143A, March, 1960.

3. J. R. Farnham, "Control of Noise and Vibration in the Unibody", SAE Preprint No. 143C, March, 1960.

4. R. H. Bollinger, and H. N. McGregor, "Practical Methods for Car Noise Reduction", SAE Preprint No. N2B, January, 1958.

5. K. Federn, "Multi-Plane Balancing of Elastic Rotors", Private Transmittal.

6. S. E. Staffeld, "Computer Analysis of Automotive Drivetrains", SAE Preprint No. 127C, January, 1960.

7. R. Plunkett, "Colloquium on Mechanical Impedance Methods for Mechanical Vibrations", Presented at the ASME

Annual Meeting, December, 1958.

8. E. Stepp, "A Computer Technique for Designing Engine Mounts to Control Shake", SAE Preprint No. 127B, January, 1960.

9. A. H. Church, "Simplified Vibration Analysis", (Series of 7 Articles), Machine Design, February 18, 1960 et seq.

10. P. H. Geiger, "Noise Reduction Manual", University of Michigan Press, Ann Arbor, Mich.

11. C. Harris, "Handbook of Noise Control", McGraw-Hill, Chap. 31.

12. R. H. MacNeal, "Vibration of Composite Systems", Project No. R-354-30-1 (Technical Report No. 4) Air Research and Development Command.

13. Rayliegh, "Theory of Sound", Vol. 1, 2, Dover Publications, Inc.

14. L. L. Salter, "Predicting Critical Speeds", Machine Design, June 25, 1959.

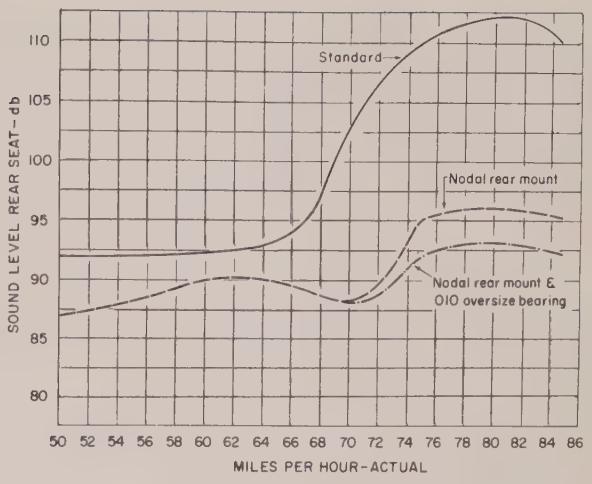

Fig. 21 — Noise reduction achieved by oversized extension bushing

Discussion

Handling Structural Problems on a Systems Basis

David C. Apps
General Motors Corp.

IT IS NOT too long ago that static testing represented the chief approach to structural problems. Static deflections, for example, measured on a body structure were taken as indices of structural adequacy, and as might be expected, some surprises were often in store during road tests of these structures. It is no more possible to predict dynamic performance from static measurements of a car than it is possible to predict dynamic performance of a simple mass-spring system by measuring the spring stiffness only and ignoring the mass.

Messrs. Bollinger and Ruhl's paper gives an elegant use of experimental procedures combined with analytical approaches. Bollinger and Ruhl pay respect to Mr. Staffeld of Chrysler, noting that he was able to predict drivetrain bending frequencies from design information only. The author's proceed by saying "If experimental components are available, a shaker can be used to determine their individual or assembled vibration responses."

If I may be allowed to prophecy or two, I have no doubt that in the not too distant future, we will be handling the problems discussed, and those alluded to, on a systems basis. The engine and its mounts, the car structure as related to shake, and drivetrain beaming and torsional characteristics will undoubtedly be handled as a system. It would appear, too, that with the start already made, the system characteristics will ultimately be predicted from paper designs.

I feel that here lies the real future in automotive dynamics: the prediction from a paper design of the dynamic performance of a system. In this way, costly mistakes can be avoided and a modified design substituted early in the history of the product.

A Radioactive Tracer Study of Lubricating Oil Consumption

E. S. Starkman
University of California

INFORMATION in the literature on piston ring phenomena, including lubricating oil consumption, was relatively abundant prior to the end of World War II and the widespread introduction of the turbine engine. (1)* Since then it has become relatively scarce compared to other reciprocating engine phenomena. The reasons for this situation are related to two factors:

1. The decrease in emphasis occasioned by phasing out of aircraft piston engines.

2. The difficulty which is entailed in obtaining data on oil consumption.

Measurement is made difficult principally by the minute rate of consumption which is encountered in the range of practical consideration. For example, a presently acceptable rate of lubricating oil consumption in a 5 qt capacity, 8-cyl engine amounts to approximately 1 qt per 1000 miles, or about 1 cc per mile. Converting this to a number which might better suit research purposes, this level of consumption corresponds to a rate of approximately one part in 1000 of total crankcase oil charge per cylinder per hour at 30 mph.

Reciprocating engine lubricating oil consumption usually has been determined by the application of what can be called a differential method of measurement. This is done either on a batch basis, (2) where the oil is periodically removed from the engine and weighed, or on a continuous basis where the oil is stored on a balance or scale externally of the engine. (3) Considering the limitation in accuracy of weighing, both of these methods are subject to a number of critical drawbacks, including.

1. The excessive time necessary for a single determination.

2. The low reliability resulting from the consumption rate being a small proportion of the total weight.

3. Oil leakage which is a complicating factor if it is significantly large.

4. Masking of transient phenomena.

5. Variable holdup in the engine.

In addition, the differential weight method does not account for the influence of foreign material, either solid or liquid, which originates from the fuel and contributes to erroneous indication of oil consumption rate.

These are reasons then why research into the phenomena associated with oil consumption has been sparce and often

*Numbers in parenthesis designate References at end of paper.

subject to argument. Considerable of the information which is available is commendable because, among other reasons, it has resulted from long, arduous and tedious experiment.

Tritium Tracer-Scintillation Counter Technique

An expeditious way to investigate lubricating oil consumption, and the scheme which was used for the purposes of this research, is to tag the lubricating oil with a radioactive tracer and to count the activity at all of the exit routes by which the oil or its degradation products leave the engine. A number of tagging schemes are possible, including the use of carbon-14 (C^{14}) and tritium (H^3). A method for the use of tritium tagged lube oil was developed by Shell Development Co. (4, 5, 6) The method was adapted for this investigation. Arguments with regard to reasons for the choice of tritium as the radioactive tracer may be found in the above references and will be dwelt upon briefly here.

Tritium (1/2-life of 12.5 years) can be incorporated chemically through the simple expedient of using it in gaseous state to hydrogenate a slightly unsaturated lubricating oil. This is done in the presence of a simple nickel catalyst and at high pressure, with the tritium well diluted with hydrogen. A drawback, on the other hand, is that tritium emits only low energy beta particles, and while this low energy emission is a desirable characteristic from the standpoint of safety, special instrumentation must be used for the detection of the emission. This problem has been solved successfully by using a liquid scintillation counter technique (4, 5).

The liquid scintillation counter method used in this research will be briefly described here. The principal feature of the method is the ability for the β energy liberated by H^3 to be transformed into light emission in a scintillator solution in which it is contained. Each such emission results in a single light pulse of short duration which can be detected by a photomultiplier tube. Since the energy level of the light flashes from the scintillator are extremely weak, they are seen by the photomultiplier tube at about the same level as its own thermionic photocathode emissions (noise). To eliminate the larger part of this noise, two photomultipliers are utilized, viewing the sample at right angles, and a circuit is supplied which counts only the coincident pulses at an energy level approximating that of the tritium emission. With a coincident resolving time of about 0.2 microseconds and with operation at 0 to -10 C (to further lower thermionic emission) and careful selection of photomultiplier tubes for low noise level, it is possible to count samples very adquately with relatively modest tritium concentrations.

A sample containing H^3 which is to be counted, usually 1 ml of either the lubricating oil or water, is added to a liquid phosphor. Standard phosphor solution in this research was 65 ml of 67% vol toluene and 33% vol ethyl alcohol, containing 4 gr/liter diphenaloxazole and 15 mg/liter diphenylhexatriene, the latter to shift the wave length of the resultant light pulses to a more advantageous part of the spectrum. Because the light ultimately emitted is very weak, the counting must be done in total darkness, and the samples must also be dark adapted for at least 20 to 30 minutes in order to allow decay of the fluorescence excited by sunlight. Counting is done in a simple, small commercial refrigerator to reduce the temperature and photomultiplier noise, and simultaneously it serves as an excellent light-tight box.

As noted, only 1 cc of the organic or inorganic liquid sample containing tritium is required to make a determination of activity. When burned, the consumed lubricating oil yields the tritium incorporated into water; the unconsumed portions contain the tritium in a relatively volatile organic material, either totally or partly unoxidized. A further desirable consequence of using tritium is thus an ability to easily distinguish the totally burned from the partly burned products of lubricating oil consumption. This is accomplished by collecting and rating two samples, one consisting of condensed water in the untreated exhaust or blowby and the other which has first passed through an oxidizing furnace before being condensed.

Engine and Operating Conditions - A standard, single cylinder, 3-1/4 in. by 4-1/4 in. overhead valve CFR engine with a special piston and pinned rings (two compression and two oil) was used to obtain all the data reported here. Except where noted, the engine was usually operated at 1800 rpm, normally aspirated, and with room air supplied for combustion. Spark advance was nominally 35 deg btc, and compression ratio 6:1. The crankcase was not vented but was maintained at a vacuum of about 1/2 in. water less than atmospheric. Fuel-air ratio was near chemically correct.

Preparation of Sample - The oil sample was prepared as follows: A 100 HVI oil was chromatographically separated. The monoaromatic fraction was then hydrogenated with hydrogen diluted tritium, and the resulting tagged fraction was blended back with the other fractions. The treated oil corresponding to an SAE 5W viscosity was substantially identical to the original, except for the added radioactivity and the slightly higher saturation. A concentration of 65 millicuries of tritium per 2500 gr of oil was found satisfactory for carrying out the research which will be described. Under the conditions of investigation, the coincidence counting technique was also found satisfactory at a 3 to 5% efficiency level. (Subsequent to this investigation, the efficiency of counting has been increased to a level of approximately 12%.)

Technique and Sampling Procedure - As noted previously, only 1 cc of oil or water sample is required for a determination of radioactivity. Furthermore, even at very low lube oil consumption rates, dilution of lubricating oil degradation products in either the exhaust gases or blowby gases is not sufficient to interfere with the ability of the scintillation counting method to discriminate the variation in concentration of tritium. These two factors together allow the rate of lubricating oil consumption to be determined by collect-

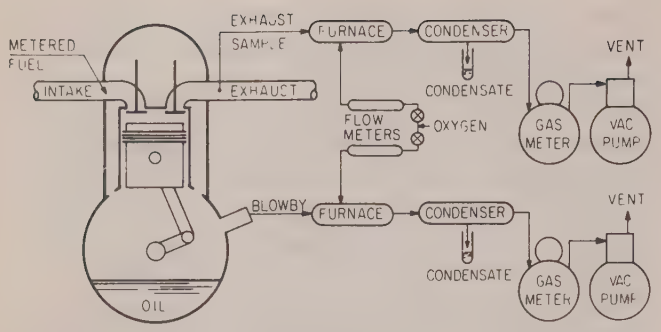

Fig. 1 — Diagram of sampling system

ing and condensing only 1 cc of the water and combustion products in either the blowby gases or the exhaust stream Only a small fraction of the exhaust gas needs to be condensed for satisfactory short period determinations, but normally all of the blowby has to be so treated. A collection period of about one minute is usually sufficient for obtaining a single sample.

Exhaust gas was collected directly from the exhaust stream at the exit from the engine through a probe which was inserted into the center of the exhaust pipe. All of the blowby was passed through a similar collecting scheme. A diagram of the system is shown in Fig. 1.

The amount of oil leaving by way of the exhaust is obtained by a direct determination of the radioactivity of the water of combustion. Most of the water of combustion comes from the fuel. Much less than 1% comes from the lubricant. The fuel composition determines the ratio of water of combustion to fuel flow rate. Thus it is most important to obtain accurate measurement of fuel flow rate. This was done by a weight displacement method. Fuel flow determinations were made as simultaneously as possible with collection of the exhaust of blowby samples.

The computational procedure is shown in the Appendix. As can be seen it is necessary only to know the fuel composition, approximate lubricant composition, fuel flow rate, and crankcase lubricating oil activity level. For ease of computation, isooctane was used as fuel for the majority of the tests. To put the results on a comparative basis, periodic determinations were made of the count rate on known activity level standard samples.

A correction was necessary to account for the water which was not condensed at the 32 F temperature of the condenser system. For computational purposes, it was assumed that the gases leaving the condenser were saturated with water at 32 F. At this temperature, the amount of water which will pass through the condenser is only 4% of that usually present in the exhaust or blowby stream, and corrections were made accordingly.

Unburned or partly burned fuel and lubricant were treated, where their proportionate presence was to be determined, by passing through a copper oxide matrix, supplied with oxygen, and were as a result converted to water and carbon dioxide.

Comparison between Tracer and Weight Determined Oil Consumption Rates

For determination of the reliability of the tracer technique, a direct comparison had to be made to a periodic weight determination of the drained oil. The oil was weighed on a balance with least count of 1 gr. Although carried out with extreme care, this method of oil consumption measurement suffers from the previously listed problems and from the time consumed. For example, even with the standardized drain procedure the oil consumed during a particular run could indicate considerable variation. This amounted to as much as 10 gr under some conditions where consumption was only 2 gr per hr.

Comparative results between weight method of determination of oil consumption rate and tritium tracer technique are shown in Fig. 2. The trend of the rate of oil consumption curves reflects the fact that the engine was undergoing break-in during the period shown. Even so, acceptable level of agreement is indicated between the isotope method and weight method, particularly if the cumulative consumption curves are compared. It is also interesting to observe that while the indicated rates are far from being identical, the radioactive technique method shows the more believable trend throughout the break-in period in which the comparison was made. It can be noted that the equilibrium operating level after break-in at full load was about 1.5 gr per hr. This would correspond to about 1500 miles per qt on an 8-cyl, 30 mph basis. Before the engine was fitted with new rings, and prior to this break-in period, some limited data were obtained which indicated a consumption level of 20 gr per hr.

Consumption and Origin of Material in Exhaust and Blowby

As shown previously, the amounts of lubricating oil leaving by way of the breather or the exhaust are readily determined by measurement of the activity level of a sample. The method inherently also gives the relative amounts of the resultant water originating from fuel and from lubricant hydrogen (or tritium). Further, bypassing the sample around the copper oxide furnace before condensing yields, by difference, how much material leaving the engine was completely oxidized and how much was not.

Fig. 3 is a plot of the results of two consecutive series of tests made for the dual purpose of ascertaining repeatability and for determining the relative amounts of the consumed oil which leaves by way of the crankcase breather and by exhaust under moderate oil consumption, full load, 1800 rpm operating conditions. Both tests shown in Fig. 3 were made using the same analysis train for exhaust as for blowby and switching the sample lines accordingly. Comparisons of the

0.25 gr per hr via blowby to the average of 2.4 gr per hr going out the exhaust indicate that about 90% of the lubricating oil loss was via the exhaust. This same ratio of almost 10 was found in nearly all of the tests carried out, including the 20 gr per hr tests refered to previously.

Fig. 4 shows the comparative amounts of completely oxidized and partly oxidized lubricating oil which leave the engine as exhaust gas. In reducing the data from which Fig. 4 was plotted, the assumption was made that the tritium concentration in the incompletely oxidized material from the oil was the same as that which had already been converted to water in the engine. This same assumption was made throughout the remainder of the work reported here. Interpreting the data in this manner indicates about 15% of the lubricating oil which went out the exhaust was in an incompletely oxidized state.

It will be noted from comparing Figs. 3 and 4 that even though engine operation was the same, oil consumption was at different levels. This was a normal observation of the transient character of oil consumption and a reflection of the ability of the tritium tracer technique to indicate accurately the transient and variable conditions of oil consumption which would have gone undetected by weight methods.

Fig. 5 is a comparison of completely burned and partly burned lubricating oil which leaves by way of the blowby gases. It can be seen that approximately 50% of the lubricating oil hydrogen in the blowby was in the partly oxidized state. A computation also showed that 99% of the partly oxidized material in the blowby originated in the fuel and 1% came from the lubricant. This agrees with conclusions of other authors. (7) Of the fuel originated material, about 60% was only partly oxidized.

The gross circulation mechanism directly deduced from this evidence is that some of the oil passes into the combustion chamber, is cracked or partly oxidized, mixed with partly or completely burned fuel, and then recirculated into the crankcase by combustion pressure. Fig. 6 is a flow diagram for the oil and fuel and their degradation products as they must circulate in the engine.

The abundance of partly burned fuel in the blowby is undoubtedly related to the proximity of the wall at the point where the combustion gases become mixed with the oil. The wall has been shown to quench combustion reactions. (8) The significantly large amount of unburned oil going out the exhaust may be related to the observations of Beaubien and Cattaneo (9) that oil is thrown from the piston predominantly during the breathing stroke.

The conclusions about lubricating oil consumption drawn

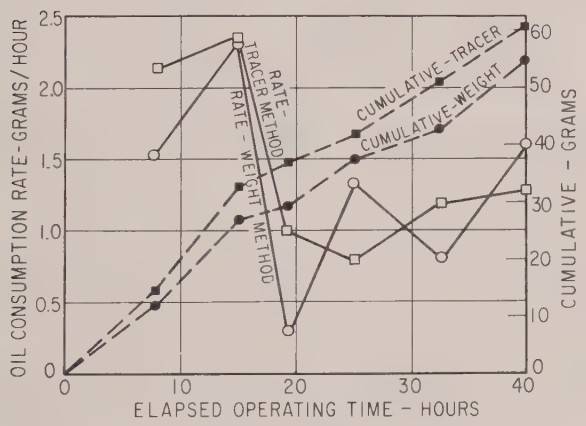

Fig. 2 — Comparison between weight and tracer methods of measuring oil consumption

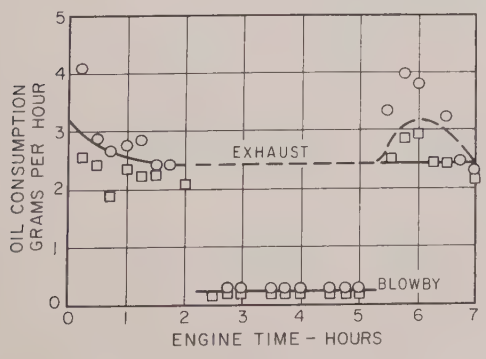

Fig. 3 — Oil consumption via blowby and exhaust

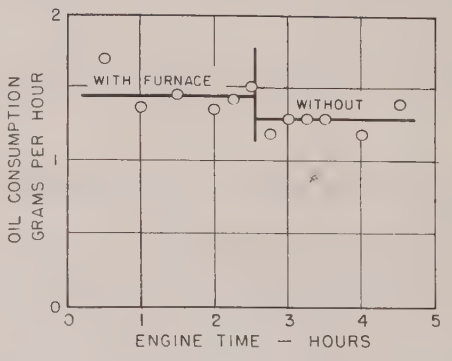

Fig. 4 — Comparative amounts of burned and unburned oil in exhaust

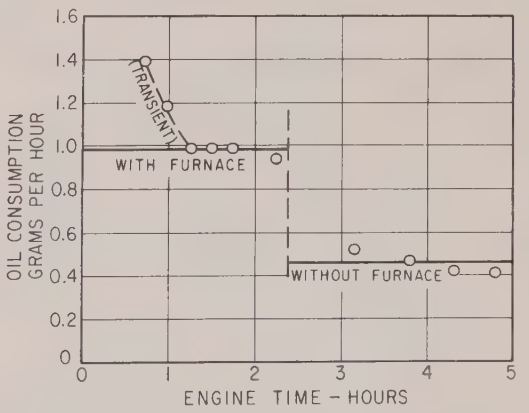

Fig. 5 — Comparative amounts of burned and unburned oil in blowby

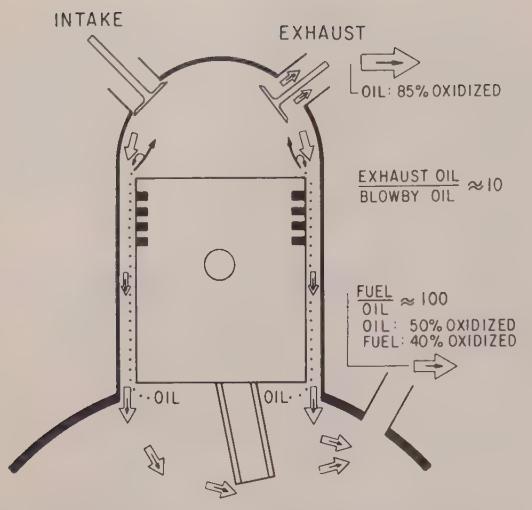

Fig. 6 — Diagram of lube oil consumption phenomenon (solid arrows represent oil, hollow arrows represent fuel)

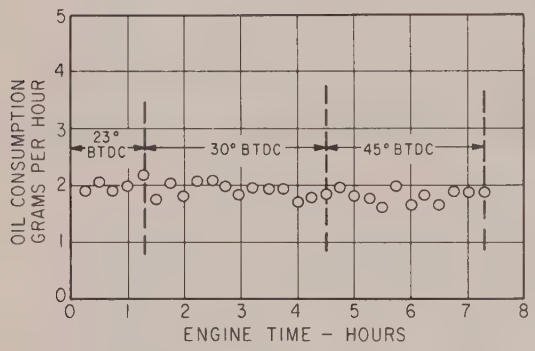

Fig. 7 — Influence of spark advance on oil consumption

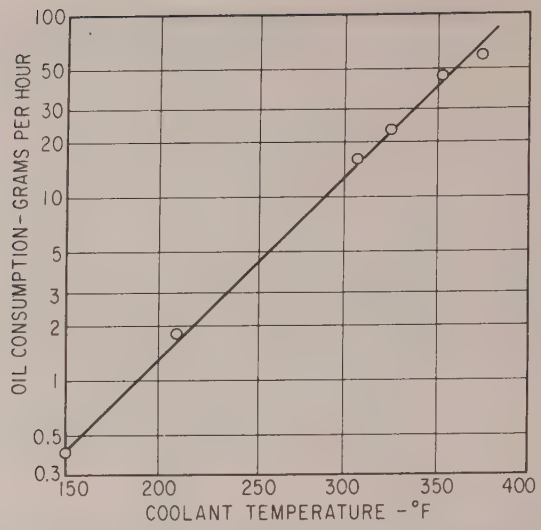

Fig. 8 — Influence of jacket temperature on oil consumption

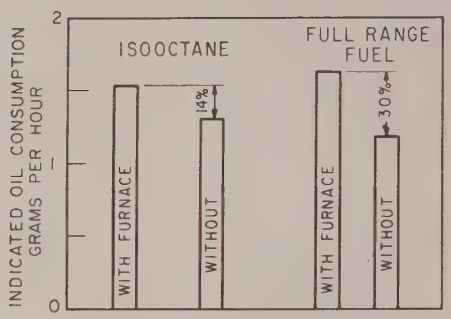

Fig. 9 — Influence of fuel composition on oil consumption

thus far in a program devoted primarily to development of the tracer method are an indication of what might be accomplished in very little time through the use of the tritium tracer-scintillation counter method. The application which can be made to the study of the source of air pollution precursors are also apparent.

Influence of a Few Selected Engine Operation Factors - Once the validity of the tritium tracer technique was established, a number of engine variables were selected for investigation. Ignition timing was one of these.

A relatively narrow range of spark settings, 23 to 45 deg btc, was surveyed under full load, 1800 rpm, engine conditions. The results are shown in Fig. 7. Over the range investigated, spark setting had no significant influence. It was later shown, however, that ignition timing could influence, oil consumption, but this was through the effect it has on abnormal combustion. (5)

Influence of Jacket Temperature - Fig. 8 shows the results of tests made to determine the influence of jacket temperature on lubricating oil consumption. Engine operating conditions were always full load, 1800 rpm, and bulk oil temperature was 245 F. The results plotted on semi-log coordinates substantially form a straight line, showing the exponential influence of coolant temperature. This is an observation relative to oil consumption which is related to reports by others. (10) In the range of normal jacket temperatures, 150 to 210 F, the consumption rate increased by a factor of 3, or from about 0.5 gr per hr to about 1.5 gr per hr. As the temperature was raised to 375 F, the oil consumption increased to a level of about 60 gr per hr or by a factor of greater than 100 over low temperature oil consumption.

Influence of Fuel Composition - Fig. 9 shows the results of comparative tests on isooctane, which was normally used as fuel for this investigation, and a full range representative motor fuel, the volatility of which is contained in the Appendix. The oil consumption rate for the two fuels, as measured after being completely oxidized, under these full load, 1800 rpm, 210 F jacket temperature conditions was quite comparable.

When the exhaust samples were allowed to bypass the combustion furnace, the results disclosed that whereas with isooctane approximately 14% of the material was unburned, 30% was unburned with the full range fuel. One explanation for the difference relates to the heavier ends in the full range fuel. These heavy ends not present in the case of isooctane

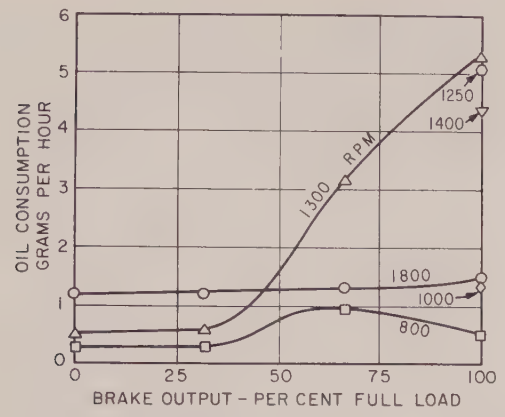

Fig. 10 — Influence of speed and load on oil consumption

would accumulate in the ring belt area of the piston, changing the character, perhaps the viscosity of the mixture of material in that area, and the state to which it becomes oxidized before being discharged from the cylinder, either into the exhaust or into the crankcase. While the total amount of oil leaving is not greatly changed, that which does have is somewhat less oxidized. This observation may have some significance to the problem of air pollution. (7)

Influence of Speed And Load - Figs. 10 and 11 include the results of an investigation into the composite effects of speed and load. Within the range of speeds involved, 800 to 1800 rpm, it is evident that a disproportionate increase in oil consumption occurred at about 1300 rpm and at full load. At 2/3 load, a hump is also evident, but at 1/3 and no load, no such magnification is apparent. It is concluded, therefore, that there must have been a peculiar relationship with speed and load which had a large controlling influence in the lubricating oil consumption. These reasons constitute the basis for the remainder of this paper and the theory for abnormal lubricating oil consumption which will be developed.

Theory for Abnormal Lubricating Oil Consumption

Figs. 10 and 11, which show the relationship between oil consumption and engine speed and load, are strikingly similar to curves which are obtained as a result of the forced vibration of a simple elastic system with one degree of freedom. The relationships are the same as that between amplitude and frequency of vibration with damping as a parameter. The analogy between oil consumption and the forced vibration system requires only that oil consumption be similar to displacement and that engine load correspond inversely to extent of damping. In its most simple form, and assuming viscous damping, an equation describing the vibrating system appears familiar (11) as:

$$m\frac{d^2x}{dt^2} + c\frac{dx}{dt} + kx = P_o \sin \omega t \qquad (1)$$

where:

- m = mass of body
- x = amplitude of the vibration
- t = time
- c = damping factor
- k = spring constant
- P_o = magnitude of the exciting force
- ω = angular velocity

all in consistent units.

The analogy suggests that oil consumption, at least in this case, was controlled by some part of the engine mechanical system which was excited to vibration at about 1300 engine rpm and in so doing increased the rate of oil consumption over that to be found at higher or lower speeds in the range investigated. The analogy also requires that the amplitude of the vibration must be influenced by load, or more specifically, by cylinder pressure. The piston rings satisfy the requirements for this vibrating part.

The so-called flutter of piston rings has been reported previously in the literature. (1, 12) Since other investigators (13) have also shown that the gas pressure behind the top compression ring is substantially that of the combustion chamber, and that the gas pressure behind rings below the top compression is relatively unrelated to combustion pressure variation, the top compression ring becomes subject to specific interest for its vibrational characteristics. The observation that the top ring can be controlling to oil consumption has also been reported in the literature, but the conclusion was drawn from entirely different evidence than will be shown here. (3, 9)

For illustration, consider Fig. 12 which is a schematic representation of the piston ring-belt area with the cylinder taper exaggerated. The piston ring, while admittedly restrained by friction, is free to move either radially or vertically in the groove. It can also revolve around the groove, but this latter movement is very minor and in the engine from which the data were obtained, the rings were actually pinned. Movement in a radial plane results in the ring expanding and contracting. Movement in a vertical plane necessitates no change in dimension of the ring.

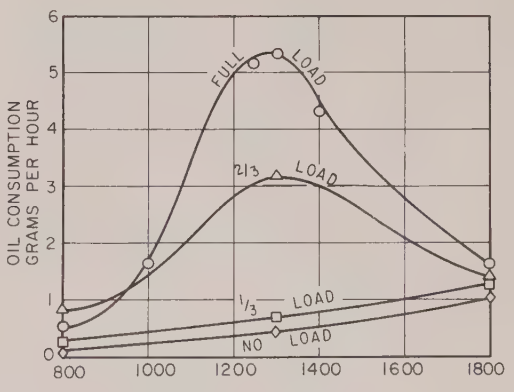

Fig. 11 — Influence of speed and load on oil consumption

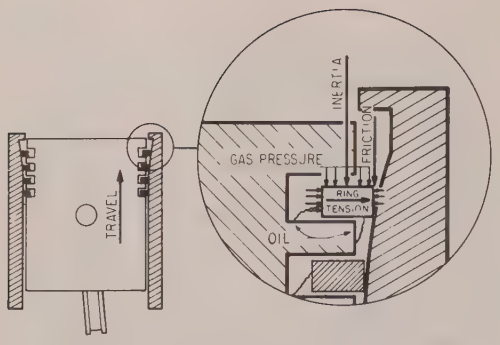

Fig. 12 — Forces acting on piston ring

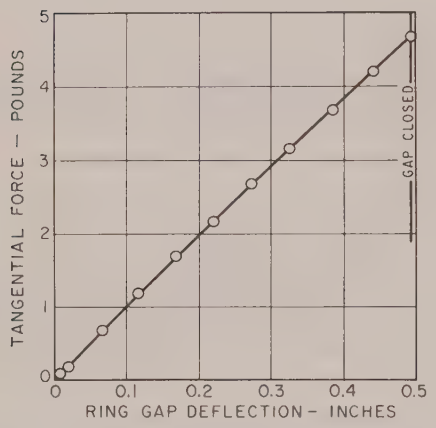

Fig. 13 — Piston ring deflection characteristics

The major force to cause the ring to move radially in a cylinder is that which results from the ring operating over the taper at the top of the stroke. (14, 15) In the absence of taper, little or no radial movement should occur. Other factors, such as the variation in thickness of oil film between ring face and cylinder wall, due to cyclic velocity changes, (16, 17) have very little effect. On the other hand, the effect of gas pressure is implicitly evident in Figs. 10 and 11, and thus gas pressure also must have an influence. The effect of gas pressure and its relationship to the forces on the top ring in a tapered cylinder is to allow a force to be exerted radially inward against the face of the ring in the area of the taper and thus reduce the resulting restraining and damping friction of the ring on the cylinder wall.

The forces which cause the ring to move vertically in the groove are functions of gas pressure, fluid friction, solid friction, if present, and inertia. (9) If a vibration of the ring is responsible for the phenomenon which was experienced, the above review of the forces acting on the ring would lead to the conclusion that a radial vibration was the type which was experienced.

To investigate further the thesis that ring vibration could be responsible for abnormal oil consumption under some conditions, analytical and experimental determinations were made of the natural frequency of vibration of the top compression ring. A computation was first undertaken to determine the natural frequency of the ring of the type used in the engine. A special rig was constructed by means of which it was possible to measure the circumferential force necessary to close the ring. Fig. 13 shows the results of the determination of the force-deflection characteristics. Similar rings tested by the manufacturer gave comparable results. The deflection test showed the ring to have an almost linear rate of 9.6 lb per in. of deflection. The compression ring used for the example weighed 0.0446 lb. Applying a simple first order approximation to obtain the natural undamped frequency, in accordance with the differential Eq. (1), presented previously and of the form:

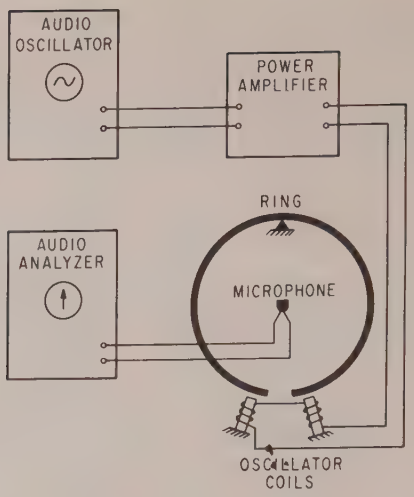

Fig. 14 — Schematic diagram of audio oscillator and frequency analysis system

$$\omega = \sqrt{\frac{1}{2}\frac{k}{m}} \qquad (2)$$

gave a natural frequency for the ring of 45.9 cycles per sec. This corresponds to about 2800 cycles per minute and is more than twice the engine speed at which the maximum oil consumption occurred.

The vibrational characteristics of the ring were further investigated by application of a simple procedure in which the ring was exposed to a magnetic field driven by an oscillator. The response of the ring was measured by placing a microphone in close proximity to the ring and analysing the output with an audio frequency spectrometer. A schematic diagram of the system is shown in Fig. 14. The lowest frequency which would cause the lightly suspended compression ring to vibrate was about 33 cycles per sec, which corresponds to 1980 cycles per minute. However, the audio output from the ring showed it to be vibrating with the second harmonic of this frequency. This characteristic of the ring to vibrate at twice the exciting frequency was an important and significant observation.

An additional computation was made of the natural frequency of vibration of the ring in a radial mode by a semi-empirical method of Pliskin, Edwards and Brundy. (18) This computation gave a frequency that corresponded very closely to the 66 cycle per sec frequency encountered in the tests made with magnetic induction of vibration.

It is obvious that the natural frequency of vibration of the compression ring does not correspond well with the engine speed at which the oil consumption was a maximum. But, as has already been shown, the ring can be excited to vibrate at its lowest mode of natural frequency by a half order forcing function. Furthermore, all of the measurements and computations were made for an undamped or unrestrained ring. If the extent of damping in the engine is taken into account, the frequency of vibration will be greatly reduced from that measured or computed.

Noting that the undamped frequency of vibration of the ring based upon the most simple of the analysis was about 2800 cycles per minute, that a more sophisticated determination yielded a natural frequency close to 4000 cycles per minute, and that the maximum oil consumption occurred at 1300 cycles per minute, a first order approach was made to determine the probable magnitude of damping which would account for the speed in the engine at which the ring appeared to be vibrating. Also taken into account was the potential for the ring to be excited by a forcing frequency half that of its natural frequency. The extent of damping was computed by assuming that the simple equation for the vibrating system presented previously would be a good approximation, since more sophisticated relationships are not available. Under these circumstances, the damped natural frequency of the ring would be expressed by:

$$q = \sqrt{\frac{k}{m} - \left(\frac{c}{2m}\right)^2} \qquad (3)$$

where all of the symbols are as indicated previously and in addition:

q = damped natural frequency
c = damping factor

For the purpose of determining c, the damping factor, from the above equation, it was assumed that the 1300 cycle per minute observed phenomenon was related to the 2000 cycle half frequency of the ring under undamped conditions as the 1400 cycle simple system frequency would compare to a new fictitious damped simple system frequency. This fictitious new frequency, which was inserted into the equation in order to solve for the extent of damping was computed to be 1840 cycles per minute. This yielded a damping factor of 0.595 lb sec/ft.

The further computation of the critical damping factor c_c by the relationship:

$$c_c = 2\sqrt{mk} \qquad (4)$$

gave a value of 0.8 lb sec/ft.

While this is only a approximation of the actual system, comparison of the computed factors of c and c_c yields the important conclusion that if the phenomenon of excessive oil consumption was due to a vibration of the top piston ring, the vibration was very close to being critically damped. Reference is made to standard texts on the subject of mechanical vibrations for a more complete discussion of the character and influence of the damping factor on a vibration system. (11)

Taking into account the thickness of oil film and the probable operating temperature of the oil in the ring area, (19) the results of the determination of the magnitude of the viscous damping necessary to explain the frequency shift showed that the viscosity of the lubricating oil, in this case a 5W, could not have accounted for the total damping forces acting on the ring by at least an order of magnitude. The frictional forces between piston ring and cylinder wall would therefore have to be the major contributor to the damping factor. It follows that if this force is of a non-viscous nature. Eq. (1) is a further approximation because of the assumption of viscous damping. Since the character of the damping is unknown at this time, a viscous approach will have to suffice.

An unrewarding attempt was made to determing the magnitude of the forcing function P_o which would be applicable to the phenomena observed in the engine. It was concluded that a further analysis of these factors would require more complete data and a better approximation to the system than that of a single degree of freedom with periodic alternating external force and with viscous damping.

Notwithstanding any limitations for the actual system to be completely correlated to such a simple system as envisaged, the phenomenon has been very substantially accounted for in all of its characteristics by the analysis performed. It is therefore proposed that under some operating conditions, the frictional characteristics of the combined lubricating oil. fuel residue and lacquer, in the ring groove and on the ring face to cylinder wall surface; the taper in the cylinder; and the forces exerted on the ring by combustion gases, ring tension and inertia, yield a phenomenon which can cause abnormal oil consumption in a manner which is analogous to the damped vibration of a spring-mass system. This is not intended to imply that all cases of abnormal oil consumption past the rings can be related to ring vibration, but the theory does help to explain many observations having to do with oil consumption and control.

For example, the success resulting from the use of expanders behind piston rings in badly tapered cylinders may be explained easily by noting the effect the expander has on two factors. Both are related to the increased ring tension. One factor is the countering of combustion pressure on the face of the ring. The other is the increase in the natural frequency which results from the greater spring constant which is provided.

In applying the theory to observations of the trend of oil consumption with increasing engine speed it must be recognized that the rings in an engine vary greatly in those characteristics which contribute to their ability to be excited to vibration. Such things as variable tension, amount and character of deposits in the ring groove, and taper in the cylinder are all influencing. It could be predicted, and is not surprising, therefore, that oil consumption does not peak in a multicylinder engine at some intermediate speed. Contrarily, it is a usual observation that oil consumption increases disproportionately with speed, and in some instances. dramatic increases have been experienced at speeds which could be termed "critical."

Conclusions

1. Tritium tagging of the lubricating oil and scintillation counting of the resulting water of combustion make a rapid, reliable, safe method for determining lubricating oil consumption.

2. Use of the method shows that a large part of the lubricant leaves the engine only partly burned and that about ten times as much lubricant leaves the engine with the exhaust as with the blowby gases.

3. Whereas spark setting and fuel composition appear to have little influence on oil consumption; speed, load and abnormal combustion have major influences.

4. There are conditions of abnormal oil consumption in the speed load spectrum which can be due to a radial vibration of the piston rings.

Acknowledgement

The author is indebted to Robert A. Coit and Vincent P. Guinn for their contribution in the use of the method described in this paper; to Roy Thorpe and John Zachar for preparation of the tagged oil samples; and to Shell Development Co., by whom they are employed, for allowing publication of the data obtained by the author during a period when he was also employed by this organization. Gratitude is additionally expressed to Edward Takemori, a former student, for his efforts in connection with the determination of the natural vibrational frequency of the piston rings.

Appendix

Exhaust Sample Oil Consumption Determination.

$$C_X = \left[R_X \frac{V}{T}\right] \left[\frac{N_X}{N_S}\right] \left[\frac{100,000}{N_O}\right] \qquad (A)$$

where:

C_X = oil consumption rate, gr per hr

R_X = ratio of vol of water of combustion to vol of fuel and oil

V = volume of fuel, ml

T = time to consume V ml fuel. hr

N_X = indicated radioactivity level of exhaust sample, counts per minute/cc

N_S = indicated radioactivity level of a standard sample, counts per minute/cc

N_O = indicated radioactivity level of 1 gr of oil, counts per minute (when standard sample indicates 100,000 counts per minute).

Blowby Sample Oil Consumption Determination.

$$C_b = \left[R_b G_b\right] \left[\frac{N_b}{N_s}\right] \left[\frac{100,000}{N_o}\right] \qquad (B)$$

where the symbols in Eq. (B) are the same as in (A) except for subscripts b referring to blowby and:

G_b = condensate collection rate, ml per hr

Ratio of Water of Combustion to Fuel and Oil.

(For stoichiometric case only since all organic matter is usually burned to H_2O and CO_2 in combustion furnace.) If the fuel or lubricant is hydrocarbon of composition C_nH_m:

$$C_nH_m + \left(n + \frac{m}{4}\right) O_2 \rightarrow nCO_2 + \frac{m}{2} H_2O \qquad (C)$$

$$R = \left(\frac{\frac{18}{2} m}{12\,n + m}\right) \text{(sp. gravity of hydrocarbon)} \qquad (D)$$

Thus for isooctane (C_8H_{18}):

$$R = \frac{9 \times 18}{12 \times 8 + 18} (0.722) = 1.025 \text{ ml } H_2O \text{ per ml } C_8H_{18}. \qquad (E)$$

The base lubricant used in these studies was 100 HVI neutral which had the composition shown in Table 1. The average composition of the lubricant, based on 350 mole wt, is:

$$C_{25.19}H_{47.72}$$

and

$$R = \frac{\frac{18}{2} \times 47.72}{350} (0.862) = 1.057 \text{ ml } H_2O \text{ per ml tube}$$

For almost all exhaust samples, the ratio of oil to fuel is very small, less than 1%. Therefore R_X can be assumed equal to R for fuel only. For blowby samples, a similar assumption would result in a maximum error of the difference

Table 1 - Composition of 100 HVI Neutral

Saturates	84%	$C_nH_{(2n-1.5)}$
Monoaromatics	14%	$C_nH_{(2n-8)}$
Dicyclic aromatics	2%	$C_nH_{(2n-14)}$
Probable average mole wt =	350	
Specific gravity	= 0.862	

Table 2 - Typical Fuel Range Fuel Properties

71%w Full Range Thermal Cracked
29%w Full Range Straight Run

I.B.P. F		110	60	280
5%		144	70	308
10		159	80	345
20		180	90	395
30		205	95	421
40		226	F.B.P.	422
50		256		
Sp Gr 60/60	0.753			
TEL	2-1/2 ml per gal			
Carbon %w	85.73			
Hydrogen %w	14.02			

between R for fuel and R for lubricant if all the water came from lubricant. For isooctane and the lubricant above, this could only, therefore, be 3.2%. Actually the error would usually be more like 1%, based on a 2:1 ratio of fuel to lubricant in blowby. Typical fuel range fuel properties are shown in Table 2.

References

1. M. D. Hershey, "Bibliography on Piston Ring Lubrication," NACA TN 956, October, 1944.

2. C. W. Georgi, "Motor Oil Consumption Characteristics," SAE Transactions, Vol. 3, No. 3, July 1949, 431-443.

3. J. S. Coon, and D. E. Loeffler, "Routes of Crankcase Oil Loss," SAE Transactions, Vol. 67, 1959, 59-70.

4. V. P. Guinn, "Liquid Scintillation Counting in Industrial Research," Liquid Scintillations Counting, C. J. Bell, Jr., and F. M. Hayes, ed. N. Y.: Pergamon Press, (1958), 166-182.

5. V. P. Guinn and R. A. Coit, "Measuring Oil Consumption with Tritium Tracers," Nucleonics, Vol. 17, No. 12, December 1959, 112-117.

6. D. E. Cooper, D. L. Courtney and C. A. Hall, "Radioactive Tracers Cast New Light on Fuel Distribution," SAE Transactions, Vol. 67, 1959, 619-639.

7. P. A. Bennett, M. W. Jackson, C. K. Murphy, and R. A. Randall, "Reduction of Air Pollution by Control of Emission from Automotive Crankcases," 1960 SAE Annual Meeting, Preprint No. 142A, February 1960, and SAE Journal, Vol. 68, No. 3, 30-36.

8. W. A. Daniel, "Flame Quenching at the Walls of an Internal Combustion Engine," Sixth Symposium on Combustion, Reinhold Publishing Co., 1957.

9. S. J. Beaubien and A. G. Cattaneo, "Piston Lubrication Phenomena in a Motored Glass Cylinder Engine," SAE Journal, Vol. 54, No. 10, October 1946, 60-67.

10. J. K. Patterson and R. C. Gregor, "Lubrication Factors Affecting Passenger Car Oil Consumption," Preprint No. 252, SAE National Fuels and Lubricants Meeting, Cleveland, November 1957.

11. J. P. Den Hartog, "Mechanical Vibrations," New York: McGraw-Hill Book Co., Inc., 4th edition. 1956.

12. J. C. Nettles and J. A. Meyer, Jr., "Piston Ring Vibration and Breakage," NACA ARR E 5 G 06, also E-44, August 1945.

13. A. R. Ford, and B. J. Robertson, "Gas Pressures Behind Piston Rings," Automotive Industries, Vol. 75, No. 4, July 25, 1936, 118-119.

14. S. W. Sparrow and T. A. Sherger, "Cylinder Wear, Where and Why," SAE Transactions, Vol. 31, 1936, 117-125.

15. M. E. Estey, "Answer to Today's Piston-Ring Problems," SAE Journal, Vol. 64, No. 3, March 1956, 39-43.

16. P. deK. Dykes, "Mechanism of Oil Loss Past Pistons," Proceedings, Instn. Mech. Engrs., Vol. 171, No. 11, 1957, 413-26.

17. S. Eilon, and O. A. Saunders, "A Study of Piston Ring Lubrication," Proceedings, Instn. Mech. Engrs., Vol. 171, No. 11, 1957, 427-443.

18. W. A. Pliskin, J. E. Edwards, and F. P. Brundy, "The Vibration of 'Free-Free' Curved Bars," Journal of Applied Physics, Vol. 14, No. 8, August 1943, 410-417.

19. D. Frazer, A. R. Klingel, and R. C. Tupa, "Friction and Consumption Characteristics of Motor Oils," Industrial and Engineering Chemistry, Vol. 45, No. 10, October 1953, 2336-2342.

Discussion

Questions Concerning Radioactive Tracer Study

P. A. Bennett, and C. R. Begeman
General Motors Corp.

This paper illustrates an interesting application of radioactive tracers to, admittedly, a very difficult problem. However, the paper raises a number of questions which we would like to ask of the author.

Prof. Starkman assumed for his calculations that the gases leaving the condensers were saturated with water at 32 F. It

Table A - Moisture Content of Exhaust and Blowby Gases

	Approx. Normal Moisture Content (Grains/lb)	Probable Moisture Content After Condenser (gr/lb, Air Sat. at 40% F	Correction Factor, %	
			Probable	Prof. Starkman
Exhaust	600	36	6	4
Blowby	150	36	24	4

has been our experience that it is very difficult to reach a dew point below about 40 F when utilizing a coil at 32 F to cool engine exhaust gases. Were direct measurements of the dew point of the gases leaving the condensers made to substantiate the assumption of a 32 F dew point?

In addition, it was stated that "The amount of water which will pass through the condenser is only 4% of that usually present in the exhaust or blowby stream." This statement assumes that the exhaust and blowby gases have equal mointure contents. Although blowby and exhaust gas moisture contents will be equal after passing through the copper oxide furnace, they are not equal when the gases bypass the furnace as was the case in obtaining the data of Figs. 4 and 5. The effect of this difference in moisture content is illustrated by the data in Table A.

Although the exhaust gas moisture content will vary with fuel, airfuel ratio, and other factors, the exhaust gas moisture content is of the order of 600 grains per lb of dry exhaust gas (Table A). Normal blowby moisture content is of the order of 150 grains per lb. If the dew point of the gases leaving the condenser is actually about 40 F, the moisture content is about 36 grains per lb. Accordingly, although the exhaust gas correction factor is not widely different from the 4% assumed, the blowby correction factor may be in error about 6-fold.

Fig. 6 indicates that some 90% of the lubricant loss was via the exhaust. This ratio is supported by the data in Fig. 3. Consideration of the data of Figs. 4 and 5 suggests that the ratio of lubricant loss in the exhaust gases to the lubricant loss in the blowby gas was not always 10 but may be as low as 1.5. How much variation in this ratio occurred from test to test at widely different engine operating conditions? What were the operating conditions associated with the data of Figs. 4 and 5?

We would not expect that the ratio of oil leaving the engine in the exhaust gas to the amount of oil leaving in the blowby gas would remain constant with widely varying oil consumption rates, as reported by the author, unless the blowby rate paralleled the changes in total oil consumption. What variations in blowby rates were observed?

Under some conditions a significant amount of the total oil loss in the exhaust gas could be due to leakage past the valve guides. Was any attempt made to determine the ratio of the amount of oil leaking down the guides to that going past the rings? What effect would oil leakage down the guides have on the author's conclusions?

The legend in Fig. 6 indicates that the oil leaving with the exhaust gas is about twice as "oxidized" as the oil leaving the crankcase vent. On the basis of this information the author concluded that" . . . some of the oil passes into the combustion chamber is cracked or partially oxidized, mixed with partly [or] completely burned fuel, and then recirculated to the crankcase by combustion pressure. Fig. 6 is a flow diagram for the oil and fuel and their degradation products as they must circulate in the engine." Although we would agree that a certain amount of the oil passing the rings into the combustion chamber probably eventually returns to the engine crankcase, the limited data presented in the paper do not constitute proof of the proposed mechanism.

Why was a 5W oil chosen for the experimental program? We would expect that the radical effect of cylinder wall temperature on oil consumption with increasing temperature would result from the use of a less volatile lubricant.

The reasoning that the oil consumption at 1300 rpm was due to vibration of the piston ring is interesting and suggestive of good detective work. Although the author strongly advocates that a resonant ring vibration is the explanation, it was not proved that the oil consumption at 1300 rpm was due to this cause. A stronger case might be made directly by showing that the rings resonate at this engine condition, or indirectly by changing the natural frequency of the ring to establish that such changes alter the oil consumption characteristics of the engine.

In discussing the magnitude of the viscous damping necessary to explain the shift in vibration frequency from theoretical to observed, the author mentioned that "The frictional forces between the cylinder wall and ring would, therefore, have to be the major contributor to the damping factor." However, since he has assumed that the vibration is radial, the friction of the ring on the wall would be essentially zero except during those periods when the ring was extended. On the other hand, we would expect a frictional force between the ring and the top or bottom of the ring groove. The presence of oil between the ring and the top or bottom surface of the ring groove would be expected to result in viscous damping of a radially vibrating ring. Would

the author comment on this as a possible source of damping?

In addition, before the proposed technique can find wide application, potential users must have additional information concerning the limitations of the technique. For example, approximately one minute was required to collect a sample for analysis. Therefore, the technique would appear to have limited utility as a method for studying instantaneous oil loss rates.

It is required, of course, that the samples analyzed be representative of the total exhaust or crankcase vent gases. In this connection we would like to ask how much tritium was left in the combustion chamber deposits, in the exhaust system, or the sample lines? Unless the tritium loss was a constant percentage of the total tritium in the sample at various operating conditions, some difficulty would be encountered in interpreting the data.

Use of Tracer Technique

A. M. Brenneke
Perfect Circle Corp.

IMPROVED techniques for accurately determining oil consumption are something Perfect Circle is always seeking. We are particularly pleased that Prof. Starkmen chose to investigate the tracer technique because we believe the ultimate solution to the problem lies in this method. These remarks will be confined to the application and use of the tracer technique.

Our company had a brief speculative fling at the tracer method for measuring oil consumption in 1951. Knowing that iodine was compatible with lubricating oil, we consulted a commercial lab, who confirmed that an isotope of iodine could be blended with lube oil, and contracted with this same commercial laboratory to supply tracers and supervise a preliminary investigation in our lab. Iodine 131 was used and a geiger tube was buried in a water-cooled thin-walled tube in the exhaust pipe of a single cylinder test engine. It was hoped that this would give a direct, continuous, and instantaneous oil consumption indication. The counter clacked away when the engine was started, but continued after the engine was shut down. The combustion products had condensed in the exhaust system for something more than 27 ft downstream from the engine. It appeared that we might salvage the project if we accepted a sampling procedure. Since this did not seem to offer any advantage over the method which was being used then, our venture into tracer technology was abandoned and hasn't since been revived.

Since 1945 we have been using a rather simple system that gives a continuous strip chart record of oil consumption, which approaches an instantaneous consumption indication with a reasonable degree of accuracy. A constant oil level is maintained in the engine sump by an overflow pipe, and oil is pumped from the sump to a tank on recording scale at a rate of about 2 G.P.H. Oil is pumped from scale tank back to the sump by another pump at half that rate. Hence, any oil leaving the engine is removed from the scale tank. This low rate of circulation through the scale tank permits use of high sensitivity scales, and a quite accurate consumption rate indication can be obtained in as little as 1 hr after engine temperatures are stabilized. Oil temperature must be held within ± 2 F for good accuracy.

We congratulate Prof. Starkman for the great progress his work represents over our early efforts. It is hoped that he will continue its development until it is a practical tool for every day lab use. We believe that to realize this, development must continue until the technique yields a continuous rate indication, preferably on a cylinder by cylinder basis. Also, to completely satisfy the requirement, equipment should be portable enough for vehicle installation.

In conclusion, we should like to suggest the possibility that some of the peculiarities of speed, load, and oil consumption are due to variations in oil consumed via the valves and guides, rather than a function of piston ring vibration. It is not unusual for as much as 75% of average gross oil consumption to be by this route and the percentage varies widely with speed and load.

Tracer Technique — Too Costly?

M. M. Roensch, and
J. C. Brabetz
Chevrolet Div.
General Motors Corp.

THIS PAPER SHOWS the radioactive tracer technique to be a valuable research tool in the analysis of engine oil consumption. Among its more promising applications, I would include:

1. Evaluating transient behavior of oil consumption; that is, the instantaneous effects of varying a single engine operating condition.

2. Determining oil consumption of individual cylinders, by sampling each exhaust port.

3. Anti-smog investigations. (Unburned hydrocarbon detection).

We find, however, that most investigations can be conducted to our satisfaction using less complex equipment. The cost of equipment and highly trained personnel could only be justified by a great need for the information that the tracer equipment could provide.

Prof. Sparkman lists several disadvantages for the "oil weigh" method that we do not find too objectionable:

1. "Excessive time for single determination". - It is true that oil consumption rate by the tracer method can be determined immediately. However, the test must be carried on for a period of at least 3 or 4 hr to assure that the rate is not changing. In this time, the constant weigh method would tell the same story.

2. "Low reliability resulting from small consumption rates". - We find the constant weigh method reliable even at low consumption rates when the following conditions are met:

a. Accurate scales are employed.

b. Weight readings are taken every 15 to 30 minutes.

c. Engine temperatures are maintained at stabilized conditions.

The slope of the plotted readings shows when the oil itself has become stabilized from dilution, and when the consumption rate becomes uniform.

3. "Oil leakage being a complicating factor when using the weigh method". - Care is usually taken for an oil economy program. However, if some leakage does occur, it can be recovered by wiping rags, which are carefully weighed prior to and after the test run.

4. "Variable oil retention by engine". - When engine temperature is held constant in the constant weight method, oil retention apparently does not vary, as evidenced by steady scale readings as the test progresses.

The author does not state whether the weigh oil consumption method shown in Fig. 2 was actually drain-and-weight or constant weigh. It appears from the reading intervals (4 to 8 hr) that the drain-and-weigh method was used for comparison with the tracer-method. It seems likely that the results would be in much better agreement if the constant weight had been used, and readings recorded every 15 to 30 minutes. This would have insured against the probability of having the use wild readings.

The information shown in Table B typifies the clear cut answers our present laboratory facilities can give. We wished to measure the effectiveness of a cylinder head change in reducing abnormal oil consumption in experimental engines.

The cause was known: oil was being lost via the valve stems at turnpike cruising speeds. The proposed solution was considerably less costly than valve stem seals, and later proved effective in production, as the laboratory data had predicted.

Our present methods are made-to-order for work such as this. When more elusive information is needed, more elaborate methods will be used. The method Prof. Sparkman advocates seems well qualified for the latter category.

Table B - Oil Economy Comparison

Engine	Cylinder Heads	Oil Economy (MPQ) (At Turnpike Speeds)
A	Experimental	357
	Production	2080
B	Experimental	425
	Production	2085
C	Experimental	329
	Production	1800
	No Overhead Oiling	2092

Advantages of Tracer Technique

L. A. McReynolds
Phillips Petroleum Co.

A VERY USEFUL contribution has been made in this paper which presents a rapid method for determination of lubricating oil consumption. We agree that direct measurement of lubricating oil consumption is difficult, time-consuming and often inaccurate. Hence, the new method dependent upon chemical incorporation of tritium as radioactive tracer and the use of a liquid scintillation counter to measure the amount of oil being consumed should find widespread use. Tritium, being as isotope of an element that is a constituent of all hydrocarbons, may be introduced into hydrocarbon components at either specific or random positions. Present cost for tritium is approximately $2.00 per Curie and the required liquid scintillation instrumentation is now, or certainly soon will be, available in most well-equipped research laboratories. We hope and expect, therefore, that the method described and applied to study of certain factors affecting lubricating oil consumption in single cylinder engines, will be used by many and extended to studies in multi-cylinder engines.

The amount of oil consumption in a given engine can have marked and significant effects on engine deposits that affect useful performance life. This is indicated by the results of some tests run recently in our laboratory in a CLR oil test engine. The engine operating procedure employed consisted of cyclic operating conditions alternating between idle at 9.5 air-fuel mixture and wide open throttle operation at 15.5 air-fuel mixture. Water out temperature was maintained at 125 F. Not included in the total operating time were controlled shutdown periods. The results of two different tests are shown in Table C. The same engine, the same operating conditions, the same fuel and the same oil were employed. The only difference in the two tests was in the rate of "oil consumption". In Run 1, "oil consumption" was accelerated by forced additions every 40 hr. If necessary, some oil was withdrawn at each of these periods so that 2 ozs of new oil were required to bring the level back to the original full position. Run II was carried out with no forced additions and the oil consumption at the end of the test was approximately 1/3 of Test No. 1. Attention is called to the very significant differences in engine cleanliness ratings, particularly sludge, oil screen plugging, and oil ring plugging. These differences are far greater than could be accounted for by reproducibility shortcomings. Extrapolating test results from this same engine operated under somewhat different conditions but with uniform oil consumption,

Table C - Effect of Oil Consumption on Engine Cleanliness

	Run I		Run II
Engine	-	CLR	-
Operating Conditions	-	Controlled Cycle	-
Fuel	-	MS Seq. V Reference	-
Oil	-	"C"	-
Total Operating Time, Hr		206-1/4	
Oil Consumption, oz	14.7(a)		4.9
Piston Varnish	8.0		7.8
Sludge	41.5		27.9
Oil Screen Plugging, %	2		85
Oil Ring Plugging, %	20		55

(a) Accelerated by forced additions

Table D - U. S. Oil Consumption Trends in Passenger Cars

	Average Miles	Average Qt Makeup	Average Qt Makeup/10,000 Miles	
1954	10,127	10.00	9.87	
1955	9,492	9.77	10.29	
1956	8,979	8.43	9.39	
1957	9,304	8.12	8.73	-17% over 1954
1958	9,364	7.67	8.19	-20.4% over 1955

Based on National Petroleum News 1959-1960 Fact Book

it is believed that the differences shown are at least as great as those which would be obtained between a non-additive oil and a detergent oil comparable to many commercial products now being recommended for Service MS.

Accurate data on oil consumption in passenger car engines are difficult to find in the literature. However, from various sources we are quite sure that oil consumption is steadily becoming less in passenger cars. Several factors account for this. The designer is consistently improving this understanding and practical application of factors affecting oil consumption from a design standpoint. Metallurgy and surface finishes have improved. Additionally, the petroleum technologist has developed improved lubricating oils over the years which, among other things, have shown steady improvement in ability to reduce engine wear. The general trend toward reduced oil consumption levels is indicated by Table D which shows data based on information published in the National Petroleum News, 1959-1960 Fact Book. It can be seen from these data that oil consumption in passenger cars operated in the United States has decreased from 17-20% in the last 5 years.

The data in Table C indicate that oil consumption rates have a marked influence on the punishment that a given oil takes in the crankcase of a given engine during a given operational period. These data also suggest that as oil consumption characteristics of passenger cars improve, consideration should be given to more frequent oil drain periods if the common objective of both the automotive and petroleum industries to prolong new car performance is to be observed.

How often to drain oil is a question that has sometimes been argued with more emotion than technical fact. The information and techniques presented by Prof. Starkman should stimulate the procurement of more data concerning oil consumption. This, in turn, should be of considerable aid to the question of sound oil drain practices.

Use of Tracer Method for Single and Multi-Cylinder Work

R. A. Coit, and
V. P. Guinn
Shell Development Co.

THE CONVENTIONAL way of determining the rate of oil consumption in an engine operating under fixed conditions, as Prof. Starkman has discussed, is the weight loss method. This method has certain obvious disadvantages, some of have been enumerated. We would like to add three more to the list:

1. Variations in consumption rate during a given run, such as on startup, are not detectable.
2. Different routes of oil loss cannot be distinguished.
3. The results are affected by changes which the condition of the engine undergoes during long runs.

These shortcomings are circumvented by the radioactive method involving the use of tritium-labeled lube oil. In

this method, incomplete combustion of sampled material introduces impurities in the condensed exhaust water which can interfere with the liquid scintillation counting of the water. One reason the bleed stream is passed through a hot copper oxide oxidizer before condensation is to insure complete combustion of all organic matter to CO_2 and H_2O. This is very essential in the case of the loss via crankcase breather gases, since here most of the material is only partially oxidized. In this respect, further investigation of the type of data shown by Prof. Starkman in Fig. 5 may be desirable.

In the Shell Development laboratories this method has been used, not only for single-cylinder oil comsumption studies, such as those described by Prof. Starkman, but also for multi-cylinder engine work. In a modern, high performance V8 engine, we obtained a smooth curve with oil consumption increasing as engine speed increases. Apparently there was no peculiar relationship with speed and load which had a controlling influence on the lubricating oil consumption in the multi-cylinder studies - unlike the single cylinder case discussed by Prof. Starkman.

In multi-cylinder oil consumption studies, this method can be invaluable in determining individual cylinder contributions to the overall engine oil consumption. This type of determination may also be quite useful in studying interactions with engine combustion phenomena. We have found a 50% increase in oil consumption through the combustion chamber during preignition, for instance.

Another application of interest is the determination of the route of engine oil consumption, other than those disclosed, for instance, past the piston rings or down through the valve guides in an overhead V8 engine. Such data can easily be obtained by separating the valve or top deck oil supply from the main sump.

The method itself is straightforward, and can now be carried out with commercially available apparatus, that is, a commercial liquid scintillation counter. During the early work on this method oil consumption rates as low as 0.1 gr/hr were readily measured. With recent improvements in the liquid scintillation method, rates as low as 0.01 gr/hr are detectable without increasing the tritium content of the oil. In addition, a relatively new method of tagging the oil with tritium is now available. This tritium gas exposure method of Wilzback simplifies considerably the preparation of the labeled oil. Tritium (radioactive hydrogen) is an excellent tracer for such work, as it is both inexpensive and easy to handle. It emits no gamma radiation, only very low energy beta particles, and hence there is no shielding problem.

Author's Closure to Discussion

IT IS QUITE OBVIOUS from the nature and extent of the discussions that very serious and detailed consideration has been given by the discussors to both the method of the radioactive technique and to the theory for abnormal oil consumption which was proposed.

A number of specific questions have been raised by Messrs. Bennett and Begeman. On the specific subject of condenser efficiency, a very thorough effort was made to insure an efficient condenser system. This was checked and proved by setting up multiple condensers in series with increasingly colder materials (below 32 F) flowing in the condenser side. The negligible amount of condensate found after the first pass was sufficient evidence to conclude that the system used was condensing at what must have been much higher efficiencies than they experience. It should further be pointed out that Table A does not show, as Bennett and Begeman state, a 6-fold "error". Even if the situation is as they interpreted, a much more modest figure of 20% neglect to account for the total material would result. This, they are certainly aware, is well within the limits of experimental error of other oil consumption determination methods.

It is recognized and pointed out in the text that Figs. 4 and 5, in comparison to Fig. 3, show levels of lubricating oil consumption which were radically different. Fig. 3 shows data obtained shortly after the engine was overhauled and the piston rings replaced. Figs. 4 and 5 represent data obtained prior to that overhaul when the total lubricating oil consumption rate was at a much higher level. This is noted in two places in the text. In the tests reported, the ratio of lubricant loss in the exhaust gas to lubricant loss in the blow-by gas was always near 10 to 1, as shown in Fig. 6.

The blow-by rate indeed varied with engine conditions. However, the information regarding the changes corresponding to the various tests is not reported here because this factor was not felt to be of great consequence.

With regard to the question of oil consumption past valve guides, the valves were separately lubricated with non-tagged material, and as pointed out in the discussion by Messrs. Coit and Guinn, this portion of the consumption can be quite well determined by auxiliary tagging means.

With regard to a last technical point, that of the influence of the frictional force between the cylinder wall and the piston ring, the influence would be primarily in the contribution the face friction makes to the ring face to ring land pressure.

As a general closing comment, it must be repeated that what was attempted in the paper, in addition to presenting the method, was to represent a possible mechanism for abnormal lubricating oil consumption. Questions of proof of inferential theories are implicit. It is difficult to present completely convincing proof of a theory in the stage of development that corresponds to that given here. This does not, should not and will not, however, preclude this author from coming to the conclusions which were drawn from the experimental data. There is no denying, as far as he is concerned, the exceedingly strong evidence that a vibration of the piston rings can be construed to contribute to excessive oil consumption. The author is most happy to allow this to stand in the record on the evidence available, particularly as a challenge for future investigators.

U. S. Lunar Travel Program

Col. Donald H. Heaton
National Aeronautics and Space Administration

THE NASA LUNAR program has as a long range objective manned landings on the lunar surface and the establishment of a lunar base as an outpost for scientific observation and exploration. This long range goal we feel is possible of achievement through extensions of scientific knowledge and technology at our command today. No new scientific discoveries need be made and no new technological breakthroughs appear necessary. However, a vast amount of effort and money must be invested and a rather considerable span of time must be devoted to an aggressive and carefully integrated program before manned lunar flights become a practical reality.

There is a great deal we need to learn about the cis-lunar environment: for example, the types, intensity and energy levels of radiation, together with the time variation of these and other space environmental factors. We need to refine our ability to predict space environmental phenomena for the protection of our lunar travelers even as our meteorologists forecast the weather which is the primary environmental hazard to flight within our atmosphere.

Instruments are being designed to detect the presence of energetic particles, together with magnetic field measurements, which will determine the absence or presence of trapped radiation belts. Scientists are particularly interested in particle streams from the sun because they present a serious hazard to space travel. It is known that the flux of protons on occasion is 350 times greater than the normal cosmic ray intensity and that the duration of the proton beam is on occasion long enough to be a lethal dose for a man in space. There are two solutions to this problem:

1. Shield the space traveler.
2. Provide a prediction capability that will minimize the risk of a short excursion into space.

The data obtained from these experiments will establish the amount and kind of shielding necessary. For example, if it is found that the stream of particles is isotropic it will be necessary to completely enclose the man; whereas, if the particle stream is directional, orientation of a shield between the man the sun would be adequate.

Of course, another question arises when man lands upon the moon. Will it be necessary for him to remain close to a landing craft containing shielding or will it be possible to predict flares far enough ahead of time to allow him to venture considerable distances from the landing craft? As can be seen the answers to these questions will definitely affect the design of the lunar manned spacecraft and the makeup and duration of missions assigned early lunar explorers.

Providing launch vehicles with the capability of imparting escape velocity to the mass of the lunar manned spacecraft and all of its equipment for landing on the lunar surface and returning safely to earth will be a major task. Although we can see no gaps in fundamental knowledge nor

lack of promising technical approaches to the design and development of the launch vehicles and spacecraft, we face an engineering and testing effort which, with supporting laboratory and space research, assumes the proportions of a major national undertaking.

Lunar Program within Overall NASA Program

The NASA program of space exploration can be divided into three phases, which, though sequential in character, exhibit considerable overlap in time. The first of these is the program for scientific exploration of the region surrounding the earth by means of scientific earth satellites and sounding rockets. Execution of this program is the responsibility of the Goddard Space Flight Center. This program covers a number of scientific disciplines and areas of investigations such as geodesy and gravitation, the upper atmosphere, magnetic and electric fields, the radiation belts, micrometeorite concentrations and effects, the sun and solar terrestrial relationships, the stars and bioscience. From this listing it is evident that, although the scientific earth satellite program supplies information indispensable to the design of spacecraft which must traverse this zone enroute to and from the moon and planets, it also pursues very important scientific goals of its own.

Such projects as the unmanned orbiting geophysical observatory and the orbiting astronomical observatory will remain active perhaps throughout the second, or lunar phase of the space exploration program. It is this phase with which this paper will deal.

The third or planetary phase will have its major buildup after the lunar program is well underway. Early phases of the planetary program will use not only the technology built up in the course of the earth satellite and lunar programs, but also some of the same launch vehicle and spacecraft hardware.

Each of the three phases of space exploration mentioned (earth satellite, lunar, and planetary) in itself has three stages which again show appreciable overlap. These stages are:

1. Development of required technology and carrier hardware.
2. Unmanned exploration.
3. Manned exploration.

Each of these stages will be followed by an exploitation of the potentialities of the newly opened frontier.

The moon is, of course, the next logical step in space exploration beyond instrumented earth satellite operations. It is relatively close to the earth, a mean distance of 238,875 miles, with a flight time via a minimum energy transfer ellipse of 90 hr. The flight trajectory we will use for the unmanned program will take 66 hr and was selected because the payload sacrifice was tolerable and the shorter transit time eased the guidance problem and permitted the lunar landing, or injection into a lunar orbit, to be viewed from this hemisphere. Furthermore, the period of the lunar orbit about the earth affords a launching opportunity approximately every 28 days, on a direct ascent trajectory and much more frequently if a "parking orbit" is employed. This contrasts to one opportunity every 1-1/2 years for Venus, our nearest planet.

Unmanned Lunar Program

The exploration of the moon with unmanned spacecraft has a number of objectives of great importance to science. The scientific significance of lunar exploration arises from the fact that its surface has not been subjected to the erosion of winds and water, and therefore may carry a record of the early history of the solar system. This record has been lost forever on the earth, Mars, or Venus, and is only available on the moon. The moon may also have on the layer of dust which has accumulated on its surface, organic molecules which will give us a clue to the development of physical life on the earth.

The primary scientific objective of the lunar science program is the exploration and investigation of the moon for the information which it can provide on the history of the earth-moon system and on the origin of planetary bodies in the solar system. Also, as has already been mentioned, chemical analysis of the surface dust which has accumulated over many aeons may turn up organic molecules, precursors of living organisms, which may prove to be of immeasurable importance to the biological sciences. Moreover, the exploration of the lunar surface, and the analysis of its physical and chemical properties, are necessary steps in the planning and designing of manned instrument stations and the solution of the problems of construction and life-support for a manned lunar station.

Finally, the unmanned lunar program affords an invaluable opportunity to test design approaches and subsystems such as terminal guidance systems, landing techniques, and landing gear designs which may later be incorporated in manned systems and measurably reduce the cost of developing and testing expensive manned spacecraft systems and the risk involved in initial manned flights.

The missions which are planned to implement this program include lunar orbiters, rough and soft landing packages, and mobile vehicles for unmanned exploration. Fig. 1 shows the projects which constitute the unmanned lunar program.

The first significant step toward accomplishing the unmanned program will be made in NASA's Ranger program. An earlier and limited attempt to place an instrumented satellite around the moon with the Atlas Able 5 vehicle was not successful because of launch vehicle failures.

Development is underway on experiments for the study of

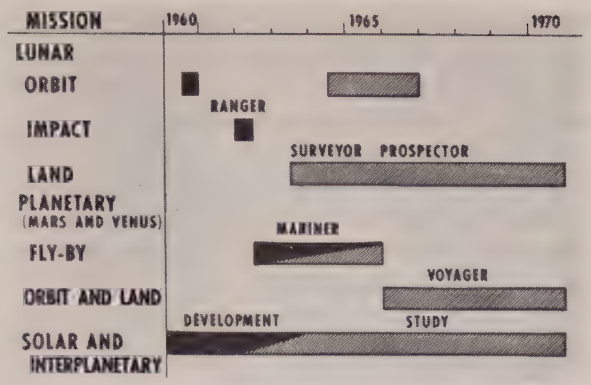

Fig. 1 — Program plan

the moon with contact instrumentation under the Ranger program. Ranger experiments include vidicon camera and television systems, gamma ray spectrometers, and seismograph systems.

All lunar missions visualized require the use of specific techniques, most of which are to be tested in the Ranger flight series. Taken in order of employment during a typical flight, these techniques might be as follows:

1. Time-dependent guidance parameter settings and launch of the vehicle.
2. Injection into a so-called "parking orbit," a more or less prolonged coast, which places the vehicle at the proper location in space for departure into the desired lunar trajectory.
3. Acceleration from parking orbit to escape speed with guidance to place the vehicle on a nearly standard departure path.
4. Tracking and telemetry during the above phases, followed by orbit computation and an orbit correction maneuver upon command.
5. Data communication during transit, followed by an accurate retro-maneuver for orbit around or landing on the moon.
6. Automatic experimentation in lunar orbit or after landing, with data transmission over a high-gain communication link.
7. Semi-automatic data handling after reception.

The Ranger spacecraft, as depicted in Fig. 2, is being developed by the Jet Propulsion Laboratory. A version differing primarily in the instrumentation carried will, we hope, be used on the early planetary missions to Mars and Venus. In the Ranger series, this spacecraft will be launched by the Atlas Agena B vehicle which can handle a heavier payload than the Atlas Able and also has the capability not possessed by the Atlas Able of upper stage engine restart and coasting flight attitude control which permit the Agena stage, with its spacecraft, to coast in a parking orbit to the point in space where a second interval of rocket operation will put the Ranger on its ascent trajectory to the moon. This capability greatly augments the lunar launching opportunities per year.

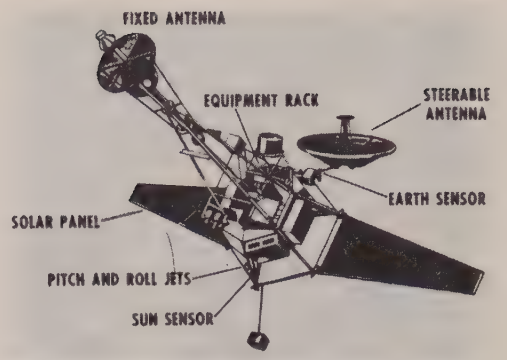

Fig. 2 — Spacecraft for ranger and mariner series

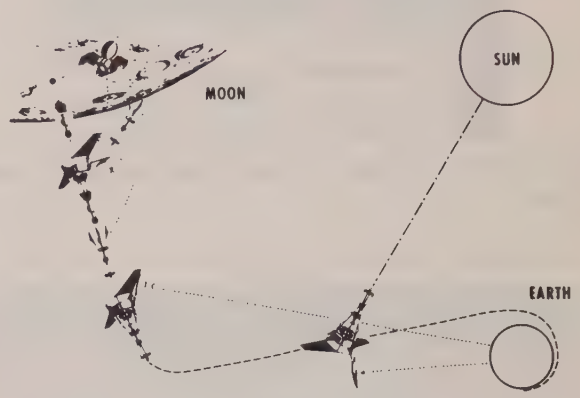

Fig. 3 — Ranger flight and terminal maneuver

The Ranger flight and terminal maneuver are shown in Fig. 3. During the early stages of the flight, the spacecraft employs the attitude control jets shown in the figure to maintain three-axis attitude control with its antenna pointing toward the earth and its solar panels toward the sun. Radio tracking reveals any necessary course corrections, which the spacecraft then makes on command by orienting itself for a midcourse rocket firing and then reorienting itself with its principal axis toward the sun for travel through cis-lunar space. As the spacecraft approaches the lunar surface, it orients itself on command along the vertical descent path and begins taking high resolution television pictures plus gamma-ray spectroscopy recordings. At the lowest possible altitude the survivable capsule is slowed by retrorocket for a rough but safe landing.

The Ranger spacecraft just described is well along in development, as is its scientific payloads. First test launch will take place in the latter part of 1961. The actual lunar landing series is scheduled for 1962.

Spacecraft Planned for More Advanced Unmanned Missions

The next spacecraft to be undertaken as part of the unmanned lunar program is Surveyor. It is to be designed for

Fig. 4 — Artist's concept of surveyor for soft lunar landings (Centaur)

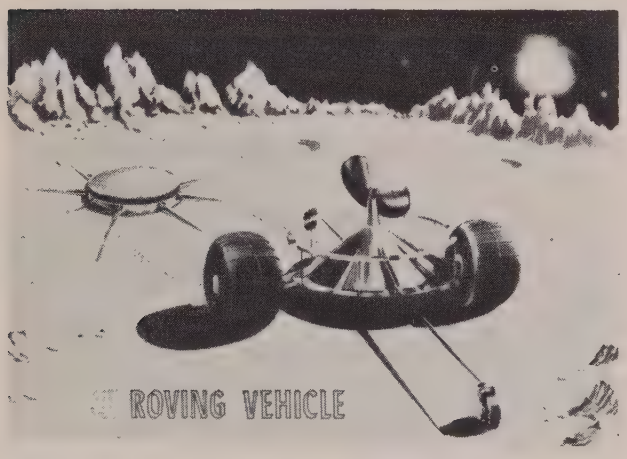

Fig. 5 — Prospector for lunar landing (Saturn)

the lunar soft-landing mission using a Centaur launch vehicle. An artist's conception of this spacecraft is displayed in Fig. 4. This spacecraft will be designed to deposit a moderately heavy (100-300 lb) scientific payload on the lunar surface.

The Surveyor will deposit on the moon scientific instruments capable of making the first direct measurements of the chemical and physical properties of the lunar crustal material. A drill will extend these measurements to a few feet below the surface of the moon. The measurements themselves will be made with instruments similar to those now used in earth-bound geochemistry and geophysics; that is, X-ray fluorescence spectrographs, gamma-ray spectrographs coupled with neutron activation equipment, densitometers, thermal and electrical devices for measuring conductivities, and gas chromatographic analyzers for detecting the presence of organic molecules (some of which are believed to have been detected in the interior of meteorites). Mass spectrometers, gravitometers, and seismometers will probably be included, though perhaps not in the earliest soft-landing vehicles. The soft-landing spacecraft will be equipped with vidicon cameras and a selection of lenses enabling both panoramic and close-up photographs of the surrounding moonscape and lunar surface material.

These soft-landed analytical laboratories will enable us to understand in great detail the nature of the moon's surface in a few selected spots. In order to extend our knowledge progressively over the whole moon, it is necessary to correlate the characteristics of the sample locations with the characteristics of other portions of the moon untouched by these landed spacecraft. For this purpose, a precision lunar orbiter will conduct a geophysical and geochemical survey of the whole moon from a distance of a few hundred kilometers above the surface. This vehicle will photograph the moon's surface with a range of resolutions available on command from earth. It will conduct a complete gamma-ray analysis of the regions over which it flies. Other spectral analyses will be included if instrumentation techniques and soft-landing measurements indicate their desirability. By this means, we will attempt to extend the analyses made directly on the spot to an understanding of the whole moon.

Prospector, a lunar soft-landing spacecraft requiring the Saturn launch vehicle, is currently under study by the Jet Propulsion Laboratory, and by the Marshall Space Flight Center for JPL. As now envisioned, the Prospector spacecraft would consist of a soft-landing "truck" plus several alternate payloads such as the mobile vehicle pictured in Fig. 5. This mobile laboratory would have first priority as a Prospector payload. It would be capable of exploring throughout a radius of about 50 miles, terrain permitting, and would obtain more data than could be obtained with Centaur launched nonmobile spacecraft. It is anticipated that the mobile vehicle would be used in areas of particular interest as highlighted by previous flights with Centaur.

Manned Lunar Flight

The benefits that might accrue from the manned exploration of space are, in a large measure, unknown. It is certainly clear that no amount of instrumentation will tell us as much about the moon, or the planets, as man himself will be able to tell.

We should, therefore, state only one broad objective for the manned space flight program: "To provide the capability for manned exploration of space."

With this objective in mind, we have developed a program that is broadly outlined in Fig. 6. At this point it should be stated that official approval of this program has

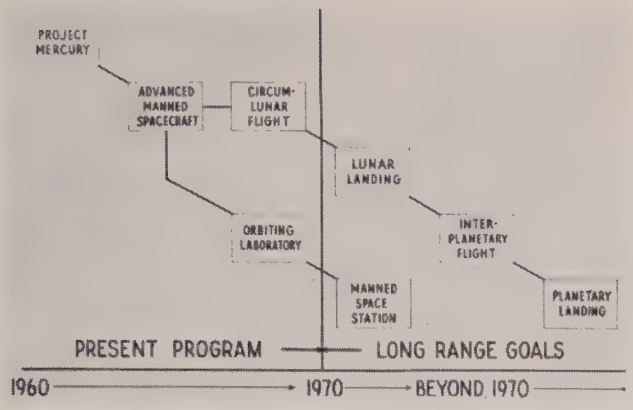

Fig. 6 — Manned spaceflight program

not yet been obtained. Rather, this presentation includes what we now believe to be a rational and reasonable approach to a long-range development program leading to the manned exploration of outer space. Manned flight to the moon is, as mentioned earlier, an intermediate, a major step in the long-range spectrum of manned space flight depicted in Fig. 6.

The initial step in this program is Project Mercury: a project designed to put a manned satellite into an orbit about 120 miles above the earth's surface, let it circle the earth three times, and then bring it back safely. Project Mercury, it is believed, is an essential step before we can proceed with other, more difficult manned space missions. It is true that all the plans for scientific exploration of space assume that eventually man will participate in that exploration. However, although all of us think men can be useful in this new environment, no one knows for sure.

If it should turn out that men cannot perform useful work in space, it is quite possible that the direction of a substantial portion of our efforts will have to be changed. So it is important to find out about man's capabilities in space, and Project Mercury is the simplest way to learn what we need to know, at the earliest possible date. As is well known, indications from Cdr. Shepard's historic suborbital flight have given us some rewarding positive information in this area.

The determination of man's capabilities in a space environment is, however, only one of the benefits that will be derived from Project Mercury. Of equal importance is the technical knowledge being gained during the design, construction, and operation of the first spacecraft specifically engineered for manned flight in space. The accomplishment of Project Mercury will mark a tremendous step forward; man's venture into space will immeasurably extend the frontiers of flight. The speed of flight will be increased by a factor of 8 over present achievement, and the altitude by a factor of 5; the environment encountered in space flight will be one that heretofore has not even been approached. This extension of the flight envelope has required major technical advancements in many diverse fields, including aerodynamics, biotechnology, instrumentation, communications, attitude control, environmental control, and parachute development, and so forth. By its very advanced nature, therefore, Project Mercury has opened the door for the next step in the manned space flight program.

This next step involves the development of a manned spacecraft designed to allow man to perform useful functions in space. This spacecraft should ultimately be capable of manned circumlunar flight, as a logical intermediate step toward future goals of landing men on the moon and the planets. The design of the spacecraft should also be sufficiently flexible to permit its use as an earth-orbiting laboratory, as a necessary intermediate step toward the establishment of a permanent manned space station. In this decade, therefore, our present planning calls for the development and construction of an advanced manned spacecraft with sufficient flexibility to be capable of both circumlunar flight and useful earth-orbital missions. In the long range, this spacecraft should lead toward manned landings on the moon and planets, and toward a permanent manned space station. This advanced manned space flight program has been named "Project Apollo."

The design for an ultimate circumlunar flight will require the solution of many, but not all, of the problems associated with a manned landing on the moon; this is particularly true of the atmosphere reentry and recovery terminal phase. The mission will require a considerable amount of trajectory control, thereby imposing rather severe requirements on the navigation and control system. Manned circumlunar flight is the ultimate manned mission consistent with our planned booster capability, that is, with the Saturn vehicle used in a direct ascent mission. The Saturn C-2 vehicle can be used for the manned lunar landing mission, but only by means of orbital assembly and refueling techniques. In order to confer escape velocity without orbital staging to the mass represented by an Apollo spacecraft fitted out to land on the moon and return to earth, a much larger vehicle than Saturn will be required.

Before circumlunar missions are attempted, earth-orbital flights will be required for spacecraft evaluation, for crew training, and for the development of operational techniques. In conjunction with, or in addition to, these qualification flights, the spacecraft can be used in earth orbit as a laboratory for scientific measurements or technological developments in space. In order to achieve this multiplicity of missions, it may be desirable to employ the so-called "modular concept" in the design of the advanced manned spacecraft. This concept is illustrated in Fig. 7.

In this design concept, various buildup blocks or "modules" of the vehicle system are employed for different phases of the mission. Basically, the spacecraft is conceived to consist of three modules:

1. A command center module.
2. A propulsion module.
3. A mission module.

In a manned lunar landing version, there is a good chance that the additional velocity increment required for lunar landing will dictate a fourth lunar landing module. The command center would house the crew during the launch and reentry phases of flight; it would also serve as the flight control center for the remainder of the mission. It is anticipated that this module will be identical for both the circumlunar and the earth-orbital missions.

The propulsion module would serve the primary function of providing safe return to earth in case of an aborted mission. In this sense, it might be compared with the escape tower and retro-rockets on the Mercury capsule. In addition, for circumlunar flight, this component should have the capability of making midcourse corrections; it might also be used to place the spacecraft into an orbit around the moon and eject it from that orbit. In an earth-orbital mission, the propulsion module should permit a degree of maneuverability in orbit or rendezvous with other vehicle. Once again, it may be desirable to provide identical propulsion units for both orbital and circumlunar flights.

The command center and propulsion units together might be considered, for some applications, as a complete spacecraft, even without the mission and lunar landing modules.

The mission module would differ for the various flight missions. For circumlunar flight and lunar landings, it would be used to provide better living quarters than the command center can afford, and some equipment for scientific observations. (Detailed design studies may well indicate that the command center and lunar mission modules should be combined into a single package.)

For earth-orbital flight, the mission module can be considerably heavier than for circumlunar flight. Hence this module can usefully serve as an earth-orbiting laboratory, with adequate capacity for scientific instrumentation and reasonably long lifetimes in orbit. Of all the modules mentioned, only the command center unit would be designed with reentry and recovery capability. Fig. 8 illustrates some of the requirements for the command center module.

This module must be designed to reenter the earth's atmosphere at essentially parabolic (or escape) velocity - about 36,000 fps. It will have to withstand the severe heating encountered at these velocities, and it must be statically over the entire speed range from 36,000 fps to the landing speed.

A degree of maneuverability will be required to stay within the limits of a rather narrow flight corridor. The boundaries of this corridor are determined by maximum tolerable loads or heating, on the one hand, and minimum aerodynamic loads to cause reentry in a single pass, on the other hand. The amount of maneuverability can be minimized through the provision of adequate midcourse propulsive corrections.

The maneuverability provided for corridor control should also permit a landing at a fixed point (or within a small area) on earth.

A conventional airplane-type landing is not required. Instead, vertical landings using parachutes or other devices are acceptable. Because of the world wide aspects of these missions, the vehicle must be capable of surviving both ground and water landings.

An important design consideration is that safe recovery must be possible for both normal and aborted missions. As in the case of the Mercury capsule, it is expected that the most severe requirements will stem from some of the off-design conditions.

There has been a great deal of discussion concerning the role to be played by the pilot in a space mission. Under the assumption that Project Mercury will demonstrate that man can indeed perform useful functions in space, we believe that in all future missions the primary control should be onboard.

This guideline is not to be construed as implying that there would be no automatic guidance or control systems on board Certainly there are many functions that can better be performed automatically than manually. But the basic decision-making capabilities, and some control functions, are to be assigned to the man.

Because of the possibility of a catastrophic failure of any

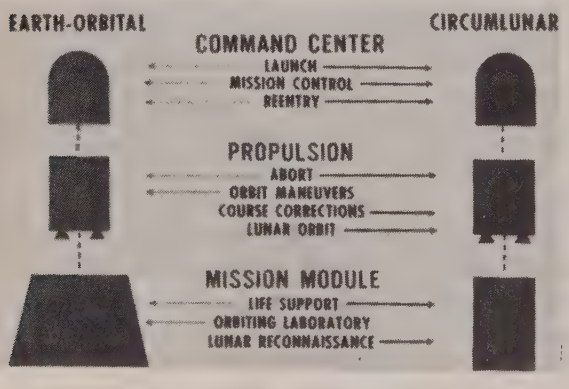

Fig. 7 — Modular concept

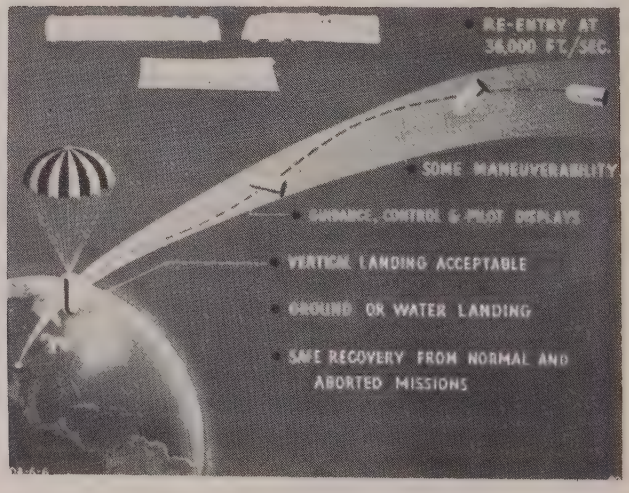
RE-ENTRY AT 36,000 FT./SEC.
SOME MANEUVERABILITY
VERTICAL LANDING ACCEPTABLE
GROUND OR WATER LANDING
SAFE RECOVERY FROM NORMAL AND ABORTED MISSIONS

Fig. 8 — Command center module

Table 1 - Requirements for Propulsion Module

Primary	Secondary
Safe recovery from aborts	Lunar orbit
Course corrections	Maneuvering in earth orbit
Return from orbit	

of the vehicle stages, the spacecraft must be equipped with sufficient propulsion to permit safe crew recovery from aborted missions. Such capability must be provided for an abort at any speed up to maximum velocity and should be independent of the launch propulsion system. Some of the requirements for the propulsion module are summarized in Table 1.

Preliminary studies have indicated that, for a circumlunar mission, roughly 1/3 of the permissible spacecraft weight will be required for onboard propulsion. In a normal mission, this same propulsion may be applied for course corrections, both while approaching the moon and when returning to earth. As mentioned earlier, the propulsion that must be carried for emergency considerations may, in a normal mission, be sufficient to place the spacecraft into satellite orbit around the moon.

In a manned lunar landing mission, the propulsion module would be used for lunar takeoff and escape, and as I mentioned earlier, for lunar landing as well, unless, as will probably prove a lighter solution, an additional fourth module is used. A fourth landing module, if incorporated, would be employed for course corrections enroute to the moon, whereas the propulsion module would provide midcourse adjustments on the return flight. Preliminary studies suggest that about 85% of the total weight at earth escape velocity must be invested in on-board propulsion.

For the earth-orbital mission, the propulsion module would again serve the primary function of providing safe return capability from aborted missions. If it is not needed for this purpose, then the available impulse might be used for maneuvering in orbit and for orbital rendezvous with other satellites.

We have tentatively specified that the advanced manned spacecraft should be designed for a 3-man crew. Our concept is that, during launch and reentry, this crew would be located in the command center unit but, for the remainder of the flight, at least two of the crew members would be in the mission module.

The use of a pressure suit in the command center module may be acceptable; but the mission module should definitely be designed to permit "shirtsleeve" operations, that is, operations without the use of pressure suits. We believe that pressure suits, as currently envisioned, would not be acceptable for the duration of a lunar flight.

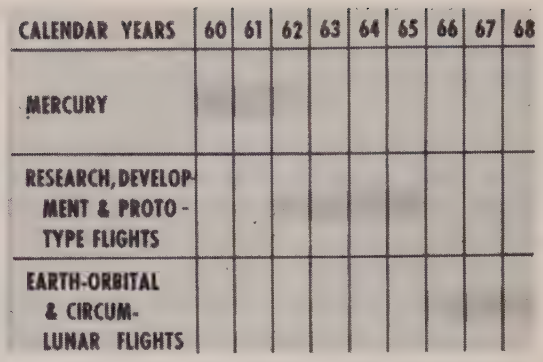

Fig. 9 — Flight program

The foregoing requirements apply for both the lunar missions and the earth-orbital mission. However, there are other requirements that differ widely between the two types of flight. For example, the lunar mission module requires an environmental control system that need only provide for about 1 week's life support; on the other hand, it may be desirable to keep the earth-orbiting laboratory in space for periods ranging from 2 weeks to 2 months.

The lunar module would carry only a minimum amount of instrumentation required to complete the mission, whereas a great deal of instrumentation for scientific measurements and observations should be provided in the orbiting laboratory.

Planning thus far has led to a proposed overall timetable for the advanced manned spacecraft program, as presented in Fig. 9.

Three companies have been selected to participate, by contract, in a program of system design studies. However, it should be emphasized that this program has no official standing as yet. Present thinking, however, is outlined in Fig. 9 to indicate the probable course of future flight events. It should be noted that major Mercury flights will probably continue for several years.

Research and development, and prototype flights of the advanced manned spacecraft are listed to start in 1962 and to end in 1965. Early flights in this series would be used to verify final design criteria for the spacecraft shape and its heat protection. The plan is to use Atlas-Agena-B as the launch vehicle for these missions. Following the Atlas-Agena flights, the Saturn vehicle will be used for full-scale development and prototype flights.

Earth-orbital missions, using the final spacecraft, could conceivably begin in 1966, with circumlunar missions following as soon as the state of both technical and aeromedical knowledge permits such flights.

Launch Vehicles

In launch vehicles as in spacecraft, the NASA quest for reliability begins with the principle of multiple use of a minimum number of different vehicles. The lunar program

will employ three Atlas-based launch vehicles, the Saturn and possibly a still more advanced and larger vehicle, which is presently the subject of early conceptual studies called NOVA.

The first Atlas-based vehicle, the Atlas Able 5, depicted in Fig. 10, has marginal performance. Its main virtue is availability. It was not successful in the few launch attempts conducted and the program has been terminated. The Atlas Agena B, shown in Fig. 11, offers a greatly improved payload capability. The Agena B, as mentioned earlier, is capable of coasting in a parking orbit under full attitude control, and of engine restart for injection into a lunar transfer trajectory. The Agena B second stage has been used very successfully in the Air Force Discoverer series, for example, Discoverer 25, whose capsule was recently successfully recovered. The Air Force will also use the Atlas Agena B for the Samos and Midas Programs. As a result of the Air Force programs, the basic design will have had a number of firings before the first one is used for a NASA mission. This common usage of a vehicle in both Air Force and NASA programs is a way of attaining the extensive buildup of operating experience so important to reliability. It is planned to use this vehicle for scientific earth satellites as well as for the Ranger rough lunar lander. It can loft a 750-lb spacecraft on an escape trajectory to the moon when launched from the Atlantic Missle Range.

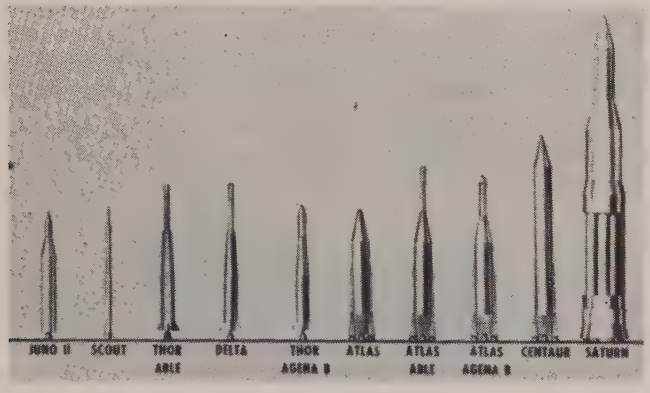

Fig. 10 — U. S. launch vehicles

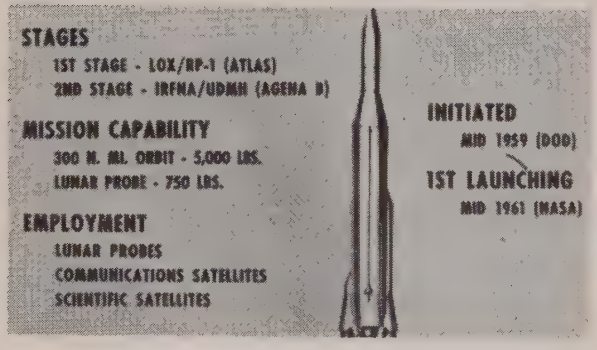

Fig. 11 — Atlas — agenda B

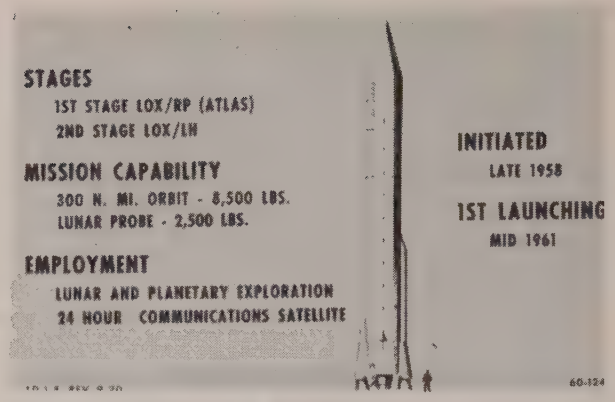

Fig. 12 — Centaur

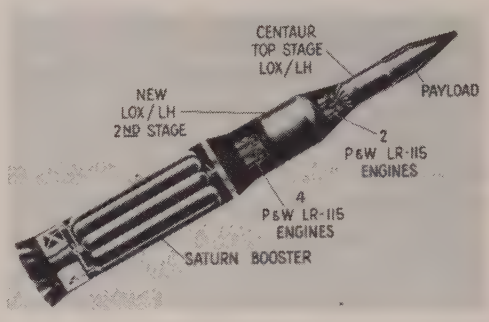

Fig. 13 — Saturn

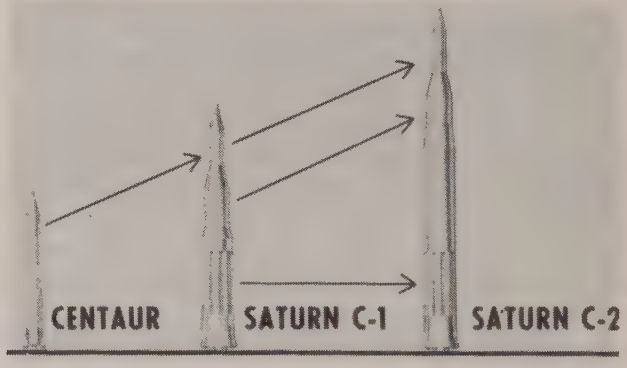

Fig. 14 — Large vehicles under development

Fig. 12 depicts the Centaur, which will be used to launch the Surveyor on soft lunar landing and precise lunar orbiting missions. The Centaur pioneers use of liquid hydrogen as a high energy fuel. The increased specific impulse of this fuel gives the Centaur a 2500-lb payload capability or about three times the payload of the Atlas Agena B on a lunar probe mission. The Centaur will be used by the Department of Defense as well as the NASA. In fact, the Centaur performance objectives originally stemmed from the DOD requirements for the 24 hr Advent communications satellite. The importance of the Centaur to NASA, however, is more far-reaching than merely the requirements for the Centaur vehicle itself because of the use of its second stage as a top stage on some versions of Saturn. In fact, liquid hydrogen

is coming to dominate the whole launch vehicle picture both as a fuel for chemical rockets, and as a working fluid for nuclear rockets.

The initial or C-1 version of the Saturn vehicle, shown in Fig. 13, is being developed under the management of Wernher von Braun's team at the Marshall Space Flight Center. Its first stage consists of a cluster of eight engines of the type used in the Thor, Jupiter, and Atlas, with a total thrust of 1,500,000 lb. On top of it we will use one or two hydrogen-oxygen stages. Fig. 14 displays a further extension of the policy of multiple use of hardware in order to achieve reliability. Note that the Centaur stage serves under the designation S-V as the top stage of the Saturn C-1, and of the planned but as yet unapproved second model of Saturn we call C-2. The S-IV stage employs six of the same rocket engines used by Centaur and S-V in a twin installation, again with an eye to reliability and minimum development costs through repetitious use. We get a C-2 from a C-1 by inserting one new hydrogen-oxygen stage beneath the S-IV stage. Incidentally, in four stages the C-2 will have 18 engines of only three types. Other versions of Saturn have been similarly examined.

We are embarked on a study program, both in-house and on contract, to define the NOVA vehicle which will follow Saturn. The principal mission we are using as an objective in these planning studies is that of injecting an Apollo spacecraft, configured for the lunar landing and return mission, on an escape trajectory to the moon without benefit of orbital refueling. Competitive studies are looking at orbital assembly and refueling using vehicles of the Saturn family.

The NOVA studies which are being linked to the Apollo studies, are carefully planned to yield the answer as to the best launch vehicle approach to the direct flight manned lunar mission. It is entirely possible that these studies may lead us to the conclusion that we should use both the Saturn orbital refueling and the NOVA direct ascent approaches, with the NOVA being employed initially as an automated truck to haul unmanned cargoes of supplies to support an Apollo spacecraft launched by the Saturn using orbital refueling.

The NOVA studies are considering nuclear as well as chemical upper stages and all are concentrating on using for first stage power various numbers of the 1,500,000-lb thrust single chamber F-1 engine presently entering its demonstration firing phase at Rocketdyne under a NASA development contract. Large solid rockets are also candidates for the NOVA Booster.

This has been a broad view of the NASA lunar program. As can be perceived, it is an evolutionary program. Initial phases are underway, others are approved and in earlier stages of development. Still others are collections of ideas which we are trying to sort out and shape into definite form with the invaluable and enthusiastic help of industry, science, and other government agencies.

Analysis and Simulation of Automobile Ride

Robert H. Kohr
Research Laboratories, General Motors Corp.

THE STUDY of automobile ride began shortly after the first automobile was built and has continued to the present day. Due to the complexity of the suspension system much of the work on ride has necessarily proceeded on the basis of empirical experience. In general, ride has been improved largely by means of specific cut and try modifications on prototype vehicles under the guidance of expert test driver opinion. Numerous attempts have also been made to analyze the suspension system mathematically but these have been only partially successful. It is the purpose of this paper to define the ride problem, to relate briefly the significant analytical efforts of the past, and to give in detail the use of modern high speed computing equipment in a new attempt to solve it.

Definition of Ride Motion

The automobile considered as a rigid body may experience any of six different types of motion. In the automobile these six motions are denoted by the linear velocities u, v, and w and the angular velocities p, q, and r as shown in Fig. 1. The axis system is fixed in the car and moves as the car moves. Because the automobile possesses a plane of symmetry, the symmetric degrees of freedom (u, w, and q) do not couple with the asymmetric degrees of freedom (v, p, and r). Consequently, it is possible to break the problem of automobile dynamics into two separate problems: the first involving motion in the plane of symmetry called longitudinal motion and the second involving motion out of the plane of symmetry called lateral motion.

The fore and aft motion in the plane of symmetry, denoted by u, relates to the acceleration and braking characteristics of the car and is called the "performance" motion. The up-and-down and pitching motions in the plane of symmetry, denoted by w and q, are together considered the primary "ride" motions of the car, while the three remaining motions (yawing, rolling, and sideslipping) are generally associated with steering control and are called the "handling" motions.

Since the "ride" and "handling" motions are largely uncoupled it is possible to study them separately. Consequently a study of "ride" can be begun by studying only two motions, bouncing and pitching.

Historical Development of Ride Analysis

The earliest work of importance in analyzing ride was done in England by Rowell (1).* This work was done at such an early date (1922) that shock absorbers had not come into general use and the only damping in the suspension was due to friction in the leaf springs. Rowell's analytic work in the realm of undamped, free vibration was later extended by Guest (2) and Olley (3). As is frequently the case, the automobile suspension system is such a nonlinear complex that analytic efforts to understand suspension performance quickly bogged down. It became apparent that computer simulation of some sort would be required to solve the suspension problem. The first analog computer used in suspension analysis was a mechanical differential analyzer built specifically for the task by Schilling and Fuchs in 1941 (4). It solved the suspension problem for only a single degree of freedom but did permit the inclusion of a nonlinear characteristic for the shock absorber. A particularly important use of this computer was the determination of transient vertical acceleration characteristics as experienced by the passengers, and how these transients could be varied by altering the shock absorber characteristics.

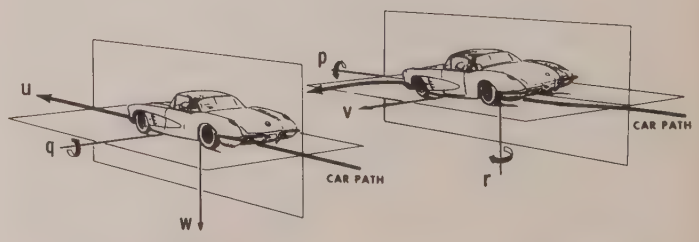

Fig.1 —Separation of longitudinal and laterial motions

* Numbers in parentheses designate References at end of paper.

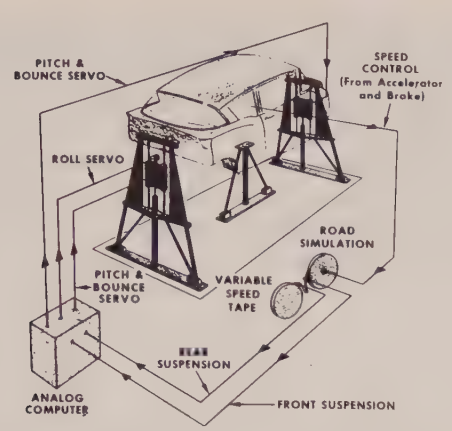

Fig. 2—Schematic view of the ride simulator

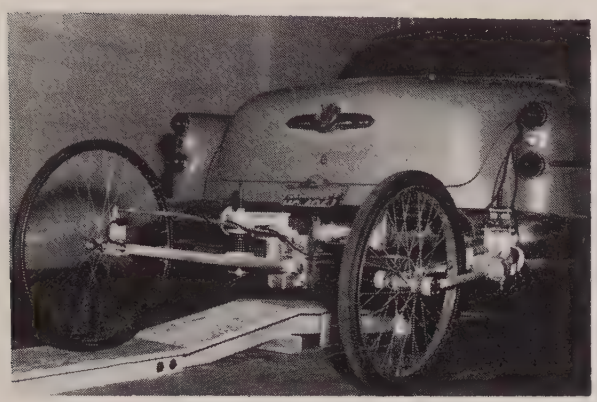

Fig. 3—Instrumental wheel used to measure road waves

A further advance in the analysis of ride was made by Jeska in 1953 when a 4-deg of freedom model was studied (5). The motions considered were the vertical motions of the front and rear wheels together with the bounce and pitch of the body. The analysis included an actual road wave, measured by a photographic technique, and a transportation lag equal to the car's wheelbase divided by the car's forward velocity. The incorporation of the transport lag was made necessary by the fact that a road disturbance which excites the front end of the car will also excite the rear of the car at a known later time. Good agreement was obtained between the analog simulation and experimental data obtained by driving a car over a known stretch of road.

General Ride Problem

It can be seen that prior to the beginning of this study the analysis of ride had been concerned primarily with the suspension system. A small amount of work had been done on passenger tolerance to vibration but not in sufficient detail to be useful. There was little or no data on the types of irregularities present in various road surfaces and because of this lack, investigators were using single sine waves or step bumps (curbs) for input disturbances. Viewed in an overall sense the ride problem can be seen to be threefold in nature because it concerns the road, the car, and the passenger. Consequently, a complete analysis of ride must take into consideration all three quantities.

Ride Analysis Through Simulation

Subsequently it became apparent that high speed analog computers could be successfully employed to solve the equations of ride motion in greater complexity than had previously been attempted. Tape recorders had been developed satisfactorily such that if a road wave could once be recorded on magnetic tape, it could then be "played" into the analog computer as an input disturbance to the suspension system. By using two pickup heads the road wave could be determined at two points analogous to the front and rear wheels of the car. There only remained the problem of inserting the passenger into the analysis. It seemed reasonable that the best way to include the passenger in the analysis was to put him in physically. This has been accomplished by constructing a servo-controlled motion simulator which can seat two passengers and which follows the motions determined by the analog computer. An overall schematic view of this system, which is called a Ride Simulator, is shown in Fig. 2. It is composed of:

1. A tape recorder to provide road wave inputs into the system. The signal of the tape is picked off at two points simulating the front and rear wheels of the car. The tape speed is variable and by speeding up the tape, the car being simulated is also "speeded up."

2. An analog computer which takes in the signals from the tape recorder and, from these inputs to the car's suspension, determines what car body motions would result. The analog computer runs in "real time", which means that the ride responses that are generated by the computer occur at the same rate as would the equivalent ride responses of a real car on a real road.

3. A motion simulator to reproduce the car body motions determined by the computer. The simulator is comprised of a portion of a standard car body and is driven by electrohydraulic servo-mechanisms whose inputs are output voltages from the analog computer. Two passengers may be accommodated in the motion simulator and the driver may control the speed of the car by pressing the brake or accelerator which sends a signal to a small computer which determines the resulting car speed and which, in turn, sends a speed signal to the tape recorder.

Since the Ride Simulator is comprised of three rather complex components, the following sections of this paper will be devoted to a detailed description of each part.

Tape Recorder

Determination of Road Profiles - As previously noted, a source of real difficulty in simulating automobile suspensions has been the lack of detailed data on road profiles. Numerous efforts have been made in the past to determine road profiles, among them are direct surveying methods and specialized surveying methods using a light beam as a space reference. In general, the shortcomings of these methods are that they are tedious and that they are not adaptable to long stretches of road (10 or 20 miles). General Motors is currently exploring another possibility -- that of obtaining the vertical accelerations induced in a towed wheel as it is rolled along the road and then integrating the acceleration twice to obtain displacement. The wheel used in this work, shown in Fig. 3 is essentially a bicycle wheel fitted with a special tire. Also shown in this figure is a standard fifth wheel which is used to generate a speed signal. The wheel is preloaded with a low rate spring to maintain contact with the ground. The wheel-spring combination acts as a low-pass filter with a break frequency of about 60 cps. The accelerometer output is passed through a high-pass filter that has a slope of 18 db per octave and a break frequency of one-half radian per sec. This filter is composed of operational amplifiers, as shown in Fig. 4, and the double integration is performed within the loop. In Fig. 4, S^2X represents the acceleration input and Y is the displacement output. Although there remains considerable work to be done before this system is completely satisfactory, a number of successful short time runs has been made. An oscillograph record of one of these runs is shown in Fig. 5. The road profile used in this test was a home-made triangular bump. The acceleration resulting when the wheel rolled over the bump is shown in the center of Fig. 5 and the displacement, recovered successfully by a double integration, is shown at the top. The measure of the wheel suspension displacement is used primarily as an event marker on the oscillograph record.

In addition to recording particular sections of various road surfaces, it is also possible to characterize the road surface statistically. Then by use of electronic noise generators and appropriate filters, it is possible to determine ride responses for a known statistical input without recourse to recording of actual roads. Although there is very little data available on highways, the statistical approach, employing power spectral densities, has been satisfactorily used to determine ground loads induced in aircraft when taxiing over rough runways (6).

Time Delay Generation - Once the road waves have been recorded on magnetic tape, there remains the problem of providing the inputs to the front and read suspension. For cars with equal front and rear treads, the road input functions for the wheels on each side of the car are identical but displaced with respect to each other by the length of the wheelbase. Previously a number of special purpose road function generators had been built in order to overcome this obstacle. In the case of the Ride Simulator, a general purpose magnetic tape unit was utilized to provide the delay in addition to acting as the input road wave generator (7). This unit, shown in Fig. 6, utilizes a modified commercial tape transport with two magnetic heads. The lower head is used for recording purposes, and both heads are used for re-

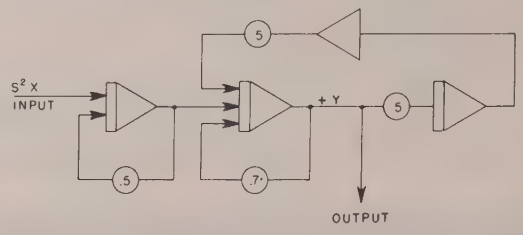

Fig. 4—Filter integrator circuit

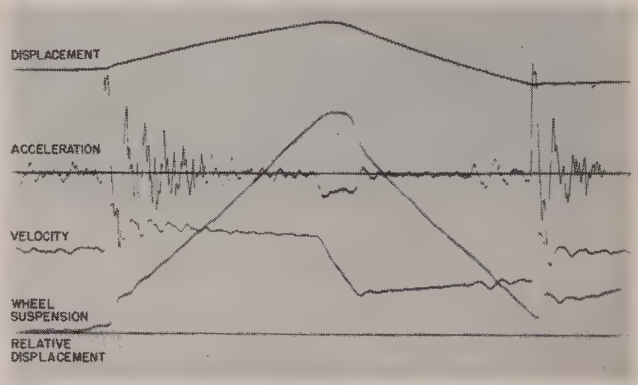

Fig. 5—Triangular road wave determined by instrumental wheel

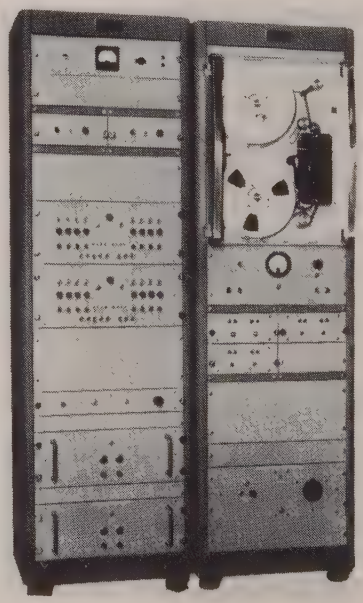

Fig. 6—Tape recorder used for road wave generation and time delay

producing purposes. When the signal is picked off by both the lower and the upper heads there is a delay in the signal of T = d/V sec, where d is the distance between the heads and V is the tape speed. The tape speed is directly analogous to the car's speed and, similarly, the spacing between the magnetic heads is analogous to the car's wheelbase. Each head will handle two channels of information so that one channel represents the road function under the right side of the car, the other, the left.

The tape recorder employs pulse-width modulation as a recording means. The delay range available is 0.04-1.5 sec. The tape speed control is continuous over the range 4 in./sec - 40 in./sec. This corresponds to car speeds in the range 15 - 150 mph. The unit will accept signals in the frequency range of 0 - 30 cps. Input and output impedances are similar to those normally associated with analog computer amplifiers.

Automobile Simulation

Seven Deg of Freedom Model - The car model simulated in the computer is the 7 deg of freedom system shown in Fig. 7. This system considers the vertical motions of all four wheels plus the bounce, pitch, and roll of the body. Although the early analysis of ride motions did not include roll effects, the high human sensitivity to roll displacements literally dictates that rolling motions be incorporated in a complete ride study. Only typical car dimensions and parameters are given in this figure to reduce clutter. The simulation of this system involves summing the forces on each wheel and summing the forces and torques that act on the body.

The general procedure is shown in Fig. 8. The system is put into motion by the road wave input which enters the tire. The difference between the road wave input and the wheel motion, acting through the tire characteristic, produces the tire force. Motion of the wheel mass results from the difference of the tire force and the suspension force. The suspension force is produced by the difference of wheel motion and body motion acting through the suspension characteristic. Finally, the body motion results from the action of the suspension force upon it. Lagrange's equations were employed to derive the equations of motion of the ride system. These equations are given in detail in the Appendix.

In order to determine numerical values of the parameters required in the equations of motion, it was necessary to measure the inertia, spring, and damping characteristics of the body, suspension and tires. For the study a typical 1958 production car was chosen. Fortunately, most of the required parameters could be measured on existing test apparatus. For example, the pitching moment of inertia was measured by swinging the car as part of a compound pendulum. Spring rates were determined on a standard test rig that applied force to the suspension and measured the resulting deflections. Shock absorber characteristics were determined by a stroking machine which gave shock absorber force as a function of input velocity. Tire damping was measured by applying a sharp pulse of force to the tire and determining the time the oscillation required to damp out. In all, there are 37 car parameters used in the simulation. Typical car parameters are given in the Appendix.

Analog Computer - With the equations of motion and the car parameters in hand, the car ride response was determined on an analog computer. The computer solves the equations of motion by summing the various forces acting on each mass or inertia. Fig. 9 shows this procedure for one

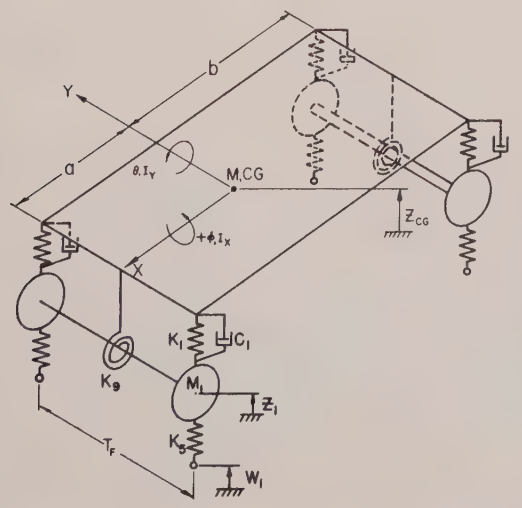

Fig. 7—Seven deg of freedom suspension system

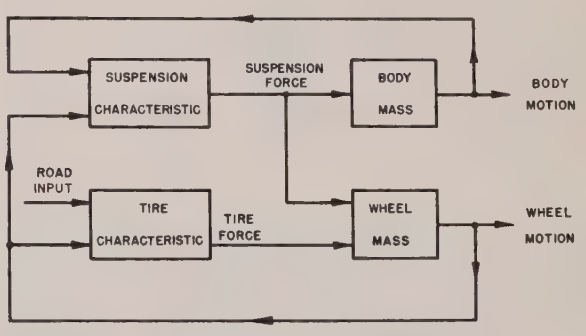

Fig. 8—Block diagram of suspension system

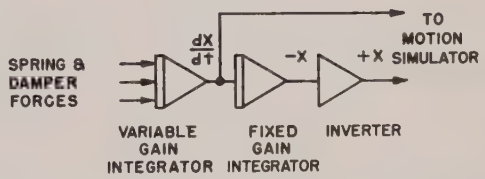

Fig. 9—Integration of acceleration to displacement

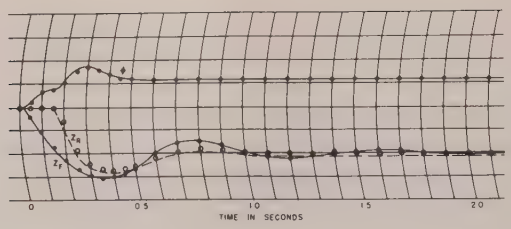

Fig. 10—Comparison of analog and digital solutions

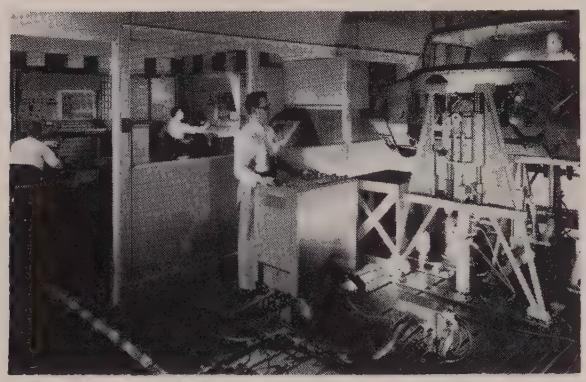

Fig. 11—Overall view of ride simulator showing computer, motion simulator, and control console

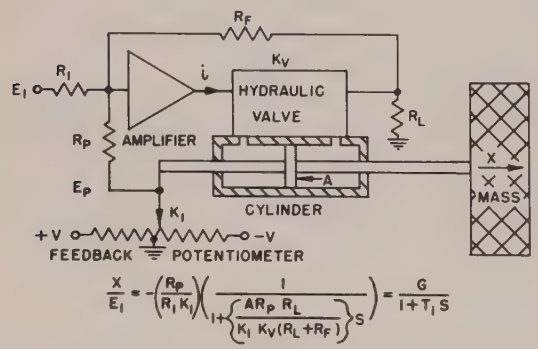

Fig. 12—Schematic diagram of simulator servo system

end of the car whose vertical motion has been denoted by the coordinate X. The forces acting on the mass of this end of the car are summed at the variable gain amplifier which is used as an integrator. The acceleration of this mass is equal to the sum of the input forces divided by the mass under consideration. The variable gain amplifier of Fig. 9 performs the three functions of summing the forces, dividing by the mass, and integrating the resulting acceleration into velocity. In Fig. 9 this velocity is denoted as the output (dX/dt) of the variable gain integrator. The velocity is then integrated in a second fixed-gain integrator to produce the displacement -X. The displacement signal is then inverted to +X by the inverter. In the computer there are seven circuits like the one shown in Fig. 9 together with nonlinear function generators to represent the springs, shock absorbers, and tires. The outputs of the computer representing the motion of the front, rear, and roll of the car are fed to the motion simulator. It should be noted that not only the displacement signal X but also the velocity signal dX/dt is fed to the motion simulator. The reason for this will be made clear in a later section.

The analog computer used to solve the equations is a general purpose unit, no special equipment being required. In all, 82 operational amplifiers are required to solve the problem and provide coordinate transformations, and as many as 16 function generators may be used depending on how many nonlinearities are considered.

Comparison Between Analog and Digital Solutions - An analog computer solution of the linear 7 deg of freedom system is given in Fig. 10. The corresponding digital check solution is indicated by dots. The input used was a step bump or curb on the left side of the car only. The three traces show the roll response (ϕ), the front end vertical motion (Z_f), and the rear end vertical motion (Z_r). The car parameters are those of a typical production car traveling at 45 mph. This simulation was carried out in real time, and the agreement between the analog and digital computers is quite good.

Motion Simulator

A view of the motion simulator together with the control console which controls it is shown in Fig. 11. The body which can carry two passengers is shown without hood and fenders. The weight of the body and frame are supported by hydraulic pressure in the central cylinder. The hydraulic pressure is supplied by an accumulator which also acts as a very low rate spring. Vertical motions at the front and rear of the car are provided by valve-controlled hydraulic cylinders. These servo-cylinders exert vertical forces on movable pads which are guided on rails. These pads are connected to the ends of the car frame and, consequently, when the pad moves the car frame moves also. The servo cylinders are located approximately at the centers of percussion in order to prevent the front servo from loading the rear and vice versa. Roll actuation is provided by a rotary actuator mounted on the rear movable pad. It is carried up and down in pitch and bounce and as a result there is no appreciable coupling between pitch, bounce and roll. It is worth emphasizing that the central cylinder supports the entire weight of the car body and passengers, and that the servos are used only to provide dynamic forces to produce motion. The valves which control the flow of oil to the servo-cylinders are actuated by voltages supplied by the computer. A block diagram of one of the servo systems is shown in Fig. 12. The input to the servo is the voltage E_1 and the output is X. The servo loop is

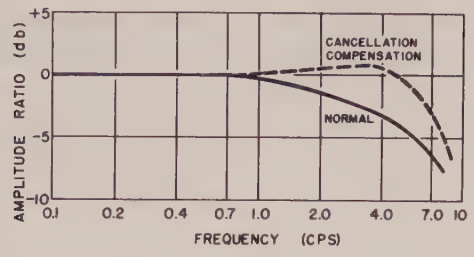

Fig. 13—Frequency response of motion simulator servo

completed by a voltage E_p supplied by movement of the wiper on the feedback potentiometer. The transfer function of this simplified system, which neglects oil spring effects and numerous nonlinearities, is X/E_1, which is the inches of simulator movement per volt input to the servo. It can be seen that the transfer function can be written as:

$$\frac{X}{E_1} = \frac{G}{1 + T_1 S} = \frac{\text{In. of Displacement}}{\text{Volt Input}} \qquad (1)$$

Thus it may be seen that the system will not give good reproduction of output frequencies much higher than $1/T_1$ radians per sec. Fortunately, the analog computer provides a way around this frequency limitation. For example, if the system were perfect, the system response to a voltage E_c from the computer would be:

$$\frac{X}{E_c} = G \qquad (2)$$

If the simulator is to track a voltage E_c it can be shown that the servo input E_1 should be made equal to $E_c + T_1 S E_c$. To prove this set:

$$\frac{X}{E_c} = \frac{X}{E_1}\frac{E_1}{E_c} = G \qquad (3)$$

But since $X/E_1 = G/(1 + T_1 S)$, it is clear that:

$$E_1 = E_c\,(1 + T_1 S) = E_c + T_1 \frac{dE_c}{dt} \qquad (4)$$

Thus it may be seen that if the motion simulator is accurately represented by the simple transfer function $G/(1 + T_1 S)$ that the simulator may be made to track a voltage E_c from the computer provided that the input voltage to the servo is the tracked voltage $E_c + T_1$ times its time derivative. Fortunately, this derivative already exists in the computer and it is a simple matter to multiply it by T_1 and feed it to the servo. This action effectively cancels an unwanted pole in the transfer function. The effect of this cancellation compensation is shown in the frequency response curves of Fig. 13. It may be seen that the normal servo system has a bandwidth of about 4 cps (the bandwidth is the maximum frequency at which the amplitude ratio is within ±3 db of the amplitude ratio at zero frequency). The effect of cancellation compensation is to extend the bandwidth to 7 cps. It is also clear that the transfer function of the system is more involved than the simple formula shown previously. The main performance figures of the Ride Simulator are given in Table 1. The bandwidth figures given represent the performance of the servos when cancellation compensation is used.

Table 1 - Ride Simulator Performance Figures

	Bounce	Pitch	Roll
Maximum Acceleration	1250 in./sec^2	1150 deg/sec^2	500 deg/sec^2
Maximum Velocity	40 in./sec	48 deg/sec	240 deg/sec
Maximum Displacement	± 5 in.	± 6 deg	± 10 deg
Bandwidth	5 cps	5 cps	4 cps
Positional Accuracy	0.020 in.	0.025 deg	0.10 deg

The simulator performance requirements originated in road test data which determined extremes in each of the variables. The road data were determined by driving an instrumented test car over a number of different bumps at various speeds and determining the peaks of the acceleration, velocity, and displacement transients. From a collection of these curves, an extreme for each variable was obtained. A comparison of the observed maximum of each motion variable with the corresponding Ride Simulator performance is shown in Table 2.

It may be seen that the Simulator has the capability of reproducing the extremes of real car motion with the exception of bounce displacement. This is not considered a major drawback since a 5 in. bump, which the Simulator can accommodate, represents a violent disturbance to the passengers at almost any road speed.

In addition to providing a means of extending the apparent servo bandwidth, the computer calculates the coordinate transformation required when the center of gravity of the simulated car does not correspond with the fixed pivot of the motion simulator. By means of another coordinate transformation it is possible to provide the sensations of rear seat ride to passengers occupying the front seats of the motion simulator.

Comparison of Overall Response to Real Car Response

The real point of a ride simulator is that the simulator will produce to a high degree of fidelity the motions experi-

Table 2 - Comparison of Ride Simulator and Real Car Performance

	Bounce	Pitch	Roll
Maximum Acceleration			
Real car	230 in. /sec^2	180 deg /sec^2	395 deg /sec^2
Simulator	1250 in. /sec^2	1150 deg /sec^2	500 deg /sec^2
Maximum Velocity			
Real car	30 in. /sec	14 deg /sec	28 deg /sec
Simulator	40 in. /sec	48 deg /sec	240 deg /sec
Maximum Displacement			
Real car	6 in.	5 deg	9 deg
Simulator	5 in.	6 deg	10 deg

enced by a real car on a real road. To prove out the complete system a typical production car whose parameters had been completely determined was instrumented with an integrating accelerometer and then was driven over a triangular bump at 20 mph. The triangular bump used in this work was 60 in. long and 4.8 in. high. Then the Ride Simulator was put through the same procedure, namely:

1. An identical triangular bump was recorded on magnetic tape and played into the computer by the Simulag.
2. The computer determined what the car's responses should be and sent motion signals to the motion simulator.
3. The simulator moved representing the motion of the car over the bump.

To demonstrate the fidelity of the overall simulator, the integrating accelerometer was removed from the car and was installed in the same location in the motion simulator body. The results of this test which compare the response of a typical 1958 production car with a simulated version of the same car are shown in Fig. 14. A comparison of accelerations is shown at the top of this figure and a comparison of displacements at the bottom. The agreement is generally good. The oscillations in the acceleration trace for the production car are due to a stiffer rear floor pan where the accelerometer was mounted.

Conclusion

The Ride Simulator has demonstrated its ability to reproduce the on-the-road ride response of real cars. The way is now open to evaluate new suspension systems without recourse to expensive component constructions and to study the passenger and seat combination under closely controlled conditions. The Ride Simulator is an important step forward in ride analysis because it will enable improvements in ride to be made with a minimum of time and effort.

References

1. H. S. Rowell, "Principles of Vehicle Suspension," IAE Proceedings, Vol. 17 (1922-1923), 455-536.
2. J. J. Guest, "The Main Free Vibrations of an Autocar," IAE Proceedings, Vol. 25 (1925-1926), 505-547.
3. M. Olley, "Independent Wheel Suspension - Its Why and Wherefores," SAE Journal, Vol. 34, No. 3 (1934), 73-81.
4. R. Schilling and H. O. Fuchs, "Modern Passenger Car Ride Characteristics," ASME Trans., Vol. 63 (1941), A 59-A 66.
5. R. D. Jeska, "A Comparison of Real and Simulated Automobile Suspension Systems," University of Michigan, Willow Run Research Center, UMM-117, February, 1953.
6. C. K. Grimes, "Development of a Method and Instrumentation for Evaluation of Runway Roughness Effects on Military Aircraft," AGARD Report 119, May, 1957.
7. M. M. Brenner, "A New Dead Time Simulator for

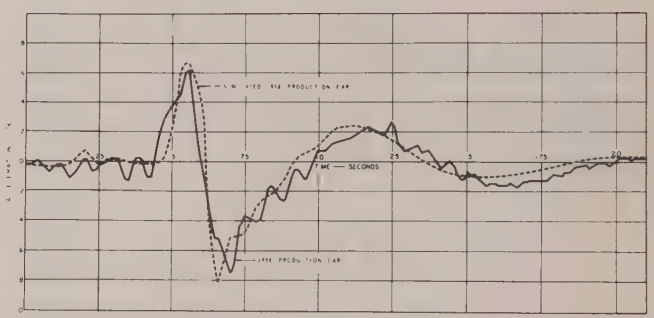

Fig. 14A—Acceleration comparison of real and simulated cars passing over triangular bump

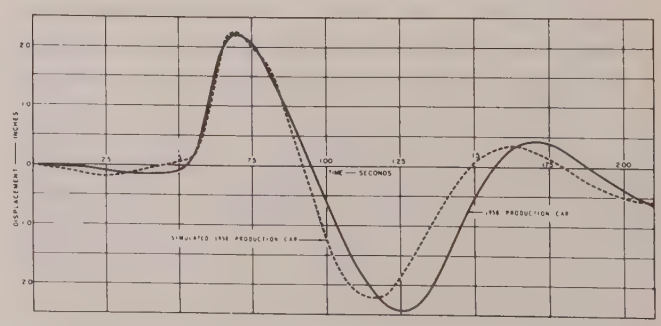

Fig. 14B—Displacement comparison or real and simulated cars passing over triangular bump

Electronic Analogue Computers," Proc. National Simulation Council, 1957, 6.0 - 6.9.

Appendix I

Notation and Axis System

Fig. 15 shows a schematic view of an automobile with three orthogonal axes fixed in the body. Fig. 16 shows a schematic view of a typical independent front suspension while Fig. 17 shows a schematic view of a typical rear suspension incorporating a solid rear axle. These front and rear suspensions are typical of those encountered on current passenger cars. Quantities are positive as shown in Fig. 15.

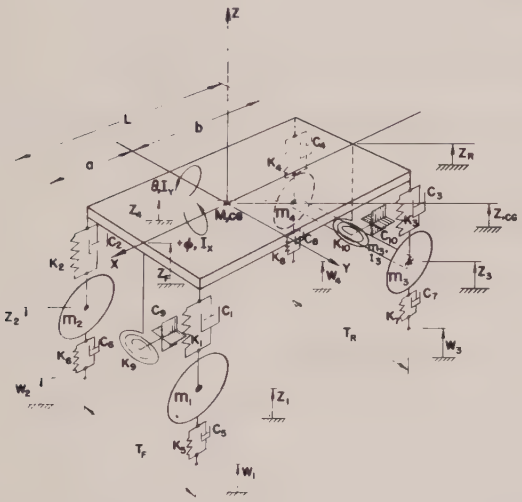

Fig. 15—Complete schematic of seven deg of freedom suspension system

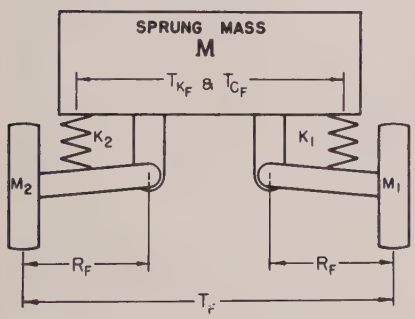

Fig. 16—Schematic view of typical independent front suspension

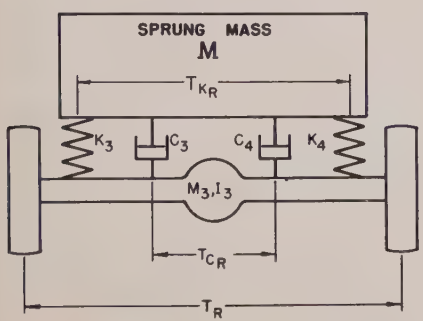

Fig. 17—Schematic view of typical rear suspension

Axis System

X, Y, Z = See Fig. 15 for axis orientation. These axes are fixed in and move with the automobile.

Displacements

W_1, W_2, W_3, W_4 = Vertical displacement of the ground under the wheels, ft

Z_1, Z_2, Z_3, Z_4 = Vertical displacement of the wheels, ft

Z_F = Vertical displacement of the sprung mass at the front wheel centerline, ft

Z_R = Vertical displacement of the sprung mass at the rear wheel centerline, ft

Z_{CG} = Vertical displacement (bounce) of the sprung mass center of gravity, ft

ϕ = Angular displacement of the sprung mass (roll) about the X axis, radians

θ = Angular displacement of the sprung mass (pitch) about the Y axis, radians

All displacements are in absolute coordinates and are measured from the static equilibrium position.

Inertia Quantities

M_1 = Unsprung mass, left front wheel, slugs

M_2 = Unsprung mass, right front wheel, slugs

M_3 = Total unsprung mass at rear, slugs

M = Sprung mass, slugs

I_X = Moment of inertia of the sprung mass about the X-axis, slug-ft^2

I_Y = Moment of inertia of the sprung mass about the Y-axis, slug-ft^2

I_3 = Moment of inertia of the mass M_3 about an axis through its center of gravity parallel to the X-axis, slug-ft^2

Spring Terms

K_1, K_2, K_3, K_4 = Spring rates between wheels and sprung mass, lb/ft

K_5, K_6, K_7, K_8 = Tire spring rates, lb/ft

K_9 = Front roll spring rate (roll bar), ft lb/radian

K_{10} = Rear roll spring rate (roll bar), ft lb/radian

Damping Terms

C_1, C_2, C_3, C_4 = Damping factors between the sprung mass and the wheels, lb-sec/ft

C_5, C_6, C_7, C_8 = Damping factors of the tires, lb-sec/ft

C_9 = Front roll damping, ft-lb-sec/radian

C_{10} = Rear roll damping, ft-lb-sec/radian

Dimensions

L = Wheelbase, ft

a = Distance from the front wheel centers to the c.g. of the sprung mass, ft

b = Distance from the rear wheel centers to the c.g. of the sprung mass, ft
T_F = Front wheel tread, ft
T_R = Rear wheel tread, ft
T_{K_F} = "Tread" of front springs (Fig. 16), ft
T_{C_F} = "Tread" of front dampers (Fig. 16), usually equal to T_{K_F} in independent front suspensions, ft
R_F = Distance from front swing arm pivot to wheel, ft
T_{K_R} = "Tread" of rear springs (Fig. 17), ft
T_{C_R} = "Tread" of rear dampers (Fig. 17), ft

Dimensionless Parameters

N_F = Gear ratio between the front spring and front wheel, $(R_F - T_F/2 + T_{K_F}/2)/R_F$
N_{K_R} = Gear ratio between rear wheels and rear suspension spring, T_{K_R}/T_R
N_{C_R} = Gear ratio between rear wheels and rear dampers, T_{C_R}/T_R

Appendix II

Equations of Motion - The following equations describe the ride motions of an automobile by considering the vertical motions of each of the four wheels, as well as the bounce, pitch, and roll of the body. For convenience, the bounce and pitch are replaced by the motions at the front and rear of the body (Z_F and Z_R). For the relatively small motions encountered in ride a simple linear transformation may be used to relate Z_F and Z_R with the bounce and pitch motions. In the following equations a dot over a variable indicates a time derivative, for example $\dot{Z}_1 = dZ_1/dt$.

Sum of Forces on Left Front Wheel

$$M_1\ddot{Z}_1 + N_F^2(C_1\dot{A} + K_1A) + (C_5\dot{G} + K_5G) - \frac{1}{T_F}(C_9\dot{E} + K_9E) = 0 \quad (5)$$

Sum of Forces on Right Front Wheel

$$M_2\ddot{Z}_2 + N_F^2(C_2\dot{B} + K_2B) + (C_6\dot{H} + K_6H) + \frac{1}{T_F}(C_9\dot{E} + K_9E) = 0 \quad (6)$$

Sum of Forces on Left Rear Wheel

$$W_1\ddot{Z}_3 + W_2\ddot{Z}_4 + \left(\frac{1 + N_{C_R}}{2}\right) C_3\dot{\bar{C}} + \left(\frac{1 + N_{K_R}}{2}\right) K_3C + \left(\frac{1 - N_{C_R}}{2}\right) C_4\dot{\bar{D}} + \left(\frac{1 - N_{K_R}}{2}\right) K_4D + (C_7\dot{P} + K_7P) - \frac{1}{T_R}(C_{10}\dot{F} + K_{10}F) = 0 \quad (7)$$

Sum of Forces on Right Rear Wheel

$$W_1\ddot{Z}_4 + W_2\ddot{Z}_3 + \left(\frac{1 - N_{C_R}}{2}\right) C_3\dot{\bar{C}} + \left(\frac{1 - N_{K_R}}{2}\right) K_3C + \left(\frac{1 + N_{C_R}}{2}\right) C_4\dot{\bar{D}} + \left(\frac{1 + N_{K_R}}{2}\right) K_4D + (C_8\dot{Q} + K_8Q) + \frac{1}{T_R}(C_{10}\dot{F} + K_{10}F) = 0 \quad (8)$$

Sum of Forces on Front End of Sprung Mass

$$R\ddot{Z}_F + S\ddot{Z}_R - N_F^2(C_1\dot{A} + K_1A) - N_F^2(C_2\dot{B} + K_2B) = 0 \quad (9)$$

Sum of Forces on Rear End of Sprung Mass

$$T\ddot{Z}_R + S\ddot{Z}_F - (C_3\dot{\bar{C}} + K_3C) - (C_4\dot{\bar{D}} + K_4D) = 0 \quad (10)$$

Sum of Torques Tending to Produce Roll

$$I_X\ddot{\phi} - N_F^2T_F(C_1\dot{A} + K_1A) + \frac{N_F^2T_F}{2}(C_2\dot{B} + K_2B) - \frac{T_R}{2}\left(N_{C_R}C_3\dot{\bar{C}} + N_{K_R}K_3C\right) + \frac{T_R}{2}\left(N_{C_R}C_4\dot{\bar{D}} + N_{K_R}\right)K_4D + (C_9\dot{E} + K_9E) + (C_{10}\dot{F} + K_{10}F) = 0 \quad (11)$$

where:

$$A = (Z_1 - \frac{\phi T_F}{2} - Z_F)$$

$$B = (Z_2 + \frac{\phi T_F}{2} - Z_F)$$

$$C = \frac{Z_3}{2}(1 + N_{K_R}) + \frac{Z_4}{2}(1 - N_{K_R}) - Z_R - \frac{\phi T_{K_R}}{2}$$

$$\bar{C} = \frac{Z_3}{2}(1 + N_{C_R}) + \frac{Z_4}{2}(1 - N_{C_R}) - Z_R - \frac{\phi T_{C_R}}{2}$$

$$D = \frac{Z_3}{2}(1 - N_{K_R}) + \frac{Z_4}{2}(1 + N_{K_R}) - Z_R + \frac{\phi T_{K_R}}{2}$$

$$\bar{D} = \frac{Z_3}{2}(1 - N_{C_R}) + \frac{Z_4}{2}(1 + N_{C_R}) - Z_R + \frac{\phi T_{C_R}}{2}$$

$$E = \phi - \frac{Z_1 - Z_2}{T_F}$$

$$F = \phi - \frac{Z_3 - Z_4}{T_R}$$

$$G = Z_1 - W_1$$

$$H = Z_2 - W_2$$

$$P = Z_3 - W_3$$

$$Q = Z_4 - W_4$$

$$W_1 = \frac{M_3}{4} + \frac{I_3}{T_R{}^2}$$

$$W_2 = \frac{M_3}{4} - \frac{I_3}{T_R{}^2}$$

$$R = \frac{Mb^2 + I_Y}{L^2}$$

$$S = \frac{Mab - I_Y}{L^2}$$

$$T = \frac{Ma^2 + I_Y}{L^2}$$

It may be noted that A and $\dot{A}$ apply to spring K_1 and shock absorber C_1 respectively in the left front wheel equation. However in the left rear wheel equation C applies to spring K_3 while $\bar{C}$ applies to shock absorber C_3. This situation occurs because the front spring and shock absorber are coaxially mounted but this is not true in the rear where the spring "tread" and the shock absorber "tread" are not equal.

Appendix III

Typical Parameter Values - The parameters given below pertain to a typical 1958 production car with two passengers in the front seat.

Inertia Parameters

M_1, M_2 = Front unsprung masses, 3.00 slugs each
M_3 = Rear unsprung mass, 9.67 slugs
M = Sprung mass with passengers, 123.03 slugs
I_X = Roll inertia, 524 slug ft^2
I_Y = Pitch inertia, 2541 slug ft^2

Spring Parameters

K_1, K_2 = Front spring rate, 4577 lb/ft
K_3, K_4 = Rear spring rate, 1275 lb/ft
K_5, K_6, K_7, K_8 = Tire rate, 13,775 lb/ft
K_9 = Front roll stabilizer rate, 7956 lb-ft/radian
K_{10} = Rear roll stabilizer rate, none (no stabilizer)

All the spring rates given above are nonlinear to some degree. The values given above are linearized values obtained by fitting a straight line to each spring curve at its origin (static position).

Damping Parameters

C_1, C_2 = Front damping characteristic, 81.50 lb-sec/ft
C_3, C_4 = Rear damping characteristic, 68.44 lb-sec/ft
C_5, C_6, C_7, C_8 = Tire damping characteristics, 1.0 lb-sec/ft
C_9, C_{10} = Roll damping characteristics, none
F_F = Front friction level, 42 lb
F_R = Rear friction level, 4 lb

All the damping rates above are extremely nonlinear. Like the spring terms, they have been linearized by fitting a straight line to each damper curve at the zero velocity point.

Dimensions

L = Wheelbase, 9.79 ft
a = Distance from front wheel centers to the CG of the sprung mass, 4.17 ft
b = Distance from rear wheel centers to the CG of the sprung mass, 5.62 ft
T_F = Front wheel tread, 4.90 ft
T_R = Rear wheel tread, 4.90 ft
T_{K_F} = Front spring tread, 4.08 ft
T_{C_F} = Front damper tread, 4.08 ft
R_F = Distance from front swing arm pivot to wheel, 1.29 ft
T_{K_R} = Rear spring tread, 3.19 ft
T_{C_R} = Rear damper tread, 1.59 ft

Fuel Injection and Positive Ignition
A Basis for Improved Efficiency and Economy

C. W. Davis, E. M. Barber, and Edward Mitchell
Texaco Research Center

HEAT ENGINE cycles involve three essential phases: compression, heat addition, and expansion. Other things being equal, the efficiency of converting heat to work increases with the ratio of compression and expansion. This trend is so well-known to engineers and even to the general public, that compression ratio and efficiency have come to be virtually synonymous. Historically, increases of compression ratio have been important considerations in the development of more efficient engines.

Once a sufficiently high compression ratio has been attained, it appears that other considerations, particularly those associated with the heat addition phase of the cycle, may provide a more rewarding basis for further developments. Two of the most important of these other considerations are:

1. The high thermodynamic efficiency associated with the combustion of lean mixtures.

2. The practical economic value of utilizing broad boiling range fuels with no octane or cetane number specifications that can be produced from crude oil in high yield and with low processing charges.

A combustion process that exploits these two important factors and has other desirable characteristics has been under development at the Texaco Research Center-Beacon for some years under the name, Texaco Combustion Process. The concept of this process has been described in earlier publications (1, 2, 3). The present paper reports progress on engineering development of the process and illustrates the application of the process to a variety of sizes and types of engines. Because of the large amount of engineering research that has been done, it has been necessary to confine this paper to a brief outline of the principal factors, and study methods involved, and a sampling of the results.

Method of Operation

The Texaco Combustion Process (TCP), illustrated schematically in Fig. 1, involves a coordination of fuel injec-

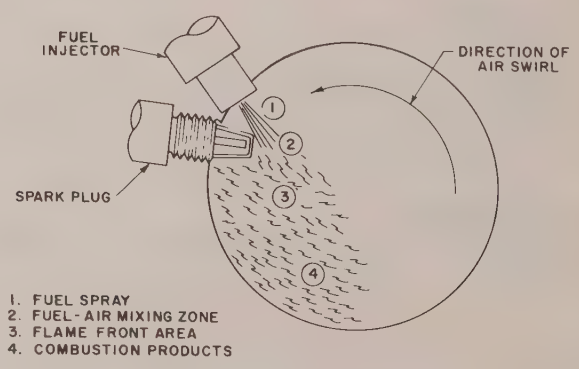

Fig. 1 — Texaco Combustion Process

*Numbers in parenthesis designate references at end of paper.

tion and positive ignition with swirling air. When combustion is to begin, near the end of the compression stroke, fuel injection is initiated and the first increment of fuel is ignited to establish a flame front immediately downstream from the nozzle. As injection continues the additional mixture supplied to the flame front is burned approximately as rapidly as it is formed.

High-speed motion picture studies of the Texaco process have been made in a two-stroke-cycle loop scavenged engine equipped with a quartz observation window as a cylinder head. Fig. 2 shows a schematic diagram of the test arrangement and a photograph enlarged from a selected frame of one of the high speed motion pictures. It is evident that actual combustion, shown by the photograph, closely follows the idealized concept of the Texaco process.

Many characteristics of the Texaco process are direct consequences of the coordination of air swirl, fuel injection, and positive ignition that is illustrated in Figs. 1 and 2. It is useful to note these characteristics in comparison with diesel and gasoline engine combustion characteristics as follows:

TCP in Comparison to Diesel - Positive, immediate ignition of the first increment of fuel eliminates the need for high compression ratio and cetane number to achieve compression ignition, It also eliminates the ignition delay that is characteristic of the compression ignition process.

The maximum pressures and rates of pressure rise that occur with Texaco Combustion are considerably lower than is typical of compression ignition. Combustion loads, noise, and shock are correspondingly less severe, and the heavy rigid structural characteristics of diesel engines are not required. The positive ignition feature virtually eliminates the carbon formation associated with the compression ignition reaction so that the Texaco process achieves higher air utilization, and results in exceptionally good cold starting and warm up characteristics.

TCP in Comparison to Gasoline - Injection of the first increment of fuel at the time of ignition eliminates the possibility of preignition with the Texaco Process. Combustion of the remaining fuel substantially as rapidly as it is injected eliminates knock, regardless of the octane number of the fuel, since unburned mixture does not have enough residence time for the pre-knock reactions to occur.

Load control is obtained by regulating the duration of fuel injection in proportion to the desired engine output, with full load duration corresponding to about the time for one air swirl. This injection duration will impregnate the entire air charge with fuel in about stoichiometric proportions. Thus, the entire TCP operating regimen is on the lean side of stoichiometric and load control does not require intake throttling.

The foregoing comparative Texaco process characteristics imply freedom to choose compression ratio and/or supercharge regardless of the octane or cetane number of available fuels, and the ability to utilize lean mixtures.

Fig. 3 presents a theoretical comparison of the Texaco, otto, and diesel cycles. Curves of thermal efficiency versus mixture strength are shown for the Texaco cycle at 10:1 compression ratio and for Otto (gasoline) and diesel cycles at their conventional compression ratios. The efficiencies are for the fuel-air cycles with no heat loss, with instantaneous events, with idealized constant pressure combustion for the diesel and with idealized constant volume combustion for the Texaco and gasoline cases. The figure highlights several important characteristics to be looked for in the subsequent Texaco process engine performance data:

1. The high efficiency of the lean mixture, constant volume combustion Texaco case contrasts with the rich mixture gasoline case of comparable compression ratio, and with the much higher compression ratio, constant pressure combustion, diesel case. This will show up in engine test results by TCP part-load fuel economies being as good as those for comparable diesel engines and very much better than those for gasoline engines.

2. The Texaco process air utilization is greater than that of the diesel case but less than for the gasoline case at its maximum power mixture strength. This shows up in engine performance by TCP smoke limited mean effective pressures being generally greater than for comparable diesels but not so high as for gasoline engines at their maximum power mixture strength.

Since Texaco process characteristics include the elimination of octane and cetane numbers as relevant fuel qualities and permit the use of hydrocarbon fuels of very broad boiling range, TCP engines have good "all fuel" character-

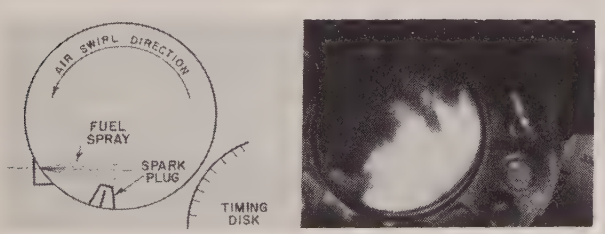

CAMERA VIEW LAYOUT SAMPLE FRAME FROM FILM

Fig. 2 — High speed motion picture studies of Texaco combustion

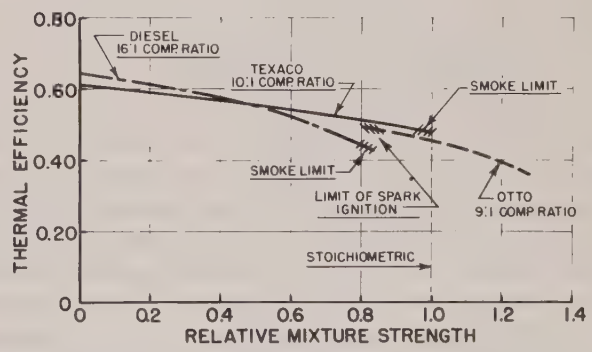

Fig. 3 — Operating ranges and theoretical efficiencies of several engine cycles

istics. They can operate essentially interchangeably on a variety of fuels such as light furnace oils, kerosine, jet and diesel fuels, motor and aviation gasolines. More important, however, the ideal TCP fuel is simply a clean hydrocarbon mixture, boiling between 100 and 700 F with no octane or cetane number specification, which can be made from crude oil in very large yields with minimum processing costs. The jet fuel, JP-4, which has extensive production and distribution at low cost, is an approximation to this ideal and this type of fuel has been used most extensively in the TCP development work.

Engineering Development of the Texaco Process

The authors' company is not a manufacturer of internal combustion engines and this fact determined that emphasis should be placed on gaining a good understanding of the process and of the principles involved in applying it to a variety of types and sizes of engines rather than on developing a finished version of any one engine. This work has resulted in a number of useful design and construction details for those engine components that relate to the Texaco process and also in a procedure for estimating the performance of a proposed TCP engine. Both the components and the estimating procedure have been verified by construction and test of a substantial number of laboratory type single and multicylinder Texaco process engines.

The principal special considerations for applying the Texaco process to an engine are:

1. To provide a means for inducing air swirl.
2. To select a combustion chamber in which the induced air swirl will persist.
3. To select a suitable fuel spray and a proper location for it relative to the air swirl.
4. To select an ignition source and a proper location for it relative to the fuel spray and air swirl, and a proper timing relative to the fuel spray.

The earliest studies of the Texaco process were made in a single cylinder CFR engine of the type used for supercharged knock testing, and this became the point of departure and reference for the ensuing development work. In this engine, air swirl was induced by a shroud on the intake valve; the combustion chamber had the shape of a flat disk; a diesel injection nozzle that produced a broad spray was located at the periphery of the combustion chamber with its centerline diagonally across and downstream in the air swirl, and a spark plug was located downstream of the nozzle. The approximate geometrical arrangement is shown in Fig. 2.

Development of Air Swirl and Volumetric Efficiency - The installation of a shrouded valve in the conventional intake port of the initial CFR engine setup served to induce air swirl but it seriously restricted the air intake to the engine. Studies of this problem resulted in two experimentally determinable characteristics that define the quality of a port and valve with respect to induced air swirl and volumetric efficiency. These are:

1. Swirl Efficiency: This is essentially the momentum of the swirling air divided by the momentum of the air flowing through the port and valve. It is determined by simple steady flow tests.
2. Flow coefficient (4): This is comparable to an orifice coefficient. It is also determined by simple steady flow tests.

Shortly after these concepts were established several port and valve designs were developed that had relatively favorable values of swirl efficiency and flow coefficient. One of these, designated as MkII, is shown on Fig. 4. It was selected for general use and applies to all four stroke cycle engine data presented hereafter.

Beyond establishing the swirl efficiency and flow coefficient concepts and developing a reasonably good port and valve design, many additional questions arose, such as: size and location of the port and valve to yield a desired air swirl and volumetric efficiency; the required amount of air swirl; the influence of combustion chamber shape; and the effects of valve timing. These questions required answers from a substantial number of engine tests with variations in the engine design and construction. A brief summary of the principal results is presented by Fig. 4 in combination with the following discussion:

1. Air swirl rate can be designated by n/N, the ratio of the air swirl rpm, n, to the engine rpm, N. n/N can be treated as a design and combustion constant independent of engine rpm. n/N, induced through the port and valve, is determined from the swirl efficiency and flow coefficient, the bore and stroke of the cylinder, the dimensions of the port and valve and the valve timing and lift data.
2. "Gulp Factor" (4), defined as the ratio of the nominal velocity to the velocity of sound through the port and valve, is a useful index of relative volumetric efficiency characteristics. Gulp factor, ϕ, is determined from bore and stroke, engine rpm, flow coefficient, port and valve dimensions

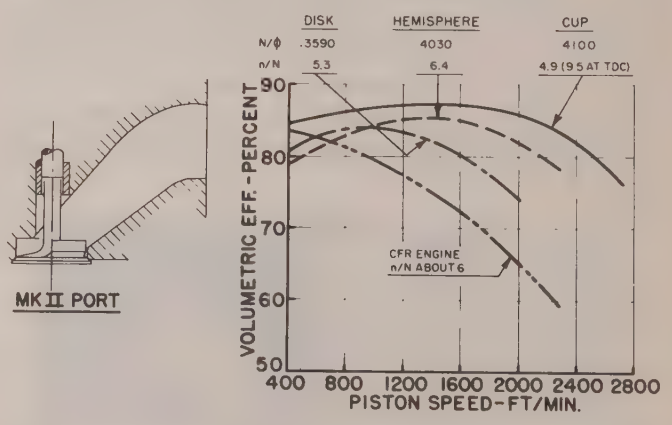

Fig. 4 — Effects of intake porting and combustion chamber on volumetric efficiency and air swirl rate

and valve timing and lift data. N/ϕ, the engine rpm at which a nominal sonic velocity through the port and valve is attained, is a valid index of the maximum speed at which useful volumetric efficiency will occur.

3. The n/N value that exists at approximately the top center position of the piston relates to combustion performance. With the flat disk combustion chamber this value of n/N is substantially equal to the induced air swirl, but if the combustion chamber is made more compact than the disk, conservation of momentum of the swirling air will cause the top center n/N to be greater than the induced air swirl.

4. The Texaco process can operate on a variety of top center n/N values but because of correlation of full load combustion duration with heat losses, low values of n/N adversely affect thermodynamic efficiency. Satisfactory efficiency requires n/N values of 6 or greater.

5. With the swirl port and valve design it was established that volumetric efficiency responds to cam timing almost exactly as any other poppet valve system. For example, late intake valve closing and large overlap tend to increase high speed volumetric efficiency but at the expense of low speed efficiency. Since these timing effects are an established part of engineering technology the practice has been to adopt as a standard the CFR knock test engine cam timings*. This timing applies to all curves of Fig. 4 and to all other four-stroke-cycle engine data presented herein.

As in current automotive practice, intake manifold branch length and diameter has been chosen to favor volumetric efficiency. Single pipes were used for the single cylinder engine data of Fig. 4, except for the CFR, and similar individual passages are used on each cylinder of multicylinder engines.

From the data of Fig. 4 and the foregoing summary of the related investigations, it appears that progress has been made to the point at which air swirl and volumetric efficiency are not really limiting to engine performance for a wide range of applications. Also, now that the techniques of this type of development have been established additional improvements can be expected; unshrouded valves in combination with the most compact combustion chamber appear particularly interesting both for improved volumetric efficiency at high speeds and for simple construction.

Combustion Chamber Shape and Location of Injection and Ignition Sources - As mentioned in the previous paragraphs, combustion chambers having more compact shapes than the flat disk are favorable to air swirl and volumetric efficiency. They also are of advantage with respect to thermal efficiency and to maximum speed for regular ignition. More compact combustion chambers that have been investigated quite fully are a hemispherical combustion chamber

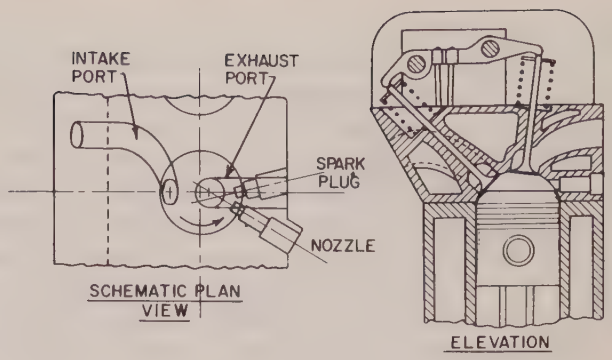

Fig. 5 — Hemispherical combustion chamber engine

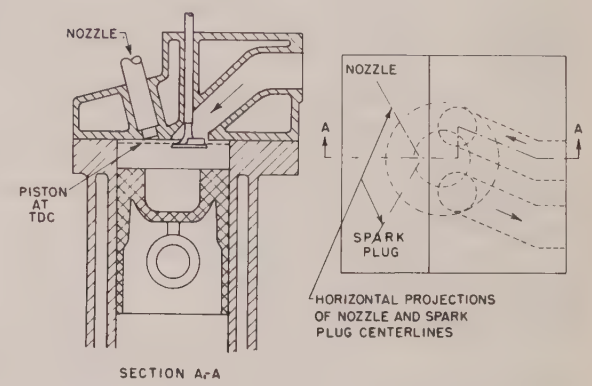

Fig. 6 — Cup combustion chamber engine

(Fig. 5) and a cup combustion chamber (Fig. 6). The relative advantages of these combustion chambers with respect to thermal efficiency and maximum speed are summarized below:

1. Thermal Efficiency: Heat loss that occurs during combustion causes a reduction of thermal efficiency. The magnitude of this loss is related to the surface to volume ratio of the combustion chamber; the larger the surface to volume ratio the greater the heat loss. Comparative surface to volume ratios, based on 10:1 compression ratio top center combustion chamber proportions with 3-1/2 in. bore and 3-3/4 in. stroke are 6.05:1, 4.60:1 and 3.44:1 for the flat disk, hemispherical and cup combustion chambers respectively.

2. Maximum speed: The swirling air tends to deflect the fuel spray and disturb its relationship to the ignition source. It also tends to blow out a spark or cool a glow plug. These effects are proportional to the linear velocity of air flow at the injection and ignition sources and they become troublesome when the velocity gets to or above 300 fps. The more compact combustion chmabers make it convenient to install the injection and ignition sources at a smaller radius than the peripheral position employed with the disk chamber (Fig. 1). This results in their being exposed to lower linear air velocity even at higher air swirl rates and higher engine speeds. Also, the air swirl production and volumetric efficiency characteristics of compact chambers are such that

*Intake opens 15 deg btc, closes 50 deg abc; exhaust opens 50 deg bbc, closes 15 deg atc.

higher speed is feasible.

Fig. 7 presenta a summary of the combined effects of compacting the combustion chamber on indicated mean effective pressure at constant values of indicated specific fuel consumption over a speed range. (The schematic illustrations of the various combustion chamber types in Fig. 7 show an arbitrary orientation of the exhaust port for improved clarity.) The relative levels of indicated mean effective pressure and the speed ranges are in general accord with the foregoing discussion of the combustion chamber effects. In the case of the cup combustion chamber the maximum range

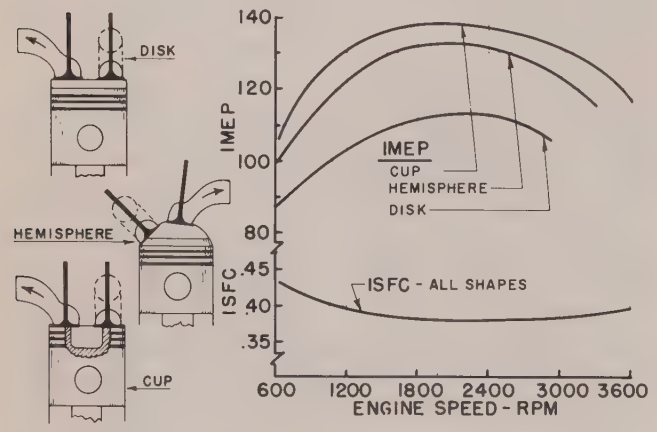

Fig. 7 — Effect of combustion chamber shape on TCP engine performance

Fig. 8 — Typical fuel spray for TCP engine

for the data is 3600 rpm but this has been held for mechanical reasons not related to the combustion process and the incipient misfire point is known to be above 3600 rpm.

Type, Relative Location and Timing of Fuel Spray and Ignition Sources - Detailed descriptions of the spray and ignition source locations are outside the scope of this paper but they may be inferred from the several drawings and photographs that are included, and they are spelled out in some detail by Reference 5. Generally speaking, the spray is directed downstream and across the swirling air such that all of the air can be impregnated with fuel, and the ignition source is positioned directly downstream in the air swirl from the spray but outside of the envelope of the spray. The spray and ignition sources should be located as closely adjacent as possible; the arrangement suggested by Fig. 1 being preferable to that of Fig. 2. Too close a position has not been obtained, because of limitations due to the physical size of the injection nozzle and the spark plug.

Fig. 8 shows a stroboscopic photograph of a typical spray observed in normal atmosphere. The spray results from flow through a simple orifice with a short length to diameter ratio as illustrated by the enlarged nozzle valve section of Fig. 9.

It has been found that the Texaco process can operate with virtually any positive source of ignition such as a glow plug or a spark plug. A glow plug is particularly intriguing since it would always be available when the first injected fuel reached it; however, no very satisfactory glow plugs have come to our attention. A spark plug, with the spark produced by more or less conventional coil and breaker systems, has been used almost exclusively in the investigations. With spark ignition, timing is a consideration because a spark having adequate incendiary power must exist when the first fuel is at the spark gap. Fortunately, most spark ignition systems produce a spark which has a finite duration of incendiary power so that there is appreciable margin for error in making spark timing coincide with injection timing. Actuation of the ignition breaker by the lift of the fuel in-

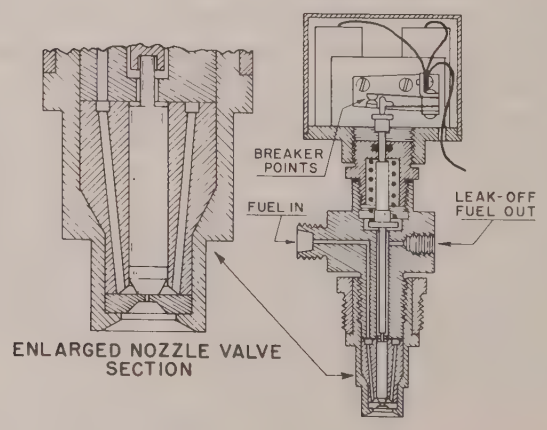

Fig. 9 — Nozzle assembly with ignition breaker

jection nozzle valve, as illustrated by Fig. 9, is a convenient way of assuring automatic coordination of fuel injection and spark timing.

The spark plugs are regular automotive types excepting that the center electrode is slightly longer than usual and the ground electrode is U-shaped with both ends welded to the plug body.

Fuel Injection and Spark Ignition Systems - Attention has been concentrated on gaining an understanding of TCP engine injection and ignition system requirements and of the system characteristics to satisfy these requirements rather than on the detailed development and refinement of any specific system. As they were needed for engine operations, systems have been assembled "breadboard" fashion from commercially available components plus a few homemade ones. These systems have been convenient enough to use and they have done a reasonably good job of satisfying engine requirements. This handling of the problem is justified on the basis that, in the long run, these systems will be supplied by specialist organizations who are well qualified to provide the required technical characteristics and with due regard for system reliability and manufacturing economy.

In the assembly of Texaco process fuel injection systems, standard diesel injection components by American Bosch, Frederick Deckel (West Germany), Demco, Robert Bosch (West Germany), and Hartford Machine Screw Co. have been used. The Texaco process involves, among other things, operation over wider speed and fuel quantity ranges than the diesel engines for which the systems were developed originally. It has been gratifying to observe that these components adapt fairly well to fulfill TCP's wider requirements, not perfectly, but well enough to produce the engine performance results reported in this paper. The Appendix presents a discussion of the principal injection system characteristics as they relate to several aspects of TCP engine performance, and points out that systems engineered for TCP engine applications can yield significant improvement in TCP engine performance over that presented in this paper, particularly at the extremes of operating conditions.

Ignition systems also have been assembled using commercially available components by Champion, Delco, Mallory, and others, often in combination with homemade parts. As compared to a typical gasoline engine of the same compression ratio, a Texaco process engine exhibits a somewhat lower maximum breakdown voltage (because of the fuel) spray), and requires a somewhat higher secondary current. The spark timing must be coordinated with fuel injection; however, TCP does not require any greater precision of timing and can possibly tolerate less. Spark plug selection need not consider preignition or fouling by lead deposits since preignition is eliminated and, even if leaded fuel is used, lead deposits do not appear in the combustion chamber or on the spark plugs. Although conventional distributor ignition systems have been used extensively, the automatic coordination of timing that results when the beginning of injection

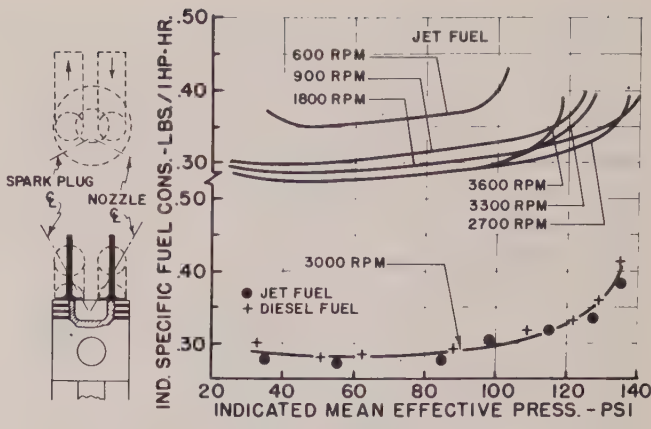

Fig. 10 — Indicated performance of TCP engine with a cup combustion chamber

is used to actuate the ignition (Fig. 9) is so convenient that it rates first consideration. The concept of injection actuated ignition is not limited to the nozzle valve operated breaker system illustrated in Fig. 9 as there are a variety of other sites in the fuel injection system from which an appropriate ignition actuation signal can be obtained. It appears that ignition system suppliers will have little difficulty in providing systems engineered for TCP engines.

Performance Results with Several Four Stroke Cycle TCP Engines

Studies have been made on a substantial number of four-stroke-cycle engines at 10:1 compression ratio with bores ranging from 3-1/4 to 5-3/4 in. and strokes from 3-3/4 to 6 in. A brief review of three cases will serve to illustrate many TCP engine performance characteristics.

Cup Combustion Chamber - Fig. 10 illustrates the arrangement of a 49.7 cu in. displacement (3-3/4 in. bore by 4-1/2 in. stroke) cup combustion chamber single cylinder engine for the Texaco Combustion Process and shows typical performance characteristics. The upper curves of the figure show indicated performance data obtained at several different engine speeds. The lower curve shows data for both diesel and jet fuel at 3000 rpm.

In many respects this is the most interesting of the four cycle TCP engine developments. With cylinder dimensions, valve timing and other details adjusted to the intended use, the existing performance is in the range of suitability for a variety of applications such as taxicabs, tractors, delivery trucks, pumping units and motor boats in all of which the Texaco process characteristics would have considerable value to the user. In addition there is room for appreciable growth in pe formance both from engineering development of the port, valve and combustion chamber, along the lines mentioned earlier, and from engineering the injection system (Appendix) to better adapt it to Texaco engines. It is thought that the growth potential is sufficient to yield performance

suitable for many automotive applications.

TCP Engine Installed in Automobile - The principal engineering development of the Texaco process has been accomplished on single cylinder engines but with several checks to determine how the results applied to multiple cylinder engines and to see how they worked out under service type conditions. One of the first such projects was the construction of a six cylinder engine for installation and test in a 1950 Canadian Plymouth car. A six cylinder L-head gasoline engine that fits into the vehicle was obtained and modified for Texaco process operation. Modification involved providing a fuel pump drive, a new cylinder head and, of course, a conversion to overhead valves. The original gasoline engine for the vehicle had been 218 cu in. displacement and the engine for the Texaco process was made at 3-1/4 in. bore by 4-1/2 in. stroke for a nearly equal displacement of 224 cu in. A disk combustion chamber and a MkII port and valve producing a swirl rate of slightly less than 6 were used in the Texaco process engine (Fig. 7).

Fig. 11 shows comparative chassis dynamometer car performance tests for the car with its original gasoline engine and with the TCP engine. The original target had been for the full throttle rear wheel traction to be about the same with no change except the engines. As the figure shows, this target was fulfilled well enough that acceleration and hill climbing capability of the vehicle is substantially the same with either engine, except at the extremes of speed, so that the comparison is primarily in terms of fuel economy, fuel quality requirement and other secondary performance characteristics.

The vehicle with the TCP engine was used for extensive dynamometer and road tests and for both cross-country and local trips. Several 2000-5000 mile cross-country trips have been made by one man who purchased fuel supplies en route; gasoline, kerosine, and diesel fuel were purchased and used in indiscriminate mixtures as available from service stations. Tank mileage* for the vehicle with the Texaco engine works out to be just about equal to the level road miles per gallon of the prevailing driving speed, as shown by Fig. 11, for cross-country driving. In local driving values of 30-35 mpg have been observed where 10 to 15 is more typical for a comparable gasoline engine.

After some 20,000 miles the engine was inspected. All bearings, shafts, and pistons, were in excellent condition. Application of the Texaco process at 10:1 compression ratio to a 7:1 compression ratio gasoline engine structure evidently was satisfactory. The vehicle with the Texaco engine installed is still used occasionally, but it is essentially obsolete.

*Trip miles divided by total gallons of fuel used.

*Waukesha Motor Co.'s 180-DLC diesel engine.

Four-Cylinder Hemispherical Combustion Chamber Engine - A TCP conversion has been made to a 144 cu in. displacement 4-cylinder engine of 3-1/2 in. bore by 3-3/4 in. stroke*. The Texaco hemispherical combustion chamber design including the MkII port and valve, a Roosa-Master fuel injection pump, and a nozzle valve actuated ignition system were used. Five of these assemblies, designated as Model 144-HCC, have been constructed for experimentation in our own and other laboratories.

The construction of these engines is illustrated by the outline drawing (Fig. 5) and by the photographs (Figs. 12-13).

Performance characteristics of this conversion are illustrated by Figs. 14-18. In all cases the engine was equipped with an air filter and all accessories except for a fan and muffler. The results shown are observed data uncorrected for ambient conditions which were in the range of 29.50-30.00 in. barometer and 75-85 F atmospheric temperature.

Fig. 14 shows brake specific fuel consumption versus brake horsepower at several engine speeds.

Fig. 15 shows the variation of several performance characteristics with engine speed.

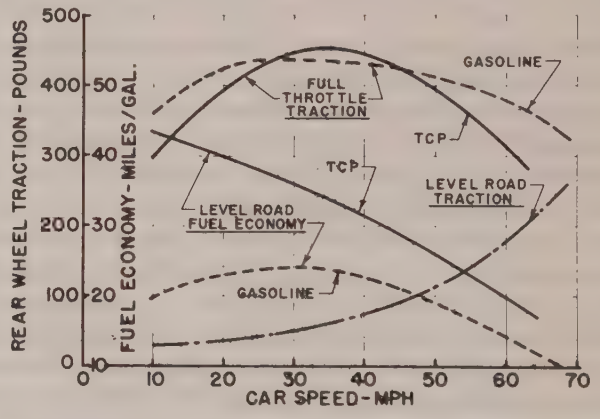

Fig. 11 — Performance of a 1950 plymouth car with gasoline and TCP engines

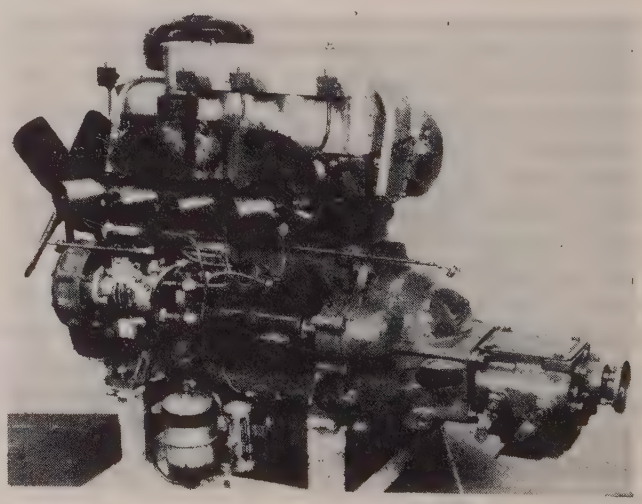

Fig. 12 — Model 144 — HCC engine

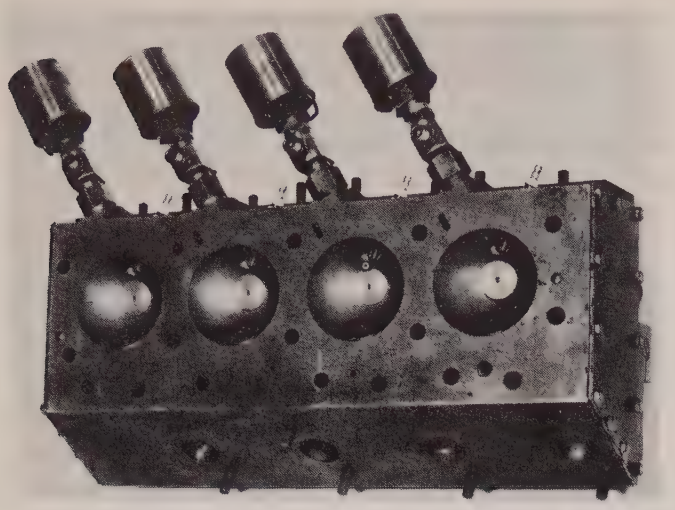

Fig. 13 — Cylinder head for Model 144 — HCC engine

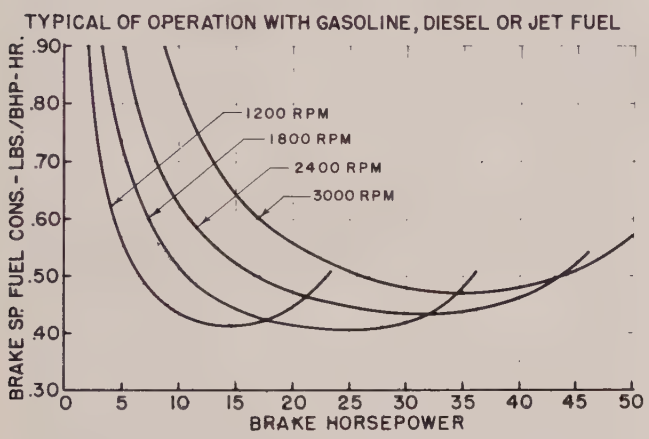

Fig. 14 — Brake performance of 144 — HCC engine

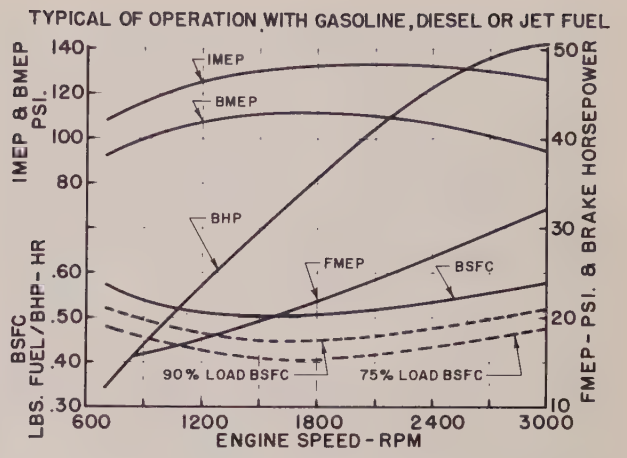

Fig. 15 — Full load performance of 144 — HCC engine

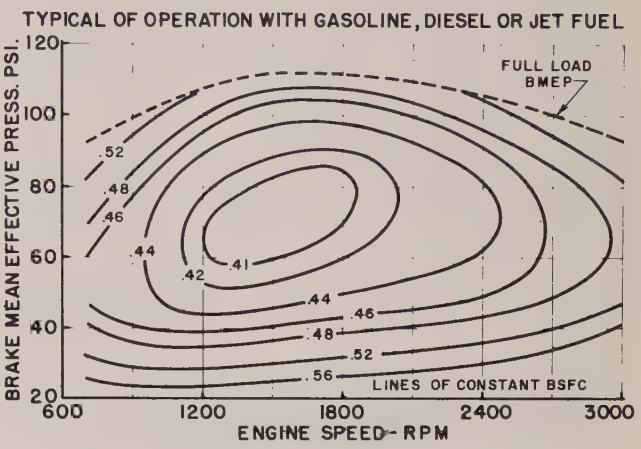

Fig. 16 — Performance map for 144 — HCC engine

Fig. 16 shows a "performance map," that is, lines of constant specific fuel consumption on the coordinates bmep and engine speed.

In the foregoing data the full load values are determined by a "smoke limit" that occurs at 95-100% of stoichiometric mixture strength regardless of the fuel. These TCP smoke limit settings are for a smoke intensity that makes the exhaust somewhat more noticeable than the exhaust of a gasoline engine but not as visible as that of many diesels. Fig. 15 shows that friction of this engine is high and that there is some performance penalty from this source. This high friction relates to the basic engine construction, it is not a characteristic of the Texaco process.

Multifuel capability is illustrated by Fig. 17 which shows performance on three fuels: gasoline, jet fuel and diesel fuel. For better clarity curves were not drawn through the points on the figure. Large changes of density and viscosity, between diesel fuel and gasoline cause the injection pump to deliver less gasoline than diesel fuel and the maximum quantity control on the injection pump is adjusted to compensate.

A variety of indicator diagrams have been taken with a balanced pressure indicator at speeds of 700 through 3000 rpm, at several loads and with gasoline, jet and diesel fuel. Typical diagrams for full load, 1800 rpm operation on the three fuels are shown by Fig. 18 on crank angle versus pressure coordinates. From the entire set of diagrams it appears that full load maximum pressures fall in the range, 675-750 psia with maximum rates of pressure rise in the range 35-40 psi per crank angle deg. There are no significant changes with fuel.

Accurate estimates of the performance characteristics that a Model 144-HCC engine would produce in many applications can be made based on the preceding dynamometer tests. Two cases of some interest are:

1. Farm Tractor: Diesel and gasoline versions of the same engine that was converted to make the Model 144-HCC are used in a commercial farm tractor. Comparative belt performance data are shown in Fig. 19. The diesel and gasoline

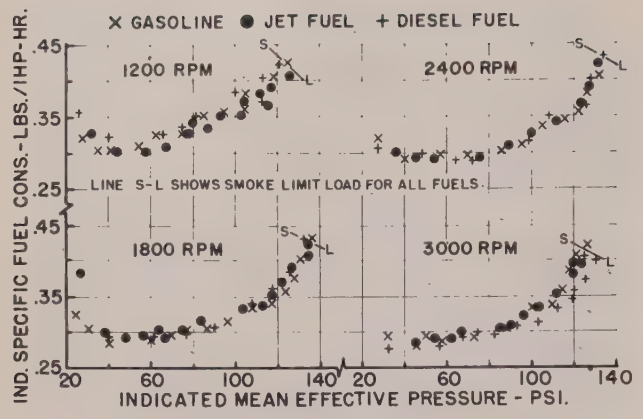
× GASOLINE ● JET FUEL + DIESEL FUEL
1200 RPM
2400 RPM
LINE S-L SHOWS SMOKE LIMIT LOAD FOR ALL FUELS
1800 RPM
3000 RPM
IND. SPECIFIC FUEL CONS.-LBS./IHP-HR.
INDICATED MEAN EFFECTIVE PRESSURE - PSI.

Fig. 17 — Indicated performance of 144 — HCC engine with three fuels

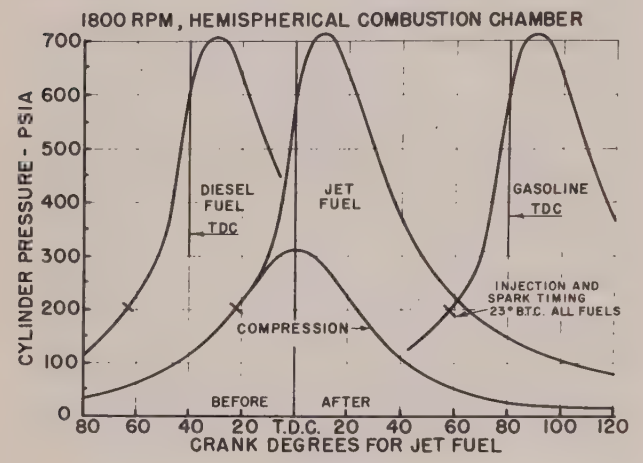

Fig. 18 — Full load P-T diagrams with three fuels

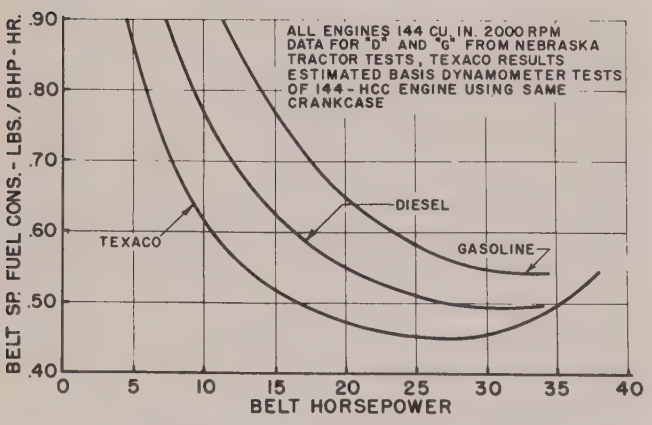
ALL ENGINES 144 CU. IN. 2000 RPM
DATA FOR "D" AND "G" FROM NEBRASKA TRACTOR TESTS, TEXACO RESULTS ESTIMATED BASIS DYNAMOMETER TESTS OF 144-HCC ENGINE USING SAME CRANKCASE
DIESEL
TEXACO
GASOLINE
BELT SP. FUEL CONS.-LBS./BHP-HR.
BELT HORSEPOWER

Fig. 19 — Tractor performance comparison gasoline, diesel and Texaco engines

values are directly from Nebraska Tractor Test reports and the TCP values are estimated on a comparable basis.

2. Jeep: The Model 144-HCC has about the same displacement as a Jeep engine and it could be installed in a Jeep vehicle. Fig. 20 shows a vehicle performance comparison of the Model 144-HCC with the L- and F-head Jeep gasoline engines. The gasoline engine data are direct chassis dynamometer test results and the Model 144-HCC is calculated from the engine performance and the vehicle characteristics. To equalize rear wheel traction an axle ratio change was assumed with the Model 144-HCC. The increase in vehicle miles per gallon would be very large.

These engines have been developed only for laboratory test purposes to illustrate the characteristics of the Texaco Combustion Process and the potential value of burning lean mixtures of broad boiling range fuels having no octane or cetane number requirements. It appears that they are suitable for this purpose.

The Texaco Combustion Process in a Two Stroke Cycle Engine

Several two-stroke-cycle engine applications have been investigated. The most interesting of these was based on an opposed piston engine of 3-3/4 x (3-3/4 x 3-3/4) in. bore and stroke with 10:1 compression ratio. The general con-

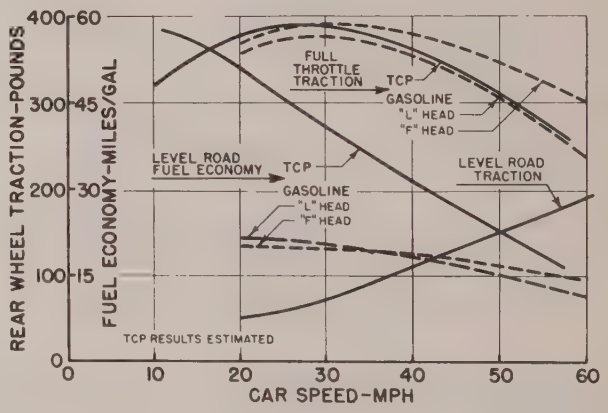

Fig. 20 — Comparative performance of Willys 4-cyl station wagon with gasoline and TCP engines

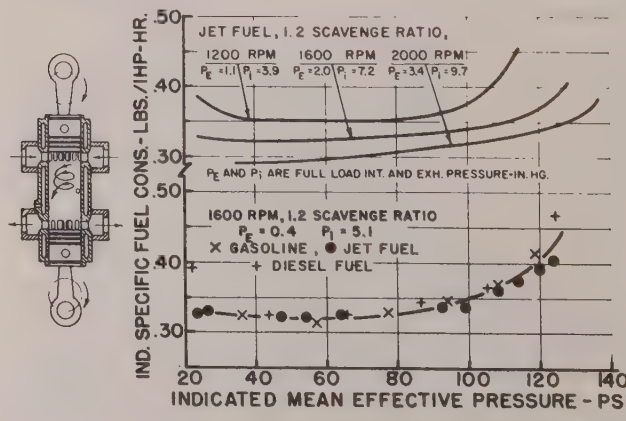
JET FUEL, 1.2 SCAVENGE RATIO,
1200 RPM 1600 RPM 2000 RPM
P_E AND P_I ARE FULL LOAD INT. AND EXH. PRESSURE-IN. HG.
1600 RPM, 1.2 SCAVENGE RATIO
P_E = 0.4 P_I = 5.1
× GASOLINE, ● JET FUEL
+ DIESEL FUEL
IND. SPECIFIC FUEL CONS.-LBS./IHP-HR.
INDICATED MEAN EFFECTIVE PRESSURE - PSI.

Fig. 21 — Indicated performance of a two stroke cycle opposed piston TCP engine

figuration is illustrated by Fig. 21. It turned out that a successful application hinged on developing an intake port design that would produce a predictable air swirl rate and a good scavenging efficiency.

Flow tests of models correlated with engine tests, in a study extending over several years and involving many models and engine port designs, eventually led to a reasonably good understanding of the two-cycle port design problem and to a construction having adequate swirl and scavenging characteristics. Thereafter, development of good Texaco process operation was an essentially routine application of the principles previously outlined, and performance of the type illustrated by Fig. 21 resulted. It will be noted from the figure that the pressure drops associated with air flow through the engine are unusually low. This in combination with the excellent imep versus isfc performance makes the two-stroke-cycle design a most interesting one to consider for a high performance engine.

For small cylinder displacements, in the range of 35-70 cu in. per cylinder, the opposed piston configuration tends to have relatively large envelope dimensions. In this displacement range a uniflow scavenged design with ported intake and poppet exhaust tends to be more compact. The air swirl and scavenging design principles worked out in the opposed piston development and the Texaco Combustion Process principles will be directly applicable to this more compact configuration. This type of TCP engine would be particularly attractive for a wide range of industrial, marine, and automotive uses.

Some Other Characteristics of TCP Engine

Cumulative experience with the Texaco Combustion Process automatically included observation of a variety of secondary factors which have an important bearing on the usefulness of the process.

Flexibility - Response to "throttle" changes is immediate and without misfire or backfire or the hesitation sometimes associated with carburetors.

Cold Starting and Warmup - Cold starting characteristics are excellent; prolonged cranking, air heaters, priming fluids or other starting aids are not required, even at very low temperatures. The primary requirement is for a cranking speed high enough to produce a reasonable injection and this depends on the injection system and application in question (Appendix). No attempt has been made either to improve starting characteristics or determine the minimum starting temperatures; however, several engines have been started in the range of -40 to -50 F. For example, the Model 144-HCC engine has been started in less than 10 sec at -50 F; a warm battery and some crankcase dilution is needed at this temperature to develop the required cranking speed, about 200 rpm.

Warmup after starting appears not to be a combustion consideration; the engine operation is smooth and regular and, except for initial high friction due to cold lubricating oil, full power can be developed immediately.

Lubrication and Deposits - Although controlled endurance tests have not been conducted, individual engines have been operated several hundred hours without overhaul or modification except for injection and ignition equipment maintenance. Using commercial grade lubricants there has been no evidence of severe or unusual lubrication requirements or of unusual deposits or wear. Combustion chamber deposits always have been very light.

Exhaust Gas Conditions - A detailed quantitative comparison of TCP with gasoline and diesel exhaust composition has been beyond the scope of the work to date. Nevertheless, fairly extensive observations have been made and, as would be expected with lean mixture operation and positive ignition, the concentration of incomplete combustion products is low. Thus, under normal load conditions hydrocarbon content of the exhaust is in the range of 200-400 ppm (mass spectrometer analysis) and CO concentration is nil, while for deceleration no fuel is injected. Idle exhaust odor similar to that encountered with diesel engines may or may not be apparent with TCP engines depending on injection system characteristics (Appendix). In a balanced consideration of all factors the TCP exhaust condition appears favorable.

Conclusions

The development of efficient and serviceable engines that can make the desirable characteristics of the Texaco Combustion Process available for general use appears to involve three major phases:

1. Development of a sufficiently precise understanding of the combustion process per se to insure that it can be handled in a predictable engineering manner.

2. Engineering research to establish and verify the factors influencing the efficiency and performance of a TCP engine and to develop both design principles and usable construction details for the related engine components and accessories.

3. Development of TCP engines for specific applications with due regard to the detail refinement, durability, and cost of the engine and its accessories in relation to its value to users for various services.

It is considered that the developments outlined in this paper represent satisfactory accomplishment on the first two of these three phases and that a solid engineering basis has been established for the development of engines for specific applications. At present levels of performance TCP engines should be attractive for a variety of uses in which efficiency and economy are most important considerations. With some predictable additional developments, TCP engines should be of value in a wider range of automotive applications.

Acknowledgement

The authors wish to express their appreciation to the many persons in the Texaco organization and elsewhere who have contributed advice, assistance, equipment, and skilled services that were invaluable to the progress of this work. The combustion photography investigations were conducted under a research contract by the Engineering Research Department of the Pennsylvania State University, under the supervision of Prof. W. E. Meyer.

Appendix I

Selection of a fuel injection system for a Texaco process engine involves many of the same considerations as for a diesel engine and the theory and practice of applying these systems is well known. Accordingly, only a few of the characteristics as they relate to selection for TCP and to engineering systems more specifically for TCP requirements, a procedure that would yield superior TCP performance, will be discussed:

System Size - Size is selected so that the amount of fuel required for full load will be discharged from the nozzle in the desired number of crank angle degrees. For TCP the desired crank angle degrees are related to n/N and can be estimated as $\frac{0.8 \times 360}{n/N}$, in which the 0.8 factor results from the fact that the spray from a simple orifice propagates somewhat faster than the air swirls so that the air charge can be impregnated with fuel in about 80% of a complete swirl. The pump displacement characteristics and the discharge characteristics of the nozzle orifice are then the primary factors in system size with second order effects relating to the compressibility and length of the system between the pump plunger and the nozzle orifice. Final selection involves systematic variation of the system characteristics over a small range to adjust or verify the calculated sizing. Our use of the simple nozzle orifice plate sealed by a flat seat check valve illustrated in Fig. 9 had its origin in the ease with which orifice sizes could be varied for such experimentation. The design is admirable for this purpose but the exact detail of it could not be recommended for long time service.

Effects of Speed - It is inherent in the hydraulic characteristics of fuel injection systems that the duration of injection increases with increasing engine rpm and that the beginning of injection tends to retard; both of these characteristics relate to the compressibility and length respectively of the system between the pump plunger and the nozzle orifice.

The change of injection duration with speed means that optimum impregnation of air with fuel occurs at only one speed, at lower speed not all of the air is impregnated and at higher speed some of the fuel is injected into vitiated air. Theoretical analysis and experimentation verify that a major portion of the high and low speed droop of TCP engine mep versus rpm curves, for example, the curves for the cup and hemisphere on Fig. 7, can be attributed to this injection system characteristic. Analgous effects of changing injection duration occur in diesel engines but because of the lesser speed range of typical diesel engines the rewards, in improved high speed performance, for minimizing the change of injection duration with speed are not so apparent. Improvements of this characteristic can be attained by reductions of system volume, and by the use of variable orifice area nozzles.

Against an injection system's natural tendency to retard the time for beginning of injection with increasing speed, the Texaco process prefers advance of timing with increasing speed, this preference being analogous to the gasoline engine's preference for a more advanced spark timing at higher speed. Various fuel injection pump accesories are available to adjust injection timing with speed and these have been used for TCP. These devices have been designed to provide a slight advance for diesels up to their characteristic speeds of 2400-2700 rpm. As applied to TCP engines with maximum speeds of 3000-3600 rpm some of them barely offset the inherent retard and produce little if any of the desired advance. Redesign to accomplish a greater advance for this wider speed range is relatively straightforward and will be of advantage to high speed TCP performance.

Maximum and Minimum Injection Quantities - Ideally, a fuel injection system should be able to inject regularly any amount of fuel from the maximum quantity to nothing and maintain a well-formed spray over this range of quantities at any speed from maximum to zero. Actual systems do very well but they are not ideal in that they exhibit minimum quantities and speeds at which they will inject regularly and produce a well-formed spray. The maximum quantity that can be injected is also a function of speed and often falls off severely at cranking speeds. These characteristics relate to the pump leakage path, the method of pump quantity control and the maximum quantity setting, the compressivility of the system, the fuel being used, and other factors. The effects on engine operation are primarily on starting and idling and operation at extreme light loads. Similar cuases and effects exist for diesel engines but again the rewards for system improvements are greater for TCP.

1. Cold Starting. Texaco process engines start readily even at very low temperatures, when a cranking speed is reached that provides regular injection of a sufficiently large quantity of fuel to support operation. This speed may range from 60 to 250 rpm depending on the application. In contrast, a diesel engine usually requires fairly elaborate starting aids to initiate combustion below 0 F so that the incentives to develop regular injection at low rpm have not been very great for diesel injection systems.

2. Idle and Light Load. Texaco process engines of 35-40 cu in. displacement per cylinder idle on about 4-5 cu mm per injection compared with approximately 8-10 cu mm for typical diesel engines. The available injection systems usually fail to provide completely regular sprays below the 6-8 cu mm level. Consequently, the systems are marginal for TCP engines of this displacement although they are adequate for most diesel engines. Texaco process engines may or may not idle regularly and without odor depending on whether or not the injection system is producing a well-developed spray. In case it is not the idle will be rather irregular and an odor resembling that of a diesel on idle will occur because the spark fails to ignite the fuel. The odor produced by a diesel engine idling is basically related to the spontaneous ignition process at the low temperature conditions of idle rather than to the injection system. Thus, there is an incentive to engineer the injection system for small injection quantities to obtain a superior result made possible by the Texaco process.

In the foregoing discussion the basis for selecting a suitable fuel injection system has been outlined. Incidental to this, attention has been given to certain deficiencies of existing systems insofar as they apply to TCP engines, as contrasted to the diesel engines for which the systems were developed. Several suggestions are made for re-engineering the systems to better adapt them to the Texaco process. It should be clearly understood, however, that the purpose of this re-engineering would be to yield improvements over the Texaco process results presented by this paper.

References

1. E.M. Barber, Internal Combustion Engine and Method of Operating Same, U.S. Patent No. 2,484,009, October 11, 1949.

2. E.M. Barber, J.B. Malin, and J. J. Mikita, "The Elimination of Combustion Knock," Journal of Franklin Institute, Vol. 241, No. 4, (April 1946).

3. E.M. Barber, B. Reynolds, and W.T. Tierney,"Elimination of Combustion Knock - Texaco Combustion Process," presented at SAE Summer Meeting, French Lick, Indiana, June, 1950.

4. J.C. Livengood and J.V.D. Eppes, "Effect of Changing Manifold Pressure, Exhaust Pressure, and Valve Timing on the Air Capacity and Output of a Four Stroke Engine Operated With Inlet Valves of Various Diameters and Lifts," Massachusetts Institute of Technology, NACA Technical Note 1366, (December 1947).

5. E.M. Barber and C.W. Davis, Internal Combustion Engine, U.S. Patent No. 2,864,347, December 16, 1958.

Discussion

Performance of the TCP Engine

J. K. Jensen
John Deere Tractor
Research & Engineering Center

PERFORMANCE of a Texaco Combustion Process engine obtained during a development program in our laboratory in cooperation with the Texaco Research Center is shown in Fig. A. Our work with TCP included manufacture and operation of two cylinder engines of 5-3/4 x 6 in., 5-1/2 x 6-3/4 in., and 5-1/2 x 6-3/8 in. dimensions operating at rated speeds of 1000-1150 rpm. All work was done with the flat disc combustion chamber and the Mark II intake port referred to by the Texaco authors. The data chosen for presentation in the curve is for the 5-1/2 x 6-3/8 in. size at 1125 rpm since Nebraska Tractor Test data is available for the gasoline version of this engine. This curve agrees with the general performance levels for the flat disc chamber shown by the authors. It is experimental evidence that their calculated comparison of gasoline and TCP tractor performance in Fig. 19 is substantially correct.

Earlier publications on the Texaco Process emphasized the multifuel aspects of the combustion system. I am pleased to note that in the current paper the process has been allowed to stand on its own merits in competition with Otto and Diesel cycles. The multifuel capability was convincingly demonstrated on the engines we built and stands unquestioned. However, the economic worth of this feature to a farmer is doubtful. Inquiry was made of two major oil companies to determine the possibility of refining and distributing a fuel acceptable for TCP engines but cheaper than No. 2 diesel fuel. The most optimistic estimate was a 1¢/gal f.o.b. refinery price advantage to the special TCP fuel. After taxes, transportation, and ordinary distribution costs are added, the percentage price advantage showed little promise of being sufficient to justify the problems of distribution of a special fuel.

From the standpoint of a typical engine builder, the Tex-

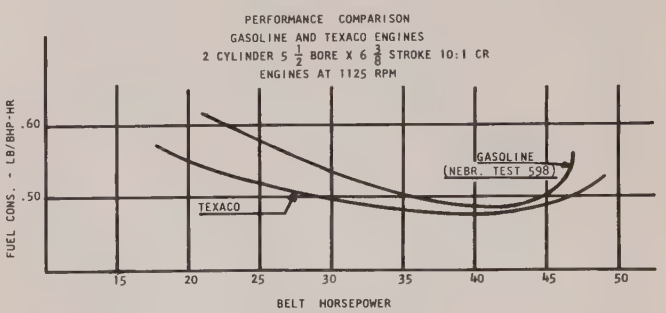

Fig. A — Performance comparison gasoline and Texaco engines 2 cyl 5½ bore times 6⅜ stroke 10:1 compression ratio engines at 1125 rpm

aco Combustion Process offers the operating advantages claimed for it by the authors and presents few unusual problems associated with the main engine structure. The principal difficulties seem to lie with the accessories, injection and ignition equipment, which are customarily constructed for the engine builder by a specialist manufacturer of this equipment. For example, our laboratory work demonstrated that it was possible to build an ignition system which gave acceptable, if not entirely satisfactory, operation. However, this system was constructed by the engine experimenter and not by an ignition equipment supplier. Efforts in our laboratory by three ignition equipment manufacturers failed to produce a satisfactory system. The time spent by any of the three was not great and none was even close to admitting defeat. However, their work progressed far enough to indicate that the ignition requirements of TCP as we then understood them were unusual and that more than a slight warming over of production automotive systems would be required.

Cost penalities associated with TCP lie primarily in the accessory equipment. The incentive to overcome these difficulties could come from the engine builders since accessory manufacturers would respond to serious requests from their OEM customers for this equipment. The likelihood that such a request will be made is reduced by the uncertainty of success in providing accessory equipment at a cost which would make a TCP engine competitive. It would be unfortunate if this impasse were to prevent utilization of a combustion system having many advantages.

Possible Application of TCP Method — Military Use

Errol J. Gay
Consultant

THIS DISCUSSION will not attempt a technical comment of the paper, but will confine its comment to possible use of the process.

In May, 1960, this discussor presented a paper at the Detroit meeting of the API, Division of Refining. The title of the paper was, "The Military Mission of the Multi-Fuel Engine, and Its Fuel Requirements." The Army needs best possible fuel economy to lighten its logistics load and to obtain maximum operating range for its vehicles. The Army engines should be able to burn gasoline or mixtures of gasoline and distillates. This is important, since in a war emergency the distillates demand for essential civilian needs, Air Force, and Navy may add up to more than can be produced by the petroleum industry.

It is also most essential that the Army be able to procure engines for most of its wheeled vehicles from existing industry tooling. The Texaco Combustion Process engine might prove useful in meeting these above noted requirements. This might be especially useful in the class of engines that now power the 1/4 ton, 3/4 ton, and 1-1/2 ton vehicles.

The TCP, a Descendant of the Diesel and Spark Ignited Engines

A. E. Cleveland
Ford Motor Co.

IT IS PROBABLY more than coincidental that the combustion system described by Messrs. Davis, Barber, and Mitchell combines most of the good features and some of the bad features of spark ignited and diesel engines. Current development trend has produced diesels with increasingly lower rates of pressure rise and less cetane sensitivity and spark-ignited engines with increasingly high compression ratios and higher rates of pressure rise together with combustion problems no longer sensitive to octane improvement. Table A shows how much of the combined engine is represented by this Texaco Combustion Process.

From the table, one might conclude that the result of this marriage has produced in the TCP engine an off-spring more resembling its compression ignition parent than its spark ignition parent, resembling the latter only in its requirement for some sort of spark or glow plug ignition and its resultant more moderate rate of pressure rise. It partakes diesel engine economy characteristic at part throttle in its ability to burn fuel in an excess of air and to eliminate the necessity of air throttling and consequent pumping losses at part load. It also has the most undesirable characteristic of its diesel ancestry, that of being combustion or smoke limited at full power. This results in practical limitation of speed and power output for engine size and weight. How serious these limitations may be are determined by the skill

Table A - Combined Features of the Compression Ignited and the Spark Ignited Engine, which are Present in the TCP Engine

Compression Ignited	Spark Ignited*
Fuel burned in excess air*	Fuel/air ratio limited near chemically correct
Smoke limited full power*	Air limited full power
Unthrottled air*	Throttled air
Fuel injector required*	Fuel injector & carburetor, optional
Rate of pressure rise, 100 psi/deg	Rate of pressure rise, 40 psi/deg*

*Features of TCP engine

of the designer of combustion chambers and injector nozzles. That the authors and their associates have made considerable progress along these lines especially with cup type combustion chamber is evidenced from the results shown in Fig. 7. However, this is still about 20 imep short of a comparable modern spark ignition engine performance curve. this compares, however, very well with diesel performance curves.

The fuel injection requirement, although a familiar problem to diesel investigators, is a matter of some concern to those whose acquaintance is largely with the high volume cost conscious spark ignited engine. The carburetor is never so much appreciated as when replaced with a fuel injector which a cost-conscious management has prescribed somewhere within the cost limitations of a carburetor. A carburetor does quite naturally (for free) many things which a fuel injector must be paid and educated to do. However, these are all fundamental challenges to the skill of the development engineer. That the end result justifies the effort seems quite evident from the curves. Figs. 14-16. It is, perhaps, of interest to note in conclusion that this part throttle economy characteristic also partakes of its diesel ancestry and appears fundamentally the same as similar diesels checked in the same laboratory.

Installation of TCP Engine in an Automobile

Peter Ashurkoff
General Motors Engineering Staff

SEVERAL features of the Texaco Combustion Process have a special appeal for the automotive engineer. The most intriguing of these are the ability to burn lean mixtures efficiently and to operate on a wide range of fuels without regard for cetane or octane quality.

In their paper, the authors point out that the proper coordination of air swirl, fuel injection and positive ignition is the key to effective operation of the Texaco Combustion Process. The authors have done extensive research and development on the system and have obtained experimental results which verify the theoretical concepts of the process for which they should be congratulated. They suggest that sufficient engineering knowledge of the process has been developed and that the presently obtainable performance is attractive enough to warrant development of engines for specific applications.

The authors cite several examples where application of the Texaco Combustion Process would be advantageous. Two of the suggested applications concern low performance vehicles: a farm tractor and a jeep. A third application discussed in the paper is the installation of a TCP engine in an automobile. It is this application to which most of the following discussion is directed.

To demonstrate the fuel economy advantage of the TCP engine, a comparison is made of chassis dynamometer tests of a 1950 Canadian Plymouth with its original gasoline and with a TCP engine. For a valid economy comparison, equal acceleration performance is required since performance and economy are directly related. Generally, for a particular engine, a suitable compromise must be made between performance and fuel economy. The economy of any car can be improved if performance is sacrificed.

The authors state that a satisfactory match in performance was obtained, except at the extremes of speed. However, in Fig. 11, the TCP engine shows a loss in power of approximately 17% at 60 mph. This loss would presumably be higher at higher engine speeds. This might be tolerable if these engine speeds occurred only for car speeds above 60 mph. However, during an acceleration, engine operation at these higher speeds must be considered at relatively low car speeds, and presumably would reduce the car acceleration performance appreciably. Furthermore, it is known that fuel economy and performance are favorably affected by an increase in compression ratio. The TCP engine had a compression ratio of 10 whereas the compression ratio of the original Plymouth engine was only 7. Consideration of these factors would indicate that the higher fuel economy of the TCP engine installed in this car cannot all be attributed to the Texaco Combustion Process.

Recently, at General Motors Engineering Staff, we had an opportunity to test a Model 144 HCC Engine modified by the Texaco Research Center to operate on the Texaco Combustion Process. We were interested in comparing the results of this combustion with those of a conventional throttled gasoline engine. We wanted to make this comparison on the same engine with only minor modifications in order to eliminate as many uncontrolled variables as possible.

The performance results which we obtained with this engine operating on the Texaco process agree substantially with the results reported in this paper except at the high speeds. At the higher speeds and loads, we obtained somewhat higher fuel consumption values. We also found that the engine was very sensitive to small changes in ignition and injection characteristics. This was particularly evident when operating on diesel fuel, since any irregularity in ignition or injection resulted in audible knock. The complexity of the system used to time and coordinate injection and ignition made it difficult to pin point the trouble when engine performance deteriorated. Of course, difficulties of this nature are to be expected in working with any experimental setup. It is interesting to note, however, that proper operation of the Texaco Combustion Process, at this stage of its development, requires optimum operation of the component parts.

To operate this engine as a conventional spark ignition engine, the following modifications were made:

1. The shrouded intake valves were replaced with standard valves.

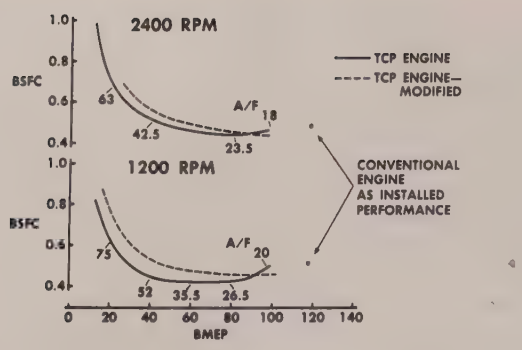

Fig. B — Brake specific fuel consumption versus brake mean effective pressure at 1200 and 2400 rpm

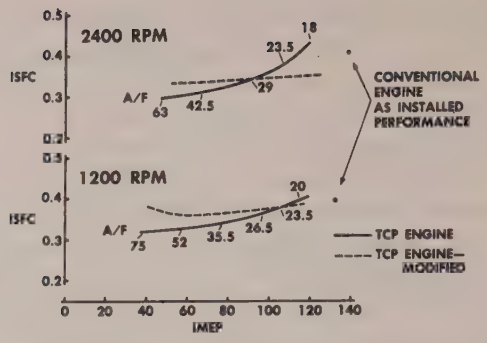

Fig. C — Brake specific fuel consumption versus brake mean effective pressure at 1200 and 2400 rpm, replotted on indicated basis

2. The fuel injection timing was changed so that injection occurred early on the intake stroke.

3. The injection actuated ignition system was replaced with a conventional distributor system.

This modified engine was then retested on the dynamometer for part load fuel economy. Fig. B shows curves of brake specific fuel consumption versus brake mean effective pressure at 1200 and 2400 rpm for the two combustion systems. Measured A/F values are indicated on the Texaco Combustion curves. The curves shown for the conventional spark ignition system do not extend to full throttle but only out to a manifold vacuum of 4 in. of Hg. because preignition was anticipated at high loads. Maximum bmep for a conventional engine at this compression ratio would be about 120 psi. This comparison indicates that the effectiveness of the Texaco Combustion Process deteriorates in this engine at high loads.

These same results are replotted on an indicated basis in Fig. C. The curves obtained for the conventional spark ignition system are essentially flat in accordance with theory, whereas the curves obtained for the Texaco process increase with load. These curves cross at progressively lower imep values and higher A/F ratios as the speed increases. We conclude from these data that maximum utilization of the air and fuel does not occur at the higher loads and speeds.

The TCP engine demonstrates good part load economy in comparison with a conventional spark ignition engine but is unable to match the high performance requirements of a passenger car engine. Actually, the Texaco Combustion Process is very similar to the diesel engine in this regard. It appears that the principal advantage of the TCP engine will be in applications where its ability to burn a wide range of fuels is of paramount importance.

Crank-Piston Gas-Generator Locomotives

L. H. Tengner
Aktiebolaget Gotaverken
Goteborg, Sweden

AMONG THE various kinds of prime movers known today, the turbine is the one best suited for automotive propulsion. Its torque-speed relation combines good efficiency at high speeds with the possibility of obtaining high torques at low speeds and start. With suitable design of the blading it is possible to obtain ratios between stalling and full-speed torques of 5/1 and above, and yet keep the overall efficiency at very good values in the upper speed range.

Among the existing methods of transforming the energy of fuel oil into mechanical work, there exists none more efficient than combusting the fuel within an engine cylinder where pressures of some 1000 psi and temperatures of several 1000 F may be allowed without harming the combustion chamber walls.

For automotive work it has been a natural solution of the propulsion problem to combine these desirable features into one engine. Thus, the special variety of compound piston-and-turbine engines called gas generator has been developed. Prof. London (1)* has made a good classification of the compound piston-and-turbine engines. Fig. 1 is a diagram of the subfamily of piston-type gas-generator engines, similar to his classification.

In the diagram Prof. London's denominations "free-piston" and "crank-piston" engines are used for the gas-generator part of the compound engines. In the free-piston engines the movement of the pistons is not restricted by mechanical means; in the crank-piston types the pistons are connected by rods to one or several crankshafts, fixing their stroke and end positions. Prof. London advocates the free-piston line and much has been published about the development work done in this field by Sigma, General Motors, Ford, and others. Less has been told about the crank-piston gas-generator development. Such development, however, has been performed. For many years Aktiebolaget Gotaverken has been experimenting with gas generators of this type and several installations have been made. Around 1950 the Orion designers started work on the crank-piston line. As may be seen from Fig. 1, the Gotaverken gas generators use piston-type compressors as do the free-piston engines, whereas the Orion engine uses two centrifugal compressors.

Review of Development

Aktiebolaget Gotaverken was founded in 1841 as an engineering works. Later, shipbuilding became the main interest. However, engineering activity has always been maintained and the company produces diesel engines, turbines,

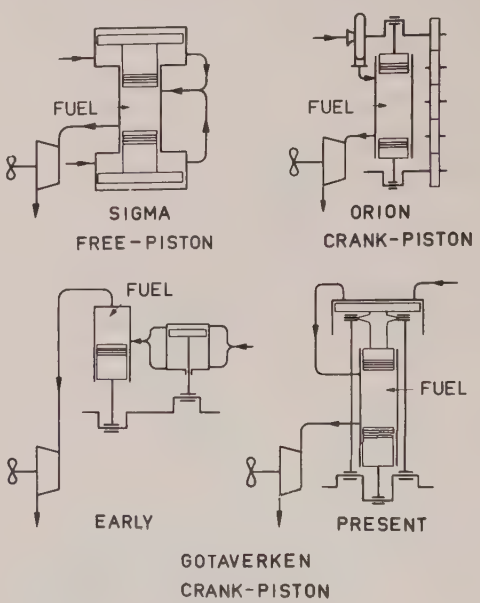

Fig. 1 — Gas-generator engines

*Numbers in parentheses designate References at end of paper.

and boilers.

The company was studying gas-generator designs as early as 1923. The basic principles and early patents were developed by Erik Johansson (2), who supervised the gas-generator work at Gotaverken until 1959. His calculations for a locomotive engine were first tested in an experimental unit built in 1926 and in three ship installations of 300, 1000, and 6500 shp, which were completed between 1931 and 1940. Two of these engines had been in service about 25 years when they were replaced.

In 1933 the powerplant of a 300-hp diesel-hydraulic locomotive was replaced by a gas generator with a 500-hp gas turbine. This locomotive was tested during 1934-1937 in regular service on several railways. However, the output was too small for the service in question, and the reversing was too slow. In railroad circles the interest was very high and it was suggested that a larger locomotive with faster reversing would be the answer. However, for several reasons further experiments were postponed. The locomotive was scrapped and its gas generator installed in a tug where it remained for 12 years doing daily work in the harbor.

These gas generators (altogether nine units) were all 2-stroke diesels with scavenge air ports in the cylinder wall and one outlet valve in the cylinder cover. They embodied from one to six working cylinders per engine and were built integral with double-acting reciprocating air compressors having one to three cylinders. The experimental unit, the 300- and 1000-hp units, and the 500-hp unit (when used on the tug) were combined with reciprocating-type propelling engines built similar to steam engines and fed with gas delivered by the gas generators. In the 6500-hp installation, as well as in the 500-hp unit when installed on the locomotive, the gas was fed to turbines, which were connected by means of reduction gears to the propeller shaft and locomotive wheels, respectively.

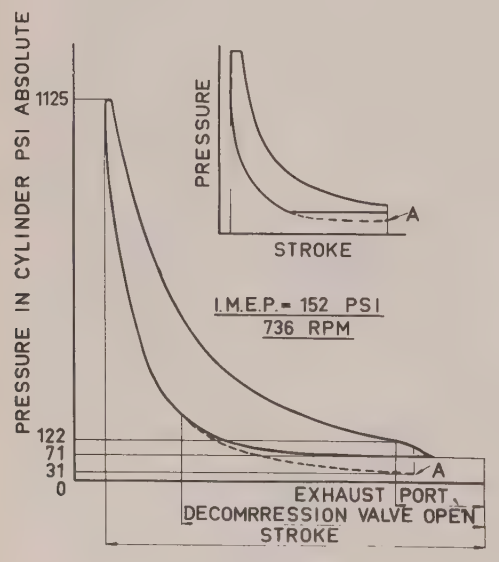

Fig. 2 — Locomotive T1 indicator card

Shortly after World War II the Swedish State Railways were on the lookout for a diesel locomotive to replace the existing steam engines on lines where the volume of traffic did not warrant electrification. Their requirements asked for a locomotive with 1000 hp at the wheel rims, a maximum tractive effort in the neighborhood of 30,000 lb, and a maximum speed of 56 mph. Existing locomotives, however, were found to be far too heavy for the tracks of such secondary lines. Gotaverken designed a new gas-generator engine for a locomotive developed by AB Motala Verkstad. The result was a locomotive which fulfilled the above requirements, had a sufficiently low axle load, and could guarantee a fuel consumption at full load of 0.44 lb/shp/hr calculated at the wheel rims. In 1950 the State Railways placed an order for a first experimental locomotive; in February, 1955, shop tests and preliminary tests in the locomotive were concluded, and the locomotive put into regular service in southern Sweden.

In this prototype locomotive, officially designated T1, the gas generator is a 2-stroke opposed-piston engine with reciprocating compressors. The power engine is a gas turbine fed from the gas generator.

Basic Features

Thermodynamic studies of the free-piston gas generator in combination with a power turbine have been made frequently in the past 10 years. As there is no fundamental difference in their application to the crank-piston gas-generator engine, they will not be repeated here.

There are, however, some features of the Gotaverken gas generator, which are of special interest and deserve a closer study.

The compressor pistons of the Gotaverken gas generator are crank-bound, which means that the dead centers of the pistons are fixed. This makes it possible to make the clearance between the compressor piston and the compressor cover very small - in T1 only 5/64 in. - which ensures a small clearance volume and a high volumetric efficiency of the compressor.

For safety reasons, the clearance between piston and cover in the free-piston gas generator cannot be kept at such small values. This means that much lower volumetric efficiencies must be contended with. With increased load the free pistons are working closer to their outer positions. The clearance volume of the compressors then is the largest and the compressor efficiency the smallest at the moment when the requirements for combustion air and compressor efficiency are maximum.

On the other hand, the binding of the working pistons to a crankshaft would give a constant compression ratio in the working cylinder. This ratio can not be reduced below the point where safe cold starting is no longer guaranteed. With increasing load and scavenge air pressure, both compression

and combustion pressures rise to values not tolerable in a diesel cylinder. In order to avoid this, the Gotaverken gas generators are equipped with a compression regulator, which changes the compression ratio according to the load and achieves a substantially constant combustion pressure over the main part of the load range.

Fig. 2 illustrates the effect of the compression regulator. The diagram shows an indicator card taken in the working cylinder of the present locomotive at full load, as well as a schematic version of the same cycle. The cycle is generally also representative of earlier gas generators. When the piston moves towards its inner position, a connection is kept open between the combustion chamber and the exhaust pipe during an interval. The length of this interval is adjusted according to the scavenge pressure in such a way that the compression and combustion pressures follow the desired relationship to load and speed. The means of keeping this connection open and the governing mechanism will be described later.

If the compression line in Fig. 2 is extended down to point A, the pressure in this point defines the degree of supercharge of the gas generator. In this case the pressure at point A is 31.4 psi absolute. F guring a scavenge air pressure of 17.8 psi absolute for a naturally aspirated engine, the supercharge degree amounts to 75%.

In this connection it may be appropriate to point out that in compound piston-and-turbine engines the pressure in the charge-air pipe does not define the supercharge degree of the diesel engine. It would do so if the compression ratio were kept within a narrow margin around the ratio common for naturally aspirated engines. But in order to keep the combustion pressures within reasonable limits, it is usually necessary to work with considerably reduced compression ratios, and many systems are working with variable compression ratios. Under such circumstances it is necessary to bear in mind, when discussing compound engines of the types in question, that the charge air pressure tells nothing about the actual supercharge degree, compression pressure, or the thermal load of the engine components.

At light load and idling any gas generator still must deliver a certain amount of gas in order to keep running. If this minimum amount of gas exceeds the momentary requirements of the power turbine, the excess gas must be blown off or its energy destroyed in some other way. Naturally, the speed of rotation or oscillation should be kept as low as possible in order to reduce the loss in gas and power. Because a crank-piston engine can run at a much lower speed without stalling than a corresponding free-piston engine, the fuel consumption at idling and low-load conditions is much more favorable with the crank-bound type. Without any special arrangements for its improvement, the idling fuel consumption of the T1 locomotive is only 8% of the full-load consumption. The gas pressure then is only about 3.6 psi gage.

Crank-Piston Gas-Generator Locomotive "Gota"

As already mentioned this 500-hp locomotive originally was equipped with a 300-hp diesel engine with hydraulic drive to the wheels. In 1933 it was rebuilt and equipped with a Gotaverken gas generator with a gas turbine and a reverse-reduction gear of Ljungstrom design and Nohab manufacture (3).

The locomotive was originally of type 2-4-2 but was later rebuilt to 2-6-2 arrangement. It weighed 62 tons fully equipped. Maximum speed was 44 mph. The starting tractive effort was about 13,000 lb. The locomotive had driver's cabins in both ends and as it made use of the full loading gage, a passage could be arranged between the two cabins along the machinery.

The gas generator consisted of a 4-cyl 2-stroke diesel engine directly coupled to a 2-cyl double-acting air compressor delivering its air at 61 psi gage into the scavenge air pipe of the diesel. As described above, the scavenge air was admitted to the cylinders through scavenge ports in their lower part, the exhaust gases leaving the cylinders through an exhaust valve in the cylinder cover. This exhaust valve was operated by a Klug valve gear. This valve gear opened the exhaust valve at a fixed position of the crankshaft regardless of speed and load, whereas timing of the closing point was varied with the gas pressure in the exhaust pipe. When idling and at low loads up to 7 psi gage gas pressure, the compression period was 85% of the stroke. With increasing gas pressure, the exhaust valve closed later and later until above 40 psi the compression period remained constant at 40% of the piston stroke. In this way the variable compression ratio discussed before was obtained and safe conditions for starting and low loads guaranteed, as well as acceptable values of compression and combustion pressures over the upper speed and load range of the gas generator.

Four working cylinders were coupled to two double-acting compressor cylinders. At a speed of 350 rpm, the gas generator delivered its maximum of gas to the turbine at 57 psi gage; but when idling with the shutoff valve to the turbine closed and the blow-off valve open, the gas pressure was 7 psi gage and the idling speed 100 rpm.

The gas turbine and the reverse-reduction gear were of the Ljungstrom patented design for steam turbine locomotives. The turbine was of full admission type with one impulse stage and fourteen stages of reaction type. The design resulted in a ratio of 3.8/1 between tractive efforts at start and maximum speed.

The reversing mechanism of the double-reduction gear included an eccentric-mounted secondary pinion, which could be alternatively meshed with either one of two gear wheels, giving different direction of rotation to the jackshaft. The eccentric bearings of the pinion were rotated by means of a nut-and-screw mechanism. The time required for reversing was very long; but it was thought that as switching service was not foreseen, the required reverse maneuvers

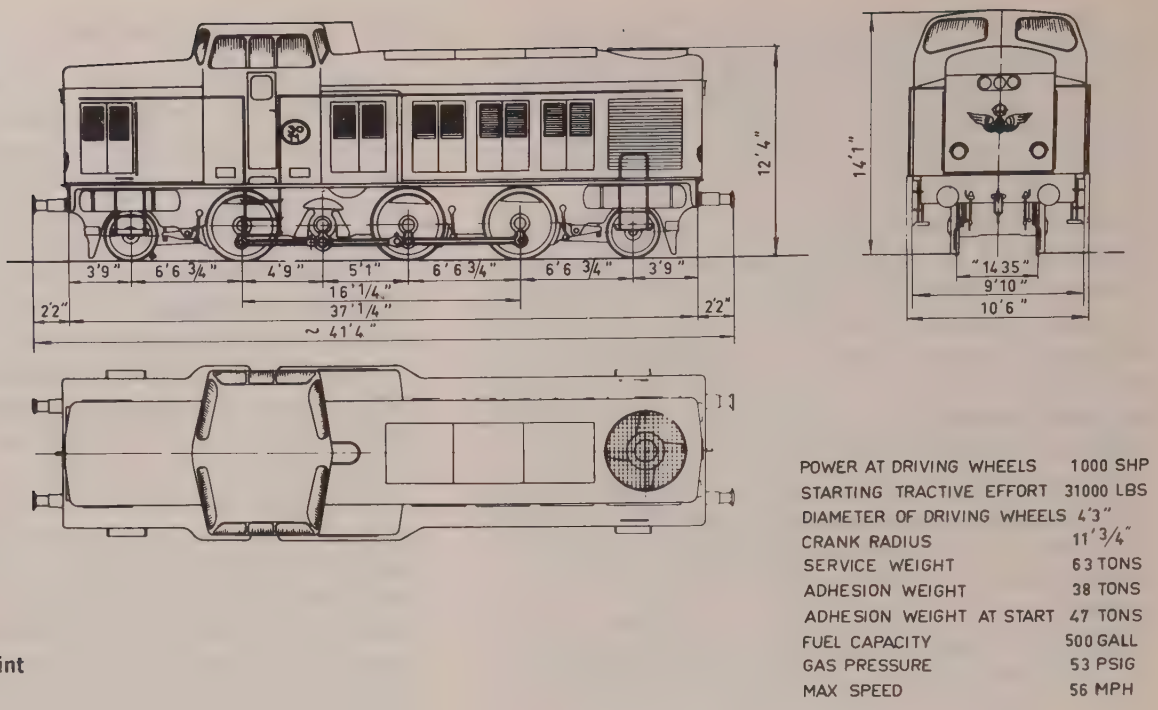

POWER AT DRIVING WHEELS	1000 SHP
STARTING TRACTIVE EFFORT	31000 LBS
DIAMETER OF DRIVING WHEELS	4'3"
CRANK RADIUS	11'3/4"
SERVICE WEIGHT	63 TONS
ADHESION WEIGHT	38 TONS
ADHESION WEIGHT AT START	47 TONS
FUEL CAPACITY	500 GALL
GAS PRESSURE	53 PSIG
MAX SPEED	56 MPH

Fig. 3 — Dimension print of locomotive T1

would not be frequent.

The auxiliary equipment was similar to that of the present T1 locomotive and will not be described in detail. At that time the Swedish passenger trains were heated by steam, and instead of the alternator of the T1 a steam boiler for 70 psi gage was installed for train heating. The boiler could be heated alternatively or simultaneously by exhaust or an oil burner.

The experiences gained from the locomotive, as well as its further history have already been related. Some of the tests were made on the then private Halmstad-Nassjo-Railroad, where later the present locomotive T1 was put into operation.

Swedish State Railways Locomotive No. T1

The gas generator used in the prototype locomotive delivered to the Swedish State Railways in 1955 is of crank-piston type with five vertical working cylinders and five compressor cylinders placed above the former. It delivers gas at 53 psi gage and 930 F through a shutoff valve to the turbine, which is bolted to the reverse-reduction gear. The latter transmits the power to a jackshaft, which is coupled by means of rods to the three driving shafts. The energy content of the gas before the turbine is 1300 gas hp. The turbine converts this to mechanical energy at 12,500 rpm and the output delivered to the locomotive wheels exceeds 1000 shp at speeds between 25 and 44 mph. The locomotive is designed for a maximum speed of 56 mph.

The locomotive is of type 2-6-2, built with a rigid frame. Fig. 3 shows a dimension print of the locomotive. The locomotive is equipped with two-wheel trucks at both ends. The jackshaft is situated between No. 2 and No. 3 axles. The locomotive is built for passenger and freight service on 1435-mm track. The six driving wheels have a diameter of 51 in. The fixed wheelbase is 16 ft, 5 in., and the total length over the buffers approximately 42 ft. The total weight of the locomotive is 63 tons. The adhesion weight is 38 tons, giving an axle load of 12.7 tons; but this may be increased during starting or periods of very low speed to 47 tons by pneumatically rebalancing the wheel spring system.

In accordance with Sedish diesel locomotive practice, the locomotive has a central driver's cabin raised above the machinery hoods. The latter are made 40 in. narrower than the cabin, which in combination with the elevated position of the cabin gives an excellent field of view in both directions.

The gas-generator engine is placed under the larger hood and in the end section of the latter, the radiators are situated together with the cooling fan and gear. The main part of the electric equipment is under the short hood. Fig. 4 shows the arrangement.

Between the gas generator and the driver's cabin and partly under the latter, the reduction gear is supported by roller bearings on the jackshaft and stayed in the locomotive frame by a reaction member. The gas turbine is flange-mounted on one side of the gearcase, and between the gas generator and the turbine a combined shutoff and blow-off valve is inserted. Above the turbine an exhaust silencer is placed connected to the blow-off pipe.

The gas generator has power take-offs at both ends. At the radiator end a short cardan shaft transmits power to two belt-driven compressors for starting and braking air, respec-

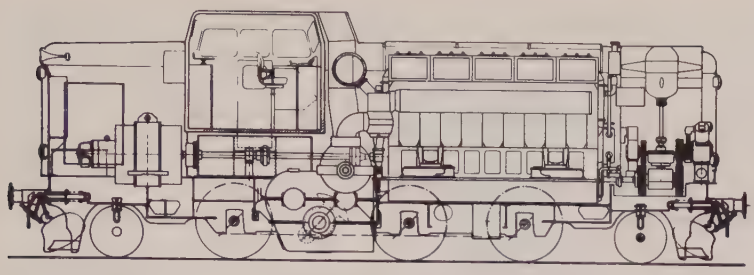

Fig. 4 — Longitudinal section through locomotive T1

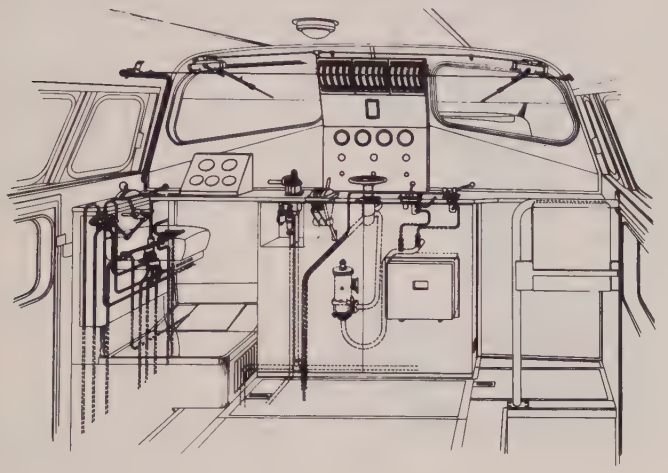

Fig. 5 — Driver's cabin in locomotive T1

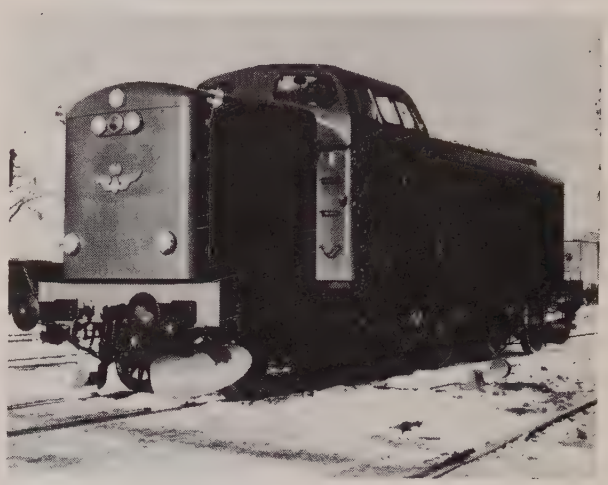

Fig. 6 — Gotaverken gas-generator locomotive T1

tively, and over a bevel gear and a hydraulic coupling to the radiator fan in the roof of the hood. The fan takes the air through the two radiators in the sides of the hood and exhausts it upwards. The speed of the cooling fan is automatically adjusted according to the cooling water temperature by means of a thermostat governing the slip of the hydraulic coupling. Water-cooled lubricating oil coolers are used for the gas generator, as well as the reduction gear. A small d-c generator for charging the battery is also driven from this end.

At the other end of the gas generator a longer cardan shaft passes above the reduction gear and turbine and below the cabin to an alternator capable of delivering 150-kva alternating current of low frequency to the electric heating system of the train. The Swedish railroads are electrified to a large extent and the current used is alternating single-phase current of 1000 v and 16 2/3 cps. All standard gage coaches have heating equipment suited for this current and it was necessary to provide a sufficient supply of electric power for this purpose. On the prototype locomotive, the alternator is connected to the gas generator as described above. The speed thus follows the speed variations of the gas generator at varying loads. The latter is allowed to run between 360 and 720 rpm when the alternator is used, and the alternator speed then changes between 500 and 1000 rpm, giving a frequency variation between 16 2/3 and 33 1/2 cps. A carbon-pile voltage regulator of special design keeps the voltage constant at 1000 v regardless of the speed. Later locomotives with diesel or gas-generator machinery will have a separately driven alternator with constant speed and frequency.

The alternator is situated under a short hood together with the necessary switchboard and a battery of 150 amp-hr and 24 v. Two communicating fuel tanks of 500 gal combined capacity are placed under the driver's cabin.

Fig. 5 gives a view inside the driver's cabin seen at the driver's eye level. The long hood may be seen through the windshield and on both sides an excellent view of the ground may be had over the low hood. In the other direction the visibility is even better over the short hood. Two identical driver's stands are arranged diagonally, each equipped with a combined lever for the operation of the pneumatic control system for the gas-generator output and for the braking of the single locomotive, a train braking control, the most important instruments for supervision of locomotive and gas-generator speeds, air and oil pressures. Push buttons are used for sanding and increasing the adhesion weight.

The instrumentation visible between the windshields was special for this prototype locomotive and has already been reduced to normal standards. Below the instrument board the starting gear for the gas generator may be seen and a valve for filling the brake air system from the starting air tank, a feature of great value for speeding up the filling of the

brake system immediately after starting up and when connecting to a long train.

A switchboard for the alternator is placed on the opposite wall. The cabin is provided with aerotempers, a toilet cabinet with basin, discharge pipe and water container, and a hot plate.

Fig. 6 is a photograph of the locomotive. Table 1 lists specification of the Gota and T1 locomotives.

Gas Generator - The diesel part of the gas generator consists of a 5-cyl 2-stroke opposed-piston engine with only one crankshaft equipped with three cranks between each pair of journal bearings. The middle crank is displaced 180 deg in relation to the side cranks. The lower piston is connected by a short rod to the middle bearing, the upper piston by two long rods to the side cranks. Junkers once built a truck engine of similar design. The single-acting compressor pistons are connected by intermediate yokes to the upper working pistons. The bearings in the upper ends of the side rods are seated on pivots extending from the yoke. Fig. 7 shows schematically the design of the gas generator, turbine, and reduction gear.

The working cylinders are equipped with scavenge air ports in the lower part and exhaust ports in the upper part. The flow through the ports is controlled by the respective pistons. A perspective sketch of the complete piston and rod assembly is shown in Fig. 8. The upper piston assembly is made as light as possible. The working piston is cast in aluminum alloy with a heat resisting steel top supporting the first piston ring. The compressor piston and the yoke are of forged steel. A photograph of the upper piston assembly is shown in Fig. 9.

The lower piston is made of cast iron with a heat-resisting steel top, oil-cooled, and very heavy in order to counterbalance the weights of the upper piston assembly.

In this way, using the inherent properties of the opposed-piston system; it has been possible to attain a complete balancing of the oscillating forces of the first order for each individual cylinder, and thus for the whole engine. Consequently, for each separate cylinder number there is complete freedom to choose a firing order, which gives the least possible external couples of the second order. The increased weight of the lower piston also decreases the bearing load on the crank bearing by 25%

The crankshaft is designed to fulfill the requirements of Lloyd's Register of Shipping for main engines in ships. The revolving masses are completely balanced within each cyl-

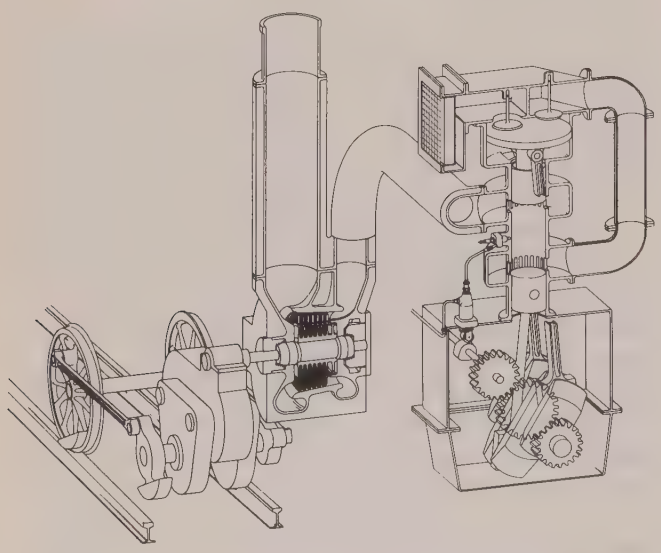

Fig. 7 — Simplified diagram of gas-generator engine

Table 1 - Specifications of Gota and T1 Locomotives

Locomotive	"Gota"	"T1"
Gas generator		
Working cylinders		
Type	Single acting	Opposed piston
Number of cylinders	4	5
Diameter of cylinders, in.	10 7/8 (275 mm)	7 7/8 (200 mm)
Stroke of upper piston, in.	-	7 7/8 (200 mm)
Stroke of lower piston, in.	15 3/4 (400 mm)	11 13/16 (300 mm)
Compressor cylinders		
Type	Double acting	Single acting
Number of cylinders	1	5
Diameter of cylinders, in.	22 (560 mm)	25 3/16 (640 mm)
Stroke of piston, in.	14 3/16 (360 mm)	7 7/8 (200 mm)
Speed, rpm	350	720
Gas horsepower	-	1300
Scavenge air pressure, psi gage	61	57
Gas pressure	57	53
Gas temperature, F	840	930
Turbine		
Number of impulse stages	1	1
Number of reaction stages	14	6
Speed, rpm	8000	12,500
Output at driving wheels, shp	500	1000
Starting tractive effort, lb	13,000	31,000
Maximum speed, mph	44	56
Adhesion weight, ton	38	38 (47)
Total weight, ton	62	63

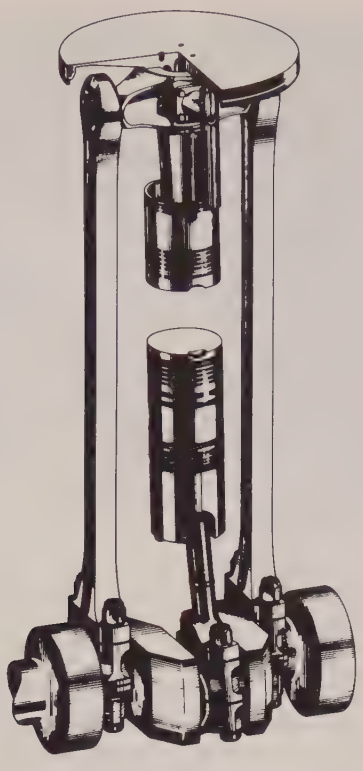

Fig. 8 — Piston and crank rod assembly

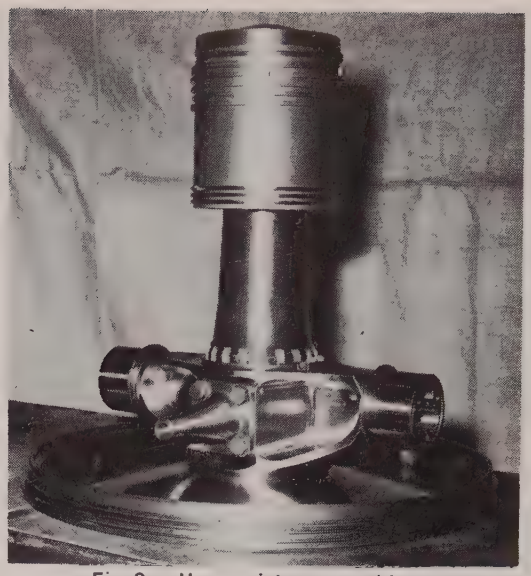

Fig. 9 — Upper piston assembly

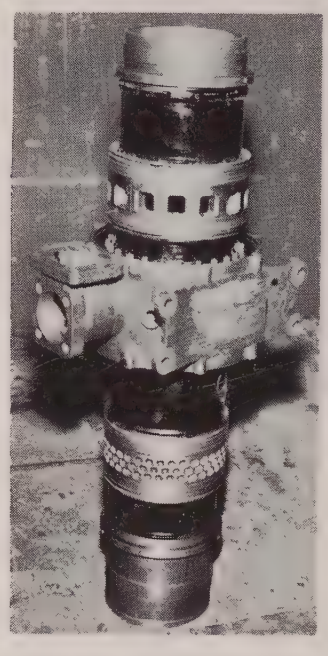

Fig. 10 — Working cylinder without jackets

inder and thus for the complete engine. The journal bearings are made with such a large diameter that they act as webs for the two adjoining cranks, which gives a considerable reduction in cylinder center distance. These unusual bearings, with a length to diameter ratio of only 0.28 and a periphery speed of 2500 fpm, have operated to complete satisfaction without any modifications.

The working cylinders are made as complete assemblies (Fig. 10). The center section forming the combustion chamber is equipped with seatings for the different valves and positioning lugs for bolting to the engine frame. It was originally cast in steel as shown in the photograph but has later been replaced by a forging with a welded-on cooling water jacket. The cylinder liners are made of centrifugally cast iron, have rectangular scavenge and exhaust ports, and are bolted with ground flanges against the combustion chamber. Welded jackets with spaces for cooling water, scavenging air, and exhaust surround the liners. In the picture the jackets are removed. The lower liner shown has scavenge ports of an early design.

Two complete views of the gas generator are shown in Figs. 11 and 12. The former shows the scavenge air side of the engine. The frame of welded steel plate consists of one lower, horizontally split case, housing the crankshaft; and one upper likewise horizontal case enclosing the compressor cylinders. The two cases are permanently joined together by vertical cases above each journal bearing. These cases enclose the long side connecting rods. The working cylinder units are positioned in the spaces between the vertical cases and bolted with their center parts to them. The cylinder liners project into the upper and lower horizontal cases and are sealed against the latter by means of spring-loaded oil seals. They are free to expand vertically with changes in temperature.

The air compressors deliver the scavenge air at maximum pressure of 57 psi gage into the upper scavenge air pipe. This is connected at both ends with the lower pipe from which the air is conducted through the scavenge ports into the cylinder. The vertical portions of the scavenge air pipe incorporate scavenge aircoolers. Their purpose is to keep the scavenge air temperature below the critical value of approximately 420 F, above which the lubricating oil (necessarily accompanying the scavenge air) might get ignited by sparks thrown out through the scavenge ports. This temperature, however,

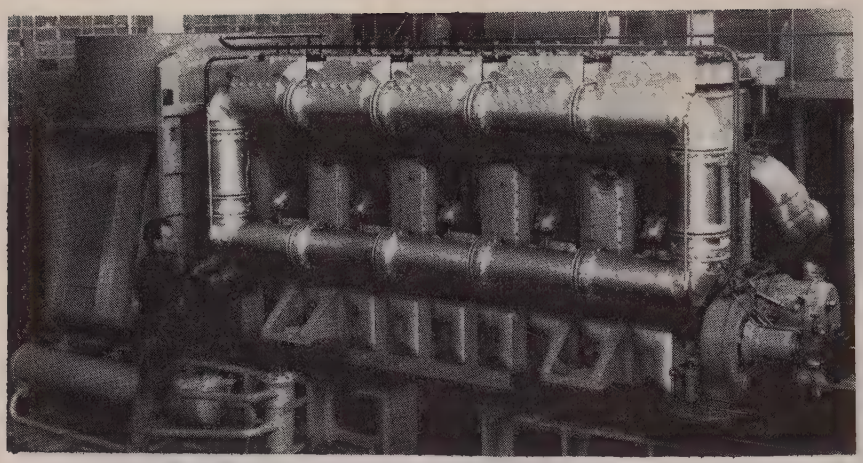

Fig. 11 — Gas generator, scavenge side

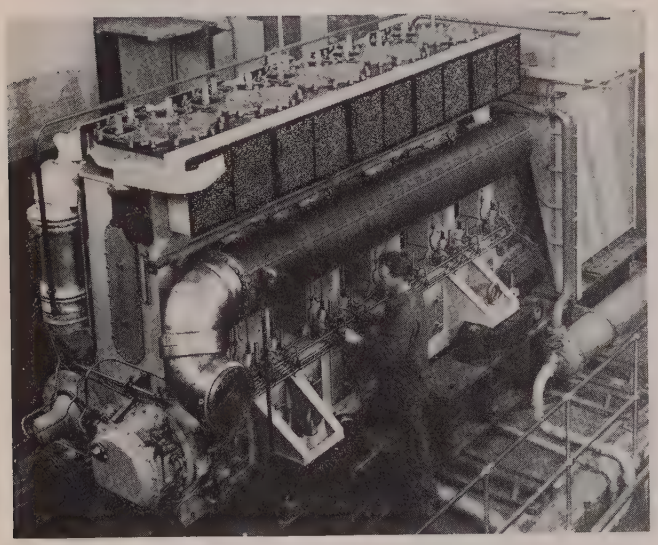

Fig. 12 — Gas generator, exhaust side

is reached only during very hot summer days, so the coolers are seldom used.

To the right in Fig. 11 the compression regulator and behind it the hydraulic governor may be seen. Above the latter the flexible gas delivery pipe is visible. In the picture the gas generator rests on rubber mountings, but during testing the engine was found to be sufficiently vibration free that the rubber suspension could be discarded and the engine solidly bolted to the engine frame. Subsequent experience with the locomotive has justified this simplification. To the left the casing for the cooling fan is erected in its proper position and to the far right part of the cardan shaft to the train heating generator is seen. The complete shafting system was tested in the shop in order to verify the calculations of the torsional vibrations in the system.

Fig. 12 shows the opposite side of the gas generator with the compressor covers with their intake and discharge valves and the intake air filters. The gas delivery pipe is situated below the filters, which are in direct connection with openings in the hood. These air passages are protected from the heat of the gas pipe by insulated panels.

The gear end of the gas generator is shown in Fig. 13. The bottom wheel is bolted to the crankshaft and drives the two camshafts at engine speed via the intermediate wheel, which is coupled to the alternator shaft. The right-hand camshaft operates the fuel pumps, two per cylinder. The left-hand shaft operates the compression regulating valves. These valves, a closer view of which may be had in Fig. 14, are situated in the cylinder center part and when open allow part of the cylinder contents to escape into the exhaust header during the beginning of the compression stroke. The valves are actuated via push-rods from the left-hand camshaft. During idling conditions, the valves are open simultaneously with the scavenge ports. However, with increasing scavenge air pressure the compression regulator turns the camshaft relative the camshaft, thus delaying the closing stroke of the valves and the beginning of the compression. The resulting influence on the compression and combustion pressures has already been described.

The governor (Fig. 15) is of the hydraulic type and incorporates speed sensitive idling and maximum speed governors, as well as an output regulator affected by the pressure in the pneumatic control system. The idling governor can be set from the driver's cabin alternatively at 200 or 360 rpm, the latter speed being used when the train heating generator is in use.

Shutoff and Blow-Off Valve - The shutoff valve is hydraulically operated and closes the inlet to the turbine when the pneumatic control system is blown off. At the same time the blow-off valve is opened and releases the gas flow into the silencer. At the turbine outlet the flow is so smooth that the exhaust can be released directly to the atmosphere without undue noise.

Turbine - Fig. 16 shows a longitudinal cut through the turbine. It has seven stages, the first one of impulse type and the remaining six of reaction type. The maximum speed is 12,500 rpm and at maximum gas pressure it delivers approximately 1100 shp to the reduction gear. It is supported in white metal bearings and has a block-type thrust bearing

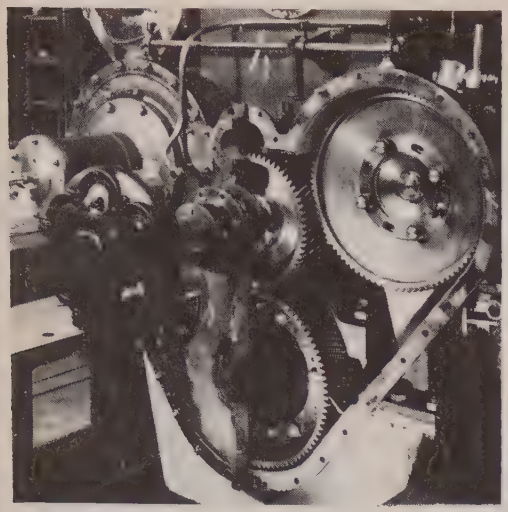

Fig. 13 — Gear train on gas generator

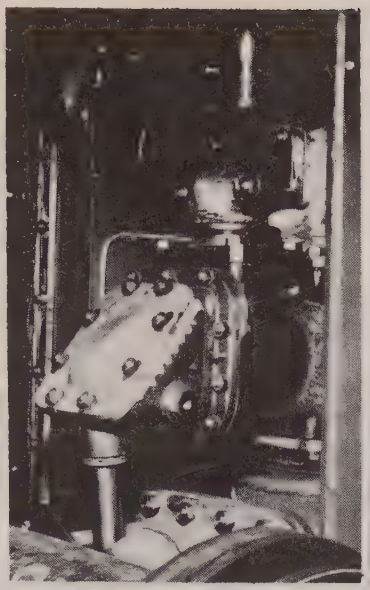

Fig. 14 — Compression regulating valve

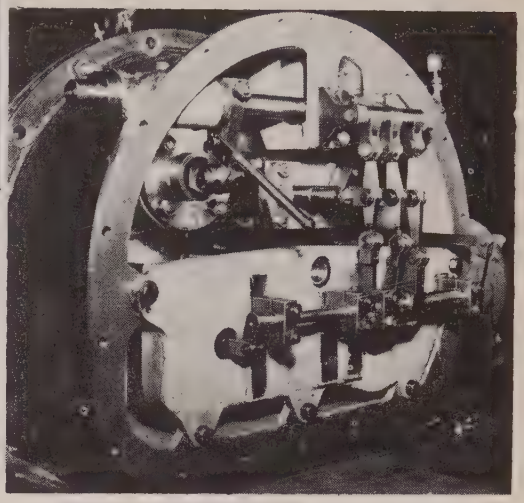

Fig. 15 — Hydraulic governor

at the outer end. An overspeed governor closes the gas shutoff valve when the maximum speed is exceeded by 15%. As the maximum gas temperature is in the neighborhood of 900 F, the blading can be made of standard heat-resisting steel without resorting to expensive creep-resisting varieties.

Reverse-Reduction Gear - A photograph of the complete gear box is shown in Fig. 17 and a partly cut-away drawing in Fig. 18. The turbine is bolted to the U-shaped flange surrounding the input shaft. Its weight is partly taken up by spring supports against the locomotive frame in order to lessen the load on the mounting flange. The turbine is connected to the pinion by means of a torsion shaft passing through the hollow pinion. The latter is of double helical type and rotates in white metal bearings specially designed to take the heavy loads from the starting torque with no oil film in the bearings, and also to suit the quite different requirements at the maximum speed of 12,500 rpm.

The pinion meshes one of two equally large intermediate gear wheels supported by white metal bearings on the two intermediate shafts. Inside the wheel are two hydraulically operated friction clutches, which connect the respective wheel and shaft when engaged. In each end of the intermediate shafts gear teeth are cut, which mesh two corresponding gear wheels on the jackshaft. The rims of the latter are elastically mounted on the hubs. By engaging one or the other of the two clutches the primary pinion is connected to the jackshaft over two or three meshes, giving forward or reverse rotation of the jackshaft. A lubricating oil pump driven by the gear operates in parallel with a similar pump on the gas generator and safeguards the oil supply when the locomotive is towed with the gas generator shut off.

The jackshaft is supported on spherical roller bearings in the locomotive frame and the gearcase rests upon the jackshaft via another set of similar bearings. As mentioned earlier a reaction member takes the reaction torque from the jackshaft. The intermediate shafts are also supported in roller bearings.

Fig. 19 is a cut-away perspective drawing of the locomotive showing the different components in their actual places.

Control System - Fig. 20 is a schematic drawing of the control system. The heavy solid lines indicate pressure oil and the dotted lines compressed air. A common pressure oil system is used for lubrication of the turbine and the gear, as well as for the control functions. As already mentioned two pumps operate in parallel, driven by the gas generator and the gear, respectively. The oil pressure is kept at 100 psi. The oil is fed to a servo valve operated by the pressure in the pneumatic control system. When this pressure reaches about 15 psi, the valve admits oil to the servo piston of the gas shutoff valve and opens the valve. At the same time the blowoff valve is closed.

Another branch conducts oil through an orifice plate to the bearings of the turbine and the primary pinion. A third branch conducts oil to the reversing slide valve, which is operated by air from the reversing valves in the cabin, and admits the oil to the proper friction clutch which then engages. Simultaneously, the other clutch is disengaged by releasing its oil content into the gear case. Part of the oil

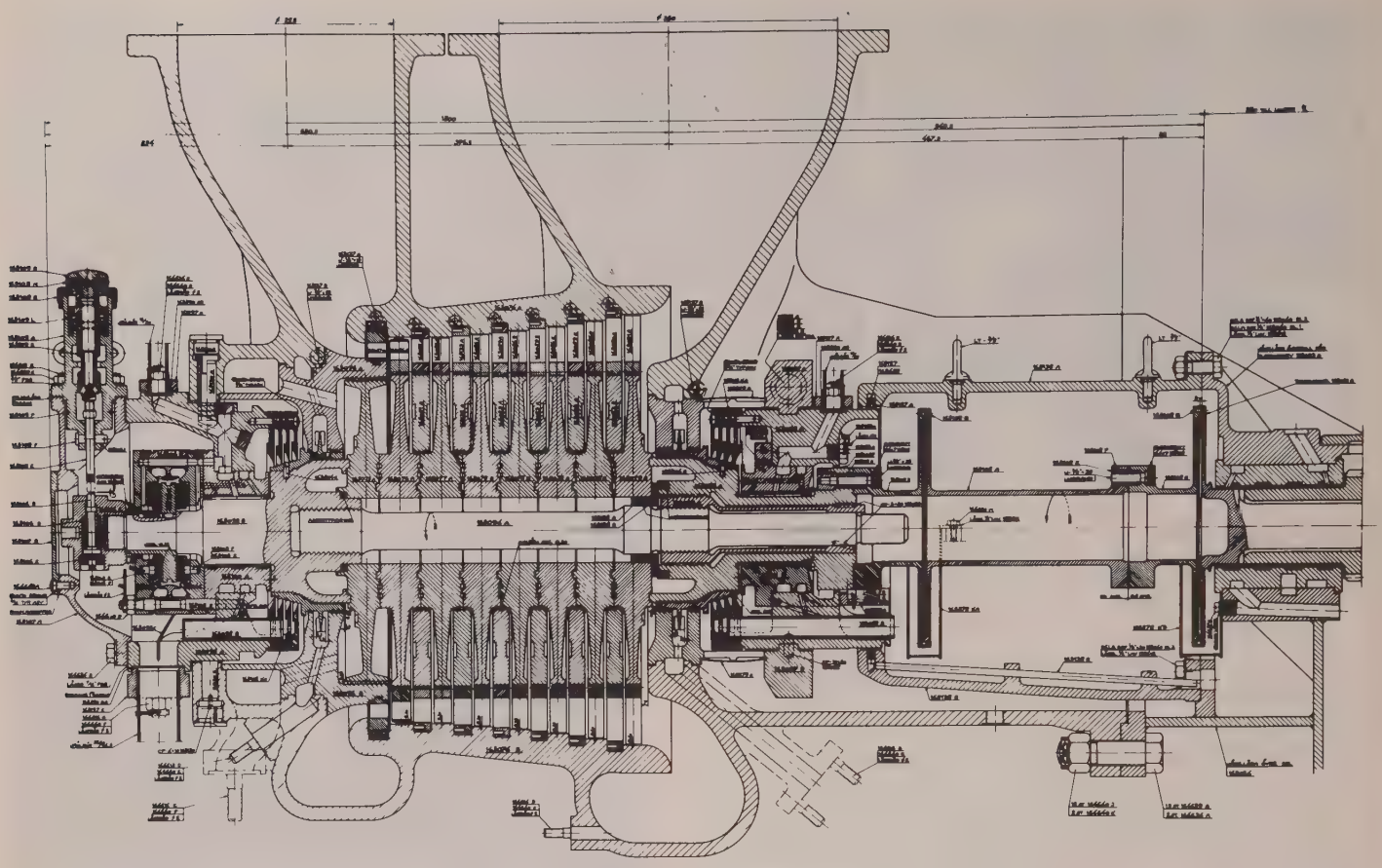

Fig. 16 — Gas turbine of locomotive T1

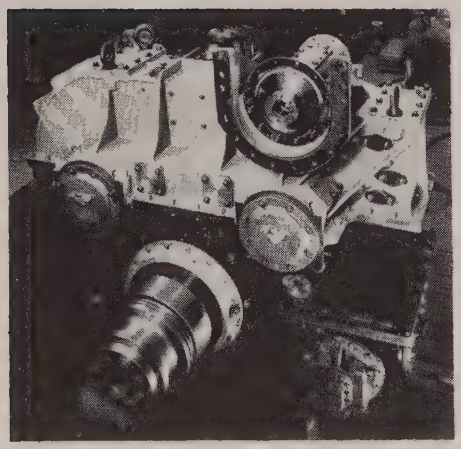

Fig. 17 — Reverse reduction gear

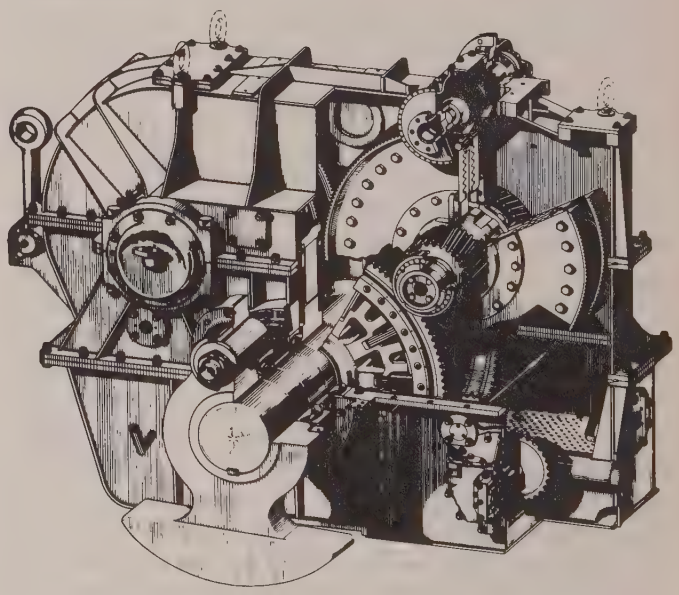

Fig. 18 — Cut through reverse-reduction gear

is transmitted at about 20 psi to the spray nozzles of the reduction gear.

From the oil pump on the gas generator, a part of the oil is conducted through a separate filter to the slide valve system in the governor of the gas generator. The slide valve are actuated by an idling flyball governor, an output regulator, and a maximum-speed governor, and determine the position of the servo piston connected to the racks of the fuel pumps.

The pressure air is taken from the brake air system, a reduction valve keeping the pressure at 56 psi before the con-

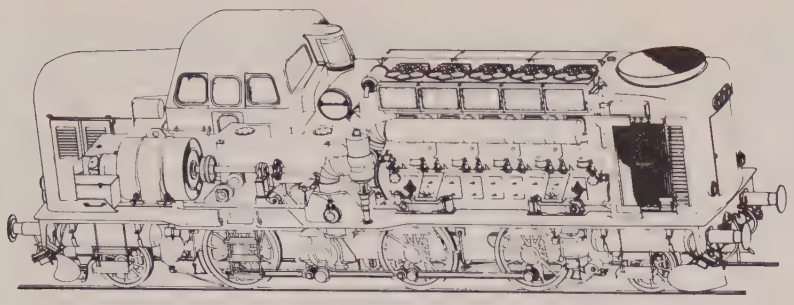

Fig. 19 — Machinery arrangement in T1

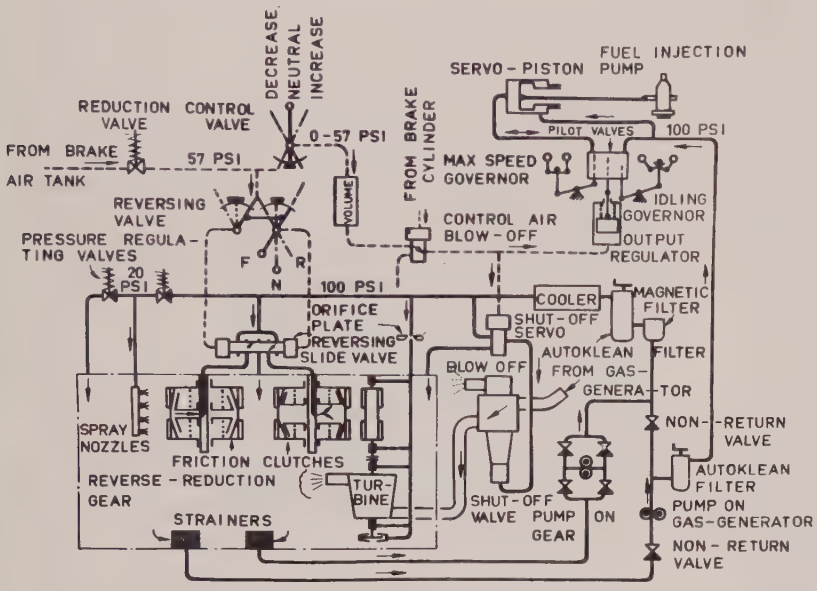

Fig. 20 — Control air and lubricating system

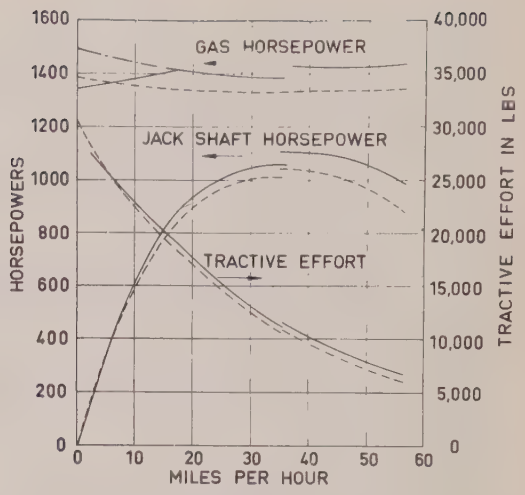

Fig. 21 — Locomotive T1, output and tractive effort

trol valves. As has already been mentioned, the reversing slide valve is operated by the reversing valve in the cabin. The variable pressure in the pneumatic control system (the magnitude of which via the output regulator governs the fuel rack position of the gas generator under load) is changed by feeding air into or releasing it out of the system by means of the control valve in the cabin. As already stated, the gas shutoff valve before the turbine is automatically opened when the control air pressure reaches 15 psi. Further pressure rise actuates the output regulator and increases the fuel rack setting, thereby increasing the speed and output of the gas generator and the torque of the turbine.

To each pressure level in the pneumatic control system, a certain fuel rack setting corresponds. At maximum gas pressure the pressure drop in the action stage of the turbine is nearly critical; consequently, the gas flow through the turbine is approximately constant and independent of the speed of the turbine. Thus, the gas generator speed is almost independent of the turbine speed; this is actually valid also for part load. The consequence is that a certain fuel rack setting corresponds approximately to a certain gas output, a certain gas pressure and a certain gas-generator speed, independent of the locomotive speed.

When braking the locomotive, a certain level of the brake cylinder pressure operates a servo valve, which blows off the pneumatic control system, thereby bringing the gas generator to idling conditions and closing the shutoff valve to the turbine.

Experiences During Tests and Operation

The complete engine was tested in the shop and several changes made before final testing and delivery. The gas generator was first run alone against a calibrated nozzle until its function was judged satisfactory. When running the gas generator together with the turbine and reduction gear certain difficulties arose. The available water brake coupled to the jackshaft could manage speeds only above 250 rpm, corresponding to about 38 mph. Below that value the torque of the jackshaft exceeded the capacity of the brake. The lower speed range had to be tested with the water brake coupled to one of the intermediate shafts. The starting tor-

que was measured with the rotor of the brake locked to its housing.

Fig. 21 shows a diagram over the output and tractive effort measured during the final delivery tests in the shop. Solid lines refer to intercooled charging air, dotted lines to the uncooled state. The curves all represent a gas temperature of 932 F. As expected under these conditions, the gas horsepower is higher when the scavenge air is cooled. The halves of the curves for cooled scavenge air do not meet, owing to an improvement made in the aircoolers between the two runs. The downward slope in the left part of the curve depends on the fact that themaximum-speed governor has come into action and restricted the speed to 750 rpm by reducing the fuel injection rate.

Nor do the curves for brake output meet at 38 mph. Improvements in the mechanical efficiency of the reduction gear were made simultaneously with the transfer of the brake. The left half of those curves are barely influenced by the changes at low speeds, but around 30 mph the curves should be raised to meet the right-hand halves.

As may be seen from the curves, the overall efficiency of the engine is maximum at 38 mph. At this speed the measured brake output was 1110 and 1040 shp with cooled and uncooled scavenge air, respectively.

The starting tractive effort calculated out of the measured starting torque was 31,000 lb with uncooled air and the ratio between this torque and the corresponding value at maximum speed was about 5/1. The measured fuel consumption at 38 mph and a brake output from the jackshaft of 1000 shp was 0.445 lb/shp-hr, including all losses down to the jackshaft. At the idling speed of 200 rpm, the fuel consumption was measured to 35 lb/hr, corresponding to 8% of the full-load consumption.

By May, 1960, the locomotive had operated about 130,000 miles. However, this includes a long period out of operation after conclusion of the first stage of testing. During that stage many "bugs" had to be overcome, as would be expected with a new design. Troubles with the auxiliary equipment, such as the drives of the alternator and air compressors, caused much delay but have been overcome.

The gas-generator engine has required adaptations in several respects, but has demonstrated its suitability for locomotive duty. The locomotive has been found to perform well in various types of service. Mainly, it has been used with fast mixed passenger and freight trains on the Halmstad-Nassjo line in Southern Sweden, a stretch of hilly and curvy track with many gradients of up to 1.7% and a total difference in altitude of 1100 ft. The distance is 122 miles and a round trip is made daily with about 20 stops on the upjourney and somewhat fewer on the way down.

The operation of the locomotive is very simple. There is one lever for forward or reverse; and once it is placed in the proper direction at the start of the trip the gear is not touched during the whole trip, as there are no gear changes necessary. One lever is used to increase or reduce the air pressure in the control system, each pressure representing a certain gas output regardless of the speed. Also, it has been found that new drivers rapidly get accustomed to the management and behavior of the locomotive.

In the gas generator, slight damages to the crank bearings occurred at an early stage. They could be attributed to restricted oil circulation in the bearing and were remedied by a modification of the oil grooves. Certain modifications of the scavenge ports have improved the performance of the gas generator. Oil cooling of the wall separating the suction and delivery chambers in the compressor covers and oil cooling of the lower pistons had to be introduced. Further, the driveshaft of the hydraulic governor broke several times despite changed designs and had to be provided with an elastic coupling, which has worked satisfactorily.

The most severe difficulty, however, has been caused by the thermal loading of the walls of the combustion chamber. When the cast-steel center sections of the working cylinders were designed in 1950, available experience regarding the possible heat transfer through the walls indicated a value around 40,600 Btu/sq ft/hr, corresponding to a temperature gradient in the undisturbed wall of 114 F per in. The optimum wall thickness was calculated with this value as a basis.

After one year of test runs in the testing bay and another year in actual service, cracks started to develop at the inner surface of the center sections. The cracks started from the holes for the compression regulating valves and later also from the openings for the smaller valves. For some time it was possible to repair the cracks by welding with good success; but it was ultimately necessary to redesign the center sections entirely and replace them in the locomotive.

The temperature gradient was measured in the wall of the center section of a single-cylinder experimental gas generator of identical dimensions, which in the meantime had been erected in the research department. The temperature gradient at full load was measured to 470 F per in., corresponding to a heat transfer of nearly 165,000 Btu/sq ft/hr. The formulas and curves from the interesting report by Alcock, Robson and Mash (4) were also applied to this problem. With due consideration taken to the different conditions an extrapolation from their results gave a value for the heat transfer through the wall of 140,000 Btu/sq ft/hr.

A new center section was manufactured of forged heat-resistant steel with a thickness only half the original one and with welded-on cooling water jacket. It was thoroughly tested in the single-cylinder engine and has performed excellently up to date. New combustion chambers of this design have lately been installed in the locomotive. At the same time, the cooling system of the locomotive was modified with increased cooler capacity. A verdict about the behavior of the new combustion chambers can not be made until after at least a year of continuous operation.

The turbine has given very positive performance. The blading stays clean and neither deposits nor erosion have been observed. A layer of soft soot formed after lengthy running

at low loads is entirely blown off as soon as higher loads are applied. The blading of the impulse wheel has been renewed with the thickness of the leading edge increased, as the original very thin edges did not keep their form when subject to the hot gases. The inlet side radial bearing initially suffered from the heat of the turbine rotor. As long as the gas generator was running, a continuous flow of lubricating oil was conducted through the turbine bearings, removing the heat transferred to them from the rotor. When the gas generator was stopped, however, the lubricating oil flow ceased and the temperature of the bearings began to rise. Measurements of the bearing temperature showed that the maximum temperature of the inlet side bearing was reached first after several hours and was so high that serious damages to the bearing could be expected. Luckily, no serious accidents happened. A battery-driven circulating oil pump was installed for cooling of the turbine bearings after the gas generator stops; no damage to the bearings has occurred since then. The pump is started manually, when the gas generator is stopped, and stops automatically after 1 hr.

The reverse-reduction gear has given excellent performance. The oil grooves in the bearings of the pinion have been modified in order to guarantee a sufficient supply of lubricating oil to the bearing surfaces under all conditions, from the very heavy starting load at zero speed to the maximum speed of 12,500 rpm. After the last modification, the bearings have worked to entire satisfaction for nearly 50,000 miles. The rest of the gear has not been opened up since the locomotive was delivered in 1955. There have been no indications of abnormal conditions. Inspection of the gear teeth, in so far as possible through the inspection holes, has shown no signs of excessive wear or overloading of the teeth.

Future Development of T1 Type Locomotive

The experiences gained from the T1 locomotive operating on the Swedish State Railways has been very valuable. In order to operate the heaviest freight trains handled by the railroad, a somewhat higher output is required. A revised and modernized design has been drawn up for the railway authorities. It includes a 6-cyl gas generator delivering 1560 gas hp, corresponding to 1200 shp at the wheels. For the reduction gear, there is a choice between the double reduction gear with only one gear ratio and a triple reduction gear with two gear ratios (enabling a change in gear ratio during running). In the former case, a very simple and easily operated gear gives a starting tractive effort of 37,000 lb. In the latter case, a more complicated gear is necessary, but the starting tractive effort may be increased to a theoretical value of over 50,000 lb, which is practically limited to about 33% of the adhesion weight. At the same time the region of optimum consumption is spread out over a wider range of speed and load.

Referring to the development of the gas generator proper, tests are being conducted with chromium-plated steel liners, improvements in scavenging and compression regulating equipment are under way, and the possibility of effecting the variation in compression ratios by increasing the clearance volume (instead of releasing part of the cylinder contents through a valve) have been investigated.

Future of Crank-Piston Gas Generators

Naturally the line chosen by Gotaverken with crank-bound gas generators is not limited to the two main types of generators described here. Plans have been made up for the conversion of a highly supercharged lightweight diesel engine, developed for the Swedish Navy, to a gas generator. This engine, which was described in 1957 (5), consists of an opposed-piston 2-stroke diesel engine with two crankshafts connected by a helical gear train. With the scavenge air pressure of 25 psi gage this 10-cyl engine develops 3200 shp at 1000 rpm with a weight including the supercharger of 18,200 lb.

Redesigned as a gas generator with 64 psi gage scavenge air pressure and a speed of 950 rpm, this engine would deliver 3250 gas hp corresponding to 2800 shp from the turbine. The compression of the scavenge air would be effected in two stages with intermediate cooling. For the first stage a centrifugal compressor with a pressure ratio between 1.5/1 and 2/1 would be supplied and for the second stage a rotating positive displacement compressor of Lysholm design, both positively driven from the engine and together consuming all its power.

The turbine could be connected to the wheel by suitable reduction gear, cardan shafts, and bevel gears in the bogies; or it could be coupled to an electric generator with standard traction motors at the wheels, in which case the increased losses in the transmission would have to be taken into account.

References

1. A. L. London, "Compound Piston-and Turbine Engines," ASME Transactions, Vol. 81, 1959, p. 259.

2. H. G. Hammar and E. Johansson, "Thermodynamics of New Type of Marine Machinery," Trans. Inst. Mar. Eng., Vol. LI, 1939, p. 139.

3. A. C. Hardy, "Diesel Boiler," Diesel Railway Traction, Oct. 6, 1933, p. 504.

4. J. F. Alcock, J. V. B. Robson, and C. Mash, "Distribution of Heat Flow in High-Duty Internal-Combustion Engines," CIMAC Conference, Zurich, 1957, p. 723.

5. E. Johansson and L. Thulin, "Highly Supercharged Two-Stroke Light-Weight Diesel Engine," CIMAC Conference, Zurich, 1957, p. 167.

Mating Materials in Unlubricated, High Load, Low Speed,

L. E. Fuller
Linde Co.

THERE ARE many wear problems such as high-temperature valves, control linkage bearings, pneumatic cylinders and seals where the selection of materials presents a considerable problem. This has created the need for mating material data, particularly where new materials with only limited prior use are to be considered. Conditions of these high-temperature applications, at relatively low speeds and high loads, require operation with no lubricant or lubricants with limited effectiveness. A large number of material combinations was evaluated by the author in laboratory wear tests designed to be generally representative of these service conditions. Samples had a form typical of complete face seals or plain thrust bearings. Description of equipment, procedures, methods of evaluation, and results are included in this report.

All data presented are from tests run in air with no lubrication at a speed of 10 fpm under an apparent contact load of 500 psi at temperatures of 1000 and 1400 F.

For test conditions described herein, and undoubtedly under a wide range of conditions of unlubricated wear in air at high temperature, the following conclusions were made:

1. Special hard materials including carbides and oxides have better mating properties with certain other hard materials and metal alloys than the mating unlike metals or the like metals which were tested. Coefficient of friction and wear rates are both lower for hard material versus hard material and hard material versus metal combinations than for metal versus metal combinations.

2. Among the special hard materials tested, those hav-

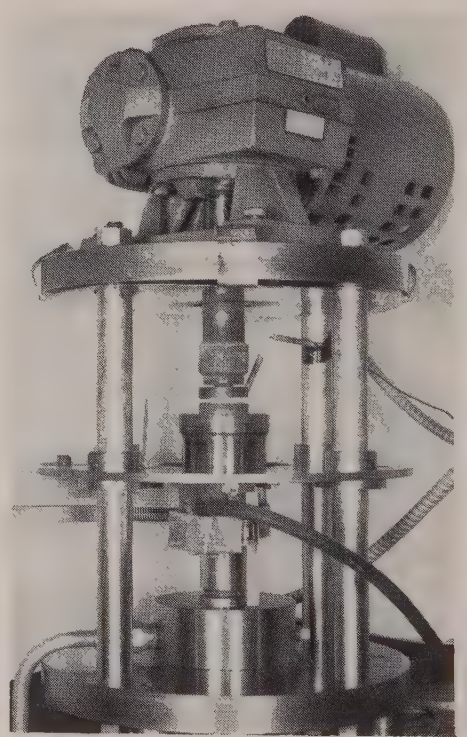

Fig. 1 — Hydraulically loaded and centered wear test machine with heater removed

Wear Tests at High Temperature in Air

ing a multiphase structure had better self-mating properties than single-phase material.

3. With suitable mating materials, wear at high temperature is predominantly by adhesion; that is, effects of oxidation, surface fatigue, and abrasion are small. The simplified wear theory affords a good approximation for predicting wear.

Equipment

A wear test machine was designed to provide for frictionless hydraulic loading and centering of a lower stationary sample (Fig. 5B) against an upper rotating sample (Fig. 5A). The lower sample is mounted on a special hydraulic piston which provides a means for axial loading as well as measurement of friction-created torque. This machine was built to replace an earlier one which had a ballbearing-mounted lower sample-holder. Operating conditions were conducive to fretting of the ball bearings, resulting in an increase in static friction; hence inaccuracies in measured coefficient of friction were experienced.

Two views of the hydraulic machine are shown in Figs. 1 and 2, and a perspective cross-section is shown in Fig. 3. The stationary motor mount is supported on a frame which is constructed in such a way that loading forces do not cause misalignment. A one-piece, thermally insulated coupling drives the rotary sample. The lower stationary sample-holder is similarly designed to help protect the hydraulic system from high temperature. Two pins extend radially from the stationary sample-holder. One pin is attached to a calibrated extension spring for measuring friction while the other

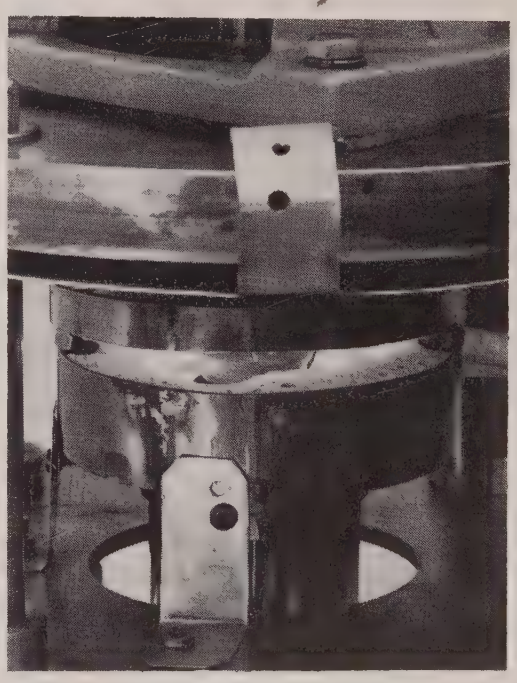

Fig. 2 — Wear sample area of wear test machine with heater cover propped open

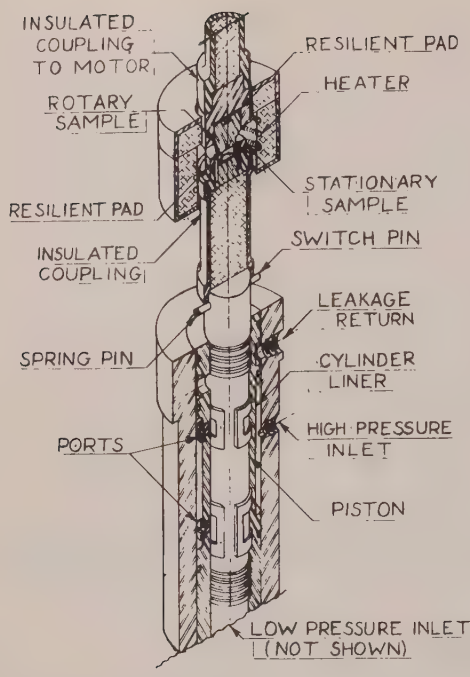

Fig. 3 — Sketch of hydrostatically centered and loaded wear test machine

contacts the operating appendage of a microswitch. The spring tension adjusting mechanism is designed to permit precise measurement of spring elongation with a depth micrometer. When friction exceeds a preset value fixed by the amount of tension on the spring, the microswitch disconnects the drive motor. An elapsed time meter records the drive motor "on" time. The heater is constructed of a stainless-steel outer shell and cast refractory to provide thermal and electrical insulation for the Nichrome V radiant heating element. A thermocouple with a recording potentiometer was used to monitor temperature. A variable transformer on the heater power supply provided the means of controlling temperature.

The hydraulic loading and centering system consists of a small packaged hydraulic power unit, suitable piping and controls, and a specially designed cylinder and piston shown in Fig. 3. The hydraulic circuit diagram is shown in Fig. 4. Water cooling in the reservoir and on the pump discharge line is used. Flow of hydraulic fluid is divided into two portions:

1. The major portion flows at full pump pressure into the wide groove between the cylinder liner and outer shell to feed six capillary ports in the liner arranged in two rows of three with equal spacing.

2. The smaller portion of flow is diverted through the flow controller, thence to the pressure regulator, and into the bottom of the cylinder to apply controlled axial loading to the bottom of the piston.

With no pressure on the hydraulic system the piston rests at the bottom of the cylinder. When pressure is applied to the bottom of the piston it is forced upward until wear samples contact each other and axial loading force is established. This vertical movement of the piston provides the space necessary to install and remove wear samples. In the raised position, the three equally spaced recessed pads in each of two rows on the piston are in alignment with the six inlet ports in the cylinder liner. Leakage past the straight-through labyrinth at the bottom of the piston and past the circumscribing walls of recessed pads flows upward through interconnecting circumferential and axial grooves in the piston to the leakage return near the top of the cylinder. The lands and grooves on the piston above the leakage return prevent leakage out of the top of the cylinder.

Hydraulic centering forces are derived from pressure differences between the recessed pads on the piston. If the piston is off center, radial clearances between the pad walls and cylinder wall will be unequal. Flow out of the pad varies as the cube of this clearance. For capillary-type ports which are used in this machine, pressure drop is proportional to flow rate. Since flow through an entry port must be equal to flow out of the aligned recessed pad, pressure drop through ports varies as required by varying clearance. Therefore, if one pad has less than normal clearance its fluid pressure will be high while the pad on the opposite side will have greater than normal clearance and its fluid pressure will be low. If the piston becomes inclined to the axis of the cylinder, which will occur if the mating surfaces of wear samples are inclined, the clearances of the two pads in the same vertical sector will be unequal and a force couple will be created which resists the force causing inclination of the piston. This force balance is essential in preventing contact between the piston and cylinder to provide a system which is practically free from static friction. Even with no external force the piston will not be perfectly centered dimensionally because of imperfections in parts. The piston will be centered in the sense that it is surrounded by equal pressure areas or force fields.

Procedure and Evaluation

Samples were installed, the thermocouple was secured to contact the stationary sample with very light pressure at a point immediately adjacent to the rotary sample, and heating was started at the beginning of each work day. Quartz felt pads were used for resilient backing of both samples. Load was applied by controlling pressure of fluid entering the bottom of the cylinder with the pressure regulator. (Pressure multiplied by the area of the piston minus the weight of the piston-sample holder assembly is equal to applied axial load.) Average contact pressure on the samples was equal to the applied load divided by the apparent contacting area of the mating samples. This area was the same for all tests and is 0.0580 sq in. computed from the 0.407 in. ID of the

Table 1 - Mating Compatibility Chart Rating and Test Temperature, F

	LW-1	440C Stainless Steel	M2 Tool Steel	LW-5	Haynes Alloy 25 (L-605)	LA-2	LC-1A	Inconel-X
LW-1 Coating	E 1000							
440C Stainless Steel	E 1000	F 1000						
M2 Tool Steel	G 1000	P 1000	P 1000					
LW-5 Coating	G 1000	G 1000	F 1000	G 1400				
Haynes Alloy 25	G 1000	F 1000	P 1000	E 1400	F 1400			
LA-2 Coating	F 1000	F 1000	F 1000	G 1400	E 1400	P 1400		
LC-1A Coating	G 1000	G 1000	F 1000	G 1400	G 1400	E 1400	E 1400	
Inconel-X	P 1000	P 1000	P 1000	P 1400	P 1400	P 1400	P 1400	P 1400

Symbols: E-excellent; G-good; F-fair; P-poor. See text for explanation of rating

Composition and condition of materials is given in the Appendix.

reamed hole in the center-of-stationary samples and the 0.490 in. OD of the rotary samples.

Friction measurements were made during momentary running at the start of each test and at different temperatures during warmup. Continuous running was started when test temperature was attained. Friction measurements were made periodically during continuous running which continued until 20 minutes before the end of the work day. Friction was again measured at various temperatures during momentary running while the machine was cooling down. Another friction measurement was made with samples at room temperature the morning after the test was completed. Thus, all friction values except at test temperature were momentary. Duration of all tests was slightly over 7 hr, except in cases where wear was so rapid that the rotary sample-holder started to scrape on the stationary sample outside the intended wear track.

Nearly all samples with good wear resistance gained weight during high-temperature tests. This illustrated the impossibility of determining wear by weight loss. The unrubbed areas of samples were used as a datum plane from which heights of adjacent rubbed areas were measured with an electric comparator gage. The maximum sensitivity of this gage was 10 Mu in. per division and differences of 5 Mu in. could be read easily. Samples were traversed radially under the tracer point of the comparator to determine the maximum wear depth at 90 deg intervals. The depth of wear track was taken as the average of these four measurements. Wear rates were computed by dividing the wear-track depth by the running time and sliding speed.

All combinations having good gross wear resistance were examined closely under the microscope to determine the extent and nature of surface damage. Qualitative data, particularly in cases where materials have good resistance to gross wear, was often more important than quantitative data. Quantitative and qualitative data were combined to arrive at a classification for mating material combinations using the following definitions:

1. Excellent - Light wear with slight surface damage to moderate wear with no surface damage other than smooth wear.
2. Good - Light wear with moderate surface damage to moderate wear with light surface damage.
3. Fair - moderate wear with moderate surface damage to rapid wear with light surface damage.
4. Poor - Moderate wear with heavy surface damage to gross wear with moderate surface damage.

Coefficient of friction is not used directly in this classification.

Table 2 - Results of High-Temperature, Low Speed, Dry-Sliding Wear Tests

Test Conditions: No lubricant, speed = 10 fpm, load = 500 psi, apparent contact pressure, temperature as indicated.

Mating Materials Rotary / Stationary	Wear Rates, 10^{-6} in. Depth per 1000 ft	Test Temp., F	Coefficient of Friction
LW-1 Coating	23	1000	0.25
440C Stainless Steel	12		0.34 R.T.
440C	117	1000	0.26
440C	17		0.43 R.T.
LW-1	35	1000	
M2 Tool Steel	20		
440C	42		0.29
M2	254		0.50 R.T.
M2	357	1000	0.30
M2	134		0.45 R.T.
LW-1	33	1000	0.20
Haynes Alloy 25	8		0.28 R.T.
LW-1	43	1000	0.33
LW-1	24		0.46 R.T.
440C	172	1000	0.43
Haynes Alloy 25	73		0.36 R.T.
M2	314	1000	0.40
Haynes Alloy 25	50		0.34 R.T.
LA-2 Coating	14	1000	0.27
440C	108		0.35 R.T.
LA-2	29	1000	0.23
M2	197		0.40 R.T.
LA-2	9	1400	0.17
Haynes Alloy 25	7		0.25 R.T.
LA-2	Gross failure	1400	0.16
Inconel-X	510		0.31 R.T.
LW-1	16	1000	0.42
Inconel-X	546		0.53 R.T.
LA-2	31	1000	0.28
LW-1	54		0.30 R.T.
Inconel-X	9000	1400	0.34
Inconel-X	9000		0.52 R.T.
LA-2	9	1400	0.16
LW-5 Coating	63		0.27 R.T.
LW-5	32	1000	0.30
440C	14		0.48 R.T.
LW-5	22	1400	0.19
Haynes Alloy 25	17		0.35 R.T.
LW-5	79	1000	0.27
LW-1	18		0.44 R.T.
LW-5	59	1000	0.32
M2	31		0.50 R.T.
LW-5	51	1400	0.29
Inconel-X	260		0.57 R.T.
LW-5	26		0.21
LW-5	17		0.34 R.T.
LC-1A Coating	29	1400	0.19
Haynes Alloy 25	13		0.32 R.T.
LC-1A	11	1400	0.15
LA-2	4.3		0.27 R.T.
LC-1A	13	1400	0.19
LC-1A	12	1400	0.34 R.T.
LC-1A	9	1400	0.23
Inconel-X	450		0.49 R.T.
LC-1A	37	1000	0.33
440C	5.1		0.46 R.T.
LC-1A	52	1000	0.35
M2	16		0.49 R.T.
LC-1A	11	1400	0.22
LW-5	19		0.37 R.T.

Table 2 - (Cont'd)

Mating Materials Rotary Stationary	Wear Rates, 10^{-6} in. Depth per 1000 ft	Test Temp., F	Coefficient of Friction	Mating Materials Rotary Stationary	Wear Rates 10^{-6} in. Depth per 1000 ft	Test Temp., F	Coefficient of Friction
Haynes Alloy 25	62	1400	0.28	440C	63	1000	0.27
Haynes Alloy 25	43		0.43 R.T.	Inconel-X	314		0.58 R.T.
Haynes Alloy 25	240	1400	0.33	M2	84	1000	0.24
Inconel-X	2050		0.40 R.T.	Inconel-X	497		0.60 R.T.

NOTE: R.T. refers to coefficient of friction measured before samples were removed from the test machine after the high-temperature test run was completed.

Results

Table 1 shows the cross-mutual compatibility ratings of all possible combinations of eight different materials. Table 2 presents the numerical wear rate and coefficient of friction values. Fig. 5 shows typical samples ready for test while Figs. 6-12 show the surface condition of several typical after-test samples. Materials are identified in the Appendix as to composition and condition corresponding with designations in the tables.

Discussion of Results - Of all combinations tested to date, chromium carbide coating (LC-1A) versus aluminum oxide coating (LA-2) was the best and LC-1A mating with itself was second. Among the coatings, tungsten carbide (LW-1) was best for mating with hardened steels. Aluminum oxide (LA-2) was best for mating with cobalt-base superalloy, but poorest for mating with itself. Chromium carbide (LC-1A) was best for mating with itself and aluminum oxide. Mixed chromium and tungsten carbide (LW-5) was excellent for mating with itself and with cobalt-base superalloy (Haynes Alloy 25). The generally better mating compatibility of cobalt-base superalloy compared with nickel-base superalloy (Inconel-X) was expected. Some recent wear data show that nickel-base alloys containing noteworthy amounts of molybdenum and/or tungsten have better wear and galling resistance than those in which chromium is the only principal alloying constituent.

The tables include only a minor faction of all combinations tested. They do include all materials for which complete cross-mutual compatibility has been determined. No claims are made that the best combinations reported represent the best possible choice of mating materials. Materials included should be considered as representing rather broad classes. Individual types among these classes may be superior to those presented.

There seem to be four possible explanations why some of the harder materials wore more rapidly than some of the softer ones:

1. Possible surface or subsurface fatigue of harder materials may result in incipient pitting and cracking, causing accelerated formation of loose particles.

2. Oxidation may form a lubricative film on some softer materials and accelerate formation of loose particles on harder surfaces.

3. Embedment of loose particles in the softer material may occur, thus reducing measurable depth of wear by an

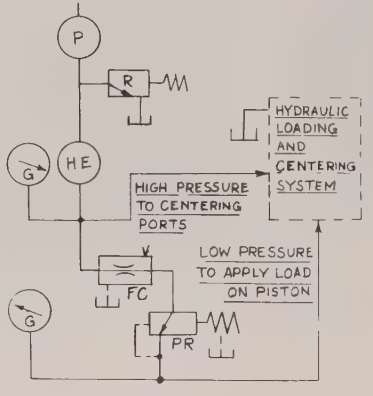

Fig. 4 — Schematic of hydraulic circuit for hydrostatically loaded and centered wear test machine

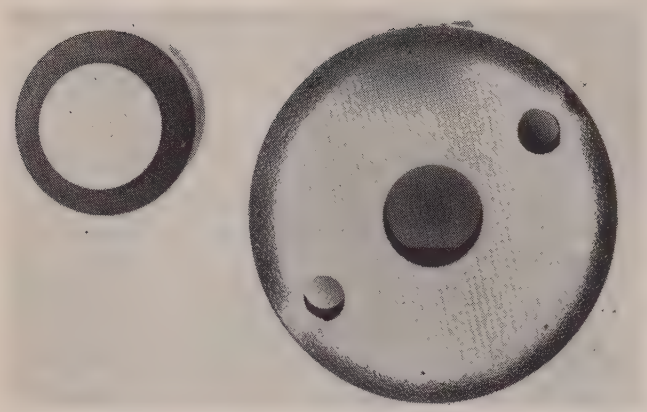

Fig. 5 — Rotary wear sample (left), stationary wear sample (right). Both samples are coated, ground and lapped, ready for test

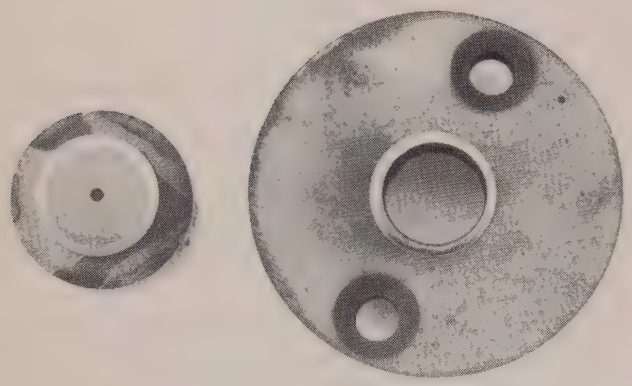

Fig. 6 — LW-1 coating (rotary) versus 440C stainless (right) after 7 hr wear test at 1000 F. No lubricant, load 500 psi, speed 10 fpm

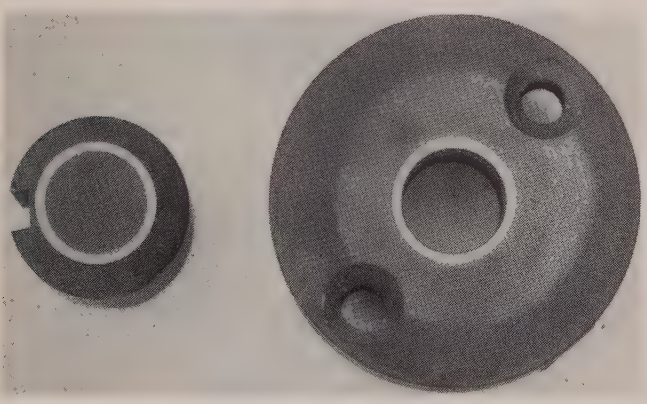

Fig. 7 — LW-1 coating (left) versus LW-1 coating after 7 hr wear test at 1000 F. No lubricant, load 500 psi, speed 10 fpm

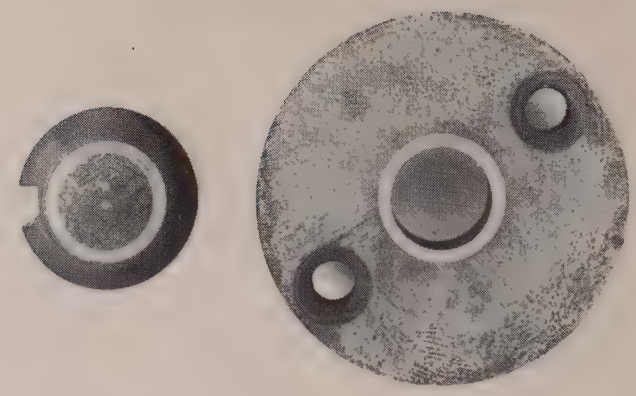

Fig. 8 — 400C stainless (rotary) versus M2 tool steel (right) after 7 hr wear test at 1000 F. No lubricant, load 500 psi, speed 10 fpm

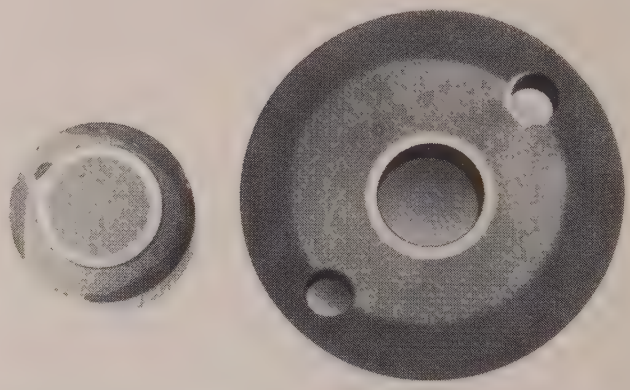

Fig. 9 — LC-1A coating (left) versus LC-1A coating after 7 hr wear test at 1400 F. No lubricant, load 500 psi, speed 10 fpm

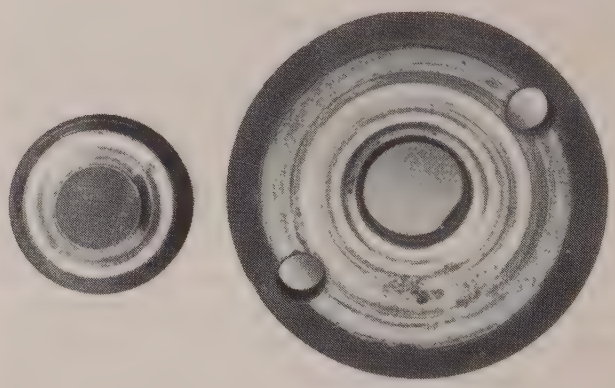

Fig. 10 — Inconel X (left) versus Inconel X after 4 hr wear test at 1400 F. No lubricant, load 500 psi, speed 10 fpm. Note extremely deep wear in intended wear track and wide track on stationary sample caused by rubbing on rotary sample holder

undetermined amount.

4. Binder material adhesion in a coating may be weaker than adhesion formed by the wear process so that shear in the binder phase rather than in wear-formed adhesions may occur.

Because of the influence of No. 3, above, and inevitable material transfer, total wear, considering transplanted material as wear, is not accurately assessed by measuring wear depth. However, the measurment of wear depth is the true criterion of useful service life. Among the combinations

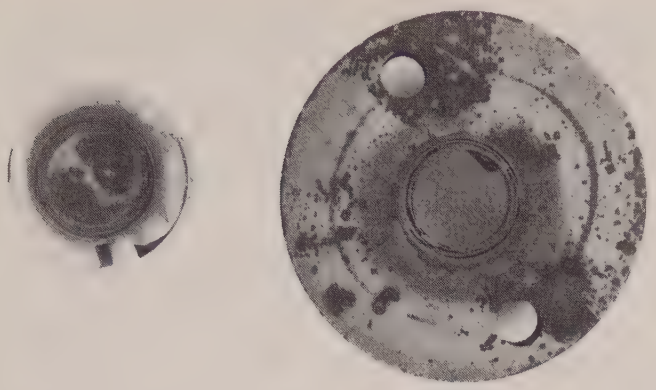

Fig. 11 — Haynes alloy No. 25 (left) versus Haynes alloy No. 25 after 7 hr wear test at 1400 F. No lubricant, load 500 psi, speed 10 fpm

Fig. 12 — LC-1A coating (left) versus LA-2 coating (rotary) after 7 hr wear tests at 1400 F. No lubricant, load 500 psi, speed 10 fpm

listed, the results show clearly the advantages of the hard coatings as mating surfaces compared to uncoated metals. Surface conditions apparent on the photographs of Figs. 5-12 are further evidence of these advantages.

Values of coefficient of friction listed at test temperature are average. There was no great change noted during steady operating conditions for the better mating combinations. Values at room temperature after tests are generally higher than those obtained when starting with new samples. Some data on coefficients of friction at various temperatures during warmup and cooling down were obtained. In most cases peak values were observed between 850 F and 600 F during cooling. None of the coefficients of friction values listed are in the range where the materials could be considered as self-lubricating. However, in cases of the better combinations, coefficients of friction are in the range of some recently published data on a high temperature dry lubricant (1).* Generally, the materials which maintain hardness at high temperature are expected to have lower coefficients of friction. Formation of adherent oxide films may account for the lower values at high temperature, but lower shear strength of adhesions at high temperature may also be a factor.

Correlation of Theory and Results

In the interpretation of data and test results it may be adequate to state simply the order of performance of materials. However, it seems desirable to include some comparison between results and theory. A good starting point is the simplified theory of friction and wear. According to the adhesive theory of friction and wear, they are both predominantly the result of a mechanism whereby minute adhesions are formed between surface asperities in contact with each other. This theory indicates that friction and wear are both proportional to normal load and inversely proportional to hardness.

Bowden and Tabor (2) determined the predominating influence on friction to be adhesions. The adhesive frictional force can be expressed as:

$$F = WS/A \qquad (1)$$

where:

W = Normal load
S = Average shear strength at weakest section in vicinity of adhesions
A = Total of areas subjected to shear

The shear strength of adhesions will depend on such factors as melting temperatures and mutual solubility and wetability of the two mating materials in addition to environmental factors such as atmosphere and temperature. Chemical dissimilarity of pure mating metals is generally considered favorable for obtaining minimum shear strength.

The area of adhesions formed is inversely proportional to the flow pressure of the material. The flow pressure is practically equivalent to the yield point. Thus, Eq. 1 may be written as:

$$F = WS/P \qquad (1a)$$

where:

P = Yield point

Since penetration hardness is approximately 1/3 of the yield point, friction may be expressed as:

$$F = WS/3p \qquad (1b)$$

where:

p = Penetration hardness in pressure units

*Numbers in parentheses designate References at end of paper.

Although yield point is more generally known for common metals, penetration hardness is easier to measure for all materials, and more accurately determined for brittle materials, especially for thin cases and coatings. Coefficient of friction then, is expressed as:

$$f = F/W = S/3p \quad (2)$$

Because of the many factors influencing the shear strength it is difficult to estimate coefficient of friction for complicated material systems.

Archard (3) developed the concept of a probability that adhesions would, upon breaking, produce loose fragments. On this basis wear due to adhesions has been expressed by the equation:

$$V = KWL/P \quad (3)$$

where:

V = Volume of wear of the softer of two mating materials, mm^3
K = Probability defined by Archard (called the adhesive wear coefficient)
L = Sliding distance, mm
W = Normal load, kg
P = Flow pressure, kg/mm^2

As explained previously in connection with friction, penetration hardness can be substituted for flow pressure, so Eq. 3 may be written as:

$$V = KWL/3p \quad (3a)$$

where:

p = Penetration hardness, kg/mm^2

Eq. 3 is the physical description of the simplified wear theory. It may be expected to apply in all cases of two solids in mutual sliding contact, since the formation of adhesions always occurs, even for contacting materials of extreme dissimilarity (4).

Rabinowicz (5) presented approximate values of the adhesive wear coefficient for broadly classified materials depending on lubrication. He obtained excellent correlation between the amount of wear calculated with these coefficients and actual wear measurements in some practical applications.

Calculations of wear coefficients using the data from Table 2 were made. For purposes of calculation, hardness at test temperature was estimated by multiplying measured room temperature hardness by the ratio of ultimate strength at test temperature to ultimate strength at room temperature. No such data was available for the special hard material coatings, so estimates of hardness at temperatures are, in fact, educated guesses. There could be an error of perhaps 30% in hardness, but this is not sufficient to change the wear coefficient by half an order of magnitude, or to the extent that the predominating wear mechanism would be judged incorrectly. Calculations for simplifying substitution of data directly from Table 2 are presented below.

Eq. 3a is converted to English units, thus:

$$V, \text{in.}^3 = \frac{K \times W, \text{lb} \times L, \text{in.}}{3p \text{ kg/mm}^2 \times 1420 \frac{\text{lb mm}^2}{\text{kg in.}^2}} = \frac{KWL}{4260p} \quad (3b)$$

Eq. 3b is transposed to:

$$K = \frac{4260pV}{WL} \quad (3c)$$

For all samples:

$$V = hA_t \quad (4)$$

where:

h = Depth of wear
A_t = Area of wear track

h is taken from Table 2, so L = 12,000 in.

$$W = P_c A_c \quad (5)$$

where:

P_c = Contact pressure
A_c = Apparent contact area

P_c = 500 psi. Therefore:

$$K = \frac{4260 \text{ h } A_t \text{ p}}{500 \text{ } A_c \text{ } 12,000} \quad (6)$$

and, since $A_t = A_c$:

$$K = \frac{4260 \text{ h p}}{6 \times 10^6} = 7.1 \times 10^{-4} \times h \times p \quad (7)$$

Table 3 shows the comparison between values obtained using test data from Table 2 and those presented by Rabinowicz (5). Correlation between calculated values and published values is very good for the first three combinations listed. It should be pointed out that the material designations in Ref. (5) do not necessarily accurately describe the hard material coatings. LA-2 should be classed as a nonmetal, but the other coatings consist of hard carbides with a distinct binder metal phase, and should be classified as cermets, intermediate between metals, and nonmetals. Wear coefficient for the Inconel-X versus Inconel-X combination could be at least one order of magnitude larger than the calculated value. This combination wore so fast that the ro-

tary sample-holder rubbed on the stationary sample. The wide wear track is visible in Fig. 11. Depth in the intended wear track only was used for calculation. The low-wear coefficient of Haynes Alloy 25 mating with LA-2 is not surprising, considering the unusual wear properties of cobalt-base materials. In the case of LC-1A mating with itself, the wear coefficient is about three orders of magnitude less than the expected value for like metals. Perhaps it is unfair to classify LC-1A as a metal since it is a multiphase material consisting of chromium carbide with a nickel-chromium alloy binder. The fact that this material mating with itself gives better performance than can be expected of unlike metals, and, in fact, is practically equal to nonmetal versus metal in performance, is considered unusual.

Calculated values of wear coefficient are significant because they show that test conditions and equipment produced the most common of wear mechanisms, that is, adhesion. Therefore, the data can be regard as typical and reliable for application to practice for systems in which adhesion is the predominating wear mechanism. This condition can usually be satisfied by expert design and selection of mating materials.

Table 3 - Adhesive Wear Coefficients

Mating Materials	[a]Hardness, kg./mm^2	K, Adhesive Wear Coefficient Calculated from Data	from Ref. (5)
[a]LC-1A Coating versus LA-2 Coating Coating	750	5.9×10^{-6}	5×10^{-6} nonmetal versus metal
Inconel-X versus Inconel-X	130	8.4×10^{-4}	5×10^{-3} like metals
440C Stainless versus [a]Haynes Alloy 25	200	1.0×10^{-5}	2×10^{-4} unlike metals
LA-2 Coating versus [a]Haynes Alloy 25	200	0.99×10^{-6}	5×10^{-6} nonmetal versus metal
LC-1A Coating versus LC-1A Coating	750	6.8×10^{-6}	5×10^{-3} like metals

[a]Wear coefficients and hardness values are for the softer material of the mating pair.

References

1. H.E. Sliney, "Lubricating Properties of Lead Monoxide-Base Coatings of Various Compositions at Temperature to 1250F." NASA Memo. 3-2-59E.

2. F.P. Bowden, and D. Tabor, "Friction and Lubrication of Solids." Oxford University Press, 1950.

3. J.F. Archard, "Contact and Rubbing of Flat Surfaces." Journal of Applied Physics, August, 1953, 981.

4. R.W. Sakman, J.T. Burwell, and J.W. Irvine, Journal of Applied Physics, Vol. 15, 1944, 459.

5. E. Rabinowicz, "New Coefficients Predict Wear of Metal Parts." Product Engineering, Vol. 29, June 23, 1958.

Appendix A — Table of Composition and Condition of Materials in Wear Tests

LW-1: Linde Flame-Plated coating, tungsten carbide with 6-8% Co, ground and lapped.

440C Stainless Steel: C 0.95-1.20, Mn 1.0 max., Si 1.0 max., Cr 16-18, Mo 0.75 max., Ni 0.5 max., S 0.03 max., Ph 0.03 max., hardened and drawn to 55-57 RC, ground and lapped.

M2 Tool Steel: C 0.82, Mn 0.25, Si 0.25, Cr 4.25, Mo 5.0, W 6.25, Va 1.9, hardened and drawn to 62-64 RC, ground and lapped.

LW-5: Linde Flame-Plated coating, 25% tungsten carbide, 7% Ni, remainder mixed chromium-tungsten carbides, ground and lapped.

LA-2 Linde Flame-Plated coating, 99+ % AL_2O_3, ground and lapped.

LC-1A: Linde Flame-Plated coating, chromium carbide with 15% (80 Ni-20 Cr) alloy, ground and lapped.

Haynes Alloy No. 25: Ni 9-11, Cr 19-21, W 14-16, Fe 3.0 max., Mn 1-2, Si 1.0 max., C 0.05-0.15, Co remainder, wrough, cold finished, ground and lapped.

Inconel-X: Ni 70 min., Cr 14-16, Fe 5-9, Ti 2.25-2.75, Nb + Ta 0.7-1.2, Al 0.4-1.0, Cu 0.2 max., C 0.08 max., S 0.01 max., equalized and aged to Rockwell C 36 min., ground and lapped.

Cord Fatigue in Fleet-Tested Tires

W. G. Klein, M. M. Platt, and W. J. Hamburger
Fabric Research Laboratories, Inc.

OF THE SEVERAL TYPES of tire failure encountered, one of the most discussed and least understood has been so-called "tire cord fatigue." The only point of real agreement has been that fatigue failure is characterized by circumferential cracks in the regions of maximum flexing. Since such failure is usually initiated in the inner ply, which is subject to considerable compression, the name "compression fatigue" has frequently been applied.

Undoubtedly, a considerable amount of private research has been done on this subject which, due to the economic advantages involved, has remained unpublished, but to our knowledge two recent pieces of research bearing pertinently on the problem have come to the public's attention. They are those of Williams, et al. (1)* and Entwistle, et al. (2). These articles are considered of particular interest because they deal with the properties of cords and filaments removed from tires rather than, as with the bulk of the work in the field, laboratory fatigue tests whose correlation with service conditions has been difficult to establish. Before noting the points of agreement and disparity among these articles and our own, it would be well to describe briefly the manner in which the tires were used.

All tires considered were fleet tested. In the Williams and Entwistle work, they were subjected to conditions of overload and underinflation for mileages up to about 30,000, while in the present work the tires were run at rated pressures and loads up to 100,000 miles.

The most important point of agreement in all three is that cord strength losses are at a maximum in the flex zone and that filament strength losses are much too small to account for cord strength losses. Thus, it is assumed that broken filaments, rather than a degradation of those intact, are responsible for cord strength losses. This has been semi-quantitatively justified by examination of weakened cords.

The most important point of disagreement is the rate of cord strength degradation. While Williams states that a linear rate of cord strength loss with mileage exists and concludes that this rate is an index of fatigue resistance, both the Entwistle work and our own show an initial low-mileage nominal loss of strength followed by a long period of very gradually diminishing strength, and consequently require a more complicated view of the mechanism of fatigue. Such a view will be presented and justified logically, if not conclusively.

The resolution of this disparity is of importance in two ways:

1. The roles of materials and construction cannot be properly understood without a knowledge of the basic mech-

*Numbers in parentheses designate References at end of paper.

anisms involved in fatigue.

2. The very inexact art of accelerated laboratory fatigue testing cannot be improved without knowing what goes on in a tire.

It is the purpose of this paper to present the results of tire analyses made on tires from a New York taxi fleet and to suggest conclusions which might be drawn on the basis of these, the above referenced articles, and several conferences with major tire producers.

This work has been jointly sponsored by the following Tyrex viscose tire yarn and pulp producers: American Viscose Corp.; American Enka Corp.; Buckeye Cellulose Corp.; Courtaulds (Canada) Ltd.; Industrial Cellulose Research Ltd.; Industrial Rayon Corp.; North American Rayon Corp.; Rayonier, Inc.

The Taxi Fleet Test

A complete description of the taxi fleet test, together with some early observations on tread wear, retreadability, etc., is found in a paper by Breazeale (3). The present brief description is simply to familiarize the reader with the test conditions.

All tires were made by the same manufacturer at the same time and all are 7.50 x 14 tubeless. Five different tire cords were used and each was represented by 100 tires in the fleet. Table 1, reproduced from the above reference (3), gives the pertinent construction parameters of the tires involved in this test.

Each of the Tyrex Viscose Cords series was supplied in duplicate by two different producers, hereinafter designated simply as "A" and "B." Thus, while five different cords were used, there are only three nominal types. Each of the five different cords was represented by a sampling of from 6 to 14 tires. The exact number of each can be found by reference to subsequent graphs where the points for the individual tires are plotted.

It should be noted that the values shown in Table 1 are for the bone dry state. All testing in the present work was done at 70 F, 65% relative humidity, and is thus not directly comparable to the above.

This test differs from most others in that rated pressure and load were maintained under constant surveillance, thus avoiding accelerated degradations which might not be correlative with normal wear.

Tires for analysis were selected from the test in two ways:

1. At selected intervals of mileage, a few tires not exhibiting any outward signs of fatigue were removed from service for dissection and analysis.

2. All tires diagnosed as fatigue failures were similarly dissected and analyzed.

*Photographs courtesy of U. S. Rubber Co., Detroit, Mich.

Table 1 - Construction Parameters of Test Tires

Material	1100/2 Tyrex Viscose Cord	1650/2 Tyrex Viscose Cord	840/2 Nylon
Ends/inch	36	27	30
Twist	15x15	12x12	12x12
B. D. Tensile	23.7	36.6	30.3
Carcass Tensile	3400	3940	3640

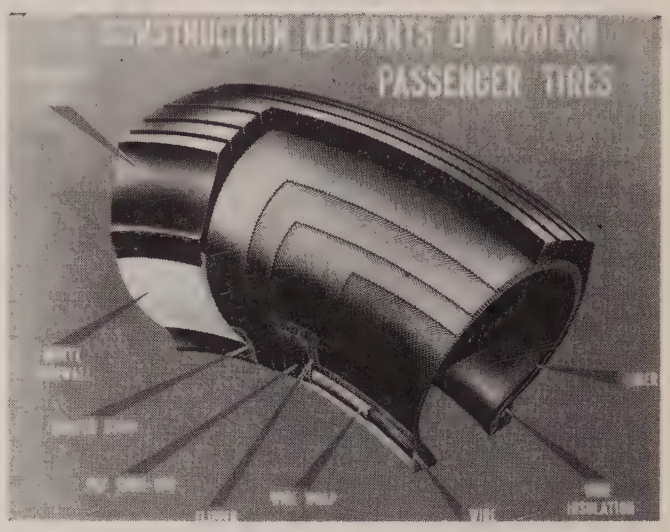

Fig. 1 — Construction elements of modern passenger tires

Data are included here covering 0 - 100,000 miles with recapping occurring at approximately 20,000-mile intervals.

TESTS PERFORMED-Figs. 1 and 2* show respectively cutaway and cross-sectional views of passenger tires. The cutaway view is from a tubeless tire similar to those considered in this report; the cross-section is from a tube type, differing primarily in the substitution of a tube for the liner. It will be convenient for the reader not familiar with tire construction to refer to these from time to time during the following discussion and descriptions.

The tires were dissected by cutting out a segment of about 90 deg and stripping off the rubber liner. This exposed the first, or inner, ply cords to easy removal. Four separate areas of investigation can be defined:

Cord Strength - Cords were stripped from the first ply and tested at low extension rates on an Instron Tensile Tester using capstan jaws and a free gage length of 2 in. Three regions of the cord were considered:

1. Crown - the center of the test specimen at the center of the cord, corresponding to the crown position on the tire.

2. Flex - the center of the test specimen about 3-1/2 in. from the center of the cord, corresponding to the region of maximum flex-compression, a position about one-third

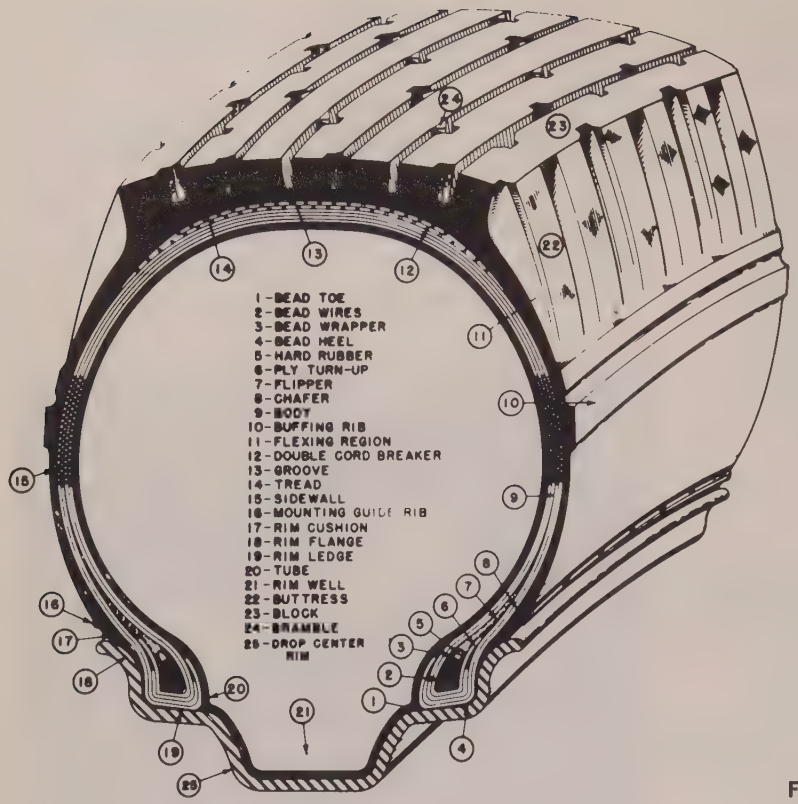

Fig. 2 — Cross-section of tire

of the way from Nos. 11 and 12 on Fig. 2.

3. Lower sidewall - the center of the test specimen at about 6 in. from the center of the cord. This is close to where the No. 9 appears on Fig. 2.

These tests were performed with whatever rubber remained on stripping the cord from the tire, still attached. The variability of cord breaking strength was extremely low and it was rarely necessary to make more than 10 breaks to establish a sufficiently accurate estimate of the strength (± 0.5 lb).

Filament Strength and Elongation - The same three regions were considered for filaments as for cords. The filament specimen length, however, was only 1 in. Filaments were removed from the cords in two ways:

1. By partially slitting the rubber coating on 1-1/2-in. pieces of cord and carefully opening the cord by untwisting. Individual filaments could then be teased out.

2. By chemically stripping the rubber from the cords, thus exposing all fibers to easy removal.

Sufficient statistical accuracy was usually established for any given point by the examination of 25 fibers. All fibers were measured for denier on a vibroscope before tensile testing.

Cord Adhesion - To measure cord adhesion, the carcass section was turned inside out and every other cord removed. The carcass was then placed on the lower cross-head of an Instron and one of the remaining cords, partially stripped, fastened in the upper jaw. As the cross-head moved down, the carcass was manipulated so as to keep the direction of cord pull normal to the carcass surface. In this manner, stripping force was plotted as a function of position of the tire.

Visual Evaluation - The physical appearance of the carcass and cords was noted at all stages of dissection. In addition, the cord structure was more closely examined on those from which all rubber had been chemically removed.

Experimental Results

Cord Strength - Figs. 3 - 7 show the breaking strength of cords removed from tires as a function of tire mileage. While the strengths for all three regions -- flex, center or crown, and lower sidewall -- are given, the curves are drawn to represent the flex zone values only.

Note that for all types considered the trend is the same; an initial nominal drop in strength followed by a long period of essentially constant strength and, in some cases, a further small drop somewhere between 60,000 and 100,000 miles. This latter drop cannot be very well defined, however, since no points were obtained between 60,000 and 100,000 miles and a single tire of each series was examined at 100,000. Nonetheless, the fact that all five showed a similar behavior suggests that the general level, if not the exact magnitude of the end points, is correct.

Three individual points on these curves deserve special comment.

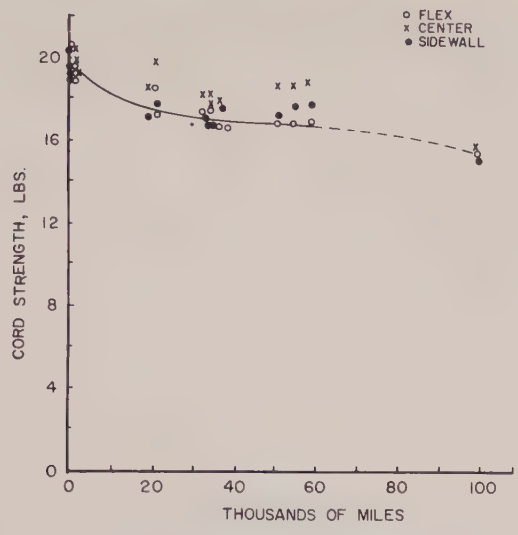

Fig. 3 — Cord strength versus tire mileage, Viscose A, 1100/2

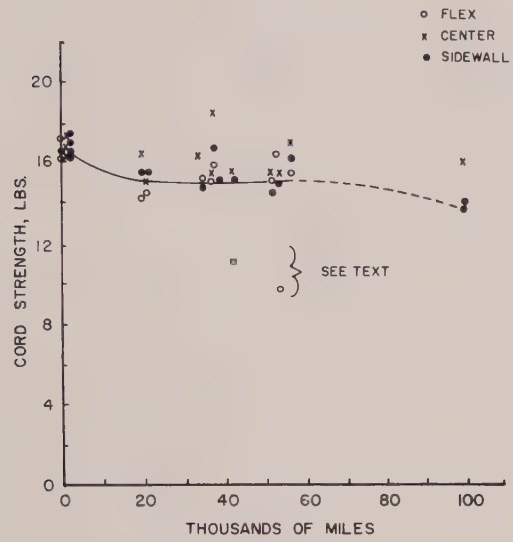

Fig. 4 — Cord strength versus tire mileage, Viscose B, 1100/2

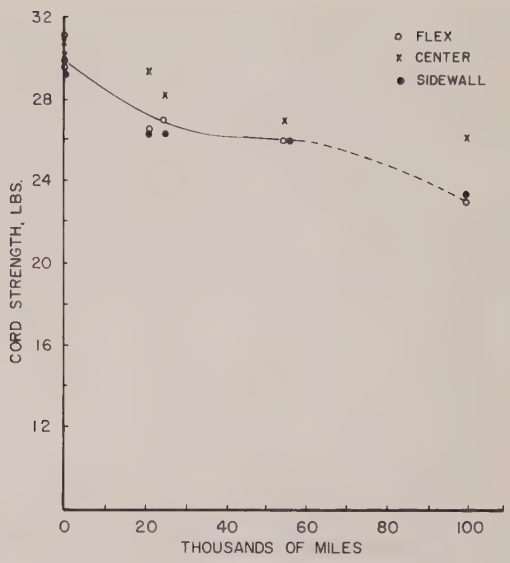

Fig. 5 — Cord strength versus tire mileage, Viscose A, 1650/2

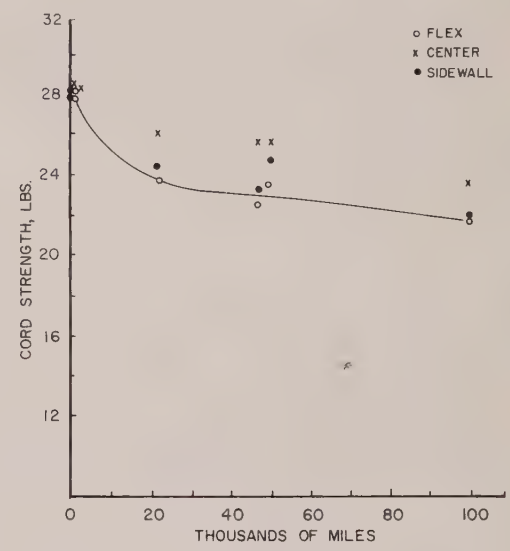

Fig. 6 — Cord strength versus tire mileage, Viscose B, 1650/2

1. The two low points in Fig. 4. These were due to obvious physical damage to the cords and will be discussed further in the section on visual evaluation.

2. There is a low point at about 60,000 miles in Fig. 7, the nylon graph. The cause here is lowered fiber strength, and this will be amplified later in the general discussion of fiber properties.

It is of interest that although the strength of the nylon cord remains quite high in the crown, or center region, its degradation rate in the flex zone is substantially the same as that of the Tyrex viscose cords.

Fig. 8 presents a normalized composite of the curves from Figs. 2-7. Shown in this form, the quantitative similarity of the five becomes obvious.

In addition to the above low-speed tensile testing, a group of 1100/2 Viscose B cords were evaluated under impact tensile loading conditions by American Enka Corp., using a previously published technique (4). The results are plotted in Fig. 9. While the impact strengths were higher than the static strengths, no differences in trend were noted with respect to mileage. While the cords were tested at full length, the break is always in the weakest or flex zone. Thus, a direct comparison can be made to the curve of Fig. 4, which is for the same type cord tested at low speed. Except for the different level, the curves are very nearly identical, even the two aberrant weak points appearing at the same relative level.

Filament Strength and Elongation - Fig. 10 shows the relationship between tire mileage and the strength of fibers removed from the flex zone of these tires. These fibers were removed from the cords by mechanical means only. Clear-

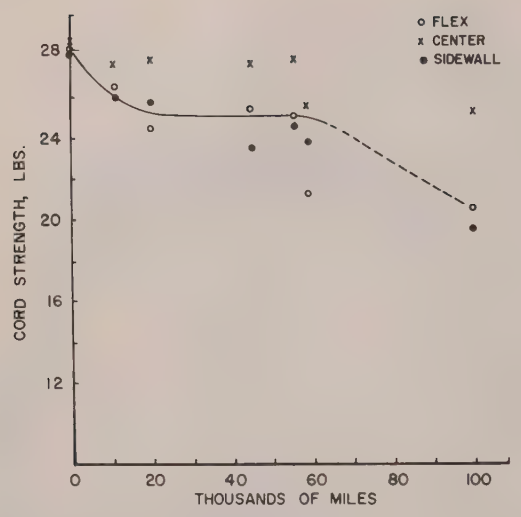

Fig. 7 — Cord strength versus tire mileage, nylon, 840/2

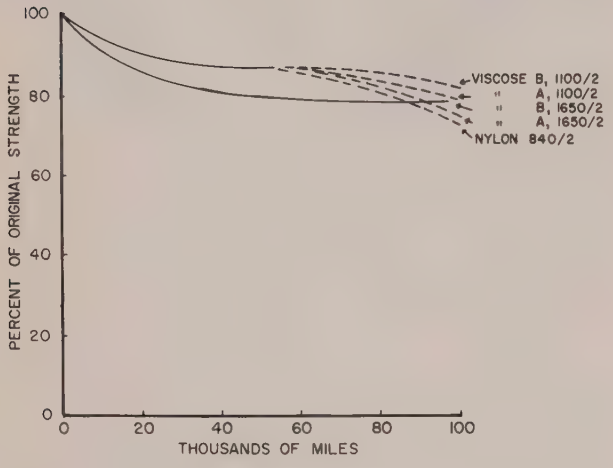

Fig. 8 — Percent residual cord strength versus tire mileage

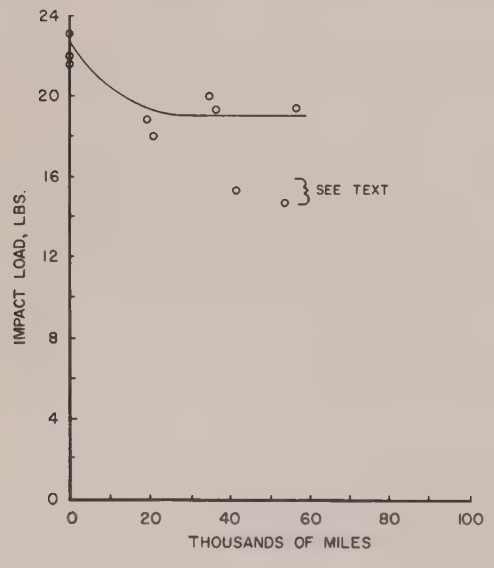

Fig. 9 — Impact cord strength versus mileage, Viscose B, 1100/2

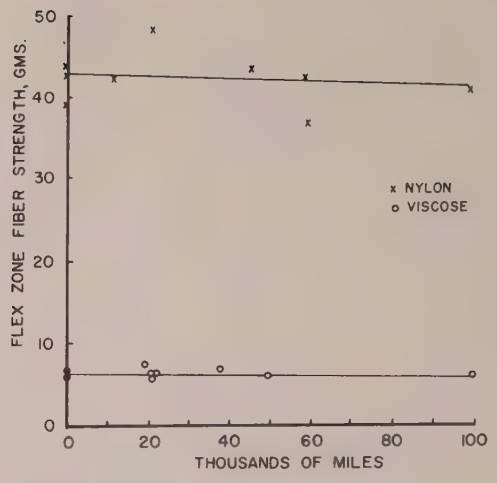

Fig. 10 — Flex zone fiber strength versus tire mileage

ly, while there appears to be a slight degradation with mileage, the amount is small, very much smaller than what would be necessary to account for cord strength losses. The sole exception is the low nylon value at 60,000 miles, which corresponds to a similarly low cord strength (Fig. 7).

The denier of the nylon filaments is about 6.0, and the Tyrex viscose, 1.6. Thus, the absolute difference in strength level is no more than would be expected on the basis of the slightly higher tenacity of nylon.

Fig. 11, filament rupture elongation versus mileage, shows a similar slight trend toward decreased elongation. However, the data are rather scattered and one could hardly attach much significance to the change.

There is always the possibility in a biased sampling of this sort, wherein fibers on the outside of cords could not be tested, that significant errors in interpretation might be made. To obviate this possibility, fibers from chemically stripped cords were tested and the tensile properties of the outside fibers, previously imbedded in rubber, compared to those from the inside of the cord. The treatment itself caused a slight shrinkage and degradation of tensile properties, so no comparison is made to mechanically removed fibers.

Fig. 12 is a plot of the tenacity of the inside versus the outside fibers from the same cords. The line drawn is not through the points, but is rather an equal tenacity reference. If there were no difference between the two regions, the points would be scattered randomly about this line. The fact that there is a strong tendency for the points to aggregate below the reference shows that the outside fibers were definitely weaker. The important point, however, is not that the outside is weaker, but that the same tendency is manifest for both new tires, indicated by X's, and used tires, shown by circles. Thus, it must be concluded that the strength differential is due to factors other than use, most probably either processing or rubber removal.

Fig. 13 is similar to Fig. 12 but shows the rupture elongation relationship between inside and outside fibers. The

same sort of conclusions apply here as for Fig. 12.

Having established the validity of using the inside fibers as a reference, it is reasonable to examine the relationship between the tensile strength of mechanically removed inside fibers and the strength of cords similar to those from which they came. It might be supposed that this relationship would show less scatter and more correlation than either of the individual plots versus mileage. Fig. 14 shows that this is not the case and the major cause of cord strength loss does not reside in a loss of fiber strength.

In addition to the above tensile investigations, some work was done using X-ray techniques to evaluate changes in fine structure. This work was done by Kraessig and Kitchen of Industrial Cellulose Research Ltd., using a technique soon to be published. The parameter studied was lateral order factor ($F_{L.O.}$), which for samples of the same degree of polymerization has been found to be linearly related to tensile strength. The results obtained are shown in Table 2.

Within the limits of fiber variability and experimental error, the data in Table 2 can be considered supporting evidence to the tensile test findings above, wherein there was shown a slight tendency to fiber strength loss with mileage. The assumption of the same degree of polymerization is currently being checked.

Cord Adhesion - It is generally accepted that adhesion of cords to the rubber somehow plays an important part in the fatigue life of the cords. A gross picture of adhesion can be obtained by the method described previously. The general levels of adhesion (as measured by the stripping test) are shown in Fig. 15. The new tire and 100,000-mile tire are from the Viscose A, 1100/2 series, while the indoor wheel plot is a typical curve taken from the work of Entwistle. Note that the highest loss of bonding force occurs in the region of maximum flex (between 3-1/2 and 4 in. along the cord from the center of the tire). The trend is the same for both wheel and fleet tested tires, but it was observed by Entwistle that the effect was less consistent on fleet tested tires. This lack of consistency can be seen in Fig. 16, where the flex zone stripping force is plotted against tire mileage for a number of 1100/2 cord tires. The trend toward lower adhesion is definite, but the variability is large.

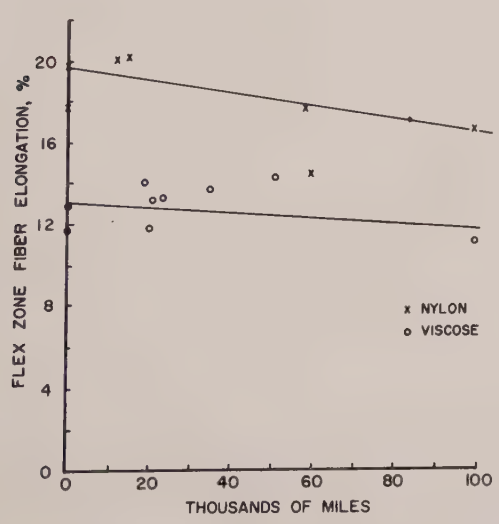

Fig. 11 — Flex zone fiber elongation versus tire mileage

Table 2 - Results of X-Ray Test to Evaluate Changes in Fine Structure

Cord	Tire Mileage	$F_{L.O.}$
Viscose B, 1100/2	0	6.69
Viscose B, 1100/2	57,000	6.69
Viscose B, 1100/2	100,000	6.14

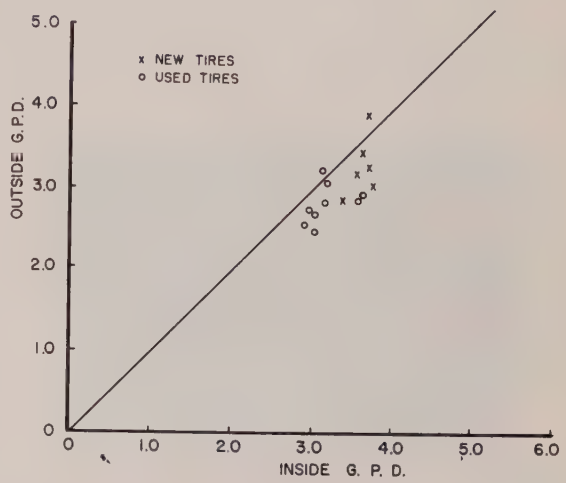

Fig. 12 — Comparison of tenacity of fibers from inside and outside of cords

Figs. 17 and 18 show very little correlation between stripping force and cord strength. This is not to say that adhesion and cord strength are unrelated, but simply that the gross nature of the test and the high variability of the data do not permit such a relationship, even if true, to be established. It is also circumstantial evidence suggesting that adhesion breakdown is significant only when relatively complete, thus leading to the so-called catastrophic failure.

Visual Evaluation - In the course of tire and cord dissection, a number of qualitatively important observations were made:

1. After removal of the inner layer of rubber, small discrete cracks were sometimes evidenced in the thin layer still remaining over the cords. Such regions were invariably associated with severe strength loss in the cords beneath.

2. Chemical removal of rubber from such cords showed excessive local fiber breakage, the extent of which was approximately that required to account for the excessive cord strength loss.

3. Such damage, when it occured, was always at a filling yarn cross-over and at the helical line of singles yarn contact in the cord. A typical damaged cord is shown in

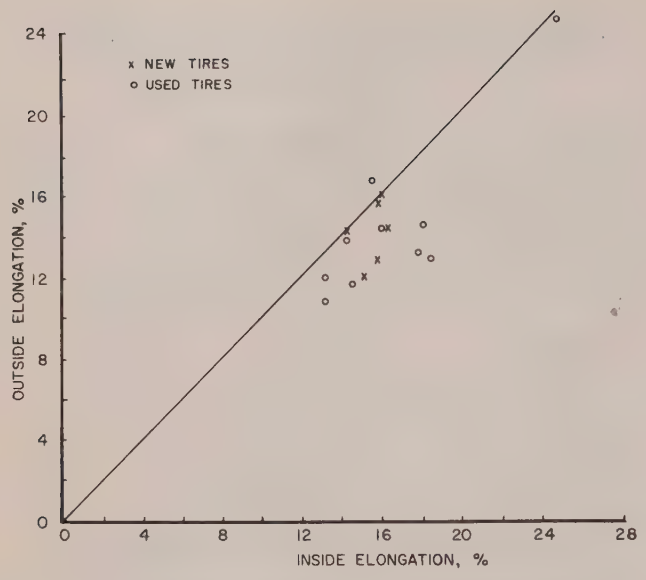

Fig. 13 — Comparison of elongation of fibers from inside and outside of cords

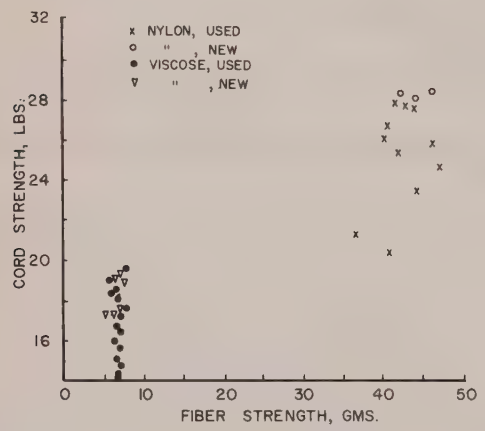

Fig. 14 — Fiber strength versus cord strength

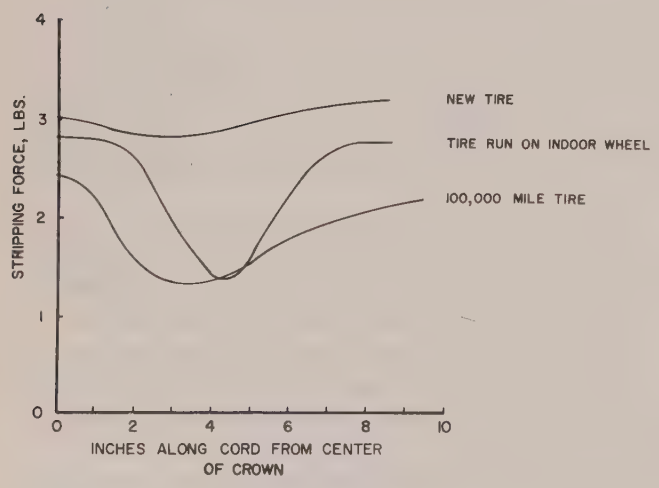

Fig. 15 — Cord stripping force versus cord position as influenced by tire mileage

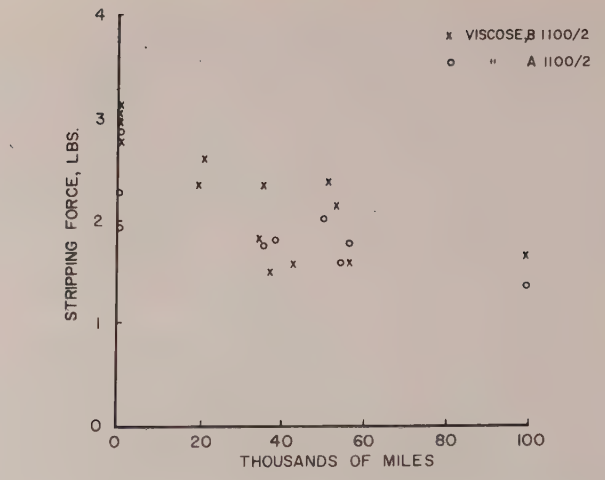

Fig. 16 — Flex zone cord stripping force versus mileage

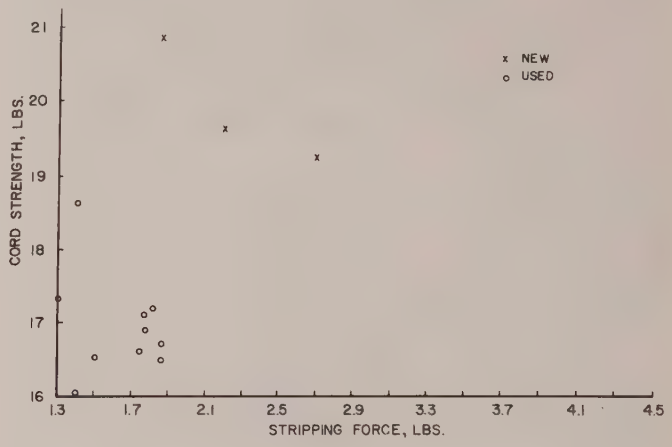

Fig. 17 — Cord strength versus stripping force, Viscose A, 1100/2

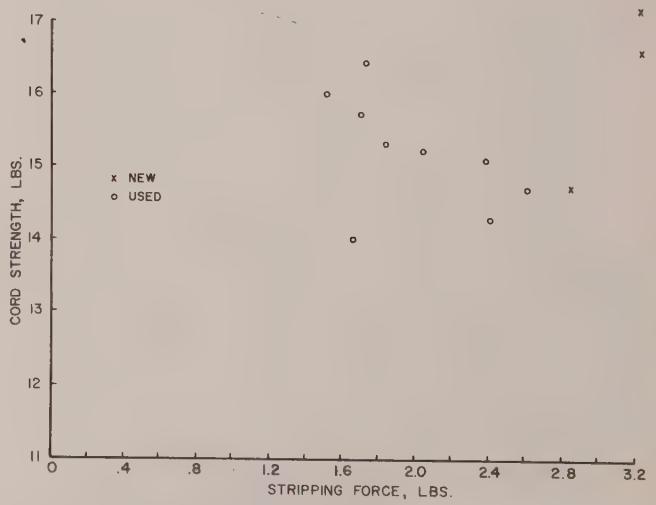

Fig. 18 — Cord strength versus stripping force, Viscose B, 1100/2

Table 3 - Fatigue Failure Test

Code	Cord	Mileage at Failure	Cord Strength (lb) Crown	Flex	Sidewall	Filament Strength Flex Zone (gr)
Viscose B	1650/2	50,066	27	24	25	
Viscose B	1650/2	48,498	23	22,23	24	6.3 (1.6 denier)
Viscose B	1650/2	0 (control)		27.5		6.5
Nylon	840/2	59,469	28	23	25	
Nylon	840/2	52,356	27	14,23	24	27.4 (6.0 denier)
Nylon	840/2	0 (control)		28.0		44.0

Fig. 19 — Viscose cord showing damaged flex zone

Fig. 19. This particular cord is representative of those giving the low values at 42,000 and 54,000 miles in Fig. 4 and 9. Since this type of damage followed the circumferential flex line quite uniformly, it is suspected that the damage was due to some period of underinflation.

TIRES CLASSIFIED AS FATIGUE FAILURES - Four tires additional to those already discussed were diagnosed symptomatically as fatigue failures; that is, they exhibited the characteristic circumferential breaks in the flex zone. Cords from all and filaments from two were examined in the same manner as the tires previously discussed herein. The results are given in Table 3.

For the fatigue failed tires, strengths of cords in the flex zone were determined:

1. For cords adjacent to the failure.
2. For cords far removed from the failure.

Where two values are given in Table 3 the lower one pertains to those cords adjacent to the failure region. Where only a single value is given, no dependence on location was found.

Note that in the case of the two failed Tyrex viscose tires, cord and filament strengths are no different than those found for unfailed tires at the same mileage (Fig. 6). No large reduction in cord strength has been observed. Observation of the cords from the Tyrex viscose tires when stripped of rubber indicated only mild filament breakage, occurring exclusively at the filling cross-overs.

Fig. 20 shows a chemically stripped viscose cord replaced in its original position on the inner surface of the carcass. Note the multiple areas of filament breakage, each occurring at a filling cross-over. This region is centered in the flex zone. The tire from which this picture was made failed in fatigue. It did not come from the taxi fleet test, but

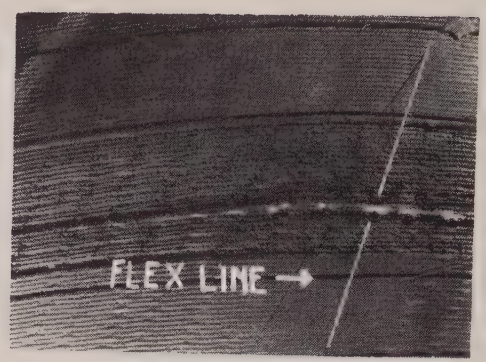

Fig. 20 — Viscose cord showing multiple damaged areas at filling cross-overs

is shown because it is an extreme example of the type of damage described above.

For the failed nylon tires, substantial reduction in cord and filament strength was observed only in the case of the 52,356-mile tire, in the flex zone adjacent to the region of failure. For this tire, filament strengths were also drastically reduced, a loss of about 40% being found in contrast with a loss of about 50% in cord strength. Additional losses resulting from some fiber breakage may be present in this nylon cord, but such breakage has not yet been observed.

Discussion

Several important facts have been established with respect to cords and filaments from the taxi fleet test. It would be of interest now to enumerate these and evaluate their general significance in the light of the works of Williams and Entwistle, which were done under different conditions.

1. The problem of fatigue has not manifested itself as a consistent degradation of cord tensile properties. In no case has there been either a failure or an appreciable weakening of cord strength which could be associated with a continuous degradation. Even in fatigue failed tires, cords adjacent to the failure were in general of normal strength. Thus, it is concluded that the cord fatigue process, once initiated, runs a rapid course to failure.

Entwistle, on the basis of both indoor wheel and fleet tested tires (overloaded and underinflated in both cases), concludes that "... fatigue failure in a tire is often a catastrophic process during which cord strength rapidly falls to zero but which is not preceded by significant and progressive loss of strength." Williams, however, states that fatigue failure stems from progressive loss of cord strength in the flex zone. This work, like Entwistle's, was done on overloaded and underinflated tires.

2. We have shown that after an initial, relatively rapid, loss of cord strength there follows a long period in which the rate of loss is very small.

Entwistle, though his mileage scale was compressed due to the accelerating action of overloading and underinflation, states substantially the same thing. Williams differs here, and concludes from his work that the loss in cord strength is linear with mileage. The cause of the initial loss is as yet unexplained.

3. Fiber tensile properties degrade at a very low rate; large losses in cord strength are attributable to fiber breakage at discrete points. Here there is complete agreement among the three investigations.

In two isolated cases, both nylon, significant loss of fiber tensile strength and rupture elongation was found. The reason for this has not been established.

4. Fiber breakage appears to occur primarily in the flex zone and at filling yarn cross-overs. It seems to follow the helical line of contact between the two singles in the cord. Williams is not so explicit but is in general agreement. Entwistle likewise agrees. Neither mentions any observation on the role of the filling yarns.

5. Significant local rubber damage (cord-rubber separation), not shown by the stripping test, but rather by visual observation, appears to accompany large cord damage.

Williams does not consider adhesion. Entwistle, on the other hand, has considered localized bond failure quite extensively with respect to both indoor wheel and fleet tested tires. Our observations are in general agreement with his, which are much more extensive than our own. Apparently, local bond failure gives rise to excessive local fiber strains leading to early failure.

The only real lack of agreement in all of the work discussed comes from Williams' contentions that:

1. Loss in cord strength is linear with mileage.
2. This loss progresses to an ultimate fatigue failure.

It is our feeling that this discrepancy is due not to a fundamentally different phenomenon or a difference in techniques, but rather to the interpretation of the data. Williams' conclusions are based on two plots, one containing three points, the other, two. In the case of the three-point plot, the locus is apparently linear, but considering the small differences in strength shown by these points and a normally anticipated variability, characterization of a linear relationship is questionable. Clearly, a straight line can be drawn through the two points of his other plot, but no functional relationship can be established from this. Once having agreed that a progressive linear loss does not exist, the assumption that such a loss leads to fatigue failure is obviously no longer tenable.

In conclusion, it seems apparent that, in general, cords do not become progressively weaker until failure, but rather fail suddenly; that the failure is not associated with a degradation of fiber tensile properties; and that localized bond failure is frequently, if not always, associated with such cord failure.

For the tires studied it is not possible to establish differences between Tyrex viscose and nylon in fatigue since the number of failures was small and all occurred at high mileages. Similarly, rates of degradation of tensile strength of cords containing either fiber type could not be distinguished from each other.

References

1. Williams, Hannel, and Swanson, Ind. Eng. Chem., 45 (1953), 796.
2. Entwistle, Jones, and Pittman, "Recent Advances in Tyre Yarns." Coventry: Courtaulds, December, 1958.
3. Breazeale, ASME Paper No. 59-SA-52.
4. Parker and Kemic, Technical Symposium on Rayon Tire Yarn Progress, Akron, Ohio (Jan. 23, 1958).

Mach 3 Wing Structures Stiffened Skin versus Sandwich

Jack C. Joanides, Stanley C. Mellin, and Leslie M. Lackman
North American Aviation, Inc.

THE MOST WIDELY used wing structures are the wide column and plate constructions. Most wide column structures have been stringer panels which are stabilized at intervals by ribs. Plate construction is characterized by thick cover plates supported by a series of longitudinal webs. Both types of structure have proved successful for aluminum aircraft.

With the advent of Mach 3 aircraft, materials being considered are steel and titanium. Both materials are denser than aluminum and, therefore, need higher strengths in order to achieve strength/weight ratios similar to those experienced with aluminum.

Titanium and steel alloys already available exceed the tension strength-to-weight ratio of aluminum. For compression, the strength-to-weight comparison with aluminum is not as favorable. For both plate and stringer panel construction, the use of higher-strength material will reduce the equivalent thickness. This decrease in the thickness of material tends to lower the allowable compression stress that can be developed. Compression stability allowables are typified by the equation.

$$F_{cr} = \frac{k \quad \pi^2 E}{12\,(1-\mu^2)} \qquad \left(\frac{t}{b}\right)^2 \qquad (1)$$

(Symbols are identified in the appendix.) For the same structural width b and for equal weight, the ratio of the elastic buckling stress of steel to aluminum is approximately

$$\left(\frac{F_{STL}}{F_{AL}}\right)_{cr} = \frac{E_{STL}}{E_{AL}} \qquad \left(\frac{1/3\ t_{AL}}{t_{AL}}\right)^2 = \frac{1}{3} \qquad (2)$$

This indicates a need for more sophisticated stiffening systems. Two such systems are the integrally stiffened grid plate and honeycomb sandwich. This paper will be concerned with the efficiencies of these two types of structure.

Numerous papers have been presented comparing the structural efficiency of wings. Most of these studies have presented the unit weight or the solidity of the structure versus structural index parameters such as N/b_s and N/h. This type of chart provides a very rapid estimation of the comparative unit weights which can be summed up to obtain wing box weights. The simplicity of these charts is possible because the internal loading is usually limited to spanwise bending moments. Compression and tension covers of most straight wings and swept wings with high-aspect ratios are designed by spanwise bending. However, the wing planform chosen for this study (as shown in Fig. 9) is a delta wing with an aspect ratio less than two. Chordwise bending moments are

significant on this wing as will be shown in the detail internal wing loads.

Design Mission and Insulation Requirements

The thermal stability limits of JP-6 are such that any prolonged periods of flight at supersonic Mach numbers require thermal protection from aerodynamic heating. This protection is required to prevent fuel vaporization and/or to conserve the sensible heat available in the fuel for use as a coolant for equipment aboard the aircraft. The fuel vaporization problem may be eliminated, within practical limits, if the fuel tanks are pressurized. The amount of thermal protection required may be reduced by the proper sequencing of the fuel, providing the limits of travel in center of gravity of the aircraft are not violated. It is apparent that an aircraft designed to operate at supersonic Mach numbers must have a thermally optimized fuel system.

Thermal protection of fuel is a very important structural consideration in the design of Mach 3 aircraft. This is because insulation requirements can be an important item in the total weight. Pressurization of the fuel tanks reduces insulation requirements but adds weight to the wing skin panels.

The lower moment of inertia of the integrally stiffened skin results in high stresses due to bending. Stiffened skin will be designed to a low pressure. The honeycomb design is not as sensitive to pressure stresses and will be designed to a higher pressure.

In order to establish the amount of thermal protection the fuel requires on any given supersonic cruise aircraft, it is necessary to know or assume the following:

1. The design mission profile: altitude, Mach number, and engine fuel flows versus mission time.
2. The order in which the fuel tanks are emptied.
3. The fuel tank geometry: areas wetted by fuel versus pounds remaining.
4. Fuel venting pressurization schedule.

For this paper, it was assumed that a major portion of the fuel aboard the aircraft was contained in the wings. The fuel tank arrangement and the fuel sequencing are shown in Fig. 1. The mission profile is shown in Fig. 2. The fuel tank vent system was assumed to be pressurized during high-speed cruise. The insulation required to prevent fuel boiloff for a 9 psia and a 4 psia vent system has been determined. At these pressures JP-6 fuel vaporizes at approximately 260 F and 190 F, respectively.

The amount of thermal protection required by each of the tanks was determined by setting up a heat balance for each tank and solving for fuel temperature versus time using various thermal conductances. The solution of the differential equations involved in the heat balance was accomplished by use of the IBM 7090 digital computer. The insulation requirements for the conditions assumed are shown in

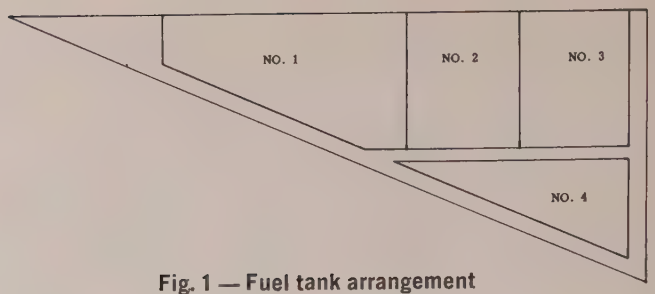

Fig. 1 — Fuel tank arrangement

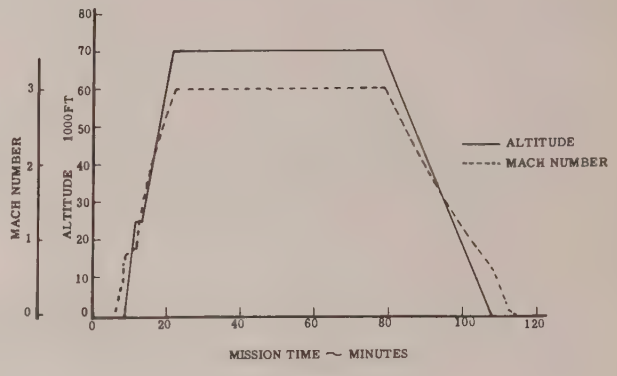

Fig. 2 — Mission Profile

Table 1 - Insulation Requirements

Tank No.	Maximum Permissible Thermal Conductance at 325 F Mean Temp Btu/(hr) (ft^2) (F) 9 psia system	4 psia system
1	No requirement	No requirement
2	5.5	3.7
3	8.3	5.2
4	No requirement	No requirement

Table 1. For the thickness of brazed honeycomb or fiber glass necessary to meet the requirements listed in the foregoing chart, Fig. 3 was used.

No attempt has been made to completely optimize the insulation requirements on the wing tanks presented in this paper. To obtain an optimum insulation configuration, the fact that the maximum aerodynamic heating rate occurs on the lower surface of the wing, must be considered. This requires more insulation on the lower surface of the wing and a lesser amount on the top. This method of insulation also aids in reducing the effect of aerodynamic heating on the fuel during the emptying period of the tank. Actually, from a heat transfer standpoint, the wing is the most inefficient fuel stowage space in an aircraft because the geometry of most wings results in the highest aerodynamically heated area per pound of fuel of any fuel stowage area in the aircraft. To offset this, it is the usual practice to empty the fuel con-

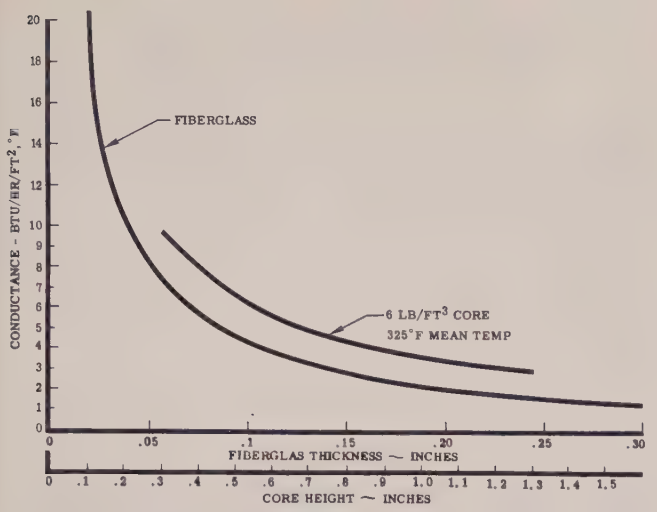

Fig. 3 — Estimated thermal conductance of PH15-7 Mo brazed honeycomb and insulating properties of fiberglass

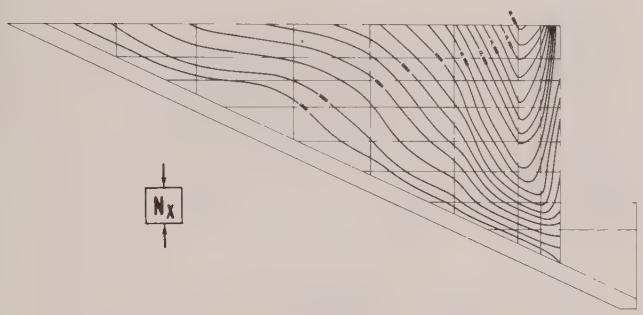

Fig. 4 — Spanwise axial load curves lb/in. — ultimate

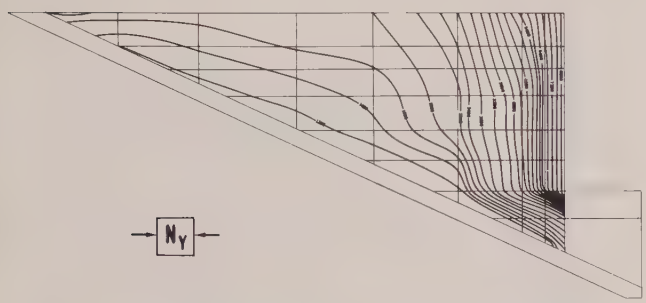

Fig. 5 — Chordwise axial load curves lb/in. — ultimate

tained in the wings early in the mission if the center of gravity of the aircraft allows.

Wing Loading

By optimization of the climb and descent speeds through the lower altitudes, the design speed-altitude profile can be determined so that both the gust and maneuver loads may have nearly equal influence on the structural design. Gust conditions would generally be critical on the forward portion of the wing and maneuver conditions would be critical for the aft portion. A composite design condition using these

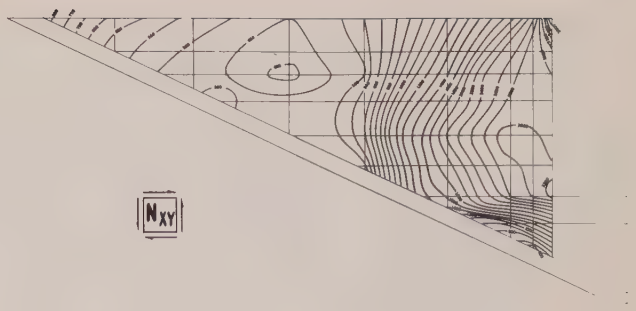

Fig. 6 — Skin panel shear flows lb/in. — ultimate

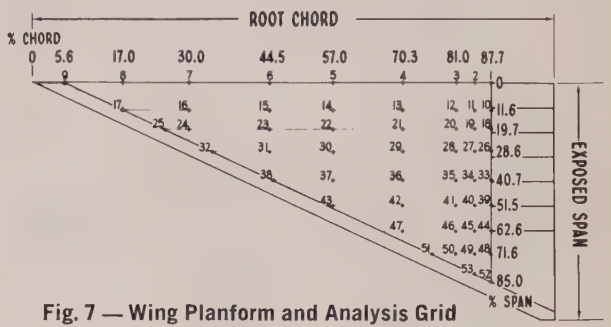

Fig. 7 — Wing Planform and Analysis Grid

two loading conditions is used for the analysis. This results in the spanwise and chordwise compression loads and skin shear flows shown on Figs. 4, 5, and 6. The structure will be sized for these loads at each of the 53 grid point locations shown in Fig. 7. Unit vertical shears at the 53 grid points are tabulated in Table 2.

There is a 30-40 F temperature differential between the lower skin panel and the upper skin panel. This difference will be neglected and the structure will be optimized for these loads at a uniform structure temperature of 480 F. Requirements for the bottom wing covers result in skin thicknesses very nearly the same as the top cover. Therefore, for this study, the wing structure will be optimized for the bottom covers having the same loading as the top covers.

Material Properties

Properties of the materials investigated for skin panels and spars are shown in Fig. 8 and Table 3.

Wing Spar Webs

The structural index curves shown in Fig. 9 represent the three types of shear webs considered in this study. These are:

1. Corrugated panel.
2. Honeycomb sandwich.
3. Sheet-stiffened skin.

The purpose of these curves is to readily compare the different types of spars without the effect of attaching members and minimum gage restrictions

Table 2 - Unit Vertical Shears at 53 Grid Points

Grid Point	Unit Shear P_s - lb/in.	Grid Point	Unit Shear P_s - lb/in.
1	10,000	28	1,800
2	5,700	29	730
3	2,920	30	650
4	1,050	31	500
5	870	32	260
6	870	33	5,510
7	800	34	3,140
8	650	35	1,420
9	650	36	650
10	7,920	37	510
11	4,870	38	290
12	2,290	39	4,720
13	970	40	2,310
14	800	41	1,090
15	760	42	520
16	650	43	380
17	410	44	3,450
18	7,120	45	1,550
19	4,300	46	610
20	2,020	47	300
21	810	48	1,250
22	710	49	800
23	650	50	460
24	500	51	300
25	400	52	700
26	6,540	53	300
27	3,650		

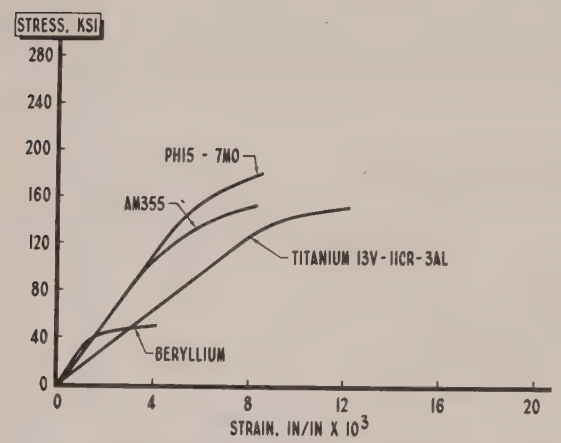

Fig. 8 — Compressive stress — strain curves — 480 F

The equivalent allowable shear stress (F_{seq}) was computed using the effective thicknesses and then adjusted for different densities. The material used for the basis of these curves is all-beta titanium alloy.

Table 3 - Material Properties at 450 F

Material Properties	PH15-7M6	AM-355	All-Beta Titanium	Beryllium
Density (lb/in.^{3})	0.277	0.282	0.175	0.066
Thermal Conductivity Btu / (in.) (hr) (ft^2) (F)	124	126	68.4	1073
Coefficient of Thermal Expansion (in./in.) / 10^{-6}	6.1	6.65	5.4	7.36
Poisson's Ratio	0.30	0.31	0.33	0.03
Heat Treatment (psi)	200,000	200,000	185,00	None
F_{TU} (KSI)	182.5	183	162	61.3
F_{TY} (KSI)	162	133	148	51
F_{CY} (KSI)	176	143	148	46.5
F_{SU} (KSI)	117.5	119.8	97.2	39.4
$E_T/10^6$	27.1	26.75	15.8	40.5
$E_C/10^6$	28.1	27.75	15.8	40.5
$G/10^6$	10.63	10.38	5.94	20
*$F_{0.7}$	182	146	150	37
*$F_{0.85}$	165	125	147	34

*Ramberg-Osgood Stress-Strain Parameters

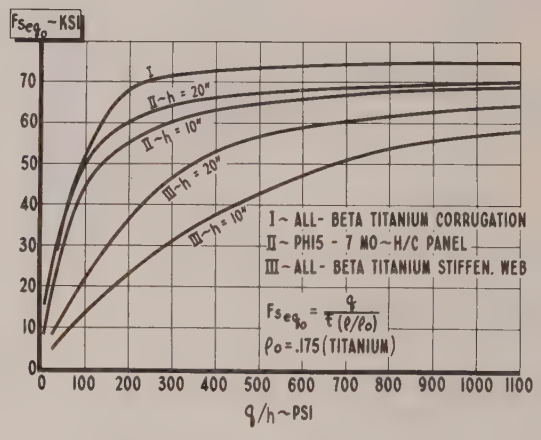

Fig. 9 — Efficiency of shear webs at 480 F

A direct weight comparison can be made from these curves to select the optimum type of shear web. On this basis, the corrugated panel was chosen as the optimum spar web for this study.

Utilizing the structural index curves from Fig. 9, each grid point was sized for optimum thickness by assuming various spar spacings. For practical reasons, a minimum gage of 0.01 in. was imposed on the corrugated panels. The ef-

fective thickness of the spar was computed from the equation

$$\bar{t}_{spar} = \frac{(q/F_{seq}) \times h/2}{b} \quad (3)$$

The effect of including the spar-to-skin attachments in the selection of optimum spar spacing was considered. This was accomplished by adding the effective thickness of the attachments to the effective thickness of the spar ($\bar{t}_{spar}$).

$$\bar{t}_{attach} = \bar{t}_{spar}\,(4/h + 1/b) \quad (4)$$

Integrally Stiffened Plate Covers

The waffle-like stiffened skin is illustrated in Figs. 10 and 11; the assumptions made in the minimum weight analysis of the stiffened skin construction are as follows:

1. The effect of asymmetry which induces bending under axial load before buckling is neglected. Crawford has shown, for a one-sided stiffened system, that although bending is produced by the application of axial load, the critical stability load is essentially the same (13).

2. In computing the elastic constants of the integral waffle-like stiffening from Ref. (4), the shearing and twisting stiffnesses of the ribs are assumed to be zero (that is, β and β' are equal to zero). Seide investigated this assumption for a typical 45 deg skew-angle configuration and found the approximate method to be adequate (4).

3. The effect of the fillet radius, r_w, and the cutting head radius, r_1, are neglected in the optimization, but the weight due to r_w and r_1 is included in the final weight of the wing.

It is assumed that local buckling failure will occur on a 45 deg plane. At about 1/2 of the grid points, the biaxial loads are far from being equal, which means that the principal stress plane is not about 45 deg. These grid points were investigated when the optimum stress on the 45 deg plane was at compression yield. It was found that the stress did not exceed tension ultimate at any other plane. Since one aircraft requirement is that there be no failure at ultimate load, this assumption seems reasonable.

Minimum Weight Analysis - From Figs. 12 and 13, the following relationships are obtained:

$$N'_y = \frac{(N_x + N_y)}{2} - N_{xy} \quad (5)$$

$$N'_x = \frac{(N_x + N_y)}{2} + N_{xy} \quad (6)$$

$$N'_{xy} = \frac{(N_x - N_y)}{2} \quad (7)$$

where + direction of forces is shown in Figs. 12 and 13.

The critical stress for a rib fixed on the bottom, simply supported at the ends, and free on the other edge, is

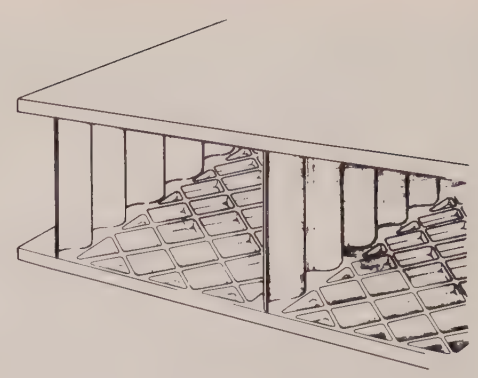

Fig. 10 — Stiffened sheet structure

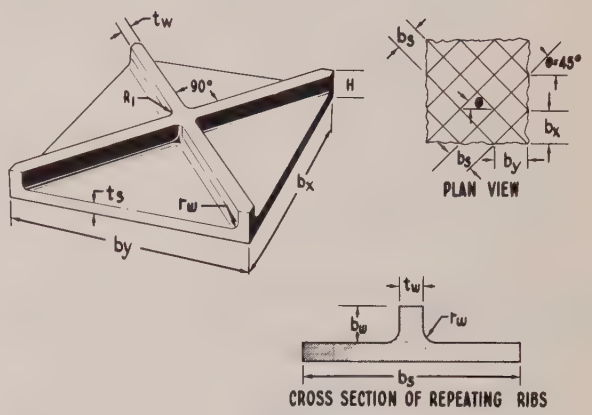

Fig. 11 — Integrally stiffened plate

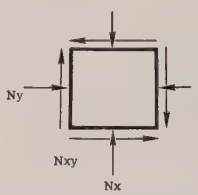

Fig. 12 — Direction of forces

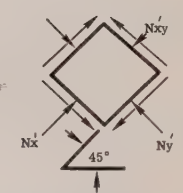

Fig. 13 — Direction of forces

$$f_x = \frac{1.3\pi^2}{12\,(1-\mu^2)}\,\frac{E}{(t_w/b_w)^2} \quad \text{(neglecting fillet radius)} \quad (7a)$$

$$\eta = E_T/E, \text{ with } f_x \leq F_{cy} \quad (7b)$$

The critical buckling coefficients for a plate with ends clamped a/b = 1 are

$$K_{cy} = K_{cx} = 10.4,\ K_s = 14.71 \quad (8)$$

The relationship between the in-plane buckling loads may be expressed by the following interaction equation:

$$\frac{f'_x}{F'_x} + \frac{f'_y}{F'_y} + \left(\frac{f'_{xy}}{F'_{x_{\bar{y}}}}\right)^2 = 1 \quad (9a)$$

where:

$$F'_x = F'_y = 10.4\,\pi^2\eta E\,(t_s/b_s)^2/12\,(1-\mu^2) \qquad (9b)$$

$$F'_{xy} = 14.71\,\pi^2\eta E\,(t_s/b_s)^2/12\,(1-\mu^2) \qquad (9c)$$

Substitution of Eqs. 9b and 9c into 9 a yields

$$f'_x = -\frac{\left(\frac{1}{F'_x} + \frac{\alpha}{F'_y}\right) + \sqrt{\left(\frac{1}{F'_x} + \frac{\alpha}{F'_y}\right)^2 + \frac{4(\phi)^2}{F'_{xy}}}}{2\,(\phi)/F'_{xy})^2}$$

where:

$$\alpha = \frac{\frac{(N_x + N_y)}{2} - N_{xy}}{\frac{N_x \times N_y}{2} + N_{xy}} \qquad (9d)$$

$$\phi = \frac{\frac{(N_x - N_y)}{2}}{\frac{(N_x + N_y)}{2} + N_{xy}} \qquad (9e)$$

Equating the two local allowables and neglecting the effect of plasticity yields

$$r_t = r_b \left[\frac{-\frac{1+\alpha}{10.4} + \sqrt{\left(\frac{1+\alpha}{10.4}\right)^2 + 4(\phi/14.71)^2}}{2.6\,(\phi/14.71)^2} \right]^{1/2} \qquad (10)$$

The average thickness of the plate neglecting r_w and r_1 is

$$\bar{t} = t_s\,(1 + 2r_b r_t) \qquad (11)$$

The effective load carrying thickness neglecting r_w is

$$t_a = t_s\,(1 + r_b r_t) = N'_x/t_x \qquad (12)$$

General instability equations for wafflelike stiffened plates simply supported with a/b = ∞ are as follows:

1. Shear equations from Ref. (6)

$$N_{xy_{allow.}} = C_a D_1/(b/2)^2 \qquad \text{If } x < 1 \qquad (13a)$$

$$N_{xy_{allow.}} = \frac{C_b\sqrt{D_1 D_3}}{(b/2)^2} \qquad \text{If } x \geq 1 \qquad (13b)$$

where:

$$x = u_y + 2D_K/D_1 \qquad (13c)$$

$$C_a \doteq 8.0 + 6.0x - .8x^2 \qquad (13d)$$

$$C_b \doteq 13.3 - .3x \quad \text{for } 1 \leq x \leq 5 \qquad (13e)$$

$$C_b \doteq 11.8 \quad \text{for} \quad x > 5 \qquad (13f)$$

2. Biaxial compression equation from Ref. (14).

$$N_{x_{allow.}} = \frac{\pi^2}{b^2}\left\{(K_c - 2)\left[D_1 D_2\left(1 - \frac{b^2 N_y}{\pi^2 D_2}\right)\right]^{1/2} + 4D_K + 2u_y D_1\right\} \qquad (14)$$

where for a/b = ∞ $K_c = 4.0$

Using the relationships obtained in Eqs. 5 to 14, the following optimum weight analysis was programmed on an IBM 7090.

1. Vary spar spacing (b values of 6, 9, 12, 15, and 18 in. were used).
2. Vary r_b (r_b varied from 0.05 to 1.50 in program).
3. For each value of r_b, calculate r_t from Eq. 10.
4. With a value of (b_w/t_w), calculate f_x allowable from Eq. 7a. (From Eqs. 7a, 11, and 12, it is obvious that the higher the value of (t_w/b_w), the lower the value of t; therefore, in the IBM 7090 program, $(b/t)_w$ first value was taken as 1 and varied to 200.)
5. Calculate t_s from Eq. 12.
6. Calculate the values of b_s, t_w, b_w.
7. Calculate D_1, D_K, μ_y (note that $D_1 = D_2$, $\mu_y = \mu_x$). Equations for these constants are given in Ref. (2), with the values of $\beta' = \beta' = r_w = 0$.
8. Calculate $N_{x_{allow.}}$ from Eq. 14; Ref. (3) suggests the following plasticity correction:

$$N_{x_{plast.}} = N_{x_{allow.}} \quad \frac{^{x}E_{sec}}{E} \qquad (15)$$

where:

$$E_{sec} = \frac{\sigma}{\epsilon}, \quad \epsilon = N_{x_{allow.}} \quad /E_1$$

and σ stress corresponds to ϵ on material property stress strain curve

9. Calculate $N_{xy_{allow.}}$ from Eq. 13a or 13b, depending on value of x; Ref. (3) suggests the following plasticity correction:

$$N_{xy_{plast.}} = N_{x_{allow.}} \times \frac{G_{sec}}{G} \qquad (16)$$

where:

$$G_{sec} = \frac{T}{\gamma'}, \quad \gamma' = \frac{N_{xy_{allow.}}}{G_K}$$

and T shear corresponding to on material property curve.

10. Calculate $N_{x_{cr}}$ from the following interaction equation:

$$N_{x_{cr}} = \left[1 - \left(N_{xy}/N_{xy_{plast.}}\right)^2\right] N_{x_{plast.}} \qquad (17)$$

11. If $N_{x_{cr}}$ is less than actual applied N_x, go back to step 4 and take larger value of b_w/t_w. This procedure is con-

tinued until $N_{x_{cr}} \geq N_x$.

12. Select new value of r_b in step 2 and repeat process. Fig. 14 shows the results for grid point 6.

13. After $\bar{t}_{skin}$ has been found for all values of r_b, a new value for the spar spacing is taken (step 1) and the whole process is repeated. Fig. 15 portrays the results of stiffened skin sizing calculations for grid point 6. (See Fig. 9.) $\bar{t}_{skin}$ is plotted versus spar spacing for the AM355 material.

14. The final step in the optimization program is the summation of the stiffened skin weight and the spar weight. The titanium spar weights are converted to an effective steel thickness as shown in the $\bar{t}_{spar}$ curve in Fig. 15. The summation of the t_{skin} and the $\bar{t}_{spar}$ yields a total $\bar{t}$ for each spar spacing. The lowest point of the $t_{skin} + \bar{t}_{spar}$ curve (Fig. 15) gives the minimum $\bar{t}$ for grid point 6.

Fig. 16 shows typical cross sections of optimized stiffened sheet under three conditions of loading.

Honeycomb Sandwich Covers

Honeycomb sandwich panels can fail by general instability of the total panel or local instability of the facing sheets. Equations will be developed to determine the facing sheet thickness and core density required to prevent the two modes of failure for given loads, geometry, and properties.

General Instability

Uniaxial Compression - The failure of a honeycomb panel by general instability due to uniaxial compression can be predicted by the formula (Ref. 7):

$$\frac{F_{c_{cr}}}{\eta} = \frac{E_f \pi^2 D}{E_1} K \qquad (18)$$

where

$$K = K_F + K_M \qquad (19)$$

and

$$D = \frac{E_f}{12(1-\mu^2)} \left[3t_f^2 \frac{(2c + 2t_f)^2}{2t_f} + 2t_f^3 \right] \qquad (20)$$

$$D = \frac{E_f c^2 t_f}{6(1-\mu^2)} \left[3 + 6K_t + 4K_t^2 \right] \qquad (21)$$

in which

$$K_t = \frac{t_f}{c} \qquad (22)$$

Eqs. 20 through 22 assume that the two facing sheet thicknesses are equal and that the core has no flexural rigidity.

The extensional stiffness of the panel, neglecting the modulus of elasticity of the core, is

$$E_1 = 2t_f E_f \qquad (23)$$

Substituting Eqs. 21, 22, and 23 into Eq. 18 yields

$$\frac{F_{c_{cr}}}{\eta} = \frac{K \pi^2 E_f}{12(1-\mu^2)(b/c)^2} \left[3 + 6K_t + 4K_t^2 \right] \qquad (24)$$

Assuming K_f is negligible an can be ignored, $K = K_m$. K_m for a simply supported panel can be found from the fol-

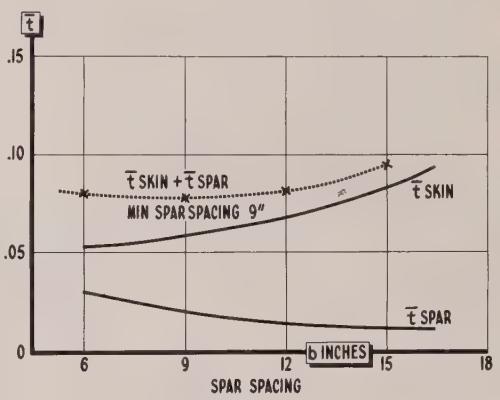

Fig. 15 — Optimization of wing box at grid point No. 6

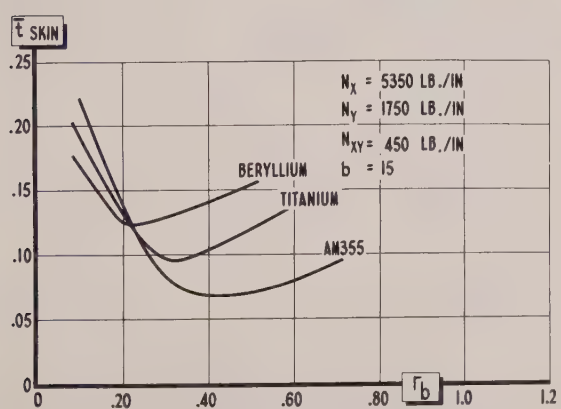

Fig. 14 — Optimization of ± 45 deg grid — grid point No. 6

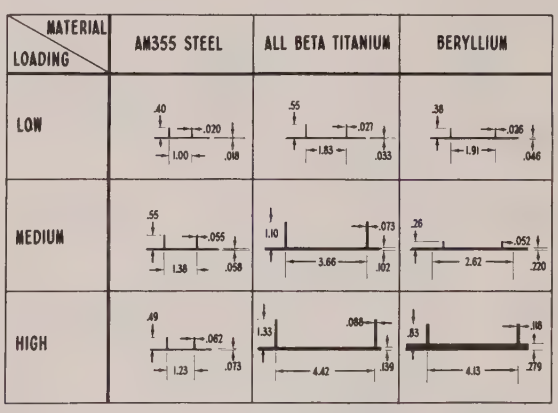

Fig. 16 — Typical cross section of optimized stiffened sheet structure

lowing equations:

$$K = K_m = \frac{1 + (a/bm)^2}{1 \quad + (bm/a)^2} \tag{25}$$

$$J = \frac{2\,(b/c)^2\, G'_c\,(1 - \mu^2)}{\pi^2\ E_f\ K_t} \tag{26}$$

assuming that the quantity

$$\left[3 + 6K_t + 4K_t^2\right] = 3(1 + K_t)^2 \tag{27}$$

If K_t^2 is negligible, Eq. 24 becomes

$$\frac{F_{c_{cr}}}{\eta} = \frac{K\ \pi^2\ E_f\,(1 + K_t)^2}{4\,(b/c)^2\,(1 - \mu^2)} \tag{28}$$

Shear - The formula for the citical shear stress in the plane of the panel is: (7)

$$F_{s_{cr}} = \frac{\pi^2\ G_f\ D}{b^2\ N_s}\quad K_s \tag{29}$$

where

$$K_s = 4/3\left[\frac{4 + 3\,b^2/a^2}{1 + (1/3J)\,(13 + 9b^2/a^2)}\right] \tag{30}$$

for the simply supported case, and

$$J = \frac{2\,(b/c)^2\ G'_c\ (1 - \mu^2)}{\pi^2\ E_f\ K_t\ (1 + K_t)^2} \tag{31}$$

The panel flexural rigidity is, of course, identical to that shown in Eq. 21:

$$D = \frac{E_f\ c^2 t_f}{6\,(1 - \mu^2)}\left[3 + 6\ K_t + 4K_t^2\right] \tag{32}$$

$$N_s = G_f\,(d - c)$$

and

$$\frac{F_{scr}}{\eta} = \frac{K_s\ \pi^2\ E_f\,(1 + K_t)^2}{4\,(b/c)^2\,(1 - \mu^2)} \tag{33}$$

Biaxial Compression - The basic plate buckling equation for biaxial compression is

$$\frac{N_x\,(m/a)^2}{E_R}\left[\left(\frac{m^2}{a^2} + \frac{n^2}{b^2}\right)\frac{\pi^2\ E_R}{G'_c\ c}\cdot\frac{t_f\,(c + t_f)^2}{2\,(1 - \mu^2)} + 1\right]$$

$$+ \frac{N_y\,(n/b)^2}{E_R}\left[\left(\frac{m^2}{a^2} + \frac{n^2}{b^2}\right)\frac{\pi^2\ E_R}{G'_c\ c}\cdot\frac{t_f\,(c + t_f)^2}{2\,(1 - \mu^2)} + 1\right]$$

$$= \frac{t_f\,(c + t_f)^2}{2\,(1 - \mu^2)}\left(\frac{m^2}{a^2} + \frac{n^2}{b^2}\right)\pi^2 \tag{34}$$

This equation can be expressed as

$$\frac{K_x m^2}{m'}\left[\frac{1}{J} + \frac{(a/b)^2}{m'}\right] + \frac{K_y\,(n')^2}{m'}\left[\frac{1}{J} + \frac{(a/b)^2}{m'}\right] = 1 \tag{35}$$

where

$n' = n\,(a/b)$

$m' = m^2 + (n')^2$

$J = G'_c\ cb^2/\pi^2 D$

$D = E\ t_f\,(c + t_f)^2/2\,(1 - \mu^2)$

m = number of half waves in X direction

n = number of half waves in Y direction (36)

The procedure for computing the allowable load is as follows:

1. Compute J (Eq. 36).
2. Find K_X, given

$$\gamma = \frac{K_y}{K_x} = \frac{F_y/\eta}{F_x/\eta} \tag{37}$$

3. Find γ_i from the equation

$$\gamma_i = (1 - \gamma + \gamma^2)^{1/2} \tag{38}$$

4. Find $(F_{c_{cr}}/\eta)/\ KE\ (10^{-6})$

5. $$\frac{F_{c_{cr_x}}}{\eta} = \left[\frac{F_{c_{cr}}/\eta}{KE(10^{-6})}\right]\quad (K_x\ E\ x\ 10^{-6})$$

6. Determine $F_{x_{cr_x}}$. γ_i from the plasticity correction curve (Fig. 17).

7. $$F_{c_{cr_x}} = \frac{F.\,\gamma_i}{\gamma_i} \tag{39}$$

8. $$MS = \frac{F_{c_{cr_x}}}{f_x} - 1 \tag{40}$$

Biaxial Compression and Shear - This type of loading is analyzed by the stress ratio concept, utilizing the approximate interaction equation:

$$R_c + R_s^2 = 1 \tag{41}$$

where

$$R_c = \frac{f_x}{F_{c_{cr_x}}} \quad \text{or} \quad \frac{f_y}{F_{c_{cr_y}}} \tag{42}$$

$$R_s = \frac{f_s}{F_{s_{cr}}} \tag{43}$$

$$\frac{f_x}{\eta},\ \frac{f_y}{\eta},\ \&\ \frac{f_s}{\eta} = (K_x,\ K_y\ \&\ K_s)\ \frac{\pi^2 D}{2b^2 t_f}\ \text{respectively} \tag{44}$$

Local Instability - Honeycomb sandwich panels are subject to two forms of local instability, intracell buckling and face wrinkling.

Intracell Buckling - Intracell buckling is a local instability of the faces. If the face thickness is reduced while the cell size and material are held constant, a value of face thickness will be reached at which the face will buckle between the cell walls. This phenomenon will occur over the entire face of the panel with concave surfaces in all cells.

Because of possible core damage and the precipitation of premature wrinkling failure, the intracell buckle should be prevented. Satisfactory prediction of intracell buckling for uniaxial compression can be made by using the following experimental equation (9).

$$F_{ci} = .9\, E_R\, (t_f/s)^{3/2} \tag{45}$$

where

$$E_R = \frac{2E\ E_T}{E + E_T} \tag{46}$$

A family of typical intracell buckling curves can be seen in Fig. 18.

Wrinkling - A wrinkling failure of a honeycomb facing sheet occurs because of the instability of a thin sheet on an elastic foundation. Two distinct modes of failure are possible, symmetrical and antisymmetrical, as shown in Fig. 19. For large values of K_t, (t_f/c), the wrinkle will be antisymmetrical and the critical stress will be a function of K_t. For small values of K_t, however, the wrinkle will be symmetrical and the critical stress will be a function only of the material properties of the core and face.

$$F_{cw} = 0.5\, (E\eta\, E_C G_C)^{1/3} \tag{47}$$

where

$$\eta = (1/4E)\,(E_s + 3E_t)$$

$$K_t \leq 0.075$$

Biaxial Compression and Normal Pressure - The prime concern for checking a panel with this loading condition will be local stresses induced by bending and shear. However, the of panel deflections on aerodynamic qualities must also be considered.

The bending stresses at the center of the panel can be determined from the following basic equations:

$$K_{mx} = \frac{16\,(a/b)^2}{\pi^4} \sum_{m=1,3}^{\infty} \sum_{n=1,3}^{\infty} \frac{(-1)^{(m+n/2-1)}\,(m^2 + \mu\, n^2 a^2/b^2)}{m' n \left\{ \dfrac{1}{(m')^2 - \left(\dfrac{N_\lambda}{G'_c c\,(1+K_t)^2}\right)\left(J\,(a/b)^2 + m\right)\left(in^2 + \gamma (n')^2\right)} \right\}} \tag{48}$$

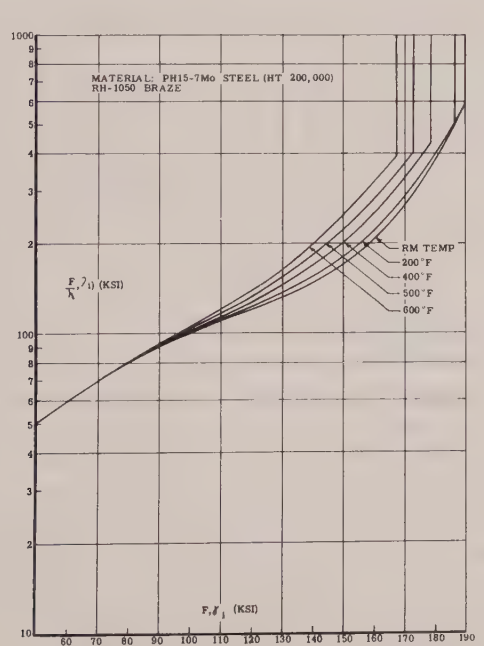

Fig. 17 — F/η versus F, for various δ i

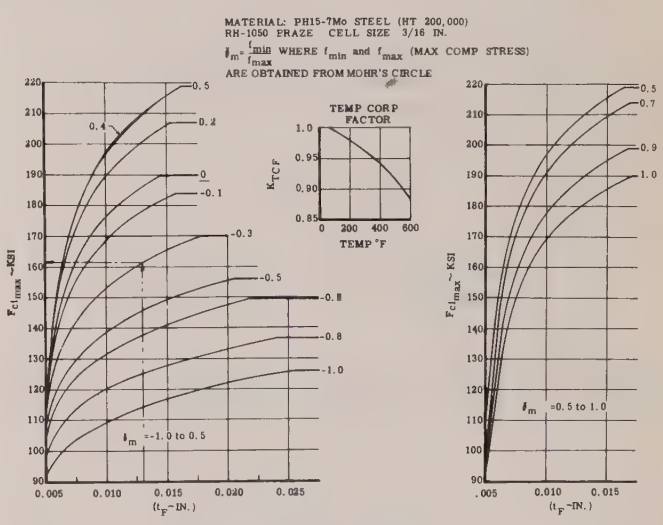

Fig. 18 — Intracell buckling

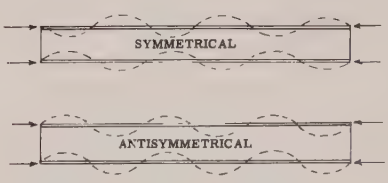

Fig. 19 — Two modes of wrinkling failure

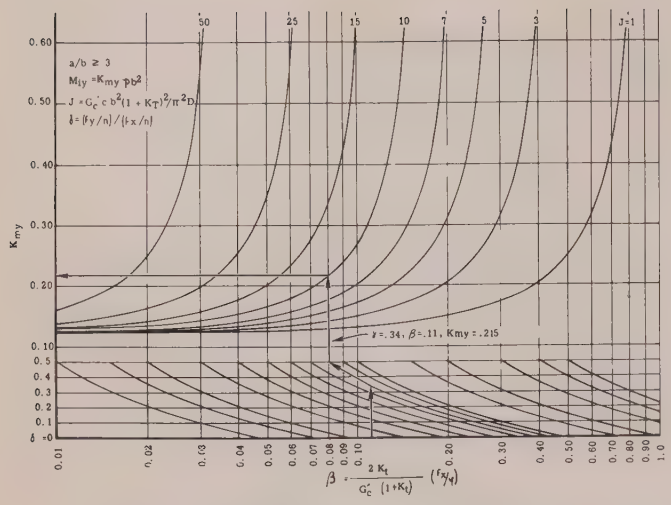

Fig. 20 — Curves plotted to evaluate K_{mx} and K_{my}

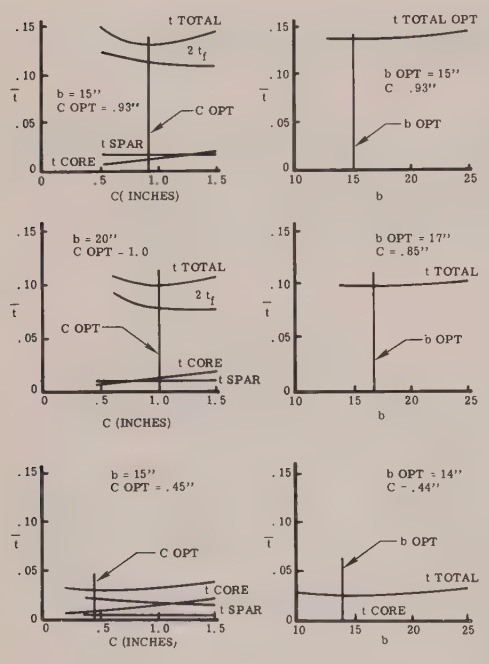

Fig. 21 — Results of computed facing sheet requirements, t_f, added to equivalent t's for core, braze, and spars

$$K_{my} = 16\,(a/b)^2 \sum_{m=1,3}^{\infty} \sum_{n=1,3}^{\infty} \frac{(-1)^{(m+n/2-1)} \left[(n')^2 + \mu m^2\right]}{mn' \left\{ (m')^2 - \left(\frac{N_x}{G'_c\, c\,(1+K_t)^2}\right)\left(J\,(a/b)^2 + m'\right)\left(m^2 + \gamma\,(n')^2\right)\right\}} \quad (49)$$

	LOADING		
	LOW	MEDIUM	HIGH
FACE THICKNESS	.006	.0390	.0573
CORE THICKNESS	.44	.85	.93
SPAR SPACING	14	17	15
SPAR WEB THICKNESS	t_w =.0119	t_w =.0247	t_w =.0340

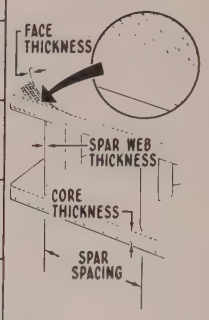

Fig. 22 — Typical cross section of optimized sandwich structure

where

$$M_{ix} = K_{mx} pb^2$$
$$M_{iy} = K_{my} pb^2$$
$$J = G_c c b^2 (1 + K_t)^2/\pi^2 D$$
$$D = E t_f (c + t_f)^2 / 2 (1 - \mu^2)$$
$$\gamma = \frac{f_y/\eta}{f_x/\eta}$$

Curves have been plotted to evaluate K_{mx} and K_{my} (Fig. 20).

The honeycomb panel optimization utilizing the equations developed in this section was performed by an IBM 7090 program. A wing was assumed to have a certain fixed spar spacing and core depth and was sized for this configuration. Spar spacing was varied from 7.5 in. to 30 in., while core depths were varied from 3/8 in. to 1-1/2 in. Twenty wings were sized at each of the 53 grid points. As each individual grid point would require approximately 3/4 of a man-hour for computation, it can be seen that the IBM program was invaluable in this study.

The results of computed facing sheet requirements, t_f, were added to equivalent t's for the core, braze, and spars in Fig. 21. The curves at the left show these summations for typical high, medium, and low load regions; t versus c is plotted for a fixed spar spacing. The low point in the t_{total} curve is, of course, the optimum sizing for the given fixed spar spacing. A direct measure of the penalty for a nonoptimum b/t is shown by comparing t_{total} for the core depths in question.

The effect of the variable spar spacing must be evaluated next. Curves of t versus c are plotted for each spar spacing considered. The optimum point for each of these spar spacings is plotted on the t versus b curves on the right-hand side of Fig. 21. A curve is drawn through these points. It is seen that these curves also have an optimum point. This point determines the optimum spar spacing and core depth for the loading at each grid reference point.

A weight breakdown for the optimum honeycomb wing is shown in Fig. 22.

Conclusions

The structural and insulation requirements for a Mach 3.0 delta winged aircraft have been computed for integrally stiffened wings and a steel honeycomb wing. The comparisons have been made for designs that take advantage of the capabilities of each type of construction.

Panel sizing was affected substantially by chordwise loads and pressure loads. The result is a decrease in the optimum spar spacing, as compared to the optimum for uniaxial loading and an increase in total wing weight. Because of the smaller moment of inertia of the integrally stiffened skin, this type of construction was found to be more sensitive to chordwise loads and pressure loads than the honeycomb panels. Final optimum sizes and spar spacings reflect these effects. (See Figs. 21 and 22.) A realistic optimization of a delta winged aircraft must include more than uniaxial loadings.

This study optimized each of the 53 points for the four wings considered. The weights (shown in Table 4) are based on the optimum configuration for each point. Further study indicates that a practical wing design - one with a minimum of changes in section and spar spacing - would result in very close agreement with the ratios obtained for total wing weights.

The corrugated spar design utilized for this study is a very efficient shear web. The shear web is important in the optimization, as any change in spar weight is reflected in optimum spar spacing and, therefore, total weight.

Insulation requirements are an important factor in the design of a Mach 3.0 aircraft with transport-type mission requirements. The relatively low thermal conductance of honeycomb is an advantage of this type of panel construction. The flat curves in Fig. 21 show that additional core depth and additional insulation can be obtained for little additional weight.

The weight breakdown shown in Table 4 illustrates the supporting structure weights, cover weights, and the weight of insulation for the sum of the left and right wing panels. The future potential of beryllium is well illustrated by these results. This was the lightest wing in spite of the very low compression yield allowable stress of 46,500 psi. The efficiency of honeycomb sandwich construction is also well illustrated by the fact that it is only 10% above the beryllium wing weight, while the AM-355 stiffened skin wing is about 70% greater. Comparison of the titanium stiffened plate with the steel stiffened plate indicates that an all-beta titanium sandwich wing would probably be lighter than the PH15-7Mo wing. Advancement of the state-of-the-art of brazing high-strength titanium alloys is indicated.

Table 4 - Wing Weight Breakdown

Wing	PH-7 M0 Sandwich	Integrally Stiffened Skin AM-355	All Beta Titanium	Beryllium
Spars	1500	2758	2422	1822
Insulation plus retainer	0	1800	1800	1800
Top & bottom wing covers	9465	12712	10142	6421
Total Wing weight	10965	17270	14364	10043

Appendix I — Symbols

a - Width or length of loaded or unloaded edge of panel (in.)
b - Width or length of loaded edge of panel (in.)
b_s - Spacing of skew ribs (in.)
b_w - Rib height (in.)
c - Depth of core or subscript denoting core (in.)
d - Total panel thickness (in.)
D_K - Twisting stiffness relative to x and y directions
D_1 and D_2 - Bending stiffness in x and y directions, respectively
E - Facing sheet modulus of elasticity in compression
E_1 - Extensional stiffness = E (d-c)
E_R - Reduced modulus of faces (psi)
E_S - Secant modulus from compression stress-strain curve (psi)
E_T - Tangent modulus of faces (psi) from compression stress-strain curve
f - Subscript denoting facing sheet
f_s - Calculated shear stress (psi)
f_x - Calculated stress in x direction (psi)
f_y - Calculated stress in y direction (psi)
f'_x - Applied local compressive stress (psi)
f'_y - Applied local compressive stress (psi)
f'_{xy} - Applied local shear stress (psi)
F_{ccr} - F_{ccr_x} - F_{ccr_y} - Compression panel buckling stress
F_{scr} - Critical buckling stress for shear (psi)
F_{ci} - Compression intracell buckling stress in faces of honeycomb panel (psi)
F_{cw} - Compression panel wrinkling stress in faces of honeycomb panel (psi)
F_{cy} - Compression yield stress (psi)
G_f - Shear modulus of facing sheet (psi)
G_K - Shear stiffness of plate in xy plane
G'_c - Core shear modulus (psi)
H - Overall height of skin plus ribs
J - A parameter representing the ratio of shear to flexural stiffness
K, K_s, K_x, K_y, K_m - Panel buckling coefficients, constant
K_{1y}, K_{1x} - Coefficients in local plate buckling equation for compression
K_{mx}, M_{my} - Pressure bending moment coefficients
m - Number of buckled half waves in x direction
$m' = m^2 + (n')^2$

M_{ix}, M_{iy} - Bending moment per inch in the x and y directions
MS - Margin of safety
n - Number of buckled half waves in Y direction
$n' = n\,(a/b)$
N_x, N_y, N_{xy} - Load per in. (lb per in.)
P - Axial load (lb)
r_b - Ratio of b dimension of stiffener and skin ($r_b = {}^{D}w/b_s$)
r_t - Ratio of t dimension of stiffener and skin ($r_t = {}^{t}w/t_s$)
r_w - Skew rib fillet radius (in.)
r_1 - Cutting head radius (in.)
R_c - Compression stress ratio f_c/F_c
R_s - Shear stress ratio f_s/F_s
t_a - Effective in-plane load-carrying thickness (in.)
t_s, t_f - Single spacing sheet thickness (in.)
t_w - Rib thickness
τ - Effective thickness of stiffened plate (in.)
' - (Prime) refers to in-plane loads on 45 deg plane on integrally stiffened skin - primes are defined individually for honeycomb panels
ϵ - Compressive strain
η - Plasticity coefficient
γ - Shear strain, f_y/f_x, or N_y/N_x
γ_i - $(1 - \gamma + \gamma^2)\,1/2$
σ - Compressive stress
F - Shear stress
K_t - t_f/c

References

1. George Gerard, "Minimum Weight Analysis of Orthotropic Plates Under Compressive Loading," Journal of the Aerospace Sciences, Vol. 27, No. 1, January 1960, 21-26.

2. Norris F. Dow, Charles Libore, and Ralph E. Hubka, "Formulas for the Elastic Constants of Plates With Integral Waffle-like Stiffening," NACA Report No. 1195, 1954.

3. Norris F. Dow, L. Ross Levin, and J. L. Troutman, "Elastic Buckling Under Combined Stresses of Flat Plates With Integral Waffle-like Stiffening," NACA, TN 3059, January, 1954.

4. Paul Seide, "The Effectiveness of Integral Waffle-like Stiffening for Long, Thin Circular Cylinders Under Axial Compression, Part I: "Chemically Milled Sheet," Part II: "Mechanically Milled Sheet," Thompson-Ramo-Wooldridge Corp., 1956.

5. Edgar Seydel, "The Critical Shear Load of Rectangular Plates," NACA, TM 705, April 1933.

6. Edgar Seydel, "Wrinkling of Reinforced Plates Subjected to Shear Stresses," NACA, TM 602, January 1931.

7. "Sandwich Construction for Aircraft," Part II, MIL-HDBK-23.

8. Nickolas J. Hoff, "Bending and Buckling of Rectangular Sandwich Plates," NACA, TN 2225, November 1950.

9. C. B. Norris, W. S. Erickson, H. W. March, C. B. Smith, and K. H. Boller, "Wrinkling of the Facings of Sandwich Construction Subjected to Edgewise Compression," Forest Products Laboratory, Report No. 1810, November 1949.

10. P. P. Bijlaard, "Analysis of the Elastic and Plastic Stability of Sandwich Plates by the Method of Split Rigidities," IAS Preprint No. 259.

11. P. P. Bijlaard, "Thermal Stresses and Deflections in Rectangular Sandwich Plates," IAS Preprint No. 777, January, 1958.

12. S. Timoshenko, "Theory of Plates and Shells," McGraw-Hill Publishing Co., Inc., 1940.

13. F. Crawford, "A Theory for the Elastic Deflections of Plates Integrally Stiffened on One Side, NACA, TN 3059, 1956.

14. W. H. Wittrick, "Correlation Between Some Stability Problems for Orthotropic and Isotropic Plates Under BI-Axial and UNI-Axial Direct Stress," The Aeronautical Quarterly, August, 1952.

The NSU-Wankel Rotating Combustion Engine

Dr. Walter G. Froede
NSU Notorenwerye A. G.
Germany

THE PRINCIPLE of the engine is based on certain geometrical relations between trochoidal curves and corresponding envelope configurations. The curves themselves were known to the ancient Greeks.

Rotary mechanisms using trochoidal rotors or housings have been suggested during the last decade of the 19th century. Probably none of these engines was ever built or tested. Most of the combinations consisting of a trochoidal body and a secondary body, shaped according to the envelope, are not very useful for application in a compressor or a combustion engine. The most efficient configuration was found by Mr. Wankel in 1954, comprising an outer body with an inner contour of a two-lobed epitrochoid cooperating with an inner body, the circumference of which is shaped according to the corresponding inner envelope. This combination contains three working chambers which vary their size according to a sinus function. Depending on the shape of the trochoid, which may be outwardly bent all over or may show two waisted sections, the ratio of maximum to minimum volume is designated.

During the development of the engine, it proved favorable to have the outer body stationary, and make the inner body perform a planetary rotary movement. This arrangement is generally called KKM (Kreiskolbenmaschine), and permits the location of the intake and exhaust ports, as well as the spark plug, in a stationary member of the engine. The relative rotation of the inner body without its housing will be easily understood by demonstration in pictures.

The major phases are shown in Fig. 1, which has been published frequently and may be considered to be generally

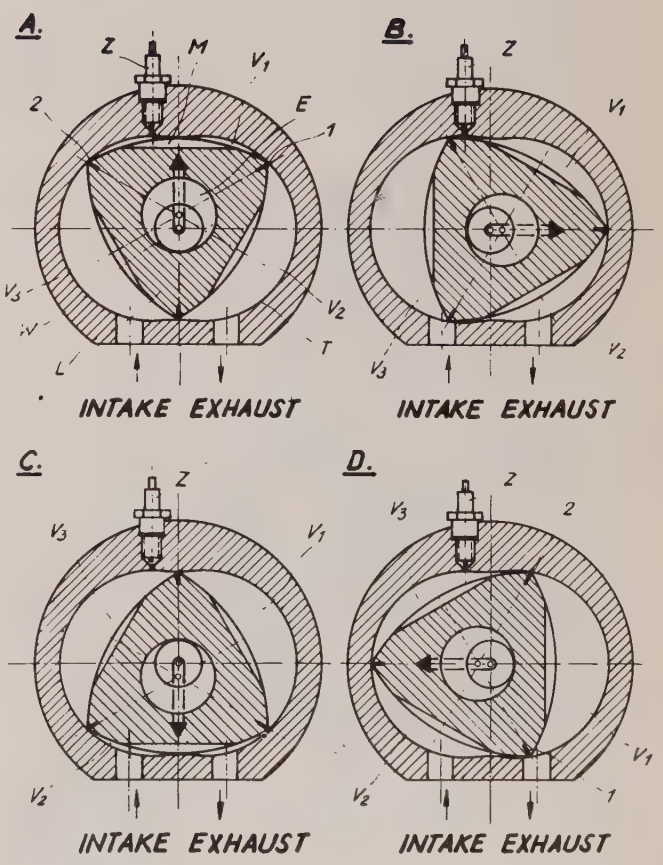

Fig. 1 — Gas change of NSU-Wankel engine using peripheral ports

known. The process of the 4-cycle operation is described on Fig. 1, so that no additional explanation seems to be necessary. Compared to the innumerable suggestions about rotary combustion engines which will be found in literature, the NSU Wankel design shows three basic features which are necessary to provide an adequate function:

1. Low sliding velocities of the sealing elements against the surrounding housing, even at high rpm's.
2. Continuous metal-to-metal contact between sealing elements and housing.
3. The body which is carrying the sealing component must be shaped to permit cooling jackets close to the seal groovings.

All these suppositions are fulfilled with the Wankel layout.

The first KKM, working as a combustion engine, was run on the test stand at Neckarsulm in July, 1958. Starting in October, 1958, the Curtiss Wright Corp. entered a license agreement, and since that time has been executing research development. Although there is only a limited capacity for this basic novel development, the present status appears to be very promising. All experience up to now was gained with the two-lobed epitrochoid, whereas the three-lobed engine is still in the designing stage. For certain applications, a three-lobed type may prove superior.

The shape of the trochoid may be defined by the ratio of the major axis to the minor axis, or by the ratio of the generating radius to the eccentricity, or by the maximal leaning angle between the apex of the inner rotor with regard to the normal on the trochoid. Only a narrow range has been examined up to now.

In all cases, the engines were run on gasoline and combustion was initiated by spark plugs. The possibility of applying the diesel process is still in the planing stage; however, it appears to be promising.

The first publication of the experiments was made in January, 1960, when a full-day symposium was held at Munich, Germany. The first technical paper was printed by the MTZ (Motortechnische Zeirschrift) in February, 1960. These publications, as well as a large number of semitechnical articles in various journals, started a serious discussion about the value and the possibilities of the NSU-Wankel design. Some of the comments given by technical authorities were truly enthusiastic; other were very skeptical and negative. The main arguments against the rotary combustion engine will be dealt with in the following section.

Comparison between Rotary Combustion and Reciprocating Engine

An important difference between the two types is obviously the shape of the combustion chamber in all phases from top dead center to bottom dead center. For the process of combustion, it is important that in the rotating combustion engine the volume, which includes the burning gas, is traveling while the combustion process takes place.

Generally, the rotating combustion engine must be considered as a true positive displacement engine, the working chamber of which includes a precisely defined size with a defined compression or expansion ratio. The compression and expansion takes place within closed and sealed volumes. The swept volume of each working chamber is defined by the difference between minimum and maximum volume.

Compression Limits - The compression ratio is limited by the shape of the trochoid, as demonstrated by Fig. 2. The maximum compression ratio will be obtained if the outer walls of the rotor are shaped exactly according to the inner envelope. Fig. 2 compares three trochoidal shapes with maximal leaning angles of 15, 25, and 50 deg. The first combination shows an epitrochoid which is oval shaped and outwardly bent all over its circumference. The second example demonstrates a slightly waisted curve, whereas the third comprises an almost sharp-edged, waisted portion. All three engines contain the same chamber volume, and by comparison it is obvious that a waisted trochoid permits

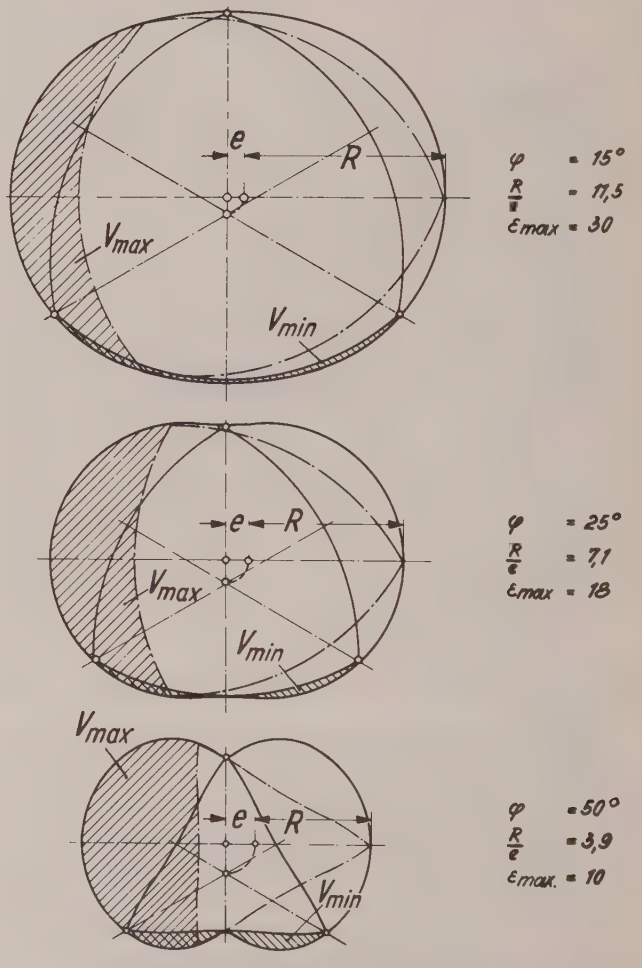

Fig. 2 — 2-lobe epitrochoid with inner envelope effect of trochoid-shape on overall dimension of engines comprising identical swept volume

smaller total dimensions, whereby the maximal possible compression ratio is superior for the oval-shaped layout.

These relations are shown in more detail in Fig. 3, which compares the swept volume and the possible compression ratio for different trochoidal shapes characterized by the maximal leaning angle. Besides the values for the ideal compression ratios, two more curves are drawn, indicating the compression ratio with various sizes of recess in the flanks of the rotor which represent the combustion chamber. If the engine is designed for a diesel process, the useful range for the leaning angle will be between 15 and 20 deg, whereby the volume of the recess should be approximately one-half of the minimum of the working chamber. Engines working on the otto principle may use leaning angles between 20 and 30 deg. They will contain a recess in the rotor flanks of about the same size as a minimum chamber volume. The comparison is based on engines with the same length of the major axes of the trochoid.

Tightness of Sealing System - Almost every comment and criticism emphasizes the fact that, different from the piston ring arrangement in reciprocating engines, the rotating combustion engine has only one sealing line of contact. Therefore, it can never reach the same tightness as a piston inside a round cylinder bore. However, it must be considered that each piston ring requires a gap, which is necessary because of different temperature expansion of piston and cylinder. The sealing system of the rotating combustion engine has no gap, except the required clearance within the fit of all components.

The major difference between the two systems is that a worn piston ring inside a worn cylinder has an enlarged gap, whereas, regardless of wear, the continuous sealing line of contact along the periphery of the rotor stays tight. Actually, the leakage of a reciprocating piston engine is not critical considering the loss of gas and loss of power, which amounts to 0.5% or less of the combustion air. It is necessary to use several piston rings because underneath the gap of ring No. 1 a considerable overheating of the piston surface occurs. A critical zone like this does not exist in the sealing configuration of the rotating combustion engine. The elements of the sealing system, which are shown in the exploded layout in Fig. 4, comprise a radially movable apex seal blade, which is located in a radial groove in the center plane through the apex. Close to both side walls, the radial inner portion is guided in axially movable interconnecting bolts. The side sealing strips extending from apex to apex are in overlapping engagement with these bolts. All parts are preloaded toward the surrounding walls of the housing by wave springs. The main sealing force is produced by the gas pressure itself and, therefore, is variable during the relative movement of the rotor. The end face sealing elements are in contact with the side wall of the housing on a plane surface area, whereas the apex seals possess only a sealing line of contact. Fortunately, the wear along this sealing line is extremely small, due to the fact that the leaning angle be-

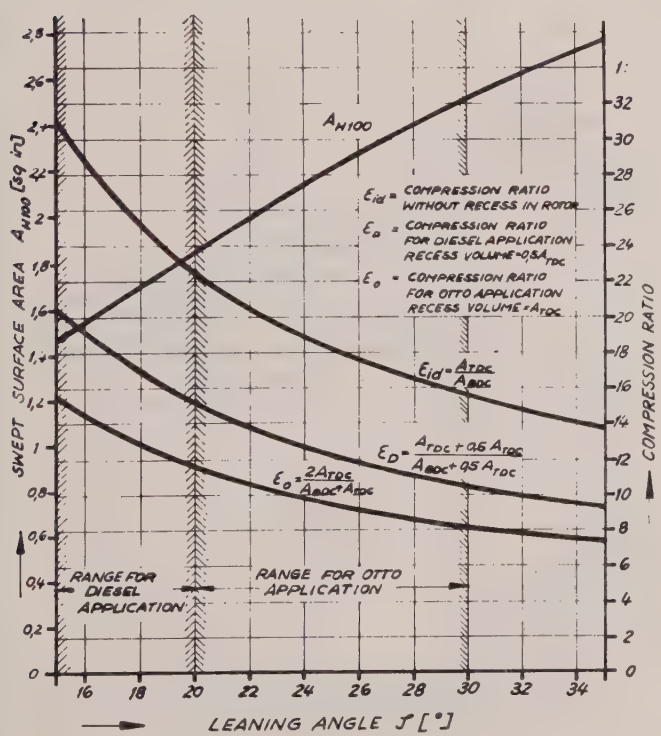
SWEPT SURFACE AREA A_{H100} [sq in.]
COMPRESSION RATIO
A_{H100}
ε_{id} = COMPRESSION RATIO WITHOUT RECESS IN ROTOR
ε_D = COMPRESSION RATIO FOR DIESEL APPLICATION RECESS VOLUME = 0.5 A_{TDC}
ε_o = COMPRESSION RATIO FOR OTTO APPLICATION RECESS VOLUME = A_{TDC}
$\varepsilon_{id} = \frac{A_{TDC}}{A_{BDC}}$
$\varepsilon_D = \frac{A_{TDC} + 0.5\,A_{TDC}}{A_{BDC} + 0.5\,A_{TDC}}$
$\varepsilon_o = \frac{2A_{TDC}}{A_{BDC} + A_{TDC}}$
RANGE FOR DIESEL APPLICATION
RANGE FOR OTTO APPLICATION
LEANING ANGLE γ [°]

Fig. 3 — 2-lobe epitrochoid relation between maximum leaning angle and swept surface area, respectively. Maximal compression ratio based on an engine size of 100 mm for major axis

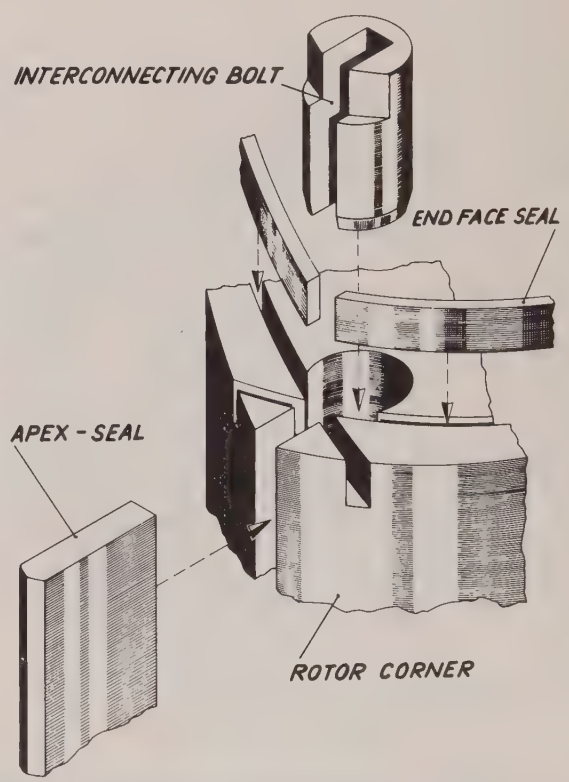

Fig. 4 — Components of seal arrangement

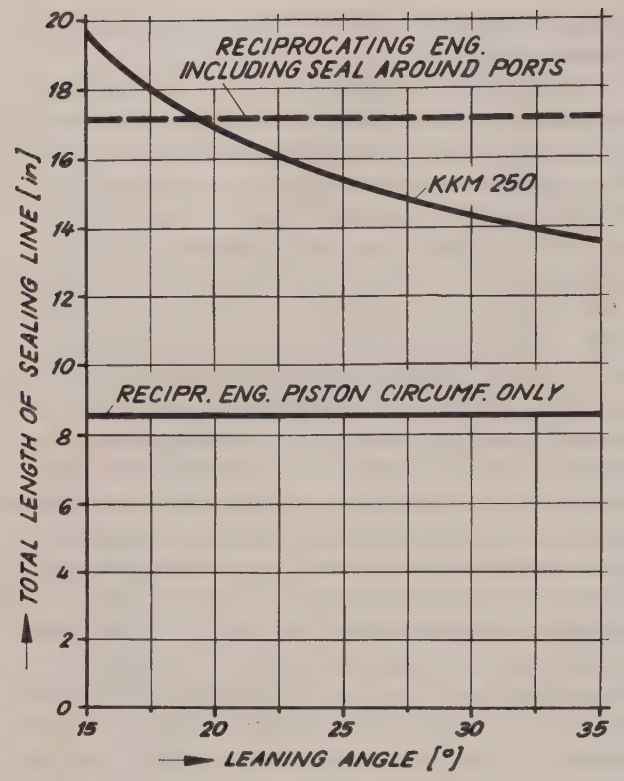

Fig. 5 — Length of sealing line for square reciprocating engine 15.3 cu in. compared to KKM 250 with various leaning angles

tween the plane of the apex seal and the surrounding wall is varying during relative motion of the rotor. By the swinging movement of the apex seal, the line of contact travels around the top of the seal and the metallic contact is to a certain extent reduced by wedge effect of lubricant and gas.

Length of Sealing Line - Another comment which is very frequently presented, refers to the total length of the sealing line. Fig. 5 shows a comparison of the sealing length of a reciprocating engine with a swept volume of 15.3 cu in. and a rotating combustion engine with the same displacement. The diagram depicts that with larger leaning angles - that is, with more waisted shapes of the trochoid - the sealing length is reduced. Applying a leaning angle of 30 deg, the difference in length of sealing contact of a rotary engine as compared to a recipricating engine is only 65%. If the sealing line around the valve seats of a 4-stroke engine is added to the sealing line along the periphery of the piston, the comparison becomes favorable even for the rotating combustion engine.

Surface-Volume Ratio - Another difference in the reciprocating engine is to be found in the surface area of the combustion chamber in the position of top dead center. During this phase, the high temperature causes heat losses to the cylinder walls and the cooling medium. It may be expected that the larger surface area of the rotating combustion engine is a reason for heavy losses. The heat distribution will be considered later, in connection with the test stand results. The actual comparison of surface area is demonstrated in

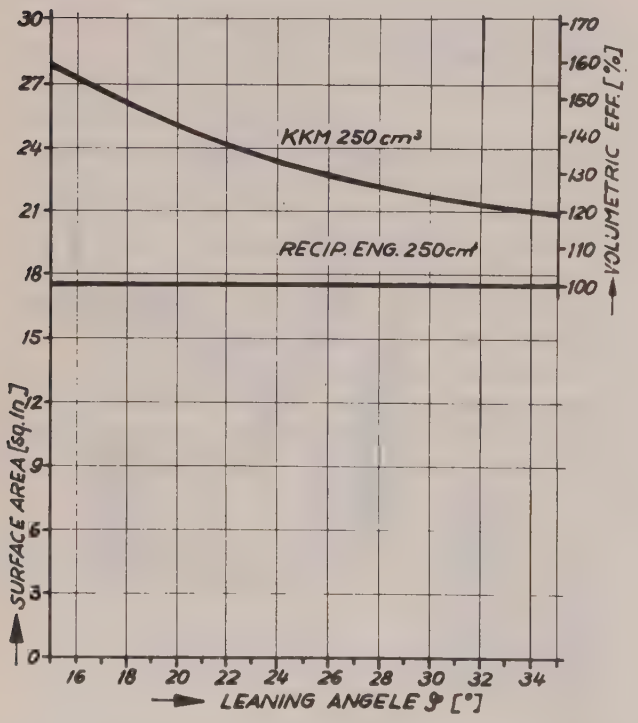

Fig. 6 — Comparison of surface area in tdc between square reciprocating engine to KKM 250 with various leaning angles

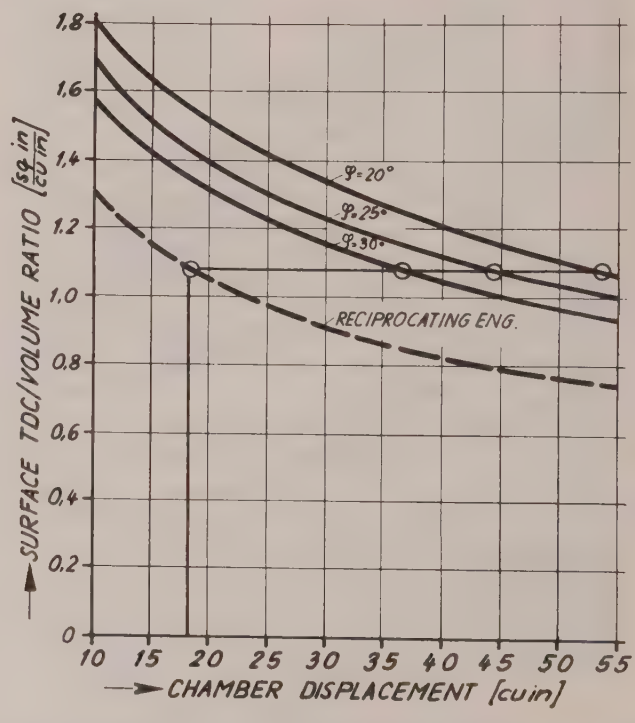

Fig. 7 — Surface per volume ratio for square reciprocating engine and KKM with different leaning angle for various chamber displacement

Fig. 6. Once more, engines are compared with a swept volume of 15.3 cu in. With trochoids of stronger waisted shapes, the difference in surface area gets down to 20-30%.

For the heat losses, it is important to consider the ratio of surface area to the displacement of the working chamber. This is shown in Fig. 7. This ratio becomes more favorable with larger swept volumes of the unit. A reciprocating engine with a cylinder volume of 18 cu in. - which is a frequent size in European automobile engines - shows a surface-to-volume ratio of 0.42. The same ratio can be obtained in a rotating combustion engine with 30 deg leaning angle by enlarging the chamber volume to 36 cu in. This enlargement is not critical, because no inertia forces are limiting the engine size.

Sliding Velocities - A further subject of criticism is a high sliding velocity of the apex seals along the trochoidal surface, which is considered to be far higher than on comparable reciprocating engines.

Fig. 8 shows the actual data, comparing again a 15.3-cu-in. reciprocating and rotating engine size. As demonstrated by the polar diagram around the trochoid, the sliding velocity at 5000 rpm stays between 29-67 fps, whereas the piston speed in the reciprocating engine varies between 0-57 fps. The leaning angle in this case is 23 deg, which is actually embodied in the test engine KKM 250. The graph shows that the maximum sealing velocity of the apex seals is only 16% higher than on the reciprocating counterpart.

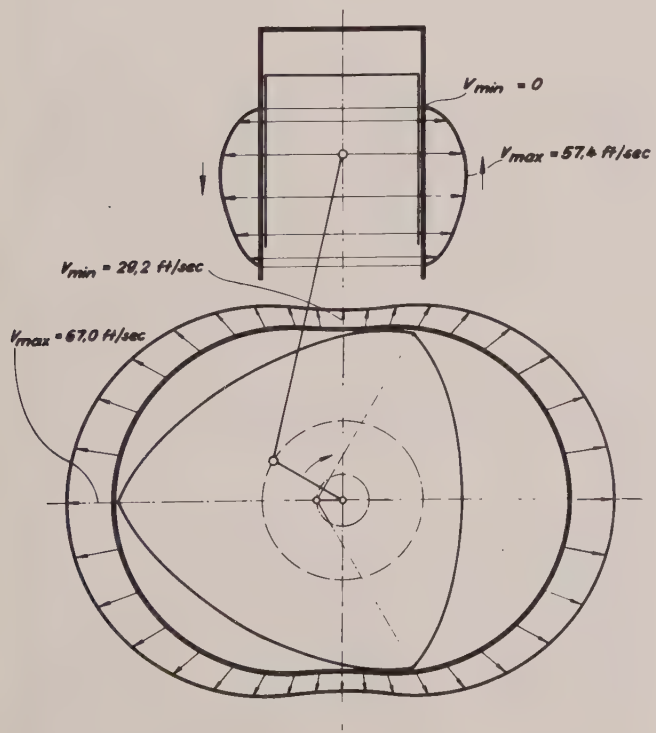

Fig. 8 — KKM 250 — sliding velocities comparing rotating combustion engine and reciprocating engine displacement, 15.2 cu in., 5000 rpm

Technical Data on KKM 250

Description of Layout - The general layout of this engine is shown in Figs. 9 and 10. The engine was designed merely for test stand operation. For this reason, roller and needle bearings were used to reduce the risk of seizing to a minimum. For this engine, the leaning angle was chosen comparatively small, with consequent comparatively high theoretical compression ratio, so that the location and shape of the recesses can be varied widely, whereas no attention was paid to minimum weight.

The peripheral wall, as well as both end walls of the housings, include water jackets for the cooling liquid. The rotor itself is oil cooled. The oil is fed through the hollow shaft and emerges through radial holes in the center plane of the eccentric. After passing the needle bearing which supports the rotor, it flows into the hollow interior of the rotor and pumped out by means of a stationary scoop.

Arrangement of the intake port in the peripheral as well as in the end wall was tested. Generally, a peripheral intake resulted in higher volumetric efficiencies, whereas the side intake helped to reduce the fuel consumption. The exhaust port was in all cases arrenged in the periphery of the center housing with a generally radial direction.

The cooling water flow was kept to approximately 10 gpm, whereas an oil flow of 1 gpm proved to be sufficient for lubrication, as well as for cooling.

The sealing system was modified during the text stand experiments and composed, as already demonstrated by Fig. 4,

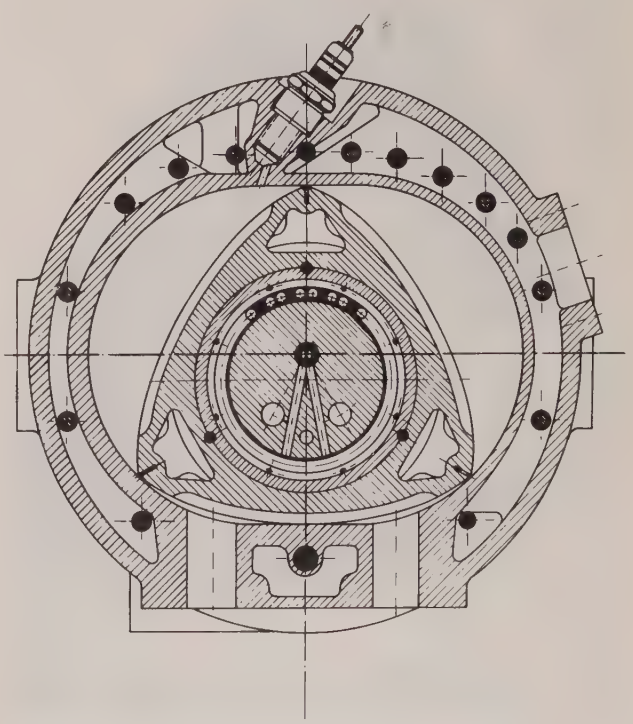

Fig. 9 — KKM 250 — cross section taken in center plane

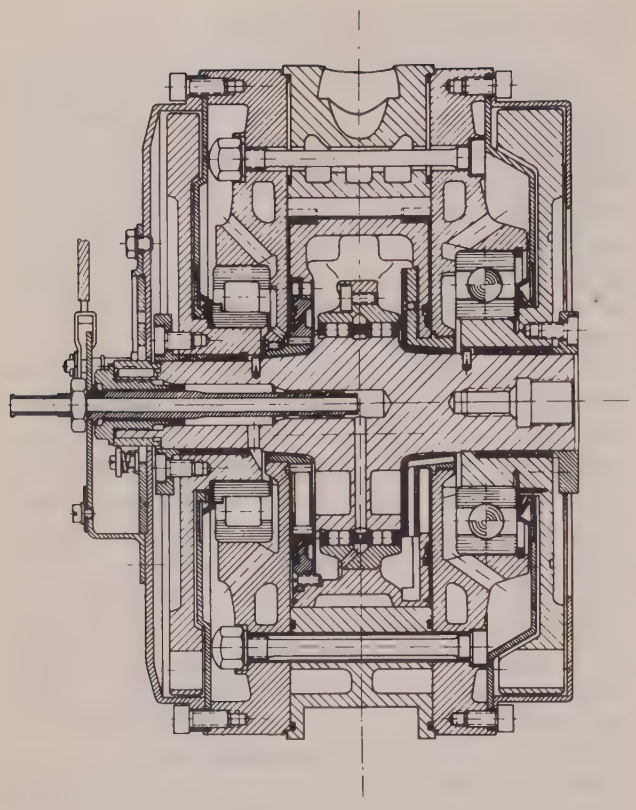

Fig. 10 — KKM 250 — longitudinal section

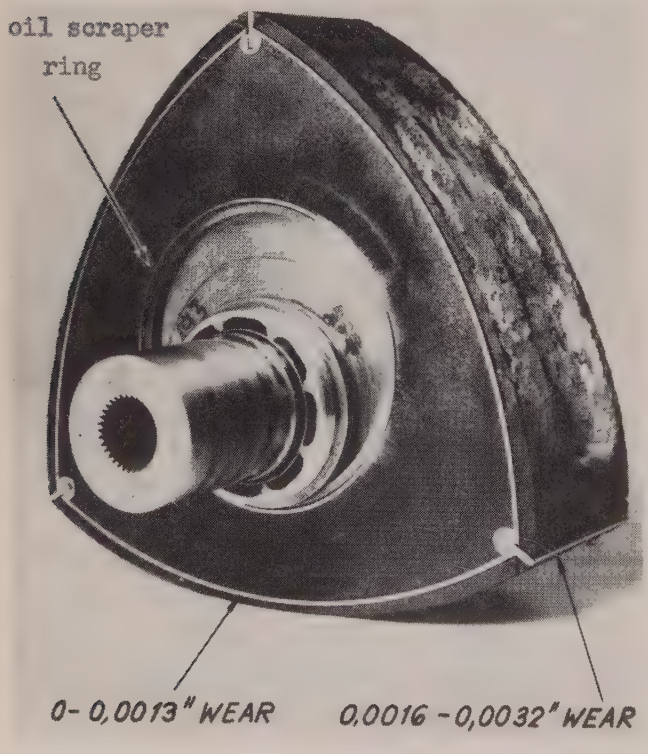

Fig. 11 — Photo of rotor KKM 250 taken after 100 hr endurance run

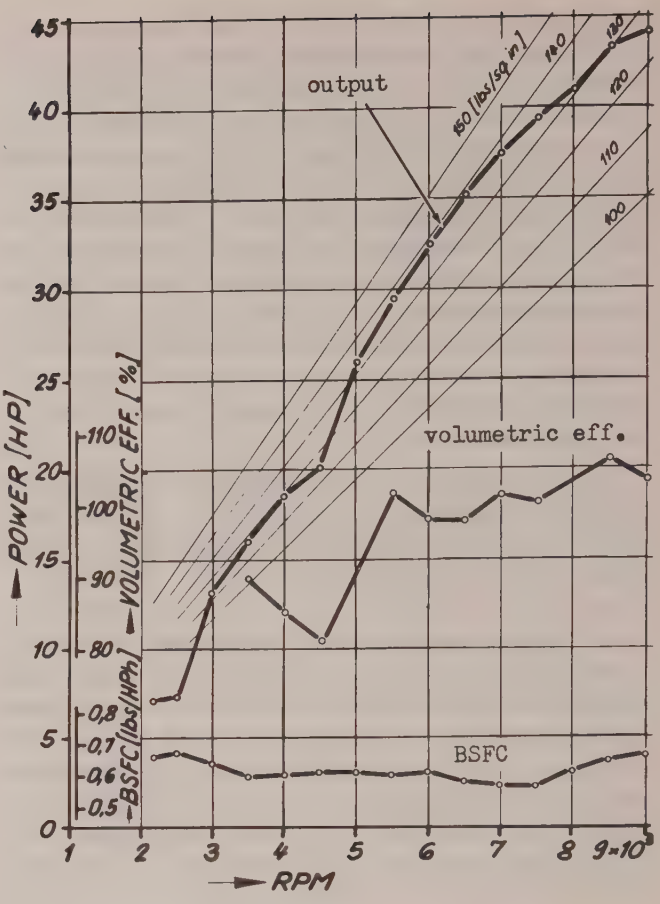

Fig. 12 — KKM 250/1 — test stand performance without muffler

which configuration proved best up to now. The oil scraper rings, which are located in both end faces of the rotor, have a loose fit in the corresponding recesses. The tightness between the rotor and the oil ring is obtained by plastic 0-rings. The oil-retaining method proved so tight that even on 100-hr endurance tests no measurable oil consumption from the sump could be observed.

The complete rotor, as shown in Fig. 11, demonstrates very clearly that only the sealing line of contact is in metal-to-metal touch with the surrounding housing. The photo was taken immediately after a 100-hr test without any cleaning. The intermediate space between the gas seals and the oil seal is covered by a gummy deposit which can easily be wiped off.

Various materials were tested for the major components of this engine. Nodular cast iron proved satisfactory for the rotor, whereas the housing was cast in aluminum 12% silicon, aluminum 18% silicon, cast iron with different quantities of phosphorus, nodular cast iron, and steel. The surface of the housing comprised a molybdenum spray coating on the plane surfaces of the end walls of the housing, which coating was used on cast iron as well as on aluminum parts. The trochoidal surface was soft nitraded, hard nitrated, or chromium plated. Recent tests with molybdenum or steel spray

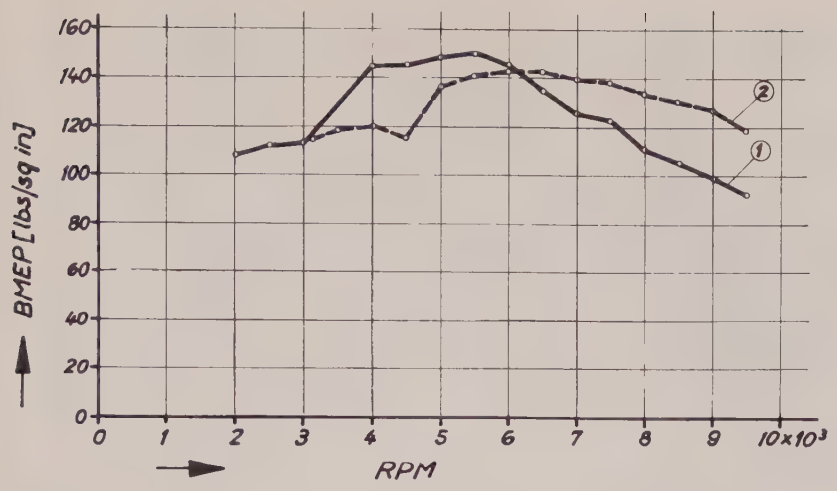

Fig. 13 — KKM 250/5 — BMEP versus rpm peripheral intake port of various size, 1=22mm diameter, 2=18x27mm rectangular

coated peripheral housing walls are still on the endurance tests.

The spark plug is normally mounted in the peripheral wall in its center plane. To reduce gas bypass from one chamber to the other when the apex seal is sliding over the spark-plug hole, the plug itself is inserted in a prechamber, and the only connection to the combustion chamber is through a flame hole of 3-mm diameter. Various locations of the spark plug have been examined. It proved that on rotors with a high compression ratio a spark plug in the leading part of the combustion chamber is favorable, whereas medium and low compression ratios require a trailing location of the plug. On test engines with high bmep, the use of extremely cold plugs is necessary. At present, the lifetime of a spark plug is between 50-70 hr at full throttle.

Performance on Test Stand - The performance data of the KKM 250 are depicted by diagrams. Fig. 12 gives the output, volumetric efficiency, and bsfc versus rpm. From the rays it becomes visible that mep's up to 150 psi were obtained. The volumetric efficiency is extremely high, peaking at 120%, due to ram effect and assisted by the straight intake which goes from a downstream carburetor right into the growing working chamber.

The bsfc is not yet as low as expected. Variations of compression ratio, shape and location of combustion chamber, spark-plug arrangements, and type of fuel are necessary to find the combination which gives a minimum fuel consumption.

The character of the bmep versus rpm of the engine can be affected by different sizes of the intake port. Fig. 13 gives an example of this relationship. Application of a small round intake port with 22-mm diameter results in high bmep in the lower speed range and a steady drop above 5500 rpm. A large intake port of rectangular shape changes the maximum of the bmep to a higher speed range and brings up high power at top speed.

The performance at partial load is shown in Fig. 14. The test was taken at a constant speed of 5500 rpm, reducing the

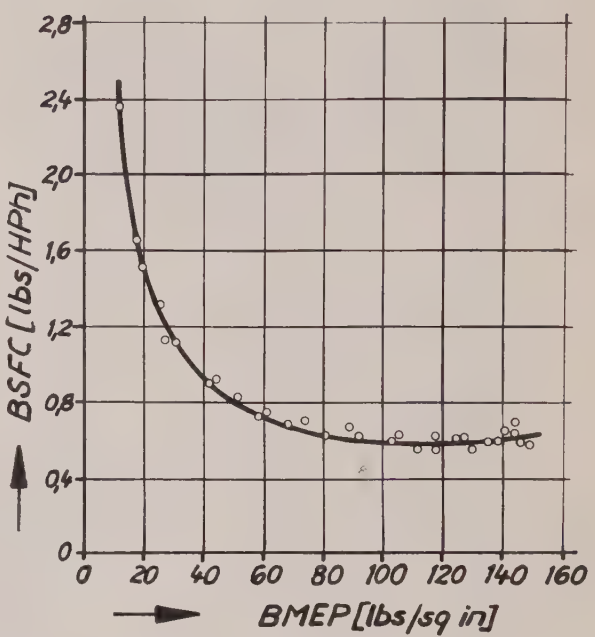

Fig. 14 — KKM 250/5 — BSFC at part load, constant speed, n=5500 rpm, peripheral intake 22mm diameter

bmep from 150 to 10 psi. For a surprisingly wide range, the fuel consumption stays almost constant, which is unusual for a 4-stroke engine. Apparently, up to a bmep of 80, combustion and sealing is perfect; whereas, at high lead, either a leakage or a slow combustion takes place, which may be responsible for a comparatively high fuel consumption. These relations are presently examined in detail, using indicator cards and ionization pickups, to obtain some closer information about the progress of combustion inside the working chamber.

As an example of pressure conditions in the rotating combustion engine, four indicator diagrams are shown in Fig. 15. This research program was carried out at "Institut für Motorenbau Dr. Huber" in Munich. These cards were taken at dif-

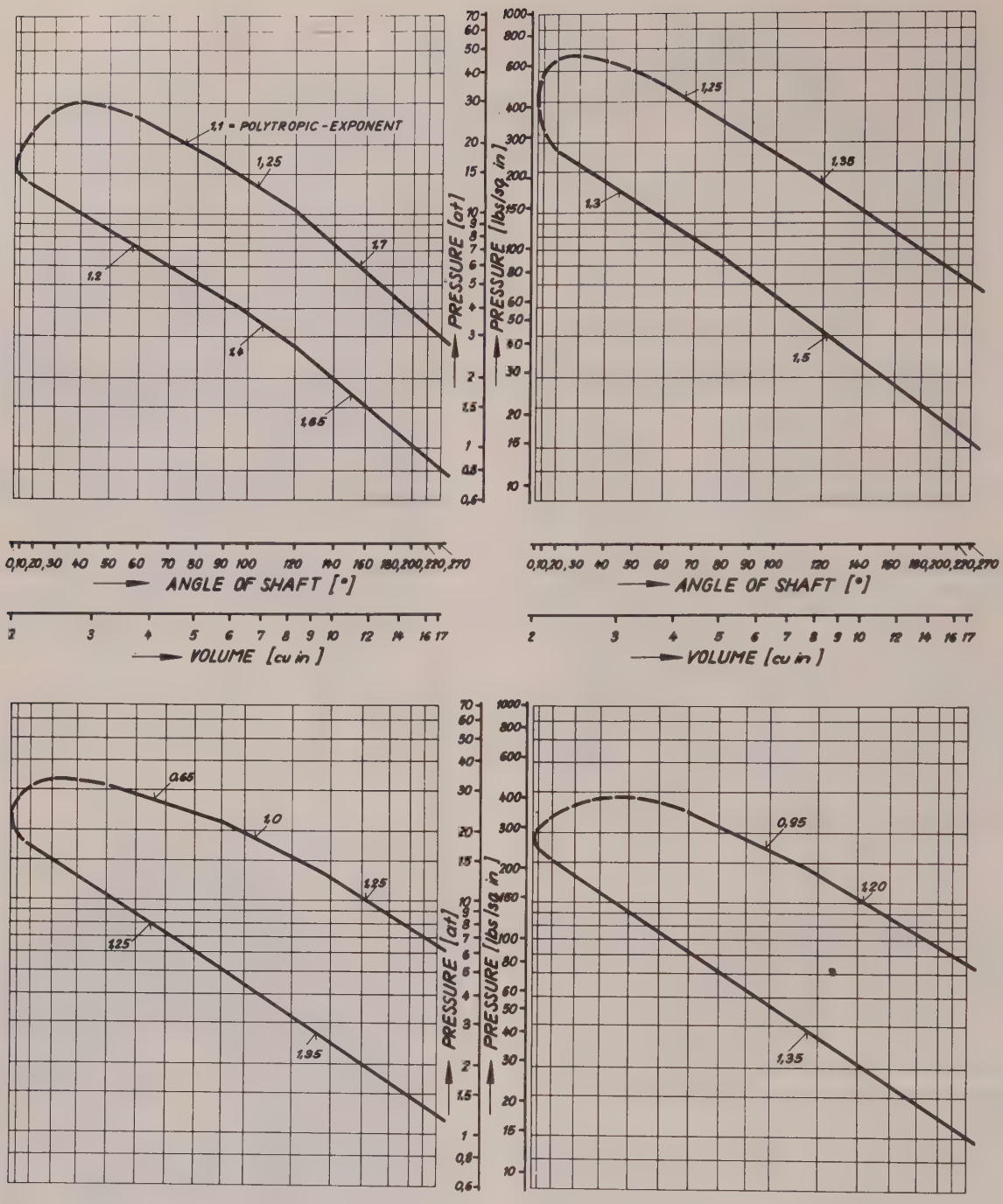

Fig. 15 — KKM 250/5 — logarithmic evaluation of indicator cards taken at full load and different rpm

ferent speeds at full throttle. The plotting in a logarithmetical scale depicts that the compression line approaches the theoretical slope of 1.4 at high rpm. At low speed, leakage from the leading working chamber causes a steep slope during the first part of the compression line, whereas leakage to the following working chamber becomes visible as a reduced inclination of the pressure rise occurs toward the end of the compression process.

The pressure rise during combustion is optimal at about 4000 rpm, whereas, at high speed, the combustion is obviously slow, so that the final slope of 1.3 is never reached. These four diagrams, which were taken at a comparatively low-power engine, demonstrate that for economic operation the speed limits are set by leakage at the low side and by slow combustion at the high side of the speed range.

Considering the effect of fuel air ratio on power and fuel

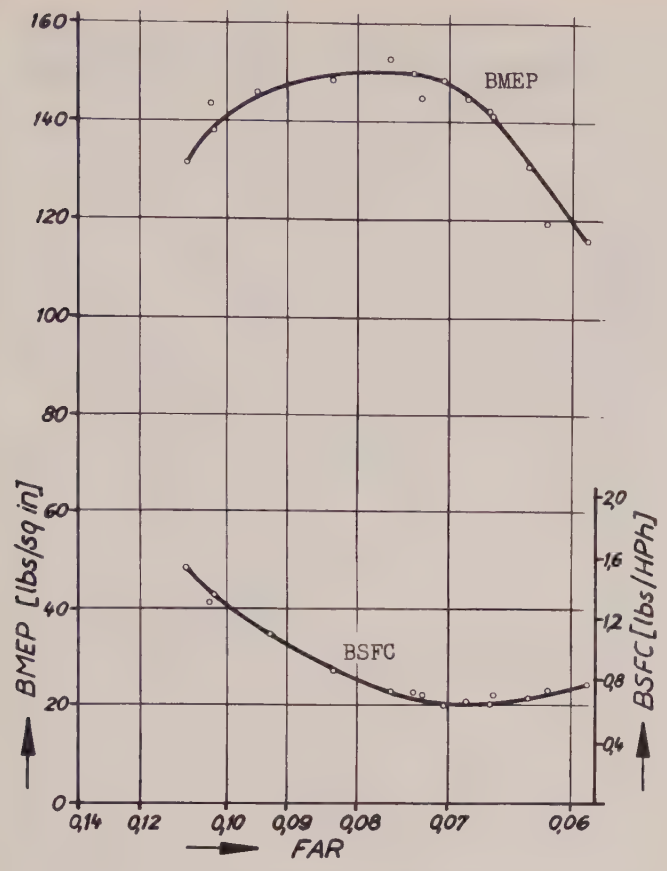

Fig. 16 — KKM 250/5 — BMEP and BSFC versus fuel air ratio

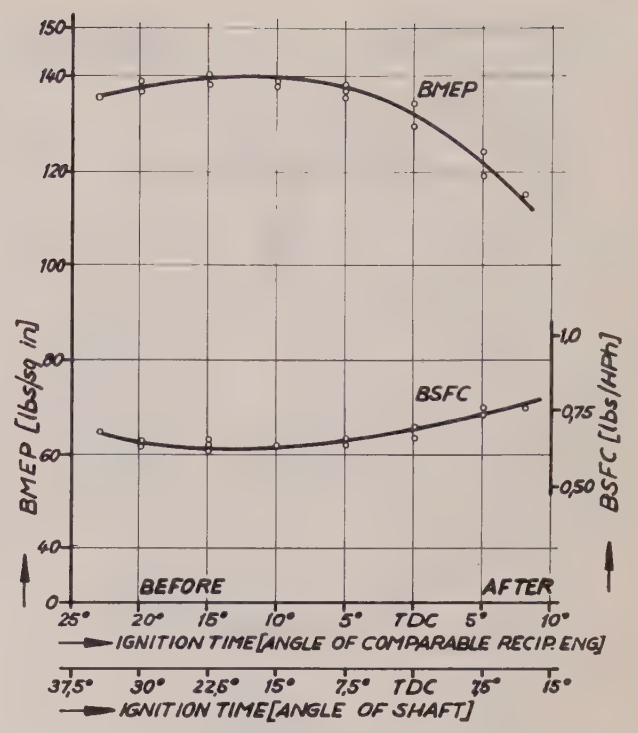

Fig. 17 — KKM 250/2 — effect of ignition timing on BMEP and BSFC, constant speed = 5500 rpm

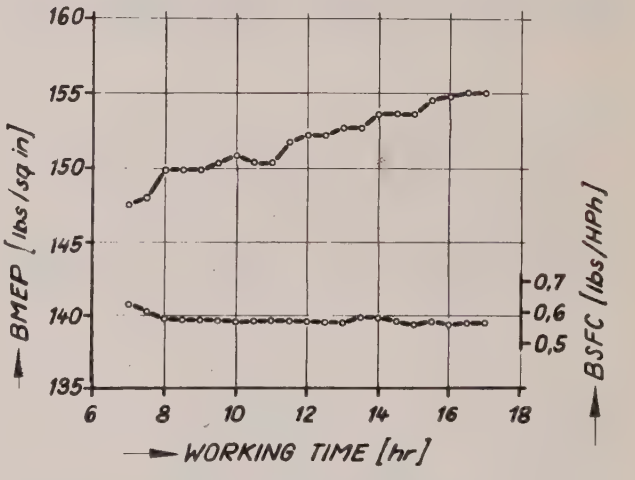

Fig. 18 — KKM 250/11 — typical break-in process during first 10 hr full-throttle 5500 rpm

consumption, details may be taken from Fig. 16. The engine may be leaned out approximately the same way as a reciprocating type. The maximum of bmep is a few per cent on the rich side, whereas the best fuel consumption will be noticed at a fuel/air ratio of 0.069, which is on the lean side(for German commercial fuels).

The diagram in Fig. 17 depicts the relationship between bmep and fuel consumption versus the ignition time. The angle of ignition must be considered different from a reciprocating type of engine, because of the fact that intake, compression, expansion, and exhaust stroke each extend over 270 deg of shaft angle. This means that the time expiring between ignition and top dead center is 1.5 of the time in a reciprocating engine which has the same preignition. For this reason, two scales are shown in the horizontal line of the diagram. One shows the actual ignition time as defined by the position of the eccentric shaft, the second scale shows the angle of a comparable reciprocating engine.

It will be noted that the spark advance is comparatively short, considering the speed of 5500 rpm, at which the best results are obtained between 10 and 15 deg spark advance. The graph shows a minute influence of timing, which may be explained, again, by slow combustion.

Until now, no defined procedure for break-in of the engine has been established. Generally, the test engines are assembled, mounted on the test stand, and, after a few minutes of warmup run, operated at full throttle. Actually, a break in period is favorable, as demonstrated by Fig. 18. During a 10 hr test with a green engine, a steady increase of bmep and a slow descent of fuel consumption can be noted.

For the function of the engine, it is of vital importance to keep the temperature of the center housing in adequate limits. Fig. 19 is a plotting of the temperatures along the periphery of the trochoidal housing. Using cast iron or aluminum for this part has a serious effect on the maximum

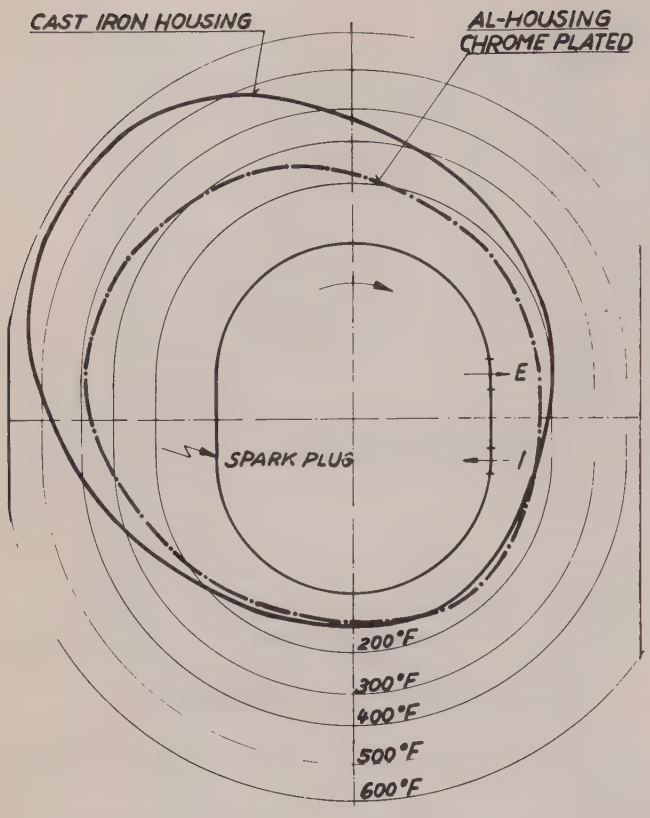

Fig. 19 — KKM 250 — temperature distribution along periphery of housing, taken in center plane 1mm from surface

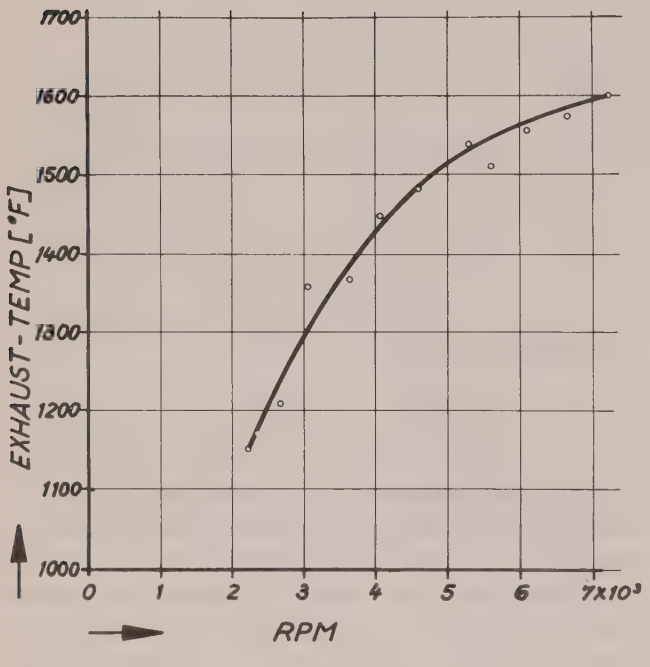

Fig. 20 — KKM 250/7 — exhaust temperature at full-throttle

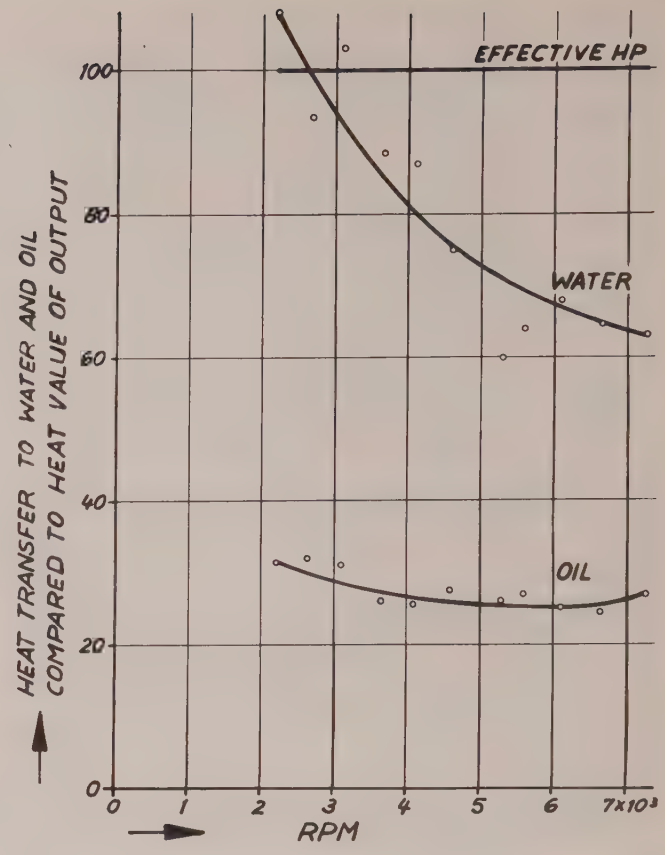

Fig. 21 — KKM 250/7 — heat distribution, full-throttle

temperature. The distribution of temperature is very similar in both cases. The maximum was found in a location in which top pressure and temperature of combustion are present. Maximal temperatures of less than 400 F, which were measured in the aluminum housing, are low enough to secure the stability of lubrication. High temperatures in the cast iron housing were found in one of the first experimental parts. By improved cooling arrangements, they could be reduced to well below 500 F.

Temperatures of the exhaust gas versus rpm at full throttle are shown in Fig. 20. Compared to reciprocating engines with similar mean effective pressures, the exhaust temperatures are on the high side. This, again, indicates a slow combustion, especially at high rpm. For instance, at a speed of 7000 rpm, gas temperatures of 1600 F were found. On the other hand, the heat transfer to the cooling water is considerably reduced at high rpm's. Details of this relationship are plotted in Fig. 21. The heat transfer to water and oil are compared to the heat value of the engine output. Rating the engine output as 100%, it will be seen that, at 2500 rpm, the heat transfer to the water is the same as the heat value of the power, whereas, at 7000 rpm, only 62% of this amount is transferred to the cooling water. The oil takes between 25-30% of the effective power. Part of this may be additional energy wasted inside the rotor for shaking the enclosed liquid.

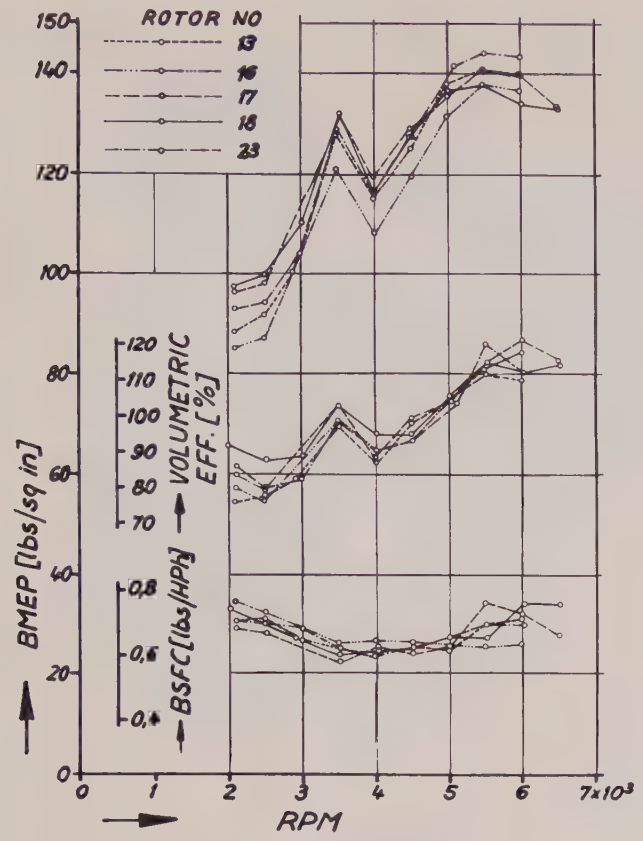

Fig. 22 — KKM 250/7 — performance data test of 5 different rotors in the same housing

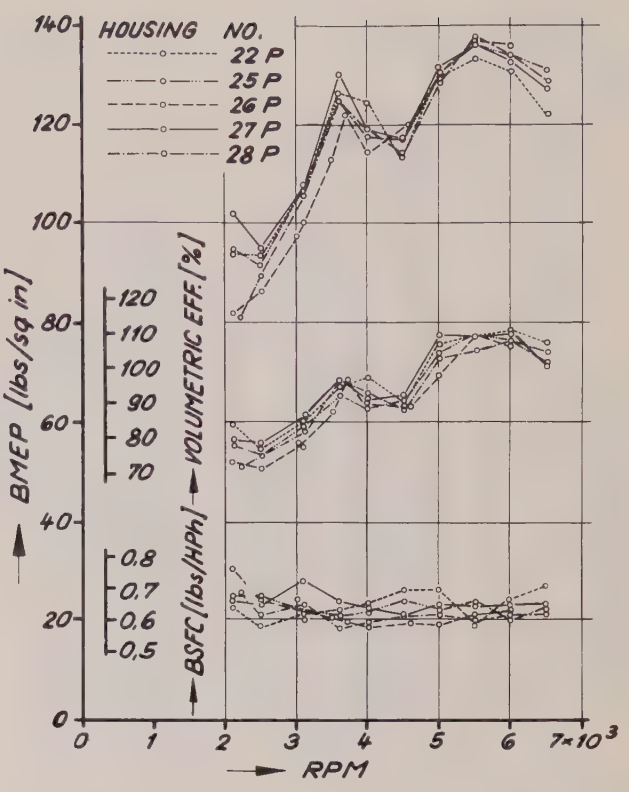

Fig. 23 — KKM 250/8 performance data, test of 5 different center housings with same rotor

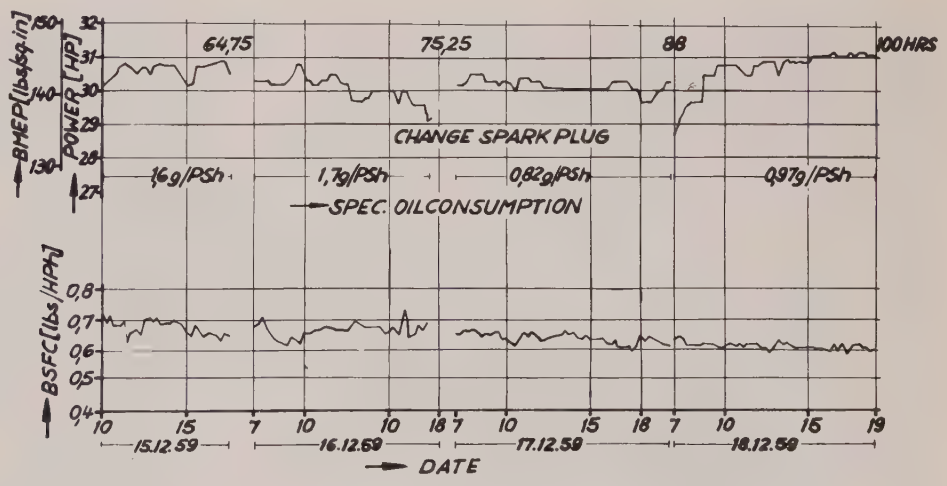

Fig. 24 — KKM 250 — end of 100 hr endurance test, 5500 rpm full-throttle

The tolerance for the accuracy of the housing and for the fit of each sealing component inside the rotor are not yet clarified. Extended series of test stand runs will be necessary to find out these data. Apparently, the requirements are not extremely high, as demonstrated by Figs. 22 and 23. Fig. 22 shows the performance data of one engine, whereby five different rotors were mounted. The effect of this interchange on bmep, volumetric efficiency, and specific fuel consumption is less then 5%, which seems to be tolerable. Similar conclusions may be drawn from the Fig. 23, in which the results are plotted for five different center housings mounted in the same engine. Again, the differences are minute and the performance stays identical in a very narrow range.

Durability - The durability of the NSU Wankel engine is feature which has been questioned very often by critical observers. During the first year of development, performance was the most important point and effort was concentrated toward this target. A couple of 100-hr test runs with full throttle were considered to be sufficient to prove the possibility

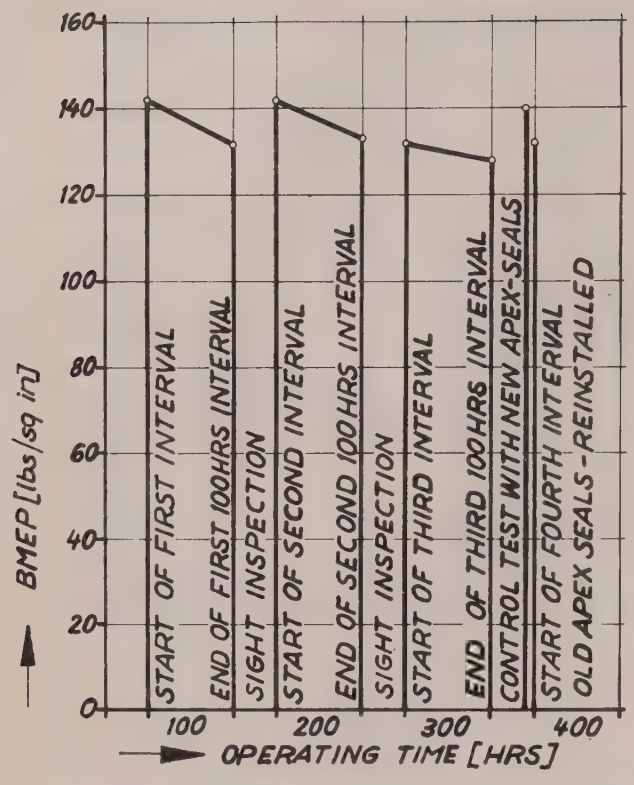

Fig. 25 — KKM 250/6 — loss of power during an endurance run, no parts exchanges, constant speed = 5000 rpm, constant load = 102 lb/sq in.

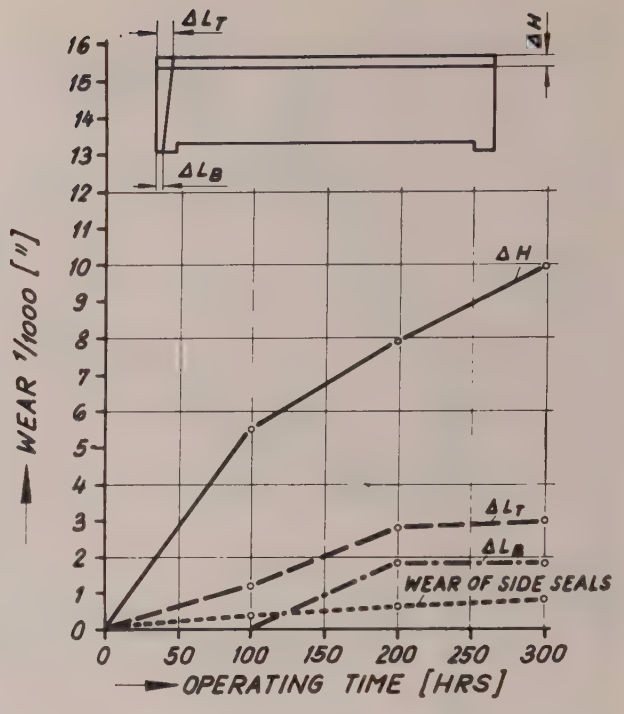

Fig. 26 — KKM 250/6 — wear of seal components during endurance run, constant speed — 5000 rpm, constant load = 102 lb/sq in.

DESIGNATION	PART. NO.	TOTAL TIME [HRS]
ROTOR	8	883
APEX SEALS	13/16	410
SIDE SEALS	8/1	883
INTERCON. BOLTS	8	883
OIL SEAL	8/1	883
OIL SCOOP	8	883
INTERNAL TOOTH GEAR	8	883
CENTER HOUSING	48	410
SIDE HOUSING DRIVE	13	668
SIDE HOUSING ANTI DRIVE	10	658
EXTERNAL TOOTH GEAR	10	658
SHAFT	5	838
FLYWHEEL	2	810
BEARING. ROTOR	11	657

Fig. 27 — KKM 250 — maximal lifetime of major components, deadline October 29, 1960

of attaining adequate lifetime.

One of these tests, which was carried out more than a year ago, is depicted in Fig. 24. This comprised an aluminum housing with a chrome-plated surface. Even during the last period of this endurance run, the output and specific fuel consumption were still improving. The only interruption that happened during these tests was an occasional change of spark plug. For the future, it may be necessary to develop special plugs which are extremely cold, or to change over to a different ignition system, such as condensor-discharge or low-voltage ignition.

The necessity of comparing the qualification of different material for the trochoidal housing, as well as for the apex seals, required longer endurance tests. An example is given in Fig. 25. This test was done with a KKM 250, running at 75-80% of its maximal bmep. The speed was kept constant at 5000 rpm. The operation at constant speed is known to be very hard for the lifetime of the engine, because of the constant frequency of seal oscillations which have a tendency to generate chatter marks. Other engines, which have been running in test cars, never showed distinct chatter marks, as they are operated all over the speed and load range.

As demonstrated by the diagram, the output gradually went down; this was determined by full-throttle tests taken in intervals of 100 hr. After completion of 300 hr total, new apex seals were mounted, of the original dimensions and the same material. The replacement of these apex seals brought back original bmep within 1%. After a short test, the worn-out seals were reinstalled and the endurance test is still going on. (It was terminated by break of two apex seals after 950 hr total.)

The wear of all sealing components is shown in Fig. 26. The wear in radial direction of the apex blade is not critical, considering the total dimension in this direction which would

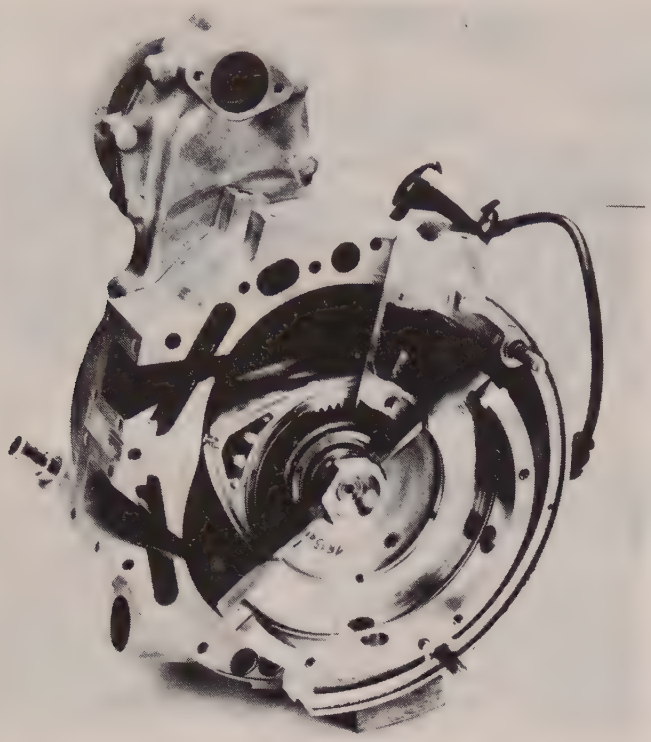

Fig. 28 — KKM 400 — view from flywheel side (housing partly cut away)

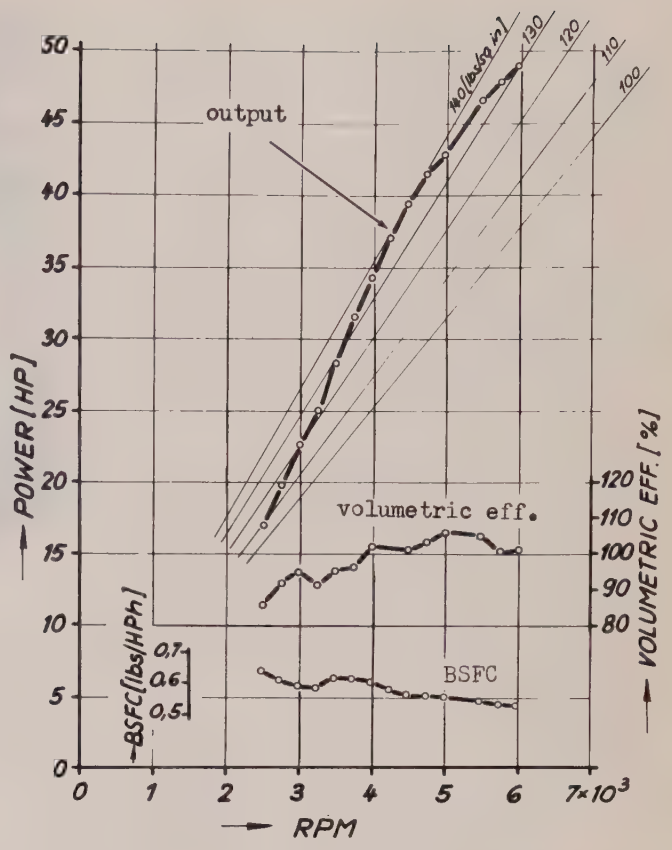

Fig. 29 — KKM 400/1 — test stand performance without muffler

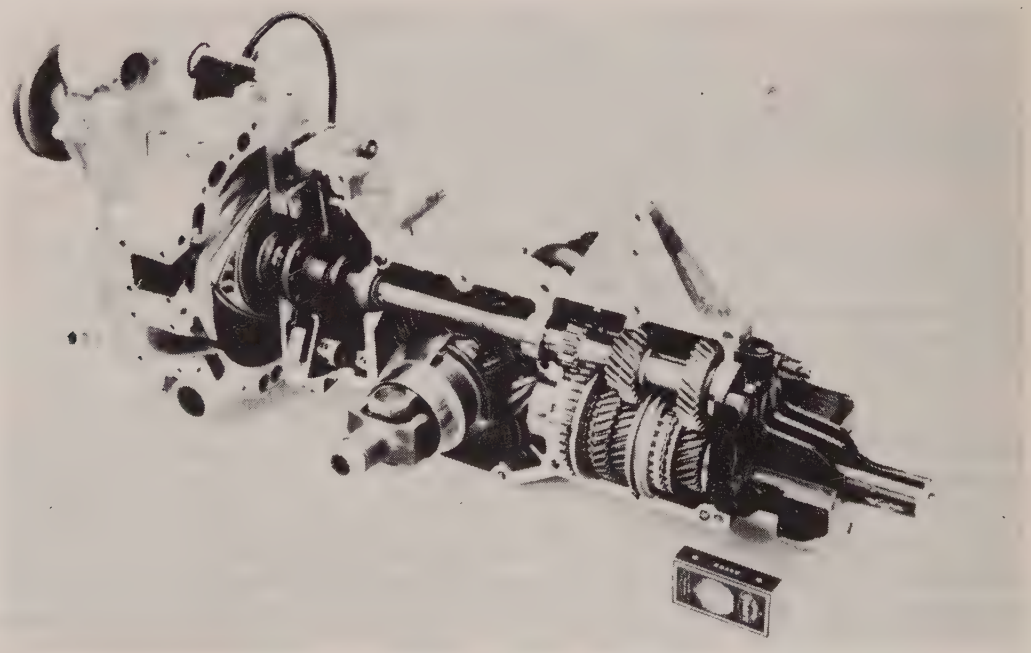

Fig. 30 — KKM 400 connected to gearbox (Volks Wagen type) for application as automobile engine

permit far more wear without effect on the sealing qualities. What actually causes the drop in power is the wear at the end faces of the apex blade, which is more severe at the outer radial part, so that the seal changes from a rectangular shape to a trapezoid shape. This effect easily can be avoided by a different design of the apex seals.

The wear of end face seals and interconnection bolts is minute; the same applies to wear of the oil scraper rings. The maximal lifetime of all major parts of the engine, as tested by now is plotted in Fig. 27. These data are prelim-

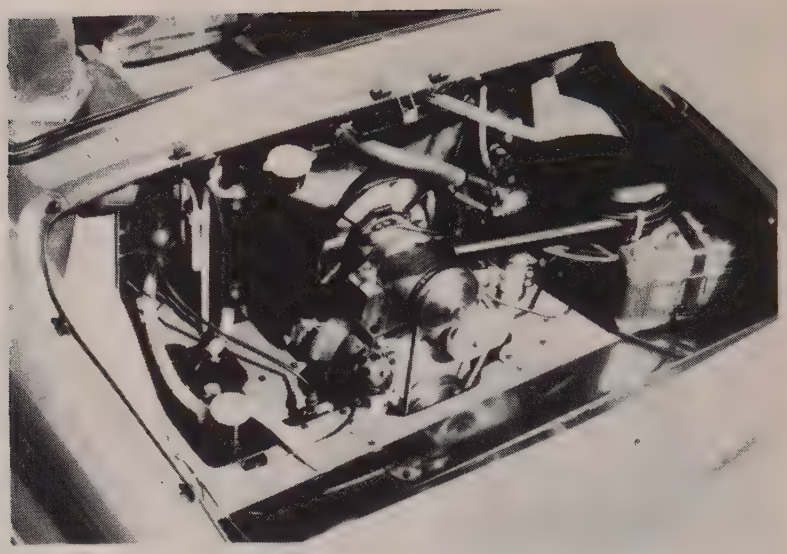

Fig. 31 — Installation of KKM 400 in engine compartment of NSU-Sportprinz

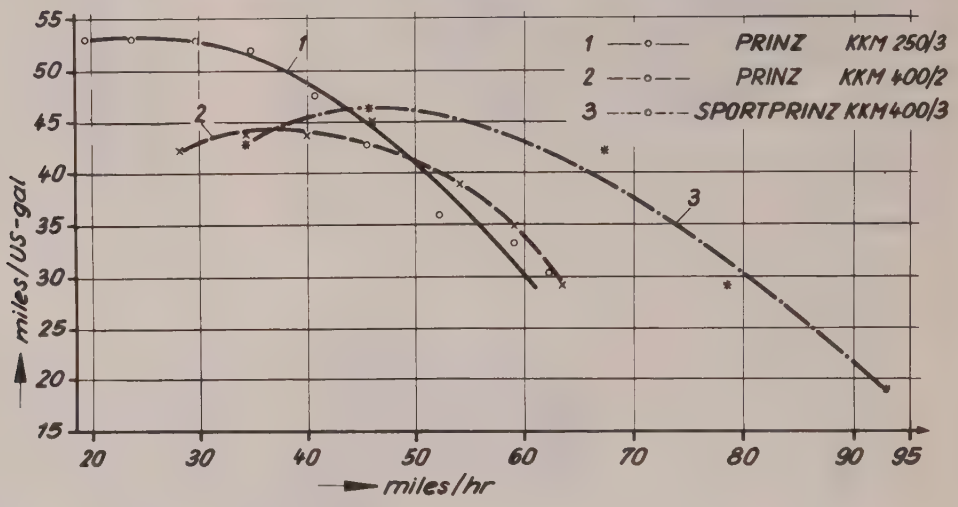

Fig. 32 — Road test mileage (preliminary results) average results on level road both directions

inary, as the endurance tests are still going on. Approaching a lifetime of 1000 hr for most of the involved items appears to be promising enough, especially as the best material combinations have not yet been examined over longer periods.

Layout, Performance and Application of KKM 400

The experience which was gained during the first year of experimental work on the KKM 250 was embodied in the layout of the KKM 400, which has a swept volume of 400-ccm per working chamber (equivalent to 24.4 cu in.) This engine was already designed for a possible installation as automobile prime mover. A photo with partly cut-away housings is shown in Fig. 28. The leaning angle of the trochiodal combination was chosen 28 deg, thus reducing the overall shape considerably. The total weight of the engine itself, without accessory and comprising an aluminum rotor and all alluminum housings, is 48 lb. Cooling system and lubrication arrangements are similar to the KKM 250, and do not require any specific description.

The performance, as plotted in Fig. 29, reveals a maximum of 140 psi at a speed of 4500 rpm. The top speed shown in this diagram is 6000 rpm, at which almost 50 hp were drawn from the engine shaft. The volumetric efficiency is again above 100% within the range of 4000-6000 rpm. The specific fuel consumption approaches the 0.5 line at high speed, whereas the lean engine (not shown in this diagram) still permits more economic consumption data.

The KKM 400 was combined with a 4-speed transmission of the Volkswagon type, which includes the differential. The complete power unit is shown in Fig. 30. It is obvious that the engine itself becomes an extremely small part of the whole powerplant. A photo of the installation in the NSU Sport-Prinz car is an impressive demonstration of the reduction of volume, compared to a reciprocating engine of a similar power rate. (See Fig. 31.)

The road testing of these cars was not carried out with high priority, so that up to now three test units have covered no more than approximately 30,000 miles. The starting requires a speed of about 300 rpm's, the idling speed can be set at 800 rpm, pickup and acceleration are excellent. The maximum speed of this car is close to 95 mph.

The fuel consumption is well below the results of comparable reciprocating units. Fig. 32 depicts the mpg for the examined speed range, whereby a KKM 250 in a standard body of the NSU Prinz is compared to a KKM 400 in the same vehicle and a KKM 400 installed in the Sport-Prinz version.

Conclusion

It was the purpose of this paper to submit a brief survey of the present status of development of the NSU Wankel engine. In criticizing the results, it must be considered that the basis of experience is far too narrow to obtain any optimal solution. Although the engine comprises only a small amount of major components, it permits a multitude of variations and combinations, which require a very careful and thorough research program.

The few types of experimental engines that have been built and tested up to now do prove, that for certain estimated configurations, results have been obtained which are not too far from performance and endurance data as realized in highly developed modern reciprocating engines. These estimates, for instance, refer to: chamber size, trochoidal contour, chamber width, port size, intake and exhaust timing, shape and location of combustion chamber, location of spark plug, compression ratio, dimensions of sealing elements, fit of sealing elements, type of fuel and lubricant, and so on.

On the other hand, it is evident that this rotating combustion engine is free of vibrations, requires a fraction of overall volume, permits extremely light weight per hp, and contains a minimum of components. None of the engine parts requires exotic material or high machining precision, leaving no question that production cost can be cut down to a fraction of reciprocating 4-stroke engines of the same output.

It can not be foreseen which size or application of the rotating combustion engine will be the first for production. It appears doubtful whether possibility of operating at high rpm will be utilized soon or the speed range would be reduced to accommodate the requirements of the accessories. Applying of the diesel combustion is still in the design status and on aircooling the first experience is just being collected. The only fact which has to be emphasized is that during the past years of development nothing showed up that indicated a barrier which could not be overcome. It appears to be only a problem of research effort to designate the time at which this type of engine will be ready for production.

Discussion of this paper will be found on page 200.

Curtiss-Wright's Developments on Rotating Combustion Engines

M. Bentele
Curtiss-Wright Corp.

ALTHOUGH Curtiss-Wright's agreement with NSU and Wankel covers the full scope of sizes and configurations of rotating combustion engines, we concentrated our development efforts from the beginning on the single rotor KKM type with a stationary rotor housing and a 3-cornered rotor rotating at 1/3 crankshaft speed.

Our first experimental engine, known as the RC6, has a displacement of 60 cu in., which means eight times more than NSU's engine KKM 125 which was in its initial test phase at the time we started designing our engine. Its general arrangement is illustrated in Figs. 1A and 1B.

In order to arrive at the optimum design of the power section, we investigated the effects of various geometric variables such as the K factor K = R/e which represents the ratio of the generating radius R of the trochoid to its eccentricity e, the ratio of the axial width of the chamber a and its breadth b at its maximum volume, and different porting configurations. The effects of the K factor on the displacement of the engine, the areas and timing for side ports, the overlap, and the combustion chamber shape are rather complex and cannot be expressed in simple formulas mainly due to design considerations, such as the accommodation of gas and oil seals. The general relationships have been amply described (1-5),* and our own conclusions led to the selection of a single K factor for an experimental gasoline engine which allowed us to accommodate for the air intake a single side port, dual side ports, and peripheral ports within one engine size, with a minimum modification to the important components. A specific design for either a dual side port or a peripheral port would have permitted a greater axial length of the engine, with a resulting reduction of R and the "diameter," and an increase of its speed for the same apex velocity, but other considerations, such as mechanical loads and shaft deflections, made it advisable to postpone these investigations until we had a better understanding of the basic engine.

A diesel version will necessitate a higher K factor in order to attain a higher compression ratio.

Experimental Engine RC6

The mechanical design of the experimental engines is conservative without special efforts toward a low weight (6, 7). The crankshaft runs in two main sleeve bearings adjacent to the eccentric, and in two more bearings outside the balance weights. The flywheel is separately mounted and easily changed for the investigation of its effect on the engine operation and torsional vibration characteristics. The

*Numbers in parentheses refer to the References at the end of the paper.

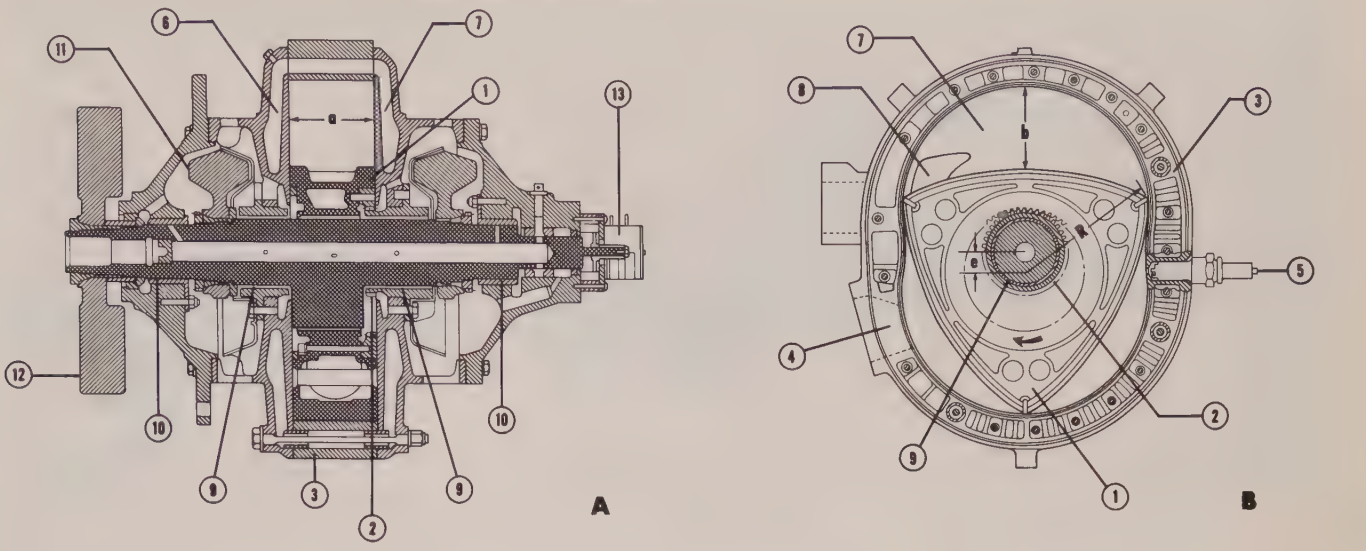

1. Rotor with internal rotor gear
2. Stationary gear
3. Rotor housing
4. Exhaust port
5. Spark plug
6. Side housing - drive side
7. Side housing - anti-drive side
8. Intake port
9. Main bearing (inner)
10. Main bearing (outer)
11. Balance weight
12. Flywheel
13. Ignition contact maker

a = Axial width of chamber
R = Generating radius
e = Eccentricity
k = R/e
b = Maximum breadth of chamber

Fig. 1 — Experimental engine — (A) longitudinal, (B) cross section

structure of the engine housings employs double walls interconnected by ribs. The outer relatively thick walls stay at low and uniform temperatures and maintain the shape of the inner walls which are thin, and thus reduce the temperature rise between the coolant side and combustion gas side. The heat transfer rate varies along the rotor housing perimeter to a considerable extent since any particular location is not exposed to the complete gas cycle but only to a portion of it. The combustion zone reaches a considerably higher average gas temperature and heat input. To match this distribution, the cooling was designed as a multi-pass forced-flow system where the coolant flows back and forth through the rotor housing and between the side housings, and the heat transfer parameters of the coolant passages are adjusted accordingly. These passages are easy to manufacture, clog-free, and avoid vapor accumulation.

The rotor and side housings are located by dowels and clamped together by numerous bolts which are spaced consistent with the gas loads and located within the cooling passages and hollow dowels.

The rotors were made from forged aluminum or cast nodular iron. The outer rotor walls are, unlike the rotor housing, exposed to the complete cycle, and the heat input is thus more uniform. Various cooling arrangements have been developed, all based on using the lubricating oil as the coolant (7).

Typical performance figures achieved with the 60 cu in. size presented in Table I for the normally aspirated engine.

Supercharging had essentially the same effect on output as experienced with reciprocating engines although extreme supercharging was not explored.

The friction mean effective pressure at low speed is important for the starter requirements, especially at low ambient temperatures, and for the idling characteristics. Tests in this area have shown that the engine does not have a high breakaway torque such as reciprocating engines have. The highest torque occurs at a moderately low speed where the mechanical friction is low but apparently the work done during compression is not fully recovered by the expansion due to some deficiency of the gas sealing at these low speeds. This loss disappears at slightly higher speeds which give the

Table I - RC6 Performance Data*
(Side Intake Port)

Power	100 hp at 5500 rpm
BSFC at Best Power	0.54 lb/hp/hr
Min BSFC	0.47 lb/hp/hr
Max Volumentric Efficiency	89%
Min BSAC	7.1 lb of air/hr/BHP

*Status as of Oct. 1960.

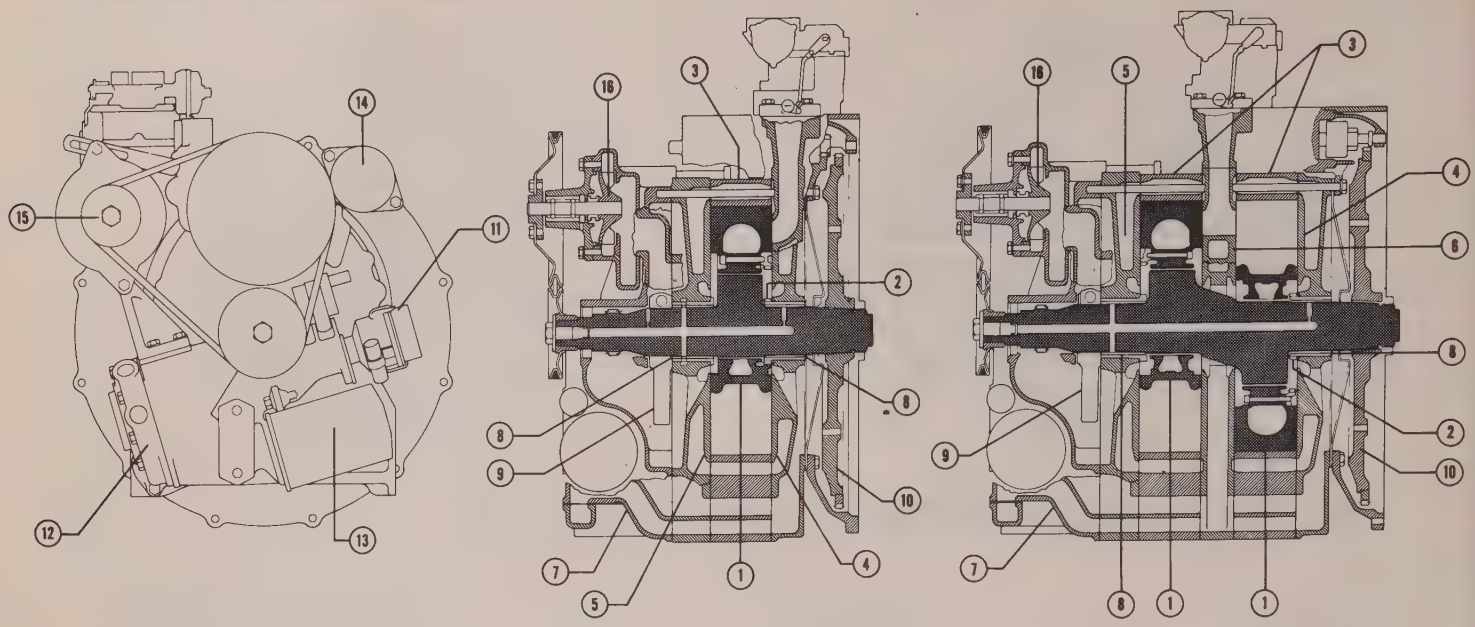

1. Rotor
2. Stationary gear
3. Rotor housing
4. Side housing - drive side
5. Side housing - anti-drive side
6. Intermediate housing
7. Accessory housing
8. Main bearing
9. Balance weight
10. Flywheel cum balance weight
11. Ignition contact maker
12. Oil pumps
13. Oil filter
14. Starter
15. Generator
16. Water pump

Fig. 2 — Single and twin powerplants

lowest friction mean effective pressure of the engine. At higher speeds, the expected rise occurs as a result of losses by mechanical and gas friction, oil churning, and heat dissipation.

Starting of the engine, down to temperatures below 0 F, was consistently accomplished with speeds in the order of 200 RPM. Recently, we have also started a small engine with a spring operated starting device and with a rope pulled by hand. The starting speed in itself does not appear to be the only factor for starting the engine. Various indicator diagrams during the starting procedure have shown that a high acceleration results in firing in the first few cycles of the engine.

Powerplants

Based on the experimental engine, which had all accessories test stand driven, a single and twin powerplant were designed. The longitudinal sections and rear view are shown in Fig. 2. The front and rear section of the single and twin are essentially identical, the second power section of the twin is a mirror image of the single, but the rotor and rotor housing are identical. The shaft and bearing arrangement is very much simplified, the flywheel is combined with its adjacent balance weight; and the outboard bearings are eliminated; either engine has only two main bearings.

The arrangement, size and weight of the accessories do not permit obtaining the full benefit of the compactness of the power sections, and further efforts to "miniaturize" these appear to be worthwhile.

The instantaneous rotor torque of a twin is very much better than that of a single as is shown in Fig. 3 which depicts the torques for a 450 hp engine laid out as a single, twin, and four rotor configuration with geometrically similar power sections and equal apex velocity. The twin eliminates the negative torque and its torque peak is considerably lower than that of the single. The four rotor engine gives a very small torque variation. The mean torque decreases for the twin and four due to their smaller trochoid sizes and correspondingly higher rated speeds by a factor of $\sqrt{2}$.

FOUR ROTOR ENGINE 4RC6

There a numerous possibilities for stacking power sections to a four rotor engine and after their careful evaluation, we selected a configuration, again based on the 60 cu in. components with the following ground rules:

1. In-line arrangement of the major trochoid axes, that means, in-line of the intake and exhaust ports, and the spark plugs.

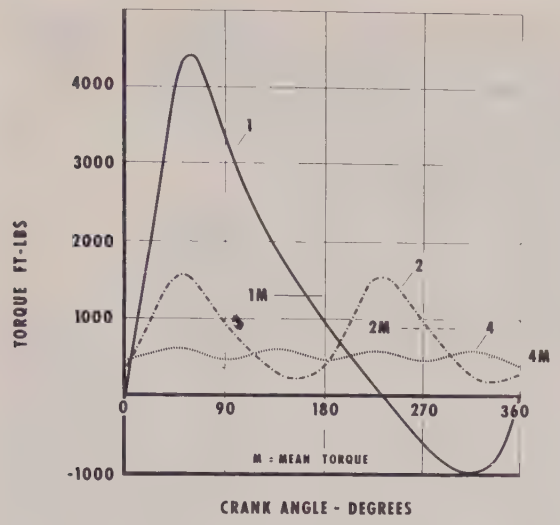

Fig. 3 — Instantaneous and torque for single (1), twin (2), and four (4) rotor engines

Fig. 4 — Four rotor engine 4RC6 — view of spark plug side

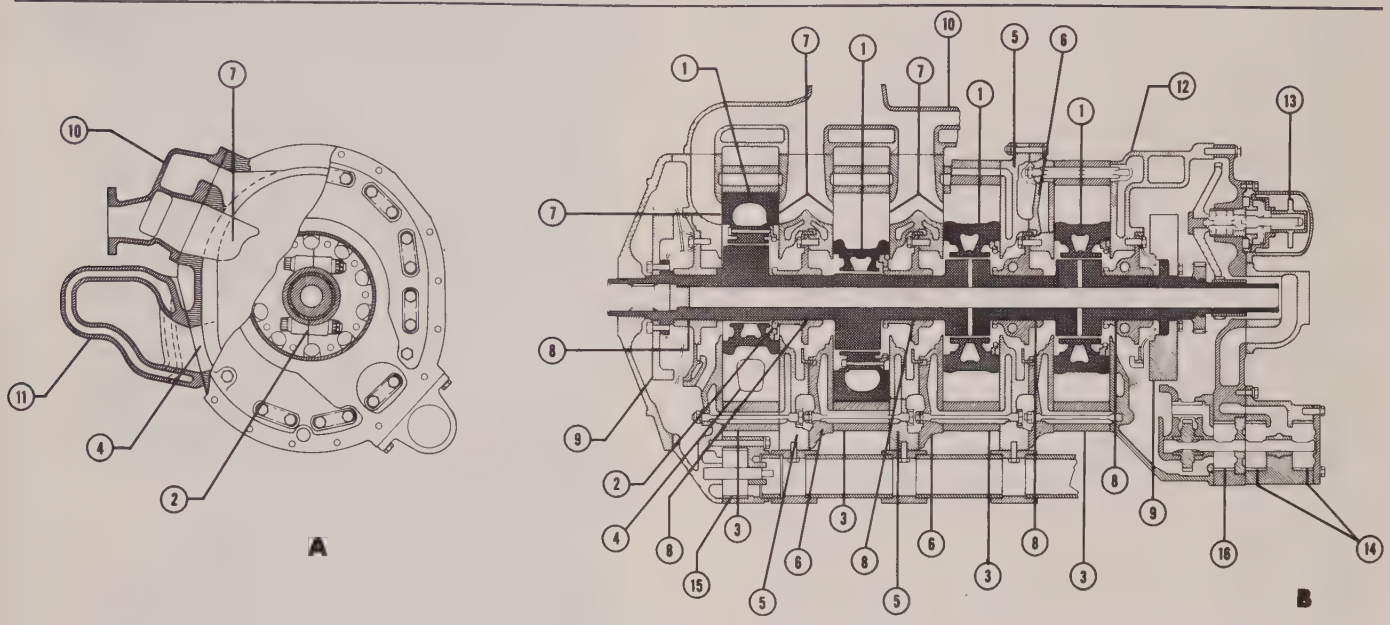

1. Rotor
2. Split stationary gear with main bearing
3. Rotor housing
4. Exhaust port
5. Side housing - drive side
6. Side housing - anti-drive side
7. Intake port (dual intake)
8. Main bearing
9. Flywheel cum balance weight
10. Intake manifold
11. Exhaust manifold
12. Accessory gear box housing
13. Ignition contact makers
14. Oil pressure pumps
15. Oil scavenge pump - front
16. Oil scavenge pump - rear

Fig. 5 — 4RC6 engine — cross and longitudinal sections

2. An integral 1-piece crankshaft.
3. Uninterrupted sealing faces of the side housings.
4. Parallel flow of the coolant and lubricant through the four power sections. The parallel flows had, apart from their advantages design-wise, the plus factor that all analytical and test results from the single unit could be readily applied to the four unit engine.

Fig. 4 pictures a side view of the engine which clearly illustrates some of these in-line features and the short length and low height for which this engine was designed. Fig. 5 shows cross and longitudinal sections of the engine. The integral crankshaft can be accommodated within the intermediate side housings by splitting these in a plane perpendicular to the engine axis and by splitting the bearings and sta-

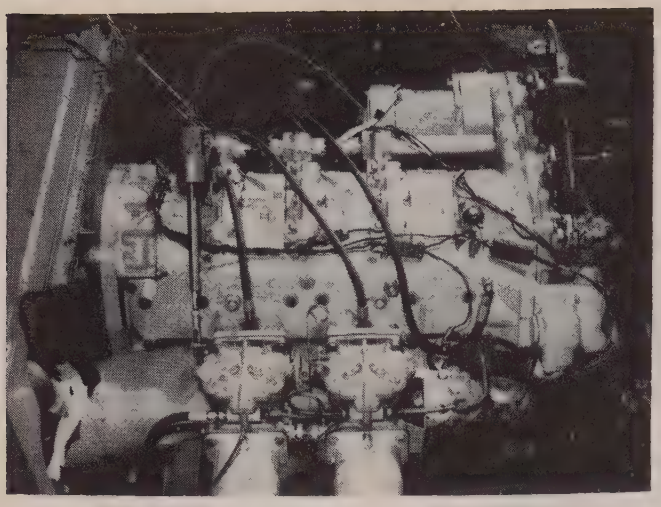

Fig. 6 — 4RC6 engine on test stand — carburetor side

tionary gears in a plane including the axis as illustrated. Assembly of the engine starts from the accessory gear box housing on the right to which the first main bearing with the inserted crankshaft is attached. Rotor and rotor housing follow, the rotor being slipped over the eccentrics of the shaft, and the addition of the side housing makes the power section complete. Rotor and side housings are doweled and clamped together in the same way as on the engines above. The second bearing and gear is assembled onto the shaft, bolted together, and piloted in the side housing. The side housing of the second power section is then piloted and bolted to the adjacent housing and the same sequence as before applies for this and the following power sections.

This crank arrangement provides for power cycles at 90 deg intervals with the firing order of 1-4-2-3, but it leaves a small couple which has to be compensated by a balance weight at either end of the shaft. This penalty is, however, not serious since an additional torsional mass is probably desirable in any case and the in-line arrangement provides for simple and light intake and exhaust manifolds, cooling lines, and so forth.

The crankshaft serves as the oil supply to the power sections. The return oil is delivered to the oil cooler and oil tank by two scavenge pumps located at the lower front and rear end of the engine.

The coolant is distributed by a tube along the housings, the exits are collected by the intake manifold which is thus heated for better fuel distribution at low ambient temperatures. In order to achieve a good air and fuel distribution, two carburetors and dual side ports were employed.

This was the first multi-rotor engine designed and built anywhere and we were ready for some surprises. We got them but, fortunately, most of them were pleasant ones. Assembly of the engine did not pose any serious problem since all important components and their relative positions can be inspected during the assembly procedures in the same manner as on the single unit engine.

Fig. 7 — 4RC6 engine on test stand—¾ rear view carburetor side

Table 2 - RC19 Preliminary Performance Data

Power	782 BHP at 1525 rpm
BMEP	106 psi
Volumetric Efficiency	83%
BSAC	7.9 lb/hr/BHP

Figs. 6 and 7 show the engine rigidly mounted on the test stand with the engine accessories and the conventional instrumentation.

Only a few minor usual mishaps interrupted the first test series of this engine. Although the flow and torque variations, as shown before, are very small, observation of the smooth engine running confirmed this in an even more dramatic manner than figures can.

Fig. 8 depicts the full throttle performance of the first test engine, culminating in a maximum output of 425 hp at 6500 rpm, and showing relatively flat torque and fuel consumption curves.

Size Effects, RC19

In order to investigate the size effect on various engine phenomena, the linear dimensions of the RC6 engine were literally blown up approximately three times to a 30 times bigger displacement of 1920 cu in., and such an engine, designated RC19, was built and tested. Only dimensions and features which affected stresses, heat transfer, and thermal gradients were adjusted. The engine configuration is essentially that shown in Figs. 1 and 2. It had dual side ports

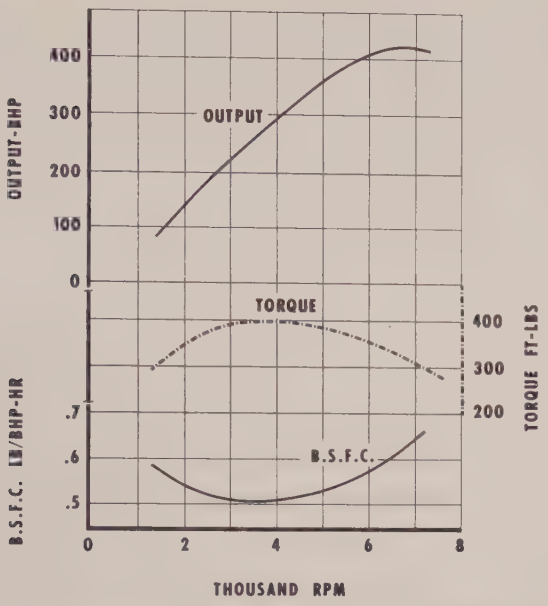

Fig. 8 — Engine performance of 4RC6

Fig. 9 — RC19 engine — assembly of power section

each connected to a carburetor with manual control. Fig. 9 demonstrates the size of the power section.

This engine also started and ran at the first attempt, and its operation was quite normal. Its breathing capacity proved very ample, even at high apex velocities, and the preliminary testing demonstrated the power potential of this engine size. However, it exhibited a phenomenon which did not occur on the smaller size engines with standard fuel, namely, detonation. It took place when standard fuel air mix-

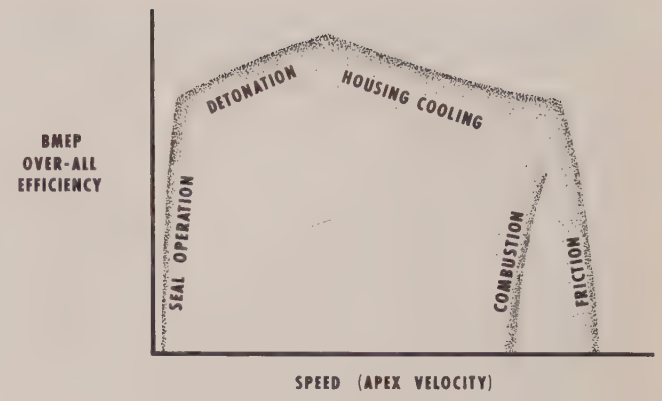

Fig. 10 — Design parameters

tures and full throttle opening were approached. In this first test series, attractive power and fuel consumption figures could therefore not be realized and further investigation of this deficiency is required. It is too early to say that the size of the combustion chamber is the main cause of detonation. On the other hand, the engine helped to clarify other phenomena which were exaggerated due to the size and could more readily be investigated by instrumentation than on the smaller engine. Table 2 gives the initial RC19 performance.

Design Parameters

Progress in the technical evaluation and application of the rotating combustion engine has been made in a displacement range of 1:250, namely, from some 7-1/2 to 1900 cu in., and a survey of the design parameters of this new prime mover is warranted. Fig. 10 represents an attempt to classify these parameters and to assess them in the form of relationships of brake mean effective pressure or overall efficiency versus speed or apex velocity.

By increasing the speed and gas velocities of a given size engine, the first problem encountered is combustion. Apart from the influence of the fuel type, combustion is affected by the manifold and porting arrangement, the combustion chamber shape, the transfer velocities inside the combustion chamber during the transition through tdc, and the spark plug location. We have developed an adequate combustion characteristic for current ratings and additional work is underway to improve it also for higher speeds and velocities, that is, higher power. However, since part of the combustion chamber shape is solely determined by the geometry of the trochoid and the rotor envelope, the combustion phenomenon will present a challenge at the high speed and high power end.

Another factor will then limit power and economy with increasing speed, namely, friction caused by the friction of the rotor and its bearing, the churning of the scavenge oil within the power section, by losses due to the motion of the cooling oil inside the rotor, and by gas friction. Knowledge

on all of these factors, both qualitatively and quantitatively, leads to design features which will reduce their detrimental effects.

At the low speed end, the engine performance is, apart from the porting, timing, and overlap of intake and exhaust, mainly influenced by the effectiveness of the gas seals. It was already indicated that seal operation is significantly affected by speed, and although improved seal designs helped this feature considerably, it appears that this limit is more severe than with reciprocating engines.

An increase of the brake mean effective pressure, for example, by supercharging, will raise the heat transfer rate to the rotor housing in its combustion section to such an extent that attainment of a wall temperature consistent with operational requirements is no longer assured. Of course, not very much can be done about the heat transfer on the combustion gas side but it has to be fully investiaged in order to arrive at an adequate cooling configuration on the coolant side. This heat transfer problem can only be partially resolved by analytical procedures, certain phases of which have to be supplemented by experimental testing. As a result of these evaluations, satisfactory relationships between the engine operating factors could be achieved.

On the coolant side, steady-state and transient conditions have to be considered and the thermal properties of the housing material, the wall thickness of the housings, the coolant passage configuration, and the coolant medium play important roles and leave sufficient room to the ingenuity of the designer. Liquid coolants offer more margin in this respect than air, and early rotating combustion engines therefore employed water exclusively as a coolant.

Apart from the effect on friction, the rotor cooling does not appear to be a factor for the thermal limitation of the engine.

The last parameter is detonation which appears to reduce the permissible effective pressure at the low speed end, especially with large displacements. However, it has not been fully investigated as yet since it did not bother us with engines smaller than the RC19.

References

1. F. Wankel and W. Froede, "Bauart und gegenwärtiger Entwicklungsstand einer Trochoiden- Rotationskolbenmaschine," MTZ MOTORTECHNISCHE ZEITSCHRIFT, Vol. 21, Ed. 2, 1960.

2. W. Froede, "Entwicklungsarbeiten an Dreh - und Kreiskolben-Verbrennungsmotoren," VDI-ZEITSCHRIFT, Vol. 102, March 11, 1960.

3. "Rotary Piston Engine Symposium," Anonymous, The Engineer, February 26, 1960.

4. R. F. Ansdale, "The NSU-Wankel Rotary Engine," Automobile Engineer, May 1960.

5. W. Froede, "Konstruktion und Prüfstandsergebnisse eines Kreiskolbenmotors KKM von NSU-Wankel," paper presented at the 8th International FISITA Congress, The Hague, May 1960.

6. "Rotating Combustion Engine," presented by R. T. Hurley at SAE Metropolitan Section meeting on March 10, 1960 (SAE Preprint No. S-236 and 1961 SAE Transactions).

7. R. T. Hurley, "Curtiss-Wright Rotating Combustion Engine Delivers 2 hp Per Cu In.," SAE Journal, June 1960, and 1961 SAE Transactions.

Discussion

How Rotating Combustion Engine Design Compares to Reciprocating Engine Design

Paul Huber
Ford Motor Co.

FOR THIS DISCUSSION I will avoid an elaboration of the major problems of the engine-sealing and thermal distoration- and will confine my comments to a few points which arise when this particular form of an epitrochoid engine is discussed with engineers who have not spent a great deal of time studying it. The question always exists as to how this engine compares in design detail with the reciprocating engine with which they are already familiar.

For example, the rotor has a large area exposed to combustion gas, and the resultant gas force acts on a line through the centroid of the rotor. This centroid lies on a circle about the output power shaft center at a radius equal to the eccentricity, which is therefore equivalent to the crank radius on a conventional engine (Fig. A). When the calculations are carried through we find that the bearing loading is approximately that which would be encountered in a reciprocating engine with a bore/stroke ratio of 5. This results in bearing loads on the order of 2000 lb/in.^{2} maximum. The bearing is located in a hot region, but every indication exists that normal heavy-duty engine bearings should be successful.

Another similarity to an engine of high bore/stroke ratio is found when we investigate the detail of the combustion chamber. The surface area is unusually great. If we calculate the bore and stroke of a disc chamber of a cylinder having the same displacement and surface area we find we have a bore stroke ratio of 3/1. This is obviously a large step since the highest ratio in American production is 1.4/1.

Fig. A — Schematic of rotor

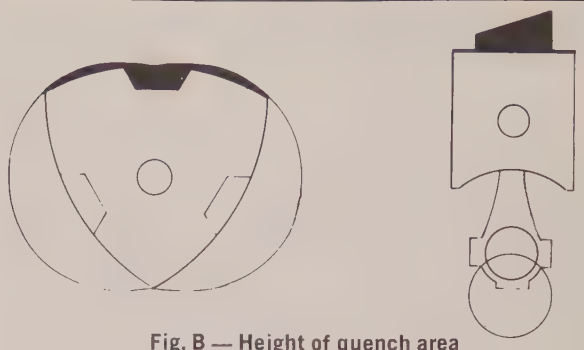

Fig. B — Height of quench area

We have been successful in developing chambers with acceptable economy to a bore/stroke ratio of 2.5/1, so this of itself does not appear to be insurmountable. However, a factor which may prove to be of major importance is the height of the quench area (Fig. B).

Because the outer surface of the rotor is limited by mechanical clearance to the housing, the thickness of the chamber at points A & B cannot be less than approximately 0.136 on the 15.3 cu in. chamber and 0.27 on the 60 cu in. chamber. This results in three important problems at 8/1 compression ratio:

1. About 1/3 of the clearance volume lies outside the central combustion chamber.

2. The flame travel distance is 20-50% more than the 3/1 bore/stroke engine, and the height is much greater than is desirable for quench area. The net result will likely be poor combustion efficiency, and high heat loss. It is worth while to note that the German engines report about 0.6 lb/hp-hr specific fuel consumption probably at maximum power mixture ratio while Curtiss Wright reports 0.47 at best economy. The first is at 8/1 compression ratio while that of Curtiss Wright is not stated. Since Curtiss Wright group may be helped by their larger chamber size, it would appear that this rotary combustion engine may prove to have a fuel consumption a little higher than that we now observe in a reciprocating engine.

The sliding velocity discussion presented by Dr. Froede is another item on which a bore/stroke similarly comparison can be made. Dr. Froede compares with a square engine of the same displacement at the same speed. Since the heating of the seal, wear, etc. is primarily a function of the average speed, we can easily show that the rotary engine has an average speed of 3220 ft/min. at 5000 rpm, whereas the reciprocating engine has an average speed of 2240 ft/min. To raise this last average to that of the rotary engine we would have to use a bore/stroke ratio of 0.647/1. One American car has a bore stroke ratio of 0.733, while 0.652 is still in production in Great Britain. We must conclude that, at the same power shaft speed, the rotary combustion engine is the equivalent of a very long stroke reciprocating engine. Furthermore, one of the advantages emphasized in the description of the rotary engine is its ability to operate well at much higher speeds: to 9000 rpm in the example of the 15.3 cu in. engine. At this speed the average seal velocity would be 5800 ft/min. We have had no experience with such velocities, but since a considerable amount of the published data on the rotary is terminated without reaching peak horsepower, we suspect that seal life may be important factor at these speeds.

Bentele's Closure to Discussion

MR. HUBER'S statements are very reasonable and indicate that he has done considerable analytical work on this engine configuration. However, in order to draw definite conclusions from his analogies, all factors have to be considered and there, I feel, important effects have been missed and should be included.

The rotor of a Rotating Combustion Engine does not exert side forces on the housings as the piston of a reciprocating engine does; the bore/stroke ratio is, therefore, irrevalent. Our analyses and experiments have shown that the "transmission efficiency" from the gas force to the shaft torque is good and at comparable speeds higher than that of a reciprocating engine.

We agree that the sliding velocities of some Rotating Combustion Engines are higher than conventional piston speeds--the 4RC6 at 6500 rpm compared with the Ford Falcon shows that--but it is well known that the highest cylinder wear, and also probably ring wear, does not occur at the highest piston velocity but at the reversals of the pistons. In this respect, we have an advantage because "we do not stop." The combination of continuous sliding in one direction, oscillating motion of the apex seal, and a hydrodynamic effect between seal and rotor housing results in a tolerable wear of the apex seals.

Our combustion chamber shape is, judged by conventional standards, "not the best in the world," but the "Rotating Combustion" apparently produces, apart from the quenching effect, additional turbulence which improves combustion to a higher degree than comparisons with area/volume ratios, quenching areas, and flame lengths, would indicate. Less effective combustion and higher mechanical efficiency compensate each other so that the BSFC of Rotating Combustion Engines is competitive to reciprocating engines.

Problems Connected with NSU-Wankel Engine

Carl H. Meile
International Harvester Co.

THE NSU ENGINE has the appeal of novelty that any new and different mechanism acclaims. This is especially true when it can be demonstrated to work. Although there have been many attempts throughout the years to modify and improve on the basic reciprocating crank engine, most have met with commercial failure. In more recent years, there has been an increased tempo in the development and promotion of new internal and even external combustion engines. The gas turbine and free piston engines are prime examples. Now we have the Wankel rotary engine.

From an engineering or technical point of view, these efforts are noteworthy. The NSU engine exhibits ingenuity and inventiveness. The possibility of producing shaft power with a simple rotor and eccentric is certainly a departure from our present engine forms. The gentlemen and companies fostering this development are to be congratulated.

From an economic point of view, however, there are many questions that arise. Each objection, whether apparent or real, must be answered before this engine can become a commercial success. Granted, the engine is small in size for the horsepower and it can be built of conventional materials with familiar tooling practices, I would like to submit a list of trying obstacles which I am sure the promoters must be overcome:

1. Can reliability of the seals be achieved within a reasonable development period? If this is several years away, for example, the target for life will have to be advanced because present day engines are going to continue improvements in reliability and life also.

2. The biggest restriction for the NSU engine in the commercial vehicle field is the apparent long term development which must be accomplished to achieve diesel combustion efficiencies (200 BMEP). This should really be stated as turbocharged diesel, for herein lies the real competitor for many years to come.

3. Cost of production must either be substantially lower than for present gasoline engines, or a gross benefit in performance must be demonstrated to compete in the passenger car market. The remarkable performance and reliability of today's engines produced at the lowest relative cost in history makes it doubly difficult to encroach upon this market.

4. Applications to motor trucks and farm tractors will be hampered by high specific fuel. Applications to construction equipment will be attractive, provided the engine can be scaled up in size to meet the future power requirements of these vehicles.

There is one more point which should be emphasized. In today's thinking, we correctly evaluate performance of the entire power train system. It is performance at the wheels that is a true measure of successful vehicle. This evaluation demands a consideration of the transmission requirements for this engine. If the high speed of the NSU engine requires more elaborate gear reduction, this may offset some of its advantages. One should not be misled by dynamometer calibrations in making comparisons. For example, we frequently hear of the high specific fuel consumption of a gas turbine versus a diesel engine. The gas turbine has a built-in "hot" torque converter. To be fair, a diesel specific fuel reading should be taken after the torque converter. A similar situation may exist with the Wankel engine where useful power at useful shaft speeds can be measured.

In closing, the following specific questions are submitted:

1. What are the potential thermodynamic efficiencies in the NSU engine compared to a turbocharged diesel with intercooling?

2. Do you think the combustion chambers are capable of sufficient modification to permit multi-fuel operation?

Bentele's Closure to Discussion

IN ANSWER to Mr. Meile's questions, reference is made to the presentations themselves and to the comments in answer to Mr. Huber's questions. The diesel aspects have not been evaluated experimentally yet, and it would be premature to predict on the basis of analytical studies only. The other comments are well taken but we are also well aware of them and work toward successful solutions. Gas turbines operate at higher speeds and find applications.

Defects of NSU-Wankel Design

John P. Soltau
Joseph Lucas, Ltd.

FOR MANY YEARS, our company, as accessory manufacturers, have been closely linked with engine makers in all the fields of travel; and from our experience, the Wankel design seems to suffer from certain basic defects which are:

1. Lack of intake or squish turbulence which will slow down the combustion rate.
2. A very long, not compact combustion chamber.
3. A narrowing end-gas flame path.
4. A shielded spark plug uncooled by the working gases.

I would like to have the author's view on how these problems, which we think are fundamental, have been or will be solved. Also, Fig. 15 shows some log. P-log. V diagrams from which it would appear that heat is still being released at an expansion ratio of four, or half way down the working stroke, assuming a compression ratio of 8/1. In a piston engine, working on a normal air-fuel ratio, combustion has ceased, in the worst cases, at an expansion ratio smaller than two.

The author mentioned the possible use of "special fuels"

to hasten combustion and I would like to have more details on this. In practice, we have found that pure benzene, will only improve the burning speed by about 20%, and to quicken this process still further, one has to use such carburates as H_2, CO mixtures or pure H_2.

Bentele's Closure to Discussion

These questions have been amply answered by previous comments and publications.

Oral Discussion of Bentele and Froede Papers

reported by
Lawrence E. Maizga
U.S. Army Ordnance

WHAT MATERIAL is used for sealing?

Author's Reply: The best coating for the aluminum housing is either chrome or molybdenum plating.

Question: What is the lube oil consumption?

Author's Reply: Two gr/hp hr which is considered very reasonable.

Question: Is the engine sensitive to fuel octane?

Author's Reply: Only limited work has been done in regard to fuel sensitivity, but it indicates that the engine is insensitive to octane number. One test phase involved the use of a special gasoline having an octane rating of 30. No knocking was noted.

Question: Are the seal's spring loaded?

Author's Reply: There is a small preload affected by wave-springs to obtain primary contact but sealing thickness is accomplished by gas pressure acting at the rear of the seals.

Question: Isn't it true that the shape of the combustion chamber is not favorable to quick combustion of the gas?

Author's Reply: "This is true and I (Dr. Froede) admitted it. In our studies to date this has not proven to be important. When and if it does become important, I think two spark plugs could be used."

Question: Isn't it true that the spark plug doesn't receive proper cooling and would have low endurance?

Author's Reply: It is true that cooling is difficult, therefore we use a very cold plug and get 100 hr endurance.

Question: What is the idle speed?

Author's Reply: Idle speed as low as 500 rpm with smooth firing was obtained.

Question: Are thin apex seals better than thick one's?

Author's Reply: Apex seals of various thickness were tested and ranged from very thin to very thick. Best results were obtained somewhere in between.

Question: What is the fuel consumption at idle?

Author's Reply: No date on idle fuel consumption has been taken to date.

Metallic Tracer Method

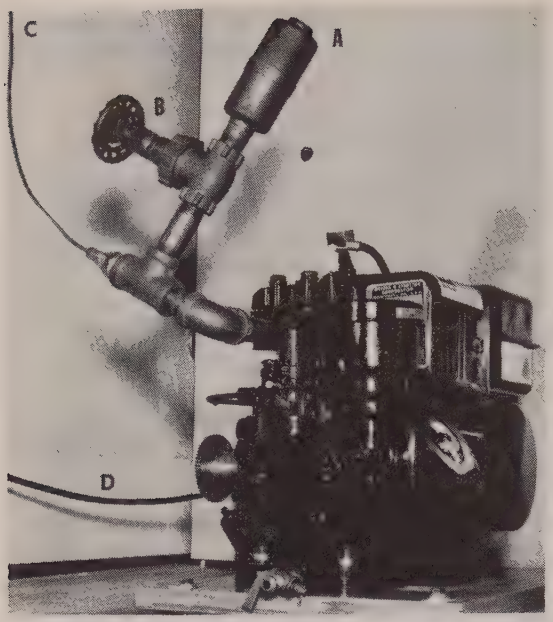

Fig. 1 — Single cylinder, 4 cycle engine used for measuring lubricant tracer in exhaust. A — main exhaust, B — gate valve, C — sample line, D — tachometer

F. R. Bryan, J. C. Neerman, and J. E. Hinsch
Ford Motor Co.

FROM TIME to time engine engineers have emphasized the fact that current methods in use for measuring oil consumption of automotive engines are less than fully satisfactory. The accepted methods involve extended operation of an engine, and gravimetric or volumetric measurement of the crankcase oil before and after the operating period. This is a reasonably accurate method providing sufficient engine operating time is involved, and providing the single integrated value is desirable. Ideally, however, an instantaneous detecting, and continuous recording system would be preferred. With this objective in mind, several possible analytical systems have been considered, and one particular method has been tested in principle and found to have interesting possibilities.

This method, which has now been tried in principle, consists of tracing a lubricant additive through the engine and detecting it quantitatively in the exhaust. The tracer fraction cannot be purely hydrocarbon in nature since molecular species derived from the lubricant are not distinguishable from molecular species of a fuel after both have been subjected to combustion. Therefore, an elemental tracer which is indestructible in the normal combustion process is desirable. The tracer atom should not be a component of engine fuel, or air; and should be detectable in very low concentrations. These considerations led to the selection of an alkali metal as the tracer element, and flame photometry as the means of detection.

Some preliminary calculations indicated that 0. 5% by weight of tracer metal in the lubricant should be measureable in automotive exhaust by means of flame photometry. Assuming oil consumption of an engine to be of the order of 1 gr/min, the tracer would be emitted at the rate of 0. 005 gr/min. Also, assuming exhaust flow to be about 50 cfm, approximately 1700 gr of exhaust would be emitted per minute. The concentration of metal in the exhaust stream would therefore be in the neighborhood of 3 ppm. Since sodium is known to be detectable to 0. 01 ppm in flames when the sample is introduced in the form of an aqueous mist, it was reasonable to expect to detect 3 ppm of sodium in exhaust with some degree of accuracy.

Outline of Experiment

A lubricant containing approximately 0. 5% sodium in the form of a sodium mahogany soap is used in a single cylinder, 4-stroke engine. A small portion of the engine exhaust is blended with a constant supply of auxiliary air and fed into the burner of a commercial flame photometer. The photometer measures the difference in intensity between the sodium line emission at 5893 A and a reference wavelength at 6078 A.

Photometer readings are taken to determine the effect of experimental variables such as photometer sensitivity, engine rpm, exhaust restriction, and auxiliary airflow. With these experimental parameters fixed, additive concentrations are varied stepwise from 0. 0 to 0. 48% sodium in order to establish relationships between sodium concentrations in the oil, and in the exhaust, with corresponding photometer

for Determining

Lubricant in Engine Exhaust

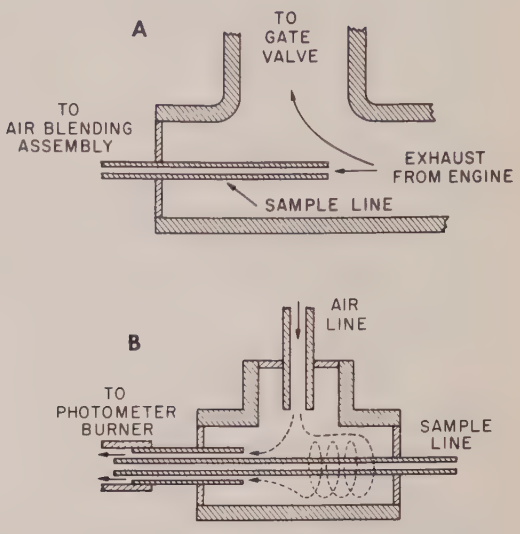

Fig. 2 — Sampling system. A — exhaust sampling assembly, B — air blending assembly

readings. Sensitivity of the method in terms of engine oil consumption is determined by comparing photometer readings with gravimetrically determined oil consumption values.

Equipment

Engine - A Briggs and Stratton, Model 60302, single cylinder engine, which has a horsepower rating of 2.25 maximum at 3600 rpm is used. Piston displacement is 6.65 cu in., and crankcase capacity is 1.25 pt. The engine (Fig. 1) is operated on nonleaded fuel and for these experiments no load was applied. An electronic tachometer with magnetic pickup indicates rpm directly. A gate-valve is installed in the main exhaust line just ahead of the muffler as a means of controlling exhaust flow into the sampling line.

Sampling Line - The exhaust sample line leading to the flame photometer is attached to the main exhaust ahead of the gate-valve in a manner which allows passage of particulate matter directly into the relatively small (1/16 in. ID) sampling line (Fig. 2A). The sample line continues as an unbroken tube directly into the base of the flame burner. Air is combined with the sample by means of a concentric outer tube (1/4 in. ID) which joins the sample line a few inches from the photometer (Fig. 2B). Airflow is measured and regulated to provide fixed flow rates from 1 to 2 cfm.

Photometer - A Baird-Atomic Model KY Flame Photometer (Fig. 3) was selected because of several features especially desirable for this experiment. The burner of this photometer is designed to operate a relatively low pressures, and yet will accommodate large sample volumes. Therefore, the flame is relatively large, and a reasonable percentage of exhaust sample can be fed directly into the burner without encountering a restrictive orifice. Matching the large flame is a large aperture optical system employing interference filters for wavelength resolution. This is a relatively efficient light system since no narrow slit is involved, as would be necessary with prism and grating spectrophotometers. The Baird-Atomic photometer is also equipped with multiplier type phototubes which provide the sensitivity necessary for this type of experiment.

The instrument is of the double-beam type (Fig. 4) allowing two wavelengths to be measured simultaneously. One beam measures the element line, and the second beam provides either a standard reference signal or a background compensating signal. In this experiment the second beam provides a background correction which partially compensates for incandescence due to soot in the exhaust. The 6708 A

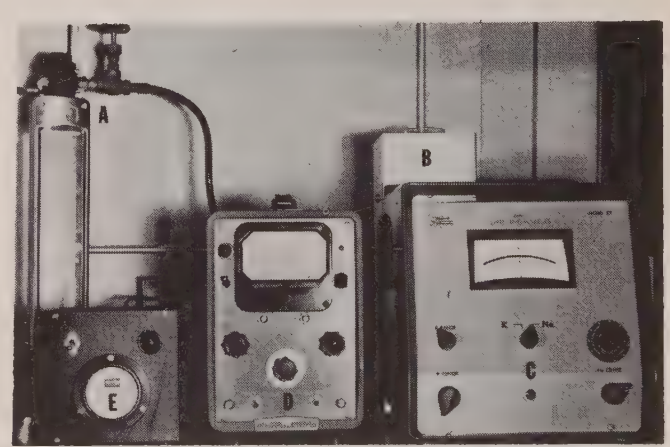

Fig. 3 — Instrumentation for measuring sodium in exhaust. A — auxiliary air flowmeter, B — photometer burner, C — photometer, D — tachometer, E — timer

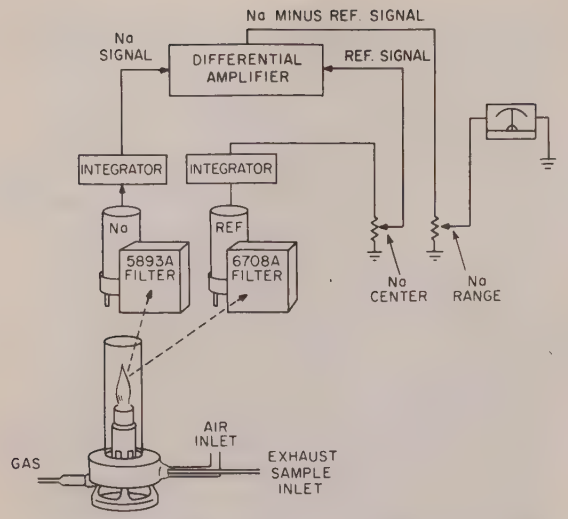

Fig. 4 — Simplified diagram of Baird-Atomic filter photometer used to detect sodium

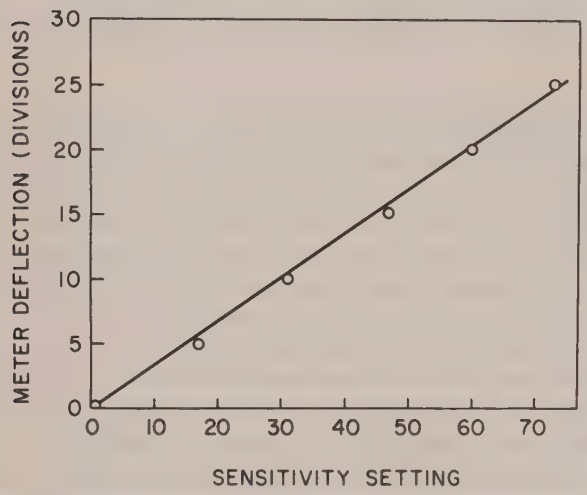

Fig. 5 — Meter response versus sensitivity setting — showing linear characteristic of photometer sensitivity control

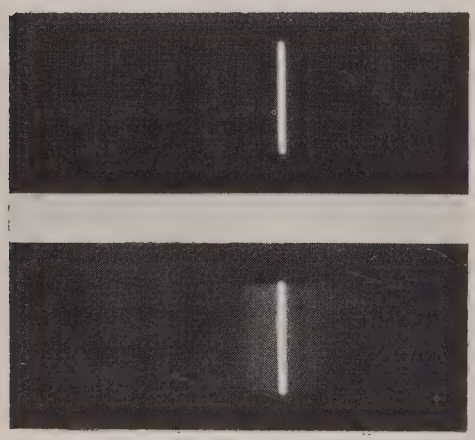

Fig. 6 — Three and twelve min photographs of the flame and sample taken through a Bunsen spectroscope. Background is noticeable in the lower (12 min) exposure

pass-band of the reference filter is designed to measure lithium. Since lithium is not present in the exhaust, however, this wavelength serves to measure background contributed by the sample and allows the instrument to indicate the difference between background at 6708 A and sodium emission at 5893 A. Ideally, a background correction obtained from a wavelength immediately adjacent to the sodium lines would be more desirable.

Experimental Procedure

Photometer Settings - The sensitivity range of the photometer is controlled by means of the "Na range" potentiometer (Fig. 4). Since the amplification factor becomes one of the experimental variables, the relationship of sensitivity setting to meter deflection needs to be known. A minimum detectable signal of 0.1 division was applied by slightly attenuating the reference signal (dark current, since no light source was involved) with sensitivity setting at zero. Sensitivity was then increased in steps to provide relationships between sensitivity settings and corresponding meter deflections. These values are plotted in Fig. 5. The response is essentially linear; doubling the sensitivity setting doubles the meter reading. This makes it possible to compare directly readings obtained over the full range of photometer sensitivities. The photometer zero is normally set by adjusting the "Na center," or reference signal potentiometer. This is done with the flame burning, but without the sample flowing.

Burner Operation - The burner is a modified Fisher laboratory burner with natural gas orifice. Air and sample enter the burner through a large annular opening at the base of the burner. A glass chimney protects the flame from drafts. Air is supplied at the rate of 1 to 2 cfm. The nonluminous flame is 1 in. in diameter at the base, and about 3 in. high.

The burner is designed to handle air suspensions of aqueous mists containing sodium or potassium salts in solution. An engine exhaust sample after cooling is somewhat similar in physical makeup, with the added complexities, however, of organic liquids and vapors together with metallo-organics, particulate carbon, metallic carbonates, and oxides. An exhaust sample from an engine operated with a sodium additive, and collected by means of a standard industrial hygiene type air sampler, revealed a dark, wet, oily substance with no visibly distinct particles which might contain the sodium. Spectrographic analysis of the material, however, revealed a high sodium concentration.

The burner flame, when supplied with exhaust from an engine with sodium additive, shows a visibly yellow color. In order to determine whether this color is due primarily to sodium line emission or to incandescent carbon, a small Bunsen spectroscope was used to view and record the spectrum. Fig. 6 shows two photographic exposures of the en-

tire visible spectrum. Although some background is evident in the longer exposure, the intensity is primarily due to sodium emission.

Engine Operation - Since oil consumption was suspected of being a function of engine rpm, this variable was investigated prior to establishing a set of standard engine operating conditions. Oil containing 0.48% sodium be weight was used in the engine. The main exhaust gate-valve was left fully open and engine rpm varied from near the stalling speed of 1000 rpm to over 3000 rpm. The photometer, at a sensitivity setting of 40, provided meter deflections from 0.5 to 9 divisions (Fig. 7). Readings showed considerable fluctuation, but a trend is discernible. Sodium signal is roughly proportional to rpm. Tachometer readings indicated that rpm values fluctuated at each setting by almost ±100 rpm. This might have occurred because the engine had no load, or because the air-vane governor was inadequate. The trend in the data does show that sodium signal is affected by engine rpm, and that tests should be conducted with controlled rpm. A speed of 3000 rpm was arbitrarily selected for subsequent tests.

Exhaust Control - The amount of exhaust sample going to the photometer can be controlled to some extent by means of the gate-valve in the main exhaust line. Closing this valve tends to force more exhaust into the smaller sample line (Fig. 1). Closing the valve too far, however, will cause malfunctioning of both flame and engine. Within the specific range of 1-2 turns, nevertheless, sodium signal is proportional to valve closure, as shown in Fig. 8.

From a fully open position to 1-turn closed the valve is ineffective due to design of the valve. From a position of 1 turn to 3-1/2 turns the gate closes rather uniformly, forcing more sample to the flame. However, after 2 turns, and with the valve aperture about half closed, the flame is inclined to fail and the engine noticeably labors. Because of the great dependence of sodium signal on the exhaust valve setting, it was decided to sacrifice sensitivity for reproducibility and run the tests with the main exhaust fully open.

Auxiliary Air - The amount of air fed to the flame in this case needs to be in the range of 0.4-2.1 cfm in order to support combustion of the natural gas fuel fed to the burner. Construction of the burner base and inlet system makes it expedient to introduce sample and auxiliary air together into the burner. Since the air dilutes the sample, it would be expected that sodium signal would vary somewhat inversely with amount of air fed to the burner. This general relationship is confirmed in the data presented in Fig. 9.

An appropriate nominal airflow rate would be 1 cfm. A somewhat higher flow of 1.8 cfm was adopted, however, primarily because the burner could be lighted more handily at the top of the chimney under this condition. Again sensitivity to sodium is considerably sacrificed by choosing the relatively high airflow rate. Airflow is satisfactorily regulated within ± 0.05 cfm by means of a Fischer-Porter flowmeter and needle valve.

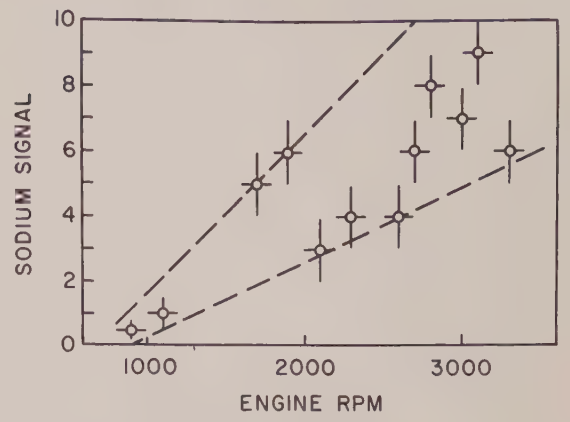

Fig. 7 — Engine rpm versus sodium signal — showing trend toward increased signal with increased rpm

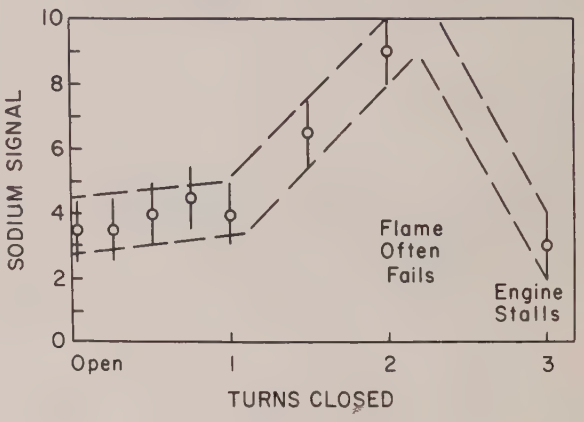

Fig. 8 — Main exhaust valve versus sodium signal — showing effect of valve closure on photometer reading

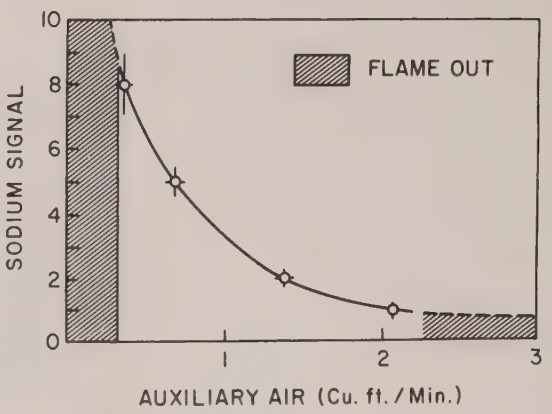

Fig. 9 — Auxiliary air versus sodium signal — showing stable flame range, and effect of auxiliary air on photometer reading

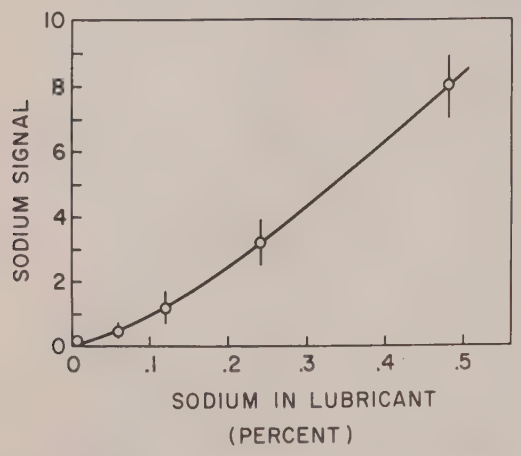

Fig. 10 — Sodium in lubricant versus signal — showing close proportionality between sodium concentration and photometer reading. (Main exhaust — open, Engine rpm — 3000, Auxiliary air — 1.8 cu ft/min, Photometer sensitivity — 40)

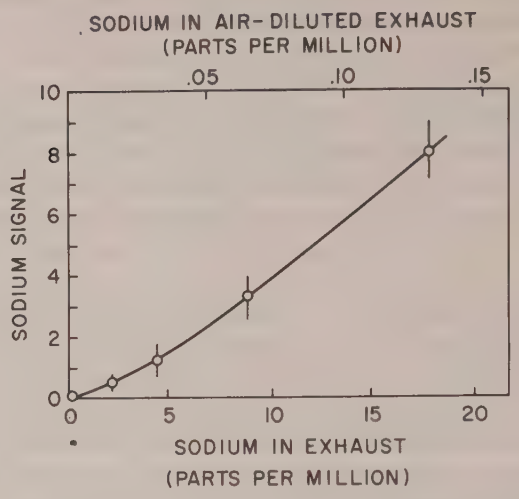

Fig. 11 — Calculated sodium in exhaust and in air-diluted exhaust versus sodium signal. (Main exhaust — open, Engine rpm — 3000, Auxiliary air — 1.8 cu ft/min, Photometer sensitivity — 40)

Results

Sodium Signal as Function of Sodium Concentration - Having determined the degree of control necessary on some of the major experimental variables, measurements were obtained to establish the reliability of the method. With fixed engine and photometer parameters, measurements were made using a series of additive concentrations in the engine lubricant. The engine was operated at 3000 rpm with the exhaust valve fully open. Auxiliary air was adjusted to 1.8 cfm, and photometer sensitivity set at 40 scale divisions.

Lubricant containing 0.48% sodium was blended with neutral base oil to provide oils with sodium concentrations of 0.0, 0.06, 0.12, 0.24, and 0.48% sodium by weight. The engine was run with each of these lubricants and the sodium signal was read from the photometer. The data are plotted in Fig. 10. The sodium signal varies directly, as expected, with the sodium content of the lubricant. The slight nonlinearity is not immediately explainable and is similar in magnitude to the experimental error.

The amounts of sodium detectable in the lubricant, the exhaust and the air-diluted exhaust can be calculated from the data presented in Fig. 10, together with the independently measured oil consumption, exhaust flow, and airflow values. An oil consumption test over a period of 4 hr of engine operation provided a consumption rate of 0.30 gr/min. The 0.48% sodium in the lubricant provides a photometer reading of 8 divisions. Since the meter can be read to ±0.5 division, approximately 0.05% or 500 ppm sodium in oil are detectable at the 0.3 gr/min oil consumption rate and a photometer sensitivity of 40. (Instrument sensitivity can be increased, if necessary, by a factor of 2.5.)

Detected sodium in terms of fraction by weight of the exhaust can be calculated by considering oil consumption rate together with total exhaust flow rate. Exhaust produced by the engine under these same operating conditions, as measured by a Rockwell gas meter, and after cooling to essentially room temperature, was 2.5 cfm (71 l/min). Using a volume to weight conversion factor of 1.15 gr/l, the exhaust flow rate becomes 81.4 gr/min. Since 500 ppm sodium in the oil is detectable, and assuming all of the oil is emitted in the exhaust, the sodium in exhaust is then detectable to 2 ppm. A plot of sodium in exhaust versus sodium signal is shown in Fig. 11.

The portion of the exhaust actually fed to the flame, as measured by a bubble flowmeter, is 0.38 l/min (0.44 gr/min). This quantity is mixed with a flow of 1.8 cfm (58.6 gr/min) of air to support combustion of fuel in the flame. Thus, the ratio of exhaust to air as the sample enters the flame is 0.007 and the sodium detected in the air-diluted exhaust is, therefore, estimated to be less than 0.02 ppm. (See upper abscissa, Fig. 11.)

Sodium Signal as Function of Oil Consumption - In order to determine the usefulness of the sodium signal in terms of engine oil consumption, it was necessary to provide a range of oil consumption values. This could have been done by employing a series of similar engines in various states of repair. A simpler procedure, however, was the use of the same engine with a series of piston ring modifications.

The engine, as received from the factory, and as operated on the previous tests, used oil at the rate of 0.30 gr/min. Under our standard operating conditions (3000 rpm, open exhaust valve, 1.8 cu ft of auxiliary air per minute, photometer sensitivity of 40) the sodium reading, using 0.48% sodium in the oil, averaged about 9 divisions. Since

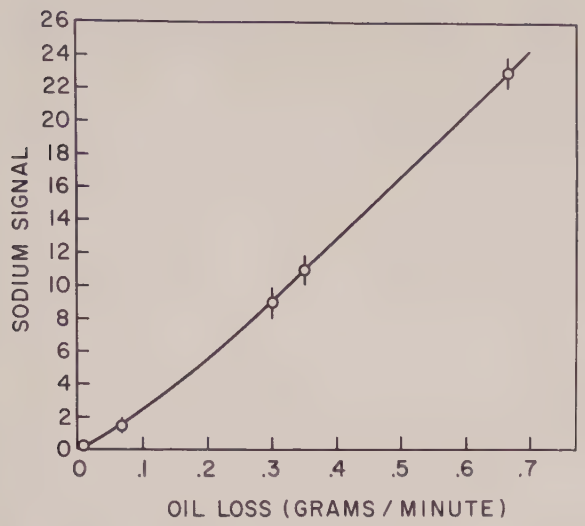

Fig. 12 — Oil consumption versus sodium signal — showing an almost linear relationship between oil consumption rate and photometer reading. (Main exhaust — open, Engine rpm — 3000, Auxiliary air — 1.8 cu ft/min, Photometer sensitivity — 40)

the engine was in essentially new conditions it was sent to the shop with instructions to modify for increased oil consumption. The oil ring (bottom ring) was lapped 0.001 in. on the circumference. In this condition, however, the oil consumption over a 4 hr period showed a lower rather than higher consumption rate. Oil loss amounted to only 0.08 gr/min, while the photometer reading averaged only 1.5 divisions. Obviously the engine was now in better condition in respect to oil consumption than previously.

The engine was next modified more drastically by grinding two 0.005-in. flats on the center and bottom rings. In this condition oil consumption amounted to 0.35 gr/min, and photometer readings averaged 10.5 divisions. Although oil consumption rate in this case was only 0.05 gr/min greater than the original rate, it was encouraging to find the two consumption rates resolved by means of the sodium signal. A further modification of the engine involved an additional two 0.005 in. flats on each of the bottom two rings. The resulting oil consumption rate was 0.67 gr/min, and the sodium signal averaged 23 divisions.

The oil consumption versus sodium signal relationship for the four engine conditions is plotted in Fig. 12. The gravimetrically determined oil loss in terms of grams per minute bears an essentially linear relationship to the potometer reading. Considering the ± 1 division fluctuation in sodium signal during supposedly steady state engine operations, the minimum detectable change in oil consumption rate is 0.05 gr/min under the conditions of this experiment.

Conclusions

A metallic lubricant additive in low concentrations can be detected and measured quantitatively in engine exhaust by means of emission spectroscopy. Flame excitation of the exhaust sample provides sufficient sensitivity of detection for alkali metal additives. Sodium, in particular, can be detected in exhaust in concentrations of the order of 1 ppm. Potassium or lithium tracers would be expected to have nearly the same detectabilities as sodium. Rubidium, calcium, and strontium should be detectable in quantities of a very few parts per million. An optimum additive content in the oil would be a compromise between an amount sufficiently large to provide the measuring accuracy required, and an amount small enough to avoid mal-lubrication of the engine.

The rate of lubricant loss through the exhaust system can be nearly instantaneously indicated and recorded. The time constant is largely dependent on the length and diameter of the sampling line between engine and photometer. In the experiments described, the time lag was about 2 sec, but no doubt could have been reduced to less than a second.

The future utility of a continuous and almost instantaneous measurement of lubricant in exhaust is intriguing from several standpoints. First, it would provide a means of studying short term oil consumption characteristics as a function of engine operating variables. Also, the method may be used to shorten the time necessary to obtain oil consumption data under any given set of operating conditions. A rapid method of checking oil consumption may establish the feasibility of 100% production inspection of new engines. The possible advent of sealed crankcases emphasizes the desirability of pre-determining and limiting oil consumption at the time of engine assembly.

Discussion

Sampling Methods

Petroleum Division
British Petroleum Research Center

THE AUTHORS' approach to the difficult problem of continuously measuring lubricating oil consumption is both novel and of considerable interest. It appears that the method for determining the tracer is satisfactory. The slight curvature of the curves in Figs. 10-12 was probably due to some nonlinearity in the detector, which would, of course, be unimportant if a preliminary calibration such as that in Fig. 12 was obtained.

It appears that one of the main difficulties in operating the suggested system to measure oil in engine exhausts lies in the method of sampling. It seems rather unlikely that with the present sampling configuration the sodium concentration of the sample would be the same as the mean concentration in the exhaust gas. This would not invalidate the method as long as the exhaust gas flow pattern was always

the same. But if the method were applied generally, it would be difficult to interpret results because the flow pattern would vary widely with speed and load. Because of the variation in flow pattern, the sodium concentration in the sample would no longer be a fixed multiple or fraction of the mean sodium concentration in the exhaust gas. In fact, the effect of changing the exhaust conditions by partially closing the gate valve cited in the paper, showed how sensitive the system was to changes in the exhaust gas flow pattern.

The existing system would undoubtedly be very useful in testing oils in the laboratory under constant engine conditions, but the sampling errors could give misleading impressions of the true effect of speed and load on oil consumption. This may account for some of the scatter in Fig. 7. We suggest that the following may be applied to obtain more representative samples of the exhaust gas.

1. The probe should be placed in the center of a straight length of an exhaust pipe which is fitted to the exhaust manifold.

2. Use isokinetic sampling if the sodium is in particle form larger than 10 microns, that is, ensure that the speed at which the gas flows in the sampling probe is the same as that in the main exhaust system to prevent separation of solid particles.

Application of Metallic Tracers to Engine Research

P. A. Bennett, and C. R. Begeman
General Motors Corp.

THE AUTHORS have presented a very interesting application of flame photometry to the problem of determining engine oil consumption. In addition, the work is an example of the new approach often needed to solve a difficult problem. However, the paper raises a number of questions. Potential users of the technique need additional information before the proposed method can find wide application.

One of the major limitations of the proposed method is that it must be calibrated against a more fundamental method of measuring oil consumption. This may have to be done for every operating condition and for different engines.

It would appear that the method may not permit the determination of instantaneous oil consumption rates. In this situation, the volume of gas fed to the photometer must be known as a fraction of total exhaust flow at each engine condition, or the sample must be proportional to the total gas flow. Do the authors know if they obtained proportional flow in their system? What was the sampling flow rate and was it constant for a given engine operating condition? Did deposits accumulate in the sample line to decrease the sample flow rate?

Table A - Calcium in Combustion Chamber Deposits

Test Duration	48 hr
Total Oil Consumed	250 gr
Calcium content of oil (0.8%)	2 gr
Total Combustion Chamber Deposits	25 gr
Calcium content of deposits (2.0%)	2.5 gr
Calcium in Combustion Chamber Deposits, Total Calcium Lost From Crankcase	25%

It is required, of course, that the sample fed to the photometer be representative of the total exhaust composition. However, starting with a clean engine, a certain amount of additive metal will remain in the engine combustion chamber, exhaust system, or the sample lines. This may be illustrated by Table A.

These data were obtained using an oil which contained a relatively large amount of calcium. Multiplying the total amount of oil consumed by the oil calcium content gives a value of about 2 gr of calcium lost from the crankcase during the 48 hr test. Combustion chamber deposits removed from the engine at the completion of the test weighed 25 gr and subsequent analysis established that about 2% of this was calcium. Accordingly, some 25% (25 x 0.02/2.0) of the total calcium consumed remained in the combustion chamber. Do the authors have any information concerning the amount of sodium remaining in the combustion chamber deposits in their tests?

Also, the sampling line in the Ford apparatus would appear to be relatively cool. This would lead to condensation or precipitation of material. Did the authors observe such material accumulation in the sampling line?

Sodium retention in some part of the engine or sampling system may account for the nonlinearity of the authors' curve of sodium signal versus lubricant sodium content shown in Fig. 10. At low sodium concentrations, any sodium lost in deposits may be a significant portion of the total exhaust sodium content. That is, the observed signal may be a relatively small part of the signal which would have been observed had no losses occurred. At high concentrations, the sodium lost in deposits would probably be a smaller percentage of the total exhaust sodium content. In order to apply the Ford method at all rigorously, it is necessary that the rate of sodium deposition in different parts of the engine or sampling system be determined for each operating condition.

A significant amount of lubricant is lost from an engine via the breather tube. Would the authors comment on the

possible application of their technique to the measurement of oil loss from this source?

We believe that the proposed method has considerable promise as a tool for measuring oil losses from engines. We hope that the authors continue tnis work with the objective of developing a technique for measuring the instantaneous rate of oil loss from engines.

Authors' Closure To Discussion

THE AUTHORS wish to acknowledge the comments of Messrs. Bennett and Begeman, especially in calling proper attention to the several considerations necessary in the application of metallic tracers to engine research.

The purpose of the single experiment described was to demonstrate the feasibility of a concept. It was not intended at this stage to produce a completely engineered instrumentation system. The potential of the technique seemed sufficiently promising, however, to warrant reporting at this time. The authors agree that considerable development and engineering would be required to render the method absolute and universally applicable.

Depending on the intended application, several avenues of further work are apparent. It should be possible (though not easy) to make an absolute calibration of the burner-photometer response per gram of sodium passing through the burner in unit time. Proportional, or better yet, isokinetic sampling would certainly be desirable for applicability of the method under widely varying exhaust flow rates such as would be encountered in engine variable studies.

It is recognized that retention of the tracer metal could be a serious problem in either research or engine inspection applications. There is very likely retention of sodium in several parts of the system. The remarkable aspect is that the rate of deposition appears to be substantially constant under the conditions of the experiment. If the slight nonlinearity of response is due to sodium retention we are pleased that the effect is this small.

There are several changes which we would recommend as improvements. The sampling line should be shorter for faster response. The sampling tube should probably be of larger diameter, and externally heated to prevent condensation of moisture. Although the photometer optics and electronic circuitry appear to be adequate, a larger and more rugged burner would be desirable.

We have not considered metallic tracers for the determination of breather tube losses because of the impending obsolescence of external type breathers.

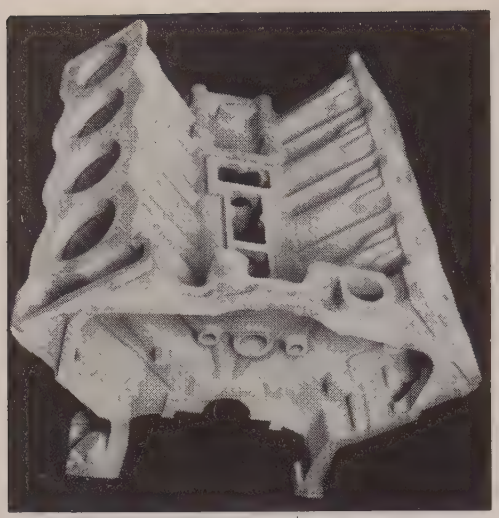

Fig. 1 — Cast aluminum V-8 diesel cylinder block

Stress Analysis of Aluminum

H. W. Van Camp
Aluminum Co. of America

THIS PAPER describes the application of experimental stress analysis in the development program of a cast aluminum V-8 diesel cylinder block. (See Fig. 1). This wet liner type block is part of the new compact, lightweight military engine, model LVDS 1100, developed for the Ordnance Corps by the Caterpillar Tractor Co. (Figs. 2 and 3). It is an 8-cyl, 4-cycle, 90 deg V-type engine with a 5.4 in. bore and 6.5 in. stroke. Displacement is 1.193 cu in. Liquid-cooled and supercharged, it is rated at 580 hp at 2200 rpm. With accessories, the engine weighs only 2485 lb or 4.3 lb/hp. The cylinder block weighs approximately 300 lb. The approximate dimensions of the complete engine are 52 in. long, 48 in. wide, and 43 in. high.

Production and service requirements dictated that the block be designed for the economical permanent mold process. Alloy 355, with a T7-type heat treatment, was chosen on the basis of castability, properties, and stability. The prototype parts were sand-cast in the same alloy.

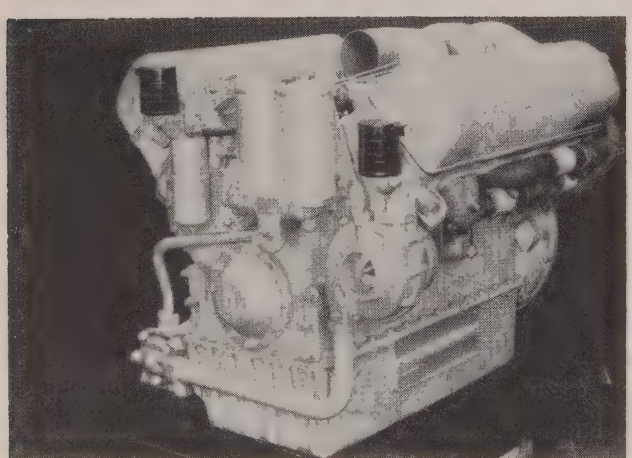

Fig. 2 — Military engine, model No. LVDS 1100

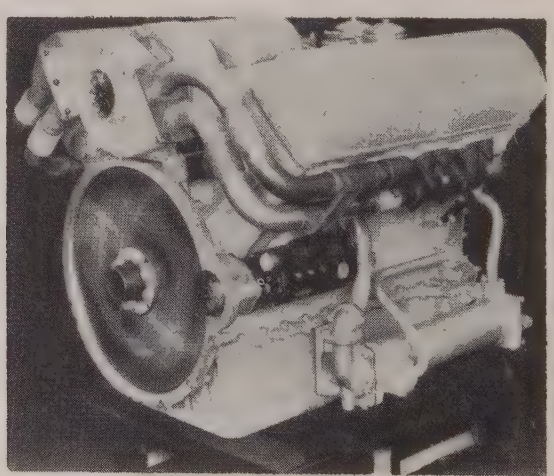

Fig. 3 — Military engine, model No. LVDS 1100

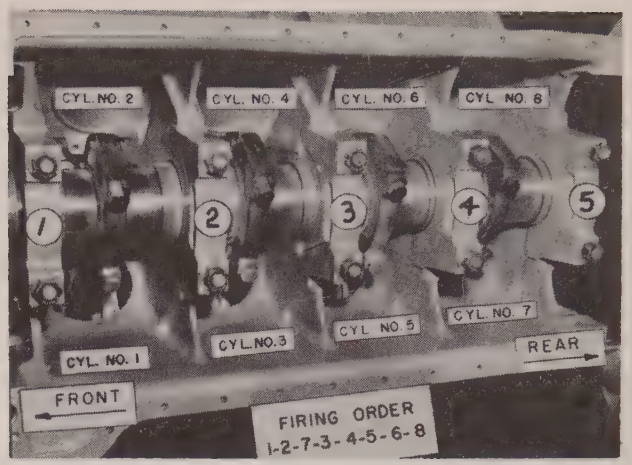

Fig. 4 — Bottom view of block showing straight shaft installed

V-8 Diesel Cylinder Block

Alcoa was fortunate in being able to work with Caterpillar on the block and other aluminum components from the early design stage. This was advantageous, since the experience of both companies in their respective fields could be incorporated in the prototype castings.

Testing of V-8 Block

Machined castings were provided for both stress analysis and engine tests, making it possible to conduct the two simultaneously. To further expedite the program, the stress analysis was made by using simulated loads based on actual cylinder pressure measurements and computed bearing forces. Through this program, difficulties encountered in one test did not delay the other, and the test information was developed more rapidly.

The components used in this test program included the block with cylinder liners installed, cylinder heads, pistons, and connecting rods. In order to facilitate testing and inspection of Stresscoat patterns, the crankshaft was replaced by a straight shaft and the oil pan was removed. Fig. 4 is a bottom view of the block showing the straight shaft installed, the orientation of the cylinders and bearing caps, and the firing order of the engine.

Two types of loads were simulated:

1. Cylinder pressure loads.
2. Main bearing dynamic vector force loads.

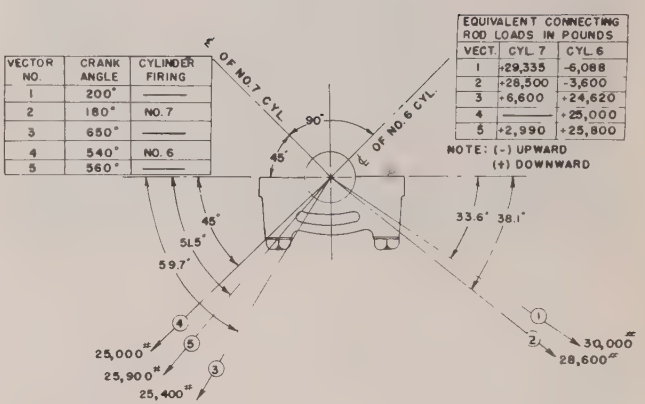

Fig. 5 — Maximum vector forces on No. 4 main bearing at 2125 psi cylinder pressure and 2200 rpm

The cylinder loads were based on a 1650-psi operating pressure. However, in testing, pressures as high as 3550 psi were applied to develop Stresscoat patterns.

The vector force loads were based on computed horizontal and vertical bearing forces at the No. 4 bearing for a peak cylinder pressure of 2125 psi at 2200 rpm. This bearing was selected, since in the firing order it is the only bearing which experiences two consecutive firing impulses from cylinders in the same bank (cylinders 6 and 8). These forces were simulated at the No. 4 bearing, by simultaneously applying cylinder pressure and inertia-type loads to the con-

necting rods of the No. 6 and No. 7 cylinders. The five maximum vector forces for one complete firing cycle were applied. These are shown graphically in Fig. 5, together with the equivalent No. 6 and No. 7 connecting rod loads.

Fig. 6 illustrates the cylinder arrangements used to produce the test loads. Cylinder pressure loads were applied, as shown at the right. The cylinder was pressurized hydraulically through an inlet adapter installed in place of the precombustion chamber. Pressures were confined to the normal combustion chamber volume by a spacer and leather cup seal on top of the piston. Inertia loads for the dynamic vector forces were obtained with a hydraulic jack, as shown at the left.

Figs. 7 shows a typical test setup. This particular one was used for the strain gage work, with cylinder pressures simulated hydraulically. In the left foreground is the strain indicator and selector box. A precision pressure gage and hydraulic pump is to the right. The large fabricated wheels attached to either end of the block were to facilitate handling of the assembly.

In the Stresscoat phase of the analysis, the complete block and the bearing caps were coated. However, cylinder pressure loads were applied only to the right cylinder bank, since the block was nearly symmetrical. Individual cylinders were loaded in increments to 3550 psi. Adjacent cylinders were loaded simultaneously as high as 1250 psi. Figs. 8-11 show the strain patterns obtained from cylinder loads and assembly loads due to torquing the cylinder head and bearing caps. The letters and numbers adjacent to each pattern identify it according to the type of stress indicated and the load producing it, as shown in Table 1. These patterns represent areas of stress concentration in the assembly where the strain exceeded 650 Mu in./in. which was the minimum strain at which cracks would develop in the brittle lacquer test. The direction and density of the pattern cracks also indicated the direction and relative magnitude of the principal stresses, providing a basis for strain gage locations.

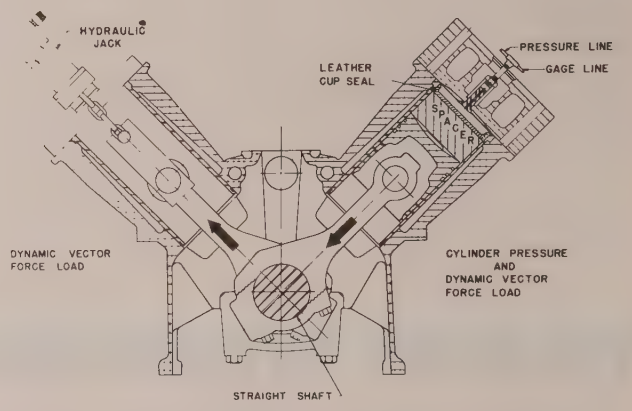

Fig. 6 — Loading arrangement for V-8 diesel cylinder block

Table 1 - Stresscoat Analysis Results
Identification of Patterns

All Stress Levels 6500 Psi or Higher

Pattern	Type Of Stress	Load Producing Pattern
PS	Compression	Bearing Cap Nuts Torqued to 200 lb-ft
17	Tension	1250 psi pressure in cylinders No. 5 and 7
18	Tension	500 psi pressure in cylinders No. 5 and 7. All bearing caps but No. 4 out
25	Tension	3000 psi pressure in cylinder No. 1
28	Tension	3000 psi pressure in cylinder No. 7
29	Tension	3550 psi pressure in cylinder No. 7
30	Tension	3000 psi pressure in cylinder No. 3
35	Tension	Head nuts torqued to 150 lb-ft
36	Compression	Head nuts torqued to 150 lb-ft

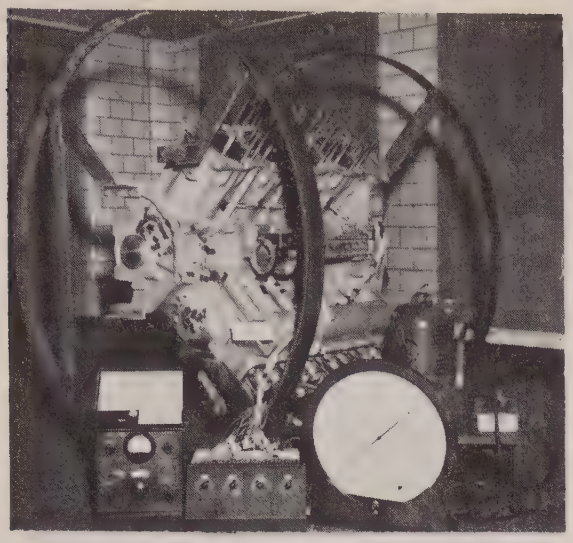

Fig. 7 — Typical test setup

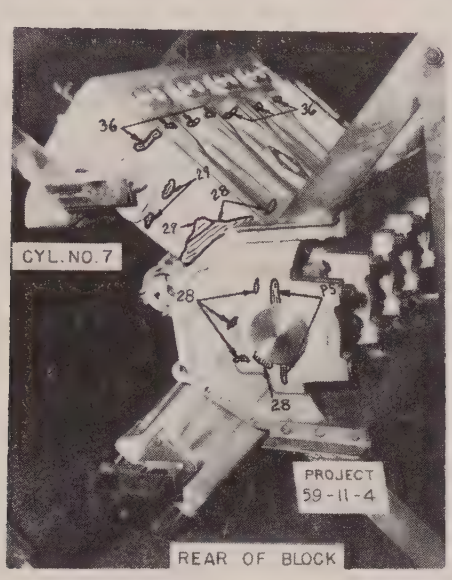

Fig. 8 — Strain pattern obtained from cylinder loads and assembly loads due to torquing the cylinder head and bearing caps

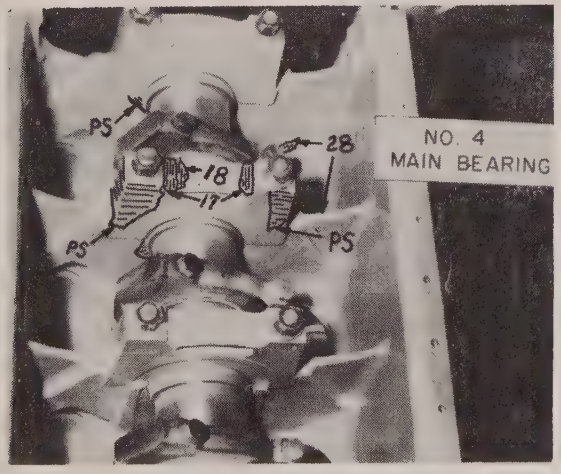

Fig. 9 — Example of strain pattern

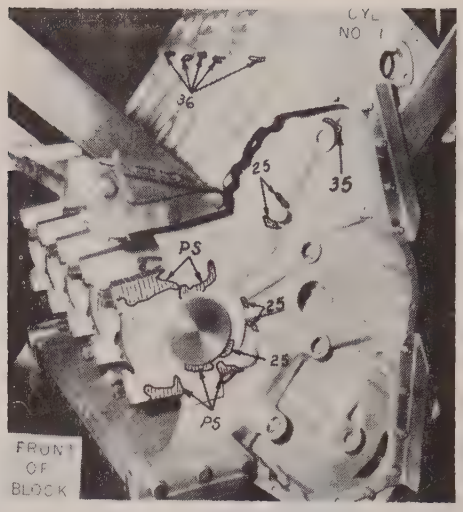

Fig. 10 — Strain pattern

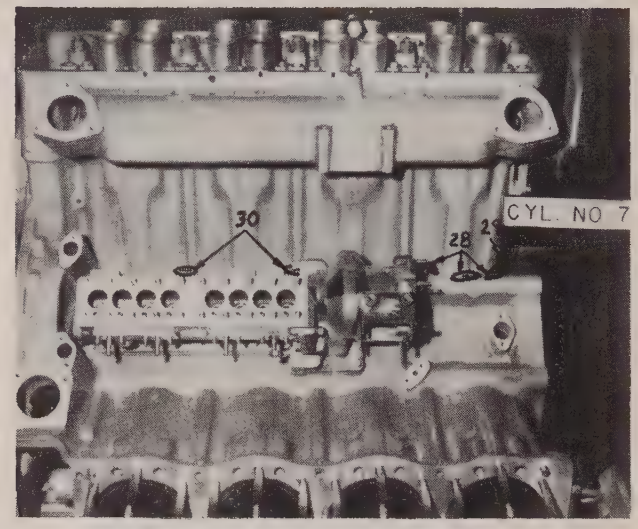

Fig. 11 — Strain pattern

Two gages were located at right angles in the stud hole of the No. 4 bearing cap, on the basis of fatigue fractures of several caps in the test engine. A typical fracture is shown at the left in Fig. 12. These fractures occurred after approximately 100 hr of operation at an average cylinder pressure of 1550 psi at 2200 rpm. The arrow indicates the fracture origin. Gages 38 and 39 were located in the stud bore, as shown in the sketch at the right. The location of gage 39 corresponded to the origin of the fracture and was oriented 90 deg to the fracture.

Thirty-three additional gages were located on the basis of Stresscoat patterns.

Three types of load were applied to determine maximum operating stresses in the gaged areas. These consisted of the following:

1. Assembly loads, due to torquing the bearing caps and cylinder head.
2. Individual and combined cylinder pressure loads in

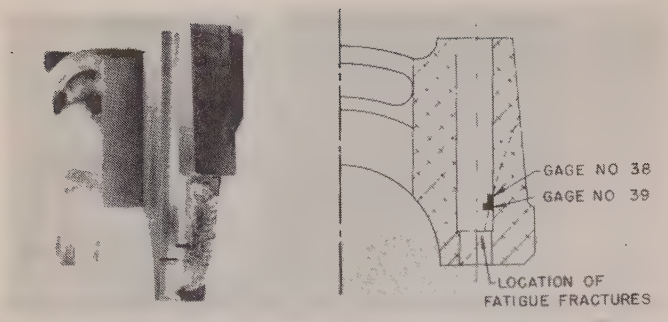

Fig. 12 — Aluminum V-8 diesel bearing cap stud bore fracture and strain gage orientation

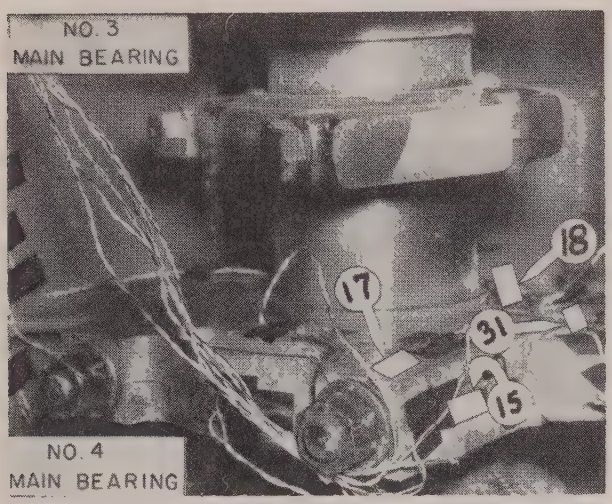

Fig. 13 — No. 4 bearing cap stud bore, gages 38 and 39

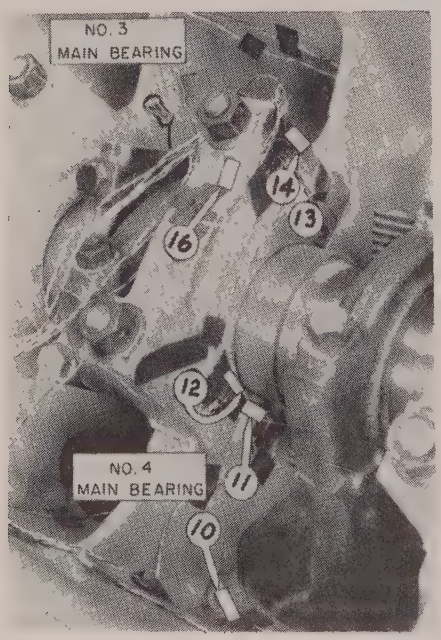

Fig. 14 — No. 4 bearing bore, tangential gage 18

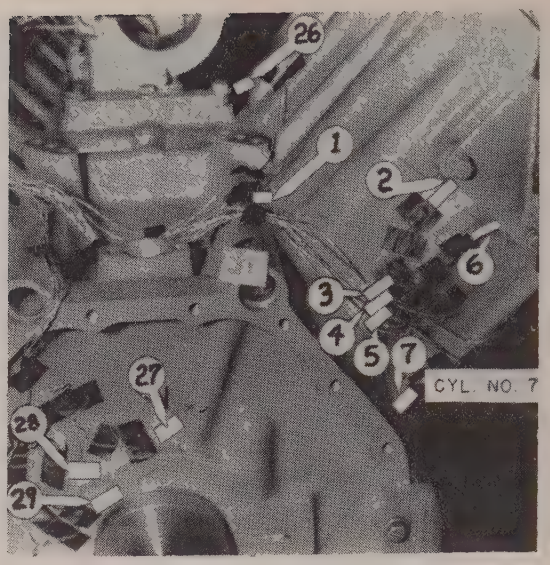

Fig. 15 — No. 4 bearing web fillet at side wall, gage 10

cylinders of both banks.

3. Five dynamic vector force loads at the No. 4 bearing. (Equivalent to 2125 psi cylinder pressure at 2200 rpm.)

A survey of the strain gage results indicated four areas having stress levels significantly higher than the others. These included:

1. No. 4 bearing cap stud bore, gages 38 and 39 (Fig. 12).
2. No. 4 bearing bore, tangential gage 18 (Fig. 13).
3. No. 4 bearing web fillet at side wall, gage 10 (Fig. 14).
4. The blend of cylinder No. 7 to block, gages 5 and 7 (Fig. 15).

Basis of Interpretation of Stress Analysis

The results of such an analysis must be weighed critically and correlated with other design factors, to effectively evaluate the strength of the design. Three basic fators are involved:

Load - The simulated loads upon which stresses are based should be representative of those occurring in service. The loads used for this analysis were considered to be equal to or higher than corresponding normal operating loads.

Stress - The loads applied to a diesel engine cylinder block are highly repetitive in nature, and fatigue resistance is the major design consideration. Since a diesel engine is expected to have a long service life and to operate at a high load factor, the operating stresses are evaluated at the endurance limit. In aluminum, this is considered to be equivalent to the fatigue strength at 500,000,000 cycles.

The stresses to be used in evaluating the block were those measured by the strain gages whose location, size, and direction were indicated by the Stresscoat analysis, except for

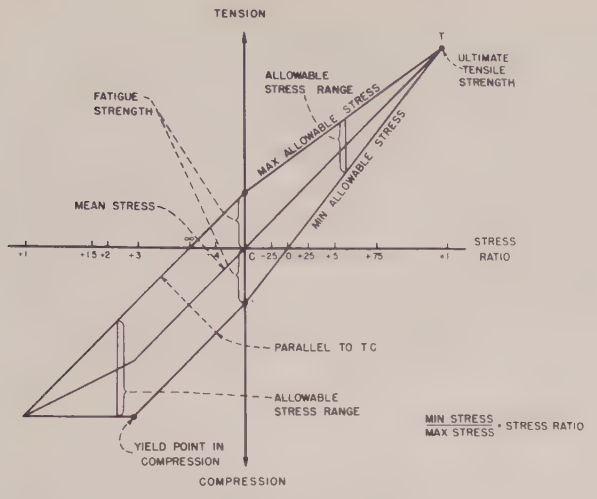

Fig. 16 — Modified Goodman diagram

those in the bearing cap stud holes.

Principal stresses were obtained in the stud hole of the bearing cap, based on the resultant of right-angle strain gage measurements taken in the direction of the maximum and minimum normal strains. Strains obtained from single gages in all of the other gaged areas provided apparent stress values. Apparent stresses based on strain indications from gages oriented by Stresscoat are adequately accurate, except in complex stress fields.

In general, static and dynamic components of stress should be considered in a cylinder block. Possible static components would be those due to residual, thermal, and assembly load stresses. Residual stress measurements were not considered necessary, because of the favorable heat treatment used. Thermal stresses were not dealt with in this investigation, as it was felt this block was properly designed to keep them at a low level. The stresses used to evaluate this design were the steady stress due to assembly of parts, and the added dynamic stress due to inertia loads and combustion chamber pressure at rated load and speed.

Material - The possibility of these measured stresses resulting in service fatigue failure is evaluated by their relationship to the envelop of an appropriate allowable stress diagram. The modified Goodman diagram, shown in Fig. 16, was chosen for this analysis. This is perhaps the most widely used technique for evaluating fatigue strength of designs. It is constructed on the basis of the static mechanical properties and fatigue data. The envelope of the diagram represents the fatigue strength of the material for a given temperature and life at different stress ratios. Fatigue failures would be expected in areas where operating stresses exceed the allowable diagram limits.

How effectively the diagram evaluates the design strength depends on the proper choice of tensile and fatigue strength values. It would be desirable to use a tensile strength based on test bars taken from representative areas of the production casting. However, in the absence of such data, 75% of the minimum properties of separately cast test bars, in the same alloy and temper as the casting, should be used. This value is representative of what can be expected in production castings of commercial quality. Certain areas within these castings may exceed this standard. If necessary, specialized casting techniques may be employed, whereby considerably higher strengths can be guaranteed in specific areas.

Selecting the fatigue strength to be used is more difficult than obtaining static properties. Fatigue data is available in the form of rotating beam, plate bending, and direct stress standard laboratory tests. Experience has shown that data from notched rotating beam tests incorporated in the modified Goodman diagram reliably predicts success or failure of production parts.

The fatigue strength used to evaluate the cylinder block was based on the published fatigue data (1)*, shown in Fig. 17. These are the scatter band limits of smooth and notched rotating beam fatigue data for sand-cast and permanent mold specimens in various alloys and tempers. It is permissible to represent the different alloy and tempers by a single set of limits, since their scatter bands are essentially the same. It will be noted that the scatter bands of the sand cast and permanent mold specimens also overlap to some extent, particularly the notched data at high numbers of cycles. The lower endurance limit of the notched permanent mold scatter band was chosen as the allowable fatigue strength of the block. Temperatures which this block would experience would not alter significantly the tensile and fatigue properties developed at room temperature.

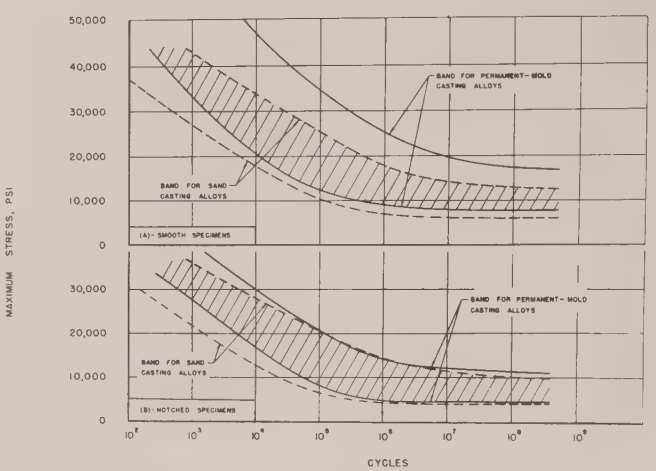

Fig. 17 — Scatter band for sand cast and permanent mold aluminum alloys

*Numbers in parentheses designate References at end of paper.

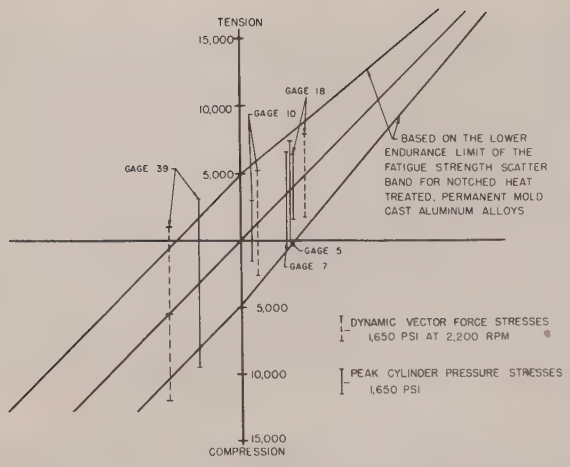

Fig. 18 — Aluminum V-8 diesel cylinder block assembly maximum cyclic stresses

Interpretation of V-8 Stress Data

The interpretation of the results was based on these tensile and fatigue values, together with the other design factor considerations previously discussed. Only the interpretation of the four higher stressed areas represented by gages 5, 7, 10, 18, 38, and 39 (Figs. 12 - 15) will be covered. These are plotted on the modified Goodman diagram, shown as Fig. 18. The vertical solid and dashed lines represent the maximum cyclic stresses produced in the four areas due to cylinder pressure and dynamic vector force loads, respectively. The stresses at gage 39 extend beyond the safe limits of the diagram, indicating that failures would occur in this area. The stresses of the other three areas fall within the diagram limits, indicating a safe stress level.

Gage 39 was located in the bearing cap stud bore, where fatigue fractures occurred in the engine after approximately 100 hr of operation. In this period of time, the cap experiences 6,600,000 load or stress cycles. In Fig. 17, the lower stress limit of the notched sand-cast fatigue data at this number of cycles is essentially the same as the lower endurance limit of the permanent mold alloys. The stresses measured at gage 39, therefore, accounted for the fatigue fractures which occurred in the initial engine tests.

Summary

This paper has discussed the role of experimental stress analysis in product design. The criteria for evaluating aluminum castings for fatigue was described in the case history of a prototype aluminum diesel cylinder block. The results discussed have been limited to four areas of the block, one of which correlated stress measurements and their interpretation with fatigue fractures which occurred in the initial prototype engine tests. This was the only area exhibiting critical stresses exceeding the allowable cyclic working stress of the block material.

Reference

1. R. L. Templin, F. M. Howell, J. O. Lyst, "Fatigue Properties of Cast Aluminum Alloys," Product Engineering, (May, 1952).

An Advanced Automotive Gas Turbine Engine Concept

I. M. Swatman, and D. A. Malohn
Ford Motor Co.

AT THE CLOSE OF the first decade of gas turbine progress within the automotive industry, it still appears that the automotive turbine is at an awkward age. The reciprocating engine, particularly the diesel, is formidable competition. Although significant advances have been made in automotive turbine research, there have not been any startling discoveries. In fact, engines developed to date represent careful refinement of principles known to the gas turbine industry for 25 years or more. While not wishing to detract from the fact that these developments have been a great stride forward, it is significant that industry has not yet made the breakthrough that would give sufficient encouragement to warrant placing an automotive gas turbine on the market in competition with reciprocating engines. The engine concept discussed in this report contains the potential for making this breakthrough.

Prior to 1957, gas turbine activity of the Ford Motor Co. was concentrated primarily on the design and development of compressor, turbine, and heat exchanger components, and on the construction of a low-pressure, regenerative gas turbine engine. While this engine indicated a potential advantage in durability, it was significantly inferior in size and fuel economy and had only marginal advantage in weight. Results of dynamometer testing and vehicle operation (Fig. 1) were satisfactory, although the engine did not appear to offer a serious threat to reciprocating engines of that period. This was particularly apparent for passenger-car application, where a replacement powerplant would obsolete a vast investment in reciprocating engine production equipment. Without an unforeseen major breakthrough in the area of materials and fabrication techniques, it appeared that the gas turbine would remain a premium-priced powerplant for a number of years.

Following a survey of applications offering sufficient production potential to interest the Ford Motor Co., it was concluded that if a significant breakthrough in concept were possible, heavy trucks would be an ideal application for the gas turbine powerplant. With judicious design, a performance advantage appeared feasible, and some weight saving could be expected. It was believed that, after suitable development, a turbine engine would have superior overhaul-life characteristics. The gas turbine would also then be placed in a market competing with premium priced diesel engines. For this application, however, it appeared that the fuel

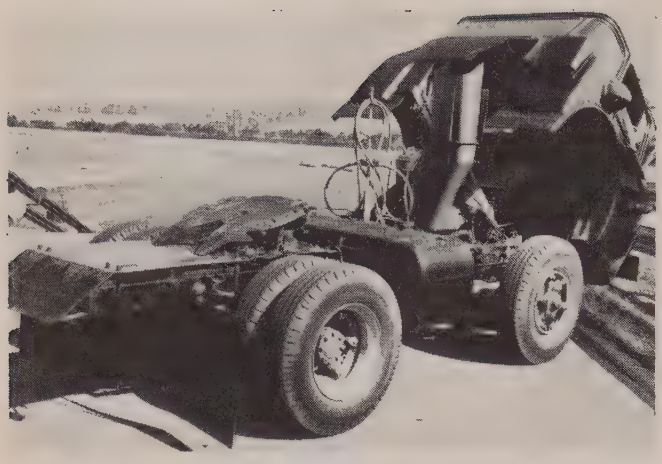

Fig. 1—Dynamometer testing and vehicle operation

consumption of the engine would have to be at least competitive (particularly at pard load) with existing gasoline, reciprocating engines, with eventual development potential comparable to the typical diesel-engine fuel consumption. The low-pressure gas turbine engine fell far short of this objective. Based on these conclusions, an intensive search of many different gas turbine cycles was undertaken.

Comparison of Gas Turbine Cycles

To obtain a basis for comparison of each cycle under consideration, assumptions for the efficiency characteristics of the components comprising the gas turbine engine were made. Table 1 illustrates the component efficiencies used in these cycle analyses. In all of the cycles investigated, a maximum single-stage compressor pressure ratio of 4:1 was assumed. The component development program previously described had resulted in compressor adiabatic efficiencies of 81.5% in 10.0-in. diameter compressor wheels at pressure ratios in excess of 4:1. Computation of the Machine Reynolds number (Re*) for the 10.0-in. diameter research compressor indicated a value of 7.25×10^5. Fig. 2 (1)**, infers that if the Re* can be maintained above 4×10^5, compressor efficiencies of 80% or better can be expected. Assumption of an adiabatic efficiency of 80% for compressor wheels down to 0.4 scale of the 10.0-in. wheel was, therefore, considered realistic. From cost and manufacturing considerations, it was believed that in the more complex cycles to be investigated, both radial and axial turbine combinations would have to be utilized. Component testing with radial in-flow turbine wheels had indicated that an adiabatic efficiency of 86% was attainable in the range of pressure ratios from 2.5:1 to 3.5:1. From the literature and available test data, it appeared that this efficiency could be maintained in small-diameter turbine wheels, since the scale effect did not appear to be a serious limiting parameter. However, in the interest of conservatism, 83% efficiency was assumed.

Consideration of the axial-flow type of turbine indicated that by maintaining pressure ratios in the order of 2:1, stage efficiencies of 88-89% were feasible. Again, however, since it was believed that wheel-tip diameters would be small, and a minimum number of stages was desired, the axial flow turbine efficiency was conservatively assumed at 86%. The remainder of the assumptions used can be considered relatively standard within the turbine industry, with the exception of the ambient-inlet and the turbine inlet temperature.

Table 1 - Assumptions

Compressor efficiency	80%
Turbine efficiency (axial)	86%
Turbine efficiency (radial)	83%
Combustion chamber efficiency	96%
Intercooler effectiveness	65%
Recuperator effectiveness	75%*
Mechanical efficiency (bearings, windage)	98%
Reduction gear efficiency	95%
Maximum cycle temperature	1700 F
Ambient temperature	100 F
Total pressure loss	(See Fig. 4)
Accessory load	0
Regenerator leakage	Equal to pressure ratio (i.e., 4% for a pressure ratio of 4:1)
Recuperator Leakage	0
Heating Value of the Fuel	18,500 Btu/lb

*Unless otherwise specified.

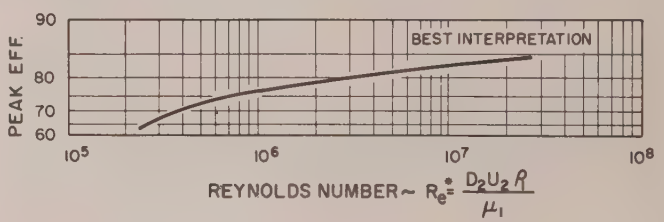

Where:

R_e^* = Machine Reynolds Number

D_2 = Impeller tip diameter, ft.

U_2 = Impeller tip speed, ft./sec.

ρ_1 = Air Density, lb/ft.^{3}

μ_1 = Viscosity, lb/sec. ft.

Fig. 2—Efficiency of similar radial compressors

** Numbers in parentheses designate References at end of paper.

The Gas Turbine in Truck Installations

Installation of a gas turbine engine in a truck does not provide an ideal air intake environment, and since gas turbines are more drastically affected by high inlet temperature than piston engines, a conservative rating of 100 F ambient was considered realistic.

With the advent of the high nickel base, superalloy turbine materials, a turbine inlet temperature of 1700 F was chosen, since, even for heavy truck operation, the full load factor is not particularly high. In the range of turbine-blade materials under consideration, the stress rupture properties are practically doubled by a reduction to 1600 F operating temperature.

Design Point Study

The method of performing the analysis consisted of calculating the engine performance, based on the assumptions outlined in Table 1, at various design pressure ratios. The data is presented graphically in Figs. 3-8, where a design point (full load) performance for each configuration of engine at various design point pressure ratios has been plotted. Thus, the resulting curves indicate the envelope of maximum specific power, minimum fuel consumption for a given cycle configuration.

Fig. 3 indicates the starting point of the study -- a reexamination of the low-pressure engine consisting of a simple-cycle, gas turbine engine with uncoupled power-turbine wheel compared with a simple-cycle plus regenerator (1) at varying design point pressure ratios and, in the case of the regenerative engine, varying design point regenerator effectiveness. From this curve, it can be seen that the simple-cycle engine attains a specific horsepower of approximately 85 at a pressure ratio of 6.5:1. However, from the fuel-economy curve, the optimum pressure ratio would be 10:1, at which condition a fuel specific of 0.68 lb/hp/hr would be expected. Understandably, the part load fuel economy would be very poor. In the case of the regererative engine, a 90% effective regenerator appears very attractive; however, at this effectiveness the matrix size is excessive. Although the specific-horsepower curve peaks at a pressure ratio of approximately 5:1, a pressure ratio of 4:1 appears to be the optimum condition for this engine configuration.

From this basic engine concept, new cycles were investigated using combinations of compressors, intercoolers, heat exchangers, reheat combustion, and turbines. The configuration for each cycle analyzed is as follows:

1. Single-spool with recuperator.
2. Single-spool with recuperator and reheat.
3. Two-spool.
4. Two-spool with reheat after the high-pressure spool.
5. Two-spool with reheat after the low-pressure turbine.
6. Two-spool with reheat after the high, and low-pressure turbine.
7. Two-spool with intercooling.
8. Two-spool with intercooling and reheat after the high-pressure turbine.
9. Two-spool with intercooling and recuperator.
10. Two-spool with intercooling, recuperator, and reheat after the high-pressure turbine.

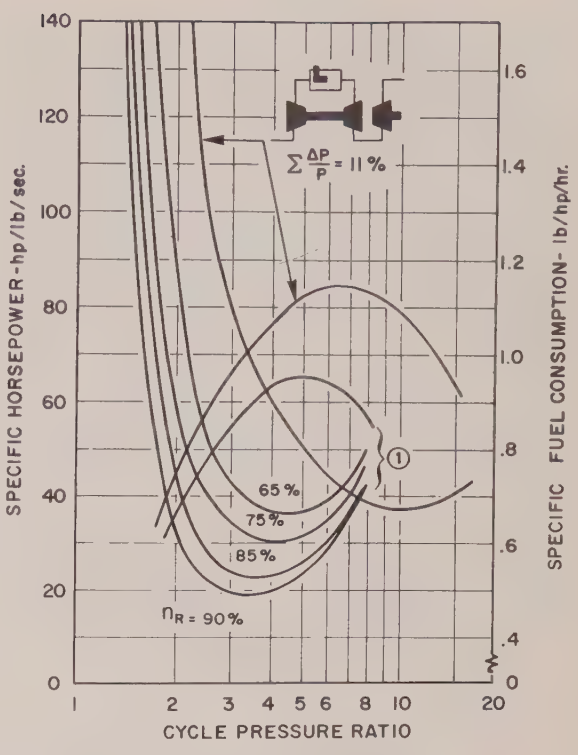

Fig. 3—Cycle comparison

Fig. 4 is a diagrammatic explanation of the concepts investigated. From the description it will be appreciated that without recourse to the more exotic gas turbine cycles -- that is, closed cycle -- one significant omission is the variable-geometry engine. This concept was disregarded on the basis of early component research where variable-geometry turbines had been tested with not too encouraging results aerodynamically and definitely poor results mechanically. In short, the "rusty gate" principle was not considered practical in an automotive turbine. Variable geometry in a centrifugal compressor is not to enticing; and since the axial compressor is too costly at the present state-of-the art, variable-geometry arrangements were completely disregarded.

Summarizing the results of the design point study, it appeared that configuration 10, a two-spool, intercooled, regenerative, reheat cycle was the best selection for a more detailed part-load investigation. Figs. 5 and 7 give the design point performance and fuel consumption of some of the less desirable cycles.

As shown in Fig. 6, the specific horsepower of Cycle 10 appeared to approach a maximum at an overall pressure

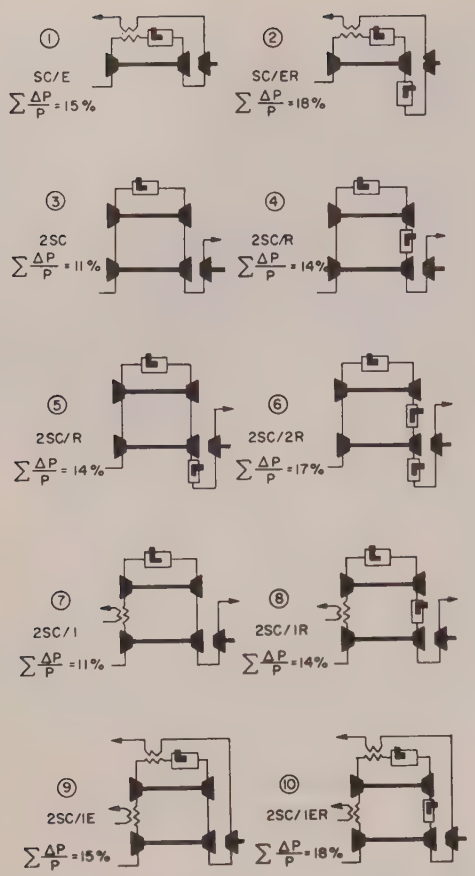

Fig. 4—Cycles investigated

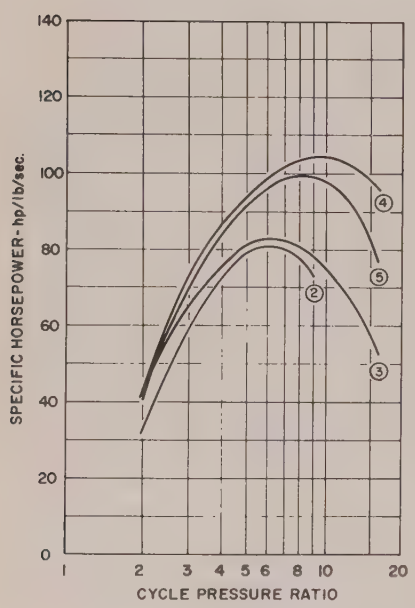

Fig. 5—Cycle comparison

ratio of 16:1, and from Fig. 8, the specific fuel consumption appeared to be relatively flat from a pressure ratio of 7:1 to 16:1.

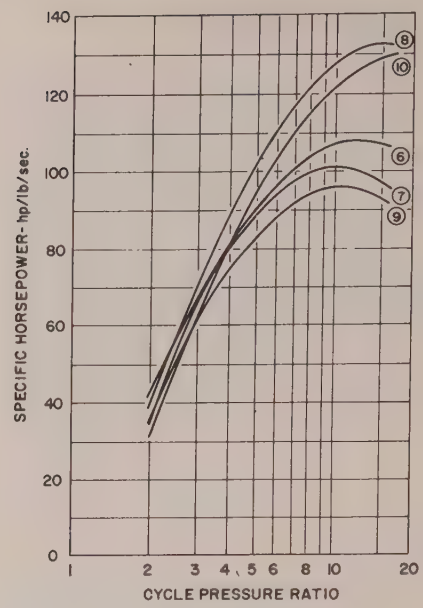

Fig. 6—Cycle comparison

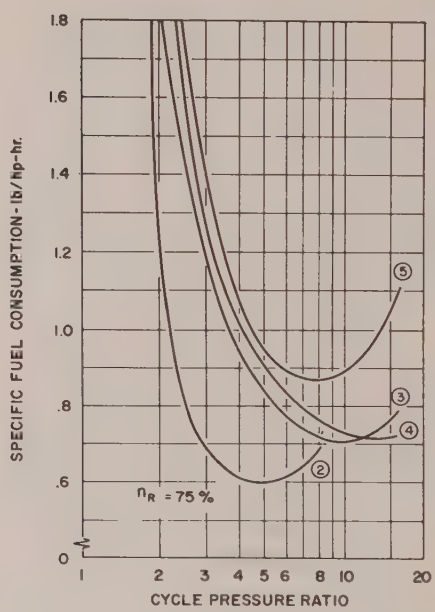

Fig. 7—Cycle comparison

Part-Load Studies

Part-load studies were undertaken following design-point sizing of the aerodynamic components. Performance maps of each of the compressors and turbines comprising the engine cycle were constructed. The part-load performance was then obtained by calculating a series of steady-state operating points down to approximately 10% of the design power.

The off-design performance (steady-state) can be calculated by several methods, the most expedient being to program the component characteristics and solve by analog and digital computer procedures. Since time precluded the programming of this cycle study, the off-design data were ob-

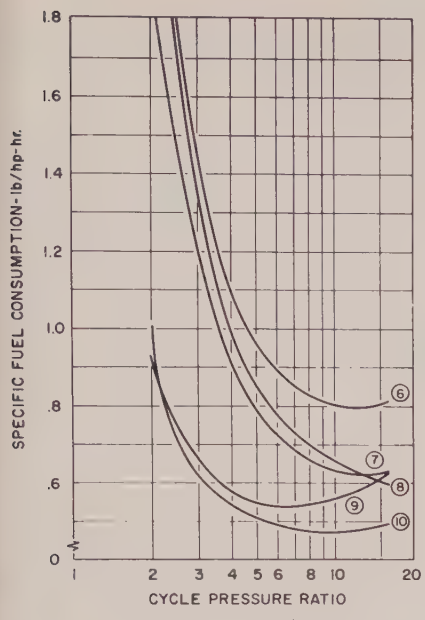

Fig. 8—Cycle comparison

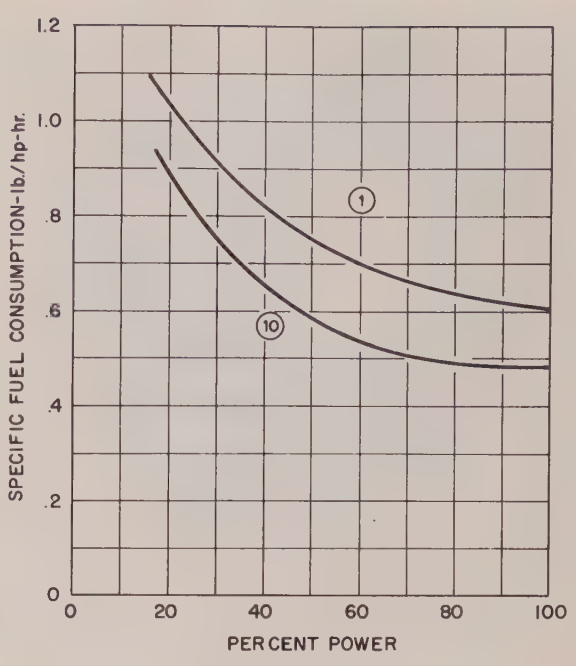

Fig. 9—Comparative part-load performance

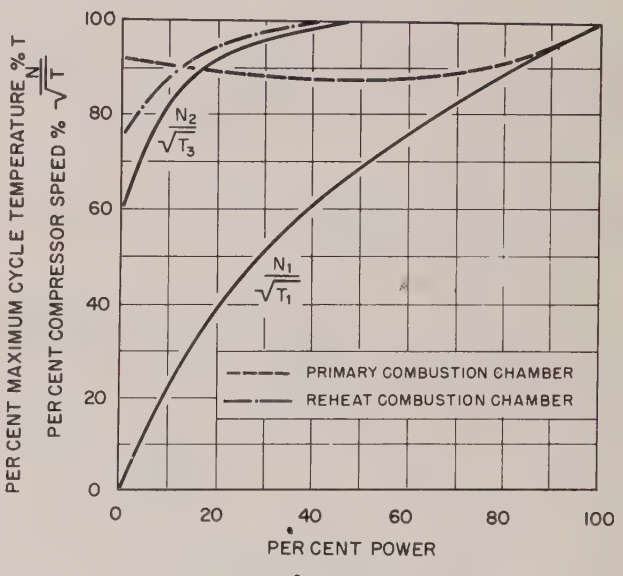

Fig. 10—Operating characteristics

tained by a graphical approach. Following construction of operating characteristic curves for the high-pressure and low-pressure compressor and turbine combinations, their off-design performance was then combined with the power turbine performance by an iteration procedure (2).

In general, the part-load fuel consumption with decreasing load will vary much as the design point studies do with decreasing pressure ratio. Cycle 10 did not follow this axiom and part-load studies were unexpectedly discouraging in that the fuel consumption increased as load was reduced at an even more rapid rate than the low-pressure cycle engine (Fig. 9).

A detailed examination of the part-load performance of this cycle revealed that the location of the power turbine resulted in the low-pressure spool turbines absorbing a majority of the available gas energy at part load, thereby maintaining a high compressor speed and airflow. This characteristic resulted in load control by rapid reduction of cycle temperature. Operation of this machine in the part-load range was analogous to one with a single-stage compressor. From these results, it was decided to reanalyze this engine cycle by placing the power turbine ahead of the low-pressure compressor turbine. Results of this analysis were significant. The effect of allowing the power turbine to absorb the majority of the available gas energy changed in operating characteristics of the low-pressure spool speed, resulting in an independent speed relationship between the high-pressure and low-pressure compressors, as shown in Fig. 10. The near constant-speed feature of the high-pressure spool combined with an almost constant reheat-burner temperature and varying airflow characteristics (for varying power requirements) for the low-pressure spool produced excellent part-load fuel economy, illustrated in Fig. 11. This arrangement attains minimum fuel consumption at 50% load. In addition, it was believed that the high idle speed and almost constant speed of the high-pressure spool above 30% load would result in improved acceleration.

Summarizing the results of the studies, it appeared that an engine utilizing Cycle 11 would result in a specific-power output of 130 hp/lb air/sec, when compared with the low-pressure regenerative engine whose capability appeared limited to approximately 65 hp/lb air/sec. At 50% load, Cycle 11 would attain a fuel specific of 0.395 lb/hp/hr, when compared with a specific of 0.75 lb/hp/hr for the low-pressure regenerative engine. As an additional bonus, it was

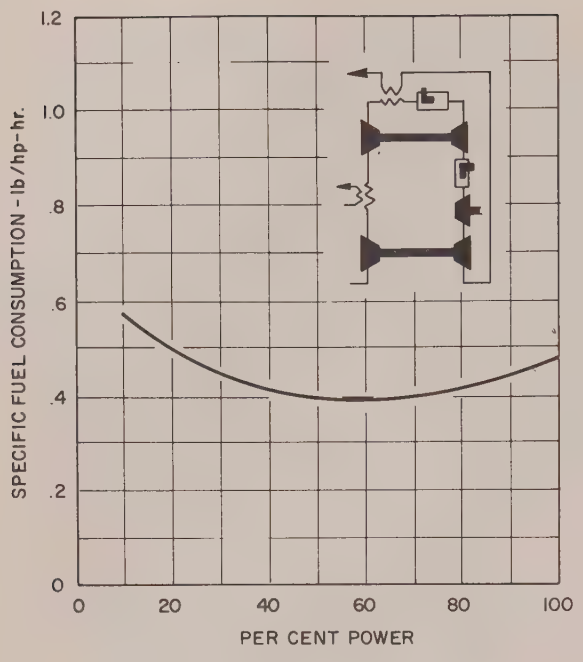

Fig. 11—Part-load performance—Cycle 11

conjectured that with twice as much power per pound of airflow in favor of Cycle 11, a very compact powerplant could be attained, and since the recuperator effectiveness assumed was only 75%, a very compact, plate-type heat exchanger appeared feasible.

Final Cycle Configuration

Final refining of the cycle configuration before proceeding with an engine design resulted in the tabulated estimates of pressure loss in Table 2, together with an overall estimate of 16.8 hp for power steering, generator, air conditioning, and airbrake compressor requirements.

Design point operating pressures and temperatures are shown in Table 3, corresponding to the stage locations illustrated in Fig. 12.

Table 2 - Pressure Losses % Δ P/P

Silencer	1.70
Intercooler	3.12
High-pressure compressor discharge duct	1.00
Recuperator	0.35
Primary combustion chamber	4.00
Interturbine duct	0.80
Secondary combustion chamber (reheat)	3.00
Outer turbine duct	0.80
Recuperator (gas side)	5.50
Exhaust duct	1.70
	21.97%

Table 3 - Design Point Operating Pressures and Temperatures

Station		Pt (psia)	Tt (^{o}R)
0	Inlet - silencer	14.70	560
1	Inlet - low-pressure compressor	14.45	560
2	Inlet - intercooler	57.80	896
3	Inlet - high-pressure compressor	56.00	682
4	Exit - high-pressure compressor	223.98	1085
5	Inlet - recuperator	221.74	1085
6	Inlet - primary combustion chamber	220.97	1426
7	Inlet - hp compressor turbine	212.13	2160
8	Exit - hp compressor turbine	84.57	1795
9	Inlet - secondary combustion chamber	83.89	1795
10	Inlet - power turbine	81.37	2160
11	Exit - power turbine	39.89	1864
12	Inlet - L.P. compressor turbine	39.57	1864
13	Exit - L.P. compressor turbine	15.92	1539
14	Inlet - recuperator	15.92	1539
15	Inlet - exhaust pipe	15.05	1203
16	Exit - exhaust pipe	14.79	1203

Mass flow	2.71 lb/sec
Drive shaft horsepower	300 hp
Drive shaft specific fuel consumption	0.566 lb/hp/hr
Fuel flow - primary combustor	112.7 lb/hr
Fuel flow - secondary combustor	57.0 lb/hr
Fuel flow total	169.7 lb/hr

The final engine configuration, designated Model 704, resulted in a performance illustrated in Fig. 13, and represents the fuel consumption attainable from an installed engine with engine-driven accessories. Of significant interest is the fuel requirement of the low-pressure 90% effective regenerative engine (1A) when rated at the same ambient, inlet, and exhaust pressure loss and the same accessory load as the 704 Engine. At 50% load, the low-pressure engine requires 0.76 lb/hp/hr of fuel compared with 0.48 lb/hp/hr for the Ford 704 Engine.

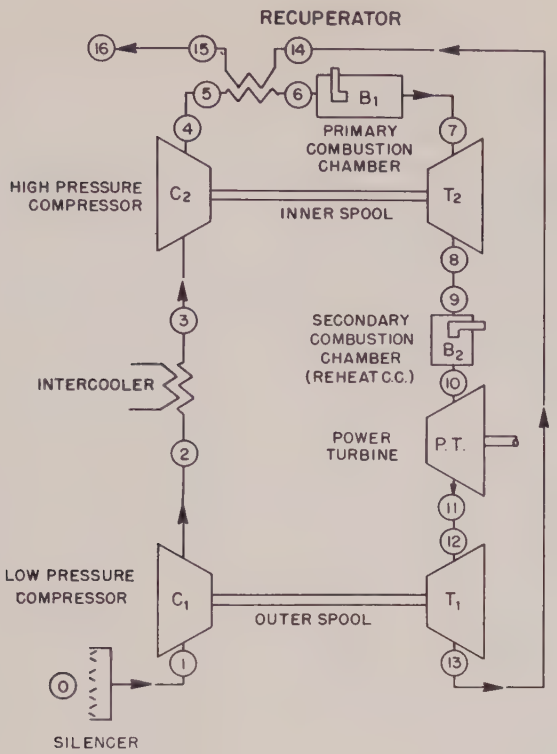

Fig. 12—704 gas turbine engine configuration

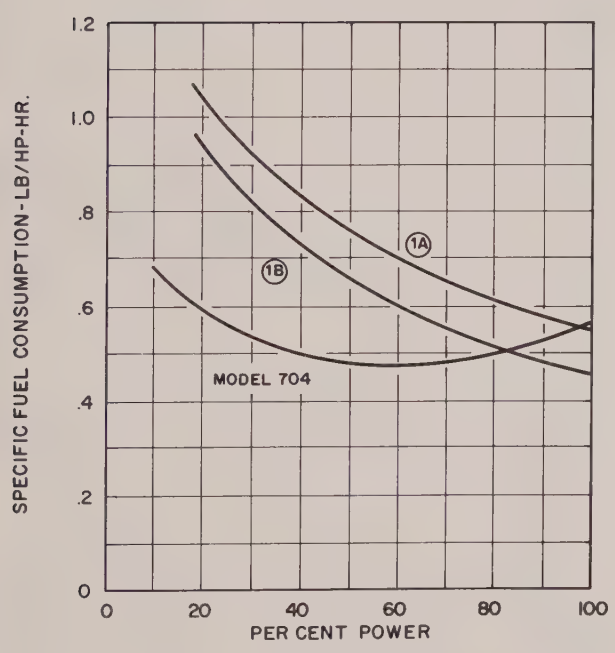

Fig. 13—Comparative part-load performance
1A=Cycle 1 at 100 F inlet air temperature with the accessory load, inlet and exit loss as the 704 gas turbine engine
1B=Cycle 1at 60 F inlet air temperature without accessory load, inlet, and exit loss

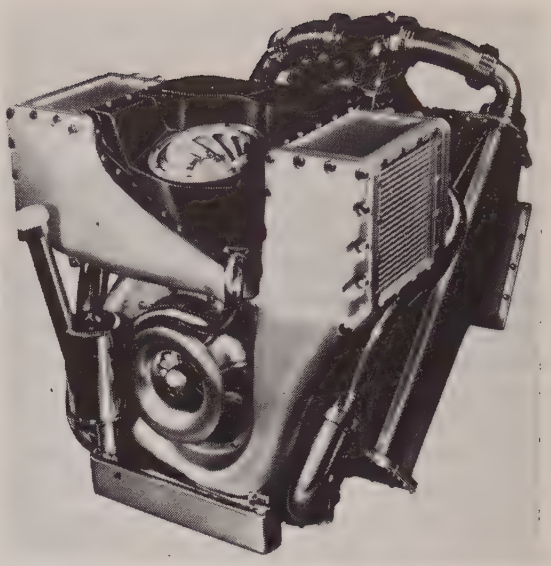

Fig. 14—Ford Model 704 300 hp gas turbine engine

Conclusions

In conclusion, it is probably appropriate to speculate on the possibilities of an engine of this concept, particularly the long-range development prospects. The engine described as Cycle 11 is now under development at Ford Motor Co. Despite what may be considered as adding complexity to an engine originally heralded as only having two moving parts, the mechanical design turned out surprisingly compact. The complete engine, including all accessories, ready for vehicle installation, is shown in Fig. 14. Mechanical reliability at the present stage of development has surpassed expectation, and with the weight little more than 2 lb/hp, a particularly attractive heavy-truck engine contender appears to be developing.

Future potential appears even more encouraging for this type of powerplant. With concerted effort in the area of improving efficiencies of rotating aerodynamic components 2% over those assumed in the cycle studies, fuel economy can surpass the present diesel engine. This, then, is our objective as the automotive turbine enters the second decade of development.

References

1. H. Davis, H. Knotts, A.M.G. Moody, "The Influence of Reynolds Number on the Performance of Turbo-machinery." Trans. ASME, Vol. 73 (1951), 499-509.

2. J. F. Dugan, Jr., "Two-spool Matching Procedures and Equilibrium Characteristics of a Two-Spool Turbo-Jet Engine," N. A. C. A., RM E 54F09.

Discussion

Future of the 704 Gas Turbine Engine

Dr. W. T. von der Nuell
Garrett Corp.

BEING UNABLE TO PARTICIPATE in this meeting, I accepted the invitation to comment on the Ford gas turbine paper which deals with one of my favorite subjects and reports about a development for which the Ford Motor Co. must be congratulated.

My personal assessment of the principle selected by Ford was expressed in my 1957 ASME paper when I said:

"The addition of air intercooling between compression stages lowers the compression work required while through reheating the expansion work can be increased; the cycle approaches more the Carnot cycle. Although the opinion has been expressed that this arrangement appears unlikely for vehicles, one may well debate this issue. For a given tip speed in the compressor, air intercooling leads to higher compression and expansion ratios which, with a given combustion-gas temperature, result in a lower temperature at the inlet to the exhaust-gas heat exchanger, thus not only simplifying its construction but also slightly reducing the significance of high heat-exchanger effectiveness. Naturally, intercooling appears simplest with gas turbines in naval installations where cool water is available. For certain applications though, air-to-air intercooling seems to deserve close consideration."

As to specific results reported by Ford, it can be said that, for instance, the compressor performance data obtained -- that is, "compressor adiabatic efficiencies of 81.5% in 10-in. diameter compressor wheels at pressure ratios in excess of 4:1" -- are remarkable indeed. Equally impressive are the power concentration, with 130 hp/lb-air/sec, and the absolute values of fuel consumption over the power range from 10-100% output. As far as can be concluded from published and personal information, the Ford approach is unique and its progress will be observed with special interest.

While, as the paper shows, the two-spool arrangement, the intercooler and the reheater and the special location of the torque-delivering turbine lead to remarkable characteristics, one can hardly overlook the fact that such a gas turbine is no longer a very simple powerplant when compared with other types. Nor can it be said that all components can easily be made to be rugged, accessible, and/or serviceable. The complexity, necessarily resulting from the desire for competitive fuel consumption characteristics, also explains why the power/weight ratio may not be so outstandingly more favorable than that of modern reciprocating or rotary engines, especially those now under development.

One must probably admit that, at present, it is still very difficult to explain why a gas turbine should take the place of, say, a diesel engine embodying a comparable amount of novelty -- that is, risk. Also, one cannot overlook that it would be rather shortsighted to compare this gas turbine of the future, which future, in production terms, might well be 5-10 years away, with diesel engines now in daily operation. It is known that given enough love through development efforts, the high-speed diesel engine has a long way to go, especially when turbocharging, charge-air cooling, improved cooling systems, and multifuel capability are included.

Now, with respect to the fuel consumption picture, the Ford engineers may well be in a position to shed a little light on some pertinent questions. In all cases, the reciprocating engine needs a variable-ratio transmission operated manually or automatically, with a strong trend to more and more automatic transmissions. In contrast, a gas turbine with a free-floating power wheel has a more attractive torque characteristic and, it has been said, would need but a single- or double-step reduction and reversible gearing. Have not some of such predictions been found to be rather debatable? When using specific fuel consumption as yardstick, would not ton miles per time unit per Btu rather than pound per horsepower-hour be a more realistic yardstick? This, aside from initial cost and maintenance, is what counts in profitable trucking. From an engineering point of view, two other important conditions for vehicles -- namely, the accelerability and the decelerability, the latter greatly depending upon the so-called braking characteristics of the engine -- deserve close scrutiny. What has been termed "variable flow geometry" may be considered as a means of influencing these characteristics of gas turbines to quite some degree.

Having this meeting near the world's largest engine and vehicle development and production center would justify the expectation that this matter of how to compare sensibly possible vehicle powerplants of the future -- gas turbines, reciprocating and rotary engines -- be dealt with most realistically. Clear presentations of all known pros and cons, sine ira et studio, appear particularly significant for the benefit of government agencies concerned with the development of future military surface vehicles. In this context, the problem of vulnerability, critical material requirements, and greatly different maintenance equipment cannot be ignored.

So, in summary and while repeating congratulations to the determined gas turbine engineers and their progress, may it be suggested that after having obtained a certain degree of perfection of new gas turbines for heavier vehicles, the question: "What is its foreseeable future?" be put high on the list of exchange of knowledge and opinions, even though we live in a time where one satellite launching may cost more than the entire gas turbine development for vehicles put together.

Questions on the 704 Gas Turbine Engine

William A. Turunen
General Motors Corp.

THE PAPER BY MR. SWATMAN and Mr. Malohm on the Ford model 704 gas turbine engine represents a tremendous amount of work, and they are to be congratulated on the excellent condensation of this work in the relatively brief confines of a single technical paper.

It is interesting to note that the authors "avoided the more exotic gas turbine cycles" in their investigations. Exotic or not, the advanced concept they have chosen for development testifies to their engineering courage.

In Fig. 13, the authors have compared the fuel consumption of their engine with a "low-pressure, 90% effective, regenerative engine." Shown in Fig. 1 is data which shows the low-pressure regenerative cycle in a more favorable position. The upper solid curve is actual test data from the GT-305 engine, which has been operational for over 2 years. The lower solid curve compares the specific fuel consumption of the advance version of the GT-305 with the 704 engine. This indicates that the fuel consumption differences between these two cycles at part throttle is considerably less than indicated in the paper. It is interesting to contemplate the actual differences which will exist when test data from the two cycles are compared.

In studying their paper, several questions have come to mind:

1. What means and how much power is required to drive the intercooler fan? Where is this allowance made in the cycle study?

2. What basic parameters are used for the fuel control systems? Are any turbine temperature-sensing elements required? How is the fuel flow to the two burners scheduled with changing power level?

3. What is the starting technique?

4. What is the running experience with the 704 and how closely does data compare to the theoretical cycle analysis?

Author's Closure to Discussion

To Mr. Turunen's discussion, the answer would be as follows:

While Mr. Turunen's data looks impressive, there is no indication of the ambient conditions and inlet and exhaust pressure losses under which this performance was achieved; also, whether any accessory load is considered.

The data in Fig. 3, we would like to emphasize, is the fuel economy attainable from an installed engine operating at 100 deg. ambient with all accessory load -- that is, air-brake compressor, power steering pump, and generator. As we stated in the text of our paper, we penalized the Ford engine 16.8 hp for these losses in the cycle studies. By comparison, if the losses are disregarded, the Ford 704 cycle engine has a fuel economy of less than 0.4 lb/bhp-hr at 50% load.

In reply to Dr. W. T. von der Nuell's comments, we wish to state the following:

While Dr. von der Nuell's suggestion for arriving at a more realistic method of computing cost of vehicle operation appears intriguing, instigating its adoption by the trucking industry would, undoubtedly, be a difficult task, particularly since the trucker, as a potential customer for the gas turbine powerplant, is obviously going to require fuel economy parameters for the gas turbine which he can compare directly with known fuel economies for the engines which he is presently using.

With regard to acceleration, the arrangement of the Ford 704 power turbine ahead of the low-pressure spool turbines allows variations in the turbine design which have resulted in improved acceleration of the compressor-turbine spool with resultant overall improvement in engine acceleration characteristics. Deceleration is a different story. This can be accomplished aerodynamically, but from design study it appears that the cost will offset the advantages. A number of very attractive transmission retarders are, however, available for this purpose and appear to be the best solution economically.

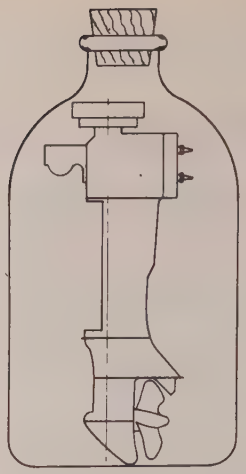

Fig. 1

Vibration and Noise Control of Outboard Motors and Other Products

James W. Mohr
Outboard Marine Corp.

NOISE CONTROL is primarily a problem of reducing engine noise. There are, of course, other noise makers of some concern, but these generally do not represent a problem until engine noise is reduced.

Vibrational disturbances are also associated with the reciprocating engine, and these contribute to the noise problems as well as to other aspects of comfort.

A good example of vibration and noise control of an OMC product is shown in the treatment of the outboard motor. It represents an approach which has proved to be successful and practical; consequently, this paper will deal primarily with it. Rotary lawn mower vibration and noise treatment, and vibration control of a three-wheeled vehicle will also be described.

Outboard Motor

The basic approach is actually rather simple. This is to build a sound barrier or enclosure around the engine or the outboard motor. In other words, as the advertising people like to say, "bottle up the noise" (See Fig. 1.)

It is obvious that there are practical problems associated with doing this, Let's look at these and then consider them in detail one at a time.

1. Effectively attaching the motor to the boat and enclosure.
2. Supplying combustion air to the enclosure (reducing air inlet noise).
3. Engine exhaust noise treatment.
4. Sealing the enclosure:
   a. where the propulsion unit protrudes.
   b. for controls.
   c. for servicing.
5. Weight considerations.

Effectively Attaching Motor to Boat and Enclosure - The purpose of the enclosure or sound barrier is, of course, to offer impedance to the noise which is radiated from the engine. To be effective there must not be a sound-conducting path between it and the engine, or the enclosure can become a more effective sound-radiating surface than the engine itself. This can be done, as shown schematically in Fig. 2, by mounting a cover to the engine with resilient mounts. The earliest production attempt at noise reduction used this method. For it to be effective, the natural fre-

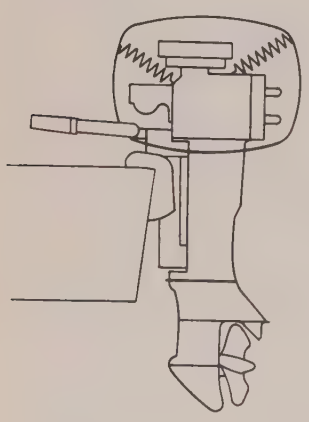

Fig. 2 — Schematic of isolated cover

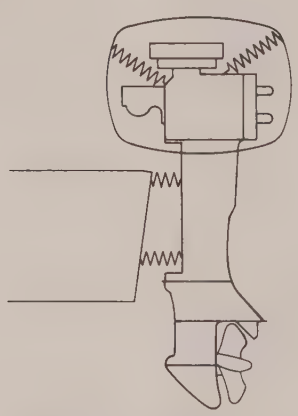

Fig. 3 — Schematic — cover isolated from motor; motor isolated from boat

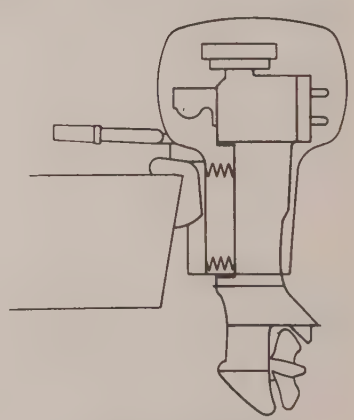

Fig. 4 — Schematic of motor isolated from boat and cover

quency of the cover and mount configuration should be as low as possible. A poor sound-conducting material such as rubber should be used for the mounts. This method actually produces a good sound barrier for engine-radiated noise, but there is still a sound-conducting path to the boat. The boat itself is usually an excellent sound-radiating surface, and acts in a way similar to the violin amplifying the sound of a vibrating string.

To have a really effective noise reduction system the engine must be isolated from the boat. It is done by means of a resilient mounting system between the motor and the boat, as shown schematically in Fig. 3. This results in:

1. Comfort — freedom from annoying vibrations.
2. Noise reduction — non-conducting path for sound.

Fig. 4 represents schematically how the methods shown in Figs. 2 and 3 can be comgined. The enclosure is fastened rigidly to the boat through a king pin or steering member, and can be thought of as a part of the boat. The engine and propulsion unit are resiliently mounted on rubber springs so the boat and cover are vibrationally and acoustically isolated from the motor.

Most important to the success of this treatment is the vibration isolation system. The design procedure follows.

In the way of review let us look at a few basic principles.

The usual purpose of a resilient mounting system is to reduce the vibrating force transmitted to the structure supporting it. The effectiveness is usually expressed as:

$$\text{Transmissibility} \qquad t = \frac{F_t}{F} \qquad (1)$$

where:

F_t = Force transmitted
F = Vibrating force at engine.

The following is an expression for transmissibility for a single degree of freedom system without damping:

$$t = \frac{1}{1 - \left(\frac{f}{f_n}\right)^2} \qquad (2)$$

It shows how t is affected by the natural frequency. A plot (without regard for sign) is shown in Fig. 5. It indicates that in order to reduce the transmitted force, the natural frequency of the device on its resilient mounts must be low relative to the exciting frequency (the frequency at which the disturbance occurs).

To design a resilient mounting system, it is necessary first to determine where and how the disturbances occur, and at what frequency. It is also necessary to bear in mind that the mounts must transmit or resist other forces (Fig. 6).

Figs. 7-9 show the exciting forces, torques, and frequencies for single, twin, and V-4 outboard motors, which are rota-

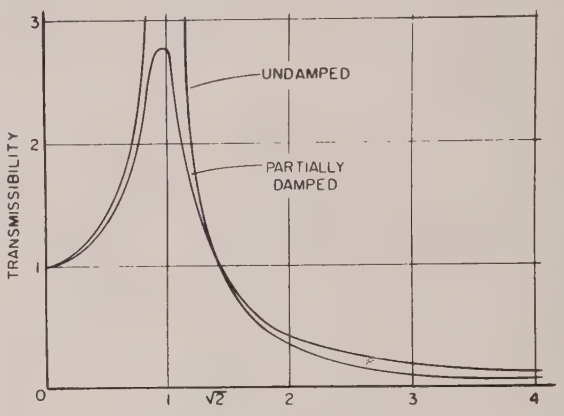

Fig. 5 — Exciting frequency / Natural frequency

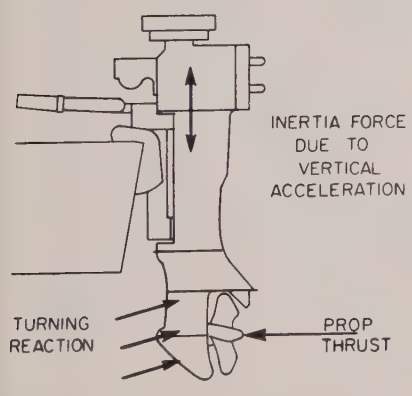

Fig. 6 — External forces

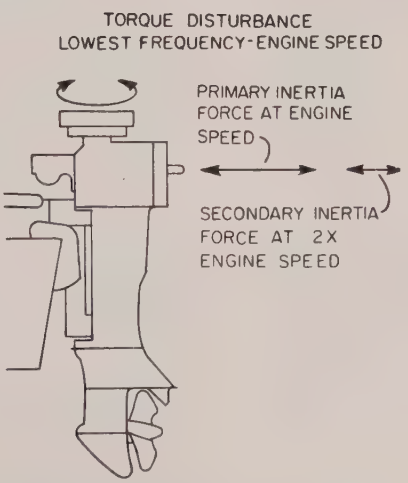
TORQUE DISTURBANCE
LOWEST FREQUENCY-ENGINE SPEED
PRIMARY INERTIA FORCE AT ENGINE SPEED
SECONDARY INERTIA FORCE AT 2X ENGINE SPEED

Fig. 7 — Vibratory disturbance — single-cyl engine

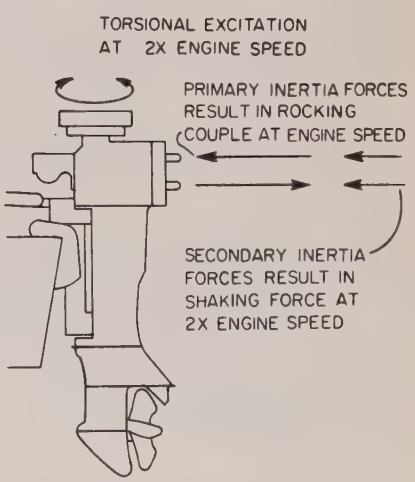
TORSIONAL EXCITATION
AT 2X ENGINE SPEED
PRIMARY INERTIA FORCES RESULT IN ROCKING COUPLE AT ENGINE SPEED
SECONDARY INERTIA FORCES RESULT IN SHAKING FORCE AT 2X ENGINE SPEED

Fig. 8 — Vibratory disturbance — twin-cyl engine

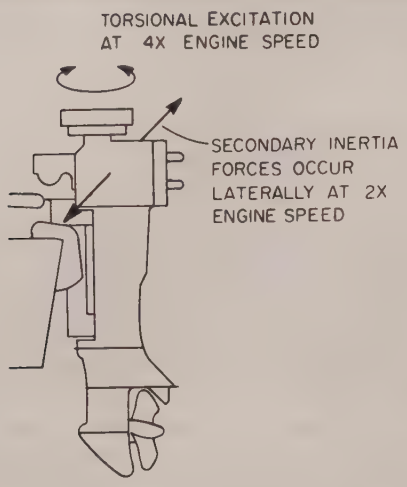

Fig. 9 — Vibratory disturbance — V4 engine

Engine Configuration	Primary		Secondary	
	Shaking Force	Rocking Couple	Shaking Force	Rocking Couple
Single Cylinder	$\frac{WrN^2\cos\theta}{35250}$ Fore Aft Plane	0	$\frac{Wr^2N^2}{35250\ell}\cos 2\theta$ Fore Aft Plane	0
Twin Cylinder	0	$\frac{aWrN^2}{35250}\cos\theta$ Fore Aft Plane	$\frac{2Wr^2N^2}{35250\ell}\cos 2\theta$ Fore Aft Plane	0
V4 Cylinder	0	0	$\frac{2\sqrt{2}\,Wr^2N^2\cos 2\theta}{35250\ell}$ Lateral Plane	0

W = Weight of Reciprocating Parts for 1 Cylinder - Pounds
r = Crank Radius - Inches
N = Engine Speed - RPM
θ = Crank angle from TDC - Degrees
ℓ = Connecting Rod Length - Inches
a = Distance Between Cylinders - Inches

Fig. 10 — Inertia forces and rocking couples for balanced outboard motor engines

tionally in balance. If the engine is not in rotational balance other disturbances will occur in the planes of unbalance.

Fig. 10 lists the equations used to calculate the magnitude of forces and couples which result from reciprocating motion of the pistons.

Fig. 11 shows the configuration of resilient mounts used by OMC for twin cylinder outboard motors. In all cases rubber mounts are indicated, and the axis of the schematic spring represents the direction of compression and tension. The mounts deflect in shear perpendicular to this axis.

For the single and twin cylinder outboard motor, the reciprocating disturbances occur in the fore-aft plane. This plane is then of most concern, and will be considered first.

The mounting system can be represented in a somewhat simplified form for purposes of analysis (Fig. 12). There are two natural frequencies. If $L_1 = L_2$ and $K_1 = K_2$ or if $K_1L_1 = K_2L_2$, the system is said to be decoupled. For a decoupled system both the translational and rotational modes of vibration occur independently. For any other condition, the modes are coupled and result at both feequencies in combined rotational and translational motion.

$$fn_1 = \frac{60}{2\pi}\left[1/2\left(\frac{C}{r^2}+a\right) - \sqrt{1/4\left(\frac{C}{r^2}-a\right)^2 + \frac{b^2}{r^2}}\right]^{1/2} \text{ cpm} \quad (3)$$

$$fn_2 = \frac{60}{2\pi}\left[1/2\left(\frac{C}{r^2}+a\right) + \sqrt{\left(\frac{C}{r^2}-a\right)^2 + \frac{b^2}{r^2}}\right]^{1/2} \text{ cpm} \quad (4)$$

$$a = \left(\frac{K_1+K_2}{W}\right)g \quad (5)$$

$$b = \left(\frac{K_2L_2 - K_1L_1}{W}\right)g \quad (6)$$

$$C = \left(\frac{K_1L_1^2 + K_2L_2^2}{W}\right)g \quad (7)$$

where:

W = Weight, lb
g = 386 in./sec/sec
L = Distance, in.
K = Spring rate, lb/in.
r = Radius of gyration about c.g., in.
K_1 = Total spring rate at 1
K_2 = Total spring rate at 2
L_1 and L_2 are + if c.g. is between K_1 and K_2
L_1 is - if c.g. is above K_1
L_2 is - if c.g. is below K_2

For the twin cylinder outboard there is a rocking couple which acts at engine speed, and a shaking force at twice engine speed. Outboard motors are run at top speed about 90% of the time and for this condition the disturbing forces are greatest. Top speed is considered to be the most important design condition. The motor on its mounts should have a second mode (highest) natural frequency of, say, 1/3 or 1/4 that of maximum speed (about 4000-5000 rpm).

The production twins have second mode natural frequencies of about 1200 rmp, and first mode natural frequencies of about 400 rpm. This results in isolation efficiencies in the order of 90% (or transmissibility of about 0.1) for disturbances occurring at engine speeds. Of course, greater isolation efficiency results for disturbances occurring at twice engine speed.

Since the outboard motor speed is variable and can be reduced at idle to, say, 500 rpm, it appears that a problem of resonance would occur when the engine speed is 1200 and 600 rpm. (See Fig. 5 when $f/f_n = 1$.) At these speeds, one would expect a multiplication of the forces (t is greater than

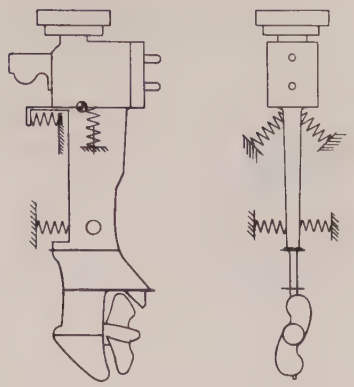

Fig. 11—Spring arrangement — twin cylinder engine

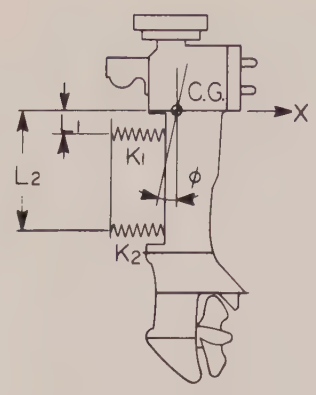

Fig. 12 — Vibratory system

1). Actually this does occur, but the disturbing forces are small at low engine speeds (F is a function of the square of engine speed), and the result is not serious. The force multiplying effect of resonance is also reduced by damping (Fig. 5). Beside the hysteresis of rubber, additional damping is provided by the lower unit being submerged. Another factor which has a bearing on the matter is described in the following:

1. When the engine runs at 1200 rpm the first order excitation which is a rocking couple should cause resonance. The second mode shape is predominately translational (Fig. 13); consequently, the excitation is not significantly magnified at resonance. Actual tests show practically no manifestation of resonance.

2. When the engine runs at 600 rpm the second order excitation which is a shaking force should also cause trouble, and does. The forces transmitted to the boat are actually somewhat larger for this case than for those described in 1. above. Actual tests do show some manifestations of resonance. The effect is not too noticeable except on light metal boats. The outboard motor is not run much of the time at low speeds; consequently, the problem isn't too serious.

The same equations are used to determine natural frequencies in the lateral plane. These are of concern for single and twin-cylinder engines having rotary unbalance, and for engines like the balanced V-4 which have only a lateral disturbance. The lateral disturbance of the V-4 occurs at twice engine speed (Fig. 9).

It is possible to use a stiffer mounting system for a V-4 engine if the rotating parts are quite adequately balanced. This minimizes the problems of clearances and stability to propeller thrust and other external forces. The V-4 system is represented in Fig. 14. All three mounts are rather flat, and have high shear and compression rates.

The isolation system must also reduce the forces caused by torque variations. Torque variation is greatest at low speeds. To be effective the rotational natural frequency about an approximate vertical axis through the c.g. must be 1/3 - 1/4 of the lowest torque: varying frequency. The

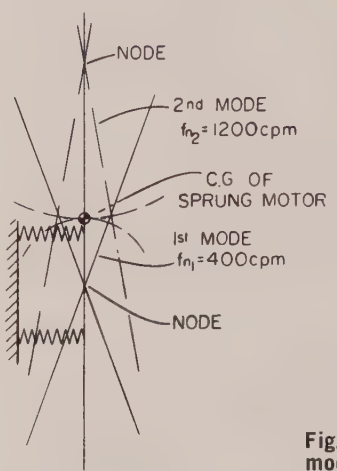

Fig. 13 — Vibratory mode shapes

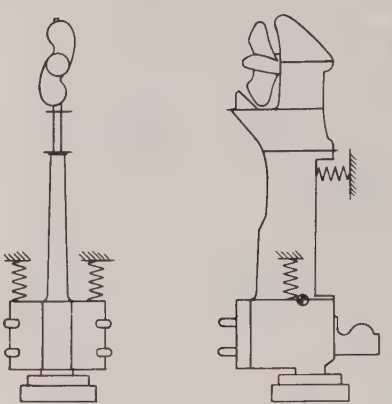

Fig. 14 — Spring arrangement — V4 engine

springs shown in Fig. 12 should ideally be positioned, so that if a couple is applied in a plane perpendicular to the axis of least moment of inertia (this axis is approximately vertical through the c.g.), the spring reaction causes rotation about the axis. The equation for the rotational natural frequency about the least moment of inertia axis is:

$$f_n = \frac{60}{2\pi}\sqrt{\frac{K_t}{J}} \quad \text{cpm} \qquad (8)$$

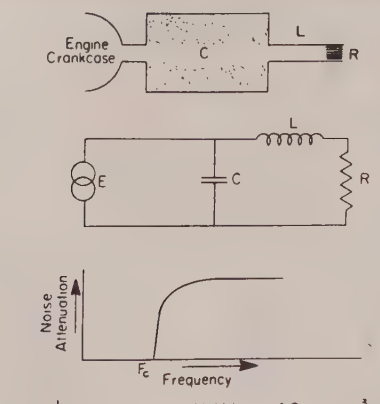
Engine Crankcase
C
L
R
E
Noise Attenuation
Frequency
$f_c = \frac{1}{\pi\sqrt{LC}}$
$C = \frac{V}{1.4\ P_o}$
$L = \frac{\rho\ l}{A}$
V = Volume of Cavity - cm³
P_o = Ambient Pressure - 1×10^6 dynes/cm²
ρ = Density of Air - 1.21×10^{-3} gm/cm³
l = Length of Tube - cm
A = Area of Tube - cm²

Fig. 15

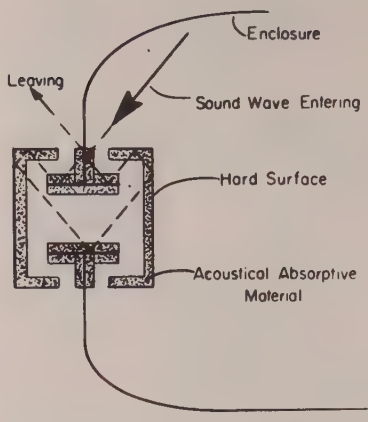

Fig. 16 — Sound trap

where:

$K_t = K_1 d_1^2 + K_2 d_2^2 \ldots K_n d_n^2$ in. -lb/radian

K = Tangential spring rate, lb/in. (all springs must be used)

d = Radial distance to axis, in.

J = Least moment of inertia in. -lb-sec^2

It is apparent that d has significant effect, and as it becomes smaller, the natural frequency becomes lower.

The rotational natural frequency of the twins are in the order of 350 cpm. Since minimum engine speed is about 500 rpm, the lowest exciting frequency is about 1000 cpm. Isolation efficiency is about 90%. Making the system softer results in more rotational motion which intensifies problems associated with clearances, connections, controls.

Supplying Combustion Air to Enclosure (reducing air inlet noise) - Original outboard motor noise reduction techniques employed an inlet silencer or muffler. Fig. 15 schematically represents the muffler and the electrical equivalent (a low pass filter). Effectiveness of this type muffler is limited by the volume it is practical to use. Reference to the electrical equivalent indicates that the capacitive effect should be large. The problem was eliminated when a sealed enclosure was used, for now the enclosure volume is the volume C of the muffler.

Good muffler design requires a tube L which in the electrical equivalent has an inductive effect. With the present system, since C is large, the magnitude of L makes very little difference. A sound trap of some type is all that is necessary. Its purpose is to allow air to enter easily and keep sound from coming out. A schematic of a sound trap is shown in Fig. 16. For a sound wave to get out it must bounce off many surfaces. If these surfaces are covered with a noise-absorbing material, the sound will be drastically reduced on the way out; on the other hand, low velocity air for combustion can flow through easily.

Engine Exhaust Noise Treatment - The exhaust from an outboard motor is passed under water, and is entrained in the slipstream of the propeller. Noise is quite adequately reduced by this process; however, the slipstream is very necessary. If the engine exhaust is merely piped under water and is not dispersed, the gas forms a channel to the air for the noise to pass through.

Sealing Enclosure - This is done where the propulsion unit protrudes, for controls, and for servicing.

The enclosure must be rather adequately sealed for it to be effective as a sound barrier. A soft rubber seal is used on the lower end of the enclosure. To get some idea of the amount of motion, bear in mind that the mounts will probably deflect a maximum of about 5/16 in. due to thrust. The lower mounts deflect in the direction of thrust, and the upper ones in the reverse direction. There is a point between the upper and lower mounts that doesn't move at all. The enclosure should cover as much of the exhaust tube as possible to impede noise radiated from it. Because of this it may be undesirable to put the seal at the position of minimum displacement, but at any position between the upper and lower mounts the displacement is less than 5/16 in.

Controls are connected with universal joint type linkages which transmit torque but have flexibility in other directions. Simple rubber seals can be used.

To facilitate servicing the engine (spark plugs, magneto), the upper part of the enclosure is removable. A soft gasket seal and over center latches are used to seal and secure it.

Weight Considerations - The weight of the enclosure is:

1. 15% of the total weight of the 75 hp outboard motor.
2. 20% of the total weight of the 40 hp outboard motor.

It seems logical to expect that the smaller motors would suffer a greater percentage of weight increase if the complete treatment is applied to them. The noise level of the smaller engines is less severe, and consequently, full treatment is not as necessary.

Lawn Mowers

Some of the problems of reducing noise and vibration for rotary lawn mowers are easier, and others more difficult to

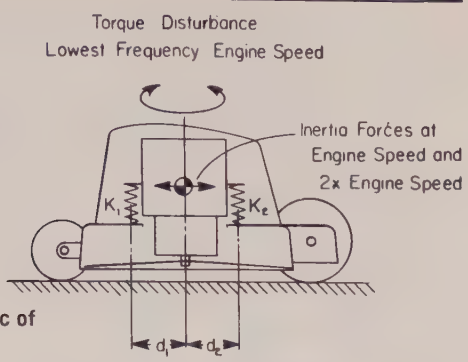

Fig. 17 — Schematic of lawn mower

solve, but the approach is basically the same.

The noise sources are:

1. Engine noise - radiated, air intake, and exhaust.
2. Blade noise.

Engine noise, both radiated and air inlet, is reduced by the same method used with outboard motors. That is, the engine is surrounded by a sound barrier or enclosure, and is vibrationally and acoustically isolated from it, and from the main housing (Fig. 17). The isolation system is actually rather easy to design provided the springs can be loactedradially close to the center of gravity.

The disturbances are shaking forces occurring at engine speed and twice engine speed, and a varying torque. The minimum torsional frequency occurs at engine speed (for a two-stroke engine). The disturbing forces act in line with the piston. The Lawn Boy engine runs at a governed speed of about 3000 rpm; consequently, the minimum disturbing frequency is 3000 cpm for both shake and torsion. Three or four rubber springs constitute a practical mounting system, and it is usually possible to place them in the plane of the c.g. Fortunately, the line of action of the exciting force acts very nearly through the c.g. As a consequence, the only modes of vibration that are of any concern are those occurring in a horizontal plane through the c. g., and the rotational about a vertical axis through the c.g.

It is fairly easy and practical to achieve a decoupled system in this case. One way is to use three mounts of the same spring rate K_1 and place them 120 deg apart at the same radial distance from the c.g. The vibratory system has decoupled modes, if a force applied through the c.g. of a body in any direction causes only translational motion. The translational natural frequency is determined by:

$$f_n = \frac{60}{2\pi}\sqrt{\frac{Kg}{W}} \quad \text{cpm} \qquad (9)$$

where:

W = Weight, lb
g = 386 in./sec^2
K = Total spring rate in horizontal plane, lb/in.

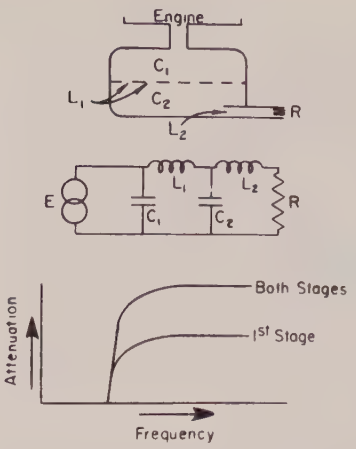

Fig. 18 — Exhaust muffler — Lawn Boy

The natural frequency should be 1000 cpm or lower for an engine speed of 3000 rpm or higher. The rotation natural frequency about a vertical axis through the c.g. should also be 1000 cpm or lower, and is determined by:

$$f_{nR} = \frac{60}{2\pi}\sqrt{\frac{K_t}{J}} \quad \text{cpm} \qquad (10)$$

where:

$K_t = K_1 d_1^2 + K_2 d_2^2 \ldots K_n d_n^2$ in.-lb/radian

J = Mass moment of inertia about vertical axis through c.g. in.-lb-sec^2

A good procedure to follow is:

1. Decide on the horizontal natural frequency, and solve for spring rate K.
2. Use the same natural frequency for rotational motion, and solve for d.

Practical limitations may force a different approach, but the designer has considerable latitude.

If rubber sandwich type mounts are used, they can be positioned to be in shear for horizontal forces, and in compression for the weight of the engine. This results in good stability.

Since the natural frequencies are in the neighborhood of 1000 cpm, resonance will occur at that speed. A governor on the engine will generally drive it through the critical speed quickly enough, after starting, so as to not cause serious problems.

The cooling air can be ducted to the engine, or away from it, or both. If it is ducted away, the air in the enclosure can also be used by the engine for combustion. A sound trap is used where the air is brought into the enclosure. On the Lawn Boy mower, the cooling air is discharged into the mower housing which is itself a fairly good sound trap.

Exhaust noise is treated with a two-stage muffler. Its principle of design is the same as for the air inlet silencer (Fig. 18).

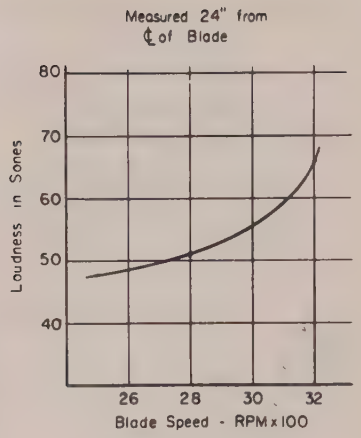

Fig. 19 — Rotary lawn mower blade noise

omrc 3 PROJECT NO. Date

Description of test: Microphone placed at approximate position of operator's ear.

Octave Bands	Model 5250 Quietflite 19" blade		Model 5210 Standard 18" blade							
	Db	Sones	Db	Sones	Db	Sones	Db	Sones	Db	Sones
O.A.	82		85							
1 (20-75)	78	5.1	81	6.8						
2 (75-150)	78	9.2	78	9.2						
3 (150-300)	70	7.4	78	12.9						
4 (300-600)	73	10.5	75	12.0						
5 (600-1200)	69	7.9	74	11.3						
6 (1200-2400)	64	6.5	70	9.8						
7 (2400-4800)	60	7.1	72	16.0						
8 (4800-9600)	53	5.2	59	8.0						
A TOTAL SONES		58.9		86.0						
B Loudest Band-Sones		10.5		16.0						
C A-B		48.4		70.0						
D .3 × C		14.5		21.0						
E B+D=Loudness		26.0		37.0						

Noise Reduction = $\frac{37-26}{37} = \frac{11}{37} = 29.8\%$

Fig. 20 — Noise data

Total noise reduction for the lawn mower has been limited by blade noise. Several years of research work were spent in an attempt to reduce noise, and not compromise cutting and delivery characteristics; but the results are still negative. Any noise-reducing scheme tried to date has resulted in poorer cutting or delivery. The only practical alternative at this time is to turn the blade at a lower speed since the noise increases rapidly with rpm (Fig. 19).

The Quietflite mower has about 30% reduction of overall noise compared with the previous model. Fig. 20 shows noise data which was taken by an independent acoustical consultant.

The effect of vibration reduction is also quite apparent to the operator of the mower.

Cushman Truckster Vibration Reduction

The truckster is a three-wheeled vehicle powered by a single cylinder 4-stroke engine (Fig. 21). The original mechanical drive system can be simply represented as shown in Fig. 22. The power frame which contains the engine, transmission, drive shaft, differential, axle and two rear wheels is fastened to the main frame at the rear with a leaf spring and was fastened at the front with a ball and socket joint. This provided a flexible suspension system, but allowed engine vibrations to be transmitted to the main frame.

Fig. 23 shows a method of resiliently coupling the power frame to the main frame. It serves the same purpose as the ball and socket joint and also reduces transmitted vibration due to inertia forces. The power frame which is pivoted on the axle, and restrained resiliently by a spring at the rear, is also resiliently restrained to rotational motion about the axle at the front.

The power frame with the engine located remotely from the pivot (axle) (Fig. 23) seems natural for a center of percussion-type mounting system. (A dynamic force through the center of percussion perpendicular to a line through the pivot and c.g. will not transmit a force at the pivot.) If the natural frequency of the frame about the pivot is low relative to the disturbing frequency, and the disturbing forces

Fig. 21 — Truckster

act at or near the center of percussion, the forces can be effectively isolated from the main frame.

The minimum vertical exciting frequency occurs at engine speed. The lowest engine speed is 800 rpm. A natural frequency of 1/3 of 800 rpm would be desirable, but difficulties with stability and excessive static deflection of the front mount prevented this. The actual natural frequency is in the neighborhood of 400 cpm. It should be less than $800/\sqrt{2}$ or 570 cpm, if force multiplication while operating at 800 rpm is to be avoided. (See Fig. 5.)

Since the vibratory mode is rotational, the following equation applied:

$$f_n = \frac{60}{2\pi}\sqrt{\frac{K_t}{J}} \quad \text{cpm} \qquad (11)$$

where:

$K_t = KL^2$, in-lb/radian
L = Distance from spring to axle, in.

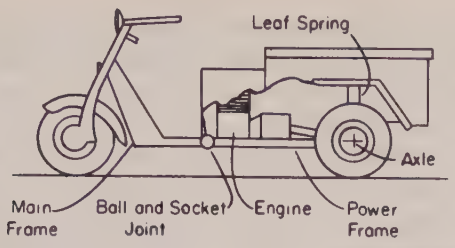

Fig. 22 — Truckster drive frame coupling

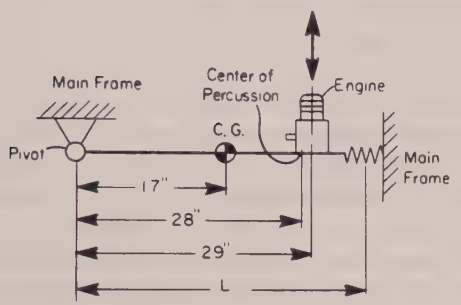

Fig. 23 — Schematic of power frame isolation system

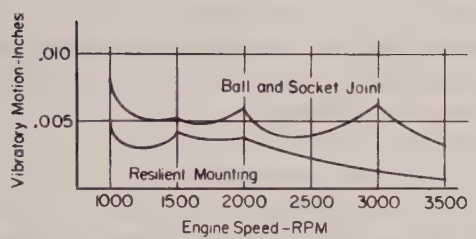

Fig. 24 — Vertical vibratory motion — driver's seat

J = Polar moment of inertia about axle, in.-lb-sec^2
K = Spring rate in vertical direction, lb/in.

Reduction of torsional disturbances was not considered a problem, since it appeared that the power frame would not readily transmit torsion to the main frame.

The engine is designed with about 60% overbalance and, consequently, there is a lateral disturbance. Lateral isolation is not too good at low speeds, but is effective above engine speeds of 1500 rpm.

Fig. 24 is a plot of vertical vibratory motion (measured at the operator's seat) comparing before and after results.

The rubber mount is positioned so it isolates in shear. Thrust to the main frame is carried in compression. Reverse loading (due to braking and backing up) is carried in tension. Fig. 25 shows how vertical and reverse deflection is limited.

References

1. Austin H. Church, "Elementary Mechanical Vibrations." New York: John Wiley & Sons Inc., 1957.

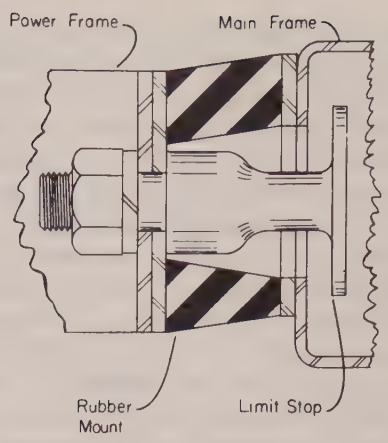

Fig. 25 — Truckster resilient mount

2. Charles E. Crede, "Vibration and Shock Isolation." New York: John Wiley & Sons, Inc. Third Printing, Jan. 1957.

3. James W. Mohr, "Noise and Vibration Reduction and Its Application to Outboard Motor." Paper presented at SAE Section Meeting, Milwaukee, Wis., October, 1955. SAE Preprint

4. Harry F. Olson, "Dynamical Analogies," New York: Van Nostrand Co., Inc., 5th Printing 1948.

5. William Tyrrell Thomson, "Mechanical Vibrations." New York: Prentice-Hall, Inc., 2nd Printing, 1949.

Discussion

Pump and Generator Noise Reduction

Robert K. Teter
Textron, Inc.

THE PROBLEMS encountered by the Outboard Marine Corp. in silencing outboard motors and rotary lawn mowers are very similar to those met by Homelite in attempting to reduce the noise level of engine generators sets.

The work done was in two areas - military and commercial. The most intensive work was in connection with generators used for military purposes. In this, the objective was to make the sets as close to inaudible as possible without hurting the performance and without increasing the size and weight beyond the point of portability.

As in the noise reduction of outboard engines and lawn mowers, the logical first step was to build an enclosure. Since the output was in the form of electricity, it was possible to use a completely tight enclosure except for a passage for air to enter for cooling and combustion and a passage for the cooling air and exhaust gases to leave the enclosure. The enclosure was made of sheet aluminum and

was lined with a layer of mineral wool; all the passages were also lined with this material. This reduced the radiated noise considerably. However, it was also necessary to isolate the generator set from the enclosure to prevent the noise from being transmitted to the enclosure and radiated from there. In some silenced sets this was done by using our conventional steel spring supports and placing the complete set on a plate resting on a pad of mineral wood. The set was allowed to float freely during operation and there was provision made for clamping the set tightly during transportation. This was effective in keeping the transmitted noise to a minimum but had other disadvantages. It was usually found desirable to remove the set from the enclosure when it was transported any distance and, consequently, there was extra time required to install the set in its enclosure when it was to be operated. To overcome this difficulty our more recent designs have had the generator sets supported by rubber vibration mounts attached to the floor of the enclosure. By using snubbers on the mounts it was possible to transport the generator set in its enclosure and by moving the engine controls to the outside of the enclosure it was possible to perform all steps of starting, operating, and stopping the generator with a considerable reduction in noise.

The principal noise source besides the radiated and transmitted noise mentioned above was the engine exhaust noise. This was minimized by using a conventional type of muffler which was discharged either into a second muffler or into a chamber of the enclosure which reduced the noise still further. The other noise sources such as the air intake noise were sufficiently suppressed by the enclosure so that in most instances nothing else was done to suppress them.

In working on this problem no attempt was made to arrive at a mathematical solution of how the enclosures should be constructed, or of what the spring rate of the rubber mounts should be. Instead we worked under the premise that best results would be obtained by (1) making the enclosure as large as possible without sacrificing portability, and (2) making the air passages as long and narrow and with as many bends as possible without detrimental effects on the operation of the engine. The selection of rubber mounts was based on the manufacturers weight rating. However, the method outlined by Mr. Mohr for designing a resilient mounting system could very readily be applied to this problem and would possibly result in a considerable improvement.

Several sizes of generators have been silenced in the manner described above and in some cases there has been a reduction in the overall sound level of better than 20 db. In all cases the chief obstacle to further improvement is the problem of cooling. Since the cooling fan of the engine was also used to provide the air circulation for the enclosure the primary consideration was to make the airflow as efficient as possible.

In the commercial aspect of silencing, an effort was made to reduce the noise of generators and also pumps used by public utility companies while working in city streets. An enclosure was made in the form of a box which could be placed over the generator or pump. The amount of noise reduction obtained by the drop-over box was not as great as for the tight box used for the military sets. We were still exceeding even the most lenient of loudness criteria, but even this reduction was helpful. These criteria vary depending on conditions such as the background noise. When emergency work is done at night in a residential area, the background noise practically disappears and no matter how quiet an engine generator set is, it is still too noisy. On the other hand, during the daytime in a street with heavy traffic even an unsilenced set does not arouse any complaints.

The drop-over box never was widely used, partly because it was not as effective as required for all conditions and because the public utilities were unwilling to sacrifice the space on their trucks required for the box. Recently, the problem is being solved by trying to reduce engine noise without an enclosure. For example, in the case of pumps a considerable reduction of noise is obtained by simply running them at a slower speed. In addition to this, a constant effort is being made to reduce the noise of the chief source, the engine exhaust muffler.

To summarize, the problems encountered in generators and pumps fall into the same categories as those encountered in outboard engines and lawn mowers and the solutions are the same as outlined by Mr. Mohr:

1. Bottle up the noise.
2. Reduce the air intake noise.
3. Reduce the exhaust noise.
4. Reduce the other noises (which would correspond to the blade noise of a lawn mower) such as engine fan noise or brush noise in a generator.

Sources of Outboard Motor Noise Level

Lowell E. Haas
McCulloch Corp.

THE FUNDAMENTAL mathematics and principles of vibration and noise control in this paper will help the engineers of the outboard motor, lawn mower, and motor scooter vehicle industries. This discussion will be confined to a brief analysis of some of the sources of outboard motor noise level.

We do not think that Mr. Mohr has done justice to his first statement, "Noise control is primarily a problem of reducing engine noise." He then states that to solve the problem his company built a sound barrier or enclosure around the engine. It is definite that if the outboard motor becomes the well-behaved powerplant that the automobile engines have become, it will have to have a true noise reduction program performed upon it in which the sources of engine noise are eliminated or drastically reduced.

The modern two-stroke cycle outboard motor, with its 1 hp/in.^{3} specific output, is a first-class noise maker. A

few of the prime reasons for this are the following:

1. Exhaust blow-down pressure.
2. Lightweight structure.
3. Caged antifriction bearings.
4. Entrained lubrication.
5. Flywheel siren effect.

Exhaust Blow-Down Pressure - A two-stroke cycle engine delivers a power stroke every downward stroke; therefore, the only time for charging the cylinder with fresh fuel-air mixture and exhausting the charge previously burned is near bottom dead center. In its simple form, the two-stroke cycle engine opens exhaust ports prior to the time of the intake port opening and approximately 20 deg earlier than a four-stroke cycle exhaust valve opens. For this reason, the exhaust gas pressure at the time of port opening is considerably higher than it is in four-stroke cycle engines. This, of course, leaves high energy in the exhaust gas, and only by drastically and quickly cooling the exhaust gas can the noise level be controlled at all. The outboard motor is fortunate in having a plentiful supply of water when it is operating so that the exhaust gas can be cooled quickly and distributed under water surface.

Lightweight Structure - Every effort is made to increase the specific power output of outboard powerheads, at the same time reducing their total weight. A 63.3 cu in. engine has recently been certified at 75 hp at 5200 rpm and, in complete and running condition, weighs 85 lb. These powerheads are made up of die case aluminum castings throughout and are subject to the inherent unbalance of the particular engine design, since aluminum is not a particularly good damping material; and since it is supplied in as lightweight sections as possible, the structure itself contributes drastically to the total noise level.

Caged Antifriction Bearings - It has been found necessary to supply connecting rod bearings and main bearings of the antifriction type as specific outputs have been increased. It has also been proved advantageous to use caged rollers or balls in these antifriction bearings rather than using full complement structures. This is because the full complement bearings have double rubbing velocity at adjacent surfaces of rollers or ball bearings and heat is generated at a greater rate than when cages separate the individual rolls or balls. Our three-cylinder engine has a total of 310 loose bearing parts in the main and connecting rod bearings. These consist of 284 rollers for connecting rods, wrist pins and center mains; 16 ball bearings in the top and bottom mains; six connecting rod bearing cages; and four center main bearing cages.

Some 6-cyl two-stroke cycle engines have over 400 loose rollers in the crank train bearings. These loose hardened steel parts operating at engine speeds up to 5500 rpm create a great mechanical clatter.

The action of the connecting rod cages contributes to the noise, since the centrifugal force at the crank radius is greater than the centrifugal action of the cage itself turning at half-engine speed upon the crankpin. Therefore, as the cage rotates upon the crankpin due to the planetary action of the rollers between the crankpin and the connecting rod bearing surface, the halves are thrown in and out against the rod or against the crankpin, thus contributing to the noise.

Entrained Lubrication - Since the crankcase of a two-stroke cycle engine is used as an air pump for charging the combustion chamber with fresh fuel-air mix, advantage is taken of this fact to secure simple structure by mixing the lubricating oil with the fuel and delivering it to the crankcase entrained in air. It has been proved that lubrication of the antifriction bearings in two-stroke cycle engines is largely a result of evaporation of the fuel from the fuel-oil mixture which impinges upon the rotating parts, leaving a film of oil on the bearing surfaces adequate enough to prevent metal-to-metal galling. Due to the fact that the airflow velocity through the crankcase of wide-open throttle, high-speed conditions is high enough to keep most of the fuel-lubricant mixture entrained in the air and carried into the combustion chamber, lubrication becomes less adequate at wide-open throttle than at low-speed or low-throttle conditions. Under no circumstances are the bearing surfaces supported on a film of lubricant as in plain bearings. Thus, sparse lubrication at wide-open throttle conditions and only sufficient lubrication to prevent galling leaves the metal surfaces free to pound upon each other and generate a high level of noise.

Flywheel Siren Effect - In order to provide a lightweight source of electrical current for electric starting motors, flywheel alternator generators are used in most modern outboards. Twelve magnets and 12 pole pieces passing each other at 5000 rpm generate considerable siren effect due to deflection of the coil pole pieces. In addition to this, the starting motor ring gear has approximately 90 teeth passing in close proximity to other metal surfaces which are stationary. This, too, adds to the total siren effect.

Reducing Airborne Engine-Radiated Noise

Cecil R. Sparks
Southwest Research Institute

THIS PAPER presents an interesting and informative discussion on several valuable techniques for controlling noise and vibration problems inherent in reciprocating engine-driven equipment.

While the vibration problems treated in this paper lend themselves well to the direct analytical approach because of the lumped constants of mass stiffness and the rest, the suppression of radiated airborne noise from the complex mechanical structure involved unfortunately does not lend itself to such a rigorous approach. Thus, some comment may be warranted in further description of the methods employed in reducing this airborne engine-radiated noise.

The difficulty encountered in an analytical approach to-

continued on page 282

FROM FOUR PLIES TO A SINGLE PLY IN STEEL CORD CASING TIRES

M. P. Baumont
Manufacture Francaise des Pneumatiques, Michelin

TO SPEAK OF "STEEL-CORD" tires is to touch upon a very important step in the evolution of pneumatic tires. In fact, one almost could apply to tires Darwin's Theory of Evolution because tires, like living organisms, have become more and more complex in their construction as the operating conditions with which they have to cope have become more and more varied. In consequence, the "Steel-cord" tire constitutes not exactly a "revolution" but rather an adaptation of tire technique to the ever-changing and increasingly expensive conditions imposed by road transportation.

Exacting Demands of Economical Transport

Beginning some years before the last war we have seen, under the constant need for less expensive transportation, higher vehicle speeds, longer hauls, ever-increasing payloads followed by a vast increase in the volume of goods carried by road. Tires, in their turn, had to be stronger, safer and, to carry a given load, of the smallest physical dimensions possible. Drivers, especially on long hauls, demanded a more comfortable ride and the more intensive running and use of vehicles posed problems of deterioration of vehicle components.

Problem of Tire Temperature

As everyone knows, the principal problem encountered in tires is that of heat generation and high internal temperatures - especially for truck tires used on long hauls. Conventional truck tires with textile casings have, for example, 12, 14, or 16 plies. During every wheel revolution every element of the tire is distorted as it comes under load and the distortion causes a slight relative movement between all the plies. Although slight, these constantly and rapidly repeated movements can cause, especially in a heavily loaded tire, a rise in internal temperature as high as 230 F (well over the boiling point of water). Obviously, the greater the tire load, and the greater the speed the greater is the rise of tire temperature.

Further, because textile casing materials are poor conductors of heat, the parts of the tire reaching the highest temperatures are in the flexion area near the beads and in the tread shoulder or buttress area (where the heat is "pocketed"). The result of this heat generation and high temperature in textile tires is a loss of tensile strength in the casing cords and a softening of the rubber compounds which impregnate the plies and bond together the various tire components; the tire is no longer "of one piece," so to speak. A relatively slight external shock, quite harmless to a cool tire, can cause dislocation of the casing; a single ply may be ruptured, but such a local rupture rapidly spreads through the whole casing thickness, culminating in a blown-out tire. Quite a high proportion of textile casing truck tires, in all parts of the world, thus perish before their treads are worn out.

Make Shift Solution

Improvement in textile casing materials and rubber compounds, better able to withstand the effects of high temperatures, did not keep pace with vehicle improvements. The lag was such that, long years ago, because it was impossible to design a satisfactory big single tire to carry a heavy load,

dual tires had to be used. Duals thus took the place of singles because the smaller dual tires, having less plies than the number needed to make a sufficiently strong big single, ran at a much lower, and relatively safe, equilibrium temperature. This is mentioned in passing simply to underline the inertia effect of habit because, in spite of the great progress made in tire construction, we still see used the dual tire solution which dates from 1908!

Story of Fight Against High Tire Temperatures

The unceasing increase in vehicle speeds and axle loads forced, nevertheless, parallel evolution in pneumatic tires. One solution was to use fewer casing plies because it is, as already mentioned, mainly interply movement which causes heat generation and high temperature; further, with many plies and correspondingly thick tire walls, heat cannot escape. Decreasing the number of plies means increasing the tire section -- which has the additional advantage of giving better heat dispersion by radiation. Increased tire section also meant, for a given tire load, a lower pressure. In fact, it is unnecessary and undesirable to retain the same pressure as was needed for the equivalent high-pressure many-plied tire. Unnecessary because the bigger section permits of carrying the load at a lower pressure while still having a safe working deflection in the tire; undesirable because a high pressure would impose too much tension on the cords of the reduced number of plies.

This was the way in which the first truck tire evolved -- for example, the old 34 x 7 high pressure replaced by the "fatter" 9.00 - 20 at a lower pressure. There are obvious limits to this approach; when high tire loads are involved, the physical dimensions necessary for such low-pressure tires would rule out their use. It thus becomes necessary to develop tires having high load ratings without increase of section.

From 1934, tire technicians turned their attention toward the use of new materials for casing construction and, since that time, rapid and parallel evolution by the chemists has led to periodic reassessment of the situation. Rayon and all other feasible textile materials -- man-made or natural -- have been tried and tested. Today, the gradually improving textile casing materials, found to be practical for general use, lose less of their tensile strength than formerly at the temperatures reached in tires; however, their "cold" strength has changed but little and in consequence no substantial reduction in the number of casing plies is possible.

Birth of Steel-Cord Casing

As early as 1934, the Michelin technicians made up their minds to take a decisive step in the development of truck tires and set about tackling the problems of using steel as a casing material because:

1. Steel is as strong at 250 F as at 60 F.
2. Its inherent tensile strength would permit using only 2 or 4 steel plies instead of the 14, 16, 18 -- or even more -- cotton or rayon plies needed (Fig. 1)

With steel they were combating, at one and the same time, the source of heat generation and its harmful consequences.

It should be mentioned here that the idea of a steel-cord casing was not by any means new -- it was as old as the pneumatic tire idea -- because the use of steel was foreseen in the famous Thomson patent which was the origin of the pneumatic; but tire technicians spoke of the use of steel only as being something beyond the bounds of possibility (Fig. 2). After prolonged research, Michelin technicians managed to make steel cords and build them into tires which were as supple as textile tires but incomparably stronger. They also

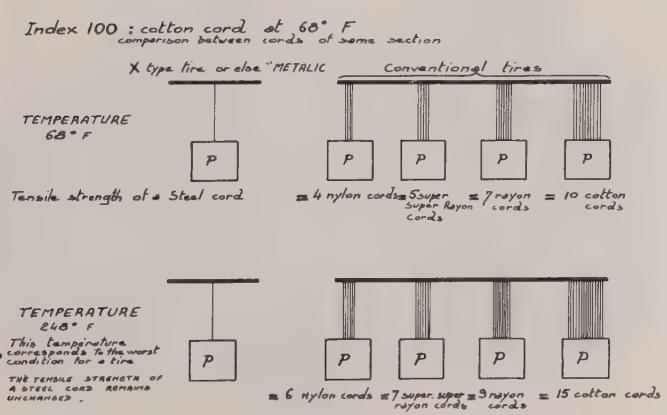
Index 100 : cotton cord at 68° F
comparison between cords of same section
X type tire or else "METALIC
Conventional tires
TEMPERATURE 68° F
P
Tensile strength of a Steel cord
= 4 nylon cords
= 5 super Super Rayon cords
= 7 rayon cords
= 10 cotton cords
TEMPERATURE 248° F
This temperature corresponds to the worst condition for a tire
THE TENSILE STRENGTH OF A STEEL CORD REMAINS UNCHANGED
= 6 nylon cords
= 7 super. super rayon cords
= 9 rayon cords
= 15 cotton cords

Fig. 1 — Comparative tensile strength of cords used in tires

UNITED STATES PATENT OFFICE.

ROBERT W. THOMSON, OF ADAM STREET, ADELPHI, COUNTY OF MIDDLESEX, ENGLAND.

IMPROVEMENT IN CARRIAGE-WHEELS, &c.

Specification forming part of Letters Patent No. 5,104, dated May 8, 1847.

To all whom it may concern:

Be it known that I, ROBERT WILLIAM THOMSON, civil engineer, of Adam Street, Adelphi, in the county of Middlesex, England, a subject of the Queen of Great Britain, have invented or discovered a new and useful Improvement in Carriage-Wheels, which is also applicable to other rolling bodies; and I, the said ROBERT WILLIAM THOMSON, do hereby declare the nature of the invention and the manner in which the same is to be performed is and by the following statement thereof—that is to say:

The nature of my said invention consists in the application of elastic bearings round the tires of the wheels of carriages for the purpose of lessening the power required to draw the carriages, rendering their motion easier, and diminishing the noise they make when in motion. I prefer employing for the purpose a hollow belt composed of some air and water tight material, such as sulphurized caoutchouc or gutta-percha, and inflating it with air, whereby the wheels will in every part of their revolution present a cushion of air to the ground or rail or track on which they run.

belt is then built up (so to speak) around the tire by riveting together a series of circular segments of leather and bolting them to the tire in the manner shown in Fig. II. The segments at two of their edges *a a*, Fig. II, are made to overlap each other, as shown, and then secured in their place by passing bolts G G, Fig. II, through the tire and felly and making them fast by nuts *g g*, Fig. II. The elastic belt C, Fig. II, is then laid upon the portions of the segments D D, Fig. II, thus made fast to the tire, and secured in its place by bringing the two remaining and as yet unjoined edges *b b*, Fig. II, of the segments together over the casing and connecting them together by rivets F F, Fig. II. A pipe I', Fig. I, through which to inflate the elastic belt with air, is passed at one place through the tire of the wheel and fitted with an air-tight screw-cap.

I prefer distending the elastic belt with air, as being more suitable than anything else for the purpose; but it may be distended with various solid substances of an elastic quality—as, for instance, metallic springs, sulphurized pieces of caoutchouc or gutta-percha or horse-hair or sponge.

Fig. 2 — Thomson patent

mastered the problem of bonding rubber compounds to steel; the bond proved to be stronger than that obtainable with cotton or rayon.

In 1936, the first steel-cord tires were used on the rail-cars which ran on the French railways (the tires, of small section, actually ran on the rail-head); but it was in 1937 that the first steel-cord tires were put into commercial service on highway vehicles. Demand soon exceeded supply -- and that remains the situation to this day. In 1939, the first "metallic" tires (as they were called) were sold in New York and, during the war years, several thousand such tires were running on American highways.

The first "metallic" tires had 4 casing plies for the larger sections and only 2 for the smaller truck sizes, but later on it was found possible to make even stronger steel cords with an even greater tensile strength (ultimate tensile 326,000 lb or 163 American tons/sq. in.). This allowed the making of a complete range of 2-ply steel-cord casing tires up to 12.00 - 20. It is tires such as these which are giving highly successful results, not only on many American roads, but all over the world.

Birth of "X" Tire

So far, we have talked only about steel-cord tires which have, as their main distinguishing feature, steel casing cords; they are built up, like conventional tires, with crisscross casing cords -- but they are designed in the light of the strength of the casing material used: that is, steel. I wish to speak now of the new step forward in tire conception -- made some years ago in Europe -- which now extends to the United States. I want to speak about the "X" tire; its development was made possible by our experience with the use of steel cords in tire construction. Contrary to the general belief that the "X" tire, with its single casing ply, is the logical continuation of our progress from multiple textile plies to only 4, then to 2, steel-cord plies, I must point out that the radial ply steel-cord casing tire is the product of a quite independent and parallel research.

Quite early research (1930) on passenger-car tires, with the object of improving comfort of ride by lowering tire pressures, had brought out the importance of "road-holding" or "road-behavior" of the car (not to be confused with tire grip or adhesion); in other words, the role of the tire in the "precision" with which a car can be driven. These studies led to an analysis of the effect of casing-cord angles, and in 1937, to the development of the so-called "Pilote" tire which has casing cords with an obtuse cord angle (we have seen, of recent years, the blossoming of this principle in your country -- known as low-profile tires). In particular, our research demonstrated that at the same time as this type of tire construction improved the "road-behavior" of the car, there was a marked reduction in the rate of tread wear.

Logically, it then became a question of pursuing this research to the limit, in order to arrive at the optimum in "road-behavior" and the associated advantage of lower rate of tread wear. The discovery of the effect of the "architecture" of a tire on its qualities and behavior led to a complete reassessment of the arrangement of its component parts -- to the application of a principle, dear to Descartes -- to make a clean sweep of all previous thinking.

Bearing in mind the two associated tire qualities already mentioned (maximum precision in driving and minimum rate of tread wear), it was possible to direct the studies of our tire technicians in two directions:

1. To design a tire best able to cope with load and speed while at the same time giving a comfortable ride.
2. To design a tire least susceptible to tread wear.

That is exactly what was done with the "X" tire; the required qualities and roles of the casing walls and of the tread were studied separately (Figs. 3 and 4). The wall plies were developed with an "archwise" arrangement of the cords -- laid on the shortest path at right angles from bead to bead. This allowed the casing cords to work in the most "rational" fashion possible when under the action of load and to cope safely with high tire working deflections. Further, when the casing is distorted under load, there is hardly any distortion transmitted to the tread (as is the case with conventional tires).

On the other hand the tread, while being very flexible longitudinally, is made rigid laterally by a triangulated arrangement of the three steel-cord crown plies; this prevents deformation ("creep" or "shuffle") of the tread in the road contact area.

What is the contribution made by Steel Cords in this matter?

Fig. 3 — Casing walls of "X" tire

1. In the casing it has permitted, by judicious choice of the steel cords used, the use of only one ply for the whole range of "X" tires. We are making at present, for example, quantities of Earth Mover tires up to the 27.00 - 33 and those have a single steel-cord casing ply.

With only one ply there is a complete absence of the shear or conflicting forces between plies which exist in all multiply tires -- there is, therefore, much less internal heating and less loss of power due to tire "drag" or "tractive resistance." Any heat which is generated in "X" tires is easily dispersed and dissipated through the thin but strong walls, and this dispersion is aided by the good thermal conductivity of the steel casing cords.

2. In the tread, it is the inherent qualities of the steel cords of the crown plies which have given the tread, in the highest degree, the characteristics which were sought.

It is thus quite evident that it is indeed "steel-cord technique" which has permitted the successful "blossoming" of the "X" tire and its development to include the very large tires now made.

I shall confine my remarks to the Steel-cord "X" (or "radial casing") tire; this is, after all, the optimum reached in the domain of truck tire design and is at present being studied by all important tire manufacturers.

Advantages of Steel-Cord Tires for Users

Let us begin by examining what advantages are reaped by users from the use of "X" or "radial" tires. There, in the final analysis, should lie our main preoccupation.

Increased Load Carrying Capacity - In selling an "X" tire to a user, one provides him with the possibility of increasing the payload carried by a given size of tire, thanks to the most effective use in the "X" tire of its component parts and constituents. If one compares the published ratings for tires of the same section, it is seen that "X" tires come definitely in the "high load capacity" category (Fig. 5). A user may thus use "X" tires to carry extra payload (within the limits

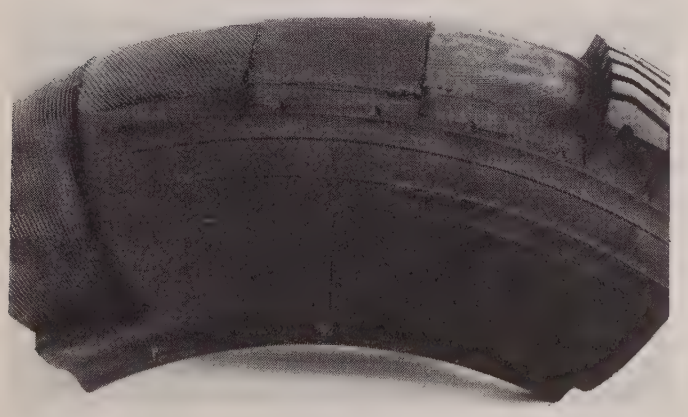

Fig. 4 — Tread of "X" tire

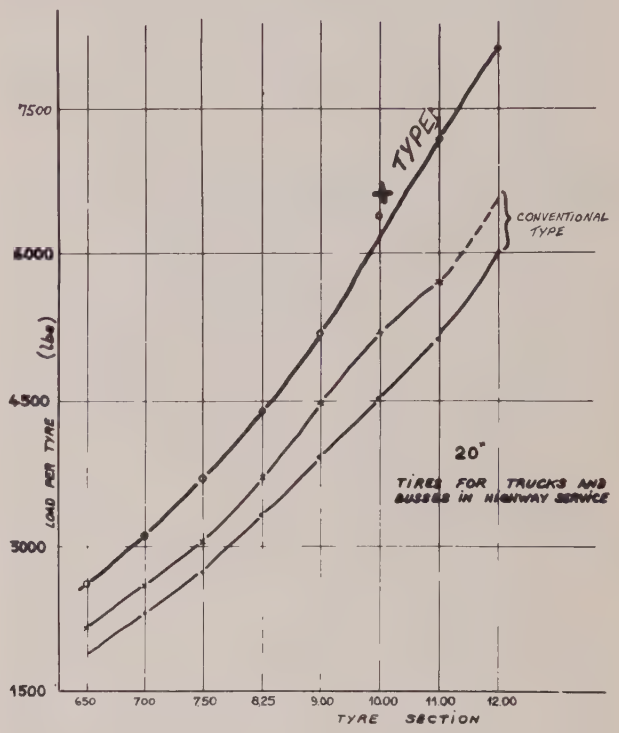

Fig. 5 — Comparative load-carrying capacity — "X" tire versus conventional

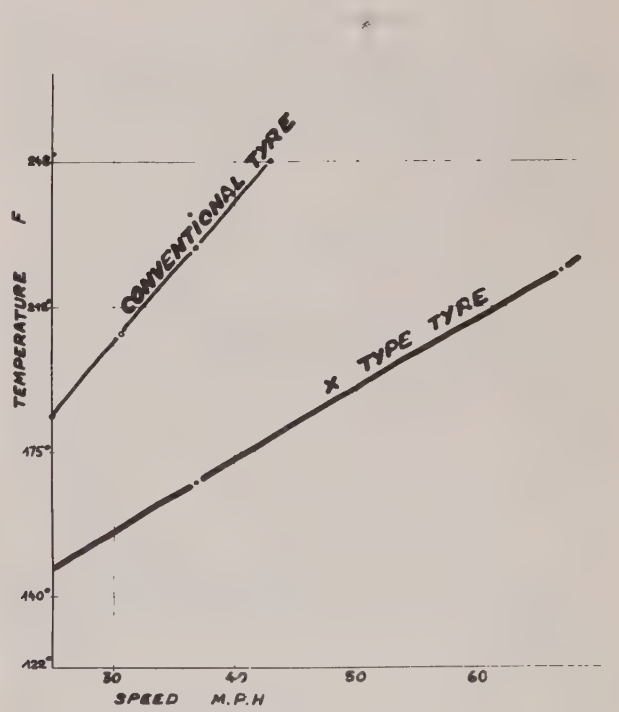

Fig. 6 — Comparative running temperature — "X" tire versus conventional

of state regulations, of course) -- or, if he does not wish, or is unable, to increase his payload, he may reduce his tire costs by fitting an "X" tire of smaller section than his present conventional tires. For example, it will be seen from Fig. 5 that 8.25 - 20 conventional tires can be replaced by 7.50 - 20 "X."

Increased Running Speeds - It is interesting to compare the equilibrium temperatures reached by tires of different types during running at various speeds. The graph (Fig. 6) is, of course, only one of many. One could argue about the figures in view of the variety of running conditions and sizes of tires in use. But, taking one case of operation on main highways, for example, one finds enormous differences in tire temperature. If one took as a criterion of safe operation the equilibrium temperature reached, the differences in permissible speeds would be very considerable!

It would be seen, for example, that with a given textile tire, a temperature of 248 F is reached at 43 mph, whereas with an "X" tire the temperature is only 220 F at 68 mph, all other things being equal. It is, of course, understood that other factors may cause variations to the results quoted and I underline the fact that they must not be taken as absolute values. Nonetheless, it is quite evident that the cool-running properties of tires of "radial" construction and with only one casing ply do permit their safe operation at higher speeds.

For this reason, in Germany, where there is a lot of heavy transport on the Autobahnen, we have been led to state officially that the ratings of our truck "X" tires up to 14.00 - 20 are suitable for sustained speeds of 62 mph. Increased payloads and increased speeds -- thanks to "X" tires -- lead to a reduction in the cost per ton/mile and to more efficient use of vehicles. It is, in fact, safe to say that many operators have already proved that the use of "X" tires has made an important contribution to the profit-earning possibilities of their undertakings.

Increase In Tread Life - The very pronounced stabilization of the tread of an "X" tire, due to the 3 steel-cord triangulated crown plies, cuts out, as already stated, the "creep" or "shuffle" of the tread in the road contact area Our studies of the behavior of treads, linked with out studies directed toward a reduction of tread wear, demonstrated the marked effect of these movements on rate of tread wear. In particular, we observed (without being surprised) the enormous reduction in rate of tread wear when triangulated crown plies were introduced.

It is possible to say, today, that the tread life of X truck tires is -- all other things being equal -- one and a half to two times as long as that of the best conventional tires. All operators know that the purchase price of a tire must be viewed in the light of its mileage performance. In the final analysis, it is not the purchase price which matters so much as the cost per tire-mile. In Europe, we have proved cases of main highway operation where the tire-mile costs have been halved by the use of "X" tires. In other areas with winding and hilly roads where tread wear is the preponderant factor, "X" tires have reduced the former cost per tire-mile by two-thirds.

Excellent "Road-Behavior" of Vehicle and Tire Grip Even on Snow and Ice - Certain factors, which do not apply in all countries and which depend both upon the temperament of the driver and on the road conditions, might well be considered at this stage. In many European countries a great deal of importance is attached to vehicle behavior; this, in our opinion, is entirely justified because the safety of the driver and vehicle depends upon good vehicle behavior; owners and drivers have a right to expect it.

Now, the very marked stabilization of the crown of "X" tires, linked with the immunity of the tread from transmitted casing distortions, results in a very pronounced reduction, compared with conventional tires, in the "deviation" from the steered path caused by external lateral forces (wind and centrifugal cornering forces). This results in a much improved directional stability of the vehicle and gives greater precision to driving, whether on main highways (where overtaking must be accurately judged) or on winding roads, of which we have so many in Europe. Further, "X" tires ensure the best road grip possible -- a valuable quality when emergency braking is necessary. This excellent grip is obvious especially on wet road surfaces, because the tread movements in the area of road contact (which, with ordinary tires, constitute in effect a commencement of tire slip) are almost entirely absent in the "X" tire.

During bad weather conditions with snow or ice on the roads, "X" tires have built up a reputation for safety and stability. In fact, in certain countries where the authorities on contemplating regulations regarding tires, users are pressing for "X" tires to be included with heavily patterned ones as being entirely suitable for snow conditions.

Question of Comfort - We have already mentioned the increasing emphasis placed upon the comfortable ride which operators demand (among other characteristics), from their tires. The low equilibrium temperatures reached in "X" tires have permitted their use at higher working deflections

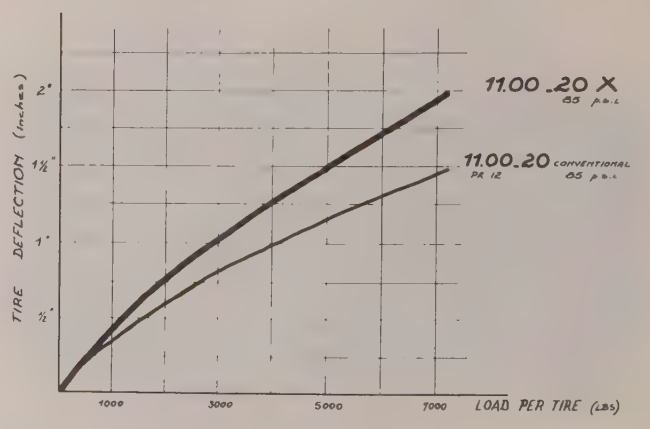

Fig. 7 — Comparative working deflections — "X" tire versus conventional

than those possible with conventional tires. The curves (Fig. 7) show the comparative working deflections of two different 11.00 - 20 tires -- one a conventional and the other a steel-cord "radial." It will be seen, for example, that at a tire load of 7000 lb, the "X" tire has 1/2 in. greater deflection. As soon as "X" tires were put on the market, this quality of greater comfort or "protection" was remarked upon by users.

Actual measurements of vibratory energy transmitted in the vertical plane by various types of tires -- including "X" -- have been made, and the results are shown in Figs. 8 and 9. These measurements were made in a manner which registered only the suspension effect of the tires; the effect of the road springs, which varies from vehicle to vehicle, was eliminated. The test vehicle was run in each case over the same 2-mile stretch of road at a constant speed of 30 mph.

The energy transmitted through the tires can be compared by measuring the area between the upper datum line and the curves. In this particular case, it is seen that, in descending order of vibratory energy engendered, the comfort increases when one passes from conventional rayon or nylon tires to "X" tires. Fig. 8 shows the test results with the vehicle loaded. Fig. 9, much more impressive, shows what happened with the vehicle unloaded with the tire pressure left at the loaded pressure values. The very marked difference between the protective qualities of the various tires and the significance of this requires no emphasis. We all know of the complaints of drivers "returning empty." Bounce, bad road holding, and noise. In this context of comfort, mention should be made of the small buildup in pressure of "X" tires during running because they run cool; this also contributes to better comfort.

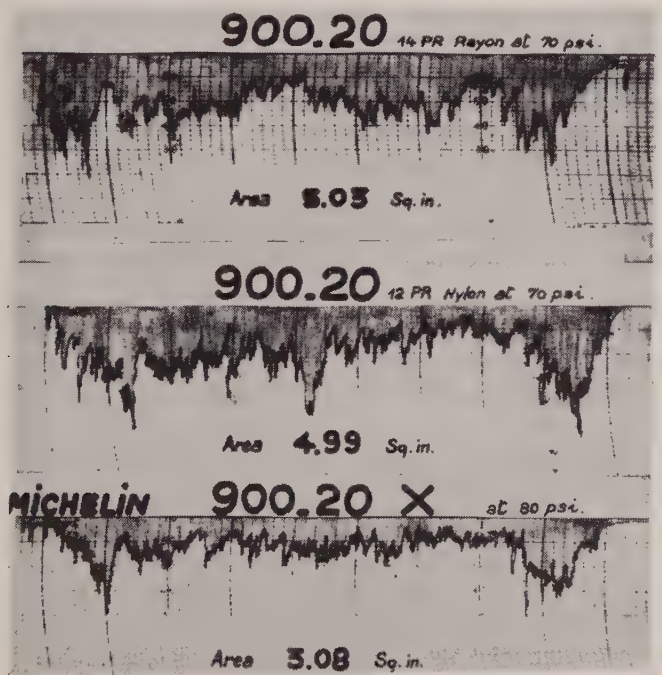

Fig. 8 — Comparison of vibratory energy transmitted in vertical plane by different tires — vehicle laden

Savings in Vehicle Repairs and Maintenance - Information obtained from operators proves that spring breakages and body damage caused by vibration have been greatly reduced, simply by use of the "radial" tires. This means marked savings on vehicle repairs. Let me quote the experience of one French operator:

Records kept of 900,000 miles running showed that, over the same routes, the replacements of complete road springs, which was 1.8 springs per 62,000 miles, fell to 0.29 springs per 62,000 miles after "X" tires were fitted -- 6.2 times less. Further running accentuated the advantages of the "X" tires because, after 1,260,000 miles, spring replacements fell from 6.2 to 9.8 times less than before "X" tires were used.

Another case investigated revealed the following facts:

Whereas in 1954 road spring breakages cost the user 20 cents per kilometer, in 1955 on the same routes with the vehicles operating from the same base, the change to "X" tires brought the figure down to 10 cents per kilometer -- a reduction of 50%.

It is quite understood that these figures are valid only for a particular case -- that is to say, one must not conclude that the use of ordinary tires inevitably causes road spring breakages. Rather, one should say "When there are road spring breakages there are less when "X" tires are used." In any case, it can be claimed safely that "X" tires on a truck, used under the conditions stipulated by the truck manufacturer, afford better protection to chassis and body

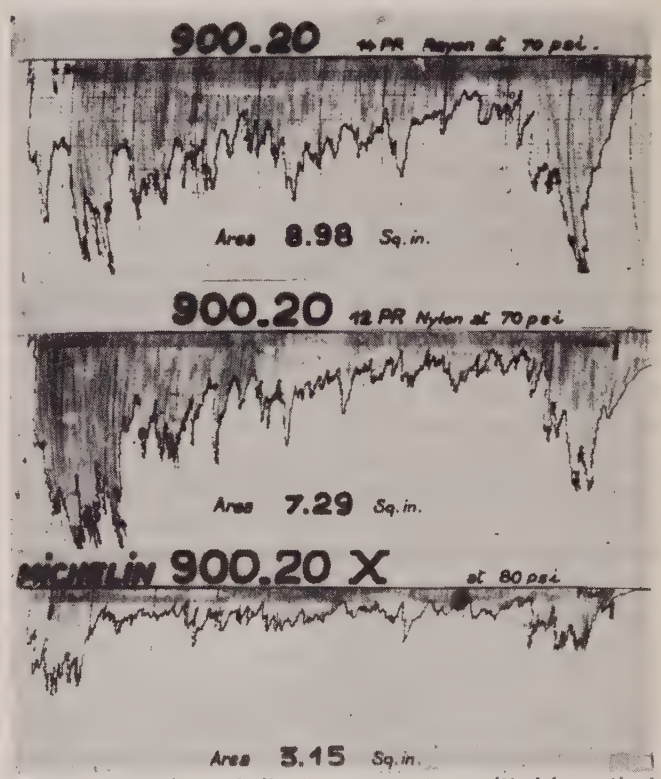

Fig. 9 — Comparison of vibratory energy transmitted in vertical plane — vehicle unladen

Fig. 10 — "X" tire retracting under shock

even if, prior to the change to "X" tires, there was no problem of broken road springs, lost studs, nuts, or bolts.

Immunity from Shock on Bad Roads - Another advantage arising from the big working deflection of "X" or "radial" tires should be pointed out here -- their immunity from shock damage. One of the first reactions to "X" tires which we encountered -- particularly in the less-developed countries -- was the fear that the single-ply walls would provide only flimsy protection against the shocks and cuts normally experienced.

It is well known that, to withstand a shock, an object must be either very hard, yet elastic, so as to repel all the energy of the shock, or very yielding, so as to absorb the shock. (The difference between hitting a golf ball and punching a pillow!)

Taking the first choice, in the case of the pneumatic tire the method adopted is to increase the number of plies (which may have harmful consequences in other directions) and to thicken up the side wall rubber in order to increase the resistance and elasticity. In the second case, the necessary protection is provided simply by so designing the tire that the walls "retract" under shock, thus almost completely absorbing the energy of the shock. That is precisely what happens with "X" tires (Fig. 10). Experience has in fact proved, statistically, that the incidence of wall damage due to shocks and cuts is rather less with "X" tires than with others. Finally, when the walls of "radial" tires are damaged, repair is easier than with other types of tire.

Saving in Fuel Consumption - When a vehicle is running, its tires, like all other moving parts, consume a certain amount of energy. It is this consumed energy which makes the tires hot and it arises from three main sources:

1. Distortion of the tire due to its deflection under load.
2. The "creep" or "shuffle" of the tread in the road contact area.
3. Distortion of the tread and casing caused by driving or breaking torque, cornering forces or any other factor imposing a slip angle on the tires.

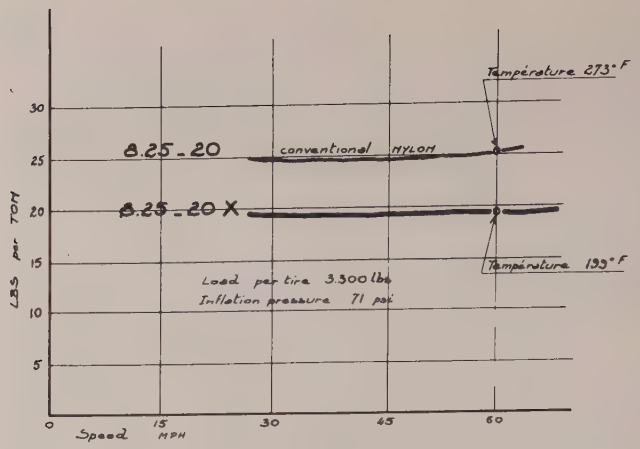

Fig. 11 — Rolling resistance

This energy expended in the tires varies according to the load and pressure and with the type of tire construction -- its "architecture." The "X" tire, lighter and having only one casing ply, offers the least resistance to flexion and, in consequence, consumes less energy when running. This is evident from the figures of equilibrium temperatures quoted earlier. Fig. 11 gives a comparison between a nylon casing tire and an "X" type steel-cord casing tire.

The energy consumed by the tire when running -- much greater in the case of the tire of classic design than in the case of the "X" -- is converted into heat. This difference in the amount of energy consumed is reflected in the temperatures reached by the tires and in the fuel consumption of the engine. For example, at 45 mph an 8.25 - 20 "X" tire has a rolling resistance of 19 lb/ton, whereas for a conventional tire of the same size, the figure is 25 lb/ton. Translated into power, this means that the "X" tire consumes 3.5 hp, or 45% more than the "X".

Other cases, investigated in France and elsewhere, lead to a similar conclusion: "X" tires consume less energy and have a higher efficiency as transmitters of power than other types of tire. In England, for example, an important manufacturer of engines -- obviously interested in obtaining the maximum miles per gallon -- made closely controlled tests at constant speeds of 30, 45, and 60 mph with the results shown in Fig. 12.

Other undertakings (vehicle manufacturers and operators) have found an improvement in mpg with "X" tires varying about 11%-16%. Obviously, such improvements obtained during controlled tests will be less marked for the "give and take" conditions of ordinary vehicle operation where random factors (which are not present during controlled tests) can influence the results obtained. Nonetheless, it is quite common to find, in big fleets using "X" tires, a reduction of fuel consumption of the order of 6%-8%.

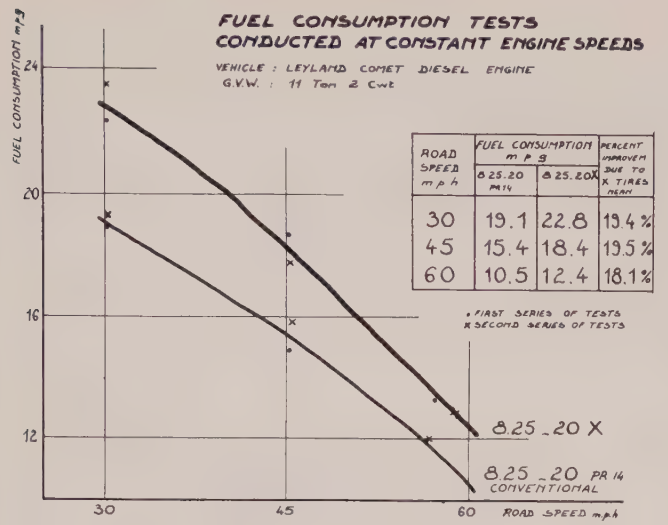

ROAD SPEED m.p.h	FUEL CONSUMPTION m.p.g 8.25.20 PR14	8.25.20X	PERCENT IMPROVEM DUE TO X TIRES MEAN
30	19.1	22.8	19.4%
45	15.4	18.4	19.5%
60	10.5	12.4	18.1%

Fig. 12 — Fuel consumption tests conducted at constant engine speeds. Vehicle — Leyland Comet diesel engine. Gvw — 11 ton 2 cwt.

In the light of the foregoing facts, one may legitimately claim that the combination of steel-cords and the new type of tire construction opens up a rosy perspective for any vehicle operator who is interested in reducing his running costs.

It is unfortunately true that operators are sometimes subjected to restrictions which are not always in the interests of the most economical transport; this explains why there is often a lag in the wide application of technical progress. Yet there remains the hope -- and we see already sings of its coming true -- that in the long run progress will prevail.

Advantages of Steel-Cord Tires for Vehicle Manufacturers

The following examination of certain other advantages of steel-cord tires of "X" type construction, is directed mainly to vehicle manufacturers. It is obvious that these latter, like ourselves as tire makers, should constantly bear in mind the interests of their customers. In this context, one has only to observe the feverish efforts in design and project offices to bring out some changes, each year, even though they be only of detail, which will improve the performance or the appearance of the vehicles to be marketed during the next selling campaign.

For a long time, both vehicle manufacturers and users have looked upon tires as mere accessories -- like headlamps or generators -- but we are happy to note that nowadays, the "education" of users in tire matters is having its effect and much more attention is being paid to the article which, in the final analysis, ensures the liaison between the vehicle and the road. This sometimes means more worries for the vehicle manufacturer whose life is made the more complex when he is well meaning, but sometimes inept State legislation concerning vehicle design and use is grafted on to his more normal technical problems.

"X" IN SINGLE FORMATION

SIZE	Section	Free radius	Laden radius	Rim	Carrying capa. US Tons	Inflation pressure	Deflection	Speed	Assembly Weight	Price Ft. comm only
14.00.20X MICHELIN	16.8	27	24.4	10.00W	11.025	105 psi	2.6	62 mph	327 lbs	104.83
CONVENTIONAL TEXTILE TIRE IN SINGLE FORMATION : NONE										
CONVENTIONAL TEXTILE TIRES "DUALS"										
1100.20 14 PR CONVENTION	11.5	21.2	20	8.0	11.025	90	1.2	50	1080	876.75
"X" DUAL FITMENT										
D20X (11.00 20X)	10.7	20.8	19.1	7.33V	11.025	102	1.7	62	1006	520.30

Fig. 13 — Selection of tire size for axle load of 11-ton tire in single formation

Let us see how "X" type tires can help vehicle manufacturers in rethinking some of their more fundamental problems. The use of higher ratings for tires of the smallest feasible dimensions permits, in particular, alteration of road spring arrangement. Springs can be more widely spaced and vehicle stability thus improved; the center of gravity can be lowered; the unspr ng mass can be decreased. Body design is also influenced -- less space taken up by wheel-arches, as an example, in one European country where the individual legal axle load is 10 tons, we are faced with two alternative tire solutions (Fig. 13):

First Solution - Duals - As already mentioned, this is the first to come in mind -- from force of habit. For 10 tons the conventional equipment is 11.00 - 20 14-ply rating. The overall width over dual tires is 24.2 in. The free radius is 21.2 in. (42.4 in. overall diameter). The laden radius is 20.0 in. (Tire deflection 1.2 in.) Inflation pressure is 90 lb for 50 mph. The weight of the rotating assembly (2 tires and wheels) is 540 lb.

The "X" dual solution is 10.00 - 20 "X". Overall width over twin tires is 22.8 in. Free radius is 20.8 in. (41.6 in. overall diameter). Laden radius is 19.1 in. (tire deflection 1.7 in.) Pressure is 100 lb for 62 mph. Weight of rotating assembly (2 tires and wheels) is 503 lb. Already it is evident that the "X" dual solution has certain advantages (Fig. 14):

1. At the same load higher speed is possible (62 versus 50 mph).

2. The working deflection of the "X" is greater at 100 lb than that of the conventional tire at 90 lb -- therefore, better protection of vehicle and load.

3. The center of gravity is lowered by the difference in laden radii by nearly an inch.

Any vehicle design men will agree that such a reduction in height of center of gravity is important from the point of view of road behavior of a vehicle and during acceleration and braking, especially when little can be done to change the "hook-up" between chassis and body. The difference in width over twin tires is not far short of 3 in. (2.8 in.), so the road spring centers could be widened by this amount,

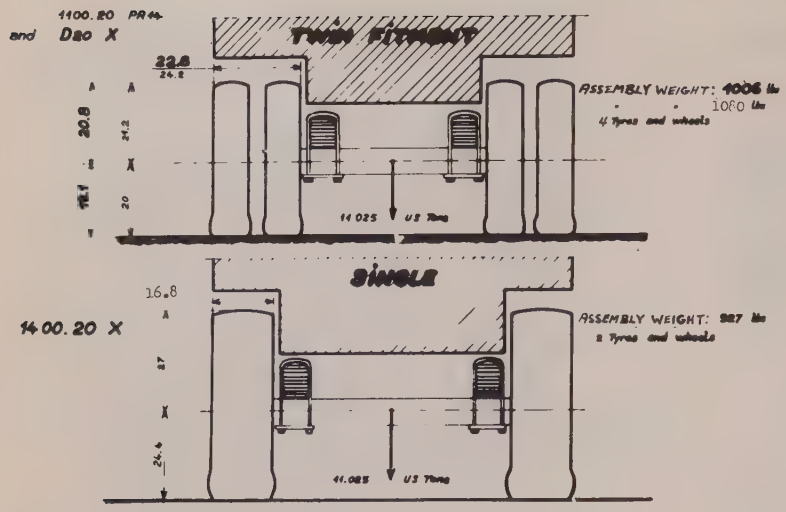

Fig. 14 — Example of comparative fitment — "X" and conventional

thus contributing, like the reduction of height of center of gravity, to better vehicle stability. If we consider a 2-axle truck, the total weight of 6 rotating assemblies is reduced from 1890 to 1720 lb -- a saving of 170 lb or 9%. This must be reflected in a reduction of power less, less wear and tear of vehicle components and improved fuel consumption (Fig. 15).

Second Solution - Singles - This merits our consideration because the advantages it brings can, in some cases, outweigh any apparent "snags" (Fig. 13). In this case, the single tire is the 14.00 - 20 "X". The section is 16.8 in. The free radius is 27.0 in. (54 in. overall diameter). Laden radius is 24.4 in. (working deflection 2.6 in.). Inflation pressures is 105 lb. The weight of the rotating assembly (one tire and wheel) is 464 lb. Compared with the conventional dual solution, the disadvantage of increase (height of the center of gravity with 14.00 - 20 "X" singles) is compensated by the enormously increased truck spring and hub spacing made possible (14.8 in. increase).

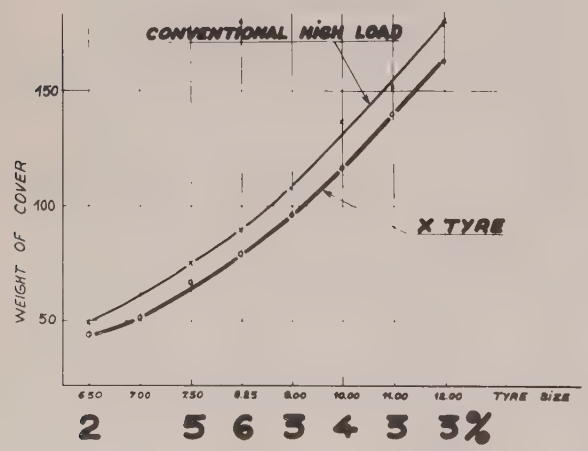

Fig. 15 — Weight saving on wheel assembly by fitting "X"-type tire

Again, even at 105 lb inflation, the deflection of the single is much greater; hence, a more comfortable ride -- especially at 62 mph, the permissible sustained speed for the "X". The reduction of unsprung mass on the rear axle (2 tires and wheels 14.00 - 20 "X" compared with 4 tires and wheels 11.00 - 20 conventional) is about 150 lb. The unequal loading between the two tires of a dual assembly is absent.

Rolling resistance, which was mentioned earlier when discussing the advantages of "X" tires for users, is less with singles than with duals; it is obviously of interest to the vehicle manufacturer to have his engine losing less of its outpub in tires, thus having extra power available for more useful purposes.

"X" Tire and Common Good

Before concluding, I should like to convey a thought which is not customary to touch upon in the context of a technical paper; yet I want to mention it because of its real importance for a country such as mine.

In effect, for any country which has no domestic production of rubber or tire textile materials -- as is the case for many European countries -- the "X" tire constitutes a means of spending foreign currency to the best advantage for the

	9.00-20 CONVENTIONAL	8.25-20X	CONVENTIONAL TIRE with 1.35 coefficient
Weight of rubber	40.44 lbs	34.41 lbs	54.66 lbs
" of cord	14.9		20.11
" of steel	2.34	21.36	
Sundries (sulfur, carbon black, ...)	22.33	23.35	30.17

Fig. 16 — Raw materials used in a tire for a 5-ton payload truck

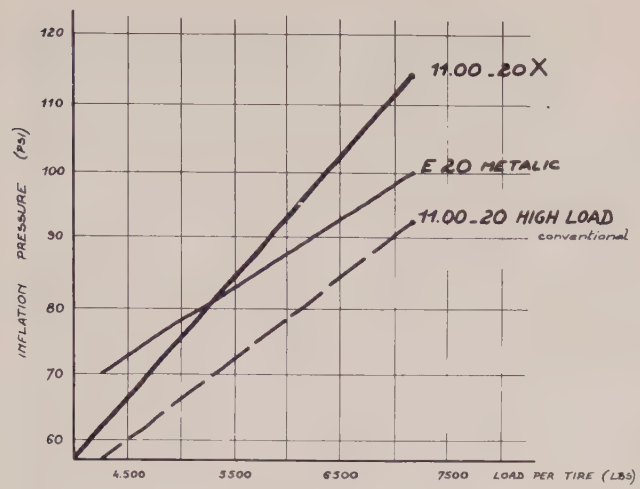

Fig. 17 — Comparative working deflections

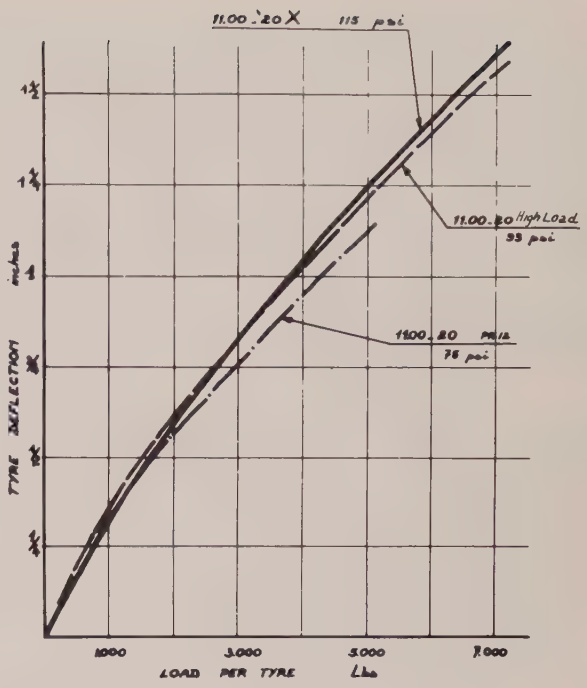

Fig. 18 — Comparative working deflections

purchase of all those imported constituants necessary for tire manufacture. For example, a 5-ton truck could be equipped with either conventional 9.00 - 20 tires or 8.25 - 20 "X". The table in Fig. 16 shows a comparison of the weights of the various constituents necessary for those two tires. However, we have shown a mere 35% increase in mileage for the "X" tire, whereas users' experience has shown that the increase may vary 35-90%.

In my country, foreign currency must be used to buy rubber, carbon black, and the materials needed for making rayon. It is evident, from the figures quoted for our 5-ton truck, that the performance of the conventional textile tires requires 67% more foreign currency than does the "X"; in other words, for the same expenditure of foreign currency the conventional textile tire only gives 60% of the mileage of the "X".

Recent tests made in various countries -- and which have been very actively pursued in the United States (I am thinking of your WASHO Road Test and of AASHO) -- have revealed the concern of governments on the subject of road development and more particularly the "preventive protection" of roads. There again, the "X" tire scores and we have not yet seen the full extent to which it may benefit road systems. The problem of roads and the factors involved in their deterioration is very complex and still very much under discussion. I propose, therefore, for the sake of simplicity, to deal with only two aspects: namely deterioration in depth and wear of surfaces.

Deterioration in Depth - Among the several factors responsible, we are obliged to include the axle weights of the vehicles using the roads. One cannot prove that the destruc-

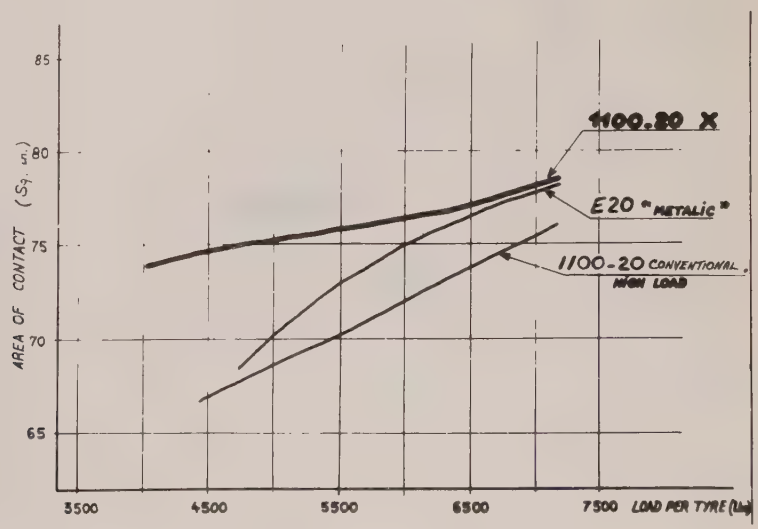

Fig. 19 — Comparative areas of road contact

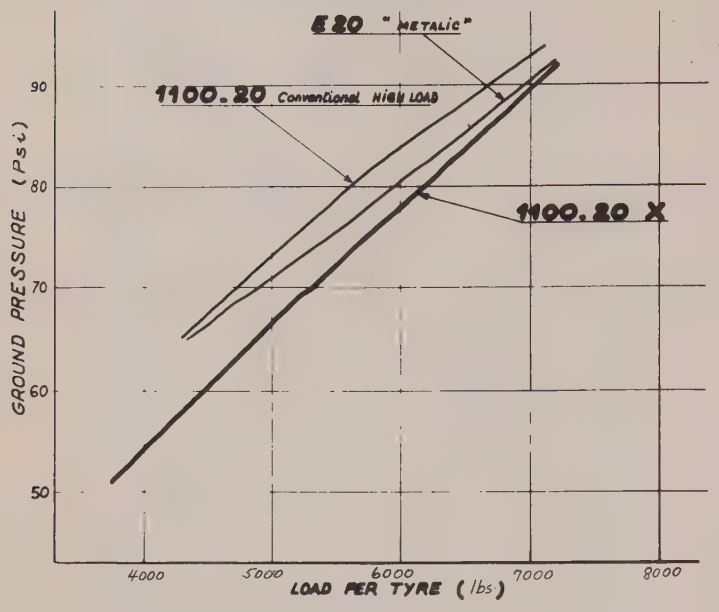

Fig. 20 — Comparative intensity of road surface loading

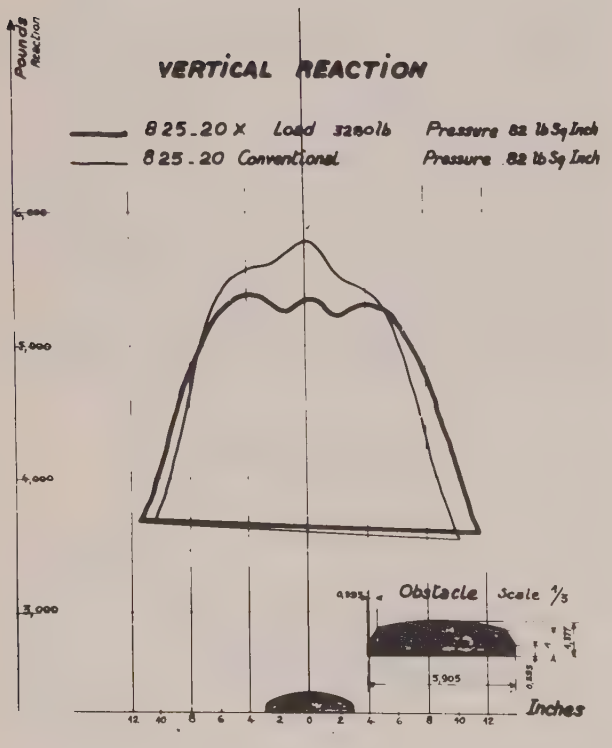

Fig. 21 — Comparative vertical reaction — "X" tire versus conventional

tive effect is directly proportional to the axle load or to some power of the axle load, but it is reasonable to admit that axle load and destructive effect vary in the same sense. Everyone agrees that it is a question of axle load and not of the total weight of the vehicle.

Has it occurred to many people, in the light of that postulate, that when it comes to distribution of gross vehicle weight, the arrangement made possible by designing for single tire equipment all round instead of duals rear (which gives a 50-50 distribution front and rear) is much to be preferred from the point of view of road deterioration in depth? With singles we have 50% front and 50% rear; with duals we have 33% front and 66% rear. For example, with 12 tons gvw, the maximum axle load with single tires is approximately 6 tons; the maximum axle load with twins rear is 8 tons.

The relatively small physical dimensions of "X" tires for a given load facilitates their use for such single tire equipments. In this matter of deterioration in depth, the dynamic behavior of the tire is equally important; the fact that the steel-cord "radial" tire can safely be used at a high working deflection results in smaller dynamic loads being exerted on the road surface.

In spite of higher inflation pressures, both "metallic" tires (with crisscrossed plies) and, in greater degree, "X" tires have larger working deflections than equivalent textile tires (Figs. 17 and 18). Further, a comparison of the areas of road contact of different types of tires carrying the same load also shows the "X" in a favorable light (Fig. 19).

It is seen that the intensity of road surfaces loading is lowest with the "X" and, therefore, the least harmful in

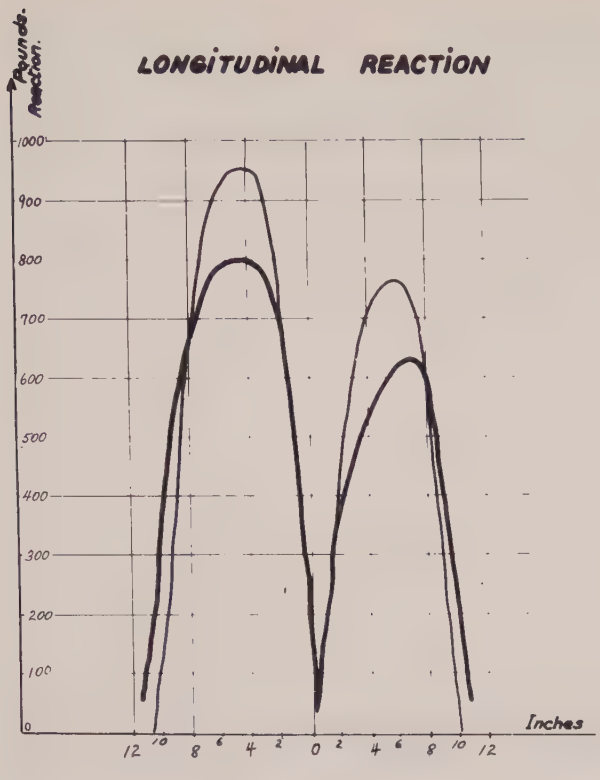

Fig. 22 — Comparative longitudinal reaction — "X" tire versus conventional

depth (Fig. 20). Included are some observed results of tests made when a tire was run over an obstacle; these tests were carried out because of the opinion expressed by some people that the stabilization of the "X" tire tread results in the tire striking any obstacle hard, thus tending, by reaction, to drive the obstacle into the road surface. Quite apart from the question of road preservation -- we can assume that the roads in question have good surfaces and no obstacles -- we can state categorically that the dynamic forces, both vertical and horizontal, engendered when a tire passes over an obstacle, are better "spread" and of lower intensity with "X" tires than they are with tires of other types (Figs. 21 and 22).

Deterioration of Surface - Among the factors revealed as being responsible for wear of road surfaces, speed and acceleration appear at the top of the list. This raises a point which we should pause to ponder: namely, if there is wear of one or the other of the two elements in contact (road surfaces and tire), there must be relative movement between them. Now, it would be extremely difficult to measure the amount of road surface wear, but it is an easy matter to measure the amount of tread rubber worn from tires. It seems reasonable to admit that if a certain type of tire, such as the "X", loses a less weight of tread rubber, of a given quality than do other types then, reciprocally, it must wear away less of the road surface.

Practical Application of High

Orville E. Cullen
Surface Combustion Division, Midland-Ross Corp.

THE PURPOSE of this paper is to explore the possibilities of high-temperature carburizing as a practical process, and to present some of the interesting results obtained while evaluating these possibilities. High temperature carburizing is considered to be at 1800 F or above, as it is recognized that considerable gas carburizing is being done at temperatures from 1700 F to approximately 1775 F.

Historical

During the early history of the carburizing process, pack carburizing or carburizing in compounds was widely used. In more recent years, gas carburizing has become the more popular method.

When pack carburizing was almost a universal practice, it was generally followed by subcritical cooling and subsequent reheating for hardening. This was done for one or both of two reasons: (1) proper disposition of excess carbon in the case or refinement of grain structure which had become coarsened during carburizing treatment, (2) relative ease of cooling the material in the box rather than attempting to remove the parts from the box at high temperature with attendant disagreeable handling of hot carburizing compound.

In view of the usual need for one and possibly two reheating and quenching operations, there was some tendency to raise carburizing temperatures to as high as 1800 F. This higher temperature became an economic consideration in pack carburizing, primarily because of the exceedingly long time required for heating. The carburizing compound provided good insulation and greatly slowed down the rate of heating the parts. Results, generally, indicated that when temperatures were 1800 F or below, grain structure was satisfactory following a subsequent single reheat for hardening.

With the acceptance of gas carburizing, the need for heating the carburizing compound was eliminated and time required for carburizing was considerably reduced. The work was heated and carburized in open loads on trays or in baskets. The process began to receive more close attention, particularly with respect to temperature. It became a commonly accepted practice to carburize at temperatures seldom exceeding 1750 F and generally not exceeding 1700 F.

Many reasons can be given for adopting these maximum heating temperatures. Some of these reasons are still valid. Others are a continuation of practices which were set up, due to limitations of the equipment or the processed work, to successfully and economically withstand carburizing temperatures above 1700 or 1750 F. Suitable heat-resisting materials were lacking for furnace construction. Carbon concentration control was difficult to attain. Distortion resulted from non-uniform heating or improper design of work

Temperature Gas Carburizing

supports.

Rates of Carburizing

Raising temperatures of gas carburizing materially increases the rate of carbon penetration of diffusion into the steel. In Fig. 1, the curves show theoretical total case depths to original carbon for various holding times at temperatures of 1700, 1850, and 2000 F. These curves illustrate the greatly accelerated rates of carbon diffusion that can be expected as the work temperature is progressively increased into the range now being considered for high-temperature carburizing. These increased rates are potential process timesavers.

Fig. 2 illustrates a very practical chart for establishing carburizing time at any selected higher temperature using the known time at 1700 F for a base figure. The apparent advantage is a substantial time saving. However, the actual time at carburizing temperature is only one of several factors affecting the overall evaluation of the gas carburizing process from a practical and economical standpoint.

Carbon Control

The iron-carbon equilibrium diagram and the associated equilibrium diagrams for the many carburizing grades of alloy steels tell us that increasing temperatures, in addition

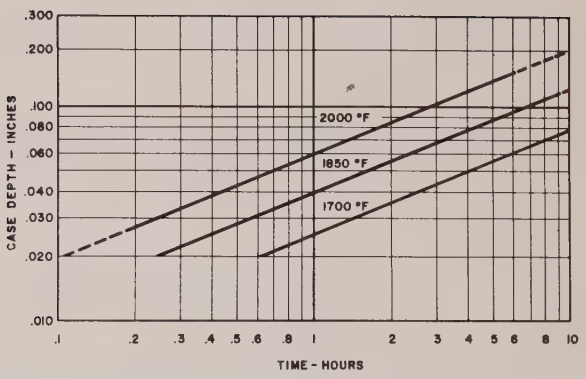

Fig. 1—Theoretical case depth versus time (total case depth — time at temperature)

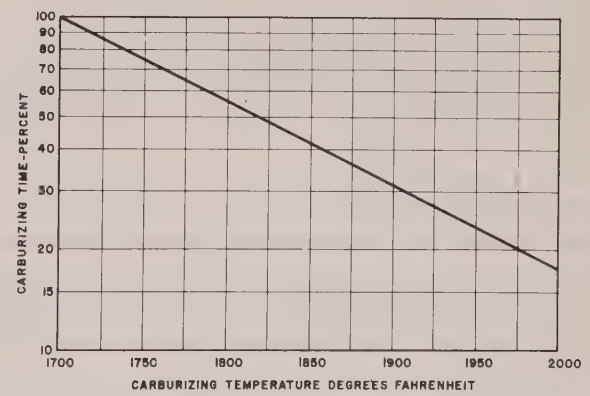

Fig. 2—Comparison of carburizing time versus temperature (base time at 1700 F = 100%)

to increasing the rate of diffusion of carbon in steel, also noticeably increase the amount of carbon which can be taken into solid solution while at carburizing temperature.

Fig. 3 shows the rather disturbing prospects of high temperature carburizing without too much carbon control. Three 1 in. diameter x 6 in. long SAE-4620 test bars were carburized at 1700, 1850, and 2000 F. Identical treating cycles were used consisting of 4 hr at carburizing temperature, plus 1-1/4 hr furnace-cooling to 1550 F and then aircooling to room temperature.

Fig. 4 shows photomicrographs of these test bars. Note the important considerations; (1) the grain size at each of the carburizing temperatures, and (2) the excess carbon in the high-temperature samples as evidenced by carbide precipitation within and around the grains.

The question of carbon control becomes one of the important considerations in high-temperature carburizing. While there may be some instances where surface carbon concentration and the accompanying type of carbon gradient through the case is not important, this certainly is not true for the vast majority of carburizing applications. Therefore, any consideration of the use of high temperatures must take into account the rather rigid specifications set up by most ultimate users of carburized work; namely, suitable depths and gradients and carefully controlled surface carbon contents in the range of 1% carbon, or under.

Fortunately, extensive work has been done during the past several years on the subject of carbon control in gas carburizing atmospheres. There are relatively few heat treating facilities today where carburizing is being carried on without some well-understood method for applying surface carbon control. The carburizing potential of furnace atmospheres is being controlled by measuring and adjusting water vapor content or dew point, carbon dioxide content or other well-publicized methods.

Most of these control methods were worked out in connection with the normal carburizing temperatures of 1700 F, or under. Naturally, some questions arise as to how successfully they may be applied when and if higher temperatures are utilized. Admittedly, there are unusual problems encountered in carbon control at higher temperatures. These problems are not insurmountable, however, and excellent results have been obtained in laboratory test work and in production facilities. There is no reason to believe that high-temperature carburizing cannot be made subject to the same limits of carbon control now specified at so-called "normal" carburizing temperatures.

As previously mentioned, there are several methods for maintaining the carbon potentials of furnace atmospheres at desired levels. For purposes of description, only one of these methods will be considered here: the use of dew point or water vapor content in the atmosphere gas as a determining factor.

Fig. 5 is a chart showing the theoretical amounts of water vapor required for carbon balance when using one type of

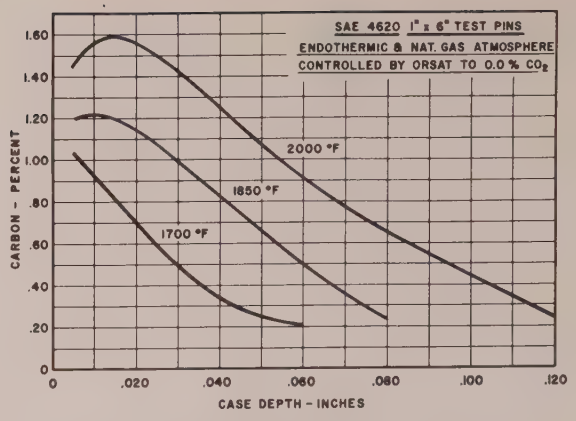

Fig. 3—Case depth versus carbon concentration

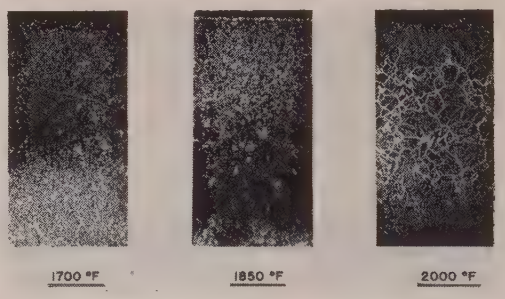

Fig. 4—Photomicrographs (originally magnified 100 times) carburized case of SAE 4620 steel 4 hr at indicated temperature

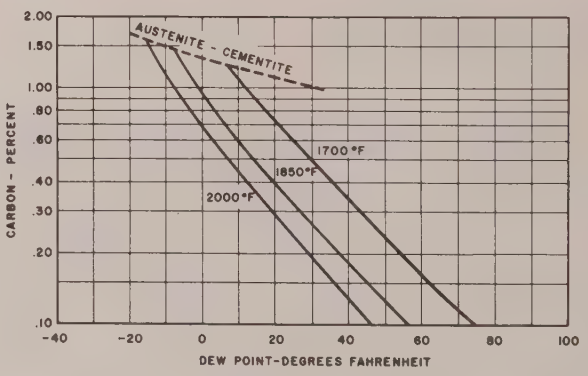

Fig. 5 — Equilibrium dew point versus % carbon in austenite endothermic base gas — 20% CO — 40% H_2 — 40% N_2

endothermic generator gas at temperatures of 1700, 1850, and 2000 F. The relationship between the dew point in the furnace atmosphere and the carbon content has been found in practice to be in quite close agreement with these equilibrium figures. The chart shows that the limits of control, as determined by variations in moisture content of the gases, become extremely narrow at 1850 F, and even more so at the higher temperatures. This same narrowing of limits of control is as much or more evident when other methods of carbon control are utilized. It becomes a matter, then, of greatest importance to carefully consider the severity of this

problem and to consider equally as carefully the selection of heating cycle and related process techniques in order to produce the desired end result.

Practical Application

How can we best recognize and utilize the techniques which are so pertinent to good results when high-temperature carburizing is used? One practical example might be cited. A heat treat specification was presented which called for carburizing SAE-1022 steel gears at 1850 F. The specification included holding the surface carbon concentration at 0.95 ±0.06% carbon and a total case depth of 0.075 in.

Fig. 6 shows a case depth - carbon concentration curve obtained from a test bar run through a furnace on a trayload of production test gears which were carburized to meet this specification. This curve illustrates that the problem of surface carbon control can be kept well in hand during high-temperature carburizing.

The type of carburized case represented by the curve is indicative of results obtained by using the "Carburize-Diffuse" technique. This is in keeping with the most acceptable method now used at 1700 F. The optimum depth relationships between hardenable case and total case must be maintained even though the ultimate maximum allowable carbon content of the case is well below the solubility limit. In order to do this, the furnace atmosphere must be held at high carburizing potential for a time, followed by control at a lower or diffusion potential to finally establish the specified surface carbon.

This particular test program specified lowering the temperature to 1650 F and equalizing, followed by aircooling to room temperature. The final heat treatment is induction hardening of the tooth areas. This specified treatment permitted taking advantage of rapid rates of carburizing at 1850 F in the high carbon potential atmosphere, followed by diffusion in an atmosphere of lower carbon potential during cooling to, and equalizing at, 1650 F. The time-temperature cycle is shown in Fig. 7. For an interesting comparison, the broken line curve in this figure shows the approximate time cycle required to diplicate the results at a maximum temperature of 1700 F.

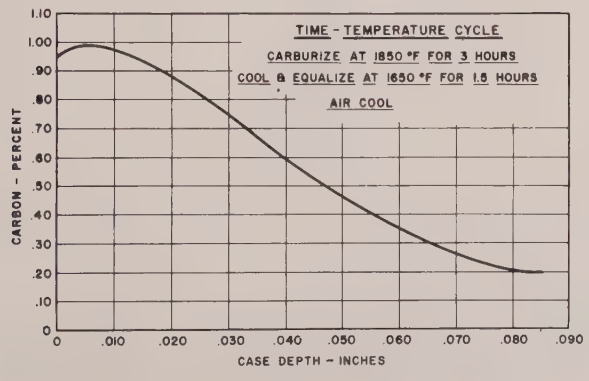

Fig. 6—Production carburizing test — 1850 F SAE 1022 gears

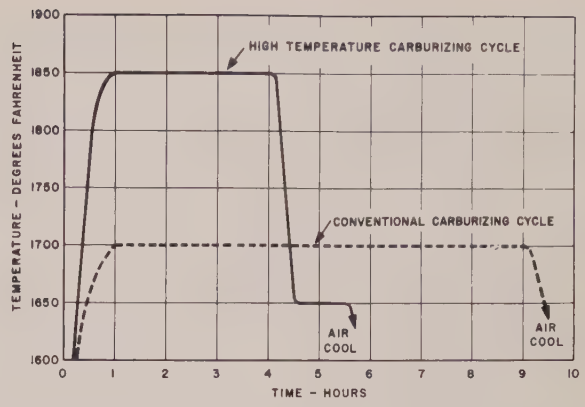

Fig. 7—Comparative time — temperature cycles for equivalent case depths

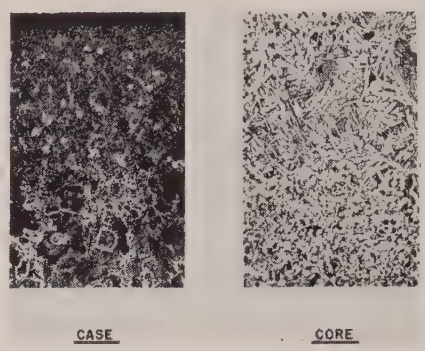

Fig. 8—Photomicrographs (originally magnifified 100 times) carburized case and core SAE 1022 steel gears (from 1850 F production test)

The photomicrographs in Fig. 8 show the case and core of the SAE-1022 steel following the carburizing and cooling cycle described above. The case and core of this material show mixed grain size with some duplexing. It was the opinion of processors of these gears that 3 hr carburizing at 1850 F exerted no unduly bad influence on the grain size of this material as compared with 1700 F carburizing.

In subsequent production load tests, SAE-1024 and SAE-1024, modified steel, gears were carburized to the same specifications with similar results. After hardening, all these gears successfully passed the physical and mechanical tests regularly applied after 1700 F carburizing and surface hardening.

Present Status of High-Temperature Carburizing

Carburizing at 1850 F has not been adopted as a result of these tests. The production tests which have been described refer to only a relatively small percentage of the total carburizing production. A variety of different steels must be carburized and tested including SAE-4027, 4620, 4815, 5120, and 8620 grades. Case depth specifications run from about

Table 1 - Production Capacities for Various Case Depths

Production Problem No. 1 - 0.100 in. Total Case Depth

	Carburizing Temperature (Time in Hr)		
Cycle	1700 F	1800 F	1850 F
Heat	3.00	3.25	3.50
Carburize	16.00	8.00	5.75
Cool to 1550 F	1.50	2.00	2.25
Total Hr	20.50	13.25	11.50
Time % vs Time at 1700 F, %	100	65	56
Net Load (100% at 1700 F), %	100	85	70
Net Efficiency, %	100	130	125

Production Problem No. 2 - 0.075 in. Total Case Depth

	Carburizing Temperature (Time in Hr)		
Cycle	1700 F	1800 F	1850 F
Heat	3.00	3.25	3.50
Carburize	9.00	4.00	2.90
Cool to 1550 F	1.50	2.00	2.25
Total Hr	13.50	9.25	8.65
Time % vs Time at 1700 F, %	100	68	64
Net Load (100% at 1700 F), %	100	85	70
Net Efficiency, %	100	125	110

Production Problem No. 3 - 0.045 in. Total Case Depth

	Carburizing Temperature (Time in Hr)		
Cycle	1700 F	1800 F	1850 F
Heat	3.00	3.25	3.50
Carburize	3.25	1.20	.60
Cool to 1550 F	1.50	2.00	2.25
Total Hr	7.75	6.45	6.35
Time % vs Time at 1700 F , %	100	83	82
Net Load (100% at 1700 F), %	100	85	70
Net Efficiency, %	100	102	86

0.045 in. to about 0.100 in., read to original carbon. Some of these carburized parts are aircooled and reheated. Others are direct quenched after lowering the temperature of the work to 1550 F. These latter are of special interest from the standpoint of any metallurgical problems related to processing time at high temperature.

This continuing program is similar to problems being carried on by several other companies and is clear evidence of the interest in the potentialities of high temperature carburizing. Also, it is evidence of the commendable caution

and soundness of approach with which we in this country appraise process changes when quality or economies of production may be affected.

At some point, and preferably early in this investigation, the economics of the process must be determined. To demonstrate the need for this information, we must first assume that the product quality has been proven to be satisfactory at the temperatures used. Furthermore, we must assume that suitable heat treating equipment is available. We believe this latter can be accepted as fact for any temperature likely to be used.

These items relate directly to ultimate decisions:

1. Temperature for carburizing.
2. Case depth.
3. Heating and cooling time.
4. Net to gross furnace load.

Temperature and case depth will fix the time for carburizing and this time will decrease as higher temperatures are used. Heating and cooling time will depend upon the geometry of the work and character of the load. Also it will change with the temperature of carburizing used. The net to gross furnace load will generally decrease with increased temperatures due to additional fixturing of the work and lighter loading because of natural decrease in strength of trays and fixtures.

Table 1 illustrates typical comparative data relating to estimated production capacities for identically sized furnaces when operated at temperatures of 1700, 1800, and 1850 F, with carburizing cycles established to produce 0.100, 0.075, and 0.045 in. total case depth.

A complete cycle analysis of this type, based on well-grounded experience or actual experimentation, should always be a preliminary step in a projected program for production carburizing at high temperatures. It brings the tempting advantages of phenominal carburizing rates into their true perspective in the overall picture.

It will be appreciated that the time values at carburizing temperatures are fixed, but heating and cooling times will change to fit particular conditions. Also net load percentages will vary somewhat depending upon the geometry of the work, its loading characteristics and the heat treating facilities considered for the job.

The above study was chosen for presentation because it represents a reasonably average picture of a number of studies carried on by different investigators. It appears to confirm the majority of opinions regarding the present practical potentials of high temperature production carburizing:

1. An operating temperature of about 1800 F usually results in optimum efficiency from the production standpoint.
2. A minimum total case depth of about 0.075 in. is required to show worthwhile economic advantages over 1700 F carburizing.

Vehicle Steering Fundamentals

William H. Baier
Armour Research Foundation

THE BEHAVIOR of the wheeled vehicle in response to steering is influenced by many factors. It is the purpose of this paper to summarize these factors and to point out the part that each plays in determining the lateral motion of the vehicle as it travels along a curved path.

Steering angles determined in accordance with the Ackermann theory of divided axle steering must be modified to account for the effects of tire slip angle. Tire slip angle, with its accompanying self-aligning torque, is modified by braking and traction effects, tire construction, and camber effects.

In addition to tire forces, the vehicle is subject to aerodynamic and inertial forces. Load transfer, arising from vehicle roll, gives rise to changes in tire cornering power by causing both camber changes and variations in tire loading. The effects of aerodynamic forces are strongly influenced by vehicle static margin and the position of the neutral steer line. Wheel alignment, and rear end roll steer effects also affect vehicle behaviour.

The effect of these forces and torques upon the basic Ackermann response is discussed in this paper. Also included are discussions of various steering gear mechanisms such as the worm and sector, worm and roller, and worm and nut, the effect of steering errors introduced by incorrect steering geometry, and the characteristics of steering phenomenon such as low and high speed wobble.

The highlights of linear system theory, borrowed from the aeronautical field, are summarized briefly at the close of the paper.

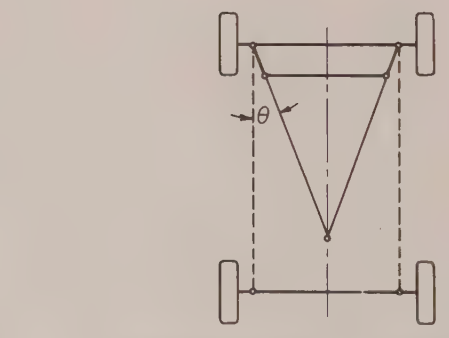

(a) ACKERMANN-JEANTAUD STEERING LINKAGE

(b) STEERING ANGLES IN ACKERMANN STEERING

Fig. 1 — Ackerman Steering relations

Ackermann Steering

The divided axle steering system used in motor vehicles was invented in 1817 by Lankensperger, a Munich carriage builder. This steering system has come to be known as the Ackermann steering system in English speaking countries. Charles Jeantaud, a French carriage builder, refined this mechanism in 1878, by noting that the axis of the wheels must meet at a common point if the vehicle is to turn a corner without slipping.

Correct Ackermann steering during a turn requires that each wheel turn about a point which is located on a extension of the rear axle center line (see Fig. 1b). Accordingly, the relation between the front wheel steering angles, α for the inner wheel, and β for the outer wheel, is

$$\cot\beta - \cot\alpha = \frac{w}{l} \qquad (1)$$

where w is the distance between the vehicle steering pivots and l the wheel base.

It is common to designate the radius of curvature about which the vehicle turns merely as,

$$R = \frac{l}{\sin\delta} \approx \frac{l}{\delta} \qquad (2)$$

Accordingly,

$$\delta = \frac{l}{R} \qquad (3)$$

is the so-called Ackermann steering angle, utilized in analyses of the vehicle lateral stability.

If the values of β, produced by the steering linkage for a given value of α, are compared to the theoretical Ackermann values it will be seen that they agree in the straight ahead position and at one other value of α. For small angles the angle of the outer wheel produced by the steering linkage is somewhat too large, while at larger angles this angle is too small.

Steering Gears

For control of the vehicle, it is necessary to convert the rotational motion of the steering wheel to the linear motions of the steering linkage which in turn moves the front wheels. This conversion is carried out by the steering gear which is ordinarily fixed to the bottom of the steering column.

The steering gear (Fig. 2), has two main functions. It converts rotary motion of the steering wheel into linear motion of the steering linkage and it also serves as a reduction gear between steering wheel motion and the front wheels. Typical gear ratios are 14/1 or higher and the total motion

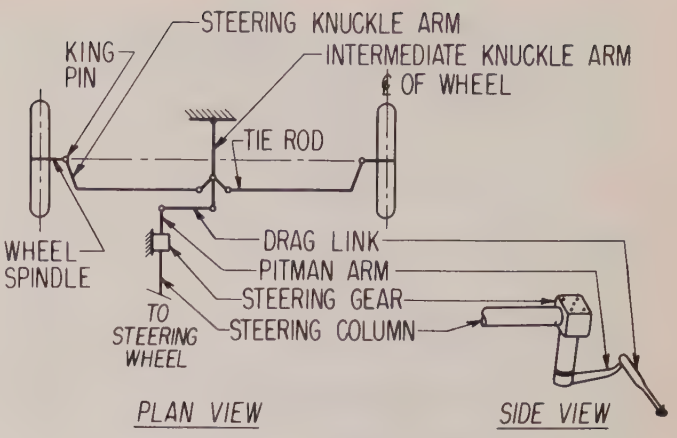

Fig. 2 — Steering linkage with intermediate knuckle arm

of the front wheels is about 80 deg, for a light passenger car.

A number of types of steering gears have been or are being built. Early designs included worm and gear, worm and sector, and worm and nut types. Skew and bevel gears have also been used.

Present steering systems, which are evolved from these basic designs include; cam and roller, cam and lever, and worm and nut types. The first two of these are derived from the worm and sector types. In the place of the worm sector, the cam and roller type employs a roller attached to the pitman arm shaft, while the cam and lever type utilizes a follower in the place of the sector gear.

Another design, used abroad, consists of a rack and pinion mechanism. Here, rotational motion of the steering wheel is converted to linear motion by the meshing of a pinion on the steering column with a rack which slides transversely across the vehicle.

Wheel Alignment

Wheel alignment is the process of keeping all the interrelated parts of the unsprung mass properly adjusted. Five factors, described below, must be properly chosen to obtain proper wheel alignment (see Fig. 3).

Toe-Out - Toe-out describes the process by which the proper Ackermann effect is obtained. An examination of an Ackermann diagram (Fig. 1b) shows that the steering arms in the typical 4-bar linkage arrangement do not travel over equal arcs. The inner wheel travels through a greater arc than does the outer wheel to permit it to travel about a smaller radius. The difference in steering angles between the two wheels is termed the toe-out. It is usually specified as the number of degrees over 20 which the inner wheel is turned when the outer wheel turns 20 deg.

Caster - Caster is the angle, measured in degrees, that the steering knuckle pivots are tilted forward or backward from the vertical, when viewed from the side. Caster is designated positive for a backward tilt. Caster tends to keep

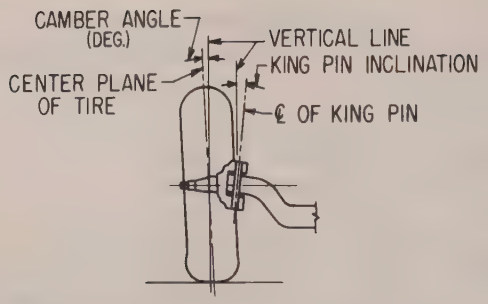

(a) CAMBER AND KING PIN INCLINATION

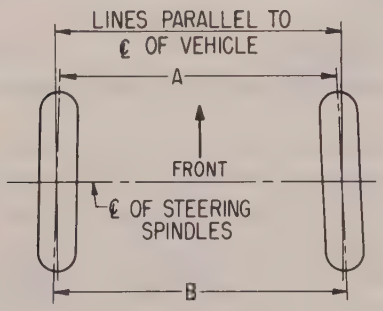

TOE-IN = B-A (INCHES)

(b) TOE-IN

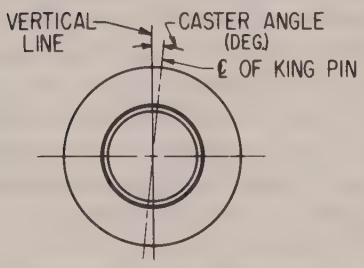

(c) CAMBER (SHOWN POSITIVE)

Fig. 3 — Factors in wheel alignment

front wheels pointed straight ahead because as the castered wheel is turned from the straight ahead it raises the front end of the vehicle slightly. When the steering wheel is released, the weight of the vehicle tends to force the wheels to the center position.

Camber - Wheel camber is the angle between the center plane of the wheel and the vertical when viewed from the front of the vehicle. Camber is considered positive when the top of the wheel leans outward. In recent years, the use of flat roads and low pressure tires has led to a reduction in camber to about 1 deg. Under ideal conditions, zero camber would result in no wheel slippage, but, because of bearing clearances and axle deflection, a slight amount of camber must be provided.

Kingpin Inclination - Kingpin or pivot inclination is the number of degrees that the steering knuckle pivots are tilted inward toward the center of the vehicle. This inclination results in a self-aligning torque as the steering wheel is turned, because a rotation of the wheel raises the vehicle slightly

Pivot inclination is generally in the range of 3 to 7 deg.

Toe-In - Toe-in is the number of inches that the wheels point in when viewed in plan. For a flat road, a zero toe-in should be maintained (14).* However, it is difficult to maintain such a condition.

Steering Geometry Errors

The path followed by the front wheels is influenced by many factors, some of which require that the theoretical Ackermann steering geometry be compromised. If the path of the wheel hub, that is, the suspension geometry, does not agree with the steering geometry, the front wheels will turn as they are deflected upwards. Road shock, felt at the steering wheel, is, in most cases, not the reflected direct shock which arises as a bump is traversed, but is, instead, the inertia (and gyroscopic) force of the wheel resulting when compromise between steering and suspension geometries attempts to change the plane of rotation of the wheel. Direct inertia and gyroscopic torques can also arise from the compromise suspension constraint of the wheel hub which results in a change in the plane of rotation during wheel motions.

In a wishbone or linked type front suspension employing equal parallel links, wheel motion is vertical for no roll of the sprung mass, hence gyroscopic torque is eliminated. The path of any point on the kingpin of such a system is an arc whose radius is equal to the length of the links. Because of conflicting space requirements, it is not always possible to obtain the theoretical steering geometry, and compromises must be made.

The most popular form of independent front suspension employs an unequal length for upper and lower links. For the case in which these links are originally parallel, the theoretically correct length for the steering connection may be

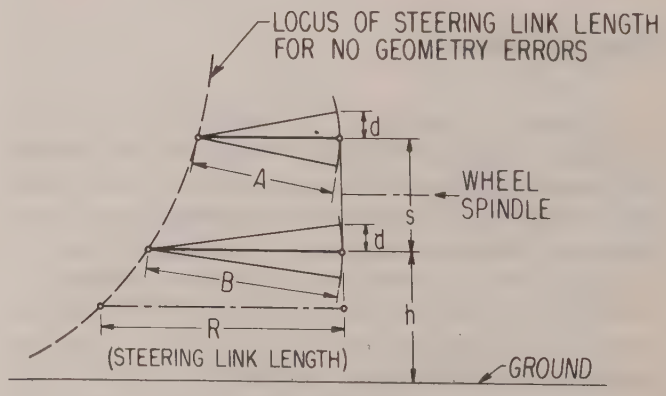

Fig. 4 — Steering link geometry

*Numbers in parentheses indicate References at the end of the paper.

established with the aid of Fig. 4.

In this figure, the horizontal displacement, of the upper and lower links for a vertical displacement d. can be shown to be $d^2/2A$ and $d^2/2B$. To avoid scrubbing of the tire on the ground, the point of tire contact should have no horizontal motion. Because the wheel is a rigid body, the horizontal deflection of a point on the wheel must be proportional to its distance above the ground.

If a steering link of length R, is at a height y above the ground (or point of zero lateral motion), the relation connecting R and y is

$$Ry = A(h+s)$$

which is rectangular hyperbola tangent to the values y=o, and R=o.

With the introduction of independent front suspension the engine was at first pushed forward. If the steering connection was kept below tht engine it had to be fairly long as was shown in the preceeding paragraph. With these long steering arms it was often possible to use only a two-piece cross steering tube without incurring too serious geometry errors. The central bell crank lever which acted as the inboard connection to the two sides of the steering arm was, in this case, not too far from the theoretical geometry.

The next step in moving the engine forward required that the steering arm be placed forward of the wheel centers. For safety reasons and because of easier Ackermann positioning, the steering arms were also raised above the wheel centers.

Because of the clearance gained between the wheel and the steering pivot axis (the steering pivot slants in at the top), the ball joint between steering knuckle and steering arm could be located farther outboard. This is an advantage because it permits a reasonable angle between the steering pivot arm and steering arm at full lock angle α , (Fig. 5), a factor which aids in the return of the wheel to the center position. Because of the high steering arm location, the steering arm radius must be short, hence a three piece steering arm or cross tube is required. This three piece gear can be furnished by using two idler levers mounted on the frame and using a cross tube to link the inboard ends of the steering arm by a cross tube.

Steering Wheel Reaction

Reactions at the steering wheel result directly or indirectly from road irregularities. If the suspension geometry is such that the plane of rotation of the front wheel changes during rebound, gyroscopic moments about the steering pivot axis will result, which may be felt at the steering wheel.

For the solid axle, the maximum torque occurs at near zero spring deflection because at this point rotation of axle center line about its midpoint is most rapid. For the parallel link system, maximum torque occurs towards, but not at, the end of deflection, because, up to a point, wheel tilt rate

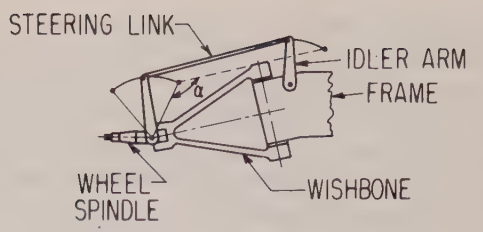

Fig. 5 — Plan view showing steering arm above wheel centers

increases with increasing spring deflection. Gyroscopic torque for such a system is zero at the nondeflected case because at this point the wheel does not tilt for an infinitesimal spring deflection.

Steering Phenomenon

Low Speed Wobble - The rotation of the front wheels of the vehicle about the kingpin axis against the flexibility of the steering linkage is termed low speed wobble. It has been found to depend on the caster angle of the front wheels, the weight on the front wheels, flexibility of the frame, and on the vehicle velocity. The resulting vibratory motion is transmitted to the steering wheel.

The following conclusions regarding low speed wobble have been established:

1. Wobble increases with increasing caster because of the greater pneumatic trail.
2. Wobble is unstable unless damped.
3. A critical velocity exists, but in practice this is not sharply defined.

In practice, it has been found that wobble decreases under wet conditions because of the reduced frictional forces which result in lower tire self-aligning torques.

Among the ways suggested to overcome low speed wobble are (15):

1. Make engine and mount system natural frequency coincident with wobble natural frequency.
2. Increase stiffness of steering linkage. In one case an increase from 720 lb/deg to 1100 lb/deg resulted in almost complete elimination.
3. Include sufficient damping to prevent an increase in magnitude of oscillation.

Because of the variation in caster angle with suspension deflection, the self-aligning torque of the tires will vary. If, in an effort to reduce wobble, caster is reduced to a small value at some conditions of suspension deflection, caster centering action may be nearly absent. The final design to reduce wobble must consider all of the factors mentioned so as to avoid a steering system which is either too heavy or too sensitive.

High Speed Wobble - High speed wobble is usually encountered in vehicles having a solid front axle. It is a rocking of the front axle about a horizontal axis near its center. It is influenced by the tire and suspension springs,

mass of the front axle, the gyroscopic torque of the front wheels, and velocity of the vehicle.

The frequency of this oscillation is increased by employing stiffer springs, higher tires pressures, and stiffening the frame. Its magnitude is reduced when caster is reduced, roll center is reduced, and it is increased when braking occurs. Damping is employed between frame and axle near the wheels to reduce oscillations.

Tire Effects on Steering

When the center plane of a pneumatic tire is directed at an angle to its direction of motion, the lateral distortion of the tread in contact with the road produces a force at right angles to this center plane (Fig. 6.) This force is called the cornering force and the angle between the direction of motion and the axis of the tire is called the slip angle. As shown in Fig. 6, the lateral distortion of the center line of the tire increases with distance along the tire center line starting at the front of the contact patch.

Because the lateral forces in the rearward portion of the contact patch are generally greater than those in the forward portion, the line of action of the cornering force generally intersects the wheel center plane at a point behind a point immediately below the center of the wheel. The moment of the line of action about a vertical line through the center of the contact patch is called the self-aligning torque because it generally tends to lessen the slip angle.

The tire cornering force is the only force acting on a car which enables it to turn a corner or resist a side wind. Self-aligning torque provides a measure of the force required to steer the car, that is, it gives measure of the "feel" at the steering wheel.

Means by which Cornering Force is Developed

The cornering properties of tires have been examined by a number of investigators (1, 5). The detailed study of the development of cornering force requires an analysis of tire-to-ground contact. Fig. 6 (from Ref. 1) shows the lateral distortion of the tire tread as a function of longitudinal distance along the contact length. Distortion of the tire is the displacement from the center plane of the wheel. This distortion gives an accurate picture of the lateral force developed because under slip angle conditions, motions at the crown and at the shoulder ribs of the tire are approximately equal. These data are replotted for both a 3 and an 8 deg slip angle (Fig. 7) where lateral force as a function of distance along contact length is shown.

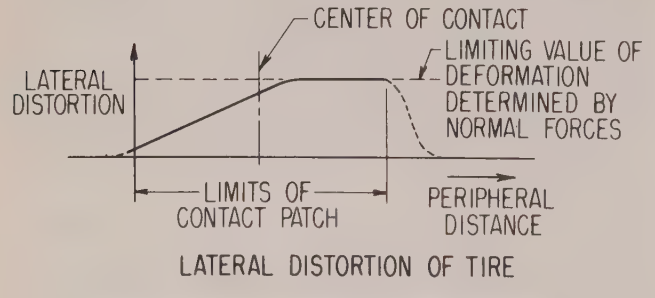

Fig. 6 — Tire characteristics during cornering

The resultant cornering force is proportional to the total area under the curve of Fig. 7. The resultant cornering force is seen to act at a point which is behind the midpoint of the contact area. The distance between the center of contact and the intersection of the line of action of the resultant with the wheel center plane is termed the pneumatic trail or caster. As is evident from Fig. 7, it is large at low slip angles and decreases with increasing slip angle and cornering forces.

The reason for the variation in cornering force and self-aligning force may be examined by considering the curves for Fig. 6. If it is assumed that a limiting value of lateral friction force exists which is determined by the contact pressure and friction coefficient, an upper limit on the lateral force per unit length of contact length is established, as shown in Fig. 6. Lateral distortion of a point on the tire tread increases as it moves along the length of the contact path. The sideways force exerts it on the ground and tire increase with its distortion. When this force reaches the limiting friction value, defined above, it remains at that value for the remainder of its motion along the contact length. It will be noted that the limiting frictional value drops as the end of the contact patch approaches, because the tire is separating from the ground and its contact pressure is decreasing.

At low slip angles, the lateral displacement is such that the limiting frictional value is not attained until very late in the contact patch. Accordingly, the total cornering force remains low and the pneumatic trail is large. For high slip angles, the lateral displacement corresponding to the limiting frictional value is attained at an earlier point in the contact patch. The total cornering force is, therefore, high and because high values of lateral force are developed ahead of the center point of the contact patch, the pneumatic trail is decreased.

The resultant of the horizontal forces in the ground plane has a line of action to the rear of the midpoint of the contact point by a distance equal to the pneumatic trail. Its direction is mainly lateral, however a slight backward com-

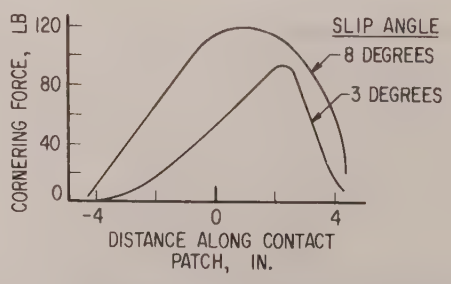

Fig. 7 — Cornering force as a function of distance along contact patch

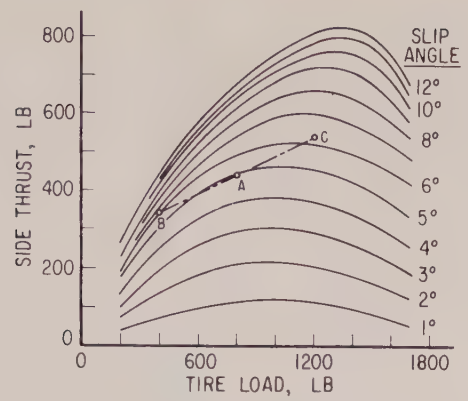

Fig. 8 — Side thrust versus load 6.00 x 16 tires at 28 lb/in²

ponent is present. This small backward component arises from tire rolling resistance or drag while the lateral component arises from cornering forces. The backward component is the same in magnitude as that developed in a freely rolling tire.

The variation of cornering force, self-aligning torque and horsepower consumption with slip angle and load has been investigated (5). Fig. 8 shows the variation of cornering force with tire loading for different slip angles. Cornering force for a given tire load increases with slip angle as described previously. Cornering force for given slip angle increases with tire loading until a maximum cornering force is developed. For further tire loading, cornering force decreases, as the frictional force in the contact patch changes from a static to slipping type.

Self-aligning torque, at constant slip angle, increases with tire loading. At constant load, self-aligning torque increases with slip angle up to a slip angle of 6 deg; above this value, self-aligning torque decreases. This angle of peak torque results as follows. At low slip angles, the line of action of the cornering forces lies near the rear of the contact patch. With increasing slip angle the resultant moves forward as discussed previously. Coincidently, the maximum cornering force developed approaches the limiting frictional value. Maximum self-aligning torque occurs at that slip angle at which the product of the magnitude of the resultant cornering force and its lever arm about the center point of the contact patch is a maximum.

The effects of inflation pressure on the three tire characteristics are shown in Ref. (1). Cornering force was shown to vary linearly with inflation pressure for constant slip angle. This results because the lateral force required to distort the tire to a given slip angle is greater for tire having a greater inflation pressure.

Self-aligning torque decreases with inflation pressure. This results because the greater forces required to distort the tires laterally, for a given slip angle, cause the cornering force to attain the limiting frictional force near the front of the contact patch.

Internal Factors - The effects of tire construction and configuration on tire cornering force, self-aligning torque, and horsepower consumption were studied in Ref. (1). The effect of increasing the rim width is to increase cornering force, to have very little (slightly decreasing) effect on self-aligning torque when the tire is run at a constant slip angle. The increased cornering force results from an increased resistance to tread distortion.

Self-aligning torques decrease slightly because at higher cornering forces more of the contact patch must generate forces at the limiting frictional values. Since this can occur only in the forward part of patch, the line of action of the resultant cornering force moves forward.

The effect of tire section width on the tire characteristics is as follows. An increase in section width results in an increase in cornering force and self-aligning torque, when measured at the same value of slip angle. These effects result because a greater value of limiting friction force can be developed by the tire as a result of its increased contact area. Even if the resultant of the total cornering force remains at the same distance behind the center of the contact patch, the higher magnitude of the resultant cornering force will result in an increased self-aligning torque.

The effect of an increase in number of plies on cornering force is negligible. The self-aligning torque at a given slip angle is less for a 6-ply tire than for a 4-ply tire. The decrease in self-aligning torque with increasing number of plies may be explained by the same mechanism resulting from an increase in rim width.

Rear End Steering Effects

The lateral behaviour of a vehicle is influenced by guidance from the rear wheels as well as that from the front wheels. Rear wheel steering, controlled by the driver, has been employed sparingly because it has been found unstable. Only at low speeds has it been found safe.

When a conventional vehicle carries a heavy load behind the rear axle, a similar effect can occur. Turning the front wheels can result in a yawing motion about a point behind the rear axle in which the rear wheels move toward the center of curvature of the path the vehicle is starting to follow. As the vehicle begins to move along the curved path, the direction of lateral forces on the rear tires reverses.

Yawing of the conventionally steered vehicle is determined by the cornering forces of both the front and rear tires. Each pair of tires provides a lateral force to resist the side forces, which causes them to slip sideways. Even when the tire planes remain parallel to the longitudinal axis of the vehicle, the slip angles of the front and rear ends of the vehicle can be different. These differences give rise to the over or understeering condition.

The principal rear steering effect introduced by a conventional solid rear axle is that resulting when the center of the axle rotates slightly, in the horizontal plane, about a

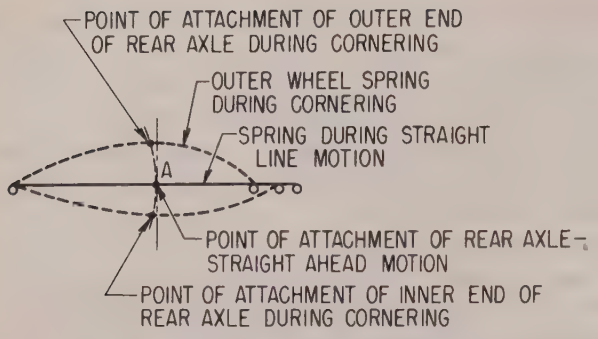
POINT OF ATTACHMENT OF OUTER END OF REAR AXLE DURING CORNERING
OUTER WHEEL SPRING DURING CORNERING
SPRING DURING STRAIGHT LINE MOTION
A
POINT OF ATTACHMENT OF REAR AXLE STRAIGHT AHEAD MOTION
POINT OF ATTACHMENT OF INNER END OF REAR AXLE DURING CORNERING

Fig. 9 — Roll steel effects in live rear axle resulting from spring deflections (asymmetrical spring eyes)

vertical axis through its midpoint. Such a rotation can result when the vehicle rolls, causing the rear suspension springs to deflect. If the point of attachment between axle and spring moves backward or forward as the vehicle rolls, the axle can rotate in the horizontal plane about its midpoint as shown in Fig. 9.

Roll Angles

The behaviour of a vehicle as it travels along a curved path is influenced by the changes in tire loadings which result from vehicle roll. In this section, the locations of the vehicle roll centers and their effect on tire loading is discussed.

The roll center of the spring mass in a given plane may be obtained as that point in the plane about which the sprung mass rotates. In general, the roll center height at either end of the vehicle is different, hence the line joining these points, ordinarily called the roll axis, is not horizontal.

Roll Center Location - The roll center location, M_o for a number of the more common front and rear suspension systems is shown in Figs. 10 and 11 (2).

Fig. 10a shows the roll center below ground level; however, by a proper choice of suspension geometry, this point may be raised. With horizontal parallel links, for example, the instantaneous center M lies at infinity and the line M-3-M_o is horizontal. Accordingly, the roll center is at the road surface.

Wheel motion in the Lancia sleeve mounting type suspension (Fig. 10b) is parallel to the axis of the sleeve. In the arrangement shown, the roll center lies below the road surface.

In the Porsche double crank suspension system (Fig. 10c) the wheel motion is vertical, hence the roll center lies at the road surface. In both of the above systems, the roll center is found by noting that wheel motion is perpendicular to the hypothetical link joining the roll center and the point of tire contact.

For the beam axle suspended by leaf springs (Fig. 11c) the roll center is at approximately the height of the spring

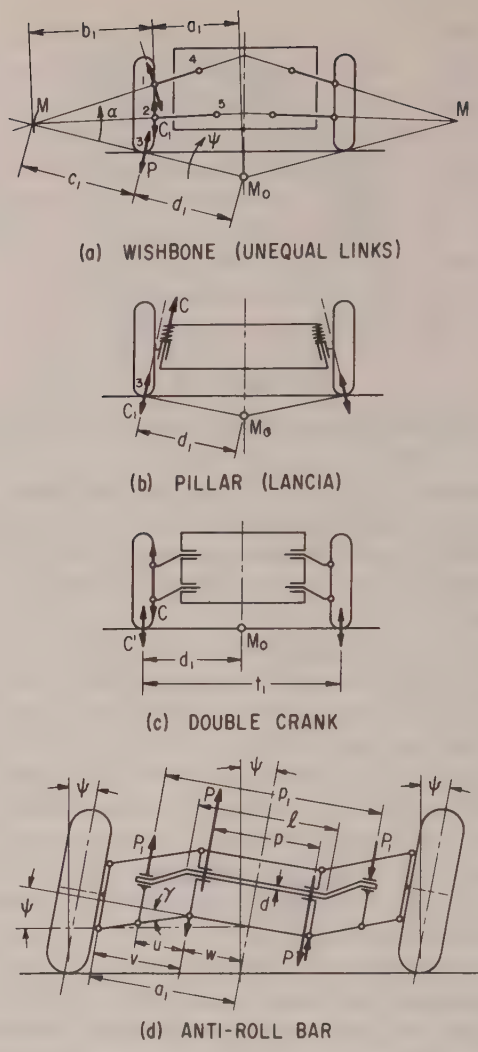

Fig. 10 — Roll centers and restoring moments for front suspensions and anti-roll bars

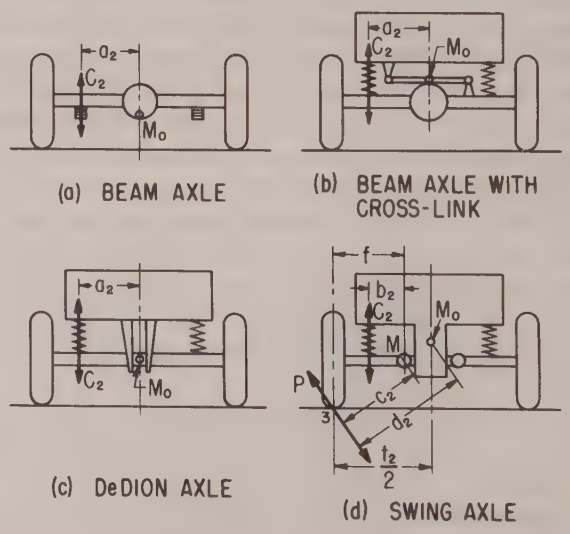

Fig. 11 — Roll centers and restoring moments for rear suspension systems

anchorages. This location is influenced by the lateral flexibility of the spring mounting.

When a cross link is used for lateral location of a beam axle (Fig. 11b) the roll center is at the point of attachment of the link to the spring mass.

For the DeDion rear axle, the roll center lies at the point of the axle about which the spring mass rotates (Fig. 11c).

For the swing axle, the roll center is located along a line joining the point of tire contact, point 3 of Fig. 11d and the swing axle joint, point M. The roll center M_o is, therefore, located above the swing axle center line when it is in the horizontal position.

Roll center height varies with spring deflection for suspensions employing links, the beam axle with lateral location link, and for the swing axle.

Restoring Roll Moments

With the roll center located, it is possible to determine the value of the restoring moment exerted by the suspension system as the vehicle rolls. Tabular values of the restoring moments introduced by the more common suspension systems are shown in Table 1.

It will be noted that in every case, the restoring couple is proportioned to the roll angle or

$$M = K\phi \tag{4}$$

where M is the restoring moment.

In some suspension systems, the effects of centrifugal force on the unspring mass causes it to exert a roll couple on the spring mass or to change the dynamic loading of the tires. These roll effects are summarized in Table 2.

It should be noted that because the roll center is above the wheel center for the swing axle, it exerts a righting moment on the sprung mass. The centrifugal moment exerted by the beam axle is not exerted on the sprung mass; however it does influence the dynamic wheel loads.

From Table 1, the suspension system restoring moments may be expressed as

$$M_{Si} = K_{Si}\,\phi \tag{5}$$

where i = 1 for the front suspension, i = 2 for the rear suspension system, and i = 3 for the anti-roll bar.

From Table 2, the unsprung mass roll moment may be expressed as

$$M_T = C_T\mu W_i = C_T\mu KW = K_T\mu W \tag{6}$$

where W_i is the weight of the unsprung mass under consideration.

The roll angle of the sprung mass for a given suspension system under the effects of a centrifugal cornering load, is

Table 1 - Restoring Roll Moments Introduced by Various Suspension Systems

System	Roll Moment 1/
Independent Linkage	$2\left(\frac{b_1 d_1}{c_1}\right)^2 C_1\,\phi$
Independent Linkage, (Parallel Horizontal)	$\frac{t_1^2}{2} C_1\,\phi$
Guided Sleeve: Double Crane	$2d_1^2 C\,\phi$
Swing Axle	$\frac{1}{2}\left(\frac{b_2 t_2}{f}\right)^2 C_2\,\phi$
Beam Axle	$2\,C_2\,a_2^2\,\phi$
Anti-Roll Bar: (Fig. 10d) Independent, Linkage	$\frac{a_1 p_1 u}{v} C_3\,\phi$
Beam Axle	$\frac{p_1^2}{2} C_3\,\phi$

1/ Nomenclature:
C_1, spring rate of lower suspension arm, lb/in. of motion of pt. 2
C, spring rate of suspension spring, lb/in. of motion of pt. 3
C_2, spring rate of suspension spring, lb/in. of motion of pt. 4
C_3, spring rate of anti-roll bar, lb/in.
ϕ roll angle of sprung mass, rad

therefore:

$$\phi = \frac{\mu W(K_C + K_T)}{K_{S1} + K_{S2} + K_{S3}} = \mu W K_R \tag{7}$$

Table 2 - Roll Moments of Unsprung Mass

System	Moment	Note
Independent	$\mu W_1 r$	Tilting
Swing Axle	$-\mu W_2(n - r)$	Restoring
Beam Axle	$\mu W_2 r$	Influences wheel loading only

where μW_i is the centrifugal force acting, r is the wheel radius and n the height of the roll axis.

where μWK_C is the centrifugal roll moment from the sprung mass.

The roll angle is therefore directly proportional to the centrifugal cornering load. It is assumed in this discussion that the tires and frame are rigid.

Dynamic Wheel Loads

Under the action of the roll moments introduced by centrifugal forces in cornering the loads imposed on the tires are changed. The outer tire is subjected to an incremental load, ΔF, (front wheel), or ΔR, (rear wheel) while the inner tire will be unloaded by an equal amount. To calculate these incremental loads it is first necessary to calculate the roll angle of the sprung mass as shown above.

Under steady-state cornering conditions, the change in tire loading caused by the roll moments acting is given by the following equations:

$$\text{Front wheels: } \Delta Fw = M_{S1} + M_{C1} + M_{S3} + M_{T1} \tag{8}$$

$$\text{Rear Wheels: } \Delta Rw = M_{S2} + M_{C2} + M_{S3} + M_{T2} \tag{9}$$

where: w is the vehicle track distance.

M_{S1}, M_{S2}, M_{S3} are the restoring motion of the front and rear suspensions, and the antiroll bar.

M_{T1}, M_{T2} are the tilting moments arising from centrifugal force on the front and rear unsprung mass.

M_{C1} is the roll moment upon the unsprung mass introduced by the centrifugal loading of the sprung mass acting at the front roll center (Fig. 12).

$$M_{C1} = \mu \frac{b}{c} m W \tag{10}$$

M_{C2} is the roll moment upon the unsprung mass introduced by the centrifugal loading of the sprung mass acting at the rear roll center.

$$M_{C2} = \mu \frac{a}{c} n W \tag{11}$$

The load transfer at the front wheels is therefore

$$\Delta F = \frac{1}{w} [K_{S1} \phi + \mu \frac{b}{c} mW + K_{S3} \phi + K_T \mu W] \tag{12}$$

$$= \frac{1}{w} [(K_{S1} + K_{S2}) \phi + \mu W (K_{L1})]$$

where:

$$K_{L1} = \mu \frac{b}{c} m + K_T \tag{13}$$

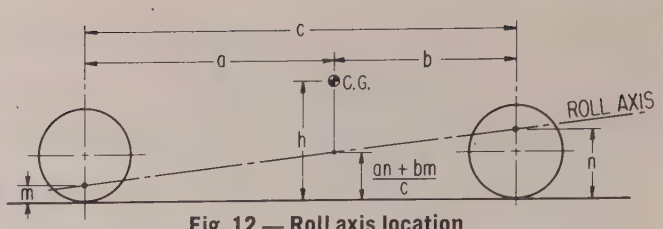

Fig. 12 — Roll axis location

The load transfer at the rear wheels is

$$\Delta R = \frac{1}{w} [K_{S2} \phi + \mu \frac{a}{c} n W + K_{S3} \phi + K_T \mu W] \tag{14}$$

$$= \frac{1}{w} [(K_{S2} + K_{S3}) \phi + \mu W K_{L2}]$$

where:

$$K_{L2} = (\mu \frac{a}{c} n + K_T) \tag{15}$$

With these equations, the load transfer for a given suspension system can be determined for a specified roll angle and centrifugal loading. In general, load transfer is found to be directly proportional to both roll angle and centrifugal loading and may be represented as

$$\Delta L = C_1 \phi + C_2 \mu W \tag{16}$$

where C_1 and C_2 are constants.

Roll Induced Load Transfer Effects on Tire Slip Angle

Tire lateral cornering force is a function of both tire slip angle and tire loading. Curves of cornering force as a function of tire loading for a number of slip angles are shown in Fig. 8 (9).

The relation which represents the cornering force, F as a function of slip angle θ, and tire load, W, may be written, in general as:

$$F = C_1\theta + C_2W + C_3\theta W + C_4\theta^2 + C_5W^2 + \text{---} \tag{17}$$

where the constants C_i are determined from experimental curves similar to those of Fig. 8.

In the load on the inner tire F_1 is equal to that on the outer tire F_2 and the law describing the cornering force is limited to second power terms and lower as in the previous equation, the slip angle θ_o, is given by

$$\theta_o = \frac{C_7 + (C_7^2 + 4C_4C_6)^{1/2}}{2C_4} \tag{18}$$

where

$$C_7 = C_1+C_3W \text{ and } C_6 = C_5W-C_2W+F \qquad (19)$$

The lateral load per tire is F which is equal to one half the cornering force required to balance centrifugal effects.

If load transfer of the amount $\Delta W=KW$ occurs, the tire loadings become

$$W_1 = (1 + K)W \text{ and } W_2 = (1 - K)W \qquad (20)$$

In this case the new slip angle is given by

$$\theta = \frac{C_7 + (C_7 + 4C_4 C_6)^{1/2}}{2C_4} \qquad (21)$$

where

$$C_6 = C_5(1+K^2)W - C_2 W+F \qquad (22)$$

It is seen that the slip angle under load transfer conditions is always greater than for the case in which the two tires are equally loaded. It is assumed in the determination of the slip angle, that both tires have the same slip angle.

Stability Margin

To provide a convenient process for the estimation of vehicle stability, the term, stability or static margin, has been introduced (3). Stability margin is defined as the horizontal distance, expressed as a percentage of the wheelbase length, between the center of gravity of the vehicle and the center of reaction of the road forces.

The center of reaction of the road forces passes through a line designated as the neutral steer line. This line is defined as a line in the fore and aft center plane of the vehicle anywhere along which a lateral force may be applied without producing yawing of the vehicle. It is assumed that the limit of adhesion of the tires is not exceeded.

Should the center of gravity of the vehicle be behind the neutral steer line, the vehicle would turn towards a lateral force applied at the center of gravity. Such a vehicle is considered to be unstable. In a stable vehicle, the neutral steer line is behind the center of gravity. This is the equivalent of understeer.

It is desirable that the passenger vehicle be stable for case of the fixed steering wheel, but, because of the self-aligning torque of the front tires, there is no need for an excessive stability margin. Excessive stability margins results in greater stabilizing motions which in turn slow vehicle response. (Ref. (3) recommends a maximum static margin of 4-6%.

Aerodynamic Effects

The aerodynamic forces acting upon a moving vehicle may be resolved into three components parallel to the longitudinal, lateral, and vertical axes of the vehicle. These forces are referred to as the resistance or drag force, the side force, and the lift force respectively. Aerodynamic forces are not of importance at lower speeds and can probably be neglected at speeds less than 50 mph.

These force's components do not act at the center of gravity of the car, hence they give rise to pitching, yawing, and rolling movements about this point. At higher speeds the lift and pitching moments generated may cause a weight transfer from front to rear wheels with a consequent change in the neutral steer line.

A significant point, however, is the location of the center of pressure defined above. For a long, streamlined body, this point lies somewhat in front of the nose of the vehicle. From the reference data on the streamlined body, this point is over 1.25 car lengths ahead of the vehicle at 2.5 deg and about 0.20 car lengths ahead at 20 deg. A very small side force acting on such a body would produce a significant yawing moment. This body represents an extreme case; however it does serve to point out the problems, introduced by aerodynamic side forces.

Fins

An automotive vehicle, in general, has a fineness ratio of less than 1/6. For a nonstreamlined vehicle it is expected that the center of pressure will be well within the wheelbase.

Ref. (3) shows that the side force for a practical streamlined vehicle is given by

$$S_b = (0.014 + 0.008 \frac{l}{d}) Aq\gamma \qquad (23)$$

where γ is the angle of attack in degrees, l is the length of vehicle and d its equivalent diameter, A its cross sectional area, and q the dynamic pressure; all units in feet and lbs.

To bring the center of pressure rearward, fine may be added to the rear of the vehicle, see Fig. 16. For such a fin, the side force generated is given by, ref. 3.

$$S_f = 0.045 A_f q \gamma \qquad (24)$$

where A_f is the fin area in ft^2

The total side force acting is therefore

$$S = S_b + S_f \qquad (25)$$

By suitable choice of fin area, the center of pressure of the vehicle-fin combination may be made to lie at any requisit point. Fin area is given by

$$S.x_{cp} = -S_b x_b + S_f x_f \tag{26}$$

and

$$S_f = \frac{Sx_{cp} + S_b x_b}{x_f} \tag{27}$$

where x_{cp}, x_b, and x_f are the distances between the front of the vehicle and the center of pressure, of the combination center of pressure of the vehicle, and of the fin, respectively.

Sudden Changes in Wind Intensity

In general, steady side winds should not greatly inconvenience the driver. However, the large responses which may occur as a result of sudden changes in wind forces may prove more difficult to control.

The behavior of a vehicle in the presence of a side wind force depends upon its aerodynamic configuration. In the case of the unstreamlined vehicle, the center of pressure is close to the center of gravity. In the case of the streamlined vehicle, the center of pressure is located near the front axle. For a streamlined and stabilized vehicle, the center of pressure can be located behind the center of gravity.

In the presence of a side wind force, the unstreamlined vehicle slips sideways away from the wind. The streamlined car, because the wind force acts almost at the front axle, develops a greater slip angle at the front than at the rear tires. Accordingly it begins to yaw at an increasing rate until the driver applies correction.

The stabilized streamlined vehicle slips sideways away from the wind. However, because the center of pressure is located behind the neutral steer line, the rear wheel slip angle is greater than the front wheel slip angle. As a result, the vehicle yaws so as to head into the wind and returns towards its original course. When the vehicle crosses its original course, the driver must apply correction.

In the ideal case, the vehicle is completely unresponsive to side wind forces. In an actual design, the vehicle should be proportioned to produce comparatively slow reactions to side forces. In this manner, the driver has time to make corrections. Ref. (3) shows that the center of pressure should be located between 2-10% of the wheelbase behind the neutral steer line to permit the vehicle to turn slowly into the wind.

Lateral Equations of Motion

In studying the lateral motion of the vehicle as it negotiates a turn, the influence of all of the effects described previously must be considered. These effects include: cornering forces and moments generated by the tires, aerodynamic forces and moments on the vehicle, rear and steering effects, change in tire rolling resistance due to roll, weight transfer effects due to roll, shock absorber forces, camber change effects and the momentum effects produced by the vehicle mass.

The lateral equation of motion can be written symbolically as:

$$\Sigma Y = Y_1 + Y_2 + Y_A \tag{28}$$

$$\Sigma N = aY_1 + T_1 + w\Delta L_1 - bY_2 + w\Delta L_2 + Y_A l + T_2 \tag{29}$$

$$\Sigma L = W_s\bar{y} + L_S + L_{SA} + Y_A h_A \tag{30}$$

where

Y_1, Y_2, Y_A are the front tire, rear tire, and aerodynamic forces,

T_1, T_2 are the front and rear self-aligning torques,

ΔL_1, and ΔL_2 are the front and rear load transfer effects,

l is the distance between cp and cg,

W_s the sprung weight,

$\bar{y}$ the distance (lateral) moved by W_s,

L_S the spring force,

L_{SA} the shock absorber force,

h_A the height of the cp.

Functionally this can be written as

$$\Sigma Y = f(\beta, r, \delta, \phi, \theta) \tag{31}$$

$$\Sigma N = f(\beta, r, \delta, p, \theta) \tag{32}$$

$$\Sigma L = f(p, \phi, \theta) \tag{33}$$

Linear Theory - In Ref. (10) the vehicle was treated as a linear system, that is, the functional relationship between the forces acting and the variables upon which they depend are assumed to be linear. For example, the relation between tire cornering force and slip angle, load, and camber was assumed to be:

$$Y_i = C_1\alpha_i + C_2 W + C_3\phi \tag{34}$$

$$= \frac{\partial Y}{\partial \alpha_i}\alpha_i + \frac{\partial Y}{\partial W} W + \frac{\partial Y}{\partial \phi}\phi \tag{35}$$

In the reference it was shown that such linearization accurately predicts vehicle behaviour under cornering conditions up to 0.3 g.

A detailed study of vehicle stability utilizing linear theory was carried out in Ref. (11). In this study, aerodynamic effects, load transfer, and roll motions were neglected. The equations of motion under such conditions are

Lateral motion -

$$M(\dot{v} + Vr) = \alpha_F C_F + \alpha_R C_R = Y_\beta \beta + Y_r r + Y_\delta \delta \tag{36}$$

Yaw motion -

$$I_Z\dot{r} = a\alpha_F C_F - b\alpha_R C_R = N_\beta\beta + N_r r + N_\delta\delta \quad (37)$$

where, for example, $Y_\beta = \partial Y/\partial\beta \ldots$ are called the stability derivatives, and C_F, C_R are the cornering stiffness of front and rear tires. The significance of the several stability derivatives is discussed below.

The side force arising from vehicle slip angle is dependent upon the stability derivative Y_β. If the vehicle performed a pure side slip motion β, the force on the vehicle would be $F = Y_\beta\beta$. Y_β may be thought of as a torsional spring constant of the vehicle because it produces a restoring moment proportional to an angular displacement.

The derivative, N_β, may be written as

$$N_\beta = \alpha C_F - b C_R$$

$$= -l(C_F+C_R)\left[\frac{C_R}{C_F+C_R} - \frac{\alpha}{l}\right] \quad (38)$$

However, $C_F+C_R = Y_\beta$ (39)

and from the definition of Static (Stability) Margin

$$\frac{C_R}{C_F+C_R} - \frac{a}{l} = \text{Static Margin} \quad (40)$$

Hence $N_\beta = -lY_\beta$ (Static Margin) (41)

or

$$\text{Static Margin} = -\frac{1}{l}\left(\frac{\partial N}{\partial Y}\right) \quad (42)$$

The static margin, therefore, determines the yawing moment provided by the tires in reacting to a side force.

The yawing moment caused by a yawing velocity is dependent upon the stability derivative N_r. If the vehicle were constrained to a steady yaw velocity r, the moment equal to $N=N_r r$ would be set up. This stability derivative determines a torque proportional to and in opposition to a yaw velocity; hence it is a yaw damping constant.

The magnitude of N_r is inversely proportional to forward velocity of the vehicle, hence yaw damping decreases with increasing speed.

The side force caused by a yawing velocity is dependent upon the stability derivative Y_r. If the vehicle were constrained to a steady yaw velocity, the difference in front and rear tire cornering forces is $Y=Y_r r$. If the front and rear tire cornering forces are the same, no net side force will appear. Y_r also decreases with increasing speed.

The yawing moment due to steer angle is dependent upon the stability derivative N_δ, which may be termed the control sensitivity. The yaw moment due to the steering angle δ, is given by $N=N_\delta\delta$.

The side force due to a steer angle is determined by the stability derivative Y_δ. The side force resulting from a steer angle δ is equal to $Y=Y_\delta\delta$.

The concept of oversteer and understeer during a steady-state turn can be examined analytically by means of the stability derivative technique. In this connection, the equations of motion during a steady-state turn, in which no yaw or side slip acceleration occurs, that is, $r=\dot{v}=0$, are solved for the curvature $\left(1/R\right)$ response to a fixed steering angle. The result is

$$\frac{1/R}{\delta} = \frac{1/l}{1+KV^2} \quad (43)$$

where

$$K = \frac{MN_\beta}{l[N_\beta Y_\delta - Y_\beta N_\delta]} = \frac{M}{lY_\delta}\frac{\text{(Static Margin)}}{\text{(Neutral Steer Point)}} \quad (44)$$

where W_R, W_F are the loads on rear and front wheels, and C_R, C_F are corresponding cornering stiffnesses. K is called the vehicle stability factor because it determines the curvature response with speed. For K negative, the radius of curvature may become zero and the vehicle is unstable when

$$V = (-1/K)^{1/2} \quad (45)$$

The steady-state steering angle required can be determined by rearranging Eq. (43). The result is

$$\delta = \frac{1}{R} + K\frac{V^2}{R} \quad (46)$$

The first term on the right side represents the Ackermann steering angle required, that is, the steering angle when tire slip angle is neglected.

As explained above, K may be either positive or negative. If K is positive, the steering required to maintain a given radius of curvature is greater than the Ackermann angle. If K is negative, the opposite is true.

Accordingly, a positive value of K corresponds to a vehicle having oversteering characteristics. A positive K corresponds to a positive static margin, a negative K to negative static margin and vehicle having zero static margin possesses a K value equal to zero.

References

1. V. E. Gough and G. R. Shearer, "Front Suspension and Tire Wear," Proc. Inst. Mech. Engr., 1955-56.

2. R. E. V. Eberhorst, Roll Angles, Auto. Engr., Vol. 41 No. 545 (Oct. 1951), 171.

3. G. E. Lind Walker, "Directional Stability," Auto. Engr., Vol. 40 No. 530, (Aug. 1950), 281; Vol. 40 No. 533,

(Nov. 1950), 370.

4. M. Platt, "Front-Steered Cars," Auto. Engr., Vol. 30 No. 394 (Feb. 1940), 35.

5. T. J. P. Joy, "Tire Characteristics as Applicable to Vehicle Stability Problems, "Proc. Inst. Mech. Engr., 1953-54.

6. D. Peters, "In the Right Direction," The Autocar, Vol. 112, No. 3337 (Jan. 29, 1960); Vol. 112 No. 3338, (Feb. 5, 1960).

7. D. Peters, "I. R. S., A Progress Report," The Autocar, Vol. 112 No. 3351, (May 6, 1960).

8. Anon, "Some Steering Problems of I. F. S.," Road & Track, Vol. 2 No. 9, April, 51), 15; Vol. 5 No. 10 (May 51), Vol. 2 No. 11, (June 51), 13; Vol. 3 No. 1, (Aug. 51), 11; Vol. 3 No. 2, (Sept. 51), 25.

9. C. Campbell, "The Sports Car, Its Design and Performance, Third Impression," R. Bentley, Inc., 1955.

10. L. Segal, "Theoretical Prediction and Experimental Substantiation of the Response of the Automobile to Steering Control," Proc. Inst. Mech. Engr., 1956-57.

11. D. W. Whitcomb and W. F. Milliken, Jr., "Design Implications of a General Theory of Automobile Stability and Control," Proc. Inst. Mech. Engr., 1956-57.

12. P. M. Heldt, "The Automotive Chasis (without Powerplant)," P. M. Heldt, 1948.

13. J. J. Taborek, "Mechanics of Vehicles," Reprinted from Machine Design, May 30, 1957; June 13, 1957; June 27, 1957.

14. Anon, "Principles of Automotive Vehicles," Department of Army Technical Manual, TM 9-8000, Dept. of Army and Air Force, January, 1956.

15. D. Bastow, "Steering Problems and Layout," Proc. Inst. Auto. Engr., Vol. 32, 124.

Scientific Highway Design for Safer Motoring

K. A. Stonex
General Motors Proving Ground

NATIONAL SAFETY Council statistics show that there has been a steady reduction in the rate of highway fatalities since 1926 when accurate data were first accumulated. This reduction has come about for many reasons. Drivers have been taught and have learned better driving practices. In the automobile industry, pride is taken in the fact that successive yearly models produce safer vehicles: cars which are quieter, smoother, easier to drive, more responsive in traffic, and with improved braking systems, steering systems, better acceleration, better visibility, and better packaging of the passenger.

Contributions of significant magnitude have been made by highway designers and builders. Before 1920, people who made automobiles were concerned primarily with dependability; the manufacturer who could produce a car which would run dependably had a commanding share of the yearly sales. At that time, the city or county or state which had a few miles of paved streets or highways had a commanding share of the successful highway transport. Just as dependability was important in the vehicle, so it was in the highway system. In the highway system, this meant all-weather roads, paved roads; and the provision of a surface which would carry traffic through all seasons of the year was a matter of primary importance and justifiable pride.

As more and more all-weather, all-year roads came into being, the problems of rapid, safe, and efficient transport became differentiated. As soon as the reliability of the vehicle was established, and the reliability of the road was established and taken for granted, the refinements of both became important. The refinements in highway and traffic engineering appeared early, first in terms of effectiveness. Since the accident always happened to somebody else, the effectiveness of the system was an element of primary interest to people who drove automobiles and transported goods before safety received much attention.

The effectiveness of the system of highways depreciated early because of the congestion. There were always people in front travelling at a slow rate (typical Sunday drivers), people turning into the road from side streets, trucks which could not maintain reasonable speed, traffic in the opposing lane which inhibited passing, and endless frustrations about getting anywhere simply because there were so many people on the road.

Justifiably, the taxpayers began to ask that the highway transportation system be improved simply because they couldn't get where they wanted to go as rapidly as they wanted to. Traffic engineering emerged as a new profession during the late 1920's and early 1930's; and highway engineering began to take into account to an increasing degree the functional utility of the highway as a design element.

Before the collection of good accident data began in the middle 1920's, the newspapers began to report more and more people killed in automobile accidents, and fewer and fewer people killed because of being kicked in the head by horses or because of bicycles going out of control and the riders plunging into a ditch or breaking their necks from falling over the handlebars.

As the problems of the highway effectiveness and safety became more clearly recognized, the design of highways matured rapidly to provide more lanes for the higher volumes of traffic, and to remove restrictions to the rapid and safe movement of traffic. Thus, there came into being one-way roads, divided highways, limited access, signal control at intersections, and separation of grade at important highway intersections. Studies of highway capacity and highway safety (in which we are primarily interested today) showed conclusively that additional investments were required to implement the effective, rapid, and safe flow of traffic, particularly in metropolitan areas.

Because the automobile and automotive transport system are revolutionizing our economy, the concept of rapid, effective, and safe highway transport across the nation has become of paramount importance. Thus, the traffic engineering and highway design principles, which first appeared essential in metropolitan developments 35 years ago, became applicable almost immediately to interurban and interstate travel.

These concepts were understood and appreciated by farsighted highway and traffic engineers more than a generation ago. As funds became available, in a few metropolitan and suburban areas they were applied even before the depression in 1929. While highway designers and traffic engineers have appreciated the basic principles involved in the construction and operation of a rapid, effective, and safe highway transport system, funds have never been adequate to meet the requirements. The deficiencies in amounts of money required have been almost paralyzing, and heavy pressures have always been imposed on highway builders to get the most miles of pavement for the money available. Because of public apathy about the highway traffic safety problem and public ignorance about the part that certain design

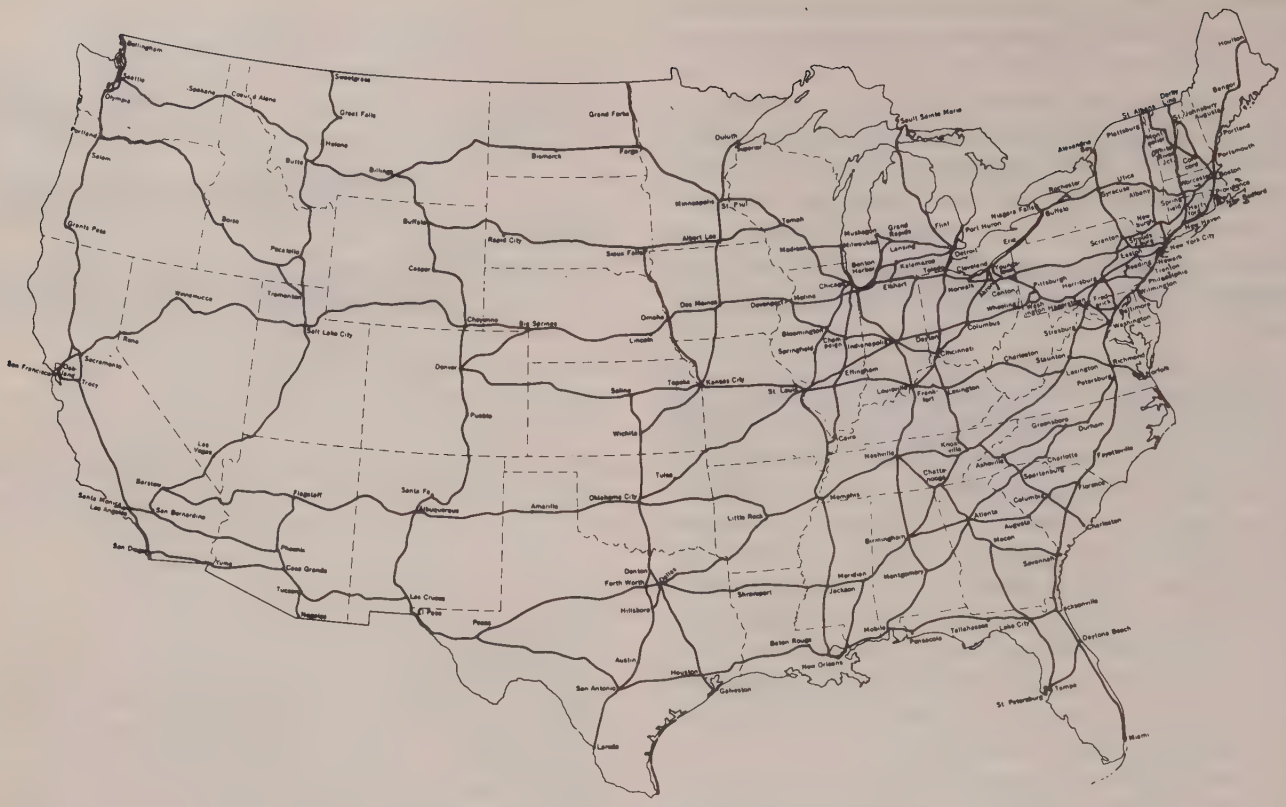

Fig. 1 — National system of interstate and defense highways

Fig. 2 — Typical scene on N.Y. Thruway showing gentle alignment, wide median, wide traffic lanes, unobstructed view, high capacity

elements play in highway safety, highway designers have never been permitted to incorporate all the safety elements required.

During the 35 years covered by the accident records, there has been a consecrated and dedicated effort by a few, then a few hundred, and then a few thousand people who are convinced that highway accidents are unnecessary and avoidable. This effort has been responsible in a large part for the steady decrease in the fatal accident rate on a travel basis. Sharing in it have been automotive engineers, highway design and traffic engineers, safety experts in many fields, the clergy, members of the press, police, radio, and TV. A major accomplishment has been to develop a better public understanding of the importance of the highway traffic safety problem and effective means by which to cope with it. As a result, highway engineers have been permitted to invest increasing proportions of highway construction funds in those features which reduce hazards; in fact, the public attitude has come to demand incorporation of these features. As a side light, it should be noted that many of the design features fundamental for highway safety also improve the flow of traffic and enhance the effectiveness of the highway.

Interstate System

This movement culminated in the Highway Act of 1956, which provided for accelerated modernization of the National System of Interstate and Defense Highways.

By this act, some 41,000 miles of highways throughout the country (Fig. 1) were established as part of the Interstate System, and enlightened standards of design were established. At the time of passage, it was intended that this system would be completed in about 15 years.

Figs. 2 - 4 show typical examples of highways constructed according to these enlightened concepts.

The standards of the Interstate System provide certain requirements with regard to alignment, profile, cross section lane width, and particularly control of access.

Control of access is required for all sections of the Interstate System. Grade separations are required except for those

intersections in sparsely settled rural areas where the traffic volumes on both roads are low, and specifically where no appreciable hazard is created, and when the traffic volume on the intersecting road is less than 50 vehicles per day.

The design speed of all highways in the system is to be at least 70, 60, and 50 mph for flat, rolling, and mountainous topography, respectively, and depending upon the nature of terrain development. Alignment, super elevation, and sight distance are to be correlated with the design speed.

For design speeds of 70, 60, and 50 mph, gradients, generally, are not to be steeper than 3%, 4%, and 5% respectively. Gradients 2% steeper may be provided in rugged terrain. Traffic lanes are not to be less than 12 ft. wide, and the usable width of the shoulder shall not be less than 10 ft, except in mountainous terrain involving high cost for additional widtn. The usable width of shoulder may be less, but at least 6 ft.

Side slopes are to be 4:1, or flatter where feasible, and not steeper than 2:1, except in rock excavations or other special conditions. These special conditions include presumably certain locations in urban areas where costs of providing this standard would be prohibitive.

The median is to have a minimum width of 36 ft, except in urban areas where right-of-way costs make this excessive. In any case, it is to be at least 4 ft.

The design standards listed above are considered minimum for the Interstate Highway System. Higher standards which represent desirable minimum standards are to be used when they are commensurate with conditions, and when the use of higher values will not result in excessive cost. In the determination of all geometric features, including right-of-way, a generous factor of safety should be employed, and unquestioned adequacy should be the criterion. All known features of safety and utility should be incorporated in each design to result in a National System of Interstate and Defense Highways which will be a credit to the nation. (1)*

During the period from the late 1930's until the Highway Act of 1956, particularly after World War II, there was an urgent demand for improved highways in some areas where anticipated usage, plus lack of other funds, justified financing as toll roads; some major examples are shown in Fig. 5.

As these facilities designed and built according to advanced and enlightened standards, came into use, it became evident that in addition to providing a highly effective highway transport system, very favorable accident rates were experienced, shown in Table 1.

The standards for construction of the Interstate Systems are comparable with those of the toll roads shown above, or higher. It seems clear that the highway traffic accident problem will be alleviated significantly when this program is completed, especially since a large proportion of the total traffic volume will be carried on the Interstate System.

*Numbers in parentheses designate References at end of paper.

Fig. 3 — Scene on N.J. Turnpike showing general alignment, paved shoulders, protected opening and overpass, grade separation, unobstructed view, wide median, wide traffic lanes

Fig. 4 — Scene on Interstate road in Ohio showing wide median with relatively mild median ditch, long sight distances, gentle horizontal and vertical curves, wide traffic lanes, and long guardrail installation protecting opening in overpass structure

Table 1 - Death Rates per 100,000,000 Miles on 13 Toll Facilities with Greatest Length and Largest Traffic Volumes

(Accident Facts - 1960 Edition)

Turnpike	Death Ratio 1959	Length Miles	Vehicle Miles (Millions)
Illinois Tollway	0.5	188	605.7
Connecticut Turnpike	1.4	129	790.0
New Jersey Turnpike	1.5	132	1343.8
Ohio Turnpike	1.8	241	981.8
Garden State Parkway - N.J.	2.1	174	1212.0
Sunshine State Parkway (Fla)	2.6	110	193.8
New York Thruway	2.8	553	2103.4
Massachusetts Turnpike	2.9	123	485.7
Pennsylvania Turnpike	3.7	470	2081.0
Indiana East-West Toll Road	4.5	157	619.3
Maine Turnpike	5.1	113	196.6
Kansas Turnpike	5.5	242	273.9
Will Rogers and Turner Turnpike (Okla)	6.1	174	295.7

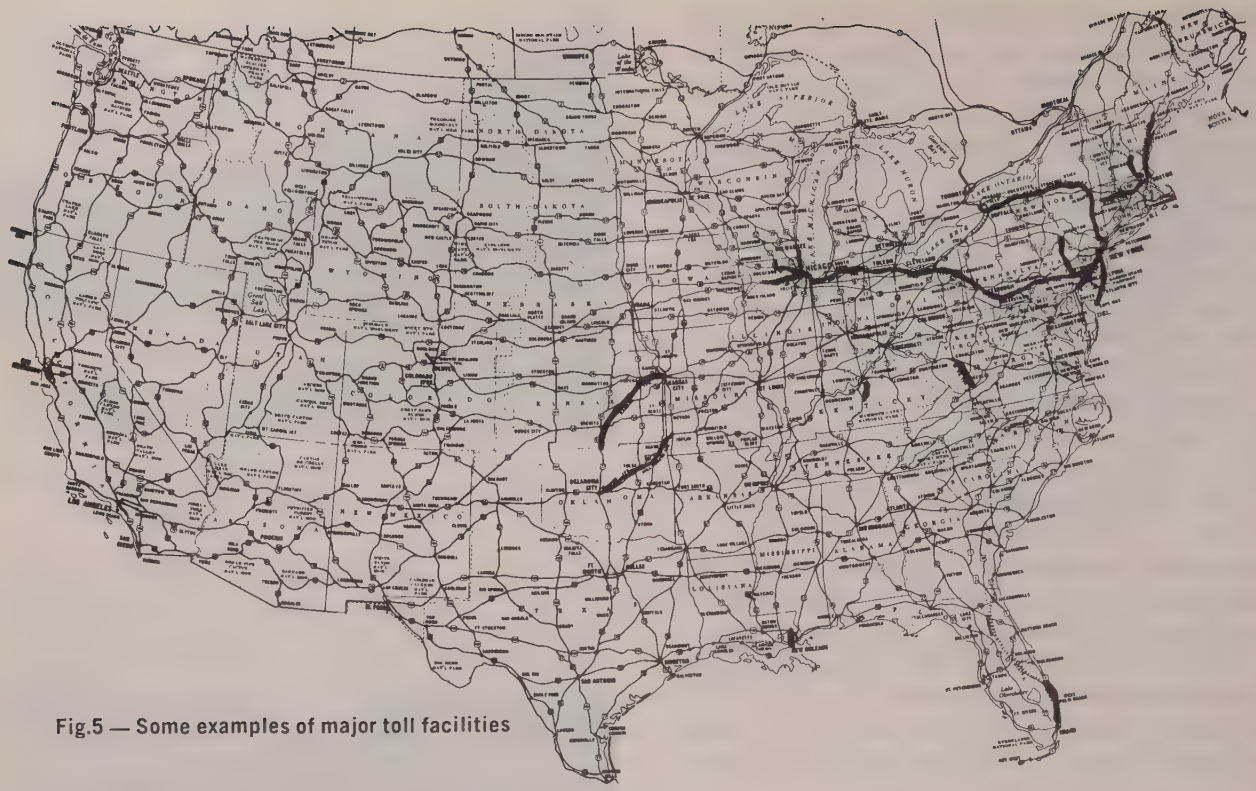

Fig.5 — Some examples of major toll facilities

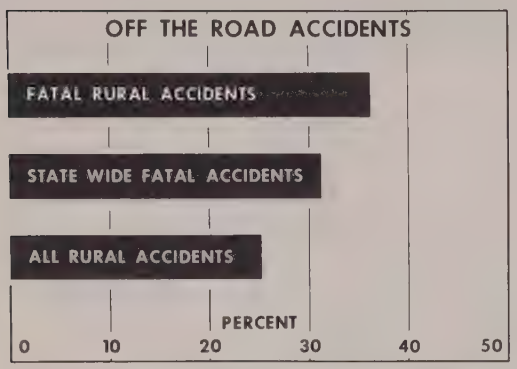

Fig. 6 — Significance of off-the-road accidents

Fig. 8 — Trees in median on controlled access road

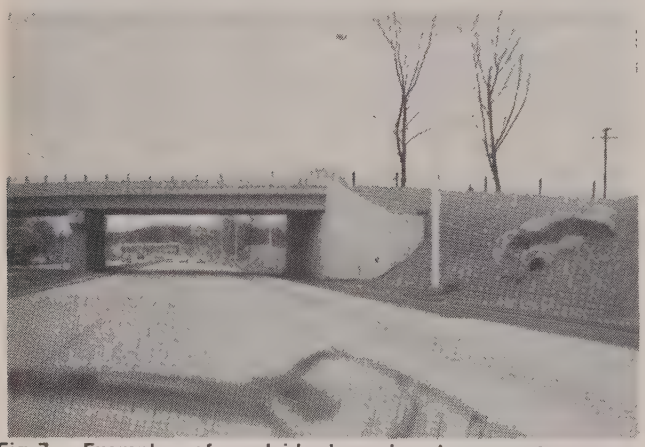

Fig. 7 — Examples of roadside hazards — lamp posts, unprotected bridge abutments and piers — on controlled access highway

Proving Ground Road Safety Problems

At General Motors Proving Ground, we have been very concerned with road safety problems.

Our primary road system was designed more than 30 years ago, and much of our operation is conducted on that part of the system. The design provided one-way operation, controlled access, elimination of grade crossings on high speed facilities, and most of the other concepts which are part of the standards of the Interstate System and the major toll roads. The primary concern of all safety engineers is to eliminate accidents. The next important concern of the in-

Fig. 9 — Sharp V ditch on modern super highway

Fig. 11 — Ditch-lined country arterial road

Fig. 10 — Tree-lined arterial road

Fig. 12 — Roadside sign with heavy supports on concrete base

dustrial safety engineer is to minimize the effect of any accident which may occur. While our road system had been designed to obviate the accidents which occur most frequently on the public highway system, too few precautions had been taken to minimize the effect of accidents resulting from the vehicle leaving the roadway.

A review of our accident statistics during the six calendar years, 1953-1958 inclusive, covering approximately 65 million test miles, revealed a total of 236 accidents, of which 72% were off-the road.

In spite of careful selection of driver personnel, the application of the best training programs we can evolve, and operation on a closed road system under adequate supervision, evidence is clear that we cannot keep our drivers on the roadway all the time. Drivers on the public highways cannot be kept on the road all the time, either, as the statistics bear out.

National Safety Council statistics show year after year that from 30% to 35% of the fatalities are incurred in off-the-road accidents, the one-vehicle non-collison type. (Fig. 6.)

It was found that our roadsides presented numerous hazards. In an attempt to apply the second precept of safety engineering (to minimize the effect of accidents), we looked at the roadsides on adjacent public highways in the hope of finding ready-made solutions. We found that these roads were designed according to the same standards as ours. We looked at the roadsides of most of the turnpikes and freeways in the north central and the northeastern parts of the country and found none of these facilities is free from roadside hazards. (2) (Figs. 7 - 9)

On any road, there are many hazards involved when a driver leaves the travelled surface, such as trees, ditches, lamp posts, bridge abutments, and traffic signs. Figs. 10-12) When our safety engineer looked at the Proving Ground road system in his study of accident potential, he found these same problems. (Figs. 13 and 14)

In the early days, trees were planted beside roads (Fig. 15) to provide shelter from rain and sun. They are beautiful, but if an automobile runs into a tree, very serious damage is inevitable (Fig. 16). According to the safety engineer, trees must be removed from the immediate roadside on all major highways (Fig. 17). In parks or residential areas, where speed regulations are observed, trees do not present a comparable hazard (Fig. 18). In areas where it is desirable to retain trees, appropriate speed controls must be imposed.

On rural roads where ditches and steep embankments occur immediately adjacent to the gravel road surface, speed control is imperative (Fig. 19).

In areas where lamp posts are erected adjacent to the

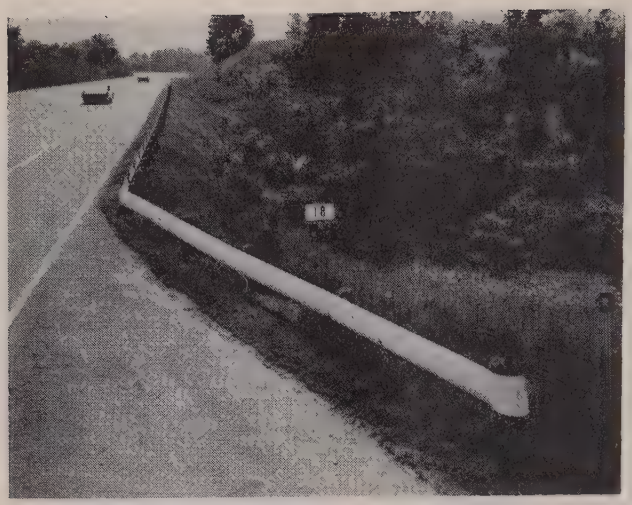

Fig. 13 — Proving Ground test track — 1926 design standard

Fig. 14 — Proving Ground roadside—Hill Route—1926 standard

Fig. 15 — Tree-lined rural highway

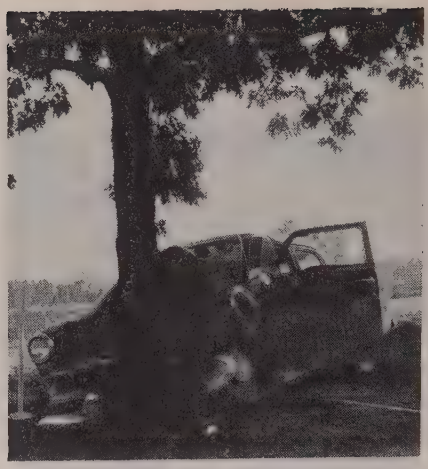

Fig. 16 — Proving Ground car-tree accident

Fig. 17 — Removal of roadside trees

highway, speed regulations should be imposed or a safe design of the lamp post, as suggested in Fig. 20, should be developed.

The standard installation of ordinary traffic signs is in itself a hazard on highways where free traffic flow occurs. Fig. 21 shows that at normal traffic speeds, a collision with a standard traffic sign may result in a serious or fatal injury to the driver or passengers.

Guardrails

In many cases, guardrails are used to protect against obstacles or unfavorable terrain conditions. The safety of guardrail design and installation, and the protection afforded to travellers, had not been evaluated in full-scale tests since the middle 1930's. At the Proving Ground, we became concerned about this problem because we had approximately 14 miles of guardrails. Tests (Fig. 22) showed that much of our installation was ineffective except for purposes of delineation. We made a series of tests to determine whether the material in the guardrail installations on the road system could be salvaged, and, following that, to determine

Fig. 18 — Example of conservative speed regulation on Parkway Drive

Fig. 19 — County road with hazardous ditch bank adjacent to paved surface

the best type of installation where guardrail could not be eliminated.

The series of tests is reported in Highway Research Board literature (3). Suffice it to say that we found that a collision with a guardrail at angles of impact and speeds normal to the freeway system was a very serious accident (Fig. 23) Tests were made to evaluate various types of guardrails construction including post design and spacing, and end treatment. The conclusion was made that guardrails should be eliminated wherever possible. Thus, in the reconstruction of our 30-year old highway system, flat gentle slopes are being built wherever possible, and guardrail are being removed. Where this is impractical economically, we are using the relatively stiff modern W-beam type of guardrail installed on posts at a spacing of 6 ft 3 in. which is half the spacing used in normal standards.

The end of the guardrail installed according to normal highway standards provides a serious and hazardous obstacle (Fig. 24). Because some guardrails are still required on the road system, we have made considerable effort to modify the end treatment to eliminate these hazards. One sugges-

Fig. 20 — Comparison of experimental low impact tripod lamp post and conventional lamp post installations

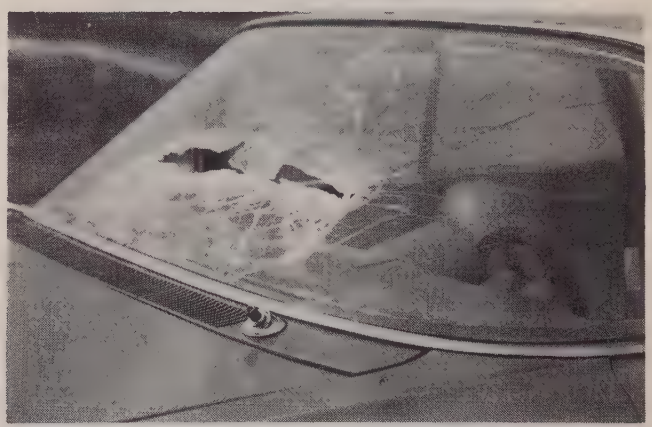

Fig. 21 — Damage from collision at 40 mph with traffic sign mounted at 42 in.

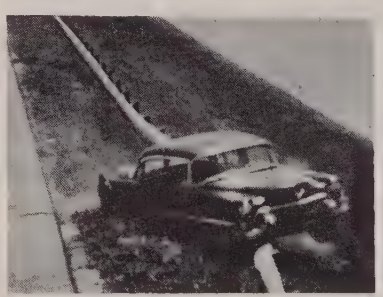

Fig. 22 — Test of 10 year old Proving Ground guardrail

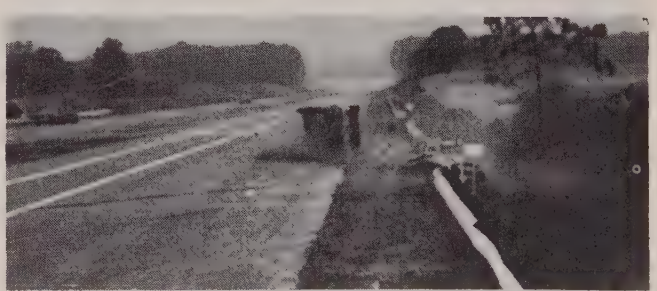

Fig. 23 — Experimental collision with guardrail at 65 mph

tion tried was to ramp the end of the rail down to the ground (Fig. 25). This type of installation was not entirely satisfactory. In the designs evaluated, the ramp was short and the car was pitched into the air too far. A longer ramp would be required to control this pitching.

Concern about this subject has beenexpressed by highway authorities, and we tested one installation suggested by the Michigan State Highway Department. This consisted of using an end section bent to a radius of 50 ft. Tests showed that this was not a complete answer to the problem (Fig. 26) because relatively high deceleration rates persisting for 0.1 to 0.2 seconds occurred.

Fig. 24 — Results of experimental collision with guardrail standard end installation

Fig. 25 — Experimental guardrail ramped end installation

Fig. 26 — Test of guardrail end section bent to 50 ft radius

One of the best solutions we have found is shown in Fig. 27. Near the logical beginning of the guardrail installation, there was a shallow ditch with a backslope about 30 in high. It was simple to bury the end of the rail in the backslope and obviate the end problem. Fig. 28 is an artist's concept of how the guardrail ends may be covered by constructing long, low mounds of earth.

Ditch Section

When the guardrail and other obstacles are eliminated, the drainage becomes of primary importance in roadside safety. We could find no information in the literature which would give criteria for rational design of ditch cross sections. In the concept of roadside safety, it is implicit that the roadside be developed so that the driver can traverse it without damage to the vehicle, or injury, or extreme shock, so that he can recover control and return to the road without incident.

In the absence of data, we made tests from which we developed the criteria to establish a rational system for road ditch cross section design. (4)

Fig. 27 — Guardrail installation with end buried in ditch backslope

Fig. 28 — Artist's concept of method of concealing guardrail end by building long, low mound of earth

To do this, we made a simple analysis of the problem and computed the severity of passage through a group of ditches with different cross sections over a range of speeds and angles of attack.

Then we built a series of ditches with different cross sections and drove cars through them at increasing speed increments over a range of angles of attack up to the limit of driver tolerance.

"Vertical" accelerations normal to the car axis were measured as an index of severity so the analysis could be verified and a value of limiting driver tolerances established. Fig. 29 shows a typical test scene.

Fig. 30 and 31 show the basis of analysis, and Fig. 32 shows the comparison of the results computed and observed. Under more severe conditions, the observed values were approximately twice the computed values. The tolerable limit which an experienced test engineer would sustain was about 1 g observed; this occurred under conditions where the computed value was about 0.5 g. The difference between the computed and observed results is attributed to the fact that discontinuities occur when the suspension system bottoms. It was concluded, therefore, that a rational criterion for ditch cross section design would be to provide that the maximum computed acceleration normal to the axis of the car would be 0.5 g. Under these conditions, the driver would experience a deceleration of about 1 g which would be about the limit tolerable without severe psychological or physical consequences.

From these data, we have developed a ditch cross section considered appropriate for a speed of 65 mph. At an angle of attack of 15 deg, the ditch would be traversable without undue shock or alarm to a driver of normal physical qualities. Fig. 33 shows the elements which must be specified, and Fig. 34 shows the significant relation between severity and length of the vertical curve.

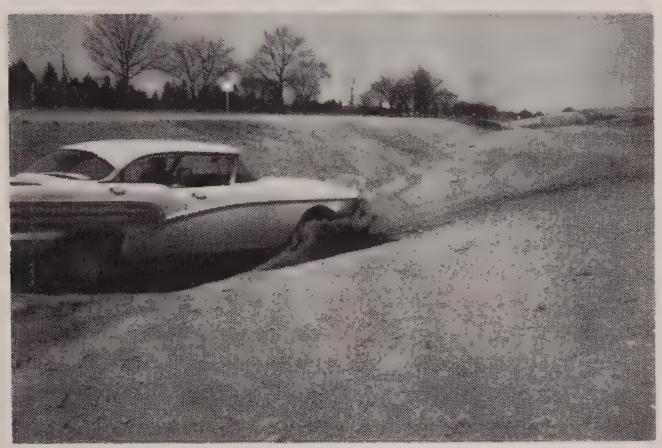

Fig. 29 — Test of experimental ditch section

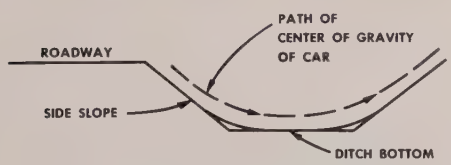

Fig. 30 — Analysis of passage through ditch

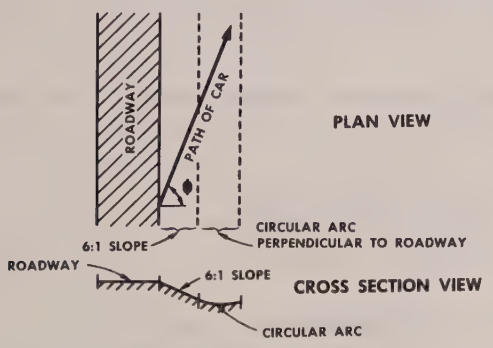

Fig. 31 — Projection of ditch section on path of car

Roadside Slope

An element of considerable importance in the roadside hazard problem is the relation of the slope of the bank and the stability of the car (Fig. 35).

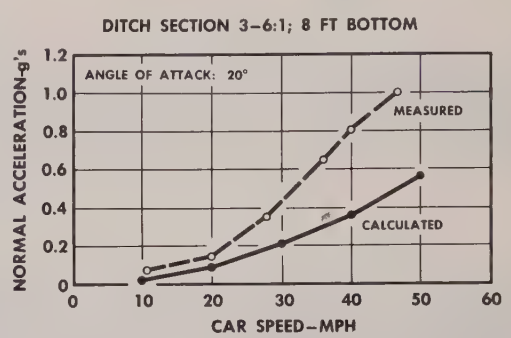

Fig. 32 — Comparison of observed and computed ditch test results

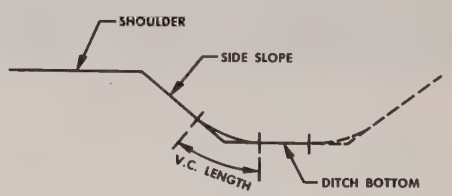

Fig. 33 — Elements of ditch cross section significant in design

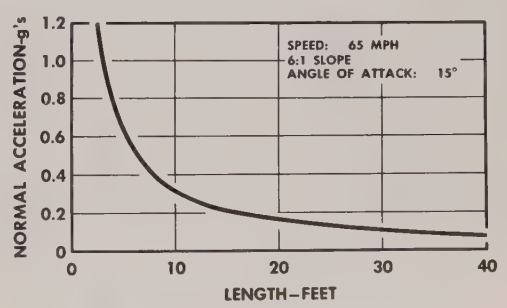

Fig. 34 — Severity in terms of normal acceleration during passage through a ditch as a function of vertical curve length

Fig. 35 — Car on test at 65 mph rolls over at top of 4:1 slope

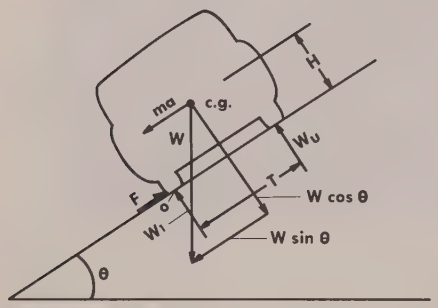

Fig. 36 — Force and moment relations of car on side slope balanced over lower wheel

Fig. 37 — Measurement of coefficient of ground reaction

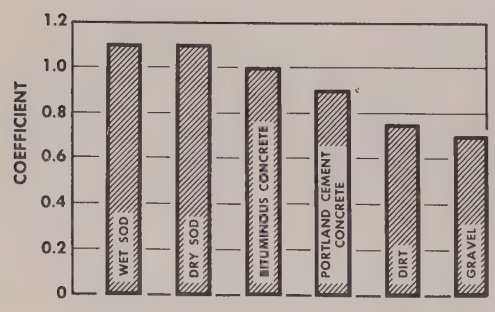

Fig. 38 — Comparison of coefficient of ground reaction on sev-

A mathematical analysis of the car stability problem (Fig. 36) shows that when a car is at a point of equilibrium of overturning on a roadside slope, the ground reaction force, F, is given by

$$F = \frac{T}{2H} W\cos\theta \qquad (1)$$

where:

T = Car tread
H = Center of gravity height
W = Weight
θ = Angle of inclination of slope

By dividing through by W, we get an expression

$$f = \frac{F}{W} = \frac{T}{2H} \cos\theta \qquad (2)$$

where:

f = A coefficient of friction or "coefficient of ground reaction"

This concept suggests that we may measure the "coefficient of ground reaction" as a characteristic of the material on the roadside slope surface, and it provides a means of specifying the performance of the roadside material if we should want to refine our construction procedures in this respect.

The factor, T/2H, is a stability characteristic of the car. Since the car stability factor, T/2H, averages about 1.4 for current vehicles, with some variation due to design considerations, it is interesting to compare this stability factor with some observations of the coefficient of ground reaction. We made some measurements on sod by the method indicated in Fig. 37 and on some other types of surfaces, and found typical results as indicated in Fig. 38. This shows that the sod surfaces had coefficient of ground reaction of approximately 1.2, either wet or dry, and it appears, thus, that there is a narrow margin between the stability factor of the car and the "frictional" characteristics of a typical roadside. This margin is so small that the importance of smooth, firm roadside slopes can hardly be ignored.

Since the car sliding down the roadside slope will be decelerated by the ground reaction force, it is of some interest to compute the deceleration rate at which the car will trip and overturn.

It can be shown that this deceleration is given by the following expression:

$$\frac{a}{g} = \frac{T}{2H} \cos\theta - \sin\theta \qquad (3)$$

where:

a = Deceleration in ft/sec/sec
g = Acceleration due to gravity

The effect of the roadside slope on the stability is shown in Fig. 39 where the percent of decrease in the deceleration required to trip the car is shown as a function of the side slope. This shows, for example, that on an 8:1 slope, which is quite flat, 6% less deceleration is required to trip the car than on a level road, and, on a steep slope, the car can be tripped much more easily. The deceleration required to overturn the car on a 2:1 slope is 20% less than that required to tip it over on a level road.

The stability factor shows by direct inspection that the value is increased as the tread is increased, and as the center of gravity height is lowered. If we take derivatives to find the rate of change, we find that the rate of change of the stability factor is negative and inversely proportional to the square of H, the center of gravity height, that is, the contribution of the center of gravity height to the stability factor varies as the negative reciprocal of H^2. Thus, the automobile designers who have progressively made lower and lower cars, with lower and lower heights of center of gravity, have increased the stability by significant amounts, and the fact that we have some margin over the coefficient of ground reaction of the normal roadside slope is undoubtedly due to the trend toward lower and wider cars.

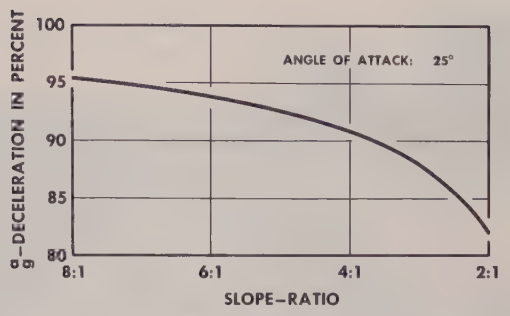

Fig. 39 — Influence of roadside slope on reduction of "tripping" deceleration

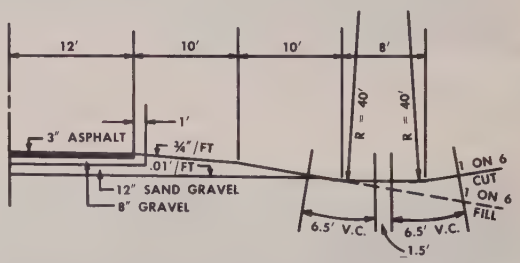

Fig. 40 — Proving Ground 1960 road cross section standard

1960 Design Standard

From our consideration of roadside hazard problems, we have developed design standards identified in Fig. 40 as the General Motors Proving Ground 1960 Road Section Design Standards. Among the elements are:

1. Where reasonably high speed may be anticipated, above 35-40 mph, the roadside will be clear of obstacles including drainage structures for 100 ft from the edge of the road.

2. Ditch cross section design to provide a maximum calculated severity of 0.5 g, normal acceleration at 65 mph at 15 deg angle of attack will be provided.

3. No guardrail will be installed unless extreme terrain requires it.

4. Where terrain considerations require, guardrail will be of the beam type with posts at 6 ft 3 in. spacing where speeds of about 35 mph may be anticipated.

Several roads representing this design concept have been constructed (Figs. 41 and 42), and we have a program current at the Proving Ground whereby the earlier roads having substantial traffic volumes are being reconstructed according to this concept. (Figs. 43-46.)

This material has been presented in other forms to numerous highway groups including national and regional meetings of the American Association of State Highway Officials, and to conferences of several of the state highway organizations, specifically Maine, New Jersey, Texas, Oregon, Michigan, and Ohio, and to the staffs of several of the turnpike authorities.

One of the questions which arises immediately is the relative cost of construction. Proving Ground roads constructed

Fig. 41 — Test road at Proving Ground constructed according to 1960 standard

Fig. 42 — Test road at Proving Ground with roadside trees set back to give an unobstructed roadside up to 100 ft from pavement edge

Fig. 43 — Proving Ground Test Track after modernization of roadside

Fig. 45 — Track access road during modernization. The steepest grade in central portion of picture is 14%. This is a one-way downhill road.

Fig. 44 — Typical scene of Test Track after reconstruction to bring roadside up to 1960 standard

Fig. 46 — Proving Ground gravel road after modernization of roadside

or reconstructed according to this standard, have included those on flat and rugged terrain. Construction cost vary widely depending upon the terrain. On one road built on nearly level terrain, the cost of construction according to the 1960 Standard was only about $9500 per mile more than it would have been if conventional standards employing steeper slopes, deeper ditches, and clearance of obstacles only to the toe of the slope or top of cuts had been used. The most expensive reconstruction was on a long, steep hill, part of which is a 14% grade, and the remainder approximately 10%. This reconstruction involved an expensive drainage system, and the cost of reconstruction above the elementary 1926 Standard was about $75,000 per mile. On our Test Track, reconstruction of the inside edge only was $47,000 per mile, but on our gravel Hill Road, which has many sharp curves and steep grades, the cost of reconstruction was about $26,000 per mile.

This investment in safety of the Proving Ground road system is a good one. We have had 14 minor accidents in areas where the roadside has been reconstructed. Without reconstruction, any one or all of them could have been fatal. We think the public highway construction standards should be raised to meet the 1960 Standard wherever the terrain permits, and that this would be an equally good investment.

Some meaningful data are being accumulated on the cost of accidents. Possibly the best are from the Masachusetts Study, one result of which is reproduced in Fig. 47. (5). This shows not only that roads with controlled access have a substantially lower cost of accidents per mile, but also that a very significant sum of money is being wasted each year per mile of highway in highway accidents. This figure shows that, on controlled access roads, the yearly accident cost per mile is approximately linear with respect to traffic volume, and that the cost of accidents is about $0.67 per vehicle for each mile of road. On roads without control of access after the volume reaches about 7000 vehicles per day, the cost of accidents is approximately $4.00 per vehicle for each mile of roadway. For example, on a road of this type carrying a traffic volume of 15,000 vehicles per day, the cost of the accidents each year is about $45,000. When we look at accident costs of $20,000 and $30,000 per mile per year, an investment of $30,000 to $50,000 per mile in original construction for safety, or reconstruction for safety, appears to be small.

To relate these traffic volumes to highways upon which

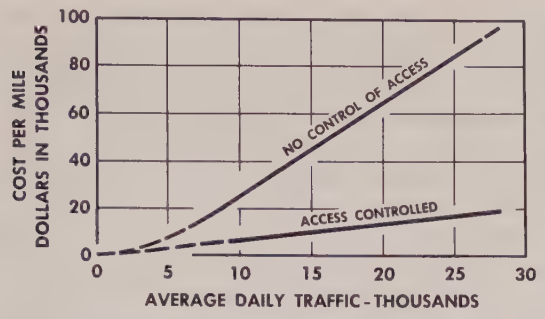

Fig. 47 — Yearly accident cost on roads with controlled access and no control of access — Massachusetts study

the traffic situation is familiar to residents of Detroit, the current average daily traffic volumes for a number of arterial highways in the Detroit area are listed. (These data are provided through the courtesy of the Michigan State Highway Department.)

Average Daily Traffic Volumes Highways in Detroit Area

US 25 -
- 18,000 at Allen Park, south city limit
- 53,000 at north Detroit city limit
- 15,000 at Mt Clemens, north city limit
- 7,000 at Marysville, west city limit

M 53 (Van Dyke) -
- 55,000 at Detroit city limit
- 14,000 at Utica, north city limits
- 5,000 at Romeo, north city limits

M 150 (Rochester Rd) -
- 10,000 from north limit Clawson to north limit Rochester

US 10 (Woodward) -
- 61,000 at north Detroit limit
- 36,000 at north Birmingham limits

US 24 (Telegraph) -
- 22,000 south Dearborn limit
- 25,000 at intersection Grand River
- 19,000 at intersection 14 Mile Road

US 16 (Grand River) -
- 36,000 at intersection McNichols
- 27,000 at intersection 8 Mile Road
- 16,000 at intersection 10 Mile Road
- 12,000 at intersection US 23
- 10,000-11,000 Brighton to Williamston
- 7,000 at Portland

M 14 (Plymouth Road) -
- 23,000 at intersection with Telegraph
- 7,500 at Plymouth east limit
- 5,000 - 7,000 Plymouth to Ann Arbor

US 112 -
- 36,000 at intersection of US 24
- 15,000-12,000 Wayne to Ypsilanti
- 6,500 at intersection of US 23
- 6,000-4,000 Saline to Sturgis

US 12 -
- 32,000 west of intersection with US 24
- 24,000 - 19,100 from US 24 to Willow Run area
- 9,000 Ann Arbor to Jackson
- 5,000-7,000 west to Kalamazoo

US 27 -
- 6,000-7,000 Lansing to Alma
- 5,000-3,000 Alma to Houghton Lake
- 4,000-3,000 Houghton Lake to Indian River

Edsel Ford X-Way -
- 124,000 at intersection of US 16

This shows that most of the arterial roads in the metropolitan area carry traffic volumes in excess of 10,000 vehicles per day, and that several of them have volumes on the order of from 30,000 to 50,000. It should be clear, then, that the accident costs reflected in this Massachusetts Study can be taken as representative of the accident costs on the metropolitan district arterial highways of the Detroit area. It seems clear that the yearly cost of the accidents on these roads would pay much of the cost of modernization even at costs reflecting urban and suburban property values.

It is estimated reliably that, nationwide, the cost of accidents is the equivalent to a tax of $0.125 per gal of fuel (6). While this may not be distributed in exactly those terms, a good portion of it is distributed in the cost of insurance, and it is fair to say that the cost of accidents to us as individuals approaches the cost of gasoline tax.

Summary

Application of high design standards in the contruction of toll facilities and comparable highways in the United States results in an accident death rate less than half of that for the country as a whole. Several of the newest and best-designed and operated of these facilities have an accident death rate much lower than the average. With the application of the highest design standards in current use, it is evidently possible to achieve accident rates as low as 1/5 that of the present national average.

We have called attention to some concepts of roadside design and elimination of roadside obstacles which are a refinement of the standards of even the newest of the modern highway facilities. We believe that the application of these concepts would achieve a further significant reduction in accident death rates on even the best of our present roads.

We believe that the application of these concepts of safe roadside design to the remainder of the public highway system, even without changes in alignment or grade of the road, would contribute very significant reductions in the total number of road accident fatalities and injuries. This belief is confirmed by experience on our own road system where, during the past two years, modernization of the roadside has

made only minor incidents out of several accidents which could have been fatal.

We believe there is need for better public understanding of the potential gains in highway safety which may be achieved by scientific design, and a need for better public support of the highway program. Even if the gains in public safety are not sufficient motivation, the cost of accidents should be.

References

1. Geometric Design Standards for National System of Interstate and Defense Highways, American Association of State Highway Officials, (1956).

2. L. C. Lundstrom, "Safety Aspects of Vehicle-Road Relationship," SAE Paper No. 66B, June 1958.

3. L. C. Lundstrom, and P. C. Skeels, "Full-Scale Appraisals of Guardrail Installations by Car Impact Tests," Proceedings of Highway Research Board, Vol. 38.

4. K. A. Stonex, "Roadside Design for Safety," Proceedings of Highway Research Board, Vol. 39.

5. Bernard B. Twombly, "The Economic Cost of Traffic Accidents in Relation to the Highway Systems," Public Roads, Vol. 31, No. 2, June 1960.

6. C. W. Prisk, "The Motor Vehicle Aspect of Traffic Safety," SAE Paper No. 209A, Summer Meeting, Chicago, Ill., June 1960.

continued from page 237 - MOHR

ward reducing radiated noise from a complex structure stems from the wide-band noise characteristics of such an engine, coupled with the fact that while mechanical impedances of the radiating surfaces may be considered lumped at low frequencies, they become distributed at higher ones. The fundamental frequency for an 3000 rpm engine is 50 cps, and thus, is in a very unresponsive region of the ear's spectral response, but it also radiated severely in other bands, as shown in Fig. A. The low pass mechanical filtration characteristics of the engine mounts serve effectively to isolate this solid borne high-frequency mechanical vibration from the boat and the engine cover. However, the response of a poorly designed cover can prove ineffective in reducing radiated noise levels and in fact make them worse in some spectral bands. Thus, serious consideration must be given in designing an adequate cover.

If the assumption is made that the enclosure is effectively sealed through the use of airtight resilient gaskets as indicated, and if intake noise is disregarded for the moment, then the transmission loss characteristics of an enclosure is a function of the area density characteristics of the enclosure for all noise above its mechanical resonant frequency. This is the so-called mass law of noise isolation and is an oversimplification of the problem for outboard engine covers, since the sections which go to make up such a structure constitute a complex multidegree of freedom system with many resonant frequencies. (An ideal noise barrier would have mass and no stiffness and hence a zero resonant frequency.) Hence, for a wide band noise source, such as an engine operating over a range of frequencies, some resonances will be inevitable, and the mass law will not apply. However, the excursion velocity of these radiating vibrations may be appreciably limited by internal damping of thick sections.

The mechanism of noise transmission from the engine cover is, of course, one of noise reradiation. If there is no structure-borne vibration utilizing this cover as a sounding board, then sound transmission through an airtight barrier is reradiated by virtue of sympathic vibrations induced by the airborne noise acting on the flexible panels of the cover.

One last concept bears mentioning, and this concerns the difference between noise transmission loss through an enclosure and noise reduction. When a noise source is confined by an enclosure, there is an accompanying sound level buildup in the near field (that is, inside the enclosure) due to reflections at wall and noise reradiation back into the enclosed volume. This reverberant buildup decreases the effectiveness of the barrier since it makes the noise source appear more severe than if no enclosure were present. This effect may be limited (particularly in the higher frequency range) by the application of sound absorbing material on the interior of the cover.

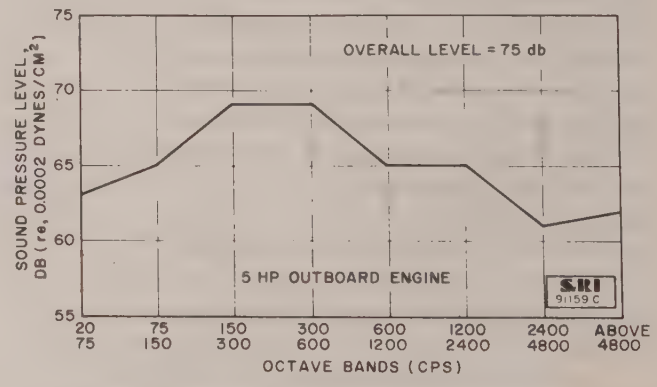

Fig. A — Frequency radiation of 3000-rpm engine

Piston Rings for Transportation Diesels

Glenn F. Hyde, Fred A. Robbins, and Paul R. Shepler
Koppers Co., Inc.

PISTON RINGS are well known mechanical elements in our modern technology, and are quite simple in their fundamental configuration. For the first 100 years of ever broadening usage of reciprocating engines, pumps and compressors, plain rectangular cross-section gray cast iron piston rings operating against gray cast iron cylinders met the functional requirements, without appreciable scientific development. The structural and frictional characteristics of unalloyed pearlitic grey iron have been so successful that this material has been the base upon which the piston ring industry has been built, and is the basis for comparison of newer ring materials. It can be safely said that the only reason a ring is fabricated of some material other than gray iron is because of the inadequacy of gray iron for one or more of the functional requirements.

Over the last 30 years, piston ring technology has become progressively more sophisticated, at an increasing rate. One of the earliest basic references in cast iron metallurgy was published in 1916 (1)*. We are in transition from art to science, but much art still prevails. We cannot as yet feed the digital computer data and end up with the solution to a piston ring problem. A list of the sciences involved in piston ring technology include: mechanics, strength of materials, fluid mechanics, pneumatics, thermodynamics, chemistry, lubrication, corrosion, metallurgy, materials compatibility, friction and wear. Pure scientists may question this list as to definition. We however, recognize that there are thousands of papers and chapters of books in existence on these subjects that contribute to the state of our technology.

It is also desirable to identify the requirements of the diesel engine builder in his application of piston rings. The engine builder expects the piston rings he applies to accomplish the following:

1. The primary function of internal combustion engine piston rings is to form a circumferential gas seal between two concentric cylinder surfaces to which reciprocating motion is applied.

2. A secondary function is to control the lubrication of the elements of the system.

3. It must contribute to high engine efficiency. This involves the control of friction horsepower as well as maintaining a gas seal.

4. It must be easy to break in, and arrive at both a good gas seal and good oil control quickly.

*Numbers in parenthesis designate References at end of paper.

5. It must be stable for life and maintain consistent performance.

6. It must be insensitive to varying environmental conditions, including fuel, lubricant, and atmospheric variables.

7. It must be flexible enough in performance to function under widely varying operational conditions in terms of load, speed, and acceleration.

8. The seal must have a benign effect on the other elements of the system. It must minimize cylinder and piston wear.

9. It must be tolerant of the over-all less sophisticated conditions that will necessarily prevail in field replacement.

10. It must be easy to install, both initially and in replacement.

11. It must be inexpensive in first cost due to the high level of competition in the engine business and the power generation business.

The mutual consideration of the requirements of the user and the sciences involved in satisfying those requirements demonstrates the technological complexities which exist. In any complex situation, it becomes necessary to select a limited approach. We shall consider, in this paper, the subject largely from the viewpoint of materials. The significant properties of modern piston ring materials will be presented, as related to wear and to other performance criteria. Coatings for piston rings have been evaluated by bench test procedure and will be discussed. Laboratory bench type wear and physical tests have been supported by engine tests; results will be evaluated. Typical transportation diesel piston ring arrangements will be discussed, both in general and with respect to the most significant features of each. Since the subjects of heat stability and fatigue of piston ring materials already covered in a previous publication of the author's company (2), it will not be covered herein.

Types of Wear

The subject of wear is a very complex one. Wear accounts for millions of dollars wasted every year in worn out engines. Since wear has received much attention in recent years now we have fair understanding of wear, it causes and in some instances its cure. There is even at the present time a special technical publication devoted entirely to wear. (3) It is recognized that wear is comprised of one or more of the following types:

1. Adhesive wear or galling.
2. Abrasive or cutting wear.
3. Corrosive Wear.
4. Surface Fatigue.
5. Minor types.

The first three types of wear listed above account for the major portion of wear encountered in piston rings and cylinders. These wear types have been extensively defined and described in the literature (4). Therefore, only a brief dissertation will be given here as related to piston ring wear.

Adhesive Wear - This type of wear is often called scuffing or galling. Early stages of adhesive wear are sometimes called incipient scuffing. According to the basic concept, adhesive wear occurs whenever two solid surfaces are in rubbing contact, whether they are lubricated or not. Because of the impossibility of making contacting surfaces of metals truly flat, local high points are subjected to extremely high pressures, often exceeding the yield point of one of the mating surfaces. This combined with relative sliding motion causes local welding of these high points and on continued sliding these points are sheared. This results in wear of the contacting metals and creates a local weld tear which will generate further wear as a loose particle or will reweld on the original surface and thereafter plow across the mating contact surface of the other part. This generally creates a condition most commonly called scuffing.

In studies of scuffing of chromium plated rings in diesel engines we have noted localized softening due to overheating of the metal. This is associated with incipient scuffing. X-Ray diffraction photograms, using the back reflection technique, of small discolored areas of the bearing face of the chromium plated rings indicate temperatures associated with incipient scuffing to be on the order of 1000-1100 F (Fig. 1).

Abrasive or Cutting Wear - In this type of wear the removal of metal from a surface is accomplished by a material which is sufficiently hard to scratch one or both of the mating surfaces. This scratching, sometimes referred to as scoring, can be accomplished by one of two means:

1. If a large differential of hardness exists between mating surfaces, the harder of the two may scratch the other one thus causing the softer to wear.

2. If a hard foreign particle, harder than either of the two mating surfaces, such as a particle of grit, is loosely rolled between the two mating surfaces, it will score or plow both surfaces as the two mating surfaces translate over one another. In some instances a hard foreign particle becomes lodged in a minute crack or crevice of one of the mating surfaces and protrudes from this surface sufficiently so that it

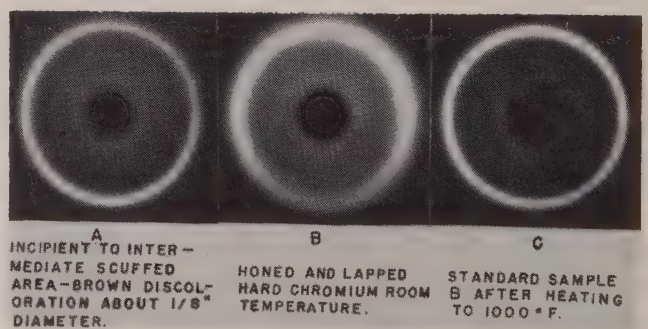
A
INCIPIENT TO INTERMEDIATE SCUFFED AREA—BROWN DISCOLORATION ABOUT 1/8" DIAMETER.
B
HONED AND LAPPED HARD CHROMIUM ROOM TEMPERATURE.
C
STANDARD SAMPLE B AFTER HEATING TO 1000° F.

Fig. 1 — Laube back reflection photograms of electrochemically plated chromium piston rings subjected to different conditions as noted: a narrowing and sharpening of diffraction ring indicated grain coarsening caused by heat, note similarity between A and C

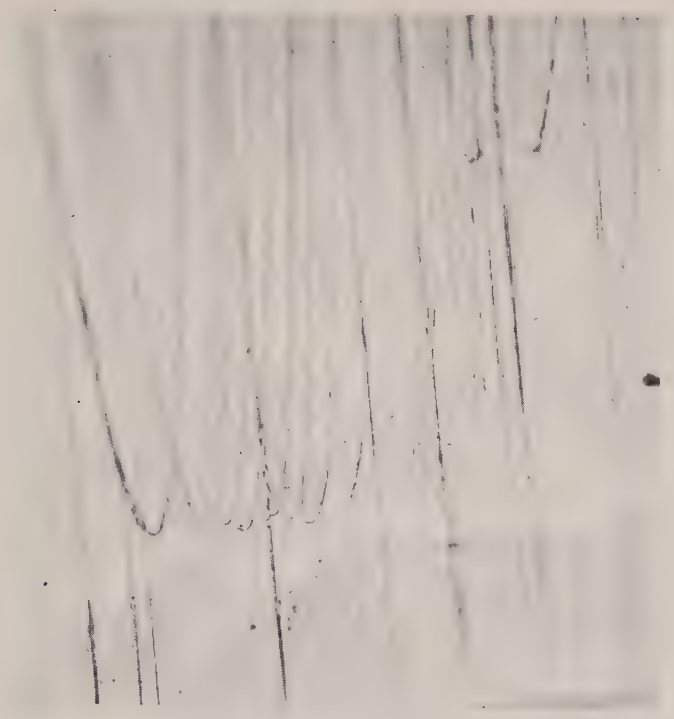

Fig. 2 — Example of abrasive wear on OD of chromium plated piston ring, 250X

scratches or plows through the other mating surface on the next stroke.

This type of wear is exhibited in Fig. 2 which shows a scratch mark on the surface of a chromium plated piston ring taken from a 4-cycle diesel engine. This scratch appears to have been caused by a single hard particle embedded in the cylinder at top ring travel. It is interesting to note that these scratch marks show the very slow rotation of the piston ring in the groove on successive strokes. It is also evident that the piston ring does not continue to rotate in the same direction but on occasion reverses direction.

Corrosive Wear - Corrosive wear takes place when a corrosive environment produces a reaction product on one or both of the rubbing surfaces and this reaction product is subsequently removed by rubbing. In many instances the corrosive by-product results in abrasive wear in addition to metal lost through corrosion.

Metallurgical Aspects of Piston Ring Materials

To meet the demand of ever increasing power and speed the piston ring industry has developed higher strength piston ring materials. Whereas gray cast iron was originally used in practically all instances, the transition has been to the malleable iron materials, to the ductile iron materials, and in some instances to specialty steels. Gray cast iron, however, has not fallen into disuse as a piston ring material for diesel engines. As a matter of fact, it still enjoys a high degree of popularity, particularly for intermediate and oil rings where operating conditions are somewhat less severe than for top compression rings.

Since gray cast iron has long been recognized as an excellent wearing material, one of the primary purposes of this paper is to examine gray cast iron from the standpoint of its various metallographic constituents and from this examination attempt to explain why it is a good wearing material. The malleable irons, ductile irons and steels will likewise be evaluated and these materials will then be compared with each other and with gray cast iron.

From Tables 1-4, it is obvious that as a family the gray cast irons have the lowest strength, the malleable rate second, the ductiles third and the steels have the highest strength. It must be admitted that the transition from gray cast iron to malleable iron has been accompanied with some sacrifice of adhesive wear properties. The ductile irons used as piston ring materials have regained some of the wear properties but not all of them. It will be seen that the adhesive wear properties of the steels, in general, are poor; however, some of the specialty steels and the eutectoid carbon steel possess some desirable wear characteristics. We will attempt to explain why these steels possess good wear properties.

Considerable research effort has gone into developing special wear resistant coatings, and special groove filling materials for irons and steels which possess borderline wear qualities. The subject of coatings and fillings will be covered in a separate section in this paper.

The piston ring industry is one of many concerned with the subject of metal-to-metal wear. Whereas gray cast iron of the unalloyed type (Table 5-A) was formerly used for practically all piston ring applications (automotive, steam, and diesel, increasing engine horsepower (BMEP) has dictated the use of higher strength materials. This has been done as a first step by utilizing two and later three types of special malleable irons: Table 5-C (pearlitic malleable) and 5-D (two hardness levels of martensitic malleable iron). The transition from gray iron to the malleables has been accompanied by an increase in piston ring strength by a factor of 3 to 4 over gray iron. Impact strength has been improved by a factor of 4 to 8 over gray iron, and the elastic modulus has been roughly doubled.

The ductile irons, Table 5-E (pearlitic ductile), has improved the strength over pearlitic malleable by a factor of about 1.5 and the impact strength by a factor of 2.6, which is roughly 17 times greater than gray iron. The elastic modulus of the ductile irons is about the same as the malleables which is approximately twice that of the gray irons.

When the irons and steels of Table 5 are arranged in order of their Modell Factor, Oberle's criterion for good wear (5), the materials fall in the order shown in Table 6.

In a broad sense, Oberle's "Modell Factor" appears to arrange materials of many different kinds and types roughly in order of their good-to-poor wear properties. However, it fails to consider metallographic material properties as they effect wear and it also fails to take the mating surface into consideration.

For example, consider the gray cast irons, Table 5-A and

Table 1 - Piston Ring Materials From The Gray Cast Iron Family (Contd.)

Maximum Allowable Transverse Stress psi	50,000	40,000	40,000 - 55,000	55,000	30,000
Transverse Modulus of Elasticity psi	12 - 16 x 10^6 at 40,000 psi	11 - 16 x 10^6 at 35,000 psi	11 - 17 x 10^6 Depending on Section	13 - 18 x 10^6	10 - 14 x 10^6
Hardness					
Section Size	R G Scale	R G Scale	R G Scale	R C Scale	R B Scale
Up to 7/32	77.5 - 91		81 - 93		
7/32 to 11/32		74 - 86	(a) 77 - 90	23 - 34	75 - 85
11/32 to 15/32		70 - 82.5	(b) 74 - 87		Bhn 137 - 176
15/32 to 5/8		66 - 79	74 - 87		
Over 5/8		57.5 - 75	68 - 84		
Impact in. lb 0.140 x 0.260 Unnotched	1.5	1.5	3.0	3.5	8.8
Coefficient of Expansion in/in/^oF	6.18 x 10^{-6}	6.18 x 10^{-6}	7.54 x 10^{-6}	7.54 x 10^{-6}	10.7 x 10^{-6}
Density lb/in.^{3}	0.256	0.256	0.264	0.264	0.264

Photomicrographs reduced in reproduction 17%. (a) section size 7/32 to 7/16 — (b) section size 7/16 to 5/8.

B; these are two gray irons both possessing the same "Modell Factor" since their hardness and elastic moduli are roughly the same. Still one material (A) is very good in wear, whereas the other (B) is a very poor wearing material. To account for this difference, a close examination and comparison of the metallographic constituents is in order.

Graphite - The graphite type shown in the photomicrograph of Table 5-A is denoted the normal flare (AFS-ASTM-Type A) graphite. It is formed from the gray iron melt at the eutectic temperature (about 2075 F) and a very noticeable amount of temperature recalescence in the cooling curve is associated with its formation. It is called normal flake graphite because the graphite is formed directly from the liquid iron during a temperature stabilization period at 2075 F. At the time of the eutectic arrest, the eutectic of austenite and graphite solidify on spherical crystallization fronts until the liquid has converted to the solid.

The graphite of Table 5-B is often called "Undercooled graphite". This type of graphite is formed on cooling as is the graphite of 5-A. However, there is no noticeable temperature recalescence in its cooling curve. Notice that in 5-B there is a very strong dendritic pattern in the structure which possesses areas devoid of graphite flakes. The dendrites of 5-B formed rapidly during cooling and the remaining liquid metal became supersaturated with carbon after the temperature of the partially solidified mass dropped below the eutectic temperature. The supersaturated liquid then suddenly ejected the excess carbon as small isolated flakes between the previously formed austenite dendrites. Tests and extensive field experience have shown the AFS-ASTM Type D graphite structure to possess poor wear properties.

The wear resistance of cylinder liners containing different graphite sizes and configurations have been tested by other investigators (6). In one such test the graphite varied from 100% AFS-ASTM Type D in one liner to various percentages of AFS-ASTM Type A graphite in additional liners. One liner contained Size 4 to 6 graphite with some AFS-ASTM Type B; another liner contained AFS-ASTM Type A, Size 3 to 4. One liner was 5150 steel. The effect of the matrix in these tests was nullified by hardening and tempering all liners so that the matrix structure of all liners were tempered martensite. The results showed the scuff resistance of the steel liner to be the lowest. The AFS-ASTM Type D graphite liner was a close second, while the liners containing the larger sizes of AFS-ASTM Type A graphite possessed the greatest resistance to scuffing. Extensive wear testing by Shuck (7) also substantiated the poor wear resistance of Type D graphite. There seems to be little disagreement among the investigators of the deleterious effect of the AFS-ASTM Type D graphite and the superiority of the larger Type A graphite.

Matrix - The matrix of both irons, Table 5-A and B, consist, upon solidifying from the melt, of gamma iron or austenite (a solid solution of carbon in iron). On cooling to room temperature the matrix structure transforms to pearlite or a

Table 1 - Piston Ring Materials From The Gray Cast Iron Family

	K-1	K-2	K-6E	K-14	#1 Ni-Resist
	100X			Picral Etch	
	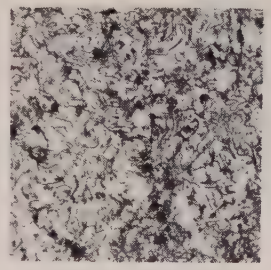		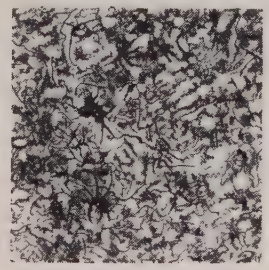	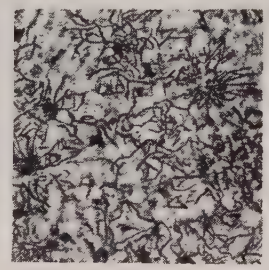	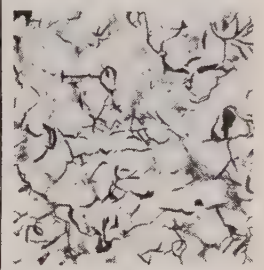
Description of Material	Unalloyed Gray Cast Iron Cast Individually in Green Sand Molds Matrix – Pearlite	Unalloyed Gray Cast Iron Cast Individually in Green Sand Molds Matrix – Pearlite	Alloyed Gray Cast Iron Cast Individually in Green Sand Molds Matrix – Pearlite and Accicular	Alloyed and Fully Heat Treated Indivi-ually Cast Iron Matrix – Tempered Martensite	A High Nickel Austenitic Gray Iron Cast Centrifugal or in Green Sand Molds
	For piston rings possessing section sizes up to 7/32 in.	For piston rings possessing section sizes over 7/32 in. up to 0.750.	For piston rings of small or large section size requiring higher strength than K-Irons.	For small or large section sizes – heavy duty service.	Used for piston rings or piston inserts where corrosion or expansivity must match aluminum.
Typical Chemistry	%	%	%	%	%
Total Carbon	3.80	3.55	3.35 - 3.90	3.35 - 3.90	2.40 - 2.80
Silicon	2.90	2.10	1.50 - 3.10	1.50 - 3.10	1.50 - 2.50
Manganese	0.60	0.60	0.60	0.60	1.25
Sulphur	0.13 Max.	0.13 Max.	0.12 Max.	0.13 Max.	0.12 Max.
Phosphorus	0.40	0.40	0.30	0.40 Max.	0.10 Max.
Nickel	--	--	--	1.10	15.0
Chromium	--	0.50 Max.	0.30	0.30	2.10
Others	--	--	0.45 Mo.	1.10 Mo.	6.50 Cu.
Mechanical Properties					
Tensile Strength (min.) psi	30,000	25,000	30,000 - 40,000	45,000	30,000
Transverse Rupture Strength (min.) psi	60,000	50,000	55,000 - 73,000	85,000	50,000

Table 2 - Piston Ring Materials from the Malleable Iron Family

100X Picral Etch

	K-Spun	F-88	K-26
	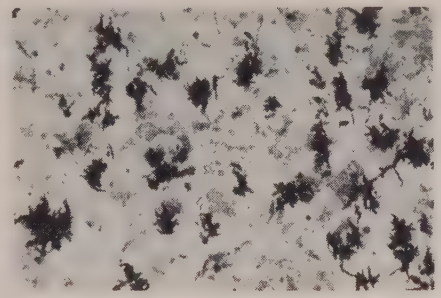	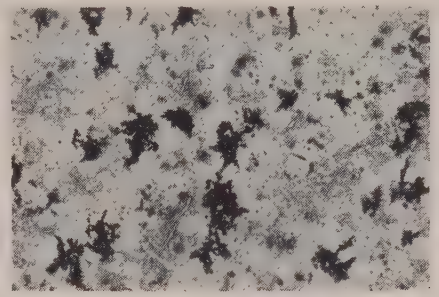	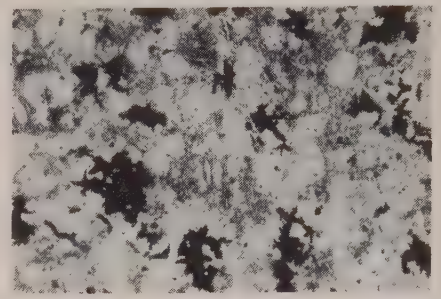
Description of Material	Unalloyed Pearlitic Malleable Iron Used for piston rings requiring high strength and impact resistance. Most generally used against hardened steel or hardened cast iron when unplated.	Alloyed Tempered Martensitic Malleable Iron Used for piston rings requiring high strength and impact resistance. Most generally chromium plated for service against cast iron or steel barrels.	Alloyed High Hardness Martensitic Malleable Iron Used for piston rings requiring high strength and impact resistance. Most generally used against chromium plated cylinder barrels.
Typical Chemistry	%	%	%
Total Carbon	2.85 - 3.50	2.85 - 3.50	2.85 - 3.50
Silicon	0.95 - 1.45	1.00 - 1.65	1.00 - 1.65
Manganese	0.75	0.75	0.75
Sulphur	0.10 Max.	0.12 Max.	0.12 Max.
Phosphorus	0.10 Max.	0.30 Max.	0.30 Max.
Copper	--	0.50	0.50
Molybdenum	--	0.50	0.50
Others	--	--	--
Mechanical Properties			
Tensile Strength (min) psi	70,000	88,000	95,000
Transverse Rupture (min) psi	117,000	146,000	130,000
Maximum Allowable Transverse Stress psi.	70,000	80,000	80,000
Transverse Modulus of Elasticity psi	$19 - 23 \times 10^6$	$20 - 24 \times 10^6$	$20 - 24 \times 10^6$
Hardness	74 - 92 R G	24 - 30 R C	40 - 46 R C
Impact Strength in. lb 0.140 x 0.260	10	10	5
Coefficient of Expansion	8.0×10^{-6} in/in/ F	8.0×10^{-6} in/in/ F	8.0×10^{-6} in/in/ F
Density	0.2625 lb/in.^{3}	0.263	0.263

Photomicrographs reduced in reproduction 10%.

Table 3 - Piston Ring Materials From the Ductile Iron Family

	K-16	K-27	K-28
	100 X Picral Etch		
	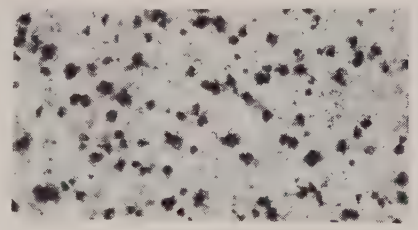	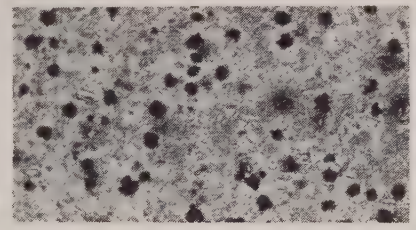	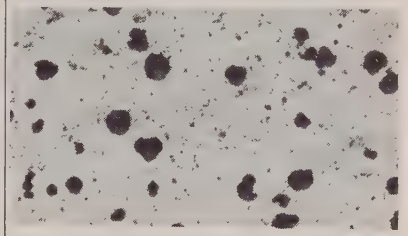
Description of Material	Unalloyed Pearlitic Ductile Iron Used for piston rings requiring high strength and impact resistance. Typical Applications: Diesel Pile Driver, Top Rings 2- and 4-Cycle Diesels 4-1/4 to 21 in. Bores.	Alloyed Martensitic Ductile Iron Used for heavy duty diesel engine applications both small and large bores. Generally chromium plated.	Alloyed High Hardness Martensitic Ductile Iron Used for direct running against chromium plated barrels of channel type. Intermediate rings and oil of small and large bore diesels.
Typical Chemistry	%	%	%
Total Carbon	3.00 - 3.65	3.00 - 3.65	3.00 - 3.65
Silicon	1.70 - 2.70	1.70 - 2.70	1.70 - 2.70
Manganese	0.50	0.50	0.50
Magnesium	0.05	0.05	0.05
Sulphur	0.03 Max.	0.03 Max.	0.03 Max.
Phosphorus	0.10 Max.	0.10 Max.	0.10 Max.
Copper	--	0.50	0.50
Molybdenum	--	0.50	0.50
Mechanical Properties			
Tensile Strength, psi	90,000	110,000	120,000
Yield Strength, psi	65,000	80,000	100,000
Elongation	3%	3%	2%
Transverse Rupture (min) psi	130,000	165,000	180,000
Maximum Allowable Transverse Stress psi	70,000	100,000	150,000
Transverse Modulus of Elasticity psi	21 - 25 x 10^6	21 - 25 x 10^6	22 - 26 x 10^6
Hardness	22 - 32 R C	24 - 30 R C	40 - 46 R C
Impact Strength in. -lb 0.140 x 0.260 Unnotched Bar (Min)	30	23	8
Coefficient of Expansion	7.4 x 10^{-6} 0.255	7.4 x 10^{-6} 0.255	7.4 x 10^{-6} 0.255

Photomicrographs reduced in reproduction 10%.

Table 4 - Piston Ring Materials from Various Steels

	SAE 9254	SAE 52100	SAE 1010 Carburized or Carbo-Nitrided	SAE 1060	SAE 1095	Nitrided Nitralloy 135 Modified	440C Stainless Steel
Description of Material	Silicon-Manganese Steel	High Chromium Bearing Steels	Low Carbon Unalloyed Steel Carburized or Carbo-Nitrided to improve Wear & Spring Properties	Medium Carbon Unalloyed Steel	Medium High Carbon Unalloyed Steel	A Special Alloy Steel Which may be Nitrided (Surface Hardened) without Quenching With Ammonia Gas	High Chromium High Carbon Stainless Steel
	Used for top rings chromium plated – small bore diesels	Used for top rings chromium plated, small bore diesel & aircraft engines	Used for oil control rings	Used primarily for fabricated steel oil control rings	Used primarily for fabricated steel oil control rings	Experimental rings in channel chromium plated barrels	Used with some success against channel chromium plated barrels
Typical Chemistry %							
Carbon	0.50 - 0.60	0.95 - 1.10	0.08 - 0.13 Carburize to about 0.90	0.65 - 0.75	0.90 - 1.03	0.38 - 0.45	0.95 - 1.20
Silicon	1.20 - 1.60	0.20 - 0.35	0.20 - 0.35	0.20 - 0.35	0.20 - 0.35	0.20 - 0.40	1.00 Max.
Manganese	0.50 - 0.80	0.25 - 0.45	0.30 - 0.60	0.60 - 0.90	0.30 - 0.50	0.40 - 0.70	1.00 Max.
Phosphorus	0.040 Max.	0.025 Max.	0.04 Max.	0.040 Max.	0.040 Max.	---	---
Sulphur	0.040 Max.	0.025 Max.	0.05 Max.	0.050 Max.	0.050 Max.	---	---
Nickel	---	---	---	---	---	Al. 0.85 - 1.20	0.50 Max.
Chromium	0.50 - 0.80	1.30 - 1.60	---	---	---	1.40 - 1.80	16.0 - 18.0
Molybdenum	---	---	---	---	---	0.30 - 0.45	0.75 Max.
Typical Mechanical Properties							
Tensile Strength, psi	220,000	237,000	215,000	160,000	215,000	145,000	285,000
Yield Strength, psi	200,000	226,000	152,000	112,000	152,000	125,000	275,000
Elongation %	9%	---	10%	13%	10%	20.5%	1.0%
Elastic Modulus, psi	29×10^6	29×10^6	$29\text{-}30 \times 10^6$	$29\text{-}30 \times 10^6$	$29\text{-}30 \times 10^6$	$29\text{-}30 \times 10^6$	30×10^6
Hardness	R C 45	R C 46.5	R C 57 - 60	R C 33	R C 57	Core RC 32 Case RC 67-70	R C 58
Coefficient of Expansion in/in/F	6.5×10^6	6.9×10^6	6.5×10^6	6.5×10^{-6}	6.5×10^{-6}	6.5×10^{-6}	6.2×10^{-6}
Density lb/in.^{3}	0.283	0.230	0.283	0.283	0.283	0.283	0.280

Table 5 - Comparison of Properties - Gray Irons, Malleable Irons, Ductile Irons, Steels

	Gray Irons		Malleable Irons	
		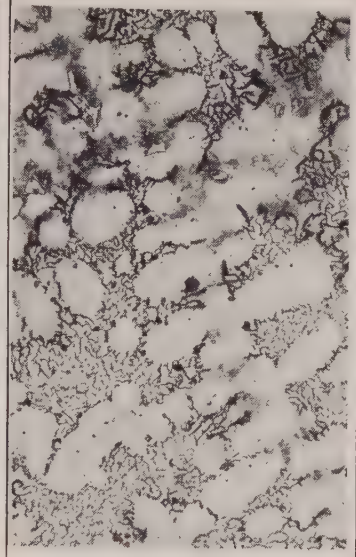		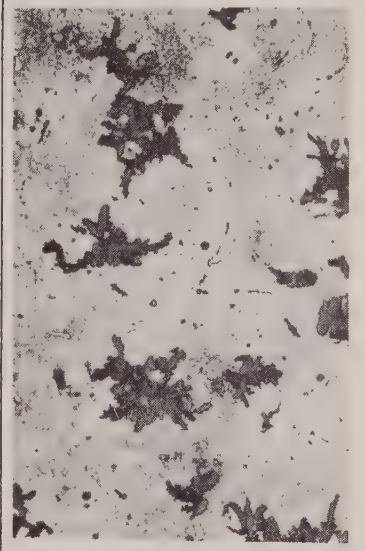
	(A)	(B)	(C)	(D & E)
	AFS-ASTM Type A 250X K-Iron	AFS-ASTM Type D 250X	Pearlitic Malleable 250X K-Spun	Martensitic Malleable 250X F-88 K-26
	A	B	C	D E
Wear Rating	Very Good	Poor	Good (−)	Good (−) Good (−)
Total Carbon	3.60	3.60	3.10	3.10 3.10
Combined Carbon	0.83	0.83	0.83	0.90 1.00
Graphitic Carbon % by % by Weight	2.77	2.77	2.27	2.20 2.10
Graphitic Carbon % by Vol	8.85	8.85	7.32	7.20 6.85
Tensile Strength Typical	35,000	32,000	92,000	105,000 144,000
Hardness	Bhn 234 R B 99	Bhn 205 R B 94	Bhn 270 R G 90	Bhn 260 Bhn 415 R C 26 R C 44
Elastic Modulus	13 x 10^6	11.5 x 10^6	22.5 x 10^6	24.6 x 10^6 24.9 x 10^6
Impact Resistance 0.140 x 0.260 Unnotched Bar	3.0	2.5	19	24 12
Density lb/in.^{3}	0.2560	0.2560	0.2625	0.2625 0.2625
Modell Factor− $\frac{\text{Bhn}}{\text{En x } 10\text{-}6}$	18	18	15	10.5 17

Photomicrographs reduced in reproduction 12%.

Table 5 - Comparison of Properties — Gray Irons, Malleable Irons, Ductile Irons, Steels

	Ductile Irons			Steels	
	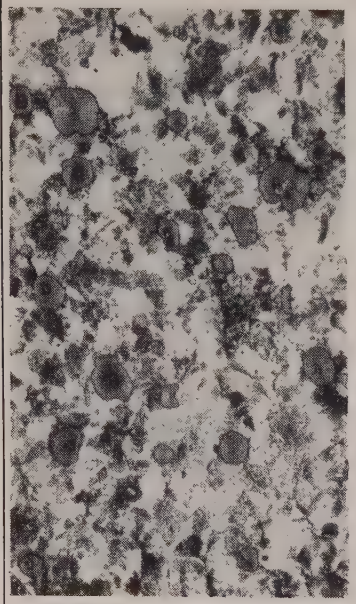	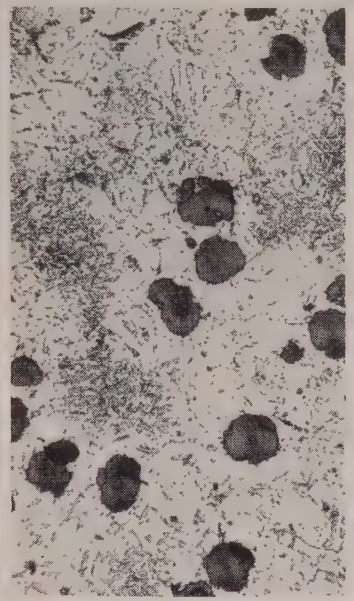		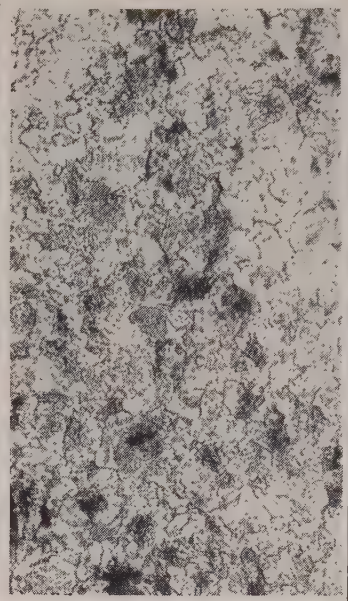	
	(F)	(G & H)		(I)	(J)
	Pearlitic Ductile 250X	Martensitic Ductile 250X		Pearlitic Steel 250X	Tool Steel 250X
	K-16	K-27	K-28	SAE 1090	
Wear Rating	F Good (+)	G Good (+)	H Good (+)	I Good wear for plain carbon steel but rates poor with the irons.	J Good (+)
Total Carbon	3.60	3.60	3.60	0.83	1.57
Combined Carbon	0.83	0.90	1.00	0.83	1.57
Graphitic Carbon %	2.77	2.70	2.60	0	0
Graphitic Carbon % by Vol	8.80	8.60	8.55	0	0
Tensile Strength Typical	128,000	138,000	150,000	115,000	300,000
Hardness	Bhn 250 R C 24	Bhn 283 R C 30	Bhn 404 R C 43	Bhn 220 R C 20	Bhn 752 R C 66
Elastic Modulus	23.0×10^6	22.9×10^6	23.4×10^6	30×10^6	31×10^6
Impact Resistance 0.140 x 0.260 Unnotched Bar	50	27	12	50	- - -
Density lb/in^3	0.255	0.255	0.255	0.283	0.304
Modell Factor $-\frac{\text{Bhn}}{\text{En} \times 10^{-6}}$	11	12.4	17.2	8	24.3

Photomicrographs reduced in reproduction 12%.

mixture of pearlite and ferrite. The interdendritic matrix material surrounding the very fine graphite is usually ferritic (pure iron or a solid solution of iron and silicon). The large dendrites of Table 5-B are usually pearlitic. The total matrix of Table 5-A is pearlitic, providing a normal cooling rate is maintained as in green sand molds, core sand, or shell molds.

Pearlite is also the eutectoid structure of steel. It contains a fixed amount of carbon (0.83%), all of which exists in the combined state as cementite Fe_3C. Cementite is a very hard and very stable intermetallic compound. The gross structure of pearlite consists of alternate platelets of the intermetallic compound Fe_3C and Ferrite (pure iron or a solid solution of iron and silicon). Cementite measures about 6.5 on Mohs scale of hardness for it will scratch Feldspar but will not scratch Quartz. On the Brinell scale it measures about Bhn 700. Ferrite is very soft, measuring only about Bhn 80.

Of all the metallographic constituents possible in plain carbon steel, pearlite is known to possess the best wear characteristics. A hypothesis is offered as to why this is so. First, pearlite is a 2-phase constituent consisting of alternate hard and soft platelets of these two materials. Any process used to rub, burnish, or polish a pearlitic structure will cause a microscopic surface relief pattern to develop such as that shown schematically in Fig. 3. When such a material is subjected to lubricated wear, the corrugated or washboard relief pattern developed at the surface serves to hold a small reservoir of oil in each small trough, thus furnishing a supply of lubricant even if the source of lubrication should temporarily be interrupted.

Pearlite wears better than other constituents of low carbon steels even under dry conditions. It is suspected that the surface relief pattern serves to hold an oxidation by-product of wear, thus it serves as a lubricant and prevents adhesive wear from occurring. Recent tests conducted in our laboratory have definitely proved that oxidation products (or by-products of wear) are in some instances lubricating. Various materials which show excellent compatibility with each other tested dry tend to gall and scuff one another when tested lubricated. The only difference has been perhaps the exclusion of the formation of an oxide in the lubricated test.

As mentioned previously, Ferrite (Bhn 80) may be the other constituent to exist as a substantial portion of the microstructure of cast iron. It is generally the matrix material which fills the interdendritic areas occupied by fine graphite flakes of Table 5-B. Ferrite has at least two strikes against it as a wear resistant material when it exists in the form of free ferrite:

1. It is soft and cannot resist penetration.
2. It is a single phase constituent which cannot develop a relief contour at the surface.

Throughout all of the many hundreds of wear tests conducted, no materials have been found to possess good wear characteristics which consist in the solid state of a soft, single phase such as the austenitic stainless steels, ferritic stainless steels, ferritic low carbon steels, aluminum, copper, or high temperature austenitic type materials (8).

Fig. 3 — Schematic sketch of pearlite showing surface relief pattern developed at surface

Consideration of Graphite and Matrix Together in Cast Iron - The graphite of Table 5-A is randomly oriented so that no large area is completely devoid of graphite; furthermore the flake size is on the order of AFS-ASTM Size 4 to 5. Graphite flake size is a manifestation of cooling rate; small sections, therefore, cool faster than large sections and possess a smaller flake size. The Type A graphite flake associated with smaller sections possess good wear properties. However, wear tests on pearlitic malleable irons and on gray irons of various graphite size show that poor wear characteristics are associated with very fine graphite (AFS-ASTM Size 8 and smaller). This is also shown in engine tests. (See Figs. 14 and 15).

The following explanation is offered to account for the difference in wear properties of these two types of gray cast iron. This theory is then extended to the malleable and ductile irons. Let us conduct a theoretical wipe test across each surface. Starting with Specimen A, a mating surface starts at the edge of the sample and moves a slight distance in. It contacts a completely pearlitic matrix and is lubricated while it passes over the long overlapping graphite flakes. The surface relief pattern of the pearlite holds the contacting surface on cementite edges and the pearlite troughs collect very slight amounts of graphite to further lubricate the mating surface as it passes. This is effective in preventing adhesive wear. Because of the long overlapping graphite flakes, no part of the moving surface fails to contact graphite or wipe across graphite as it completes its pass across the specimen. Also, the distance traversed from one graphite flake to the next is uniform and is small.

If this same wipe test should now be conducted across Specimen B, the mating surface first of all contacts a ferritic matrix, filled with very small graphite flakes. The ferrite is single phased; it is soft and the mating surface can penetrate. There are no cementite platelets or ferrite troughs to hold lubricants. The graphite, furthermore, is extremely small and possesses very little lubricating properties. Since the large dendritic areas are completely devoid of graphite, there are long distances of rubbing contact without lubrication and this starts the nucleation of adhesive wear by microscopic welding and shearing. Deterioration of this type, once initiated, will continue to progress, particularly since the remaining structure is the same.

The above explanation has been given to account for the good and poor wear properties which may exist in gray cast iron of the same Modell Factor but of different structure.

Wear Properties of Pearlitic Malleable and Pearlitic Ductile Irons - The pearlitic malleable (Table 5-C) and pearlitic ductile (Table 5-F) materials possess a matrix which is common to both pearlitic steel (5-I and the AFS-ASTM Type A graphite cast iron (5-A). The matrix, as previously described, possesses inherently good properties for wear resistance. The malleable irons, however, possess less free graphite (6.85 to 7.32% by vol) than either the gray irons or the ductile irons which possess between 8.55 to 8.85%. The graphite of the malleable irons, as indicated in Table 5-C, D and E, is derived from a high temperature malleabilizing heat treatment at which time the white iron of the ascast structure gives up its carbon to temper carbon nodules. The constituents which exist in the structure at the end of the malleabilizing treatment consist of temper carbon nodules and austenite. A controlled cooling rate after malleabilizing converts the austenite to pearlite. There are many variables which may effect the graphite nodule size and density (nodules per sq mm on a 100X screen), that is, cooling rate after casting, prequenching before malleabilizing, deoxidation practice of the molten metal, alloys added and others. Tests indicate that the most desirable graphite density for optimum wear properties lies between 80 to 110.

Graphite shape of the malleable irons may be described as nodular but not truly spheroidal. The graphite is clumped together in a ball but at the same time possesses appendages. These appendages as described by Thum and Ude (9) account for the lower mechanical properties of the malleable irons as compared to the ductile irons. However, it may be seen that this graphite, existing roughly in the shape of a ball, leaves less surface area exposed to serve as a lubricant than does the gray cast iron. The graphite configuration of the malleable irons plus the lesser quantity of free graphite than the gray irons leaves less lubricant available to lubricate a mating surface as was described in the theoretical wipe test for the gray iron, Table 5-A.

The controlled graphite density and pearlitic matrix stands in favor of the pearlitic malleables wearing well, however, because of the difference in graphite configuration, it is slightly more prone to adhesive type wear than the gray cast irons due to the longer distances existing between areas of lubrication. As previously mentioned under discussion of wear properties of the gray cast irons, free ferrite is conducive to adhesive wear. Both pearlitic malleable and pearlitic ductile irons may be produced with varying amounts of free ferrite in the matrix unless the production procedures are controlled closely. The wear properties of both the pearlitic malleable and pearlitic ductile irons are much more subject to adhesive type wear if these materials possess ferrite in the matrix. A little free ferrite closely associated with the nodules or spheroids is not generally detrimental. However, ferrite in any percentage above this leads to adhesive wear and should be avoided. Also, a burr turned up on the pearlitic malleable material is tough and strong and will tend to gall or scuff the mating surface unless removed. A similar burr on a gray iron piston ring will generally break off in a brittle manner and disintegrate into small particles which are less damaging to the mating surface. This emphasizes the need for preventing nicks or burrs with the malleable materials.

The martensitic matrix of the high hardness malleable irons, Table 5-E, is instrumental toward preventing abrasive type wear since the matrix material is hard and prevents penetration and scratching by hard foreign particles. Martensite has, however, a single phase matrix and high hardness martensite, if overheated by localized adhesive wear, can be subject to microscopic softening which may then induce further adhesive wear. The low hardness martensitic malleables are always chromium plated on wearing surfaces. These materials, however, when used under conditions of fair lubrication do well in engine service.

The Ductile Irons - The discussion regarding graphite shape of the malleable irons also applies to the ductile irons. The graphite in the ductile irons, however (Table 5-F, G and H) exist as almost perfectly shaped spheres and this accounts for the mechanical properties being substantially higher than the malleables and the gray irons. A sphere possesses the least surface area for a given volume of any other geometrical shape. From the standpoint of wear, this is a disadvantage due to less lubricity for the mating surface. However, the quantity of free graphite in ductile irons, which equals that of the gray irons, places these two materials on somewhat equal grounds in wear properties; the gray iron naturally holds the advantage in this respect because of its graphite flake configuration.

Specialty Steels - In our discussion thus far we have considered only the eutectoid pearlitic steels since this matrix material is common to the pearlitic ductile and malleable irons and the AFS-ASTM Type A graphite gray cast irons. Some of the specialty tool steels possess remarkable hot hardness properties, the ability to resist softening, even up to a red heat, the ability to maintain a cutting edge under these conditions and also the ability to resist abrasion. The steels of this type possess a high Modell Factor (24.3) due to their high hardness (67 RC) and in spite of the high modulus about 31×10^6 psi. These materials (See Table 5-J) possess excess carbide particles which in the annealed state contain high proportions of the alloying elements. These carbide particles, often called segregate, are responsible for the wear resistance of hardened high speed steel and by dissolving partially during heat treatment, provide the matrix of the steel with the necessary alloy and carbon content for hardenability, resistance to tempering, and hot hardness. Materials of this type have been shown to possess excellent dry brakeshoe type wear properties against themselves, against channel type chromium plated surfaces, against flame plated tungsten car-

bide, chromium carbides and aluminum oxide. Engine tests of piston rings made from these materials wearing against chromium plated liners show borderline scuff resistance in chromium barrels. Grooving of the tool steel rings, however, substantially decreases the scuffing tendency.

Piston Ring Platings, Coatings, and Surface Treatments

The field of platings, coatings, and surface treatments is of the utmost importance to the manufacturers of parts subjected to wear. A coating may be selected to combat any particular type of wear whether abrasive, adhesive, corrosive, or a combination of these. Coatings also enable a manufacturer of parts subjected to wear to select a base material which satisfies one requirement and a coating material which satisfies the wear requirement. For example, the proper selection of a wear resistant coating such as chromium plate enables the use of certain high strength materials such as martensitic malleable iron as a base material. The malleable iron provides the strength and the chromium provides the wear resistance. The base may also be selected to withstand high temperatures; the coating in this instance would be selected to perform under high temperature wear.

Some coatings are applied for break-in purposes. In such instances the coating is expected to be of a friable nature, and porous to hold a lubricant. Thus, more oil than normal may be supplied to surfaces rubbing against one another for the first time.

Coatings for parts subjected to wear, such as piston rings, may be divided into two general categories:

1. Wear resistant coatings.
2. Break-in type coatings.

Table 7 shows a listing of coatings, some conventional and some new to the piston ring industry. Each of these coatings have been classified according to composition, maximum service temperature F, total wear in milligrams, material compatibility rating, and tested values of coefficient of kinetic friction. The test rig used to compile these data is shown in Fig. 4. Essentially, the method of testing consists of loading the coated side face of a split piston ring against a solid ring of known composition. The solid ring is rotated and the frictional drag between mating surfaces is measured with a strain gauge linkage. Wear is measured in milligrams weight loss of the coated and solid rings, and a wear compatibility rating is given to each pair. The ratings are "Good", "Fair", or "Poor". For a pair to be rated "Good", they must possess relatively low wear weight loss and must show a smooth glazed surface. A "Fair" rating is used if the weight loss is slightly high and/or if the mating surfaces show minor adhesive or abrasive wear. A "Poor" rating is used if high wear rate is encountered or if excessive adhesive or abrasive wear is observed. These ratings are based on visual and low power binocular microscopic examination.

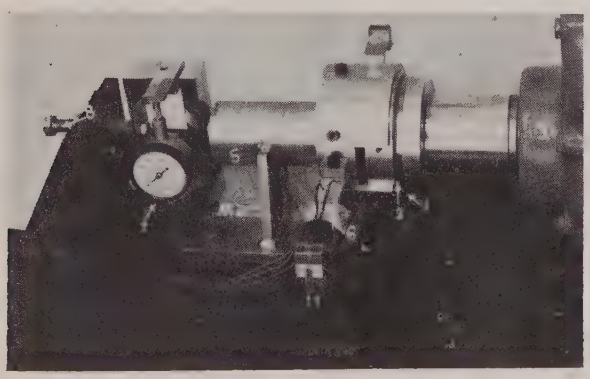

Fig. 4 — Wear and friction test apparatus

Of the coatings listed on Table 7, the hard metal type which has found perhaps the most widespread acceptance, is electrochemically deposited chromium. Surprisingly, chromium plate possesses rather poor wear properties under unlub-

Table 6 - Arrangement of the Irons and Steels in Order of Model

Material	Photo Ref. Table 5	Condition	Modell Factor Bhn / En x 10^{-6}
Alloyed Tool Steel	J	Hardened	24.3
Gray Cast Iron Type A Graphite	A	As Cast	18.0
Gray Cast Iron Type D Graphite	B	As Cast	18.0
Martensitic Ductile Iron (High Hardness)	H	Alloyed & Heat Treated	17.2
Martensitic Malleable Iron (High Hardness)	E	Alloyed & Heat Treated	17.0
Pearlitic Malleable Iron	C	Heat Treated	15.0
Martensitic Ductile Iron (Medium Hardness)	G	Alloyed & Heat Treated	12.4
Pearlitic Ductile Iron	F	Heat Treated	11.0
Martensitic Malleable (Medium Hardness)	D	Alloyed & Heat Treated	10.5
Pearlitic Steel	I	Unalloyed Pearlitic Structure	8.0

Table 7 - Coatings of Different Types

Classified According to Maximum Operating Temperatures, Dry Wear (mg. weight loss), Wear Compatibility and Coefficient of Friction

Coating	Composition	Max. Service Temp. F Oxidizing Atmosphere	Total Wear (Mg.) No Lubrication				Material Compatability No Lubrication				Coefficient of Kinetic Friction - No Lubrication			
			Gray Cast Iron (Bhn 201)	Gray Cast Iron (Bhn 432)	Chro-mium Plate	Tool Steel A	Gray Cast Iron (Bhn 201)	Gray Cast Iron (Bhn 432)	Chro-mium Plate	Tool Steel A	Gray Cast Iron (Bhn 201)	Gray Cast Iron (Bhn 432)	Chro-mium Plate	Tool Steel A
Dense Chromium Plate	Electro-lytic Chro-mium	700	78	75	-	11	Fair	Fair	-	Good	0.42	0.42	-	0.30
Sprayed Molyb-denum	Molybdenum + Carbon + Oxygen	700	16	60	327	36	Good	Good	Fair	Good	0.55	0.63	0.45	0.52
Vanderloy H	Iron Electro-plate	700	84	86	74	30	Fair	Good	Good	Good	0.40	0.47	0.58	0.47
Linde LC-1A (Cr-C)	85 Cr_3C_2 + 15% Ni-Cr	1300	48	54	-	36	Good	Fair	-	Good	0.51	0.57	-	0.39
Linde LW-1 (WC)	Tungsten Car-bide + 6-8% Cobalt	1000	33	44	-	3	Good	Good	-	Good	0.44	0.36	-	0.33
Linde LW-5 (WC)	25 WC + 7 Ni + 68 W-Cr Carbides	1200	78	51	-	12	Good	Good	-	Good	0.76	0.64	-	0.67
Plasma WC + 12 Co	Tungsten Car-bide + 12% Co	1000	12	17	-	7	Good	Good	-	Good	0.42	0.33	-	0.34
Linde LA-2 (Al_2O_3)	Aluminum Oxide	>1300	60	270	-	7	Good	Good	-	Good	0.47	0.60	-	0.51
Tungstide No. 301	Tungsten + Moly Disulphide + Silicone	600	120	25	42	81	Good	Good	Good	Good	0.09	0.08	-	0.08
Molycote X106M	Moly Disulphide + Resin + Tuluol	600	5	4	7	5	Good	Good	Good	Good	0.12	0.14	0.15	0.13
Tin Plate	Tin Electroplate	600	*	*	-	33	Poor	Fair	-	Fair	*	*	-	*
Steam Treated Cast Iron	Steam Oxidation Fe_3O_4 Coating	800	75	75	190	180	Fair	Fair	Poor	Poor	0.56	0.54	0.57	0.35
Parco Lubrite	Iron Phosphide Coating Formed In a Manganese Iron Phosphate Solution	600	24	7.8	30	34.8	Good	Good	Good	Good	0.26	0.20	0.31	0.27

*Catastrophic Wear, No data obtained

ricated bench test conditions. However, under lubricated conditions, it does exceptionally well and has been used as a wear resistant coating for top rings in many heavy duty engines.

Chromium plated rings for top grooves are often plated with porous chromium. As this term implies, the outermost surface of the chromium plated ring possesses a porosity that extends about 0.001 in. deep (see Fig. 5). The porous struc-

ture is soft and friable compared to the base chromium which possess a hardness of about 1050 Knoop. The outer porous chromium absorbs and holds oil, is of a friable consistency, and aids in engine break-in. Chromium plated rings are used in steel or cast iron cylinder bores, never in chromium plated cylinders.

Electrochemically plated hard chromium possesses an as plated hardness of about Knoop 950 to 1100 (Bhn 850-950). The extreme hardness greatly resists penetration and scratching; and this, combined with its low elastic modulus of about 15 x 10^6 psi, yields a Modell Factor of about 63.0. Electrochemically plated chromium also possesses a unique combination of high hardness, thus abrasion resistance, and corrosion resistance (10) to the sulphur type acids formed from the combustion of diesel fuels (especially the bunker type diesel fuels). For these reasons, chromium plate of the channel or pin point porosity types are being used for diesel cylinder barrels in some engines.

Hard chromium plate, when subjected to heat, will soften. From the as plated hardness of about Knoop 950 or higher, the hardness may be lowered to Knoop 550 by heating to 1220 F (Fig. 6 shows the temperature versus hardness plot for porous chromium plate). It is because of this softening tendency of chromium due to heat and the scuffing which accompanies it that we are seeking a ring coating with better high temperature characteristics.

Sprayed Molybdenum Coatings - Sprayed Molybdenum type coatings have had reported success against channel type chromium plated cylinder barrels. At the present state of development, however, this type of coating possesses poor adhesion to the base material and thus has doubtful promise as a piston ring wear resistant coating. Because its hardness is lower than chromium plate, it is doubtful that this material will wear as well under abrasive conditions.

Carbide and Oxide Coatings - Coatings of the metallic oxides and metallic carbides hold promise for piston rings

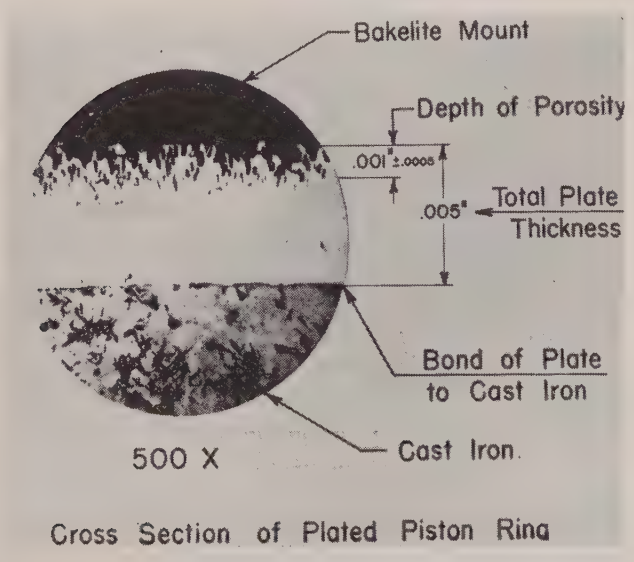

Fig. 5 — Porous chromium plate on OD surface of piston ring

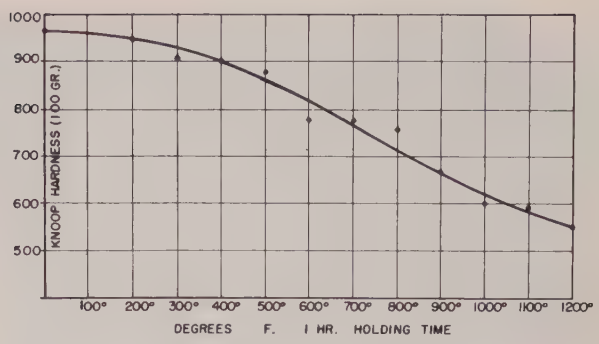

Fig. 6 — Effect of temperature on knoop hardness of electrochemically plated chromium

for high speed heavy duty engines. This is particularly true for OD coatings applied to top rings. Combustion temperatures in diesel engines exceed 3000 F. Measured and documented temperatures on the OD wearing surfaces of some top rings are on the order of 1000 to 1200 F and possibly higher under border line scuffing conditions. The metallic oxides and carbides possess metallurgical stability in these temperature ranges, they will retain their hardness which varies between VPH 1000 to 1450. Oberle's Modell Factor show Alundum (Al_2O_3) to possess one of the highest values at 143. In addition, as a general rule, these oxides and carbides possess good dry wear properties against mating surfaces of hardened tool steel and medium and high hardness cast irons. This indicates that these materials resist welding, or if welding does occur, it is of a covalent bond and is of a friable nature (11 & 12). Since these materials are compatible under dry conditions with materials commonly used for diesel engine cylinder liners, they will live and do a good job when applied to the OD wearing surface of top compression rings in high BMEP engines.

The carbide and oxide type coatings may be applied by several different methods. Some of these methods produce coatings of exceptionally good adherence to the base metal, but some do not. Also coatings of this type which have high porosity show poorly under abrasive wear as compared to the coatings of higher density.

Solid Lubricant Type Coatings - Practically all of the solid lubricant type coatings are formulations containing molybdenum disulphide as the primary constituent. Various liquid carriers are used which also serve as the bonding agent after the coatings have dried. Some of the higher temperature coatings of this type possess metallic additions such as tungsten. These additions plus a high temperature binder enable them to be used at high temperatures. Our tests show that molybdenum disulphide converts to a tri-oxide at temperatures on the order of 1000 F. The trioxide is very abrasive and this naturally produces catastrophic wear. As a general rule, the molybdenum disulphide formulations are applied over a chemically etched base, particularly the Parco Lubrite treatment for cast iron and steel.

These solid lubricant coatings, for the most part, are classified as break-in type. They are used for the purpose

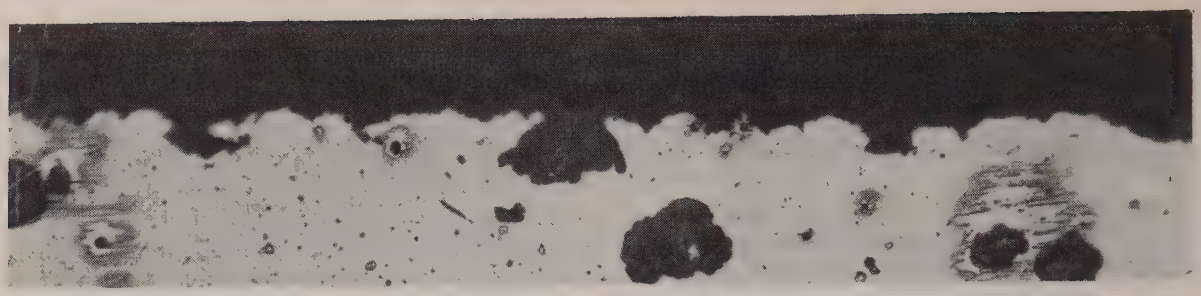

Fig. 7 — Parco Lubrite: Cross section thru treated surface showing iron phosphide coating at 500 X. Coating thickness ranges from 0.00015 to 0.00035 in.

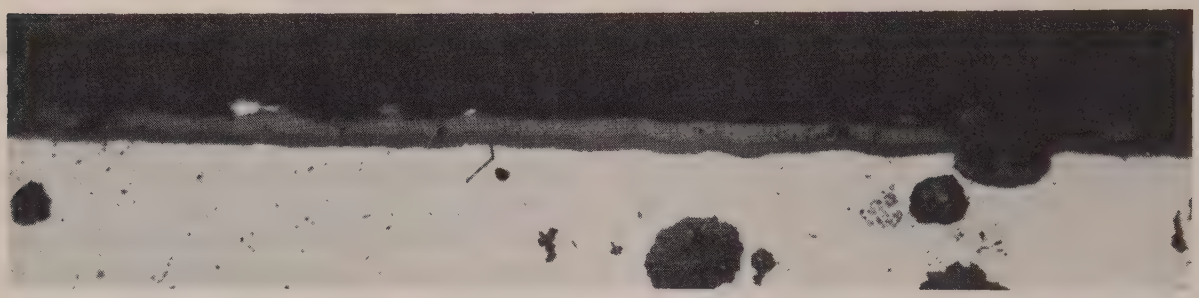

Fig. 8 — Steam treated at 1100 F for 1 hr: Coating thickness approximately 0.00035. 500 X. Note two different colored layers

of establishing compatible wearing surfaces. However, they cannot be expected to be permanent and for this reason the base metal must possess good wear properties after the break-in coating is gone. As shown in Table 7, these coatings possess low coefficients of friction, and they are successfully applied and used for certain piston ring applications for diesel engines.

Soft Metal Coatings - The soft metal coatings in general find a rather limited usage for piston rings. Soft metals such as tin plate are applied to piston rings for break-in and corrosion resistance. The soft metal allows the ring to adjust quickly to the mating surface, thereby lowering the unit bearing load.

Coatings formed by Chemical Alteration of Base Metal- Two methods presently being used for making break-in type coatings by chemical conversion of the base metal consist of (1) Steam treatment, which creates an iron oxide coating (Fe_3O_4) and (2) Immersion of ferrous parts in a manganese-iron-phosphate solution which forms a black iron phosphide type coating known as Parco Lubrite.

Both of these coatings are very thin, varying in thickness between 0.0001 to 0.001 in. as desired.

Fig. 7 shows a polished section of ductile iron with a Parco Lubrite coating varying in thickness between 0.00015 to 0.00035. Fig. 8 shows a ductile iron base material steam treated at 1100 F for 1 hr. This coating has a thickness of approximately 0.00035 in.

Fig. 9 shows friction versus speed and pressures for the Parco Lubrite treated irons, and the steam treated irons. Both coating types have been applied to several different base materials.

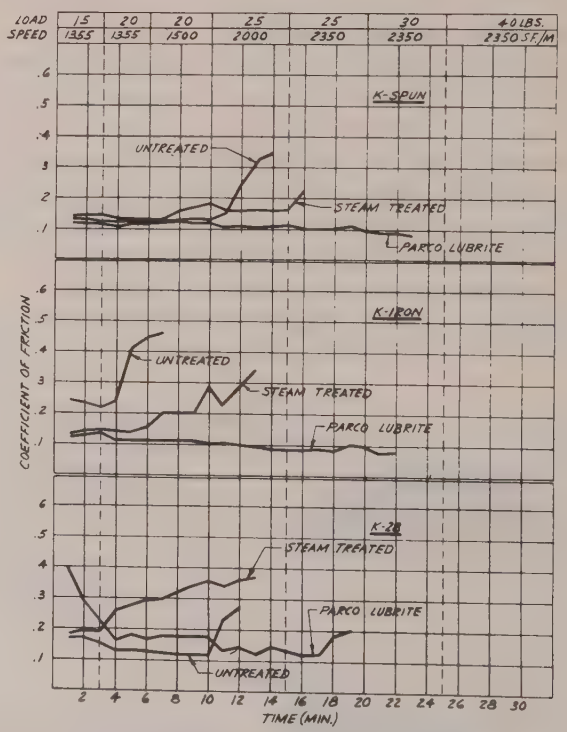

Fig. 9 — Kinetic coefficient of friction versus speed and pressure for oil absorbed parco lubrite treated irons and steam treated irons

The specimens, 3 in. dia rings, treated by the various methods to produce the coatings, were soaked in spindle oil

5 minutes and then wiped with an absorbent towel to remove all but a slight film of oil. The rings were then assembled in the test rig (Fig. 4) with one flat surface bearing against a cast iron mating surface. Unit loading between the contracting surfaces and speeds were increased as coefficient of friction was measured. This procedure was continued until the friction became excessive and/or erratic.

It is interesting to note that the highest speeds and pressures available on this test rig were insufficient to break down the Parco Lubrite coating. The steam treated samples, however, show increasing values of friction at much lower speeds and pressures.

Filled Groove Rings

Another means for reducing the scuff sensitivity of rings which have had considerable usage in certain engines is filled groove ring. Usually a material of good adhesive characteristics is mixed with a filler such as iron oxide or finely dispersed metallic or graphite particles and the resulting mixture thermo-set in multiple grooves on the OD surface of a piston ring. The filled structure is usually of a porous nature as shown in Fig. 10 and furnishes an absorptive medium for oil. The filled grooves also function to reduce the wiped axial bearing length, and carry a share of the bearing load.

Solid metals such as phosphorous bronze are also used to fill grooves on the OD of piston rings. The function of this type filling is to supply a bi-metallic bearing action with the mating surface; this results in wear reduction. (13)

Laboratory Engine Tests

Since the middle of 1958 a basic compatibility and accelerated wear test program has been conducted on a Caterpillar D318 6-cyl 4-1/2 in. bore, naturally aspirated diesel engine. The technique of accelerated wear was established by Caterpillar Tractor Co. (14). In particular, it consists of injecting two lots of 88 gr of No. 1 AC fine dust into the intake lines of the engine during 96 hr of operation at 1400 rpm and zero load. The 96 hr are broken into two 48-hr runs. The 88 gr are injected nearly uniformly during each 48 hr. Before each acceleration test there is an 8 hr compatibility test at full engine load, 96 hp, 80 BMEP at 1800 rpm. Figs. 11 and 12 show the dust feeder and part of the engine; Fig. 13 shows measurement of liners.

The program has been oriented towards establishing the basic abrasive wear relationships of the piston ring materials on iron and chrome plated cylinders, and investigation of promising ring materials for the future. The most pertinent results, which will be reported in this paper, are on top ring, liner, and ring side wear. Information is also gathered on the second, third, and oil rings but these have been of only secondary importance.

Fig. 10 — Groove filling 45 X

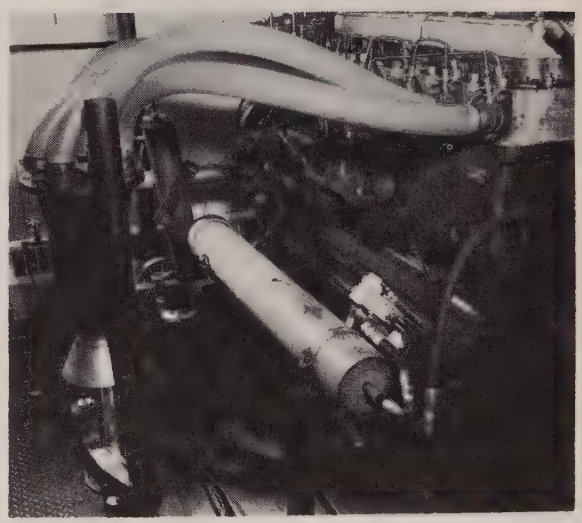

Fig. 11 — Dust feeder attached to diesel engine

It should be pointed out that this test is very specific. It includes testing abrasive resistance of the parts at moderate temperature and pressures. The results will not necessarily be pertinent for clean engines at higher temperatures and pressures but the results, doubtless, are indicative of the general wear relationships of engine materials and are supported by field experience and other laboratory data.

The test results fall into several logical categories:

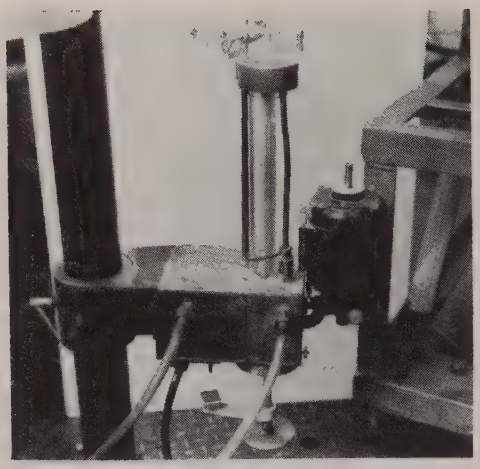

Fig. 12 — Detail of dust feeder mechanism

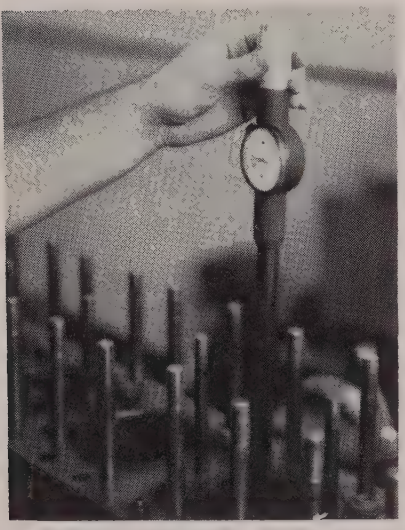

Fig. 13 — Measurement of cylinder liners with dial bore gauge

1. Iron rings in iron cylinder liners.
2. Iron rings in channel chromium plated cylinders.
3. Dense chromium plated rings in iron cylinders.
4. Experimental rings in iron cylinders.
5. Experimental rings in chromium cylinders.

Fig. 14 and 15 present individual ring and cylinder results, which are discussed in detail below.

Iron Rings in Iron Liners - Fig. 14a presents tests of various types of iron top compression rings in iron liners. The average end clearance change in 48 hr for the cases shown is 0.097 in. No attempt is made at this moment to distinguish between the various types of irons in view of the fact that there are insufficient tests for some of the irons to make a valid comparison. However, there are sufficient tests on the irons as a whole to determine an average end clearance value. Fig. 15a shows the cylinder liner wear for iron rings in iron liners to be 0.0045 in. in 48 hr as measured at the maximum wear point 31/32 in. below the top of the liner.

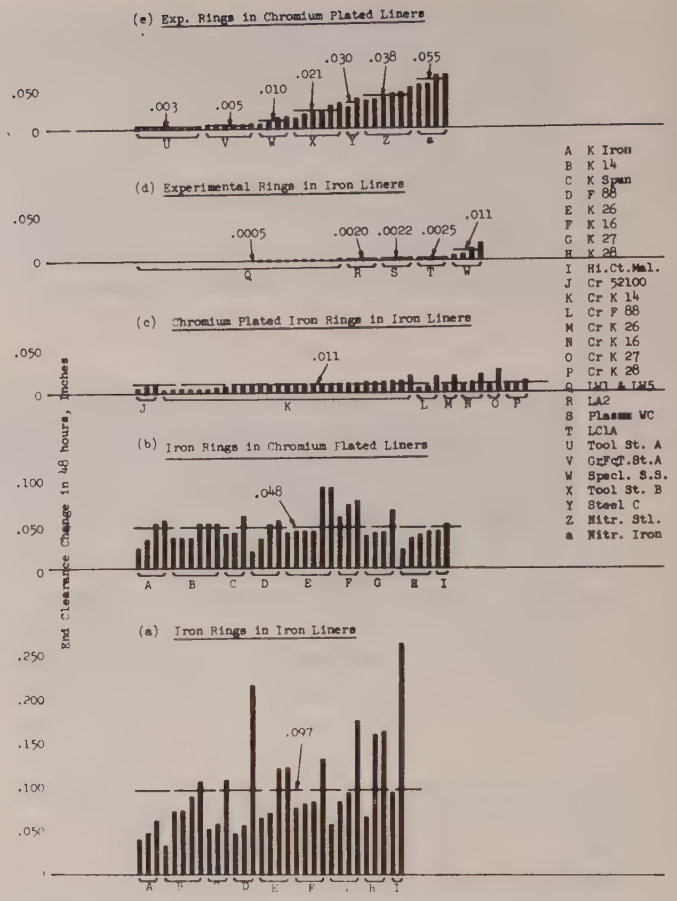

Fig. 14 — End clearance change accelerated wear tests D318 6-cyl diesel caterpillar engine

As in Fig. 14a no attempt is made to distinguish between the wear of the various types of irons due to insufficient data of any one type.

Iron Rings in Channel Chromium Plated Liners - Fig. 14b shows the end clearance changes for various iron top compression rings in channel chromium plated liners. The average end clearance change for this group is 0.048 in. in 48 hr. This is 1/2 the end clearance change for these types of rings in iron liners, 0.097 in. Fig. 15b shows the channel chromium liner wear for iron rings to be 0.0015 in. in 48 hr. This liner wear is approximately 1/3 the iron liner wear for the same type rings, 0.0045 in.

Chromium Plated Rings in Iron Liners - Since chromium plating is usually used as a facing material for top compression rings, much data have been collected on varying the base material of chromium rings in regard to its effect on face wear, if any, and its effect on side wear. It is also of interest to compare the ring and cylinder wear for chromium plated rings in iron liners with iron rings in chromium liners.

Fig. 14c indicates the end clearance change for chromium plated iron rings in iron liners to be 0.011 in. in 48 hr. It may be compared to the 0.048 in. end clearance change for iron rings in chromium liners and 0.097 in. end clearance change for iron rings in iron liners. Fig. 15c indicates

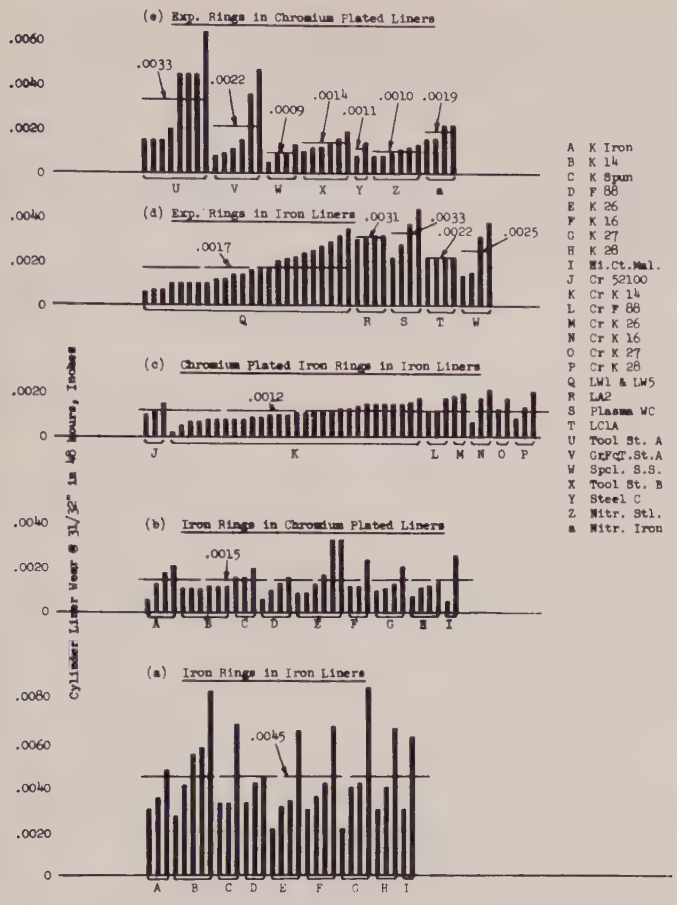

Fig. 15 — Cylinder liner wear accelerated wear tests D318 6-cyl diesel caterpillar engine

the cylinder liner wear in 48 hr for chromium plated iron rings in iron liners to be 0.0012 in. diametral wear in 48 hr. It is somewhat less than the wear of iron rings in chromium liners, 0.0015 in. in 48 hr and is approximately 1/4 the wear of iron rings in iron liners, 0.0045 in. in 48 hr.

Since the chromium plated iron rings in iron liners are at present the industry accepted standard for small bore diesel engines, the 0.011 in. end clearance change and 0.0012 in. liner wear must be equalled or bettered for a ring-liner combination to be attractive.

There are insufficient data to differentiate as to side wear occurring under the test conditions among those materials applied as the base for chromium plated rings.

Experimental Rings in Iron Liners - Fig. 14d indicates the small amount of ring wear that occurs with flame plated tungsten carbide, chromium carbide, aluminum oxide rings and a special stainless steel. The end clearance change for the LW1 and LW5 tungsten carbide plated rings is 0.0005 in. in 48 hr. This is approximately 1/20 of the chromium plated iron rings in iron liners, 0.011 in. in 48 hr; about 1/100 of the iron rings in chrome liners, 0.048 in. in 48 hr; and 1/200 of the iron rings in iron liners, 0.097 in. in 48 hr.

Fig. 15d indicates the liner wear for this group. The value of the liner wear for the tungsten carbide plated rings in iron liners is 0.0017 in. in 48 hr. This is approximately 50% greater than the chromium plated iron rings in iron liners, 0.0012 in. in 48 hr and is very slightly greater than iron rings in chromium liners, 0.0015 in. in 48 hr. However, this is very much lower than iron rings in iron liners, 0.0045 in. in 48 hr. It should be pointed out that these LW1, LW5 tungsten carbide flame plated rings are being surveyed for future use for elevated temperature conditions and additional tests in high output engines under typical operating conditions are being conducted.

Fig. 14d also shows a special stainless steel tested in iron liners with a resultant end clearance change of 0.011 in. in 48 hr. Fig. 15d indicates this special stainless steel produces an iron liner wear of 0.0025 in. in 48 hr, approximately double that of the chromium plated iron rings in iron liners, 0.0012 in. Inasmuch as the intended application of this material is in chromium liners, its performance in iron liners is of secondary importance.

Experimental Rings in Channel Chromium Plated Liners - Fig. 14e shows the end clearance changes that occur with experimental rings in channel chrome plated liners. As can be noted, extremely low wears occur with a Tool Steel A in the channel chromium liners. These end clearance changes are 0.003 and 0.005 in. in 48 hr for the solid and the grooved face designs, respectively. The corresponding chromium liner wears shown in Fig. 15e are 0.0033 in. and 0.0021 in. in 48 hr, respectively, and these are considerably higher than the 0.0015 in. in 48 hr of the irons in chromium liners.

Fig. 14e indicates that the special stainless steel previously mentioned has an end clearance change of 0.010 in. in 48 hr. This is considerably less than the end clearance change of the iron rings in chromium liners, 0.048 in. in 48 hr. Fig. 15e indicates that this special stainless steel has a chromium liner wear of 0.0009 in. in 48 hr, which is somewhat below the 0.0015 in. of the iron rings in chromium liners. Thus, this special stainless steel is attractive on both ring and liner wear and, in addition, it is reasonably wear resistant when used in iron liners, Figs. 14d and 15d. Unfortunately, this material has borderline scuff resistance, and must be altered to be attractive.

Fig. 14e shows the end clearance changes of Tool Steel B to be 0.021 in. in 48 hr. This is approximately half of the end clearance change of the irons in the chromium liners, 0.048 in. in 48 hr. Fig. 15e indicates Tool Steel B to produce a chromium liner wear of 0.0014 in. in 48 hr. This is about the same as the chromium liner wear of 0.0015 in. in 48 hr for the iron rings in chromium liners.

Fig. 14e indicates that various nitrided steels have an end clearance change of 0.038 in. in 48 hr, which is somewhat less than the 0.048 in. in 48 hr of the iron rings in the chromium liners. Fig. 15e indicates these nitrided rings produced a chromium liner wear of 0.0010 in. in 48 hr and this is approximately 2/3 of the chromium liner wear for iron rings, 0.0015 in. in 48 hr. Thus, the nitrided rings have

Table 8 - Summary of Top Ring and Liner Wear

D318 Caterpillar Diesel Engine
Dust Injection Tests

	Δ E.C.	Wear in 48 Hr Ring Side	Groove Width	Liner at 31/32 in.
Iron Rings in Iron Liners	0.097	0.0019	0.0013	0.0045
Iron Rings in Chrome Liners	0.048	0.0006	0.0009	0.0015
Cr Pltd. Ir. Rgs. in Iron Liners	0.011	0.0012	0.0010	0.0012
LW1, LW5 Plated Irons in Iron Liners	0.0005	0.0017	0.0013	0.0017
LA2 Plated Irons in Iron Liners	0.0020	0.0053	0.0030	0.0031
Plasma WC Plated Irons in Iron Liners	0.0022	0.0028	0.0012	0.0033
LC1A Plated Irons in Iron Liners	0.0025	0.0025	0.0019	0.0022
Special S.S. in Iron Liners	0.011	0.0002	0.0005	0.0025*
Special S.S. in Chrome Liners	0.010	0.0002	0.0008	0.0009*
Tool Steel A in Chrome Liners	0.003	0.0000	0.0006	0.0033
Grooved Face T.S.A. in Chrome Liners	0.005	0.0001	0.0008	0.0021
Steel B in Chrome Liners	0.021	0.0005	0.0011	0.0014
Tool Steel C in Chrome Liners	0.030	0.0016	0.0010	0.0011
Nitrided Steel in Chrome Liners	0.038	0.0003	0.0004	0.0010
Nitrided Iron in Chrome Liners	0.055	0.0002	0.0004	0.0019

*Slightly incompatible.

some attraction on both ring and liner wear.

Ring Side Wear - Table 8 gives figures on ring side wear for the various groups of top compression rings. There are enough data to indicate that the ring side wear of the iron rings is heavier in iron liners, 0.0019 in. in 48 hr, than in chromium liners, 0.0006 in. in 48 hr. The ring side wear of chromium plated iron rings in iron liners, 0.0012 in. in 48 hr, falls between the two. However, the data are too few and too scattered for each type of iron in these various groups to indicate the preference of the individual irons on side wear. The variation in side wear is doubtless considerably influenced by the amount of random rotary motion of the rings in the grooves. This motion is known to vary over

Table 9 - Wear of Ring and Cylinder Liners with all Cylinders on same Setup, over 96 hr Abrasive Wear Period

Cylinder No.	1	2	3	4	5	6
96 hr top ring wear - % of Avg.	98%	93	89	115	107	98
96 hr liner wear - % of Avg.	83	94	73	118	114	118
Combined Avg. Ring & Liner	90	94	81	117	110	108

quite a wide range due to small variations in the geometry of the motion of the piston in the cylinder.

From 30 observations of the iron rings on side wear, the side wear in the second 48 hr was shown to be at least 50% greater than the side wear in the first 48 hr.

Certain of the experimental rings used with chromium liners had very low side wear, in particular, the Tool Steel A where there was nearly zero side wear during either 48 hr period. The special stainless steel and the nitrided steel were also low on this point, 0.0002 in. in 48 hr and 0.0003 in. in 48 hr, respectively.

Single Cylinder Versus Multi-Cylinder Testing - When the testing program was formulated we intended to study only very black and white situations; situations where the wear would be reduced by a factor of at least two or three. For such condition it was thought that a single cylinder would suffice for a "yes" or "no" answer. For gray situations, it was realized—as advocated by experienced engine builders—more testing than this would be necessary. Many experienced testers have nearly zero confidence in single cylinder tests. We have frequently found the single cylinder test useful but as frequently found it insufficient. Many of our answers have been black or white for one part and gray on another. These latter require many more than a single test. Our practice seems to be evolving toward at least six tests for setups of real interest, one in each cylinder, split among at least three test periods. It will be sometime before many of the setups mentioned are so tested.

In regard to the relation of wear between the first and second 48 hr run, the second period shows, in general, about 80% of the wear of the first period. For 30 observations, the second period ring wear was 90% of the first period ring wear and the second period liner wear was 75% of the first period liner wear.

We have found that there are variations in wear among the cylinders. During one test (8/14/58) of the engine with all cylinders on the same setup, the wear of the ring and cylinder liners varied as shown in Table 9 over the full 96 hour abrasive wear period. The Table shows cylinder 4 to

be highest on wear, cylinder 3 lowest, cylinders 1 and 2 somewhat low and cylinders 5 and 6 somewhat high. We have not repeated this test to know how it duplicates results. However, during the past 2 years, cylinder 4 has frequently shown high ring and liner wear in comparison to other cylinders and frequently, but not quite as often, cylinder 3 has shown low wear in comparison to other cylinders. We suspect the general trend of the above figures still holds and thus we want to have each material, unless obviously unsatisfactory, tested on each cylinder.

Modern Diesel Engine Ring Arrangements

It is of interest to describe the piston rings and their arrangement in typical transportation diesels today. Figs. 16-27 serve this purpose. The engines have been selected to cover the general field of transportation diesels including trucks, buses, tractors, locomotives, tugs, and towboats. These engines are recently developed high BMEP machines.

Piston rings of several manufacturers are used. Many piston rings are made of proprietary materials developed by the manufacturer. Therefore, those not produced by Koppers will be identified by general metallurgical description.

At first glance, there is tremendous variety in the setups. It is not possible to select a single ring arrangement that is typical of either 2-cycle or 4-cycle engines. Behind each feature of each ring (including many characteristics not mentioned here) there is a reason. The reasons are many — experience developed on previous engines; solutions of problems at the prototype stage; correction of field problems. This paper will first establish those generalties which persist for modern high output diesel engines, and then present the most pertinent features of each setup.

Top Compression Rings - The most critical piston ring in any diesel engine is the top compression ring. It is subjected to the heaviest thermal, gas, and mechanical loads. It is subject to the most severe shock, the heaviest abrasive wear, the least lubrication, and suffers the greatest deterioration in service, both inherently and in its environment (greatest groove and cylinder wear).

The following generalities apply to top compression rings:

1. They are made of materials which have mechanical properties superior to ordinary gray iron. Superior strength, thermal fatigue, and impact resistance are required.

2. Face bearing is improved with respect to abrasion, corrosion, and/or scuffing.

3. A material of higher hardness than gray iron is used. This varies from low alloy martensitic iron Bhn 260 to dense chromium plate Knoop 1000.

4. The axial bearing width is kept narrow to maintain scuff resistance. This is established through narrow rings or face interruptions such as threading or grooving.

5. Top edge bearing is prevented due to adverse effects on oil control and scuffing. This is usually accomplished by selection of ring section. Various design technique are used such as taper facing, grooving of the back upper corner causing dishing, or tilting the top groove upward.

Intermediate Compression Rings - The intermediate compression rings fall into general categories depending upon whether the engines is 2- or 4-cycle. Introduction of intake and/or exhaust ports to the cylinder liner gives the piston and rings a valving action as well as a sealing action. Passage of rings over the ports in a 2-cycle engine, which necessarily means that segments of the ring are unsupported for a portion of each stroke, makes ring function more severe. In 2-cycle engines it is usually an advantage to make the second ring, and often all compression rings, similar to the top ring. In all cases, wear, scuff and breakage resistance are of prime concern.

The 4-cycle intermediate ring requirements are not as severe. While their function is primarily gas sealing, in high speed engines their effect on oil control is widely recognized. Bottom edge bearing is usually created, either by tapering or twisting. There is a trend to high strength materials in intermediate rings for 4-cycle engines as turbocharging produces increasingly higher BMEP.

Oil Control Rings - All engines except one of those shown have at least one ventilated oil control ring of the type with two scraping edges. They are all higher in unit pressure than is feasible with gray cast iron. High unit pressure is usually accomplished by application of abutment expanders; crimped expanders are no longer used in modern engines. Several engines create high unit pressure by utilization of a dense, high modulus material and narrow scraping faces.

General Ring Arrangements - In 4-cycle engine design through recent years, there has been a tendency to shorten pistons, decreasing the number and width of rings. The advantages of this are obvious: a more compact engine, lower friction, lower reciprocating mass, and the resulting lower bearing loads. However, the trend towards large bore and short stroke coupled with high BMEP results in increased piston thrust loads. Piston shape and fit as related to unit bearing load and rocking have become much more critical, especially with customer's desire to decrease lubricating oil consumption. These trends have kept engine, ring, and piston designers busy the last few years. It does appear feasible to design engines of this category with three compression rings and one oil control ring. However, for extremely high BMEP a fourth compression ring may be required.

Two-cycle engines appear to have reversed a trend towards three compression rings and usually utilize four. With increased charging and exhaust pressures, the upper oil ring has become primarily a gas sealing ring, with primary oil control exercised by the lower oil control rings. Piston length in 2-cycle engines continues to be dominated by the valving requirements of the piston and the necessity of preventing the upper oil ring from passing over the ports.

Discussion of Individual Ring Arrangements - Ring arrangements are listed in order by bore size. They do not

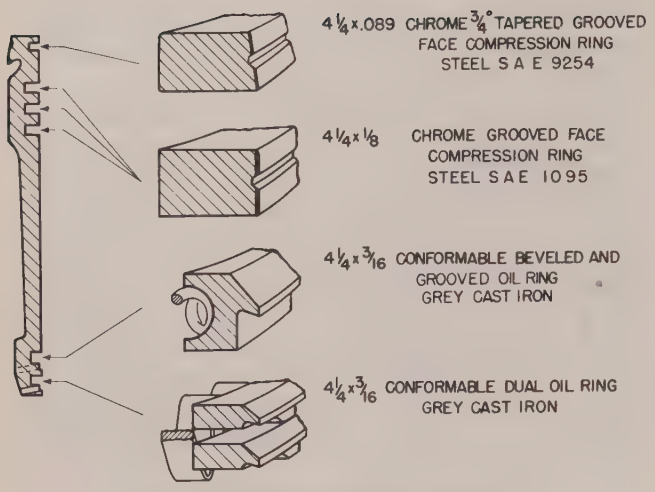
4 1/4 x .089 CHROME 3/4° TAPERED GROOVED FACE COMPRESSION RING STEEL S A E 9254
4 1/4 x 1/8 CHROME GROOVED FACE COMPRESSION RING STEEL S A E 1095
4 1/4 x 3/16 CONFORMABLE BEVELED AND GROOVED OIL RING GREY CAST IRON
4 1/4 x 3/16 CONFORMABLE DUAL OIL RING GREY CAST IRON

Fig. 16 — Supercharged 2-cycle diesel

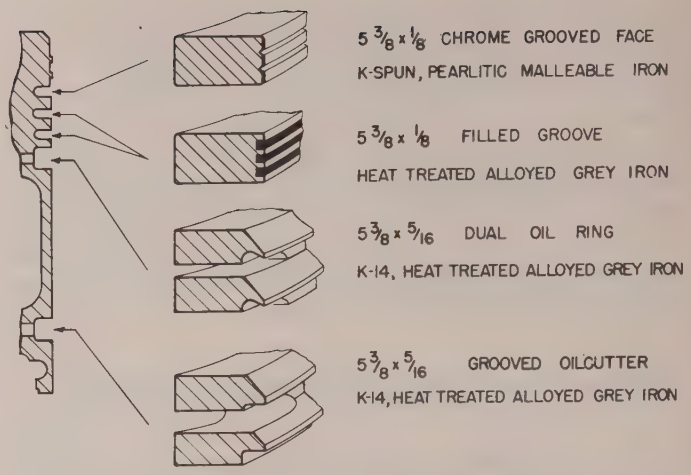
5 3/8 x 1/8 CHROME GROOVED FACE K-SPUN, PEARLITIC MALLEABLE IRON
5 3/8 x 1/8 FILLED GROOVE HEAT TREATED ALLOYED GREY IRON
5 3/8 x 5/16 DUAL OIL RING K-14, HEAT TREATED ALLOYED GREY IRON
5 3/8 x 5/16 GROOVED OILCUTTER K-14, HEAT TREATED ALLOYED GREY IRON

Fig. 18 — Turbocharged 4-cycle diesel

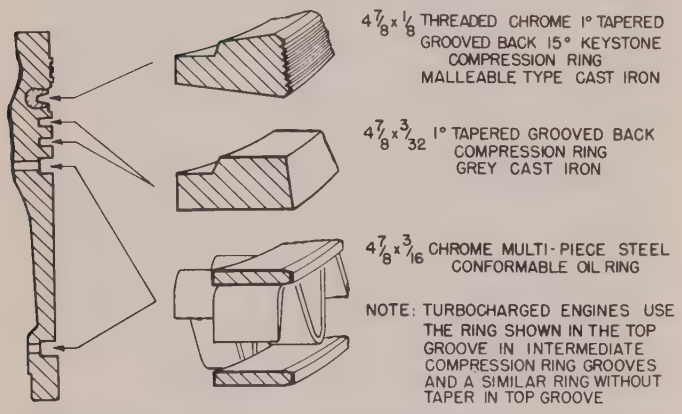
4 7/8 x 1/8 THREADED CHROME 1° TAPERED GROOVED BACK 15° KEYSTONE COMPRESSION RING MALLEABLE TYPE CAST IRON
4 7/8 x 3/32 1° TAPERED GROOVED BACK COMPRESSION RING GREY CAST IRON
4 7/8 x 3/16 CHROME MULTI-PIECE STEEL CONFORMABLE OIL RING
NOTE: TURBOCHARGED ENGINES USE THE RING SHOWN IN THE TOP GROOVE IN INTERMEDIATE COMPRESSION RING GROOVES AND A SIMILAR RING WITHOUT TAPER IN TOP GROOVE

Fig. 17 — Naturally aspirated and turbocharged 4-cycle diesel

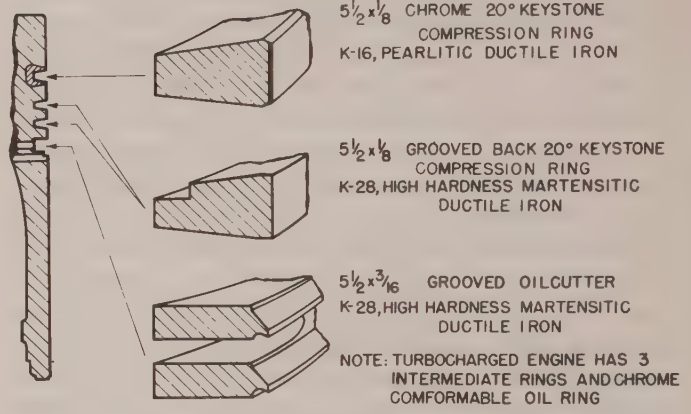
5 1/2 x 1/8 CHROME 20° KEYSTONE COMPRESSION RING K-16, PEARLITIC DUCTILE IRON
5 1/2 x 1/8 GROOVED BACK 20° KEYSTONE COMPRESSION RING K-28, HIGH HARDNESS MARTENSITIC DUCTILE IRON
5 1/2 x 3/16 GROOVED OILCUTTER K-28, HIGH HARDNESS MARTENSITIC DUCTILE IRON
NOTE: TURBOCHARGED ENGINE HAS 3 INTERMEDIATE RINGS AND CHROME COMFORMABLE OIL RING

Fig. 19 — Naturally aspirated and turbocharged 4-cycle diesel

represent the complete range in transportation diesels, but are as wide a coverage as is feasible to present in a technical paper.

Fig. 16 represents a most interesting 2-cycle ring arrangement. This engine is produced both with and without the very narrow top ring, depending upon the service requirements of the engine installation. The steel base material has been selected for its strength, and fatigue resistance. The upper oil ring groove utilizes a combination oil control and sealing ring. Note the absence of drilling behind the ring. This is for the purpose of preventing airbox pressure leakage to the crankcase. The lower oil ring consists of two independent cast iron ventilated scraping elements loaded by an abutment expander.

The arrangement shown in Fig. 17 is unique in the application of a skirt oil ring, which removes a major portion of the oil from the cylinder wall. The top compression ring applies a combination of six features, as indicated in the figure, to establish the desired performance characteristics. Other than the keystone shape, all other characteristics have been previously discussed. This keystone shape is applied to ring and groove to prevent sticking under adverse deposits.

Fig. 18 indicates an arrangement related to the type of service for which the engine is designed — high output marine application. The compression ring arrangement indicates the ultimate in scuff resistance, and the oil control is established by a multiple of unplated self-energized rings. The upper oil ring is composed of two 5/32 in. wide identical elements in a single groove.

Fig. 19 presents an arrangement for a high performance truck engine. All compression rings are high strength ductile keystone rings to insure against breakage. The ductile iron in the intermediate rings is hardened for scuff and wear resistance. The engine is built, depending upon the model, with a chromium plated ventilated oil ring with an abutment expander or a hardened ductile iron ventilated high unit pressure directional oil ring.

In Fig. 20 the ring arrangement for the only air cooled diesel military engine manufactured in this country is presented. All rings are chromium plated to control wear, since this service is extremely dusty. The use of a steel cylinder with a bonded aluminum muff results in limited scuff resistance; therefore, thread face compression rings are required.

The engine arrangement illustrated in Fig. 21 is used

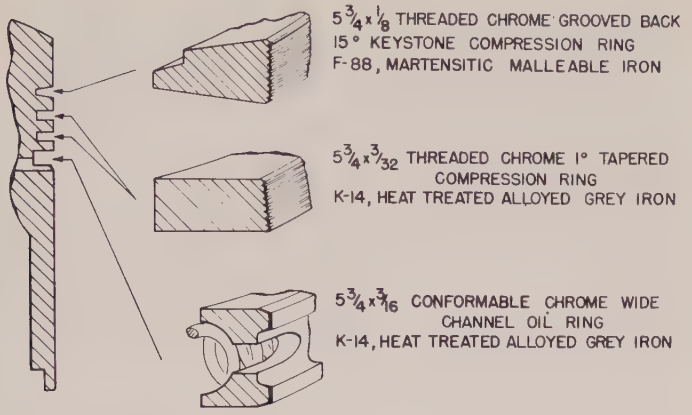
5 3/4 x 1/8 THREADED CHROME GROOVED BACK
15° KEYSTONE COMPRESSION RING
F-88, MARTENSITIC MALLEABLE IRON
5 3/4 x 3/32 THREADED CHROME 1° TAPERED
COMPRESSION RING
K-14, HEAT TREATED ALLOYED GREY IRON
5 3/4 x 3/16 CONFORMABLE CHROME WIDE
CHANNEL OIL RING
K-14, HEAT TREATED ALLOYED GREY IRON

Fig. 20 — Turbocharged 4-cycle diesel

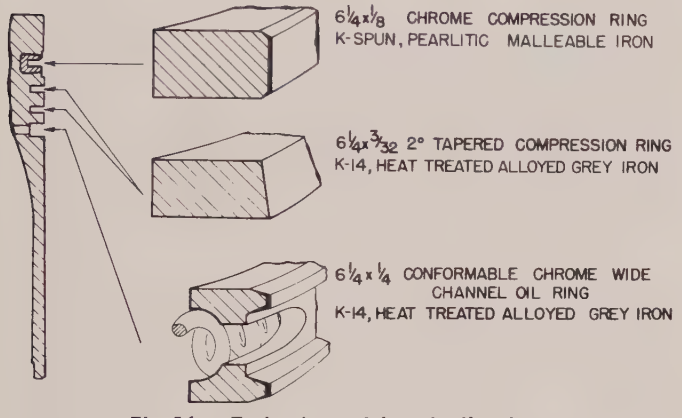
6 1/4 x 1/8 CHROME COMPRESSION RING
K-SPUN, PEARLITIC MALLEABLE IRON
6 1/4 x 3/32 2° TAPERED COMPRESSION RING
K-14, HEAT TREATED ALLOYED GREY IRON
6 1/4 x 1/4 CONFORMABLE CHROME WIDE
CHANNEL OIL RING
K-14, HEAT TREATED ALLOYED GREY IRON

Fig. 21 — Turbocharged 4-cycle diesel

largely in earthmoving equipment. The ring designs recognize the dusty operating conditions; the top compression ring has 0.010-0.012 in. chrome plate, and the conformable oil ring is also chrome plated. A cast iron insert is applied to the top ring groove to minimize wear.

Fig. 22 indicates the rings for a 2-cycle opposed piston engine used primarily in railroad and large marine service. In some cases this engine is built with chromium plated cylinders, and all compression rings are of the filled groove type. With cast iron cylinders the threaded chromium top ring is furnished. A special 2-piece sealing ring is used in the upper oil ring groove. This seals airbox pressure from the crankcase and also serves as the upper oil control ring. A single scraper oil ring is used in this engine to establish the optimum oil control for cylinder lubrication purposes.

Fig. 23 indicates the ring arrangement for the turbocharged version of a widely used railroad engine. A threaded chromium ring is used in each of the top three compression ring grooves; a tapered filled ring in the fourth groove assists in maintaining good oil control. A non-ventilated double scraper ring with bleed slots in the lower scraper is used in the upper oil ring groove, which is not ventilated. A double scraper non-directional ventilated conformable oil ring is used in the bottom groove.

The engine illustrated in Fig. 24 is used for heavy marine service. All compression rings are of filled groove type. The upper oil ring is both spring loaded and sealed joint for the purposes described earlier. A conventional hooked conform-

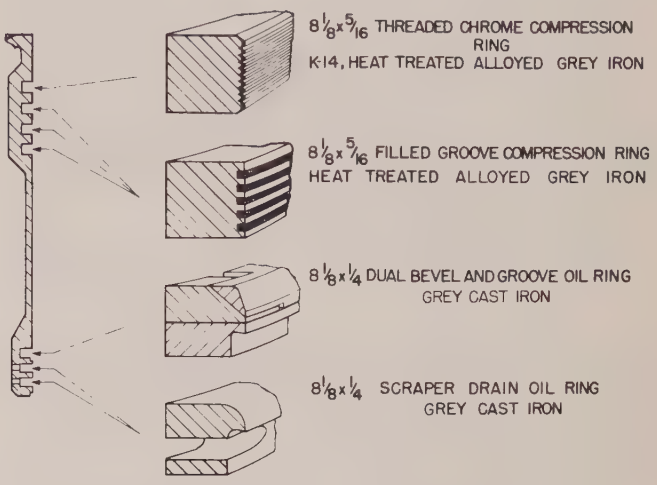
8 1/8 x 5/16 THREADED CHROME COMPRESSION
RING
K-14, HEAT TREATED ALLOYED GREY IRON
8 1/8 x 5/16 FILLED GROOVE COMPRESSION RING
HEAT TREATED ALLOYED GREY IRON
8 1/8 x 1/4 DUAL BEVEL AND GROOVE OIL RING
GREY CAST IRON
8 1/8 x 1/4 SCRAPER DRAIN OIL RING
GREY CAST IRON

Fig. 22 — Supercharged 2-cycle opposed piston diesel

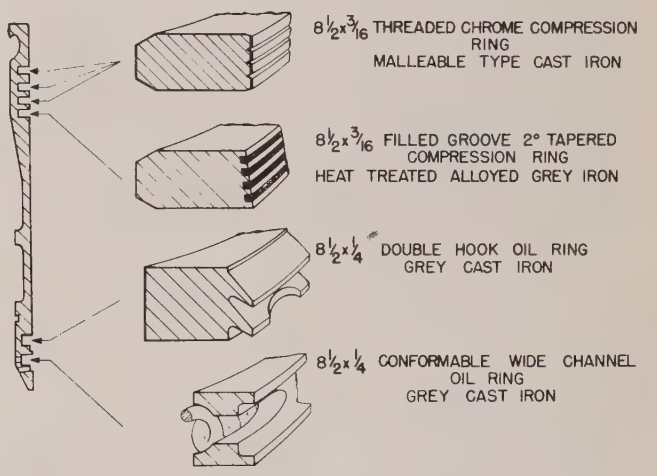
8 1/2 x 3/16 THREADED CHROME COMPRESSION
RING
MALLEABLE TYPE CAST IRON
8 1/2 x 3/16 FILLED GROOVE 2° TAPERED
COMPRESSION RING
HEAT TREATED ALLOYED GREY IRON
8 1/2 x 1/4 DOUBLE HOOK OIL RING
GREY CAST IRON
8 1/2 x 1/4 CONFORMABLE WIDE CHANNEL
OIL RING
GREY CAST IRON

Fig. 23 — Turbocharged 2-cycle diesel

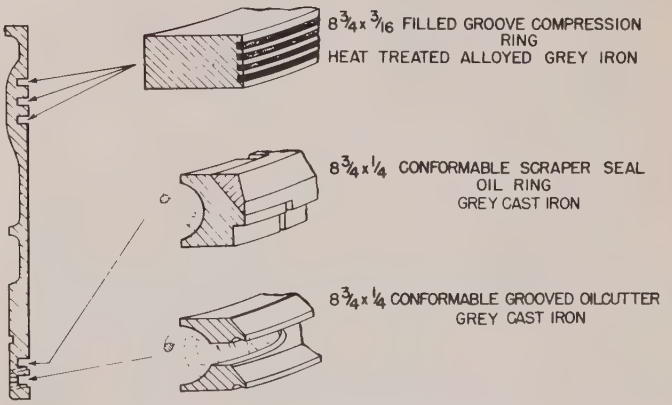
8 3/4 x 3/16 FILLED GROOVE COMPRESSION
RING
HEAT TREATED ALLOYED GREY IRON
8 3/4 x 1/4 CONFORMABLE SCRAPER SEAL
OIL RING
GREY CAST IRON
8 3/4 x 1/4 CONFORMABLE GROOVED OILCUTTER
GREY CAST IRON

Fig. 24 — Turbocharged 2-cycle diesel

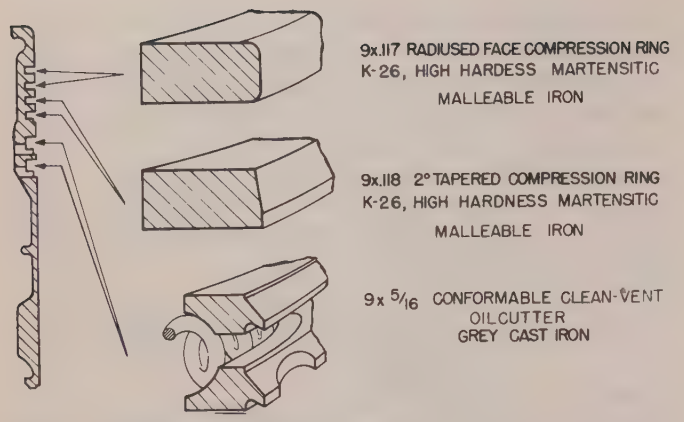

Fig. 25 — Turbocharged 4-cycle diesel chrome plated cylinder

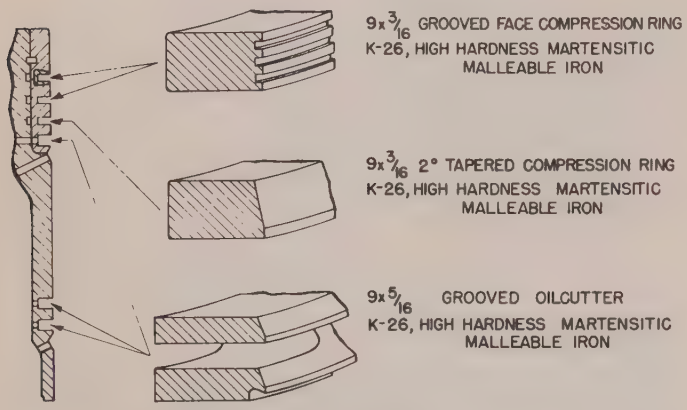

Fig. 26 — Turbocharged 4-cycle diesel chrome plated cylinder

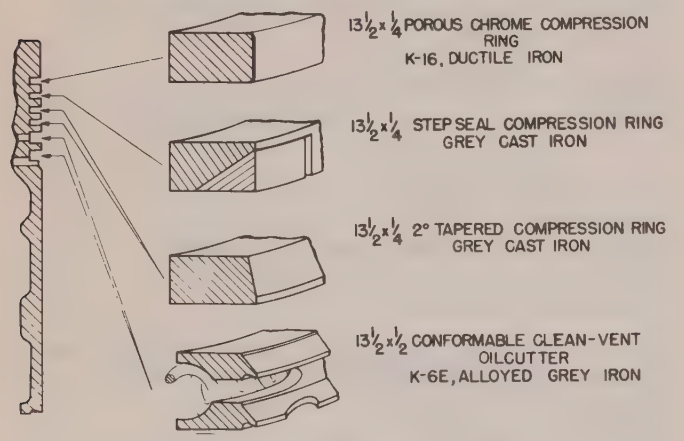
13 1/2 x 1/4 POROUS CHROME COMPRESSION
RING
K-16, DUCTILE IRON
13 1/2 x 1/4 STEP SEAL COMPRESSION RING
GREY CAST IRON
13 1/2 x 1/4 2° TAPERED COMPRESSION RING
GREY CAST IRON
13 1/2 x 1/2 CONFORMABLE CLEAN-VENT
OILCUTTER
K-6E, ALLOYED GREY IRON

Fig. 27 — Turbocharged 4-cycle diesel

able oil ring is used in the bottom groove.

Figs. 25 and 26 are both for high BMEP railroad engines utilizing chromium plated cylinders. Hardened malleable iron is used for all compression rings and in one case for the oil control ring. In the other case, a conformable ring with bleeder slots in the bottom rail is applied. These bleeder slots prevent sludge formation under dirty operating conditions.

The arrangement in Fig. 27 is for a highly supercharged and intercooled engine used for large marine installations, as well as for stationary power generation and gas pipeline service. The top compression ring is chromium plated ductile iron for breakage and wear resistance. A step seal second ring is applied to minimize ring belt and crankcase contamination. The third and fourth rings are tapered and two conformable clean vent oil rings are applied above the pin. These rings are made of a tight grain alloy iron to establish sharp narrow scraping edges not feasible with ordinary gray cast iron in this section size.

References

1. Albert Sauveur, "Metallurgy and Heat Treatment of Iron and Steel", McGraw Hill, 1916.

2. "Engineer's Handbook of Piston Rings, Sealing Rings and Mechanical Shaft Seals", Chapter II, "Fundamentals of Piston Ring Design", 3-8; Chapter XI, "Relationship of Material Properties to Piston Ring Design", 60-68. Published by Koppers Co., Inc., 1959.

3. "Wear", Elsevier Publishing Co., Amsterdam, Netherlands, published bi-monthly.

4. J. J. Burwell, Jr., "Survey of Possible Wear Mechanisms", Wear, Vol. I, No. 2, Elsevier Publishing Co., Amsterdam, Netherlands, October, 1957.

5. T. L. Oberle, "Properties Which Influence Wear of Metals", presented at AIME Meeting at St. Louis, Feb., 1951.

6. Metals Handbook. 1955 Supplement, August 15, 1955, 31.

7. A. B. Shuck, "A Laboratory Evaluation of Some Automotive Cast Irons", Trans. American Foundrymen's Society, 1948, 166.

8. E.J. Taschenberg, J.J. Brenza, J.H. Fuchsluger, R. D. Guerke, G. F. Hyde, "Evaluation of Designs and Materials for High Speed — High Temperature Rubbing Seals for Turbo Engine Application", WADC Technical Report No. 56-267, ASTA Document No. A.D. 110636, May 15, 1956. Also WADC Technical Report 56-267, Part II, Dec. 31, 1958.

9. G. H. T. Gilbert, A.M.I. Mech. E., "Factors Relating to the Stress/Strain Properties of Cast Iron", British Cast Iron Research Assoc. Journal, Vol. 6, No. 11, April, 1957.

10. W. Blum, "Electroplated Metal Coatings", Metals Handbook, 1948 Edition, 716-717.

11. A. E. Roach, C. L. Goodzeit and R. P. Hunnicutt, "Scoring Characteristics of 38 Different Elemental Metals in High Speed Sliding Contact with Steel", Trans. ASME, Vol. 78, 1956, 1659 et seq.

12. C. L. Goodzeit, "Seizure of Metal Pairs during Boundry Lubrication", Frictional Wear, R. Davies, ed. Elsevier Publishing Co., Amsterdam Netherlands, available thru Van Nostrand in USA.

13. P. S. Lane, "Wear of Diesel Engine Cylinders and Rings", Trans. ASME, Vol. 62, February, 1940, 95-110.

14. R. E. Kennemer, "Accelerated Wear Tests for Diesel Engines", SAE Journal, May, 1952, 50-53.

15. Metals Handbook, 1939 Edition, 618.

16. G. N. J. Gilbert, "Factors Relating to the Stress/Strain Properties of Cast Iron". British Cast Iron Research Journal, Vol. 6, No. 11. April 1957, Published Bi-Monthly by the Council of British Cast Iron Research Association, Alvechurch, Birmingham, England.

17. H. Morrough, "Graphite Formation in Grey Cast Irons and Related Alloys", The British Cast Iron Research Association, Journal of Research and Development, Birmingham, England: Vol. 5, No. 12, June 1955, 656. Published by Council-Alvechurch.

18. A. R. Troiano and A. B. Greninger, "The Martensite Transformation", Metals Handbook, 1948 Edition, Published by the American Society for Metals, Cleveland Ohio: 264.

19. P. Payson, "Tempered Alloy Martensites" (1958 Edward DeMill Campbell Memorial Lecture), Transactions of American Society for Metals, Vol. 51, 1959 Edition, 60. Cleveland 3, Ohio: Published by American Society for Metals.

20. C. S. Barrett, "Structure of Metals", Metallurgy and Metallurgical Engineering Series, New York and London: McGraw Hill Book Co., Inc. First Edition, 478.

21. Letter from Mr. O. I. Lemmer of the Vanadium Alloy Steel Co., Latrobe, Pennsylvania to Mr. G. F. Hyde dated November 25, 1960.

Discussion

Possibilities for Further Research

N. J. Beck
Cummins Engine Co., Inc.

THE AUTHORS are to be commended for a very timely paper summarizing piston ring materials and their wear properties.

Probably the most significant accomplishments in piston ring materials have been the development of wear resistant coatings (particularly chrome plating), high strength cast irons, and the high hardness ductile irons which exhibit good wear properties even without chrome plating. I sincerely hope that we can expect continued improvement in piston ring and liner materials until engine life between overhauls is no longer determined by piston ring or liner wear.

As part of this discussion I would like to suggest some areas for further research and development which might provide further advancement in the art of sealing combustion chambers.

Although chrome plating offers nearly a 10-fold reduction in wear rate over ordinary cast iron rings, there is no reason to believe that the optimum material has yet been found. In fact according to the authors' data, it seems reasonable to expect coatings and materials to provide another factor of ten in reduction of wear.

An area of piston ring design which deserves more attention is reduction of friction. Piston ring friction accounts for about 10 hp of engine friction in a typical truck engine. This loss amounts to over 1 kw of heat generated per cylinder. It is interesting to note that if piston ring friction could be eliminated, a cost saving of nearly $500 would be realized for 100,000 miles operation. Although piston rings and liners are performing satisfactorily in naturally aspirated engines, we are pushing them to the limit in high output turbo-charged engines. Much improvement in scuff resistance, blowby and oil control is needed before increases above about 200 BMEP are really practical.

In the detail design of piston rings, the transition from art to science has still a long way to go. The development of satisfactory piston rings remains largely empirical. The phenomenon of lubrication of piston rings has never been adequately defined; the exact forces acting on piston rings are not accurately known; detail description of ring scuffing, oil control, blow-by, and friction leaves much to guesswork.

As an example of the non-scientific manner in which piston rings are designed, the authors have illustrated the configurations of piston rings for 12 diesel engines--no two are alike. There is no other component in a diesel engine which has such a wide variation in detail design. The authors have brought us closer toward understanding why and how a piston ring works. Perhaps it can eventually be expected that pistons, rings and liners will be optimized by design based more and more on scientific facts and less on habit, superstition and folk lore.

In closing I have three questions:

1. What is the authors' opinion on the possibilities of improved wear resistant coatings other than chrome but less exotic than tungsten carbide or aluminum oxide?

2. In the authors' engine testing could the difference in wear rates among cylinders be a result of centrifugal separation affecting the distribution of dust in a manner similar to the effect on fuel distribution in a spark ignition engine?

3. Do the authors' believe that it is really necessary for 1Z engines to all use different piston ring configurations?

Authors' Closure to Discussion by Beck

THE POTENTIAL for reduction in engine friction by ring design is pointed out by Dr. Beck. Internal combustion engine designers have made considerable progress in recent years by two means:

1. Reduction in face bearing width, which allows reduced axial force from gas load and radial bearing pressure.

2. Reduction in the number of rings.

This has been accomplished with both compression and oil rings. High strength base materials, including the mal-

leables, ductiles, and steel, plus chrome plating have been required to accomplish this. Abrasive wear, unfortunately, is inversely proportional to width. Scuffing tendency, however, is directly proportional. Thus, we are faced with compromise, based on the relative values and significance of the variables at hand, and we are involved in the "non-scientific manner in which piston rings are designed" as identified by this discussor. The facts required to minimize the art involved in piston ring technology are being steadily gathered, but the application of science should be empirical for at least another generation.

Dr. Beck has asked several specific questions, which are answered as follows:

1. We believe that current materials research should make additional coatings with abrasion, scuff, and corrosion resistance available. We doubt that they will be less exotic than tungsten carbide and aluminum oxide. It is anticipated, however that these two materials and others will not be impractical, due to development of economical means of fabrication. Therefore, they will lose the exotic connotation.

2. Our dust feeder mechanically divides the dust equally to individual cylinder air inlets. Individual cylinder swirl, or air mass movement, is probably the controlling variable in wear on a cylinder-to-cylinder basis.

3. No, the engines don't all need different piston ring configurations. Two and 4-cycle engines require basic differences in design and arrangement. However, within either class pistons, cylinders, combustion, application, lubricant, fuel, maintenance, and many other variables have a major effect on ring design decisions. Even similarity for different diameters becomes specifically limiting due to the basic mathematics of piston ring design. Many similarities in ring design and arrangement do exist, but they will dominate this technology in the foreseeable future.

Concerning the Tests and Test Results

William S. Kenyon, Jr.
Detroit Diesel Co.

THIS PAPER is an excellent contribution to the never-ending search for more scientific approaches to the development of piston rings. This is especially true of the section dealing with the fundamental aspects of wear and metallurgy. Since I am not a metallurgist, I will confine my comments and questions to the portion of the paper dealing with tests and test results.

As a matter of interest, I would like to ask the authors to furnish, if possible, the following additional information:

1. What was the type of surface finish, the surface roughness, and the hardness of the iron liners used in these tests?
2. What was the piston ring groove material?
3. Were the stainless steel rings made from one of the more common types such as 440C and what was their hardness?

The authors have stated that ring coatings of the metallic oxides and metallic carbides hold promise for high speed heavy duty engines. This is partially supported by their test results which show very low ring face wear with the tungsten carbide faced rings. I wonder, however, if they feel that these coatings have practical application for volume usage at the present time or in the near future. In considering these coatings, we have found that the cost for applying them is too prohibitive to make their use practical at the present time.

It has been our experience that some stainless steels have sufficiently improved high temperature properties to make them attractive from this standpoint without an excessively high cost penalty. It was, therefore, interesting to note in this paper that stainless steel rings also appear to have reasonably good wear properties. It was further pointed out, however, that the material must be altered to be attractive from the standpoint of scuff resistance. I would like to inquire as to what specific alteration or alterations might be made.

One must agree with their decision to settle on multi-cylinder rather than single cylinder testing. I wonder if an analysis has been made as to the reasons for the wear being generally higher during the first 48 hr test period as compared to the second 48 hr period.

In closing I would like to comment on the excellent job the authors have done in discussing and presenting pictorially the different ring arrangements currently in use by the various engine manufacturers. It is most interesting to be able to make this direct comparison.

I would again like to congratulate the authors on a very fine paper and thank the chairman for the opportunity of presenting this discussion.

Authors' Closure to Discussion by Kenyon

REFERRING to Mr. Kenyon's paragraph 3:

1. The type of surface finish is a honed cross-hatched finish. Surface roughness is about 20 Mu in. Hardness at surface is about 50 RC, at 0.008 in. depth, about 20 RC and at base (about 0.016 in. deep) about 95 R_B.

2. The groove material is believed to be centrifugally cast grey cast iron (equivalent to Koppers K8).

3. A modified 440C with additions of Mo and V was used. Hardness was 65 RC.

Referring to Mr. Kenyon's paragraph 4: We are presently working not only on the development of these materials to run properly in engines but also on means to supply these rings at an attractive cost. These coatings, of course, will be more expensive than chromium plated piston ring but not excessively so.

Referring to Mr. Kenyon's paragraph 5: The alterations

mentioned will be in mechanical and/or chemical constituents, the latter referring to changes in amounts of Mo and V.

Referring to Mr. Kenyon's paragraph 6: We believe this is a matter of wearing off the high points of both the ring material and the liner material and the lower wear rate thereafter.

Comments on Metallurgical Aspects

Dallas Lunsford
Perfect Circle Corp.

DISCUSSER'S Comment: The authors state, "Wear accounts for millions of dollars wasted every year in worn out engines," To say that wear accounts for millions of dollars each year in maintenance and replacement of engines is one thing, but to say that it is wasted is another. Most engineers and engine builders are constantly working to provide the best known materials, designs, and workmanship to promote the longest possible life of their product consistent with the economic requirements.

Authors' Reply: No comment.

Discusser's Comment: "Metallurgical Aspects of Piston Ring Materials" - This section refers to Oberle's "Modell Factor" and indicates that it does not hold true, particularly for two gray irons A and B shown in Table 5. The statement is made that these two materials have the same "Modell Factor", yet A shows good wear and B poor wear. Several wrong assumptions are made for these two materials and in particular for material B. (There is no question about material B being poorer with respect to scuffing and wear resistance.) We wish to comment as follows:

a. The combined carbon of 0.83% for both materials is incorrect. This percentage is only true for a plain carbon steel of eutectoid composition.

Authors' Reply 2a: With regard to the materials A and B the combined carbons of the specimens from which these were taken were 0.81% exactly. I have stated in the paper that "The interdendritic matrix material of Spec. B surrounding the very fine graphite is usually ferritic (pure iron or a solid solution of iron and silicon)." In light of this the combined carbon of this specimen could easily be 0.6% or even 0.5%.

2b Discusser's Comment: The inference is made that the matrix of both materials is pearlitic, and therefore the only difference is in the graphite. It is obvious that considerable free ferrite is present in material B which would have a very detrimental effect upon its scuff and wear resistance. This is acknowledged later in the paper, but the early statement is misleading.

Authors' Reply 2b: The discusser's statement is incorrect. The three subsections entitled Graphite, The Matrix, and Consideration of Graphite and Matrix Together in Cast Iron, all discuss in turn the pertinent characteristics of Material B. Together, these three paragraphs relate metallographic structure to scuff tendency, and definitely indicate the significance of free ferrite.

2c Discusser's Comments: The data showing a modulus of elasticity of 11.5×10^6 psi for Material B is contrary to all factual data and experience, particularly with regard to piston rings. A piston ring material having a microstructure similar to that shown for B Table 5 would have a modulus of elasticity more in the order of 17×10^6 psi. Making this one change in the calculations would give a "Modell Factor" of 12 and place this material more nearly in proper position with regard to the arrangement shown in Table 6.

Authors' Reply 2c: Perhaps the modulus value for the specimen B is lower then typical for this type of structure, although it is a real value. Usually when the modulus is raised, the hardness for cast iron sections of this type is also. Therefore, the "Modell Factor" remains reasonably the same for type A graphite irons and Type "D" graphite irons. Referring further to Ref. (7), Heats 312 and 378 specifically show lack of correlation of Modell Factor and wear rating. In fact both heats show a poorer wear rating with increased Modell Factor.

It was also mentioned by the Authors' during the discussion that gray cast iron does not possess a true elastic modulus. Gray cast iron is not an elastic material and the elastic modulus changes with different values of stress. It is necessary, therefore, in the piston ring industry to specify the stress of a piston ring part in order to obtain a given elastic modulus.

This is illustrated in the Fig. A which shows the changing values of elastic modulus for the two gray cast irons K-1 and K-2, as compared to the malleable irons K-Spun, F-88 and K-26 which show constant elastic moduli values up to their yield points. The two steel materials K-60 and K-61 also possess true elastic properties as shown. Because of this non-elastic property of gray cast iron, possessing no true elastic modulus value it is possible that the Modell Factor should not be used to rate gray cast iron on wear.

2d Discusser's Comment: With regard to the description of the graphite structure of materials A and B, it is the type

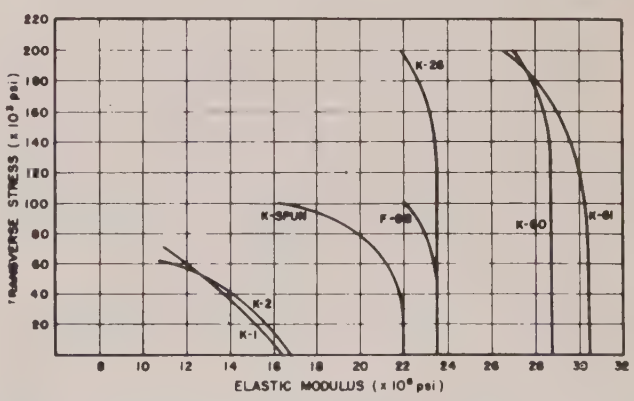

Fig. A — Change in transverse modulus of elasticity with increased stress for different piston ring materials

D (undercooled graphite) which would be considered as eutectiform, rather than that shown for material A.

Authors' Reply 2d: The term "eutectiform" is used in the paper to describe the structure shown for material A in the paper. This expression was used by the authors' to attempt to define the AFS-ASTM Type A graphite structure as was described by Morrough (17) where he states, "It seems now generally agreed that the normal flake graphite arising from the eutectic transformation is deposited directly from the liquid and not indirectly as a result of carbide decomposition". The term "eutectiform" seems to us to clearly describe the formation of the type A structure as described by Morrough - graphite formed from the eutectic.

Morrough uses the term "undercooled" to describe the type D structure and the term "Normal Flake" to describe the type A structure.

As pointed out by Mr. Lunsford, however, the term "eutectiform" has had prior usage to describe the type D graphite structure. For this reason this term as used in the paper is confusing and will be changed to read either "Normal Flake" or "Type A" graphite cast iron.

Discusser's Comment: "The Matrix" - The statement that pearlite contains a fixed amount of carbon (0.83%) is true only for a plain carbon steel as mentioned earlier. The eutectoid composition of pearlite in cast iron is somewhat lower (more in order of 0.65% carbon) and varies with respect to the silicon content, assuming normal cooling and solidification. It might also be mentioned that the hardness shown in this same paragraph for "ferrite" will vary somewhat in accordance with the silicon content.

Authors' Reply: The classic definition of a pearlitic cast iron is stated to be as follows (15): "Pearlitic iron is cast iron with a pearlitic matrix. So defined, any iron containing from 0.60 - 0.90% combined carbon is a pearlitic iron. With regard to the hardening effect of silicon in ferrite, this is well known.

Discusser's Comment: "The Matrix" - The statement is also made that of all the metallographic constituents possible in plain carbon steel, pearlite is known to possess the best wear characteristics. This seems to completely ignore the fact that in nearly all applications of steel components where wear resistance is a requirement, the part is heat treated to provide a higher hardness, martensitic microstructure.

Authors' Reply: The inference here was to convey the thought that of all metallographic constituents possible in plain carbon steel (0.90% carbon and below) that pearlite possesses the best adhesive wear characteristics. The intent was to point out that for the best wear properties ferrite should be avoided.

I cannot agree with Mr. Lunsford that we have completely ignored the excellent wear properties of fully hardened steels. This is so stated in the paper under the discussion of Specialy Steels which states that, fully hardened alloy steels possess excellent abrasive wear characteristics. These steels possessing a hardness on the order of 67 RC and a Modell Factor of about 24.3 possess excellent dry brake-shoe type wear properties against themselves, against channel type chromium plated surfaces, against flame plated tungsten carbide, chromium carbides, and aluminum oxide.

Discusser's Comment: "Wear Properties of Pearlitic Malleable and Pearlitic Ductile Irons" - The statement is made that optimum wear properties are obtained with a graphite density in the range of 80 - 110 nodules per sq mm. Undoubtedly this refers only to the pearlitic malleable material and not to pearlitic ductile material, although it is not so clearly defined.

Authors' Reply: We had assumed that since these comments were under a section referring exclusively to malleable irons that it was clear that it referred only to the malleables. We wish to affirm that Mr. Lunsford's speculation is correct on this point. We would like to add; however; that although this statement was meant to apply only to the pearlitic malleable irons, we have found a similar deleterious effect on the wear properties of the ductile irons when the graphite density becomes very large with small graphite.

Discusser's Comment: "Wear Properties of Pearlitic Malleable and Pearlitic Ductile Irons" - Reference is also made in this section to martensite as being a single phase matrix, and therefore as previously stated earlier in the paper for single phase matrix, indicates that martensite is not a good microstructure for scuff and wear resistance.

First, we wish to take exception to the statement that martensite is a single phase matrix. We believe it to be quite similar to the phases in pearlite, except that it consists of extremely fine or minute distribution of the Fe_3C constituent. We do agree that the martensitic structure is more readily annealed, or in case of the cast irons, a second stage graphitization takes place more readily under conditions of high temperature than with the normal pearlitic structures.

Authors' Reply 6a: Martensite of the iron-carbide system is defined by Troiano and Greninger (18) and Barrett (20) as a constituent possessing a body centered tetragonal lattice. Certainly no additional words need be said to prove that martensite as a metallurgical constituent is single phased.

Tempered martensites, however, do possess precipitated carbides. In the unalloyed and low alloyed steels and cast irons the precipitation of these carbides result in softening of the matrix material as was stated in the paper and this often results in the initiation of adhesive wear and scuffing. Mr. Lunsford states that "He agrees that the martensitic structure is more readily annealed". We would like to point out that in the Specialty Steels also stated that these steels possess remarkable hardness stability to temperatures as high as 1000 to 1100 F. With regard to the hardness stability of these materials and the issue pertaining to martensite, Mr. O. I. Lemmer (21) reports as follows:

"The rigorous definition of martensite as a single phase constituent which exists as a super-saturated solid solution of carbon in ferrite holds specifically for unalloyed marten-

site in the as quenched condition. During tempering, iron carbide is rejected from the solid solution. This results in minor softening and reduction of the tetragonal lattice structure. Depending upon the extent of tempering, these reactions continue until the rejected carbide becomes visible microscopically and the lattice dimensions are congruent with ferrite. Nevertheless, it may be considered that martensite itself is still a single phase exclusive of the precipitated carbide.

High speed steels show a parallel but somewhat complex reaction on tempering, partly because a significant amount of austenite is retained after quenching. Consequently, during tempering, two reactions occur simultaneously; the first is the softening and carbide precipitation described above, while the second is a conditioning of the retained austenite.

Considering the primary martensite only, its softening does not proceed continuously with higher tempering temperatures. Actually, the iron carbide, which is the first carbide rejected during tempering, redissolves as tempering temperatures approach 600 F and a more complex alloy carbide precipitates in its place. The rejection of this secondary carbide increases the hardness of the structure up to the tempering temperature of approximately 1000 F.

This reaction alone does not account for the significant increase in hardness observed at temperatures in the neighborhood of 1000/1100 F. Actually, transformation of the conditioned austenite to martensite during cooling from the tempering temperature accounts for most of the hardness increase. The change in the primary martensite manifests itself metallographically as a darkening of the previously undefined matrix."

6b Discusser's Comment: The authors' are apparently not convinced about the better scuff and wear resistance of pearlite. In the section discussing various piston ring combinations and applications, reference is made to the ultimate in scuff resistance where the top ring is chromium plated and all the unplated rings are given a full heat treatment to provide a martensitic structure. Reference is also made to the fact that all the intermediate rings are hardened for better scuff and wear resistance.

Autnors' Reply 6b: The discusser assumes that the authors' have related the ultimate in scuff resistance to the base material of the rings involved inasmuch as he is discussing base material structure. This is not true. It is associated with the utilization of:

1. Grooved face top chromium plated rings.
2. Filled Groove Intermediate rings.

Both of these ring configurations are highly scuff resistant and widely accepted as such.

The eleven arrangements shown obviously indicate the need to balance ring material properties and design factors for the application, we are not advocating the universal use of pearlitic irons.

With reference to Mr. Lunsford's next comment, the application called for a material to resist breakage, hence the selection of ductile iron. The effectiveness of hardening malleable and ductile irons to control scuffing and abrasive wear is well accepted.

By-Pass Engine Noise

F. B. Greatrex
Rolls-Royce, Ltd.

This paper received the
1960 Wright Brothers Award.

FOR SOME TIME it has been generally agreed that the next generation of civil transport engines should be jet engines of low jet velocity. We as a firm are flattered to note that it is now also agreed that these engines should be of the by-pass type which we have pioneered. A diagrammatic view of this type of engine is shown in Fig. 1.

As far as its jet noise is concerned, the noise has got to be determined from a central hot jet of moderately high velocity which may be surrounded by an annular cool jet of rather lower velocity. For optimum thermodynamic performance these two jets must be mixed and allowed to discharge at a uniform velocity through a single nozzle. But this mixing process is precisely that which produces jet noise. Thus, it is not immediately obvious that this is also the optimum arrangement for minimum noise. It might, for example, be quieter to discharge the two jets through two separate nozzles. We must, therefore, examine this mixing process carefully in order to find the optimum arrangement.

Jet Mixing Processes

In the general case, where a central jet of velocity Vj is surrounded by an annulus of air of infinite extent, having a velocity Va, the significant part of the mixing region is that shaded in Fig. 2. The outer boundary of the mixing region spreads at an angle θ to the axis, and the inner boundary spreads at an angle ϕ to the axis, where θ and ϕ vary with the ratio of Va to Vj, as shown in the lower diagram. This simplified picture is not by any means a com-

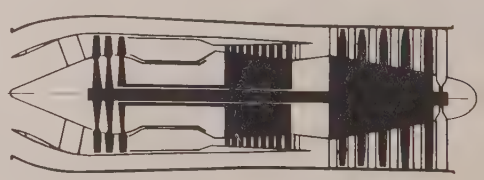

Fig. 1 — Schematic of by-pass engine

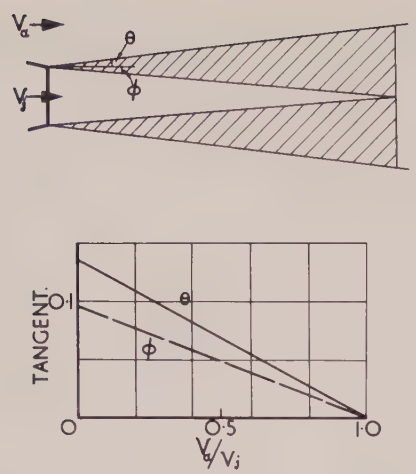

Fig. 2 — Mixing of high velocity jet in low velocity air

pletely true picture of the spread of a jet in air (1)*, but it is sufficiently accurate for our purpose in examining noise. It can be seen that when Va is zero the core is about 5 diameters long, whereas when Va = Vj there is no mixing and the core is infinitely long (neglecting temperature effects).

It is generally agreed that most of the jet noise is generated in the initial part of the mixing region up to the end of the core of unmixed jet, and that the noise per unit length of the jet is constant in this region (2, 3). For out purposes it is good enough to assume that all the noise is generated in this region and none downstream of the end of the core. We would then expect the noise of this jet to be related to its core length, as well as to its area and relative velocity, that is a relationship of the form

$$\text{noise} \propto Aj \times \text{core length} \times (Vj - Va)^n \qquad (1)$$

where n is around 8 to 10. The only new feature of this expression is the dependence of the noise on the core length. It seems reasonable to bring in the core length in this way, since the volume of the mixing region is also proportional to Aj x core length. Before we use this expression to examine the noise of a by-pass engine, its validity should be checked as much as possible.

NOISE IN FLIGHT AND ON GROUND - One obvious check is to compare noise measurements made on a jet engine on the ground where Va = 0, and in flight where Va = the flight speed. Fig. 3 shows this comparison for all the tests we have made of noise from an Avon engine in a Canberra as it flies overhead (4). The line on this graph is derived from the best mean line through all our ground test points of the peak overall sound pressure level heard by an observer walking along a line 500 ft from the axis of the jet engine. To be exact, it is a line 5 deg from this to allow for the fact that over the range

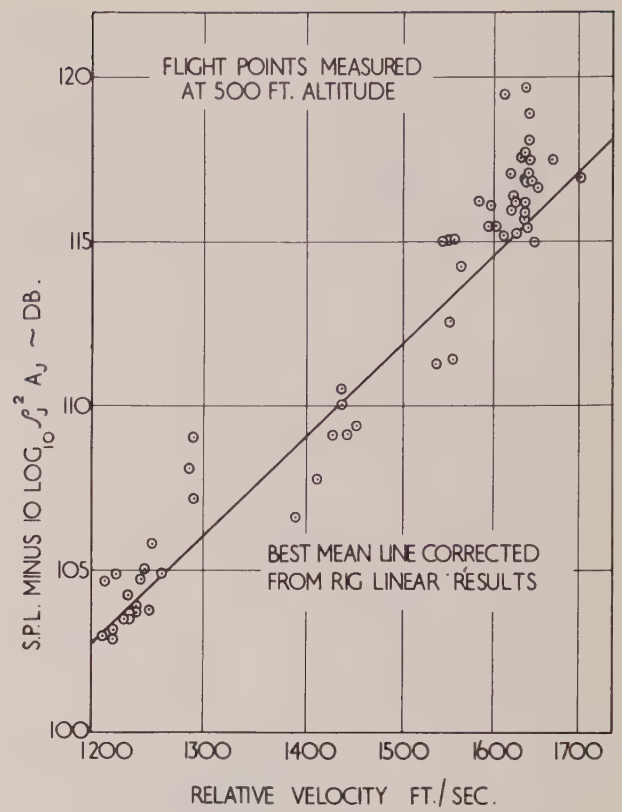

Fig. 3 — Flight noise measurements

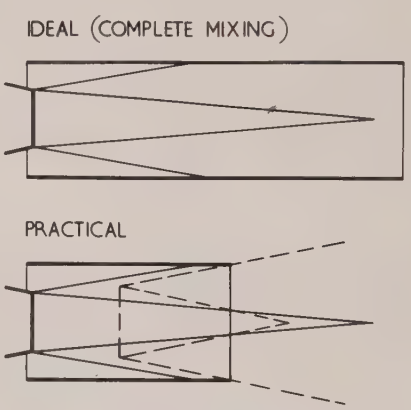

Fig. 4 — Ejector mixing processes

of flight speeds in which we are interested the jet is usually at an angle of incidence of about 5 deg to the flight path. The actual line has been corrected by a factor depending on the altitude and the variation of core length between ground and flight conditions. The points are from the flight tests and are plotted at the appropriate relative velocity between jet and air. The scatter of the points is considerable but this core length correction does enable us to account for the fact that the noise is apparently higher at a given relative velocity in flight than at that absolute velocity on the ground.

EJECTORS - Circular Nozzles - A very similar mixing process occurs in an ejector (Fig. 4) and again we can try

*Numbers in parenthesis designate References at end of paper.

to account for measured results. In the ideal case (shown in the upper part of the figure) the jet mixes completely with the induced air and is then discharged at a uniform and, of course, much lower velocity from the outlet. Ideally, therefore, we would expect to get the mixing noise due to Vj-Va as in the flight case, plus the noise from the mixed velocity at outlet (though this latter, as can be seen below, is in fact negligible in practice). There is, however, a complication in the case of an ejector system on an engine on the ground, because the action of the ejector is to induce an air flow round the nozzle which results in a low static pressure at this point, with the static pressure rising back to atmospheric at the outlet of the ejector. Due to this depression at the inlet the jet velocity is itself slightly raised and this velocity must drop slightly along the core. Similarly, the air velocity must also drop along the ejector, and for calculation purposes it seems reasonable to assume that the relative velocity remains constant along the core.

In practice it is not possible to use an ejector long enough to allow complete mixing in this way, and a more practical configuration is that shown in the lower figure. In this case the core would protrude out of the end of the ejector, and it is clearly no longer possible to assume that mixing is taking place at the previously considered relative velocity between core and induced air. In fact this last portion of the core must be mixing much more, as if it was the last part of a hypothetical jet mixing with static air, as shown in the diagram. In this case, therefore, we would expect part of the noise to be generated at the relative velocity Vj - Va and part at Vj in proportion to the respective areas and core lengths concerned. On this basis we have calculated the attenuation to be expected by the use of an ejector, and compared these calculations with measurements.

For a basic jet of 1600 fps jet velocity, the induced air velocities are shown on Fig. 5 for a series of ejector area ratios ($\bar{A}$) and length/diameter ratios (in terms of the original jet area and diameter). The increasing jet velocities and the relative velocities between jet and air are also shown. The corresponding attenuations, calculated as described above, are shown in Fig. 6, plotted against length/diameter ratio. The left-hand parts of the curves are those for which the calculated core protrudes from the end of the ejector so that the noise of its mixing with static air must be allowed for. (Since the static pressure must have risen to the atmospheric value at this point the velocity in the core has been assumed to be that of the basic jet, not the new velocity associated with the depression at the inlet to the ejector.)

The first interesting fact to emerge from the calculations is that the attenuation is actually less for larger area ratios, in contradiction to the theories put forward in our earlier paper referred to above (4), but on reflection this appears to be a more reasonable result. It is clearly legitimate to discard one hypothesis in favour of another in the hope of ultimately arriving at the truth.

On the graph have also been plotted a number of experimental points, some obtained on a small scale jet engine of 5 in. nozzle diameter and some on a full scale Avon engine, all as the reductions in peak overall noise heard by an observer walking nearly parallel to the jet axis as described above, and all for a basic jet velocity of 1600 fps. The test points are undoubtedly scattered but the agreement between calculation and measurement is very reasonable at the small ejector lengths which can be used in practice. We attribute the high attenuations at larger ejector lengths to a change in directivity of the noise due to multiple reflections inside the ejector.

Another interesting deduction that can be made by means

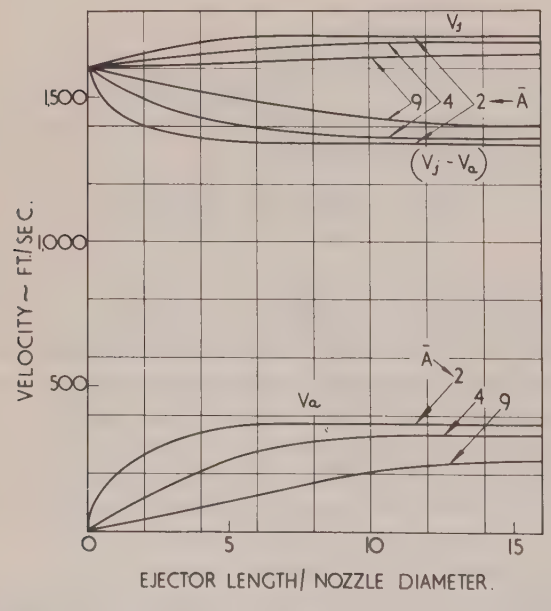

Fig. 5 — Velocities induced by ejectors — 1600 fps original jet velocity

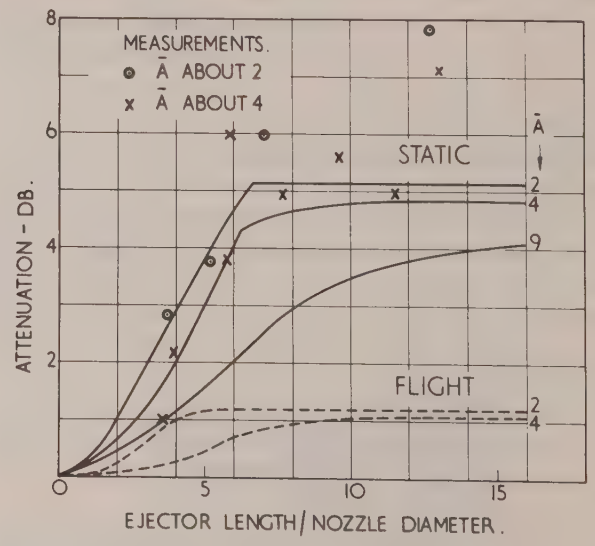

Fig. 6 — Estimated and measured attenuations for various ejectors — circular nozzles

of these calculations is to examine what happens in flight. In this case the fitting of an ejector only increases the air velocity past the nozzle very slightly. The corresponding calculated flight attenuations are also shown on Fig. 6. It can be seen from this that an ejector giving about 5 db attenuation on the ground would only be expected to give about 1 db in flight. We have been hoping to do some specific tests of this effect on our Canberra aircraft but have not yet been able to arrange it. It would therefore be extremely interesting to know if the Douglas Aircraft Co. has noticed any effect of this sort with their ejector on the DC-8.

Silencing Nozzles - Douglas, of course, is using their ejector not with a conical nozzle but with a silencer, the advantage of this being that as all the core lengths are reduced with a divided nozzle so are the ejector lengths for the same attenuation. But, to be exact, this should be for the same induced velocity, and it is not necessarily the same thing. Here we will digress for a moment on the subject of silencers, although it is hoped that they will not be needed on future bypass engines.

We know that part of the attenuation produced by a silencing nozzle is due to the fact that some of the individual jet mixing regions are shielded from 'view' by others. A simple experiment (4) on two circular jets, examining the noise first in the plane through the jets and then in the plane normal to this, illustrates that one jet can effectively shield the noise from another. Fig. 7 shows that even with the jets widely separated we get 3 db attenuation relative to a single nozzle of the same total area. As the jets are brought nearer together the attenuation increases. We have hitherto rather weakly ascribed this to interference' between the jets, without trying to specify the nature of this interference. But we know that the action of a silencer is to induce an axial air flow into the jets and it may be the consequent reduction in relative velocity which produces the remainder of the attenuation, just as with an ejector. This sort of hypothesis has been stated many times before though no systematic attempts have been made to correlate this induced velocity with the attenuation.

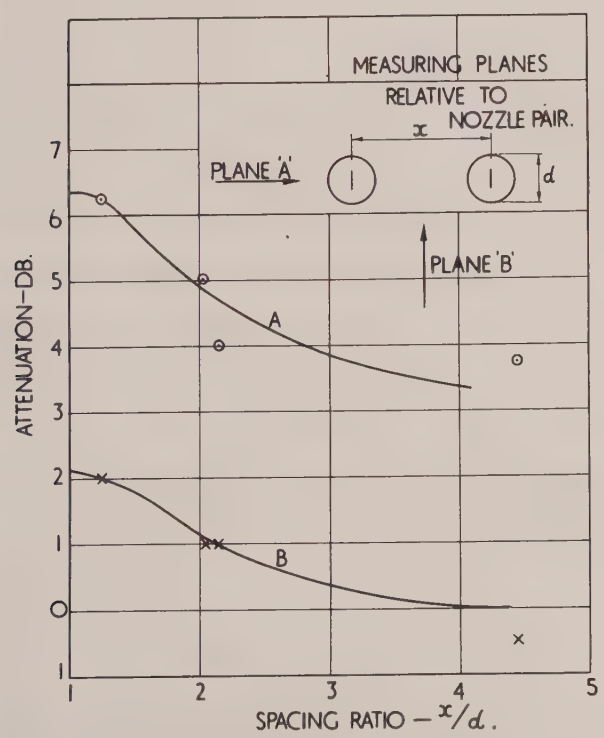

Fig. 7 — Measured attenuation form pair of nozzles

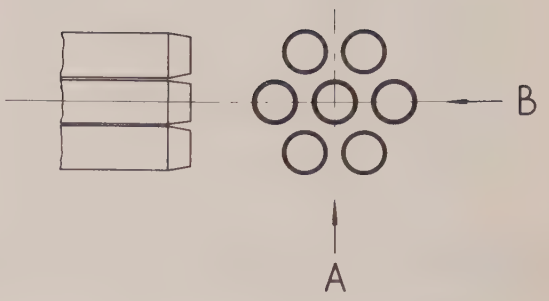

Fig. 8 — Seven-tube silencing nozzle

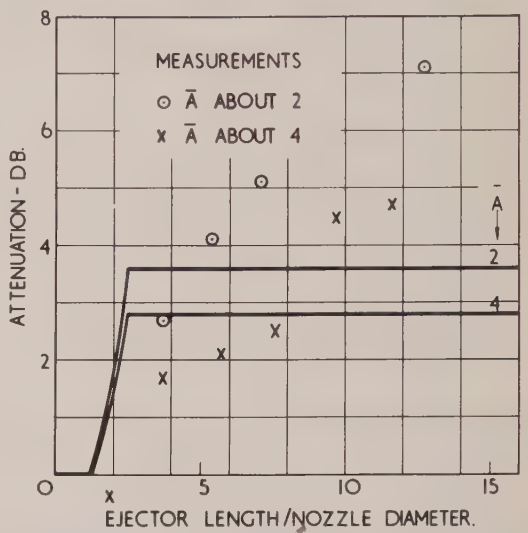

Fig. 9 — Estimated and measured attenuation for various ejectors — 7-tube silencing nozzles

Consider the case of the 7-tube silencer shown in Fig. 8, which by itself gives an attenuation of about 4-1/2 bd at 1600 fps jet velocity. Looked at in direction A, two whole jets plus three half jets can be seen, making 3-1/2 jets in all, and in view B, three jets can be seen. Clearly about half the jets are shielded, and we would expect 3 db attenuation due to this effect. To account for the remaining 1-1/2 db attenuation we would need a new relative velocity of 1525 fps. Allowing for the depression at the nozzle outlets the jet velocity would increase to 1625 fps, an induced

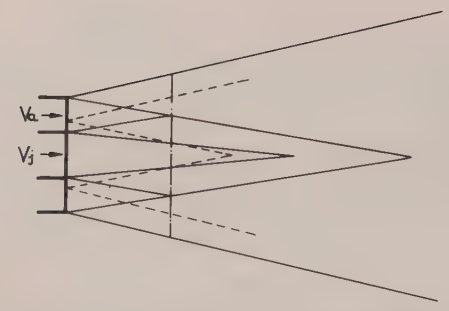

Fig. 10 — Mixing of low velocity annular jet co-planar with high velocity central jet

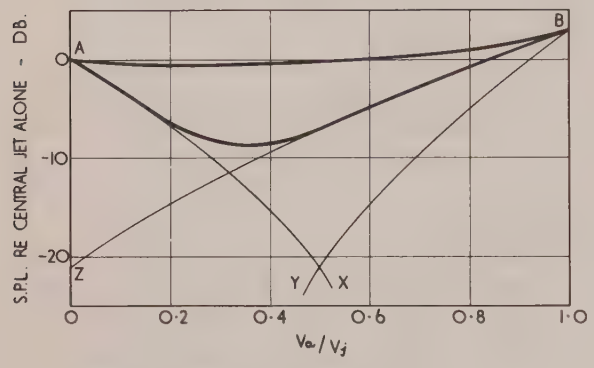

Fig. 11 — Noise of co-planar jets — $\bar{A} = 2$

velocity of 100 fps. Reverting now to our ejector calculations, in this case for a series of ejectors of increasing length fitted to this 7-tube nozzle, it is clear that they cannot produce any additional attenuation until they are long enough to induce at least this same air velocity of 100 fps. On the other hand, each individual tube diameter is about 0.4 times that of the original nozzle and all the core lengths will be reduced by the same factor. Hence only for very small ejector lengths will the cores protrude so that we must add the noise of their mixing with static air. The calculated curves are then of the form shown in Fig. 9. A number of experimental points are also shown in this graph and it can be seen that the agreement with the calculations is again not too bad for short ejector lengths. We have not made any attempt to calculate what happens in flight with this sort of nozzle plus ejector arrangement because the behaviour of a silencer by itself in flight is not at all readily predictable. Its performance must depend on how readily air can penetrate into the central part of the nozzle against an adverse pressure gradient in flight compared with a favourable pressure gradient on the ground. Judging by the calculations for the circular nozzle, however, it does not seem likely that much additional attenuation will be obtained from the ejector in flight.

CO-PLANAR JETS - One further case we can consider is where the annulus air and central jet emerge separately but in the same plane, as in Fig. 10. In this case there are three mixing regions to consider,

1. The annulus air mixing with static air if it were a large jet of area $\bar{A}$.

2. The central jet mixing with the annulus air at the relative velocity Vj - Va.

3. The part of the central core protruding downstream of the first mixing region and assumed to be mixing with static air again as if it was part of the hypothetical jet shown.

Once again we can calculate the noise corresponding to these different mixing regions in terms of the jet areas, core lengths, and velocity differences concerned, and compare with measurements.

It might be thought that we should take into account the shielding of the noise from the inner mixing region by the outer mixing region but in fact this consideration need not be taken into account. This shielding can only be significant when the velocity difference in the shielding region is at least of the same order as that in the shielded region, or in other words when Va is equal to half of Vj or greater; under these conditions the noise from the inner mixing region is so much less than that of the original jet that it contributes nothing to the total noise in any case.

This can be understood more readily by referring to Fig. 11 which has been drawn to illustrate the various processes for an annular air jet of area equal to that of the central jet (that is $\bar{A} = 2$). The diagram shows the resultant noise level relative to that of the central jet alone, plotted against the velocity ratio annulus/central jet. Clearly when the velocity in the annulus is zero the noise is the same as if the annulus were not there, giving point A zero db at $\frac{Va}{Vj} = 0$. Equally clearly, if the velocity in the annulus is the same as that in the central jet, the noise is that from a larger jet of twice the area, giving point B + 3 db at $\frac{Va}{Vj} = 1$. How the noise varies between these points is more complicated.

Consider first the noise in the mixing region between the central jet and the annulus air, assuming for the moment that it extends to the end of the core. As Va increases, the relative velocity in this region decreases, so that when $\frac{Vj - Va}{Vj} = 1/2$, for example, the noise should be down (on an 8th power law) to $(1/2)^8$, but because of the increased core length up by a factor of 2, i.e. down by 21 db. This noise will therefore vary according to the line AX, going through the point 21 db down at $\frac{Va}{Vj} = 1/2$.

Similarly, if the noise from the outer mixing region of the annulus air were also complete, it would be that of a jet of area twice the area of the central jet varying as $\frac{Va^8}{Vj}$. At $\frac{Va}{Vj} = 1/2$, therefore, it would be 24 db down on the noise at $\frac{Va}{Vj} = 1$, and this variation of noise would be represented by the line BY.

It is also of interest to consider how the noise would vary if it came from a uniformly mixed jet spread over the total

area. At $\frac{Va}{Vj} = 0$ this would be a jet of half the velocity through twice the area of the central jet (assuming incompressible flow) and the noise would be 24 db down on point B. This variation of noise is given by the line BZ.

Reverting for the moment to ejectors, this diagram shows that the noise of an ejector system of area ratio 2, and long enough to mix completely and to contain the core of the initial mixing region, will be obtained by adding the two noise components given by the lines AX for the internal mixing noise, and BZ for the noise of the mixed jet emerging from the end of the ejector. The lower of the two heavy lines on Fig. 11 shows the sum of these two components. Since an ejector of this sort can only induce a maximum $\frac{Va}{Vj}$ of about 0.2, the working point is at the left-hand end of this diagram, and the noise of the mixed jet emerging from the end of the ejector is well down on that of the internal mixing.

On the other hand, this curve also defines the noise from a by-pass engine if the two streams are discharged into a pipe at a pressure just above atmospheric and allowed to mix completely before being discharged again. In this case the working point is towards the right-hand end of the diagram, so that the noise of the mixed jet predominates. In practice the two streams would be mixed at a considerably higher pressure, and lower velocities, so that the internal mixing noise would be even lower.

For the co-planar nozzle of Fig. 10, the noise will be the sum of that produced by a proportion of the internal mixing region given by AX plus a proportion of the outer annulus mixing region given by BY plus a proportion of the original central jet mixing with static air. Clearly the high jet velocity makes the last of these terms overwhelmingly the more important, and it will only be eliminated for very large area ratios for which the outer mixing regions completely shield the inner one; and in fact area ratios of at least 10 are needed for this.* For the area ratio of 2 of Fig. 11 the calculation gives the upper of the two heavy lines, and it can be seen that over the greater part of the range of $\frac{Va}{Vj}$ the noise is essentially the same as that of the inner core alone, and that there is no significant attenuation produced by discharging the annulus air round the central jet.

We have carried out some tests on co-planar nozzles of this type of four different area ratios ranging from 1.77 to 5.14. The two 'theoretical' lines of Fig. 11 have been calculated for compressible flow and using the correct index of noise variation with velocity, and plotted on Fig. 12. It will be seen that even with an area ratio of 5.14 only a small degree of attenuation is predicted for the co-planar nozzle. The results are rather sketchy but it would be fair to deduce

*For the individual mixing regions of a silencing nozzle the effective area ratios are, of course, quite large.

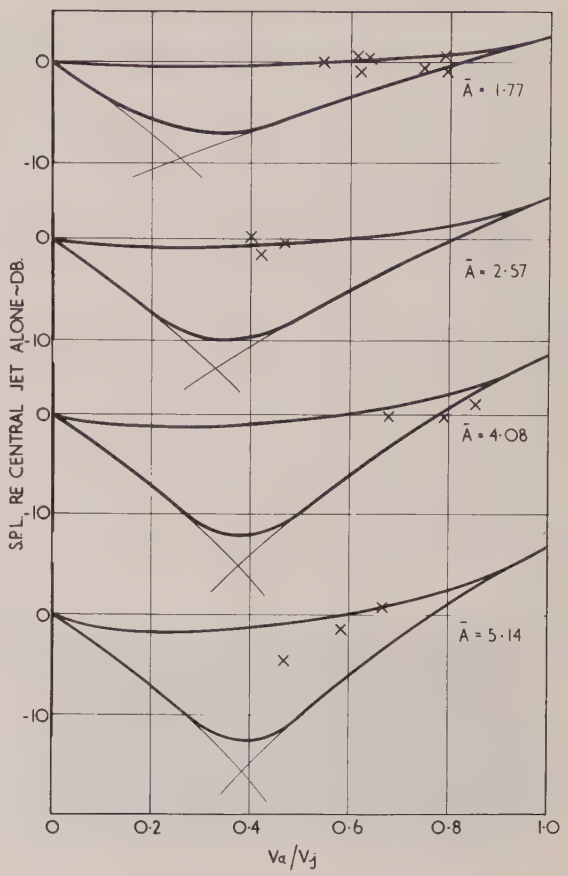

Fig. 12 — Noise of co-planar jet — comparison of estimation and measurement for various values of Ā

from them that for area ratios up to 4 and velocity ratios $\frac{Va}{Vj}$ up to 0.8 the noise of the co-planar jet is predicted, that is the same as that of the original central jet. These results are in excellent agreement with some reported a long time ago by Tyler and Perry (5) in which they investigated the noise from several co-planar jets at a velocity ratio of 0.67. Their area ratios were 1.33, 1.67, and 3.4, and in every case they found that the noise of the co-planar jet was the same as that of the central jet. Incidentally, at this velocity ratio our own results still agree very closely even in the case of the largest area ratio tested, for which the measured attenuation at low values of $\frac{Va}{Vj}$ seems to be between the two 'theoretical' curves.

Optimum Jet Arrangement

In the case of an actual by-pass engine, with by-pass ratio around 1, the area ratio is about 2 so that we can use Fig. 11 to examine its noise. Velocity ratios are in the range 0.65 to 0.75. The conclusions to be drawn are:

1. For separate discharge of low velocity cool air and high velocity hot gas there is clearly no advantage to be

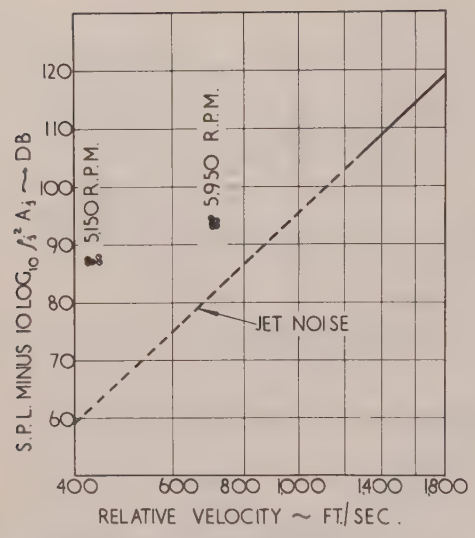

Fig. 13 — Overall noise measurements on approach — one engine at 500 ft

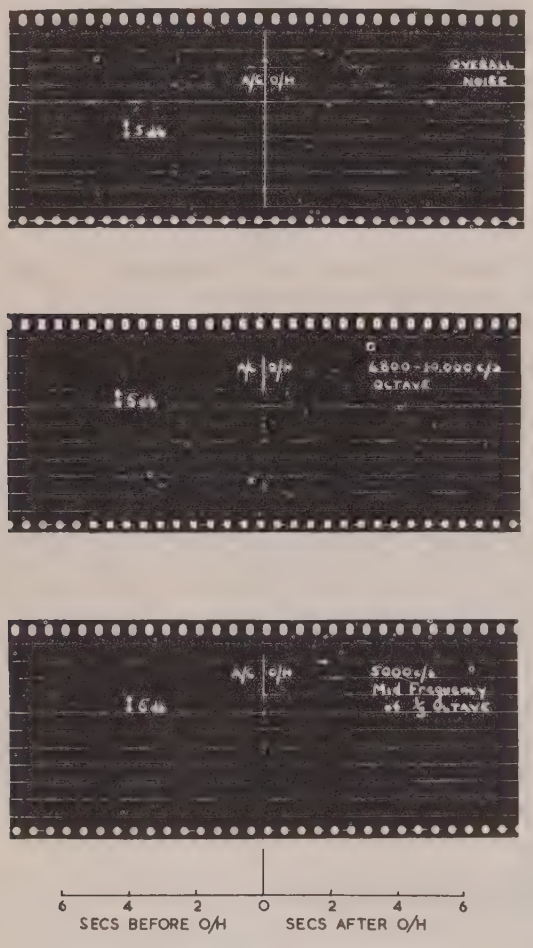

Fig. 14 — Variation of noise with time

gained by surrounding the gas jet by an annulus of air in a co-planar nozzle. The noise will still be the same as that of the hot gas jet alone.

2. If the two streams are mixed before being discharged as a uniform jet there is a significant reduction in noise over the hot gas jet alone (quite apart, of course, from any gain in thermal efficiency). Exactly as in the case of the ejector, the mixing length can be shortened by using a mixer not unlike a silencer.

Approach Noise

Until comparatively recently it has been jet noise during take-off which has caused most disturbance to communities around airports but the noise on approach with the engines throttled back is now found to be equally disturbing. At Los Angeles, for example, most take-offs are made over water and it is the approaches over land which disturb most, while at New York and London the use of silencers and of noise abatement take-off procedures has reduced the take-off noise of the current jet aircraft to a level where complaints concerning the approach noise have become equally numerous — and, of course, the jet noise of these by-pass engines, even unsilenced, will certainly be no worse than that of the silenced existing engines.

IS IT JET NOISE? - What do we know about approach noise? We know that it has a lot of discrete frequencies in it which are very irritating but there is also a loud white noise component. The first point to consider, therefore, is whether this is still jet noise or whether it all comes from the compressor.

We have made many measurements of the noise from an Avon engine in a Canberra aircraft flying overhead at high thrusts, and we have recently extended these down to the low thrust end of the scale. By using two engines together at approach rpm we have been able to fly the aircraft over at about the same forward speeds as we have been able to do with one engine at high rpm. Fig. 13 shows some of the results. The line (taken from Fig. 3) shows the variation of jet noise with relative jet velocity and it can be seen that around 6000 rpm the measured overall noise is some 13 db above the jet noise, around 5000 rpm it is some 27 db above. Clearly this is not jet noise.

SPECTRUM ANALYSIS - Fig. 14 shows typical traces of the variation of this noise with time as the aircraft flies overhead. The top trace is for overall noise, the second for noise in the top octave, and the third for noise in the 1/3 octave centered above 5000 cps. It can be seen that the white noise varies quite smoothly as the aircraft flies overhead but that the high frequency traces show a double peak, a first peak when the aircraft is overhead, and a second peak about 2 sec later. The 1/3 octave analysis uses a band width of ± 13% in frequency; clearly with these discrete frequencies present we need a narrower band-width. We have therefore made an analysis of the noise heard at various instants of time with some equipment having a band-width of ± 3% (for 3 db down on the peak) over the frequency range from about 500 to 8000 cps. The results are shown on Fig. 15 for

times from 4-1/2 sec before the aircraft is overhead to 5-1/2 sec after it is overhead. It can be seen that the noise has the general characteristics of a white noise having a maximum intensity in the region around 600 to 800 cps, with a number of peaks superimposed on this. The width of the peaks shown on this diagram is not of course a true measure of the sharpness of the peak of the actual noise, both because of the finite band width of the analyser and because the rpm of the two engines used during the tests were not exactly the same but were 2% apart. It is quite clear, however, by actually listening to the noise, that true discrete frequencies are present, and it is, therefore, fair to assume that the peaks on these curves represent at their peaks the magnitude and frequency of the discrete tones present.

VARIATION OF NOISE WITH TIME - From these graphs we can obtain the variation of sound pressure level against time for the various components of the noise, as shown in Fig. 16. The overall noise is taken directly from the trace and is shown rising to a peak about 1 sec after the aircraft has passed overhead, a peak of 87 db in this case when the aircraft was at 500 ft altitude.

In the lower part of Fig. 16 the lines are drawn for the calculated variation in frequency of notes emitted by the compressor as heard by an observer on the ground. The variation is, of course, due to the Doppler effect as the aircraft flies overhead. The speed of the aircraft is such that the frequency of the note heard when the aircraft is flying away from the observer is almost down to half that which is heard as it flies towards him. The fundamental blade passing frequencies of the 1st, 2nd and 3rd stages of the compressor have been plotted, and also the 2nd harmonic of the 1st stage;the points on both graphs are the peak values of noise, and of the frequency at that peak, taken off the previous curves at the various moments of time. It can be seen that the 1st stage fundamental can be clearly identified over the whole period of time on the graphs, since the measured frequencies agree very closely indeed with the theoretical ones. Similarly the 2nd stage fundamental can be identified over most of the time scale although there is a gap around 1/2 to 1 sec after the aircraft has passed overhead, during which it is not possible to identify it. There is a faint trace of the 3rd stage fundamental but the graphs are not reliable enough to show it accurately. On the other hand, there is very clear evidence of the 1st stage 2nd harmonic rising very rapidly to a peak just after 1 sec after overhead, and falling again very rapidly, also very clearly identifiable by the frequency peaks agreeing very closely with the theoretical.

It is, of course, possible that there is also some 2nd stage 2nd harmonic present, but the frequencies of this component would be beyond the range of the equipment used during these tests, and in fact would be above or near the limit of the audible range during most of the fly-over.

When listening to this noise it is particularly difficult to grasp exactly what one is hearing because of the big variation of frequency due to the Doppler effect as the aircraft

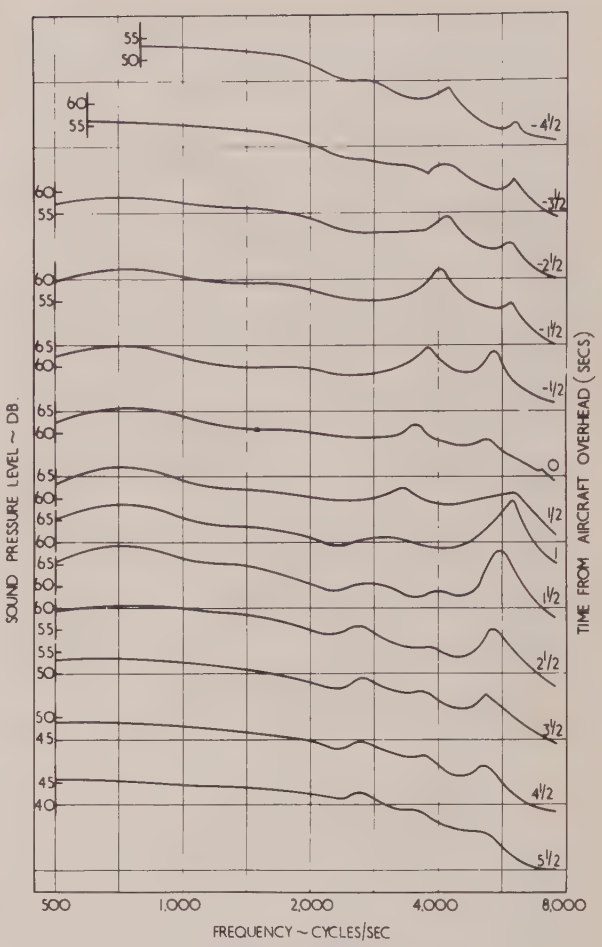

Fig. 15 — Change of spectrum with time

flies past, but this graph makes it clearer. As the aircraft approaches, the overall white noise builds up slowly, rising to a peak around 1 sec after the aircraft has passed overhead, and then falling again quite slowly.

We have also plotted the mean spectrum levels of this white noise as db per cycle for the 7th and 8th octaves which contain the discrete frequencies. The corresponding octave levels are 34 db higher for the 7th octave and 37 db higher for the 8th octave. Considering the 7th octave, it can be seen that at a point about 1/2 sec before the aircraft passes overhead the octave level has reached 71 db. The 1st stage fundamental has been rising rapidly to a peak at this moment of 65 db, and it is therefore contributing slightly to the total noise in this octave and is, of course,'colouring' it very very distinctively. This 1st stage fundamental then falls off slightly, but around 1 sec after overhead it is reinforced by the 2nd stage fundamental which has dropped sufficiently in frequency by this time to appear in the 7th octave, although they are both some 10 db down on the white noise in that octave at that moment. Considering now the noise in the 8th octave, at about 1/2 sec before overhead, the white noise is at a level of 64 db; the 2nd-stage fundamental actually reaches the same level at this point before it falls off again,

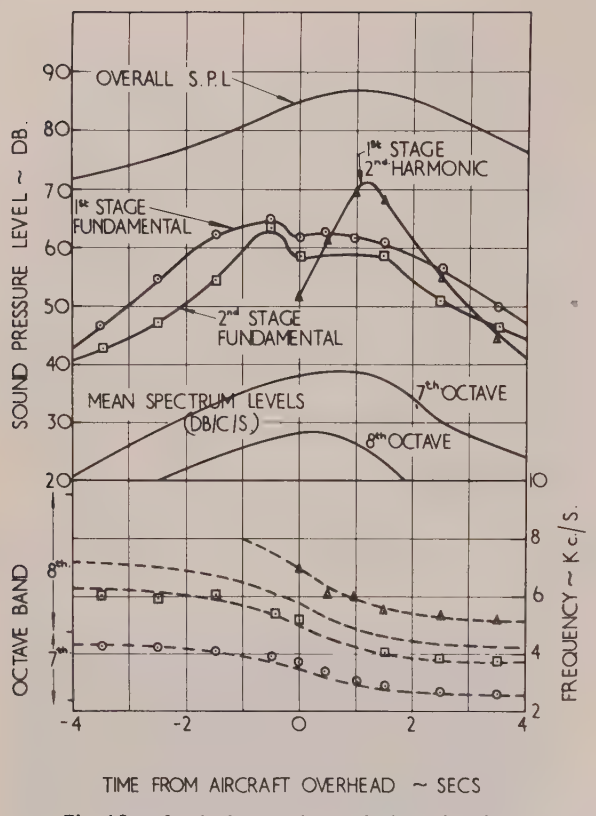

Fig. 16 — Analysis of noise variation with time

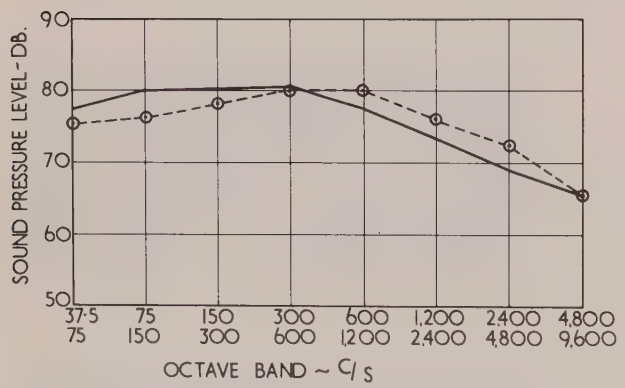

Fig. 17 —Comparison of flight and ground test spectra

to be succeeded by the very rapid rise in the 1st stage 2nd harmonic, which reaches a peak of 71 db at 1.2 sec after overhead, some 9 db above the level of the white noise at that moment. The double peak shown in the original traces of Fig. 14 is clearly first a peak of the 2nd stage fundamental and then a peak of the 1st stage 2nd harmonic.

DIRECTIVITY - The fact that this white noise and these discrete frequency noises rise and fall at different rates, and peak at different times, suggests that they have quite different directivities. Part of this effect is, however, due to the rapid variation of atmospheric attenuation with frequency at high frequencies. Measurements on an engine running statically on the ground at these approach rpm show that it is the noise in front of the compressor, within ±30 deg of the engine axis, which is the loudest, both for the white noise and for the discrete frequencies. But as the aircraft flies overhead this noise has to traverse a long path before it reaches the observer on the ground and suffers considerable attenuation.

It is therefore very difficult to correlate reliably the noise heard in front of the compressor from an aircraft flying overhead with that from an engine running on the ground. However, it is the noise radiated around 90 deg to the engine axis, to be exact between about 60 deg and 120 deg to the axis, which is most important to the observer, and this gives a much more satisfactory correlation. Fig. 17 shows the octave analysis of the noise measured at 90 deg to the engine axis from one engine in the Canberra while running on the ground at the same rpm as used in flight. The noise was actually measured for one engine at 100 ft distance and has been corrected to the 500 ft altitude of the flight tests by inverse square law plus an extra attenuation in db per thousand ft of 0, 0, 0, 1/2, 1-1/2, 4, 7, 12 db respectively in each of the standard 8 octaves (6), and then increased by 3 db for two engines. This is the full line on the graph; the points are the noise levels at this angle (that is, at 1/2 sec after overhead) from the flight tests, and are the mean of four runs of the aircraft at this rpm. It can be seen that both the noise level and the variation with frequency are in extremely good agreement.

CALCULATION IN TERMS OF COMPRESSOR CHARACTERISTICS - It seems, therefore, that there is no mysterious difference between the approach noise from the aircraft in flight and that from an engine running on the ground.

We have therefore attempted to account for this noise in terms of the characteristics of the compressor concerned.

White Noise - The white noise could be produced by the shedding of vortices from the blades. It must then be largely a function of the work done on the air in its passage through the blade row. The noise should therefore be a function of $M \Delta T$ where M is the mass flow through the engine and ΔT the temperature rise through the stage of blades under consideration. It seems reasonable to assume for this white noise that we need only consider the 1st stage of the compressor, since we have found that the white noise produced by one jet at any rate will completely shield that produced by another behind it, and something of the same sort of mechanism may be well taking place here. There is in fact a formula derived from measurements on ventilating fans (7) which can be expressed as:

$$\text{Space average S.P.L.} \propto (M\Delta T)^{1.5} \times (M.\Delta T)/B^{0.27} \qquad (2)$$

where:

B = Number of blades

We have used this expression to predict the space average white noise for certain Avon and Conway engines at a distance of 50 ft away, over a range of rpm. The calculations

are of course quite elaborate, involving detailed knowledge of the compressor characteristics, and the results are shown as the lines in Fig. 18. The formula has been used to give the variation of noise only; the absolute level has been arbitrarily fixed to agree with the 8100 rpm point for the Avon (the dotted part of the Avon line is the operating range of rpm of the bleed valves which are open at low rpm and closed at high rpm). The different sets of points shown for the Avon are measurements made on an engine on two different occasions, while those for the Conway are measurements made on two different engines. The calculation of the space average S.P.L. over the hemisphere round the front of the engine has been carried out for only a few rpm although the results are available at very many different rpm. It can be seen that the formula predicts the variation of noise of the Avon extremely well; the same formula (with its constants chosen for the Avon) evidently predicts the Conway noise very closely also, both its variation and its level agreeing well with the measured points, although there are signs of departure from the predicted line at the bottom end of the rpm range. The excellent agreement with the Avon results, in spite of a very discontinuous variation with rpm, is sufficient to discount any suggestion that this noise might be combustion noise, rather than compressor noise.

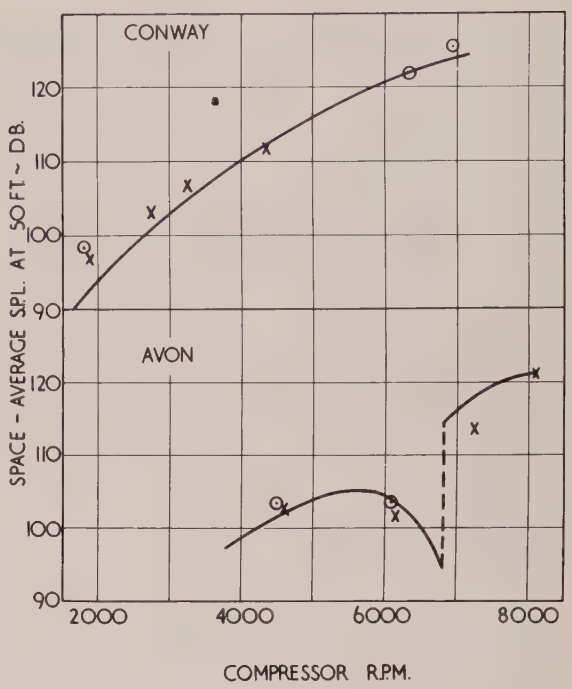

Fig. 18 — Comparison of measured and estimated compressor noise — white noise

Discrete Frequency Components - For the discrete frequency noise we have drawn an analogy with propeller noise as calculated by Gutin for the dipole noise due to the lift of the blades. Gutin's formula as quoted by Hubbard (8) can be reduced to the form:

$$\text{Space average S.P.L.} \propto M^2 \eta \, \Delta T / D^2 (1-r^2)^2 \qquad (3)$$

where:

η = Stage efficiency
D = Tip diameter
r = Hub/tip ratio

In obtaining this formula we have been able to replace the Bessel function term in the original expression by a constant, which means that we are left with no way of distinguishing between the levels of the various harmonics of the noise. As a first step, therefore, we have examined how this formula predicts the variation of fundamental frequency noise from the compressor.

On Fig. 19 the lines show the predicted variation in space average S.P.L. for the 1st and 2nd stages of the Avon compressor, the constants being chosen to agree reasonably well at the top end of the rpm scale for the 1st stage. For the 2nd stage an arbitrary reduction of 5 db* has been applied over the whole rpm range. The measured points on Fig. 19 have been extracted at the appropriate frequency, and it can be seen that the prediction of the 1st-stage noise is very good, but that of the 2nd stage is poor at low rpm. A similar comparison has been made on Fig. 20 for the 1st and 2nd stages of the Conway (the calculations being made using the constants chosen for the Avon). Again it can be seen that both the level and the variation of noise for the 1st stage is predicted quite well, and again that of the 2nd stage is reasonable except at the low rpm end.

These two attempts to correlate the approach noise of our engines with their compressor characteristics are so far quite encouraging. As far as we know, these are the only two sources of noise which are significant in our engines, but it seems likely that there is at least one other type of noise which can occur. This can be described as a 'siren' noise, produced by the pressure field round each compressor blade being driven past an obstacle such as a stator blade at very high rotational tip speeds. This would of course be a discrete frequency noise at the same frequency as the lift noise described above, and would be expected to rise particularly rapidly in intensity at high rpm. The Avon

*The justification for this is that the analysis of the flight tests shown on Fig. 16 gives an average level for the 2nd stage fundamental relative to the 1st stage fundamental (allowing for the variation in attenuation with distance of the frequencies concerned) of -2 db. On the other hand, the calculation gives +3 db increase. We have therefore arbitrarily assumed that noise from the 2nd stage of the compressor is attenuated by 5 db in passing through the 1st stage.

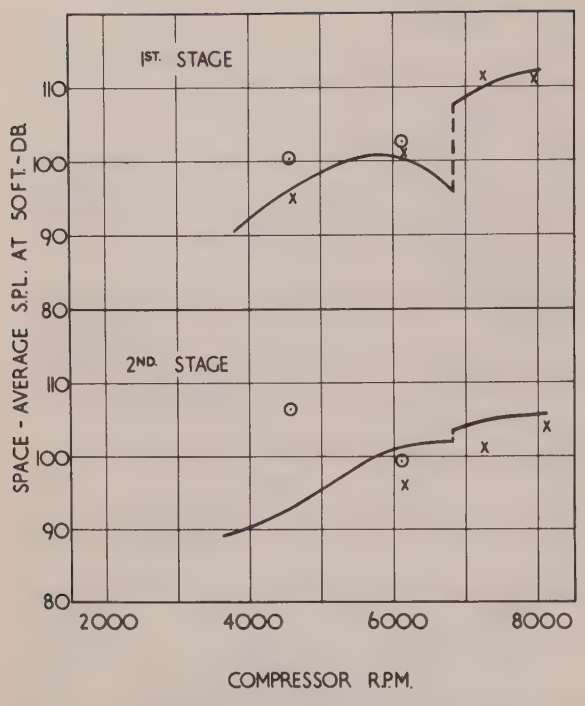

Fig. 19 — Comparison of measured and estimated compressor noise — discrete frequency component — Avon

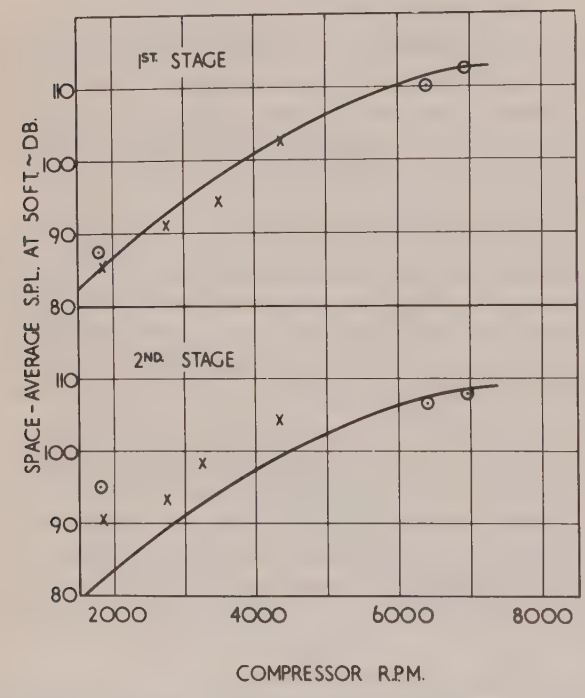

Fig. 20 — Comparison of measured and estimated compressor noise — discrete frequency component — Conway

and Conway results show no evidence of this type of noise, and we have not observed it on any of our other axial-compressor engines. This is not surprising, of course, as there are no large differences in the basic designs of the front stages of our compressors whether they are on plain jet engines, by-

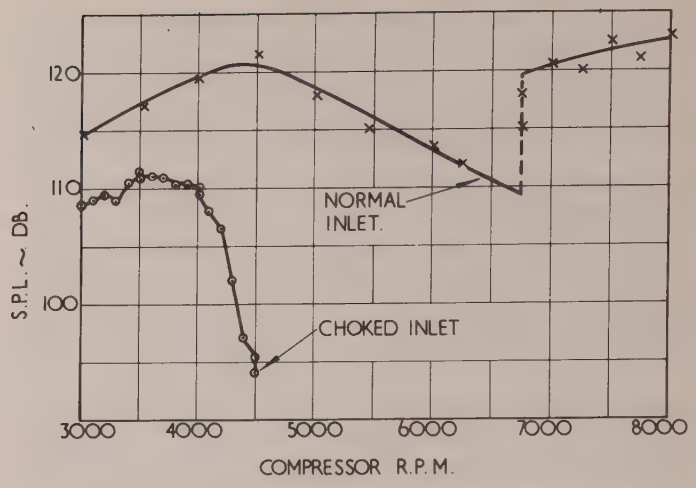

Fig. 21 — Effect of choked intake on compressor noise

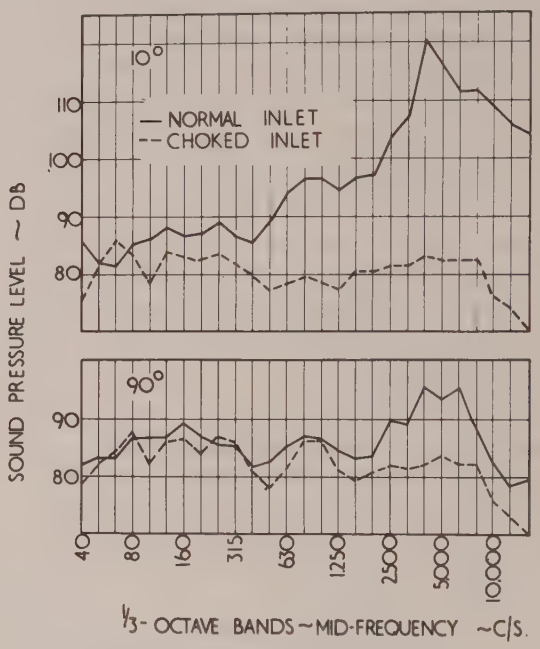

Fig. 22 — Effect of choked intake on noise spectrum

pass engines or even propeller-turbine engines, only small variations in the parameters such as hub/tip ratio. This 'siren' noise may, however, be important in the case of the adaptation of an existing engine to make it into a by-pass engine, where it may not be possible to avoid very high rotational tip speeds, even though the blade loadings can be kept quite normal by using a sufficient number of stages.

POSSIBLE METHODS OF REDUCTION - As to what can be done about compressor noise, the only clue offered by the formulae seems to be that to reduce the noise it is necessary to reduce the blade loading, that is, the stage temperature rise. To do this in the basic design of the engine means increasing the number of stages in the compressor so that as usual a compromise is involved, in this case between the

conflicting requirements of lower noise and light weight.

It may be possible to achieve some reduction of noise by lining the inlet duct with acoustic lagging, at the expense of weight and increased specific fuel consumption. Another method that has been suggested is to adjust the area of the inlet so that the air reaches sonic velocity at a throat through which the noise is not able to travel forward (except of course in the boundary layer). Unfortunately, this poses a severe mechanical problem, because this throat must have an area only around 1/3 of that which is normally used; the inlet losses corresponding to this small area at normal take-off and cruising thrusts would obviously be so prohibitive that any mechanism must be designed to be absolutely fool-proof in its fail safe characteristics.

However, there is no doubt that such a device undoubtedly has an enormous effect on the noise coming out of the front of the engine, as has also been demonstrated by Curtiss-Wright Wright. Fig. 21 shows the variation in overall sound pressure level at a point 50 ft in front of the intake at 10 deg off the engine axis for an Avon engine. The upper curve shows how the noise varies with rpm over the whole rpm range when fitted with a normal inlet. The lower curve shows the corresponding figures when fitted with an inlet with a central bullet designed to choke at 4500 rpm. It can be seen that there is about 28 db reduction in noise under these conditions. The upper graph of Fig. 22 shows the 1/3 octave analysis of the noise at this point in the two cases. It can be seen that there is a reduction of as much as 20 db in the white noise, and nearly 40 db in the discrete frequency components. Unfortunately this spectacular reduction in noise is not achieved at 90 deg to the engine axis, as the lower graph of Fig. 22 shows. At this point there is no significant reduction in the white noise, and, of course, the flight tests have shown that it is the noise transmitted in this direction which is important. There is around 10 db reduction in the discrete frequency components which would probably be very valuable.

Conclusions

Summing up, it can be said that the jet noise of the by-pass engine, of by-pass ratio around 1, designed for efficient mixing of by-pass and hot gas streams before being discharged to atmosphere, will be some 4 db quieter than if the two streams are discharged separately. As far as the compressor noise on approach is concerned, there is no reason for the noise of the by-pass engine to be any worse than that of existing engines of the same thrust; we are learning about the mechanism of this noise, and as a result we shall be able to reduce it though there is still a considerable amount of work to be done on the subject.

Acknowledgements

The author wishes to acknowledge with gratitude the assistance of his colleagues at Hucknall in preparing this paper, and to thank Rolls-Royce, Ltd. and the Ministry of Aviation for permission to publish it.

References

1. H. B. Squire, "Jet Flow and its effect on Aircraft," Aircraft Engineering, March 1950, 62-67.

2. K. K. Neely, B. Etkin and H. S. Ribner, "Noise Research in Canada: Physical and Bio-Acoustic," Paper read at the First International Congress in the Aeronautical Sciences, Madrid, September 8-13, 1958.

3. G. M. Lilley, "On the Noise from Air Jets," Aeronautical Research Council Report ARC. 20,376, September 1958.

4. F. B. Greatrex and D. M. Brown, "Progress in Jet Engine Noise Reduction," Paper read at the First International Congress in the Aeronautical Sciences, Madrid, September 8-13, 1958.

5. J. M. Tyler and E. C. Perry, "Jet Noise," Pratt and Whitney Aircraft Report No. PWA. Inst. 451, April 9, 1954, Prepared for presentation at the SAE Meeting in New York, April 14, 1954.

6. Bolt, Beranek and Newman, Inc., "Studies of Noise Characteristics of the Comet 4 Jet Airliner and of Large Conventional Propeller-driven Airliners," Report prepared for the Port of New York Authority, October 1958.

7. C. F. Peistrup, J. F. Wesler, "Noise of Ventilating Fans," J. Acoustical Soc. Amer., March 1953.

8. H. H. Hubbard, "Propeller Noise Charts for Transport Airplanes," National Advisory Committee for Aeronautics Technical Note No. TN 2968, 1953.

Discussion

Discrepancy in Relation for Noise Generation?

Edmund E. Callaghan
Lewis Research Center
National Aeronautics & Space Administration

IN THE PAPER by F. B. Greatrex, there appears to be a discrepancy in the relation for noise generation proposed.

Greatrex gives

$$\text{noise} \propto A_j \times \text{core length} \times (V_j - V_a)^n \qquad (a)$$

Now, core length is given from Fig. 2 as

$$\text{core length} = \frac{\sqrt{\frac{A_j}{\pi}}}{\tan} = \frac{\sqrt{\frac{A_j}{\pi}}}{(.1 - .1\frac{V_a}{V_j})} = \frac{10\sqrt{\frac{A_j}{\pi}}\,V_j}{V_j - V_a} \qquad (b)$$

Hence,

$$\text{noise} \propto A_j^{3/2} \times V_j \times (V_j - V_a)^{n-1} \qquad (c)$$

If we take the case where $V_a = 0$ then

$$\text{Noise} \propto A_j^{3/2} V_j^n \qquad (d)$$

which is not in agreement with the usual Lighthill relation of

$$\text{noise} \propto A_j V_j^n \qquad (e)$$

It has been well established that noise is proportional to Aj rather than $A_j^{3/2}$, and in fact, it is just this change which causes the line in Fig. 3 to agree so well with the data. It would appear that the use of core length in the relation is not therefore justified and some other explanation is required.

The section of the paper dealing with approach noise is excellent and is a unique contribution to the literature.

Author's Closure to Discussion

MR. CALLAGHAN is quite right in taking me to task for getting the "dimensions" wrong in my suggested relationship for jet noise, and I can only plead that I suggested "a relationship of the form.....". Writing instead of "core length", the ratio "(core length)/(core length for $V_a = 0$)" puts this right without altering my argument.

I am grateful for his kind words on the second half of the paper.

The Performance of Springs at Temperatures Above 900 F

William R. Johnson and Ronald D. Crooks
Associated Spring Corp.

ENGINEERING demands for metals to stand high temperatures have also come to the spring designer. Resilient elements for use in jet engines, rockets, aircraft wheel brakes, power nuclear reactors, steam plants, and a host of other applications are called on to sustain elastically stresses at elevated temperatures with little or no creep or stress relaxation. As the ambient temperatures increase, the problem becomes increasingly difficult. Zimmerli and Woods' (1)* work anticipated many of the automotive industry's demands by reporting spring data at temperatures up to 650 F. Matters and Lochen (2) added information on some high temperature alloy springs up to 1400 F. The most widely used data source published to date for high temperature spring designers is a Technical Bulletin of the International Nickel Co. (3) A brief discussion of the phenomena involved in the behavior of high temperature springs was given in an article in the Mainspring (4).

The analysis of spring failure at elevated temperatures is not a simple matter. For the purpose of this discussion, simple helical compression springs will be considered, although many of these remarks will apply to other configurations. The spring is basically a resilient element designed to deliver a force over a distance. Because of space limitations, it is usually designed with as high an elastic stress as possible. Its loading is almost always unidirectional. At high temperatures spring failure is usually caused by setting or plastic flow. If this setting occurs under constant load conditions it is called creep. Under fixed height conditions, setting is called relaxation. During creep the load is constant throughout, despite the shortening of the spring. In the case of relaxation, the load (and stress) diminish as relaxation proceeds. At elevated temperatures, where plastic flow may be appreciable, a fatigue test at constant deflection may cause enough stress relaxation so that the fatigue life may be as good or better than at room temperature, although the spring may actually have failed due to lack of ability to sustain the desired force. Consequently, at elevated temperatures excessive setting is generally the criterion for failure.

Setting of a Spring

The setting of a spring under load, whether it is creep or relaxation, occurs in two stages. If the yield point is exceeded, very rapid plastic flow occurs. Then, if the load is maintained, flow takes place on a time dependent basis,

*Numbers in parentheses designate References at end of paper.

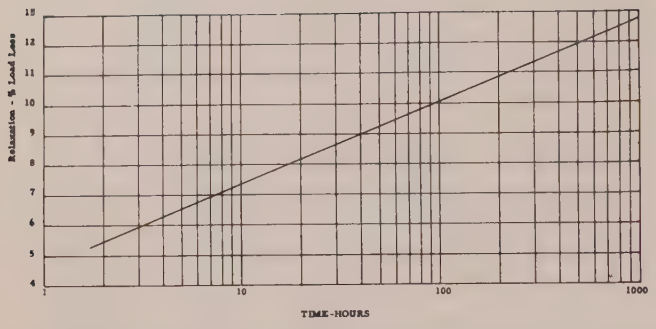

Fig. 1 — Stress relaxation of highly stressed spring at room temperature, 0.062 in. music wire spring, initial test stress 200,000 psi

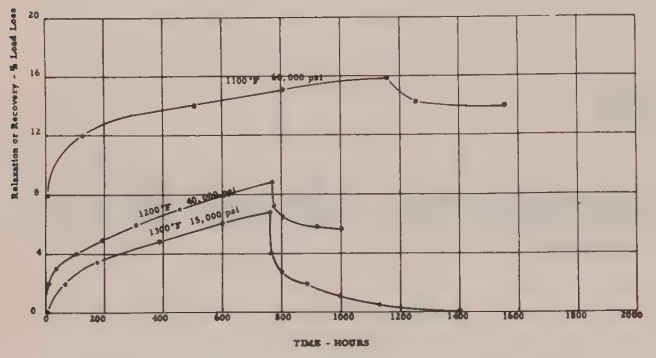

Fig. 2 — Stress relaxation and recovery of triple heat treated No. 1 temper Inconel X alloy springs at 1100, 1200, and 1300 F

at a decreasing rate. This phenomenon may be detected at room temperature in highly stressed springs (Fig. 1), although it is much more noticeable at elevated temperatures. This second stage of setting was called by Lubahn (5) anelastic flow, and defined as "flow caused by a sufficiently low constant stress which is non-instantaneous and completely recoverable isothermally in a sufficiently long time." Thus a spring cold set to a high stress level will grow or increase in length if its stability is upset by slightly raising the temperature or mechanically shocking it while it is unloaded. Similarly the spring which has been set at elevated temperature will recover a portion of the set if it is maintained at temperature under a lesser load or no load.

Theoretical interpretation of this recovery is difficult in a spring geometry. The torsional stresses in a spring are not uniform through the cross-section, as are the tension stresses in a creep specimen. Some of the recovery of the unloaded spring is the recovery of anelastic flow or creep recovery as described by Lubahn, but some may be the flow due to relief of residual stresses which were induced by the plastic flow of setting. These effects are so marked in springs that the effect of the inducing of residual stresses, their maintenance, and their relief must be considered, even at temperatures up to 1200 F for long periods of time. A typical relaxation - recovery curve on a spring is given in Fig. 2 from unpublished data of the International Nickel Co.

One of the basic difficulties in the interpretation of spring relaxation data is the problem of converting strains measured on many sizes and types of springs into comparable stress values. Presently the most accepted practice for helical compression springs is to use the formula

$$S = K \cdot \frac{8PD}{\pi d^3} \qquad (1)$$

$$\text{or} \quad S = K \cdot \frac{FGd}{\pi D^2 N} \qquad (2)$$

where:

S = Stress - psi
D = Pitch diameter - in.
K = Wahl's constant
N = Number of active coils
P = Load - lb
D = Wire diameter - in.
F = Deflection - in.
G = Shear modulus - psi

Since most spring stress calculations are made using Eq. (2), the shear modulus G must be known at the test temperature. From practical experience, it is known that the curvature correction, or Wahl's factor K, does not make stress calculations completely consistent for all spring configurations. Use of a common formula by all concerned, however, permits comparison of test data from spring tests, although we do not seem to be able to translate the data from tension creep, creep rupture, and relaxation tests run on bars to spring applications, except in a most general sense.

Test Materials

For operating temperatures above 900 F, most of the ferrous base materials will not sustain sufficient stress, in spring applications, without excessive relaxation. For service above 900 F, the spring temper materials direct-aged are not useable because of excessive relaxation. One of the greatest problems has been getting suitable size wires of acceptable quality. For example, three separate samples of one wire alloy were obtained, each time with heavy seams which so lowered the spring rate that interpretation of the data was impossible. Since Inconel X is the most readily available material in a range of wire sizes, it has been used as the basic experimental material. The samples were No. 1 temper wire, aged 16 hr at 1350 F after coiling. The Haynes 25 alloy and Hastelloy C were aged 4 hr at 1200 F after coiling. The S816 was heated to 1400 for 16 hr, and the Refractaloy 26 was aged at 1350 F for 24 hr. Other high temperature alloys have been tested when available, including D979, Rene 41, and A286. Most of the wires were 0.060 to 0.080

in. in diameter.

Testing Techniques

Test springs were coiled cold by standard spring making techniques. They were made of such dimensions that the spring index was about 7.5, the middle of the range for normal design. The ends were squared and ground. Subsequent heat treatments were carried out in air furnaces after any cold drawing lubricants, such as lead or copper, were removed. Relaxation tests were conducted on springs by the nut-and-bolt method, in which the spring is measured cold, locked up at the test deflection between two washers on a nut and bolt assembly, all heated for the desired length of time, cooled, and removed from the assembly for retesting. The test deflection is determined by calculation from the spring dimensions and the shear modulus at test temperature. No allowance was made for bolt expansion in the test. Creep tests on springs were made by loading three springs, in series, on a vertical arbor with a dead weight to give the desired stress. (Fig. 3). In this set up the variation of modulus with temperature did not enter into the stress calculations. Tests were made with a minimum of three springs at each condition. Control tests showed that the total cumulative relaxation of a spring was unaffected by temperature cycling. That is, a spring relaxed as much in a continuous 400 hr test as it would in a series of tests whose cumulative time, under load at temperature, was 400 hr.

A simple material evaluation test was developed, using a modified wire torsion tester developed at the Associated Spring Co. (Fig. 4). In this tester a straight length of the test wire is twisted through a predetermined deflection, corresponding to the desired stress, and heated while fixed in position. Measurements of the set are made periodically by releasing the load and checking the deviation from zero under no load at temperature. These measurements must be made immediately after load release, because recovery starts at once at the test temperature. This equipment is useful for quick material evaluation tests, since short lengths of wire can be tested and the sample does not need to be cooled for each measurement. Data obtained on springs by the nut-and-bolt method involve measurements at room temperature where no recovery can occur. The experimental differences that can arise between tests, in which relaxation data are measured at test temperature and at room temperature, can be appreciable if this phenomenon of recovery is overlooked.

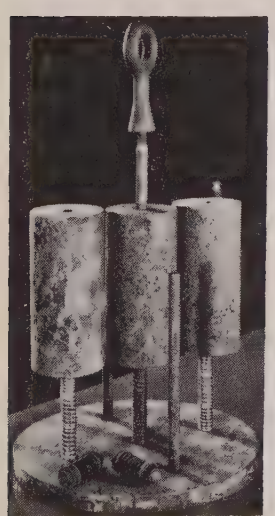

Fig. 3 — Dead weight loading fixture for creep tests and bolts for relaxation tests

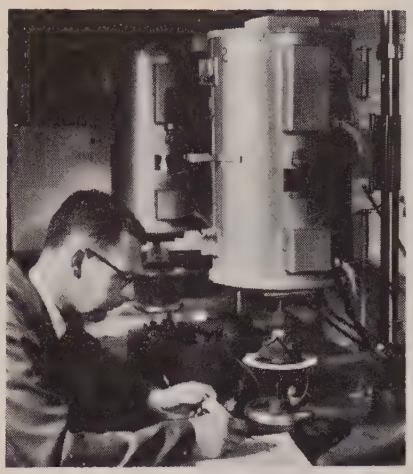

Fig. 4 — High temperature wire torsion tester

Test Results

The test data for relaxation and creep are presented as a percent of load loss with time for given test conditions of stress and temperature. This load loss figure actually represents a loss of deflection, but the two are directly proportional. The set in inches (or degrees for the wire tension tester) divided by the test deflection, times 100 is reported as the percent load loss. The data are plotted on a semi-logarithm basis against the log of time at temperature.

Some data obtained on the wire torsion tester are plotted in Fig. 5. Note that the plots are essentially straight lines on a semi-log basis. They do not go through zero relaxation; the intercept at zero time would represent the initial plastic flow due to the lower yield point at the elevated temperature. A plot such as this serves as a rough ranking of potential spring materials under given conditions of stress and temperature. Note that two factors control the total amount of relaxation:

1. The initial relaxation due to plastic flow.
2. The time dependent anelastic flow.

Some materials have shown a high initial relaxation and a low rate of anelastic flow, while others are just the opposite. This means that the relaxation-time data lines may cross, and materials which may be best for short operating times will not necessarily be so for longer times. This condition also changes with operating temperature, so that some alloys which have a high initial relaxation but a low flow

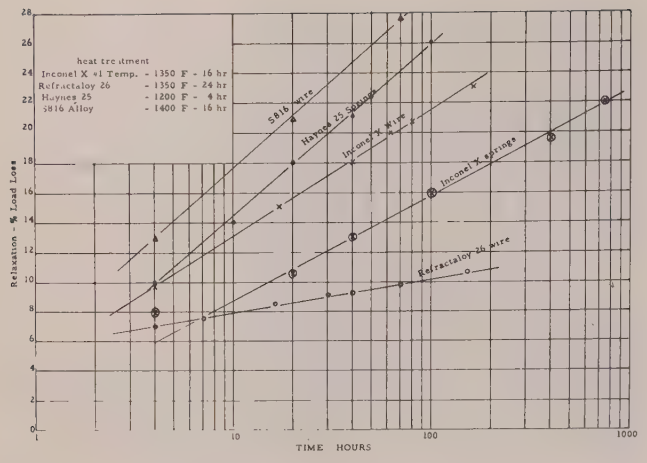
heat treatment
Inconel X +1 Temp. - 1350 F - 16 hr
Refractaloy 26 - 1350 F - 24 hr
Haynes 25 - 1200 F - 4 hr
S816 Alloy - 1400 F - 16 hr
S816 wire
Haynes 25 Springs
Inconel X Wire
Inconel X springs
Refractaloy 26 wire
Relaxation - % Load Loss
TIME HOURS

Fig. 5 — Stress relaxation of springs and straight wire specimens at 1000 F, initial stress 40,000 psi

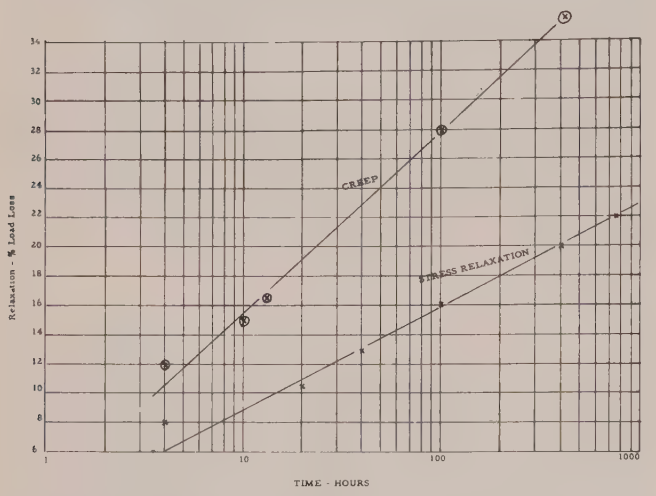

Fig. 6 — Creep versus stress relaxation in Inconel X alloy springs tested at 1000 F and initial stress of 40,000 psi (No. 1 temper Inconel X aged 1350 F, 16 hr)

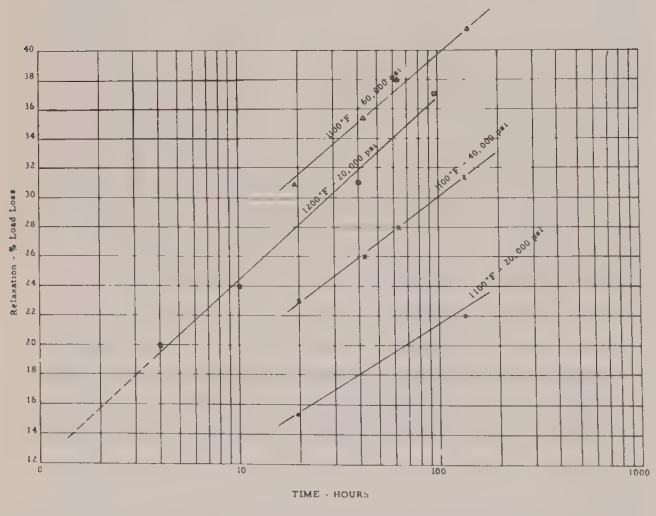

Fig. 7 — Stress relaxation of springs of Inconel X alloy at 1100 and 1200 F (No. 1 temper Inconel X aged 1350 F, 16 hr)

rate may look increasingly better as the test temperature is increased.

Creep or Relaxation - Fig. 6 is a plot of creep and relaxation on the same type of spring, with the same initial stress. Both are losing load at a constant rate on a semi-log time basis, but the rate of load loss is appreciably higher under conditions of creep or constant load. Because of test difficulties with creep loading, most of the subsequent tests have been run as relaxation tests.

Relaxation Data - Figs. 5 and 7 represent the relaxation of various spring materials at temperatures of 1000 F through 1200 F. In Fig. 5, at 1000 F, the alloy Haynes 25 shows a low initial relaxation but a high rate of anelastic flow. Thus, springs made of this material are poorer than those of Inconel X at longer test times. This condition is the same at temperatures below 900 F, but reversed above 1000 F.

Relaxation and Recovery - Fig. 8 shows relaxation and recovery data obtained by alternately loading and unloading springs and wire torsion samples at temperature. These tests were run in an Instron tester fitted with a furnace (Fig. 9). The significant point here is the tendency of a spring to recover anelastically after a loading period. This effect is the basis of a spring treating process known as heat setting, in which a spring is over-loaded at temperature for a short time to impart a tendency to grow or resist a lower load at temperature.

Effect of Heat Setting - One of the "tricks of the trade" of the spring maker is heat setting, in which a spring is loaded and heated to a temperature higher than the desired operating temperature. In this process the spring sets, but it is made initially longer than desired, so that after heat setting the spring is of the desired dimensions. This operation removes the initial plastic flow from the spring, and, furthermore, builds up a favorable residual stress pattern in the spring to resist further setting. Such a heat set spring will withstand relaxation markedly better than a non-set spring. Cold setting has no such beneficial effect on relaxation.

In fact, a drastically heat-set spring will actually gain load, and exhibit recovery or negative relaxation, during test under load, if the heat-set time, temperature, and stress have been sufficiently high as compared with service stress and temperature. Of course, if a heat-set spring is unloaded at temperature, it will recover rapidly. The heat setting process is thus best for a steadily load spring, and not for one intermittently loaded, although some gain may be expected due to the allowance for the initial plastic flow.

One of the unexpected results of this series of tests has been the discovery of the fact that the beneficial effects of heat setting are transient. The heat set springs (Figs. 10-12), show in most cases some slight initial recovery, then a period of no relaxation, and finally a period in which relaxation begins and proceeds at a rate equal to the rate of relaxation of a non-heat-set spring. In other words, the period of stability conferred by heat setting is not indefinite. It may last from a few hours to almost a thousand, but ultimately re-

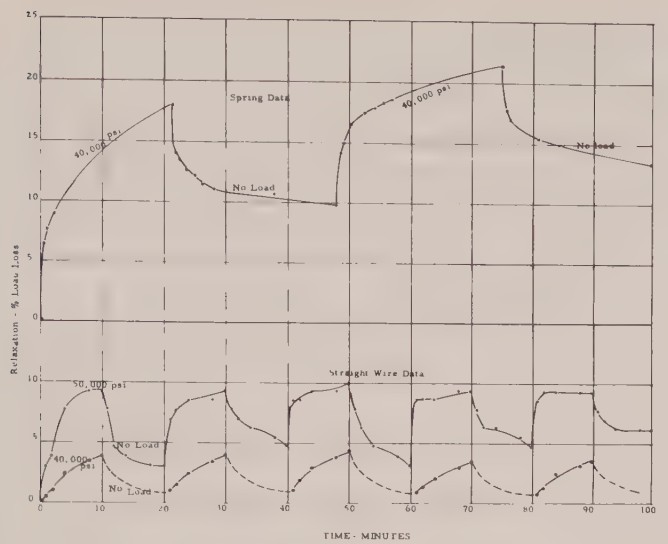

Fig. 8 — Stress relaxation and recovery of Inconel X alloy springs and straight wire samples at 1000 F (No. 1 temper Inconel X aged 1350 F, 16 hr)

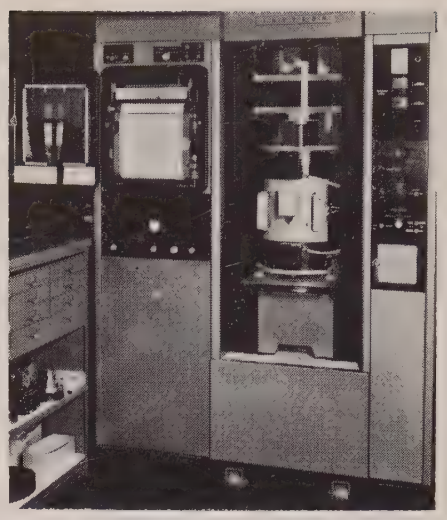

Fig. 9 — Setup for measuring spring relaxation and recovery continuously

laxation begins as if there had been no heat setting. The period of delay appears to be related to the severity of the heat setting operation for a given alloy and given test conditions. Unfortunately, severe heat setting operations, although they confer stability, result in a greater amount of initial recovery. So far, it is not known how to make a spring that will show zero relaxation indefinitely under load at temperatures above 900 F. However, this ideal can be approached if a precision heat-set spring is calibrated at temperature to allow for any recovery.

Summary

Data are presented on the performance of statically loaded spring materials for temperatures up to 1200 F and up to 1500 hr. Stress relaxation proceeds at a constant rate if the time is plotted on a log basis, and cautious extrapolation of test data may be justified. Heat-set springs exhibit markedly better performance with close to zero or actually negative relaxation, but this is a temporary effect only, dependent on the heat setting process, and extrapolation of test data may be quite dangerous.

In the range of temperatures, stresses, and time used in these tests, Inconel X, No. 1 temper, appears to be the best of the commonly available spring materials, although one sample of Refractaloy 26 has given better results, particularly as the temperature goes up. Unpublished data of the International Nickel Co. have indicated that spring temper Inconel X given the triple heat treatment of 2100 F for 2 hr, plus 1550 F for 24 hr, plus 1300 F for 20 hr may be expected to give comparable results at these temperatures. However, this heat treatment must be applied to already coiled springs, necessitating supporting arbors. Tests are being run on this

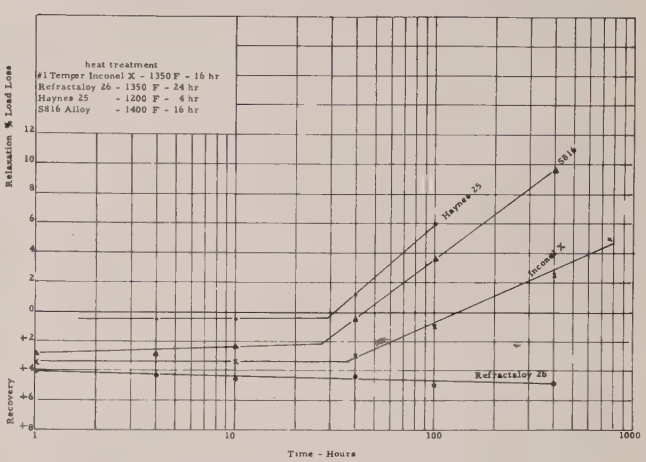
heat treatment
#1 Temper Inconel X - 1350 F - 16 hr
Refractaloy 26 - 1350 F - 24 hr
Haynes 25 - 1200 F - 4 hr
S816 Alloy - 1400 F - 16 hr
Relaxation % Load Loss
Recovery
S816
Haynes 25
Inconel X
Refractaloy 26
Time - Hours

Fig. 10 — Stress relaxation of heat-set springs at 1000 F and initial stress of 40,000 psi

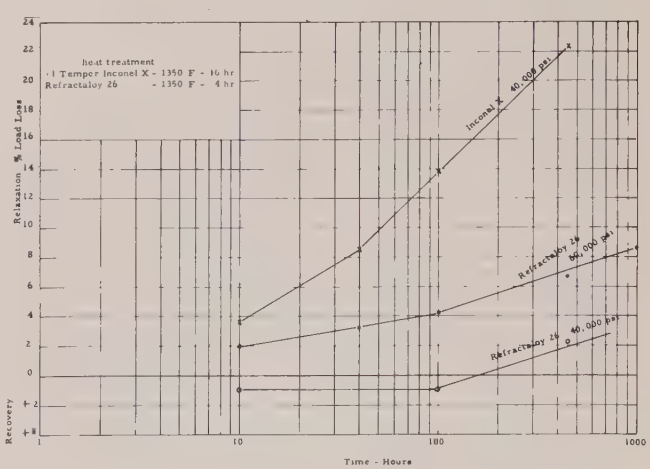
heat treatment
#1 Temper Inconel X - 1350 F - 16 hr
Refractaloy 26 - 1350 F - 4 hr
Relaxation % Load Loss
Recovery
Inconel X 40,000 psi
Refractaloy 26 40,000 psi
Refractaloy 26 40,000 psi
Time - Hours

Fig. 11 — Stress relaxation of heat-set springs at 1100 F

type of heat treatment.

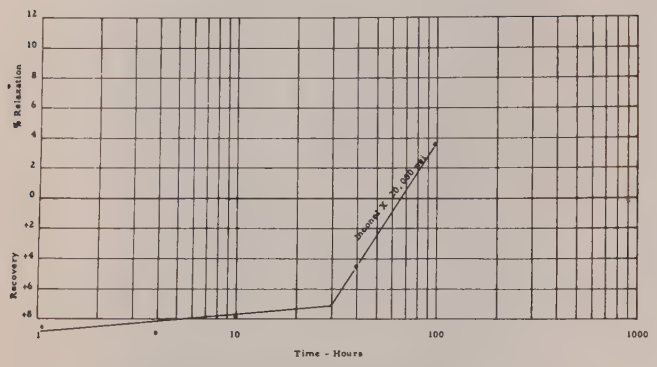

Fig. 12 — Stress relaxation of heat-set springs at 1200 F

References

1. F. P. Zimmerli and W. P. Wood, "Effect of Temperature on Endurance Limit and Relaxation of Spring Materials", SAE Transactions Vol. 62, 1954, 557-565.

2. R. G. Matters and R. E. Lochen - "Materials for Helical Compression Springs for Use at Constant Deflection from 600 to 1400 F", Proceedings of ASTM Vol. 56, 1956.

3. Inco Nickel Alloy Helical Springs, Technical Bulletin T35, International Nickel Co., May 1955.

4. "High Temperature Springs", The Mainspring, Associated Spring Corp., Spring 17, Coil 3, October-November 1957.

5. J. D. Lubahn "The Role of Anelasticity in Creep, Tension, and Relaxation Behavior", Transaction of the ASM., Vol. 45, 1953, 787-838.

Secondary Power Systems for Space Vehicles

D. B. Mackay
North American Aviation, Inc.

This paper received the 1960 Manly Award.

THE MOST EFFICIENT means known today for converting heat energy into shaft power is a turbine or reciprocating engine. The Rankine vapor cycle would probably be used, although in some cases, Brayton and Stirling cycles may be considered as possible alternates.

Ambient temperatures have considerable influence on earth powerplant performance. The condenser is cooled by water or air, and temperature and pressure of the vapor are directly related to the environment. In space, the vapor is condensed by transferring its heat to space by radiation, and the pressure and temperature are controlled by the radiator area and the other factors influencing radiation heat transfer.

For a space vehicle, the powerplant weight is a significant item and must be reduced to a minimum. If the heat energy for a given plant is assumed, as indicated in Fig. 1A, to come from a nuclear reactor, the reactor weight is essentially constant for a wide range of energy output. With the exception of the radiator, the other components are more or less fixed in weight when power output is specified. Thus the radiator is the only item which can be altered for a significant change in overall system weight. Further, it is expected that weight of the radiator will depend largely on the effective radiator area. The conditions for obtaining minimum radiator area are therefore important features in controlling powerplant design.

A method for analyzing cycles to obtain minimum radiator area has been developed (1)*. This method is applicable to one class of fluids used in the Rankine cycle and was employed in obtaining a comparison of mercury and rubidium. Other work pertaining to the same subject and adopted for a limited number of other fluids is presented in Ref. (2). Since the publication of these reports, NASA has analyzed space powerplants and has proposed the use of sodium as a working fluid (Ref. 3). Ref. (4) proposes the use of sulfur for a small space powerplant, and still others have suggested potassium. For these reasons, methods for analyzing the fluids and predicting their performance are combined here into a single source for easy reference.

A portion of the work in the analysis presented in this paper is directed toward analyzing cycles and fluids to obtain minimum radiator area. Also, other physical characteristics such as vapor volume, pressure, and quality are analyzed and comparisons are made for the more promising fluids. Because Ref. (1) demonstrates the fact that superheating rubidium vapor has little effect on optimum turbine exhaust temperature, and because the other liquid metals be-

*Numbers in parentheses designate References at end of paper.

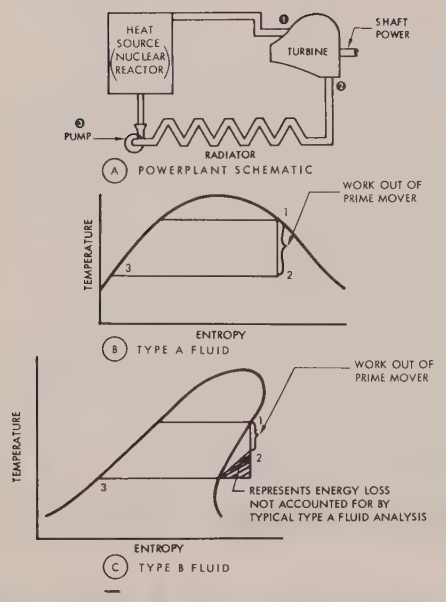

Fig. 1 — Theoretical cycles for type a and type b fluids

have in a similar manner, no analysis is presented here for the superheat cycle. It is desirable to maintain dry or nearly dry vapor at the turbine inlet, and therefore, because a fluid comparison is being made, only the basic direct cycle illustrated in Fig. 1A was analyzed.

In performing this analysis, two classes of fluids are encountered. The fluids for which direct parameters for fluid performance are derived have been designated as Type a fluids. Unfortunately, not all fluids can be analyzed by these parameters, and individual analyses are required. For convenience, the latter fluids have been designated as Type b fluids. A recent publication (Ref. 5) contains much of the information needed for all these analyses.

Rankine cycles using saturated vapor at the turbine inlet for the two classes of fluids (Types a and b) are illustrated in Fig. 1. The conditions of the expanding vapor in an ideal prime mover are shown by the portion of the cycle between points 1 and 2. For Type a fluid, point 2 is in the "wet" region, and the temperature at point 2 is equal to the saturated liquid temperature at point 3. For Type b fluid, the vapor expands in the superheat region, and the temperature of the vapor leaving the ideal prime mover exceeds saturation temperature. Also, the rejection of heat from the cycle from points 2 to 3 is at constant temperature for a Type a fluid but at partially varying temperatures in a Type b fluid. A fluid exhibiting Type a characteristics can be analyzed by the method demonstrated in Ref. (1), while a fluid with inherent Type b properties requires a lengthy, independent analysis. Possible working media for space powerplants include the fluids shown in Table 1.

Cycle Analysis

Type a Fluids - To establish useful parameters, it is convenient to consider the three cycles shown in Fig. 2:

1. Carnot cycle.
2. Ideal fluid cycle.
3. Actual liquid-vapor cycle.

The performance of the Carnot and ideal fluid cycles is easily predicted. In the Carnot cycle, heat is added to a working fluid as it changes from state 4 to 1. (See Fig. 2A.) Work is then extracted from the fluid while passing from 1 to 2, and heat is rejected along the line shown as 2 to 3. The work done by the fluid in passing through the cycle is equal to the shaded area W_c, and the heat rejected per cycle is shown by the area Q_r. The heat added is equal to the sum of the areas W_c and Q_r.

If the ideal cycle is modified to include only inefficiency effects in the prime mover, the cycle shown in Fig. 2B results. Here, the fluid expands in an inefficient engine from state 1 to 2 along an irreversible path shown with a dotted line. The result of this inefficiency is to increase the size of the heat rejection area Q_r, with the increase at the expense of the work cycle. The actual work is less than the ideal work. The portion of the cycle from 3 to 4 is identical to that of the Carnot cycle in which no external heat is added to the fluid during the change of temperature from 3 to 4. Thus, if the fluid were a liquid, its specific heat would be equal to zero. A liquid specific heat equal to zero is the basis used here for defining an ideal fluid.

The actual liquid-vapor cycle takes into account actual fluid properties as well as an inefficient prime mover. If an ideal expansion process is assumed as a limiting case, this cycle would conventionally be classed as a Rankine cycle. If attention is confined to the particular case where the vapor enters the turbine in a dry and saturated condition, then the cycle for a number of fluids can be drawn as shown in Fig. 2C. The difference between this cycle and the ideal fluid cycle is that heat is added to the liquid along the path between 3 and 4, at which time the liquid is heated to the boiling point. Continued heat beyond this point is at constant temperature, and the liquid is converted to 100% vapor when point 1 is reached. The effect of having an inefficient fluid is shown by the area W_{theo} being smaller than the area W_c, represented by the rectangular area shown for the ideal cycle. The heat added to the fluid is also reduced to a smaller degree, but a larger portion of the added heat ends up in the rejected heat area, Q_r. An inefficient prime mover further reduces the output energy and again adds its waste energy to the rejected heat.

In the optimization of a cycle and selection of the best fluid, the actual cycle thermal efficiency is of paramount importance. In its most useful form, it is expressed in terms of the fluid temperatures at the prime mover inlet and exit. For the Carnot cycle, this efficiency can be expressed as

$$\eta_c = \frac{T_1 - T_2}{T_1} = 1 - \frac{T_2}{T_1} \quad (1)$$

and for the ideal fluid cycle as

$$\eta = \eta_t \left(1 - \frac{T_2}{T_1}\right) \quad (2)$$

When an actual fluid cycle is considered, the equation for thermal efficiency becomes more complicated and an evaluation of an actual fluid cycle is needed. Referring to Fig. 2C, the energy available as work in the cycle is equal to the area designated W_{theo}, whereas in the Carnot cycle this area would be the rectangular area W_c shown in Fig. 2A. Points 1 and 3 of the actual cycle must coincide with points 1 and 3 for the Carnot cycle. The relationship or ratio of the two areas can be defined as a work factor f or

$$f = \frac{W_{theo}}{W_c} \quad (3)$$

The thermal efficiency of any actual heat cycle can be written as

$$\eta = \frac{\text{Output}}{\text{Input}} = \frac{\dot{w} W_a}{\dot{w} Q_a} = \frac{\dot{w} W_a}{\dot{w} Q_n + \dot{w} W_a} \quad (4)$$

The actual work output is the product of the theoretically available work, times the turbine Rankine efficiency, or

$$W_a = \eta_t \, W_{theo} \quad (5)$$

Combining Eqs. 3 and 5,

$$W_a = f \, \eta_t \, W_c \quad (6)$$

Substituting values from Eq. 6 into Eq. 4,

$$\eta = \frac{f \, \eta_t \, W_c}{Q_r + f \, \eta_t \, W_c} \quad (7)$$

The work from the Carnot cycle is

$$W_c = (T_1 - T_2)(S_1 - S_4) \quad (8)$$

The heat rejected from the actual cycle is equal to the amount lost from the ideal cycle plus the amount made unavailable by the inefficient prime mover, or

$$Q_r = T_2 (S_1 - S_4) + (1 - \eta_t) \, f \, W_c \quad (9)$$

Combining Eqs. 7, 8, and 9,

$$\eta = \frac{f \, \eta_t (T_1 - T_2)(S_1 - S_4)}{T_2 (S_1 - S_4) + f (1 - \eta_t)(T_1 - T_2)(S_1 - S_4) + f \, \eta_t (T_1 - T_2)(S_1 - S_4)} \quad (10)$$

After simplication,

$$\eta = \frac{(T_1 - T_2) f \, \eta_t}{T_2 + (T_1 - T_2) f} \quad (11)$$

This can further be reduced to

$$\eta = \eta_t \, \eta_{theo} \quad (12)$$

where

$$\eta_{theo} = \frac{1 - \frac{T_2}{T_1}}{1 + \left(\frac{1}{f} - 1\right)\left(\frac{T_2}{T_1}\right)} \quad (13)$$

It should be noted that the theoretical efficiency expressed by Eq. 13 depends only on the temperature ratio and the value of f and plays a key role in predicting thermal effi-

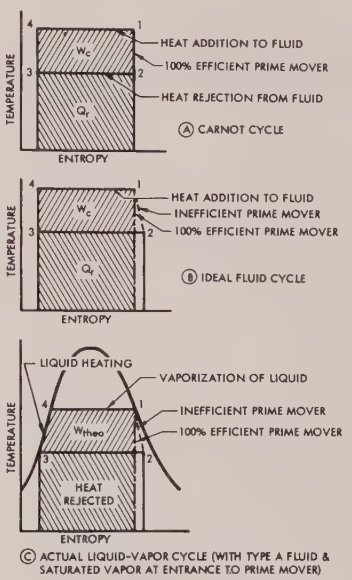

Fig. 2 — Comparison for Carnot cycle with actual cycles for type a fluids

Table 1 - Possible Working Media for Space Powerplants

Type a	Type b
Water	Diphenyl
Ammonia	Dowtherm A
Mercury	Sulfur
Rubidium	Aluminum bromide
Sodium	Large number of hydrocarbons
Potassium	
Cesium	

ciency.

An alternate form for thermal efficiency can be obtained by combining Eqs. 12 and 13. From these equations, the efficiency can be written as

$$\eta = \frac{\eta_t \left(1 - \frac{T_2}{T_1}\right)}{1 + \left(\frac{1}{f} - 1\right)\frac{T_2}{T_1}} \tag{14}$$

Further, if a substitution is made wherein

$$g = \frac{1}{f} - 1 \tag{15}$$

then

$$\eta = \frac{\eta_t \left(1 - \frac{T_2}{T_1}\right)}{1 + g\left(\frac{T_2}{T_1}\right)} \tag{16}$$

A convenient method for the evaluation of the work factor f has already been published (1), and an equation for obtaining the numerical value was given as

$$f = \frac{1 + \frac{h_{fg1}}{CT_1} + \frac{\frac{T_2}{T_1}}{1 - \frac{T_2}{T_1}}\left(\log_e \frac{T_2}{T_1}\right)}{\frac{h_{fg1}}{CT_1} - \log_e \frac{T_2}{T_1}} \tag{17}$$

The term $h_{fg1}/C\,T_1$ in Eq. 17 is an easily determined parameter expressing the fluid properties, and is designated here as a fluid parameter. Eq. 17 also shows that the work factor f for saturated vapor at the entrance to the prime mover is only a function of the temperature ratio T_2/T_1 and the fluid parameter $h_{fg1}/C\,T_1$. A high value of the fluid parameter for a given temperature ratio will result in a high value of the work factor f. Thus, a fluid parameter of high value is a desirable property because high values of f yield high thermal efficiencies. This convenient parameter can be used to evaluate the performance of a fluid in the Rankine cycle.

For certain types of analyses, it is desirable to express efficiency as a product of three terms:

1. Efficiency of the Carnot cycle.
2. Efficiency of prime mover.
3. Fluid efficiency factor η_f which takes into account deviations due to the cycle and working fluid.

With these notations, Eq. 12 becomes

$$\eta = \eta_c\ \eta_t\ n_f \tag{18}$$

The value of η_f can be found by combining Eqs. 1, 12, 13, and 18.

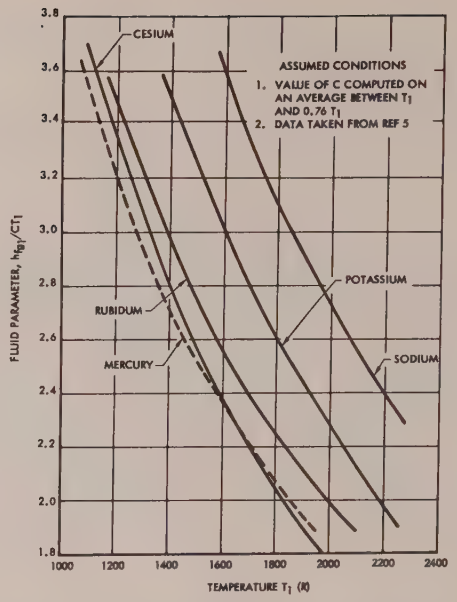

Fig. 3 — Fluid parameters for type a fluids

$$\eta_f = \frac{1}{1 + \left(\frac{1}{f} - 1\right)\left(\frac{T_2}{T_1}\right)} \tag{19}$$

Eq. 19 is basic for the evaluation and comparison of fluids.

Having established a set of equations for evaluating fluids, it is now possible to apply them to real fluids. Figs. 3-7 show a number of relationships existing between the fluid parameter, temperature, and cycle thermal efficiency.

Fig. 3 shows fluid parameters for a number of possible fluids. The highest values were obtained for sodium. Many fluids have lower values, but no fluids with parameters below that of mercury are shown. Water, for example, has a value of only 0.593 at a temperature T_1 of 1000 R. It appears that the liquid metals (i.e., sodium, potassium, rubidium, cesium, and mercury) stand in a class by themselves, with high-value fluid parameters. The values shown for the fluid parameters are lower at higher temperatures. In fact, the fluid parameter becomes zero at the critical temperature. This is due to two factors, both of which predict a zero value. The latent heat is equal to zero, and the specific heat of the liquid is equal to infinity. Thus, as higher temperatures are used in the prime mover, fluids of higher critical temperatures will be needed.

To study the effects of fluid parameters on the work factor f, the relationship shown by Eq. 17 was plotted in Fig. 4. As stated previously, high values for f are obtained with high values for the fluid parameter. Also, as shown, the value of f decreases with a reduction of the temperature ratio. Values of f in excess of 0.9 are attainable over a wide temperature ratio for all of the liquid metals shown in Fig. 3.

The work factor f is related to thermal efficiency as shown by Eqs. 11 and 13. The useful curves of Fig. 5 were ob-

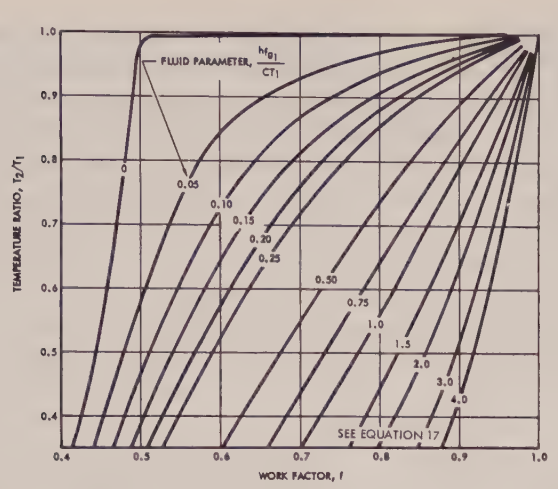

Fig. 4 — Relationship between work factor and fluid parameter

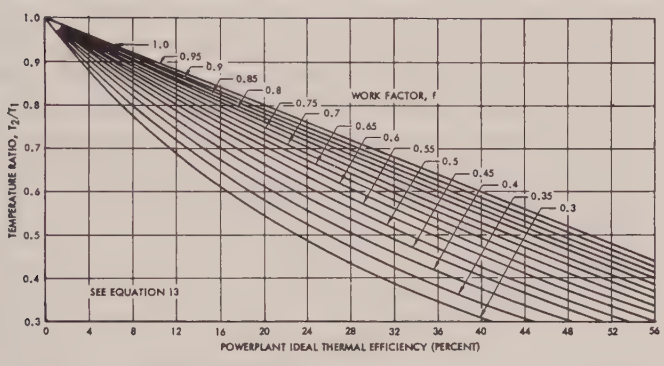

Fig. 5 — Powerplant thermal efficiency as function of work factor

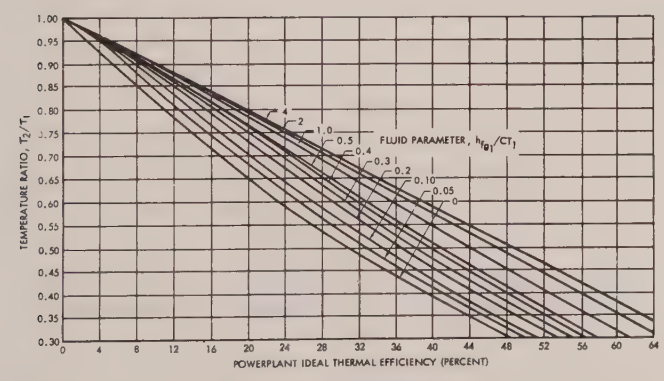

Fig. 6 — Powerplant thermal efficiency as function of fluid parameter

tained from Eq. 13. Thermal efficiency is highest for values of f approaching 1. Because a value of 1.0 is attainable only with the Carnot cycle, this line is the maximum value attainable for any cycle. It has been demonstrated that rather high values are possible from the liquid metals. Therefore, values within 2 to 3% of the Carnot cycle are possible for the theoretical cycle.

Another extremely useful curve can be obtained by cross plotting the data of Figs. 4 and 5 to eliminate the work factor f. However, better accuracy was obtained in this study by using arbitrarily assumed values of the fluid parameter. These values were substituted into Eq. 17, and the value of f was computed for a number of arbitrarily selected temperature ratios. The resultant values of f were then substituted into Eq. 13. By using the selected temperature ratios, the ideal thermal efficiencies shown in Fig. 6 were computed. The ideal thermal efficiency can be quickly obtained with these curves. Further, if actual efficiency is desired, this too can be easily obtained by using Eq. 12.

The thermal efficiency was also expressed by Eq. 18, wherein the value of η_f was given by Eq. 19. However, to obtain a set of curves in the most useful form, values of f were evaluated by Eq. 17 for assumed temperature ratios. These temperature ratios and the computed values of f were substituted into Eq. 19 and the value of efficiency factor η_f computed. The data obtained from Eqs. 18 and 19 were then plotted for convenience on Fig. 7. As shown, the values of η_f approach 100% for all fluid parameters at a temperature ratio of 1, and are greater than 90% for all temperature ratios shown when the liquid metals are used in the Rankine cycle. These efficiency factor values are remarkable and point to the futility of attempting to improve powerplant performance by using a binary fluid or a regenerative cycle.

To further demonstrate cycle performance, a specific case is considered. Assume a rubidium powerplant is operating at 1800 R with a temperature ratio T_2/T_1 equal to 0.75. From Fig. 3, the fluid parameter $h_{fg1}/C\ T_1$ equals 2.243. Applying this value to the curves of Fig. 7, the value of η_f is found to be equal to 94%. In other words, the Carnot efficiency is reduced by a factor of 6% due to the use of a Rankine cycle with rubidium as a working fluid. It does not seem justifiable to complicate the cycle when an improvement of only 6% is theoretically possible.

Type b Fluids - It is possible to compare the performance of Type b fluids by establishing efficiency curves for each fluid, or by use of a fluid efficiency factor η_f as established for Type a fluids. The latter factor can be obtained by combining Eqs. 12 and 18, or

$$\eta_f = \frac{\eta_{theo}}{\eta_c} \qquad (20)$$

Accurate theoretical efficiency is not easily predicted for Type b fluids because of the lack of information on the fluid properties. However, the available data were analyzed and the results compared.

The fluids analyzed include diphenyl, Dowtherm A, aluminum bromide, and sulfur. The first three were considered because of their relatively high thermal stability, and sulfur was considered because it is an element with favorable vapor pressure characteristics. The thermal efficiencies of Dowtherm and diphenyl were obtained by planime-

tering the areas on the diagrams presented in the appendix of this paper, and the results are shown in Figs. 8 and 9.

Reliable data were not obtainable for sulfur. The temperature-entropy chart (Fig. A-4 of the appendix) should be regarded as approximate because the areas planimetered do not agree with the available energy data taken from the same data source. To approximate the thermal efficiency, sulfur was regarded as though it were a Type a fluid, and an approximate loss due to the area in the superheat region was determined from Fig. A-4. For a temperature ratio of 0.75, an approximate correction of 14% in the value of η_f was obtained. Smaller corrections should be used if larger temperature ratios are considered.

A similar but less extensive analysis was made for aluminum bromide using the data of Ref. 5. However, for this fluid, the data for the fluid in the superheat region is unsatisfactory for computing the conditions of the fluid. Because the saturated vapor curve is nearly vertical, however, the loss of energy in the superheat region appears to be much smaller than was found for sulfur. An approximate reduction of 5% in the value of η_f was assumed for this fluid when the temperature ratio T_3/T_1 is equal to 0.75.

As a final comparison, values of the fluid efficiency factor η_f were computed at a temperature ratio of 0.75 for a number of Type a and Type b fluids. The results are presented in Fig. 10. The values shown for sodium, potassium, rubidium, and mercury fall in a narrow band between 94 and 97%. Sulfur, aluminum bromide, Dowtherm A, and diphenyl have much smaller values. Considering only the last four compounds, aluminum bromide has the highest efficiency (approximately 76% at 1100 R). The values on the curves for aluminum bromide, Dowtherm A, and diphenyl fall quite rapidly as the temperature T_1 increases, showing the severe limitations of the Type b fluids analyzed.

Sulfur has another adverse thermodynamic property which should also be noted. The molecular structure is not constant, but changes from one form to another depending upon such factors as temperature, pressure, and time of exposure to the environment. Sulfur is known to exist as S_1, S_2, S_6, and S_8 forms, or as mixtures of these depending upon conditions. This peculiar characteristic makes difficult the establishment of equilibrium fluid properties and the prediction of the performance of sulfur in an actual prime mover.

The data of Fig. 10 point out the shortcomings of using any fluid except those in the liquid metal class. If the other fluids are considered for any reason, then modifications such as employed in a steam powerplant should also be considered. The use of liquid heating by the extraction of vapor from the turbine or by the use of exhaust vapor from the

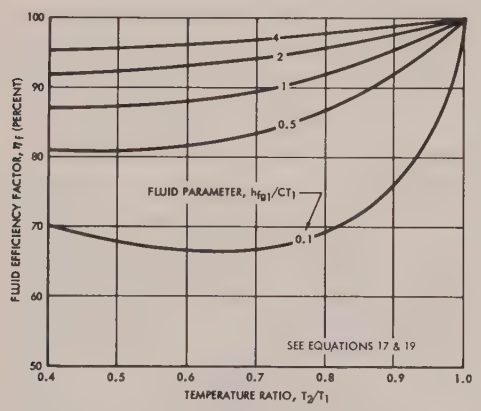

Fig. 7 — Fluid efficiency factor as function of fluid parameter

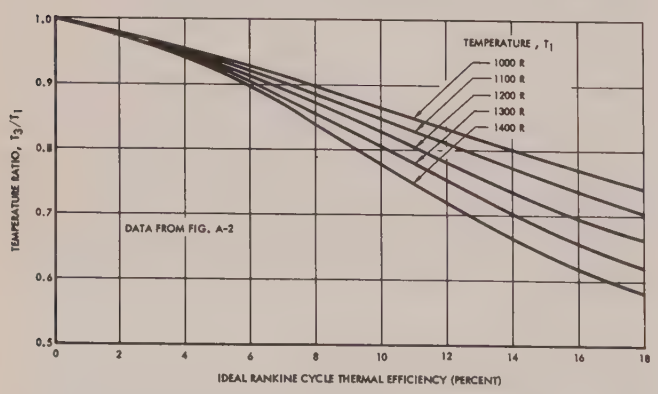

Fig. 8 — Thermal efficiency for diphenyl

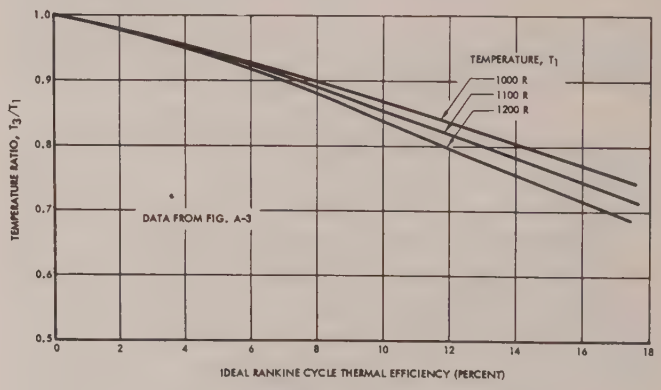

Fig. 9 — Thermal efficiency for dowtherm A

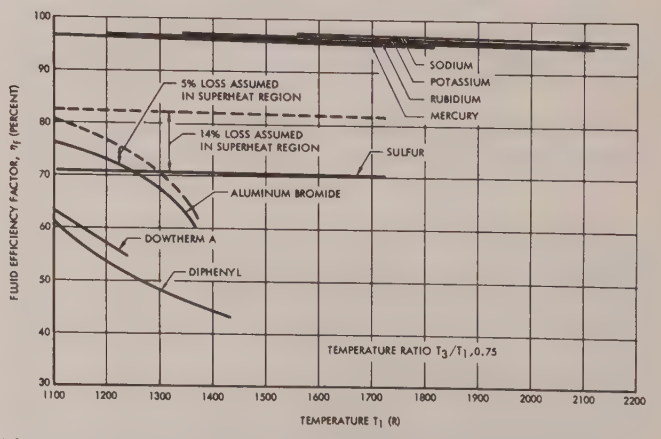

Fig. 10 — Comparison of fluid efficiencies for type a and type b fluids

prime mover will improve cycle performance. Without such improvement, the efficiency will be very low.

Powerplant Radiator Area

An equation expressing the radiator area can be obtained by modifying Eq. 4. The product, $\dot{w}\ W_a$, is the Btu equivalent of a kw-hr of work. By substituting its numerical value, Eq. 4 becomes

$$\eta = \frac{3413}{\dot{w}\ Q_r + 3413} \tag{21}$$

When Eq. 21 is solved for the heat rejected per kilowatt of power produced,

$$\dot{w}\ Q_r = 3413\left(\frac{1}{\eta} - 1\right) \tag{22}$$

It can be assumed in a heat-power cycle that the temperature level in the radiator will be high enough that celestial radiation would have little effect on the radiator surface temperature. Even radiation from the sun (430 Btu/(hr)(sq ft) at the earth's mean orbit) can be largely reflected from a normal white surface with little effect on the ability of the radiator to dissipate heat at the radiator temperature. Therefore, this source of heat was also omitted from the calculations. Neglecting the small temperature difference between the working fluid and the outer wall, the heat rejected from the cycle is

$$\dot{w}\ Q_r = C_1\ A_e\ T_2^4 \tag{23}$$

where

$$C_1 = (\epsilon_a + \epsilon_b)\sigma \tag{24}$$

in which C_1 is a constant for computing the heat radiated from a unit of radiator area.

The constant C_1, as defined in Eq. 24, takes into account the heat transfer from two sides of a heat exchanger. However, Eq. 24 is easily adapted to a configuration which emits heat from one side only. It is only necessary to retain the surface emissivity of the radiating surface and to equate the emissivity of the other surface to zero when computing the value of C_1. The value of the effective area is related to the physical size of the radiator (i.e., width and length). In the case that extended areas of nonuniform temperature are considered then the actual area can be converted to an effective area of uniform temperature equal to T_2. Substituting values from Eq. 23 into Eq. 22, and solving for the area.

$$A_e = \frac{3413}{C_1\ T_2^4}\left(\frac{1}{\eta} - 1\right) \tag{25}$$

Eq. 25 is basic to all direct cycles.

The radiator area for a Carnot cycle can be readily derived by combining Eqs. 1 and 25. Thus,

$$A_e = \frac{3413}{C_1\ T_2^4}\left(\frac{T_2}{T_1 - T_2}\right) \tag{26}$$

$$A_e = \frac{3413}{C_1\ T_2^4}\left[\frac{T_1}{(T_1 - T_2)\ \eta_t} - 1\right] \tag{27}$$

It can be observed that Eq. 27 becomes identical with Eq. 26 when η_t is equal to 1.0.

For an actual fluid cycle, values from Eq. 16 can be substituted into Eq. 25 and the area becomes

$$A_e = \frac{3413}{C_1\ T_2^4}\left[\frac{1 + g\left(\frac{T_2}{T_1}\right)}{\eta_t\left(1 - \frac{T_2}{T_1}\right)} - 1\right] \tag{28}$$

This important equation is basic for all Rankine cycles because when g is equal to 0 it becomes identical with Eq. 27 for the ideal fluid cycle, and when η_t is equal to 1 and g is equal to 0 it becomes equal to Eq. 26 for the Carnot cycle. Eq. 28 can be written in an alternate form,

$$A_e = \frac{\lambda}{(\epsilon_a + \epsilon_b)\ T_1^4} \tag{29}$$

where

$$\lambda = \frac{3413}{\sigma\left(\frac{T_2}{T_1}\right)^4}\left[\frac{1 + g\left(\frac{T_2}{T_1}\right)}{\eta_t\left(1 - \frac{T_2}{T_1}\right)} - 1\right] \tag{30}$$

The area function λ is also important. It contains only three variables: temperature ratio, T_2/T_1, turbine efficiency η_t, and the fluid properties expressed by the value of g. However, it will be demonstrated in the next section that the optimum temperature ratio T_2/T_1 is a function of g and η_t, and the value of therefore depends only upon g and η_t. Eqs. 28 and 29 are basic for determining the required radiator area.

A mathematical equation can be derived for determining the temperature relationship existing at the condition of minimum area. Differentiating Eq. 28 and simplifying,

$$\frac{dA_e}{dT_2} = \frac{3413}{C_1\ \eta_t\ T_2^5}\left\{\frac{T_1 T_2\ (1 + g)}{(T_1 - T_2)^2} - 4\left[\frac{T_1\ (1 - \eta_t) + T_2\ (\eta_t + g)}{(T_1 - T_2)}\right]\right\} \tag{31}$$

where, at minimum area,

$$\frac{dA_e}{dT_2} = 0$$

After making this substitution into Eq. 31 and simplifying,

$$4\left(\frac{T_2}{T_1}\right)^2 - \left(\frac{8\eta_t + 3g - 5}{g + \eta_t}\right)\frac{T_2}{T_1} - \frac{4(1 - \eta_t)}{g + \eta_t} = 0 \qquad (32)$$

Solving this quadratic equation, and excluding the extraneous root,

$$\frac{T_2}{T_1} = \frac{8\eta_t + 3g - 5 + \sqrt{(3g + 5)^2 + 4g - 16\,\eta_t\,(g + 1)}}{8\,(g + \eta_t)} \qquad (33)$$

Eq. 33 is an important general equation expressing the relationship between the optimum temperature ratio, the fluid properties, and the turbine efficiency.

In the special case of the Carnot cycle, η_t is equal to 1 and g is equal to 0. These substitutions into Eq. 33 reduce the temperature ratio to a constant value of

$$\frac{T_2}{T_1} = \frac{3}{4} \qquad (34)$$

For the ideal fluid cycle, g is equal to 0, and Eq. 33 reduces to

$$\frac{T_2}{T_1} = \frac{8\eta_t - 5 + \sqrt{25 - 16\eta_t}}{8\eta_t} \qquad (35)$$

The value of the optimum temperature ratio in Eq. 35 can be obtained readily for any desired value of η_t.

Temperature ratios for minimum radiator area are plotted from Eq. 33 for a variety of work factors f as functions of turbine efficiency η_t in Fig. 11. The temperature scale is magnified so the curves can be read to a high degree of accuracy, as shown by the ratio changes from 0.75 for a 100% efficient turbine to a maximum value of 0.776 at a 60% efficient turbine.

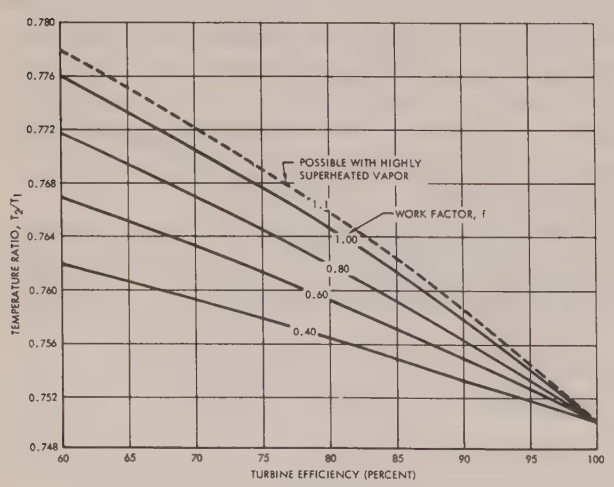

Fig. 11 — Optimum temperature ratio (direct cycle)

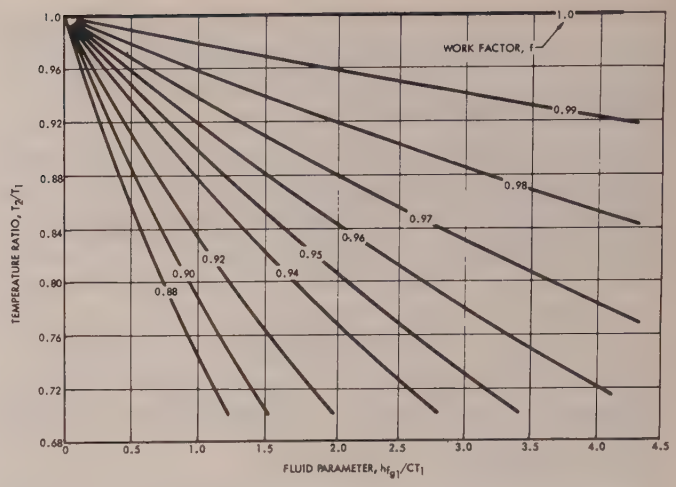

Fig. 12 — Relationship between work factor and fluid parameter

Before the data of Fig. 11 can be used in an actual fluid cycle analysis, it is necessary to determine the work factor f of the useable fluids for this cycle. In high-temperature operating regions, only a few fluids can be considered. The more promising are elements, because most known fluid compounds either partially or completely decompose at temperatures above 1000 F (1460 R). Even a number of elements change molecular form in the higher temperature regions and introduce molecular stability problems. It is difficult to predict the result upon the turbine design, radiator performance, and even the heat source operation when dealing with an unstable molecular structure. The more promising elements are the liquid metals recommended earlier, which will be analyzed further.

A set of curves relating fluid parameter, work factor, and temperature ratio, in a form useful for this analysis, were obtained by cross plotting the data in Fig. 4. The results are shown in Fig. 12. With the data of Figs. 11 and 12, it is possible to determine the optimum temperature ratio T_2/T_1 in the cycle.

If the data of Fig. 11 are superimposed on Fig. 12, using the values of work factor and temperature ratio to locate the turbine efficiency curves, a set of data results which would determine the correct temperature ratio directly from the known values of the fluid parameters. However, the operating range for an actual powerplant is located in a narrow range of temperature ratios from 0.75 to 0.776.

In order to obtain a more readable scale, the data of Fig. 12 were enlarged in the useful region and plotted in Fig. 13. The temperature ratio and work factor data of Fig. 11 were then carefully determined for a series of turbine efficiencies and superimposed on the expanded data. The resulting

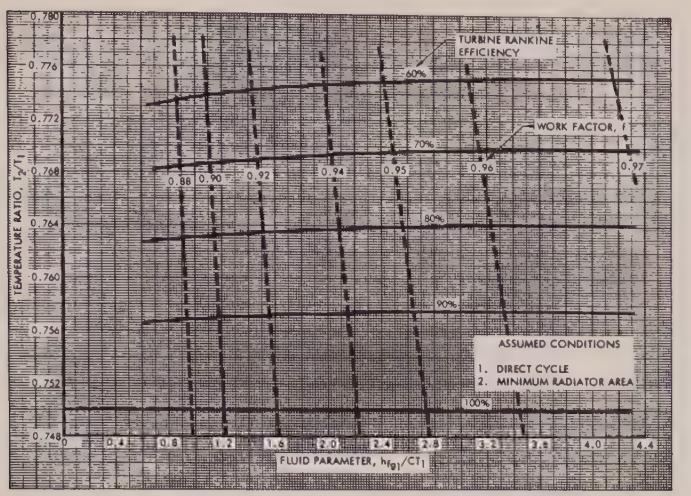

Fig. 13 — Optimum temperature ratio versus fluid parameter

curves (Fig. 13) are convenient for analyzing a fluid cycle. It is only necessary to establish the fluid parameter and turbine efficiency; with these two items, the temperature ratio and the work factor can be easily read to a high degree of accuracy.

Using the optimum temperature ratios established, the turbine exhaust temperatures were calculated and plotted in Fig. 14 for rubidium. The differences in exhaust temperatures for different turbine efficiencies are not large. The maximum change ranges from 40 to 75 R as the turbine inlet temperatures go from 1500 to 3000 R. Changes in turbine exhaust temperature are due to turbine efficiency changes from 60 to 100%.

Fluid Comparisons

Having established the optimum turbine exhaust temperature, it is possible to make physical comparisons using different working fluids with a variety of turbine efficiencies. The more important comparisons include radiator area, vapor quality at turbine exhaust, volume of exhaust vapor, working fluid flow rate, vapor pressure, and powerplant thermal efficiency. With these comparisons, a designer is able to make a more intelligent selection of the best working fluid for a powerplant.

The radiator areas can be compared either by a general analysis using the area function of Eq. 30, or by comparing the fluids individually using Eq. 28. In applying the general analysis, however, the optimum temperature ratios and the fluid work factors were established by use of Fig. 13 for a variety of fluid parameters and turbine efficiencies. The value of g was then determined by Eq. 15 for each value of the work factor. The value of the area function λ was determined by Eq. 30 for the assumed values of the fluid parameters and turbine efficiencies. For the case of an ideal fluid, the value of λ is readily computed from Eq. 30 since

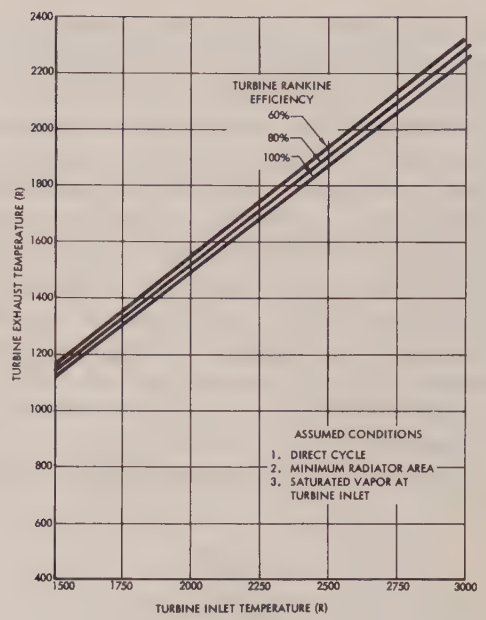

Fig. 14 — Exhaust temperature for rubidium turbine (direct cycle)

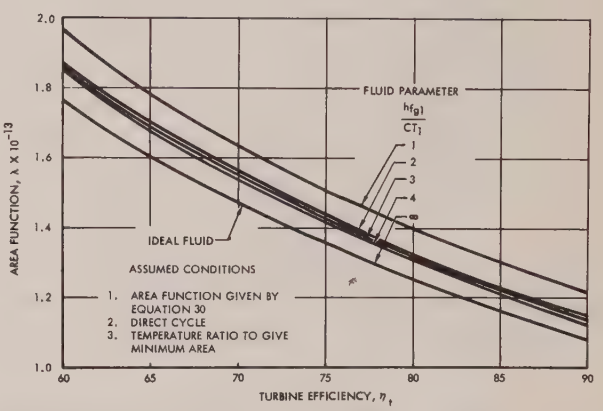

Fig. 15 — Radiator area functions

g is equal to 0 and T_2/T_1 is equal to 0.75. In presenting the results, the value of λ was plotted in Fig. 15 for the originally assumed variables.

Fig. 15 indicates that the value of λ goes up as the turbine efficiency goes down. An increase in the value of λ of approximately 55% is encountered when the turbine efficiency drops from 90 to 60%. The actual radiator area will increase by the same percentage; thus, the penalty resulting from reduced turbine efficiency is clearly illustrated.

Values for the area function λ are higher at low values of the fluid parameter, but the change is small. For example, at 60% turbine efficiency, the values of λ x 10^{-13} are 1.765, 1.847, and 1.965 for fluid parameters of ∞ (ideal fluid), 4, and 1, respectively. The 1.847 and 1.965 values represent radiator area increases of 4 and 11% above the areas required for the ideal fluid cycle. At 90% turbine efficiency, slightly higher increases in λ are encountered. When

comparing liquid metals, the difference in values of λ when one metal is replaced by another is very small. At 80% turbine efficiency for the fluid shown in Fig. 3, the increase in λ is less than 2% when changing from the lowest to the highest fluid parameter. Therefore, with liquid metals, properties other than fluid parameter (such as specific volume of vapor, flow rate, or pressure), will play a predominant role in the selection of the best fluid.

Effective radiator areas required for a powerplant can be determined by Eq. 28 or 29. Eq. 28 was used for the work presented in Fig. 16 for rubidium when black body emissivity is assumed. The effective areas, with other surface emissivities, can be obtained by dividing by 1/2 the sum of the actual emissivities.

Fig. 16 also shows the advantages of going to higher turbine inlet temperatures. The radiator area for a powerplant with an 80% efficient turbine changes from approximately 2.565 to 0.22 sq ft per kw when the temperature increases from 1500 to 2750 R. These curves also show the possible area reduction with an increase in turbine efficiency. At 2000 R for rubidium, the area reduces from 1.17 to 0.83 sq ft per kw, or approximately 29% for a change from 60 to 80% turbine efficiency.

A comparison of radiator areas for rubidium vapor cycles and Brayton gas cycles was extracted from Ref. (1) and reproduced in Fig. 17. The areas in both cases are shown to increase with reduced turbine efficiency, and the two cycles are equal when the turbine efficiency is 100%. However, at lower turbine efficiency, the curves deviate markedly and show the striking advantages of the Rankine over the Brayton cycle.

A comparison of the quality of vapor leaving the turbine when the inlet vapor is saturated is shown in Fig. 18 for liquid metals. Five fluids are compared for a turbine efficiency of 80%, but only mercury and rubidum are compared at turbine efficiencies of 60 and 100%. For 80% efficiencies, mercury has the highest quality, and progressive reductions are shown for rubidium, cesium, potassium, and sodium. The vapor quality shown for rubidium in Fig. 18 changes less than 4% for an inlet temperature change of 1000 R; the quality change for mercury is even smaller. When compared in the same temperature range, the quality of mercury is about 1% higher than that of rubidium. For an 80% efficient turbine, the minimum quality for any fluid is approximately 82% over the temperature range considered. This moisture content is slightly higher than desired, but it does not appear to present an unreasonable turbine design problem.

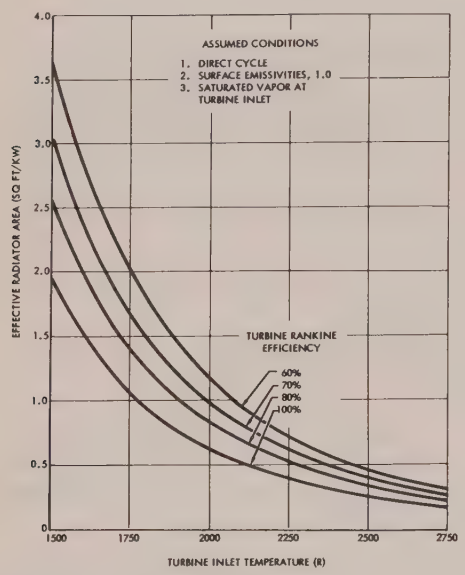

Fig. 16 — Minimum radiator area for rubidium powerplant (direct cycle)

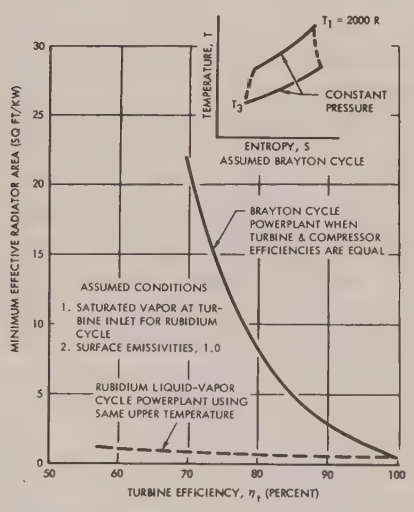
T_1 = 2000 R
T_3
CONSTANT PRESSURE
TEMPERATURE, T
ENTROPY, S
ASSUMED BRAYTON CYCLE
BRAYTON CYCLE POWERPLANT WHEN TURBINE & COMPRESSOR EFFICIENCIES ARE EQUAL
ASSUMED CONDITIONS
1. SATURATED VAPOR AT TURBINE INLET FOR RUBIDIUM CYCLE
2. SURFACE EMISSIVITIES, 1.0
RUBIDIUM LIQUID-VAPOR CYCLE POWERPLANT USING SAME UPPER TEMPERATURE
MINIMUM EFFECTIVE RADIATOR AREA (SQ FT/KW)
TURBINE EFFICIENCY, η_t (PERCENT)

Fig. 17 — Area comparison for brayton and rankine cycles

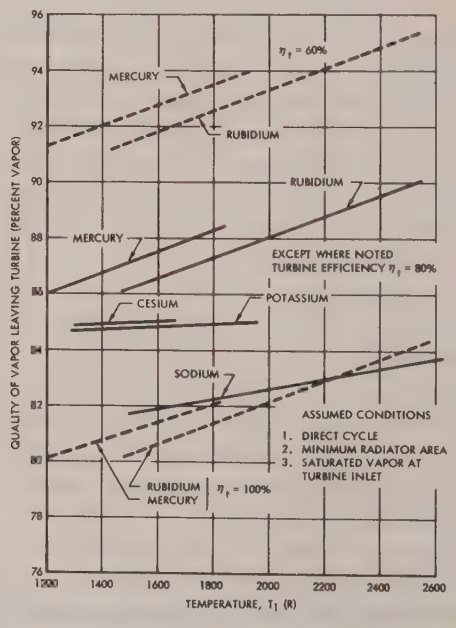

Fig. 18 — Vapor quality at turbine exhaust (direct cycle)

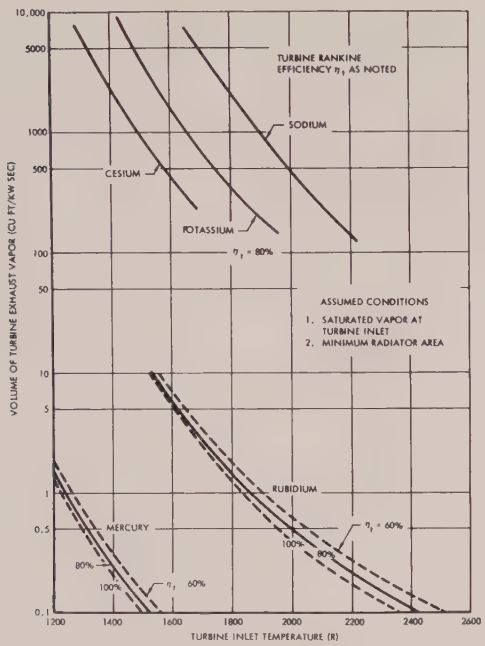

Fig. 19 — Volume of turbine exhaust vapor (direct cycle)

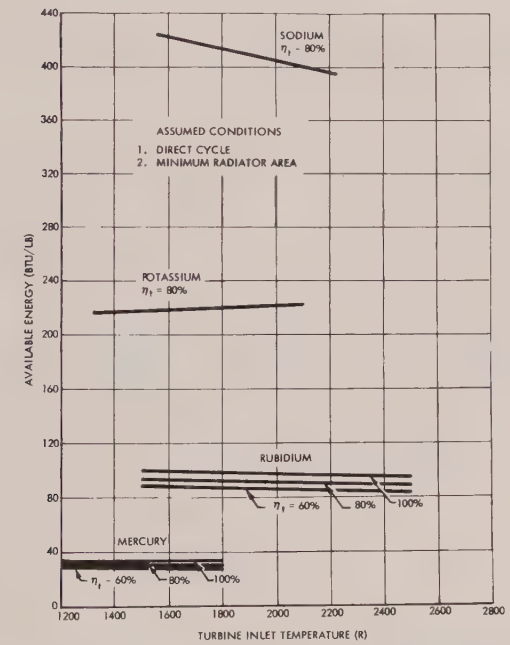

Fig. 20 — Energy available from rankine cycle (direct cycle)

The fluid cycles are further compared in Fig. 19 on the basis of exhaust vapor volume. The comparison required 5-cycle semilog paper in order to include a reasonable range for the fluids being considered. The wide differences in fluid characteristics provide the best criteria for fluid selection.

The volume of mercury vapor, much smaller than the other fluids, is approximately 1% of the volume of rubidium vapor. At 2000 R, for a turbine efficiency of 80%, the volume of sodium vapor would be 950 times that of rubidium vapor. The exceptionally high volumes presented by cesium, potassium, and sodium eliminate these fluids from consideration in the temperature range now attainable. Even the volume required for rubidium vapor will dictate a considerably larger diameter for the turbine exhaust duct than that required for mercury. Due to vapor density effects, the increase in exhaust duct size is not directly proportional to the vapor volume. Rubidium, cesium, potassium, and sodium vapors are less dense than mercury vapor. The lower densities are primarily due to lower vapor pressures, but, in addition, the molecular weight of mercury is considerably higher than that of the other elements being considered. A lower density either reduces the pressure drop in the exhaust duct or permits an increase in vapor velocity. An increased vapor velocity will only partially compensate for the large volume increase.

In designing turbine nozzles and blades, it is necessary to know the energy theoretically available in the expanding vapor. Fig. 20 shows a comparison of data computed for conditions that result in a radiator of minimum area. The theoretically available energy for sodium is considerably higher than that of any other fluid—more than 10 times the amount available in mercury, and more than four times that in rubidium. From a structural standpoint, the turbine for fluids with higher values of available energy must either be designed with higher blade speeds or with an increase in number of stages. Fewer pounds of vapor would be circulated in the cycle per unit of power output when a fluid with higher available energy is used.

Fig. 21 compares a number of fluids from the standpoint of pressure. The vapor pressure of mercury is 50 to 100 times higher than that of rubidium, while the vapor pressure

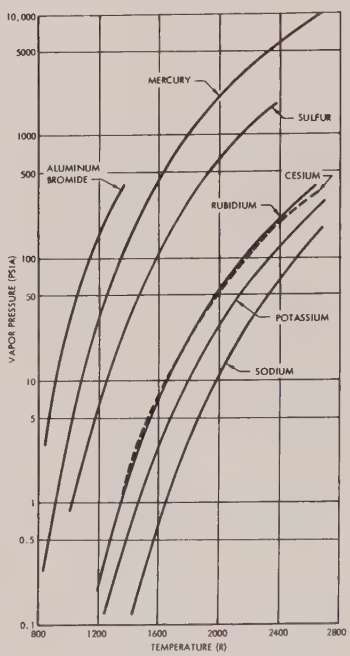

Fig. 21 — Vapor pressure comparison

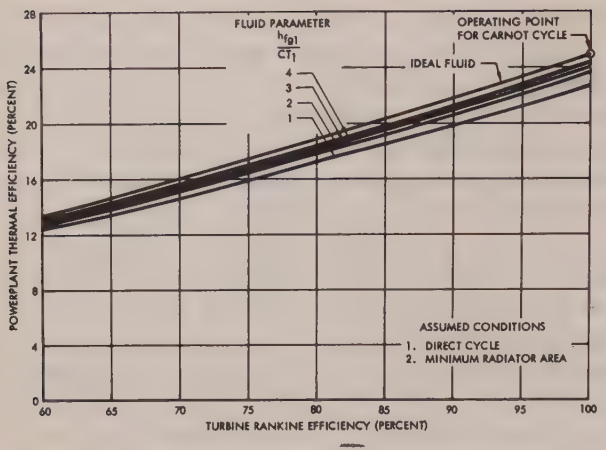

Fig. 22 — Powerplant thermal efficiency (direct cycle)

of sodium is lower than that of the other fluids. Lower vapor pressure permits the use of lightweight pressure vessels and piping.

The thermal efficiency of vapor cycles has been determined over a range of fluid parameters. (See Fig. 22.) The data for the range analyzed falls within a very narrow band of approximately 1% at a turbine efficiency of 60% and increases to slightly over 2% at a turbine efficiency of 100%. Further, because most of the fluid parameter values shown lie within 2 to 3.5, the thermal efficiency for the liquid metals is confined to an extremely narrow band with a maximum difference less than 1/2% at the maximum deviation conditions of 100% turbine efficiency.

The comparisons permit a designer to assess the advantages and disadvantages of the fluids and operating conditions in order to select the best powerplant for a particular application.

Conclusions

Type a fluids are easily analyzed. The thermal efficiency of the Rankine cycle using these fluids can be readily predicted from their fluid parameters. Fig. 3, showing the fluid parameter of the more promising fluids, can be used directly with Figs. 6 and 7 to determine the ideal cycle efficiency, with Fig. 13 to establish the optimum temperature ratio, and with Fig. 15 to obtain the area function. Thus, the analysis for the Type a fluids is expected to be very useful in space powerplant design.

No simple means for analyzing Type b fluids was found. However, the performance of all the fluids analyzed was far below that of available Type a fluids. It is therefore expected that little additional effort will be expended toward using the Type b fluids. In the future, other fluids of this type will no doubt be proposed, and similar analyses will be needed at such time. Approximate results can be obtained by assuming Type a characteristics and establishing a correction factor, as was pointed out in this study when sulfur and aluminum bromide were considered. Fluids which are shown to be low in efficiency need not be considered further.

As power producing devices, the efficiencies of the vapor cycles were found to be little different from those attainable with the ideal Carnot cycle. Therefore, the vapor cycles analyzed are probably the most efficient means of producing power which can be obtained from a heat cycle.

While it is not the object of this paper to specify the optimum vapor powerplant, it is hoped that the data presented here will enable designers to evaluate critical parameters. This study shows that some liquid metals possess properties desirable for working fluids in a heat power cycle. Mercury seems best suited for low temperatures, and rubidium, potassium, and sodium are indicated as higher termperatures are considered. For turbine inlet temperatures below approximately 1600 R, the volume of rubidium vapor leaving the turbine becomes exceptionally high and will probably present design difficulties. When temperatures above 1600 R are anticipated, rubidium should definitely be considered as a possible working fluid. At still higher temperatures, potassium and sodium can also be considered.

Appendix 1 — Thermal Efficiency of Diphenyl, Dowtherm A, and Sulfur

The ideal thermal efficiency of a cycle using a Type b fluid can be determined from a temperature-entropy diagram for the particular fluid considered. This method was used in computing cycle efficiencies for diphenyl and Dowtherm A. The temperature-entropy diagrams for saturated vapor and liquid were taken from Refs. (7) and (8). The curves in the superheat region were obtained by assuming that the specific heat of the superheated vapor was equal to the specific heat of the saturated vapor. The gain in entropy over a chosen temperature range was then computed from the relationship

$$\Delta S = C_p \log_e \frac{T_1}{T_2} \qquad \text{(A-1)}$$

where

ΔS = Change of entropy
T_1 = Upper temperature assumed
T_2 = Lower temperature assumed
C_p = Average specific heat of saturated vapor over the range T_1 to T_2

The method for determining the thermal efficiency can be explained by referring to Fig. A-1. The cycle thermal efficiency is defined as the ratio of the area for the reversible cycle divided by the area under the curve for the heating portion of the cycle. Referring to Fig. A-1, this can be written as

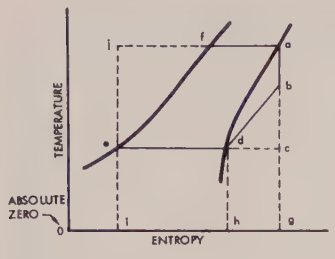

Fig. A — Diagram for computing thermal efficiency for type b fluids

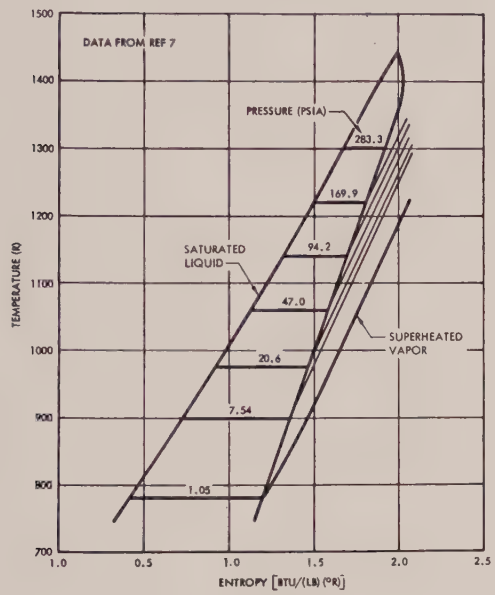

Fig. B — Temperature-entropy diagram for diphenyl

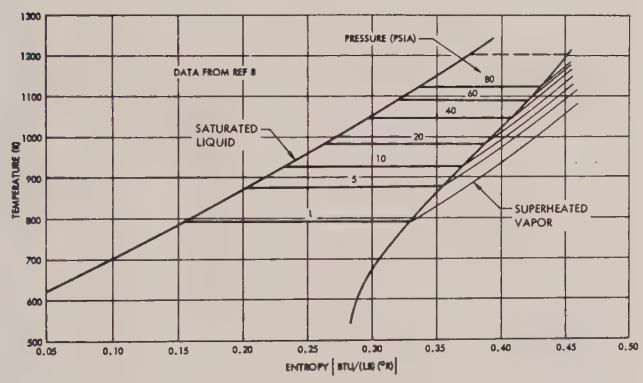

Fig. C — Temperature-entropy diagram for dowtherm A

$$\eta_{theo} = \frac{\text{Area a b d e f a}}{\text{Area a g i e f a}} \qquad (A\text{-}2)$$

The areas for Eq. A-2 were determined for diphenyl and Dowtherm A from Figs. B and C by planimetering the desired areas.

A temperature-entropy chart for sulfur taken from Ref. (6) is shown in Fig. D. These data were used for predicting the performance of this element in the Rankine cycle. However, it should be pointed out that the areas planimetered on this chart do not agree very well with the tabulations presented in the same reference, and Fig. D should therefore be regarded as approximate.

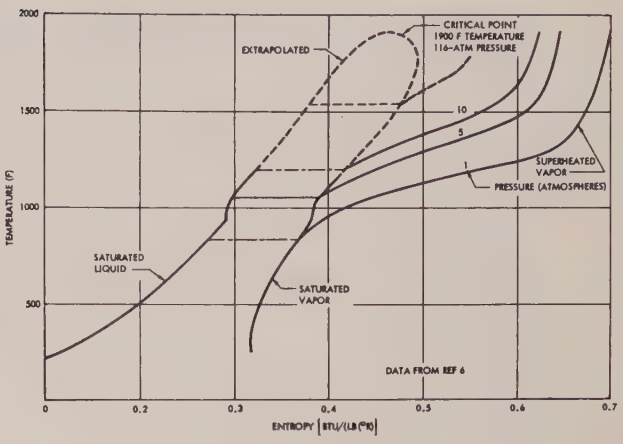

Fig. D — Temperature-entropy diagram for sulfur

Appendix 2 — Nomenclature

f	=	Fluid work factor defined by Eq. 3
g	=	Work factor term defined by Eq. 15
h_1	=	Enthalpy of vapor entering turbine, Btu/lb
h_{f2}	=	Enthalpy of saturated liquid at condenser temperature, Btu/lb
h_{fg1}	=	Latent heat of vaporization at temperature T_1, Btu/lb
h_{g1}	=	Enthalpy of saturated vapor at temperature T_1, Btu/lb
$\dot{v}$	=	Volume of discharge vapor, cu ft/kw-sec
v_{g2}	=	Specific volume of saturated vapor at turbine discharge temperature, cu ft/lb
$\dot{w}$	=	Flow rate of working fluid, lb/kw-hr
A_e	=	Effective radiator area, sq ft/kw
C	=	Average specific heat of saturated liquid, Btu/(lb) (R)
C_1	=	Radiation constant defined for Eq. 24
C_p	=	Average specific heat of fluid at constant pressure, Btu/(lb) (R)
Q_a	=	Heat added to working fluid cycle, Btu/lb
Q_r	=	Heat rejected from cycle, Btu/lb of working fluid
S	=	Entropy of working fluid, Btu/(lb) (R)
S_1	=	Entropy of working fluid entering turbine, Btu/(lb) (R)
S_{f3}	=	Entropy of saturated liquid at condenser temperature, Btu/(lb) (R)
S_{g1}	=	Entropy of saturated vapor at temperature T_1, Btu/(lb) (R)
T	=	Absolute temperature, R
T_1	=	Temperature of working fluid at turbine inlet, R

T_2 = Ideal temperature of working fluid at turbine exit, R
W_a = Actual shaft work from working fluid, Btu/lb
W_c = Work from ideal Carnot cycle
W_{theo} = Theoretical work from working fluid, Btu/lb
X_2 = Quality of vapor at turbine exhaust, % vapor
ϵ_a = Emissivity of radiator surface (usually surface facing sun)
ϵ_b = Emissivity of radiator surface (usually surface away from sun)
λ = Area function (Eq. 30)
η = Cycle thermal efficiency
η_c = Carnot cycle thermal efficiency
η_f = Fluid efficiency factor defined by Eq. 18
η_t = Turbine adiabatic efficiency
η_{theo} = Theoretical thermal efficiency
σ = Stefan-Boltzmann constant = 0.1713×10^{-8} Btu/(hr) (sq ft) (R^4)

References

1. D. B. Mackay, "Powerplant Heat Cycles for Space Vehicles," Institute of Aeronautical Sciences, Paper No. 59-104. SAE National Summer Meeting, Los Angeles, Calif. June 16-19, 1959.

2. D. B. Mackay, and E. L. Leventhal, "Solar Turbo Powerplant Design," American Society of Mechanical Engineers, Paper No. 59-A74. National Meeting, Atlantic City, New Jersey, November 29 - December 4, 1959.

3. R. E. English, and H. O. Slone, et al, "A 20,000-Kilowatt Nuclear Turboelectric Power Supply for Manned Space Vehicles," National Aeronautics and Space Administration, Memo 2-20-59E, March 1959.

4. E. B. Zwick, and R. L. Zimmerman, "Space Vehicle Power Systems," American Rocket Society, SAE Paper No. 867-59. June 8-11, 1959.

5. W. D. Weatherford, Jr., J. C. Tyler, and P. M. Ku, "Properties of Inorganic Working Fluids and Coolants for Space Applications," Aeronautical Systems Division, WADC TR 59-598, December 1959.

6. "The Sulphur Data Book," Compiled by Technical Staff, Freeport Sulphur Co., New York: 1954. McGraw-Hill Book Co.

7. Kermit Anderson, "Engineering Properties of Diphenyl," Argonne National Laboratory, ANL-5121, August 11, 1953.

8. "Dowtherm Handbook," Dow Chemical Co., Midland, Mich., 1954.

Limitation of New Approach to Thermodynamic Powerplant Analysis

Homer J. Wood
H. J. Wood & Associates

DR. MACKAY HAS presented some new approaches to thermodynamic powerplant analysis which are certain to prove of value far beyond the "space vehicle" applications on which he has concentrated his interests. In following Dr. Mackay's analysis it is well to note that there is a fundamental presumption to the effect that an expansion engine can be found which will provide the temperature ratio between heat source and condenser. This is a legitimate assumption for the temperature ratios of interest within the subject of the paper, but is sometimes not found in Rankine cycle steam plants where turbine exhaust temperatures may be somewhat above condensate temperatures. This should be kept in mind in applying the new design method to old problems. This point bears some relationship to his statement that a binary fluid would not be justified. When it is desired to deal with lower temperature ratios than about 0.75, physical limitations on expansion engine design may make binary fluids attractive.

The method of radiator size optimization used by Dr. Mackay is directly applicable only when the heat source weight is not a variable. For solar collectors the optimum temperature ratio is somewhat depressed. This depression becomes much more prominent when a portion of the mission is in Earth's shadow. In such case the use of heat storage means, such as lithium hydride, places emphasis on high cycle efficiency during the shadow period. Thus we might expect a Rankine cycle designed for such a mission to be optimized at a lower temperature ratio. In some comparisons between Stirling and Rankine cycles, this factor has not had proper evaluation. The reference paper provides easy means of making such evaluations.

Although Dr. Mackay's published analyses of Brayton cycles have not included recuperative heat exchangers, I am in agreement that such cycles offer no hope of competition with liquid metal Rankine cycles at temperature ratios of about 0.75. For the case of partial shadow operation noted above, the reduced temperature ratio might make a recuperative Brayton cycle competitive with Stirling and Rankine cycles. It would be interesting to have Dr. Mackay's comments on this point. It should be noted that practical Stirling cycles have thermodynamic characteristics very similar to recuperative Brayton cycles.

Dr. Mackay makes very plain the first-order importance of turbine efficiency in minimizing radiator size. Flow path efficiencies of 90% or above are possible in expansion engines, but formidable mechanical problems are posed with either turbine or positive-displacement expanders by the presence of liquid metal in the working fluid. A recent ARS paper by Mr. Bullock of The Garrett Corp. discusses some of these problems and shows that liquid metal erosion can be serious. On the other hand, it is evident that superheating to reduce mechanical problems is detrimental to cycle efficiency. The next few years should see much improvement in both performance and durability which can be achieved only through empirical development work. No more challenging problem has ever faced the designers of turbomachinery...

Author's Closure to Discussion

THE AUTHOR agrees whole heartedly with all of the above comments. A small amount of study has been made regarding the use of a Brayton cycle supplemented with a recuperative heat exchanger. The recuperative feature reduces the size of the waste heat radiator as well as the quantity of heat required to be supplied by either a reactor or a solar collector.

A comparison of cycle performance employing the theoretically maximum amount of improvement due to recuperative heat exchange made with one having no recuperation is shown in Fig. B. These data were obtained by selecting conditions in the Brayton cycle which gave the smallest size for the waste heat radiator and then by computing the area change due to the addition of a 100% effective recuperative heat exchanger. In the normal efficiency range

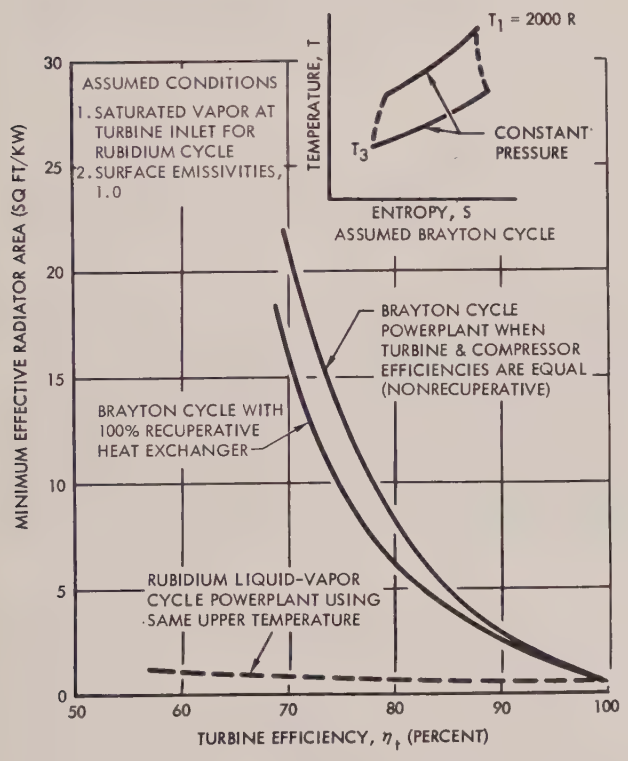

Fig. B — Cycle performance comparison

for compressors and turbines, the area reduction is approximately 25%. At the same time, the savings in heat input to the system would be almost 57% when the turbine and compressor efficiencies are 80%. Even with these improvements, the Brayton cycle is shown to be far from comparative from a standpoint of radiator area.

An interesting problem, and one which will require considerable study, is presented when one wishes to increase cycle efficiency by increasing the size of the waste heat radiator. A large number of variables are encountered, and some measure of advantage and penalty must be assessed to each. A binary fluid cycle would no doubt be required for the Rankine cycle since the turbine exhaust already contains as much moisture as can be tolerated. To improve efficiency, optimum recuperation would be needed for the Brayton cycle. After these changes, the Rankine cycle would have a higher thermal efficiency since it deviates so little from the Carnot cycle. The recuperative feature combined with the lower temperature will theoretically cause the Brayton cycle to approach more nearly the Carnot cycle. It should be pointed out, however, that the minimum radiator area comparison presented here was obtained by the use of a comparatively cold gas temperature at the compressor inlet for the Brayton cycle. Temperatures of approximately 550 and 800 R would be associated with 70 and 80% turbine efficiencies, respectively. Corresponding temperatures of approximately 1540 and 1520 R were encountered with the Rankine vapor cycle. Lowering the temperature in a radiant heat exchanger, which is already low, will have a more serious effect than if the temperature were high. Also, the operation of a Brayton cycle in the sunlight would be penalized more than would the Rankine cycle. At the lower temperatures, the solar heat input becomes a higher percent of the possible total heat output and the Brayton cycle performance will be more seriously affected. Operation in shadow would be somewhat as presented in the paper since solar heat input was neglected for that study.

A solar powerplant using the Brayton cycle has some advantages not possible with the Rankine cycle. For the Rankine cycle, the problem of operating condensers and pumps in zero gravity has not been solved to the author's satisfaction. It is felt, therefore, that more study is needed to establish the optimum solar powerplant.

The author appreciates the comments and hopes that this discussion will help to clarify the questions.

Plasma Propulsion

S. W. Kash
Lockheed Aircraft Corp.

PLASMA PROPULSION provides one of the more promising engines for futuristic space travel. In plasma propulsion propellant material can be accelerated to large velocities by the use of electromagnetic forces. The term plasma was introduced about a third of a century ago, and refers to gas containing an appreciable number of ions and electrons. The amounts of positive and negative charge, however, are equal, so that from a macroscopic point of view the gas is essentially neutral. Familiar examples of plasma devices are to be found in electric arcs, such as are used in welding, and in electric discharges, such as in neon displays.

Plasma may be properly considered a fourth phase of matter, the phase beyond the gaseous one. Plasma may be an exceptional state on earth, but it is the most prevelant state of matter in the universe. Plasma comprises the stars and much of the material in space. Plasmas and plasma phenomena are destined to play an increasingly important role in our developing technology. We may expect plasmas to be important in communication, in space propulsion, in power production, and in other areas, presently unsuspected.

The principle attraction of electrical propulsion, such as plasma propulsion, is the long range possibility it offers of providing a large ratio of payload weight to initial vehicle weight. This large ratio results from the projected use of higher velocity propellants. The larger the exhaust velocity of the propellant, the larger the payload fraction will be for any given mission. For example, Fig. 1 shows how the payload fraction varies with propellant velocity, for a vehicle velocity change of 30 km/sec. This velocity change would be adequate to carry out most interplanetary missions.

The feasibility of electrical propulsion rests on two relatively recent technological developments:

1. The development of nuclear reactors provides us with a potentially unlimited energy source.

2. The development of our ability to put increasingly greater weights into satellite orbit. Because of the large cost of lifting material into satellite orbit, however, it is advan-

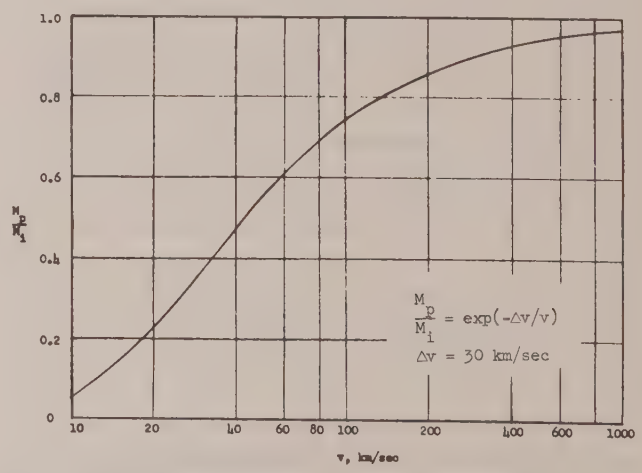

Fig. 1 — Ratio of payload mass to initial mass as a function of propellant velocity

tageous to develop space ships with as large a payload fraction as possible.

Because of power plant limitations, higher propellant velocity entails lower engine thrust. This results from the fact that for a fixed thrust, the power required is proportional to the propellant velocity. Nevertheless, by starting in a low-drag satellite orbit, a low-thrust, long acceleration-time propulsion engine can be used advantageously.

It is quite possible that the first application of electrical propulsion in space will involve the use of a small plasma engine to help stabilize a communication satellite or change its orientation. This would be followed by larger units for orbital transfer and finally by plasma engines for interplanetary travel.

Engines for Space

There are several types of propulsion engines feasible for space travel. These include:

1. Chemical propulsion
2. Nuclear-chemical propulsion
3. Propulsion by electric arc heating (plasma jet)
4. Ion propulsion
5. Plasma propulsion.

In chemical propulsion systems both the energy and propellant are contained in a fuel oxidizer mixture. This mixture is burned in a combustion chamber to produce high temperature gases. The gases are then allowed to expand through a nozzle to convert part of their internal heat energy into kinetic energy of the exhaust. Chemical propulsion units have been under development for many years and are currently being successfully operated. Unfortunately, there is a limit to the propellant velocity that can be achieved with chemical fuels. Even with fuel mixtures which combine the most energetic chemical bonds with the lightest weight atoms, it is unlikely that propellant exhaust velocities greater than 4 km/sec can be achieved.

An obvious way to achieve higher velocities is to combine a nuclear heat source with a light chemical propellant. The propellant is heated upon passing through the reactor and then accelerated by expansion through a nozzle. The velocity is limited by the temperature to which the propellant can be heated, that is, primarily by the temperature of the reactor materials. With hydrogen heated to 2000 C a velocity of about 6 km/sec could be obtained. If a practical way could be devised to deliver the kinetic energy of the nuclear fission fragments directly to the propellant, a velocity possibly 50% greater could be achieved.

Higher temperatures and velocities may be obtained by heating the gas electrically as with a plasma jet. In a plasma jet, a gaseous propellant is heated to high temperature by passing it through a high-current electric-arc (1)*. Electric forces are used to heat the gas, but not to accelerate it. The gas is accelerated by expanding it through a nozzle, as in the case of the chemical or nuclear-chemical engine. The propellant velocity of a plasma-jet engine is also limited by material temperatures, but may achieve values between 15-20 km/sec.

Ion propulsion (Fig. 2) illustrates the simplest means of accelerating material by electromagnetic forces. Ions are directly accelerated by strong electric fields, similar to the acceleration of electrons in cathode ray tubes. To maintain overall charge neutrality on the vehicle, as many positive as negative charges have to be eliminated. Furthermore, in order to provide a neutral space environment in the vicinity of the ion engine, the positive and negative charges should leave the vehicle with about the same velocity. The atomic alkali metal ions, in particular cesium, are considered most promising for the positive charges (2, 3). Electrons are usually considered for the negative charges, although heavier negative ions, such as those of the halogen atoms offer considerable promise (4).

The ion currents that can be obtained in an ion gun are unfortunately very small. A very large exhaust area composed of many small ion guns in required to get an appreciable thrust. We may expect that the thrust per unit area from an ion engine will be no greater than about 0.1 lb/ft^2 (5).

In plasma propulsion engines, a neutral plasma is accelerated with the aid of electric and magnetic fields. The magnetic fields can be provided by currents in the plasma, or they can be provided independently. The propellant energy is supplied by the electric fields; however, the magnetic fields are required to orient the gas and give it a net momentum. Operation of a plasma device does not require the separation of the positive and negative charges. The plasma device can therefore handle larger amounts of propellant and can provide a larger thrust per unit area (5).

There are two types of plasma propulsion devices:

1. The steady-state plasma-accelerator.
2. The pulsed plasma-accelerator.

The steady-state devices may be suitable for the acceler-

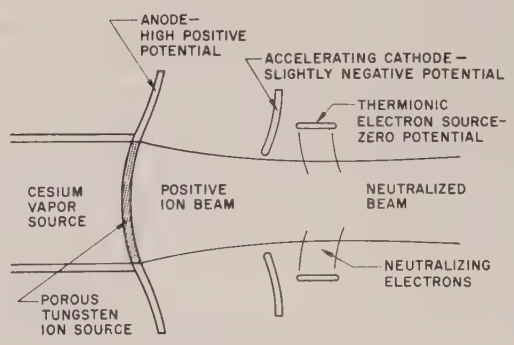

Fig. 2 — Electrostatic ion-accelerator

*Numbers in parentheses indicate references at the end of the paper.

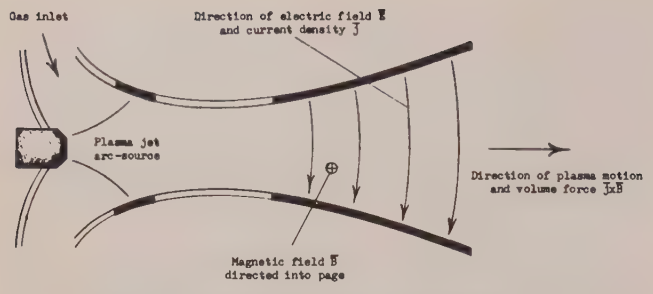
Gas inlet
Direction of electric field E and current density j
Plasma jet arc-source
Direction of plasma motion and volume force jxB
Magnetic field B directed into page

Fig. 3 — Steady-state plasma accelerator

ation of plasma to intermediate velocities, up to about 50 km/sec. The pulsed devices can be utilized to accelerate plasmas in the velocity range of about 10-500 km/sec, but are better suited for producing velocities greater than that of the steady-state devices. The basic principles involved in these devices are the same, although the technical problems are quite different. The differences are analogous to those between ac and dc electrical devices.

Steady-State Plasma Accelerator

Let us consider first the steady-state plasma-accelerator. This is often called a crossed electric and magnetic field accelerator, and is similar to that of the electromagnetic pump presently used for metal liquids. In a simple version of the crossed field device (Fig. 3), a plasma arc-jet is used to produce a high-temperature partially-ionized gas, to which some alkali metal vapor, such as potassium, may be added to increase its electric conductivity. The plasma gas then passes between a pair of electrical plates to produce a current transverse to the flow, and a set of coils which provide a magnetic field at right angles to both the current between the plates and the direction of flow. The resultant interaction between the current and the magnetic field provides the force for accelerating the gas.

As in the electromagnetic liquid-metal pump, the current also heats the moving plasma. However, by permitting the plasma to expand while being accelerated, some of the joule heating can be recovered. The expansion of the plasma also helps keep its temperature down. Since the plasma in the steady-state device is only slightly ionized (its conductivity is perhaps only 10^{-5} times that of liquid sodium), care must be exercised during the expansion lest the temperature drops so low that the conductivity of the gas becomes too small.

For the steady-state accelerator the equation of motion is

$$\rho \frac{d\bar{v}}{dt} = \rho\bar{v}\cdot\nabla\bar{v} = -\nabla p + \bar{j}x\bar{B} , \qquad (1)$$

where ρ, $\bar{v}$, and p are the plasma density, velocity, and pressure, respectively, and B is the magnetic field intensity. The current density is given by

$$\bar{j} = \sigma(\bar{E} + \bar{v}x\bar{B}) , \qquad (2)$$

where σ is the conductivity and $\bar{E}$ is the electric field intensity. If E, $\bar{v}$, and B are at right angles to each other and the flow is one dimensional, Eq. (2) can be written as

$$j = \sigma(E - vB) . \qquad (2a)$$

Note that, as in the electric motor, vxB provides a back emf that opposes the applied electric field. In plasma devices designed for the production of power, vxB is the dominant term and produces a voltage and a current flow. This is analogous to the electric generator, in which the voltage is produced by the movement of conducting elements through magnetic fields.

The energy equation for the steady-state accelerator is

$$\rho\bar{v}\cdot\nabla(e + \frac{v^2}{2}) = \bar{v}\cdot(-\nabla p + \bar{j}x\bar{B}) + \frac{j^2}{\sigma} ; \qquad (3)$$

e is the internal energy of the gas. Eqs. (1 - 3) do not include terms for viscosity or heat conduction. The important term for joule heating is included, however, in Eq. (3).

To understand the underlying principles of an ExB device, it should be noted that a charged particle under the influence of an electric field will be accelerated in the direction of the electric field. Thus, since the electric field has a component along the motion of the particle, it will increase the energy of the particle. On the other hand, the force of a magnetic field is at all times perpendicular to the motion of a charged particle. The magnetic field will therefore change the direction and momentum of the particle, but will not change its energy. In the crossed field device the energy is thus supplied through the currents set up by the electric fields. However, the thrust is obtained through the orientation of the particles by the magnetic field.

Actually, in most plasma devices, the applied fields act primarily on the electrons, because the electron mass is much smaller than that of the ion. The electrons in turn set up space-charge effects which accelerate the ions. The ions in turn collide with the neutral particles present and impart acceleration to the gas as a whole.

To date an operating steady-state crossed field device has not been built. The steady-state plasma-motor should, however, operate on voltages about an order of magnitude lower than that of the electrostatic ion-motor. It should also, in principle at least, produce per-unit-area thrusts up to 100 lbs/ft^2— about three orders of magnitude greater than that of the ion engine. For efficient operation there are several losses which must be minimized:

1. Heat is produced in the electrical circuit elements and in the magnetic field coils. This heat must be eliminated by convection cooling or by radiation.

2. Thermal energy and internal energy (energy of exci-

tation, dissociation and ionization) is carried out with the propellant exhaust. This loss is similar to that which occurs in a chemical propulsion system and becomes relatively less important as the plasma exit velocity increases.

3. The viscous boundary-layer at the electric plates takes up energy and momentum from the moving plasma. These losses increase with plasma velocity and channel length.

4. Hall currents (at right angles to both the electric and magnetic fields) can produce undesirable sideways motion in the plasma. It may be possible to reduce these somewhat by the application of auxiliary electric fields.

5. High temperatures and velocities will produce evaporation and erosion of surfaces in contact with the plasma.

Pulsed Plasma Accelerator

The pulsed plasma-accelerator will now be considered. This is an intermittently operated device and can produce a per-unit-area thrust intermediate between the ion accelerator and the steady-state plasma-accelerator (5). In this device bursts of plasma are driven by rapidly varying magnetic fields produced by large currents in the plasma discharge. There are a number of different electrode arrangements possible. Two of these are shown in Figs. 4 and 5.

In each of these, a plasma introduced into the discharge region or produced by the discharge, is accelerated by the interaction of the current elements in the plasma and the current elements in the fixed part of the discharge circuit. The accelerating forces arise from the interaction of the current elements with the magnetic field produced by the current in the discharge circuit.

These devices have been studied for several years at various laboratories including the research laboratory of Lockheed Missiles and Space Division. Often the plasma is provided by admitting a pulse of gas between the electrodes and a discharge is simultaneously triggered (6). In a number of experiments the discharge has been triggered by the gas itself. In a few experiments (7, 8) the plasma has been provided by vaporizing a metal wire which has in turn triggered the discharge. More recently the discharge has been triggered with a minute amount of material and most of the propellant has been obtained by electrode erosion (9). It would appear from these studies that pulsed plasma-accelerators can be built which will convert electrical energy into plasma kinetic energy with an efficiency exceeding 50%.

The pulsed plasma-accelerator differs in a number of respects from the steady-state plasma-accelerator:

1. Because of higher velocity and conductivity the ratio of plasma kinetic energy to plasma internal energy is greater in the pulsed accelerator than in the steady-state accelerator.

2. The acceleration of the plasma is greater and the channel length is shorter in the pulsed accelerator, so that the viscous boundary-layer losses are smaller.

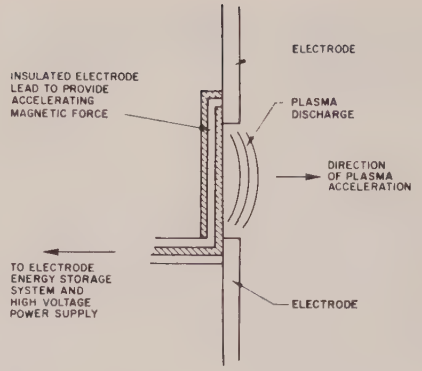
ELECTRODE
INSULATED ELECTRODE LEAD TO PROVIDE ACCELERATING MAGNETIC FORCE
PLASMA DISCHARGE
DIRECTION OF PLASMA ACCELERATION
TO ELECTRODE ENERGY STORAGE SYSTEM AND HIGH VOLTAGE POWER SUPPLY
ELECTRODE

Fig. 4 — Collinear electrode pulsed plasma accelerator

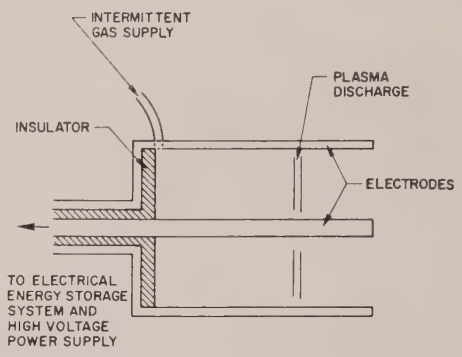

Fig. 5 — Coaxial electrode pulsed plasma accelerator

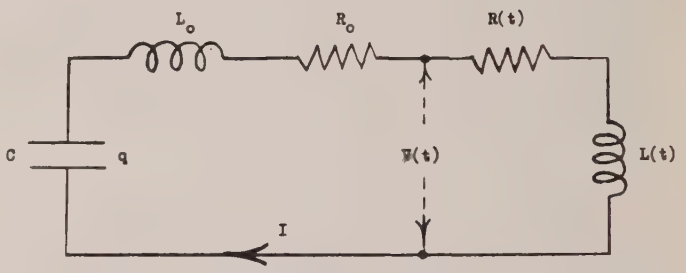

Fig. 6 — Equivalent circuit for pulsed plasma accelerator

3. In the pulsed accelerator some of the heat developed in the electrodes can be utilized and advantage can be taken of electrode erosion to provide the propellant material.

4. The currents in the pulsed plasma accelerator are very large, of the order of 100,000 amps or more, and hence the resistance of the electrical components must be minimized to reduce circuit heating losses and to prolong component life.

5. With pulsed operation the effect of circuit inductance is important. For increased efficiency all fixed inductance should be reduced as far as possible. However, the rate of change of inductance in the discharge circuit should be as large as possible.

Although the forces in pulsed devices are basically the same as those in steady-state devices, the analysis of these systems is more complicated. For the analysis it is convenient (10) to set up an equivalent circuit, such as shown in Fig. 6. The left hand part of the circuit represents the elec-

trical storage capacitor and leads; the right hand part represents the electrodes and the plasma discharge. The circuit equation for the system is

$$\frac{1}{C}q = (R_o + R + \dot{L})I + (L_o + L)\dot{I}, \qquad (4)$$

where the dot denotes differentiation with respect to time. The power into the electrodes and plasma discharge is

$$P(t) = V(t)I = (R + L)I^2 + LII$$
$$= RI^2 + \frac{1}{2}\dot{L}I^2 + \frac{d}{dt}\left(\frac{1}{2}LI^2\right). \qquad (5)$$

The first term RI^2 is the rate at which electrical energy is dissipated by ohmic heating in the plasma and electrodes. The last term represents the rate of increase of magnetic field energy. When the current is zero the magnetic field energy is zero. For good efficiency the plasma should not be ejected before the current has passed through a maximum and returned to a small value.

The term $\frac{1}{2}\dot{L}I^2$ represents the rate at which mechanical work is done on the plasma and $\frac{1}{2}\dot{L}$ can be taken as an "equivalent load impedance" for the mechanical work done on the plasma. Electrical energy in these systems is ultimately expended by ohmic heating of the circuit elements and plasma and by the mechanical work done on the plasma. Thus, for good efficiency it is important to have $\frac{1}{2}\dot{L}$ larger than the resistance $(R_o + R)$ of the circuit.

A simplified analysis can be carried through for the pulsed accelerator by considering the plasma to be driven by a magnetic piston. This assumes that the rate of rise of the magnetic field and the plasma conductivity are sufficiently large, so that there is little penetration of the magnetic field into the plasma during the time of acceleration. Accordingly, the plasma current is restricted to a thin sheath, with the magnetic field very small in front of the sheath and a maximum behind it. We may then put

$$\dot{L} = \frac{dL}{dx} \cdot v, \qquad (6)$$

where dL/dx is the inductance per unit length and v is the velocity of the moving sheath. By this relationship, we see that the efficiency is improved when dL/dx and v are increased. Further details concerning this analysis are to be found in Ref. (10).

The results of the foregoing analysis, applied to a particular case in which the plasma is provided by electrode erosion, are shown in Fig. 7. It is assumed in this case that the production of plasma is proportional to the square of the current and that the resistance and inductance per unit length are constant, equal to 10^{-2} ohm and 10^{-8} henry/cm, respectively. Fig. 7 shows how the efficiency (η) increases

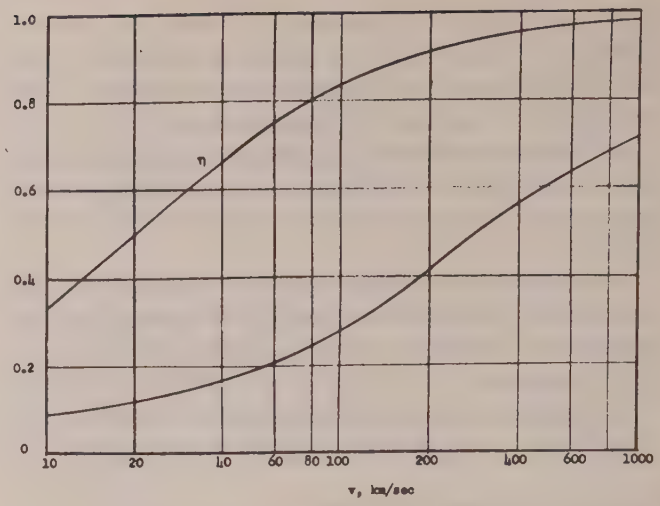

Fig. 7 — Efficiency and fraction of electrical energy expended per pulse versus plasma velocity

with velocity. The fraction of the electrical energy (f) removed from the capacitor per current surge is also shown. That this increases with velocity reflects the fact that increasing $\dot{L}$ improves the impedance match between the discharge part of the circuit and the electrical capacitor.

References

1. M. Comac, "Plasma Propulsion of Spacecraft", Astronautics, Vol. 4, (October 1959), 31.

2. A. T. Forrester and R. C. Speiser, "Cesium-Ion Propulsion", Astronautics, Vol. 4, (October 1959), 34.

3. Staff of the Ramo-Wooldridge Research Laboratory, "Electrostatic Propulsion", Proceedings of the IRE, Vol. 48, (April 1960), 477.

4. M. A. Gilleo and S. W. Kash, "Propulsion by Composite Beams of Negative and Positive Ions", American Rocket Society, Paper No. 1157-60, May 1960.

5. S. W. Kash, "A Comparison of Ion and Plasma Propulsion", Proceedings of the IRE, Vol. 48, (April 1960) 458.

6. A. Andrew and J. Fitzpatrick, "Plasma Acceleration in an Axially Symmetrical Discharge Tube", Research Report 288107, Lockheed Missiles and Space Division, May 1960.

7. W. L. Starr, "A Propulsion Device Using an Exploding-Wire Plasma Accelerator", Research Report 418236, Lockheed Missiles and Space Division, December 1958.

8. W. L. Starr and S. W. Kash, "Experimental Results with a Collinear Electrode Plasma Accelerator", American Rocket Society, Paper No. 1008-59, November 1959.

9. W. L. Starr and J. T. Natf, "Acceleration of Metal Derived Plasmas" Plasma Acceleration, Stanford, Calif.: Stanford University Press, 47.

10. S. W. Kash, "Efficiency Considerations in Electrical Propulsion", Plasma Acceleration, Stanford, Calif.: Stanford University Press, (1960), 79.

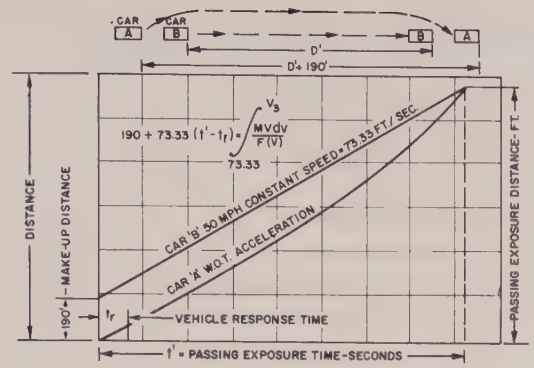

Fig. 1 — 50 mph passing exposure time simulated passing maneuver graphical definition

Computer Predicts Car Acceleration

Henry L. Setz
Ford Motor Co.

IT IS IMPERATIVE for every automobile manufacturer to be able to predict the performance characteristics of its vehicles prior to production. Before the availability of modern computers, hand solutions of complex equations were cumbersome and time consuming. Rapid reliable mechanized prediction procedures can now replace these hand calculations. Engineering procedure is materially streamlined through lessening the repetitive process of design, build and test. The resultant improvement in efficiency and lower cost warrant increased emphasis on this activity.

Ford Motor Co. has set forth desired characteristics for acceleration performance capabilities while a new passenger car design is in the embryonic stage. Specific objectives are selected for each of the following previously established criteria:

0-4 Second Start-Up Distance - The distance traveled by a vehicle at wide open throttle during a 4 second period after initial depression of the accelerator pedal.

0-10 Second Start-Up Distance - This covers a 10 second period similar to the one defined above.

50 mph Passing Exposure Time - This simulates a vehicle passing maneuver and is defined as the time required at wide open throttle to accelerate the vehicle from 50 mph constant speed through a distance 190 ft greater than that traveled by a 50 mph constant speed vehicle during the same time. The time is measured from the initial depression of the accelerator pedal beyond the 50 mph constant speed position. The 190 ft make up distance provides for adequate vehicle spacing at a 50 mph driving speed. While a downshift operation is included for vehicles with automatic transmissions, manual shift transmission vehicles are appraised on the basis of high gear operation. A graphical definition of this criterion is shown in Fig. 1.

Development of Fundamental Relationships

The problem of expressing acceleration performance criteria in terms of kinematics and engineering mechanics is basically simple. Start with the elementary concepts of motion and the natural laws which produce motion. The primary concern is with a particular type of motion called translation which denotes a displacement along a straight line path. The conventional concepts of distance, time, the rate of change of distance with respect to time termed velocity, and the rate of change of velocity with respect to time termed acceleration are associated with translation. Both velocity and acceleration have directions identical to that of the

translatory displacement. From these concepts, the differential equations defining the translatory motion of a passenger car can be expressed as:

$$v = \frac{ds}{dt} \tag{1}$$

$$a = \frac{dv}{dt} = \frac{dv}{ds} \times \frac{ds}{dt} = v\frac{dv}{ds} \tag{2}$$

$$\text{or } \boxed{ds = \frac{v}{a}dv} \tag{3}$$

$$\text{and } \boxed{dt = \frac{dv}{a}} \tag{4}$$

where

t = time - seconds
s = distance - ft
v = velocity - ft/sec
a = acceleration - ft/sec/sec

In addition to the preceding expressions for time and distance, the causes of motion and the associated concepts of force, mass and acceleration must be considered. The explanation is found in Newton's lays of motion from which the familiar relationship Force = Mass times acceleration is derived. This expression provides the link relating the vehicle's translatory motion to its cause, the resultant or net driving force at the wheels. Its mathematical expression is given below.

$$F = Ma$$

$$\text{or } a = \frac{F}{M} \tag{5}$$

The value for acceleration from Eq. (5) is substituted into Eq. (3 and 4). F, the net driving force at the wheels, is a complex function of velocity and will be expressed as F(v).

$$ds = \frac{vdv}{\frac{F(v)}{M}} = \frac{Mvdv}{F(v)} \tag{6}$$

$$dt = \frac{dv}{\frac{F(v)}{M}} = \frac{Mdv}{F(v)} \tag{7}$$

Vehicle start up performance capabilities such as the 0-4 second and 0-10 second distances may be evaluated by integrating equation (6).

$$\text{0-4 second distance } S = \int_0^s ds = \int_0^{v_1} \frac{Mvdv}{F(v)} \tag{8}$$

$$\text{0-10 second distance } S = \int_0^s ds = \int_0^{v_2} \frac{Mvdv}{F(v)} \tag{9}$$

The equation expressing the 50 mph passing exposure time t min is formulated from the graphical definition of this criterion shown in Fig. 1.

$$190 + 73.33\, t'\text{min} = \int_{73.33}^{v_3} \frac{M}{F(v)} vdv + 73.33\, t_r$$

$$\text{or } 190 + 73.33\,(t'\text{min} - t_r) = \int_{73.33}^{v_3} \frac{Mvdv}{F(v)} \tag{10}$$

The respective integral limits v_1, v_2 and v_3 from Eq. (8, 9, and 10) must be evaluated before these integrations can be performed. The integration of Eq. (7) for each performance criterion will accomplish this evaluation.

$$\text{0-4 second distance limit evaluation } \int_0^4 dt = \int_0^{v_1} \frac{M}{F(v)} dv \tag{11}$$

$$\text{0-10 second distance limit evaluation } \int_0^{10} dt = \int_0^{v_2} \frac{M}{F(v)} dv \tag{12}$$

$$\text{50 mph exposure time limit evaluation } \int_0^{t'-t_r} dt = \int_{73.33}^{v_3} \frac{M}{F(v)} dv \tag{13}$$

A graphical description of the method employed to evaluate the integrals expressed in Eq. (8-13) is found in Fig. 2. The M/F and Mv/F functions of velocity are plotted as shown. Determination of the area under the M/F function between limits prescribed for each criterion defines the respective upper limits for the integral of the Mv/F function. Subsequent determination of the areas under the Mv/F curves evaluates the respective integrals of this function. Eq. (8-13) represent all of the fundamental relationships required to express our acceleration performance criteria.

Evaluation of Performance Equations

The calculation of distance or time values from equations expressing performance criteria can be accomplished by either analog or digital type computers. Problems requiring numerous repetitive solutions such as those in the performance field are best handled by the digital type machine. Since the digital computer performs all mathematical operations by addition and subtraction, a numerical integration of the performance equations is required.

Numerical integration may be described as a particular numerical summation process commonly employed to evaluate definite integrals of a complex nature. To perform this operation an independent variable is first selected and then subdivided into a large number of increments of definite magnitudes. The equation is numerically evaluated for each successive increment of the independent variable. The incremental evaluations of the dependent variable thus obtained are summed up between prescribed limits to evaluate the integral.

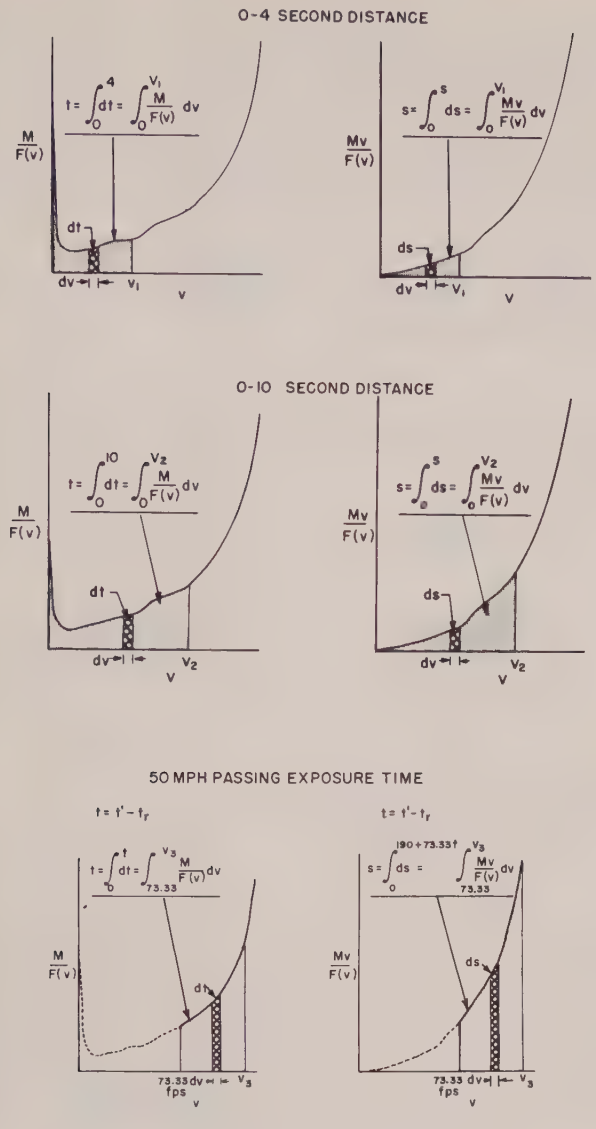

Fig. 2 — Integral evaluation — graphical description

Either time or velocity may be selected as the independent variable for numerical integration of the performance equations. Since most of our power train characteristics are expressed as functions of velocity we have selected velocity as the independent variable. The magnitude of velocity increments selected for our computer solutions is 0.50 mph.

Since Eq. (8, 9, and 10) contain specific integrals representing vehicle distance, the general equations for distance will be employed to demonstrate the evaluation procedure.

$$\text{Vehicle Distance Traveled} = S = \int_{s_1}^{s_2} ds = \int_{v_1}^{v_2} \frac{M}{F(v)}\, v\, dv$$

$$= \sum_{n} V\Delta V \left[\frac{M}{F(v)}\right] \qquad (14)$$

where ΔV = velocity increment.
V = mean velocity for each ΔV.
n = number of increments.

Eq. (15) will now be expanded to incorporate significant vehicle and power train characteristics required to evaluate the summation. It should be noted that all force terms resulting from the expansion are functions of vehicle velocity and are shown for vehicles with automatic transmission.

$$\text{Vehicle Distance Traveled (ft)} = \sum_{\eta} V\Delta V \left[\frac{\text{Mass}}{\text{Net Force}}\right] \qquad (15)$$

$$= \sum_{\eta} V\Delta V \left[\frac{\text{Mass}}{\text{Tractive Effort-Road Load Thrust}}\right] \qquad (16)$$

$$\text{where: Mass (Slugs)} = \frac{W_p M_e}{g} \qquad (17)$$

$$\text{Tractive Effort (lb)} = \frac{T_E C_{TR} R_G E_G R_a E_a}{r_t} \qquad (18)$$

$$\text{Road Load Thrust (lb)} = \frac{C_r W_p}{p} + \frac{C_D \rho A V^2}{2} \qquad (19)$$

Substituting Eq. (17, 18, and 19) into Eq. (16) and we have:

$$\text{Vehicle Distance Traveled} = \sum_{\eta} V\Delta V \left[\frac{W_p M_e}{\left(\frac{T_E C_{TR} R_G E_G R_a E_a}{r_t} - \frac{C_r W_p}{p} - \frac{C_D \rho A V^2}{2}\right) g}\right] \qquad (20)$$

A brief definition of terms for Eq. (20) is shown in Fig. 3.

A more detailed definition of terms found in Eq. (20), including descriptions of pertinent input data, is found in Appendix I. The group of terms expressing net driving force are a complex function of velocity. These are expressed in the form of empirical curves constructed from test data or as predicted curves. Several features of special interest concerning the evaluation process are described below:

Effective Mass Factor (Fig. 4) - A factor used to express power train rotating inertias as a function of the translatory mass of the vehicle. Experimentally determined factors representing many different vehicles are plotted against N/V to construct the curve shown in Fig. 4. Engine rpm car speed values are calculated for a specific vehicle and corresponding values of effective mass factor are read from the curve and substituted into Eq. (20).

0-10 MPH Time Curve (Fig. 5) - This is employed to express vehicle start up response characteristics empirically. The numerical integration of Eq. (20) is initiated from a vehicle speed of 10 mph when predicting 0-4 second and 0-10 second distances. The first velocity increment (0-10 mph) is evaluated from the curve where 0-10 mph time is plotted

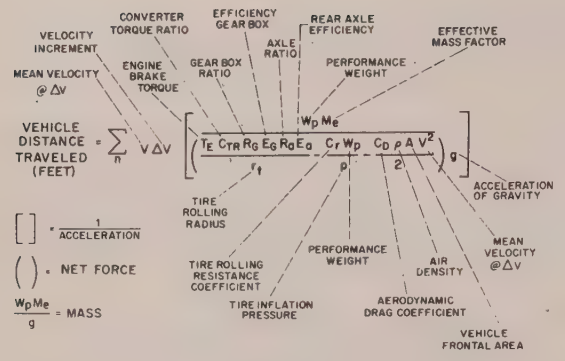

Fig. 3 — Definition of general distance equation terms

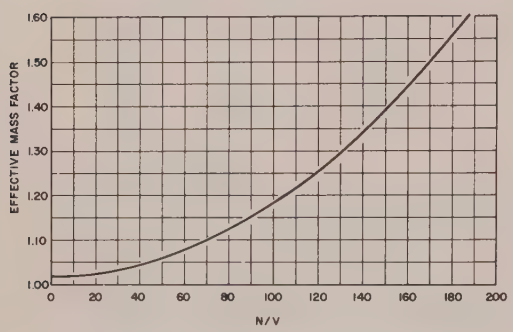

Fig. 4 — Effective mass versus N/V

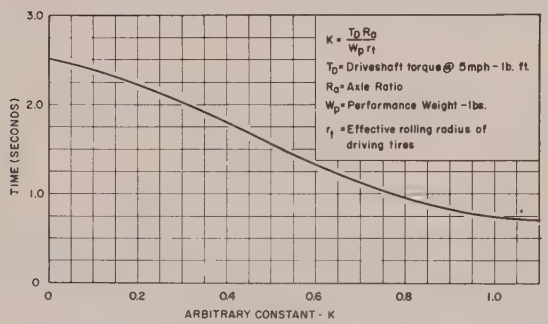

Fig. 5 — 0-10 mph time curve

as a function of an arbitrary constant K defined in Fig. 5. The curve represents an average of data compiled from tests of many passenger cars with automatic transmissions.

Engine Speed - Car Speed Relationship - This must be accurately determined to express the net driving force function of vehicle velocity correctly. The precise definition of this relationship is complicated by the presence of converter slip and the effective slip or creep between the driving tires and the road surface. Compatibility between net driving force terms from Eq. (20) and the mean velocity of each velocity increment evaluated is achieved by a driveshaft speed matching technique. The detailed description of this technique is found in Appendix II.

Vehicle Acceleration With Drive Wheels Spinning occurs when the tractive capacity of the driving wheels is exceeded by the tractive force transmitted by the power plant. The acceleration magnitudes associated with spinning drive wheels are limited to those produced by the maximum tractive forces that the road surface can react. The evaluation procedure for the numerical integration of distance includes a technique for imposing a tractive limit. The detailed description of the technique will be found in Appendix III.

Evaluation of Vehicles with Manual Shift Transmissions

The procedure previously outlined pertains to the prediction of acceleration performance for passenger cars with automatic transmissions. The performance of manual shift transmission vehicles may be predicted after making the following alterations:

1. Equation terms describing the torque converter are eliminated.
2. The procedure for matching the engine and torque converter is deleted.
3. Appropriate manual shift transmission vehicle input data are substituted.

Solution of Performance by Hand Calculation

The numerical integration of performance equations can be accomplished with the aid of an ordinary desk calculating machine. In order to reduce the human labor required to process the integration, the magnitude of the independent variable increment ΔV is increased to 5 mph. Some accuracy is sacrificed to fulfill this objective. The hand calculation process is tedious, time consuming, and continually subject to human error. A computer solution is more effective, saving both time and money.

Computer Solution Technique

Since many repetitions of solutions of the performance equations are required during the normal course of vehicle design, a digital computer was selected to perform the calculations.

A carefully devised set of detailed instructions was prepared to direct the computer during the problem solving process. This is known as a computer program which serves a dual function. The program outlined in logical sequence the detailed steps the computer must follow to solve the performance equations. It also prescribed the detailed sequence of operations necessary to transform the equations and related input data into a form acceptable to the computer.

The input data previously shown in the form of curves to facilitate illustrations were actually processed by the computer in the form of polynomial equations or tables. The in-

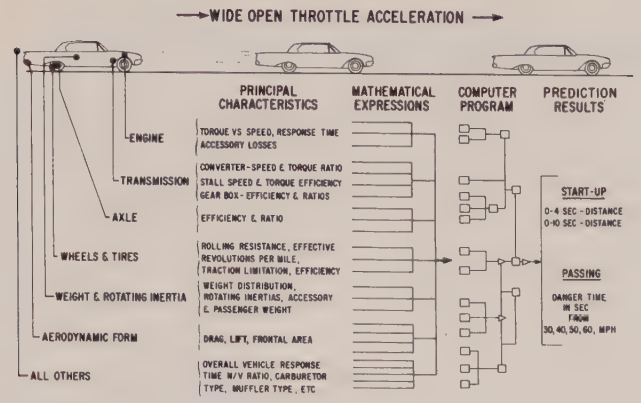

Fig. 6 — Computer solutions general flow chart

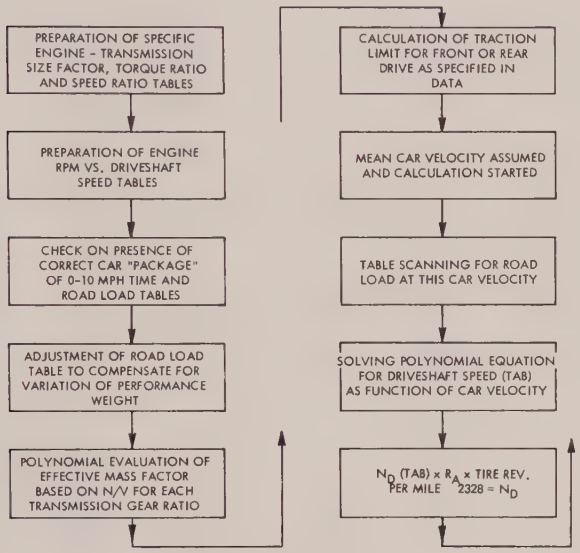
PREPARATION OF SPECIFIC ENGINE - TRANSMISSION SIZE FACTOR, TORQUE RATIO AND SPEED RATIO TABLES
PREPARATION OF ENGINE RPM VS. DRIVESHAFT SPEED TABLES
CHECK ON PRESENCE OF CORRECT CAR "PACKAGE" OF 0-10 MPH TIME AND ROAD LOAD TABLES
ADJUSTMENT OF ROAD LOAD TABLE TO COMPENSATE FOR VARIATION OF PERFORMANCE WEIGHT
POLYNOMIAL EVALUATION OF EFFECTIVE MASS FACTOR BASED ON N/V FOR EACH TRANSMISSION GEAR RATIO
CALCULATION OF TRACTION LIMIT FOR FRONT OR REAR DRIVE AS SPECIFIED IN DATA
MEAN CAR VELOCITY ASSUMED AND CALCULATION STARTED
TABLE SCANNING FOR ROAD LOAD AT THIS CAR VELOCITY
SOLVING POLYNOMIAL EQUATION FOR DRIVESHAFT SPEED (TAB) AS FUNCTION OF CAR VELOCITY
N_D (TAB) × R_A × TIRE REV. PER MILE / 2328 = N_D

Fig. 7 — Car acceleration performance calculation power train equipped with automotive transmission data-processing flow chart, IBM 650 digital computer

crement size of the independent variable ΔV selected for the numerical summation of time and distance equations is 0.50 mph vehicle speed.

A special set of forms was designed for the purpose of recording all required input data. These were made available to all engineering personnel desiring passenger car acceleration performance predictions. The coded data from a set of these forms were punched onto cards and fed into the computer.

A general schematic flow chart portraying a computer prediction of acceleration performance criteria is shown in Fig. 6.

Figs. 7-10 present in sequence the data processing flow charts applicable to the computer prediction of acceleration performance for a passenger car equipped with automatic transmission. Table 1 presents a sample of the computer output tabulation.

As the calculation proceeds, the computer prints out a

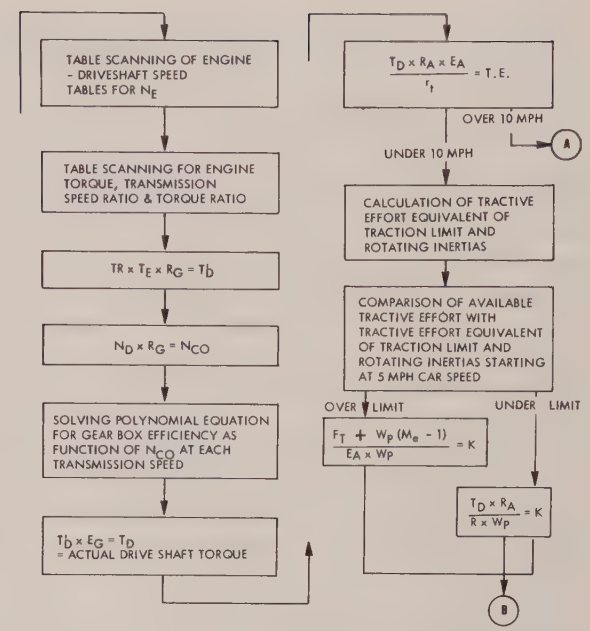
TABLE SCANNING OF ENGINE - DRIVESHAFT SPEED TABLES FOR N_E
TABLE SCANNING FOR ENGINE TORQUE, TRANSMISSION SPEED RATIO & TORQUE RATIO
$TR \times T_E \times R_G = T_b$
$N_D \times R_G = N_{CO}$
SOLVING POLYNOMIAL EQUATION FOR GEAR BOX EFFICIENCY AS FUNCTION OF N_{CO} AT EACH TRANSMISSION SPEED
$T_b \times E_G = T_D$ = ACTUAL DRIVE SHAFT TORQUE
$\frac{T_D \times R_A \times E_A}{r_t}$ = T.E.
OVER 10 MPH
UNDER 10 MPH
A
CALCULATION OF TRACTIVE EFFORT EQUIVALENT OF TRACTION LIMIT AND ROTATING INERTIAS
COMPARISON OF AVAILABLE TRACTIVE EFFORT WITH TRACTIVE EFFORT EQUIVALENT OF TRACTION LIMIT AND ROTATING INERTIAS STARTING AT 5 MPH CAR SPEED
OVER LIMIT
UNDER LIMIT
$\frac{F_T + W_P (M_e - 1)}{E_A \times W_P} = K$
$\frac{T_D \times R_A}{R \times W_P} = K$
B

Fig. 8 — Data processing flow chart — continued

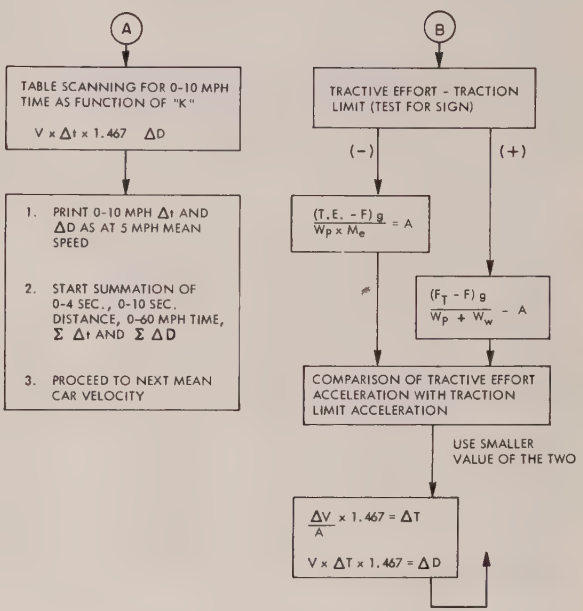
A
TABLE SCANNING FOR 0-10 MPH TIME AS FUNCTION OF "K"
$V \times \Delta t \times 1.467 \quad \Delta D$
1. PRINT 0-10 MPH Δt AND ΔD AS AT 5 MPH MEAN SPEED
2. START SUMMATION OF 0-4 SEC., 0-10 SEC. DISTANCE, 0-60 MPH TIME, $\Sigma \Delta t$ AND $\Sigma \Delta D$
3. PROCEED TO NEXT MEAN CAR VELOCITY
B
TRACTIVE EFFORT - TRACTION LIMIT (TEST FOR SIGN)
(-)
(+)
$\frac{(T.E. - F)\, g}{W_P \times M_e} = A$
$\frac{(F_T - F)\, g}{W_P + W_w} - A$
COMPARISON OF TRACTIVE EFFORT ACCELERATION WITH TRACTION LIMIT ACCELERATION
USE SMALLER VALUE OF THE TWO
$\frac{\Delta V}{A} \times 1.467 = \Delta T$
$V \times \Delta T \times 1.467 = \Delta D$

Fig. 9 — Data processing flow chart — continued

progress report of the numerical summation at the end of each successive 5 mph increment of vehicle speed. The numerical predictions of each performance criterion, vehicle shift speeds and other pertinent input data are included for reference and checking purposes.

Performance Prediction System Applications

The principal applications of the prediction system fall into the two general categories listed below.

Table 1 - Computer Output Tabulations

PB 027 PERF PROJ JONES 3 MAR 59 59 TBIRD 430-4V

GR 1	GR 2	GR 3	GR 4	SFT 1	SFT 2				
4.000	2.400	01.470	1.000		4200.000			1998.000	2829
SFT 3	P WT	D WT	AXL R	AXL E	C FRC				
4200.000	4775.000	2297.000	2.910	.965	.950			90000.000	2829
CG HT	WH BS	R R	T RPM	T MAS	T PRS				
20.600	113.000	01.093	768.000	54.000	23.000		110.000	110.000	2829

VEL	E RPM	RD LD	T EFF	DS SP	DS TQ	ACCEL	T SEC	D FT	CALC	GEAR
5.000	1799.558	83.460	3455.484	240.000	1344.958		1.086	7.964	2829	1
10.130	1947.836	84.042	2953.723	436.992	1149.661	16.763	1.108	8.289	2829	1
15.000	2153.912	87.500	2616.378	624.000	1018.358	14.772	1.579	17.145	2829	1
20.000	2419.163	93.600	2406.303	816.000	936.591	13.510	2.101	30.775	2829	1
25.000	2716.490	101.700	2239.846	1008.000	871.802	12.490	2.666	49.642	2829	1
30.000	3088.019	109.800	2150.233	1200.000	836.923	11.919	3.268	74.177	2829	1
35.000	3503.415	119.960	1972.588	1392.000	767.779	10.822	3.915	105.284	2829	1
40.000	3955.407	130.100	1812.466	1584.000	705.455	9.828	4.630	144.942	2829	1
42.500	4177.042	136.200	1719.937	1680.000	669.441	9.251	5.016	168.434	2829	1
45.000	2831.503	142.300	1363.795	1752.000	530.822	7.683	5.490	198.999	2829	2
50.000	3063.256	157.500	1336.625	1939.200	520.247	7.417	6.460	266.917	2829	2
55.000	3291.743	176.800	1275.818	2126.400	496.579	6.913	7.487	346.394	2829	2
60.000	3562.862	197.100	1202.437	2313.600	468.018	6.324	8.602	440.879	2829	2
65.000	3833.103	221.400	1139.207	2500.800	443.407	5.773	9.822	553.193	2829	2
70.000	4100.216	249.800	1076.404	2688.000	418.963	5.199	11.164	686.704	2829	2
71.500	4178.867	259.535	1050.185	2744.160	408.757	4.973	11.600	732.091	2829	2
75.000	3056.858	282.250	937.163	2843.035	364.767	4.224	12.785	859.868	2829	3
80.000	3207.817	314.700	909.942	3024.585	354.171	3.839	14.614	1068.506	2829	3
85.000	3369.116	351.250	877.141	3205.302	341.404	3.392	16.655	1316.360	2829	3
90.000	3547.262	387.800	843.659	3385.196	328.373	2.940	18.994	1617.612	2829	3
95.000	3723.542	428.350	813.988	3564.285	316.824	2.487	21.726	1989.645	2829	3
100.000	3897.892	468.900	786.523	3742.589	306.134	2.049	25.000	2459.407	2829	3
105.000	4070.134	510.950	760.178	3920.138	295.880	1.608	29.066	3072.784	2829	3
110.000	4238.431	553.000	722.519	4096.967	281.222	1.093	34.647	3956.070	2829	3
115.000	4402.094	553.000	674.020	4273.116	262.345	.781	42.630	5277.909	2829	3
118.000	4497.356	553.000	639.327	4378.500	248.842	.557	49.466	6449.316	2829	3

4 SEC	10 SEC	0-60	TIME	40 mph	50 mph	60 mph			
109.745	570.359	08.544	5.557-30mph	6.819	8.010	9.570	1800.000		2829

1. Determination of power train component characteristics required to achieve performance objectives for a vehicle design program.

2. A comparison of power train components as they effect the acceleration performance of a specific vehicle.

The first type of investigation requires the prediction of both acceleration performance and fuel economy criteria for a substantial number of hypothetical vehicles. Input data for each power train component are arbitrarily selected to cover a wide range of possibilities. The predicted values of time and distance criteria are cross-plotted versus values of fuel economy criteria for each hypothetical vehicle. Performance and economy design objectives are superimposed on these plots. Fig. 11 illustrates a sample cross-plot for several engine sizes in combination with a series of axle ratios. From this cross-plot it is evident that economy can be optimized for a given performance objective or vice versa. Variations of the cross-plotting technique can be applied for the appraisal of other component characteristics.

The second type of investigation is employed to study the

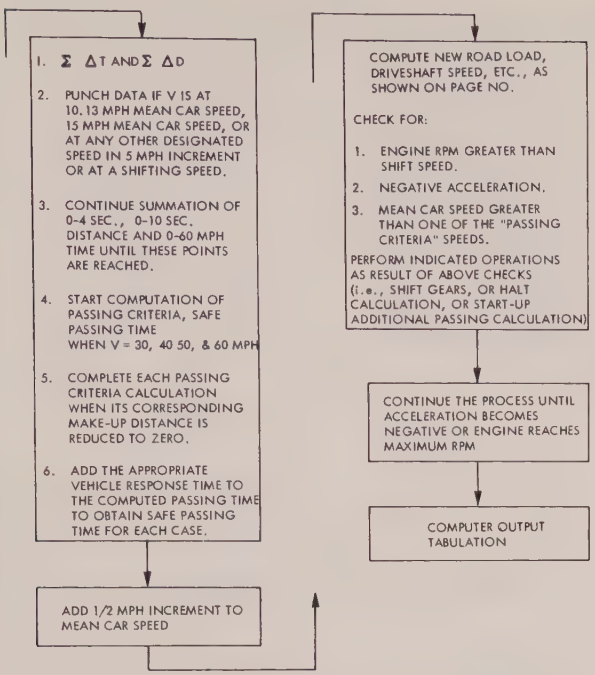
1. Σ ΔT AND Σ ΔD
2. PUNCH DATA IF V IS AT 10, 13 MPH MEAN CAR SPEED, 15 MPH MEAN CAR SPEED, OR AT ANY OTHER DESIGNATED SPEED IN 5 MPH INCREMENT OR AT A SHIFTING SPEED.
3. CONTINUE SUMMATION OF 0-4 SEC., 0-10 SEC. DISTANCE AND 0-60 MPH TIME UNTIL THESE POINTS ARE REACHED.
4. START COMPUTATION OF PASSING CRITERIA, SAFE PASSING TIME WHEN V = 30, 40 50, & 60 MPH
5. COMPLETE EACH PASSING CRITERIA CALCULATION WHEN ITS CORRESPONDING MAKE-UP DISTANCE IS REDUCED TO ZERO.
6. ADD THE APPROPRIATE VEHICLE RESPONSE TIME TO THE COMPUTED PASSING TIME TO OBTAIN SAFE PASSING TIME FOR EACH CASE.
ADD 1/2 MPH INCREMENT TO MEAN CAR SPEED
COMPUTE NEW ROAD LOAD, DRIVESHAFT SPEED, ETC., AS SHOWN ON PAGE NO.
CHECK FOR:
1. ENGINE RPM GREATER THAN SHIFT SPEED.
2. NEGATIVE ACCELERATION.
3. MEAN CAR SPEED GREATER THAN ONE OF THE "PASSING CRITERIA" SPEEDS.
PERFORM INDICATED OPERATIONS AS RESULT OF ABOVE CHECKS (i.e., SHIFT GEARS, OR HALT CALCULATION, OR START-UP ADDITIONAL PASSING CALCULATION)
CONTINUE THE PROCESS UNTIL ACCELERATION BECOMES NEGATIVE OR ENGINE REACHES MAXIMUM RPM
COMPUTER OUTPUT TABULATION

Fig. 10 — Data processing flow chart — continued

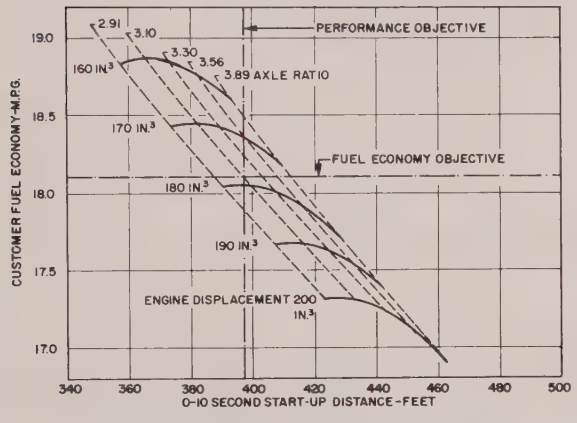

Fig. 11 — Power train optimum selection, performance versus fuel economy

comparative performance merits of two or more unlike samples of the same component such as several engines, torque converters, or axle ratios. When component characteristics are accurately represented, calculated comparisons are in many cases more reliable than test comparisons. The reason for this is that the computer can eliminate all variables associated with test measurements and their reproducibility.

Prediction System Accuracy and Cost Data

The accuracy of results derived from the computer solution of the performance equations is dependent on two principal factors.

1. The vaildity of the equations expressing the performance criteria.

2. The accuracy of input data employed to solve the performance equations.

Prediction accuracy is defined as per cent deviations from the true mean of a subsequent production vehicle. When predicting the acceleration performance for vehicles incorporating production drive train components with known characteristics, the prediction accuracy is within ± 5%. When future components with carefully estimated characteristics are incorporated, the prediction accuracy is ± 7%. Mean measured or estimated values of input data are used for all performance criteria predictions.

The accuracy associated with comparison of components will be as good as that related to the input data expressing component performance. For examples such as axle ratio comparisons, the comparative error is for all practical purposes non-existent.

Additional refinement in expression of some of the basic terms of the performance equations is contemplated to provide future accuracy improvement.

The utilization of the prediction system has been steadily increasing since its introduction. During the calendar years 1958 and 1959, over 4000 separate vehicle appraisals were processed. The volume for March, 1960, totaled 474 vehicles.

The cost and solution time requirements for computer prediction of all acceleration performance criteria for a single vehicle are very reasonable as indicated in Table 2. The corresponding average cost and time estimates for slightly

Table 2 - Prediction System Cost Data

Vehicle Transmission	Hand Calculations Time Min	Hand Calculations Cost Dollars	Computer Calculations Time Min	Computer Calculations Cost Dollars
Automatic	240	30.00	7	4.00
Manual	180	22.50	3	2.00

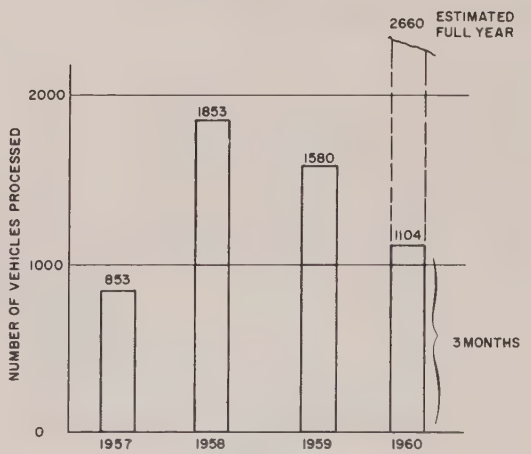

Fig. 12 — Prediction system utilization

less accurate hand calculated predictions are also listed.

The cost and time data shown for computer calculations are based on the use of an IBM 650 computer. These estimates are based on complete utilization of computer time on many different jobs. However, under most conceivable operating conditions, these costs would be no greater than double the dollar values indicated.

Future Outlook

Much remains to be done in perfecting procedures for expressing complex problems by equation systems and adapting these for solution by computers. The interrelationships of variables expressing power train component characteristics require further investigation and study to develop more precise methods of representation. Progress in this direction will be evolutionary in nature, resulting in the availability of increasingly more powerful engineering tools.

Appendix I

Detailed Definition, Eq. (20), Terms and Description of Related Input Data:

All data required to evaluate performance equations may be determined experimentally from hardware or predicted for paper vehicles and components. All net driving force terms are expressed as functions of velocity.

Engine Torque T_E versus Engine rpm Curve (Fig. 13) - The engine brake torque for the "vehicle as installed" condition corrected to a particular dry air standard for temperature and pressure.

Torque Converter Performance Curves (Fig. 14) - Include converter torque ratio C_{TR}, efficiency, input and output size factors which are plotted as functions of converter speed ratio for convenience.

Transmission Gear Box Efficiency Curves (Fig. 15) - Include a typical set of wide open throttle efficiency curves, one curve for each operational speed of a 3-speed automatic transmission gear box. These are plotted as a function of gear box input speed for convenience.

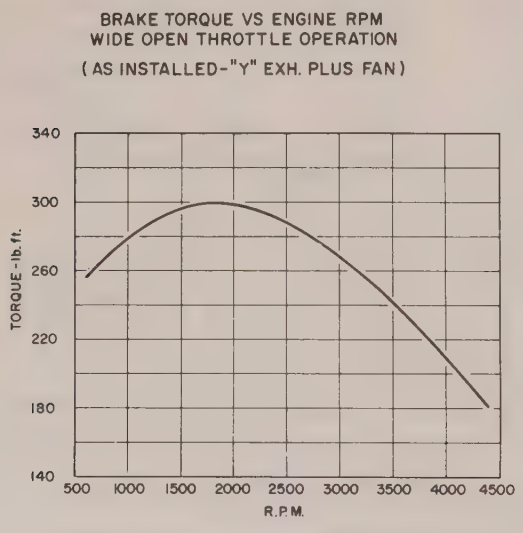

Fig. 13 — Engine performance

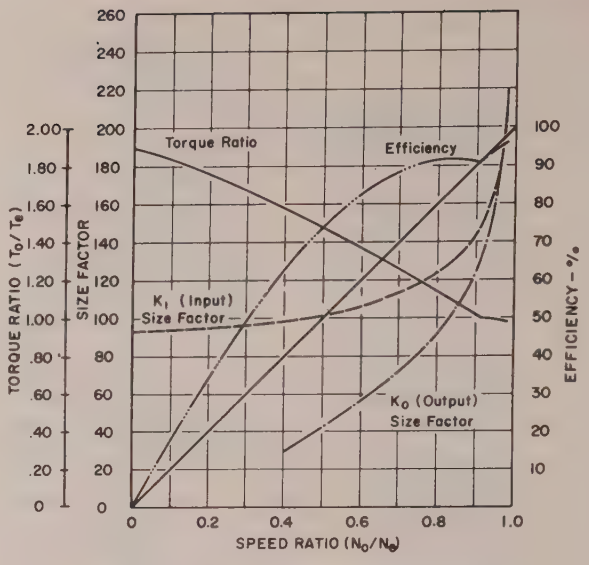

Fig. 14 — Torque converter performance

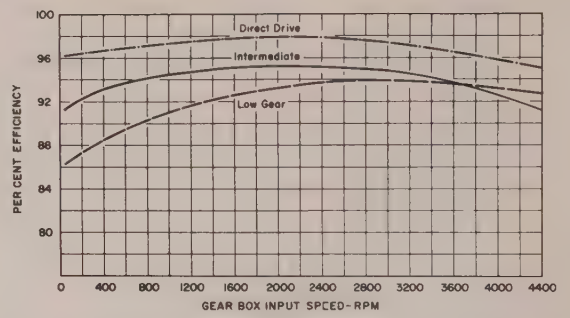
Direct Drive
Intermediate
Low Gear
PER CENT EFFICIENCY
GEAR BOX INPUT SPEED-RPM
0 400 800 1200 1600 2000 2400 2800 3200 3600 4000 4400

Fig. 15 — Transmission gear box efficiency, 3-speed automatic wide open throttle

Power Train Ratios - Such as gear box and axle ratios pertaining to the particular vehicle under consideration which are recorded for calculation purposes.

Drive Axle Efficiency E_a - This is assumed to remain constant over the speed range for wide open throttle operation.

Vehicle Performance Weight W_p - Vehicle curb weight including weight of common accessories plus a passenger complement. For conventional size vehicles the passenger complement consists of four 150 lb passengers divided equally between the front and rear seats.

Road Load Thrust (Fig. 16) - This is plotted as a function of vehicle velocity and is defined as the sum of vehicle rolling and aerorynamic drag resistances. Road load data used for prediction calculations are obtained by adjusting suitable

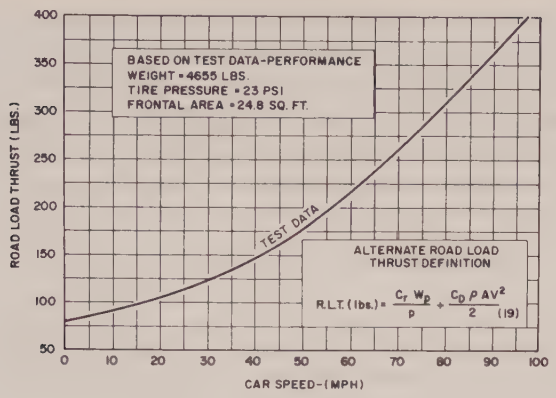
BASED ON TEST DATA-PERFORMANCE
WEIGHT = 4655 LBS.
TIRE PRESSURE = 23 PSI
FRONTAL AREA = 24.8 SQ. FT.
TEST DATA
ALTERNATE ROAD LOAD THRUST DEFINITION
R.L.T. (lbs.) = $\frac{C_r W_p}{p} + \frac{C_D \rho A V^2}{2}$ (19)
ROAD LOAD THRUST (LBS.)
CAR SPEED-(MPH)

Fig. 16 — Road load thrust

test data for differences in performance weight, tire pressure, vehicle frontal area, and aerodynamic drag coefficient. Eq. (19) shown in Fig. 16 is employed to make these adjustments. If no suitable test data are available, this equation is used to predict road load thrust.

Vehicle Tire Data - Such as rolling radius magnitudes (r_t), are determined experimentally for various tire sizes when subjected to appropriate operating conditions. Tire inflation pressures corresponding to vehicle design specifications are used for prediction calculations.

Appendix II

Engine Speed - Car Speed Relationships:
Description of Driveshaft Speed Matching Technique:

Accurate expression of the net driving-force function of velocity requires a detailed knowledge of the engine speed - car speed relationship. The principal problem is that of developing a method for expressing the mechanical N/V ratio for each operational gear of the transmission as a function of converter slip and effective driving wheel slip. The driveshaft speed matching technique solves this problem in three basic steps indicated below:

1. Determine driveshaft speed as a function of vehicle speed with effective driving wheel slip effects included.
2. Determine driveshaft torque as a function of driveshaft speed and engine torque.
3. Driveshaft torque values corresponding to the mean vehicle speed V of each speed increment ΔV are defined by equating driveshaft speed values from steps 1 and 2.

The driveshaft speed versus vehicle speed relationship is developed as follows:

$$N_D = N'_D\, k \qquad (A)$$

$$= \frac{N'_W\, k}{R_a} \qquad (B)$$

$$= \frac{\text{Wheel Revolutions}}{(5280 \text{ ft} = 1 \text{ mile})} \times V \times \frac{k}{R_a} \times 60 \qquad (C)$$

N'_D = Apparent driveshaft rpm.
N_D = Actual driveshaft rpm.
N'_W = Apparent driving wheel rpm.
k = Effective slip factor (Fig. 17).
V = Vehicle mean velocity corresponding to each particular velocity increment (ΔV) - ft/sec.

This expression is evaluated by test for each transmission gear ratio. One vehicle in each of several performance capability classes of vehicles is subjected to such tests.

This data is expressed empirically by a family of curves as indicated in Fig. 17. Similar curve families can be constructed for other cars in the same performance capability class by employing Eq. (C) to adjust the test data.

Since the driveshaft torques corresponding to the driveshaft speeds calculated by Eq. (C) are unknown, it is necessary to determine the driveshaft torque versus driveshaft speed relationship. This is accomplished by equating size factors of the engine and torque converter.

$$\text{Engine Size Factor} = K_E = \frac{N_E}{\sqrt{T_E}} \qquad (D)$$

Where T_E = Engine brake torque - lb ft from Fig. 13.
N_E = Corresponding engine speed - rpm.

The engine size factor is plotted with engine torque versus engine speed as shown in Fig. 18. The torque converter performance characteristics including its input size factor K_i are shown in Fig. 14. The matching of engine and con-

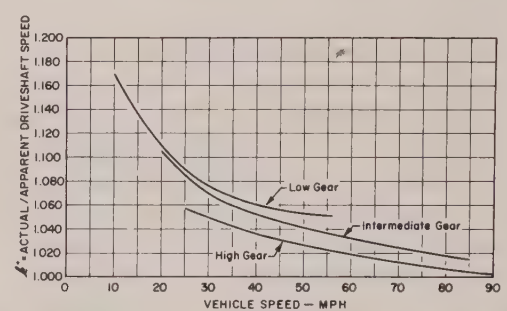

Fig. 17 — Effective slip "k" versus actual vehicle speed

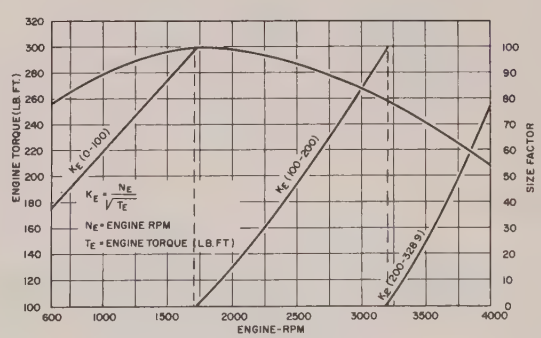

Fig. 18 — Engine torque and size factor versus engine speed

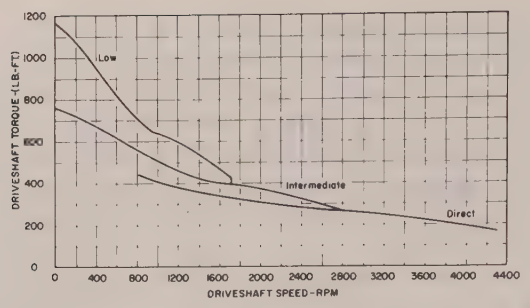

Fig. 19 — Driveshaft torque versus driveshaft speed, automatic transmission, 1-2-3 shift

verter is accomplished by setting $K_E = K_i$.

$$\text{Driveshaft Torque} = T_D = T_E C_{TR} R_G E_G \qquad (E)$$

$$\text{Converter Output Speed} = \text{Gear Box Input Speed} = N_E C_{SR} \qquad (F)$$

$$\text{Driveshaft Speed} = N_D = \frac{N_E C_{SR}}{R_G} \qquad (G)$$

where T_E = Engine brake torque - lb ft.
N_E = Engine speed - rpm .
C_{TR} = Converter torque ratio.
C_{SR} = Converter speed ratio.
R_G = Gear box ratio.
E_G = Gear box efficiency.

Eq. (E, F, and G) in combination with Figs. 14, 15, and 18 are employed to calculate the driveshaft torque versus driveshaft speed relationship for each transmission gear ratio. A specific engine torque and size factor corresponding to a particular engine speed are selected from the curves shown in Fig. 18. Since $K_E = K_i$ the converter input size factor is determined. For this specific value of K_i the corresponding values of converter torque ratio and speed ratio are read from the curves illustrated in Fig. 14. The gear box input speed is determined from Eq. (F) and the corresponding gear box efficiency read from the appropriate curve of Fig. 15. Eq. (E and G) are employed to calculate driveshaft speed and torque values which are plotted as shown in Fig. 19. The driveshaft speeds of Fig. 20 and Eq. (C) are matched to determine the driveshaft torque corresponding to a particular mean vehicle speed V.

Appendix III

Vehicle Acceleration With Drive Wheels Spinning - If the tractive capacity of the driving wheels is exceeded by the tractive force transmitted by the power plant, the wheels will break into a spin relative to the road surface. The acceleration of a vehicle with spinning drive wheels is limited to that produced by the tractive force reacted by the road surface. In all start-up performance prediction calculations maximum vehicle acceleration is limited to this value. The following equations are employed to effect this restriction.

$$\text{Traction Limit (lb)} = F = \mu W_s \left[1 \pm \frac{\mu h}{L \pm \mu h} \right] \qquad (H)$$

where $\mu = 0.95$ = Limiting coefficient of traction.
W_s = Static weight on driving wheels - lb.
h = Vehicle center of gravity height - in.
L = Wheelbase - in.

$$\text{Wheel spin occurs when T E at 5 mph} > F_T + W_D (M_e - 1.0) \qquad (I)$$

where TE = Tractive Effort - lb.
F_T = Tractive Limit - lb.
$W_p (M_e - 1.0)$ = Tractive effort equivalent of power train rotating inertias at 5 mph.
W_p = Performance weight - lb.
M_e = Effective mass factor.

The corresponding 0-10 mph time is determined from Fig. 5 with K calculated from the following equation:

$$K = \frac{F_T + W_p (M_e - 1.0)}{E_a W_p} \qquad (J)$$

K = An arbitrary constant.
F_T = Tractive limit - lb.
W_p = Performance weight - lb.
M_e = Effective mass factor.
E_a = Driving axle efficiency.

The corresponding vehicle acceleration at V = 5 mph and at V for each successive car speed increment is calculated as shown below.

$$a \text{ at 5 mph} = \frac{(F_T - F)g}{W_p + W_w} \qquad (K)$$

a = Acceleration - ft/sec^2
F_T = Traction limit - lb.
F = Road load thrust - lb.
g = 32.16 ft/sec^2
W_p = Performance weight - lb.
W_w = Rotating inertia equivalent weight of two non-driving wheels - lb.

The acceleration value obtained from Eq. (K) is compared with that obtained during the evaluation of Eq. (20). The smaller of the two is retained for the numerical integration of Eq. (20).

Production Application of High Energy Rate

E. W. Feddersen
Convair Division, General Dynamics Corp.

HIGH ENERGY RATE process is defined as the application of high energy rate to the deformation of materials without the frame work of conventional heavy machinery. Three major methods of applying high energy rate to the deformation of materials are explosive, hydroelectric, and pneumatic-mechanical.

Explosive Forming

Explosive forming is the shaping of materials by the exertion of sudden pressures from the explosion of a chemical charge. The shock wave and subsequent hydraulic action cause the material to take the shape of its die.

Normally, a medium such as water is used to transmit these forces because the intense heat generated tends to burn the material. Water, or a fluid medium, is also used because a more uniform pressure is experienced from the hydraulic action. A third less important reason for using water is the natural muffling effect it has on the sound of the explosion.

Although possessing certain advantages over mechanical presses, explosive forming cannot replace mechanical means of forming in producing high volume items. The real advantage lies in the ability to form and size large, complex sections at fractional tool costs, and the elimination of extremely large mechanical machinery.

Hydro-Electric Method

The hydroelectric method has been described as underwater lightning. Again, the sudden release of energy is applied to deform materials. In this method, electrical energy is stored in capacitors and suddenly triggered. The energy, applied through a water medium, is the same as in explosive forming. This method, like explosive forming, also has its limitations, and does not appear to be a replacement for the mechanical press. Advantages of the hydroelectric process read almost identical to those of explosive forming. However, there are two additional advantages which make it more versatile as a production method. The process is accurate and repeatable and, because of complete controllability, usable within a fully inhabited factory.

Pneumatic-Mechanical Method

A third method, called "Dynapak," is a pneumatic-mechanical means of applying high energy rate to the deformation of materials through the sudden release of compressed gas. Energy is stored in the form of compressed dry nitrogen

gas. This gas is released through a system of valves and applied to a piston. The piston, ram, and header plate are driven at very high velocity, making contact with a bolster plate. The header plate contains the punch while the bolster plate holds the die, all of which is very conventional, except the high velocities employed in the mechanical action. This method, while semi-conventional, opens new avenues of metal forming and can, in some instances, use simple punches with complicated dies.

Application of Explosive Forming

These three methods of high energy rate application range from laboratory research to full production.

Explosive forming is the forerunner, primarily because it does not require mechanical or electrical devices other than those employed for handling materials and tools. Production application of explosive forming is most prominent in the aircraft, missile, and engine accessory fields. Ryan Aeronautical Co., Aerojet General Corp., North American Aviation, Inc., Rocketdyne Division of North American Aviation, Inc., Lockheed Aircraft Corp., Boeing Airplane Co., and Convair installed facilities for research and production as early as 1957. Talco Engineering Co., Redondo Beach, Calif., and Mesa, Ariz.; and E. I. DuPont de Nemours, Wilmington, Del., are currently using explosive forming methods.

It is understandable why the main interest has been centered with the airframe, missile, and engine accessory fabricators. First, these companies generally deal in relatively small quantities of parts. Second, the parts and hardware fabricated by airframe and engine companies are usually as dynamic as the finished or completed item itself, resulting in frequent configuration change. Third, all companies are looking for ways of stretching the defense dollar, and, to be sure, a 50% tooling reduction is one way of cutting costs. Fourth, the process is different, exotic, and challenging. The process challenges the metallurgical engineer and brings into the manufacturing picture the need for scientists, in the fields of shock wave phenomenon and hydraulics.

Imaginations ran rampant when the process was first introduced to industry. At first, everyone believed that the current conventional methods would be replaced by the easier and cheaper method which used explosives. Numerous articles were written and as many speeches were made, each emphasizing that this was the panacea that the metal working industry had been seeking. Approximately, three active years have passed since the first blast of publicity. During this time, many among us have quiescently became wiser and assumed the practical approach in the use of this very important and versatile form of energy.

After the first shock wave subsided at Convair-Fort Worth, we initiated technical studies and tests on explosives and their capacity to deform material. These studies provided us with a great amount of technical data. These included effects of explosive types, shapes, and stemming on various shapes to be formed. Compilation of this data has permitted us to establish parameters of explosive type, shape, and weight to do a given forming operation. These parameters are relatively broad and we still rely heavily upon the engineer's practical knowledge of explosives and their characteristics. Continued use of explosives will generate more empirical data to be utilized in establishing more precise parameters.

In addition to the above data, we began a systematic classification of shapes which we considered to be practical to form by explosives:

1. Preformed hollow bodies (ultimate shapes).
2. Cups (drawn from flat plates).
3. Channels (straight and curved).
4. Panels (flat and contoured).

The path of least resistance was the order of business, not only at Convair-Fort Worth, in this instance, but at most other fabricators using explosives. The expansion of preformed hollow bodies and cup shapes were selected as the most economical application of this process.

Fig. 1 shows one application of explosives to the expansion of preformed hollow bodies. The ball joint is made by precutting 301 annealed stainless steel tubing and nesting one within the other. These are then placed in the die shown in Fig. 2. A light charge of prepackaged gun powder is placed inside the tube and detonated. This results in a uniform semi-airtight ball joint for the overboard dump system for the B-58 airplane. Fig. 3 shows two ball joints fitted to attaching flanges resulting in a universal joint in the anti-icing system for the B-58.

Another application of explosives to preformed hollow bodies is shown in Fig. 4. This part is a cooling shroud for a ramjet engine. In this case, a type 310 stainless steel was preformed into a cylinder and welded. It was placed in the die shown in Fig. 5 and a cylindrical charge of PETN explosives, 2 in. in diameter and 9 in. long was suspended within the chamber. The results are self evident. A complicated part was formed without the need of any machine tools. Conformation of convolutions and diameters were well within customers tolerances ±0.010 in.

In Fig. 6, we see the application of explosives in forming a regular cup shape. In this case, the requirement was for the part to be made from 301 1/2h stainless steel, 24 in. in diameter with a 4 in. chord height. The tool (Fig. 7) for this cup shaped part was made in two pieces. The base is cast Kirksite with the hemispherical form and a steel draw ring. The upper case serves two purposes: (1) it acts as a draw ring, and (2) as a water tank in which the explosive charge is placed. The formation of this hemisphere is interesting because multiple charges created stresses within the material which caused the part to warp when trimmed. Although many variations of explosive charge sizes and shapes were tried, the hemisphere could only be formed with a sin-

Fig. 1—Ball joint

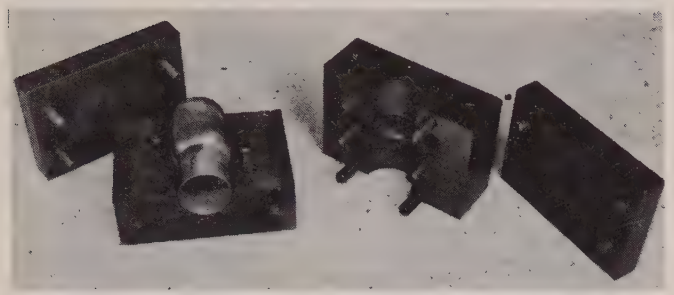

Fig. 2—Ball joint in die

Fig. 3—Ball joint production part

Fig. 4—Ramjet engine cooling shroud

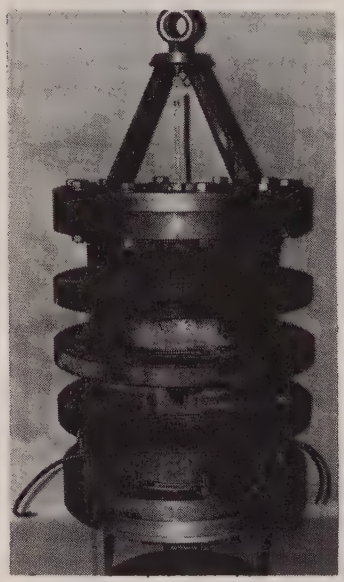

Fig. 5—Ramjet engine cooling shroud die

gle charge. The 1/2 h 301 material had to be fully trapped to prevent compression wrinkles.

Fig. 8 is an irregular cup shape selected for explosive forming because of the multiple strike and annealing operations, which were required when the part was made on the drop hammer. Operations were reduced by explosive forming from five strikes to three and from four anneals to one. The part, a mounting for a ground cooling line on the B-58, is made from 6061-0 aluminum and is formed using two 5-gram explosive charges with only one annealing required between strikes.

All parts discussed above plus many others have been made in our outdoor explosive forming installation. This installation (Fig. 9) is out-of-doors because of safety regulations established by state and local governments and company policies. These regulations, while absolutely necessary, cause the process to be normally a fair weather operation. With these limitations, plus the fact that generally the blasting site is located some distance from the main plant facility, explosive forming is economical only when applied to selected parts. The search is continuing for a practical method of generating controlled explosive forces of a desired magnitude and, yet, safe enough for in-plant detonation.

Electricity, a Substitute for Dynamite

Within the past year, Chrysler Corp., Republic Aviation Corp., and Convair announced that they have found a

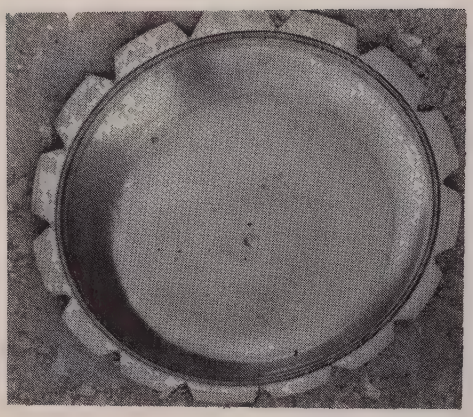

Fig. 6—Regular cup shaped application

Fig. 7—Die for regular cup shaped part

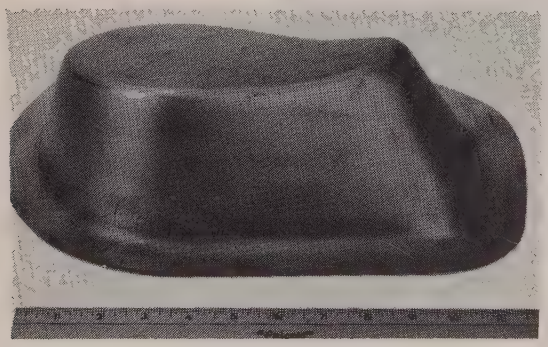

Fig. 8—Irregular cup

substitute for dynamite. The substitute is electricity. Convair engineers developed a high energy spark unit, classed as nonchemical-type high energy release method, to supplement explosive forming in study of shock waves and wave forms. Numerous experiments and tests were performed, during which it became apparent that a distinct and vast source of controlled high energy was available. Here was explosive forming that could be used indoors. Here, too, was one of the few direct applications of electricity to do work.

Initial work was done using high voltages in a range of 14,000-22,000 and 30-60 microfarads. Encouraging experiments showed that a sufficiently intense shock wave could be generated in water to form small sample parts. Sample materials were stainless steel, copper, and aluminum. Pressures obtained were in excess of 80,000 psi, well above the yield limits of the materials used in the experiments. It should be remembered that all the work done with these high voltages was done with a spark discharged from a bank of capacitors.

As additional experiments were tried, it became essential for the power of the unit to be increased. This increase in power was realized by reducing the voltage from 22,000 to 4000 and the capacity increased from 60 to 1200 microfarads and with the addition at an initiating wire. This substantial increase in energy released is highly desirable in sheet metal forming.

An added bonus was derived from the reduction of voltage. Complete elimination of corona leakages was obtained, resulting in a safer operating unit.

The energy contained in the capacitor bank is equal to 14,580 joules or 10,800 ft-lb. When this unit is fired, the initiating wire connecting the electrodes is transformed into a cylinder of metallic vapor. This vapor expands against the medium, in our case water, the inertia of which causes a pressure buildup in the approximate range from 15,000 to 20,000 atm. For example, other investigators tell us that a tungsten wire, upon vaporizing, will increase its original volume by more than 25,000 times. Surge peak of current is about 2 or 3 microsec and 40 microsec of total time is used to decay. This item, measured on a Hughes memoscope, is shown graphically in Fig. 10.

Another interesting variable, the variable wave front, was discovered and applied. This is accomplished by shaping the initiating wire. Sharp nosed, spherical, and plainer wave fronts have been observed. Each of these wave fronts can be put to use for a specific job of forming.

Fig. 9—Explosive forming site

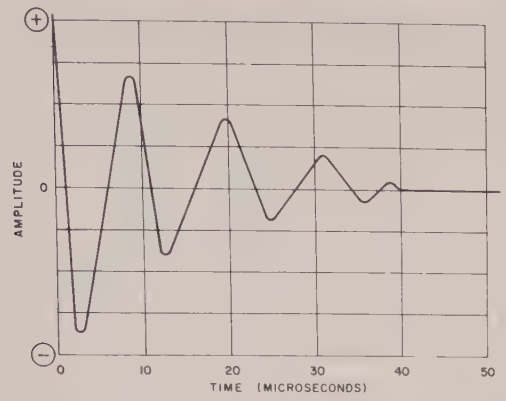

Fig. 10—Results shown by Hughes memoscope

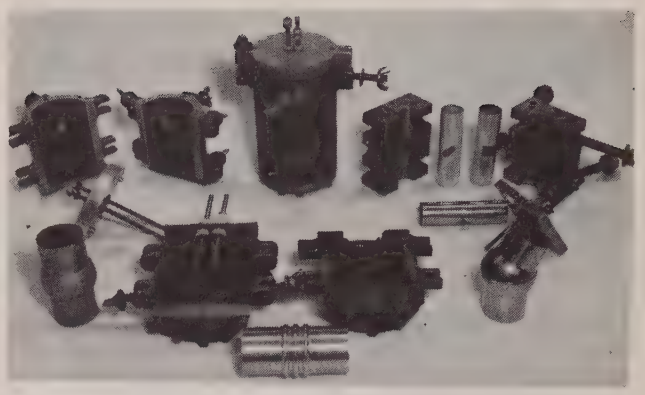

Fig. 12—Hi-vo pac dies

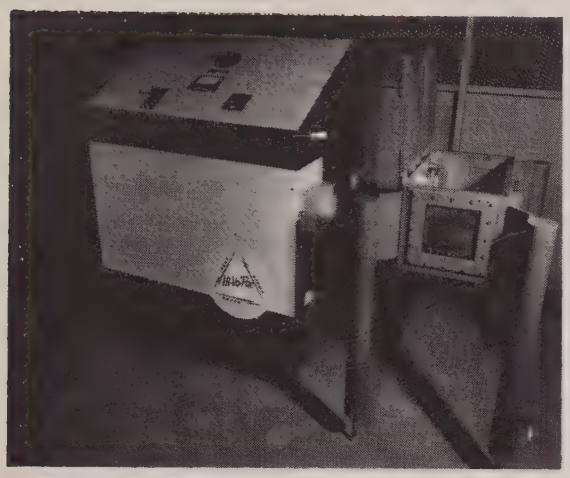

Fig. 11—Hi-vo pac unit

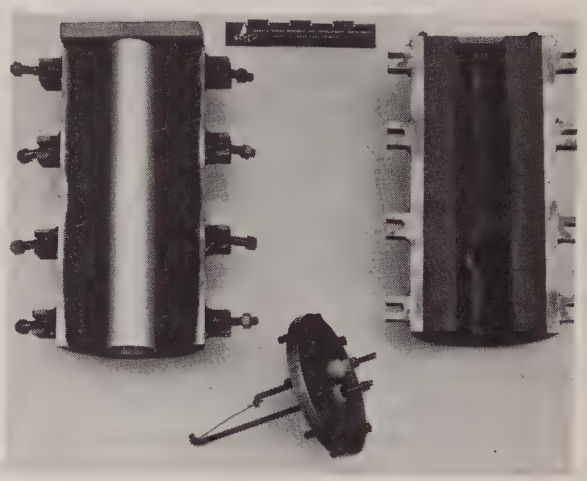

Fig. 13—Split die, blank, and die head electrode

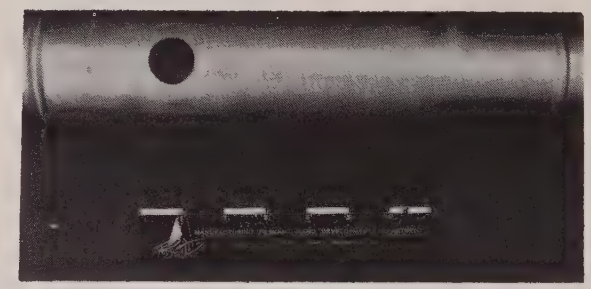

Fig. 14—Hi-vo pac finished part

The high energy spark unit is shown in Fig. 11 (HI-VO-pac unit). The portable metal box on the left contains capacitors, switching circuits, variac control of power, charging switch, and automatic or manual discharge switches. The desired voltage buildup is controlled by the variac and can be read in the voltmeter located on the control panel. Buildup and discharge after making the desired setting is initiated by merely pressing the release button. Upon activating this button, the unit charges in 6 sec and then automatically discharges. The unit is sufficiently safe for operation by nontechnical personnel and is located in the proximity of other plant activities with complete safety.

In the application of this controlled and repeatable electrical explosive force, the most obvious departure from explosive forming is the die design. Dies for high energy spark forming are completely closed. Fig. 12 shows several dies for forming airframe components. The closed die in the top center of Fig. 12 contains fixed electrodes to which is attached the initiating wire. The position of the electrode has been determined by experiments to give the most efficient wave front for the forming to be done.

Each die has its own peculiar set of electrodes and initiating wire. The dies can be completely closed because the gas volume generated by the vaporized wire is insignificant, if compared to the gas bubble created by a chemical explosive. By closing the die, full advantage can be taken of the pressure wave and, in the case of tubular parts, the shock wave is reflected off the ends, creating additional energy.

This closed die design, employed by Convair-Fort Worth, permits the use of epoxies as die material. Epoxy resins have high compression strength and reasonable wear characteristics. Standard shells, in which the pattern is held, are

of various diameters. Resin is poured while the die is being vibrated. Vibrating the die is very essential in expelling all trapped air from the resin. The die is completed in about two days, including curing time for the epoxy resins.

The following sequences are necessary operations in the forming of a part by hydroelectric process. Fig. 13 shows the split die, blank, and die-head electrode with initiating wire attached. The die is closed and the bottom plate installed. The tube to be formed has a rubber wafer installed at its base, making the tube water tight. The tube is then placed into the die cavity and the tube filled with water. The cover plate with electrodes and initiating wire is installed. The leads from the power unit are connected to the electrodes, the release button is pressed. In 6 sec, the unit charges itself and fires automatically, resulting in the finished part shown in Fig. 14. Of great interest is the fact that the operation of beading, expanding, and piercing of hole were done simultaneously.

High energy spark, like explosion forming, obviously lends itself to expanding and sizing hollow bodies. This is, therefore, the most economical use for which it has been employed. This high energy rate method will take its place among the other production processes in sheet metal fabricating shops.

Dynapak Machine

The question is always asked, "What about forgings, impact extruding, and straight extrusion? Is there a high energy rate device these industrial specialists can use?" The device in question exists and is marketed under the trade name of Dynapak. This is a pneumatic-mechanical machine which releases stored high-pressure nitrogen gas to accelerate a piston to a high velocity, thus developing a high energy rate forming process.

This principle of forming offers to the metal forming industry a high energy rate device which can be used in forging, forming, extruding, compacting, shearing, and blanking. To date, most of the effort in application development has been in forging, extruding, and "closed-cavity extrusion molding." The latter is a coined term which pertains to the extruding of a material through an orifice into a vented closed-cavity die. This process literally makes functional the concept of parts being "born to shape."

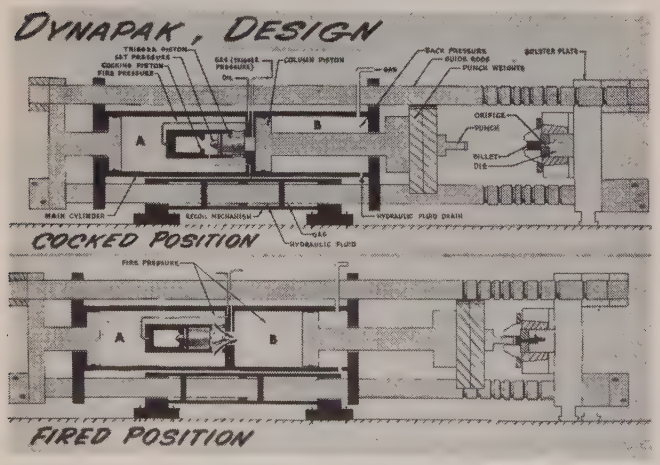

Fig. 15 — Dynapak schematic

Fig. 15 is a schematic of the Dynapak. It consists of a two-chambered cylinder, valve cocking assembly, piston ram assembly, bolster plate, tie rods, cushioning piston, nitrogen shock absorbers, and base frame. This entire unit can be mounted either in a horizontal or vertical position. The operation of the machine is simple. Chamber A is charged with nitrogen gas to the desired fire pressure. A trigger pressure is then applied to the small area between chambers A and B. This trigger pressure forces the trigger piston to an open position. Compressed nitrogen gas then passes through three large ports and acts upon the piston, driving it and the punch toward the work piece at a high velocity. Because the machine is mounted on a floating type support, the bolster plate also moves, toward the punch, when the machine is fired. The momentum from these two sources cancel each other as the part is formed. Therefore, all stresses are contained within the machine. After the part is formed, the piston is returned to the cocked position by pumping hydraulic oil into the forward section of chamber B. This action also recompresses the nitrogen gas chamber A to the original firing pressure. By changing the firing pressures, we vary the energy, and, by changing the weight, we vary the velocity of the ram.

With this, we have a fully controlled, variable high energy rate machine. But, what can be accomplished with this machine?

Application of Dynapak

Two progressive forging fabricators in the Los Angeles area decided to give this high energy rate device a whirl. The Precision Forge Co. was first. Their first customer was Convair-San Diego. Could they use this high energy rate to produce a forged gas tight corner, which would be structurally sound and require a minimum of machining? The part, shown on the right in Fig. 16, is used in the Convair 880 airliner. It was being machined from the 4-lb 10-oz blocker forging, shown on the left in the same photo, to a finish

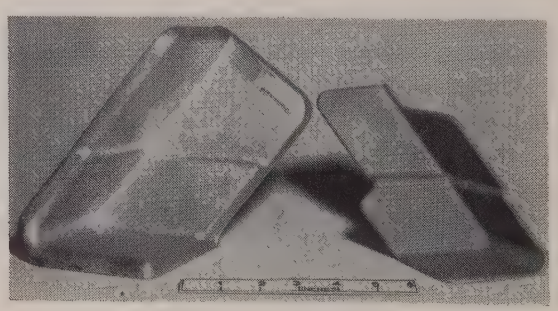

Fig. 16—Forged gas tight part

Table 1 - Savings Possible with Dynapak

	Conventional Forging	Dynapak
Tooling	$2,274.00	$3,600.00
Set Up	198.00	65.00
Unit Price	6.44	5.75
Machining		
Tooling	7,454.00	None
Unit Price	51.60	None
	$9,984.04	$3,670.75
Net Savings		$6,313.29

weight of 10 oz.

Precision Forge Co. produced the part shown in Fig. 17. This part is finished forged from 2014 aluminum alloy in two strikes. The only machining required is the flash trim and the attach hole drilling. This method of producing the gas-tight corner has resulted in the dollar savings shown in Table 1. But this is an aluminum alloy, easily worked and not too costly. What about the tough ferrous alloys?

An example of what can be done with high energy rate applied to a part made from 19-9 DL stainless steel is shown in Fig. 18A (internal view) and Fig. 18B (external view). This part had been machined from typical blocker forgings. Precision Forge Co. applied the high energy rate principle. Results included a reduction from $1200 to $600, and machining operations reduced from seven to two. The result of the above reductions was a 75% overall savings by the customer. Another major factor was realized when this process was applied to forge this flange. When forged at 2100 F and hot-cold worked at 1500F, greater strength and uniform and controllable work hardening resulted. Stated another way, this process resulted in an ASTM grain size No. 11. This is comparable to a conventional forging grain size of ASTM No. 5. These two examples of open die forging appear simple and not too difficult to make.

However, all new forging techniques, die material selection, and die design required in this field are not completely established. Continued development by forgers will be required to put this new process in full production use.

The application of high energy rates to metals has been conclusively shown to yield improvements over conventional methods. This improvement was most prevalent in open die forging experiments that were conducted by Precision Forge Co. The results of these experiments included:

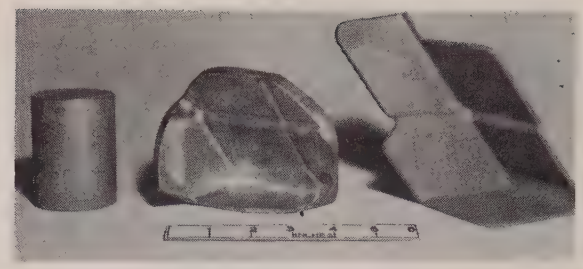

Fig. 17—Aluminum forged part

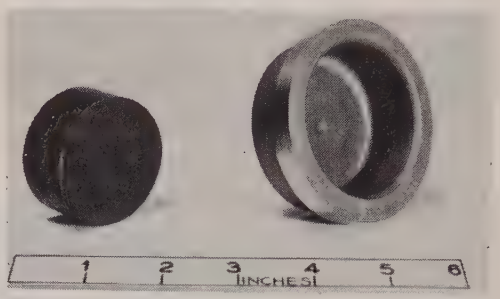

Fig. 18A—Internal view of her forged 19-9 DL

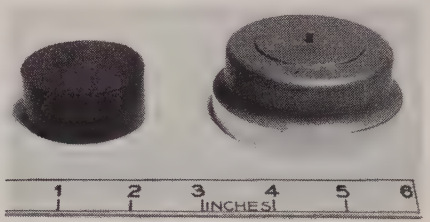

Fig. 18B—External view of her forged 19-9 DL

1. Grain refinement.
2. Improved surface finish.
3. Precision tolerances.
4. Sharper radii.
5. Thinner sections.

Closed-cavity extrusion molding is defined as the forcing of metal in a semi-solid or plastic state through a small outlet (orifice) into a defined volume (die cavity) to produce a finished or semi-finished configuration with high physical properties.

The initial work centered around the effect of moving metal through an orifice into a closed cavity. These tests were conducted using the die (XJ-35809) shown in Fig. 19. This die is designed so that various orifice ratios can be employed. An example of the results of these tests are shown in Figs. 20 through 23.

Photomacrograph shows the flow lines of a 17-4 PH stainless steel closed cavity extrusion (Fig. 20). Note the uninterrupted flow lines and the lack of slag inclusions, voids, or overlap.

In the photomicrograph (Fig. 21) the ferrite stringer (white) shows the direction of flow due to rolling. In Fig. 22 only the ends of the ferrite stringers are visible, which is to be expected.

Photomacrograph (Fig. 23) shows the flow lines in an AI-

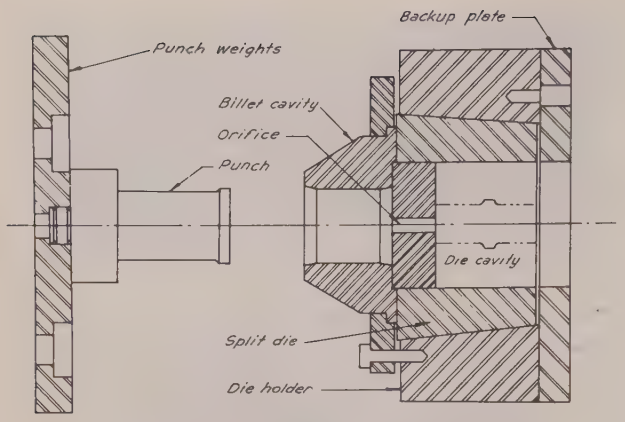

Fig. 19—Die XJ-35809

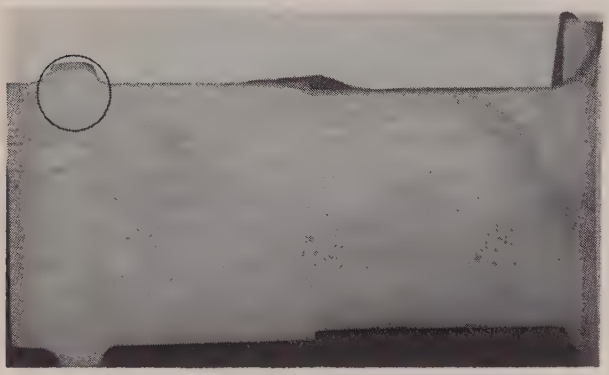

Fig. 20—Photomacrograph showing flow lines of 17-4 PH stainless steel closed cavity extrusion

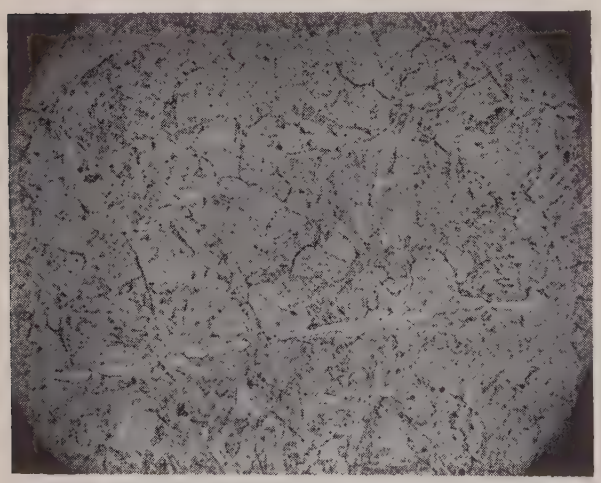

Fig. 21—Photomacrograph with ferrite stringer showing direction of flow due to rolling

SI 4130 steel closed-cavity extrusion. As with 17-4 PH, it is characterized by uninterrupted flow lines, lack of slag inclusions, voids, or overlap.

These simple tests indicate that materials did experience a fluid behavior when subjected to the high energy rates. They also indicate that the material, while no longer possessing defined longitudinal or transverse structure, did not suffer a loss of tensile properties.

Fig. 22—Photomacrograph with ends of ferrite stringers visible

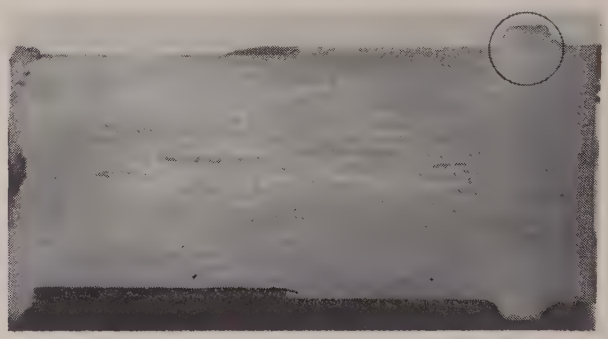

Fig. 23—Photomacrograph showing flow lines in an AISI 4130 steel closed cavity extrusion

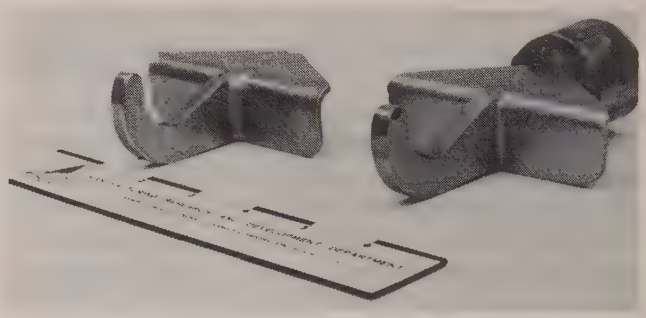

Fig. 24—B-58 canopy pod hook

Armed with this data, the next step was to select some part on the B-58 which offered a challenge. The challenge was met with the part on the left in Fig. 24. This canopy pod hook is made of AISI 4130. It is welded from two pieces, flange and hook. Certain structural problems were being experienced with this part and, from the earlier test work, it appeared that good grain structure could be realized from the application of the closed-cavity extrusion mold-

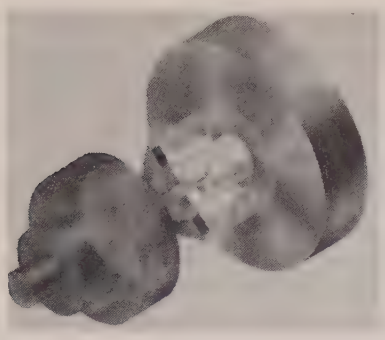

Fig. 25—B-58 canopy hook die

ing process.

The B-58 canpoy hook die shown in Fig. 25 was put in work. Die material selected was "Stentor," heat treated to hardness of 55-60 Rockwell C.

Fig. 26 defines the evaluation of the canopy hook. Note that the forging temperature, billet diameter, and billet length remained constant. On the first trial with a 6.25-in. stroke, 684 lb of weight on the ram, and 750-psi fire pressure the material barely entered the hook and flange cavity. For the second trial, only, the fire pressure was changed, with the encouraging results of more hook and more flange.

Between the second and third trial the air bleeds were increased, both at the extremities of the flange and hook. The third trial was run with increased stroke, decreased ram weight. The final trial was made after the air bleeds were again enlarged and with increased fire pressure.

The results are most dramatically portrayed in Fig. 24, with the original welded hook on the left and the Dynapak hook on the right. These tests were not without great disappointment. During the fabrication of the next successful hook, the die failed. The failure was attributed to lack of knowledge in tool steels and closer control of heat treating. Since this tool had to be rebuilt, several tool steel manufacturers were brought into the picture. They are all sympathetic and see needs for a new die steel which is tough, abrasion resistant, thermal shock resistant, and has good elongation. We hope that a new die steel will soon be formulated with these characteristics. With improved die steels, we believe that this process can literally cause complex parts to be "born to shape."

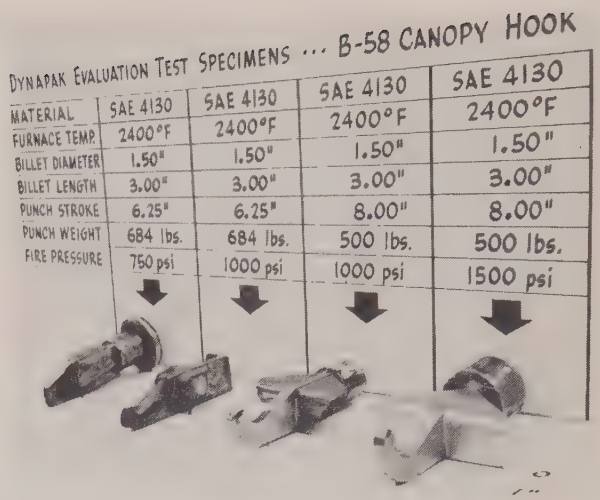

Fig. 26—Evaluation of canopy hook

Production Application of High Energy Rate

The application of high energy rate to production is feasible. However, there remains a considerable amount of development work still to be accomplished. The several processes are sound with only detail information remaining to be gathered before specific parameters are established. It must be recognized that each method of applying high energy rate has its own area of application. No one method is the panacea for the material processing industry. They should be applied only when the job cannot be done another way, the finished product will be better physically or when it can produce a part more economically.

These processes still require a great amount of manual work. Handling devices for tools and material must be improved. In addition, an entire new concept will be required in the design of quick opening dies. Die design becomes more difficult because of the high internal pressures acting upon the material and the dies.

With diligent effort from industry, it is certain that the maximum utilization of high energy rate in production will be made soon. Through the application of these new processes, we offer to the design engineers unfettered design freedom.

Case Crushing of Carburized and Hardened Gears

R. Pedersen and S. L. Rice
Caterpillar Tractor Co.

STEEL HAS BEEN HARDENED in various ways since ancient times. Hardening of steel is referred to by early Greek and Roman writers, and even the ancient Egyptians heated iron (probably meteoric iron) in a forge until, by long contact with the charcoal, the surface became carburized and hardenable. Although carburizing has probably been used more or less unintentionally for several thousand years, it was not until the comparatively recent date of 1781 that Bergman of Upsala pointed out that the difference between wrought iron, cast iron, and steel was in their carbon content. It is only within the last 50 years that carburizing has become more of a science and less of an art.

One of the most common uses for carburized and hardened steel is in heavily loaded gears. In the recent past, engineers who were acquainted with the strength requirements designed the gears, but left the selection of carburized case thickness in the hands of the experienced heat treat foreman who generally specified case depths which were proportional roughly to tooth thickness. In this manner standards(1, 2)* came into being which specify case thickness on the basis of tooth thickness.

These standards, however, are inadequate for many present day nonstandard gear designs. For example, Fig. 1 shows a pair of teeth from a standard addendum gear set and another pair from a long and short addendum set. The standard

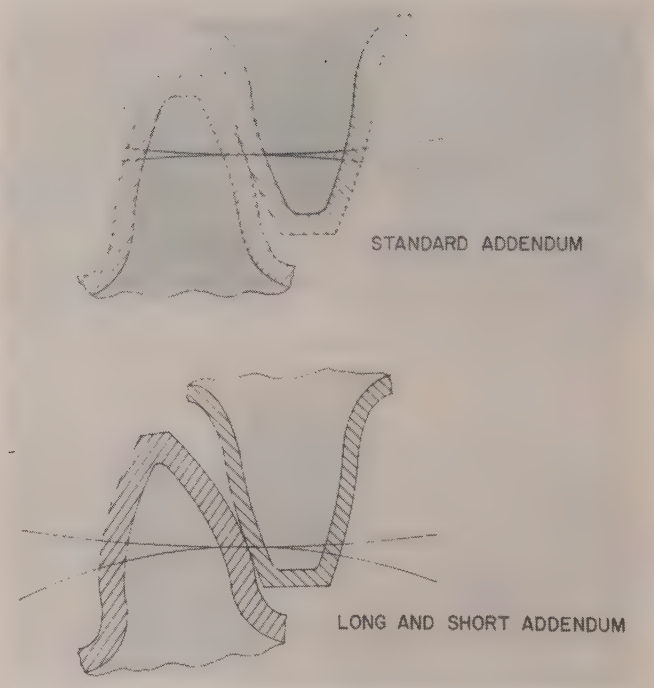

Fig. 1 — Effect of making case depth proportional to circular tooth thickness (carburized case shown crosshatched)

*Numbers in parentheses designate References at end of paper.

addendum pinion and gear have equal tooth thickness and, on the basis of the above mentioned standards, equal case depths. The long and short addendum set, having different tooth thicknesses, are given proportional case depths. Even intuitively we feel that the member having the thicker case will support the heavier compressive load. However, there are stronger reasons for believing that case thickness should be chosen on the basis of considerations other than tooth thickness, and to show these it is necessary to discuss two types of gear tooth profile failures: pitting fatigue and case crushing, as they occur on carburized and hardened gears.

This discussion is concerned only with the influence of case depth in resisting the compressive loads on gear tooth profiles. The question of how case depth is related to strength in bending is not considered. In general, however, our experience indicates that maximum strength in bending is obtained by using the thinnest case which will resist crushing.

Characteristics of Pitting Fatigue and Case Crushing on Carburized and Hardened Gears

Pitting Fatigue - Pitting occurs on the profile of a gear tooth and generally originates in the dedendum region of driving pinions in reduction gear sets. From the point of origin, a crack spreads in a characteristic V-shape toward the tip of the pinion tooth. This crack extends a short distance into the hard case and then travels nearly parallel with the surface, after which it returns to the surface. Fig. 2 shows such a crack in process of growing. Notice that the crack is at an acute angle to the surface and does not necessarily extend into the softer core material. When the main crack, or any of its offshoots, returns to the surface a flake of material is completely separated from the tooth, leaving a shallow cavity or pit. Usually the pits occur on several teeth and increase in size and number with continued operation of the gears until the remaining tooth surface is unable to sustain the load.

Fig. 2 — Crack which led to pitting in carburized and hardened gear

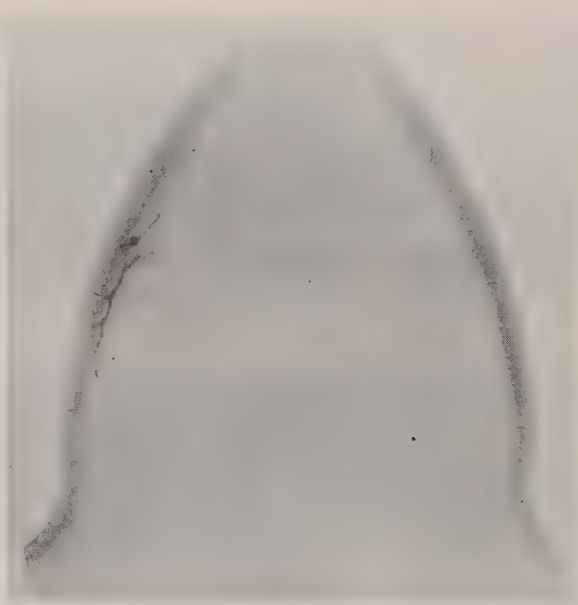

Fig. 3 — Crack which accompanied case crushing of carburized and hardened gear

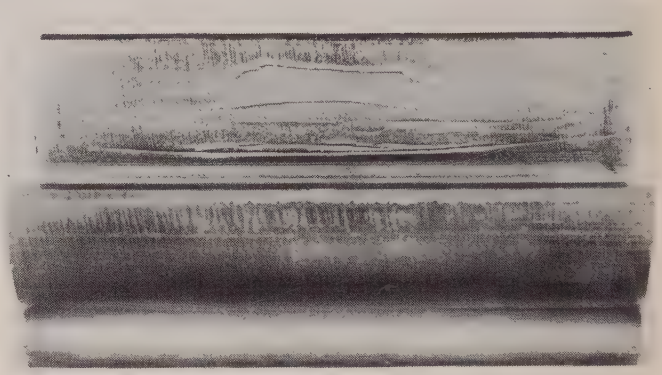

Fig. 4 — Case crushing cracks in final drive test pinion

Case Crushing - A different form of gear tooth failure which we call case crushing has been seen on a number of test gears. Fig. 3 shows a cross section of a gear tooth which failed by case crushing. Notice the marked difference in appearance of this crack from that in Fig. 2. The crack in Fig. 3 not only extends below the hard case, but most of its length is in the softer core material. Also, the offshoots which extend to the surface are perpendicular to the surface.

Fig. 4 shows the appearance of one tooth on a final drive

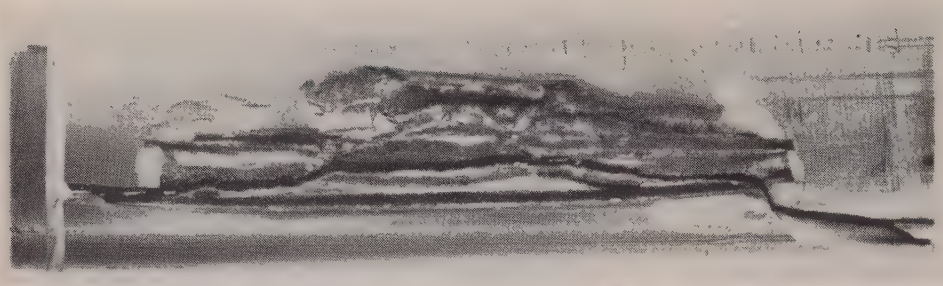

Fig. 5 — Appearance of pinion tooth from Fig. 4 after removing cracked case

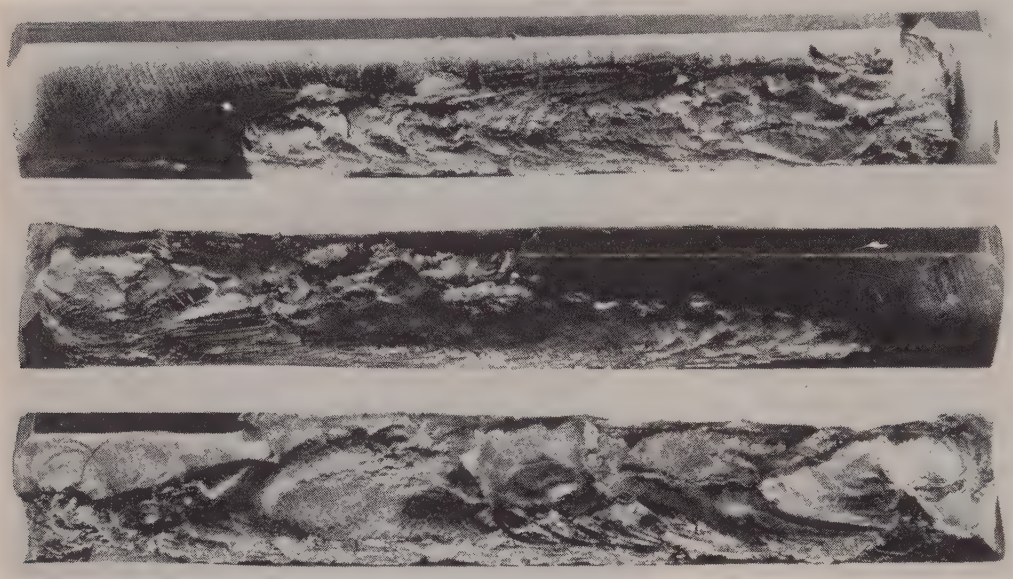

Fig. 6 — Case crushing failures from three final drive test pinions

pinion from one of our tractors used for development work. The case cracks extend across most of the tooth face width, but no pits are evident. Also, the cracks are not limited to the addendum or dedendum regions, but extend over most of the tooth profile. This is the only tooth on the pinion which showed cracks; none of the mating gear teeth were cracked. Visual evidence of case crushing commonly is seen on only one or two teeth while the remaining teeth are apparently sound. We have found, however, upon cross-sectioning apparently unmarred teeth, that some contained cracks leading to the surface.

Fig. 5 shows the exposed core material, of the same tooth illustrated in Fig. 4, after the tooth was broken off the pinion and the case fragments were removed.

Case crushing in its final stages is shown by the three examples in Fig. 6, all of which came from final drive test pinions. On the upper and middle teeth, cracks are visible in the portions of the profiles still remaining. In the region near these cracks, the walls of the cavity drop sharply from the tooth profile due to the cracks being perpendicular to the surface. On the middle and lower teeth, removal of the case proceeded so far that portions of the unloaded profiles were removed. On all three teeth the failed portion has the appearance of having been gouged longitudinally.

It is interesting to note that Merritt(3) has observed similar failures on case hardened or surface hardened gears. He calls the failure cracking or flaking and suggests a number of possible causes, among which are insufficient case depth and low core strength.

Another characteristic of case crushing failures is that visual evidence of the failure appears suddenly, often without any warning signs on the tooth surfaces, and sometimes after a long period of otherwise successful operation. Some test gears have run under constant load in our 4-square machines(4) for more than 20,000,000 load cycles, during which time, periodic inspection disclosed no unusual visible marks on the tooth surfaces. Yet within a few thousand additional cycles, one or more tooth profiles were completely destroyed. In one or two instances we have seen case crushing failures lead to gear tooth fractures through the crushed portion of the profiles.

The differences between pitting and case crushing failures are summarized by listing their chief characteristics in Table 1.

Case crushing and pitting fatigue are clearly two distinct types of failure, and early test results indicated a correla-

Table 1 - Summary of Differences Between Pitting and Case Crushing Failures

	Pitting	Case Crushing
Physical appearance	Shallow	Deep; ridged
Occurrence	Gradual	Sudden
General shape	V-shape	Longitudinal gouge
Distribution	Many teeth	One or two teeth
Direction of surface cracks	Acute angle to surface	Normal to surface

tion between the incidence of case crushing and thickness of the carburized case.

Theory of Case Crushing Failure

The investigation of case crushing failures led to a study of the shear stresses within a gear tooth. The maximum shear theory of failure is frequently used in the design of machine parts, but it is usually applied to ductile materials. We believe that case crushing failures are due, not to maximum shear, but are related to the ratio of shear stress to shear strength of the material at the subsurface level where the hardened case meets the softer core. This can be shown by describing first the manner in which the shear stress/shear strength ratio (hereafter called stress/strength ratio) is calculated, and then the results of applying the analysis to a number of test gears.

Calculation of the stress/strength ratio can, in turn, be subdivided into two parts:

1. Calculation of the subsurface shear stresses in a gear tooth.

2. Calculation of the subsurface shear strength of the material.

Calculation of Subsurface Shear Stresses - If two mating gear teeth are assumed to be equivalent to two mating cylinders having curvatures equal to those of the gear teeth at the line of contact, the subsurface stresses can be calculated by methods described by Radzimovsky(5) and based on the work of Thomas and Hoersch(6). When two cylinders are pressed together, the pressure distribution is as shown in Fig. 7. The principal stresses σ_x, σ_y, and σ_z at points in the XZ plane and at various depths below the surface can be plotted as in Fig. 8. To generalize the curves, the ordinates are in terms of b, half the width of the band of contact, and the abscissas are in terms of $p_{max.}$, the maximum contact pressure. The shear stress, τ_{45} deg, on a plane at 45 deg to the Y axis and parallel to the Z axis, is computed from the relation

$$\tau_{45 \text{ deg}} = \frac{\sigma_x - \sigma_y}{2}$$

The values of τ_{45} deg (for points beneath the surface and in the XZ plane) have also been plotted in Fig. 8, where it is seen that τ_{45} deg reaches a maximum value at a depth approximately 0.78b below the surface. The value of τ_{45} deg at this point is frequently used in applying the maximum shear theory to analyses of pitting failures.

In case hardened parts there are also residual stresses, resulting from heat treatment, that affect the stress picture. As an example of their magnitude, the residual stresses in the tangential and longitudinal directions (Y and Z directions, respectively, in Fig. 7) in a 1-3/4 in. diameter car-

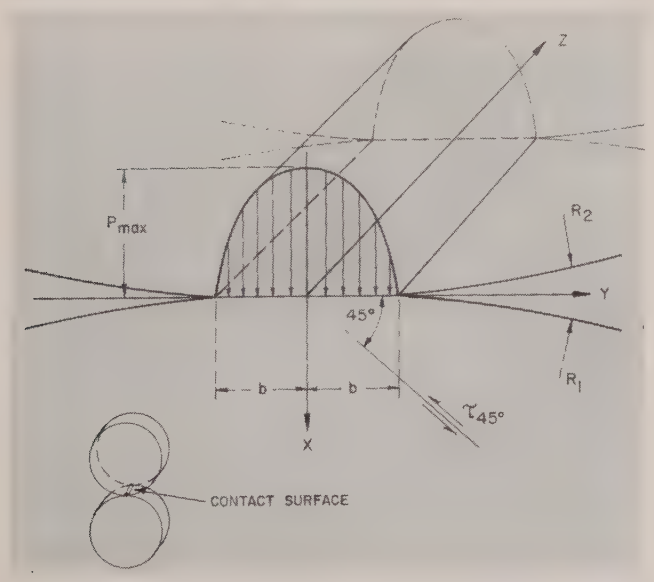

Fig. 7 — Pressure distribution on contact surface of two cylinders

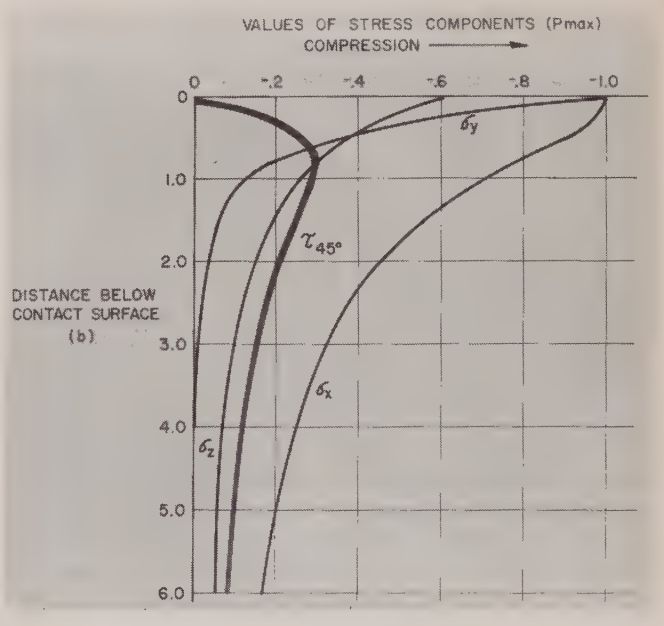

Fig. 8 — Distribution of stresses in cylinder due to normal load

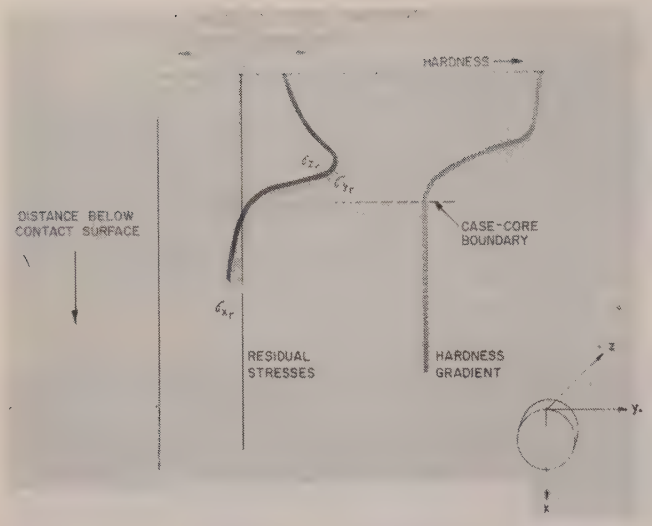

Fig. 9 — Typical residual stress components and hardness gradient for carburized and hardened cylindrical bar

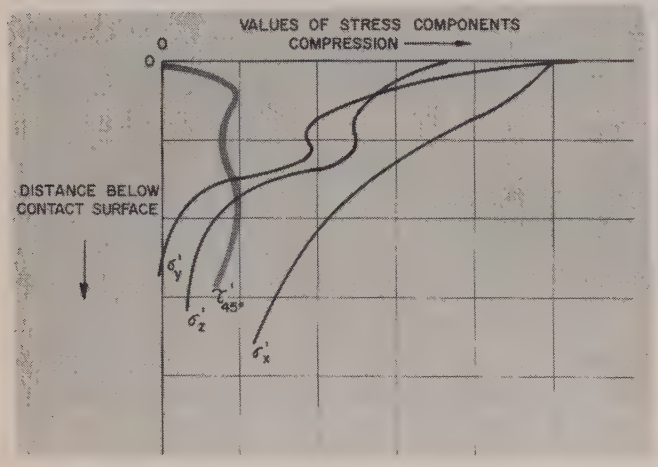

Fig. 10 — Typical stresses due to normal load and residual stresses

burized and hardened steel bar have been found to be nearly 30,000 psi in compression at the surface, and to reach a maximum of almost 60,000 psi in compression within the hardened case. When the residual stresses σ_{xr}, σ_{yr}, and σ_{zr}, in the X, Y, and Z directions, respectively, for a carburized and hardened cylindrical bar are plotted on axes similar to those in Fig. 8, the general shapes of the resulting curves are as shown in Fig. 9. The hardness gradient curve for such a bar is also shown in the figure, but is plotted with hardnesses as abscissas and depths as ordinates instead of in the usual manner. Actual values of the residual stress components can be obtained from work done by the SAE Iron and Steel Technical Committee, Division IV(7).

When the principal stresses σ_x, σ_y, and σ_z (Fig. 8) produced by pressing the two cylinders together, are added to the residual stresses σ_{xr}, σ_{yr}, and σ_{zr} (Fig. 9) in a cylinder, the resulting principal stresses, when plotted, will be similar to the curves in Fig. 10. The shear stress, τ_{45} deg, is also plotted in Fig. 10. It is evident that when the residual stresses as well as the stresses produced by the normal load are considered, the τ'_{45} deg shear stress curve has two mathematical maximum points. This shear stress curve will be used in computing the stress/strength ratio after some consideration of the method of calculating the shear strength of the gear tooth.

Calculation of Subsurface Shear Strength - The shear strength of the material can be estimated by cross sectioning the gear tooth first and obtaining a hardness gradient curve, similar to the one in Fig. 9, in the region of the line of contact. Several publications (8,9,10) provide conversions from hardness to average tensile yield strength, based on the assumption that 90% or more of the material is martensite. With the additional assumption that tensile yield strength is proportional to yield strength in shear, a curve such as that in Fig. 11, for converting hardness to average shear yield strength, can be drawn. The hardness gradient curve can then be converted to a shear yield strength curve, shown in Fig. 12. In this figure the shear yield strengths are plotted as abscissas and depths below the surface as ordinates to facilitate comparison with the shear stress curve plotted similarly.

Calculation of Stress/Strength Ratio - When a shear stress curve (τ'_{45} deg) as in Fig. 10 and a shear strength curve as in Fig. 12 are plotted to the same coordinate axes, the result is similar to Fig. 13. Although these are generalized curves, their individual shapes as well as their relationship to each other are typical for carburized and hardened gears. Fig. 13 shows that the shear stress is very near a maximum value at a depth where the hardened case meets the softer core material (the "knee" of the shear yield strength curve). In the same region, the shear stress is greater in proportion to the shear strength than at any other depth. This is illus-

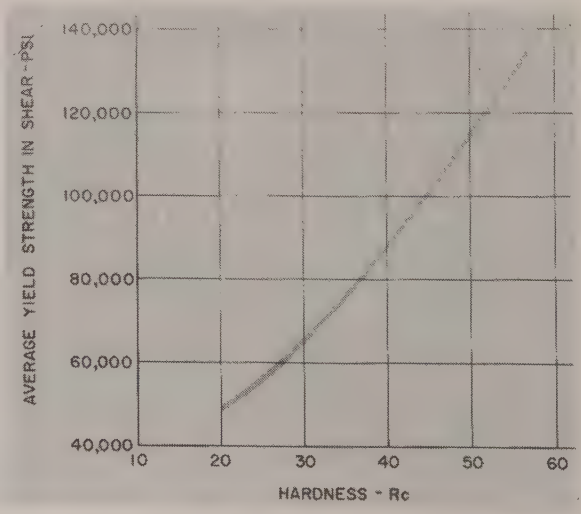

Fig. 11 — Curve for converting hardness to average yield strength in shear

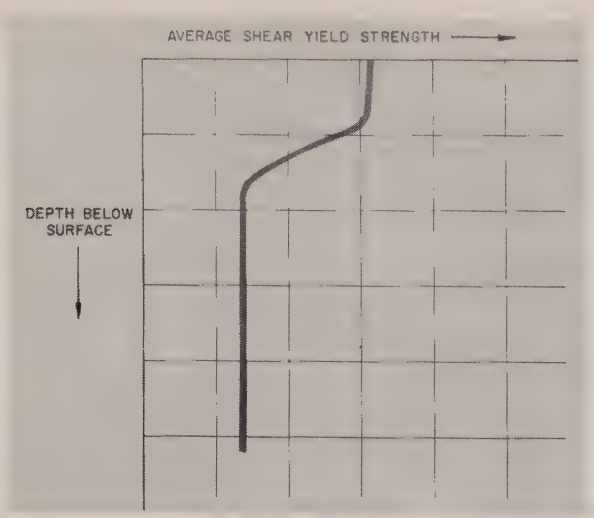

Fig. 12 — Typical shear yield strength curve for carburized and hardened gear

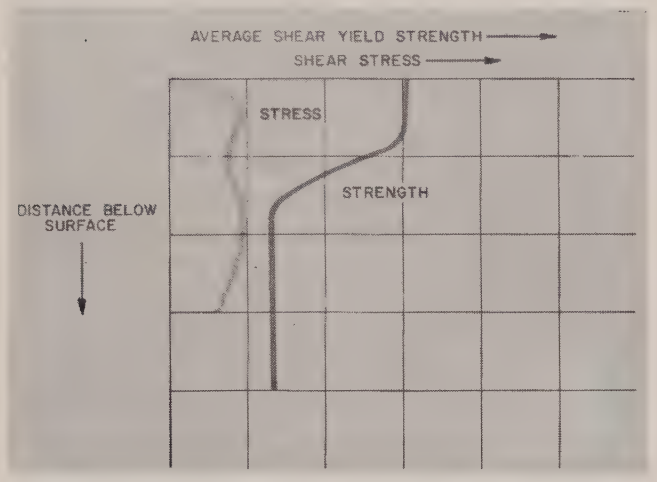

Fig. 13 — Subsurface shear stress compared to shear yield strength of carburized and hardened gear

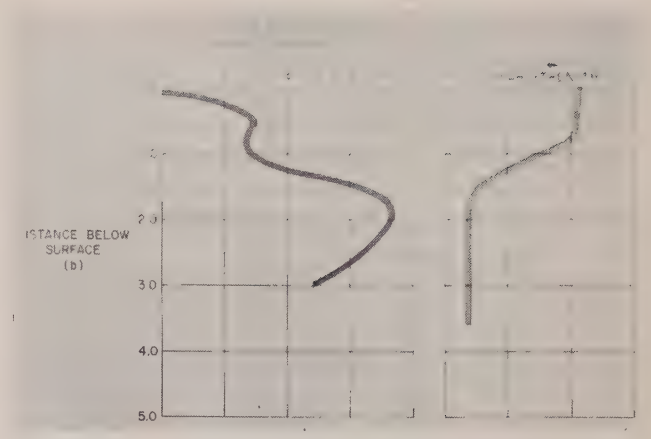

Fig. 14 — Variation of stress/strength ratio with depth

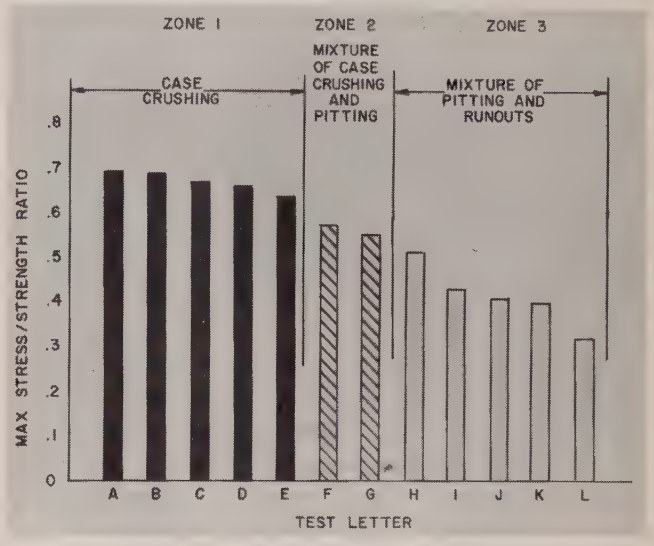

Fig. 15 — Experimental results

trated in Fig. 14 where the ratio of shear stress to shear strength is plotted against depth below the surface. The shear strength curve from Fig. 13 is repeated here for comparison.

At about the depth where case and core meet, the stress/strength ratio reaches a maximum value but the compressive residual stresses are small enough to be negligible. By comparing the two curves in Fig. 9, it is seen that the residual stresses are in fact very small at the case-core boundary (at the depth indicated by the broken line). Koistinen (11) has also observed this characteristic of residual stresses in carburized cases: "The reversal in the sign of the residual stress from compression in the case to tension in the core occurs at or very near the case-core boundary." Therefore, at the depth of the case-core boundary the shear stresses produced by the load are not affected by any residual stresses. The maximum value of the stress/strength ratio for a particular gear can then be obtained simply by computing the shear strength and τ_{45} deg due to load, both in the region where case and core meet.

Some Experimental Results

Assuming there is a critical value for the stress/strength ratio above which case crushing occurs, the above analysis was applied to a number of test gears. These include experimental final drive and bevel gears tested in our tractors as well as transmission type gears tested in the 4-square machines. All of the gears were made from SAE 8600 series or 8700 series steel and were carburized and hardened. Diametral pitches ranged from 2 to 3.

Of the gears examined, some had failed by case crushing, others had failed by pitting, and some (runouts) showed no signs of failure. The maximum stress/strength ratios, which

varied from 0.30 - 0.70, have been plotted in Fig. 15 where they have been arranged in descending order from left to right. Letter designations have been used on the horizontal axis for identification purposes only. Each letter represents the result of a single test except that test C represents 3 case crushing failures and test D represents 4 such failures. These were condensed in Fig. 15 since the gear geometries, case depths, and loads were similar.

The results fall into three categories or zones:

1. Zone 1 in which case crushing is unmistakable and where the maximum stress/strength value is above 0.60.

2. Zone 2 in which it is more difficult to decide from a visual inspection whether the failure is case crushing or an advanced stage in pitting fatigue.

3. Zone 3 in which pitting occurred on some of the gears and the remainder did not fail at all.

The zone boundaries shown in Fig. 15 are only approximate and can be defined more exactly on a statistical basis when more test results are available.

At this time we feel that the maximum stress/strength ratio should be no more than 0.55 in order to prevent case crushing. It must be emphasized that this critical value applies only to the type of failure here described as case crushing and does not pertain to pitting fatigue since, as Fig. 15 illustrates, pitting can occur when the maximum stress/strength ratio is less than 0.55.

If the above method of analysis, when applied to a particular gear set, leads to the conclusion that case crushing failure will result, one of the available remedies is to increase the strength of the material in the case-core boundary. This can be done by increasing case depth, increasing core hardness, or a combination of both. Thus it is seen that, when resistance to case crushing is considered, case depth is not necessarily related to tooth thickness, but is more strongly influenced by the radii of curvature at the point of contact, the load, and the core hardness of the material.

Throughout this analysis we have concentrated on its application to carburized and hardened gears. However, we feel the method should be applicable as well to other case hardened gears such as those which are nitrided or carbo-nitrided. A recent failure in case crushing (not included in Fig. 15) on a nitrided 12-pitch test gear in which the stress/strength ratio was 0.58 helps to confirm this opinion.

Summary

The primary object of this investigation was to produce a more rational approach to the selection of case thickness of carburized and hardened gears than is evident in present standards. This paper shows the need, and provides a method, for a more reasonable selection of case depth. This method is useful not only as a design tool but is an aid in determining the cause of failure on gear tooth profiles. Equally important, we feel, is the separation of a distinct type of failure, case crushing, from the large number of gear tooth profile failures usually simply called pitting fatigue. By thus narrowing the field, the continuing investigation of pitting fatigue can be pursued more directly and, we hope, more fruitfully in the future.

References

1. "Standards," American Gear Manufacturers Association, AGMA 241.01.

2. Darle W. Dudley, "Practical Gear Design." New York: McGraw-Hill Book Co., 1954. First Edition, 165.

3. H. E. Merritt, "Gears." London: Isaac Pitman & Sons, 1954. Third Edition, 314.

4. R. P. Van Zandt and B. W. Kelley, "Gear Testing Methods for the Development of Heavy Duty Gearing." SAE Quarterly Transactions, Vol. 3, 1949.

5. E. I. Radzimovsky, "Stress Distribution and Strength Condition of Two Rolling Cylinders Pressed Together," Univ. of Illinois Eng. Expt. Sta. Bull. 408, Feb. 1953.

6. H. R. Thomas and V. A. Hoersch, "Stresses Due to the Pressure of One Elastic Solid Upon Another," Univ. of Ill. Eng. Exp. Sta. Bull. No. 212, 1930.

7. "Residual Stress Distribution on Standard Specimens," SAE Div. IV ISTC, June, 1955.

8. "Heat Treating Republic Alloy Steels," Republic Steel Corp., 1949.

9. "Metals Handbook," American Society for Metals, 1939 Edition.

10. "SAE Handbook," Society of Automotive Engineers, New York, 1960.

11. D. P. Koistinen, "Distribution of Residual Stresses in Carburized Cases, and Their Origin," Transactions of American Society for Metals, 1958, Vol. 50.

Case Crushing as opposed to Pitting

H. E. Merritt
Consulting Engineer

THIS IS AN interesting and valuable paper on a somewhat neglected aspect of gear failure. One must agree with the author's contention that the basing of case depth on tooth thickness is unsound, but is it not true to say that it is more commonly based on the diametral pitch? This avoids the anomaly represented by Fig. 1, because the use of long and short addendum makes little difference to tooth thickness at the mean depth.

The authors make a good case for the theory that case crushing is a form of fatigue failure in shear. What might be underlined is the basic difference between this form of fatigue failure, and the fatigue failure called pitting. The

latter, usually begins as a tensile fatigue failure at the surface under the influence not only of the tensile component of the static Hertzian stress system, but also of the tangential stress due to friction and the thermal stresses(1). Pitting failures give a log-S/log-N plot exactly comparable to that in bending fatigue; but it would appear that there are not yet enough data to permit case-crushing fatigue to be so plotted.

It is suggested that a case-crushing failure may be triggered by a surface crack,and developed by the stresses which would ultimately cause pitting. Such a crack would change the stress-distribution below the surface in a rather radical way. In the writer's experience, case-cracking is a quite rare phenomenon, and would not normally be expected in teeth having case depths of the order shown in the illustrations in the paper, at least as regards Fig. 2. The case-depth in Fig. 3 seems rather shallow for a heavily loaded pinion.

The authros presage rather than amplify a specific method of arriving at the desirable case depth. The starting point is a criterion of contact stress. In British practice, the criterion introduced by the writer some 30 years ago is the "surface stress criterion S_c" which represents the load per inch of line of contact per inch of relative radius of curvature. In association with "zone factors"charted for the range of tooth-number combinations, the quantity S_c is an explicit and known item in calculation.

The width of the band of contact w (= 2b) is then given by:

$$w = 3.05\, F_c \sqrt[m]{S_c \cdot E} \qquad (A)$$

where:

F_c = load per inch of line of contact
E = modulus of elasticity of the (similar) gear materials

The case depth would then be made equal to K. w where K could be derived, for any material, by the kind of analysis given in the paper. The general result is that the case depth, for a given pitch, will increase as the harmonic mean of the numbers of teeth in the mating gears.

A point that should be made in connection with the pitting of case hardened gears (and it may have some connection with case crushing as well) is the vulnerability of the teeth along the pitch line (the intersection of the pitch cylinder with the tooth surface). As the band of contact passes across the pitch line, the surfaces still in contact reverse their direction of relative sliding. This can lead to a form of surface failure which the writer calls "pitch-line fissure" and is quite different in appearance from ordinary pitting; it can occur quite early, whilst regular pitting of addenda and dedenda does not occur.

One might also refer to the question of how case depth is to be specified, since the values derived from the appearance of a fracture, etching, and microhardness testing are all different.

Reference

1. B. W. Kelley, "The Importance of Surface Temperature to Surface Damage," in "Engineering Approach to Surface Damage". Univ. of Michigan Press, 1958.

Stress-Strength Relationships and Case Depth Determination

J. D. Graham
International Harvester Co.

SEVERAL contributions have been made to gear technology in this paper.

1. The definition and clearly detailed description of a badly confused type of gear failure is timely regardless of the name used to describe it.

2. The extreme importance of an understanding of stress-strength relationships where gradient stresses exist is accented and an approach to the problem outlined.

3. Perhaps most welcome, another nail is driven into the coffin for the idea of case depth based on chordal thickness of the gear tooth.

Case Crushing, or Spalling - The failure described by the authors as case crushing has been called by several names over the years. In this paper it is carefully and clearly described and I am thoroughly in agreement with the details of this description. Many engineers have chosen to call this failure "spalling" and it is so designated by the American Gear Manufacturers Association, even though the definition is somewhat vague. This paper should lead to a clear understanding of this type of failure as contrasted with other types of surface damage, and perhaps to a universal adoption of a properly descriptive name.

That this is a clearly different phenomenon than pitting is well brought out. To emphasize the distinctive nature of spalling, attached are three photographs of hypoid pinions, tested under very heavy load. Fig. A shows the presence of a crack in the center of the tip of the tooth. In this type of pinion such a crack usually precedes spalling. This tip crack is apparently confined to hypoid pinions - it is undoubtedly related to the unique progression of a small contact area towards the tip of the pinion accompanied by heavy sliding friction. The origin of this crack is still a matter of discussion. It is possible that subsurface failure of the type shown in Fig. 3 may progress to the tip of the tooth for its first exit to the surface, and we have evidence that this is sometimes the case. We have also considered the possibility that this crack is formed by progression of plastic flow in the area of maximum stress-strength ratio to the tip of the tooth, some-

Fig. A — Hypoid pinion — crack in center of tip of tooth

Fig. B — Hypoid pinion — appearance of cracks on tooth face

Fig. C — Hypoid pinion — more advanced case of spalling

what the way a toothpaste tube may split at the bottom if squeezed too hard.

Fig. B shows the appearance of cracks on the tooth face, very similar to those shown by the authors in spur gears, Fig. 4.

Fig. C illustrates a more advanced case of spalling. The tip crack can still be seen, as can the typical cracks in the tooth face, and the longitudinal gouged appearance.

Stress-Strength Relationships - The attempt to understand the performance of critical parts such as gears by relating stress and strength gradients is well remembered from Woodvine's work of the early twenties - in fact charts such as the authors' Fig. 13 are often called Woodvine diagrams. However, little use has been made of them in the literature, and the present paper demonstrates a graphic new approach in the use of a stress-strength ratio curve. The obstacles to this technique (as in many areas of engineering), are primarily our ignorance of real values, and the necessity to make assumptions that are often rather vague concerning residual and applied stresses. The results, however, are demonstrably more reliable than the alternatives of guesswork and tradition.

In considering failure of the hypoid test pinions discussed above, this approach was attempted but was handicapped by the extreme complexity of applied stresses in hypoid gears

and inability to calculate these stresses on a specific basis. Fig. D shows the shear strength distribution near the surface of two pinion teeth at the pitch line. When run at severe overload, pinion A failed by bending fatigue at the root of the tooth with no sign of spalling, while pinion B developed the typical subsurface failure previously shown. The conventional shear stress distribution is shown, and while the maximum shear stress reached in this test cannot be properly determined, it is obvious that the principles brought out by Mr. Pedersen and Mr. Rice are demonstrated here.

To further illustrate this point, Fig. E shows a number of test pinions all run at the same severe overload. It can be seen that the strength at a depth of 0.100 in. below the pitch line is directly related to the occurrence of spalling.

Case Depth Determination - For years metallurgists have attempted to discourage the practice of fixing case depth requirements on the thickness of a gear tooth, but have often been brought back to this practice by lack of some sound theoretical approach. This paper makes an important contribution to our growing knowledge in this manner. Two points need to be accented, however.

1. The determination of stresses in a gear may be a complex problem, depending upon the gear design and application, and considerable difference of opinion exists in determining applicable strength factors from a hardness traverse.

In applying the approach described in this paper to very similar gears using the exact methods of calculation used by the authors, advantage can be taken of their experimental work. In all other cases the critical stress-strength ratio should be determined experimentally, since this figure is relative and not specific.

2. Considering only the relationship shown in Fig. 13 it would appear that case depth is relatively unimportant and core hardness alone needs to be controlled. As pointed out by the authors, this is not the case. I feel sure that this apparent contradiction arises from the fact that the maximum stress-strength ratio is not always located at the case-core junction.

These factors accent the need for more information relating theoretical evaluation of gears with their performance, and the authors have made a lasting contribution to this information.

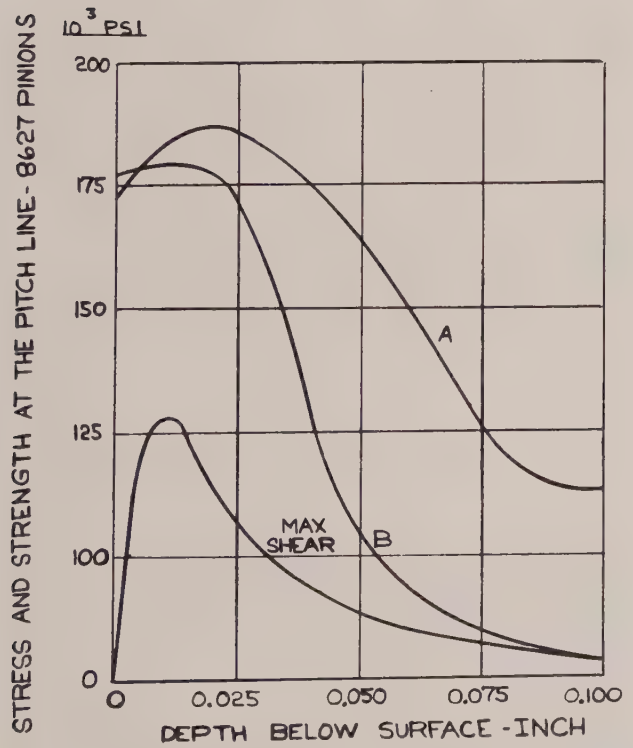

Fig. D — Shear strength distribution near surface of two pinion teeth at pitch line

Author's Closure to Discussion

We wish to thank Dr. Merritt and Mr. Graham for their formal discussions of the paper, as well as others who have personally expressed interest in the subject matter.

As Dr. Merritt implies, we do not have enough data to attempt to plot case-crushing failures on a log S/log N chart. Since these failures depend not only on the applied stress but also on the state of the residual stresses (which are in turn the result of case depth), it may prove more profitable to plot some function of the maximum stress/strength ratio against number of load cycles, when more test results are available. The case depth in Fig. 3 was deliberately made shallow, since the test gears had a case depth range of 0.5-2.2 mm.

Mr. Graham has drawn attention to the assumptions which were made in determining the average shear yield strength from a hardness traverse. The conversion curve of Fig. 11 is based on the assumption that yield strength in shear is half the yield strength in tension. As Mr. Graham points out our particular assumptions influenced the value (0.55) which we determined experimentally to be critical for the maximum stress/strength ratio. Different assumptions would lead to a somewhat different critical value.

In reference to Mr. Graham's second comment ragarding Fig. 13, we believe the apparent contradiction can be clarified by illustrating the state of subsurface stresses for a "normal" case depth and for a reduced case depth under the same externally applied load.

Fig. F diagrams the shear stress curve (τ_{45} deg) due to load, the strength curve. and the matching residual stresses. Fig. G is similar to Fig. 13. These two figures merely illustrate the stress and strength conditions for a given load and hardness gradient.

If the case depth is now halved but core hardness is unaltered (as in Fig. H), the strength gradient curve and the

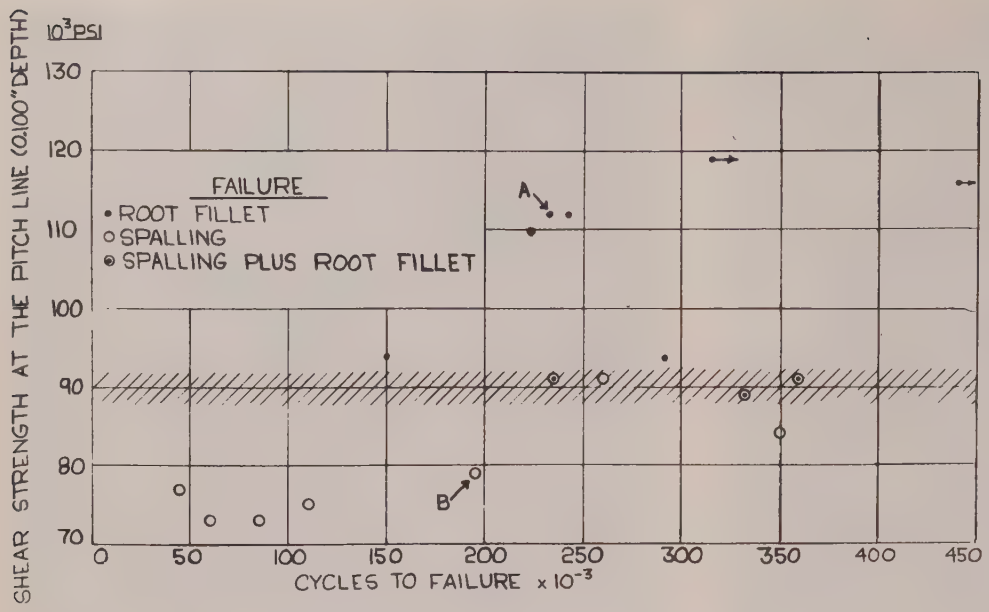

Fig. E — Number of test pinions run at same severe overload

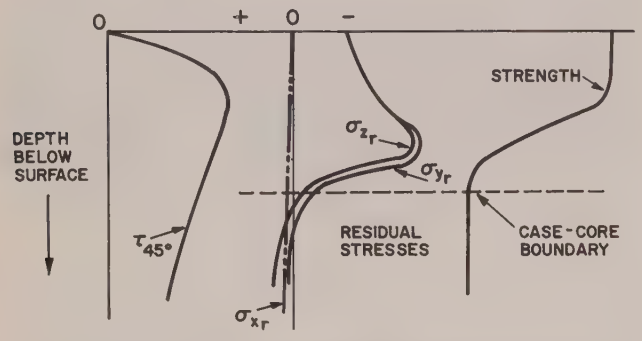

Fig. F — Shear stress curve (T45 deg) due to load, strength curve, and matching residual stresses

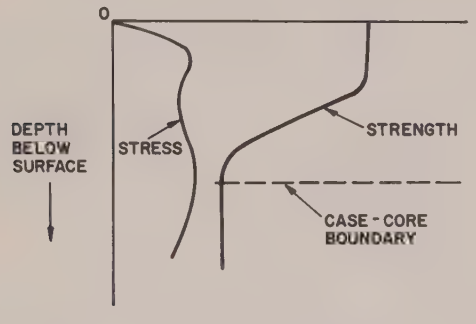

Fig. G — Stress and strength conditions for given load and hardness gradient

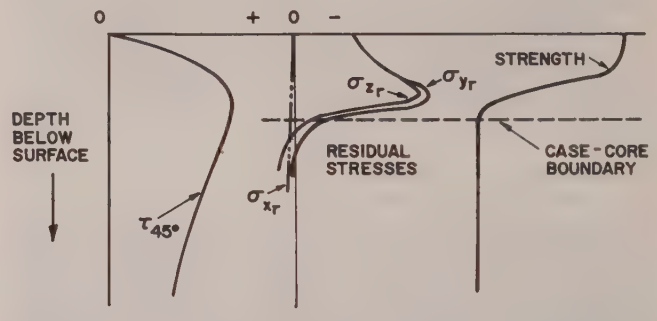

Fig. H — Case depth halved but core hardness is unaltered

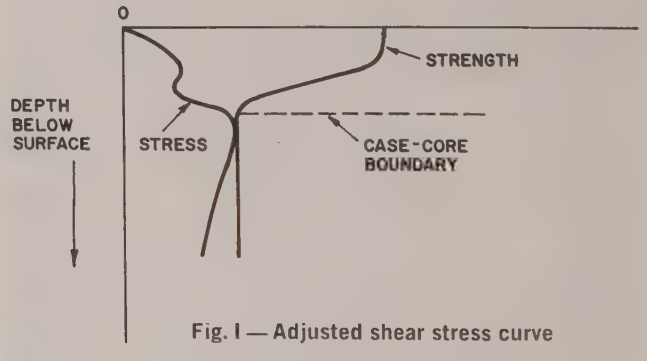

Fig. I — Adjusted shear stress curve

residual stresses change - although we are assuming the stress value at the surface as well as the maximum value will be approximately the same as for the original case depth. The applied shear stresses (τ_{45} deg) do not change since the load is unchanged.

The new residual stress curves bring about an adjusted shear stress curve like that in Fig. I. Here the second "maximum point" on the stress curve is again near the nose of the strength curve and close to the case-core boundary. Also, the maximum stress/strength ratio is higher than it was for the thicker case.

Thus, we feel control of case depth is as important as control of core hardness. But a change in case depth affects not only the strength curve but also the adjusted shear stress curve.

Handling Requirements

O. J. Winkelmann
Chrysler Corp.

THE FIRST requirement in a paper intended to discuss automobile handling is to define the term "handling," itself. A simple way to approach this is to say that whereas "ride" has to do primarily with the carrying of vertical loads and the isolation of road-originated dynamic forces from the passengers, "handling" has to do with the lateral support given the car by the tires and suspension system.

More specifically, it can be described as the car's behavior when it is steered into a path, and its ability to stay on that path. If a car can be controlled with ease, if it has good inherent directional stability, and if it can be driven safely for hours on available roads and at accepted speeds with no undue strain on the driver, we can say that this car handles well.

There are two parts of the handling problem to be considered: the car or machine and the driver. This car-driver combination or control system includes objective and subjective qualities. This discussion will deal primarily with the objective part, the car.

We will assume that the ability and general requirements of the driver as a part of the control system are well enough known by the automobile engineer to enable him to include properly the subjective part of the handling problem in his considerations.

It should be stressed, however, that considerable research work is desirable to understand better the car-driver control system.

This leaves us with control and stability of the machine, or lateral response in the three degrees of lateral freedom: yaw, roll, and side-slip.

The problem can be analyzed by breaking it down into its essential properties. First of all, there is a relatively firm and constant support for the car -- the four footprint areas of the tires. All forces acting on the car are reacted at these four spots. For good handling the results of the forces acting at these spots must be predictable and consistent under the ever-changing conditions to which the car is exposed. Considering that these conditions include such widely varying circumstances as straight-ahead driving, cornering, accelerating, braking, fighting side winds, pitching, bouncing, yawing, and rolling, all on a wide variety of road surfaces and shapes, we can appreciate the complications encountered in making a vehicle that does indeed handle well.

With this in mind, it can be said that an automobile must satisfy the following five requirements:

(1) Cornering ability

Briefly, this means that the car must be capable of withstanding a maximum amount of lateral acceleration per degree of tire slip angle.

(2) Directional stability

The car must have steering characteristics built in which make it directionally stable. It is not sufficient that the steering tendency merely be neutral.

(3) Wind stability

The car must not wander in gusty side winds.

(4) Response

Proper response to the driver's commands is essential for good control.

(5) Feed back

The car must somehow indicate to the driver what the moment-to-moment conditions are at the tire footprint areas.

All of the above requirements are dependent only upon the mechanism of the automobile. They are valid whether or not the driver is anywhere near the car and as such can be evaluated for the steady state and transient conditions.

The handling characteristics of a car can be tailored by taking advantage of tires, weight distribution, suspension geometry, suspension deflection, roll stiffness distribution, and location of the center of aerodynamic pressure. In so doing, of course, the engineer must know the type, the magnitude, and the direction of the forces and moments likely to be introduced either by the driver through the use of the steering wheel, or from the outside by wind and road disturbances.

Dynamic Attitude Control

Before going further with a detailed discussion of the five main handling requirements, it is necessary to consider another area of typical high-powered American cars with low wheel rates which can restrict us in selecting the geometry of the front and rear suspensions required for best handling. This is dynamic attitude control, or the reduction of pitching, which must be provided for in order to maintain a flat ride during acceleration and braking.

Pitch is introduced to the car not only by road irregularities but also by dynamic load transfer under acceleration and braking. It can be controlled -- but not entirely eliminated -- by careful attention to the geometry of the front and rear suspension systems.

Let us examine some of the choices open to the designer in working to restrict pitching. Fig. 1 is a simplified free body diagram of a conventional rear-drive car with unsprung differential and brakes. The acceleration inertia force $W/g \cdot a$ acts at the center of gravity and at the rear wheels. The dynamic load transfer from the front to the rear is represented by the formula $W/g \cdot a \cdot h/I$. If the kinematic instant center of the rear suspension is located anywhere along the line of action of the resultant R of these forces, no displacement of the rear springs will occur under acceleration. This is because the resultant force has no moment arm with which to apply a torque about the instant center.

However, since there is no fore-and-aft force on the front suspension, nothing similar with its geometry can be done to prevent the front end of the car from rising under acceleration, except to decrease it somewhat by using a high front wheel rate in rebound. To reduce or even eliminate pitching, however, we can select an instant center location for our rear suspension above the neutral line so that the rear of the car rises with the front.

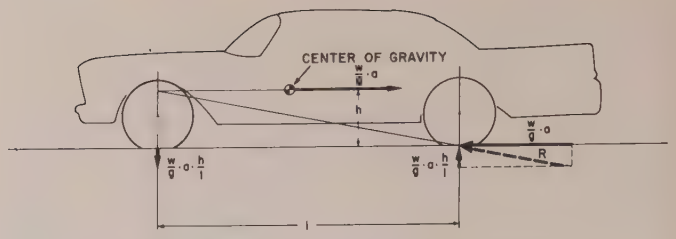

Fig. 1—Dynamic forces on the car during acceleration

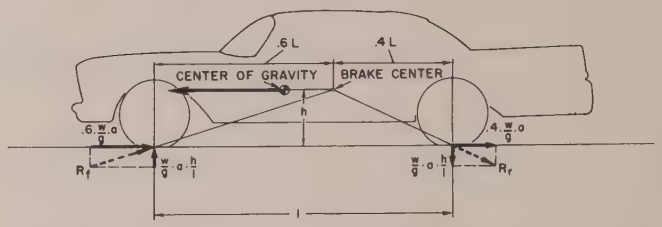

Fig. 2—Dynamic forces on the car during braking. Brake torque distribution 60% front, 40% rear

Fig. 2 shows the same car when braking, with a brake torque distribution of 60% front and 40% rear. Again, if the instant centers of the front and rear suspensions are located along the lines of action of the two resultants R_f and R_r, the car will stay at its normal static height under braking.

Fig. 3 shows the car with the neutral, or zero deflection, lines for both braking and acceleration. As was noted earlier, it is permissible to deviate from the neutral line, depending upon the design objective. For practical purposes, the instant center may be located anywhere within the area of a sector on both sides of the neutral line. These sectors, or areas of freedom, are shown in the illustration. In general, the dark areas are considered desirable, and the lighter areas questionable.

Obviously, in all cases a compromise must be made between the car's attitude under acceleration and under braking. We must also keep in mind the limitations imposed by the need to avoid harshness and change of wheel caster.

Appendix I gives a sample calculation of car attitude control considerations which may help the understanding of these relationships.

Fig. 4 illustrates the conditions for a car with sprung differential and sprung rear brakes. Note that the instant center of the rear suspension has to be located quite high. Since this can interfere with other car design features, the designer must accept more of a compromise in dynamic attitude with this type of rear end design.

Fig. 5 shows the requirements for a high-powered car with front and rear springs interconnected. Because of the ex-

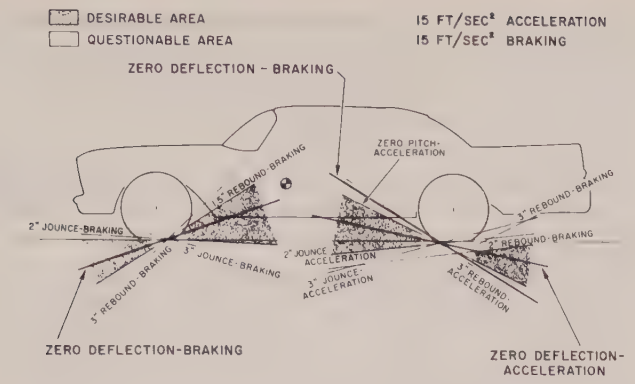

Fig. 3—Instant center location for attitude control with a live rear axle and unsprung brakes front and rear

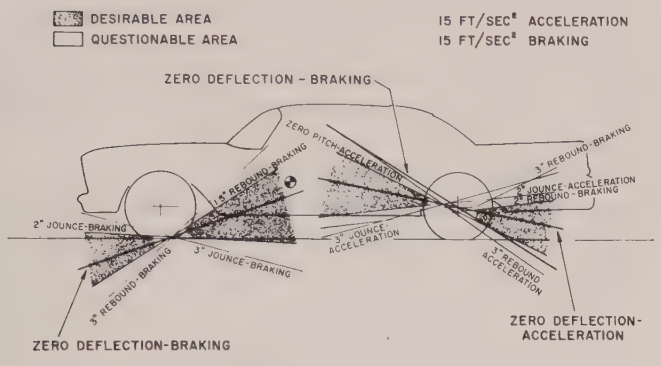

Fig. 4—Instant center location for attitude control with a rear sprung differential, sprung rear brakes, and unsprung front brakes

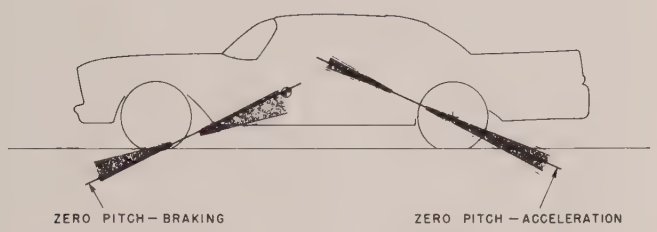

Fig. 5—Instant center location for attitude control with interconnected springs, sprung differential, sprung rear brakes and unsprung front brakes

tremely low pitch rate of such a design, the possible locations for the instant centers are very restricted.

These limitations on front and rear suspension geometry complicate the handling problem because they can affect the selection of roll steer, roll axis location, and the physical location of suspension pivot points. In addition it is important to take care that in controlling attitude, excessive tire scuff, brake hop, or power hop are not built into the car.

With this background behind us, we can now redirect our attention to the subject of handling requirements. As noted earlier, five requirements must be satisfied if the car is to handle well:

1. Cornering ability.
2. Directional stability.
3. Wind stability.
4. Response.
5. Feedback.

Cornering Ability

Ultimate cornering ability is an important criterion of the handling properties of a car. In the absence of complete tire data at high slip angles, the best measure of cornering ability seems to be the lateral acceleration per degree of slip angle. To eliminate the weight factor and simplify comparisons it is convenient to use the cornering coefficient, which is cornering power per unit vertical load - lb/(deg x lb). Thus, we try to develop a car concept which allows the tires to develop the maximum cornering power, or force per degree slip angle, of which they are capable.

Theoretically, the best that can be done in this respect would be achieved -- to take the simplest example -- with a vehicle having its center of gravity located at the ground, equal weight distribution, roll axis along the ground, a tire camber angle of zero degrees, no power applied to the driving wheels, and equal tire sizes and pressures.

Although most American cars do specify equal tire sizes and pressures, the other characteristics of the ideal vehicle are somewhat more difficult to attain.

The center of gravity is, of course, unavoidably located somewhere above ground level. Because of this, dynamic load transfer to the outer wheels takes place during cornering, resulting in a loss of total cornering force of the four wheels at a given slip angle. This is due to the well-known fact that the curve of lateral force versus vertical load for a typical tire is not linear, but convex.

This can be seen in Fig. 6, in which the tire is assumed to be operating at a slip angle of 12 deg. With an equal vertical loading of 1000 lb per tire, the total cornering force generated is 3100 lb Now, assuming a weight transfer of 48% to the outside tires, which amounts to 480 lb per tire at 0.6g lateral acceleration, we see that the total cornering force has dropped to 2630 lb, or a net loss of 470 lb cornering force for the car. This same loss of cornering force would also apply in the event of dynamic load transfer under braking and acceleration.

Other sources of reduced cornering forces associated with the center of gravity are the jacking effect of certain independent rear suspensions, unequal front and rear roll stiffness, and the nonhorizontal roll axis inherent in most automobiles. The latter two are involved in the steering characteristics of the car and will be mentioned again later.

Unequal weight distribution caused by static loading adversely affects cornering force in the same manner as does dynamic weight transfer.

Since drive thrust must use a goodly portion of the tire's potential reacting force, it subtracts considerably from the cornering force of the driving wheels, be they front or rear.

The unfavorable camber of front and rear independent suspensions also detracts from cornering force. As a matter of fact, the ideal car ought to give us more than zero camber. It should be designed so that no matter which way it is turning, the outside wheels have negative camber and the inside wheels positive.

Fig. 7 shows the cumulative detrimental effect on lateral support at 12 deg maximum tire slip angle caused by these deviations from our ideal symmetrical vehicle.

The first bar represents the symmetrical car with even weight distribution, center of gravity at the ground, and no power applied to the wheels. This vehicle can withstand 0.78g lateral acceleration at a 12 deg slip angle.

Introducing a reasonable center of gravity height, as in Bar II, the permissible lateral acceleration drops to 0.63g.

In Bar III, the incorporation of an independent front suspension, with its associated camber variation, brings it down to 0.57g.

Changing now to a 55-45 weight distribution, and installing a front sway bar, leaves 0.55g lateral acceleration at 12 deg maximum slip angle, as shown by Bar IV.

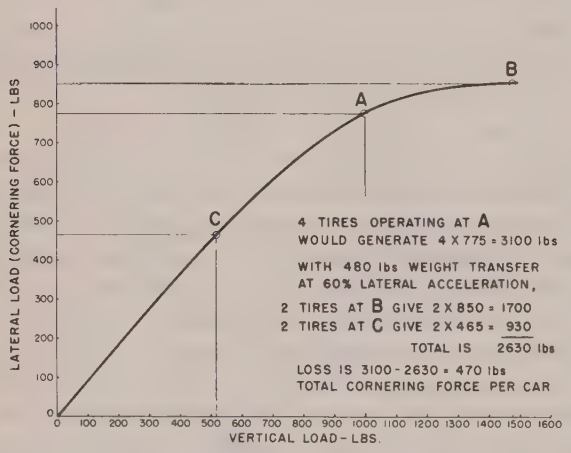
LATERAL LOAD (CORNERING FORCE) - LBS
VERTICAL LOAD - LBS.
A
B
C
4 TIRES OPERATING AT A
WOULD GENERATE 4 X 775 = 3100 lbs
WITH 480 lbs WEIGHT TRANSFER
AT 60% LATERAL ACCELERATION,
2 TIRES AT B GIVE 2 X 850 = 1700
2 TIRES AT C GIVE 2 X 465 = 930
TOTAL IS 2630 lbs
LOSS IS 3100 - 2630 = 470 lbs
TOTAL CORNERING FORCE PER CAR

Fig. 6 — Lateral force versus vertical load. Typical tire operating at 12 deg slip angle

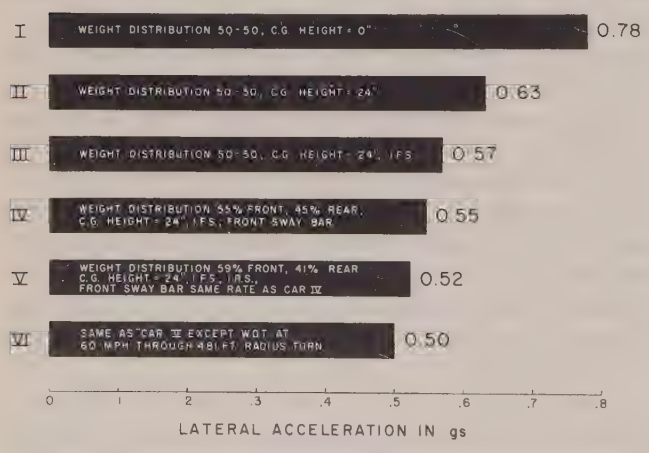
I WEIGHT DISTRIBUTION 50-50, C.G. HEIGHT = 0" 0.78
II WEIGHT DISTRIBUTION 50-50, C.G. HEIGHT = 24" 0.63
III WEIGHT DISTRIBUTION 50-50, C.G. HEIGHT = 24", I.F.S. 0.57
IV WEIGHT DISTRIBUTION 55% FRONT, 45% REAR, C.G. HEIGHT = 24", I.F.S., FRONT SWAY BAR 0.55
V WEIGHT DISTRIBUTION 59% FRONT, 41% REAR C.G. HEIGHT = 24", I.F.S., I.R.S., FRONT SWAY BAR SAME RATE AS CAR IV 0.52
VI SAME AS CAR V EXCEPT W.O.T. AT 60 MPH THROUGH 481 FT. RADIUS TURN 0.50
LATERAL ACCELERATION IN gs

Fig. 7—Lateral acceleration at 12 deg tire slip angle

The addition of a well designed independent rear suspension together with increased front roll stiffness to maintain the same understeering effect as with the solid rear axle, brings the lateral acceleration to 0.52g.

Finally, applying full power to the rear wheels of our car at 60 mph while going through a turn of 481 ft in radius leaves the car capable of withstanding only 0.50g, as shown by Bar VI.

It should be mentioned here that the 12 deg slip angle can be maintained for all four tires of the car in the first two examples, on the front tires only of the next three, and on the rear tires only for the last example.

The calculations associated with the above values are performed in Appendix II.

All of the calculations are based on the tire data shown in Fig. 8. Note that cornering forces are shown only up to 12 deg of slip angle. This is because available data over 12 deg are scarce and incomplete. As additional reliable data in this area is developed by the tire industry, the suspension designer will welcome it eagerly.

It should be pointed out that all of the foregoing assumes that the tires maintain continuous contact with the ground. In practice this is, of course, not always possible. An in-

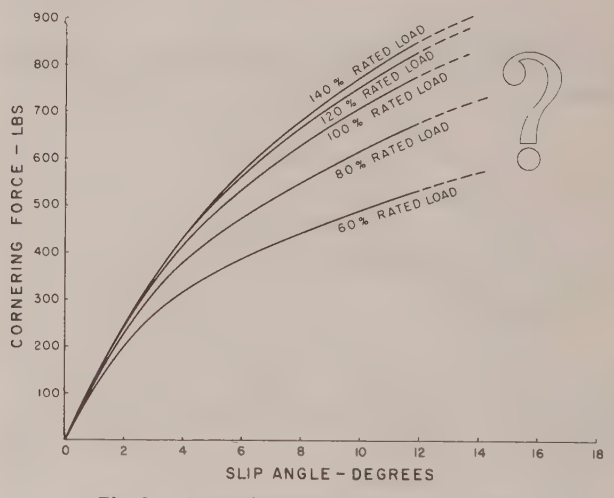

Fig. 8 — Cornering force versus slip angle

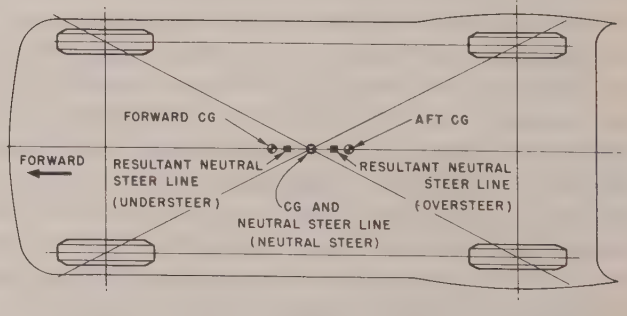

Fig. 9—Effect of center of gravity shifts on neutral steer line location

dependent suspension with less unsprung mass and no coupling between the wheels as with a solid axle permits the tires to follow the road contours better, and thus to reclaim some of the lost cornering force.

Directional Stability

As mentioned earlier, it is not sufficient that a car have a neutral steering characteristic. This is because as such a car encounters different loading, driving, and maintenance conditions, the steering tendency would shift back and forth from understeer to oversteer, resulting in a confusing control situation for the driver.

As shown in Fig. 9, a symmetrical car will have its center of gravity and its neutral steer line both located at the midpoint of the car. The neutral steer line may be defined as that line at which lateral forces applied to the car do not cause yawing. If that line passes through the center of gravity, as on a symmetrical car, we can see that loads or inertia forces acting at the center of gravity will not cause yawing. Such a vehicle is a neutral steering car.

To avoid a neutral steering car, it is necessary to separate the center of gravity and the neutral steer line. One way to do this is simply to move the center of gravity forward or rearward.

When the center of gravity is moved, the neutral steer line follows it, but does not move quite as far. This is because of the tire characteristics discussed earlier which result in a lower cornering coefficient of the overloaded front tires and a higher cornering coefficient of the underloaded rear tires. Thus, the line at which a lateral load is applied and does not cause yawing - the neutral steer line -- falls behind the center of gravity. The same is true in reverse, when we move the center of gravity rearward.

To put it very simply, when the neutral steer line is behind the center of gravity, the car will understeer; when it is ahead of the center of gravity, the car will oversteer. The distance between the center of gravity and the neutral steer line expressed in per cent of wheelbase -- but not at all dependent on their location relative to the midpoint of the wheelbase -- is a measure of the magnitude of the steering effect.

An understeering car will be directionally stable. This is because the centrifugal force at the center of gravity resulting from any deviation in course will tend to counteract and minimize the effect of the disturbance causing the deviation.

Conversely, an oversteering car will be unstable because the effect of a side load ahead of, behind, or at the center of gravity will be magnified by the centrifugal force. Centrifugal force increases with the square of the car speed, and for any given car a critical speed will exist at which, unless the driver quickly takes proper corrective action, even the smallest side load will result in a ground loop.

The stability of the understeering car directly benefits the driver. He can afford to take his eyes off the road for a moment without being in danger of finding the car moving in a different direction when he looks back. He can bring the car smoothly into a curved path and achieve a state of equilibrium in that path without difficulty. He can leave the path for one with different curvature, or return to the straight ahead condition and again maintain equilibrium on the new path -- all with a stable, easily controlled automobile.

For simplicity this discussion has been restricted to a single means of separating the center of gravity from the neutral steer line. This end can also be reached by other means, primarily in the tires and suspension system. We will not, however, go into any detail here. At this time let us content ourselves with the result -- that a certain degree of understeer is built into the car.

I say a certain degree of understeer, because while a considerable amount is required to avoid a shift from understeer to oversteer, for good cornering ability the degree of steering effect should be small. Thus another compromise must be reached.

Wind Stability

As already established, for best directional stability both in turns and in the straight ahead condition, the center of gravity should be located in front of the neutral steer line. This is the only arrangement which will be considered during the discussion of the car's remaining directional sense, wind stability.

Fig. 10 shows an understeering car with two different locations for the center of gravity and neutral steer line. Also shown is the wind force acting at the aerodynamic center of pressure of the car. Location of the center of pressure is the primary factor in the wind stability of an automobile.

In today's passenger cars, the center of pressure is normally located close to the front wheels, ahead of the center of gravity and the neutral steer line. This is an undesirable condition for wind stability. As can be seen in the illustra-

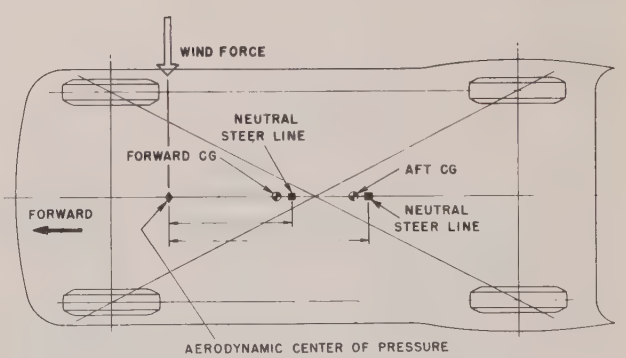

Fig. 10—Aerodynamic moment arms of two different understeering cars

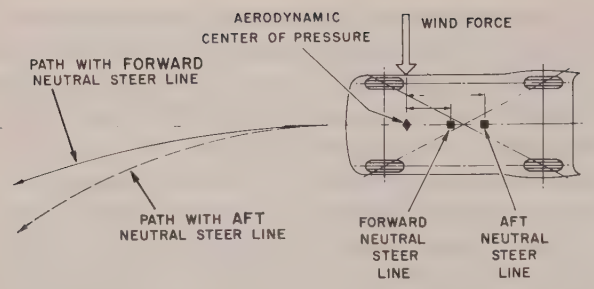

Fig. 11—Effect of aerodynamic moment arm on the path of two different understeering cars

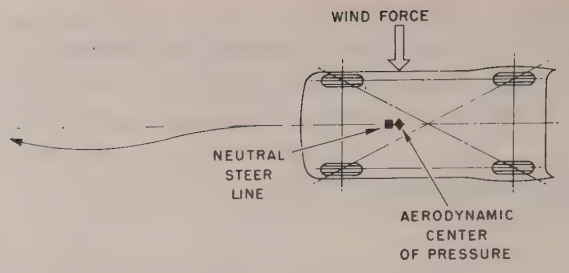

Fig. 12—Path of aerodynamically stabilized car

tion, the wind force acts on a moment arm about the neutral steer line, and causes the car to rotate or yaw. This not only introduces a side drift, but causes the car to steer off the road in the direction of the wind. Obviously, with a rearward neutral steer line, the moment arm of the wind force is appreciably greater than with the forward location, and the effect on the car is that much more severe.

Fig. 11 shows that the longer wind moment arm for the rearward location of the center of gravity and neutral steer line produces a more severe curvature away from the intended path than does the shorter moment arm. Although in both cases the driver must make a correction to stay on the road, the car with the center of gravity at the rear is the less windstable of the two.

The wind stability of either car may be improved by moving the center of pressure rearward through the use of fins or other measures. If it were possible to move it behind the neutral steer line, we would have for all practical purposes an automatically windstable car.

Fig. 12 illustrates this condition. The first response of our windstable car to a side wind load is to drift in the direction of the load. Gradually, however, the small difference in slip angles of the front and rear tires produces a steering angle which overcomes the drift and causes the car to cross its original path. The small path deviation involved here minimizes the need for driver correction to the point where strong gusty side winds require no more attention than do lateral disturbances introduced by very small irregularities in the road.

Response

The fourth requirement of car handling is proper dynamic response for good control. The transient behavior of the automobile has not yet been fully investigated. A more complete understanding of the dynamic control and stability problems associated with car handling may have to await further work in the research field.

However, it can be agreed that even with this limitation, very acceptable handling can be and has been built into present-day passenger cars. Let us discuss the lateral response of an automobile. This involves all three degrees of lateral freedom -- yaw, side slip, and roll.

The yaw velocity response of a car to steering wheel displacement has to be high enough and free from overshoot so that precisely controlled travel along a selected path is possible for the operator. The mass, displacement, available damping, and the inherent steering characteristic of the car, and the means by which this characteristic is achieved, determines the time required to change from one steady state to another.

A car leaving a straight path for one with a constant radius of curvature must be accelerated from zero to a constant yaw velocity and to a constant yaw angle relative to the path. The yaw velocity is introduced by the steering angle needed to make the car follow the curved path if no inertia forces were involved. The yaw angle is required to bring the rear tires into a slip angle position at which they can develop their share of the cornering force for a given lateral acceleration of the car.

The amount of the yaw angle and the time required to build it up and maintain it determine more than anything else whether or not the response and, therefore, the control of the car is satisfactory.

It has already been explained how the smallest yaw angle for a given lateral acceleration -- or in other words, the highest amount of cornering power or lateral stiffness -- can be achieved. Remember that the closer the car comes to the ideal car, the higher is the lateral stiffness.

Of the other two degrees of lateral freedom, side slip has only a minor effect on car response and can be neglected for all practical purposes.

Roll, however, does have an effect on speed of response, although it does not directly alter the car's path.

Overall response time can be shortened by using fast responding steering effects. All such effects are introduced directly by the tires without involving any appreciable secondary effects. Among these are:

1. Unequal weight distribution.
2. Unequal tire sizes or tire pressures.
3. Roll axis inclined in the side view.
4. Suspension deflection steer.

Deflection steer is an effect caused by actual deflection of the axle or wheel support. Because of the relatively small mass and the high mounting rate involved, it is a high frequency system with fast response. It is of interest to note

that deflection steering does not significantly decrease cornering force, a fact also true for the slower-responding roll steer.

The slow-responding steering effects are -- with the exception of jacking -- all coupled with body roll, which being itself of relatively low frequency is responsible for the slow response of the others. Among these are:

1. Different roll stiffness distribution, front and rear.
2. Tire camber change.
3. Jacking of one end of the car under lateral acceleration caused by undesirable suspension geometries.
4. Roll geometry steer.
5. Toe steer.

The remaining factor influencing lateral response is damping. A steering wheel displacement pulse or step input should not introduce an objectionable roll or yaw oscillation before reaching the steady state again.

Feedback

The last of the important handling requirements is feedback to the driver. The driver controls the car by means of steering wheel displacements and torque applied to the steering wheel. While so doing, he sees, hears, and feels the lateral response to his inputs. He observes to a certain degree the acceleration, velocity, and displacement of the car as it yaws, sideslips, and rolls. In addition, he has the benefit of torque feedback through the steering gear back to his hands. This torque feedback is a valuable source of information with regard to the decisions the driver must make continuously to keep the car safely on the desired path.

This feedback is the self-aligning torque generated at the footprint areas of the front tires. It varies with the friction coefficient between the tire and road surface, and with the slip angle of the tires. It enables the driver to feel slippery road surfaces, and to detect by the fast decrease of aligning torque shortly before tire skidpoint, and impending skid.

To provide good torque feedback, it is important to use low mechanical and hydraulic friction in the wheel supports, steering linkages, and steering gear. Caster change can distort the torque feedback. On the other hand, however, by building in sufficient positive caster, the reversal of self-aligning torque at high slip angles can be avoided.

Kingpin inclination and toe-in, are of constant value, and affect returnability of the front wheels; they do not contribute any information to the driver.

Having reviewed the operational handling requirements for an automobile, I will conclude by summarizing the major design requirements which permit us to achieve our goal:

1. Maximum cornering ability per degree of slip angle.
2. Good directional stability through locating the neutral steer line behind the center of gravity.
3. Good wind stability through locating the center of aerodynamic pressure as close as possible to the neutral steer line.
4. Proper responding steering effects for good control.
5. Adequate feedback for maximum driver information.

Since we are dealing with the practical rather than with the ideal, in trying to reach the design goal we must make the best possible compromises between these requirements for good handling, and possibly conflicting requirements for other considerations.

Appendix I

Rear wheel deflection during acceleration for a given instant center location on a rear drive car with unsprung differential.

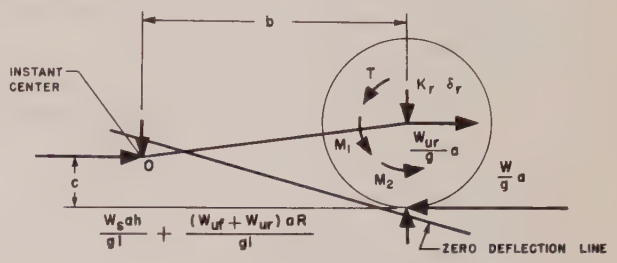

W = 3500 lb --------Total weight to car
W_s = 3000 lb --------Sprung weight
W_{uf} = 200 lb --------Front unsprung weight
W_{ur} = 300 lb --------Rear unsprung weight
a = 15 ft/sec^2 ----Acceleration
h = 25 in. -------Height of center of gravity of sprung mass
g = 32 ft/sec^2 ----Acceleration of gravity
l = 100 in. -------Wheelbase
K_r = 200 lb/in. -----Rear wheel rate (sum for 2 wheels)
δ_r = ----------Rear wheel deflection in inches
R = 12 in. -------Tire rolling radius
b = 40 in.
c = 8 in.
T = 0 ---------- Torque not reacted by suspension linkage (zero for unsprung differential)
M_1 = 0 ---------- Polar inertia moment of wheels (neglected)
M_2 = 0 ---------- Rolling friction moment (neglected)

$[\Sigma M_O = 0]$

$$\delta_r = \frac{\frac{W_s ahb}{gl} + \frac{(W_{uf} W_{ur})\, abR}{gl} - \frac{Wac}{g} + \left(\frac{W_{ur}a}{g}\right)(C - R) + \frac{T + M_1 + M_2}{bK_r}}{bK_r}$$

$$= \frac{\frac{3000 \times 15 \times 25 \times 40}{32 \times 100} + \frac{500 \times 15 \times 12 \times 40}{32 \times 100} - \frac{3500 \times 15 \times 8}{32} + \left(\frac{300 \times 15}{32}\right)(-4)}{40 \times 200}$$

= 0.19 in. of jounce

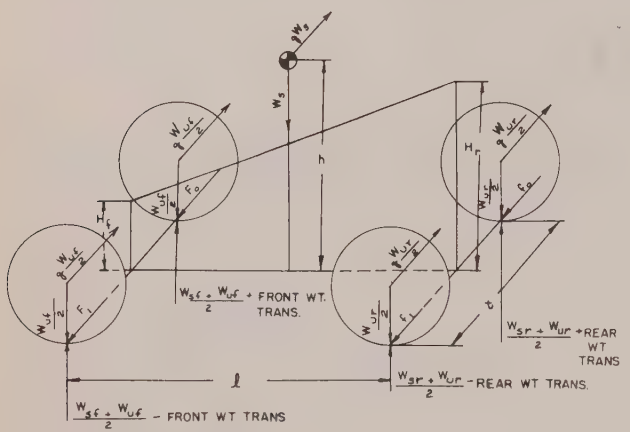

W_s = Total sprung weight, lb
W_{sf} = Front sprung weight, lb
W_{uf} = Front unsprung weight, lb
W_{sr} = Rear sprung weight, lb
W_{ur} = Rear unsprung weight, lb
h = Center of gravity height of sprung mass, in.
H_f = Front roll center height, in.
H_r = Rear roll center height, in.
K_f = Ride rate per front wheel, lb/in.
K_r = Ride rate per rear wheel, lb/in.
K_{rf} = Roll rate front, lb/in.
K_{rr} = Roll rate rear, lb/in.
R = Tire rolling radius, in.
t = Track, in.
l = Wheel base, in.
K_t = Tire rate, lb/in.
g = Lateral gravity acceleration
F_o = Front outside wheel cornering force (slip angle thrust minus camber thrust), lb
F_i = Front inside wheel cornering force (slip angle thrust minus camber thrust), lb
f_o = Rear outside wheel cornering force (slip angle thrust minus camber thrust), lb
f_i = Rear inside wheel cornering force (slip angle thrust minus camber thrust), lb

Appendix II

Calculations to determine the lateral gravity which generates a 12 deg slip angle on Car IV.

In the following calculations several minor effects have been neglected for simplification. These effects include:

1. Lateral shift of center of gravity with roll.
2. Effect of self-aligning torque.
3. Lateral shift of car as tires "roll under."
4. Effect of traction on slip angles.

Specifications of Car IV

W_s	= 3365	W_{ur}	= 415	K_f	= 115	R	= 13.1
W_{sf}	= 1980	h	= 26	K_r	= 115	t	= 60
W_{uf}	= 220	H_f	= 4	K_{rf}	= 220	l	= 120
W_{sr}	= 1385	H_r	= 10	K_{rr}	= 115	K_t	= 1100

The problem resolves itself into first determining which slip angle, front or rear, reaches 12 deg at the lowest lateral acceleration. For understeering vehicles, which Car IV is, higher front than rear slip angles are generated. Since successive trial calculations are required to solve the problem, only the mathematics of the final trial will be shown for brevity.

Final Trial - Find front slip angle generated by a 0.547 lateral gravity acceleration.

Total Weight Transfer Front at g = 0.547 Lateral Gravity

A = Sprung weight nonrolling couple weight transfer.

$$A = \frac{W_s}{t}\left[H_f + (H_r - H_f)\left(\frac{W_{sr}}{W_s}\right)\right]\left[\frac{W_{sf}H_f}{W_{sf}H_f + W_{sr}H_r}\right](g)$$

$$A = \frac{3365}{60}\left[4 + (10-4)\left(\frac{1385}{3365}\right)\right]\left[\frac{1980 \times 4}{1980 \times 4 + 1385 \times 10}\right](0.547)$$

A = 72.4 lb

B = Sprung weight roll couple weight transfer.

$$B = \frac{W_s}{t}\left[h - \left[H_f + (H_r - H_f)\left(\frac{W_{sr}}{W_s}\right)\right]\right]\left[\frac{K_{rf}}{K_{rr} + K_{rf}}\right](g)$$

$$B = \frac{3365}{60}\left[26 - \left[4 + (10-4)\left(\frac{1385}{3365}\right)\right]\right]\left[\frac{220}{115 + 220}\right](0.547)$$

B = 392 lb

C = Unsprung weight nonrolling couple weight transfer.

$$C = \frac{W_{uf}R}{t}(g)$$

$$C = \frac{220\ (13.1)}{60}\ (0.547)$$

C = 26.2 lb

Total Weight Transfer Front = A + B + C = 491 lb

D	= Static tire load = 1100		$\frac{W_{sf} + W_{uf}}{2}$
E	= Total weight transfer	= 491	A + B + C
F	= Outside wheel load	= 1591	D + E
G	= Inside wheel load	= 609	D - E
H	= Roll deflection	= 1.78 in.	B/K_{rf}
I	= Roll angle	= 3.40 deg	$H\left(\frac{360}{\pi t}\right)$
J	= Outer wheel camber relative to body	= -0.85	Front susp. camber
K	= Inner wheel camber relative to body	= -0. --	Front susp. camber
L	= Camber due to tire deflection	= 0.85 deg	$\frac{E}{K_t}\left(\frac{360}{\pi t}\right)$
M	= Outer wheel camber relative to road	= 3.40 deg	I + J + L
N	= Innte wheel camber relative to road	= 4.25 deg	I - K + L
O	= Outside wheel camber thrust[1]	= 113	$\frac{23}{1100}$ (F) (M)
P	= Inside wheel camber thrust[1]	= 54	$\frac{23}{1100}$ (G) (N)
Q	= Lateral side force of front total mass	= 1203	$(W_{sf} + W_{uf})$ (g)
R'	= Slip angle thrust required	= 1370	O + P + Q
S	= Thrust available at 12 deg slip angle		
	Outer wheel	= 850	F_o + O) Fig. 13
	Inner wheel	= 522	F_i + P)
		1372	

Therefore, a lateral gra vity acceleration of 0.547 generates 12 deg front slip angle.

[1] In the vicinity of 12 deg slip angle, camber thrust is taken as 23 lb per degree camber and is assumed proportional to wheel load.

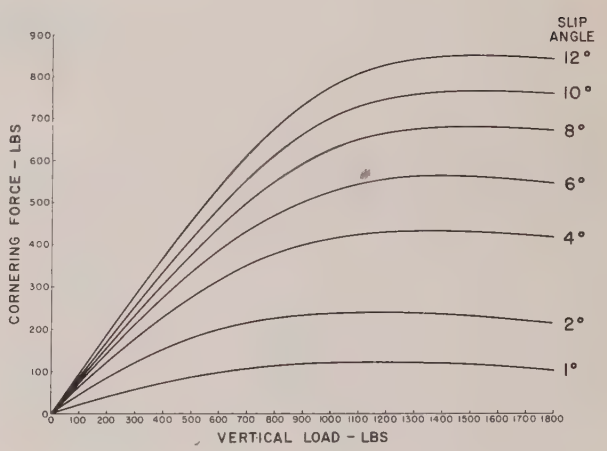

Fig. 13—Cornering force versus vertical load

SNAP 2

A Reactor Powered Turboelectric

ON NOV. 18, 1959, announcement was made of the successful operation of the SNAP 2 reactor, which was designed to power a turboelectric generator for use in space vehicles. This marked the achievement of an important milestone in the Atomic Energy Commission's space power program which began in 1955. An operational model of this small reactor will eventually provide the heat power necessary to produce several kilowatts of useful electric power for very long periods of time. It will do this completely automatically and unattended. The following is essentially a status report of the SNAP 2 project.

The fueled portion of the reactor core is contained in 61 stainless steel cylinders, 1 in. in diameter. Each cylinder contains 10-in. long fuel element with a 1-1/2-in beryllium reflector at each end. This bundle of cylinders fits into a hexagonal can which measures 8 in. across the flats and 14 in. in length. Two to 3 in. of beryllium surround the entire core, acting as a reflector. The active portion of the core (neglecting end plugs) is slightly under one-third of a cubic foot. Reactor control is accomplished by means of rotating drums made of reflector material. A model of this assembly plus a conceptual shadow shield for payload protection is shown in Fig. 1. A disassembled fuel element is shown in Fig. 2.

The reactor used in the first power demonstration is more accurately referred to as the SNAP experimental reactor, abbreviated SER. It first achieved criticality on Sept 19, 1959; and, after installation of the liquid metal coolant, it was carefully brought up to design power and temperature on Nov. 9. This test was accomplished at an AEC facility in the Los Angeles area by the Atomics International Compact Power Group. An artist's concept of this facility is shown in Fig. 3.

The reactor is shown suspended in the lower section of the steel containment shell. Two concrete plugs provide biological shielding for shutdown and power operation. Access to controls and plumbing is provided in the space between the two plugs. Heat from the reactor is dissipated by two liquid metal loops employing commercial pumps and heat exchangers. The primary loop, which becomes radioactive in operation, is housed in the first concrete shielded vault. The second loop provides ultimate dissipation of the heat to the atmosphere by an air-blast heat exchanger. This nonradioactive loop is contained in an unshielded vault. The actual reactor used in this experiment is shown in Fig. 4.

This simple, relatively low-cost experiment provided a means of conducting long-term tests of the reactor core, with a high degree of safety, before attempting to marry it to a prototype turboelectric conversion unit. The conversion unit is being developed by the New Devices Laboratories of Thompson Ramo Wooldridge Inc., Cleveland, Ohio, under

Generator for Space Vehicles

Lt. Col. Guveren M. Anderson
U. S. Air Force (Atomic Energy Commission)

a subcontract to Atomics International. A combined test involving the turbogenerator and the reactor will require a more elaborate facility in order to simulate some of the environmental conditions experienced in rocket launch and space operation. Construction of this facility is progressing at a rate which indicates a combined test late in 1960. Since ling-term reliability of the whole system is expected to be the most stringent requirement for a space system, long-term test experience on each component is imperative early in the development program. As of Feb. 12, 1960, the reactor has produced 25,000 thermal kwhr. Considerable operating experience and knowledge of the reactor control parameters will have been achieved when the combined test is attempted.

Objectives

The objective of the SNAP 2 project is to develop a space power system for use in the 1962-1963 time period. Summary specifications of this system are cited:

Life, continuous operations - 1 year
Electrical power (useful) - 3 kw
Gross weight, including radiator - less than 620 lb (unshielded)
Radiative area - less than 110 sq ft
Maintenance - none
Start-up - remote in orbit
Environment - rocket launch and space
Biological hazards - negligible during launch, abort, orbital, or post orbit
Payload dose - limits to be established primarily by transistors
Shielding - design to be determined during vehicle integration

Additional objectives are: The system should be both economical to build and capable of growth potential for higher powered systems.

In order to accomplish these objectives, the contractor was requested to:

1. Develop basic materials and physics information required to engineer the power system.
2. Develop fabrication techniques.
3. Engineer and fabricate developmental systems.
4. Perform operational and environmental tests to prove adequacy of design.
5. Integrate the power systems into the vehicle system, where appropriate.

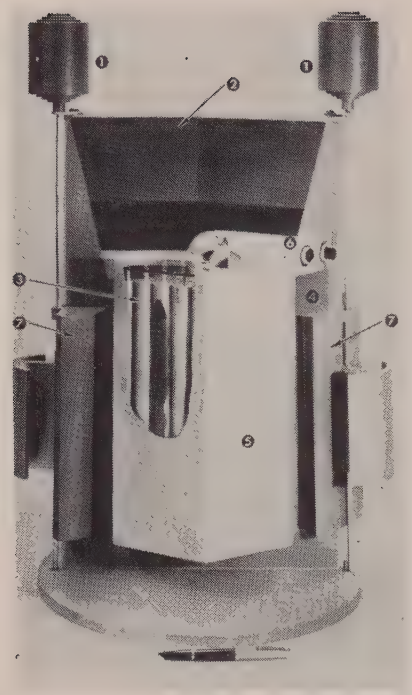

Fig. 1 — Full-scale model of SNAP 2 reactor: (1) control motors, (2) shielding, (3) fuel elements, (4) reflector, (5) core vessel, (6) coolant lines, (7) control drums

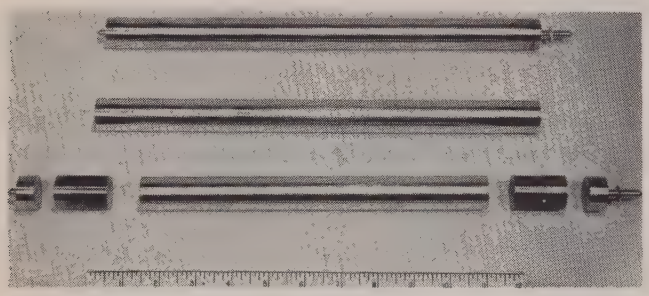

Fig. 2 — SNAP 2 — fuel moderator element

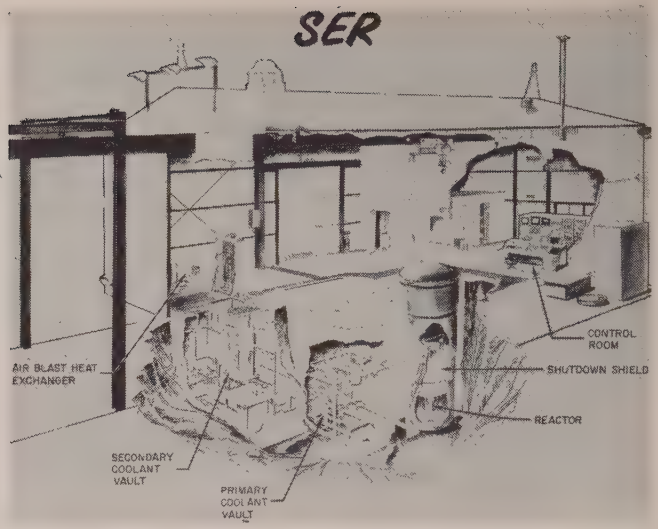

Fig. 3 — SNAP experimental reactor facility

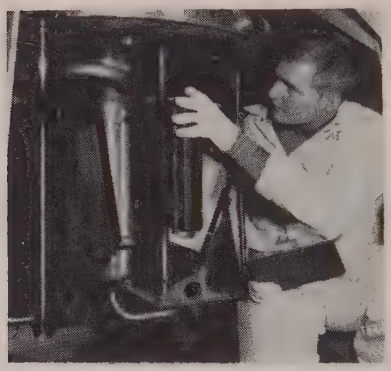

Fig. 4 — SNAP experimental reactor showing control drum and scram mechanism

6. Develop ground support equipment and handling procedures.

7. Evolve operational systems for specific vehicle systems.

Reactor

Selection of the reactor fuel form to be developed was the most critical decision made. When this had been accomplished, the upper temperature of the cycle was estimated and the conversion system parameters established. A high source temperature was necessary if the waste heat was to be rejected within the limits of the radiative area specified.

All of the fuel materials originally proposed depended on the solution of complicated materials problems, compact reactor physics, and control problems. In keeping with the time schedule, the reliability requirements, and the 1955 state of the art projections for long life power conversion and reactor systems, a 1200 F operating temperature target was established.

The cost of elevating a pound of material into a 300-mile orbit about the earth has been estimated at $15,000 per lb. Newer vehicles should reduce this figure to less than $1000 per lb. It was apparent, therefore, that SNAP 2 would be most attractive if a lightweight system capable of being launched by a variety of vehicles were achieved. In a 3 KWe system it was obvious that the reactor and shield would constitute a relatively heavy unit. The reactor, therefore, should be made as small as possible without sacrificing reliability.

To keep the weight of a small, high-temperature reactor low, an efficient, low-pressure coolant must be used. Direct boiling would allow the most efficient heat removal sys-

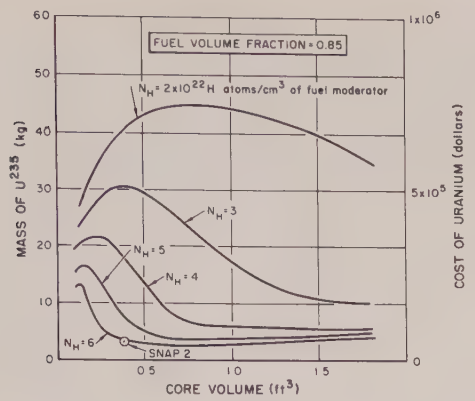

Fig. 5 — Critical mass and volume relationship for various N_h values

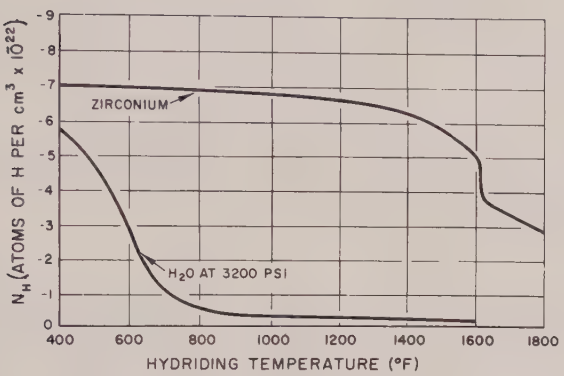

Fig. 6 — Hydrogen density versus temperature for ZrH_x and water (at 1 atmosphere)

tem. The boiling coolant, however, would impose a difficult reactor control problem; and, in addition, boiling in zero-gravity would be an added complication. As a result, a liquid metal coolant system was chosen.

There are two ways to achieve the small reactor volume needed. First, approximately 53 kg of pure, or slightly diluted, uranium-235 will result in a small fast critical assembly with a volume of about one-tenth of a cubic foot. Provisions for adequate coolant fractions would increase the critical mass to about 67 kg. The practicability of reprocessing the uranium after use in orbit would be remote. The total critical mass, therefore, can be assumed to be expended, hence a base cost of approximately $1 million for fast assembly fuel alone must be borne. In addition, material problems associated with oralloy at high temperatures preclude its use in a space application.

For the satellite missions requiring modest amounts of electrical power the second way was more economical; that is, a reasonably priced reactor can be assembled by diluting U-235 with a suitable moderator. Dilutions of the U-235 with any atom other than hydrogen results in an assembly heavier than the slightly diluted U-235 assembly noted above and achieves no reduction in critical mass for small cores. The

Table 1 - Physical Properties of Zr Hydride ($ZrH_{1.7}$)

Hydrogen density	6.25×10^{22} atom/cm³
Density	5.65 gram/cm³
K (1200 F)	13.0 ± 1.0 Btu/hr ft F
E (80 F)	9.1×10^6 psi
E (1200 F)	4.4×10^6 psi
UTS (80 F)	8000 psi
UTS (1200 F)	10,000 psi
Coefficient of linear expansion (1200 F)	6.56×10^{-6} in./in. F

effect of dilution with hydrogen is readily seen in Fig. 5. Critical mass and volume relationships are shown for assemblies of various N_H values. (N_H is the number of hydrogen atoms/cm³.) Room temperature water has 6.7×10^{22} hydrogen atoms/cc. SNAP 2 with a core of 1/3 ft and a fuel loading of only 2.7 kg U-235 is shown in contrast to systems utilizing a lower hydrogen density.

High-pressure problems would be associated with the use of water as the source of hydrogen, therefore, the possibility of using certain refractory metal hydrides was investigated. Zirconium-Hydride, ZrH_X, was found to have the properties permitting a high degree of hydrogen retention at temperatures in the range of interest. Fig. 6 illustrates relative hydrogen densities achievable with water and zirconium hydride.

Although the advantage of using the refractory metal hydride is evident, compensation must be made for the low but finite vapor pressure resulting from the dissociated hydrogen. For an N_H of 6.0×10^{22} atoms/cm³ this pressure is approximately 0.1 atmospheres at/1200 F, and increases by a factor of three, approximately, every 100 F. At 1500 F, the pressure is about 2.5 atmosphere. A slight reduction in N_H can materially reduce this pressure. Satisfactory containment materials have been developed and demonstrated which permit the use of zirconium-hydride at temperatures up to approximately 1300 F for one year with a hydrogen loss of not more than 1%. At the lower temperatures encountered in conventional terrestrial applications, good containment of the hydrogen is easily achieved with a conventional material such as stainless steel.

The U-235 fuel is alloyed with the zirconium by means of successive arc-melting operations. The resultant alloy is hydrided to form a massive homogeneous fuel-moderator material. Such a homogeneous material is superior to a heterogeneous arrangement in that all fuel and moderator

surface contributes to heat transfer. More important, the moderator dilutes the fuel such that a much higher fraction of fuel atoms can be fissioned before excessive structural damage results. Thus, the homogeneous fuel-moderator allows both maximum power density and core endurance. Homogeneity also provides a rapid-acting negative temperature coefficient which is particularly desirable for automatic control.

Integrity of the fuel element when subjected to six times the SNAP 2 power density and twice the burn-up requirement has been verified in the Materials Testing Reactor at a surface temperature of 1280 F. Current tests are being conducted at 1/2 and 1% burn-up of the total metal atoms in the fuel mixture. These rates are equivalent to roughly 1500 and 3000 MWd (t) per cu ft of core.

Power density in this element is dependent upon diameter, permissible operating temperature, thermal conductivity, and allowable temperature gradients through the element. The gradients are limited by the coefficient of expansion, elastic modulus, ultimate strength, creep strength, and Poisson ratio. Most of the properties have been determined and are listed in Table 1.

Early considerations for achieving the maximum compactness led to consideration of several core geometries. A sphere made up of fuel-bearing coencentric shells and an approximate sphere made up of fuel-bearing coencentric pipe sections (with the coolant flowing in the clearance spaces) were considered but eventually discarded in favor of the "faggot" arrangement; that is, rod or pin-type elements. The simple, straight-through flow of coolant and the ease of manufacture of these rod-type elements justified the 10% increase in core volume due to this cylindrical geometry.

If small rod diameters are used, high power densities are attainable from a variety of fuels. Small pins, however, would result in difficult design problems, higher fabrication costs, increased structural materials in the core, increased critical mass, decreased reliability and endurance. For these reasons, it is desirable to use a reasonable rod diameter and an efficient coolant such as NaK. Bulk heat fluxes obtainable from the SNAP 2 reactor fuel element material as a function of rod diameter are shown on Fig. 7. The data presented in Fig. 7 is based on a predicted thermal stress limitation which may not actually exist. Either yielding of the material or hydrogen migration could relieve these stresses allowing a much higher power density. Noteworthy is the fact that the SNAP 2 power density is only 0.156 Mw/ft^3. Development of a smaller diameter SNAP reactor fuel element in connection with the National Aeronautics and Space Administration SNAP 8 project will provide considerable growth potential for power production in the SNAP hydride reactor.

The zirconium hydride fuel material of the SNAP Experimental Reactor has demonstrated a prompt and large negative temperature coefficient which is desirable for safety

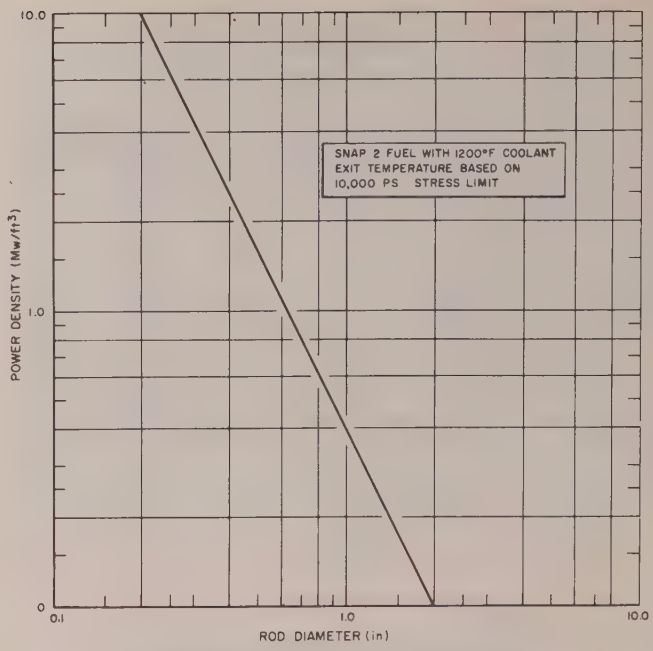

Fig. 7 — Power densities achievable with SNAP 2 reactors using various rod diameters

and good control. The average coefficient during the transition from room temperature to the operating temperature at 1200 F is -3.5 x 10^{-5} $\Delta K/K/\overset{\circ}{C}$. At the operating temperature, the coefficient is-6.0 x 10^{-5} $\Delta K/K/\overset{\circ}{C}$. In case of a maximum credible accident, the prompt temperature coefficient will limit the energy release to about 50 megawatt sec. In addition, if the temperature rises to about 1700 F, hydrogen will be lost, thus providing an inherent backup safety mechanism. As a result, a catastrophic or meltdown accident is impossible.

Neutron generation time in the epithermal hydrides is 10 - 30 microsec, which is long in comparison to about 0.01 microsec in a metallic fast core. This property also offers an additional control and safety advantage.

Thus, the prompt and large negative temperature coefficient of the SNAP Experimental Reactor, attributable to the homogeneous mixing of fuel and moderator as well as to the slightly epithermal mean fission energy (0.1 ev), results in an easily controlled and safe reactor. There is zero-time lag between fuel element and neutron temperature increases because of the intimacy of the fuel atoms, the moderator atoms, and the neutrons. Instantaneous expansion of the moderator is expected to permit considerable dynamic stability, with controls providing primarily for start-up, long term burn-up, poisoning, and loss of hydrogen.

In addition, any small-core reactor has an advantage in control, because a large percentage of the neutrons are lost by leakage without resulting in fission reactions. Approximately 40% of the fission neutrons are lost by leakage from the SNAP core. The reflector thus becomes an effective means of control simply by controlling leakage. As much

as 15 to 20$ reactivity($\Delta K/K$) change can be accomplished by small control drums located in the reflector. Drums of this type can be made rugged and essentially shock-proof. Control rods requiring holes in the pressure shell, movement of fuel, or burnable poisons were other possibilities with somewhat greater complexity than the simple rotating drums used in SNAP 2.

A summary of the more important characteristics of the SNAP reactor are listed in Table 2.

Selection of Thermodynamic Cycle and Working Fluid

The maximum reactor coolant outlet temperature, the available heat sink area (110 sq ft), and a reasonable time for development, then, were the limiting factors in the choice of a thermodynamic cycle and its fluid. The Brayton, Stirling, and Rankine cycles were examined, and the latter was selected as having the best probability of success. Reactor weight is relatively independent of power conversion cycle selection in SNAP 2 since the reactor is sized by criticality rather than by power output or endurance. Thus, a power conversion cycle must be chosen on the basis of minimum component weights consistent with reliability and lifetime.

The heaviest single component in the power conversion system is expected to be the radiator. In order to obtain minimum weight for this component, the reactor should operate at the maximum feasible temperature, thus allowing a high heat rejection temperature. In the case of SNAP 2, a 1200 F reactor coolant outlet temperature has been chosen as a feasible goal for a reliable system. Furthermore, radiator size can be minimized by operating near the ideal condition:

$$\frac{T_c}{T_h} = \frac{3}{4} \qquad (1)$$

where:

T_c = Effective heat rejection temperature in absolute units

T_h = Effective heat injection temperature in absolute units

When component efficiencies and temperatures effects on material strengths are considered, the optimum temperature ratio will vary, but not by a large factor. Based on these and other considerations a radiator inlet temperature of 615 F was selected. Since the above considerations tend to fix the system temperature limits, minimum weight is required for a cycle which can operate in this range.

Comparing the various real cycles with the ideal carnot cycle shows that the saturated Rankine cycle most closely approaches the ideal cycle efficiency and thus gives the optimum system. This close approach is obtained by the isothermal heating and cooling phases of the saturated Rankine cycle which allows much better utilization of available temperature ratios than provided by other cycles such as the Stirling and Brayton.

Both the Brayton and Stirling cycles were attractive because the problems of boiling and condensing under zero-gravity conditions would not be present. The Brayton cycle was eliminated on the basis of uncertainties in producing useful shaft work within the specified conditions of temperature and radiator area. Furthermore, a system based on the Brayton cycle with an efficiency comparable to the Rankine cycle would require an excessively high source temperature (assuming optimistic compressor and turbine efficiencies). A further disadvantage of any gas cycle would be the sole dependence on the heat transfer coefficients of gases which invariably result in larger, heavier, heat exchangers.

The Stirling cycle was considered because of the successful history of the Phillips air engine, which has demonstrated reasonably good brake thermal efficiencies in small sizes. An engine based on this cycle is expected to be somewhat heavier than the Rankine for the same reason as the Brayton cycle; that is, dependence on heat transfer coefficients of gases. Although the problems of a two-phase working fluid would not be present in zero-gravity, the difficulties of lubricating cylinder walls, bearings, and any necessary gearing, as well as the difficulty of scavenging the oil from the crankcase, would present other problems. Entrainment of lubricant in the working fluid, with ensuing deposition on the interior of the thermal transfer surfaces, would probably reduce

Table 2 - SNAP 2 Reactor Characteristics

Fuel - $(Zr\text{-}U)H_{1.7}$	Homogeneous mixture
No. fuel elements	61
Size of fuel elements	1 in. D x 10 in. long
Hydrogen atoms/cm^3 at 1200 F	6.1×10^{22}
Fuel inventory	2.7 kg U-235
Reflector	2-3 in. beryllium
Coolant	NaK eutectic (in 1000 F out 1200 F)
Control	reflector drums
Temperature coefficient - (600-1200 F) average	$-3.5 \times 10^{-5} \Delta K/K/^{\circ}C$
at 1200 F	$-6.0 \times 10^{-5} \Delta K/K/^{\circ}C$
Core size (hexagonal parallele piped)	8 in. across flats x 10 in. long
Weight	213 lb
Overall dimensions	13 in. D x 16-18 in. long

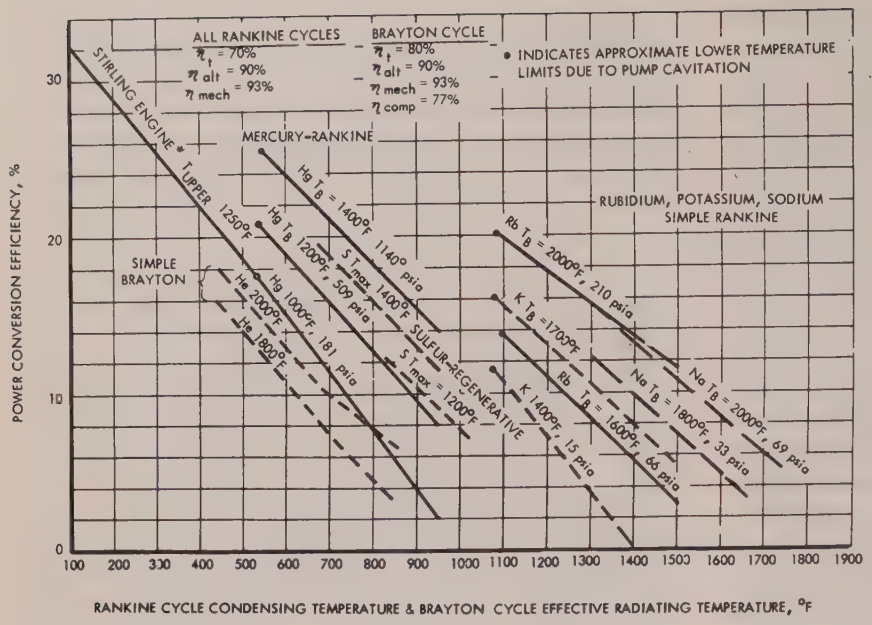
ALL RANKINE CYCLES
η_t = 70%
η alt = 90%
η mech = 93%
BRAYTON CYCLE
η_t = 80%
η alt = 90%
η mech = 93%
η comp = 77%
• INDICATES APPROXIMATE LOWER TEMPERATURE LIMITS DUE TO PUMP CAVITATION
STIRLING ENGINE * T UPPER 1250°F
MERCURY-RANKINE
Hg T_B = 1400°F 1140° psia
Hg T_B 1200°F, 509 psia
Hg 1000°F, 181 psia
RUBIDIUM, POTASSIUM, SODIUM SIMPLE RANKINE
Rb T_B = 2000°F, 210 psia
K T_B =1700°F
Na T_B = 1800°F, 33 psia
Na T_B = 2000°F, 69 psia
Rb T_B = 1600°F, 66 psia
K 1400°F, 15 psia
SIMPLE BRAYTON
He 2000°F
He 1800°F
S T max 1400°F
S T max = 1200°F
SULFUR-REGENERATIVE
POWER CONVERSION EFFICIENCY, %
RANKINE CYCLE CONDENSING TEMPERATURE & BRAYTON CYCLE EFFECTIVE RADIATING TEMPERATURE, °F

Fig. 8 — Comparison of Stirling, Brayton, and Rankine cycle efficiencies

the efficiency of any heat exchangers.

Fig. 8 illustrates that the Stirling cycle at 1250 F would achieve efficiencies comparable with a mercury Rankine cycle at 1000 F if both are held to the same heat sink temperatures. The Rankine cycle radiator is practically isothermal, while both the Stirling and the Brayton cycles have relatively large temperature drops through the radiator, thus reducing radiator effectiveness.

The Rankine cycle takes advantage of the latent heat gained from phase changes, the lower flow rates, and the isothermal heat transfer to attain high efficiencies, light weight, and good reliability within the temperature and radiator area limits. The difficulties associated with phase changes in a zero-g environment have been partially solved by utilizing the viscous properties and the velocities of the fluid to achieve phase separation in the designs of the boiler and condenser. Experiments performed by Thompson Ramo Wooldridge indicate that this design approach may be successful. The experiments include both laboratory and zero-g tests in an aircraft at Wright Air Development Division, Dayton, Ohio, in which test intervals of up to 15 sec at zero gravity were obtained.

The selection of a suitable cycle fluid is based on the pressure and temperature limitations of the fluid, its physical properties, and the availability of containment materials. A simple presentation of the temperature regimes wherein certain Rankine cycle fluids become attractive is shown in Fig. 9. Considering (1) that a reasonable upper pressure for each fluid is limited from the standpoint of containment; (2) that a reasonable low-cycle pressure in the radiator is limited from the standpoint of pump cavitation; and, (3) a minimum efficiency of 10% overall, then the temperatures of interest for each fluid can be bracketed. It is readily seen that if weight is to be saved by increasing radiator temperature, the alkali metals must be employed as working fluids. Estimated efficiencies for these fluids are also indicated on Fig. 8.

Fluids which can achieve the phase changes desired within the available temperature and pressure limits of SNAP 2 were found to be sulfur, phosphorous, and mercury. Phosphorous undergoes several complicated molecular transitions and is difficult to handle. A sulfur cycle was found to be competitive with mercury but required greater heat transfer area. Sulfur, however, was eliminated primarily on the basis of its corrosive properties.

Mercury was selected as the best cycle fluid because it had been in use in several stationary power plants in the United States, and the pressures are reasonable at modestly high temperatures, thereby permitting the use of reasonable containment methods for the vapor. A considerable amount of information has now been developed concerning the heat

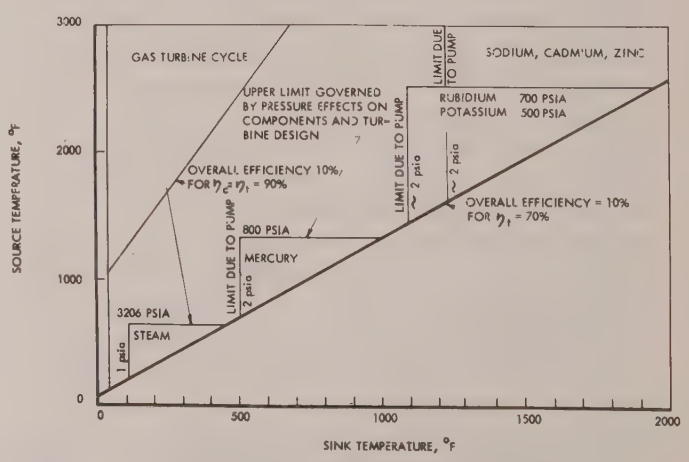

Fig. 9 — Temperature regimes for use of various liquids in a rankine cycle

transfer, corrosion, and other physical properties of mercury so that components such as boilers, turbines, pumps, bearings, and alternators can be designed and built, using mercury as a cycle working fluid, a coolant, or a lubricant.

Cycle conditions were finally selected on the basis of weight rather than efficiency. No weight penalty is accrued if the reactor is operated at an increased thermal output; however, the boiler and condenser weights can be reduced by proper combination of boiling conditions and moisture content at the turbine discharge.

The use of a once-through counterflow boiler configuration coupled with a reasonable temperature difference in the primary coolant loop allows superheating of the cycle fluid. The superheat approaches the reactor outlet temperature and is obtained with a small weight penalty. This improves the cycle efficiency slightly and, more important, reduces the moisture content of the turbine exhaust. A dry turbine exhaust will tend to ease the erosion problem and is expected to lead to a longer lived, more reliable turbine. As a result of these considerations, SNAP 2 will utilize a somewhat superheated Rankine cycle with an effective radiating temperature of about 600 F.

System Schematic

Fig. 10 is a schematic of the SNAP 2 system showing the components and flow of working fluids. NaK has been selected as the reactor coolant in this case to adapt the powerplant for remote start. The primary NaK loop is composed of the pump, reactor, and NaK section of the boiler. The secondary loop contains the components of the Rankine engine; that is, pump, boiler, turbine, and radiative condenser and subcooler. A third loop supplies the bearings,

The primary loop pump delivers 71.5 lb of NaK per min at 1000 F. NaK is discharged from the reactor at 1200 F.

The secondary loop pump discharges 45 lb of mercury per min at 175 psia. Sixteen pounds per minute are required for the bearings, 10 lb per min are recirculated through the jet pump, and the remaining 18.6 lb per min are discharged into the boiler. The boiler is heated by NaK entering at 1200 F and leaving at 1000 F and is designed for a 60 psi pressure drop which provides superheated vapor for the turbine at 115 psia and 1150 F. The superheated vapor is expanded from 115 to 7 psia producing work to drive the alternator, mercury pump, and NaK pump.

The output requirement and the operating conditions of each component may be calculated from the cycle conditions, component performance, and system output requirement. Table 3 lists the power balance in the mechanical and electrical portions of the system.

The NaK pump, turbine, alternator, and mercury pump are mounted on a common shaft supported by two mercury-lubricated journals and one thrust bearing. This combined rotating unit (CRU), shown in Fig. 11, is designed to operate at 40,000 rpm. (The actual unit is shown in Fig. 12.) The NaK pump rotor is separated from the NaK by a metallic diaphragm and the bearings are lubricated with the mercury, permitting the entire unit to be hermetically sealed.

NaK Pump

The NaK pump employs a permanent magnet rotor mounted on the CRU shaft, obviating the need for separate NaK lubricated bearings. The rotating magnetic field introduces eddy currents in the NaK which accelerate the fluid. The velocity is converted to pressure in the pump volute. This pump type was selected for its high reliability and simplicity. Efficiency was a secondary consideration.

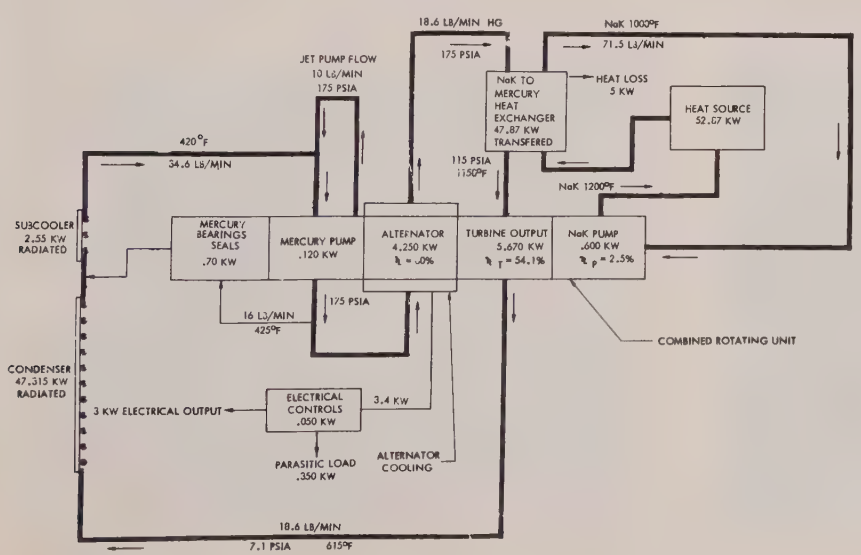

Fig. 10 — SNAP 2 cycle — schematic

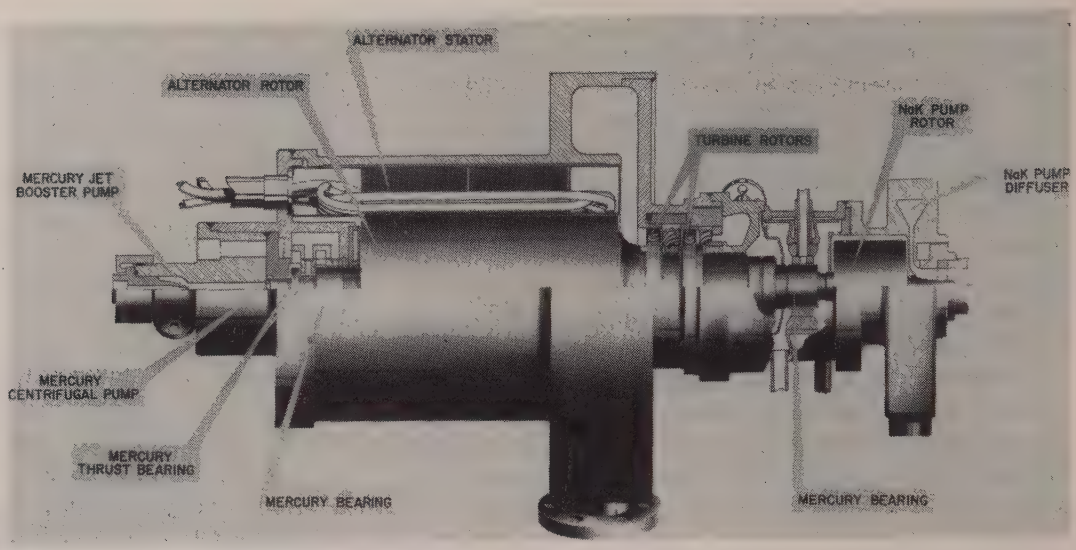

Fig. 11 — Combined rotating unit cut away

Table 3 - SNAP 2 Power Balance

Alternator Power	
Net power output	3.000 kwe
Parasitic load at rated output	0.350
Speed control	0.050
Total	3.400 kwe
Turbine Power	
Alternator $\frac{\text{output}}{\text{efficiency}}$	4.250 kwm
Bearings and seals	0.700
Mercury pump	0.120
Sodium pump	0.600
Total	5.670 kwm

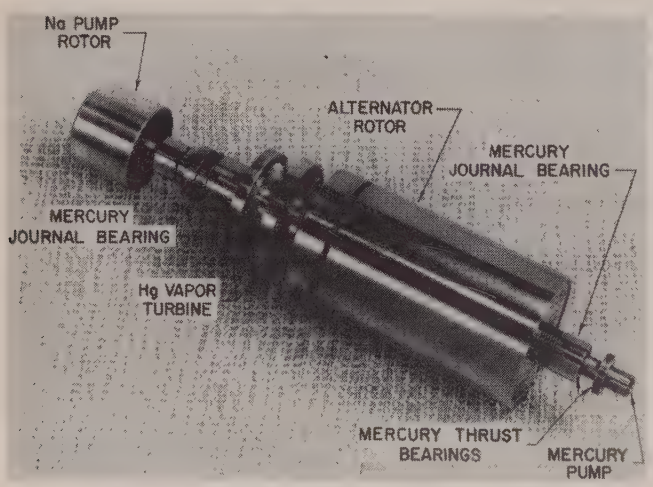

Fig. 12 — Combined rotating unit shaft assembly

Alternator

The alternator is a permanent magnet machine producing 3.4 kw at 2000 cps. The rotor is constructed of Alinco V permanent magnets and is unaffected by the high-temperature mercury environment in the CRU. The stator wound field coil is sealed from the mercury environment with a glass bore seal. The machine is a two-phase unit connected externally to produce a single-phase output.

Turbine

A full admission, two-stage, axial flow, impulse turbine extracts the energy from the mercury vapor. Two stages limit the pressure ratio per stage to a reasonable value and prevent formation of excessive moisture in the vapor as it traverses the turbine. Tests indicate that blade erosion from moisture is not a severe problem.

The SNAP 2 turbine dynamometer test package is shown in Fig. 13. From left to right are the second stage rotor, second stage stator (nozzle), first stage rotor, and first stage stator. Mercury vapor enters the first stage nozzle through the hole shown in the flat face of the first stage stator housing. Labyrinth seal grooves can be seen in the hubs of both the first and second stage rotors.

Mercury Pump

The mercury pump centrifugal impeller and the mercury-lubricated journal and thrust bearings are shown in Fig. 14. The pump impeller is only 0.30 in. in diameter. Because of the high rotation speeds, a pump discharge pressure greater than 175 psia is obtained despite the small impeller diameter. The major problem encountered in pumps of this type is the limited net positive suction head due to the low

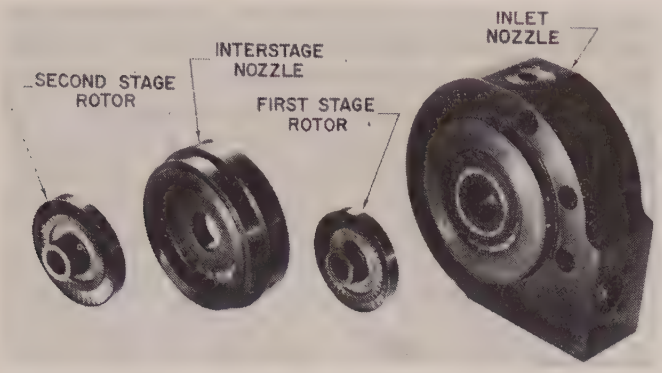

Fig. 13 — Turbine dynamometer parts

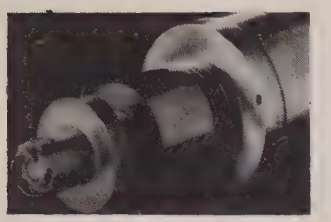

Fig. 14 — Mercury pump

condenser pressures and lack of any gravitational fluid head. This problem is solved by utilizing a jet pump to boost the pump inlet pressures.

Boiler

The boiler consists of a tube within a tube, with mercury in the inner tube and NaK in the annulus. An artificial gravitational force field results from the helical configuration and the use of turbulators in the mercury boiling section. Forces on the entrained droplets are on the order of 500 g. The 18-in. diameter boiler test loop shown in Fig. 15 is 30 ft long.

Heat transfer rates obtained during tests of the boiler were about 10, 000 Btu/ft^2-hr. These were obtained with temperature differentials of 325 -350 F at high mercury flow rates. Heat transfer rates are expected to increase through the use of increased pressure drop and velocities in the boiling realm.

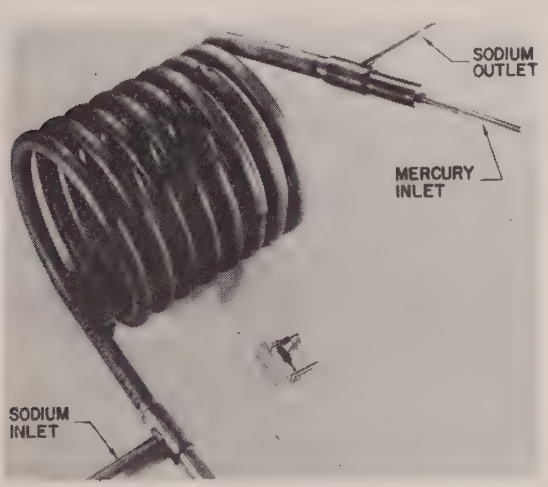

Fig. 15 — Boiler

Radiative Condenser

The condenser consists of tubes attached to a radiating surface. Mercury is condensed in the tubes and the heat transferred by conduction to the radiating surface. High vapor velocities are maintained in the tubes to drag the condensate through the condenser, thus maintaining flow stability and reasonable condenser inventories. Rotation of the vehicle will not be required to control condensation, as this can be accomplished entirely by viscous forces.

In order to prevent cavitation of the small mercury condensate pump, a subcooler section is employed in the radiator to cool the liquid mercury below the condensing temperature.

Control

A parasitic load speed control is employed. This control consists of a parasitic load in parallel with the vehicle load, with a frequency discriminator to sense speed and to govern the amount of parasitic load applied. Load is added if the frequency is too high and removed if too low. The alternator and reactor operate at all times near the design point, eliminating excursions and simplifying stability of the system. Parasitic controls are reliable and their development is straightforward.

Mercury Corrosion

The resistance of various materials to mercury corrosion is still under investigation, and progress to date is very promising. Many materials are available that easily contain mercury at the high cycle operating temperatures for long periods of time with little structural deterioration. A mass transfer problem, however, still remains. Mass transfer occurs as a result of containment materials dissolving in the liquid mercury and depositing out in lower temperature regions, the boiling sections, or flow restrictions.

Considerable materials evaluation testing has already been conducted. This has included more than 15, 000-hr of constant pressure convection loops in which boiling and condensing have simulated the action in the prototype mercury system. More than 300 glass capsule tests of many materials, surface treatments, and chemical additives have been evaluated for compatibility in boiling and condensing conditions.

The materials evaluation program is still under way. Based on the results to date, stellites, the 400 series, the

low nickel 300 series stainless steels, and the Haynes metals with suitable surface treatments, are promising for use in mercury systems.

Conversion Equipment Test Program

The major effort at Thompson Ramo Wooldridge has been in the development of the combined rotating unit (consisting of the turbine, the alternator, the bearings and two pumps), the boiler, and the control. Miniaturization of the individual components, as well as the high rotational speeds of the dynamic components, necessitated a (fine) balance between final design and performance. Considerable test experience on each component, as well as on the combined rotating units, has already been achieved.

These tests are summarized in Table 4. It should be noted that the tests include test time accumulated on the SNAP 1 program on components and CRU's that are similar in design characteristics but lower in power output than the SNAP 2 components. A summary of the present state of development of the major components is presented in Table 5. The data and operating hours are tabulated as of Feb. 1, 1960.

Combined rotating unit tests have been run at 40,000 rpm, utilizing mercury vapor to drive the turbine and mercury-lubricated bearings. The latest of thest tests was a 20-day performance test completed on Jan. 8, 1960. The speed was limited to 35,000 rpm to avoid the shaft critical speed associated only with this particular unit. No significant deterioration in performance occurred during the test, with one exception: the alternator rotor magnet strength decreased with time, causing a voltage reduction of about 2%. This has been attributed to the natural high-temperature aging of the magnet and can be avoided with proper preassembly treatment.

Table 4 - Component Development Tests

Component	Accumulated Test Time, hr
Alternator	1400
Bearings	1550
Mercury Pump	1050
Sodium Pump	60
Turbine	890
Boiler	270
Combined Rotating Unit	870*

*Includes a 20-day endurance run.

Table 5 - SNAP 2 Component Performance Status

Component	Efficiency, %		Power	
	Objective	Achieved	Objective	Achieved
Alternator	80	78	3.1 kw	3.6 kw
Bearings	NA	NA	600 w consumed	550 w consumed
Mercury Pump	10	30	240 w consumed	120 w consumed
Sodium Pump	1.8	2.4 (a)	443 w consumed	165 w (b) consumed
Turbine	55	46 (c)	5.16 kw	5.16 kw (d)

a. At full flow 5%.

b. No change at full flow.

c. Off-design data, measured at 2 kw.

d. Extrapolated.

Table 6 - Component Performance Deviations During 20-Day Endurance Test

Parameter	Mean	± One Sigma
Unit Speed, rpm	35,000	141.4
Alternator Power, w	2127	268
Turbine Inlet Temperature, F	1145.8	145
Turbine Inlet Pressure, psia	94.7	1.8
Turbine Exhaust Temperature, F	643.7	36.7
Condenser Pressure, psia	9.1	0.57
Boiler Inlet Flow, lb/min	15.03	1.2
Bearing Lubricant Flow, lb/min	18.39	0.58

During the test, some 30,000 data observations were made. Unit performance during this test is summarized in Table 6. The CRU is shown following initial testing and immediately prior to assembly for the 20-day run.

This test run was terminated because of an accidental short in the alternator field causing the load to decrease and the unit to overspeed. Disassembly of the unit showed no damage or deterioration of the unit due to the normal test operation, although some damage resulted from contact as a result of the excess speed.

Conclusions

The successful testing of the SNAP Experimental Reactor, a sodium to mercury heat exchanger, and a complete combined rotating unit has been demonstrated.

The next major step in the SNAP 2 development effort is the assembly of the CRU, boiler, and condenser into a complete power conversion system and the testing of the completed unit using a reactor as the heat source. Present status of the SNAP 2 development indicates that flight-type power systems will be available by 1963.

Potential missions which can use the SNAP 2 system include: surveillance satellites, communications satellites, space station power systems, lunar station power systems, and solar system probes.

Aircooling Versus Watercooling in

H. H. Haas
Klöckner Humboldt Deutz AG

RECENT publications on aircooling versus watercooling indicate that two items are growing to be apparent and should begin this presentation:

1. The remarkable design activity in the field of aircooled engines as is demonstrated by the many new models appearing increasingly on the market.

2. The increasing sale of aircooled engines all over the world with the surprising exception of the United States.

These two facts may indicate that the issue of "Aircooling versus Watercooling" is far from being settled.

A study of how the two cooling methods are spread reveals a rather puzzling picture (Fig. 1). Water and aircooled engines are used side by side for almost all applications from 1 to 4000 hp. Although a detailed analysis of this figure will be made later, it may serve to characterize the great span which is covered by aircooling. In fact the two extreme groups, namely the smallest, simplest, and cheapest engines as used for lawn mowers and the largest, most complicated and most expensive engines for aircraft are almost uniformly aircooled. On the other hand there is in between these two groups a wide range where the choice of the cooling system varies indiscriminately.

Obviously, the choice of the cooling system is still influenced in many instances by personal preference of the designer rather than by an impartial evaluation of the demands of the particular application.

Considering the increasing variety of aircooled engine design compared with the rather standardized features of the watercooled engine models, the picture is indeed confusing. An attempt is therefore made in this paper to review and clarify the various criteria of aircooled engines and put them, as far as possible, in relation to the needs of the agriculture and construction industry.

In comparing aircooling and watercooling emphasis is placed on the first and it is assumed that the design features of watercooling are known. Furthermore. priority is given to the diesel engine since it is this type of engine which, especially in agriculture and the construction industry, meets with growing interest.

Fig. 2 illustrates the variety in aircooled engine design and obtains a better survey, by giving a classification of the performance, depending on the specific design features. Although this chart is only slightly different from one already published in the past, it may be useful for the discussion.

The essential features of the various groups in Table 1 are roughly as follows:

1. Group A - Low-speed engines of low specific output, lowest price, long life, used primarily for continuous operation in industrial and agricultural applications.

2. Group B - High-speed engines of low output, compactness, medium life, low weight (due to high speed and light metal), used primarily for garden tractors and light applications in agriculture.

3. Group C - High-speed engines of medium output, low

Agricultural and Construction Equipment

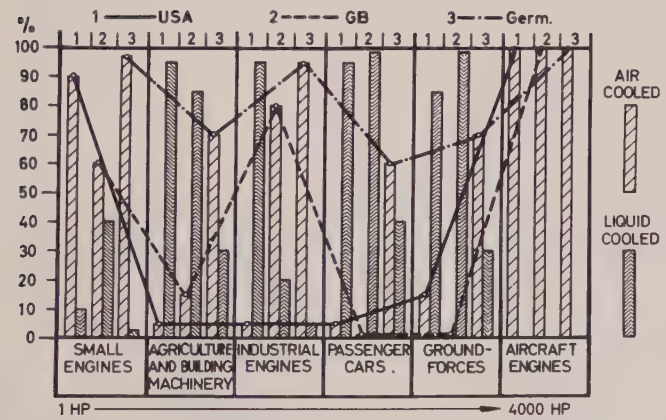

Fig. 1 — Internal combustion engines (1959), estimated percentages of air and liquidcooled engines

price due to mass production, long life, used for tractors, vehicles and equipment of all kind.

4. Group D - High-speed engines of highest performance, low weight high price, used primarily for military purposes. This group, however, may be of interest for high performance earthmoving equipment.

Application if the various groups in agriculture and building is roughly as follows:

1. Agriculture.

Garden and small tractors - Group B.

Medium-sized and heavy-duty wheel tractors - Group C.

Combines, hay balers, etc. - Group C.

Stationary (pumps, blowers etc.) - Groups A, C.

2. Earthmoving and building industry.

Small auxiliary equipment, cement mixers, etc. - Groups A, C.

Crawler tractors, loaders, excavators, scrapers etc. of medium size - Group C.

Earthmoving equipment of high performance (not yet equipped with air-cooled engines) - Group C (D).

Fig. 2 shows a comparison of Groups A, C and D and the great extent to which the specific output per cu in. depends on the design adopted.

The hp/cu in. reaches from 0.19 to 0.5 hp/cu in. Compared with the watercooled engine the specific output of the aircooled engine is in general 5-15% lower. If the design is especially elaborate, the difference may be smaller, and vice versa. This difference is due to the lower breathing efficiency and to the somewhat larger distortion of the cylinder liner when the engine operates at full load.

The power range of the aircooled engine has recently been extended upwards and downwards. The smallest engine has 4 hp at 3000 rpm. The upeer limit of commercial engines has been moved up to 600 hp with exhaust turbocharger. This progress is not due as much to aniincrease of cylinder size as to higher speed and higher bmep.

Bmep of 170 lb/sq in. have been successfully run on high-performance aircooled engines of Group D. However, the resultant peak pressure raises the mechanical and thermal stresses in the cylinder head close to safe limits. Bmep beyond 200 lb/sq in. are the domaine of liquid-cooled engines with a rigid unit-bloc structure.

Likewise is the maximum aircooled cylinder size limited

Table 1 - Average Characteristics of aircooled Diesel Engines

	Industrial A	Small Size Tractor B	Medium Size Multi-Purpose C	High Performance Military D
Bore, In.	3.0 to 4.5	2.7 to 3.4	3.5 to 4.7	5.1 to 6.1
Stroke, In.	3.0 to 4.5	3.5 to 3.8	4.4 to 5.5	5.5 to 6.9
Displacement, Cyl-Cu In.	21 to 80	20 to 33	47 to 90	113 to 204
Hp/Cyl	2.5 to 12	6 to 12	12 to 28	27 to 62
Number of Cyl	1 to 8	1 to 2	1 to 12	9 to 16
Hp/Engine	2.5 to 96	6 to 24	12 to 330	245 to 750
Speed, rpm	1200 to 1800	2000 to 3000	2000 to 2500	2000 to 2800
Hp/Cu In.	0.12 to 0.19	.26 to 0.36	0.23 to 0.32	0.24 to 0.55
Lbs/Hp	106 to 20	19 to 13	49 to 9	7 to 4.5
BMEP, psi	60 to 85	43 to 65	78 to 122	86 to 138
Piston Speed, Ft/Min.	750 to 1300	1350 to 1850	1650 to 2120	2000 to 2300
Cycle	4 - stroke	2 - stroke	4 - stroke	4 - stroke

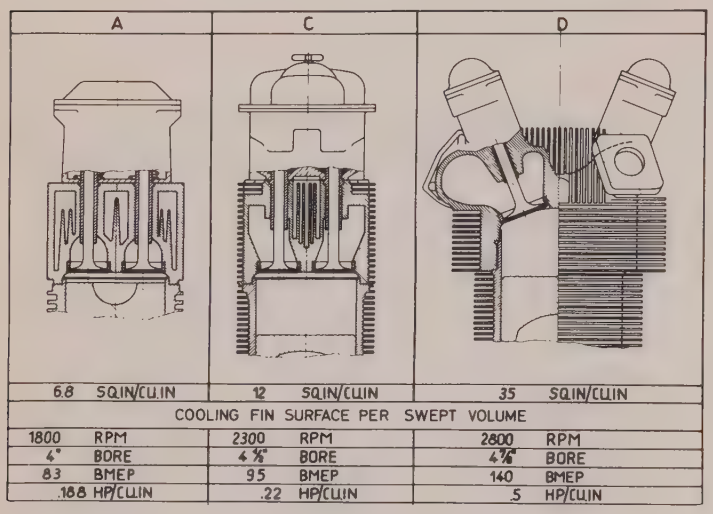

Fig. 2 — Comparison of three cylinder units

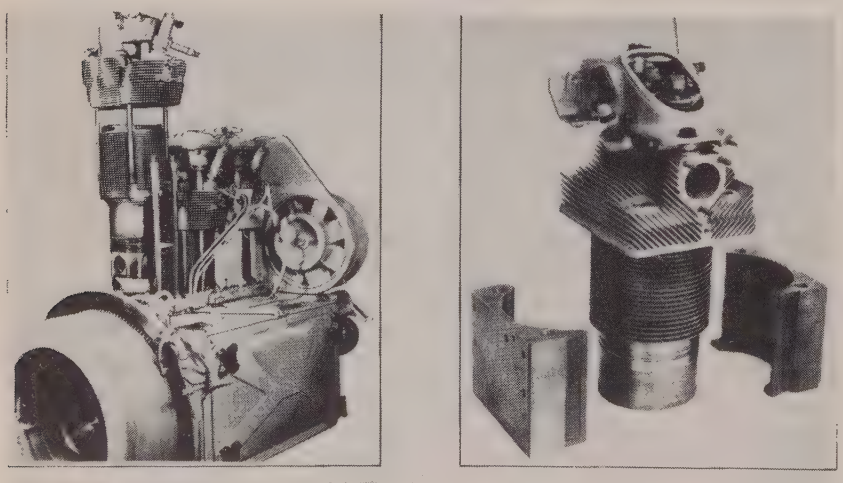

Fig. 3 — Head/liner connection

primarily by thermal problems, and a bore size beyond about 6.30 in. for both gasoline and diesel engines is not advisable.

The combustion principle is of particular importance to the aircooled engine. Inherently, the direct injection system has a lower temperature level and relieves the cooling problem. Also, accommodation of the injection nozzle is easier than arrangements with a precombustion chamber or swirl chamber. On the other hand the clogging problem of multi-hole nozzles in high-performance air cooled engines requires careful attention. Also, it is difficult to achieve smooth operation with direct injection and aircooling because of the poor insulation characteristic of a finned cylinder unit. Recently some remarkable designs of direct injection systems have been developed (MB, OM, Guldner) which evidently are aimed at utilizing the advantages of this principle. But these new engines are characterized by relatively low speeds. It is interesting to note that the majority of aircooled engines in Germany are still using the antichamber type combustion with its characteristic smooth operation, suitability for high speed, and insensitivity against fuel variations. Undoubtedly this system has its merits for application in agriculture and earthmoving equipment especially when used oversea. In any case it should be said that the choice of the combustion principle is one of the essential factors to be considered if a change from watercooling to aircooling is planned.

Design Features

The following design criteria may illustrate that a reasonable compromise between performance and durability on the one hand and price and weight on the other is much more difficult to be achieved for aircooling than for watercooling.

Fig. 2 represents three different designs of the critical section between the valves and the head/liner connection. The figure shows that the cylinders of Group C with through bolts permit a smaller cylinder spacing than the screwed connection of Group D. With watercooled engines it is usually easier to provide adequate water distribution at the bridge between the valves. The problem is more difficult with aircooled engines. Only a careful study of the fin arrangement and airflow pattern in this most critical area permits adequate control of the temperature level. A maximum number of fins with a maximum of surface should be located as close as possible to the bridge between the valves and the exhaust port. Hot spots, restriction of the heat flow and of the cooling air passage near the injection nozzle or the combustion chamber require a thorough investigation.

The high performance of Group D is accomplished by using an aluminium alloy of high temperature strength for the cylinderhead, inclined valves arranged at an angle to the engine axis permitting ample finning between the valves, and close fin spacing of 160/1000 in. through the shell moulding process. The engine of Group A has a cast iron cylinderhead, parallel valves, and fins with almost twice the fin spacing (250/1000 in.) of D which results in low manufacturing cost. It is obvious that the high-performance design of Group D involves substantially higher cost for material. Also, machining requires a larger cylinder spacing.

Design C is a compromise using aluminium for the cylinderhead, parallel or only slightly inclined, and a medium fin spacing of 220/1000 in. It is a characteristical example for a decent design compromise suitable for mass production and good performance.

Any type of cylinderhead requires high air velocities in between the valves without undue power loss. Only a careful design of the air duct system, the baffles, and fin configuration will ensure this requirement. Adequate material sections with respect to heat transfer and mechanical stresses are of great importance.

On large-size watercooled high-speed engines the number of valves can be increased and thus the volumetric efficiency improved and the thermal and mechanical stresses reduced. With aircooling more than two valves are not advisable, as the cooling fin layout would otherwise be impaired.

An advantage in favor of the aircooled individual type cylinderhead is the easier control of the casting which ensures the desired cooling effect. In contrast it is very difficult to eliminate in watercooled block-type cylinderheads casting offsets which may lead to considerable trouble in the cooling water circuit.

The cylinder liner and its ability to retain its shape under various operating conditions is of particular importance to the performance of aircooled engines. Several methods for connecting cylinder head and crankcase and for sealing the combustion chamber have been developed.

The method of using through bolts (Fig. 3) can be regarded as the standard design. It is cheap and permits a minimum cylinder spacing. On the other hand, sufficient rigidity of crankcase, cylinder liner, and cylinderhead is essential to withstand and compensate the variable tension loads of the through bolts originating from changing operating conditions.

Some manufacturers of aircooled diesel engines have started securing their cylinders to the crankcase, free from longitudinal stress. Various solutions are used. For instance, at Daimler-Benz, the head/liner unit is supported by the cooling air duct system (Fig. 3). The cylinder is screwed into the head and can freely expand in operation. Deformations should occur only at the head.

The layout of the Paxmann shown in Fig. 4a, combines the cylinderhead and cylinder in a 1-piece aluminium casting and uses a pressed-in cast iron sleeve. Head and liner are free to expand.

Fig. 4b shows a heavy-duty engine of Group D (Continental tank engine) which is designed like an aircraft engine: a steel liner with aluminium fins is screwed and shrunk tight

Table 2 - Influence of Design on Cylinder Spacing/Bore ratio

Manufacturer	Engine model	Cylinder D bore D	Cylinder spacing A	Construction	A/D
Deutz	FL 514 in-line	110 dia	150 mm	through bolts	1.36
Deutz	FL 714	120 dia	174 mm	through bolts	1.54
DB	MB 862 in-line	115 dia	184 mm	cylinder suspended	1.6
Continental	V AVDS 1790 V	5.75 dia	9 in.	cylinder suspended	1.55

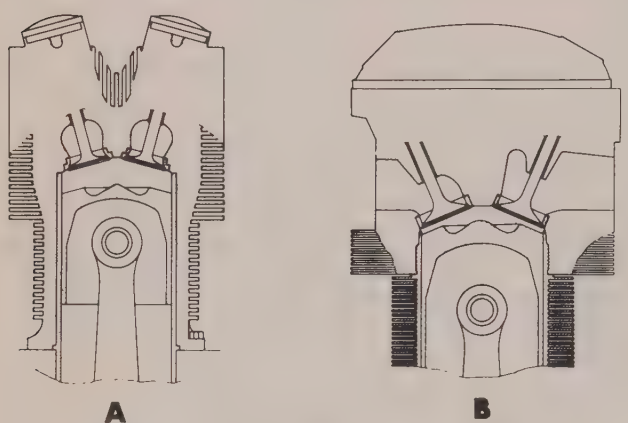

Fig. 4 — Layout of head/liner connection

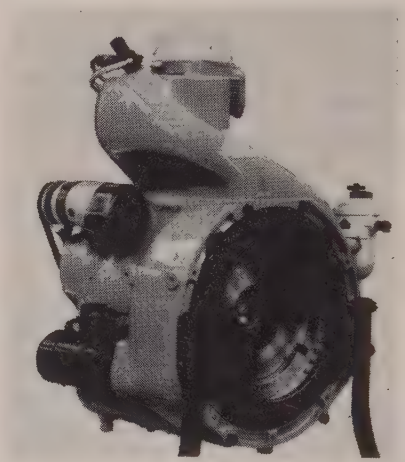

Fig. 5 — Flywheel blower

into the aluminium cylinderhead.

All these later designs embody the advantage of no deforming or bending forces distorting the liner of head. They also permit equal fin depth over the entire cylinder circumference without cut-outs or interruptions. These stress-free designs however, demand larger cylinder spacing and are more expensive. A comparison illustrating the influence of the various designs on the cylinder spacing/bore ratio is given in Table 2. For heat transfer and form stability the stress-free cylinder liners with aluminum fin jacket are very favorable since aluminium improves temperature uniformity around the circumference and in longitidinal direction of the liner, and provides quick transfer of the heat to the cooling air. In fact, compared with cast iron this type of liner lowers the temperature on the working surface by as much as 100 F and the temperature difference on the circumference by 40 F.

Aircooling also offers far more variations of the cooling fan than watercooling. It is possible to use either pressure cooling or suction cooling. The latter principle results in a somewhat better temperature distribution but requires a 10% larger size fan for discharge of the hot cooling air.

Small engines of Groups A and B use the cheap flywheel blowers (Fig. 5) which are the least expensive and are practicable up to a maximum of three cylinders.

Separately driven blower or suction fans, both designed as axial fans, are usually positioned at the engine front end, particularly for automotive engines (Fig. 6). However, in this case a uniform cooling air distribution, especially with multi-cylinder engines, can only be accomplished by careful design of the air duct system.

The most efficient and compact layout with superior air distribution is a suction fan above the engine as shown by the Continental tank engine. However, this arrangement is suitable only for V-engines and is rather expensive (Fig. 7).

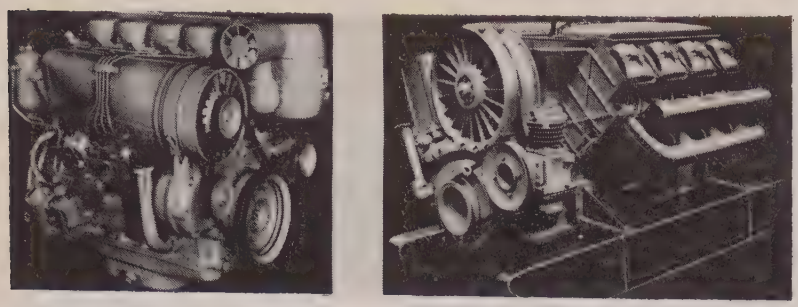

Fig. 6 — Axial fans

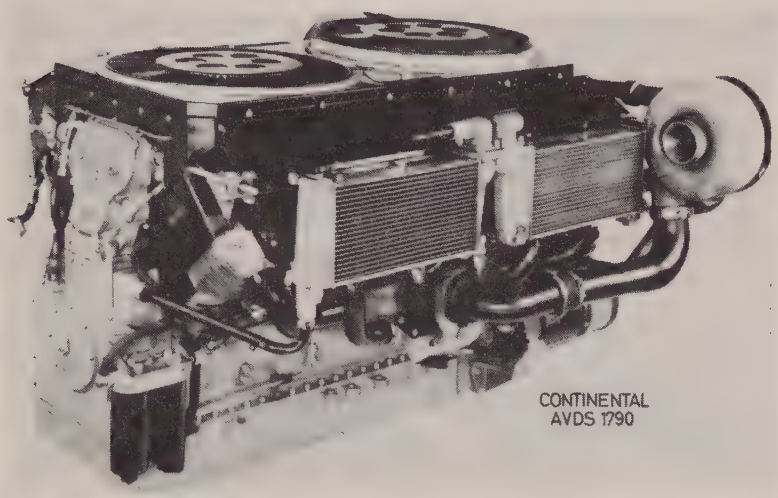

Fig. 7 — Suction fan

Centrifugal fans have good efficiency when they blow directly onto the individual cylinders. With this arrangement, adopted for many passenger cars like VW, Steyr, and Fiat, the fan input can be reduced to less than 4% of the engine output. (Fig. 8.)

A highly efficient cooling system is expected to suit the engine's cooling requirements automatically. In watercooled engines thermostats are provided in the water circuit to control the water temperature. Aircooled engines of simple design (Groups A and B) may dispense with cooling air control as the inherent high liner temperature of aircooled engines generally avoids condensation also as partial load and low ambient temperatures.

Modern aircooled engines of higher output (Groups C and D) are equipped to a growing extent with cooling air control. Although this air control is more expensive than cooling water thermostats, such an air control permits reduction of the part-load fuel consumption by reducing the cooling air flow. This control is achieved mainly by a controllable hydraulic coupling built into the blower drive and influenced by a thermostat which is depending on load and ambient temperature (Fig. 9). Incidentally, this arrangement is also proposed for high-performance water-cooled engines in order to obtain favorable consumption at partload and high speed.

Another solution is a cooling air control by thermostat-controlled flaps (Fig. 10) installed either in the air duct or in the guide vane assembly of the cooling fan. With these

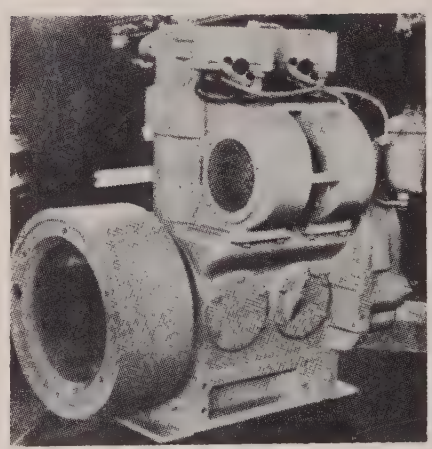

Fig. 8 — Fan with twin rotors

arrangements it must be assured, however, that the flap movement is not hampered by freezing water or dirt formation. The temperature feeler is located either in the cooling air exit or in the exhaust manifold.

In addition to the major components already discussed, there are many other parts which require particular attention with aircooling.

For instance, the crankcase has to have an especially rigid structure to compensate for the missing cylinder block. This is particularly important when the engine is a structural member of the chassis as for instance in tractors and earth-moving vehicles. Means of ensuring the necessary rigidity

include: crankcase split below the crankshaft center line, a tunnel-shaped crankcase, or a crankcase with special reinforcements through box-like elements. (Fig. 11).

Additional oil cooling is advisable on automotive engines where more heat is transferred to the oil due to the hotter cylinder liner and valve rocker chamber.

The increased flexibility and heat expansion of the cylinder unit under load must be taken into account in the layout of the valve operating mechanism which may require hydraulic valve tappets.

The oil tightness of the aircooled engine is important to prevent the cooling fins from clogging. Certain standard solutions for pushrod tubes and rocker covers have been developed which fairly meet all requirements in this respect.

Bulk and Space Utilization

Considering the engine without its cooling system, the watercooled version can be built more compactly than the aircooled one. The watercooled engine permits smaller cylinder center distances than the aircooled engine and the specific performance of the aircooled engine is somewhat lower than that of the watercooled engine. The watercooled engine, therefore, seems to require less space than the aircooled one. However, considering the engine plus its cooling system as a unit, both types of engine require about the same space. The watercooled engine offers the advantage that the bare engine is somewhat smaller and that the cooling system can be installed separately wherever the space is available. On the other hand the water cooling system is more complicated and has more components which are liable to develop trouble, such as hoses, and clamps.

The horsepower per cubic foot of total bulk is a good measure of the engine's compactness. It varies from 1 - 3 hp cu ft. in the single- and 2-cylinder engines of Groups A and B to 2.5 - 7 hp cu ft. in the larger sizes of Groups C and D, and it may be as high as 10 hp/cu ft. or more in tank engines.

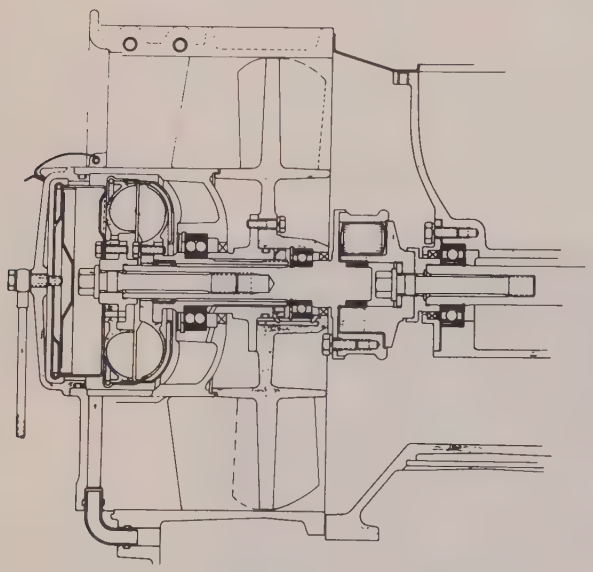

Fig. 9 — Hydraulically controlled cooling blower

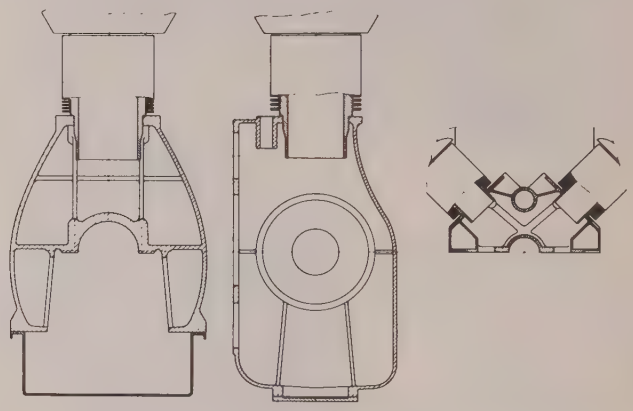

Fig. 11 — Design features of crankcases for aircooled engines

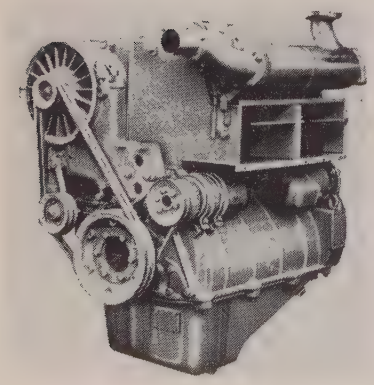

Fig. 10 — Cooling air control by thermostatically operated flaps

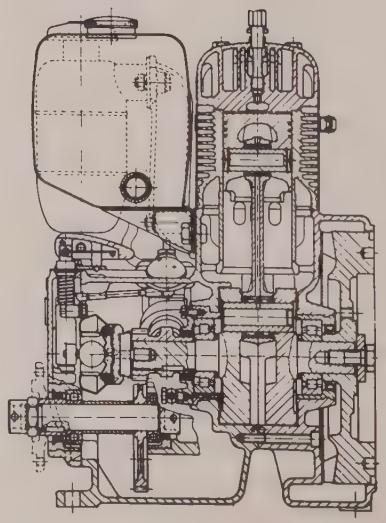

Fig. 12 — Motorenfabrik München-Sendling model DL 107

Weight per Horsepower

Since the weight of aircooled engine includes the weight of the cooling system, a weight comparison to the water-cooled engine can only be made when its cooling system is included. As mentioned already, there is no appreciable difference in weight between the two types of engines. The engine weight depends on combustion principle, speed, power range and other factors more than on the type of cooling.

The weight per horsepower (referred to rated output) on aircooled diesel engines is comparable to watercooled engines ranges between 40 lb/hp for the 10 hp engines of Group A and about 8 lb/hp of the 200 hp engines of Group C. In the high-performance Group D a 550 hp engine, for instance, has a horsepower weight of 4 lb/hp. These values refer to bare engine without fan or cooling system in order to permit a correct comparison with watercooled engines.

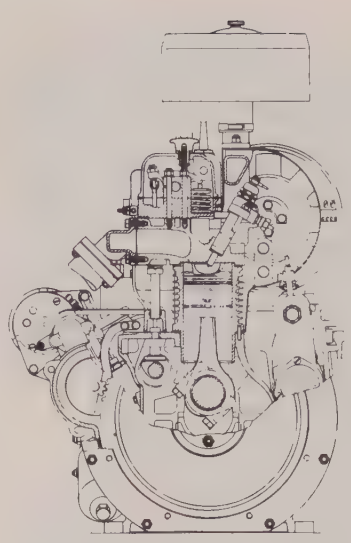

Fig. 13 — Petters, Ltd. model PC 4

Engine Models and Applications

The following demonstrates the large variety of aircooled engine design.

Motorenfabrik Munchen-Sendling, Model DL 107 (Fig. 12) Single-cylinder 2-stroke diesel engine of small output. Group B.

Basic specifications:

Bore/stroke	2.56/2.95 in.
Piston displacement	15.2 cu in.
Output	4 hp
Maximum speed	3000 rpm

Design features:

One of the smallest diesel engines. Tunnel-shaped crankcase. Built crankshaft supported in anti-friction bearings. Governor on crankshaft. Flywheel fan.

Petters Ltd., Model PC 4 (Fig. 13) - Four-cylinder 4-stroke diesel engine, in line. Group A.

Basic specifications:

Bore/stroke	3.00/3.00 in.
Piston displacement	85 cu in.
Output	20 hp
Maximum speed	3000 rpm

Design features: Direct injection, combustion chamber in piston, cast iron cylinderhead, inlet and exhaust parts on opposite sides, shrouded inlet valve, cylinder liner with short fins and wide fin spacing.

Klöckner-Humboldt-Deutz A. G., Model T1L 110 (Figs. 14 and 15) - Single-cylinder 2-stroke diesel engine, light weight. Group B.

Basic specifications:

Bore/stroke	3.16/3.94 in.
Piston displacement	30.5 cu in.
Output	9 hp
Maximum speed	2500 rpm

Design features: Direct injection, pear-shaped combustion chamber in cylinderhead, crankcase scavenging, flywheel fan, spring force starter on flywheel. The engine uses aluminum die castings to a wide extent. The cylinder is suspended and free to expand.

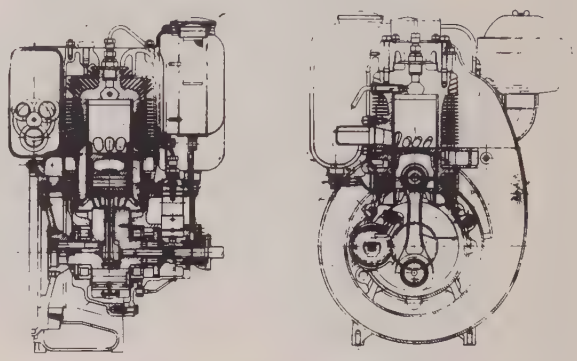

Fig. 14 — Schematic of Klöckner Humboldt Deutz model T1L 110

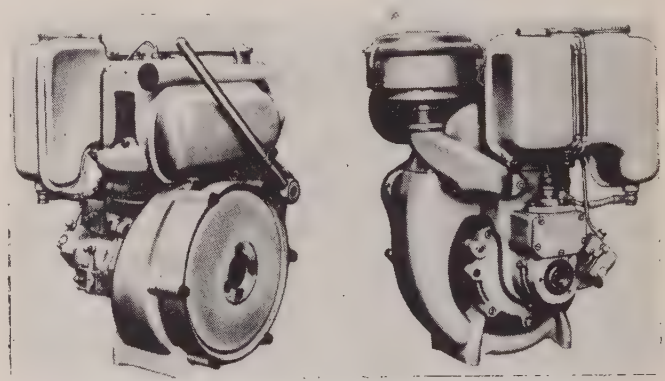

Fig. 15 — Klöckner Humboldt Deutz model T1L 110

Wisconsins Motor Corp., Model VH 4 (Fig. 16) - Four-cylinder Otto V-engine. Group C.

Basic specifications:

Bore/stroke	3.25/3.25 in.
Piston displacement	108 cu in.

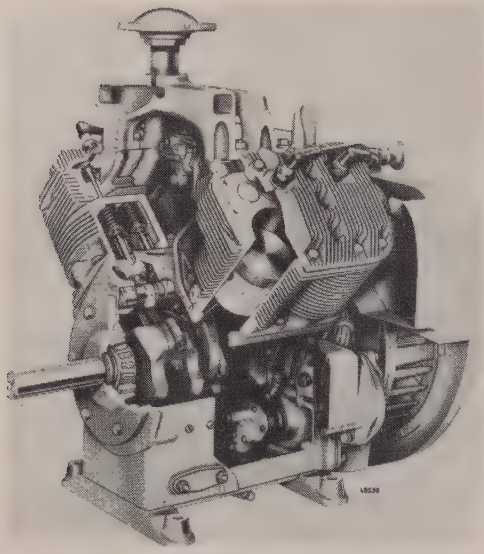

Fig. 16 — Wisconsin Motor Corp. model VH 4

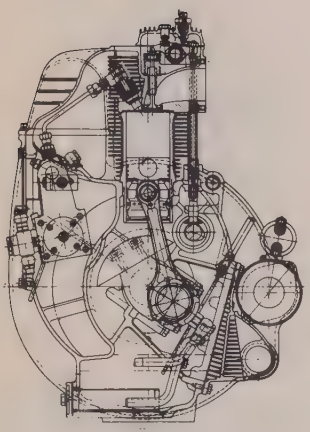

Fig. 17 — Güldner Motoren-Werke model 3 LKN

Maximum gross output 30 hp
Maximum speed 2800 rpm

Design features: Tunnel-shaped crankcase. Crankshaft carried in two anti-friction bearings. Four offset crankpins (one connecting rod per crankpin). Flywheel fan.

Güldner Motoren-Werke, Model 3 LKN (Fig. 17) - Three-cylinder 4-stroke diesel engine. Group C.

Basic specifications:

Bore/stroke	2.96/3.97 in.
Piston displacement	77 cu in.
Output	25 hp
Speed	2600 rpm

Design features: Direct injection, combustion chamber in piston, fin-cooled nozzle holder, pushrods on cooling air exit side, Alfin cylinder, tunnelshaped crankcase with diagonal division for main bearings, flywheel fan, crankcase cover designed as oil cooler.

Klockner-Humboldt-Deutz A. G., Model F2L 712 (Fig. 18) - Two-cylinder 4-stroke diesel engine. Group C. Belongs to a standardized range of in-line engines of 1, 2, 3, 4 and 6 cylinders.

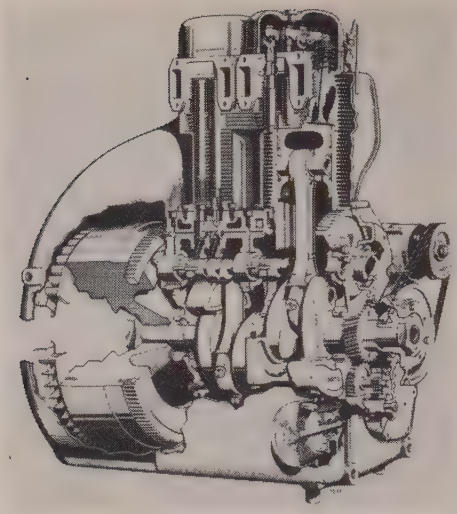

Fig. 18 — Klöckner Humboldt Deutz AG model F2L 712

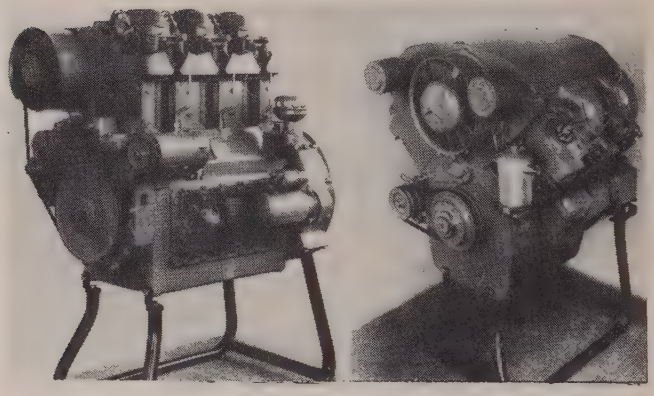

Fig. 19 — Daimler Benz AG models MB 863 and MB 864

Basic specifications:

Bore/stroke	3.73/4.73 in.
Piston displacement	104 cu in.
Output	30 hp
Speed	2800 rpm

Design features: Aluminium cylinderheads with integrally cast and insulated swirl chamber. Tunnel-shaped crankcase with central main bearing cap secured from below. Flywheel-type radial fan.

Daimler-Benz A. G., Models MB 863 and MB 864 (Fig. 19) - Four-stroke diesel engine. Three-cylinder in-line, 4-cylinder V. Group C. Standardized range of 1, 2, 3, and 4 cylinders.

Basic specifications:

Bore/stroke	4.53/5.32 in.
Piston displacement	267 and 355 cu in. respectively
Continuous output B per cylinder to DIN 6270	20 hp
Speed	2000 rpm

Design features: Direct injection. Aluminium cylinder-

head with screwed-in cast iron cylinder liner, freely suspended. Parallel valves arranged in a plane at a right angle to the crankshaft.

Carl Kaelble GmbH., Model LM 215 v (Fig. 20) - Four-cylinder 4-stroke diesel engine, in line. Group C. Range consisting of 2, 3, 4 and 6-cylinder in-line engines and 8-cylinder V-engine.

Basic specifications:

Bore/stroke	4.53/5.13 in.
Piston displacement	329 cu in.
Continuous output B to DIN 6270	66 hp
Speed	1800 rpm

Design features: Cylinderhead with interesting fin arrangement and cooled exhaust duct, inclined valves.

Tatra (CSR), Model 928 (Fig. 21) - Eight-cylinder 4-stroke V diesel engine. Group C.

Basic specifications:

Bore/stroke	4.72/5.13 in.
Piston displacement	718 cu in.
Output	180 hp
Speed	2000 rpm

Design features: Hydraulic coupling for cooling fan. Temperature feeler behind the last cylinder.

Davey, Paxmann & Co. Ltd., Model Vega 8YGA (Fig. 22) - Eight-cylinder 4-stroke V diesel engine. Group C.

Basic specifications:

Bore/stroke	6.06/6.47 in.
Piston displacement	1530 cu in.
Output	306 hp naturally aspirated
Speed	2000 rpm

Design features: Cylinderhead and cylinder cast from aluminium in one piece with a shrunk-in liner. Chaindriven cooling fan with temperature control.

The 12-cylinder version of this model delivers 600 hp when supercharged and is thus the most powerful aircooled industrial engine.

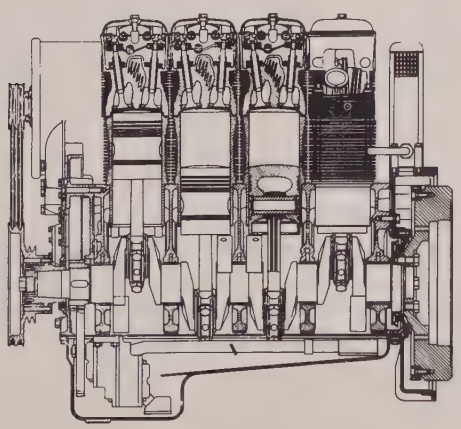

Fig. 20 — Carl Kaelble GMBH model LM 215V

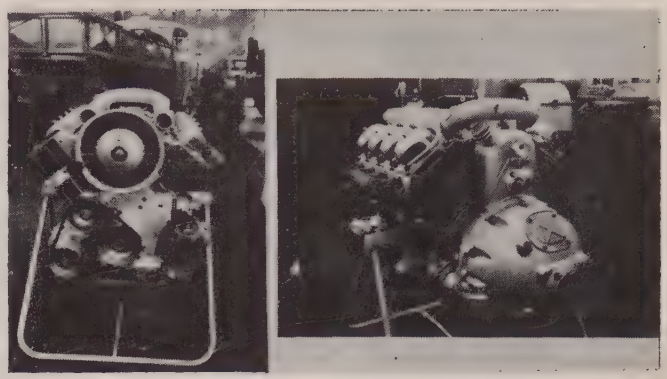

Fig. 21 — Tatra (CSR) model 928

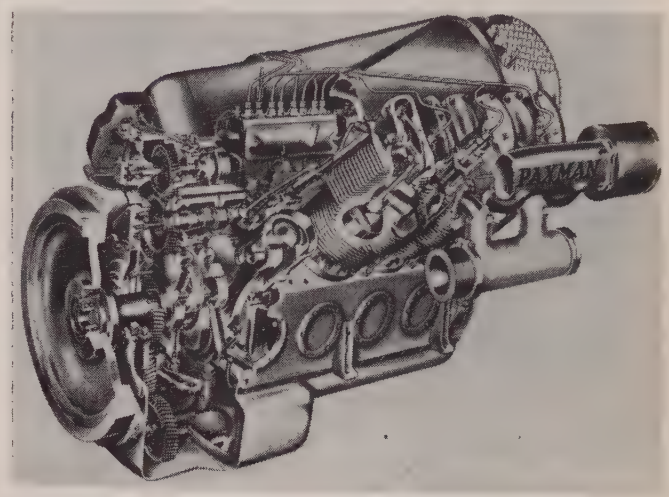

Fig. 22 — Davey, Paxmann & Co., Ltd model VEGA 8YGA

Manufacture and Operation

Manufacturing cost - The manufacturing costs of an engine depend on the weight of the raw material, the machined weight, the type of materials used, the degree of machining accuracy, time for assembly, and the like. For aircooled engines more light metal is often used. High-performance densely finned liners and cylinder heads are comparatively expensive castings. The cooling air fan is more expensive than the cooling water pump and the fan of a watercooled engine. On the other hand, a watercooled block and cylinder head are very complicated castings involving higher scrap rates and set-up cost.

A great advantage of the aircooled engine is the use of the identical cylinder unit for a wide range of standardized engines (Fig. 23) which permits mass production tooling and thus results in low machining costs. (Fig. 24).

The manufacturing costs of aircooled engines are slightly higher than those of watercooled engines but the manufacturing equipment in general is slightly cheaper and simpler. However this largely depends on the Group to which the engine belongs; aircooled engines of Group A with one and two

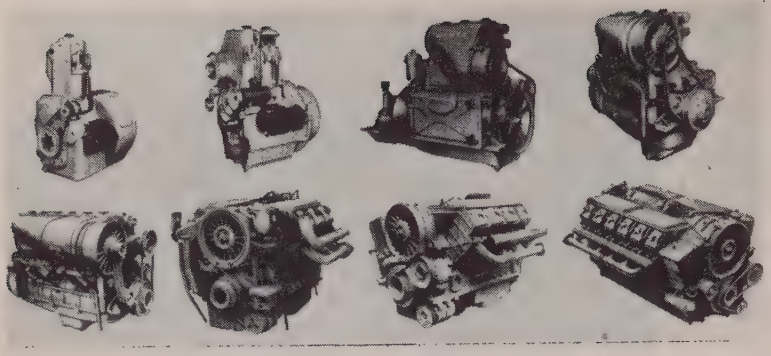

Fig. 23 — Engines built on building block principle

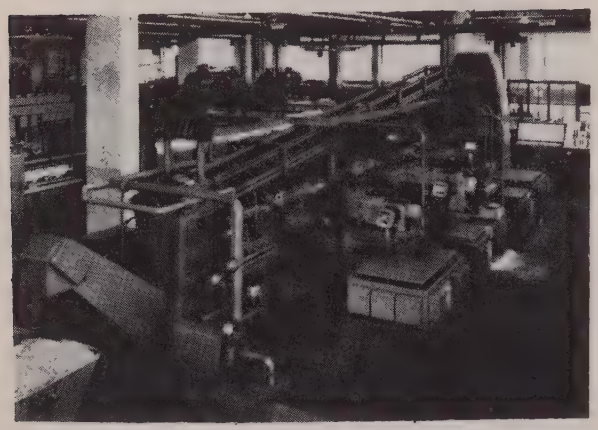

Fig. 24 — Cylinder head transfer line

cylinders may be even cheaper than comparable watercooled engines including the cooling system.

Spare Parts Service

The "building block principle" is of advantage not only to manufacturing but, also to the spare parts service. In fact, engines with one to 12 cylinders can be serviced with a small stock of identical parts. Builders using tractors, trucks, earthmoving machinery, or generator sets of varying horsepower but of an identical basic engine model are able to substantially simplify their replacement and overhaul procedures. In contrast, users of watercooled engines, built on the conventional cylinder block principle where each engine size has another cylinder block, must keep cylinderheads, gaskets and numerous other parts of different designs on stock. Fig. 25 shows, for instance, a building site using 16 different vehicles and pieces of equipment developing between 15 and 200 hp, which are all driven by engines of the same basic model (Deutz FL 514/614).

The building block principle is also very suitable for export to overseas, especially for underdeveloped countries where savings in tooling, stockparts, maintenance, and training of service personnel are essential.

Before switching to the statistics, the properties of the aircooled engine which, apart from design, appear to be of particular importance for use in agriculture and earthmoving industry will be pointed out.

Reliability of Operation

In this respect aircooling has definite merits:

1. Absence of any leakage on hoses, water pump, radiator, cylinder gasket.
2. Ability to operate satisfactorily at practically all existing ambient temperatures without the necessity for making special provisions. Frost damage is eliminated.
3. Outstanding emergency capability which permits the aircooled engine to continue operation in the event of a cooling fan drive failure, compared to the instant breakdown of a watercooled engine when a defect develops on any part of the cooling system.
4. Dispense of anti-freezes, cooling water and control equipment for pressure cooling. Elimination of corrosion on cylinder liner and crankcase through cooling water.
5. Elimination of cooling trouble through impurities in the water. Clogging up of the cooling fins of an aircooled engine by sand and dirt affects engine performance only slightly, whereas clogging the air ducts of a radiator results in boiling and complete stoppage of the engine.
6. Independence of the cooling effect from altitude, respectively from the boiling point of a liquid coolant, which may require an oversized radiator for high altitude.
7. Insensitivity to mechanical damage by blows, shocks, and vibration, compared with the very vulnerable radiator and hose system of the watercooled engine.
8. No need for frequent overhaul on radiator, thermostat and hoses during field operation.

Considering that by switching from watercooled gasoline engines to the aircooled diesel approximately 20% of failures due to the cooling system and the about 20% failures due to the ignition system, are eliminated, the growing popularity of the aircooled diesel in agriculture, earthmoving and building industries should become quite comprehensible.

The higher cylinder liner temperature of aircooled engines at part-load has also a favorable effect on the wear rate.

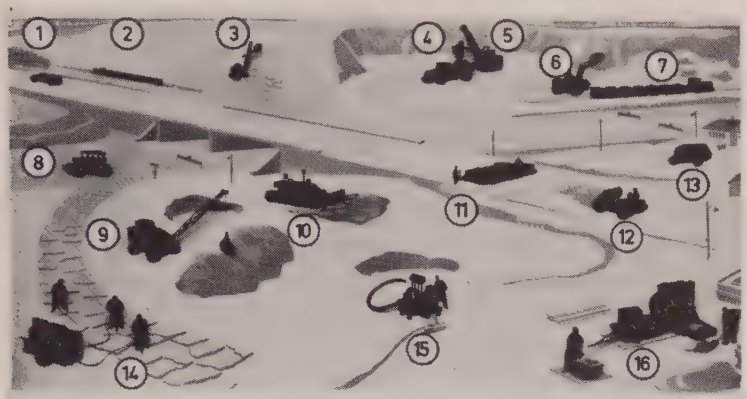

Fig. 25 — Building site using one single engine series

The cold start behaviour of aircooled engines, especially with cooling air control, is more favorable than that of watercooled engines. The mass surrounding the combustion chamber is smaller due to the absence of the cooling water jacket so that less compression heat is lost during the starting procedure.

Operating Conditions

The proper function of an engine depends largely on the roundness of the cylinder liner, the operating clearance between piston and cylinder, the tightness of the piston rings, and the sealing pressure between cylinder head and liner. The larger the actual temperature differences of the various components are, the more distortion and deformation may impede the satisfactory function of the engine.

Factors which are more difficult to control on aircooled than on watercooled engines include:

1. The great temperature difference between the cooling air inlet and exit side and between the upper and lower end of the cylinder liner.

2. Uneven distribution of the cooling air between the various cylinders.

3. Mechanical deformation of the engine components through the combustion forces.

The great variety of designs already discussed originated from the desire to tackle these problems.

Noise

The water jacket surrounding the combustion chamber of the watercooled engine has a sound absorbing effect, while the vibrating cooling fins of the aircooled engine tend to transmit the sound to the surrounding air. Accordingly, the watercooled engine is inherently superior to its aircooled rival with respect to smooth and quiet operation. However, careful research work made it possible to reduce the noise of the aircooled engine considerably. By providing a soundproof engine compartment - although this adds to the cost - noise can be practically eliminated. Automobiles equipped with modern aircooled engines and well insulated, such as the new Chevrolet Corvair and the Deutz Magirus Bus, operate at a noise level equal to any watercooled vehicle.

Cost of Development

The success of the aircooled engine in general and of the aircooled diesel in particular depends on careful design and development. While watercooling can be brought to satisfactory results with comparatively small research expenditure, aircooling requires an exact knowledge of the thermal problems, extensive practical experience, and very elaborate tests under all existing conditions. Thus, higher development cost and a longer development time are to be taken in account when aircooled engines of competitive performance and durability are desired.

In the USA aircooling plays a subordinate role, except for certain military applications, such as tanks, and a first step in car design, the Corvair built by Chevrolet.

Undoubtedly this inconclusive situation is influenced by the passenger car. In Germany after the war the small and cheap passenger car found wide acceptance. These cars have been mostly equipped with aircooled engines developed during the war. Thus this type of cooling system was introduced to wide circles. This contributed certainly to the remarkable success of aircooling in the agriculture and construction industry, as well as in many other fields, because everybody knew already that aircooled engines can operate satisfactorily. It should also be pointed out that it is the simple and robust engine of medium output where aircooling is prevailing in Germany while the heavy-duty automotive en-

gines, especially when supercharged, are still predominantly watercooled.

In underdeveloped countries the aircooled diesel engine is finding growing acceptance on account of its robustness as well as simple maintenance and parts stock-keeping.

The following diagrams give a clear picture of the development in Germany. There is, unfortunately, only little information available for England and USA.

Statistics

Air cooling versus watercooling in farm tractors in Western Germany, (Figs. 26 and 27). The percentage of air cooling in all farm tractors of German origin sold in Germany rose from 20.3% in 1951 to 54.9% in 1959.

Air and watercooling in construction machinery displayed at the Hanover Fair 1949 - 1960 (Fig. 28 - The Technical Fair at Hanover is one of the greatest displays of building machinery of all kinds. A census on how many of these machines operate with aircooled and how many with watercooled engines gives the following picture:

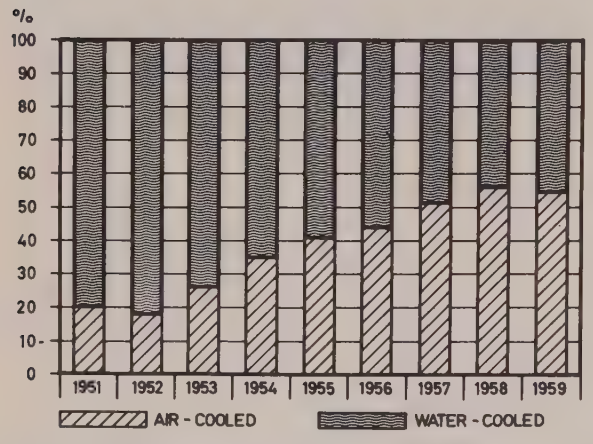

Fig. 26 — Agricultural tractors sold in Western Germany; percentages of air and watercooling

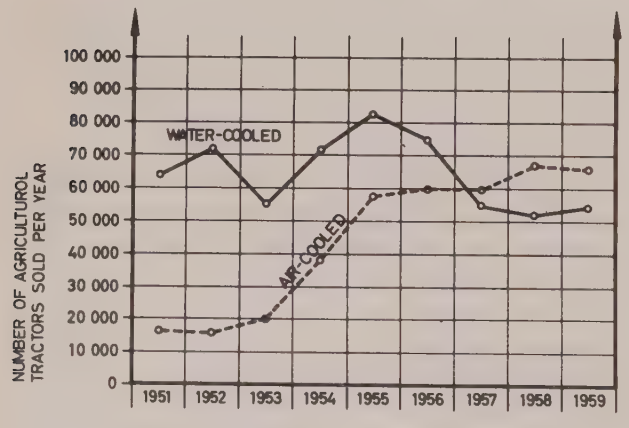

Fig. 27 — Agricultural tractors sold in Western Germany; quantities of aircooled and watercooled units

While in 1949 only 2.5% of the construction machinery was aircooled, this proportion rose steadily from year to year and reached in 1957 already 70%. The slight decrease of aircooling between 1957 - 1960 is due to the growing import of construction machinery from abroad which is exclusively water-cooled.

German makers of aircooled diesel engines (Fig. 29) In 1950 besides Deutz only three companies produced aircooled diesel engines in Western Germany. Since then the number of companies, which manufacture aircooled engines, increased steadily. While there were only four companies with eight engine models in 1950, there were 19 companies with 64 engine models in 1956.

At the same time the commercial range increases from 110 hp in 1950 to 330 hp in 1960 in Germany respectively to 600 hp in England.

Makers and models of aircooled diesel engines in Western Germany and in the world (Fig. 30) - Not only in Western Germany but also in many other countries of the world the production of aircooled diesel engines is continuously rising. This trend applies to the number of makers and models of-

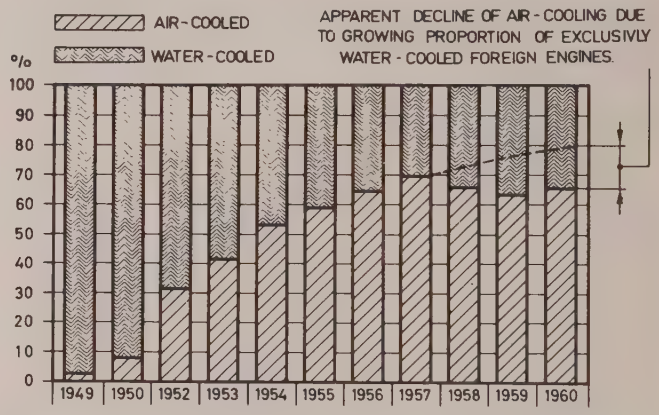

Fig. 28 — Percentages of aircooled industrial engines found at Hanover Fair

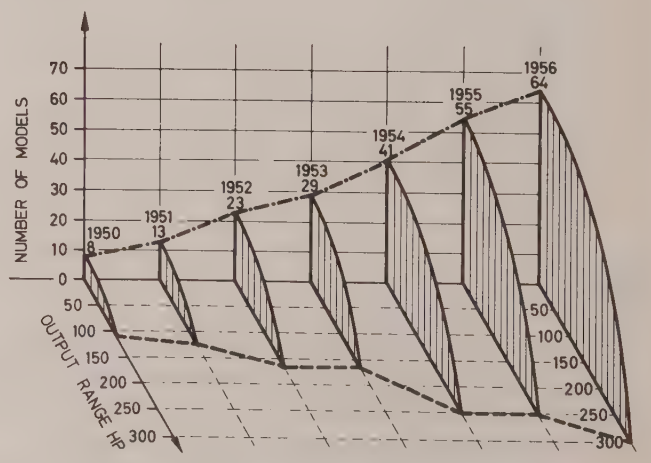

Fig. 29 — Production of aircooled engines in Western Germany, 1950-1956, models and output range

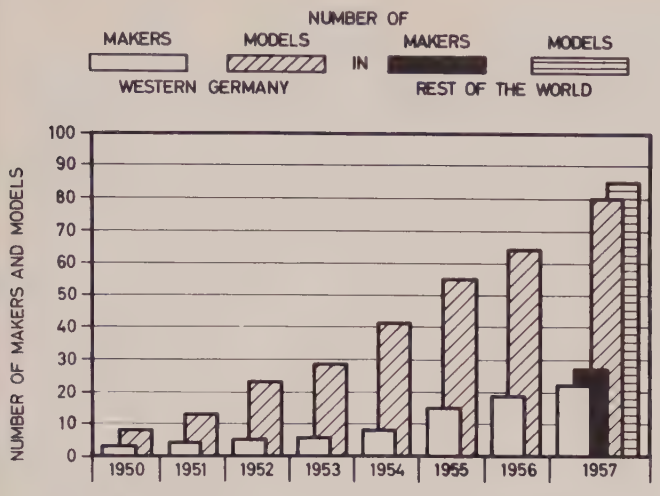

Fig. 30 — Makers and models of aircooled engines

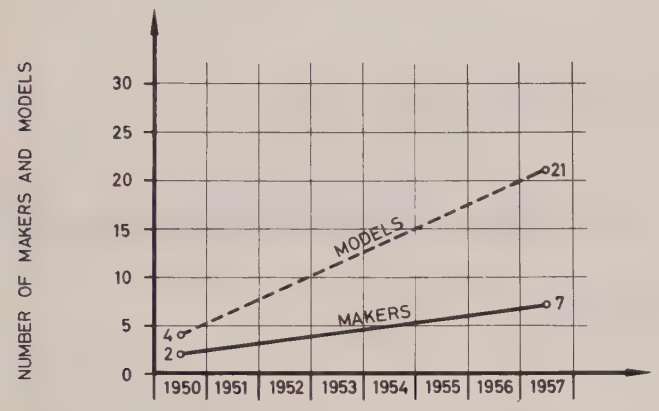

Fig. 31 — Production of aircooled engines in England, number of makers and models

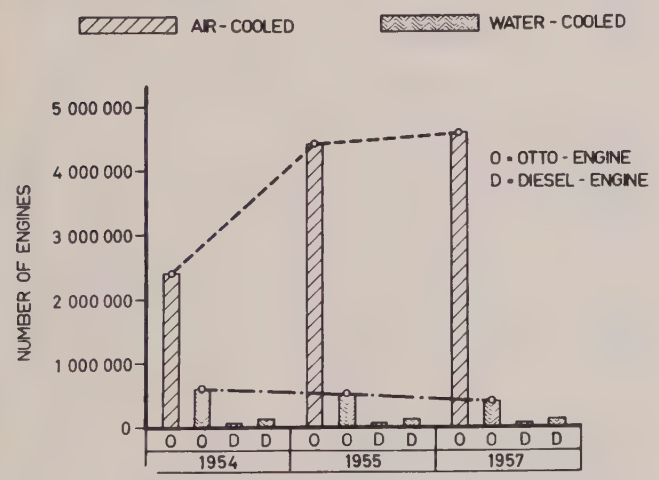

Fig. 32 — Production of J. C. engines in USA (except outboard, automotive and aircraft)

fered as well as to the total number of engines manufactured. In England, Czechoslovakia, Eastern Germany and Switzerland numerous new models of aircooled engines have been developed. In 1957 there were 22 makers with 85 models in the rest of the world.

Makers and models of aircooled engines in England (Fig. 31) - In the absence of other information, only the increase of makers and models of aircooled engines in England can be shown. The trend is likewise upward.

Sales of aircooled engines in the USA (Fig. 32) - Also in the USA the sales of aircooled engines rose between 1954 and 1957, but it seems that this was due to the growing sale of grass mowers. Although latest figures are not available, it is safe to assume that with the introduction of aircooled passenger cars the trend will continue to be upward.

Summary

Within the scope of this paper an attempt has been made to compare the advantages and problems of air and watercooling. It is, however, almost impossible to find a common denominator for the many and often opposite requirements which the cooling system must meet in agriculture and construction industry. In fact, the classification discussed under section C1 shows that almost for each particular application there is also a particularly suitable design. For this reason the author endeavoured not to pass a general judgment in favor of one or the other cooling system nor of one or the other design. The aim was rather to demonstrate that there should never be generalization but careful consideration be given to each particular installation.

Nevertheless, some essential items of this discussion should be summarized.

The aircooled engine, and in particular the aircooled diesel engine, is generally neither of lower weight nor of lower cost than the watercooled engine. Nor should aircooling be considered preferable for maximum ratings as its foremost suitability is rather within the medium performance range. The aircooled engine demands a particular and honest effort on the part of the design and development engineer to make it an equal or superior partner of the watercooled engine.

However, the aircooled diesel engine has uncontested reliability in operation under the most difficult conditions. It is this quality which has contributed most to the advance of aircooled engines.

References

1. R. Kloss, "High-Speed Aircooled Diesel Engines. -- Past and Present," SAE Section paper, Boston, Mass., 1956.

2. C.F. Bachle, "Aircooled Diesel Engine Appraisal," SAE Preprint No. 154, September, 1957.

3. H.H. Haas, and E.R. Klinge, "The Continental 750-Horsepower Aircooled Diesel Engine," SAE Transactions, Vol 65, 1957.

4. E.R. Klinge, "Aircooled Engine Design Criteria" SAE Milwaukee Section, March, 1958.

An Engine Test for Predicting the Performance of

SINCE 1952 the American Petroleum Institute Service Classification System (1)* has been widely used by the automotive industry in the United States in making passenger-car engine lubricant recommendations even though service experience has shown it to be inadequate. The primary factor responsible for this inadequacy is that the API system provides no method for determining the quality level necessary to meet the requirements of a given service. Also, extensive service experience has shown that some marketers have completely disregarded the apparent intent of the API definitions. For example, oils designated for Service MS range in quality from straight mineral oils to products which are more than adequate. (This situation is discussed further in Appendix A.)

As a result it has been decided that if the automobile industry is to continue to use the API Service Classification System, a method must be found to implement the definitions. It has been suggested (2) that a partial solution could be provided by establishing minimum performance levels for each service classification. This suggestion led to the publication of a series of engine oil performance tests for describing the oil quality level necessary for satisfactory operation of passenger-car engines under severe service conditions.

It is the objective of this paper to describe one of the engine tests which is being used to define minimum acceptable performance, in current passenger-car engines, of oils designated for MS Service. This test is commonly known as Sequences I, II, and III of the G-IV Test Sequences. Test Sequences I, II, and III will be referred to throughout the paper as "the engine test" or "the engine performance test". The paper discusses the test development, describes the engine operating conditions, points out some of the important variables, shows the correlation with service, and indicates some of the test limitations.

Test Development Criteria

In developing an engine test to define minimum lubricant performance levels for Service MS in current passenger-car engines, it was decided that the test procedure should reflect what was believed to be the intent of the API definition. For example, the definition of Service Classification MS was interpreted to mean that MS oils should provide more engine protection than ML or MM oils. Also, the protection should be sufficient to result in acceptable per-

*Numbers in parentheses designate references at end of paper.

Engine Lubricants in Most Severe Passenger Car Service

Paul A. Bennett, George K. Malone, and Chester K. Murphy
General Motors Research Laboratories

formance with respect to wear or deposits under all (including severe) operating conditions encountered by passenger-car owners. An oil formulated for average service should not be designated for Service MS.

The API Service Classification System includes engine design considerations as a variable. It was believed that the intent of the API definition was that oils designated for Service MS should perform satisfactorily in all current engine designs. This factor has two important implications:

1. Since engine designs change, the type of lubricant designated for Service MS may change.
2. The testing of lubricants in full-scale engines of current design provides some assurance that the oils will satisfactorily lubricant such engines in service.

The most important requirement was that the engine test separate acceptable lubricants from those oils which result in service problems. On the other hand, the test need not necessarily rank the best lubricants in the proper order. In addition, the test must provide satisfactory repeatability.

The engine test should include operation under conditions resulting in the condensation of moisture and acidic blowby contaminants in the engine crankcase. This is important in that most service problems are associated with low temperature engine operation. The additive depletion which occurs under these conditions can drastically change the performance of the lubricant.

The test was not intended to evaluate all the desirable oil performance properties. It was considered acceptable to include only those performance criteria which recent experience had shown to be associated with service problems.

Finally, the engine test would provide a full-scale evaluation of lubricant performance in current passenger-car engines under conditions that approximate actual service. It was anticipated that this evaluation would provide a basis for estimating the service performance of the lubricant. The test was not intended for use in routine screening of additives or lubricants.

Engine Test Conditions

Since the test procedure is readily available, (2, 3, 4), the engine operating conditions, only, are summarized in Table I. Table I summarizes the 1960 test (3) conditions. The 1958 procedures (2, 4) differed primarily in that it did

Table 1 - 1960 Engine Test Conditions
1960 Production V-8 Passenger Car Engine F

	Section A	Section B	Section C*
Speed, rpm	2500	1500	3400
Load, bhp	2	25	85
Coolant Out, F	95	95	200
Oil Sump, F	120 Max.	120	260, 265
Carburetor Air Humidity, gr/lb	80	80	80
Carburetor Air Temperature, F	80	80	80
Air-Fuel Ratio	14	14	15
Blowby Rate, cfm	0.4	0.8	2.0
Exhaust Back Pressure, In. Water	2	4	20
Crankcase Oil Filler Tube	Plugged	Plugged	Unplugged
Test Duration, hr			
Engine Time	5	30	40
Elapsed Time	30	60	40

*Section C includes evaluations of rumble made at full-throttle and 2500 rpm.

not include rumble evaluations.

As indicated in Table I, the engine performance test consists of three parts. Section A is a cam and lifter scuffing test. It consists of 10 minutes of operation at the conditions indicated, followed by a 50-minute shut-down with the coolant maintained at 95 F.

The scuffing test is included as the initial part of the procedure in that new engine parts are much more susceptible to scuffing failure than used components. The ability of a lubricant to prevent damage during the initial run-in of heavily loaded cams and lifters is a good measure of the anti-scuff performance of the lubricant.

Following the successful completion of 30 cycles under the conditions of Section A, the test is continued to Section B without oil change.

Section B is primarily a low-temperature engine rusting and corrosion test (5). This section consists of a cycle of 3 hr of operation followed by a 3-hr shut-down at a controlled coolant outlet temperature of 95 F. Upon the successful completion of 10 cycles, the test is continued to Section C without oil drain.

Section C is a high-temperature oil oxidation test. This section consists of 40 hr of continuous operation at relatively high engine speeds and loads. Section C differs from the widely used CRC L-4 procedure (4, 6) as follows:

1. A modern automotive passenger-car engine is used.
2. The test is run on used oil.

During Sections A and B water and acidic blowby contaminants accumulate in the engine crankcase. These contaminants can result in additive depletion and seriously affect lubricant performance. Section C evaluates the high-temperature stability of crankcase oils following operation in the presence of low-temperature engine contaminants.

In addition, the combustion chamber deposits are evaluated during Section C for their tendency to cause engine rumble.

Rating Procedures

Valve-lifter scuffing is determined by a visual inspection of the part. Any visible scuffing is considered evidence of failure.

Cam and lifter wear is reported as the decrease in major diameter of the cam plus the mating lifter length loss.

The rust rating system is based on a rating of ten for a perfectly clean part and a rating of zero for a part comcovered with a heavy layer of rust. The system parallels the CRC cludge and varnish rating scales which are used in evaluating sludge and varnish deposition.

The engine rumble rating is determined in terms of a series of blends of leaded isooctane and leaded benzene. Leaded isooctane, a fuel relatively insensitive to rumble, is arbitrarily assigned a rating of 100. Leaded benzene, a fuel relatively sensitive to rumble, is assigned a rating of zero. A rumble rating of 60 means that a blend of 60% leaded isooctane and 40% leaded benzene is the lowest LIB number blend capable of suppressing rumble. The higher the rating of the LIB blend necessary to repress rumble, the greater the tendency of the engine to rumble.

Some Important Test Variables

Section A - One of the most important variables is that of engine speed. This is illustrated by Fig. 1. These data (7) show that engine speed is an important variables at engine speeds below 2500 rpm. Fig. 1 also indicates that failures occur more readily when a cyclic procedure is used.

As would be expected with any scuffing or wear test, the valve-train loads must be carefully controlled.

Although some effect of engine temperature on scuffing tendency has been observed, the low temperatures and the plugged oil filler tube are specified in Section A because of their influence on lubricant performance during Section B.

Section B - The most important variables are the amount and type of contaminants which accumulate in the engine crankcase (5). The amount of material condensing in the crankcase is primarily a function of engine temperatures and the blowby rate. The cylinder wall temperature largely determines the rate of condensation. Repeatability thus re-

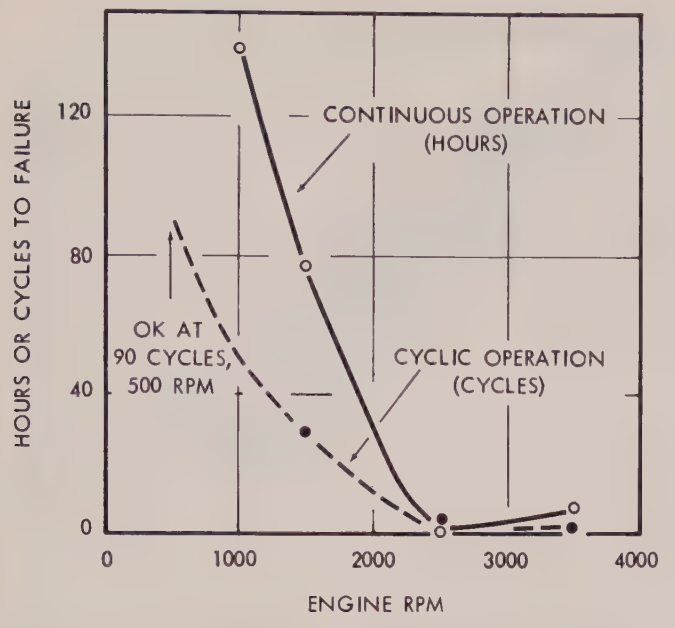

Fig. 1 — Effect of engine speed on time to scuff cams or lifters

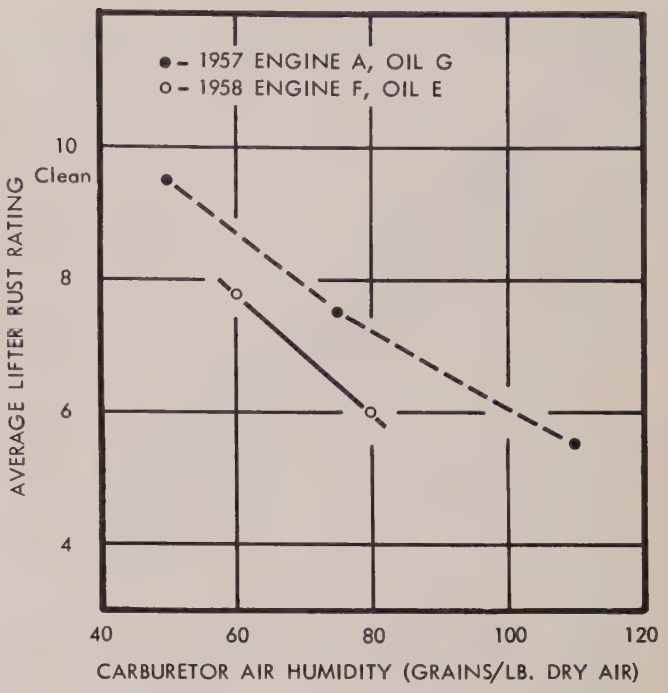

Fig. 2 — Effect of carburetor air humidity on hydraulic valve lifter rusting

quires close control of engine coolant inlet and outlet temperatures. In addition, the condensates will remain in the crankcase only if the crankcase lubricant temperature is low enough to discourage subsequent evaporation. Although engine coolant temperature is controlled during shut-down to minimize the effect of changing ambient air temperatures, optimum repeatability can only be obtained if the ambient air temperature and rate of air flow over the engine are also controlled.

The effects of blowby rate changes on rusting tendency are illustrated in Table 2. The blowby rate is a function of cylinder and ring condition, engine speed, and load. Also, the amount of exhaust gas passing through the engine crankcase can vary with the exhaust valve guide condition and exhaust back pressure. High exhaust back pressures can result in appreciable flow of exhaust gas through worn valve guides and into the crankcase.

The composition of the condensates accumulating in the engine is related to the composition of the blowby gas. The latter varies with engine speed, load, fuel, air-fuel ratio, and carburetor air humidity.

The effect of fuel composition on lubricating oil performance has been known for some time (8). Moreover, the fact that substantial amounts of fuel accumulate in engine crankcases during low-temperature operation is generally known. These facts are not surprising when it is recognized that a substantial amount of unburned fuel is present in the blowby gas (9). In addition to unburned fuel, the blowby gases contain oxidized and partially oxidized materials. Accordingly, such factors as the fuel TEL and sulfur contents (Table 3) become very important.

The blowby gas composition also varies with carburetor air humidity. It has been shown (5) that this factor is important in the rusting and corrosion of important engine parts (Fig. 2).

Table 2 - Effect of Blowby Rate on Engine Rusting and Corrosion

1958 Engine F, Commercial MS Oil O1

Section B Blowby Rate, cfm	Average Lifter Rust Rating
0.6	10.0
0.8	9.8
1.0	8.8
1.2	7.2

Section C - Section C is primarily an oil oxidation test. The important variables include engine temperature, available oxygen, crankcase oil charge, fuel, air-fuel ratio, and blowby rate and composition.

The amount of available oxygen varies with the blowby gas composition (9, 10), which is related to the engine air-fuel ratio. The amount of available oxygen is also increased by unplugging the crankcase oil filler tube during Section C.

The net effect of a number of variables related to engine air-fuel ratio is illustrated using the L-4 data shown in Table 4. The engine blowby rate can also affect the test results as indicated by the data of Table 5.

Table 3 - Change in Valve Lifter Rusting With Fuel Sulfur Content

1956 Engine C, Commercial MS Oil O3

Fuel Sulfur Content, wt. %	Average Lifter Rust Rating
0.06	10.0
0.16	9.0
0.30	7.5

Table 4 - Effect of Air-Fuel Ratio on L-4 Test Results

A/F	Piston Varnish Rating (Oil S1)	Bearing Wt. Loss, mg (55% REO 7/45% REO 12)
13.0	8.5	800
14.5	6.5	380, 275, 315
16.5	6.0	765

Table 5 - Effect of Blowby Rate on Engine Sludge and Varnish Ratings

Section C Blowby Rate, cfm	Average Engine Ratings, Individual Tests	
	Cover Sludge	Piston Varnish
1.2 to 1.4	9.8, 9.6	9.8, 9.7
2.4 to 2.6	8.8, 9.0	9.4, 9.2

Section C is also useful in evaluating the tendency of combustion chamber deposits to produce engine rumble. However, consistent results require careful control of fuel and compression ratio as is generally appreciated.

In addition, it has been shown (11) that engine rumble varies with fuel type, additive content, and air-fuel ratio with maximum rumble occurring near maximum power mixture ratios. Rumble tendencies increase with compression ratio, carburetor air temperature, engine load, and engine speed. Increasing carburetor air humidity results in decreased engine rumble tendencies.

The length of time the engine is permitted to operate at high load is important because of the resulting removal of combustion chamber deposits. Accordingly, such seemingly unimportant factors as the rate at which the throttle is opened can have an important effect on engine rumble ratings.

Test Repeatability

Table 6 and Figs. 3-6 present the results of several tests on each of a group of engine oils. The data in the figures are the ratings for individual tests on a given oil, plotted against the average for all tests on the oil. The shaded areas represent the 95% confidence level sampling errors for single tests. At a lifter rust rating of about 8 this error is ± 0.8 number. The top cover sludge and piston varnish sampling errors are about ± 0.4 number at a rating of 9. The individual test sampling errors for wear, bearing weight loss, and rumble are ± 0.0012 in., ± 50 mg, and ± 10 LIB numbers respectively at the 95% confidence level. This repeatability is considered acceptable. However, acceptable repeatability can be obtained only by careful attention to detail as outlined in the previous section.

Lubricants Evaluated

Appendix B presents a summary of some of the physical and chemical properties of some of the physical and chemical properties of 57 oils evaluated in the performance test. With the exception of three CRC Reference Oils, all were commercial products designated by the marketer for Service MS. The commercial oils were selected on the basis of available service performance data and to illustrate performance differences that may be observed. An examination of Appendix C indicates that these oils cover a wide range of base stocks, additive treatments, and viscosity grades.

Performance Variations with Commercial Oils

Table 7 is a tabulation of results obtained using both the 1958 and the 1960 procedures. Some of the data are averages of two or more tests of a given oil. Inspection of Table 7 indicates very wide variations in lubricant performance with oils designated for Service MS. This is further illustrated by the photographs of Fig. 7. It is impossible to reconcile such extremes in lubricant performance with the statement that "Under Service MS, the engine should receive from the lubricating oil the maximum possible protection against wear and deposits under all operating conditions." (12)

Correlation with Service Performance

Table 8 compares engine test results with service scuffing and wear data. These data show that oils (Group 1) which resulted in field service scuffing failures also result in failure in the engine performance test.

In two instances, Oils D3 and D4 (Group 2) which are considered about borderline with respect to scuff perform-

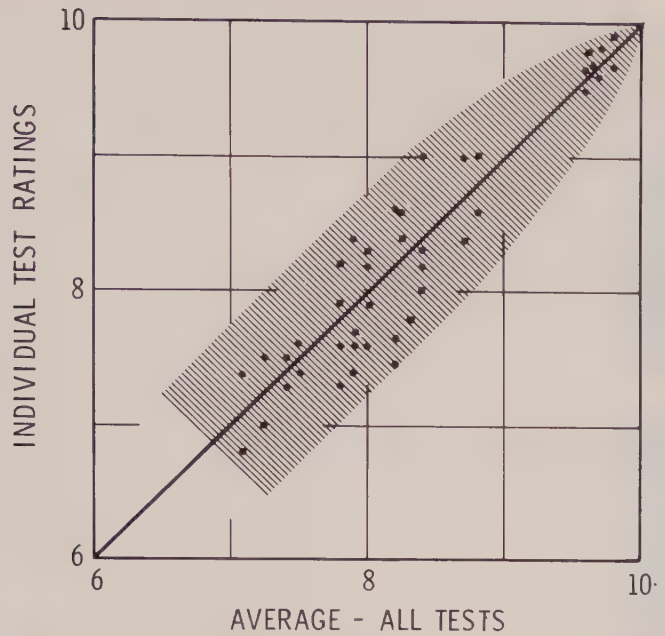

Fig. 3 — Variation in average valve lifter rust ratings

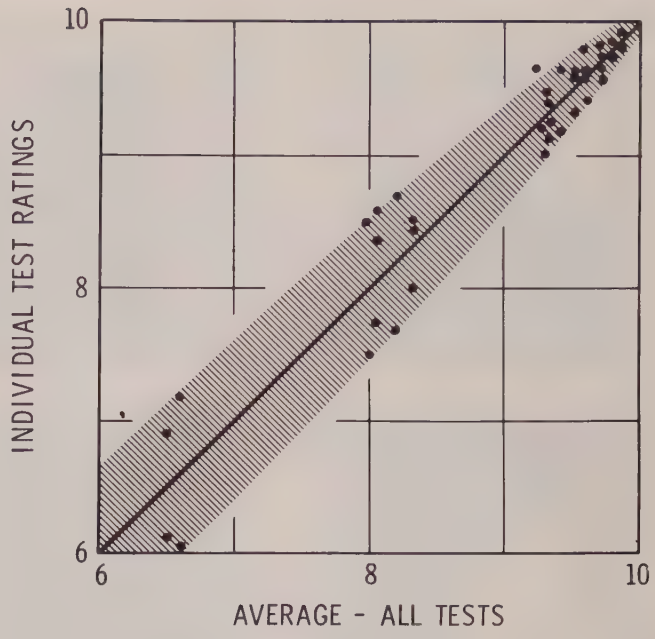

Fig. 5 — Variation in average piston varnish ratings

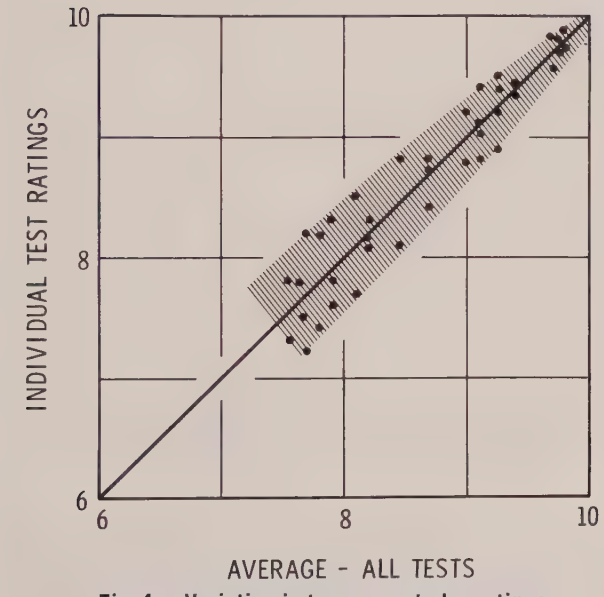

Fig. 4 — Variation in top cover sludge ratings

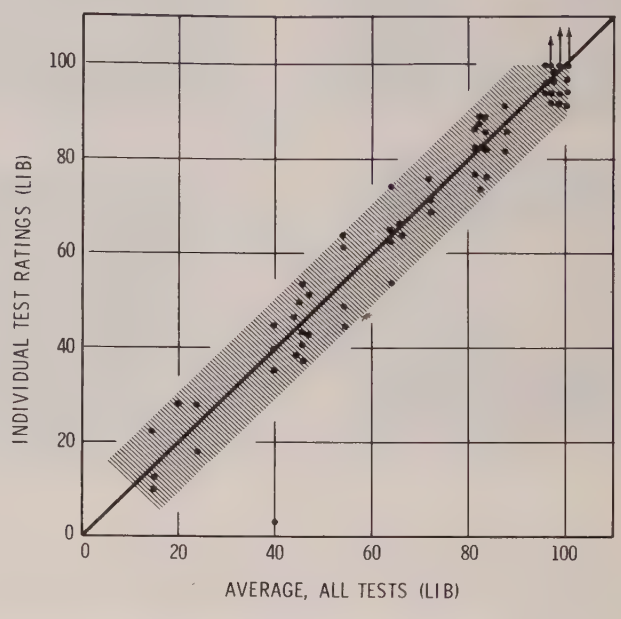

Fig. 6 — Variation in rumble ratings

ance, the type of failure observed in service was different than that predicted by the engine test. The service performance of such oils is not acceptable.

Group 3 oils show that products acceptable in service also pass the engine test. Oils B3, D2, D5, and Q2 are reformulations of Oils B2, D1, D4, and Q1 respectively. Table 7 includes data for a large number of other oils which are satisfactory in the engine test and have resulted in no known field service scuffing problems.

The Group 4 oils of Table 8 point out one of the limitations of the engine test. Field failures have been observed with a limited number of oils that pass the test. These differences in severity may be due, in part, to fatigue, differences in additive depletion, or oil dilution.

Table 9 shows a correlation of the engine performance test with the short-trip rusting test described in Appendix C. The engine test and the short-trip service test show the same ranking of lubricants with respect to anti-rust performance.

Table 10 shows the correlation of the engine performance test and service rusting experience for a group of commercial MS oils. The service data are a compilation of information from company-owned cars in general transportation

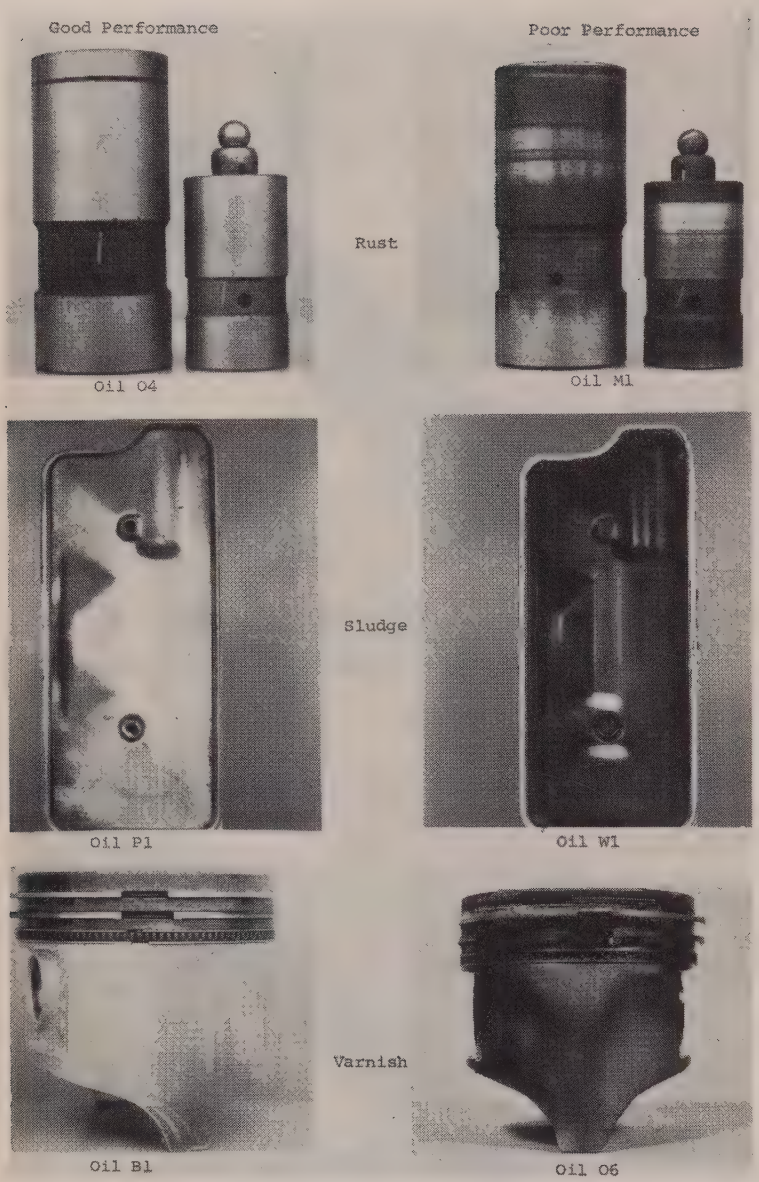

Fig. 7 — Variations in performance noted with various commercial MS oils

service and data from service reports. These data also show a satisfactory correlation of engine test results with service experience.

Figs. 8 and 9 show the correlation of engine test and service sludge and varnish deposition data. The service data are results obtained with company-owned cars in general transportation service. This type of service is representative of relatively long-trip operation and includes a minimum of short trips. In general, oils acceptable in service rate essentially clean in the performance test. The engine test does not differentiate among top quality lubricants with respect to either sludge or varnish deposition.

Fig. 10 compares engine performance test rumble ratings with road test data (13) for several commercial MS oils. The road test data were accumulated in four different groups of cars. Three of these were production vehicles ranging in compression ratio from 9.75 to 10.5:1. Commercial gasolines were used in accumulating the combustion chamber deposits in these cars. The experimental 12:1 compression ratio car was fueled with a gasoline containing one theory of phosphorus (11). These data show that the engine performance test provides the same ranking of lubricants with respect to rumble tendencies as has been observed on the road.

Summary

Service experience has indicated a need for implementing the API Service Designation MS as applied to current passenger-car engine lubricants. An engine performance test has been developed to evaluate oils with respect to scuffing, wear, rust, corrosion, deposits, and rumble under con-

Table 6 - 1960 Engine Performance Test Repeatability

Oil	Cam or Lifter Scuffing	Cam plus Lifter Wear (In. x 10^4)		Avg. Rust Rating		Avg. Sludge Rating		Avg. Varnish Rating		Brg. Wt. Loss (mg)	Rumble Rating (LIB No.)	Oil Consumption (qts)
		Avg.	Max.	Lifter	Engine	Top Cover	Engine	Piston	Engine			
I	No	25	32	8.3	7.6	8.8	9.2	9.5	9.8	118	94	2.2
	No	33	51	8.0	7.2	8.8	9.1	9.2	9.6	102	95	2.4
	No	28	41	8.2	7.6	8.8	9.2	9.4	9.6	166	100	1.9
	No	30	47	9.0	8.2	8.4	9.0	9.2	9.6	75	95	3.8
G1	No	29	40	8.4	7.8	7.8	8.8	9.1	9.6	182	54	2.6
	No	30	40	7.8	7.0	7.6	8.9	9.0	9.6	189	37	2.8
	No	22	32	8.6	8.0	8.3	9.0	9.7	9.8	146	43	3.9
C1	No	31	45	8.2	7.0	8.3	9.0	9.6	9.8	39	100+	2.9
	No	28	34	8.3	7.2	8.1	9.0	9.4	9.7	20	98	2.2
	No	24	39	7.9	6.5	8.1	8.9	9.8	9.8	92	94	2.7
	No	22	35	7.6	6.0	8.2	8.9	9.6	9.8	36	96	3.7
O2	No	32	46	9.6	8.8	8.9	9.4	9.7	9.8	---	87	3.2
	No	29	38	9.5	8.4	9.5	9.6	9.7	9.8	61	83	2.6
	No	26	33	9.8	9.2	9.4	9.5	9.6	9.8	65	87	3.2
	No	22	28	9.6	9.2	9.2	9.4	9.8	9.9	64	73	4.0
P1	No	33	41	9.8	9.2	9.8	9.9	9.9	10.0	188	22	3.0
	No	24	37	9.7	8.7	9.8	9.7	9.8	9.8	171	13	---
	No	30	47	9.6	8.6	9.8	9.8	9.8	9.8	123	10	2.7
J	No	24	30	7.6	7.1	9.1	9.2	9.6	9.8	82	100+	2.1
	No	28	39	7.4	7.2	9.0	9.2	9.6	9.7	76	98	3.5
	No	21	28	8.6	7.4	9.1	9.2	9.4	9.6	74	100+	4.2
D1	Yes											
	Yes											
	Yes											
	Yes											

Table 7 - Results of Engine Tests of Reference and Commercial MS Oils

Oil	Cam or Lifter Scuffing	Cam plus Lifter Wear (In. x 10^4) Avg.	Max.	Avg. Rust Rating Lifter	Engine	Avg. Sludge Rating Top Cover	Engine	Avg. Varnish Rating Piston	Engine	Brg. Wt. Loss (mg)	Rumble Rating (LIB No.)	Oil Consumption (qts)
						1958 Tests						
A1	No	31	40	9.2	7.5	9.4	9.6	9.8	9.9	734	---	4.0
A2	No	--	--	7.5	7.4	7.6	8.5	9.8	9.6	113	---	5.5
A3	Yes	--	--	---	---	---	---	---	---	---	---	---
B2	Yes	--	--	---	---	---	---	---	---	---	---	---
B3	No	--	--	---	---	---	---	---	---	---	---	---
D1	Yes	--	--	---	---	---	---	---	---	---	---	---
D2	No	--	--	---	---	---	---	---	---	---	---	---
D3	No	37	60	8.7	8.4	7.7	8.7	9.8	9.8	221	---	3.3
D4	Yes	--	--	---	---	---	---	---	---	---	---	---
D5	No	23	34	9.7	9.0	8.5	8.8	9.5	9.7	---	---	---
F1	No	21	31	6.2	6.4	9.0	9.2	9.7	9.8	91	---	3.2
J1	Yes	--	--	---	---	---	---	---	---	---	---	---
J4	Yes	--	--	---	---	---	---	---	---	---	---	---
J5	Yes	--	--	---	---	---	---	---	---	---	---	---
J6	No	17	27	---	---	8.2	8.8	8.8	9.2	---	---	3.0
L1	No	22	33	7.6	7.2	9.0	9.2	9.2	9.4	---	---	2.8
L2	Yes	--	--	---	---	---	---	---	---	---	---	---
L5	No	--	--	---	---	---	---	---	---	---	---	---
M1	No	15	24	5.4	5.0	9.6	9.7	9.8	9.8	103	---	3.2
M3	No	35	49	8.9	8.5	8.0	8.6	9.0	9.2	38	---	3.5
N1	No	21	33	8.6	8.1	8.8	8.9	9.1	9.6	1300	---	3.0
O1	No	28	41	9.8	9.6	9.0	9.3	9.7	9.8	124	---	4.8
O6	No	28	45	4.0	5.0	7.3	8.2	5.5	7.6	---	---	4.3
P1	No	26	33	9.2	8.5	9.8	9.8	9.9	9.8	79	---	4.0
Q1	Yes	--	--	---	---	---	---	---	---	---	---	---
Q2	No	--	--	---	---	---	---	---	---	---	---	---

Table 7 - Results of Engine Tests of Reference and Commercial MS Oils (Cont)

Oil	Cam or Lifter Scuffing	Cam plus Lifter Wear (In. x 10^4)		Avg. Rust Rating		Avg. Sludge Rating		Avg. Varnish Rating		Brg. Wt. Loss (mg)	Rumble Rating (LIB No.)	Oil Consumption (qts)
		Avg.	Max.	Lifter	Engine	Top Cover	Engine	Piston	Engine			
						1958 Tests						
R1	No	32	55	5.4	5.6	7.4	8.6	7.6	8.5	85	---	3.2
T1	No	--	--	---	---	---	---	---	---	---	---	---
U1	No	--	--	---	---	---	---	---	---	---	---	---
						1960 Tests						
A4	No	23	34	9.5	8.6	9.8	9.8	9.8	9.8	75	82	3.3
B1	No	20	31	8.6	8.0	9.8	9.8	9.9	9.9	105	68	1.3
C1	No	26	38	8.0	6.8	8.2	9.0	9.6	9.8	61	100*	2.9
D1	Yes	--	--	---	---	---	---	---	---	---	---	---
E1	No	23	47	9.8	9.2	8.8	9.2	9.5	9.8	53	90	2.7
E2	No	22	35	8.6	7.6	9.4	9.6	9.8	9.8	102	100+	2.0
G1	No	27	37	8.3	7.6	7.9	8.9	9.3	9.7	172	45	3.1
G2	No	40	55	8.8	7.6	9.3	9.4	9.7	9.8	92	10	2.9
J2	No	--	--	6.8	6.0	9.7	9.7	9.7	9.8	70	49	2.9
J3	No	23	37	9.4	8.0	9.8	9.8	9.9	9.9	42	72	0.8
J7	No	20	26	9.4	9.0	9.1	9.4	9.6	9.8	37	97	2.1
K1	No	20	28	9.6	9.3	9.4	9.4	9.8	9.8	39	40	3.0
L3	No	36	57	7.6	6.4	9.2	9.4	9.6	9.8	226	18	2.8
L4	No	27	47	9.6	9.0	9.2	9.4	9.7	9.8	156	25	4.2
L6	No	20	27	9.8	8.9	9.7	9.8	9.9	9.9	184	62	---
L7	No	20	30	7.4	6.9	9.6	9.5	9.7	9.8	154	92	2.8
M1	No	30	42	7.0	5.7	9.8	9.8	9.7	9.8	152	45	3.0
M2	No	21	29	7.4	7.6	9.6	9.6	9.6	9.8	178	47	2.3
N2	No	22	32	9.0	7.6	9.4	9.4	9.6	9.7	105	100+	4.5

(continued on next page)

Table 7 - Results of Engine Tests of Reference and Commercial MS Oils (Cont)

Oil	Cam or Lifter Scuffing	Cam plus Lifter Wear (In. x 10^4) Avg.	Max.	Avg. Rust Rating Lifter	Engine	Avg. Sludge Rating Top Cover	Engine	Avg. Varnish Rating Piston	Engine	Brg. Wt. Loss (mg)	Rumble Rating (LIB No.)	Oil Consumption (qts)
O2	No	28	36	9.6	9.0	9.2	9.5	9.7	9.8	63	85	3.3
O3	No	38	62	9.8	9.2	8.8	9.3	9.9	9.9	85	45	4.3
O4	No	23	35	9.8	9.2	9.8	9.8	9.8	9.9	50	65	1.9
O5	No	25	40	9.8	9.3	9.3	9.4	9.5	9.8	67	93	3.1
O7	No	29	41	6.6	5.0	7.8	8.6	8.4	9.2	213	78	2.6
P1	No	29	42	9.7	8.8	9.8	9.8	9.8	9.9	161	15	2.8
U2	No	25	42	7.1	7.2	9.1	9.2	9.4	9.6	147	100+	2.0
V1	No	36	47	9.7	8.8	9.2	9.4	9.8	9.8	35	78	3.1
W1	Yes	125	705	7.4	6.0	7.6	8.4	6.2	8.4	238	100	3.5
REO 132	No	20	28	6.8	6.2	7.7	8.8	8.0	9.2	132	55	3.2
REO 145	No	18	27	9.6	8.7	9.7	9.7	9.8	9.8	144	28	4.2
REO 147	No	27	46	9.6	8.5	9.8	9.8	9.9	9.9	105	47	1.9

*Estimated (See Table 6)

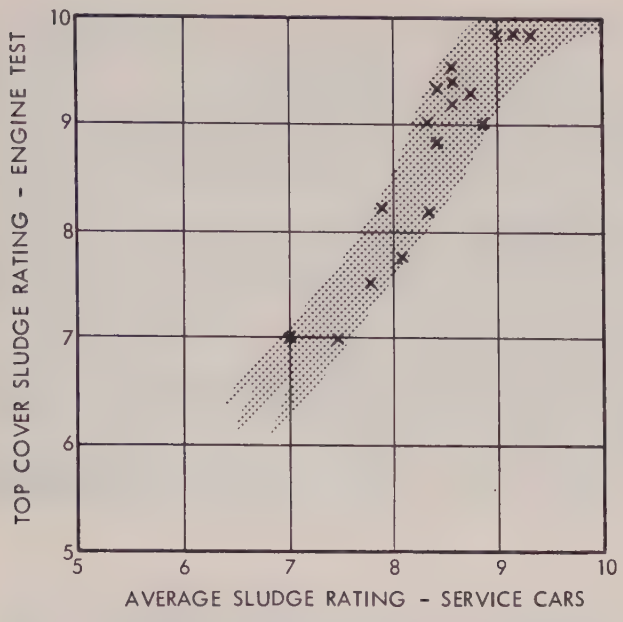

Fig. 8 — Comparison of engine performance test and service sludge ratings

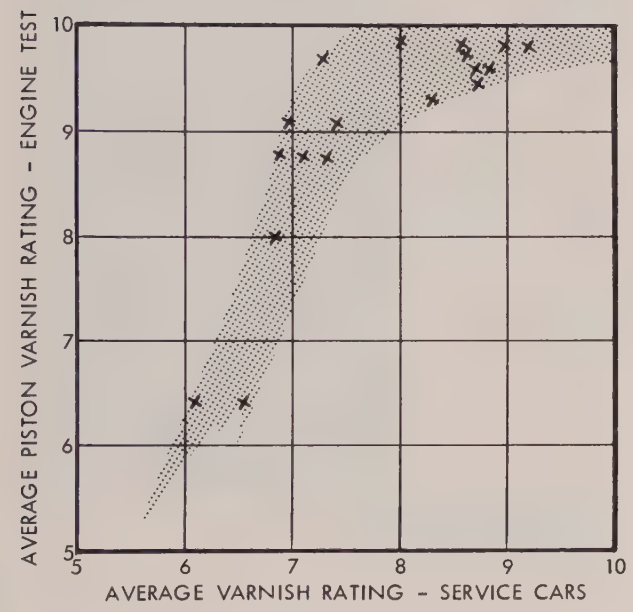

Fig. 9 — Comparison of engine performance test and service varnish ratings

ditions typical of those existing in service. Experience has shown this test to be useful in establishing minimum performance levels, with respect to the above criteria, for oils designated for Service MS in current passenger-car engines.

Acceptable repeatability is indicated by the data presented. The data also show that satisfactory repeatability can be obtained only if all of the important test variables are properly controlled. The data obtained under these conditions correlate well with the field performance of representative commercial lubricants.

Table 8 - Correlation of Engine Test with Service Scuffing and Wear Data

Group	Oil	1958 Engine Test Results	Field Service Experience
1	L2	Fail (scuffing)	Scuffing Failures
	B2	Fail (scuffing)	Extensive Scuffing Failures
	A3	Fail (scuffing)	Extensive Scuffing Failures
	D1	Fail (scuffing)	Extensive Scuffing Failures
	J4	Fail (scuffing)	Scuffing Failures
	Q1	Fail (scuffing)	Scuffing Failures
2	D3	Borderline (wear)	Scuffing Failures
	D4	Fail (scuffing)	Excessive Wear
3	B3	Pass	No Reported Failures
	D2	Pass	No Reported Failures
	Q2	Pass	No Reported Failures
	D5	Pass	No Reported Failures
4	T1	Pass	Scuffing Failures
	U1	Pass	Scuffing Failures
	L5	Pass	Scuffing Failures

Table 9 - Correlation of Engine and Short Trip Rusting Test Results

Oil	1960 Engine Test	Average Lifter Rust Rating Short Trip Tests (Cars C and D)
O3	9.8	10.0
P1	9.7	9.0
N2	9.0	8.5
L3	7.6	8.0
M1	7.0	6.0

Appendix A — Engine Lubricant Performance Testing — Why?

This section is devoted to a discussion of some of the reasons for the engine builder's interest in lubricant performance testing.

The Engine Builder and Lubricant Performance - The engine manufacturer is directly concerned with engine lubricant performance for several reasons. For example, the design engineer recognizes that the ultimate design is influenced by the intended lubricant. The choice of material

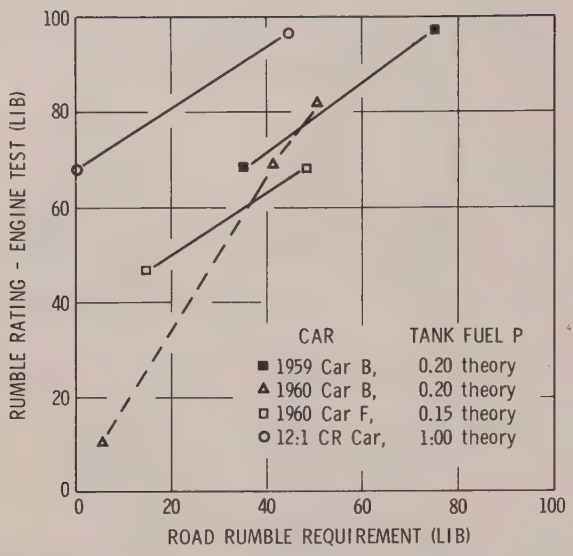
RUMBLE RATING - ENGINE TEST (LIB)
ROAD RUMBLE REQUIREMENT (LIB)
CAR TANK FUEL P
1959 Car B, 0.20 theory
1960 Car B, 0.20 theory
1960 Car F, 0.15 theory
12:1 CR Car, 1:00 theory

Fig. 10 — Comparison of engine performance test and road rumble requirements

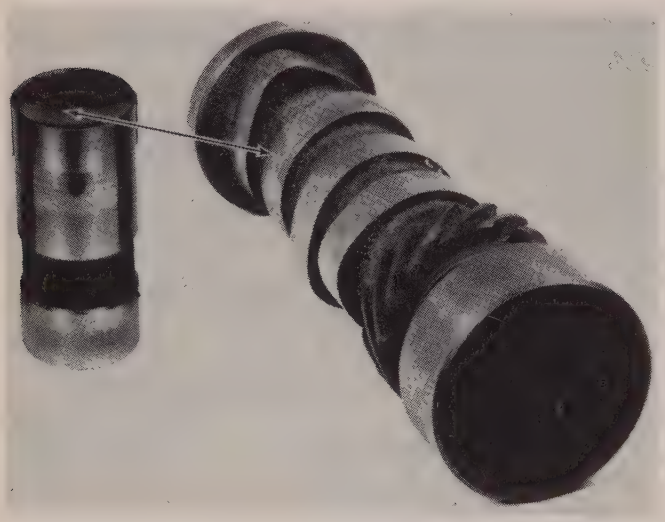

Fig. 11 — Typical catastrophic cam lobe and lifter failure showing badly damaged cam lobe and corresponding dished lifter

for a given part and the loads this part will carry are directly related to the lubricant. Therefore, the lubricant is as much a material of design as are the steels, cast irons, or other materials used.

The development engineer recognizes that the lubricant is also an important factor in engine performance. Accordingly, if he is to evaluate the effects of engine design changes on the performance of a vehicle, it is necessary that representative development oils be selected. It is obviously a physical impossibility to include all the various lubricant types in the engine development program. Moreover, the development oil must be selected with considerable care. If these oils are representative of the best commercial lubricants, the manufacturer is assured of service problems when lower quality oils are used. In fact, most past lubricant service problems have resulted from the service use of engine oils which differed markedly from the oils used in developing the engine. In addition, developing an engine to operate on minimum quality lubricants leads to excessive manufacturing costs and the desired engine performance may never be obtained.

When the engine is released for production it becomes the responsibility of the equipment manufacturer to recommend, to the customer, a type of lubricant which will insure satisfactory service performance. This problem is complicated by

1. The unsatisfactory performance of some filling station lubricants as shown in Table 7 and Fig. 3.

Table 10 - Correlation of Engine Test and Service Rusting Results

Oil	1960 Engine Test Average Lifter Rust Rating	General Service Experience
E1	9.8	Good, occasional trace rust
O2	9.6	Good
C1	8.0	Satisfactory to good
L3	7.6	Light rust
M1	7.0	Poor
REO 132	6.8	Poor, considerable rust

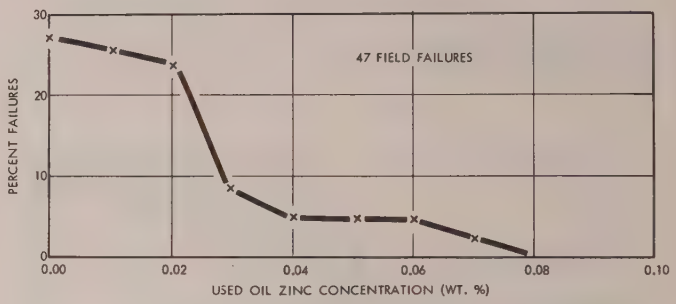

Fig. 12 — Frequency distribution showing the relationship of cam and lifter failures to zinc concentration in used oil

Table 11 - Comparison of Second and Third Line MS Oils

Oil	Lifter Rust	Top Cover Sludge	Piston Varnish
O1 (Second Line)	9.8	9.0	9.7
O6 (Third Line)	4.0	7.3	5.5

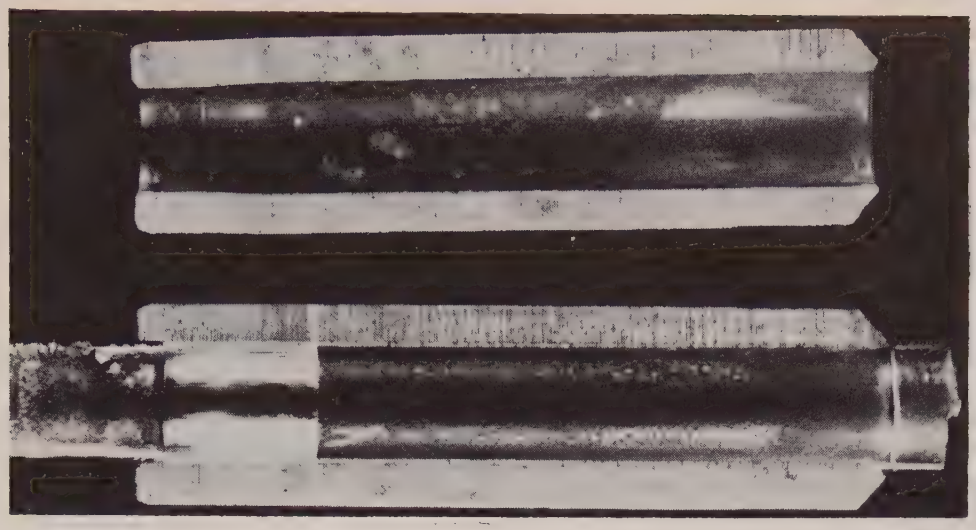

Fig. 13 — Rusted exhaust valve stem and guide, 1959 make B, 4000 miles of service

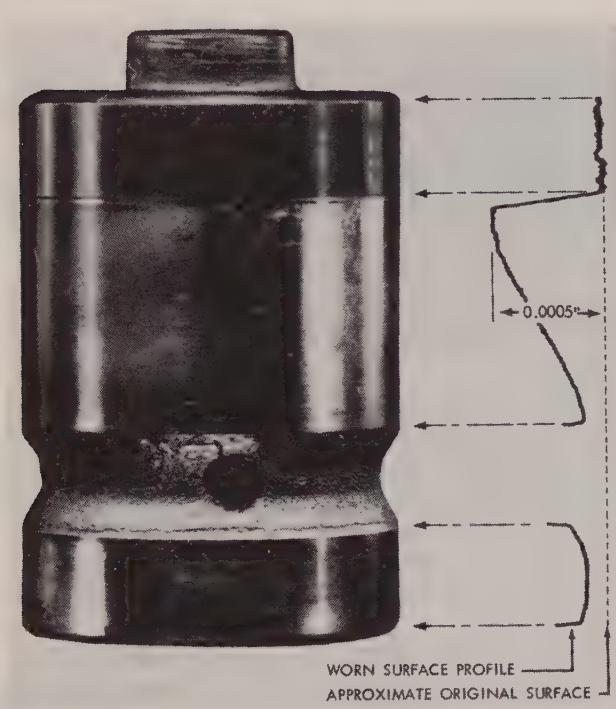

Fig. 14 — Profile of badly worn lifter plunger, 4000 miles service, commercial MS oil

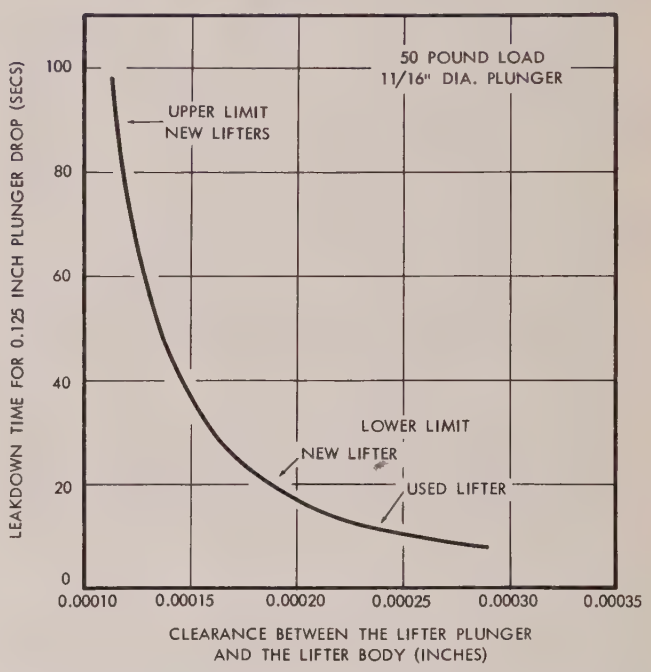

Fig. 15 — Variation of hydraulic valve lifter leakdown time with plunger-body clearance

2. The lack of a reliable oil classification system.

In fact, it is currently impossible to write recommendations which will insure the service use of suitable lubricants. Nevertheless, if lubricant misapplication results in service problems, it is the equipment manufacturer who must pay the direct warranty cost and/or the indirect cost resulting from the decreased public acceptance of his product.

Accordingly, the lubrication problems facing the equipment manufacturer includes the selection of a lubricant performance level and an oil change interval for design purposes, and of selecting representative development oils to provide maximum equipment life and performance at the lowest total cost to the customer. The ultimate problem is that of insuring that the customer use lubricants which will perform at least as well as the development oil. These factors emphasize his concern about oil classification systems.

API Service Classification System - Since 1952 the only oil classification system available to the automobile industry has been the American Petroleum Institute Service Classification System. The history leading to the development of this system has been discussed by Round (1). The current description is available in the SAE Handbook (12).

In general, the API System establishes three types of service for gasoline engines. These may be summarizes as fol-

lows:

1. Service ML - Service typical of operation under light-duty or favorable operating conditions.

2. Service MM - Service typical of moderate to severe operation conditions.

3. Service MS - Service typical of operation under unfavorable or severe types of service.

The above definitions and a study of the API Service Classification System indicate that one objective was to establish three different service classifications which could be satisfied by the use of three different lubricants of varying performance levels. It would also appear that it was the intent of the system that oils designated for Service MS represent the best available lubricants.

This is important in that a study of the marketing practices of the petroleum industry has indicated that many companies sell three quality levels in their filling stations. These may be defined as follows:

1. First Line Oils - These are generally premium-priced, multiviscosity grade products. Such oils generally result in good to excellent service performance although there are some notable exceptions.

2. Second Line Oils - These products are usually single viscosity grade oils with somewhat lower additive treatments, selling at a nominal price reduction from first line products. Many of these oils result in adequate performance.

3. Third Line Oils - These products are usually oxidation-inhibited mineral oils or oils containing minimum additive treatments. These oils do not provide adequate performance.

However, contrary to what would appear to be the intent of the API Service Classification System, all three of the above oil quality grades have been designated for Service MS by some marketers. This practice leads to completely unacceptable performance with many MS oils. For example, this paper contains data for a second and third line oil marketed by one petroleum company. These data are summarized in Table 11. The designation of third line oils of this performance level for Service MS is absolutely contrary to the apparent intent of the API Service Classification System.

Service experience has proven the API Service Classification System inadequate. The primary reason is that no means were provided for insuring that a lubricant designated for a particular service met any performance requirements.

Field Service Problems Related to Use of Commercial MS Oils - During the last three years a number of service problems have been encountered which were directly related to the use of inadequate oils designated for Service MS. These problems are discussed in the following paragraphs.

1. Scuffing and Wear - The most serious problem involved the catastrophic wear of cams and hydraulic valve lifters. Fig. 11 is a photograph of a typical failure. The following examples illustrate the problem.

One example involves a Mid-Western town which had two automobile dealers handling the same make of vehicle. Over a 6-month period the first dealer reported catastrophic cam and lifter failures in 28 new automobiles. This dealer was using an engine oil subsequently shown to be deficient in anti-scuff performance. The second dealer was handling acceptable competitive oils and had no service failures.

Another example involves a customer who replaced four camshafts within 2000 miles. His dealer also used an engine oil deficient in anti-scuff performance. After the fourth failure, the customer, being a man of some discretion, changed to a competitive brand of oil and encountered no further cam failures.

These and similar field failures stimulated an intensive investigation of the problem. At one point in the investigation used oil samples from engines with failed cams and lifters were analyzed with some of the results shown in Fig. 12. These data indicate that the incidence of failure decreased rapidly at used oil zinc contents greater than 0.02%. No failures were observed where zinc contents were greater than 0.07%. These data suggested that the problem was related to the absence of zinc dialkyldithiophosphate additives, one additive known to provide excellent lubricant anti-scuff performance.

The data of Fig. 12 and the case histories reported above suggest that the cam and lifter failures were associated with particular lubricants. In fact, it was subsequently shown that only a small number of lubricants were actually involved. For example, some 73% of the failures noted in Fig. 12 were associated with lubricants marketed by a single company.

Another problem involved the wear of fuel pump eccentrics. While this problem was not of the catastrophic variety, engine failures have occurred due to the inability of the fuel pump to supply a sufficient quantity of fuel. This problem has also been related to the use of lubricants having very low zinc contents. In general, the use of oils having higher zinc contents has resulted in reduced eccentric wear.

Although service experience has indicated that the use of zinc-containing additives provides one solution to these problems, other additives can also impart the desired performance (14).

2. Rust and Corrosion - The rusting and corrosion of hydraulic valve lifters and valve stems illustrates another service problem which can be related to oil quality. A photograph showing a badly rusted exhaust valve stem is shown in Fig. 13. The valve stem stuck in the guide due to rust accumulation during storage. Rusting may also result in the sticking of hydraulic valve lifters.

The rusting and corrosion of hydraulic valve lifters can also cause rapid wear of these critical engine parts as is illustrated by Fig. 14. This high rate of wear was due to the fact that the corrosion product ". . . is a common grinding compound. Low temperature operation, therefore, accelerates wear in two ways: First, by causing corrosion . . . and secondly, by the corrosion product causing abrasive

Fig. 16 — Badly varnished valve lifter

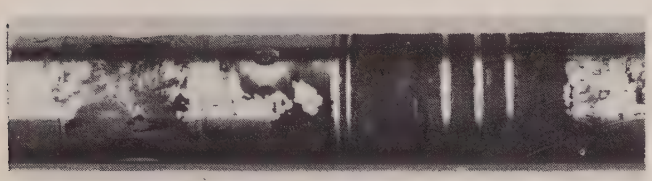

Fig. 17 — Badly varnished rocker-arm shaft

wear." (15)

Plunger wear is important since lifter body-plunger annular clearances must be closely controlled to provide the of higher compression ratios in passenger car engines is engine rumble. Although the severity of this problem varies widely with a number of factors, the engine lubricant used is one of the variables which must be considered (11).

During the last two years several engine manufacturers have decreased engine compression ratios because of service problems related to rumble, although this problem has been of major concern only in some geographical areas. Rumble can result in emphatic customer complaint despite the fact that rumble alone has not been observed to have caused engine damage.

desired performance. Fig. 15 indicates that the maximum clearance which will result in an acceptable leakdown time is about 0.00024 in. Fig. 14 illustrates an instance where an increase in this dimension of 0.00050 in. occurred in only 4000 miles of operation. This relatively small wear is sufficient to result in unacceptable lifter performance.

3. Sludge and Varnish Deposition - Service problems relating to sludge and varnish deposition can occur as a result of lubricant high temperature instability and instability resulting from some combination of low- and high-temperature operation.

Lubricant instability at high operating temperatures has caused hydraulic valve lifter sticking. An example is shown in Fig. 16.

Another service problem involved the sticking of rocker arms and bending of push rods due to the accumulation of varnish on the rocker shaft (Fig. 17). This was due to varnish deposition observed with certain lubricants following combinations of short-trip and high-temperature service. Additive depletion during low-temperature short-trip operation can be sufficiently severe that excessive oxidation and sludge and varnish deposition will occur during subsequent high-temperature operation.

4. Engine Rumble - The major factor limiting the use

Appendix B — Physical and Chemical Properties of Oils Evaluated

Oil	SAE Grade	Viscosity, cs		VI	TAN	TBN	Ba	Elemental Analysis, Wt. %		
		100	210 F					Ca	P	Zn
A1	10W	36.2	5.8	110	0.9	2.0	ND	0.11	0.06	0.06
A2	10W-30	---	---	---	---	---	0.51	T	0.12	0.09
A3	20W	69.6	8.4	99	0.7	3.0	0.47	0.07	ND	ND
A4	30	112.9	11.8	100	1.9	1.9	1.32	T	0.16	0.09
B1	10W-30	75.9	12.6	142	1.8	1.2	0.34	ND	0.13	0.12
B2	20W	---	---	---	---	---	0.20	T	0.05	0.04
B3	20W	75.8	9.3	107	2.8	0.5	0.22	T	0.09	0.07
C1	20W	77.0	9.7	112	2.9	2.2	ND	0.17	0.12	0.11
D1	20W	67.1	8.3	100	0.1	1.4	0.35	ND	0.04	ND
D2	20W	63.7	9.0	121	0.6	1.5	0.35	T	0.06	0.06
D3	10W-30	57.5	9.6	140	1.4	3.5	0.67	ND	0.06	0.06
D4	10W-30	71.2	11.2	137	0.4	3.6	1.30	T	0.04	0.04
D5	10W-30	73.1	11.3	135	0.5	3.5	1.20	T	0.09	0.09
E1	10W-30	68.5	11.4	141	3.2	3.9	0.83	ND	0.12	0.11
E2	10W-30	70.8	11.4	139	3.2	2.5	ND	0.28	0.09	0.12
F1	10W-30	69.6	12.0	144	2.6	1.7	0.07	0.13	0.09	0.10
G1	10W-30	65.8	10.5	137	2.4	2.1	0.40	T	0.15	0.12
G2	10W-30	65.2	10.7	140	2.4	2.1	0.36	T	0.14	0.08
J1	10W-30	66.1	9.6	127	2.0	2.8	ND	0.25	0.09	---
J2	10W-30	62.2	9.9	136	Nil	Nil	ND	T	0.12	0.02
J3	10W-30	67.7	10.8	138	Nil	Nil	ND	T	0.07	0.02
J4	5W	---	---	---	---	---	ND	0.17	ND	ND
J5	20W	78.9	9.4	104	3.0	8.7	ND	0.16	ND	ND
J6	10W-30	66.6	11.1	141	3.3	5.8	ND	0.32	0.09	0.12
J7	20W	77.5	8.9	95	---	---	ND	0.37	0.08	0.09
K1	10W-30	72.1	12.0	141	2.6	2.4	1.47	ND	0.15	0.08
L1	10W	39.1	5.9	101	2.0	0.9	0.20	T	0.12	0.08
L2	5W-20	36.4	7.6	156	---	---	0.30	ND	0.07	ND
L3	10W-30	69.7	11.0	137	2.8	1.7	0.66	T	0.21	0.11
L4	10W-30	68.3	11.0	138	2.1	2.0	0.78	T	0.22	0.12

APPENDIX B - PHYSICAL AND CHEMICAL PROPERTIES OF OILS EVALUATED (CONT)

Oil	SAE Grade	Viscosity, cs		VI	TAN	TBN	Elemental Analysis, Wt. %			
		100	210 F				Ba	Ca	P	Zn
L5	10W-30	69.2	10.4	131	---	---	0.18	T	0.07	ND
L6	30	122.5	12.2	97	1.6	1.0	0.58	T	0.21	0.13
L7	30	124.8	12.4	98	0.9	0.5	0.23	T	0.13	0.10
M1	10W-30	64.8	12.6	151	2.2	0.2	ND	T	0.12	0.12
M2	10W-30	74.0	12.7	144	2.8	0.4	ND	ND	0.12	0.11
M3	20W	81.4	9.4	100	1.1	1.5	T	0.09	0.05	0.06
N1	20W	73.5	8.8	102	0.5	1.9	0.32	T	0.09	0.08
N2	20W	75.4	9.2	105	1.3	1.4	0.37	T	0.10	0.08
O1	10W	45.4	7.2	125	1.9	2.7	0.75	T	0.09	0.09
O2	20W	73.7	9.4	111	1.7	3.3	0.72	ND	0.08	0.09
O3	10W-30	66.2	10.6	137	1.6	2.6	0.72	ND	0.09	0.08
O4	20W	73.9	9.2	108	1.3	4.0	0.62	T	0.10	0.08
O5	30	129.8	11.9	87	1.3	3.8	0.82	ND	0.09	0.10
O6	10W	37.8	5.9	111	0.9	1.5	ND	T	0.06	0.08
O7	20W	76.7	8.8	94	1.0	0.4	0.02	T	0.06	0.08
P1	10W-30	72.2	11.1	135	1.9	3.8	0.70	T	0.08	0.08
Q1	10W-30	80.4	13.1	140	0.3	1.1	0.58	T	0.09	ND
Q2	10W-30	64.2	10.4	138	1.6	2.2	0.53	ND	0.15	0.07
R1	20W	71.8	9.2	112	Nil	0.1	0.01	T	0.01	ND
T1	10W	38.8	6.1	112	0.5	1.7	ND	0.07	0.04	0.04
U1	10W	41.5	6.2	104	0.4	2.0	0.40	0.03	0.07	0.05
U2	30	111.7	11.9	103	1.9	3.6	0.49	T	0.09	0.10
V1	10W-30	75.3	12.2	140	1.4	2.5	0.72	T	0.05	0.06
W1	10W	47.1	6.7	103	Nil	0.3	0.05	T	0.03	0.05
REO 132	10W-30	73.1	11.7	139	1.3	0.1	T	T	0.08	0.09
REO 145	10W-30	74.0	11.8	138	1.0	3.2	0.42	ND	0.14	0.08
REO 147	20W	48.7	6.6	96	2.2	1.0	0.32	T	0.09	0.09

T Trace ND Not Detected

Appendix C — Short-Trip Service Tests

The short-trip service tests consisted of a 3-month period of operation between November and April. New cars were used. The cars were broken in on factory-fill oil and carefully checked to insure that break-in proceeded uniformly, blowby rates were satisfactory, and that engine air-fuel ratios, operating temperatures, and warm-up rates were uniform.

Following assurance that the break-in was satisfactory, the cars were driven in home-to-work transportation service. The drivers were rotated daily and required to abide by the following regulations:

1. No car was driven more than 4 miles at any one time.
2. The accumulated mileage would not exceed 4 miles in any 4-hr period.
3. No car was driven more than 40 mph at any time.
4. Idling was not permitted except as necessary in traffic

The cars were parked outside at all times and the commercial premium-grade gasoline used had a sulfur content of 0.02%.

References

1. G.A. Round, "The New API System of Service Classifications," Proceedings of American Petroleum Institute, Vol. 32, Division of Marketing, Section 32, (1952), 44.

2. "Engine Test Sequences for Evaluating Oils for Service MS," Report of ASTM Subcommittee G-IV, 1959.

3. "Method for Testing Crankcase Oils for Most Severe Service (MS)," GM 4477-P, Revised 1960. General Motors Manufacturing Standards, Materials and Processes.

4. "Engine Tests for Evaluating Crankcase Oils," SAE Handbook, 1960, 228.

5. P.A. Bennett, "Engine Rusting in Service and Dynamometer Tests," Lubrication Engineering, Vol. 16, Nov., 1960, 529.

6. "Oxidation Characteristics of Crankcase Lubricating Oils," Method 3402, Federal Test Method Standard No. 791, Lubricants, Liquid Fuels, and Related Products; Methods of Testing, General Services Administration, Washington 25, D. C.

7. P.A. Bennett, "Some Observations Related to Engine Cam and Lifter Wear," Proceedings of Engine Wear Symposium, Southwest Research Institute, San Antonio, Texas, May, 1958.

8. A.C. Pilger, Jr., "Field Testing of Motor Oil and Gasoline," SAE Quarterly Transactions, Vol. 2, 1948, 354.

9. P.A. Bennett, C.K. Murphy, M.W. Jackson, and R.A. Randall, "Reduction of Air Pollution by Control of Emission from Automotive Crankcases," SAE Transactions, Vol. 68, 1960, 514.

10. R.S. Spent, C.L. Wolfe, and D.R. Stevens, "Nitrogen Oxides, Combustion, and Engine Deposits," SAE Transactions, Vol. 64, 1956, 797.

11. R.F. Stebar, W.M. Wiese, and R.L. Everett, "Engine Rumble -- A Barrier to Higher Compression Ratios?" SAE Transactions, Vol. 68, 1960, 206.

12. "Internal Combustion Engine Service Classifications," SAE Handbook, 1960, 286.

13. R.F. Stebar, and W.M. Wiese, Private Communications.

14. P.A. Bennett, "A Look at the Effects of Lubricant Additives on Surfaces," Presented at the SAE National Fuels and Lubricants Meeting, Tulsa, Oklahoma, November, 1958.

15. L.H. Mulit, and F.W. Kavanagh, "Lubricating Oils for Internal Combustion Engines," SAE Journal (Trans.) Vol. 48, March, 1941, 98.

A Consideration of the Deposit Ignition Mechanism

F. W. Bowditch, and T. C. Yu
General Motors Corp.

THE PROBLEM of deposit-induced surface ignition in gasoline engines has been recognized for about 40 years. As early as 1918 T. A. Boyd (1)*, using one of Midgley's early indicators, recorded pressure cards of pre-ignited gasoline engine explosions. Since then, a number of abnormal combustion phenomena which can be traced to deposit ignition as the origin have been identified; for example, preignition, wild-ping, and, more recently, rumble.

Despite the long history of interest in the subject, the mechanism of ignition by hot surfaces, whether caused by deposits or by hot spots in the combustion chamber, is not well understood. This should not be surprising, since the ignition mechanism of spark knock, which has received considerably more attention than deposit ignition, has not been completely elucidated. Nevertheless, the problem of deposit ignition in today's automotive engines is one of serious proportions, gradually approaching the problem of spark knock in overall importance. It therefore requires continued effort to understand the mechanism of deposit ignition so that the most effective remedial measures can be determined.

In this paper, a comparison is made of the ease of ignition in an operating engine of various fuel-air mixtures by both engine deposits and hot wires. From the results of this study, a model of the mechanism of deposit ignition is proposed, based upon the assumption that the basic surface ignition process is the same regardless of the type of surface Although the model is not adequate to satisfactorily explain all known experimental data, verifying experiments reported herein, together with the fact that the model is consistent with most experimental data, indicate that it is worthy of consideration.

* Numbers in parentheses designate References at end of paper.

Equipment and Procedure

Two different sets of equipment were used in obtaining the data discussed herein. One was used in finding the deposit ignition resistance of fuels and the other to determine the time and surface temperature for ignition by hot surfaces. Both techniques were applied in the same operating engine.

APPARATUS USED FOR DETERMINATION OF DEPOSIT IGNITION RESISTANCE OF FUELS - The most difficult problem in finding the deposit ignition resistance of fuels is to provide a reproducible deposit condition in a reasonable length of time. This problem was attacked by using a deposit aspiration technique, originally proposed by Sabina, Mikita, and Campbell (2), whereby engine deposits were introduced to the engine through the induction system. This technique eliminates the time-consuming process of building up deposits in the combustion chamber.

Fig. 1 shows a schematic view of the equipment. To introduce deposits, 0.1 gr of 65-80 mesh engine deposits were loaded into the check valve through the deposit filler hole. The actuating switch was then depressed. This allowed the

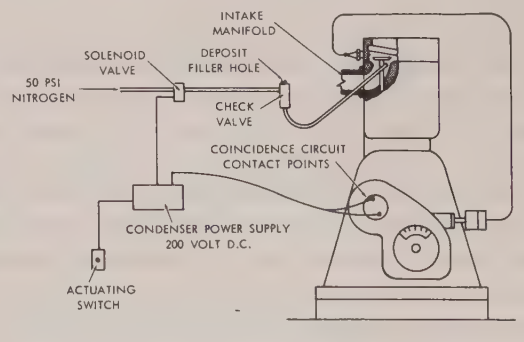

Fig. 1 — Schematic of deposit aspiration apparatus

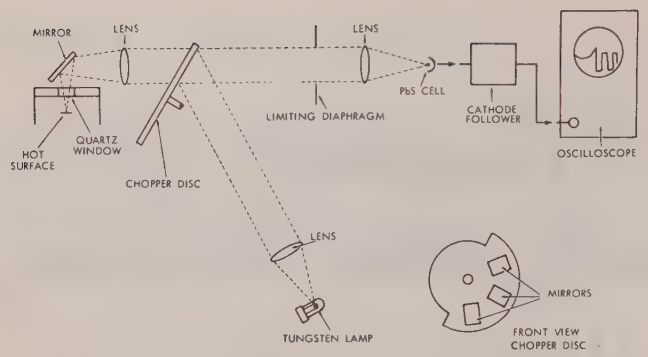

Fig. 2 — Schematic of optical temperature-measuring system

Fig. 3 — Schematic of surface radiation oscillogram

solenoid valve to open when the coincidence circuit contact points driven by the engine were closed. The contact points were set so that the nitrogen plus deposits reached the underside of the engine intake valve just as it opened. This allowed the nitrogen and deposits to enter the combustion chamber during the intake stroke and provided about 180 deg of crankshaft rotation to complete the aspiration process. This technique produced relatively short-lived, but great, deposit activity.

Measuring the amount of deposit activity was accomplished by determining the time of occurrence of peak cylinder pressure in each of the 20 cycles immediately following aspiration. The average of these values was compared with the average time of peak cylinder pressure for the 20 normal explosions just preceding aspiration. The greater the difference between the two average times of peak pressure, the greater the deposit activity or the lower the ignition resistance of the fuel being tested.

In order to monitor the times of occurrence of consecutive peak cylinder pressures, an electronic counter called the peak pressure distribution counter was designed and built by the physics department of the General Motors Research Laboratories. The instrument is discussed in detail in a paper by Weller, Schubring, and Fitch (3) and is similar to the one described more recently by Hyatt, Tomsic, and Mellinger (4).

The engine deposits used in the aspiration system could be either synthetic or actual engine deposits. Numerous attempts were made to produce synthetic deposits, but the problem of obtaining an intimate association of carbon and lead salts was never solved satisfactorily. The deposits used in these experiments were actual deposits scraped from a multicylinder engine operating on a commercial fuel and oil.

The test engine used in this series of experiments was a L-head ASTM-CFR engine having a compression ratio of 6.75:1. Table I shows the engine operating conditions. These operating conditions were chosen after considerable experimentation. While the effects of most of the engine operating variables on the severity of deposit ignition were already known, the problem here was to provide the maximum sensitivity in measuring deposit ignition resistance of fuels.

APPARATUS USED IN DETERMINING TIME OF IGNITION AND SURFACE TEMPERATURE - Various stationary hot surfaces ranging from deposit pellets to chromel wires were used in the study of surface ignition with an operating engine. Part of this study required the measurement of both the time of ignition of the gaseous mixture and the relative surface temperatures of the hot surfaces at the time they caused ignition.

An ionization gap was used to indicate when ignition occurred. A special 10-mm AC spark plug (number 458-JAA) with electrodes extended about 9/16 in. was used as the ionization gap. This gap was positioned in the head of the engine such that the gap was approximately 1/8 in. from the hot surface, causing ignition. By applying 45 v dc to the ionization gap, sufficient current flow through the gap was available to trigger other electronic equipment when the gap became ionized. The output of the gap was fed through a pulse shaper to the peak pressure distribution counter referred to earlier. The counter produced a visible display of distribution of times of gap ionization (in terms of crank angles) for 100 consecutive cycles. From this information, an average time of ionization was calculated. This time was taken as the average time of ignition by the hot surface, since the assumption was made that the time required for a flame front to travel the 1/8 in. from the wire to the gap was constant, regardless of fuel.

An optical system utilizing a lead sulfide cell was constructed to measure the surface temperature of the igniting surface at the time of ignition. Fig. 2 shows a schematic representation of the system. For convenience of discussion, the instrumentation can be broken down into the optical and electrical portions.

The functions of the optical portion were to focus the radiation from the hot surface onto the lead sulfide cell and to provide a means of standardizing the cell. A 3/8 in. diameter quartz window was mounted in the cylinder head directly over the hot surface. Radiation from the hot surfaces that passed through the quartz window was reflected off a front-surfaced mirror into a collumating lens and focused by a second lens close to the cell.

Standardization of the hot surface radiation was accomplished by providing a tungsten lamp in an additional optical path. The lead sulfide cell was exposed to the tungsten lamp

about one-quarter of the time by means of three front-surfaced mirrors mounted on a light chopper disc which was driven at one-half engine speed. The disc was so constructed that, as shown in Fig. 2, one-half of the time the lead sulfide cell was exposed to the radiation from the hot surface in the engine and the remainder of the time exposed alternately to the radiation from the tungsten lamp and to the radiation from the portions of the disc assumed to be at room temperature.

The electrical portion of the temperature-measuring system consisted of a lead sulfide cell, a cathode follower, and an oscilloscope. Lead sulfide cells are infrared sensitive, photoelectric devices whose resistances change in proportion to the amount of radiation received. By applying a fixed voltage to the cell and measuring the current variation, a signal proportional to radiation was obtained. For the data cited herein, a Cetron E 706 lead sulfide cell was used. This cell had a time constant of about 60 mu sec.

A sketch of a characteristic oscillogram produced by the temperature-measuring system is shown in Fig. 3. The three square waves represent standardizing signals from the standardizing portion of the optical circuit. The tops of the square waves were caused by the radiation from the tungsten lamp and the bottoms by the radiation from the room-temperature portions of the disc. The standardizing section of the disc served not only as a means of signal calibration, but also as a means of blocking out the relatively intense gas radiation due to combustion that would otherwise saturate the lead sulfide cell.

The right-hand half of the trace represents the variation in radiation of the hot surface from about the beginning of the intake stroke until combustion is initiated. Point A on the trace represents the time that ignition occurs. The last portion of the trace represents radiation from both the hot surface and the hot gases. The temperature of the surface just prior to ignition was the important temperature in these studies; therefore, the radiation at Point A was the crucial value.

The optical lead sulfide system has three major advantages:

1. The system has a sufficiently high frequency response to follow the transient temperature variations of a hot surface in an engine running at 1000 rpm.

2. The optical system measures surface temperature, believed to be the critical temperature as far as surface ignition is concerned, rather than average mass temperature.

3. There is no physical connection between the optical system and the object being measured. Thus, the igniting surface may be changed without disturbing the temperature-measuring apparatus.

The major disadvantage of the optical system is the fact that it does not provide a direct temperature reading. To convert the output of the lead sulfide system into temperature readings, it would be necessary to know the emissivities of the ignition source. Such information is not readily available. Since relative temperatures were sufficient for most of the experiments, the disadvantage of not knowing the emissivities did not prove to be a serious handicap in the present investigation.

Table 1 - Engine Operating Conditions

Engine speed	1000 rpm	Coolant temp.	360 F
Throttle	Fully open	Oil Temp.	180 F
Inlet air pressure	Atmospheric	Spark advance	tdc
Inlet air temperature	Ambient	Air-fuel mixture	10% rich

The engine and operating conditions (Table 1) for this series of experiments were the same as those used for the deposit ignition experiments described previously.

Data and Discussion

DEPOSIT IGNITION RESISTANCE RATINGS OF FUELS - As mentioned previously, the major difficulty in finding deposit ignition resistance of fuels is to provide reproducible engine deposit conditions from cycle to cycle and from rating to rating. In order to circumvent as much of the difficulty as possible, two steps were taken.

1. Leaded iso-octane-benzene (LIB*) reference fuels were run as standards, along with the fuels to be rated.

2. By randomly changing the order in which the fuels are rated, and by rating each fuel including the standard ones a number of times, statistical procedures could be used to arrive at average ratings and to determine if significant differences existed between the fuels.

The so-called standard or LIB reference fuel series is made up of blends of leaded iso-octane and leaded benzene. Each blend contains 3 ml tel/gal to ensure that the antiknock quality of the blends is sufficiently high to suppress spark knock under most conditions. Since iso-octane has a high resistance to deposit ignition and benzene a low resistance (5), blends of the two form a reference fuel system that can be used in rating the deposit ignition resistance of fuels. The LIB numbers assigned to these blends are equivalent to the volume percentage of leaded iso-octane in the blend.

The deposit ignition resistance ratings of fuels are expressed as the LIB reference fuel equivalent in deposit ignition resistance as defined by the difference in time of peak cylinder pressure technique described previously. Each fuel was run a total of 16 times in random order; so each rating is an average of 16 determinations.

Table 2 shows deposit ignition resistance ratings of a number of hydrocarbons. With the exception of furan and methanol, each rating shown is an average of at least three ratings, or three times 16 determinations.

* Originally proposed by the Combustion Chamber Deposits Group, Coordinating Research Council.

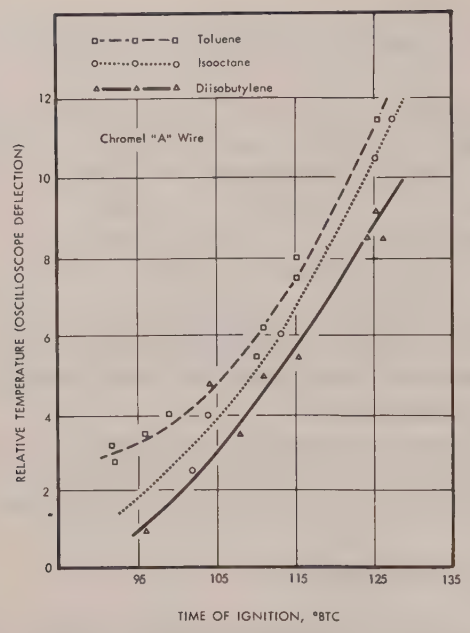

Fig. 4 — Effect of surface temperature on hot spot ignition

Table 2 - Resistance of Fuels to Ignition by Engine Deposits as Determined by the Engine Aspiration Technique

Fuel		Rating LIB Number
2,2 Dimethylbutane	High Resistance	120
Isooctane		100
2,3 Dimethylbutane		86
Diisobutylene		57
Cyclohexane + 3 ml tel/gal		51
Toluene		42
Furan		30
Benzene		0
Propane		-12
Methanol		-110
Ethylene	Low Resistance	-175

The brackets shown on the data indicate that any two fuels within the same bracket are not significantly different at the 95% confidence level. These significance-determinations were made by use of the statistical method described by Duncan (6).

Obviously, methanol and ethylene ratings represent gross extrapolations of the reference fuel system, since benzene with an assigned LIB rating of zero represents the reference fuel with the least resistance to deposit ignition. The ratings of methanol and ethylene are included, however, to give an indication of the range of deposit ignition resistances of hydrocarbons which can be used as fuels in spark ignition engines.

Even though the total range of deposit ignition resistance ratings vary from 120 to -175, or about 300 LIB numbers, most commercial fuels appear to fall in a 25-LIB range between 50-75 LIB numbers (7). Very little data are available to indicate whether or not the fuel ratings shown in Table 2 would be the same if determined in a multicylinder engine on the road. However, the ratings shown by Stebar, Wiese, and Everett (7) of toluene and 2,3 dimethylbutane, using a multicylinder engine road-rating technique, does show good agreement with the ratings shown in Table 2 for these two fuels.

HOT SPOT IGNITION RESISTANCE RATINGS OF FUELS - Another form of ignition which, superficially at least, bears a resemblance to deposit ignition is hot spot ignition. It was thought that a careful study of the hot spot ignition resistances of fuels in the same engine and under the same engine operating conditions as was used in obtaining the data shown in Table 2 might provide a clue to the mechanism of deposit ignition. Therefore, such determinations were carried out using the L-head ASTM-CFR engine and the operating conditions shown in Table 1.

A chromel "A" wire, 0.040 in. in diameter, was used to simulate the hot spot. The wire was bent into a U-shape, 3/8-in. long, and brazed to the center electrode and threaded body of a 14-mm glow plug in place of the original resistance wire. The wire was heated electrically by use of a 6 v storage battery and the temperature of the wire was varied by changing the current in the wire with a carbon stack rheostat.

The time of the ignition caused by the hot wire and the relative surface temperature of the wire were determined by the methods described previously.

There are two obvious means of finding the relative resistances of a group of fuels to ignition by such a hot wire:

1. Vary the temperature of the wire to produce a constant time of ignition, regardless of fuel. The temperature of the wire for each fuel then can be assumed to be a measure of the resistance of the fuel to hot spot ignition. Preferably, such a method would require that the absolute temperatures of the wire be determined.

2. Maintain the wire temperature constant at the time of ignition. Then the time that ignition occurs can be used as a measure of ignition resistance.

During experimentation using both methods, it was discovered that the data showed some variation. Therefore, a number of readings were required so that a statistical average could be obtained. The latter method of finding ignition resistances of fuels was preferred, since the time of ignition could be recorded automatically by the electronic counter described earlier.

To determine whether both methods produced the same ranking of fuels, a series of experiments was run using isooctane, di-isobutylene, and toluene. From these experiments, the times of ignition were determined for a series of apparent wire temperatures. The results are shown in Fig. 4. As shown in the figure, the relative ignition resistances of these three fuels did not vary, regardless of whether

a constant time of ignition or a constant wire temperature and variable ignition time was used to rate the various fuels. This rating was assumed to reflect the relative hot spot ignition resistances of the fuels.

The actual procedure of maintaining a constant wire temperature at the time of ignition was accomplished by setting the tungsten lamp in the optical temperature-measuring system at a predetermined temperature and varying the chromel wire current until the wire signal at the time of ignition gave the same vertical oscilloscope deflection as did the tungsten lamp signal. This condition is represented in Fig. 3 by having Point A on the hot wire portion of the trace equivalent to the tops of the calibration square wave.

The predetermined temperature was chosen so that the wire would ignite fuels of both high and low ignition resistance and still not cause fuels of low ignition resistance to backfire through the intake valve. The wire temperature at the time of ignition then was maintained identically for all fuels by adjusting the wire current as required.

To facilitate the comparison of the ignition resistances of a number of fuels, an interlocking chain block experimental design (8) was used in conjunction with Duncan's statistical analysis (6), mentioned earlier. This procedure minimized any bias in the data due to run-to-run variation within fuels, as well as day-to-day variation in average ratings. It also provides a method of finding significant differences between fuels. This procedure required that each fuel be rated four times in a prescribed order and that each rating be an average one of 100 consecutive engine explosions. The necessary data was conveniently accumulated by the electronic counter.

Table 3 shows the hot wire ignition resistance ratings of 10 fuels, as determined by the procedures just described. The fuels are arranged in decreasing order of ignition resistance. The earlier the time of ignition, the lower was the resistance, since the wire was always adjusted to produce the same temperature just prior to ignition, regardless of fuels or times of ignition. The brackets on the data again indicate that fuels within the same bracket are not significantly different at the 95% confidence level.

Among the hot spot ignition results in the literature, two series of experiments are particularly pertinent to the present investigation. One of these was a series of experiments run in operating engines by a group of laboratories for the Combustion Chamber Deposits Group, Coordinating Research Council (9). In these experiments, an electrically heated glow plug was used as the source of ignition. The minimum glow plug current that would cause ignition was used as the measure of ignition resistance.

The results obtained in this manner are not in agreement with those shown in Table 3. This is not surprising, since the CRC program participants assumed that the wire temperature was a function of wire current alone, whereas for the results reported herein no such assumption was necessary.

To determine the effect of this assumption, a series of

Table 3 - Resistance of Fuels to Ignition by a Hot Wire in an Operating Engine

Fuel		Time of Ignition Deg btc
Methane	High Resistance	No Ignition
Toluene		82.0
Propane		84.0
Iso-octane		96.0
2,2 Dimethylbutane		102.0
Di-isobutylene		103.7
Indonene		106.2
2,3 Dimethylbutane		112.3
Benzene		114.0
Ethylene	Low Resistance	>150 (backfired)

experiments were run with the procedure used by the CRC Program participants. At the same time, the temperature of the wire producing ignition was measured by the previously described optical system. It was found that if wire current was used as the measure of wire temperature, the results were the same as those obtained by the CRC Program participants. However, if the optical indication of the temperature of the wire just prior to ignition was used, then results consistent with those shown in Table 3 were obtained.

It would appear from these experiments that heat transfer between the hot wire and the surrounding gases materially affects the temperature of the wire. When the wire current was held constant, experiments with benzene, toluene, cyclohexane, and iso-octane showed that the surface temperature of the wire, as measured with the optical temperature-measuring system, varied with the fuel used and with the engine operating conditions. It would therefore appear that wire current is not a satisfactory index of wire temperature in an operating engine.

A series of experiments performed by Agnew and Bowlus (10) is also of interest. These experiments were carried out in a constant volume bomb. Centrally located within the bomb was a nickel-chromium wire which was heated electrically. The wire was heated at a rate so that ignition occurred in 3 sec. The wire temperature was monitored through a small window in the bomb with a calibrated photoelectric cell.

Table 4 shows the results of these experiments.

The fuels marked with an asterisk were also rated in the engine experiments reported in Table 3. A comparison of the relative rankings of the fuels in Tables 3 and 4 shows good agreement, despite the wide differences in experimental conditions.

PROPOSED MECHANISM OF DEPOSIT IGNITION - As can be seen in Tables 2 and 3, comparison of the experimental results which were obtained in the same engine, under the same engine operating conditions but with different sources

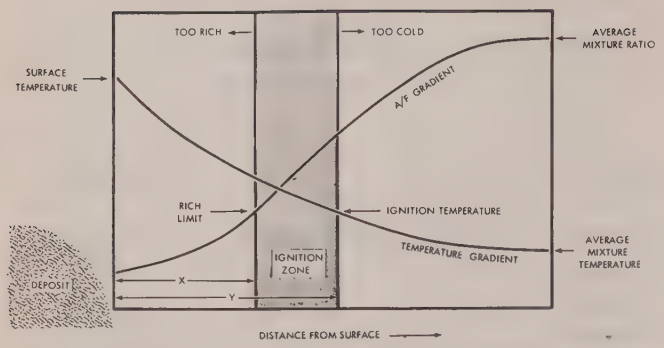

Fig. 5 — Schematic illustrating ignition by engine deposits according to proposed ignition mechanism

Table 4 - Resistance of Stoichiometric Air-Fuel Mixtures to Ignition by a Hot Wire - Constant Volume Bomb Experiments (10)

Fuel	Wire Temperature Just Causing Ignition, F
*Methane	> 2300
*Toluene	2240
*Propane	2215
*Iso-octane	2210
*Benzene	2170
n-Hexane	2150
Butane	2140
Cyclohexane	2140
Ethane	2080
n-Heptene	2050
*Ethylene	1900
Acetylene	1760

of ignition, shows that ignition resistances of fuels vary with the type of surface causing ignition. If it is assumed that basically the ignition mechanisms are the same with a variation to account for the difference in surface characteristics, then an interesting speculation as to the mechanism of ignition by hot surfaces can be made.

Briefly, the proposed mechanism stipulates that a fuel-air mixture, upon contact with a hot surface, will be heated and ignition of the mixture will occur if the following two conditions are simultaneously satisfied:

1. The composition of the mixture is within the limits of inflammability.

2. The temperature of the mixture is above the ignition temperature.

With certain materials -- for example, engine deposits -- combustion of the surface causing ignition occurs. When this takes place, oxygen must be consumed in the process. The removal of oxygen from the mixture creates an oxygen deficiency in the mixture adjacent to the surface.

It has been well established that combustion can occur only within fairly narrow limits of air-fuel ratios--the two

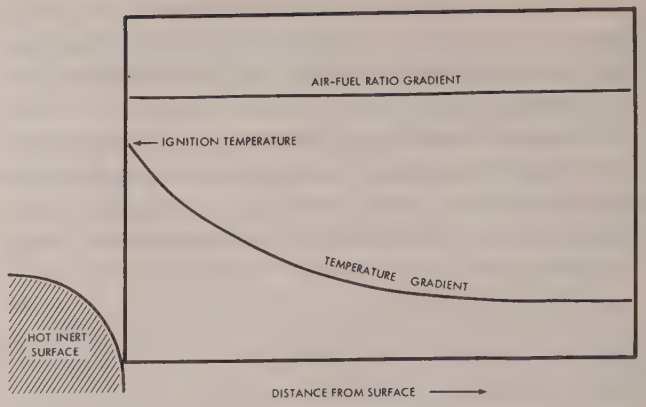

Fig. 6 — Schematic illustrating ignition by inert surfaces according to proposed ignition mechanism

limits of inflammability (11). In the case of deposit ignition, the engine deposit may consume so much oxygen that the air-fuel ratio of the mixture immediately adjacent to the deposit surface may exceed the rich limit of inflammability. If ignition is to take place under these circumstances, it must do so at a distance from the deposit surface where the air-fuel mixture is within the flammability limits.

If it is further assumed that for surface ignition of any type to occur some critical volume of air-fuel mixture must be heated by the surface to the ignition temperature of the mixture, then the further this critical volume is from the surface, the hotter the surface must become to cause ignition because of heat transfer considerations (based on thermal theory of ignition). The combination of local temperature and air-fuel ratio considerations constitutes the basis of the proposed mechanism of ignition by hot surfaces in general and deposits in particular.

A schematic illustration of a case in which deposit ignition would occur according to the proposed mechanism is shown in Fig. 5. As shown in the figure, the temperature of the mixture surrounding the deposit is assumed to decrease as the distance from the surface increases, until the average mixture temperature is reached. Also, the air-fuel ratio of the mixture is assumed to increase as the distance from the surface increases, until the average ratio of the mixture is reached.

Up to a distance X from the deposit surface, the air-fuel mixture surrounding the deposit is too rich to burn, because the deposit has consumed too much of the local oxygen supply. At distances greater than Y from the deposit surface, the air-fuel mixture temperature is too cold to cause ignition. Since a zone exists which is greater than distance X from the deposit surface, but less than distance Y, then both the temperature and air-fuel requirements for ignition are satisfied simultaneously and ignition should occur.

In the case where the surface causing ignition does not consume oxygen, the mixture requirement for ignition is no longer important. As shown schematically in Fig. 6, a temperature gradient will still exist in the immediate neighborhood of the surface as before. However, the air-fuel ratio

will now be independent of distance from the surface. Therefore, as soon as the surface reaches the ignition temperature of the air-fuel mixture, as shown schematically in the figure, ignition will occur at the surface proper.

There are a number of complicating effects which have thus far been ignored. For instance, it has been well established (11, 12) that dilution of CO_2 and N_2 can have a very substantial effect on the limits of inflammability. Also, information regarding the effect of mixture ratio on the ignition temperature is not complete. Investigations by Spencer (13), as well as our own, showed that mixture ratio had negligible effect on hot wire ignition temperature for the range of mixture ratios commonly encountered in operating engines. However, whether this finding can be extended to the limits of inflammability has not been determined.

It has been known for a number of years that some surfaces are catalytic and conducive to certain surface reactions. As an example, consider the ignition experiments of Coward and Guest (14). In their experiments, it was found that platinum wire, though very active catalytically, required a higher temperature to ignite fuel-air mixtures than a surface of equal dimension but of lesser catalytic action. On the other hand, when a cold jet of hydrogen and oxygen mixture was allowed to stream over cold platinized asbestos, the asbestos became red hot and ignition of the mixture followed.

The explanation (15) applied to this set of seemingly contradictory facts was that surface reaction reduced the the availability of the fresh mixture near the surface of the platinum wire. Consequently, the temperature required for ignition was increased. In the case of platinized asbestos, however, since the heat conductivity is poorer than that of platinum wire, the platinized asbestos material attains higher surface temperatures and ignition is more likely to occur.

It is interesting to note the similarity of this explanation with the present explanation of deposit ignition where oxygen near the deposit surface is consumed by the combustion of the deposit, and as a result, gas phase ignition occurs at some distance from the deposit surface.

Catalytic surface reactions probably also occur during the ignition process by hot surfaces in operating engines. As was shown, this type of reactions exerts considerable influence on surface temperature and local mixture air-fuel ratio. However, when these two factors have been duly considered as they are in the proposed ignition mechanism, the principal effects of catalytic surface reaction on ignition are taken into account.

There is another area in which surface reactions might have influence on surface ignition. That is the possibility that surface reactions may produce reaction products with lower ignition temperatures than the parent hydrocarbon. At present, we know of no way to evaluate this possibility.

CORRELATION OF EXPERIMENTAL RESULTS WITH PROPOSED IGNITION MECHANISM - Surface temperature was suggested in the proposed ignition mechanism as being one of the influential parameters in the ignition process by hot surfaces. Experiments were performed to assess the importance of this variable on ignition using both inert and oxygen-consuming surfaces.

Temperature Effect--Inert Surfaces - Since it was necessary to change the surface temperature of the igniting source independent of operating conditions, a glow plug was used as the igniting hot spot. The temperature of the glow plug was varied by changing the glow plug current and the radiation emitted by the glow plug was taken as a measure of its surface temperature.

Fig. 4 shows the effect of relative surface temperature (in terms of oscilloscope deflection) on the ignition tendency (measured by time of ignition) for toluene, iso-octane, and di-isobutylene. It can be seen that ignition tendency is dependent upon the surface temperature; the greater the surface temperature, the greater the ignition tendency.

Temperature Effect--Oxygen-Consuming Surfaces - In this series of experiments, the igniting surface used was a small cylindrical pellet (1/4-in. in diameter and 5/16-in. long) made of 10% PbO and 90% carbon. The pellet was suspended about 1/8 in. from the combustion chamber wall by a small wire.

The temperature effect on ignition by the pellet (an oxygen-consuming surface) is shown in Fig. 7. As with the case of the hot wire, ignition tendency increases with surface temperature. Both Figs. 4 and 7 support the proposed ignition mechanism that surface ignition is dependent upon the surface temperature.

Surface Effect - In order to investigate the effect of surface on the ignition process, the ignition tendencies of a number of surfaces were compared. The surfaces tested consisted of a selection of metallic wires and strips, porcelain pellets, alumina pellets, engine deposit pellets, and pellets

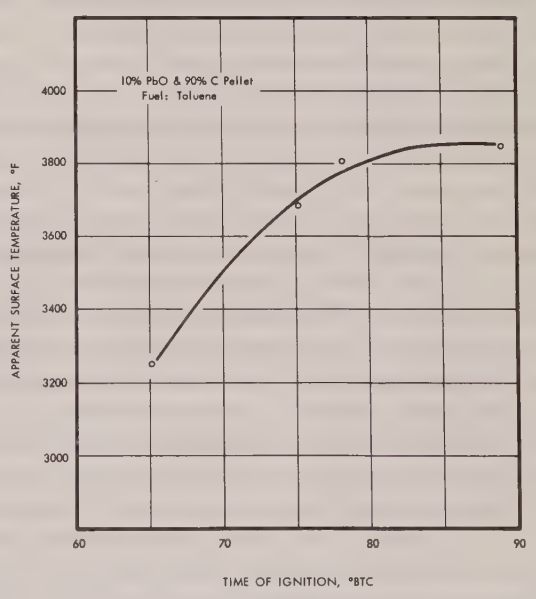

Fig. 7 — Effect of temperature on ignition by oxygen-consuming surfaces

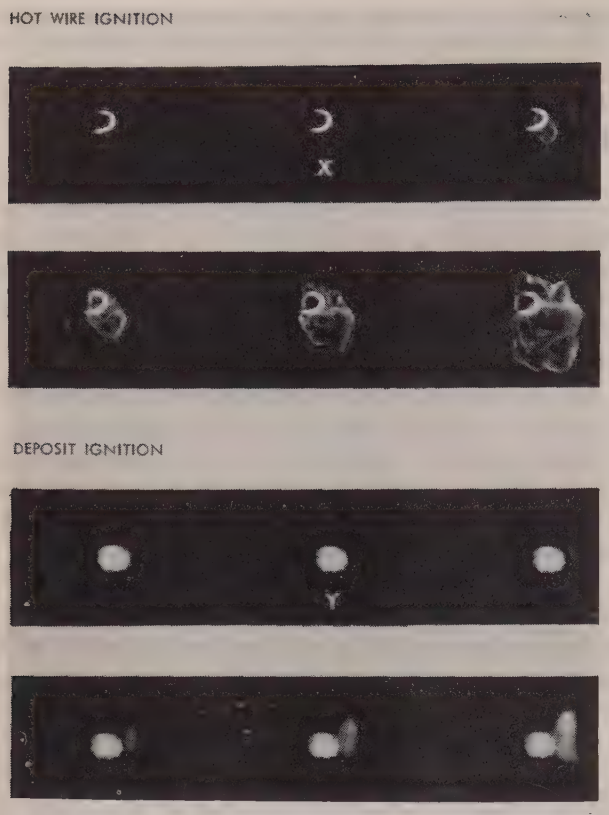

Fig. 8 — High-speed flame photographs of ignition processes by hot wire and engine deposits

made of various proportions of PbO and carbon. The experiments were carried out under the same operating conditions as described in Table 1, and the fuel used was toluene.

Since it was not possible to heat these surfaces electrically, the surface temperature was increased by advancing the timing of the spark discharge. This increased the duration of exposure of the surfaces to the hot combustion chamber gases. When the surface was heated up sufficiently, surface ignition would start. Then the spark discharge was turned off and self-sustaining surface ignition occurred.

The surface temperature required to ignite a given fuel-air mixture at a given time was found to be dependent upon the type of surface; in other words, the abilities of various surfaces to cause ignition were not the same. The most pronounced difference was found between engine deposits and hot spot surfaces. To ignite a toluene-air mixture at 75 deg btc, deposit pellets required an apparent surface temperature of about 3710F, while an electrically heated chromel wire needed only about 3100 F. It thus appears that surface temperature is not the sole parameter controlling the ignition process.

The major difference between engine deposits and hot spots is that the former are combustible while the latter are not. Observations through the quartz window in the combustion chamber of the test engine showed that the engine deposit and PbO + C pellet surfaces glowed brightly when surface ignition took place and that the pellets disappeared after a few minutes of engine operation. This appeared to indicate that combustion of the pellets was indeed occurring.

The proposed mechanism of ignition is consistent with these experimental observations. Since ignition is proposed to occur at some distances from a combustible or oxygen-consuming source of ignition, but at the surface of a non-combustible or non-oxygen-consuming one, the required surface temperature to cause ignition is expected to be higher for a combustible source than for a non-combustible one.

Combustion Movies of Deposit Ignition and Hot Spot Ignition - In order to verify the deduction that the point of ignition is, indeed, dependent upon the amount of oxygen the igniting surface consumes, high-speed movies were taken in an operating engine of the ignition processes caused by inert and engine-deposit surfaces. The inert surface was a U-shaped chromel "A" wire mounted as a glow plug and heated electrically. The oxygen-consuming surface was a 1/4 in. diameter by 5/16 in. long pellet made of engine deposit and was attached to the combustion chamber wall by a small wire. The igniting surface was mounted midway between the intake and exhaust valves of the L-head single-cylinder engine described earlier. The operating conditions were the same as those shown in Table 1 and the fuel was toluene.

Fig. 8 shows six consecutive frames from the high-speed movies taken of hot wire and deposit ignition. The glowing U-shaped hot wire is clearly visible in the upper photographs and ignition of the fuel-air mixture is seen to take place in the frame marked X.

The lower photographs show the burning deposit pellet with ignition of the gaseous mixture barely visible in the frame marked Y. The deposit ignition photographs are not as sharply defined as the hot wire ignition ones, because the burning engine deposit rapidly coated the quartz window with a thin layer of lead salts before photographs could be taken.

As can be seen in frame X, hot wire ignition took place at or very close to the wire surface; however, as shown in frame Y, ignition occurred at a distance from the deposit surface--the distance in this case being about 1/16-in.

Summarizing, the experimental results appear to support the proposal that both the surface temperature and the air-fuel ratio of the local ignition mixture are important parameters affecting surface ignition. It should be pointed out, however, that the local air-fuel ratio is the same as the average mixture ratio in the combustion chamber when the igniting surface does not consume oxygen. This is proposed as the reason why fuels react differently to deposit ignition than to hot spot ignition. The former is caused by an oxygen-consuming surface while the latter is caused by an inert surface.

Surface Ignition Resistance of Fuels - The proposed mechanism of ignition stipulates that surface temperature and local mixture ratio at the time of ignition exert important influences on ignition by hot surfaces. If these are the predominant influences on ignition, then a consideration of

temperature and mixture ratio limitations should permit the prediction of deposit ignition resistances of fuels. The two fuel properties which appear most clearly related to surface temperature and local mixture requirements are ignition temperature and rich limit of inflammability.

Ignition temperature is the minimum temperature to which the mixture must be heated in order to obtain ignition. Experimentally, the ignition temperature may be determined by measuring the minimum surface temperature required for ignition by an inert surface: that is, a surface which does not enter into the ignition process chemically. It is only when ignition takes place at the surface proper that ignition temperature and surface temperature are equivalent.

When a fuel-air mixture having a high ignition temperature is ignited by a hot surface, the surface temperature required for ignition also will be high. It follows that the higher the ignition temperature, the greater the ignition resistance of the fuel, all other conditions being equal.

When the igniting surface consumes oxygen, the ignition mechanism predicts that the mixture at the surface is rich in fuel but deficient in oxygen. The minimum distance from the surface beyond which ignition can occur is, therefore, dependent upon the rich limit of inflammability. Thus, a fuel having a lean rich limit has high deposit ignition resistance, all other conditions being the same.

Table 5 shows the deposit ignition resistance, the hot wire ignition resistance, and the rich limit information for the six fuels for which complete data are available. The deposit ignition resistance and the hot wire ignition resistance data are taken from Tables 2 and 3 respectively. The data shown in Table 5 are relative rankings, 1 being the fuel with the greatest ignition resistance and 6 the one with the least resistance. If the ignition source (a chromel wire) used in determining the hot wire ignition temperature is assumed to be inert, the hot spot ignition temperature is equivalent to the ignition temperature. Therefore, it may be assumed that the hot wire resistance is directly related to the ignition temperature.

The information shown under the rich limit classification in the table is the limit in terms of the percent of stoichhiometric air-fuel ratio (16). The numbers in parentheses represent the rankings of the fuels only on the basis of the rich limit information (shown with 1 again representing high resistance and 6 low resistance).

Combined consideration of the rankings shown under the hot wire ignition resistance and rich limit should, ideally, predict the ranking shown under deposit ignition resistance. In the actual case, however, the correlation is not always consistent. For instance, 2,2 dimethylbutane has intermediate resistance to hot wire ignition (ranking of 4) and also an intermediate rich limit ranking (4). A consideration of these two rankings predicts an intermediate deposit ignition resistance, rather than the high resistance it is shown to have. Of the remaining five fuels, toluene, benzene, and ethylene predictions are reasonably good, while iso-octane and especially propane predictions are poor. The reason for the failures is not clear. Perhaps the effects of dilution and temperature on the rich limit, not considered in the correlation, are responsible.

Table 5 - Relative Rankings of Fuels Based on Deposit Ignition Resistance, Hot Wire Ignition Resistance, and Rich Limit

Fuels	Relative Ranking: Deposit Ignition Resistance	Relative Ranking: Hot Wire Ignition Resistance	Rich Limit % Stoich. A/F
2,2 Dimethylbutane	1	4	28.5 (4)
Iso-octane	2	3	27.8 (5)
Toluene	3	1	31.0 (2)
Benzene	4	5	29.8 (3)
Propane	5	2	35.3 (1)
Ethylene	6	6	16.4 (6)

As mentioned previously, H_2O, CO_2, and other inert gases have substantial effect on the flammability limits of many fuels. The effect of dilution is to narrow the flammability limits. Therefore, the rich limit of a fuel is changed in the presence of diluents, and dilution would be expected to have a substantial influence on the deposit ignition resistances of fuels.

For most mixtures, it has been shown that there is a straight line relation between the limit of inflammability and the mixture temperature (17). The flammability limits widen with increasing temperature. If this factor is taken into account, the ranking of the fuels shown in Table 5 may also change considerably. For example, propane has a very high ignition temperature: that is, a ranking of 2 under hot wire ignition resistance. Therefore, the rich limit of propane at the ignition temperature would be expected to be considerably richer than that shown in Table 5. This would lower its predicted deposit ignition resistance and would make its ranking more consistent with the data shown in Table 5.

While it is realized that both dilution and temperature must be considered in connection with the rich limit, unfortunately, sufficient information is not available to permit a proper evaluation of these factors. Consequently, it is not possible at the present time to resolve whether the proposed ignition mechanism is sufficient to explain the differences in ignition resistances of fuels. However, as was shown, the mechanism can be used to explain some otherwise unexplainable experimental facts. It is our belief that the proposed ignition mechanism is worthy of serious consideration, despite the lack of positive confirmation here.

Effect of Engine Operating Conditions - A number of operating variables have been shown to have influence on deposit ignition. It is of interest to consider some of these

findings utilizing the proposed mechanism of ignition, both as a check on the validity of the mechanism and to illustrate how it can be applied to actual situations.

Compression Ratio and Inlet Air Temperature - The influence of compression ratio and inlet air temperature on deposit ignition was reported by Stebar, Wiese, and Everett (7). It was found that increasing the compression ratio raised the rumble (a form of deposit ignition requirement. These findings are in agreement with the proposed ignition mechanism. Increasing either the compression ratio or the inlet air temperature increases the mixture temperature. With a high mixture temperature, the surface temperature required to heat the mixture to its ignition temperature is lower. Moreover, for most mixtures, the rich limit becomes richer with increasing mixture temperature. There fore, the proposed mechanism predicts that ignition will take place closer to the igniting surface and thus will occur more readily. Both the temperature and mixture ratio parameters predict the effect of compression ratio and inlet air temperature shown experimentally.

Air-Fuel Ratio - The effects of air-fuel ratio reported in the literature are not consistent. Stebar, Wiese, and Everett (7) found that the deposit ignition tendency is the greatest near maximum power mixture. Results of Melby, Diggs, and Sturgis (18), however, showed deposit ignition tendency increased with lean mixtures.

The proposed mechanism predicts that as the overall mixture becomes leaner, the rich limit will be reached closer to the igniting surface. As a result, the ignition tendency increases with lean mixtures.

However, there is another factor which should be considered--dilution by nitrogen. As the proportion of air increases when the mixture becomes leaner, the ratio of nitrogen to fuel increases. Investigations by Coward and Jones (17) showed that the rich limit becomes leaner as the percentage of inert diluent in the mixture increases. The net effect of excess nitrogen in the mixture is to reduce the deposit ignition tendency.

Summarizing, the proposed ignition mechanism predicts that increasing the air-fuel ratio increases the ignition tendency until the dilution effect of nitrogen becomes predominant.

Inlet Air Humidity - The effect of humidity was also investigated by Stebar, Wiese, and Everett (7). Their finding reveals that deposit ignition tendency decreases with increasing humidity. This finding is in agreement with the proposed mechanism, since water has a pronounced effect on the rich limit (17). The rich limit becomes leaner in the presence of water vapor. As discussed earlier, this would reduce the ignition tendency. There is also the effect of reduced mixture temperature with high humidity. Both of these effects help to suppress the ignition tendency with increasing humidity.

Engine Speed - The investigation by Stebar, Wiese, and Everett (7) also showed increasing deposit ignition tendency with increasing engine speed. From the standpoint of the proposed ignition mechanism, this is to be expected. Increasing engine speed would increase combustion chamber wall temperatures, which in turn increase the tendency toward surface ignition.

Also, as discussed earlier, the region adjacent to the deposit surface is deficient in oxygen. This prevents ignition from occurring at the surface proper. The generally higher level of turbulence at higher speeds would ease this situation by bringing fresh mixture to the deposit surface and thereby increasing the ignition tendency.

Again, both the mixture ratio and surface temperature concepts of the proposed mechanism predict the results found experimentally.

Concluding Remarks

A mechanism for surface ignition has been proposed. It stipulates that if surface ignition is to occur, the fuel-air mixture must be heated above its ignition temperature and at the same time its composition must be within the limits of inflammability.

The proposed mechanism is consistent with most experimental data available. This mechanism provides an explanation for the difference in surface temperature requirements to cause ignition for different surfaces, the difference in deposit and hot spot ignition resistances of fuels, and the fact that ignition sometimes occurs at a distance from the surface causing ignition.

The proposed mechanism is not complete. Consideration of the joint effects of temperature on rich limits, and of rich limits on ignition temperature have not been elucidated, nor are the total effects of dilution known. All of these factors need to be incorporated into the proposed mechanism in order to fully evaluate it. However, it does offer a reasonable basis for prognostication and does suggest new areas of research.

Acknowledgments

The authors take this opportunity to express their appreciation to Messrs. Weller, Schubring, Fitch, and Colcer of the Physics Department for assistance with problems incident with the operation of the peak pressure distribution counter; to Mr. K. C. Peng of the Data Processing Department for his assistance in the application of the statistical chain block procedure; to the members of the Fuels and Lubricants Department for their assistance in the preparation of the manuscript.

References

1. T. A. Boyd, "Engine Flame Researches," SAE Trans., Vol. 45, No. 4 (1939), 421-32.

2. J. R. Sabina, J. J. Mikita, and M. H. Campbell, "Pre-Ignition in Automotive Engines," Proc. API 33, III (1953), 137-150.

3. E. F. Weller, Jr., N. W. Schubring, and M. E. Fitch, "A Peak Pressure Distribution Counter for Engine Fuel Studies," Proc. National Electronics Conference, Vol. 12 (1956), 197-211.

4. K. Hyatt, V. J. Tomsic, and C. A. Mellinger, "Surface Ignition -- A New Look with a New Instrument" paper presented at SAE Summer Meeting, Atlantic City, N. J., June, 1959.

5. Coordinating Research Council, Inc., Combustion Chamber Deposits Group, Private Report.

6. D. B. Duncan, "Multiple Range and Multiple F Tests," Biometrics, Vol. 11, No. 1 (March, 1955), 1-41.

7. R. F. Stebar, W. M. Weise, and R. L. Everett, "Engine Rumble--A Barrier to Higher Compression Ratios?" SAE Trans. V 68 (1960), 206-216.

8. J. Mandel, "Chain Block Designs with Two-Way Elimination of Heterogeneity," Biometrics, Vol. 10, No. 2 (June, 1954), 251-272.

9. Coordinating Research Council, Inc., Combustion Chamber Deposits Group, Private Report.

10. D. A. Bowlus, "Effect of Time on the Hot-Wire Characteristics of Twelve Hydrocarbon-Air Mixtures" M. S. Thesis, Purdue University, June, 1960.

11. H. F. Coward, and G. W. Jones, "Limits of Flammability of Gases and Vapors, "Bureau of Mines Bulletin 503, 1952.

12. W. Jost, "Explosion and Combustion Processes in Gases," Translated by H. O. Croft, New York: McGraw Hill, 1946, 1st ed., 133-135.

13. R. C. Spencer, "Preignition Characteristics of Several Fuels Under Simulated Engine Conditions," NACA Report 710, 1941.

14. H. F. Coward and P. G. Guest, "Ignition of Natural Gas-Air Mixtures by Heated Metal Bars," J. Amer. Chem. Soc., Vol. 49 (1927), 2479-2486.

15. W. Mason and R. V. Wheeler, "The Ignition of Gases, Part II. Ignition by a Heated Surface. Mixtures of Methane and Air," J. Chem. Soc., Vol. 121 (1922), 2070-2091. Also W. Mason and R. V. Wheeler, "The Ignition of Gases. Part IV. Ignition by Heated Surface. Mixtures of the Parafins with Air," J. Chem. Soc., Vol. 125 (1924), 1869-1875.

16. Propulsion Chemistry Division, Lewis Flight Propulsion Laboratory, "Basic Considerations in the Combustion of Hydrocarbon Fuels with Air," NACA Report 1300, 257-258.

17. H. F. Coward, and G. W. Jones, op. cit., 1-10.

18. A. O. Melby, D. R. Diggs, and B. M. Sturgis, "An Investigation of Preignition in Engines," SAE Trans., Vol. 62 (1954), 32-39.

Discussion

Effect of Time on Ignition Reaction

A. J. Pahnke
E. I. du Pont de Nemours & Co.

BOWDITCH AND YU have shown that ignition of hydrocarbons by deposits differs from ignition by metallic hot spots and have proposed that oxygen depletion in the gaseous layer adjacent to the surface of the deposits accounts for the differences between the relative ignition resistances of hydrocarbons in aspirated deposit and hot spot tests. Oxygen depletion and the effect of the rich limit of inflammability appear to be a reasonable explanation; however, these differences also may be ascribed to the amount of time available for ignition reactions. With aspirated deposits, this time is very short; with hot spots, this time may be long and the course of the ignition process can be considerably different.

Considering first the aspirated deposit case, the deposit particles move through the fuel-air charge, continually contacting new volumes of the fuel-air mixture. This movement, coupled with a probable twisting motion, reduces the thickness of the boundary layer and eliminates any quiescent regions near the particle. As a result, the time available for chemical reactions to take place prior to ignition is very short and the ignition process approaches that of spark ignition. In agreement with this hypothesis, aspirated deposit ignition resistances of hydrocarbons obtained by Bowditch and Yu(1)* generally correlate with minimum spark ignition

Table A - Aspirated Deposit Ignition Resistance

	LIB Number Bowditch and Yu(1)	Minimum Spark Ignition Energy, Millijoules Calcote, et al(2)
2,2-Dimethylbutane	120	1.64
Iso-octane	100	1.35
Di-isobutylene	57	0.56
Cyclohexane + 3 ml tel/gal	51	1.38*
Toluene	42	1.3
Furan	30	0.23
Benzene	0	0.55
Propane	-12	0.31
Methanol	-110	0.22
Ethylene	-175	0.10

* Unleaded value.

* Numbers in parentheses designate Reference at end of paper.

Table B - Hot Spot Ignition Resistance

	Time of Ignition, Deg btc Bowditch and Yu(1)	Spontaneous Ignition Temperature, F Jackson (3)	Critical Compression Ratio 600 rpm, 350 F A.P.I. RP-45(5)
Methane	None	-	13.0
Toluene	82.0	1094	11.4
Propane	84.0	940	8.8
Iso-octane	96.0	837	6.6
2,2-Dimethylbutane	102.0	824	5.1
Di-isobutylene	103.7	788, 587	7.3
2,3-Dimethylbutane	112.3	790	7.4
Benzene	114.0	1097	-
Ethylene	150	-	5.6

Table C - Effect of tel on the Surface Ignition Resistance of Iso-octane

	Average Number of Ignitions
Iso-octane	37
Iso-octane + 1.5 ml tel/gal	38
Iso-octane # 3 ml tel/gal	39

energy values determined by Calcote, et al(2), as shown in Table A. Considering that the minimum ignition energy data were obtained at atmospheric pressure, the agreement is surprisingly good.

In the case of hot spot ignition, the igniting source is stationary and conceivably has a thick boundary layer associated with it. In addition, located near most hot spot ignition sources is a quiescent zone of fuel-air mixture where precombustion reactions can occur and contribute to the overall ignition process. The time available for these oxidation reactions can be relatively long, and the overall ignition process approaches that of knock.

In support of this concept is the general agreement between hot spot ignition data obtained by Bowditch and Yu and spontaneous ignition temperatures obtained by Jackson(3), who used a technique which involved dropping a few drops of hydrocarbon into a heated vessel and observing the occurrence of ignition. This comparison is shown in Table B.

Benzene stands out as a notable exception. A comparison of the Bowditch and Yu hot spot data with critical compression ratio data (5), presented in the table, also shows a good order of agreement. A further consideration of critical compression ratios obtained at other speeds and temperature suggests that critical compression ratios obtained at a lower speed and a higher temperature would correlate even better. In general, the hot spot data appear to correlate with data from other processes which involve gas phase autoignition.

The effect of tetraethyl lead further suggests that the difference between aspirated deposit and hot spot results may involve ignition delay as an important factor. A series of experiments in our laboratory showed that tetraethyl lead did not change the ignition resistance of iso-octane to floating deposits. An engine was operated under part-throttle conditions to accumulate deposits. Each hour, a test fuel was introduced into the engine and a switch was made to high-load conditions for 30 sec. On the basis of a large number of tests with clear and loaded iso-octane, tetraethyl lead did not exhibit any effect on preignition, as reported in Table C.

On the other hand, tetraethyl lead markedly increases the hot spot surface ignition resistance of iso-octane. Downs and Pigneguy(6), using a metallic hot spot as an ignition source, found that 4 ml of tetraethyl lead increased the preignition-limited performance of iso-octane by 0.75 compression ratio units. Morris(7), using a spark plug as an ignition source, found that 3 ml increased the preignition-limited manifold air pressure by 12%; 6 ml raised it 23%. Wimmer (4), using an isolated graphite pellet as a hot spot, found that 3 ml of tetraethyl lead increased the surface ignition-limited compression ratio by 1.3 units.

The increased surface ignition resistance obtained with tetraethyl lead in hot spot tests indicates that reactions similar to those leading to knock probably are an important phase of the hot spot ignition process. This is not the case for ignition by floating deposits, as evidenced by the lack of any effect with tetraethyl lead. In summary, it appears that ignition delay time may be another factor accounting for the difference between hot spot and aspirated deposit results.

References

1. F. W. Bowditch, and T. C. Yu, "A Consideration of the Deposit Ignition Mechanism," paper presented at the June, 1960 SAE Meeting, Chicago, Ill.

2. H. F. Calcote, C. A. Gregory, Jr., C. M. Barnett, and Ruth B. Gilmer, "Spark Ignition, Effect of Molecular Structure," Ind. Eng. Chem. 44, (1952), 2658.

3. J. L. Jackson, "Spontaneous Ignition Temperature of Pure Hydrocarbons and Commercial Fluids," N. A. C. A. Research Memorandum RME 50, J10 (December, 1950).

4. D. B. Wimmer, "Some Factors Involved in Surface Ignition in Spark Ignition Engines," SAE Tulsa Meeting, November, 1956.

5. A. P. I. RP-45, "Knocking Characteristics of Pure Hydrocarbons," published by ASTM (1958).

6. D. Downs, and J. H. Pigneguy, "An Experimental

Investigation Into Preignition in the Spark-Ignition Engine," Proc. Inst. Mech. Engrs. (London), Automobile Division, IV (1950-1951), 125-149.

7. W. E. Morris, unpublished data presented to C.R.C.

Authors' Closure to Discussion

THE TIME hypothesis advanced by Mr. Pahnke warrants serious consideration. While it would be expected that a deposit particle would move about in the combustion chamber of an engine, it would appear to us more likely that the particle would move with the gaseous mixture so that the relative movement would be less between deposit and mixture than between a stationary ignitor and the mixture. This would argue that more time for precombustion reactions would be available in the case of the moving deposits than for the case of the stationary ignitor.

In the experiments reported in our paper where a hot wire and deposit pellets were used alternately in the same location in the engine as ignitors, it was found that under similar engine operating conditions the hot wire ignited mixtures more readily than did the stationary deposit pellets. As reported in the paper, deposit pellets had to be approximately 600 F hotter than a hot wire in the same location in order to be equally effective in igniting fuel-air mixtures. This does not appear to be consistent with Mr. Pahnke's hypothesis.

Concurrent Pyrolytic and Oxidative Reaction Mechanisms in Precombustion of Hydrocarbons

C. E. Welling, G. C. Hall, and J. S. Stepanski
Ford Motor Co.

IT IS GENERALLY postulated that the first step in the oxidation of an alkane consists in the abstraction of a hydrogen atom probably by an oxygen molecule, with formation of an alkyl free radical. The further reaction of the alkyl free radical through peroxide formation and various peroxide decomposition mechanisms has been studied in both gaseous and liquid systems by a relatively large number of investigators. In gas phase oxidations near atmospheric pressure, however, the production of lower olefins has been observed with propane [1]*, n-butane [2], isooctane [3], and neohexane [3] and explained by assuming a decomposition of some fraction of the original free radicals derived from the fuel. Production of lower olefins from n-hexane cool flames has been reported [4] and their origin ascribed [5] to degradation of free radical hydroperoxides. to the dismutation of higher free radicals, and to stripping of a hydrogen from an ethyl free radical.

In a few cases the production of olefins with the same number of carbon atoms as the original fuel has been observed. Generally, these results come from work with rich mixtures near atmospheric pressure and the production of olefin passed through a maximum with increasing temperature. Observations have been reported on ethane[6], propane [7, 8], and n-butane [2], and the respective investigators have suggested stripping of a hydrogen from the original free radical by oxygen or by a reactive species such as HO_2. In a recent review [9] the following three possibilities for elementary reactions to produce such olefins are enumerated. ($R\cdot$ = original free radical derived from the fuel; RO_2^* = excited peroxy radical):

1. $RO_2^* \longrightarrow$ olefin + HO_2
2. $RO_2^* + X \longrightarrow$ olefin + HO_2 + X
3. $R\cdot + O_2 \longrightarrow$ olefin + HO_2

It is pointed out that deactivation of RO_2^* and rearrangement may occur instead of decomposition, giving rise to various oxygenated species. In addition, the deactivated alkyl peroxy radical, $ROO\cdot$ may through hydrogen abstraction be stabilized as an alkyl hydroperoxide, ROOH.

The reaction possibilities pointed out above for production of synthetic hydrocarbons during oxidative attack on fuel appear to have received little attention in engine studies. Appreciable quantities of ethylene and propylene in a ratio of roughly 10/1 have been reported in motored engine work with n-pentane [10]. These olefins were believed to have resulted from the breakdown of larger alkyl radicals. In another study[11], the production from n-heptane of large amounts of unsaturates together with oxygenates and hydrogen peroxide was observed in motored engine exhaust under conditions milder than the autoignition limit. The splitting of an alkylperoxy radical to give an unsaturate and a HO_2 radical was suggested as a source of a part of the hydrogen peroxide found.

In the course of a study of preflame reactions of single pure hydrocarbons in a motored single-cylinder (CFR) engine, observations of reaction product composition have been made with particular attention to the synthetic hydrocarbons found present in some abundance. The work involved partition chromatography analysis of samples, withdrawn from the engine combustion chamber through a fast acting magnetic valve, to determine stable reaction products. The observed conversion of a part of the reacted fuel into synthetic hydrocarbons is of interest as it reflects relative reaction rates. It is also an aid in understanding the evident alterations in fuel that occur in passage through a fired engine during periods of incomplete combustion such as an automotive decleration.

*Numbers in parentheses designate References at end of paper.

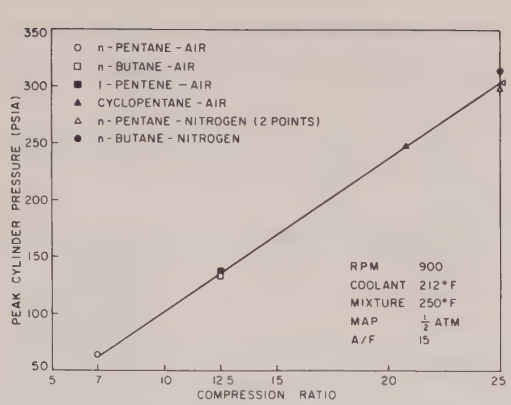

Fig. 1 — Engine performance observed with non-reacting mixtures

Objectives

The first purpose of this paper is to relate synthetic hydrocarbon products from a motored engine with the following types of precombustion reactions:

1. Cracking - Thermally induced decomposition may follow formation of alkyl free radicals produced by abstraction of a hydrogen atom from a fuel molecule.

2. Hydrogen Stripping - In the presence of oxygen, the original free radical from the fuel molecule may have a second hydrogen stripped off to yield a stable olefin containing the same number of carbon atoms as the parent molecule.

3. Peroxide Formation and Decomposition - The complex mechanisms involved yield oxygenated compounds, and to some extent small hydrocarbon molecules. These mechanisms have been rather definitively studied for several hydrocarbon fuels both in motored and fired engine operation with respect to the oxygenated products[12].

A second objective is to show that all of the above reaction paths appear to run concurrently and to originate from a common reactant--the original free radical produced by abstraction of a hydrogen atom from a fuel molecule. Furthermore, each reaction path may be a chain mechanism that serves to maintain the concentration of the original common free radical reactant.

Lastly, some implications of the above view of the precombustion reactions will be discussed.

Apparatus and Procedures

Engine - An ASTM Motor Method engine received the following modifications:

1. The ice tower was disconnected and room air was drawn directly into the intake surge tank. In experiments with controlled oxygen, metered nitrogen and oxygen streams were fed from cylinders into the inlet surge tank with the air entry blocked.

2. A gate valve placed in the carburetor inlet pipe, 5-1/2 in. below the intake surge tank, permitted control of intake manifold pressure. This pressure was monitored with a damped mercury manometer connected to a flush tap in the manifold close to the manifold thermometer entry.

3. Fuel bowls and related equipment were removed. A spring-loaded check valve was placed in the new fuel line as close as possible to the carburetor jet and volume from check valve to jet was minimized by packing with small pieces of drill rod. The C_5 fuels were delivered at around 10 psig with a metering pump running at 100 pulses/min, that drew fuel from a calibrated liquid burette. Fuel flow was smoothed with a small buffer volume, partially gas filled, between pump and check valve. Cycle-to-cycle fuel flow, as judged by pressure traces and random autoignitions, was as good and long period fuel rate constancy was better, than that achieved with needle valve metering. N-butane, however, was metered with a needle valve and liquid flow meter from a tank placed on scales sensitive to 0.1 g.

4. Micrometer mounting was modified to permit high compression ratios.

5. A pressure pickup (Li or Kistler types) replaced the spark plug and a Cox sampling valve was placed in the detonation meter opening.

6. For nitrogen-fuel runs, atmospheric oxygen was excluded by sealing the induction system, maintaining a positive nitrogen pressure of 2 or 3 in. water in the crankcase, and maintaining a positive nitrogen pressure within a mylar film bag that enclosed the rocker arm assembly and was sealed to the cylinder head. (With operation at 1/2 atmosphere manifold pressure, it was found that gas leakage down the valve guides with normal tolerances contributed 3/4 of a per cent or more to total discharge at the exhaust.

Airflow through the engine, to establish air/fuel ratio, was measured by taking the flow from the exhaust surge tank through a dry test meter. Cylinder pressure versus crank angle timing and sampling valve position versus timing were displayed on the oscilloscopes. The time base, developed in this laboratory, depended upon the use of a knife-edged magnetic pickup to sense passage of degree marks on the flywheel periphery. The train of marker pulses so generated was faithful to the flywheel graduations. An electrometer preamp[24] designed by Rosen of this laboratory was employed with Kistler pressure pickups.

Fuels - Phillips "pure grade" n-butane and n-pentane were used. The 1-pentene used was Phillips "technical grade," and cyclopentane was obtained from Brothers Chemical Co. Chromatographic inspection of the fuels provided against possible identification of an impurity as a reaction product.

Operation - Typically, the engine was motored on air alone until operating temperatures stabilized. Compression ratio and manifold pressure were then adjusted. A measurement of net airflow was then made and the fuel rate chosen for the desired air/fuel ratio. Fuel was then started and its rate adjusted. With operation stabilized, sample withdrawal through the sampling valve could begin. The sample stream was split, a minor portion being taken through a short con-

nection into the sample collection system. Sampling periods were usually 5-10 min long and permitted monitoring fuel flow and the pressure trace. The values generally used for the basic engine variables are shown in the heading of Table 4.

The behavior of the engine as a gas compressor is shown in Fig. 1. The peak cycle pressures on the curve were obtained with air (or nitrogen)/single hydrocarbon mixtures at compression ratios such that little, if any, reaction occurred. The points were obtained over a space of some 15 months that embraces all of the work reported. The standard intake manifold pressure of 1/2 atmosphere (measured with a damped manometer) that prevailed for these tests resulted in a cylinder pressure of 6.6 ± 0.3 psia at the time the intake valve closed, as measured at compression ratios of 12.5/1 and 17/1 with a balanced diaphragm pressure indicator.

Deviations from the relation shown in Fig. 1 occurred when n-pentane/air and 1-pentene/air mixtures were subjected to increasing compression ratios approaching autoignition. The difference between observed peak cycle pressure at stated compression ratio and peak cycle pressure for a non-reacting mixture at the same compression ratio (taken from Fig. 1) is plotted in Fig. 2. Net heat releases as the autoingntion limit is approached are indicated for n-pentane and 1-pentene. The precombustion reactions of n-butane as autoignition is approached are appreciable from the standpoint of fuel destruction as shown by analysis but give no observable heat release before expansion. (At a compression ratio of 21.75, definite autoignition in the engine did not occur, but inaudible pressure rises at around 60 deg atc were noted and severe ignitions occurred in the exhaust surge tank. Consistent autoignition occurred at a compression ratio of 22/1.)

Analysis for Precombustion Products - A typical precombustion sample gas consisted of a mixture of gases and vapors of which all but H_2, N_2, O_2, CO, and CH_4 could be recovered for analysis in a liquid nitrogen-cooled trap. The condensate could then be analyzed for C_2 to C_5 hydrocarbons and CO_2 and on occasion for oxygenated compounds. The noncondensable gases were nonroutinely determined in effluent from the condensate trap or on whole sample gas by gas chromatography, orsat, and mass spectroscopic analysis. Hydrocarbons above methane and carbon dioxide were determined by two-stage series gas chromatography using both partition and adsorption columns.

At gas flow rates of approximately 100 cc/min through the liquid nitrogen-cooled trap it was possible to take one liter volumes of synthetic samples containing 200 ppm of ethane or ethylene and to recover and determine the C_2 hydrocarbon to within ±5%. Since ethylene concentrations in engine samples were generally above 200 ppm it is believed that ethylene recovery was quite complete. Since ethane concentrations found in the engine sample gas were in the range 0-200 ppm, trapping may not have been complete at the low end of the concentration range.

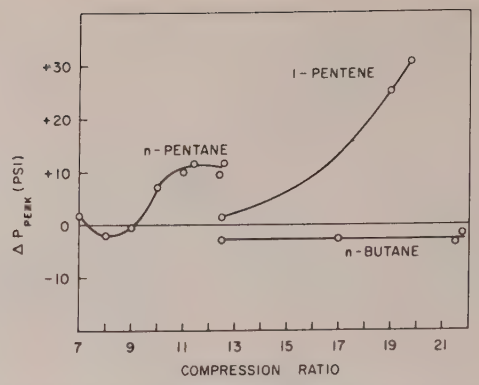

Fig. 2 — Pressure deviations from the curve of Fig. 1 as autoignition was approached

Blank tests were made, motoring the engine without fuel, that established the lubricating oil did not contribute detectable quantities of light hydrocarbons of interest nor carbonyl compounds detectable with 2,4-dinitrophenylhydrazine[12].

Oxygenates including individual carbonyl compounds were detected and identified qualitatively by gas chromatography using tricresylphosphate and polyglycol columns at 230 F. The list of oxygenates positively identified include formaldehyde, acetaldehyde, propionaldehyde, acrolein, acetone, methanol, ethanol, propanol, and tetrahydro-2-methylfuran. Many of the original identifications required collecting material under a chromatographic peak as it was eluted and making use of IR or MS inspection. We are particularly indebted to James Neerman of this laboratory for the mass spectroscopic work leading through recognition of mass and structure to the identification of tetrahydro-2-methylfuran. This compound presumably is formed by δ stripping in an intramolecular oxidation of a pentyl peroxy radical as suggested by Boord[5].

Experimental Results and Discussion

Evaluation of Cracking Reactions - The cracking of n-pentane and n-butane via the thermal decomposition of pentyl and butyl radicals, respectively, is well described by free radical reaction mechanisms[17], and various experimental studies[13, 14, 15, 16] with n-pentane are in general agreement. Simpler hydrocarbons and (in some cases) hydrogen are the expected primary products.

In considering precombustion reaction products from the engine it appeared that the same pattern of synthetic hydrocarbons was present (together with other materials) that would result from considerable cracking of free radicals derived from the fuel. It seemed desirable then to establish with certainty that the pattern of products from thermal decomposition in the engine was the same as that known to occur in pyrolyses of the same pure hydrocarbon under conditions quite different from those prevailing in the engine.

In the case of n-pentane, for instance, it was also particularly desired to establish that only small relative amounts

Table 1 - Hydrocarbon Product Ratios from Engine Decomposition and from Low-Pressure Pyrolysis of n-Pentane

Reference	This Work		(13)		(15)	(14)		(16)	(17)	
System	Engine		Flow		Flow	Static		Static	Theoret.	
Test Designation	6A	6B	2	3	--	(a)	(b)	(b)	--	--
Temperature, F	1047(c)	1053(c)	1040	1040	1200 -1380	1020	1020	1040	570	1830
n-pentane destruction, %	1.0(d)	1.4(d)	7.8	4.9	0(e)	--(f)	--(f)	--(f)	(g)	(g)
Product mole ratios:										
Propylene/Ethylene	0.72	0.73	1.16	1.0	(1.4)	1.15	1.0	--	1.0	0.35
Propylene/1-Butene	2.8	2.7	1.9	1.8	1.9	--	--	5.0	2.0	2.0
Ethane/Ethylene	0.17	0.13	0.76	0.79	(1.2)	1.1	1.0	--	1.0	0
Propane/Propylene	0.0	0.0	0.05	0.04	0.0	0.08	0.11	0	0	0
1-Butene/2-Pentenes	3	4	4.8(h)	5.3(h)	--	--	--	~25	∞	∞

(a) Uninhibited pyrolysis.
(b) Nitric oxide present to inhibit free radical reactions.
(c) Estimated as indicated above.
(d) n-Pentane equivalent of recovered synthetic hydrocarbons x 100/recovered n-pentane.
(e) Extrapolated back to zero destruction.
(f) Destruction not explicitly stated.
(g) Secondary reactions not considered.
(h) Ratio involves total pentenes.

of pentenes were produced from decomposition of pentyl radicals, since it is the production of pentenes that distinguishes the second mechanism postulated above.

Accordingly, decomposition of n-pentane was observed in a motored CFR engine test at a high compression ratio (25/1) to attain suitable reaction temperature and 1/2 atmosphere intake manifold pressure. For this test the engine was supplied a 15/1 (wt) mixture of prepurified nitrogen-n-pentane and air was excluded as completely as possible. Some leakage of oxygen into the engine occurred, but its concentration in the engine exhaust did not exceed 0.2 vol% either during preliminary operation when no n-pentane was being charged or during the test period. Samples were taken through the magnetic valve at 15 deg after top center (atc). On the basis of estimated peak temperature* of about 1050 F, and available reaction time** of about 2 millisec, it is concluded that the rate of n-pentane decomposition much exceeded normal pyrolysis and may be termed oxygen-sensitized. Typical oxidation reactions appeared to have been insignificant; a qualitative test for carbonyls with 2, 4-dinitrophenylhydrazine was negative and the ratio (moles C-atoms in synthetic hydrocarbons)/(moles C-atoms in CO_2) was about 35/1.

Table 1 summarizes the distribution of synthetic hydrocarbon products from the engine test and contains, for comparison, results obtained by others on the pyrolysis of n-pentane in low-pressure static and flow systems. The theoretical predictions of Rice, obtained by application of a free radical mechanism to n-pentane cracking are included. For convenience, all results are shown in terms of mole ratios; where necessary, literature data were recast into these ra-

* Estimated from peak pressure observation, combustion-chamber volume, moles of charge per cycle (corrected for clearance volume) and assumption of PV = nRT.

** The reaction time is arbitrarily taken as that interval around top dead center piston movement in which gas temperature would be within 90 F of the peak temperature as determined from the pressure trace.

Table 2 - Hydrogen Product Ratios from Engine Decomposition and from Low-Pressure Pyrolysis of n-Butane

Reference	This Work	(2)	(13)		(18)
System	Engine	Static	Flow		(a)
Test Designation	B1A	175 S			
Temperature, F	1132	932	1067		
n-Butane Destruction, %	~0.2	2.22	11.3	10.5	
Product Mole Ratios:					
Propylene/Ethylene	2.2	2.2	1.9	1.9	1.3
Propane/Propylene	0(b)	0.05	0.05	0.07	0
Ethane/Ethylene	0(b)	1.1	0.71	0.81	1
Propylene/Butenes	No butenes found	3.7	5.0	----	3.4
Propylene/2-Butenes		----	12	----	----

(a) Product ratios are calculated from the author's summary of literature data; the temperature range is restricted to that permitting isolation of initial products.

(b) No propane or ethane was found.

tios from the original product analyses.

The following conclusions may be drawn from Table 1.

1. Thermal decomposition of pentyl radicals in the engine tests with short reaction times and high nitrogen pressure gives essentially the same products and product distribution as obtained in low pressure pyrolyses of pure n-pentane.

2. Production of pentenes is not predicted by the simplest free radical mechanism for pyrolysis. Experimentally, Frey and Hepp and Jach and Hinshelwood observed yields of one molecule of (total) pentenes for 5 and 25 molecules, respectively, of 1-butene, the latter being an expected pyrolysis product. In the engine tests one molecule of 2-pentene was produced for 3 to 4 molecules of 1-butene. When corrected for probable production of 1-pentene (which was not resolved in these particular chromatographic analyses) to permit comparison with the literature values for total pentenes, the engine product ratio becomes one molecule(total) pentene to 2 to 3 molecules 1-butene. This ratio sets the upper limit for pentene production through thermal decomposition of pentyl radicals.

3. 1-butene is a major product of pentyl radial decomposition and is considered the best available quantitative indicator of the cracking reaction because of a low probability of its formation by other mechanisms and for practical reasons related to sampling and analysis.

A study was also made of n-butane. It was chosen because the literature affords a reasonably clear picture of its pyrolysis products and because it has greater resistance to precombustion attack, as witnessed by its higher octane number compared to n-pentane. In Table 2 a comparison is made of product distribution from engine test B1A at compression ratio 25/1 on nitrogen/n-butane mixture and results from the literature[2, 13, 18] on pyrolysis of n-butane at low pressures.

In test B1A oxygen content of the exhaust stream was 0.1 - 0.2%, as indicated by the Beckman magnetic oxygen analyzer. Qualitative tests of the engine sample gas for carbon dioxide and for carbonyl compounds were negative. About 0.2% destruction of n-butane was observed.

Table 3 - Relative Rates of Pentyl Radical Decomposition

Test	Mixture (15/1)	Compression Ratio	MAP	1-Butene/ 2-Pentene
6A	Nitrogen/ n-pentane	25/1	1/2 atm	3
6B	Nitrogen/ n-pentane	25/1	do.	4
4A	Air/ n-pentane	8/1	do.	0.12
4C	Air/ n-pentane	8/1	do.	0.11

It will be seen from Table 2 that the engine test gave a propylene/ethylene ratio typical of butyl radical decomposition by free radical mechanisms. No butenes were found although the literature on low-pressure pyrolysis of n-butane reports minor amounts of butenes. It appears proper to use propylene production as an indicator of the cracking reaction with n-butane.

With the above background and choice of 1-butene and propylene as indices for the thermal decomposition of pentyl and butyl radicals, respectively, it is possible to consider normal precombustion.

Cracking and Hydrogen Stripping in Precombustion of n-Pentane - Anaylsis of sample gas taken at 15 deg atc of the compression-expansion cycle of the motored CFR engine operated with a 15/1 air/n-pentane mixture and at conditions a bit below the autoignition threshold, reveals the presence of the same synthetic hydrocarbons (1-butene, propylene, C_2) reported above as products of carbon-carbon bond breaking in pentyl radicals. There is also, however, an order of magnitude increase in relative production of pentenes that indicates more or less equal consumption of pentyl radicals by cracking and by the hydrogen stripping to produce pentenes.

A comparison of relative rates of pentyl radical decomposition versus conversion to pentene in 15/1 nitrogen/fuel and air/fuel mixtures in respective engine tests is shown in Table 3. The relative rates of the 2 reactions in each test are expressed as the mole ratio of a product of decomposition (1-butene) to a product of the pentenes forming reaction (2-pentene, cis- and trans-isomers summed) contained in a gas sample taken from the cylinder during the test.

A complete tabulation of engine conditions and sample analysis for the tests above and all other engine tests will be found in Table 4. In connection with our choice of sampling time at 10-15 deg atc it is to be noted that the same ratios of synthetic hydrocarbons were found in a few samples taken at tc as in 15 deg atc samples. Excluding cases in which, at near autoignition conditions, there was evidence for delayed reactions, no change in synthetic hydrocarbon ratios was noted between 15 deg atc samples and occasional exhaust samples.

While the elementary reactions involved in hydrogen stripping are still in doubt, a reaction sequence may be suggested similar to that outlined by Satterfield and Reid(7) to describe the observed production of propylene and hydrogen perioxide in the slow oxidation of propane. The sequence for n-pentane would be as follows:

1. $C_5H_{12} + [x] \longrightarrow C_5H_{11}\cdot + HX$
2. $C_5H_{11}\cdot + O_2 \longrightarrow C_5H_{10}$ (a pentene) $+ HO_2\cdot$
3. $C_5H_{12} + HO_2\cdot \longrightarrow C_2H_{11}\cdot + H_2O_2$

Step 1 shows initiation of reaction through the production of a pentyl free radical. The reaction is carried on as a chain mechanism by steps 2 and 3. It should be noted that the pentyl free radical has a certain independent probability of cracking before step 2 is complete. Another independent probability exists for formation of a relatively stable peroxy radical ROO · that would lead to a peroxide.

Influence of Temperature: Tests made at the same values of intake manifold pressure, mixture composition (15/1 air/fuel ratio), and so forth, but raising compression ratio from near the minimum that would yield detectable quantities of products to the autoignition threshold increased the attack on the n-pentane. At the autoignition threshold the production of 2-pentenes was about 7 mole %, based on n-pentane fuel. 1-pentene amounted to 2-3 mole % on the fuel. At the same time a change in the relative rates of the concurrent reaction mechanisms occurred. This can be seen from Table 5.

Relative rate of decomposition of pentyl radicals is seen to be increased by about a factor of 3 over the available compression range. This indicates that a higher activation energy is involved in the decomposition reaction than in interaction of oxygen to produce pentenes.

A similar trend was found in working with very lean mixtures (air/n-pentane = 77-78) which at the same intake manifold pressure and other conditions as above permitted a higher compression range. Results are shown in Table 5.

Some further tests were made in which a nitrogen-oxygen blend was substituted for air and a mixture fed the engine with blend/n-pentane at the nominal ratio of 15/1(Table 5).

Again the overall effect of increasing severity of conditions is a 5-fold increase in relative rate of fragmentation of the fuel.

Oxygen Concentration: Two tests were made in which the mole ratio, oxygen/n-pentane, in the mixture had the extreme respective values 1.3 and 42. The first ratio was arrived at by using a nitrogen - 3.5% oxygen blend in place of air; the latter with a 78 A/F mixture. Both runs were at the same intake manifold pressure and with compression ratios adjusted to give the same peak pressure (± 2-3 psi). Results are shown in Table 6.

Since oxygen is postulated as a reactant in the mechan-

Table 4 - Engine Test Conditions and Sample Gas Composition

Intake manifold pressure - 380 mm Hg Abs (a) Coolant - 212 F Oil - 135 ± 15 F
Sampling time - 15 deg atc, except as noted Rpm - 900 Mixture - 250 F

Test	C.R.	A/F	Oxygen Content (Vol %)	Airflow g/min	Peak Press psia	Condensate Sample Composition as Component Ratios					Carbonyls mg/l	Calc Peak Temp, F
						A	B	C	D	E		
Air/n-Pentane Mixture												
1A	12.5	15		83.2	---	0.39	3.4	59	5.3	0.041	65	---
1.5A	12	14.9		82.9	137	0.38	3.2	24	4.0	0.036	--	963
3A*	10.0	15.0		83.6	109	0.27	4.0	49	3.7	0.022	--	849
3.5A	9.0	14.5		80.2	---	0.24	4.0	67	4.1	0.0095	--	715
3.5B	9.0	15.1		81.8	88	0.20	3.8	47	4.3	0.011	41	700
4A*	8.0	14.6		80.6	71	0.12	3.3	86	8.1	0.0026	--	597
4C	8.0	14.4		78.6	75	0.11	4.1	43	5.2	0.0012	14	654
5A	12.5	78.0		86.6	143	0.24	2.3	240	2.6	0.017	43	924
7A	17.0	77		87.5	209	0.60	3.1	79	3.9	0.056	13	1061
Nitrogen + Oxygen/n-Pentane Mixture												
10.5A	13.25	14.8	10.5	82.1	146	0.25	3.3	48	2.9	0.014	34	914
11B	14.25	14.5	3.6	81.6	146	0.08	3.8	(b)	(b)	0.00016	0	832
12A*	23.5	15.1	10	84.8	292	1.29	3.2	16	6.5	0.10	27	1129
Nitrogen/n-Pentane Mixture												
6A	25.0	14.8	0.1	85.0	304	3	2.8	6	4.5	0.0019	0	1047
6B	25.0	15.2	0.2	85.0	304	4	2.7	8	4.2	0.0026	0	1053
						F	G			H		
Air/n-Butane Mixture												
B2A	21.25	15		89.0	---	0.77	1.8			0.016	--	---
B3A	12.5	15.6		84.8	133	0.29	1.5			0.0052	--	830
B4A	17.0	15.1		85.2	193	0.68	1.6			0.0066	--	943
B5A	21.5	15.9		85.6	253	----	---			------	5	1110
Nitrogen/n-Butane Mixture												
B1A	25.0	15.2	0.1	82.9	315	(c)	0.46			0.0017	0	1132

(a) This value measured with a damped manometer and used for control; it gave 6.6 ± 0.3 psia pressure in cylinder measured with a balanced pressure diaphragm at the time the intake valve closed.

(b) No ethane or ethylene.

(c) No 2-Butene.

* Sampled at 10 deg atc.

$A = \frac{\text{1-Butene}}{\text{2-Pentene}}$ $B = \frac{\text{Propylene}}{\text{1-Butene}}$ $C = \frac{\text{Ethylene}}{\text{Ethane}}$ $D = \frac{\text{Ethane + Ethylene}}{\text{1-Butene}}$ $E = \frac{\text{1-Butene}}{\text{Unreacted n-Pentane}}$

$F = \frac{\text{Propylene}}{\text{2-Butene}}$ $G = \frac{\text{Ethylene}}{\text{Propylene}}$ $H = \frac{\text{Propylene}}{\text{Unreacted n-Butane}}$

Table 5 - Concurrent Reaction Mechanisms

Test	C.R.	O_2 in Blend, %	1-Butene/ 2-Pentene
4A	8/1	--	0.12
4C	8/1	--	0.11
3.5A	9/1	--	0.24
3.5B	9/1	--	0.20
3A	10/1	--	0.27
1A	12.5/1 (autoignition	--	0.39
1.5A	12.4/1 threshold)	--	0.38
5A	12.5/1 (A/F = 78)	--	0.24
7A	17/1[a] (A/F = 77)	--	0.60
10.5A	13.25/1[b]	10.5	0.25
12A	23.5/1[c]	10	1.3

(a) This compression ratio was established as the autoignition threshold for an air/n-pentane mixture of 55/1.

(b) This compression ratio was chosen to yield the same peak pressure as in tests with air at C.R. = 12.4.

(c) Autoignition threshold.

ism producing pentenes, it might have been expected that the 1-butene/2-pentene ratio would have decreased from 11B to 5A; the opposite was observed. Apparently the higher effective temperature of 5A (calculated to be about 90 F above 11A) more than offset the oxygen concentration effect. This higher temperature may be explained by the order of magnitude greater attack on the fuel at the higher oxygen concentration.

It appears, therefore, that over the range of 3-21% oxygen in the mixture that oxygen concentration has no important effect upon pentene production versus decomposition. The transition to predominantly pyrolytic or oxygen-sensitized pyrolytic processes that was found in the nitrigen/n-pentane tests must, therefore, occur below 3% oxygen in the mixture. A similar situation is found in the work of Appleby, et al[2], on the decomposition of n-butane in the presence of oxygen. In their work at constant temperature, oxygen concentrations from 0.48 to 8.5% caused no significant change in the propylene/butene mole ratio in products that may be calculated from their data. This ratio should have the same significance for n-butane reactions as does the 1-butene/2-pentene ratio with n-pentane reactions.

Table 6 - Effect of Oxygen Concentration

Test	C.R.	Relative O_2 conc. in Mixture	O_2/n-pentane	1-Butene/ 2-Pentene
11B	14.25	1	1.3	0.08
5A	12.5	6	42	0.24

Table 7 - Abundance of Butene in Various Butane Mixtures

Test	Mixture	C.R.	Propylene/ 2-Butenes
B1A	Nitrogen/n-butane (15.2/1)	25/1	No butenes found
B3A	Air/n-butane (15.6/1)	12.5/1	0.3
B4A	Air/n-butane (15.1/1)	17/1	0.3
B2A	Air/n-butane (15/1)	21.25/1*	0.8

*Autoignition threshold.

Hydrogen Stripping with n-Butane Fuel - Butenes were found in relative abundance in samples from precombustion of air/n-butane mixtures. Since it was shown above that no butenes were produced in the engine test with nitrogen/n-butane it seems clear that hydrogen stripping by oxygen is the source of butenes. Results with engine conditions constant, save for compression ratio, are summarized in Table 7. The propylene/2-butene ratio is employed to show the relative rates of decomposition and hydrogen stripping.

Precombustion reactions of n-butane just under the autoignition threshold were more limited than with n-pentane. Yield of carbonyl compounds was less than 10% of the yield from n-pentane and conversion of n-butane to total synthetic hydrocarbons was approximately 1/4 that for n-pentane.

Precombustion Reactions with 1-Pentene - The precombustion of 1-pentene was observed at compression ratios around 19 with the usual engine operating conditions. The principal observations were:

1. Hydrogen stripping occurred to yield 1,3-pentadienes.
2. Product distribution of 4-carbon and smaller synthetic hydrocarbons resembled that found by Gorin, et al[19], in cracking 1-pentene. However, we obtain for the mole ratio propylene/(butenes + butadiene) values of 0.25 to 0.5 while Gorin found 1 to 1.2 at somewhat higher temperatures.
3. No isomerization of 1-pentene to 2-pentenes was detected.

Production of Hydrogen in Precombustion - In engine tests with air/n-pentane mixtures, limited quantities of hydrogen were found and determined semi-quantitatively. A source is suggested by the ethylene/ethane ratios of 30-100/1 that prevailed in the engine samples as opposed to ratios near unity that are reported for low pressure pyrolysis (Table 1).

It appears that ethyl radicals formed by decomposition of pentyl radicals or otherwise would have two paths to ethylene and one to ethane, as follows:

4. $C_2H_5\cdot \longrightarrow C_2H_4$ (ethylene) + H·
5. $C_2H_5\cdot + O_2 \longrightarrow C_2H_4 + HO_2\cdot$
6. $C_2H_5\cdot$ + RH (fuel or other species with reactive hydrogen) $\longrightarrow C_2H_6$ (ethane) + R·
7. H· + RH $\longrightarrow H_2 + R\cdot$

Probability for reaction 6 is obviously lower in a stoichiometric air-fuel mixture than in an undiluted n-pentane pyrolysis. If reaction 4 is coupled with 7 then a mode of formation of molecular hydrogen is supplied. (Wall recombination of hydrogen atoms might occur also.)

In cool flame oxidation of rich mixtures of ethane at around 1000 F, Gray[6] found evidence for concurrent operation of reactions 4 and 7 and of 5. In his work, product mole ratios of ethylene/hydrogen of around 4/1 occurred. We observed ethylene/hydrogen ratios as high as 9 in lean-mixture test 7A and as low as 0.5 in test 12A with 10% oxygen and quite high peak cycle temperature.

Synthetic Hydrocarbons from Peroxide Oxidation Mechanism - In the above discussion the observed production of 1-butene was employed as an index of the decomposition of pentyl radicals and it was assumed to have no other origin. Various radical recombination reactions might yield 1-butene but they appear to be of low probability. However, another mode of formation of 1-butene that might be hypothesized would involve the formation of a primary pentyl hydroperoxide $C_4H_9CH_2OOH$ which might degrade to C_4H_9CHO or C_4H_9OH as suggested by Boord[5]. Decomposition of the aldehyde would produce a butyl radical that could undergo hydrogen stripping to butene; dehydration of the C_4H_9OH would likewise yield butene. It seems reasonable to assume, along the line suggested by Boord, that the formation of a primary hydroperoxide may be only 1/6 or 1/5 as probable as formation of secondary hydroperoxides in the case of n-pentane. This limited probability, together with the multistep processes required to go from the primary hydroperoxide to butene, make the contribution of the overall mechanism to the observed 1-butene production likely to be insignificant. It is concluded, therefore, that 1-butene can be regarded as primarily a product of the pyrolytic decomposition of pentyl radicals. (An experiment with the terminal position of n-pentane labeled with C^{14} should be helpful in evaluating transient formation of valeraldehyde.)

Other mechanisms following the original formation of hydroperoxides in the oxidation of n-pentane may yield propylene and ethylene; such are:

(1) Formation and degradation of secondary alkyl hydroperoxides as outlined by Boord.

(2) Attack on propionaldehyde or higher aldehydes to yield an acyl radical which decomposes to yield an alkyl free radical and carbon monoxide[5, 22]. The ethyl radical so formed from propionaldehyde would in the engine be expected to be converted to ethylene as discussed in the preceding section. (Attack on carbonyl compounds is quite vigorous in the engine in precombustion of n-pentane as evidenced by the rate of fall of carbonyl concentration from a peak at 15 deg atc to a lower value at say 25 deg atc as shown by Davis, et al[12] and confirmed in this laboratory.)

If a product mole ratio of 2/1 for propylene/1-butene is accepted for pyrolysis of n-pentane (Table 1) then propylene in excess of this ratio is the sum of that coming out of mechanisms 1 and 2. Propylene/1-butene ratios of 3.3-4/1 were observed with stoichiometric air/n-pentane mixtures, suggesting that 1/3 to 1/2 of the total propylene came out of peroxide decomposition mechanisms or from valeraldehyde and/or butyraldehyde decompositions.

In considering excess ethylene, adjustment must be made for the reactions of ethyl radicals in the presence of oxygen to produce mostly ethylene. A direct comparison, therefore, cannot be made with ethylene yield versus 1-butene in oxygen-free pyrolysis. Instead, a reference point from pyrolysis is obtained by considering the mole ratio, (ethylene + ethane)/1-butene. In pyrolysis of n-pentane the experimental values for this ratio are close to 3 although Rice's theory would give a value of 4, increasing to 5.75 with increasing temperature. In typical engine tests with stoichiometric air/n-pentane mixture, the value of the ratio ranged from 3.6 to 5.0, averaging 4.2. This suggests that a maximum of about 30% of the total ethylene found had its genesis in peroxide mechanisms.

The criteria developed just above may be applied to engine tests 6A and 6B that were made with oxygen concentrations of 0.1 - 0.2% and in which no detectable carbonyl compounds were produced. It may be concluded that perhaps 25-30% of the propylene and 20% of the ethylene did not come from pyrolysis.

Hydrogen Peroxide - In the analysis of precombustion sample gas from air/n-pentane mixtures close to autoignition conditions, only very small concentrations of alkyl hydroperoxides were found and hydrogen peroxide only to the extent of 1-5 mole % equivalent of the pentenes produced. Tests were, therefore, made in which a 3% aqueous solution of hydrogen peroxide was pumped in place of fuel to form a mixture with air (16/1) that was inducted into the motored engine at a compression ratio of 12/1. Only 1-3 % of the original hydrogen peroxide concentration could be found in the sampling valve gas, even when sampling was advanced to 50 deg btc or with the mixture temperature reduced to about 80 F. A part of the hydrogen peroxide decomposed within the cylinder, for after the tests the top of the piston was free of previously accumulated carbon deposits. The absence of substantial amounts of hydrogen per-

oxide in fuel tests may, therefore, largely reflect the catalytic activity of the walls of the apparatus.

Sturgis[23] has observed that increasing and substantial amounts of hydrogen peroxide are found in motored engine exhaust with n-heptane and isooctane fuels as the autoignition limit is approached. The increases roughly parallel the simultaneous increases in total olefins found. Downs, et al[21] observed a double peak to total peroxides concentration in the sampled end gas of a fired engine versus crank angle at sampling, with mixed isooctanes fuel. The early peak may be associated with alkyl hydroperoxides from the peroxide mechanism of oxidation with probably some hydrogen peroxide. The late peak might be predicted to contain a greater amount of hydrogen peroxide resulting from hydrogen stripping.

In view of the above, it seems likely that hydrogen stripping is accompanied by formation of HO_2 free radicals and that at least a portion of the HO_2 will react with fuel to produce hydrogen peroxide and fulfill the chain mechanism. Furthermore, Satterfield and Stein[20] have proposed a step in the gas phase decomposition of hydrogen peroxide as follows:

$$8.\ HO_2\cdot + H_2O_2 \longrightarrow H_2O + O_2 + \cdot OH$$

This reaction would destroy hydrogen peroxide and the HO_2 precursor of hydrogen peroxide as well. The hydrogen stripping chain, however, might be continued, for the OH radical should serve to strip hydrogen as HO_2 is postulated to do.

Conclusions - The cracking and hydrogen stripping reactions in precombustion of a paraffin fuel are indicated to afford sources of H atoms, HO_2 free radicals and perhaps indirectly of OH free radicals. Since one or more of these species are generally believed to be the active agents in autoignition, it appears that cracking and hydrogen stripping may contribute to autoignition.

The residual hydrocarbons in automotive exhaust are comprised of synthetic hydrocarbons and unreacted fuel. The C_1 - C_4 fraction is primarily synthetic, and the C_2 - C_4 species are reported as largely olefinic, as would be expected if generated from cracking or decomposition of peroxide structures and with perhaps some hydrogen stripping. Synthetic olefins and diolefins would be expected in the C_{5+} fraction as a result of hydrogen stripping acting on paraffin and olefin components of the fuel.

Acknowledgment

Acknowledgment is made of the contributions of W. A. Cannon, N. Lisicki, and J. L. Parsons in the development and application of the analytical procedures.

References

1. C. N. Satterfield and R. C. Reid, "Fifth Symposium on Combustion," p. 511, New York: Reinhold Publishing Corp., 1955.

2. W. G. Appleby, W. H. Avery, W. K. Meerbott, and A. F. Sartor, J. Amer. Chem. Soc., Vol. 75 (1953), 1809.

3. F. F. Rust and D. D. Collamer, J. Amer. Chem. Soc., Vol. 76 (1954), 1055.

4. P. E. Oberdorfer, PhD. Dissertation, The Ohio State University, June, 1954.

5. C. E. Boord, Presented before Division of Petroleum Chemistry, Amer. Chem. Soc., April 7-12, 1957.

6. J. A. Gray, J. Chem. Soc., 1953, 741.

7. C. N. Satterfield and R. C. Reid, J. Phys. Chem., Vol. 59 (1955), 283.

8. V. Shtern, Zhur. fiz. Khim., Vol. 28 (1954), 613.

9. C. F. H. Tipper, Quart. Rev., Vol. 11 (1957), 313.

10. E. W. Malmberg, M. L. Smith, J. E. Bigler, and J. A. Bobbitt, "Fifth Symposium on Combustion," p. 385, New York: Reinhold Publishing Corp., 1955.

11. A. J. Pahnke, P. M. Cohen, and B. M. Sturgis, Ind. Eng. Chem., Vol. 46 (1954), 1024.

12. W. C. Davis, M. L. Smith, E. W. Malmberg, and J. A. Bobbitt, SAE Transactions, Vol. 63 (1955), 386.

13. F. E. Frey and H. J. Hepp, Ind. Engr. Chem., Vol. 25 (1933), 441.

14. K. U. Ingold, F. J. Stubbs, and C. N. Hinshelwood, Proc. Roy. Soc., London, Vol. A 208 (1951), 285.

15. H. Shanfield and R. O. King, Can. J. Tech., Vol. 34 (1956), 10.

16. J. Jach and C. N. Hinshelwood, Proc. Roy. Soc., London, Vol. A 231 (1955), 145.

17. F. O. Rice and K. K. Rice, "The Aliphatic Free Radicals," p. 102, John Hopkins Press, 1935.

18. E. E. Royals, "Advanced Organic Chemistry," p. 125, Prentice-Hall, Inc., 1954.

19. E. Gorin, A. G. Oblad, and R. F. Schmuck, Ind. Eng. Chem., Vol. 38 (1946), 1187.

20. C. N. Satterfield, and T. W. Stein, J. Phys. Chem., Vol. 61 (1957), 537.

21. D. Downs, A. D. Walsh, and R. W. Wheeler, Phil. Trans. Roy. Soc., Vol. A 243 (1951), 463.

22. G. Skirrow and C. F. H. Tipper, Seventh International Symposium on Combustion, 1958. 134.

23. B. M. Sturgis, SAE Transactions, Vol. 63 (1955), 253.

24. P. J. Rosen, Proceedings of the National Electronics Conference, Chicago, Illinois, October, 1958.

Discussion

Mechanisms Involved in Vapor Phase Oxidation of Hydrocarbons

J. F. Kunc, H. S. Roblee, Jr.
Esso Research & Engineering Co.

THE AUTHORS are to be complimented for tackling and at least partially unraveling some of the threads of an important and extremely complex problem. It has been amply demonstrated by many investigators that a tremendous amount of chemistry can take place ahead of the advancing flame front in the spark-ignited engine. The nature of this chemistry determines whether the material ahead of the flame will continue to burn smoothly or will ignite spontaneously at some point in the process to cause knock. It is generally conceded that knock will occur if the critical concentration of some chemical compound or compounds is exceeded. However, neither the nature of these compounds nor their critical concentration is known.

Much research has been done on the problem of the mechanisms involved in the vapor phase oxidation of hydrocarbons. In spite of this fact, however, our over-all knowledge of the field remains sketchy and woefully incomplete. Many theories have been proposed but none of them have been adequately proved. The basic difficulty rests in the nonselectivity of both oxidative and pyrolytic reactions. As a consequence, as the authors and others have shown, if a mixture of a single pure hydrocarbon with air is heated, a host of intermediate compounds are formed before the carbon is all converted to CO_2 and the hydrogen is all converted to water. The individual intermediates may be either more or less resistant to knock than the parent compound. A brief description of a study we conducted on a lean mixture of 2-methylpentane with air in a rapid compression machine illustrates the complexity of the situation. In this experiment, the mixture was rapidly compressed and then rapidly quenched 1 millisec prior to the time it would have ignited spontaneously if it had not been quenched. At this time about 70% of the 2-methyl-pentane had disappeared. Analysis of the quenched sample using gas chromatographic and Time-Of-Flight mass spectrometric techniques revealed the presence of at least 40 chemical compounds not in the original material. These included 14 different olefins and a wide variety of oxygenated materials.

In agreement with the findings of the authors, the studies which we have made using the rapid compression machine indicate that at least certain hydrocarbons do readily undergo pyrolytic and oxidative reactions simultaneously under temperature and pressure conditions comparable to those prevailing in engines. Under severe conditions the reactions can be extensive provided they are allowed to proceed for a sufficient period of time (for example, more than a few milliseconds). In engines operating at reasonable speeds, however, the time that the reactants are exposed to really high temperatures and pressures is relatively short (usually 2 millisec or less). No conclusions regarding the significance of these reactions in terms of their influence on engine power output or knocking can be drawn at this time.

As a matter of interest in connection with the general question of the vapor phase oxidation behavior of hydrocarbons, Fig. A presents the results of ignition delay experiments conducted by Esso Research on the five isomers of hexane in admixture with air in a rapid compression machine. As might have been anticipated, their ignition delay times roughly parallel their antiknock characteristics. Of more interest, however, is the shapeoof the pressure time curves. It will be noted that the increase of pressure with time becomes much more gradual in progressing from n-hexane to 2, 3-dimethylbutane. This indicates that 2, 3-dimethylbutane undergoes reaction much more slowly than n-hexane and the other isomers exhibit intermediate reactivities. Based on gas chromatography of quenched samples taken during the ignition delay period, all of the hexane isomers undergo both oxidative and pyrolytic reactions prior to spontaneous ignition as indicated by the presence of both oxygenated and olefinic compounds.

Pyrolysis and oxidation reactions usually convert hydrocarbons to both higher and lower molecular weight materials. It would be of interest to learn whether the authors observed the formation of high boiling materials in the course of their studies. Conceivably, determination of the oxygen content of the high molecular weight materials might be quite revealing in helping to decide whether the reactions involved were predominantly pyrolytic or oxidative in nature.

In conclusion, we would like to inquire whether the authors plan to continue their study and, if so, what general plan of attack is being considered. Since oxidation reactions are generally exothermic, whereas pyrolysis reactions are endothermic, it might be interesting to determine the overall exo- or endo-thermicity of the reactions taking place in the motored engine by making temperature as well as pressure measurements.

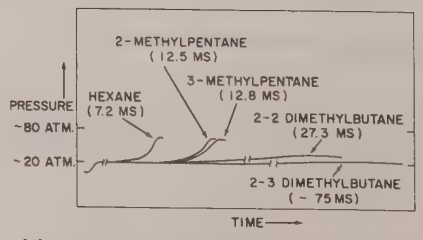

Fig. A — Ignition delay and pressure-time path reflects differences in oxidation behavior of hexane isomers

Chemical Kinetic Problems

P. R. Ryason
California Research Corp.

THE AREAS covered by the research reported in this paper are very extensive. We limit our comments to certain aspects of the chemical kinetic problems. Both static and flow experiments on thermal decomposition of hydrocarbons are very much influenced by the walls of the container. The time required in the motored engine compression of a hydrocarbon-air mixture is so short as to make it unlikely that wall reactions are important in the combustion chamber proper. Another important factor is that the laboratory experiments were carried out under isothermal conditions, whereas a rapidly varying time-temperature history occurred in the engine. In view of the extreme temperature dependence of reaction rates and the sensitivity of free radical reactions to surface conditions, we believe it is difficult to compare rigorously the experimental engine and laboratory data. Even in laboratory experiments, the Rice mechanism is regarded as not inconsistent with the observed rates of thermal decomposition. Generally, this mechanism is regarded as exhibiting the possibility that free radicals may be important in hydrocarbon decomposition. More direct proof of the presence of free radicals is always required in each case.

Product ratios similar to those predicted by the Rice mechanism are not sufficient proof the reactions are, in fact, free radical in nature. Inhibition by nitric oxide is more conclusive evidence that free radicals are present in the system. The authors are asked if they have any data on the effect of nitric oxide in the motored engine decomposition of hydrocarbons? The author's scheme is reasonable, but additional evidence is required to prove the contention free radicals are present. The exact mechanism is complex and probably involves chain reactions. Many parallel reaction paths with common intermediates, in a nonsteady situation, make the interpretation of observed rates difficult. The surest experiments are those which involve some direct interaction with a postulated intermediate. Reactions with a reagent, such as nitric oxide, or direct observation by optical or mass spectroscopy are examples that come to mind of such direct interactions.

Whatever the exact mechanism, the production of olefins is of particular interest. Do the authors have data on the olefin production from higher paraffin homologues? Can any general statements be made concerning the types of olefins likely to be synthesized in the engine from aliphatic hydrocarbons boiling in the gasoline range?

Cracking Reactions and Hydrogen Stripping

C. Walcutt
Ethyl Corp.

THE AUTHORS have given us additional evidence to support the idea that cracking reactions and hydrogen stripping are some of the initial steps in hydrocarbon degradation. It is suggested that, in the case of pentane, hydrogen stripping by oxygen accounts for the pentenes observed while cracking reactions account for the butenes. This concept seems to fit in well with their experimental data.

A reduction in oxygen concentration would be expected to reduce the tendency for oxygen to strip hydrogen from the parent molecule, and thus increase the ratio of butene to pentene, as found experimentally.

A point that might be elaborated on a little is their finding that the ratio of butenes to pentenes increases with increased compression ratio. Some years ago, in trying to account for the proknock effect of a precool flame reaction with no evidence of heat release,* we use a reaction mechanism proposed by Wilson**. His concern, like that of Dr. Welling, was to account for the olefins and hydrogen peroxide formed during the oxidation of a paraffin. It is of interest to note that this reaction mechanism, as shown in the following equation,

	ΔH, Kcal/mole
$RCH_2CH_2\cdot + O_2 \longrightarrow RCH = CH_2 + HO_2\cdot$	-4
$RCH_2CH_3 + HO_2\cdot \longrightarrow RCH_2CH_2\cdot + H_2O_2$	0
$RCH_2CH_3 + O_2 \longrightarrow RCH = CH_2 + H_2O_2$	-4

is quite similar to the one used by Dr. Welling to account for the olefins obtained in his motored engine studies. This reaction mechanism indicates that only a small amount of energy is required for hydrogen stripping as compared to what would be required for thermal decomposition and formation of butenes. This, then, fits in well with the findings of Dr. Welling and his co-workers; namely, that high compression ratio and more energy input to the gases increases the ratio of butenes to pentenes.

The authors attempted to compare their engine data with conventional data obtained in reaction vessels and flow systems. Although qualitative comparisons may be possible, it would appear rather dangerous to make quantitative com-

*R. E. Wilson, Doctorial Thesis, Massachusetts Institute of Technology, 1953.

**C. Walcutt, J. M. Mason, and E. B. Rifkin, "Effect of Preflame Oxidation Reactions on Engine Knock," Ind. Engr. Chem., Vol. 46 (May, 1954), 1029-1034.

parisons, because of the large differences in contact time between conventional systems and engines. The longer contact time in conventional systems would allow the reaction to more nearly reach an equilibrium state. Consequently, it is difficult to see how quantitative comparisons would be possible. Also, I believe the point is not well established that cracking reactions and hydrogen stripping, which lead to olefinic constituents in unburned fuels during precombustion, are the reason for the existence of olefins in exhaust residuals after combustion.

Mention was made that only very small concentrations of alkyl peroxides and hydrogen peroxide were found. We have done some experimental work where the sampling apparatus we used was similar to that used by Dr. Welling. In our case, however, the CFR engine was spark ignited. We had no difficulty in finding increasing concentrations of carbonyls and peroxides as the flame front approached the end zone at knock-limited operating conditions. We were unable, however, to get satisfactory results with instrumental methods and had to resort to wet chemical procedures.

Frequent reference is made in the paper to "airfuel" ratios in systems without oxygen or with oxygen reduced from the normal level in air. I suppose what is meant by "airfuel" ratio is the ratio of diatomic gases to fuel. Another item I wish to comment on is the method of measuring airfuel ratio in the engine. It is explained that the engine is first run on air without fuel and the air consumption is measured. Then, the amount of fuel required is calculated and introduced into the intake manifold. Since an engine is a volume breathing device, the fuel vapors, to the extent that they are evaporated before the valve closes, would reduce the previously measured air consumption. This would then invalidate the previous calculations; the engine would be operating richer than intended. Perhaps it was assumed that all the pentane was evaporated in the intake manifold and an allowance was made for its volume. This would not, however, allow for the reduction in intake-manifold temperature due to fuel evaporation and the resulting increase in engine volumetric efficiency.

Authors' Closure to Discussion

HIGH BOILING materials that were observed in our studies were oxygenates. No hydrocarbons of greater molecular weight than the fuel were observed. The experimental conditions are thought to strongly favor the unimolecular decomposition of a radical or its reaction with reactants of relatively high concentration (fuel or oxygen) rather than with another hydrocarbon radical which is also in low concentration.

No data were obtained on the influence of nitric oxide on precombustion reactions. With respect to olefin production from gasoline range aliphatic hydrocarbons in a fired engine, limited data indicate lower olefins, presumably from pyrolysis, predominate but higher olefins which could have been produced by hydrogen stripping are also present.

With respect to the pyrolysis of pentyl radicals under a variety of conditions, problems of heterogeneous reactions and secondary reactions do exist as has been suggested by the discussors. Also, the unimolecular decomposition in gas phase of 2-pentyl radical, for example may invariably give the same products but unless the reactivities of primary and secondary hydrogens in n-pentane are in the same ratio for all attacking species a variation in relative quantities of 1-, 2-, and 3-pentyl radicals produced and of their decomposition products could readily occur between precombustion and oxygen-free pyrolysis. In the present work the overall variations do not appear to be large except for the ethane-ethylene case. The most significant feature of the pyrolysis of n-pentane is that it fails to produce pentanes in quantity as precombustion may do.

In measurements of air volume and mixture ratio fed the engine, allowance was made for volume of fuel vapor. The manifold heater was adjusted to maintain constant manifold temperature with or without fuel.

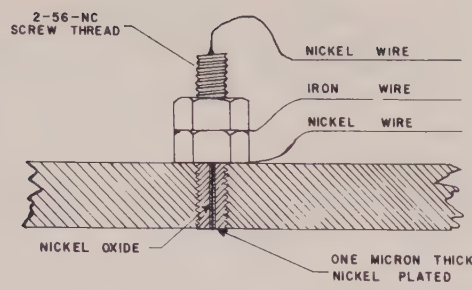

Fig. 1—Thermocouple construction and installation

Unsteady Heat Transfer in Engines

Vern D. Overbye
A. O. Smith Corp.
(previously of University of Wisconsin)

James E. Bennethum
General Motors Corp.

O. A. Uyehara
University of Wisconsin

P. S. Myers
University of Wisconsin

A THERMOCOUPLE, whose junction is located one micron below the surface of the combustion-chamber wall of an engine, was used for the following studies, together with appropriate oscillographic equipment, to give recordings of the combustion-chamber metal surface temperature as a function of time. Data were taken in two ways:

1. Deliberately keeping the thermocouple free of deposits.

2. Deliberately building up deposits over the thermocouple.

The first procedure, plus suitable mathematical analysis, gave instantaneous heat transfer rates through the gas-metal interface. This permitted evaluation of heat transfer coefficients in unsteady heat transfer. The data and accompanying analysis suggest that the concept of the heat-transfer coefficient h is of questionable utility and validity in unsteady heat transfer. A theoretical analysis and correlation of experimental data are presented.

The second procedure shows that deposits from different fuels have markedly different effects on heat transfer and heat transfer rates. An empirical analysis of the experimental data is presented. A theoretical analysis permits estimation of the thermal properties of the deposits and of the gas-deposit interface temperature as a function of time.

While two studies with different objectives are reported herein, the basic instrumentation was nearly the same. The most important instrument, which was common to both studies, was a thermocouple as described by Bendersky (1)*. The thermocouple construction and arrangement is shown in Fig. 1 as well as the usual method of installation in the engine. As shown in Fig. 1 the nickel wire is insulated electrically (and thermally) from the iron body by a nickel-oxide film formed on the wire. The iron is drawn down on the nickel wire by a wire-drawing die. After metallurgically polishing the end of the resulting concentric cylinders, a layer of nickel is evaporated on the end; thus the thermocouple junction is located at the nickel-iron interface. The nickel evaporation can be controlled to obtain various thicknesses. A one-micron-thick layer was used for the work reported herein, although some observations were made with thermocouples having a 5-micron-thick layer. The lower iron nut, shown in Fig. 1, together with the iron and nickel wires clamped by this nut, form a second thermocouple. The junction of this thermocouple is located between the wall and the nut. Its output then is a measure of the wall temperature on the water side. The iron wire is common to both thermocouples.

The thermocouple records the metal temperature at the thermocouple junction which, for present purposes, is the same as tne gas-metal interface temperature. Its response to sudden temperature changes of gases in front of it is also excellent. Bendersky (1) reports measurements where the rate-of-change-of-metal temperature with time was as high as 800 F per millisecond, which was roughly ten times the maximum values measured in this work.

Two CFR engines were used for the investigations, al-

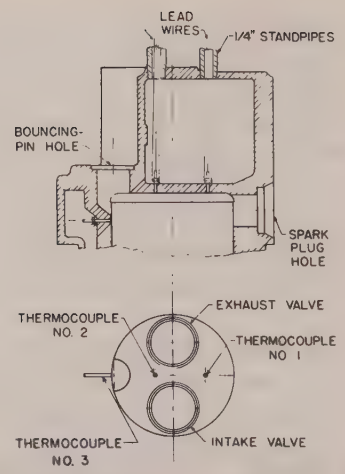

Fig. 2—Location of thermocouples in engine

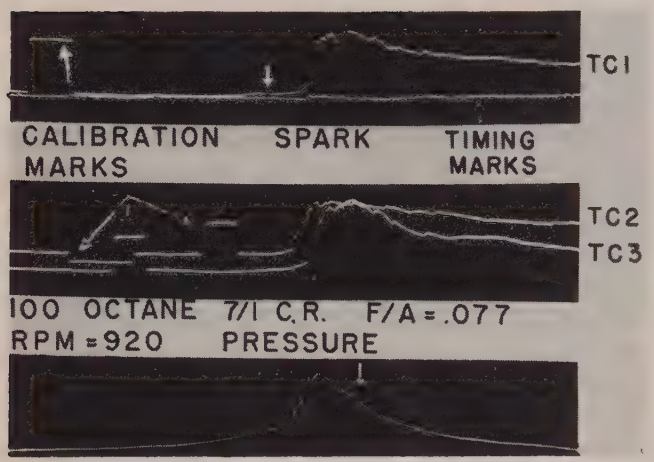

Fig. 3—Typical drum camera record showing data obtained

though some of the earlier work was done with a Lauson oil-test engine (2) and an Ethyl test engine (3). The thermocouples were installed in the same locations in both CFR engines, as shown in Fig. 2.

The CFR engines were not always fired from the same place. The reader is cautioned to note the place from which the engine was fired if he attempts to draw any conclusions regarding flame speeds or other similar phenomena.

The output from each thermocouple was amplified by a low-noise, high-gain d-c amplifier (4), and the output of the amplifiers was displayed on a bank of oscilloscopes. The oscilloscopes were photographed by means of a drum camera. A typical trace with the pertinent features labelled is shown in Fig. 3.

The engine used to obtain data with clean thermocouples was equipped with an American Bosch fuel injector and pintle nozzle in the intake manifold as well as a shrouded intake valve. Cylinder gas pressure was recorded with a Li-Draper transducer and associated d-c amplifiers. All data were obtained with the engine fired from the spark plug hole.

The engine used in the deposit studies was equipped with a carburetor and unshrouded intake valve, and it was fired

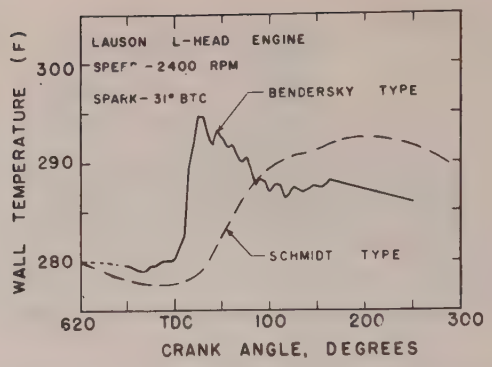

Fig. 4—Comparison of two different types of thermocouple

from the bouncing pin hole. Other differences between engine instrumentation will be noted where applicable.

Both engines were equipped with dynamometers to measure power output. Crank angle degree markers to indicate piston position were obtained by means of a magnetic device (Fig. 3). The interference on the traces when the engine was sparked provided a convenient spark detector (Fig. 3).

Section I — Tests Without Deposit

Early investigators recognized that inner metal surface temperature variation could be expected in operating engines. As a matter of interest Donkin (5) inserted small mercury-in-glass thermometers in the cylinder walls of a steam engine and observed a periodic rise and fall of the mercury with the engine operating at 35 rpm. Coker (6) used a thermocouple, galvanometer, and point-by-point technique to record wall temperature variations in a spark-ignition engine. Nusselt (7) used a bomb to obtain fundamental knowledge of heat transfer coefficients. Dahl (8) developed theoretical relationships for cyclic temperature and stress variations in a cylinder wall. The peak predicted thermal stress was 4900 psi compression in the example used. Eichelberg (9, 10) used thermocouples located at a slight distance beneath the gas-metal interface in slow speed diesel engines to develop a correlation for the heat transfer coefficient h as a function of average piston speed, cylinder pressure, and cylinder gas temperature. This correlation has been used in many subsequent investigations and computations for heat transfer in diesel engines. Meier (11) was inspired by the theoretical studies of Ptriem (12, 13) and developed a gold resistance thermometer suitable for recording wall temperature variation in an engine operating at 2000 rpm, but heat transfer computations were not performed. Elser (14) used Eichelberg's technique to measure diesel engine wall temperatures and developed a correlation for h in dimensionless form. In a recent investigation by Vincent (15), Eichelberg's formula for h was used to predict thermal loadings of diesel engine cylinder walls, which were compared with experimental data, but no attempt to determine unsteady heat transfer was reported.

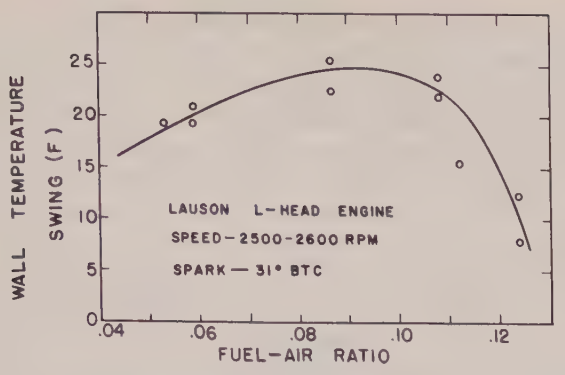

Fig. 5—Wall temperature swing versus fuel-air ratio with an L-Head engine

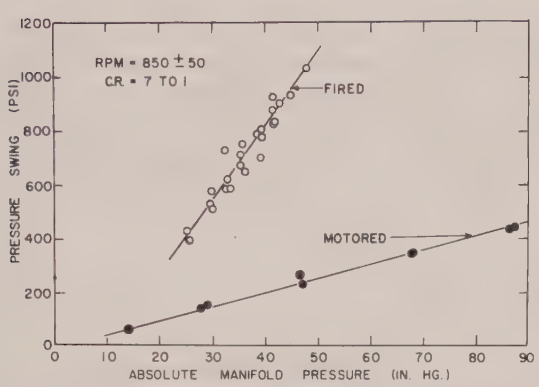

Fig. 6—Pressure swing versus manifold pressure in a fired and motored engine

Attempts have been made to measure wall surface temperature at the University of Wisconsin for the past ten years. Schmidt (3) formed an iron constantan thermocouple using a plug made of cylinder head material as one of the elements. He ground down the resulting junction to make it as near to the surface as possible. Although temperature variations were recorded, the resulting data were not suitable for extended heat transfer computations. Pless (2), under the direction of T. J. Schweitzer, used a thermocouple developed by Bendersky (1) to record wall temperature variations in a Lauson oil test engine with good success. A thermocouple as described by Schmidt (3) was also inserted in the head of the engine. Fig. 4 shows the response of each of the thermocouples under similar operating conditions. It may be seen from Fig. 4 that the Bendersky type thermocouple is far superior to the older type, since many surface temperature variations are present in the response of the newer high-speed thermocouple. Data were obtained by Pless with the engine operating at full throttle, 31 deg spark advance, speed of 2500-2600 rpm, and varying air fuel ratio. These data are presented in Fig. 5. The term "wall temperature swing" used in the figure represents the difference between the maximum and minimum temperatures during the cycle. The large decrease in wall temperature swing at very rich fuel air ratios may be partly due to deposit formation during the test run.

Table 1 - Clean-Engine Operating Conditions

Intake Manifold Pressure	Variable
Compression Ratio	7/1
Speed	830 +/- 4 rpm
Spark Advance	18 deg btc
Air-Fuel Ratio	14.75 +/- 0.33
Inlet air Temperature	80 +/- 3 F
Exhaust Pressure	Atmospheric
Fuel	Iso-Octane

Overbye (16) used the Bendersky type thermocouple and a theoretical analysis in studies with a spark-ignition CFR engine. This is the basis for the studies of heat transfer and heat transfer coefficients presented herein.

Surface temperature measurement and subsequent heat transfer analysis is desirable for an operating internal combustion engine for three principle reasons:

1. To account for heat transfer during an engine cycle analysis.
2. To determine cyclic thermal stresses in the wall material.
3. To determine the effect of heat flow on volumetric efficiency.

The investigation described herein is concerned primarily with the first reason.

The surface thermocouples, test engine, and instrumentation previously described were used to determine the effect of various operating conditions on the wall temperature variation of a clean engine. The data obtained were analyzed, using heat transfer equations developed in the Appendix, to determine the magnitude of heat transfer through the wall surface. An attempt was made to correlate the data with more easily determined engine parameters, such as speed, cylinder gas pressure, and cylinder gas density. If this task proved to be insurmountable, it was hoped to at least express the derived quantities in more commonly accepted terms such as heat transfer coefficients.

Unleaded fuel (iso-octane) was used in all fired tests (except for iso-octane-normal heptane mixtures for 70 octane data). Air was used in motored tests. The thermocouples were cleaned prior to each series of runs by inserting a nylon brush saturated with acetone through the spark plug hole and gently swabbing the thermocouple surfaces. The fired tests shown in this section were performed with nearly stoichiometric air fuel ratio such that deposit formation during the test run was very small. It will be seen that initial data could be reproduced at the end of a series of prolonged tests.

Fired Data

Variation of Intake Manifold Pressure - One of the variables studied quite intensively was variation of the intake manifold pressure in a fired engine. The operating conditions, which were held constant except when deliberately

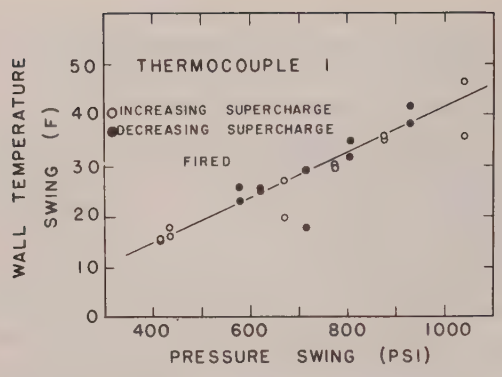

Fig. 7—Wall temperature swing at thermocouple 1 versus pressure swing in a fired engine

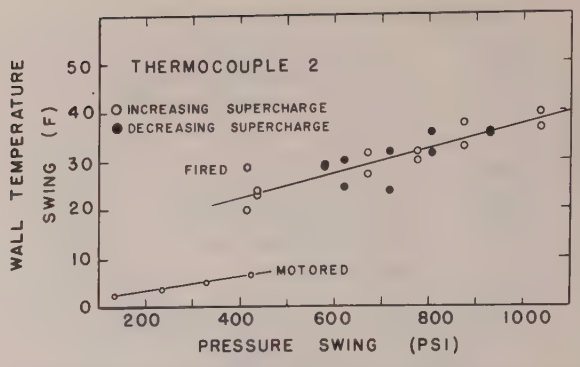

Fig. 8—Wall temperature swing at thermocouple 2 versus pressure swing in a fired and motored engine

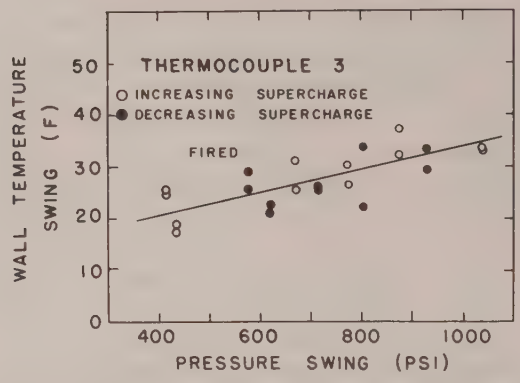

Fig. 9—Wall temperature swing at thermocouple 3 versus pressure swing in a fired engine

varied, are shown in Table 1. It may be noted from the table that the air fuel ratio was slightly richer than stoichiometric. This was chosen so that the engine would operate satisfactorily over the entire range of intake manifold pressures used in the tests and yet deposit formation would be slight. Visual examination of the combustion chamber thermocouple surfaces showed a slight cloudiness after the series of tests, which required approximately 2 hr to complete.

The effect of manifold pressure on cylinder gas pressure in the fired engine is shown in Fig. 6. The figure also shows the effect of intake manifold pressure on cylinder gas pressure in a motored engine, which will be discussed in detail in later sections. The difference in maximum and minimum gas pressure during the cycle was found to be a convenient correlation variable, and it will be referred to as "pressure swing". A similar variation in wall temperature is obtained in taking the difference in maximum and minimum wall surface temperature during the cycle, which, as previously stated, will be termed "wall temperature swing".

Figs. 7-9 show variation of wall temperature swing as a function of pressure swing at thermocouples 1, 2, and 3 respectively. Fig. 8 also shows the variation of wall temperature swing at thermocouple 2 in a motored engine, which will be discussed in detail in later sections. It will be noted on the figures that two data points occur for each value of pressure swing. These two temperature swings were obtained from two successive cycles of recorded wall surface temperature variation. The pressure swing abscissa is the arithmetic mean of two successive pressure cycles. The data are presented in this manner to emphasize cycle-to-cycle temperature swing variation. Cycle-to-cycle pressure variation, on the other hand, was usually less than 2% peak pressure; thus the average pressure swing was used. The trend of increasing wall temperature swing with increasing pressure swing is present in each of the figures as may be expected intuitively. This intuition will be confirmed later in heat-transfer-coefficient analysis. Also the figures show that data points obtained during decreasing supercharge runs (obtained later in the test period) agree with points obtained during increasing supercharge. Thus the effect of deposit formation on wall surface thermocouples under these operating conditions appears negligible.

It will be noted that the curves in Figs. 7-9 have significantly different slopes and that the slope of the motored curve in Fig. 8 is different from the slope of the fired curve. Presumably the difference between the fired curves is due to location, i.e., gas movement or head construction - the difference between the fired and motored slopes in Fig. 8 is that of gas composition, and the difference in ordinate is probably due to gas-wall temperature differences.

Variation of minimum wall surface temperature at each of the thermocouples is shown as a function of cylinder pressure swing in Fig. 10. Here the steady-state level of the surface temperature is seen to increase with cylinder pressure swing. The obviously greater increase in minimum wall surface temperature at thermocouple 2 may be explained by its location in the engine. Thermocouples 1 and 3 are installed in relatively large areas of uniformly thick metal adequately covered with cooling water, while thermocouple 2 is installed near the exhaust valve where the metal thickness is nonuniform and the flow of cooling water is definitely restricted. These relative locations of the three thermocouples may also explain later peculiarities in heat transfer computations.

Finally, the variation of water jacket metal surface temperatures as measured by the water jacket thermocouples is

shown as a function of cylinder pressure swing in Fig. 11. The trend of the water jacket surface temperatures is seen to be similar to the trend of minimum combustion chamber surface temperatures, but the slopes of the curves are lower. Incidentally, Fig. 11 shows that the water jacket surface temperatures are always higher than those of the continuously boiling coolant, which was water.

Variation of Intake Valve Position - The data shown in the preceding section were obtained with the shrouded intake valve positioned such that the shroud opened toward the spark plug hole. Fig. 12 shows a section of the temperature level above the minimum value in the cycle as a function of crank angle for thermocouples 1, 2, and 3, with the intake valve orientated in this manner. Examination of Fig. 12 reveals that thermocouple 1, which is nearest to the spark plug, does not respond first in the cycle, but rather thermocouple 2 is the first to respond. In fact, Fig. 12 shows thermocouple 3 responding before thermocouple 1. This indication of burning characteristics in the combustion chamber suggested that variation of the inlet valve position affects flame patterns.

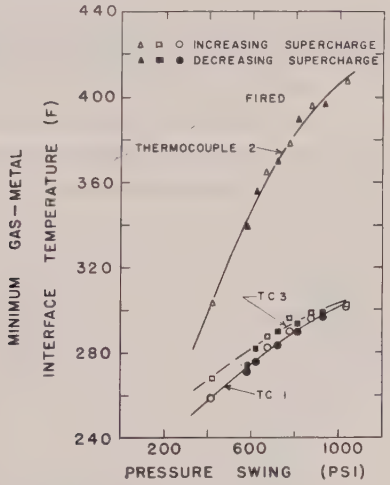

Fig. 10—Minimum gas wall interface temperature versus pressure swing for three thermocouples in a fired engine

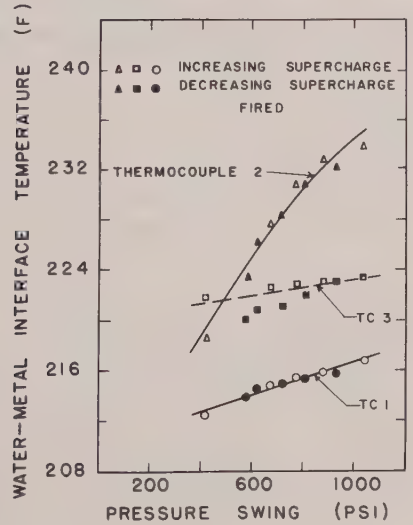

Fig. 11—Water-metal interface temperature versus pressure swing for three thermocouples in a fired engine

The intake valve was rotated 90 deg clockwise, so that the shroud opened toward the exhaust valve. Fig. 13 is a section of surface temperature variation above the minimum value at thermocouples 1, 2, and 3 as a function of crank angle with the intake valve in this position. It may be seen from Fig. 13 that the flame progresses across the chamber as if it were passing through a relatively quiescent mixture, since it is assumed that the thermocouple responds sharply when the flame front passes by the thermocouple location. Fig. 13 also shows that thermocouple 3 does not respond until late in the cycle even though it is "looking" at the flame front traveling across the chamber; this suggests that radiant heat transfer is not significant during combustion.

In view of the effect of orientation of the shrouded valve on thermocouple response in the fired engine, an arbitrary definition is made that the intake-valve position with the valve shroud opening toward the spark-plug hole is a position of "maximum turbulence", while the position with the shroud opening toward the exhaust valve is termed the position of "minimum turbulence." Several test runs with the valve shroud rotated 180 deg from the maximum and minimum turbulence positions showed no significant variation in test results obtained with maximum or minimum turbulence positions respectively. However, the response of thermocouple 1 does indicate that the effect of turbulence on flame pattern is reduced with the intake valve orientated, as recommended by ASTM, as compared with the shroud opening toward the spark plug hole.

Fig. 14 shows the wall temperature above the minimum level at thermocouple 1 as well as cylinder pressure as a function of crank angle in the supercharged condition of minimum turbulence. It is seen from Fig. 14 that the thermocouple response is a sudden small jump and a gradual increase in temperature with time. Fig. 15, on the other hand, shows the wall surface temperature variation above the minimum level at thermocouple 1 as well as cylinder pressure as a function of crank angle in the supercharged condition of maximum turbulence. Here it is seen that the initial temperature rise carries the wall temperature to nearly the maximum value achieved during the cycle.

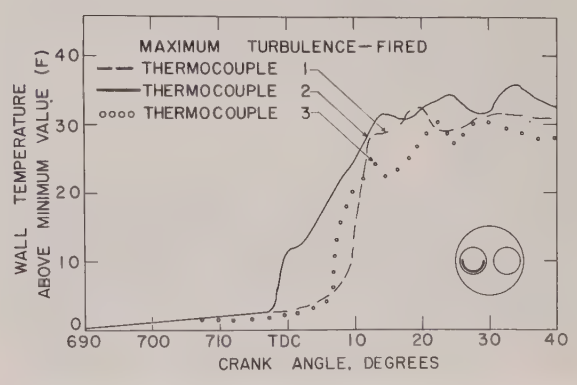

Fig. 12—Wall temperature versus crank angle for three thermocouples in a fired engine with minimum turbulence

The wall temperature responses shown in Figs. 14-15 may be explained in part by the pressure-time history in each figure as well as knowledge of factors affecting steady-state heat transfer. Two factors will be considered:

1. A driving force (temperature difference between the gas and wall).
2. Heat transfer resistance of the gas adjacent to the wall.

In the fired engine with minimum turbulence (Fig. 14) the temperature of the gas in front of the thermocouple will increase abruptly due to combustion from its initial compression temperature as the flame front passes. The difference in the gas and wall temperature at this time in the cycle is the driving force. The gas film thermal resistance is comparatively high due to low turbulence and low density. After the flame front passes thermocouple 1, the temperature and density of the gas in front of thermocouple 1 will increase with time as a result of the burning of the rest of the charge. The burned gas may also be more turbulent than the unburned gas. These factors, then, slowly increase the driving force and decrease the film resistance of the burned gas in front of thermocouple 1 as the flame front advances across the chamber. The final result is for the wall temperature to steadily increase after the small initial rise until the cylinder charge is burned.

In the fired engine with maximum turbulence (Fig. 15) the pressure trace indicates that the gas in front of thermocouple 1 will burn from an initial temperature which is slightly higher than that in Fig. 14. The gas turbulence and density are also increased when compared with Fig. 14. Since the pressure record in Fig. 15 and the temperature records in Fig. 12 show the gas in front of thermocouple 1 to be one of the last parts of the end gas to burn, there is little chance for gas temperature or density increase after the initial inflammation. The conditions of a large driving force, low film resistance, and small charge remaining to burn determine the wall temperature variation shown in Fig. 15.

The wall temperature swing, minimum temperature level, and water jacket surface temperature did not change appreciably with the intake valve oriented in either a position of maximum or minimum turbulence. An attempted explanation of these phenomena will be deferred until after a discussion of motored data.

Since distance along a line from the spark plug to each thermocouple is known, it is possible to determine average flame speed in the condition of minimum turbulence. The assumption was made that the thermocouple shows it most rapid response as the flame front passes. Fig. 16 shows var-

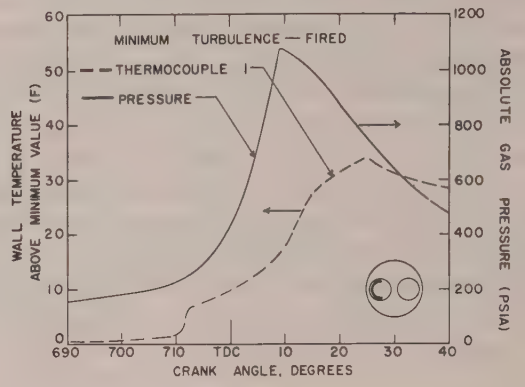
MINIMUM TURBULENCE — FIRED
THERMOCOUPLE 1
PRESSURE
WALL TEMPERATURE ABOVE MINIMUM VALUE (F)
ABSOLUTE GAS PRESSURE (PSIA)
CRANK ANGLE, DEGREES
690 700 710 TDC 10 20 30 40
0 10 20 30 40 50 60
0 200 400 600 800 1000 1200

Fig. 14—Wall temperature at thermocouple 1 and gas pressure versus crank angle in a fired engine with minimum turbulence

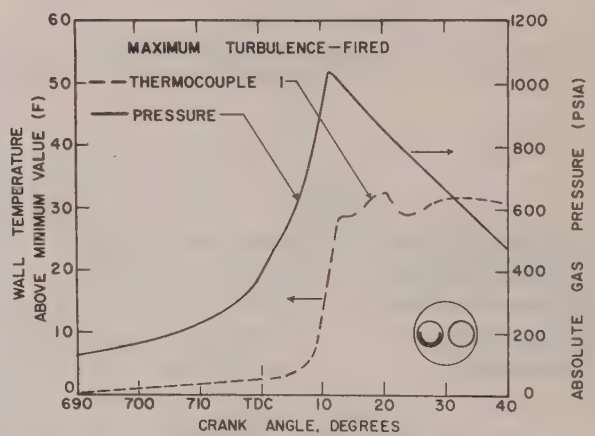
MAXIMUM TURBULENCE—FIRED
THERMOCOUPLE 1
PRESSURE
WALL TEMPERATURE ABOVE MINIMUM VALUE (F)
ABSOLUTE GAS PRESSURE (PSIA)
CRANK ANGLE, DEGREES
690 700 710 TDC 10 20 30 40
0 10 20 30 40 50 60
0 200 400 600 800 1000 1200

Fig. 15—Wall temperature at thermocouple 1 and gas pressure versus crank angle in a fired engine with maximum turbulence

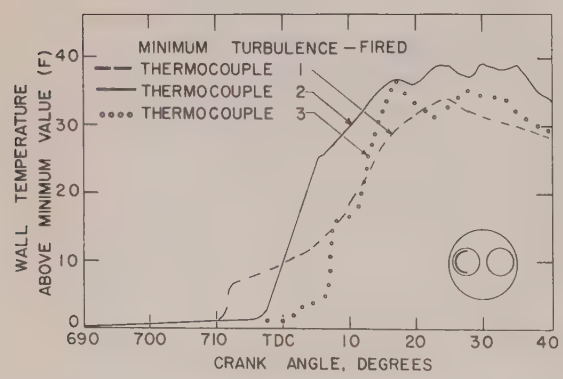
MINIMUM TURBULENCE — FIRED
THERMOCOUPLE 1
THERMOCOUPLE 2
THERMOCOUPLE 3
WALL TEMPERATURE ABOVE MINIMUM VALUE (F)
CRANK ANGLE, DEGREES
690 700 710 TDC 10 20 30 40
0 10 20 30 40

Fig. 13—Wall temperature versus crank angle for three thermocouples in a fired engine with maximum turbulence

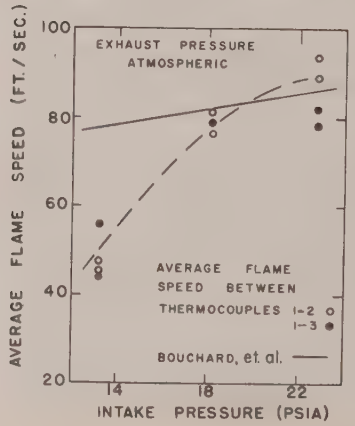

Fig. 16—Average flame speed versus intake manifold pressure in a fired engine with minimum turbulence

iations of flame speed averaged between thermocouples 1 and 2 and flame speed averaged between thermocouples 1 and 3 as a function of intake manifold pressure. A relationship between flame speed and intake pressure as found by Bouchard (17) by means of flame photography is shown as a solid line in Fig. 16. Bouchard's study was conducted by averaging about 15 flame photographs obtained from an L-head engine on which the intake and exhaust pressures were equalized. Fig. 16 is not an attempt to duplicate the earlier investigation since intake and exhaust pressures were not equalized in the present studies, but it does suggest that surface thermocouples may be used to obtain flame patterns and average flame speeds in a clean engine.

Miscellaneous Fired Data - A theoretical investigation of heat transfer phenomena in an engine (Appendix) indicates a definite (but as yet undetermined in its entirety) relationship between the temperature variations within the gas volume and temperature variation on the wall surface. One theoretical derivation indicates that wall temperature variation is a miniature replica of the gas temperature variation. These theoretical studies are intriguing in light of observations made while the engine was knocking.

It has been shown in Fig. 3 that the wall surface temperature increases abruptly from a low temperature before the flame front passes to a high temperature after the flame front passes when an unsupercharged engine is operated with isooctane as fuel. Fig. 17 shows an example of the wall temperature variation at the thermocouples when the engine was operating at maximum turbulence with audible, light knock using 70 octane fuel. It appears in Fig. 17 that a slight burning occurs in front of thermocouple 1 prior to the sudden temperature increase, which is characteristic of nonknocking operation. This phenomenon indicates that either a slight burning occurred in the gas volume in front of thermocouple 1 prior to the time the flame front normally arrived or that the resistance of the gas film decreased very markedly. This is perhaps not too unexpected, but the following rather rapid decrease in wall temperature just prior to the arrival of the flame front is quite unexpected.

One possible explanation would be that the thermocouple responded to burning gas which was swept away due to turbulence before the normal flame front arrived. However, it is difficult to see why this event occurred only during knocking operation. Another explanation would be that the thermocouple responded to ionization in the flame front, but since its impedance is low, this explanation is not satisfactory either.

The phenomenon shown in Fig. 17 occurred on approximately 25% of the recorded temperature cycles with the engine operating at 7/1 compression ratio and 70 octane fuel, and it occurred frequently in later data obtained with the engine knocking during supercharge operation at 7/1 compression ratio using 100 octane fuel.

An interesting result in a heavily knocking engine with a 9/1 compression ratio and sparked from the bouncing pin hole is shown in Fig. 18. In studying Fig. 18 it should be remembered that the normal temperature swing under these conditions would be around 30 F. It will be seen in Fig. 18 that thermocouple 1 had a temperature swing just slightly greater than normal, while thermocouple 2 experienced an initial temperature swing of approximately normal magnitude, followed by a constant temperature region, and this was followed by another temperature rise of roughly twice the normal variation. Not enough work was done to explain the details, but Fig. 18 does illustrate the way in which the thermocouple might be used to study knock.

Wall surface temperature variation at thermocouple 1 is shown in Fig. 19 as a function of crank angle for an early spark and a late spark. These data were obtained early in the investigation before completely satisfactory calibration techniques were developed. Hence, it is probable that the

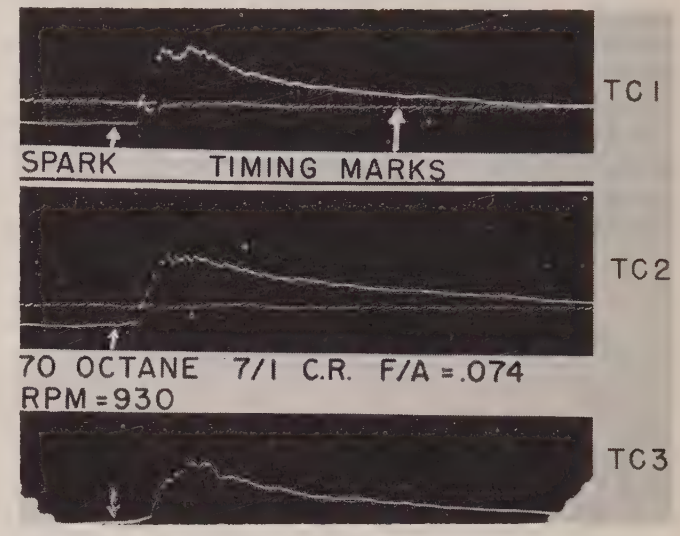

Fig. 17—Wall temperature versus crank angle for three thermocouples in a fired engine with light knock

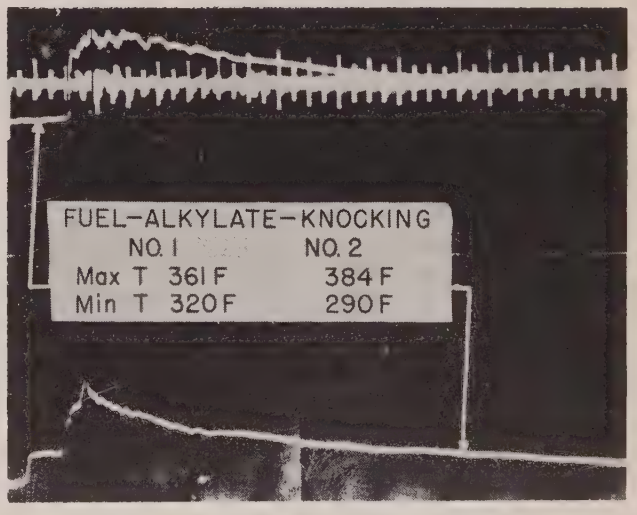

Fig. 18—Wall temperature versus crank angle for two thermocouples in a fired engine with heavy knock

data presented in Fig. 19 are a few per cent too large, but the relative variation is significant. It is seen that an early spark results in gases burning late on the compression stroke and early on the expansion stroke with a resulting increased wall temperature swing, whereas a late spark results in gases burning late on the expansion stroke with a resulting decrease in wall temperature swing. Heat transfer computations for these curves are interesting and are presented later.

Motored Data

It was realized (and will be conclusively proved later) that any correlation between instantaneous heat transfer in a fired engine and other operating parameters would be extremely difficult to formulate, despite the simple correlation for h found by Eichelberg (10) in a diesel engine. Thus it was decided to measure the wall surface temperature in a motored engine where the variable of chemical reaction is eliminated. The results were not too successful, as the chance of all amplifiers exhibiting satisfactory signal-to-noise ratios and stability simultaneously at the extremely high gain required to record motored wall surface temperatures was small. Also a set of new thermocouples were installed in the engine head and water leakage was experienced occasionally at thermocouples 1 and 3. Hence, the data presented in this section were obtained from thermocouple 2.

Fig. 20 shows a section of wall temperature variation versus crank angle at a condition of high intake manifold pressure (43.1 psia). This figure illustrates the general shape of the temperature-time history and indicates the magnitude of the maximum wall surface temperature variation recorded. It may be noted from Fig. 20 that the wall surface temperature variation peaks about 10 deg after tdc, while the gas temperature is expected to peak at tdc or a few crank angle degrees before tdc. This observation may be explained by the relative temperatures of the gas and wall. The gas temperature begins to decrease near tdc, but its value is still higher than that of the wall surface. Hence, heat will continue to flow to the wall from the gas, and the wall surface temperature will continue to rise until the rate of heat conduction into the inner wall material exceeds that from the gas to the wall surface. At this time the wall surface temperature will begin to decrease.

Fig. 21 shows variation of wall temperature swing with cylinder pressure swing and, also, the effect of maximum and minimum turbulence on wall temperature swing. If the gas temperature variation is assumed identical in all runs (identical intake gas temperature and compression ratio), it may be deduced that heat transfer coefficients increase with increased cylinder gas density and swirl velocity, since wall temperature swing increases with these variables.

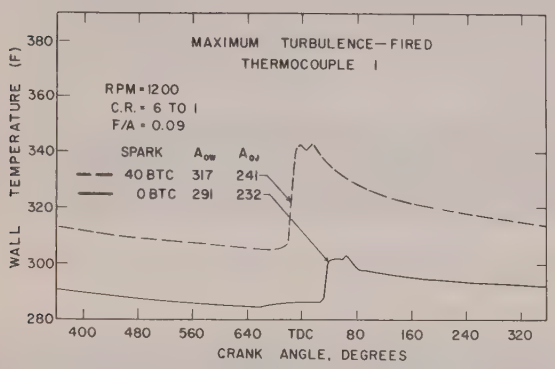

Fig. 19—Wall temperature at thermocouple 1 versus crank angle in a fired engine with variable spark

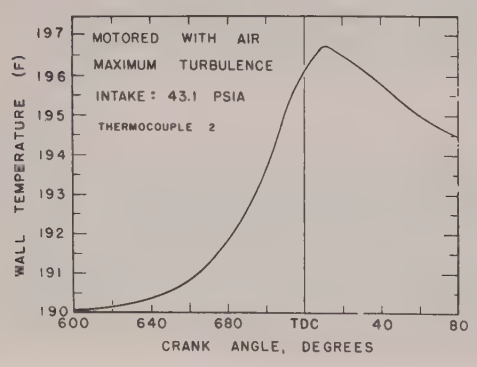

Fig. 20—Wall temperature at thermocouple 2 versus crank angle in an engine motored with air

Analysis of Data

General - The general equation for time variation of energy within the control volume (Appendix) may be reduced to Fourier's heat equation for a solid by assuming conduction to be the only mode of energy transport. The periodic surface temperature recorded by the thermocouple may be synthesized by a trigonometric series and the temperature profile into the cylinder wall may be determined. The surface heat transfer may then be obtained by differentiating the temperature profile equation with respect to distance and taking the limit as the surface is approached. These operations are detailed in the Appendix.

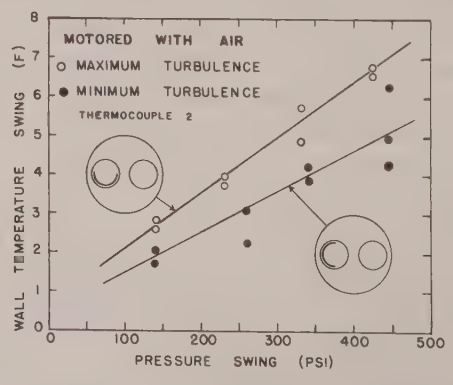

Fig. 21—Wall temperature swing at thermocouple 2 versus pressure swing in an engine motored with air with maximum and minimum turbulence

The procedure followed in determining the heat transfer for cycles representative of a given operating condition in the motored or fired engine was to pick a cycle that fell on the line through the data of Figs. 7-9, and 21 and completely analyze the cycle for heat transfer. A further requirement that data for all three thermocouples fall on their respective lines was used when possible.

Heat transfer was computed using 144 equally-spaced ordinates as sampling frequency on these selected temperature records. An IBM 650 Data-Processing machine greatly reduced computational effort and allowed analysis of a considerable amount of data.

Cylinder gas pressure-time variation was used along with the measured engine air flow and perfect gas equation to provide an average gas temperature-time variation during the cycle. In the fired engine an assumed exhaust gas temperature at the end of the exhaust stroke permitted determination of the weight of residual gas in the cylinder. A cycle analysis, detailed in Ref. (16), determined whether or not the assumed temperature was satisfactory. In the motored engine with a 7/1 compression ratio, the peak gas temperature was estimated to be 1215 R from experimental data presented in Ref. (18), and the pressure and volume variation with time permitted determination of gas temperature at each successive piston position during compression and expansion.

Heat Transfer in a Motored Engine - Heat transfer through the gas-wall interface as computed from the surface temperature variation in Fig. 20 is shown in Fig. 22 along with heat transfer from a temperature record obtained with the engine motored at atmospheric manifold pressure. Fig. 22 shows that the supercharged engine has both a higher positive heat transfer and greater negative heat transfer than that in the unsupercharged engine.

The effect of turbulence on heat transfer in a motored engine is shown in Fig. 23. The manifold conditions and speed are identical for both thermocouple records used to compute heat transfer curves shown in Fig. 23. The steady-state values show that turbulence is clearly a factor which tends to increase heat transfer in a motored engine.

Heat Transfer in a Fired Engine - Variation of instantaneous surface heat transfer for two supercharge conditions is shown as a function of crank angle in Fig. 24 for thermocouple 1. Peak heat transfer rates are seen to increase with supercharge in the fired engine, but the difference in the two conditions is not extreme.

A portion of surface heat transfer rates computed for temperature-time records shown in Figs. 14 and 15 are presented in Fig. 25. The condition of minimum turbulence does show

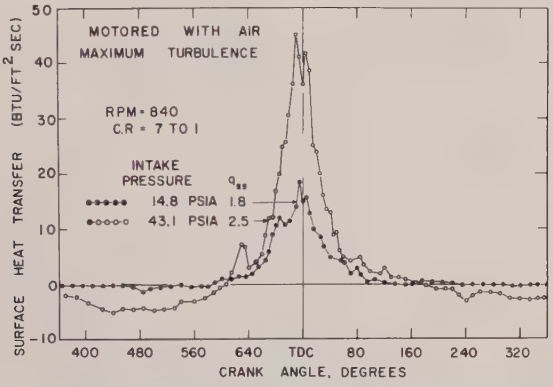

Fig. 22—Surface heat transfer at thermocouple 2 versus crank angle in an engine motored with air and variable supercharge

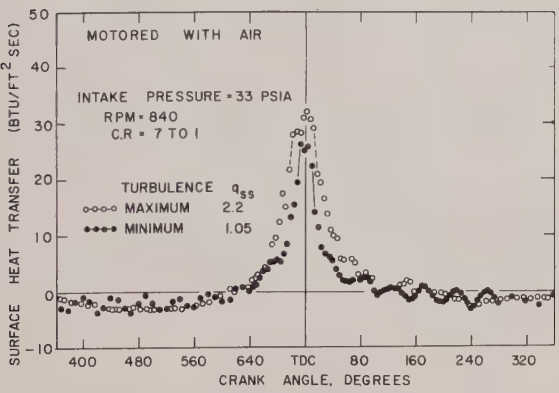

Fig. 23—Surface heat transfer at thermocouple 2 in an engine motored with air and maximum and minimum turbulence

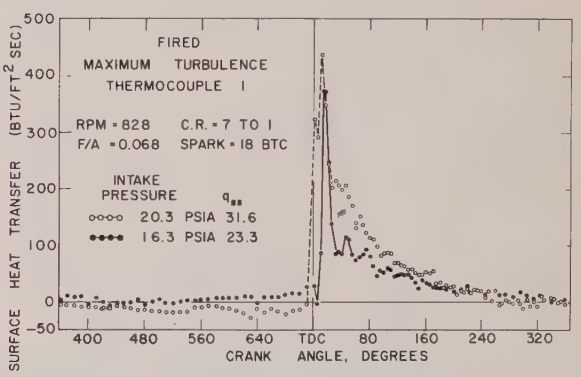

Fig. 24—Surface heat transfer at thermocouple 1 versus crank angle in a fired engine with variable supercharge

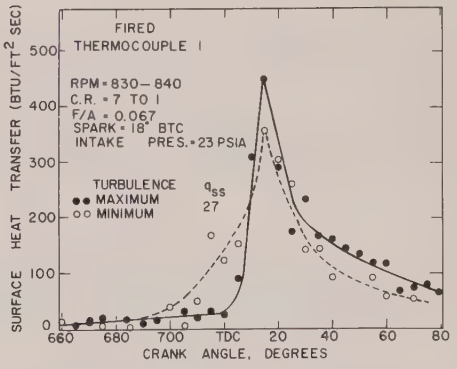

Fig. 25—Surface heat transfer at thermocouple 1 versus crank angle in a fired engine with maximum and minimum turbulence

heat flux rates increasing earlier in the cycle, but the difference is not extreme.

Fig. 21 shows that intake valve orientation has a great effect on wall temperature variation in a motored engine for a given manifold condition, and the effect is more pronounced at high pressure swings. However, the manifold pressure required to obtain high swirl velocities is much larger than any manifold pressures used in the fired engine (Fig. 6). Hence, the small effect of intake valve orientation on wall temperature swing, minimum temperature level, and heat transfer rates (Fig. 25) in the fired engine may be explained in part by the fact that initial swirl velocity variation in the fired engine is not as great as in the motored engine.

The variation of spark advance, which produced the temperature-time records shown in Fig. 19, is the parameter for difference in heat transfer rates shown in Fig. 26. Early spark results in a high rate of heat flux early in the cycle, while a late spark results in low heat flux rates late in the cycle.

The overall heat transfer is a function of the integral value of the rate of heat transfer at all points in the combustion chamber. Ref. (19) indicates that with rumble the increased rate of combustion (corresponding in some ways to an earlier spark) increases the heat transfer coefficients enough to cause a significant decrease in work output. Thus a large heat flux q and a small area may cause more transfer of available energy than a lower heat flux late in the cycle with a larger exposed area.

Fig. 27 illustrates the general shape of heat transfer variation computed with temperature-time variations obtained from thermocouple 2. The disturbing thing about Fig. 27 is that heat transfer is never negative, i.e., from the wall to the gas. This may be explained mathematically by the heat transfer equation (Eq. A-4, Appendix), which consists of a steady-state part and a fluctuating part. The steady-state heat transfer at thermocouple 2 is large, with the engine operating at maximum turbulence, and the fluctuating component never becomes sufficiently negative to result in negative heat transfer. A physical explanation of this condition is that gas swirl in the combustion chamber causes gas to pass over the hot exhaust valve and then pass in front of thermocouple 2. Two-dimensional heat transfer might also explain this observation.

Thermocouple 3 did not exhibit any unusual behavior, and it may be seen from Figs. 7-9 that the variation of heat transfer would be similar to that at the other thermocouples. Thermocouple 3 did exhibit negative heat transfer.

Heat Transfer Coefficients - Correlation of experimental data for heat transfer from a fluid to a solid under steady-state conditions is always expressed with heat transfer coefficients. These concepts have been applied to unsteady heat transfer (Appendix), but new problems arise.

The procedure used for obtaining heat transfer coefficients in an engine consists of measuring the wall surface temperature, computing surface heat transfer, computing an average gas temperature, and applying Newton's Law of Cooling. Eichelberg (10) presented data obtained from a diesel engine by use of heat transfer coefficients and obtained a relationship as follows:

$$h = 0.0564 \sqrt[3]{v_o} \sqrt{P T_g} \qquad (1)$$

where h = instantaneous heat transfer coefficient (Btu/ft^{2}hr R)

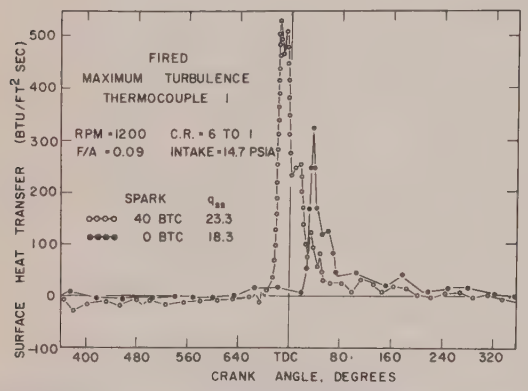

Fig. 26—Surface heat transfer at thermocouple 1 versus crank angle in a fired engine with variable spark

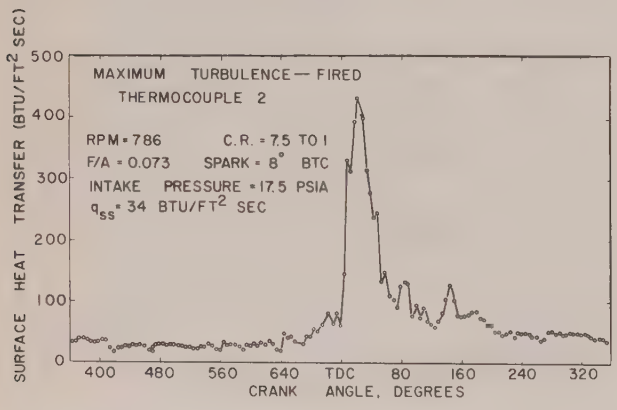
MAXIMUM TURBULENCE — FIRED
THERMOCOUPLE 2
RPM = 786 C.R. = 7.5 TO 1
F/A = 0.073 SPARK = 8° BTC
INTAKE PRESSURE = 17.5 PSIA
q_{ss} = 34 BTU/FT^2 SEC
SURFACE HEAT TRANSFER (BTU/FT^2 SEC)
CRANK ANGLE, DEGREES

Fig. 27—Surface heat transfer at thermocouple 2 versus crank angle in a fired engine

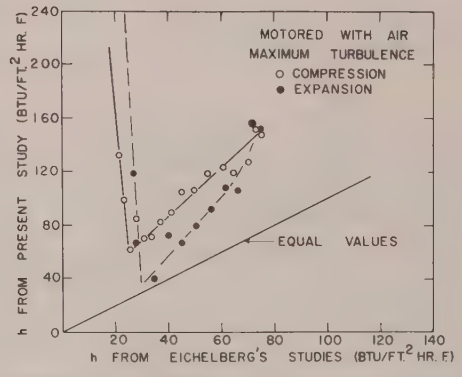

Fig. 28—Heat transfer coefficients, h, from this study versus h from Eichelberg's study for an engine motored with air

v_o = mean piston velocity (ft/sec)

P = gas pressure (psia)

T_g = gas temperature (deg Rankine)

Fig. 28 is a comparison of the heat transfer obtained with the motored engine divided by the temperature difference between a computed gas temperature and the average wall surface temperature and a heat transfer coefficient computed by Eichelberg's equation from the measured pressure and computed temperature. The experimental computation results in infinite values at some places on the compression and expansion stroke, while Eichelberg's relationship predicts finite values. It should also be noted that the numerical values are different.

Fig. 29 is a comparison of the same quantities in a fired engine on the expansion stroke. The data are scattered, but no infinite coefficients are obtained. Again the numerical values are different.

Since the concept of a heat transfer coefficient meets the most severe test when the gas temperature nearly equals the wall temperature, two plots were made showing the behavior of the surface heat transfer, the difference between gas and wall temperature, and the resulting heat transfer coefficient during this part of a motored and fired cycle. These data are presented in Figs. 30 and 31. Both figures show that the gas temperature nearly equals the wall temperature when the heat transfer is zero. However, the possibility of the conditions of zero heat transfer when the gas temperature equals the wall temperature in all required locations in Figs. 30 and 31 are very remote. The behavior of heat transfer and gas temperature - wall temperature difference was investigated and is summarized in the Appendix. The models used in the theoretical analysis are highly idealized but infinite values of heat transfer coefficients are predicted in one example.

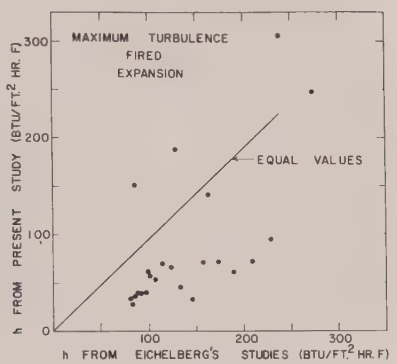

Fig. 29—Heat transfer coefficients, h, from this study versus h from Eichelberg's study for a fired engine

Correlation of Motored Data - Since heat transfer correlations could not be derived from theoretical considerations even for motored data, it was decided to use the thermal energy equation (Appendix) as a guide for determining significant correlating parameters. A number of assumptions were made (Appendix) in order to obtain a solvable relationship with the limited data obtained during a test. The end result for the case in which degradation of mechanical energy into thermal energy due to internal fluid friction is zero results in a rather simple correlation:

$$N_o^* = \text{Function of } (P^*, Pe') \quad (2)$$

The symbol N_o^* is related to the surface heat transfer by the relationship

$$N_\delta^* = L_o q_o / k_g T_o \quad (3)$$

The symbols are defined in the Appendix. Briefly, the surface heat transfer at any particular crank angle is a function of cylinder pressure at that crank angle and the engine operating condition.

The Péclet number (Pe') in Eq. 2. involves both air density in the manifold and average engine speed. Fig. 32 is a plot of the functional relationship expressed in Eq. 2 with the same Péclet number obtained by varying the engine speed and intake manifold density.

A number of plots similar to Fig. 32 were constructed with several different Péclet numbers. The linear approxi-

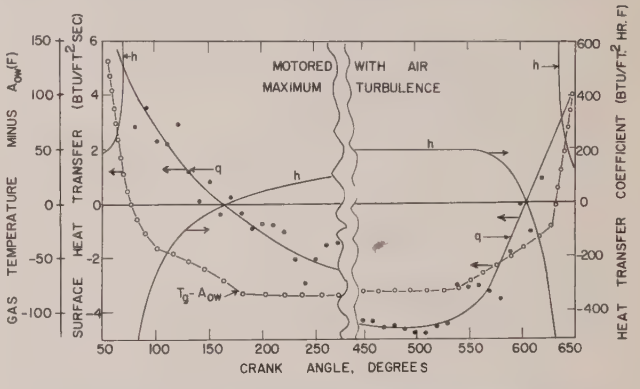

Fig. 30—Gas temperature minus average wall temperature, surface heat transfer, and heat transfer coefficients versus crank angle in an engine motored with air

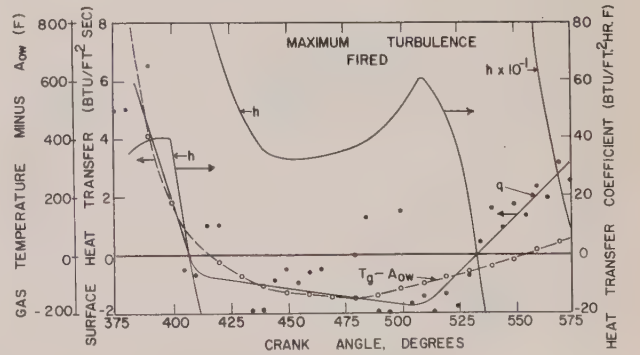

Fig. 31—Gas temperature minus average wall temperature, surface heat transfer, and heat transfer coefficients versus crank angle in a fired engine

mation used in Fig. 32 provided good agreement with the data in all cases. A summary of the motored data obtained with the engine operating at maximum turbulence is presented in Fig. 33. A general equation for the N_o^* - P^* plane may be expressed as

$$\frac{1}{3600} N_o^* = Pe' \times 10^{-4} (0.26\ P^* - 0.035) + 0.1\ P^* - 0.02 \quad (4)$$

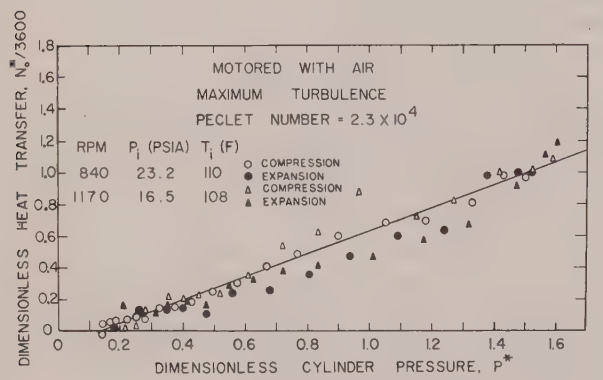

Fig. 32—Dimensionless heat transfer versus dimensionless pressure in an engine motored with air with a constant peclet number from different manifold pressures and rpm

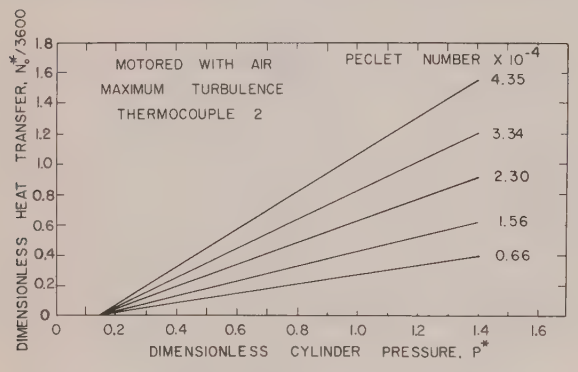

Fig. 33—Dimensionless heat transfer versus dimensionless pressure for several peclet numbers in an engine motored with air

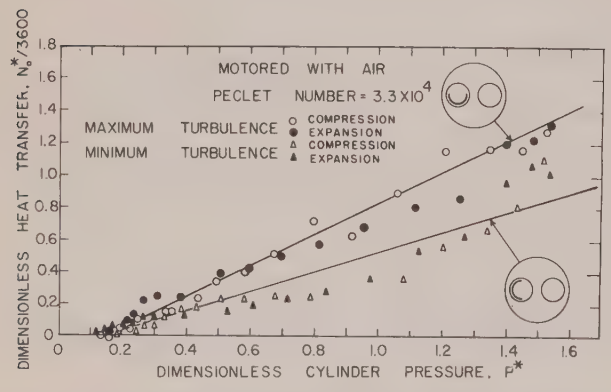

Fig. 34—Dimensionless heat transfer versus dimensionless pressure in an engine motored with air at maximum and minimum turbulence with a constant peclet number

Fig. 34 illustrates the effect of turbulence on an N_o^* - P^* plot for a particular Péclet number. This difference may be explained in part by the fact that mechanical energy degradation to thermal energy was neglected. If this term is included, velocity profiles must be known in the gas volume. This information was unavailable.

The data correlation shown in Fig. 33 was obtained from theoretical considerations and did not present difficulties experienced when attempting to use heat transfer coefficients.

Natural curiosity would demand that Eq. 4 be expressed in terms of cylinder gas temperature and density rather than cylinder pressure and checked to see if heat transfer q_o may be expressed as a heat transfer coefficient h and a gas temperature - wall temperature difference. If this operation is performed, the result states that heat transfer is a function of gas temperature rather than the difference between the gas and wall temperature. Thus it cannot be rearranged to be expressed in terms of h.

Correlation of Fired Data - It has been shown in Fig. 29 that finite heat transfer coefficients are obtained during the expansion stroke of a fired engine, but the correlation with Eichelberg's (10) equation for h was not good. Hence, the equation for N_o^* as a function of dimensionless cylinder pressure and Péclet number was tried for a fired engine. The results are shown in Fig. 35. It may be seen from Fig. 35 that the compression part of the cycle agrees quite well with a motored engine during compression, but the expension part has much higher N_o^* for a given P^* than in a motored engine. This may be attributed to the fact that chemical energy release occurs in a fired engine. Thus the amount that N_o^* is higher is undoubtedly a function of air-fuel ratio.

Since it has been seen that density and the temperature difference between the wall and gas affect heat transfer, an empirical method of correcting Fig. 35 for the expansion stroke presents itself: the density at a particular position on the expansion stroke is the same as the density at the same crank angle on the compression stroke. Thus the P^* at the same crank angle on the compression stroke would be used. The temperature effect due to chemical energy release may be accounted for by multiplying N_o^* on the expansion by a ratio of the gas temperature on the compression stroke at the same crank angle minus the average wall temperature (ΔT_{comp}) to the difference between the gas temperature and wall temperature on the expansion stroke (ΔT_{exp}). If ΔT_{comp} were zero at the same time N_o^* were zero, this correction technique might be satisfactory. However, as shown in Figs. 30 and 31, this is not generally true. Thus this correction technique is not satisfactory at small values of N_o^*. A plot of this empirical correction is shown in Fig. 36. The method outlined has not been studied in any detail to see if other deficiencies are present.

One interesting observation is characterized by the heat transfer coefficients obtained using heat transfer data from thermocouple 2 presented in Fig. 27. Variation of h with crank angle is shown in Fig. 37. When the exhaust valve

opens there is an increase in the heat transfer coefficients. These phenomena were observed to increase with pressure at the point of blow-down. Hence, it is quite probable that the increased heat transfer coefficient variation during exhaust is a function of cylinder gas passing over thermocouple 2 as it enters the exhaust port. Although the same gas temperature was used to compute h at thermocouples 1 and 3, the increasing values of h during exhaust were observed only at thermocouple 2.

CONCLUSIONS

The purpose of this section has been to measure the surface temperature variation at three locations in a CFR engine without deposits and determine the effect of operating conditions on wall temperature variation. The data were used to determine heat transfer rates through the combustion chamber wall surface, and an attempt was made to correlate heat transfer with operating parameters. Several conclusions may be made from the resulting data:

1. The temperature of the combustion chamber wall surface varies in minimum temperature level and temperature swing with operating conditions and also location in the combustion chamber. Orientation of the shrouded intake valve affects flame patterns, which in turn affects the rate of wall temperature response and the time in the cycle at which the wall temperature rise occurs.

2. The maximum heat transfer rates in unsteady heat transfer may differ by as much as a factor of 20 when compared with the steady-state values, i.e., the amount of heat actually reaching the cooling water per unit time. This clearly indicates that considerable heat is transferred from the gases to the wall during combustion and expansion and then transferred back to the gases during intake and compression. The steady-state rates vary with location in the combustion chamber, and this affects the instantaneous heat transfer during the cycle.

3. The heat transfer coefficient concept offers many problems and the correlation of Eichelberg (Eq. 1) does not agree with experimental results found in this study for either a fired or motored engine. This may be due to the fact that the data used by Eichelberg (10) were obtained in a diesel engine with thermocouples located beneath the combustion chamber surface, whereas data in this study were obtained with a surface thermocouple in a spark-ignition engine.

4. A theoretical analysis (Appendix) suggests a correlation for heat transfer in a motored engine, which gave quite good results when applied to experimental data. However, the correlating equation (Eq. 4) could not be reduced to a heat transfer coefficient equation which tends to confirm reservations concerning the use of the concept of h. Also the effect of turbulence on heat transfer could not be accounted for in a single correlation with the experimental data available. This is to be expected since the correlation did not involve turbulence as a variable.

5. A theoretical analysis including chemical reaction could not be completed because of nonlinearities and complexities of the defining equations.

6. Although Eichelberg's equation (Eq. 1) does not agree with the experimental data of this study, it is a simple expression, and it is an attempt to account for three factors important to heat transfer in an engine: turbulence, gas density, and gas temperature - wall temperature differences. The study outlined in this section does not present a more satisfactory correlation for heat transfer in a fired engine

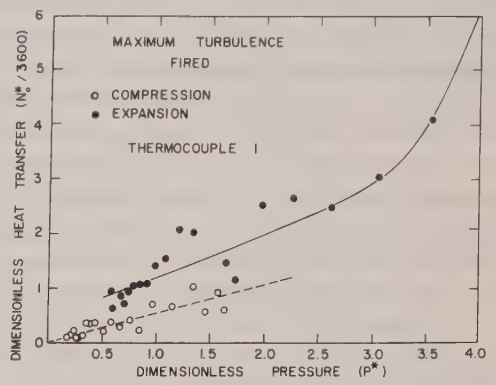

Fig. 35—Dimensionless heat transfer at thermocouple 1 versus dimensionless pressure in a fired engine

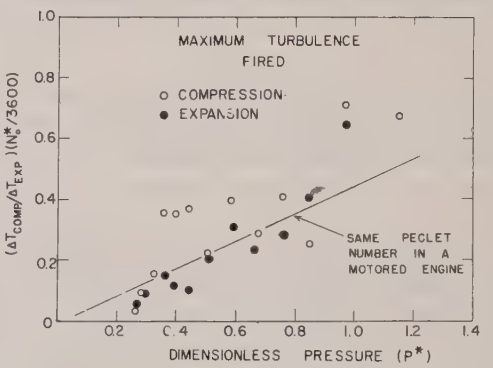

Fig. 36—Modified dimensionless heat transfer at thermocouple 1 versus dimensionless pressure in a fired engine

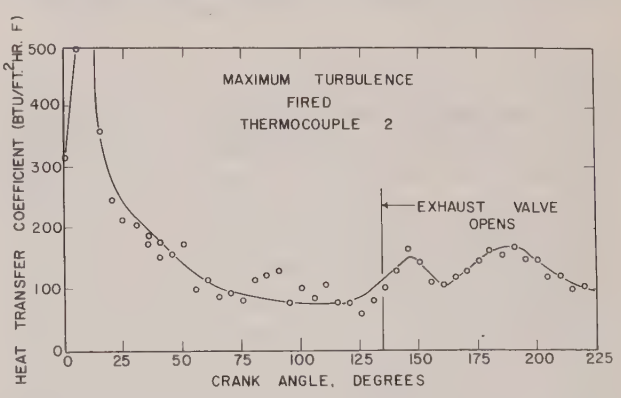

Fig. 37—Heat transfer coefficient at thermocouple 2 versus crank angle in a fired engine

and our present state of knowledge in this area must be regarded as unsatisfactory.

Section II — Test With Deposits

Combustion chamber deposits have always been a problem in spark ignition engines. As early as 1925 an article was published by Orelup (20) which summarized the state of the problem at that time. Since then considerable time and effort have gone into the investigation of deposits and numerous articles have been published on the subject. The majority of this work has centered around techniques used to evaluate the influence of the deposits formed on engine performance. These investigations employ various methods such as measurement of engine octane requirement increase (ORI) and air consumption (21), preignition counting (22), high speed combustion photography (23), and simulated deposits (21, 24). It is unfortunate that in this 35 yr period comparatively little has been learned about the physical properties of the deposits and the part they play in influencing the performance of the engine. In part this has been due to a lack of instrumentation and techniques which could be used in such studies. What little work has been carried on along these lines has produced results which are of limited utility because of the uncertainty in the relation between the measured quantities and the deposit characteristics.

The surface thermocouple presented an excellent opportunity to obtain information about combustion chamber deposits without having much influence on their normal formation and behavior. Because of the type of measurements made there is a definite relation between the data and the thermal properties of the deposits making their evaluation possible.

The work presented in this section represents the initial step in the application of the surface thermocouple to the study of combustion chamber deposits. Therefore considerably more work will be required to substantiate some of the conclusions. However, it is hoped that this presentation will suffice to stimulate interest in the techniques used and subsequently lead to a better understanding of the problem.

Instrumentation

Preliminary tests showed that it was necessary to remove the thermocouple from the engine after every run for cleaning and inspection. However, the thermocouple lead wires are delicate and it was found impractical to do this with the normal method of installation. For this reason a special thermocouple plug was designed to eliminate the installation problem without complicating the heat flow.

The plug was made of cast iron equal in thickness to the combustion chamber wall and threaded with a 1/8 in. tapered pipe thread. The plug was drilled and tapped in the center for the 2-56 thread of the thermocouple. The water jacket side of the plug has four milled holes to accommodate an installation tool. The complete assembly of the thermocouple plug unit is shown in Fig. 38, where it can be seen that the thermocouple is flush mounted in the plug. It was necessary to match each new plug to the tapped hole in the cylinder to insure a tight fit when the plug was flush with the combustion chamber surface. If this was not carefully carried out, water and/or gas could get into the threads and distort the heat transfer picture. This technique permitted easy installation and removal of the thermocouple without breakage of the lead wires or disturbance of the deposits covering the thermocouple.

Fig. 38—Thermocouple plug assembly

For these studies thermocouple 3 was not used. In addition, pressure-time data were not recorded although pressure-time oscillograms were visually observed.

Test Procedure

Since the influence of the first layers of deposit formed during the early portion of each test was so significant, a special starting technique was adopted to control the operating conditions during this period. The technique involved the following steps:

1. The engine was motored at 1000 rpm with the intake manifold heater on and no fuel flowing. This was continued until the coolant temperature and intake air temperature reached constant values.
2. The fuel pump was actuated and the ignition switch turned on with the throttle wide open. The time of the first firing was recorded as the beginning of the run.
3. Initial data were recorded as soon as the intake mixture temperature, coolant temperature, and cylinder wall temperatures reached a constant value.
4. The engine was put on the automatic cycle control.

In tests where lubricating oil consumption is a factor, this procedure may need amending. However, for the tests conducted in this work it was quite satisfactory.

After each run was completed, the thermocouple plug units were removed from the engine and the combustion chamber scrubbed with a nylon brush saturated with acetone. It was found impossible to remove all of the deposit from the

Table 2 - Comparison of Typical Deposit-Accumulation Cycles

	Cycle Used in this Study		Cycle A		Cycle B	
	Idle	WOT	Idle	WOT	Idle	WOT
Cycle Duration	120 sec	120 sec	50 sec	150 sec	50 sec	150 sec
Engine Speed	800 rpm	1000 rpm	900 rpm	900 rpm	600 rpm	900 rpm
Air-Fuel Ratio	9-10/1	13.5/1	12.6/1	13.4/1	11.5/1	13/1
Spark Timing	5 btdc	5 btdc	tdc	tdc	tdc	tdc
Compression Ratio	9/1	9/1	8/1	8/1	7/1	7/1
Jacket Temperature	Boiling		155 F	155 F	150 F	150 F
Mixture Temperature	140 F	110 F	--	120 F	--	112 F
Oil Temperature	Not controlled		160 F	160 F	160 F	160 F

combustion chamber in this way because the configuration of the chamber made some regions inaccessible from the outside. However, all the deposit was removed from the area surrounding the two thermocouple locations and as much as possible was removed from the rest of the chamber.

The fuel system was flushed with the fuel to be used in the next test and then left empty.

A comparison of the cycle employed in this work with two cycles used by other investigators is given in Table 2. Basically it consists of 2 minutes of rich idle and 2 minutes of wide-open-throttle operation (WOT). The idle speed was as low as possible without causing firing difficulties.

The mixture temperature was controlled with a 1000-watt intake manifold heater. The temperature of the WOT condition was held at 110 F. At idle this setting gave a temperature of about 140 F because of the reduced air flow. The humidity of the intake air was held constant at 27-32 grains per lb of dry air by the use of an ice tower. The lubricating oil temperature was not controlled since a synthetic lubricating oil (Plexol) was used and it was believed that it did not contribute appreciately to deposit formation.

The data were recorded at varying time intervals during the run. The intervals were short, about 15 minutes, at the beginning of the run and at times when comparatively rapid changes were observed. These intervals were lengthened to one hr when the changes were less rapid. The data were recorded during the WOT portion of the cycle. Unfortunately, it was impossible to record all the required data in the normal 2-minute period of WOT operation so this period had to be extended to approximately 5 minutes.

A run was considered complete when no significant changes with time were observed in the data. At this time the final data were recorded and the engine shut down. The thermocouple plug units were removed from the engine as soon as possible for observation.

Three complex hydrocarbon fuels were tested (Table 3). These fuels, alkylate, base, and aromatic, are primarily composed of paraffins, olefins, and aromatics, respectively. Three ml/gal of TEL was added to the base and aromatic fuels. In addition, in some tests the base and aromatic fuels contained a considerable amount of tri cresyl phosphate (0.45 theory). These fuels were blended and stored in 55 gal drums to ensure uniformity throughout the test.

Table 3 - Description of Complex Hydrocarbons

	Light Alkylate	80/20 FCC/Alkylate	80/20 Reformate/Straight Run
Reference Name	Alkylate	Base	Aromatic
Deg API Gravity	70.4	60.7	48.4
Reid Vapor Pressure	4.6 psi	7.0 psi	6.5 psi
Boiling Range			
IBP	110 F	110 F	110 F
EP	340 F	413 F	402 F
TEL Added	None	2.95 ml/gal.	3.00 ml/gal.
TCP Added	None	None & 0.45 Theory	None & 0.45 Theory

Table 4 - Description of Pure Hydrocarbons

	Family Classification	Boiling Point	°API Gravity	Vapor Pressure
Iso-octane	Paraffin	210.6 F	71.8	0.8 psi
Dio-iso-butylene	Olefin	215.0 F	65.0	1.55 psi
Benzene	Aromatic	176.2 F	28.5	1.53 psi
Toluene	Aromatic	231.1 F	30.9	0.5 psi
Xylenes	Aromatic	282.0 F	31.7	0.13 psi

Table 4 shows the characteristics of the pure hydrocarbons studied.

Results

The raw data obtained were in all cases oscillograms similar to Fig. 3. Inasmuch as the raw data are voluminous, it is impractical to present it here. Instead, selected observations and analysis of the raw data will be presented.

Two methods of approach were used in the data analysis: empirical and analytical. Both methods are described below.

Empirical Analysis - Several changes were observed in the temperature-time diagrams which could be directly attributed to the formation of deposit over the junction. A typical clean and dirty thermocouple trace are compared in Fig. 39. The significant changes are marked and are discussed in detail below:

1. Slope. At the time the flame front passes the thermocouple junction, the temperature of the gas changes abruptly from that of the unburned gas to that of the burned gas. This abrupt change in temperatures causes a correspondingly abrupt change in temperature at the gas-wall interface. The temperature rise of the clean junction is found to be extremely rapid, while that of the covered junction is much less. This shows the influence of the thermal properties of the deposit in distorting the temperature fluctuation before it reaches the thermocouple junction. The tangent of the angle which this portion of the temperature-time diagram makes with the horizontal reference line is used to describe this deposit influence and is called the "Slope".

2. Maximum-Minimum Cycle Temperatures. During each cycle, the thermocouple junction temperature passes through a maximum and minimum value. On a clean thermocouple, the maximum occurs shortly after the flame front passes the junction while the minimum occurs during the in-

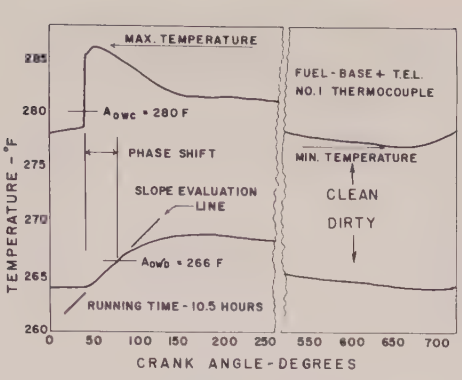

Fig. 39—Typical temperature recordings from a clean and dirty thermocouple

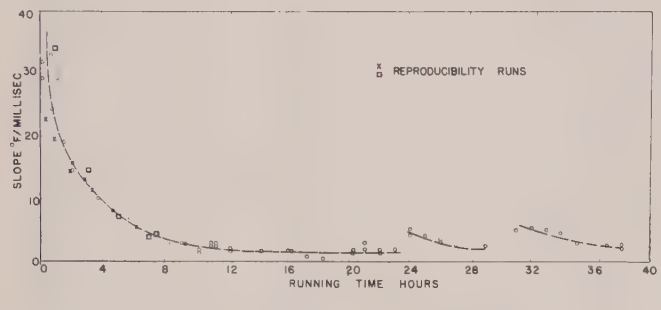

Fig. 40—Alkylate reproducibility runs

take stroke when the relatively cold fresh charge is coming in. The formation of deposit over the junction tends to reduce the absolute value of the temperature measured, because of the heat transfer through the wall, and to reduce the amplitude of the temperature variation between the maximum and minimum values.

3. Time-Averaged Temperature, A_O. This symbol is defined precisely in the Appendix. As its name indicates, it is a time-average value of the temperature over one cycle.

4. Phase Shift. The influence of the deposit on the thermocouple temperature can also be described by the displacement of the point of intersection of the temperature-time trace and the time-averaged temperature A_O. This quantity will be used in the unsteady-state analysis discussed later in this work. For lack of a better name, it is referred to as the Phase Shift.

Complex Fuels

The first tests were run with the alkylate fuel. The results of three runs are plotted in Fig. 40 using the slope as the variable. The two initial runs were made to check the reproducibility of the data. These two runs were arbitrarily discontinued after 8 hr of running. After plotting the data, it was obvious that an equilibrium condition had not been reached and a longer period of running was required. Consequently another run was made which continued for 20 hr. The engine was then shut down but the deposits were not disturbed. The next day the engine was started again and the

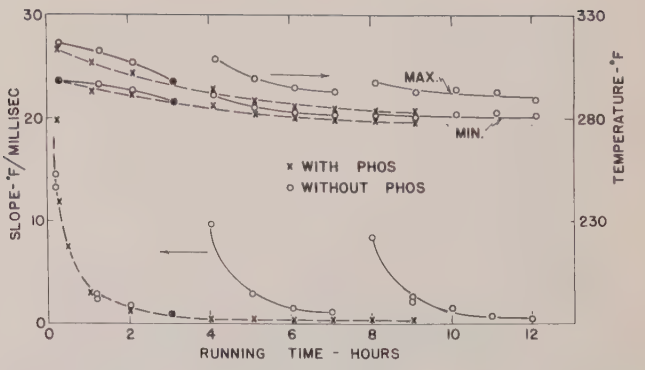

Fig. 41—Leaded base fuel with and without phosphorous added

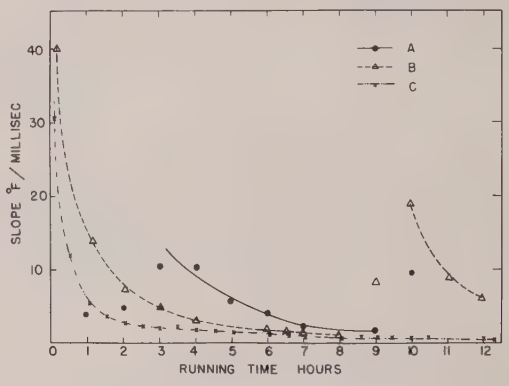

Fig. 42—Comparison of leaded base fuel runs using data from thermocouple 1

test continued. As can be seen, the early data were repeatable. While the discontinuities which occurred came only after the engine had been stopped and allowed to cool down, it is not clear whether the discontinuities were a result of shutting the engine down or of the increased running time.

The second series of tests were conducted with the leaded base fuel with and without tri cresyl phosphate. Fig. 41 is a plot of the slope and maximum-minimum cycle temperatures recorded with thermocouple 2. When the base fuel without tri cresyl phosphate was used, several discontinuities appeared in the data at regular intervals during the run. Both the slope and maximum-minimum cycle temperatures indicated that something was happening either to the thickness or the character of the deposits. When the leaded base fuel with tri cresyl phosphate was run, the data for the early part of the run was identical with that for the base without tri cresyl phosphate but no discontinuities were observed and the deposit appeared to have reached equilibrium in 4 hr. However, observation was continued for 5 additional hr and still no change was detected.

Further runs with the tri cresyl phosphate added to the leaded base fuel showed no discontinuities. Additional runs without the tri cresyl phosphate added are shown plotted, with slope as the variable, in Figs. 42 and 43, for thermocouple 1 and 2 respectively. It is apparent that the discontinuities were always observed, although the frequency varied from

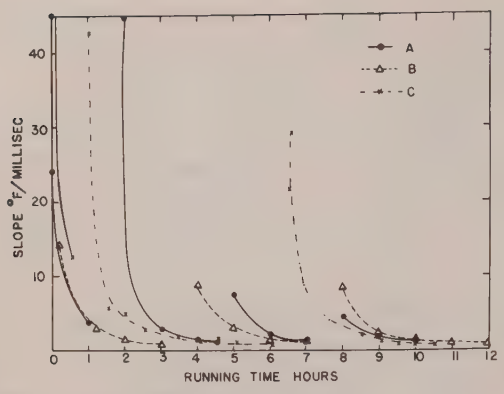

Fig. 43—Comparison of leaded base fuel runs using data from thermocouple 2

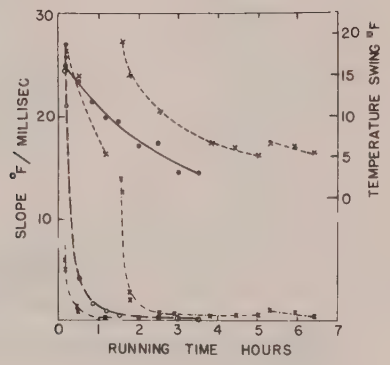

Fig. 44—Leaded aromatic fuel with and without phosphorous added

run to run. There was, however, a rough relation between the frequency at the two thermocouple locations: the frequency at the number two location was approximately twice that of the number one location for each run.

A third series of runs were made with the aromatic fuel with and without tri cresyl phosphate. In general, the same comparative results were found. Its addition to the fuel eliminated the discontinuities from the data (Fig. 44). The one big difference is the appearance of the discontinuities at irregular intervals.

An additional observation was that both fuels, when run without the tcp added, exhibited a considerable amount of knock during the WOT portion of the cycle. The intensity of the knock was associated with the discontinuities in the data. At the beginning of a run or immediately after a discontinuity appeared the intensity and frequency of the knock was low, but they would increase until the appearance of another discontinuity.

One obvious explanation for the cause of the discontinuities would be that the deposits break away from the thermocouple. It would follow that the effect of tri cresyl phosphate was to prevent breaking off of the deposits.

Another explanation for the influence of the tri cresyl phosphate in these tests is the effect it has on the ignition temperature of the deposit formed. Table 5, taken from Ref. (25), shows the results of studies of the influence of various lead compounds on the ignition temperature of carbon. The

Table 5 - Ignition Temperature of Lead Compound-Carbon Mixtures

(Lead compound concentration 0.2 mole % based on Pb)

Lead Compound Added to Carbon	Concentration Wt. %	Ignition Temp., F.
(None	--	1030
Acetate	5.95	510
Iodide	7.14	570
Basic chloride	4.15	605
Basic bromide	4.82	650
Peroxide	3.82	660
Bromide	5.76	685
Monoxide	3.58	695
Chloride	4.42	715
Fluoride	3.96	725
Carbonate	4.26	730
Basic carbonate	4.18	740
Basic sulfate	4.19	765
Borate	4.93	795
Formate	4.73	800
Nitrate	5.23	820
Arsenate	5.46	895
Sulfide	3.83	935
Chromate	5.10	960
Sulfate	4.80	960
Pyrophosphate	4.81	1030
Orthophosphate	4.31	1030

lead compounds normally found in combustion chamber deposits, lead chloride, lead bromide, and basic lead sulfate, all reduce the ignition temperature of carbon significantly. The compound formed by the addition of tri cresyl phosphate, i.e., lead ortho-phosphate, has no influence on the ignition temperature of carbon. The discontinuities could, therefore, be attributed either to the burning away of the outer layers of deposit or to the burning away of the carbon in these layers thus increasing the thermal conductivity of the deposits. Combustion of the deposit could take place when lead compounds which lower the ignition temperature are present.

Both of these explanations can account for the severe knock encountered. In the first case the pieces of deposit could be large enough to remain in the chamber and serve as sources of ignition and in the second the burning deposits on the wall would serve the same purpose.

Fig. 45 presents a comparison of the effect of these three complex fuels on the slope. This comparison shows that the aromatic deposit affects the thermocouple readings more in the same period of operation than the olefin deposits. Both

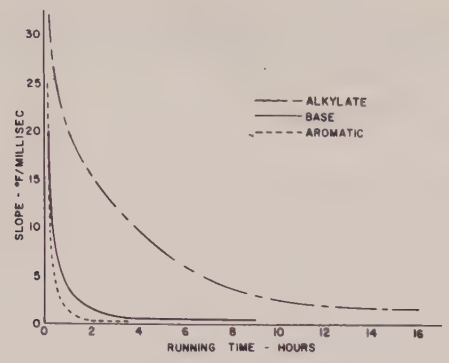

Fig. 45—Comparison between complex fuels

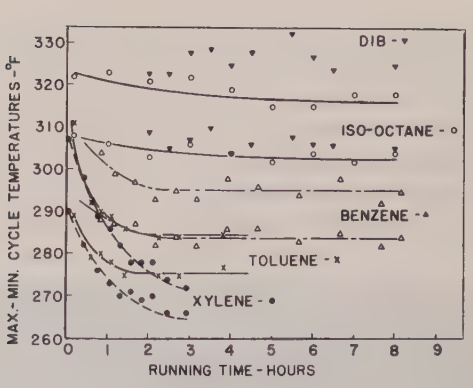

Fig. 48—Pure fuel temperature comparison at thermocouple 2

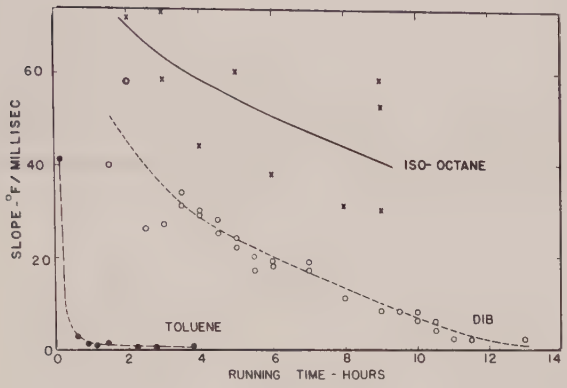

Fig. 46—Comparison between pure fuels

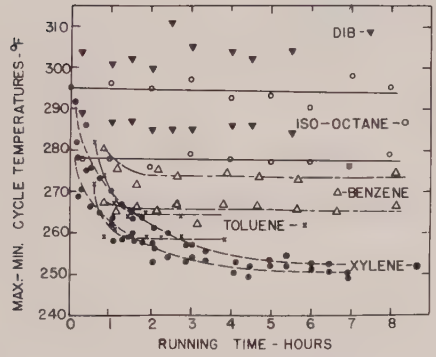

Fig. 47—Pure fuel temperature comparison at thermocouple 1

of these have a much greater effect than the paraffin deposits.

In the figures previously shown deposit equilibrium was reached, from a heat transfer standpoint at least, in times that are short in comparison with equilibrium from ORI standpoint (21). This may result from the fact that ORI represents an integrated effect over the entire cylinder while the data shown here are for one point in the cylinder. It is also interesting to note that deposit-induced ignition seems to reach equilibrium in times comparable with those shown in this paper (22). It is also possible that the equilibrium values in this paper are not truly equilibrium values, but merely conditions where the rate-of-change is imperceptible (see later discussion on limitations).

Pure Fuels

The pure fuel studies were conducted with two different objectives in mind;

1. The general effect of the hydrocarbon structure.
2. The effect of boiling-point variation with the same basic structure.

The results for the three different fuel structures are shown in Fig. 46 with the toluene being considered representative of all the aromatic investigated. The results are identical with those found with the complex fuels; the effect of the toluene deposits is the largest with the olefin and paraffin deposits following in decreasing order. The reason for the large amount of scatter above a slope of 25 F/millisecond is the reading accuracy. Since this is a measurement of the tangent of an angle, the reading accuracy becomes quite critical for angles greater than 80 deg. Visual comparisons and angle measurement show that the variation for the iso-octane was within +/- 1 deg for consecutive data points. However, this represents a slope variation of 15-20 F/millisecond.

The maximum-minimum cycle temperatures are used to compare fuel structure data in Figs. 47 and 48. Here it is found that the olefin fuel, DIB, does not have an effect intermediate between the paraffin and the aromatic but rather has less effect than either of the others at both thermocouple locations. A typical temperature-time record for DIB is shown in Fig. 49 where it can be seen that the temperature shows its usual abrupt rise, but then it rises rather slowly to its maximum value (compare with Fig. 3). It should be noted from Figs. 47 and 48 that although the numerical values are different between the two thermocouples, the same trends are shown.

Figs. 47 and 48 also present data on maximum-minimum temperatures for the three different boiling-point aromatics studied. The data show that the higher the boiling point the lower the maximum-minimum cycle temperatures. When corresponding data are plotted with the slope as the variable,

Figs. 50 and 51, the same conclusion is reached, i.e., the higher the boiling point the greater the influence. The only significant difference here is that for three aromatics the slope appears to have reached a terminal value which is roughly equivalent at both of the thermocouples. This indicates a limiting deposit formation of constant thickness and thermal properties has been reached. As will be shown later, this would seem to indicate a limiting value of $s/\sqrt{\alpha}$ (see later discussion on limitations).

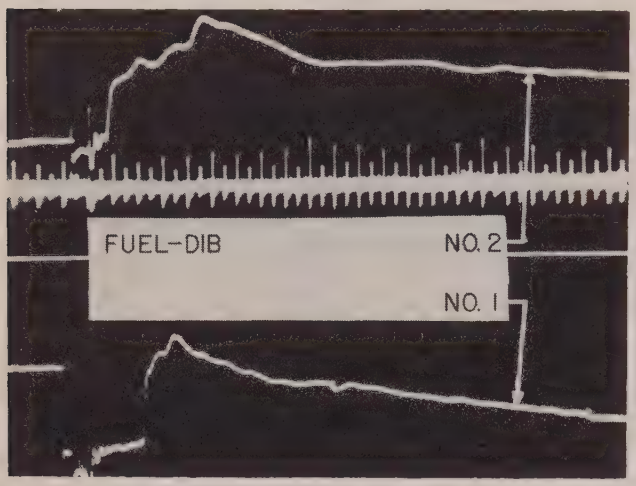

Fig. 49—Typical oscillogram for DIB

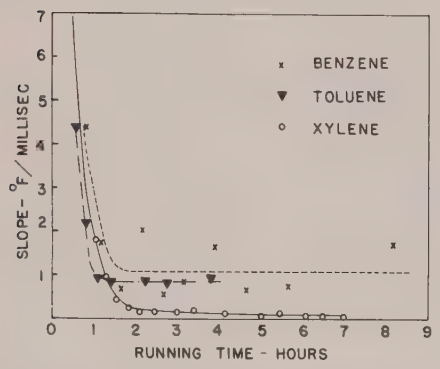

Fig. 50—Comparison of three pure aromatics at thermocouple 1

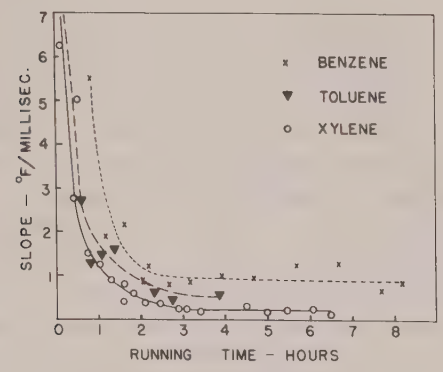

Fig. 51—Comparison of three pure aromatics at thermocouple 2

Mixtures of Pure Fuels

Weiss (26) has studied the effect of mixtures of pure fuels on the empirical parameters of slope and maximum-minimum temperatures. Two different types of mixtures were considered: (1) a mixture of two "dirty" fuels and (2) a mixture of a "dirty" and "clean" fuel.

Figs. 52 and 53, which were taken from Ref. (26), consider toluene and xylene as representative of the "dirty" fuels. Probably the most important implication of the data is that a mixture of two "dirty" fuels does not produce a "clean" fuel.

Figs. 54 and 55, again from Ref. (26), consider xylene as the "dirty" fuel and iso-octane as the "clean" fuel. It is apparent in these figures that a small amount of a "dirty" fuel has a deleterious effect when mixed with a "clean" fuel.

Theoretical Analysis - The basic heat transfer problem involved here is that of heat flow through a composite ma-

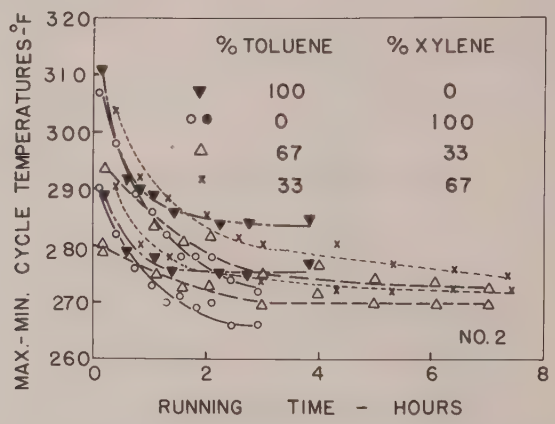

Fig. 52—Temperature comparison of toluene-xylene mixtures

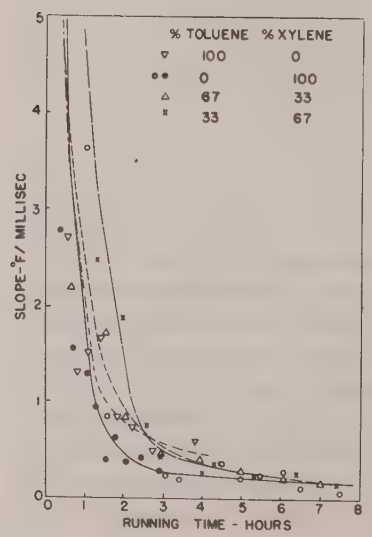

Fig. 53—Slope comparison of toluene-xylene mixtures

terial. By making some simplifying assumptions, it becomes possible to analyze the problem from both the steady-state and unsteady-state point of view. The following is a description of the analysis and the results which were obtained by applying it to the observed data.

Steady-State - The problem is shown in diagramatic form in Fig. 56. The same net heat flow must pass through both the deposits and the wall. The temperature on each side of the combustion chamber wall are measured and the thermal properties of the wall are known. By making a few simplifying assumptions, the net heat flow from combustion gases to the cooling water can be computed. These assumptions are:

1. The heat flow is one dimensional and perpendicular to the wall.

2. The wall is homogeneous and has constant thermal properties throughout.

3. The thermal conductivity of the wall is independent of temperature. This leads directly to the expression for the net heat flow (see Appendix for definition of symbols not defined here):

$$q_{ss} = \frac{(A_{ow} - A_{oj})\, k_w}{a} \qquad (5)$$

where q_{ss} = steady-state heat flow Btu/hr-ft^2

These values can be readily determined from the data so that the net heat flow can be computed and plotted as a function of running time. This information is presented in Figs. 57 and 58 as computed from data observed at thermocouples 1 and 2, respectively. The initial values at zero running time correspond quite well for all the fuels tested. The influence on the heat transfer follows the trend as deduced from the earlier discussions. The deposit formed by the paraffin fuel has little influence on the net heat flow while the aromatic deposits have considered effect, actually reducing the heat flow at this point in the cylinder by some

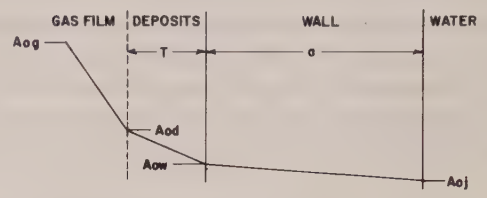

Fig. 56—Diagram of steady-state heat transfer problem

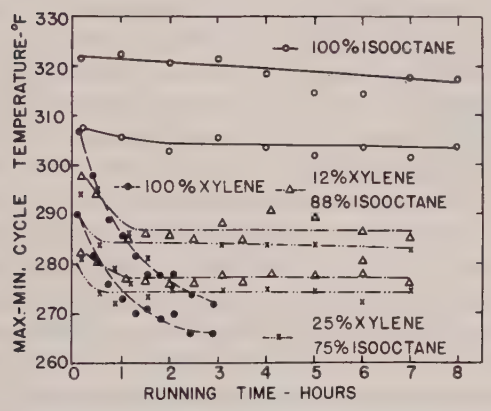

Fig. 54—Temperature comparison of iso-octane-xylene mixtures

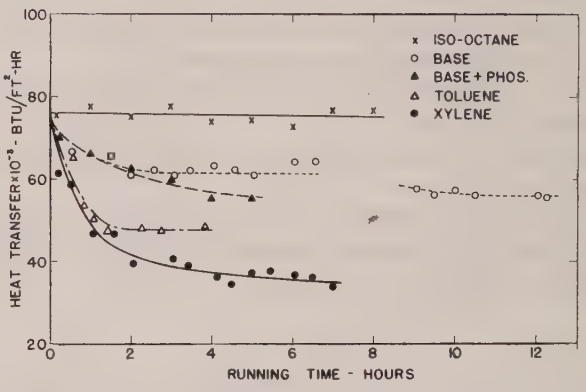

Fig. 57—Steady-state heat transfer at thermocouple 1

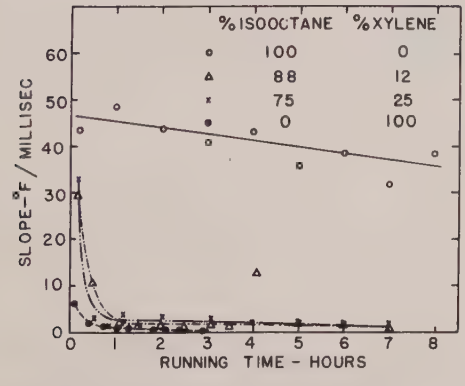

Fig. 55—Slope comparison of iso-octane-xylene mixtures

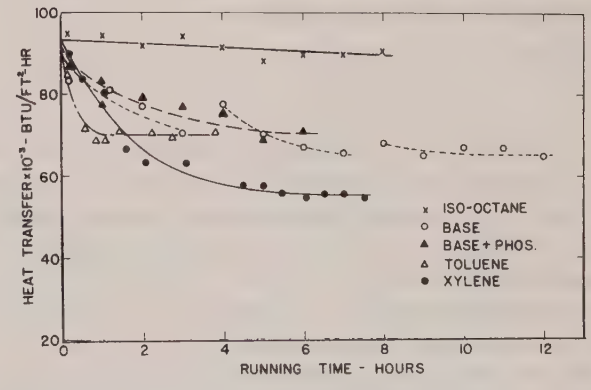

Fig. 58—Steady-state heat transfer at thermocouple 2

40-50%. The olefin deposits again have an intermediate effect. It is quite obvious that the initial deposit formed over the surface causes the most significant reduction in net heat transfer.

Fig. 59 presents data from Ref. (27) where the heat transfer to the cooling water was measured under deposit-forming conditions using a heat collector, i.e., a water-cooled probe extended into the combustion chamber. The trend shown is similar to that in Figs. 57 and 58. However, Fig. 60 presents data from Ref. (21), again taken under deposit-forming conditions. In this case, the heat transfer was determined by a heat balance on the engine cooling water and represents the integrated effect over the entire cylinder. The trends are obviously different. The two trends are not inconsistent if deposits were formed initially over the thermocouple (or probe) and later spread to the rest of the combustion chamber. In this connection, it should be noted that the thermocouples were deliberately located in what are probably cooler locations in an attempt to satisfy the condition of one-dimensional heat transfer and that the heat collector probably is at low temperature because of its design.

More information may be obtained by making the following additional assumptions:

4. Time-averaged gas temperature remains constant with and without deposit.

5. Time-averaged thermal resistance of the gas film (h_o) remains constant with and without deposit.

6. The deposit is homogeneous and has constant thermal properties throughout.

7. The thermal conductivity of the deposit is independent of the temperature.

8. There is no constant resistance between the deposit and the wall. The general expression for the net heat flow through the wall can now be written as:

$$q_{ss} = \frac{A_{og} - A_{oj}}{\frac{s}{k_d} + \frac{a}{k_w} + \frac{1}{h_o}} \qquad (6)$$

Without deposits, the thermal resistance of the deposit, s/k_d, is zero and the equation reduces to:

$$q_{ss} = \frac{A_{og} - A_{oj}}{\frac{a}{k_w} + \frac{1}{h_o}} \qquad (7)$$

At this point, it is necessary to assume either a value of A_{og} or h_o. A value was assumed for A_{og} for three reasons:

1. The results were found to be relatively insensitive to changes in this value.

2. If the same value is used throughout, all the results can be compared on a relative basis.

3. Estimations of A_{og} were available in the literature.

Eq. (7) was then rearranged and the value of h_o computed. For the value of A_{og} used, 1200 F, the value of the film coefficient was reasonable (around 100 Btu/ft^2-hr-F) and compared favorably with the mean value determined in the clean engine work (16).

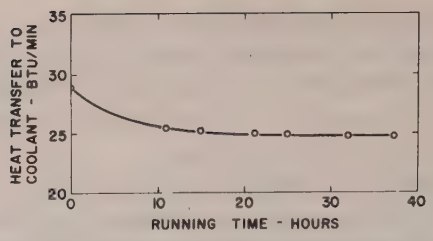

Fig. 59—Steady-state heat transfer measured with the heat collector

Since the net heat flow can be computed at any time during the run from Eq. 5 and q_{ss} is thus known, Eq. 6 now can be rearranged and solved for the deposit resistance. Once these values are known, the time-averaged deposit surface temperature, A_{od}, can be computed by applying the simple heat transfer equation to the deposit:

$$q_{ss} = \frac{k_d}{s}(A_{od} - A_{ow}) \qquad (8)$$

The time-averaged deposit surface temperatures were computed in this way for the three pure aromatic fuels with the results as shown in Fig. 61. These curves seem to indicate a limiting surface temperature value which is different for each fuel. When studying Figs. 50 and 51, there were indications that the equilibrium value of $s/\sqrt{\alpha}$ was different for the three aromatic fuels. As will be shown later, the data of Fig. 61 would indicate that the equilibrium values, of s/k_d were different for the aromatic fuels.

Further examination of this analysis shows that for the assumptions made all the computations are based on two measured values, i.e., the mean temperature of the deposit-wall interface, A_{ow}, and the mean temperature of the wall on the water-jacket side, A_{oj}. Since the temperature on the water-jacket side of the wall was found to be essentially constant the only variable is A_{ow}. This means that a considerable amount of information can be obtained from an examination of trends shown in the maximum-minimum cycle temperature plots.

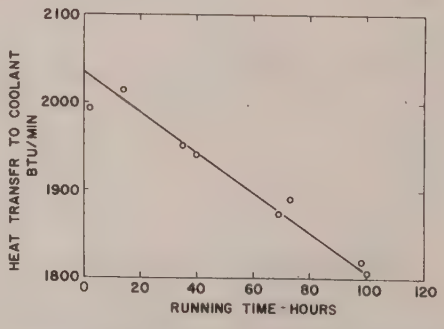

Fig. 60—Steady-state heat transfer from cooling water energy balance

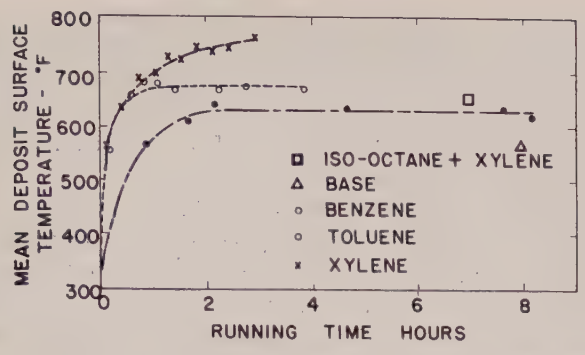

Fig. 61—Calculated mean deposit surface temperatures

Unsteady State - The unsteady-state conditions can be idealized as shown in Fig. 62. As is shown in the Appendix, an expression is derived in the Appendix for the temperature variation on the deposit surface in terms of the deposit properties and the measured temperature variation at the deposit-wall interface with the aid of some simplifying assumptions. There are three unknowns involved in Eq. A-5, k_d, ρc and s. It is therefore necessary to evaluate these quantities before the computations can be made.

At the end of each test, the engine was shut down immediately after the last data were recorded and as soon as temperatures would allow, the thermocouple plug was removed. The plug was first examined visually and then a high magnification microscope was used to determine the mean thickness of the deposit by focusing first on the plug surface and then on the deposit surface and determining the travel of the microscope barrel. Typical deposit thicknesses measured at the two locations are given in Table 6. Using the steady-state theory, it is possible to calculate the thermal conductivity, k_d, once the thickness s is known.

This leaves only the heat capacity, ρc, of the deposit unknown. At present, no experimental means of determining this value is known. The solution was therefore carried out by varying the value of the heat capacity, ρc, and examining the temperature-time curves which resulted.

Two criteria were used to determine when a reasonable solution was obtained. These were:

1. The computed temperature-time curve must pass through its mean temperature at the same crank angle that the clean curve passed through its mean temperature.

2. The rate of temperature rise on the surface of the deposit must be equal to or slightly greater than that on the clean surface.

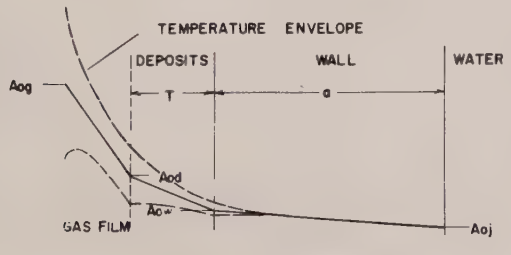

Fig. 62—Diagram of unsteady-state heat transfer problem

The first criterion is based on the phase shift previously defined in Fig. 39. If it is assumed that the accumulation of deposit in the cylinder has little effect on the flame front or flame speed, this simply says that the deposit caused a phase shift in the temperature-time curve, the magnitude of which could be determined from a comparison of the point of intersection of the time-averaged temperatures of the clean and dirty thermocouple with the respective clean and dirty temperature-time curves. For the same reasons, the rate of temperature rise on the deposit surface would be expected to be similar to but greater than that on the clean surface because of the difference in thermal properties of the wall and the deposit. For example, if the deposit had a very low thermal conductivity and heat capacity relative to that of the wall it would be expected that the temperature of the deposit surface would more closely follow the temperature of the gas. In the limit, if the thermal conductivity and heat capacity of the deposit were zero, the deposit surface temperature would be expected to follow the gas temperature exactly.

Table 6 - Typical Deposit Thickness Values

Number One Location (In.)	Number Two Location (In.)
0.0031	0.0034
0.0054	0.0066
0.0025	0.0050
0.0032	0.0051
0.0030	0.0027
0.0005	0.0020
0.0034	0.0028
0.0018	0.0017
0.0017	0.0030
0.0016	0.0029

Fig. 63 shows the results of one of these calculations using data from the base fuel without tri cresyl phosphate added. Comparison is made between the experimental temperature-time curve for the clean and the dirty conditions and the computed curve for the deposit surface corresponding to the dirty condition. The heat capacity, ρc, was assigned as initial value of unity, which was at first considered low, but which was to be increased until the two criteria were satisfied. When the measured thickness and the value of the thermal conductivity, computed from the steady-state values, were used with this value of unity both criteria were satisfied. To be sure that this was the most reasonable solution, the value of the heat capacity was increased; however, all other values led to oscillations in the computed temperature-time curves which seemed too large to be reasonable.

Earlier in the development of the unsteady-state theory an assumed temperature-time curve was theoretically imposed on the surface of an assumed deposit and the temperature-time curves at the deposit-wall interface were computed for various deposit properties and thickness. It was found that these computed curves were very similar to the curves experimentally determined with the thermocouple. One of these computed curves was then used as if it had been determined experimentally to investigate the effects of using different values of the deposit properties and thickness in the computations. Fig. 64 shows the results of these later calculations. As can be seen, when the value of the heat capacity, ρc, was made large, the solution contained large temperature oscillations. For this reason, whenever unreasonably large oscillations were found in the computed temperature-time curves it was concluded that the value of the variable being studied was larger than reasonable. It should be clear from a study of Fig. 3 that oscillations can be expected at the gas-deposit interface and thus considerable judgment is involved in the decision as to when the oscillations are unreasonably large.

In order to examine the effect of different deposit characteristics on the deposit surface temperatures, a second set of calculations was made using data obtained from an unleaded fuel. The results of these computations are shown in Fig. 65. Unfortunately, the first criterion could not be satisfied in this set of calculations for two reasons:

1. There was a great deal of variation in the time that the flame front reached the thermocouple.

2. The point at which the mean temperature intersected the computed temperature-time curve occurred very early in the cycle.

The reason for the variation in time of arrival of the flame front at the thermocouple could be either poor ignition or variation in the flame speed. No effort was made to determine what caused the irreproducibility since these computations were carried out some time after the actual run was made. However, the results did satisfy the second requirement and, as would be expected, the lower thermal conductivity of this deposit caused a much higher deposit surface temperature. Here again an increase in the heat capacity, ρc, above unity caused large temperature oscillations and the value unity was considered correct. The lower value of the thermal conductivity, k_d, for the unleaded fuel seems reasonable although the same value of ρc between the leaded and unleaded fuel does not.

The fact that the first criterion could not be satisfied was not too discouraging. Applying phase shift to any complex wave is difficult. Although the application of this type of thinking to a single wave is fairly straight forward, the combination of several waves to form a complex wave does not allow for a simple addition of the phase shifts.

Table 7 compares values of thermal conductivities of deposits formed by leaded and unleaded fuels given in Ref. (28) with those used in these computations. Obviously there is a marked difference. Unfortunately there was no explanations of how the values in Ref. (28) were obtained. This is a very significant factor and the fact that the values obtained in this work were determined with the deposit in place in an operating engine should not be overlooked.

The instantaneous heat transfer at the solid-gas interface was computed for a clean and dirty run made with leaded base fuel. Eq. A-4 of the Appendix was used for the clean wall calculations and Eq. A-6 for those with deposit. The results are compared in Fig. 66, where the instantaneous heat transfer is plotted as a function of crank angle.

The accumulation of deposit is shown to have reduced the steady-state heat flow by 13% while it decreased the peak instantaneous value by 72%. Since the heat transfer is always positive, the flow is always in one direction: from gas to solid. This is not what would be expected since the solid temperature is at least 200 F hotter than the fresh charge entering the engine. However, this condition was also found in the clean engine investigations, (Fig. 27), and probably indicates that the charge has been heated appreciably before reaching this location in the cylinder.

One significant feature of these curves is that they are quite similar except for the region near tdc. One would expect that the heat transferred in and out would be quite different since the thermal properties are significantly different

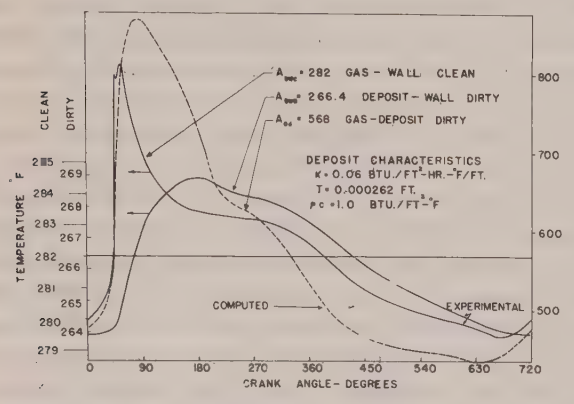

Fig. 63—Computed deposited surface temperatures for a leaded fuel

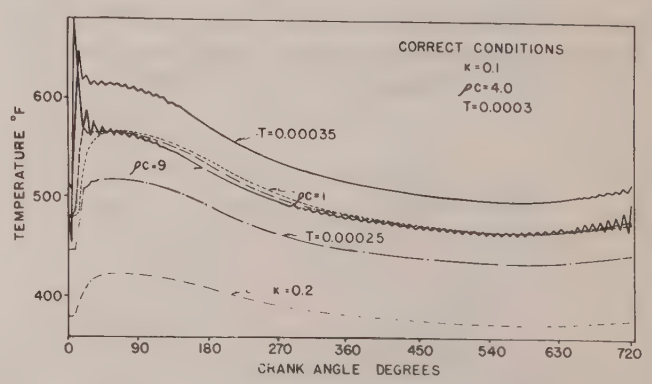

Fig. 64—Influence of varying thermal properties on computed temperature curves

for the two surfaces. This leads one to wonder what is required of the deposit for it to have a significant influence on engine operation. One obvious requirement is the ability to absorb and reject large quantities of heat. This requires relatively high values of thermal conductivity and heat capacity as well as a sufficient temperature difference between the gases and the deposit surface to cause heat to be transferred. If the conductivity is low the heat capacity is not important since large quantities of heat can not penetrate into the material anyway. However, if the conductivity is high, a high heat capacity is also necessary to be able to store up the heat which will later be released to the cool fresh charge.

The wall also has a high heat capacity and thermal conductivity. Therefore, the heat will not remain in the deposit but will leak out the other side to the cooling water via the wall. In order to reduce this leakage it appears that a thermal insulating barrier must exist either between the deposit and the wall or in the deposit next to the wall. There are two possible ways this could occur:

1. The contact resistance between the wall and deposit could contribute materially as a thermal insulator.

2. It has been shown (29) that the composition of the deposit changes with thickness and time, in such a way that the amount of carbon present is substantially reduced in the latter layers to form, while the amount of lead present increases. Because the carbon has a relatively low thermal conductivity as compared with the lead the required type of composite thermal properties would result.

It should be noted then that a nonleaded fuel would probably find it difficult, but not impossible, to form the required type of deposit, i.e., a deposit with nonuniform properties, while a leaded fuel whose deposits had the ability to "burn out" the carbon in the layer next to the gases and leave predominantly lead compounds of high heat capacity in this layer would readily form deposits harmful from the heat transfer standpoint. Thus one might logically conclude that the discontinuities found in the leaded fuel data (Figs. 41 and 44) were the result of the "burning out" of the carbon.

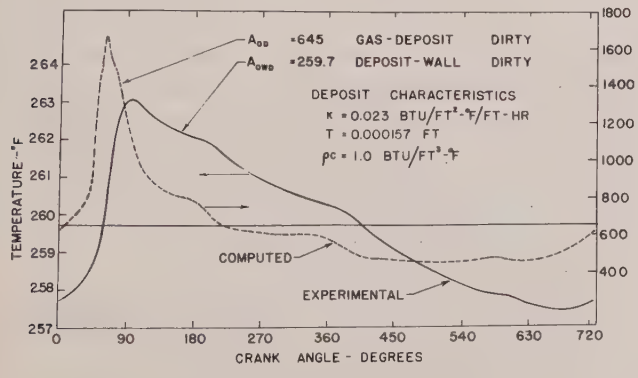

Fig. 65—Computed deposit surface temperatures for an unleaded fuel

Limitations

The surface thermocouple is basically a temperature measuring device and, therefore, it is influenced by the deposit properties which alter the heat flow ro and from the junction. Both steady-state and unsteady-state quantities are present and both contribute to the temperature measured with the thermocouple. However, each is influenced by a different grouping of the deposit properties. The steady-state or time average temperature at the wall surface is influenced by the total thermal resistance of the deposit which is equivalent to the ratio of the deposit thickness to its thermal conductivity, i.e., s/k_d. The unsteady-state temperature is dependent on the deposit properties which govern the penetration of surface temperature variations into the material. These properties appear as the ratio of deposit thickness to the square root of the thermal diffusivity, i.e., $s/\sqrt{\alpha} = s\sqrt{\frac{\rho c}{k_d}}$. Unfortunately, both of these groups have the greatest influence on the measured temperatures when they are comparatively small. As they become progressively larger the sensitivity of the measured values to changes in either ratio becomes much smaller. As the deposits build up over the junction a condition can be ultimately reached where it becomes impossible to distinguish between significantly different types of deposit. This dictates that all comparisons should be made while the measured values are representative of a given set of deposit properties. This can only be

Table 7 - Comparison of Thermal Conductivities of Deposit of Leaded and Unleaded Fuels

k = Btu/Hr-ft^2 - F/ft

	Mikita	Present Work
Leaded Fuel	0.217	0.06
Unleaded Fuel	0.138	0.023

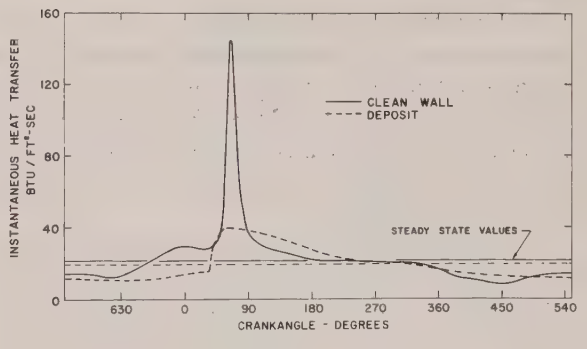

Fig. 66—Computed instantaneous heat transfer at gas-solid interface

accomplished at low values of the ratios, which occur early in the runs when the deposit thickness, s, is comparatively small.

In general the trends which are predicted from the theory are shown to exist in the data. All measured values change significantly early in the runs and then are found to level off. If deposit continues to build up, a change will occur in the temperature, but it may be too small to be perceptible in the recorded data.

Conclusions

The purpose of this section has been to measure deposit-wall interface temperature variations at two locations in a CFR engine with deposits. The data obtained were used in two ways:

1. An emiprical analysis using the slope and maximum-minimum cycle temperatures to compare the deposits formed by various types of fuels.
2. An analytical analysis to determine the thermal properties of the deposits, the gas-deposit interface temperature variations, and the instantaneous heat transfer at the deposit surface.

Several conclusions may be made from the results of this section:

1. The surface thermocouple provides a simple and effective method with which the influence of deposits on heat transfer can be determined at particular locations in the cylinder in relatively short times.
2. The thermal characteristics of the deposits and their resulting effect on heat transfer is significantly influenced by the chemical structure and boiling point of the fuel as well as the additives which are used.
3. A small amount of a "dirty" fuel blended with a "clean" fuel is sufficient to cause the mixture to produce deposits which are similar to those produced by the "dirty" fuel alone.
4. The thermocouple data, coupled with the deposit thickness measurements, make possible the calculation of the thermal conductivity of the deposit and the time-average temperature of the deposit-gas interface. This is significant since it is done without disturbing the deposit or imposing any unrealistic conditions on the overall heat transfer picture.
5. The theoretical analysis suggests a means of computing the heat capacity of the deposit and the deposit-gas interface temperature-time history from the thermocouple data. However, the results of this work indicates that a re-evaluation of the assumptions is in order. Some consideration should also be given to the accuracy of the computational techniques employed.
6. It appears that greater harm due to deposits, i.e., decreased volumetric efficiency and high gas temperatures during compression, would occur primarily in connection with nonhomogeneous deposits. This is in direct contrast with the assumption made in the present analysis, as this subject requires further investigation.

Acknowledgment

The work presented in this paper covers a span of 10 yrs. Thus the authors, V. D. Overbye, J. E. Bennethum, O. A. Uyehara and P. S. Myers, represent those individuals who were present at this, a reportable stage, of the project. Thomas Schmidt, T. J. Schweitzer, Loren Pless, Rodney Abramson, and Melvin Weiss all contributed materially to the project. In addition, grateful acknowledgment is due General Motors Corp. Research Laboratories and Ethyl Corp. for support over the 10 yr period via unrestricted scholarship grants. The Pure Oil Co. and Standard Oil Co. (Indiana) contributed equipment and supplies. The Wisconsin Alumni Research Foundation and College of Engineering supported the project in many ways. The University of Wisconsin Numerical Analysis Laboratory aided in data reduction. Prof. H. W. March aided in the mathematical analysis.

Appendix

Consider a small control volume fixed in space and located either in the wall of the cylinder, in the deposits, or in the gases within the combustion chamber. Ref. (30) shows that the energy variation within this volume is given by

$$\frac{\partial}{\partial t}\rho cT = -(\nabla \cdot \rho cT\vec{v}) - (\nabla \cdot \vec{q}) - (\tau : \nabla \vec{v}) + \left(\frac{\partial \ln 1/\rho}{\partial \ln T}\right)_p \frac{Dp}{Dt} + \rho T \frac{Dc}{Dt} + q_i \qquad \text{(A-1)}$$

m m

where
- t = time
- ρ = density
- c = specific heat at constant pressure
- T = absolute temperature
- v = velocity considered as a vector
- q = heat flux considered as a vector
- τ = shear stress - a tensor
- P = pressure
- q_i = rate of energy conversion inside the control volume
- D = symbol indicating substantial derivative

Basically Eq. A-1 states that the energy variation is caused by convective energy transport, conduction, frictional effects, pressure work, effects due to variable specific heats, and internal energy conversion, i. e., combustion.

If our consideration is initially limited to a solid, it can logically be assumed that:

1. Convective heat transfer is zero.
2. Frictional effects are zero.
3. Density is independent of temperature and pressure.
4. Pressure work is zero.
5. Internal energy conversion is zero.

If in addition it is assumed that:

1. The specific heat is constant.

2. The thermal conductivity is constant.
3. The heat transfer is one dimensional.

Eq. A-1 reduces to the familiar one-dimensional Fourier equation for unsteady heat transfer in a solid:

$$\frac{\partial T}{\partial t} = \alpha \frac{\partial^2 T}{\partial x^2} \qquad \text{(A-2)}$$

where $\alpha = k/\rho c$
k = thermal conductivity
x = distance

Experimentally it was demonstrated that the wall temperature on the water side did not fluctuate with time, i.e., the combustion chamber temperature variations were damped out. The boundary conditions which must be satisfied if Eq. A-2 is to be applied to the wall are (See Fig. 67 for physical model):

a) $T_w = A_{ow} + \sum_{n=1}^{\infty} [K_n \cos n\omega t + G_n \sin n\omega t]$ at $x = 0$

b) $T_w = A_{oj}$ = constant at $x = a$

where A_o = time-averaged temperature defined mathematically as

$$A_o = \frac{1}{2\pi} \int_0^{2\pi} T(\omega t)\, d(\omega t)$$

A_{ow} = time-averaged wall temperature at the gas wall or deposit wall interface as the case may be, with and without deposits
A_{oj} = time-averaged wall temperature at the wall-water interface
a = thickness of wall
K_n, G_n = Fourier coefficients
ω = angular frequency
n = harmonic number
w = subscript indicating wall

m

The solution of Eq. A-2 with these boundary conditions is (4):

$$T_{(x,t)} = A_{ow} - (A_{ow} - A_{oj})\frac{x}{a} + \sum_{n=1}^{\infty} e^{-xr} \begin{bmatrix} K_n \cos(n\omega t - xr) \\ + \\ G_n \sin(n\omega t - xr) \end{bmatrix} \qquad \text{(A-3)}$$

where $r = \sqrt{\frac{n\omega}{2\alpha_w}}$

Differentiation of a series, as represented by Eq. A-3, is permissible according to Ref. (31). Thus, differentiation of Eq. A-3 with respect to x, multiplication by k_w, and evaluation of $x = 0$ will give the heat transfer at the gas-wall interface as shown in Ref. (4):

$$q_o = \frac{k_w}{a}(A_{ow} - A_{oj}) + k_w \sum_{n=1}^{\infty} r \begin{bmatrix} (G_n - K_n)\sin n\omega t \\ + \\ (G_n + K_n)\cos n\omega t \end{bmatrix} \qquad \text{(A-4)}$$

This is the equation that was used as the basis for computing instantaneous heat transfer to a clean wall in the text.

If deposits are present and the control volume is located either in the deposits or in the wall, the same assumptions can be made and Eq. A-2 will be applicable, but the boundary conditions will be different. The additional boundary conditions to be met are:

c) $T_d = T_w$ at $x = 0$

where d = subscript indicating deposits

d) $k_w \frac{\partial T_w}{\partial x} = k_d \frac{\partial T_d}{\partial x}$ at $x = 0$

(note - these assume zero contact resistance between the deposits and wall)

e) $T_d = A_{od} + \sum_{n=1}^{\infty} [A_n \cos n\omega t + B_n \sin n\omega t]$ at $x = -s$

where A_n and B_n are Fourier coefficients.

The solution to Eq. A-2 under these boundary conditions is given in Ref. (32) while details of the solution are given in Ref. (33). The solution is

$$T_{d(x,t)} = \left(1 - \frac{xk_w}{ak_d}\right) A_{ow} + \frac{xk_w}{ak_d} A_{oj} = \sum_{n=1}^{\infty} \sqrt{A_n^2 + B_n^2} \cos(n\omega t - q_n) \qquad \text{(A-5)}$$

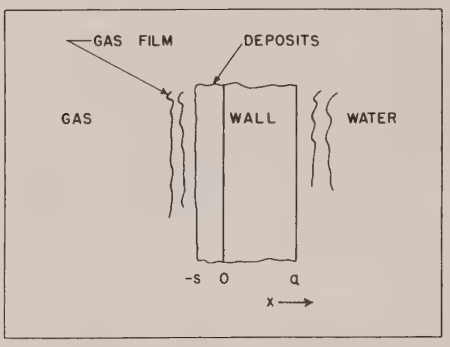

Fig. 67—Physical model of engine cylinder

where $q_n = \arctan B_n/A_n$

$A_n = \sigma e^{-px} (G_n U + K_n V)$

$B_n = \sigma e^{-px} (G_n V - K_n U)$

$\sigma = 0.5(1 + k_w r/k_d p)$

$p = \sqrt{\frac{n\omega}{2\alpha_d}}$

$U = (1 - \gamma) \sin(-px)$

$V = (1 + \gamma) \cos(-px)$

$\gamma = e^{2px} (\delta/\sigma)$

$\delta = 0.5(1 - k_w r/k_d p)$

The unknowns in Eq. A-5 have all been expressed in terms of thermal properties of the wall and deposit and the experimentally determined values of A_{ow}, A_{oj}, G_n, and K_n.

As before, if Eq. A-5 is differentiated with respect to x, multiplied by k_d, and evaluated at $x = -s$, it will give an equation for heat transfer into and out of the deposit at the gas-deposit interface. The resulting equation becomes

$$q_{(-s)} = \frac{k_d}{s} (A_{od} - A_{ow}) + k_d \sum_{n=1}^{\infty} \sqrt{\Psi_n^2 + \phi_n^2} \cos(n\omega t - \beta_n) \qquad (A\text{-}6)$$

where $\beta_n = \arctan \Psi_n/\phi_n$

$\Psi = \sigma p e^{ps} [(\lambda_n - u_n) G_n - (\lambda_n + u_n) K_n]$

$\phi = \sigma p e^{ps} [(\lambda_n + u_n) G_n + (\lambda_n - u_n) K_n]$

$\lambda_n = (1 - \gamma) \cos ps$

$u_n = (1 + \gamma) \sin ps$

and γ must be evaluated at $x = -s$, so for this case

$$\gamma = e^{-2ps} (\delta/\sigma)$$

Again the unknowns are expressed in terms of the experimentally determined values.

The temperature distribution and the heat transfer at the deposit-wall interface will be given by Eq. A-3 and Eq. A-4 respectively.

When evaluating the above equations from the thermocouple output variation, it is of course impractical to let n become infinite, i.e., to take an infinite number of harmonics as is required for the Fourier series representation of the time-temperature function. Since the time-temperature trace recorded from the thermocouple obviously has a significant high frequency spectrum (Figs. 3, 17, 18), it is desirable to use as large a value of n as is practical. Using numerical techniques outlined by Sokolnikoff and Sokolnikoff (34), it was decided that n = 72 was a realistic compromise between accuracy and practicality. Thus temperature readings were scaled from the oscillograms at intervals of 5 crank-angle deg. This number of harmonics (seventy-two) is six times that used by previous investigators (10, 14), but, considering the character of the curves shown in Figs. 3, 17, 18, it is still not sufficiently large to remove all uncertainties from the numerical procedure.

What happened in the gas has not been considered so far. It has merely been said that the temperature fluctuation in the gas induced the specified temperature variation in the wall and deposits. The next step is to find a relationship between the gas temperature and the wall temperature and try to deduce ways of finding correlating variables for the heat transfer to the wall as a function of the gas conditions.

Jakob (35) summarizes the work of Hobson (36) and Kelvin (37) who attempted to use the relationship defined under steady-state conditions

$$q_o = h_o (T_g - T_w \mid x = o) \qquad (A\text{-}7)$$

and apply it to unsteady conditions. They assume that the temperature of the gas in the main gas core varies sinusoidally with time as

$$\Theta_g = \Theta_{og} \cos n\omega t \qquad (A\text{-}8)$$

where Θ_{og} is the maximum gas temperature above the time-averaged value.

It is next assumed that the temperature variation above the time-averaged value induced in the wall is given by

$$\Theta_w = \Theta_{og} \eta e^{-rx} \cos(n\omega t - rx - \epsilon) \qquad (A\text{-}9)$$

where η, r, and ϵ are constants to be determined by the boundary condition.

It should be noted in Eq. A-9 that if $x = 0$, i.e., at the gas wall interface, the wall temperature lags the gas temperature in the gas core by an amount ϵ. This is illustrated in Fig. 68 where a first sine harmonic of both the gas and wall temperature are plotted.

Fourier's heat equation, Eq. A-2, must be satisfied throughout the wall.

The assumpations required in order to derive Eq. A-2 from the general equation for energy variation within a control volume in a medium were made. Also the boundary conditions to be satisfied for solution of Eq. A-2 are

f) the heat transfer from the gas is equal to the heat transfer through the wall surface ($x = 0$)

g) the gas temperature equals that of the wall temperature at the gas-wall interface.

Both of these conditions may be expressed by the single relationship

$$\frac{-k_w \partial \Theta_w}{\partial x} = h_o (\Theta_g - \Theta_w \mid x = 0)$$

where h_o is a time-averaged heat transfer coefficient. From these boundary conditions they find that

$$\epsilon = \arctan 1/(1 + g/r)$$

$$\eta = \frac{1}{\sqrt{1 + 2r/g + 2(r/g)^2}}$$

where $g = h_o/k_w$

Jakob (35) presents a table showing a variation of η and ϵ with g/r. Computations using typical values in engines show (16) that:

1. The amplitude of the gas temperature is greatly damped in the gas film next to the wall surface.

2. The gas temperature in the main body of the gas leads the temperature at the gas wall interface by an angular amount of 40-45 deg. Differentiation of Eq. A-9, evaluation at x = 0, and multiplication by k_w gives

$$q_o = \sqrt{2}k_w r\Theta_{og}\,\eta \cos(n\omega t - \epsilon + \pi/4) \qquad \text{(A-10)}$$

Thus if ϵ is exactly equal to 45 deg the heat transfer through the surface is exactly in phase with the temperature variations of the main body of the gas. The curve for the heat transfer for the first sine harmonic is also shown in Fig. 68. It should be pointed out that boundary condition f requires that regardless of the value of ϵ the heat transfer at the wall is in phase with a curve of the temperature difference between the gas and the wall, i.e., $\Theta_g - \Theta_w|_{x=o}$.

It is obvious from comparison of gas temperature (a function of gas pressure), wall surface temperature, and wall surface heat transfer variations in the text that the wall temperature does not lag the gas temperature by 1/8 the period, which should be 90 crank-angle deg for the first harmonic. This fact may be clarified and accounted for in the above derivation by consideration of the higher harmonics in the gas temperature variation. It may be noted from Eq. A-8 that if the Fourier coefficients are positive, Θ_g is a maximum for $\omega t = 0$, regardless of harmonic number. Also ϵ approaches $\pi/4$ more rapidly as n increases. Thus it may be seen from Eqs. A-9 and A-10 that the wall surface temperature variation and surface heat transfer will maximize at $\omega t = \epsilon/n$ and $(\omega t = \epsilon - \pi/4/n)$ respectively. Thus the maximum values of the three variations will occur more nearly simultaneously as the harmonic number of the positive Fourier coefficients increase. Negative Fourier coefficients cause a 180 deg phase shift in these effects and will thus tend to cause the gas temperature and heat transfer to become out-of-phase. In an actual engine the phase shift is apparently not large.

Because h was considered constant throughout the cycle, when in fact it varies by a factor of 5 or 10, and because no energy additions to the gas film next to the wall surface other than conduction and convection were considered, it was decided to investigate unsteady heat transfer in an engine further from a theoretical standpoint.

Pfriem (12) and Elser (14) have attempted to apply Eq. A-1 to a control volume located in the gas and thus to determine heat transfer. They make all the assumptions made in deriving Eq. A-2 except that they do not assume the pressure work and internal energy conversion to be zero.

With these very restrictive assumptions, Eq. A-1 becomes

$$\frac{\partial\Theta_g}{\partial t} = \alpha_g \frac{\partial^2\Theta_g}{\partial x^2} + \frac{1}{J(\rho c)_g}\frac{\partial P}{\partial t} + \frac{q_i}{(\rho c)_g} \qquad \text{(A-11)}$$

where J is the mechanical equivalent of heat. They further assume that:

1. Either of the last two terms or the sum of the last two terms vary periodically with time.

2. These variations are uniformly distributed throughout the gas volume.

Using Elser's analysis, which assumes that q_i varies periodically with time and that the pressure variation is zero, i.e., the variation of pressure is small compared with the time-averaged value, Eq. A-11 becomes

$$\frac{\partial\Theta_g}{\partial t} = \alpha_g \frac{\partial^2\Theta_g}{\partial x^2} + \frac{q_i}{(\rho c)_g} \qquad \text{(A-12)}$$

At a great distance from the wall the conduction is zero. If the temperature variation in this region is given by

$$\Theta_{g\infty} = \Theta_{o\infty} \sin\omega t \qquad \text{(A-13)}$$

then

$$q_i = \omega(\rho c)_g\,\Theta_{o\infty} \cos\omega t \qquad \text{(A-14)}$$

The boundary conditions to be met are:

h) $\Theta_w = \Theta_g$ at x = 0

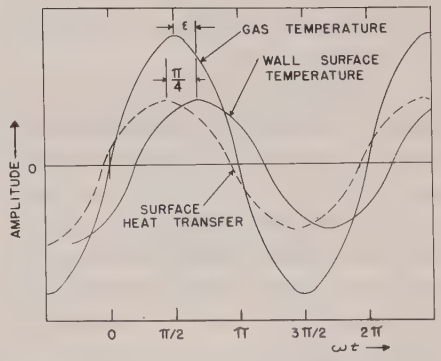

Fig. 68—Phase relationships between gas temperature, wall temperature, and surface heat transfer

$$\text{i)} \quad k_w \frac{\partial \Theta_w}{\partial x} = k_g \frac{\partial \Theta_g}{\partial x} \qquad \text{at } x = 0$$

A solution of Eq. A-12 for the gas temperature using the above boundary conditions and relations is:

$$\Theta_g = \Theta_{o\infty} \sin \omega t - \Theta_a e^{mx} \sin (\omega t + mx + \zeta) \quad \text{(A-15)}$$

where $m = \sqrt{\omega/2\alpha_g}$

Θ_a and ζ are constants determined by boundary conditions. From Eq. A-3 (for a single harmonic and zero steady-state temperature gradient in the wall)

$$\Theta_w = \Theta_{ow} e^{-rw} \sin (\omega t - rx + \kappa) \quad \text{(A-16)}$$

After some manipulation of the above equations, it is seen that

$$\frac{\Theta_{ow}}{\Theta_{o\infty}} = b_g/(b_g + b_w) \quad \text{(A-17)}$$

where $b_g = \sqrt{k\rho c}$ for the gas

$b_w = \sqrt{k\rho c}$ for the wall

The results of this analysis show that:

1. The wall surface temperature is in phase with the gas temperature at a great distance from the wall and is a miniature replica of it.

2. The heat transfer through the wall surface leads both the gas temperature and wall surface temperature by exactly 45 deg. These are very interesting conclusions (if correct) since they mean that the temperature records produced by the thermocouple (Fig. 3, 17, and 18) are miniature replicas of the gas temperature some distance from the wall. However, this derivation will lead to positive, negative, and infinite values for h if Eq. A-7 is used as a defining relationship. The assumptions made in deriving Eq. A-17 are better than those made in deriving Eq. A-9 in that the resistance of the gas film is not considered constant and that energy generation throughout the gas volume is considered. They are very unrealistic, of course, in that they consider the gas density to be constant.

Overbye (16) has considered other models using the technique of Elser (14) but found that if sufficient simplifications are made so that a solution to the equations could be obtained, the assumptions were such that the model was unrealistic. He did, however, evolve some heat transfer correlations by use of dimensional analysis with Eq. A-1 and the continuity equation. This analysis has been used for correlation of heat transfer in a motored engine in the test, and it is summarized below.

The continuity equation is needed for this analysis. Again considering the control volume located in the gas within the combustion chamber, Ref. (30) shows that the continuity equation may be expressed as

$$\frac{\partial \rho}{\partial t} + (\nabla \cdot \rho \vec{v}) = 0 \quad \text{(A-18)}$$

The objective of this correlation is to obtain relationships from Eq. A-1 relating surface heat transfer with more easily determined operating parameters by means of dimensional analysis. Five general assumptions were made which do not require grossly unrealistic concepts:

1. The gas is a perfect gas.
2. The specific heats, thermal conductivity, and viscosity are constant.
3. The gas pressure is a time variation only.
4. There is zero radial gas velocity.
5. The cylinder gas has angular symmetry in temperature and velocity.

Equations A-1 and A-18 were put in dimensionless form by the following definitions

$$T^* = T/T_o \qquad x^* = x/L_o \qquad z^* = z/L_o$$

$$P^* = P/P_o \qquad v_x^* = v_x/V_o \qquad v_\Theta^* = v_\Theta/V_o$$

$$\rho^* = \rho/\rho_o \qquad t^* = V_o\, t/L_o \qquad q_i^* = \frac{L_o\, Rq_i}{c_g P_o V_o}$$

where z = the radial position coordinate
v_Θ = tangential velocity of the gas
R = the gas constant for the gas within the cylinder.

The subscripted zero quantities were reference quantities arbitrarily chosen as

T_o = absolute gas temperature in the intake manifold
ρ_o = gas density in the intake manifold
P_o = absolute gas pressure in the intake manifold; it was multiplied by the compression ratio of the engine for data plotting.
L_o = the stroke of the engine
V_o = the average piston velocity $\cong L_o\, \omega/\pi$

The five general assumptions simplify Eq. A-1 considerably, but still many unknown variables remain in the equations, e.g., velocity distributions within the gas. It was decided to attempt to correlate motored data obtained from thermocouples 1 and 2, which were in the cylinder head. Thus three additional assumptions were made:

1. The ratio of viscous energy dissipation within the gas volume to the pressure work was negligible.
2. Radial heat transfer was zero.
3. Internal heat sources were zero, i.e., combustion was absent. Eq. A-1 in dimensionless form then becomes (with the aid of the continuity and perfect gas equations):

$$\frac{\partial^2 T^*}{\partial x^{*2}} - Pe'\, \rho^* v_x^* \frac{\partial T^*}{\partial x^*} + Pe' \left(\frac{P^*}{\rho^*} \frac{\partial \rho^*}{\partial t^*} - \frac{1}{\Delta} \frac{\partial P^*}{\partial t^*} \right) = 0 \quad \text{(A-19)}$$

where $Pe' = L_o V_o \rho_o c_g / k_g$ = Peclet Number for the gas
= product of the Reynolds No. and the Prandtl No.
Δ = ratio of specific heat at constant pressure to the specific heat at constant volume for the gas, which is taken as a constant.

The similarity between the dimensionless gas temperature gradient at the wall surface and the Nusselt No. in steady-state dimensional analysis suggests letting

$N^* = \partial T^*/\partial x^*$ at an arbitrary x^* and $N_o^* = \partial T^*/\partial x^*$ at $x^* = 0$.

The two boundary conditions on the dependent variable, N^*, become

j) $N^* = N_o^*$ at $x^* = 0$

k) $N^* = 0$ at x^* large (far from wall)

Noting that at $x^*=0$ the velocity is zero, the wall surface temperature variation is small, and P^* and $\partial P^*/\partial t^*$ are parametric equations of t^*, the simple relationship is obtained:

$$N_o^* = \text{function } (Pe', P^*) \qquad \text{(A-20)}$$

An equation similar to boundary condition i) expresses N_o^* in terms of q_o. Thus

$$N_o^* = \frac{L_o q_o}{k_g T_o}$$

The failure to include viscous dissipation terms in the above derivation may well explain the experimental observation that the resulting correlation does not correct for the effect of intake valve orientation on surface heat transfer. A rigorous discussion of this problem requires more detailed data on gas velocity variation within the cylinder. This is unavailable.

In comparing the derivations presented by Jakob (35) and Elser (14) it is convenient to neglect a steady-state temperature gradient through the wall, i.e., the time average of the gas temperature and wall temperature is equal. However, it is obvious from data presented in the text that a steady-state temperature gradient does exist and contributes extensively to the total heat transfer in certain sections of the cycle. A net transfer of heat from the wall to the gas may have considerable effect on the volumetric efficiency or octane requirement increase of the engine. The equations derived earlier in the Appendix may be used to gain some insight into the effect of wall material on the ORI and volumetric efficiency when both steady-state and unsteady heat transfer are considered.

Let Eq. A-10 express the unsteady heat transfer through the wall with n equal to unity (first harmonic), and let the steady-state heat transfer component given in Eq. A-4 also be present. Thus

$$q_o = k_w(A_{ow} - A_{oj})/a + \sqrt{2}\, k_w r \Theta_{og}\, \eta \cos(\omega t - \epsilon + \pi/4) \qquad \text{(A-21)}$$

If Eq. A-21 is then integrated with respect to time over the half period during which the unsteady heat transfer component is negative, i.e., $(\epsilon + \pi/4) \le \omega t \le (\epsilon + 5\pi/4)$, we obtain the net heat flow from the wall to the gas during this particular half period. The result of the integration yields

$$Q_t = [\pi k_w (A_{ow} - A_{oj})/\omega a] - [2\sqrt{(k\rho c)}\, \Theta_{og}\, \eta/\sqrt{\omega}\,] \qquad \text{(A-22)}$$

Now if an average gas temperature A_{og}, average wall-water interface temperature A_{oj}, and average heat transfer coefficient h_o are assumed independent of the wall material, it may be shown by a steady-state heat balance that the average gas wall interface temperature and steady-state heat transfer through the wall are functions of the wall thermal conductivity k_w. Hence the first bracketed term on the right hand side of Eq. A-22 becomes

$$Q_{ss} = (\pi k_w/\omega a)\left\{\left[(h_o A_{og} + k_w A_{oj}/a)/(h_o + k_w/a)\right] - A_{oj}\right\} \qquad \text{(A-23)}$$

The unsteady heat transfer component depends on the product of $\sqrt{(k\rho c)_w}$ and η. However, for conditions within an engine operating in the usual speed range g/r is very small ($g/r \le 0.07$). The definition of η indicates that for small g/r

$$\eta \tilde{=} g/\sqrt{2}\, r = h_o/\sqrt{\omega}\ \sqrt{(k\rho c)_w} \qquad \text{(A-24)}$$

Note that the second bracketed term on the right hand side of Eq. A-22 is independent of the wall material. Thus

$$Q_{unsteady} = -2h_o\Theta_{og}/\omega \qquad \text{(A-25)}$$

Table 8 lists the thermal properties of several wall materials ranging from good conductors to insulators. However, it is not possible to obtain a comparison between materials by means of Eqs. A-22, A-23, and A-25 without assigning numbers to the parameters assumed invariant with wall material. Thus if we let the following values be specified we may make a comparison of heat transfer effects:

$A_{og} = 1200$ F

$A_{oj} = 210$ F

Table 8 - Thermal Properties of Wall Materials

Material	k	ρ	c	$\sqrt{(k\rho c}$
Aluminum	123.0	168.5	0.248	71.7
Cast Iron	24.8	474.0	0.110	35.9
Aluminum Oxide	2.0	170.0	0.330	10.6
Zirconia	0.58	275.0	0.200	5.66

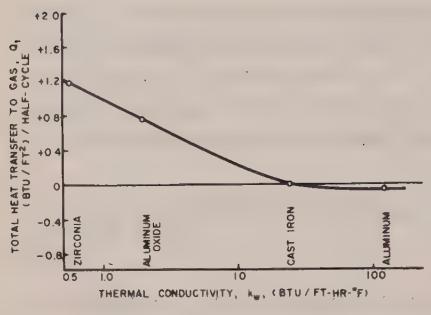

Fig. 69—Results of comparison of heat transfer effects

$\Theta_{og} = 450\pi$ F

$h_o = 100$ Btu/ft^{2}hrF

$a = 0.0248$ ft

$\omega = 60,000\pi$ rad/hr (4-Stroke cycle, 1000 rpm)

The values listed above were chosen to give $Q_t = 0$ for a cast iron wall. Thus the values of thermal conductivity from Table 8 may be used to compute Q_t and this value may be plotted against k_w. The results of this comparison are shown in Fig. 69. The interpretation of the figure is that positive Q_t indicates heat transfer to the wall from the gas, while negative values of Q_t represent heat transfer from the wall to the gas with possible decreased volumetric efficiency or increased ORI.

References

1. D. Bendersky, "A Special Thermocouple for Measuring Transient Temperatures", Mechanical Engineering, Vol. 75 (1953), 117.

2. L. G. Pless, "The Effect of Selected Operating Variables on Instantaneous Combustion-Chamber Surface Temperature", MS Thesis, University of Wisconsin, 1956.

3. T. R. Schmidt, "Instantaneous and Continuous Heat Flow Measurements in Internal Combustion Engines", MS Thesis, University of Wisconsin, 1950.

4. V. D. Overbye, "Instrumentation and Analysis for Instantaneous Heat Transfer in Internal Combustion Engines", MS Thesis, University of Wisconsin, 1959.

5. B. Donkin, "Temperature of Cylinder Walls", Railway Review, Vol. 34, (1894), 558.

6. E. G. Coker, and W. A. Scoble, "Cyclic Changes of Temperature in a Gas-Engine Cylinder", Proceedings of the Institution of Civil Engineers, Vol. 196 (1913-1914), Part II, 1-74.

7. W. Nusselt, "Der Warmeubergang in der Gasmaschine", Zeitschrift des Vereines Deutscher Ingenieure, Vol. 58, Part I (1914), 361-367, 414-417, 459-463. (Abstracted in Journal of ASME, Vol. 36 (1914), 098-0101.)

8. O. G. C. Dahl, "Temperature and Stress Distribution in Hollow Cylinders", Transactions of ASME, Vol. 46 (1924), 161-208.

9. G. Eichelberg, "Zeitlicher Verlauf der Warmeubertragung in Dieselmotor", Geb. Ing. Wes., H. 300 (1928), 61-66.

10. G. Eichelberg, "Some New Investigations on Old Combustion-Engine Problems", Engineering, Vol. 148 (1939) 463-466, 547-550.

11. A. Meier, "Messung schnellveranderlicher Zylinderwand-temperaturen", Forschung auf dem Gebiete des Ingenieurwesens, Vol. 10 (Jan. - Feb., 1939), 41-54. (Translated in N.A.C.A. Technical Memorandum 1013).

12. H. Pfriem, "Der Periodische Warmeubergang bei kleinen Druckschwankungen", Forschg. Geb. Ing., Vol. 11 (1940), 67-75. (Translated in N.A.C.A. Technical Memorandum 1048).

13. H. Pfreim, "Der Warmeubergang bei schnellen Druckanderungen in Gasen", Forschung. Geb. Ing., Vol. 13 (1942), 150-164.

14. K. Elser, "Der instationare Warmeubergang in Dieselmotoren", Mitt. 15, Inst. Thermodyn. Verbrennungsmotorenbau, ETH, Zurich, 1954.

15. E. T. Vincent, and N. A. Henein, "Thermal Loading and Wall Temperatures as Functions of Performance of Turbocharged Compression-Ignition Engines", SAE Transactions, Vol. 67 (1959), 478-488.

16. V. D. Overbye, "Variation of Instantaneous Wall Temperature, Heat Transfer, and Heat Transfer Coefficients in a Spark-Ignition Engine", Ph. D. Thesis, University of Wisconsin, 1960.

17. C. L. Bouchard, C. F. Taylor, and E. S. Taylor, "Variables Affecting Flame Speeds in the Otto-Cycle Engine", SAE Journal, Vol. 41, No. 5, 1937, 514-520.

18. M. C. Burrows, "A Fast Infrared Pyrometer for Engine Compression Temperatures", Ph. D. Thesis, University of Wisconsin, 1959.

19. R. E. Stebar, W. M. Wiese, and R. L. Everett, "New Studies Provide More Information in Engine Rumble--a Phenomenon of High Compression Ratio Engines", General Motors Engineering Journal, Vol. 7, No. 1 (1960), 23-29.

20. J. W. Orelup, and O. I. Lee, "Factors Influencing Carbon Formation in Automobile Engines", Industrial and Engineering Chemistry, Vol. 17 (1925), 731.

21. L. F. Dumont, "Possible Mechanisms by Which Combustion Chamber Deposits Accumulate and Influence Known", SAE Transactions, Vol. 5, 1951, 565.

22. D. A. Hirschler, J. D. McCullough, and C. A. Hall, "Deposit-Induced Ignition - Evaluation in a Laboratory Engine", SAE Transactions, Vol. 62 (1954), 40.

23. L. L. Withrow, and F. W. Bowditch, "Flame Photographs of Auto-ignition Induced by Combustion-Chamber Deposits", SAE Transactions, Vol. 6 (1952), 725-51.

24. C. A. Hall, "Effect of TEL Concentration on Rate-of-Requirement Increase". SAE Transactions, Vol. 5, (1951), 581.

25. G. J. Nebel, and P. L. Cramer, "Ignition Temperatures of Lead Compounds-Carbon Mixtures". Industrial and Engineering Chemistry, Vol. 47 (Nov. 1955), 2393.

26. M. Weiss, "Combustion-Chamber Deposit Study Using Pure Mixtures," M. S. Thesis, University of Wisconsin, 1959.

27. P. M. Ku, "Factors Affecting Heat Transfer in the Internal Combustion Engine," NACA Technical Note, T. N. No. 787, 1940.

28. J. J. Mikita, and W. E. Bettoney, "How Combustion-Chamber Deposits Affect Engine - Fuel Requirements," Oil and Gas Journal (July 6, 1953), 84.

29. J. L. Lauer, and P. J. Friel, "Some Properties of Carbonaceous Deposits Accumulated in Internal Combustion Engines," Combustion and Flames, (March, 1960).

30. R. B. Bird, W. E. Stewart, and E. N. Lightfoot, "Notes on Transport Phenomena", New York: John Wiley and Sons, Inc., 1958.

31. H. S. Carslaw, "Fourier Series and Integrals", New York: Dover Publications, 1930, 282-283.

32. Private Communication from Prof. H. W. March, University of Wisconsin.

33. J. E. Bennethum, "Heat Transfer and Combustion Chamber Deposits in a Spark Ignition Engine", Ph. D. Thesis, University of Wisconsin, 1960.

34. I. S. and E. S. Sokolnikoff, "Higher Mathematics for Engineers and Physicists", New York: McGraw-Hill, 1941, 545-548.

35. M. Jakob, "Heat Transfer", Vol. 1, New York: John Wiley and Sons, Inc., 297-299.

36. E. W. Hobson, "Warmeleitung, Mathematischer Teil," Encyklopeadie der mathematischen Wissenschafter, Vol. 5, Part I, Article 4, B. G. Teubner, Leipzig and Berlin (1903-1921), 186.

37. Lord Kelvin, "Linear Flow of Heat, Part II," Cambridge Mathematical Journal, Vol. 3, London: E. Johnson and Whittaker Co., 1843.

Discussion

Four Points to Consider

Lamont Eltinge, and T. O. Wagner
Standard Oil Co. of Indiana

THE AUTHORS have made a worthwhile contribution. SAE would benefit from more papers covering work that is as extensive and more engineering analyses that are as thorough as the authors'. This paper, because of type and extent of work reported, is not "light" reading; its 37 pages, 8 tables, and 69 figures encompass many complex ideas, some higher mathematics, and several assumptions that require checking for correctness and resultant effects.

Our study of the paper, although as yet incomplete, has raised several questions and made it seem that some further treatment of the data would improve understanding and application. Four of the points we encountered are:

1. Many of the curves are of temperatures at the thermocouple. They would be more informative if the data were analyzed to yield heat transfer rates, q, at the surface. For example, in Fig. 17, is the dip for TC1 accompanied by a negative q? In Fig. 15, does q exhibit a fast rise and plateau, as wall temperature does?

2. What is the exact physical significance of the slopes of the temperature-time curves? They are apparently related to the decay factor, rx. Here too the curves would be easier to understand if the data were analyzed to yield the more significant parameter, rx. We wonder if r changed or if x, alone, changed. If only x, would the change in mean thermocouple temperature show the same values of x?

3. The appendix indicated that "the wall temperature (we presume at the surface) is in phase with the gas temperature at a great distance from the wall and is a miniature replica of it." Fig. 20, which shows the thermocouple profile in a motored clean engine, shows both a phase shift and a distortion of the shape of the profile. The authors attribute the phase shift to heat capacity. They seem to have accounted for this in the appendix; but some further explanation is necessary. They do not comment on the distortion. We wonder whether a different and possibly more complex theoretical model is needed, or if the discrepancy can be attributed to experimental error. The model used allows no heat transfer from the gas outside the layer in which conduction is the only mode of heat transfer. A model that allows for some heat transfer by circulation from the bulk of gas seems more realistic, though mathematically more difficult.

4. Unsteady-state heat-transfer effects of deposits depend on engine rpm. Might the effects be greater or smaller at the 2000-4000 rpm of automobile engines than at the 800-900 rpm of their laboratory engine?

From a study of this extent, it is difficult to select the one idea that seems most significant. Our selection would be the idea that the h concept is not valid for engines. Although it is never exactly valid, for the h concept does not allow for the heat capacity of the boundary layer, it is valid in a practical sense unless neglecting the heat capacity of the boundary layer introduces significant errors. We feel the results in the paper show that such significant errors are an important possibility. However, further study of these data and of additional data seem necessary to assure that the discrepancy does not result from experimental error or assumptions in the analysis.

Despite these and other questions, the significance of this work should not be underestimated. For men interested in combustion chamber deposit problems, a careful study of all the author's analyses and results, and an effort to check, extend and apply them should prove beneficial and stimulating.

Authors' Closure To Discussion

THE AUTHORS thank the discussers for their interest in this paper.

The four points to consider are discussed below.

Unfortunately a heat transfer analysis was not made for the cycle with "preflame" reaction shown in Fig. 17. However, it is justifiable to assume that the sudden temperature change will affect heat transfer through the wall surface. The wall temperature variations shown in Figs. 14 and 15 yield slightly different surface heat transfer variations, as shown in Fig. 25. A study of temperature-time sampling frequency necessary to determine surface heat transfer is presented in Ref. (16).

It is difficult to examine a temperature-time record and predict the temperature-distance variation (which is proportional to surface heat transfer). Ref. (16) confirms the intuitive result that for a fixed material peak unsteady heat transfer increases with increased wall temperature swing and temperature-time slope. The deposit studies indicate that deposit thickness and thermal properties affect both slope and amplitude of the deposit-wall interface temperature.

The models in the Appendix are oversimplified, as shown by a constant heat transfer coefficient assumption (Eq. A-7) and a constant density gas with small pressure variations (Eq. A-12). These simplified models are presented to show that two completely different results are obtained by using either the heat transfer coefficient concept or the temperature profile concept. Experimental determination of heat transfer coefficient variation during the entire cycle and computer techniques for solving nonlinear differential equations are needed to give a more complete picture of the intricate relationship between gas processes and surface heat transfer in an operating internal combustion engine.

It is unfortunate that the engines used in this study were limited to low rpm. Refined instrumentation and calibration techniques must be developed to use the thermocouple in high speed engines. Higher engine speeds may indicate completely different wall surface temperatures and surface heat transfer because of the effect of turbulence and rpm on combustion processes within the combustion chamber.

The authors present this paper with a sincere desire that the surface thermocouple may be one additional tool to be used to study the intricacies of combustion phenomena in modern internal combustion engines.

End Gas Temperature Measurement by a Two-Wavelength Infrared Radiation Method*

William G. Agnew
General Motors Research Laboratories

ENGINE KNOCK has been under intensive seige for about 40 years. The sometimes hot, sometimes cold war against this ever-present enemy has had few casualties on either side. It has been a war of containment in which millions of miles are driven every day with a minimum of objectionable noise and practically no damage, but at the same time compression ratios, spark advances, mixture ratios, and fuel types are severely limited. We pay dearly to maintain peaceful coexistence with engine knock; yet, we have gained a great deal of ground through proving ground testing and laboratory research.

Our intelligence divisions have perhaps not fared as well as the front line divisions, since our understanding of the basic nature of knock, the essential mechanism from which it springs, is far from complete. The problem of intelligence resolves itself to understanding the mechanism by which a fuel-air mixture ignites under the influence of pressure and temperature. If this understanding were to be gained, it should have many uses. Knock could, perhaps, be outflanked by adjusting end-gas conditions more shrewdly than is done at present; the mechanism might be sabotaged with antiknock additives more neatly than is done now; or the mechanism might even be put to our own use more effectively, as is desirable in the operation of compression-ignition engines.

Such exacting operations require precise understanding and control of the fuel-air ignition process. Mixture composition, temperature, and pressure are perhaps the three most critical factors in the ignition process, and the measurement of these factors as functions of time in operating engines has been the subject of much research. Pressure measurement has been rather precisely accomplished with the most modern instruments, and the measurement of pressure development from preflame reactions in spark-ignition engine end-gases has assisted greatly in the understanding of the knock mechanism. Composition studies, by sampling valves, exhaust analysis, and spectroscopic studies, while not exhibiting great quantitative precision, have, nevertheless, contributed greatly in elucidating the chemistry of preflame reactions and in correlating this chemistry with that of cool flame reactions already widely-known outside of engine studies.

Measurement of the temperature of the (nominally) unburned fuel-air mixture in an operating engine, prior to knock or normal flame propagation in the end-gas, has been attempted only in the last ten years in a very few laboratories. These studies have been motivated by a strong desire on the part of the automotive and petroleum industries to substitute experimental observations for the many uncertain calculations, estimations, and conjectures about end-gas temperatures made heretofor. It was believed that such observations would not only contribute to an understanding of the mechanism of engine knock and help explain the influence of engine and fuel variables on knock limits, but might also be informative in the matters of residual dilution, heat transfer to combustion chamber walls, and particle ignition phenomena.

Under sponsorship of the Coordinating Research Council three methods of engine end-gas temperature measurement have been studied at the Massachusetts Institute of Technology

*This paper received the 1960 Horning Award.

and the University of Wisconsin.[1] The MIT group has developed a method based on the measurement of the velocity of sound in a narrow gap between two probes in an engine cylinder. The University of Wisconsin has studied a method involving absorption spectroscopy of iodine introduced in an engine cylinder, and has developed an additional method based on infrared emission and absorption by water vapor in an engine.

The sound velocity and infrared emission-absorption methods were both developed to a state of useful application, and a comparison of the two methods when operated simultaneously on the same engine showed good agreement.

During the last eight years of the CRC development program, General Motors Research has independently carried out its own study of still another method of end-gas temperature measurement: the two-wavelength infrared emission method. The temperature study has been carried out in conjunction with a spectroscopic study of preflame reaction products,[2] which utilized much of the same equipment. The two-wavelength method was chosen for study for several reasons. The method was thought to have certain advantages over other methods being studied, and it was felt that confirmatory data on end-gas temperatures by several independent means would strengthen a position with regard to these temperatures which would be, at best, rather shaky.

It is the purpose of this paper to describe in some detail the method, how it is applied, and to indicate some of its successes and failures in order that this method may be evaluated in relation to the other methods currently in use.

Two Wavelength Principle of Temperature Measurement

The two-wavelength radiation method of temperature measurement has been applied in many different systems and discussed in many texts.[3] Most of the applications have been with near-black radiators and with visible rather than infrared emission. These are the well-known color pyrometers used for measuring the temperatures of solid and molten metal, and carbon-forming flames. Uyehara, Myers, Watson, and Wilson[4] at the University of Wisconsin applied the two-color method to the luminous carbon radiation emanating from a diesel engine combustion chamber.

Although the Wisconsin work is the only prior application of a two-wavelength temperature measurement method to a reciprocating engine, applications to non-luminous flame gases are actually more pertinent to the present study, since spark-ignition engine end-gases emit little or no luminous radiation. Bernath, Powell, Robison, Welty, and Wohl[5] measured temperatures in a non-luminous Bunsen burner flame using the infrared water vapor bands. The equipment and technique were completely analogous to that in the present engine study. The author[6] has also discussed the application of this same technique to a jet engine combustor.

The two-wavelength radiation technique relies on the fact that the intensity of radiation from any material in thermal equilibrium varies with the temperature. If the absolute emissivity of the material at some wavelength were known, and if the instrumentation were arranged so that absolute measurements of radiant energy were possible, then a simple measurement of the radiant energy emitted at one wavelength would determine the temperature. Unfortunately, the absolute parameters are not generally known. It is possible, however, to cancel the need for many of these parameters, and reduce the influence of others if measurements are made at two wavelengths rather than at one. The fact that radiation intensity is a different function of temperature at different wavelengths makes it possible to determine temperature from the ratio of intensities, while many parameters of the optical and electronic measuring system cancel out. Two parameters, the emissivity of the radiator and the sensitivity of the detector, do not actually cancel, but at least absolute values for these factors are not needed, only their ratios at the two wavelengths. These ratios may be determined by empirical calibration.

In mathematical terms the two wavelength radiation technique may be expressed from the fundamental laws of radiation as follows:

$$\frac{I_1}{I_2} = \frac{\epsilon_1}{\epsilon_2}\left(\frac{\lambda_2}{\lambda_1}\right)^5 \frac{\left(\exp \frac{C_2}{\lambda_2 T}\right)-1}{\left(\exp \frac{C_2}{\lambda_1 T}\right)-1} \qquad (1)$$

where: I = Radiation intensity of substance at λ
ϵ = Emissivity of substance at λ
λ = Wavelength of radiation
C_2 = Planck's second radiation constant
T = Absolute temperature

This relationship is obtained from Planck's equation for a perfect black body, and it applies to any radiating substance in thermal equilibrium.

The calculable blackbody part of Eq. 1 may be expressed as:

$$\frac{B_1}{B_2} = \left(\frac{\lambda_2}{\lambda_1}\right)^5 \frac{\left(\exp \frac{C_2}{\lambda_2 T}\right)-1}{\left(\exp \frac{C_2}{\lambda_1 T}\right)-1} \qquad (2)$$

where B_1/B_2 is the ratio of emissive powers at the two wavelengths λ_1 and λ_2 for a blackbody at temperature T. At fixed wavelengths B_1/B_2 is a function of temperature only.

*Numbers in parentheses designate References at end of paper.

The instrument constants may be taken care of by:

$$I = \frac{D}{K} \tag{3}$$

where:

D = Output of detector

K = Relative sensitivity of detection system at λ

Substituting Eqs. 2 and 3 in Eq. 1 and rearranging terms gives the working relation:

$$\frac{B_1}{B_2} = \frac{D_1}{D_2}\,\frac{K_2}{K_1}\,\frac{\epsilon_2}{\epsilon_1} \tag{4}$$

If K_2/K_1 and ϵ_2/ϵ_1 are known by prior calibration, and if D_1/D_2 is measured, then B_1/B_2 may be determined. The known relation between B_1/B_2 and T (Eq. 2) then permits determination of the absolute temperature of the radiating substance.

In this work water vapor present in the engine cylinder gases was taken as the radiating substance, and the wavelengths chosen were those of two water vapor bands at λ_1 = 1.89 and λ_2 = 2.55 microns. The blackbody relationship (Eq. 2) was readily manipulated with the aid of a blackbody radiation slide rule.

In principle, at least, the two-wavelength method of temperature measurement has several advantages over the other methods currently in use. The problems of the sound velocity method associated with cooling of the measured gases by the cooled sound probes, and the uncertain effects of preflame reactions on the sound velocity are entirely absent. Turbulence of the end-gases, which may interfere with the sound velocity measurement, should have no effect on the two-wavelength method. The two-wavelength method requires only one window in the engine combustion chamber instead of two, as required by the emission-absorption method, and presumably there is no direct effect of dirtying the engine window on the temperature measurement, as long as sufficient radiation passes to obtain the measurement. The emission-absorption method suffers a direct error from any dirt deposited on the windows between calibration and measurement.

Since all three of the end-gas temperature measurement techniques now in use involve an appreciable volume of gas, the matter of temperature gradients within the measured volume is of some concern. All three measuring techniques obviously give some sort of an average temperature for the gases under study. The actual temperature gradients existing in an engine are unknown. It may be presumed, however, that late in the compression stroke the bulk of the gas is at a temperature much higher than the cylinder walls, and that this bulk of gas is surrounded by a layer in which the temperature gradually decreases to the value at the wall. Theoretical calculations[1, 7] indicate that, while the sound velocity technique tends to give a temperature corresponding closely to the mass average temperature of the gases between the probes, the infrared emission-absorption method tends to give values closer to the peak temperature in the volume under observation. As shown in Appendix A, the two-wavelength method of temperature measurement tends to give an average value still closer to the peak than the emission-absorption method. Thus, the two-wavelength method perhaps gives the most significant results for knock studies, since it tends more to indicate the temperature of the hottest gas which must eventually be first to reach spontaneous ignition in the engine cycle. Of course, if the correlation of end-gas temperature with average cylinder pressures or heat transfer through the chamber walls is of interest, then a mass average temperature might be considerably more useful.

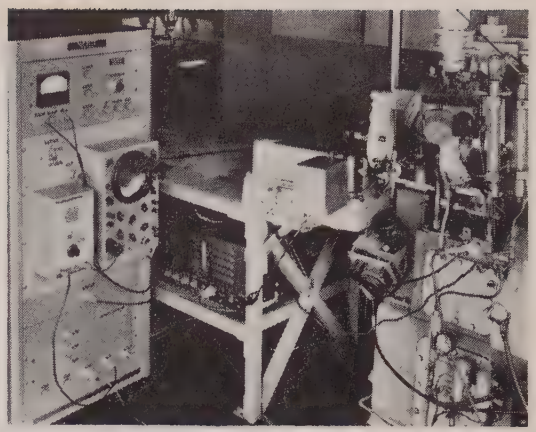

Fig. 1—Engine radiation temperature measuring equipment

It is extremely hard to compare the different methods with regard to the many practical difficulties which arise in attempts to apply such techniques to actual engine measurements. However, some of these difficulties in the case of the two-wavelength method will become evident in the following discussion.

Equipment

Fig. 1 is a photograph of the equipment for two-wavelength temperature measurement. At the right is the single-cylinder research engine; in the center is the spectrometer for detecting radiation from the engine cylinder gases; and at the left is the electronic apparatus known as the Engine Radiation Ratio Indicator. The dynamometer, operating controls, and engine utilities (water, oil, air systems) are out of view from the picture.

Engine - The single-cylinder research engine has a bore and stroke of 3-3/4 and 3-7/16 in. respectively. It was adjusted to a compression ratio of 8:6. The cylinder head is of sandwich construction, made from an Oldsmobile-type single-cylinder head of 12.0 nominal compression ratio mounted on top of a 7/8 in. thick spacer containing the "end-gas pocket" with its viewing windows.

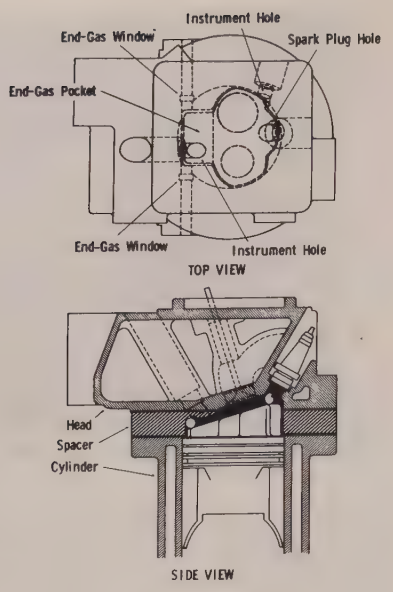

Fig. 2—Sandwich head engine combustion chamber with piston at top center

Fig. 2 shows the combustion chamber with the piston at top center, and illustrates the viewing windows, the end-gas pocket, the spark plug, and the two instrument access holes.

The aluminum piston has a built-up head which fits up into the spacer in such a manner as to keep the clearance volume small. Cooling passages in the spacer permit circulation of water from the system which cools the head and cylinder liner.

Air is supplied to the engine either from the atmosphere or from the building compressed air lines through a critical flow air-metering system. The latter system provides a relatively constant, low humidity of about 0.25% H_2O by weight. Air temperatures are controlled with an immersion electric heater in the surge tank ahead of the carburetor and electric heating tape wrapped around the intake manifold between the carburetor and the engine inlet valve. Inlet mixture temperature is indicated by an unshielded immersion thermocouple just ahead of the inlet valve in the manifold. The exhaust temperature, under motored conditions, is measured by an unshielded thermocouple in the exhaust port about 1/2 in. from the exhaust valve. Liquid fuel flows are measured with calibrated rotameters, propane flow by a critical flow metering system. Exhaust back pressure is varied with a gate valve in the exhaust manifold.

Performance measurements on this engine showed no unusual effects attributable to the sandwich combustion chamber design. The maximum IMEP at 2000 rpm was 150 psi; MBT spark advance was 31 deg at 2000 rpm; and the primary reference blend octane requirement at this condition was 98. Ionized-gap measurements of flame arrival time indicated that the end-gas pocket was actually one of the last parts of the chamber to be reached by the flame. The flame arrived in the pocket about 50 crankangle deg after ignition at the 2000 rpm maximum power condition. Cyclic variation of the arrival time was on the order of ±3-5 crankangle deg.

Optical System - Radiation from the end-gas pocket in the engine combustion chamber passes out through one of the 3/8 in. diameter by 3/16 in. thick quartz windows (the other window is not used for this work) and is focused on the spectrometer entrance slit by a quartz lens. The optical path length between the two end-gas windows is 2-7/8 in. The focal points of the lens are in the center of the engine end-gas pocket and at the spectrometer entrance slit.

A rotating shutter between the lens and spectrometer is driven by a selsyn system operated from the engine camshaft. The shutter interrupts the radiation beam for one complete engine revolution, starting to close 32 deg atc on the power stroke and reaching full-open 47 deg atc on the induction stroke. The purpose of this shutter is to provide a zero baseline for radiation on the detector and to prevent the extremely intense hot flame emission from reaching the detector and either changing its sensitivity characteristics or overloading the electronic circuits.

Between the shutter and the spectrometer slit is a multiple-wedge adjustable radiation attenuator. This optical attenuator is used to maintain a constant level of illumination on the radiation detector under the different operating conditions, thus keeping the detector in the linear portion of its operating range. The attenuator calibration also gives a measure of the relative signal intensity under the various operating conditions.

The detector signal from the hot flame radiation in the combustion chamber under some conditions is 500 times that from the unburned gases ahead of the flame front. Some of this radiation may reflect several times from various surfaces in the combustion chamber. If even a small portion of this radiation should enter the optical system before the hot flame actually reaches the window, it could interfere seriously with measurements of the unburned gas. Therefore, attempts were made to determine whether such interference does occur. A tungsten lamp was placed at various positions in the chamber, and the amount of radiation entering the spectrometer was measured. When the lamp was 1/4 in. away from the line of sight through the end-gas windows, the signal on the detector was reduced to about 1/100 of its direct value. This means that at this distance the reflected hot flame radiation may still be about five times stronger than the unburned gas radiation. Unfortunately, a light source as intense as the hot flame could not be conveniently placed in the engine. Therefore the distance at which a source of this strength would produce a negligible signal could not be determined. It can only be concluded that the hot flame probably affects the temperature measurements when it is within 1/4 in. of the windows, and very likely does not affect the measurements when it is near the spark plug at the far side of the combustion chamber.

Spectrometer - The spectrometer is a Perkin-Elmer Model 99 double-pass monochromator with a lithium fluoride prism and lead sulfide detector. The slits were kept at 2000 microns, a width necessitated by the extremely low radia-

tion intensities involved. The internal 13 cps chopper is not used, and single-pass radiation, which was found to interfere seriously with the measurements, is eliminated by masking portions of the spectrometer slits. The masking does not reduce the signal intensity appreciably, since only 1/3 of the slit length is illuminated even before masking.

In early work atmospheric air was allowed in the spectrometer, but it was later suspected that variations in atmospheric humidity were affecting the temperature measurements by varying the amount of self-absorption in the water vapor bands. From then on the spectrometer was flushed continuously with nitrogen. This change necessitated a complete recalibration of the temperature measuring technique, since both K_2/K_1 and ϵ_2/ϵ_1 were altered by the reduction in self-absorption. Much of the day-to-day variation in results, however, appeared to be eliminated.

Detector - Six different lead sulfide photoconductors were tested in an attempt to find the best detector for this work. The final selection was a Kodak Ektron lead sulfide cell with a time constant of about 800 microseconds. This time constant is barely adequate for engine studies at 2000 rpm. Several of the other detectors had much faster responses, but these detectors were completely inadequate with respect to signal-to-noise ratio.

The relative sensitivity of the lead sulfide detector at 2.55 and 1.89 microns (K_2/K_1 in Eq. 4) was determined by comparing the intensity ratio from a globar source at the two wavelengths as measured with the lead sulfide cell to the ratio as measured with a uniform-response thermocouple detector. The sensitivity ratio, K_2/K_1, determined in this manner was 0.581.

Engine Radiation Ratio Indicator (ERRI) - The ERRI has been completely described in previous publications.[8, 9] Its purpose is to permit the determination of the mean value (with respect to engine cyclic variations) of the detector signal voltage ratio at the two wavelengths. It functions as follows: The signal from the spectrometer detector, which varies with time in the engine cycle, is compared with a reference voltage level at any given instant during the engine cycle. The instant of comparison is determined by a pulse from a pulse generator which can be manually adjusted to any desired crank angle. A coincidence meter reads the percentage of cycles in which the engine signal voltage is greater than the reference level at the predetermined crank angle (thus "averaging" the engine cyclic variations). In use, the spectrometer is set to the wavelength of the weaker radiation (1.89 microns); the reference voltage level is adjusted for 50% coincidence at the desired crank angle (the reference level thus represents the mean cycle-to-cycle signal voltage); the spectrometer is then adjusted to the wavelength of the stronger radiation (2.55 microns), and this detector signal is electrically attenuated by means of a potentiometer to again give 50% coincidence. The fraction of attenuation required is equal to the ratio of the first signal to the second, and this fraction is read directly from the potentiometer dial. The dial is graduated in ten turns with 100 divisions for each turn. Thus, the signal ratio can be read directly to three significant figures. In the range of ratios used, 0.060-0.200, one division on the dial corresponds to about 5 F.

Although some consideration was given to making a continuous-recording temperature measurement system, rather than this point-by-point, cyclic-averaging system, the difficulties associated with very accurately recording the ratio of two rapidly varying voltages were thought to be out of proportion to the value of knowing the engine temperature variation throughout a single cycle.

Experimental Procedure

Like the proverbial babe-in-the-woods, our delicate end-gas temperature measuring systems venture only with the utmost caution into the savage holocaust of an operating engine cylinder. In the present study we have learned to walk in four distinct stages.

In the first stage we don't move at all, but simply look about to see what may be encountered. We make no temperature measurements, but rather see what the radiation from an engine looks like under typical motoring and firing conditions. We also examine the question of reproducibility.

In the second stage we start to move with actual temperature measurements in an engine motored with air alone. In this stage we determine the cylinder gas temperature both with the radiation technique and by calculation from pressure card data and air flow measurements using the perfect gas law. The calculated temperatures serve to calibrate the radiation technique by determining the emissivity ratio, ϵ_2/ϵ_1, and by holding on to this support we can, in fact, walk through a number of motored-air exercises, pretending to explore. This second stage, of course, makes no progress into the unknown because the radiation technique measures nothing that could not already be determined by other means.

In the third stage we let go of the support and walk alone, but we stay within the limits of a motored engine, adding various fuels this time to test the strength of our system a bit, and to allow for some exploration.

In the last stage we run pell-mell into the fired engine, acting in most respects as if we knew just about what we were doing.

The subsequent discussion will follow the general order of this experimental procedure.

Radiation from Engine

Spectra - Fig. 3 gives an indication of the types of radiation spectra obtained from the engine under typical motoring and firing conditions. Each spectrum represents the peak intensity of the unburned gas radiation plotted as a function of wavelength. The spectra are all plotted to the same

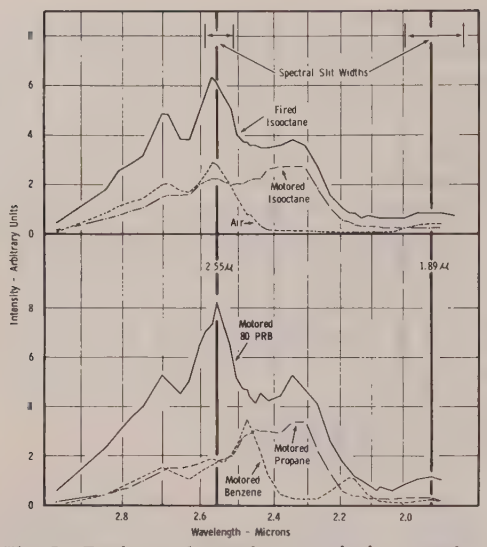

Fig. 3—Engine unburned gas emission spectra

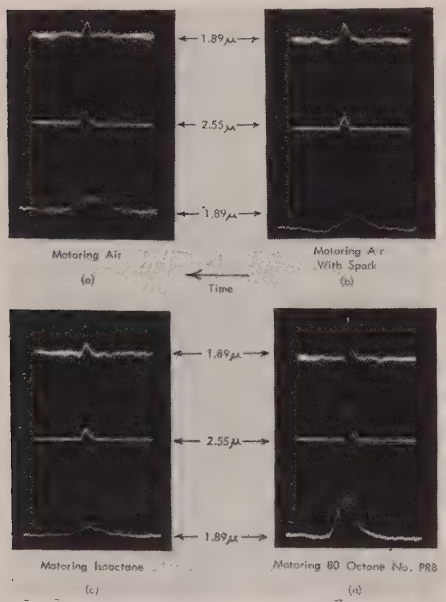

Fig. 4—Motored engine radiation traces

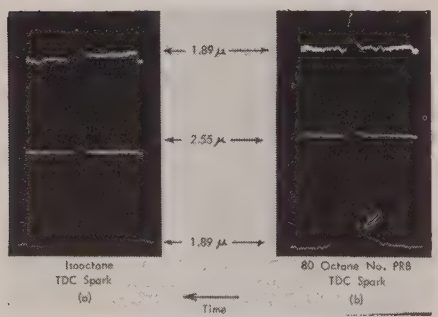

Fig. 5—Fired engine radiation traces

scale. The two wavelengths of water vapor emission at which the intensity ratio is determined are indicated by vertical lines along with the spectral slit widths resulting from the 2000 micron spectrometer slit.

The motored isooctane, benzene, and propane-air spectra have the lowest intensity; the motored air spectrum is slightly more intense at the water vapor wavelengths. The fired engine and the motored 80 octane primary reference blend spectra are considerably more intense because in these cases both the temperatures and the water vapor concentrations are higher. The water vapor content is higher in the fired engine because of residual dilution, and higher with the 80 octane fuel because of water production in the preflame reactions.

Of particular interest in Fig. 3 is the intense emission between 2.1 and 2.5 microns which apparently comes from the unreacted fuel (and perhaps partly from preflame reaction products). The spectral slit widths would seem to exclude this radiation from influencing the temperature measurements to any appreciable extent with isooctane, propane, and the primary reference blend. However, with benzene the fuel emission has a different distribution and it might be expected that the intensity reading at $\lambda_2 = 2.55$ microns would be increased by the fuel emission, tending to make the temperature readings lower than would otherwise be the case. No attempt was made to estimate the magnitude of this error.

Oscilloscope Traces - Figs 4-5 show a number of radiation traces photographed from the oscilloscope face during motoring and firing operation respectively. In each of these traces time progresses from right to left, and in the top two traces of each photograph the length of the trace corresponds to one engine cycle or 720 deg of crank angle. In most cases only a single engine cycle is recorded, although in some exposures portions of a second cycle appear. The top trace represents the radiation at 1.89 microns as it was presented for temperature measurement. The middle trace represents the radiation at 2.55 microns attenuated as it was for temperature measurement (the attenuation was on the order of 1/10). The lowest trace represents again the radiation at 1.89 microns, but this time the horizontal scale expanded.

Fig. 4A illustrates the case with motoring air. The trace is approximately symmetrical with the peak at tdc, or at most 1 or 2 deg after tdc.

Fig. 4B is identical to 4A except that the spark plug was fired at tdc. This photograph illustrates the problem of spark pickup encountered in the later fired-engine work. The small pip on the 1.89 micron trace, which occurred in spite of electrical shielding and a resistor in the high tension spark lead, introduced a serious error in the temperature measurement at the crank angle of the spark discharge. The problem was avoided by making measurements only at crank angles different from the spark timing.

Fig. 4C, when compared to 4A or 4B, illustrates the slight reduction in signal height accompanying the use of essentially non-reacting fuel-air mixtures.

Fig. 4D shows the large effect of cool flame reactions occurring with low octane quality fuels. The peak of the cool flame radiation is 8-15 deg after tdc, and the relative-

ly sharp cutoff of radiation a short time after the peak results from closing of the rotating shutter 30-40 deg atc.

Fig. 5A shows a fired engine cycle with the spark fired at tdc. The initial rise in the trace at the far right end occurs when the rotating shutter opens 30-40 deg atc on the intake stroke. The radiation level remains approximately constant throughout the intake stroke and most of the compression stroke. This radiation is presumed to come from hot solid materials in the optical line of sight--the quartz windows, deposits on the windows, and perhaps metal walls or reflections from metal walls. The spectrum of this radiation is continuous and thus could not represent gas emission. The gas emission was found to rise sharply above this level at 20-40 deg btc on the compression stroke, and the peak occurred in the vicinity of tdc. Sometime after the peak (20-40 deg atc) the radiation passes through a minimum and then starts to rise again as compression by the normal hot flame advancing across the combustion chamber finally overcomes the expansion caused by the receding piston. (The possibility cannot be ruled out that some of this increased intensity after the minimum also is contributed by reflected radiation from the hot flame itself.) The shutter is arranged to close in time to cut off the very intense direct emission from the hot flame.

The 2.55 micron trace does not show the second rise in emission after tdc as the 1.89 micron trace does. This results from the fact that as temperature increases, the 2.55 micron radiation increases more slowly than the 1.89 micron radiation (according to the laws of thermal radiation).

In order to gain an accurate measurement of the gas radiation intensity, aside from any solid continuous emission in the line of sight, the ERRI is arranged to maintain a baseline reference level[8] in the crankangle region between 70 crankangle deg before and after bdc on the intake and compression strokes. This is the center section of the flat, continuous emission portion of the cycle illustrated in Fig. 5A. In effect, this arrangement assumes that the gas emission is negligible in this portion of the cycle, an assumption which seems valid in view of the low temperature and low optical depth of water vapor during that period.

Fig. 5B demonstrates the effect of preflame reactions with a low octane quality fuel. For this case the signal was attenuated about 50% from that in the other photographs. A distinct inflection point in the trace at about 1 or 2 deg btc (as indicated by arrow) indicates the onset of preflame reactions. The signal peaks 5-10 deg atc.

Accuracy and Precision

The absolute accuracy of this temperature measuring technique is not known and probably cannot be known with certainty. The accuracy of the temperature data given here depends on:

a. The accuracy of the calculated gas temperatures for the motored air runs, which in turn depends on the accuracy of the pressure, airflow, other measurements, and on the assumptions involved in the calculation (see Appendix B).

b. The accuracy of the assumption that the temperature of the end-gas, as averaged by the radiation technique in the motored-air case, is represented by the calculated value (which requires that temperature gradients in the optical path be negligible with motored air).

c. The accuracy of the assumption that no additional factors become involved when measurements are made under conditions other than motored-air.

Since these factors may never be known for sure, perhaps it will be sufficient to rely on the "reasonableness" of the results obtained. This involves comparing the results with what might logically be expected from an engine and with results obtained by other independent, but perhaps equally uncertain, temperature measuring means. Attempts are made to check this "reasonableness" in the discussion of data to follow.

If accuracy eludes our grasp, certainly precision, or reproducibility, can be pinned down. Experience, which is illustrated in the data to follow, has shown that three classes of precision can be distinguished in this work, as follows:

1. The precision with which a single temperature reading could be made at one moment--i.e., the precision with which the ERRI attenuator dial could be set and read and a deviation from 50% on the coincidence meter was noticeable--was about +5F. This was essentially the reading precision of the instrument and included no allowance for drift in either the instrument or engine conditions.

2. The repeatability of readings for the same engine condition run from day to day or week to week with a motored engine was ±10-20 F. This variation is represented essentially by the scatter in the data on the individual curves shown later. It included the possibility of some drift in the instrument and engine operating conditions. This same precision existed for the fired engine in a given day's running.

3. The variation from day to day in the fired-engine studies, which included possible variations in ambient conditions, ranged up to ± 50 F.

It is of interest to note that the reading precision and short term reproducibility of the two-wavelength technique for temperature measurement are of the same order as those for the sound velocity and emission-absorption techniques.[1]

It appears possible that the large day-to-day variations in end-gas temperature encountered here for the fired engine may have resulted from variations in ambient humidity and its effect on burning rates in the engine. Such effects seem to have been magnified by the generally retarded spark timing used, so that power differences from day to day, apparently due to humidity changes, were also noted. Thus, it is quite possible that the ± 50 F precision mentioned in (3) above represents actual variations in engine end-gas temperatures and should not be charged to the temperature measuring technique as errors.

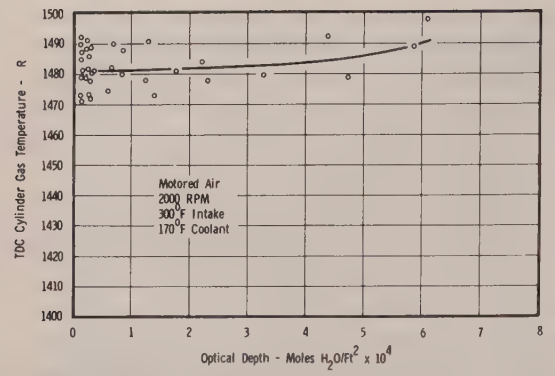

Fig. 6—Cylinder gas temperatures calculated from pressure cards with varying water vapor concentration

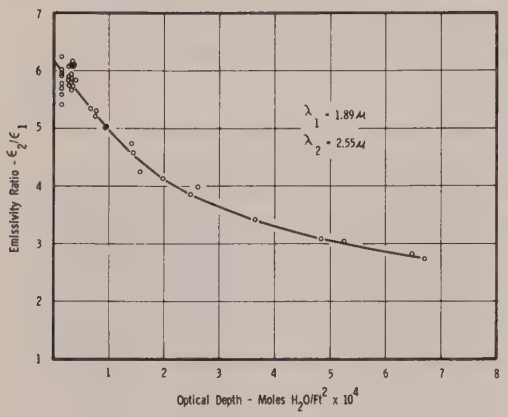

Fig. 7—Variation of emissivity ratio with optical depth

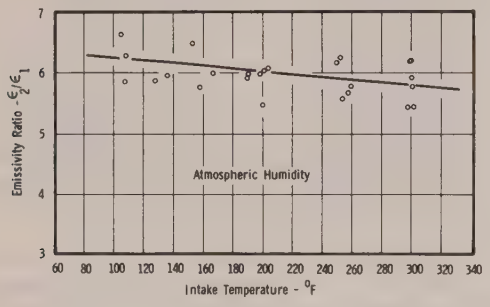

Fig. 8—Variation of emissivity ratio with intake temperature

Experiments with Motored Air

Determination of Emissivity Ratios - The emissivity ratios, ϵ_2/ϵ_1, were determined under motored-air conditions by comparing the measured radiation intensity ratios with temperatures calculated from pressure card, air flow, and exhaust gas measurements, using the perfect gas law. The method of this calculation is described in Appendix B. In Eq. 4 given earlier, B_1/B_2 was determined from the calculated temperature, D_1/D_2 was indicated by the ERRI, $K_2/K_1 = 0.581$, as mentioned previously, so ϵ_2/ϵ_1 could be calculated.

It was expected on theoretical grounds that water vapor concentration in the engine cylinder might have an appreciable effect on ϵ_2/ϵ_1, so an arrangement was made to permit the introduction of steam into the engine intake surge tank and to measure the partial pressure of water vapor in the intake air resulting from the added steam. From this the optical depth of water vapor in the engine end-gas could be computed and expressed in terms of moles of water per cu ft times the path length across the combustion chamber in ft, or moles/ft^2.

Fig. 6 shows the tdc cylinder gas temperatures calculated from pressure card data and the perfect gas law, as indicated in Appendix B, plotted against optical depth (water vapor concentration). There is a ± 10 F scatter in the data from the pressure measurements, but the trend is for little or no change in the end-gas temperature with changing water vapor concentration. An isentropic compression from fixed initial conditions would be expected to give a reduction in final temperature of the order of 50 F from the case with no water vapor to 6 $(10)^{-4}$ moles H_2O/ft^2. The deviation from the isentropic case here is unexplained, but may be associated with changing residual fraction, heat transfer, or inlet conditions.

The emissivity ratios determined as a function of optical depth are shown in Fig. 7. This curve is extremely important to the subsequent temperature determinations since it demonstrates a rather large effect of water vapor concentration on the calibration of the temperature measuring technique. The shape of the curve is explained by the fact that as optical depth increases, the absolute emissivities at each of the two wavelengths must approach the blackbody value of 1.0. Thus, the ratio itself, whatever it may be at low optical depths, must approach 1.0 as the optical depth increases.

The cluster of points around the optical depth of about 0.3 $(10)^{-4}$ moles/ft^2 represents conditions with atmospheric induction in the engine. The points at about 0.15 $(10)^{-4}$ moles/ft^2 were taken using the closed air-metering system, and the signal intensities were so low that considerable scatter in the data occurred. However, it must be recognized that a portion of the scatter in the emissivity ratio determinations actually arises from the pressure card data used in the perfect gas law temperature calculation, as evidenced in Fig. 6, and should not be charged to the radiation instrument.

It is perhaps of interest to note that for a Bunsen flame with a somewhat smaller optical depth than any measured here, and for slightly different wavelengths ($\lambda_1 = 1.819$, $\lambda_2 = 2.505$), Bernath, et. al.[3] obtained an emissivity ratio of 6.41, which shows a fairly good agreement.

Fig. 8 shows the effect of varying the engine intake temperature on the emissivity ratio. There is a slight tendency for ϵ_2/ϵ_1 to decrease as the temperature increases, but the effect is small. In Fig. 9 the data are replotted as a function of the calculated tdc cylinder gas temperature. For a 160 F change in cylinder gas temperature, the variation in ϵ_2/ϵ_1 appears to be negligible. For the same temperature

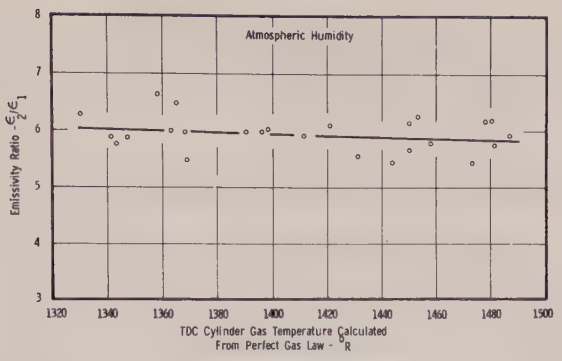
Atmospheric Humidity
Emissivity Ratio - ϵ_2/ϵ_1
TDC Cylinder Gas Temperature Calculated From Perfect Gas Law - °R

Fig. 9—Variation of emissivity ratio with cylinder gas temperature

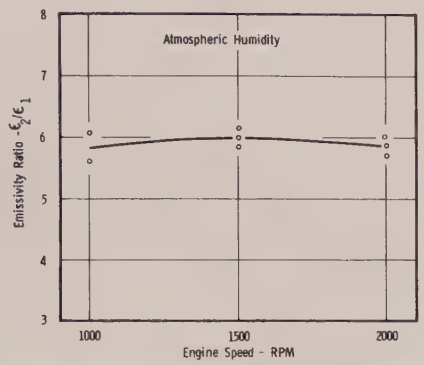

Fig. 10—Variation of emissivity ratio with engine speed

span, Bernath, et. al., [5] showed a variation in their ϵ_2/ϵ_1 from 6.45 to 6.41. Again the agreement is satisfactory.

Figs. 10-11 show that the coolant temperature and the engine speed had essentially no effect on the emissivity ratio in the ranges tested.

Temperature Measurements with Motored Air - In Figs. 12-14 the data discussed above have been turned inside out. The radiation technique is considered as "calibrated," and the temperatures calculated from the perfect gas law and the temperatures determined by the radiation technique, assuming a single value of the emissivity ratio (5.82) at atmospheric conditions from Fig. 7, have been plotted together. These results show how the temperature varies with motoring conditions and also indicate how well the radiation measurement compares with the perfect gas calculations when a constant emissivity ratio is assumed.

In Fig. 12, the scatter is fairly large, but a difference in slope of the two curves is still noticeable. This difference results from the small change in emissivity ratio noted in Fig. 8.

It is of interest to note that the cylinder gas temperature changes about 0.91 F for every degree change in intake temperature but only about 0.64 F for every degree in coolant temperature (Fig. 13) under these motoring conditions. These figures compare with values obtained from the University of Wisconsin work:[1] 0.85-1.15 F per degree of intake temperature, 0.5 F per degree of coolant temperature in a motored engine, and 0.2 F per degree of coolant temperature

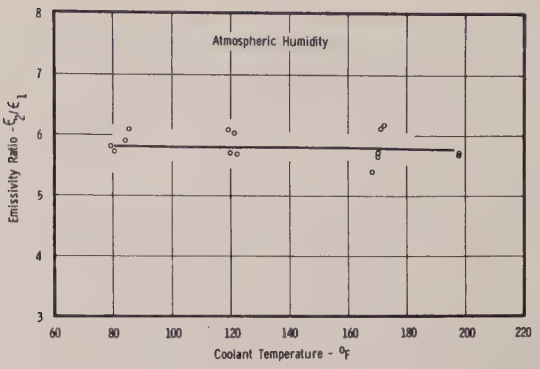

Fig. 11—Variation of emissivity ratio with coolant temperature

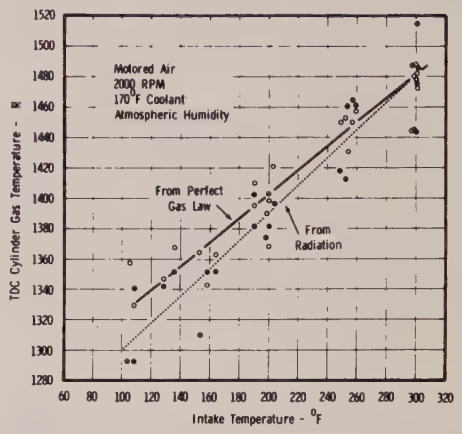

Fig. 12—Variation of tdc motored air temperature with intake temperature

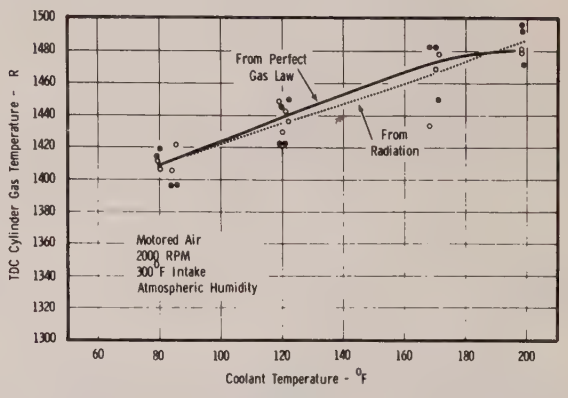

Fig 13—Variation of tdc motored air temperature with coolant temperature

in a fired engine. The MIT work[10] indicated values for peak end-gas temperature in a fired engine under somewhat similar conditions of about 1.1 F per deg for intake temperature and 0.38 F per deg for coolant temperature. The agreement is well within expectations.

The increase in cylinder gas temperature with engine speed, shown in Fig. 14, is attributed both to the reduced time for heat transfer from the gases to the cylinder walls and the reduced amount of work extracted from the fresh charge by the piston during the intake stroke at the higher speeds.[11] The latter effect results in a higher temperature

at the start of compression for higher speeds. The increase shown in Fig. 14 is about 90 F for a 1000 rpm change of speed, a figure which compares with values of around 30-80 F for a motored engine and 150 F for a fired engine found at Wisconsin,[1] and 50 F-100 F for a fired engine found at MIT[10].

Fig. 15 shows the cylinder gas temperature, emissivity ratio, and pressure as functions of crank angle in a motored engine. The reason for the drooping emissivity ratio on either side of tdc is not known. As the cylinder volume increases, the emissivity ratio would be expected to increase slightly with decreasing optical depth. The effect may be due simply to the poor detectability, since the radiation at the extremes of these data was very low. The radiation temperature was determined using $\epsilon_0/\epsilon_1 = 5.82$ from the emissivity ratio calibration curve given in Fig. 7.

It may be noted in Fig. 15 that both the radiation and calculated temperatures are nonsymmetrical with respect to tdc. The peak in both cases is 1-2 deg after tdc, whereas heat losses and gas leakage from the cylinder would both tend to make the peak occur slightly before tdc. The effect may have resulted from a slight reaction of the lubricating oil with the heated air in the cylinder. However, slight time lags in the pressure pickup and the lead sulfide radiation detector may also have been involved. In both cases, the effect seems small and should not seriously affect the general conclusions.

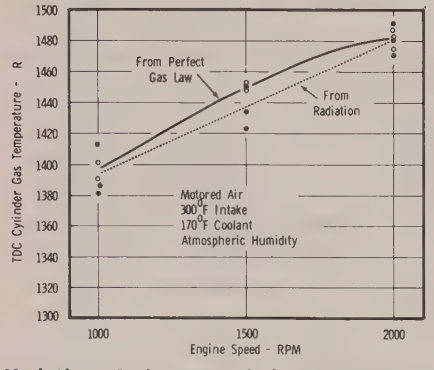

Fig. 14—Variation of tdc motored air temperature with engine speed

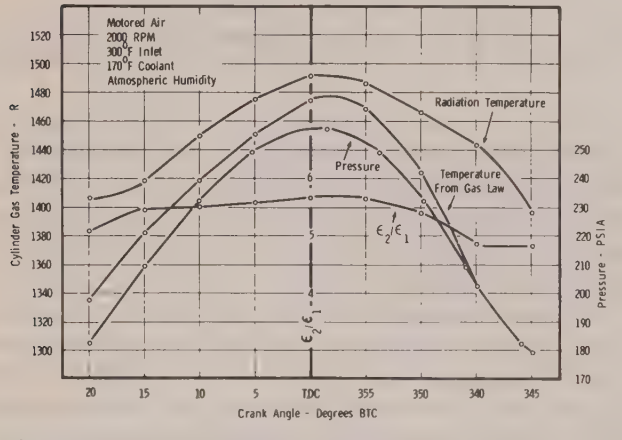

Fig. 15—Variation of motored air temperature, pressure, and emissivity ratio with crank angle

Experiments with Motored Fuel Air Mixtures

In Fig. 16 the cylinder gas temperatures attained in the motored engine with several different fuel-air mixtures are compared with that of air. The two runs for the 80 octane number primary reference blend were recorded three weeks apart and indicate the reproducibility of these data.

Benzene shows an approximately symmetrical temperature curve about tdc, indicating no preflame reaction. The 80 octane number primary reference blend, on the other hand, shows clear evidence of cool flame reaction which raises the temperature after tdc considerably above what it would normally be. Isooctane also shows a slight effect of preflame reaction, since it is considerably humped between tdc and 20 deg atc. Evidence of the preflame reactions was given also by the reduction of the horsepower required to motor the engine from 4.0 with air to 3.8 or 3.9 with isooctane and 3.3 with the 80 octane primary reference blend. The characteristic aldehyde odor of the cool flame exhaust was also evident with the low octane fuel.

It must be recognized at this point that with the occurrence of a cool flame in the engine cylinder in this case, we have the first instance in which the water vapor concentration, and consequently the optical depth, cannot be easily calculated from the known inlet conditions. Although the data in Fig. 16 are all calculated on the basis of atmospheric humidity, it is known that the cool flame reaction produces water, and, therefore, the temperatures indicated for this fuel should be corrected downward according to Fig. 7.

A correction procedure has been devised which is based on the fact that the signal strength at one wavelength is proportional both to the optical depth and to the temperature. Thus, if the relationship between signal strength and the optical depth is known by experiment, a trial and error solution permits an estimate of the optical depth and a cal-

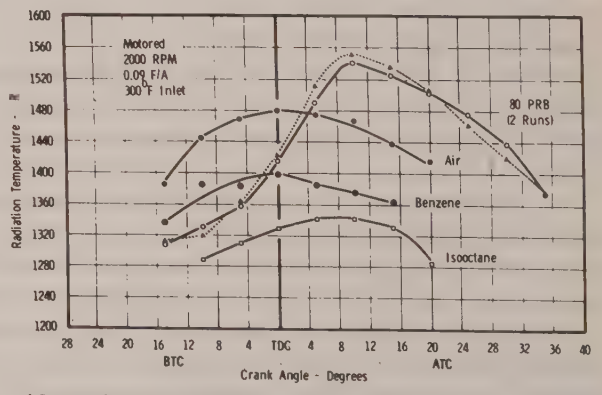

Fig. 16—Variation of radiation temperature with crank angle for various motored fuel air mixtures

culation of the corrected cylinder gas temperature. This procedure is fully described in Appendix C. Results of the correction for one of the 80 octane number primary reference blend curves of Fig. 16 is shown in Fig. 17. It may be seen that the correction is significant but does not change the character of the curve.

Fig. 18 shows the variation in cylinder gas temperature with changing fuel octane number. For a 75 octane reference blend it is concluded that the maximum temperature rise as a result of preflame reactions under these conditions is about 200 F. This may be compared with the previous experience of Downs, Street, and Wheeler[12] who recorded a 90 F rise with a fine wire resistance thermometer in a motored engine, and the MIT group[1] which recorded about 150 F rise with a fired engine.

Four different factors must be considered in explaining the fuel-air ratio effects in Fig. 19.

First of all, as the fuel concentration increases with any of the fuels, the ratio of specific heats of the mixture, k, decreases and consequently the temperature at the end of compression tends to be lower. Assuming an isentropic compression ratio of 8.6 and an initial temperature of 300 F, the final temperatures calculated for 0.08 F/A mixtures of the various fuels compared to air are shown in Table 1. The figures are in the same order as the corresponding curves in Fig. 19, but, of course, the values are much higher since they presume no heat losses during compression. Also, the magnitudes of the temperature differences are not in the same propostion as those in Fig. 19.

The second factor to be considered is that of liquid fuel vaporization. Since all of these fuels presumably passed the intake port at 300 F, only that vaporization which occurs inside the engine cylinder should be significant. The more volatile the fuel, the larger should be the portion of the total fuel supplied that vaporizes in the manifold, and the smaller should be the portion vaporized in the cylinder. On this basis, benzene should show less temperature reduction with increasing fuel-air ratio than isooctane. On the other hand, benzene has a higher latent heat of vaporization than isooctane, and so any portion which does vaporize in the cylinder should give a proportionately greater temperature reduction. Propane, of course, does not vaporize at all in the engine or manifold, and this perhaps explains the wide difference between it and the liquid fuels in spite of the small difference in isentropic compression temperatures.

The third factor is obvious from the 80 octane primary

Table 1 - Final Temperatures Calculated for 0.08 F/A Mixtures of Various Fuels Compared to Air.

Fuel	Air	Propane	Benzene	Isooctane
Isentropic Compression Temperature, R	1799	1725	1718	1699

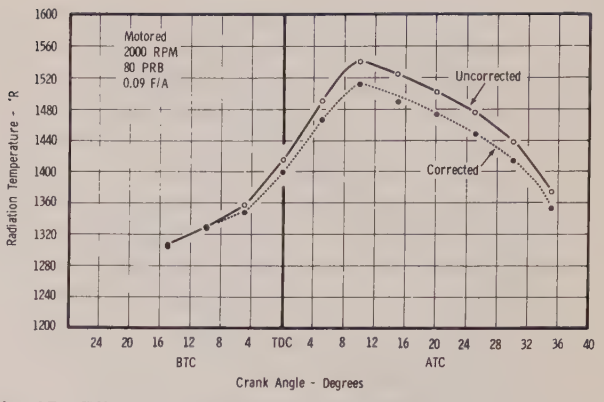

Fig. 17—Effect of the water vapor correction on the radiation temperature for a reacting fuel air mixture

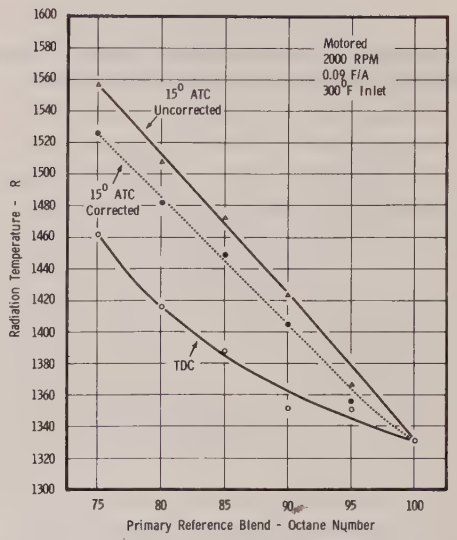

Fig. 18—Variation of radiation temperature with fuel octane number for a motored engine

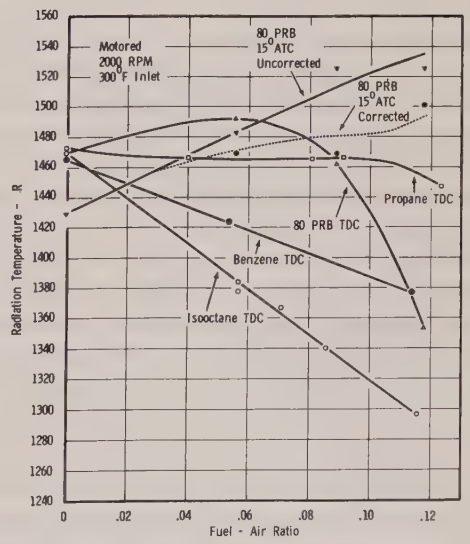

Fig. 19—Variation of radiation temperature with fuel air ratio for a motored engine

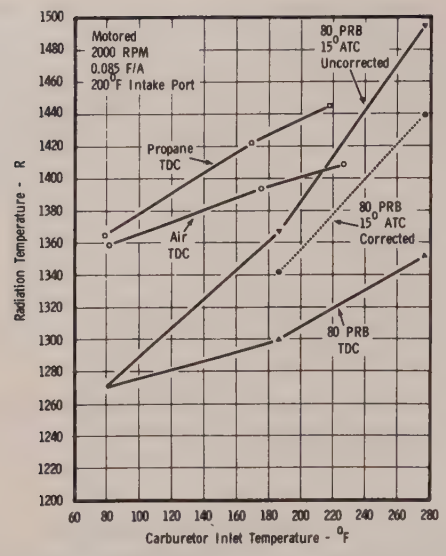

Fig. 20—Variation of radiation temperature with carburetor temperature at a constant intake port temperature

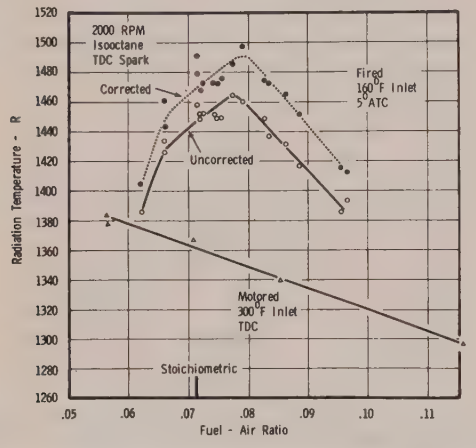

Fig. 21—Variation of radiation temperature with fuel air ratio

reference blend, which produces extensive cool flame reactions. At tdc the cool flame apparently tends to raise the temperature as fuel concentration increases, but the changing specific heat overcomes that tendency at the very rich mixtures. At 15 deg atc the temperature increases more or less continuously with fuel-air ratio as a result of the cool flame reaction, although the data are somewhat erratic at the richest mixtures.

The fourth factor involved in Fig. 19 is not obvious from the figure, but apparently involves the unshielded thermocouple in the engine input port, and is better illustrated in Fig. 20. For these tests the carburetor inlet temperature was varied with the surge tank heater while the intake port thermocouple was maintained at 200 F by adjustment of the intake manifold wall heater. With a constant intake port temperature it might be expected that the carburetor inlet temperature would have no effect on the cylinder gas temperature. However, this was not the case. As the carburetor

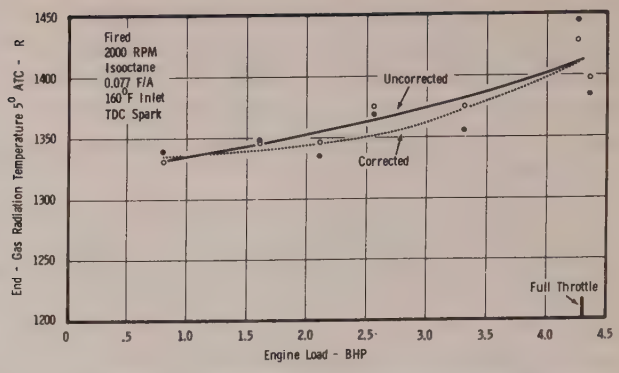

Fig. 22—Variation of end gas radiation temperature 5 deg atc with throttle position for a fired engine

temperature increased, the heat input to the wall heater in the manifold decreased and the radiation temperature at tdc in the engine increased, probably because the radiation error on the intake port thermocouple was decreased and the intake port temperature was actually going up. The fact that this effect occurred with propane and air indicates that fuel vaporization was not involved. The much larger effect with the 80 octane PRB at 15 deg atc resulted from the fact that the increasing intake temperature caused a cool flame reaction to appear. There was no cool flame evident at the lowest carburetor temperature (the signal was too weak to record a cylinder gas temperature here, but this temperature was known to be below 1270 R).

From the effects noted in Fig. 20, it was concluded that the intake port thermocouple reading was significantly affected by radiation from the manifold walls, and that the intake port temperature probably was also falsified by radiation errors during the fuel-air ratio experiments illustrated in Fig. 19. Thus, the intake port temperature may have decreased with increasing fuel-air ratio, making the curves in Fig. 19 steeper than they would have been at constant intake temperature.

Experiments with the Fired Engine

In taking the last step from a motored to a fired engine, it is immediately necessary to consider the large increase in water vapor concentration in the end-gases which results from the residual exhaust gases. In the present case, this was handled in two ways. First, the correction procedure developed in Appendix C and previously used for motored-engine cool flames was applied to one of the standard fired-engine conditions which was used repeatedly (0.08 F/A, tdc spark, 2000 rpm, isooctane). The correction factor indicated an average optical depth of $0.7\ (10)^{-4}$ moles/ft^2 and an average $\epsilon_2/\epsilon_1 = 5.30$ for this condition. This value was then used to compute radiation temperatures for all the fired-engine conditions studied. These values are indicated by circles and solid lines in Figs. 21-27, and are labeled "uncorrected" since they include no correction for variations in optical depth during the particular runs involved but only for

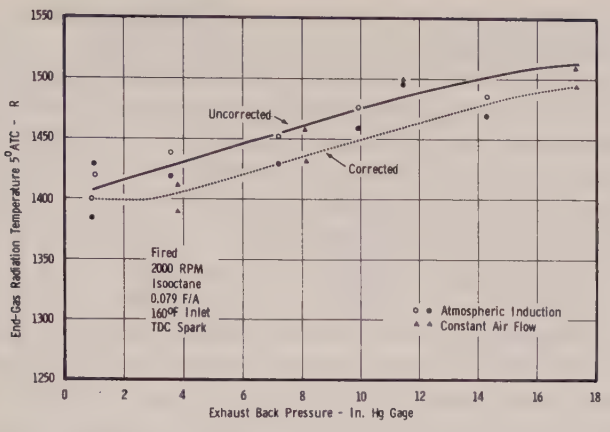

Fig. 23—Variation of end gas radiation temperature 5 deg atc with exhaust back pressure

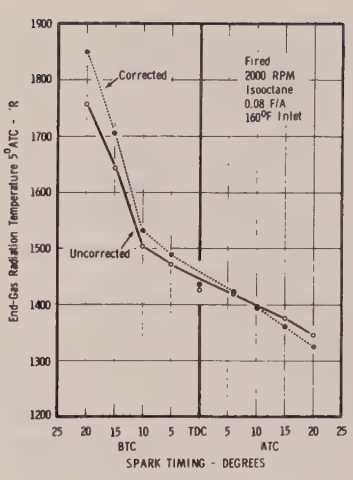

Fig. 24—Variation of end gas radiation temperature 5 deg atc with spark advance

the change from motored to fired engine. Thus, the solid curves represent the fired-engine temperatures which would result if no significant variations in optical depth occurred throughout the fired-engine operating conditions.

The second correction procedure consisted of applying the correction factor to each data point, and these results are indicated by dotted lines in Figs. 21-24. Comparison of these curves with the uncorrected curves indicates the effect of changes in optical depth during the particular run.

An additional consideration in the case of the fired engine was the possibility, mentioned earlier, that radiation from the normal hot flame in the combustion chamber might interfere with the end-gas temperature measurement at some time before the flame actually progresses all the way across the chamber. In anticipation of this problem, most of the fired-engine studies were made with a spark timing of tdc, much retarted from maximum power, in order to leave a wide range of crank angles around tdc available for measurement.

Fig. 21 shows the effect of fuel-air ratio in the fired engine compared with that in the motored engine. The temperatures were recorded at 5 deg atc in the fired engine in order to avoid electrical interference from the spark discharge. It is seen that the motored engine inlet temperature of 300 F is still insufficient to provide end-gas temperatures equal to those in the fired engine with a 160 F inlet. This difference would seem to be due to the hot residual gas dilution and much hotter cylinder walls in the fired engine as compared to the motored engine. The steeper fall of the fired engine temperatures on the rich side of maximum power fuel-air ratio (0.08) and the drop-off on the lean side would also appear to result from the effect of flame temperatures on the combustion chamber walls. The much reduced burning rates at very rich and lean fuel-air ratios would also be expected to lower the peak cylinder temperatures at the extremes of the range, although this would be compensated somewhat by corresponding increases in the exhaust residual temperatures.

These results are essentially the same as those found at MIT,[10] where the maximum end-gas temperature was found to be somewhere between the chemically correct fuel-air ratio and 20% richer. The emission-absorption technique at Wisconsin indicated a uniform decrease in end-gas temperature as the fuel-air ratio increased from lean to rich,[1] although with only three points measured, it is difficult to determine the exact shape of the curve.

Closing the engine throttle reduces end-gas temperatures, as indicated in Fig. 22. A number of interacting factors are again involved in this result: First, and probably dominating, is the 25% reduction in fresh mixture charge which was measured for the smallest throttle opening. This reduction in the amount of heat released in the engine per unit time might be expected to decrease cylinder wall temperatures and in turn the end-gas temperature. Second is the increased pumping loss (reduced amount of work extracted from the fresh charge by the piston during induction) which tends to increase the temperature at the start of compression in the same manner that increased engine speed does.[11] This effect counteracts the reduction in heat release and would tend to give a flatter curve than would otherwise be the case. Third is the increased heating of the fresh charge by a larger fraction of hot residual gases. This would tend to increase the end-gas temperature and again counteract the heat release effect. Fourth is the effect of increased residual dilution in reducing the burning rate in the engine. This factor has two compensating second-order effects: (1) it reduces the peak cycle temperature and consequently the wall temperatures, and (2) it increases the residual temperature.

These same factors are involved in a slightly different manner when the exhaust back pressure is increased (Fig. 23). This experiment was run both with atmospheric induction, in which case the fresh charge decreased with increasing back pressure, and with a constant fresh charge. Both procedures produced essentially the same effect on end-gas temperature. The indicated power reduction resulting from an increase of back pressure to 14 in. Hg was 40% with atmos-

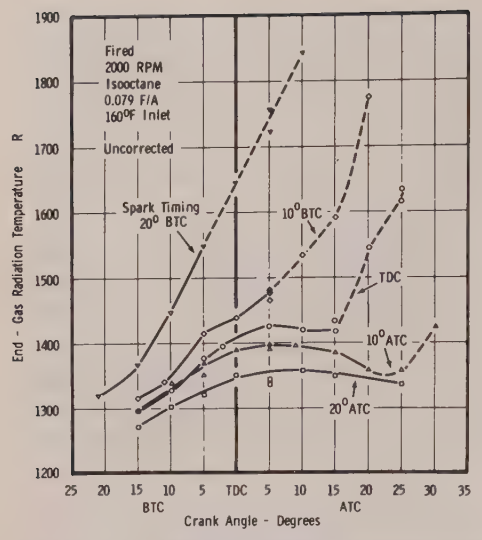

Fig. 25—Variation of end gas radiation temperature with crank angle for different spark timings

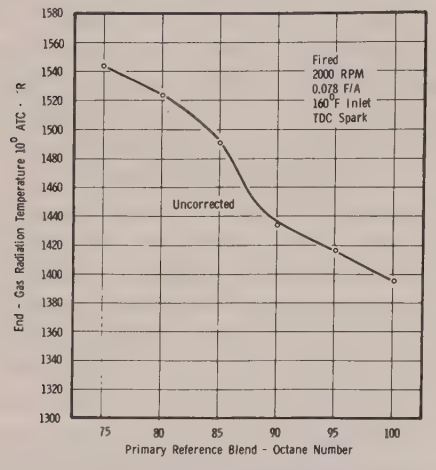

Fig. 26—Variation of end gas radiation temperature with fuel octane number for a fired engine

pheric induction and 34% with constant air flow. The air flow reduction with atmospheric induction was only 11%. It seems evident then that in this experiment, the factor of heat released per unit time, which appeared dominant when the engine was throttled, is minor or absent. Instead, the factor of increased temperature at the start of compression, due both to the increased amount and the increased temperature of the residual fraction, appears to dominate.

The results illustrated in Figs. 22-23 do not appear to be in disagreement with the corresponding data obtained by the velocity of sound technique.[10] In those results the end-gas temperature sometimes increased and sometimes decreased with increasing ratio of the exhaust pressure to the inlet pressure, depending on the particular engine conditions.

Since the correction factors in Figs. 21-23 were all relatively constant, there were apparently no significant changes in the optical depth under these conditions.

Advancing the spark timing (Fig. 24) evidently produces two distinct effects on the end-gas radiation temperature at 5 deg atc, as evidenced by the two different slopes in the curve. The slope in the flatter portion probably results from the effect of increased peak cycle temperatures (and consequently wall temperatures) compensated slightly by the reduced residual gas temperatures resulting from more efficient engine operation as the spark is advanced. With spark timings earlier than the measuring point at 5 deg atc the effect of end-gas compression by the advancing flame front might be expected to increase the end-gas temperature more steeply. However, two significant facts indicate that the change in slope in Fig. 24 arises from a more sinister cause. First, the change in slope occurs at a spark timing of 10 deg btc, not at 5 deg atc. Second, the correction factor, which is positive in this portion of the curve, indicates a decreasing optical depth rather than increasing, as would be expected from compression of the end-gas.

It appears that the sharp rise in the indicated end-gas radiation temperature at spark advances greater than 10 deg btc resulted from reflected radiation from the hot normal flame front which entered the optical path before the flame reached the end-gas. From Fig. 24 it would appear that this influence is felt approximately 15 crankangle deg after the spark fires (since it first appears with the spark 15 deg before the point at which the temperature is measured).

The same type of difficulty occurred with the data in Fig. 25. With the tdc spark advance run, the correction factor indicated a decreasing optical depth at crank angles greater than 15 deg atc, and the actual radiation traces on the oscilloscope indicated that the radiation was still decreasing at both wavelengths as late as 25 deg atc. Thus, the end-gas must have been still expanding from the downward motion of the piston. Nevertheless, the indicated temperature increased sharply 15 deg after the spark fired. The only ready explanation for this inconsistency is that hot flame radiation superimposed on that of the end-gas beginning at 15 deg atc.

Since the portions of the curves in Fig. 25 which are more than 15 deg after the spark firing all appear to be affected by the hot flame, and the correction factors for the rest of the data are all minor, only the uncorrected data are shown to avoid confusion.

Fig. 25 shows evidence of slight preflame reactions with isooctane since the curves with 10 and 20 deg atc spark timings are unsymmetrical about tdc in the same manner as the motored curve in Fig. 16. With lower octane fuels (Fig. 26) the end-gas radiation temperature at 10 deg atc rises, indicating still more extensive reaction. The data in Fig. 26 are again uncorrected because in this case the iteration correction procedure failed to converge for fuel octane numbers below 95. Here the correction tended to be in the right direction, indicating more water vapor concentration with lower octane fuels, but the amount was indeterminable. It appears that at the very high optical depths occurring in this instance (these were the highest encountered in this work)

the correction procedure breaks down for some unexplained reason. From experience with the motored engine, the increase in water vapor concentration resulting from the cool flames might be expected to have only a moderate effect on the overall trend, but the data must remain uncertain to the extent of this correction.

Fig. 27 shows the difference in the radiation temperature histories for isooctane and 80 octane primary reference blend. The data are again uncorrected. The maximum difference in the two curves is here about 150 F, in fair agreement with the motored engine, although correction for the change in water vapor concentration would be expected to reduce the difference somewhat.

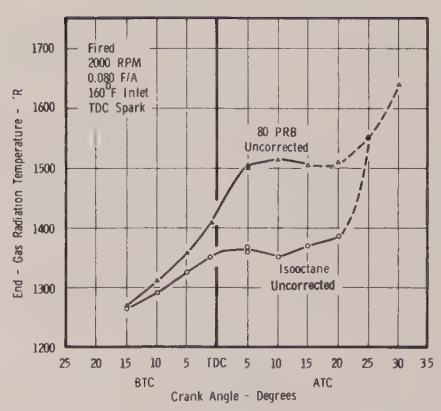

Fig. 27—Comparison of temperature time histories for low and high octane number fuels

Conclusion

Engine end-gas temperatures can be measured by the two-wavelength infrared radiation technique with adequate precision under a variety of operating conditions. Several advantages of the method recommend it over other techniques currently in use, although its most significant contribution to date appears to be its use as an independent source of information on end-gas temperatures for comparison with the other methods.

Limitations remaining with this temperature-measuring technique are concerned with the time at which radiation from the normal flame in the cylinder begins to interfere with the unburned gas temperature measurement, and the correction of the temperature readings for changes in optical depth under conditions of very high water vapor concentration. While neither of these problems is believed to have appreciably affected the general conclusions reached here, they remain as serious factors to be solved in any future application of this technique.

Unburned gas temperatures have been shown to increase with increasing inlet temperature, coolant temperature, engine speed, spark advance, throttle opening, and exhaust back pressure, and with decreasing fuel octane number. End-gas temperature is a maximum near the maximum power fuel-air ratio and decreases for richer and leaner mixtures. In general, engine cylinder wall temperatures, as affected by the peak cycle temperature, appear to have a strong influence on end-gas temperature.

Acknowledgement

Considerable credit is due to Prof. John T. Agnew of Purdue University (who is unrelated to the author) for much fruitful discussion and assistance during the course of this work, and to Merrill L. Haviland and others who have helped with the experimental work. Robert R. Bockemuehl and A. J. Gioia were responsible for the design, construction, and testing of the ERRI.

References

1. "Development of Techniques for Measuring Gas Temperatures in Internal Combustion Engines," Coordinating Research Council, Final Summary Report, New York, March, 1960.

2. J. T. Agnew, W. G. Agnew, and K. Wark, "Comparison of Emission Spectra of Low Temperature Combustion Reactions Produced in an Engine and in a Flat-Flame Burner," Sixth Symposium (International) on Combustion, New York: Reinhold Publ. Co. (1957), 894-902.

3a. "Temperature, Its Measurement and Control in Science and Industry," Am. Inst. Phys., Vol. II, New York: Reinhold Publ. Co., (1955).

3b. S. S. Penner, Quantitative Molecular Spectroscopy and Gas Emissivities, Reading, Mass: Addison-Wesley Publ. Co., (1959), 457-459.

4. O. A. Uyehara, P. S. Myers, K. M. Watson, and L. A. Wilson, "Flame Temperature Measurements in Internal Combustion Engines," Trans. ASME, Vol. 68, (1946), 17.

5. L. Bernath, H. N. Powell, G. A. Robison, F. Welty, and K. Wohl, "The Determination of the Temperature of Non-Luminous Flames by Radiation in the Near Infrared," London Conference on Heat Transfer, Joint Meeting ASME and IME, (1951), 315.

6. W. G. Agnew, "The Application of Radiation Techniques to Engine Combustion Studies," General Motors Engineering Journal, May-June, 1956, 14.

7. P. S. Myers, O. A. Uyehara, and M. C. Burrows, "Development of a Method for Measuring Gas Temperatures in the Combustion Chamber of an Engine," University of Wisconsin, Coordinating Research Council, Second Quarterly Status Report Covering Period April 1 to July 1, 1958.

8. R. R. Bockemuehl, "Gated Amplitude Ratio Indicator," Proc. Nat. Electronics Conf., Vol. 14, (October, 1958).

9. R. R. Bockemuehl, "Gated Ratio Indicator Aids Engine Research," Electronics, (March 27, 1959).

10. J. C. Livengood, C. F. Taylor, and P. C. Wu, "Measurement of Gas Temperature in an Engine by the Velocity of Sound Method," SAE Trans., Vol 66, (1958), 683. See also: C. F. Taylor, J. C. Livengood, E. A. Jeffery, and P. C. Wu, "Development of a Method for Measuring Gas Temperatures of an Internal Combustion Engine," Massachusetts Institute of Technology, Final Report, DA-19-020-ORD-3699, (September 15, 1955-September 30, 1956).

11. J. C. Livengood, A. R. Rogowski, and C. F. Taylor, "The Volumetric Efficiency of Four Stroke Engines," SAE Quarterly Trans., Vol. 6, (1952), 617.

12. D. Downs, J. C. Street, and R. W. Wheeler, "Cool Flame Formation in a Motored Engine," Fuel 32, (1953), 301.

Appendix I

Effect of Temperature Gradient on Two-Wavelength Temperature Indication - As an example, the gases in the engine end-gas pocket are assumed to have a temperature distribution as indicated in Fig. 28. The window surface temperatures are assumed to be 900 R and the maximum gas temperature 1400 R. The boundary layer in which the temperature falls by increments from the maximum value to the wall value is assumed to be 1/6 of the path length. Allowing the emissivity of the central portion of gas to be 0.1. and assuming the emissivity to be unaffected by temperature or wavelength, the emissivity for each of the smaller zones will be 0.013 by Lambert's and Kirchhoff's Laws. The contributions to the emitted radiant energy from the different gas zones can then be added up using the blackbody slide rule, as shown in Table 2.

If the emissivity in the central portion of the gas path is increased to 0.6, a similar calculation results in an average indicated temperature of $T_{average}$ = 1388 R. These figures are to be compared with the peak temperature of 1400 R and the mass average temperature of 1300 R for this distribution.

For a similar distribution it has been calculated[7] that the infrared emission-absorption technique would give an indicated temperature of about 1345 R, and the sound velocity method would give[1] a value of 1306 R. Thus, the two-wavelength method is seen to give the closest value of the three methods to the maximum temperature, and the sound velocity method comes closest to the mass average.

Table 2 - Contributions to Emitted Radiant Energy from Different Gas Zones (added up on blackbody slide rule).

At 2.55 microns

$I_1 = 0.013\ (169.3)$	$= 2.2$ watts/cm^3
$I_2 = 0.013\ (1200) - (0.013)^2\ (1200)$	$= 15.4$
$I_3 = 0.1\ (2465) - 0.013\ [0.1\ (2465)] - 0.013\ \{0.1\ (2465) - 0.013\ [0.1\ (2465)]\}$	$= 240.1$
$I_4 =$ . . . . . etc	$= 13.7$
$I_5 =$ . . . . . etc	$= 1.9$
$I_{2.55}$	$= 273.3$

At 1.89 microns

$I_1 = 0.013\ (24.1)$	$= 0.3$ watts/cm^3
$I_2 = 0.013\ (333.7) - (0.013)^2\ (333.7)$	$= 4.3$
$I_3 = 0.1\ (884) - 0.013\ [0.1\ (884)] - 0.013\ \{0.1\ (884) - 0.013\ [0.1\ (884)]\}$	$= 86.2$
$I_4 =$ . . . . . etc	$= 3.8$
$I_5 =$ . . . . . etc	$= 0.2$
$I_{1.89}$	$= 94.8$

$I_{2.55}/I_{1.89} = 2.88 = B_2/B_1$

From the blackbody radiation law:

$T_{average} = 1390$ R.

Appendix II

Sample Calculation of Cylinder Gas Temperature from the Perfect Gas Law - As an example, a motored-air condition is taken in which steam is added to the intake surge tank in order to increase the optical depth. The following engine data are observed:

N = Speed = 2000 rpm

P = Pressure at tdc from indicator = 268 psia

W_{fa} = Weight of fresh air metered to engine = 1.014 lb/min

P_{i_1} = Inlet surge tank pressure before steam addition = 28.9 in. Hg

P_{i_2} = Inlet surge tank pressure after steam addition = 29.9 in. Hg

Ti = Inlet Temperature = 300 F

Te = Temperature of exhaust gas in exhaust port = 577R

pi = Exhaust gas pressure = 14.5 psia

Vc = Volume of combustion chamber at tdc = 0.00287 ft^3

The weight of water vapor in the fresh metered air, W_{wo}, was estimated at 0.24%, or

$W_{wo} = 0.0024\ (W_{fa}) = 0.00244$ lb/min

The weight of water vapor added to the surge tank as steam, W_{wa}, is determined from the partial pressure of the water vapor and the molecular weights of air and water:

$$W_{wa} = \frac{P_{i_2} - P_{i_1}}{P_{i_1}} \frac{18}{28.97} (W_{fa}) = 0.0218 \text{ lb/min}$$

The total weight of water in the fresh charge then is:

$W_{wf} = W_{wo} + W_{wa} = 0.0243$ lb/min $= 0.243\ (10)^{-4}$ lb/cycle

and the total weight of fresh charge is:

$W_f = W_{fa} + W_{wa} = 1.0358$ lb/min $= 0.0010358$ lb/cycle

The gas constant for the wet mixture, R_m, is calculated from the values for air ($R_a = 53.3$) and water ($R_w = 85.8$) as follows:

$$R_m = \frac{R_w (W_{wf}) + R_a (W_{fa} - W_{wo})}{W_f} = 54.0$$

The weight of residual mixture trapped in the engine cylinder at the end of the exhaust stroke is assumed to be determined by the cylinder clearance volume, V_c, and the pressure and temperature of the residual gas. The residual gas temperature is assumed to be that measured for the exhaust gas in the exhaust port, Te. The residual gas pressure is obtained from the series of experiments illustrated in Figs. 29-32. Fig. 29 shows the pressures measured in the engine cylinder with a balanced diaphragm pickup during the period when the residual gas is trapped. It is noted that there is a pronounced effect of engine speed on the pressure at tdc, probably the result of surge effects in the exhaust manifold.

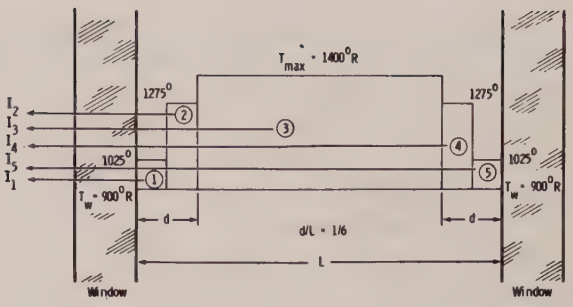

Fig. 28—Assumed temperature distribution in the optical path

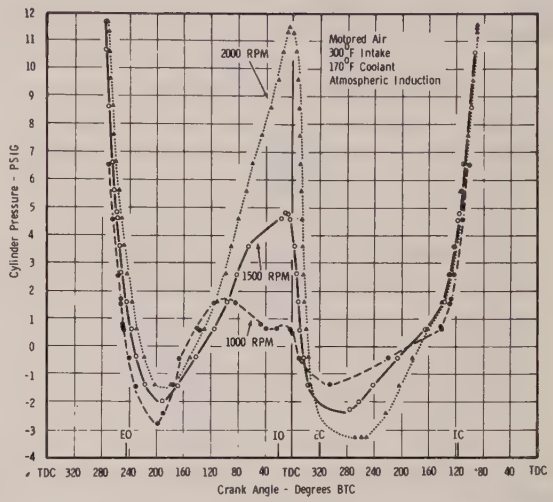

Fig. 29 — Cylinder pressure during the residual trapping period for three speeds

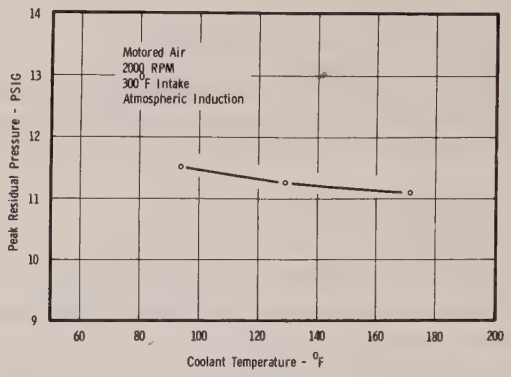

Fig. 30—Variation of peak residual pressure with coolant temperature

It was assumed for this work that the residual trapping pressure, p_r, was the value given at tdc. Figs. 30-32 show that this pressure is affected somewhat by the coolant and intake temperatures and by the amount of water vapor added. In the present example, from Fig. 32,

$p_r = p_e + 11.3 = 25.8$ psia

and the weight of residual

$$w_r = \frac{p_r V_c}{R_m T_e} = 0.000342 \text{ lb/cycle}$$

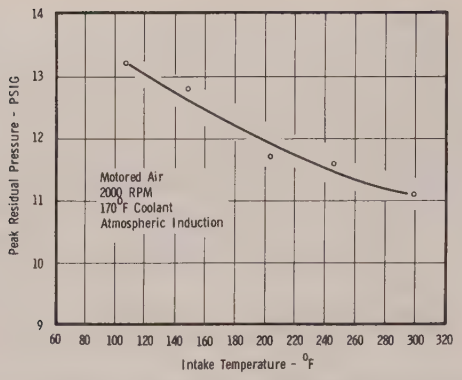

Fig. 31—Variation of peak residual pressure with intake temperature

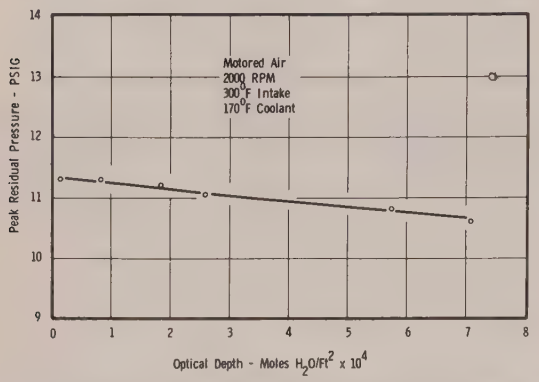

Fig. 32—Variation of peak residual pressure with water vapor concentration

The total weight of charge in the cylinder is:

$W_t = W_f + W_r = 0.001378$ lb/cycle

Tests showed the blowby for this engine to be of the order of 1% at 2000 rpm, so this factor was neglected. The perfect gas law then gives the cylinder gas temperature at tdc as:

$$T_c = \frac{p\,V_c}{R_m\,W_t} = 1491\ R$$

The optical depth is given by the path length, $X = 2.875$ in. and the concentration of water vapor in the clearance volume according to:

$$OD = \frac{W_{wf}}{18}\,\frac{W_t}{W_f}\,\frac{X}{V_c} = 1.495\ (10)^{-4}\ \text{moles/ft}^2$$

7. Repeat (3) through (6) until convergence gives the corrected temperature and the optical depth.

Taking as an example the point of Fig. 21 at 0.089 F/A, let it be assumed that several trials have led to an estimated temperature of 1452 R. Then follow these steps:

1. The reference condition (closed air metering system) has T = 1485 R, optical depth = $0.145\ (10)^{-4}$ moles/ft^2, and $I_1 = 1.13$.

2. Try 1452 R.

3. For a change in temperature from 1485 R to 1452 R, I_1 would be expected to decrease by a factor of 0.819 (from blackbody slide rule).

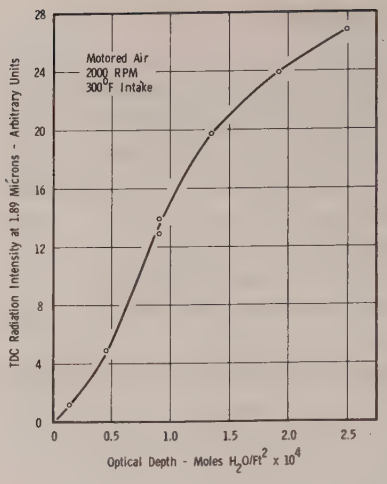
TDC Radiation Intensity at 1.89 Microns - Arbitrary Units
Motored Air
2000 RPM
300°F Intake
Optical Depth - Moles H2O/Ft2 x 10^4

Fig. 33—Variation of tdc radiation intensity at 1.89 microns with optical depth in a motored engine

4. The actual intensity was 3.34 times the reference intensity, so that an intensity increase of 3.34/0.819 = 4.08 must be attributed to increased optical depth.

5. From Fig. 33 at 4.08 times the reference intensity of 1.13, the actual optical depth must be $0.430\ (10)^{-4}$ moles/ft^2.

6. From Fig. 7, $\epsilon_2/\epsilon_1 = 5.62$, and calculating from Eq. (4), T = 1452 R.

7. The calculated temperature agrees with the assumed value, so the result is acceptable.

Appendix III

The Correction of Temperature Measurements for Optical Depth Variations - In order to calculate the cylinder gas temperature from the measured intensity ratio, it is necessary to know the emissivity ratio, and, according to Fig. 7, this in turn requires that the optical depth be known. In cases, where the water vapor concentration in the engine (optical depth) is not known, it is possible to estimate this quantity from the intensity of radiation at any single wavelength since the intensity increases continuously with optical depth as well as with temperature.

Fig. 33 illustrates a typical relationship observed between the intensity of radiation at 1.89 microns and the optical depth. These data were recorded with a motored engine operating with steam added to the intake air. This relationship varies somewhat as the engine window becomes dirty, as the optical alignment varies, and as the detector sensitivity varies. However, the correction procedure in most cases is relatively insensitive to this variation and only a crude estimation of optical depth appears necessary.

Although Fig. 33 represents the variation of intensity with optical depth at a constant temperature (see Fig. 6), in the usual case both temperature and optical depth are unknown

variables. The temperature calculation depends on the optical depth (via ϵ_2/ϵ_1), but the optical depth is determined from the intensity, which depends also on the temperature. Thus, a trial-and-error solution is required. The iteration procedure is as follows:

1. Choose a reference condition for which the temperature, radiation intensity, and optical depth are all known. (The lowest data point on Fig. 33, corresponding to the closed air metering system, was generally used.)
2. Calculate the temperature using the emissivity ratio determined from Fig. 7 assuming no change in the optical depth from the reference condition, or assume some reasonable value of the temperature.
3. Calculate the change in intensity from the reference condition which would be expected to result from the difference in temperature alone (using the blackbody law).
4. Compare the actual intensity change from the reference with that expected from temperature alone. Any difference is presumed due to a change in optical depth.
5. From the change in signal attributed to optical depth and the relationship illustrated in Fig. 33, determine the change in optical depth from the reference.
6. From the optical depth so determined, find a new value of emissivity ratio from Fig. 7 and recalculate the temperature.

Discussion

Value of the Emissivity Ratio

John T. Agnew
Purdue University

AS A CONSULTANT to General Motors, I have been working with Mr. Agnew on this particular project for several years, so it is difficult for me to make either a constructive or an adverse criticism which we have not discussed many times in the past.

I would, however, like to comment on two particular aspects of this technique of end-gas temperature measurement. The first has to do with the data shown in Fig. 12, concerning the comparison of the motored air temperature as calculated from pressure card data and the perfect gas law, and the temperature as measured by the two-wavelength radiation method. It was reassuring that these temperatures agreed quite well with a reasonable value of the emissivity ratio, but a rather disconcerting fact still remains which may need further consideration. This is the fact, as was pointed out in the paper, that the radiation temperature probably corresponds more closely to the maximum gas temperature, whereas the temperature calculated from pressure card data and the perfect gas law should correspond more closely to the mass average temperature. Since the difference between these two temperatures can be as much as 100 F at the 1000 F level, it would seem that the emissivity ratio used to calculate the radiation temperature should be revised. This assumes, of course, that the methods for calculating the mass average temperature are beyond reproach.

My second comment has to do with the primary difficulty with this method of temperature measurement; the fact that the emissivity ratio is critically dependent on the optical depth of the engine end-gas. It is believed that this difficulty could be largely overcome by improving the calibration technique for emissivity ratio as a function of optical depth. This probably could be done more satisfactorily in a separate accurately instrumented flow experiment in which the detecting instrument could view a constant temperature stream of air of known thickness and water vapor content. This more precise calibration, combined with the iterative correction technique described in the paper, should allow more accurate temperature measurement by the two-wavelength method. Such experiments would also provide calibration data relative to the temperature distribution problem.

One final point which may be lost in the presentations today concerning the various methods of measuring end-gas temperature, is the fact that we are very close to if not actually to the point where end-gas temperature can be measured, even under conditions where considerable pre-reaction has taken or is taking place. Calculation of end-gas temperature with pressure card data and an equation of state is not only difficult but probably impossible under these conditions. Therefore, we have at our disposal techniques for gaining an insight into the factors limiting the performance of internal combustion engines, insofar as the combustion process itself is concerned, whether this combustion limitation is autoignition of the end-gas, or particle ignition of the primary mixture.

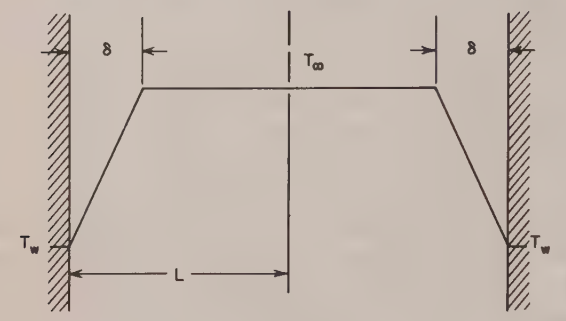

Fig. 1

Table 1 - Summary of Comparative Defined Temperatures

T_∞	= 1400 F	(Free-Stream)
T_{IR}	= 1345 R	(Gas Radiation)
T_{SV}	= 1306 R	(Sound Velocity) (4)
T_{MM}	= 1301 R	(Mass Mean)
T_{SM}	= 1320 R	(Space Mean)
T_{AM}	= 1150 R	(Arithmetic Mean)

The Measurement in an Engine by

M. C. Burrows
Lewis Research Center

S. Shimizu
Nagoya University, Japan

P. S. Myers, and O. A. Uyehara
University of Wisconsin

KNOWLEDGE of the measured pressures and temperatures in an engine can greatly aid the analyses of processes leading to combustion. Both of these properties, when properly defined and accurately measured as a function of time, can be used to study knock, heat transfer, and other phenomena.

The Subcommittee on the Fundamentals of Detonation of the Coordinating Research Council, Inc., (CRC), recognized the need for measurement of the temperature-pressure-time history of the end gas prior to the occurrance of knock in a firing engine. In 1953 they published the results of a feasibility study of four methods for measuring end-gas and compression temperatures (1)*. These methods included:

1. Thermocouples.
2. Determination of the velocity of sound.
3. Emission of electromagnetic radiation.
4. Absorption of electromagnetic radiation.

Subsequent to that study, three measuring techniques were developed, under CRC sponsorship, into instruments capable of measuring temperatures of the gases in an engine. They were:

1. The sound-velocity method at Massachusetts Institute of Technology.
2. The iodine absorption pyrometer at the University of Wisconsin.
3. The infrared radiation pyrometer, also at the University of Wisconsin.

The sound-velocity technique of temperature measurement is described thoroughly in the literature (2) (3) (4), and preliminary results obtained by the iodine absorption pyrometer have been published (5). The infrared radiation pyrometer will be described in this paper together with simultaneous and comparative temperature-time histories obtained by the other two instruments.

Factors Influencing Measured Gas Temperatures

The actual temperature measured in a given volume of gas in the chamber of an engine depends on the boundary conditions and thermal gradients present in the gas at the instant that the measurement is made. Thus, any technique for measuring the gas temperature must be analyzed for the effect of the nonisothermal behavior of the gas as well as the effect that the measuring technique itself may have on the gas volume being studied.

Unlike pressures in the engine cylinder, which are normally equalized rapidly throughout the volume of gas, temperatures are not the same in all parts of the gas when heat transfer and gas motion are present. Thus, there are vari-

*Numbers in parentheses designate References at end of paper.

# of Unburned Gas Temperatures

an Infrared Radiation Pyrometer

ous "temperatures" that can be defined in a given gas volume. In the absence of walls and high gas velocities which may cause temperature gradients, the temperature of the gas is uniform and is called the free-stream temperature. As the influence of the walls and gas movement becomes apparent, temperature must be defined, that is, free-stream temperature, mass mean temperature, arithmetic mean temperature, or average measured temperature. In addition, when chemical reactions are present, there may be temperature gradients in the molecules themselves, in which case one can speak of rotational, vibrational, and electronic temperature as well as the translational temperature of the gas molecules.

Since the temperature gradients and gas motion cannot be avoided in the operating engine, their influence must be known before the appraisal of a measuring technique is complete.

Analytical Comparison of Measuring Techniques

A convenient method of comparing the gas temperatures measured by the various techniques is that of computing an average measured temperature for each technique of a gas volume with an assumed temperature profile along its length. These temperatures can then be compared with values of the arithmetic mean temperature, mass mean temperature, and so forth, for the same volume of gas. Such a computation was made for the assumed temperature profile in Fig. 1 using the equations for the various comparative temperatures given in appendix II.

For wall temperatures of 900 R, free-stream temperature of 1400 R, and boundary layer as shown, comparative defined temperatures are summarized for a δ/L ratio of 1/3 in Table 1.

The physical meaning of the various comparative temperatures must now be considered in order to evaluate the significance of the average measured temperatures. Since the arithmetic mean temperature is merely the average of the wall and free-stream temperatures of the gas volume, it has little real value. The same is true for the space mean temperature, since it is the mean value of the temperature-distance diagram in Fig. 1. The mass mean temperature is the temperature obtained if the gases are adiabatically mixed until thermodynamic equilibrium is achieved.

The two temperatures that have the greatest significance in a gas volume within the engine are probably the free-stream or peak gas temperature and the mass mean temperature, since the first would give the maximum rate of chemical reaction and the second the energy present at a given time. If two of the measuring techniques are compared with the free-stream and mass mean temperatures for a series of temperature profiles, the results are as shown in Figs. 2 and 3. It may be seen that the sonic-velocity instrument measures a temperature near that of the mass average, and the infrared pyrometer measures a temperature close to the peak gas temperature.

The choice of the measuring technique obviously depends on the measurement of temperatures which have the greatest effect on the physical parameters being varied. For example, the peak temperature is probably the most important temperature in controlling end-gas reactions, whereas the mass-mean temperature is probably the most important temperature in controlling the total heat transfer in the engine chamber.

It may even be possible to obtain information on the actual temperature gradients in the engine chamber by simultaneously using measuring techniques with different characteristics.

Infrared Radiation Pyrometer

To measure the gas temperatures in the engine chamber before ignition, it is desirable to have the pyrometer

1. Sensitive to the low level of gas radiation present in the measuring zone.
2. Respond to extremely rapid temperature fluctuations.

3. Give consistent, reproducible, and accurate results.
4. Offer minimum interference with the engine combustion chamber.

A radiation pyrometer has the distinct advantage of having little or no effect on the gases and hence on their temperature. However, for maximum sensitivity it should utilize a wavelength band in the infrared range, since the principal radiation from the compression gases is in that range (6) (7). After considerable experimentation using water vapor as the sensing medium in the compression gases, an instrument was developed similar in principle to those utilizing sodium line reversal but much more sensitive to temperatures of the gases before ignition (7).

Principle of Operation - The required components of the infrared radiation pyrometer are shown schematically in Fig. 4. Radiation from the hollow cavity of the sources passes through sapphire windows and the gases in the engine chamber to a quartz lens which focuses the radiation on an infrared-sensitive detector. An interference filter placed between the lens and the detector restricts the radiation falling on the surface of the detector to a wavelength band from 2.5 to 2.9 microns (10^{-4} cm). Since the transmitted wavelength band corresponds to the emission-absorption bands of water vapor and carbon dioxide, radiation from those gases is transmitted to the detector along with a portion of the source radiation.

Equations describing radiation received by the detector are discussed in appendix II. Briefly, they can be summarized as follows: If the engine cylinder is assumed to have transparent walls, radiation can pass from the black-body source through the gas and filter to the detector. If there is negligible gas present in the chamber (corresponding to intake in the engine), the detector will receive radiation from the black-body source alone, restricted only by the spectral filter which transmits radiation from 2.5 to 2.9 microns. When the gas in the chamber increases in pressure and temperature (corresponding to compression in the engine), the detector will receive radiation from the gas in addition to the portion of radiation from the source that is unabsorbed.

When the absorption of black-body radiation by the gas is exactly equal to the radiation emitted by the gas itself, the radiation received by the detector will be exactly the same as that received from the black-body source alone. This condition is defined as the null point, or point at which the gas temperature equals exactly the black-body source temperature. Therefore, for every source temperature, there is a corresponding equal gas temperature, and a series of null points result in a measured temperature-time curve. The so-called null method is a point-by-point technique; that is, one gas temperature is measured at a particular time or crank angle, and a certain minimum time is required to record one complete cycle of temperature-time data from many cycles of operation.

If a mechanical chopper is placed between the black-body source and the gas in the chamber, and its blades emit negligible radiation, an additional radiant flux that is proportional to the gas radiation alone will be received by the detector. The three levels of radiation, when measured in terms of intensities, result in the following equation:

$$\ln\left(\frac{I_1 + I_3 - I_2}{I_3}\right) = \frac{C_2}{\lambda}\left(\frac{1}{T_{IR}} - \frac{1}{T_b}\right) \qquad (1)$$

where the terms are as defined in appendix I. From Eq. (1), the null method of operation is evident when I_1 equals I_2. Then it is apparent that the measured gas temperature must equal the black-body source temperature. From the equation, it appears that the gas temperatures can be measured as a function of time for the entire engine cycle with a given source temperature. However, as will be shown later, the chopped method of operation of the pyrometer does not have the accuracy of the null method and, therefore, was not used in obtaining the final engine data.

Instrument Components and Their Characteristics - The preceding analysis of the operation of the instrument included only ideal components. The limitations of the components themselves must be considered as well as the factors to be considered in applying the pyrometer to the engine environment.

The reference source for the pyrometer was a uniformly heated cylindrical cavity with a thermocouple mounted in its interior as shown in Fig. 4. The walls of the cavity were uniformly oxidized iron resulting in an overall emissivity of 0.98 for the cavity which required only a few degrees' temperature correction.

The engine was equipped with transparent windows to transmit the radiation through the engine. Artificial sapphire was used because of its strength and high transmission of radiation in the 2.7 micron wavelength range. Radiation losses through the windows as well as those due to the slow accumulation of dirt on their inner surfaces were corrected in terms of the measured temperature of the gas (see appendix II). For accurate measurements, the direct accumulation was not allowed to become greater than that which would produce a 5% reduction in transmission. In most cases this did not impose any limitations on the operation of the engine as long as excessive oil accumulation in the combustion chamber was avoided.

A 1 in. diameter quartz condensing lens stopped down to an aperture of about 0.5 in. focuses the radiation from the source and engine gases on the surface of the detector with a demagnification of 6 to 1. The short focal length of the lens (1.5 in.) keeps the length of the entire apparatus at a minimum for convenience. Limiting apertures along the entire optical length eliminate internal reflections, one cause of measurement errors. As a further precaution, the interior of the pyrometer was coated with carbon. The pyrometer was experimentally checked on a bench setup for

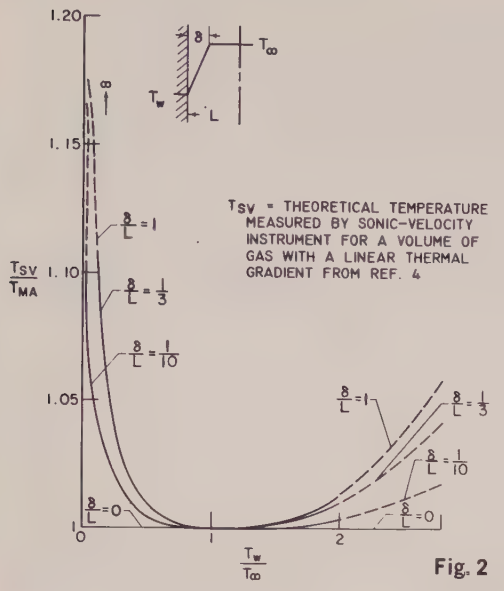

Fig. 2

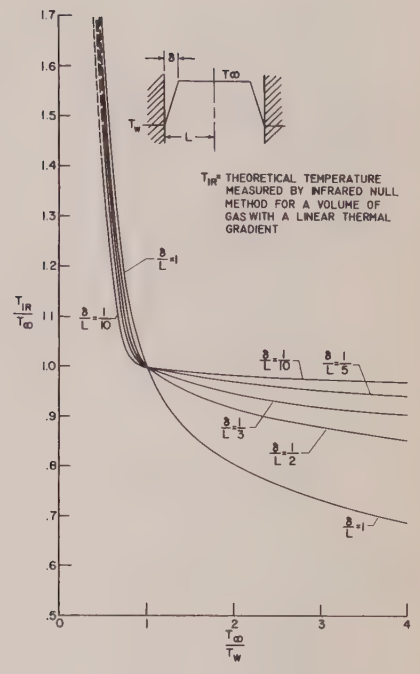

Fig. 3

optical alignment and the assurance that only radiation within the volume of gas between the windows was received by the detector.

A multilayer interference filter was used to isolate the 2.7 micron band of water vapor. Its transmission characteristics proved to be adequate for good separation of the wavelength band between 2.5 and 2.9 microns as well as overall high transmission with a maximum of 75% at 2.6 microns.

It is readily observed that all of the preceding components of the pyrometer are essential, and any one of them is capable of determining the success or failure of the instrument to measure gas temperatures adequately. However, when considering pyrometer sensitivity only, it was found that the detector was the limiting factor, since the improvements in the rest of the pyrometer were insignificant when compared with a sensitive or insensitive detector.

The maximum radiation during combustion is 10^3 times that during the compression stroke. This makes it necessary for the detector to withstand the intense radiation during the combustion and exhaust phases of the engine cycle and recover to measure the low-level radiation during the compression stroke. Initially, lead sulfide detectors were used in the pyrometer. However, when exposed to combustion radiation, they rapidly developed a fatigue characteristic that affected their response to the low-level radiation. A rotary shutter was, therefore, inserted to prevent combustion and exhaust radiation from reaching the detector. A recently developed detector (8) made of gold-doped germanium and cooled to liquid nitrogen temperature has proved to be much more stable and does not require the use of a rotary shutter. The sensitivity of the germanium detector is about equal to the lead sulfide detector for spectral radiation at 2.7 microns. The time required for the gold-doped germanium detector to respond to a step function of radiation is 0.2×10^{-6} sec as compared with 100×10^{-6} sec for evaporated-type lead-sulfide detectors. Chemically deposited lead-sulfide detectors of similar sensitivity were even slower in response (300×10^{-6} sec) and caused an error of as much as 100 R in temperature measurement when the engine was motoring at high speed.

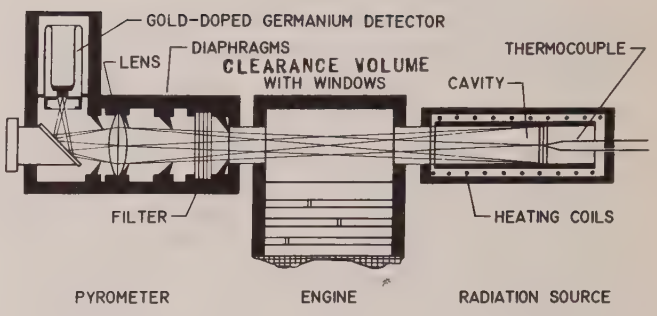

Fig. 4

The detectors used in the infrared radiation pyrometer were photoconductive in nature; that is, their resistance was proportional to the radiant energy impinging on the sensitive surface area. The detector was connected in one side of a bridge circuit as shown in Fig. 5. The bridge was coupled to a cathode follower output, and the signal was transmitted via coaxial cable to the vertical axis on an oscilloscope.

Engine Instrumentation

The infrared radiation pyrometer was used to measure the

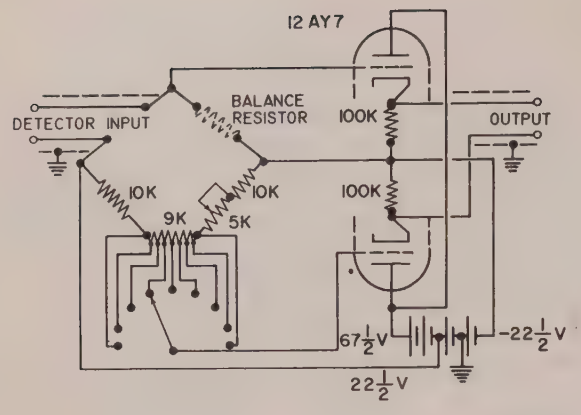

Fig. 5

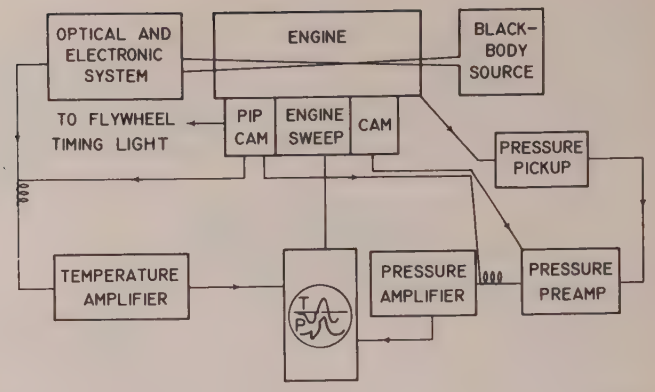

Fig. 6

gas temperatures in three different combustion-chamber configurations:

1. A modified 7-hole CFR head used during the instrument development phase.
2. A specially pocketed combustion chamber made for comparison tests in cooperation with MIT.
3. A modified ell-head combustion chamber used for comparison tests with the iodine-absorption pyrometer.

The rest of the engine consisted of a standard high-speed CFR crankcase with all of the accessory drive shafts.

Engine load was supplied by a cradled dc dynamometer. The fuel and air were metered separately by a calibrated flowmeter and critical-flow orifices, respectively, and mixed in a steam-jacketed mixing tank before entering the engine. Inlet pressure was controllable over a wide range, and exhaust pressure was held at one atmosphere. Cooling water in the jacket was controllable in the range 60 - 210 F.

To measure the compression gas-temperature by the null method, the engine was instrumented as shown in Fig. 6. Several sets of breaker points were installed on the engine accessory drive shafts to trigger the oscilloscope at the proper instant for the measurement of both the radiation and pressure signals. Fig. 7a shows the radiation and pressure signals as they would appear on the oscilloscope when the engine was motored without fuel and the oscilloscope had a long sweep duration. When the sweep duration was reduced several times, the oscilloscope display appeared as shown in Fig. 7b with line X corresponding to engine intake conditions and line Y corresponding to engine compression. The crossing point of the two lines was readily determined by adjustment of a breaker connected to a high-voltage source and timing light which illuminated the timing marks on the flywheel. The pressure-time signal was altered in shape by a breaker and calibrated potentiometer so that gas temperature and pressure could be obtained simultaneously at each crank-angle.

The black-body source was slowly heated, and the data on temperature, pressure, and crank angle were recorded. This procedure required that the data be recorded over a number of engine cycles, the average time for a complete record being 10 to 15 minutes.

Analysis of Measured Gas Temperatures

Extensive engine data were taken by the infrared pyrometer to evaluate the instrumentation and recording method. Each set of data was analyzed with regard to its reproducibility, accuracy, and internal consistency.

The reproducibility of the infrared pyrometer was checked on many motored runs taken on different days and with several different configurations of the optical system in the pyrometer. The results are shown in Fig. 8. The maximum scatter in the measured gas temperatures was ±22 R. Fired engine data by the pyrometer also showed good reproducibility over a shorter period of time (Fig. 9).

Because of the speed with which the engine phenomena occurred, the accuracy of the infrared pyrometer could not be directly measured. For this purpose, the engine was replaced by a steady-flow system which provided gas temperatures up to 1300 R and velocities as high as 60 fps. Although the pressure in the duct was atmospheric, engine conditions were approximated by artificially controlling the water-vapor content of the air passing the measuring zone in the heated duct section. The instrument responded to variations of the moisture content of the gas except when the gas and source temperatures were equal. Thus, the null point could be found without varying the gas temperature. Reference temperatures of the gas were obtained by a shielded thermocouple probe which could be traversed through the entire cross section of the measuring zone.

Accuracy of the null method of recording gas temperatures was within ±5 R of the probe temperature when sufficient water vapor was present in the hot gases passing through the duct (Fig. 10). Additional data were obtained for three different path lengths and varying water-vapor density in the gas. These results are shown as representative curves in Fig.

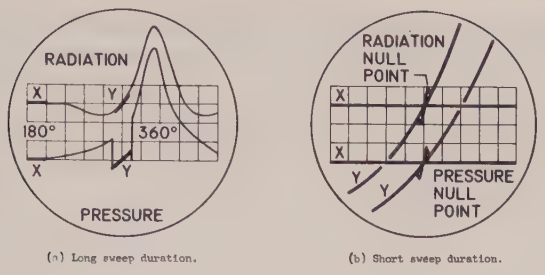

(a) Long sweep duration. (b) Short sweep duration.

Fig. 7

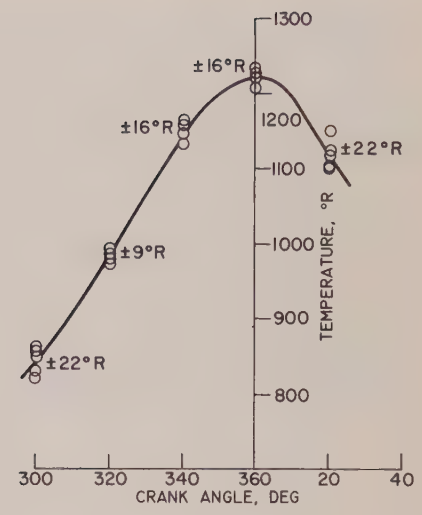

Fig. 9

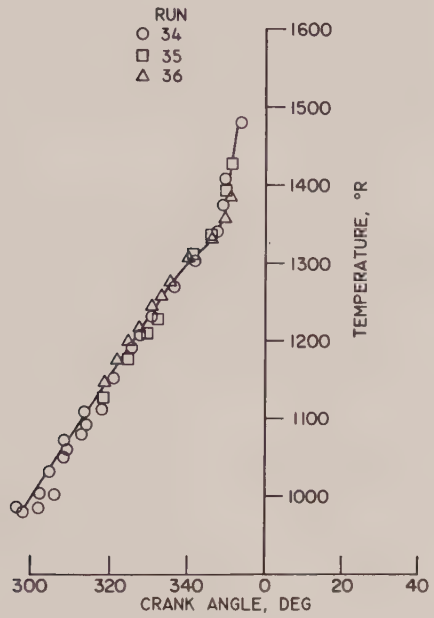

Fig. 8

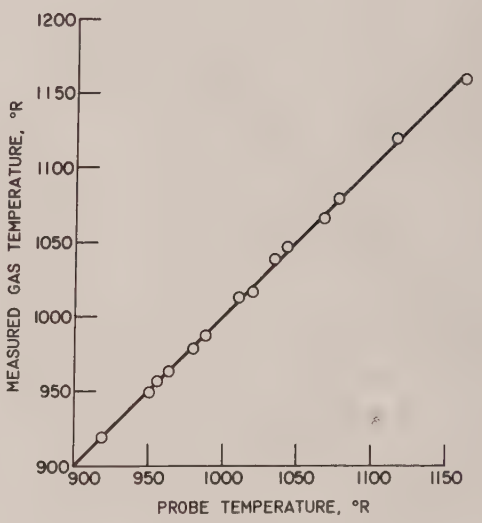

Fig. 10

11 along with the typical water-vapor density near the start of compression in the engine (intake air at 540 R and 80% relative humidity).

The chopped method mentioned earlier as a possible means of recording data showed consistent inaccuracies which varied according to the curve in Fig. 12. Engine data by this method showed that a temperature correction was necessary which depended on the black-body source temperature and the temperature difference between the black-body source and the gas. Causes for the errors in measurements by the chopped method were not obvious and could be due to:

1. Improper bandwidth of the pyrometer for nonequilibrium measurements.

2. Inequality of the total gas emissivity and total gas absorptivity for nonequilibrium conditions.

Since the null method of recording gas temperatures required no correction other than that for the source and win-

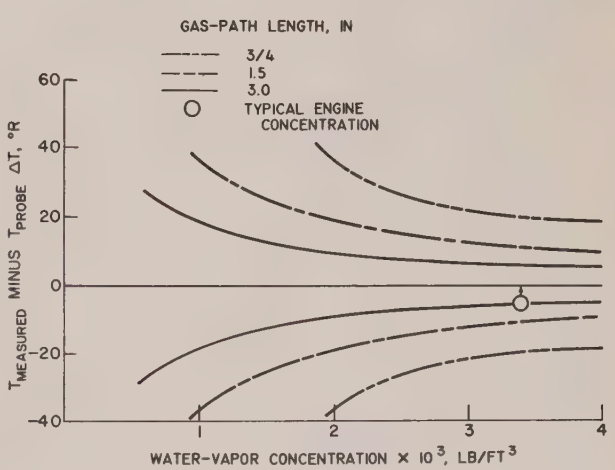

Fig. 11

dows, it was considered the best method of operation for obtaining the radiant gas temperatures reported herein. However, it did have the disadvantage of requiring a number of engine cycles to obtain a complete curve of temperature against crank angle.

To estimate the accuracy of the engine data, it was possible to compare the measured gas temperatures with those calculated for isentropic compression according to the equation

$$T_2 = T_1 (V_1/V_2)^{k-1} \qquad (2)$$

where point 1 is the point of closing of the intake valve and point 2 is any point on the compression stroke.

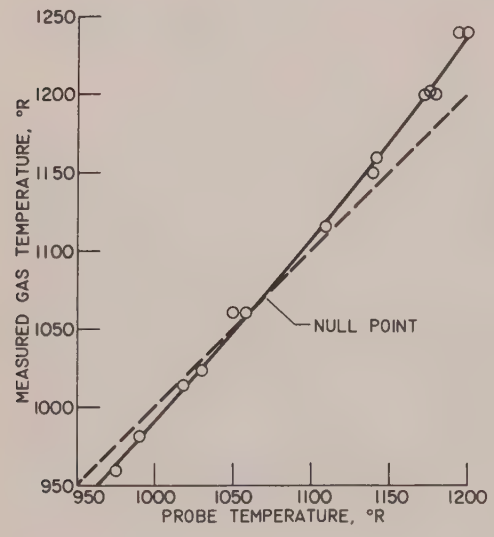

Fig. 12

Measured weight flow, estimated weight of clearance gas, and measured pressure were used to determine the initial temperature in the chamber, and Modified Air Charts (9) were used to obtain the isentropic compression data. Another comparison was made with the average temperature calculated from the measured pressure and volume and based on the measured temperature at 300 deg crank angle. Results of these comparisons are shown in Fig. 13. The motored runs show measured gas temperatures and comparative calculated average gas temperatures at three different engine speeds.

It has been stated earlier that the measured gas temperatures by the infrared radiation pyrometer departed from the mass-average temperature with increasing thickness of the boundary layer. This would be the case in the engine when the gases are compressed assuming a nearly constant value of wall temperature. It would be even more pronounced in an engine with a pocket or end-gas region where the gas path is very short.

In order to evaluate the internal consistency of the data within itself, the measured temperatures were plotted logarithmically against pressure for the motored data already discussed, and the slopes of the ln T - ln P curves were measured to find the apparent polytropic exponents for the engine processes (Figs. 14 and 15). Departure from the isentropic value n = k was considered due to the heat transfer from the gases to the walls and the thermal boundary-layer influence on the measured radiant gas temperatures.

The weight of charge derived from measured temperature, pressure, and volume was plotted against crank angle in the form W/W_{310} to show its constancy as derived from

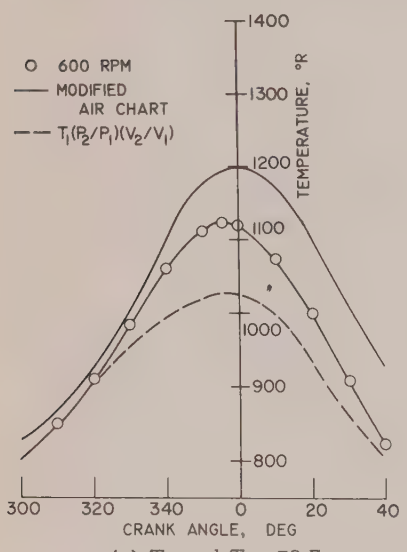

(a) T_i and T_j, 78 F

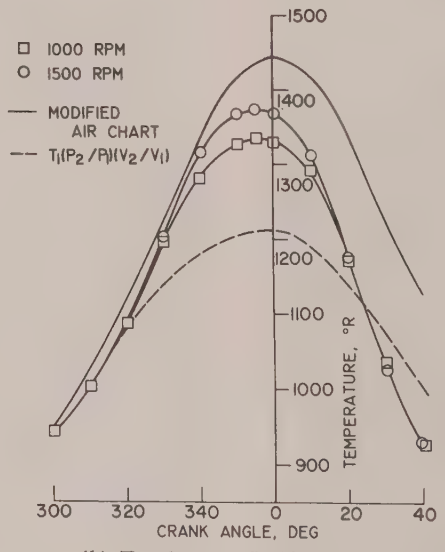

(b) T_i, 200 ± 5 F; T_j, 110 F

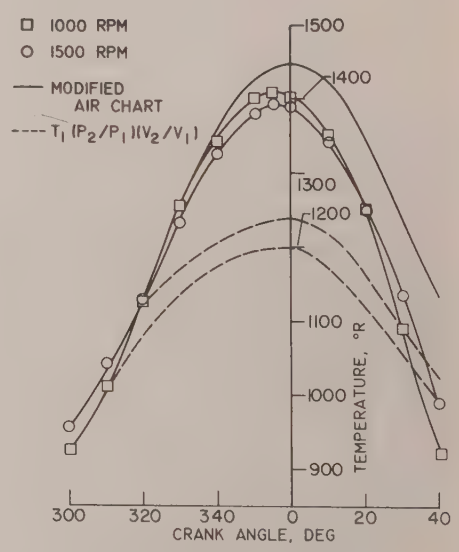

(c) T_i and T_j, 200 ± 5 F

Fig. 13

the three measured quantities. Its fluctuation with crank angle can be explained on the basis of the thermal boundary effect. Since the measured gas temperatures were above the mass-average temperature, the result was a lowering of the apparent mass weight in the cylinder as the gas temperature increased because of compression by the piston.

Comparative Engine Data

Comparative engine data were obtained on a specially pocketed chamber with the infrared pyrometer and velocity-of-sound instrument mounted as shown in Fig. 16. Simultaneous temperature measurements of the same gas volume were taken in this manner, with the pyrometer having a 3/4 in. path length and the velocity of sound transducers having a 5/8 in. path length. The final comparison of measured gas-temperatures by both techniques is shown in Fig. 17. Reproducibility limits for the simultaneous measurements varied from ±20 to ±30 R over the temperature range. Both instruments were operated under less than favorable conditions, the infrared pyrometer having a much shorter gas path than usual and the velocity-of-sound instrument a longer path than was customary.

The analytical effect of the boundary layer on the measured temperatures by the two techniques was considered earlier; now the experimental data can be compared on the basis of a temperature gradient and plotted in the form shown in Fig. 18. The shaded portion represents the final comparison data. Both the analytical and experimental data have the same trend, and the apparent increase in the boundary-layer thickness is not surprising when considering the decreasing velocity in the measuring zone as the piston approaches top dead center.

The infrared pyrometer was also used to record compara-

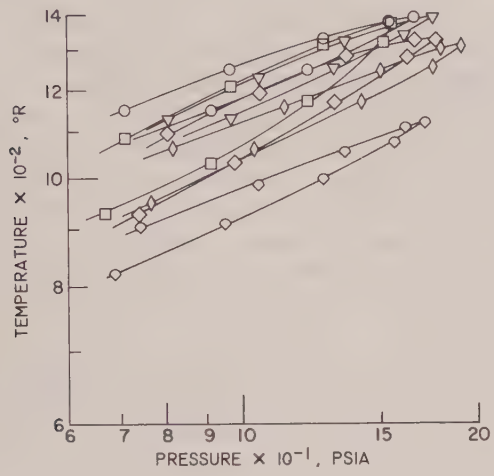

Fig. 14

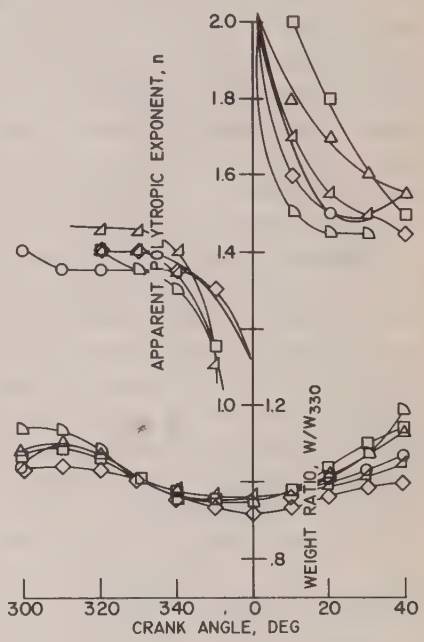

Fig. 15

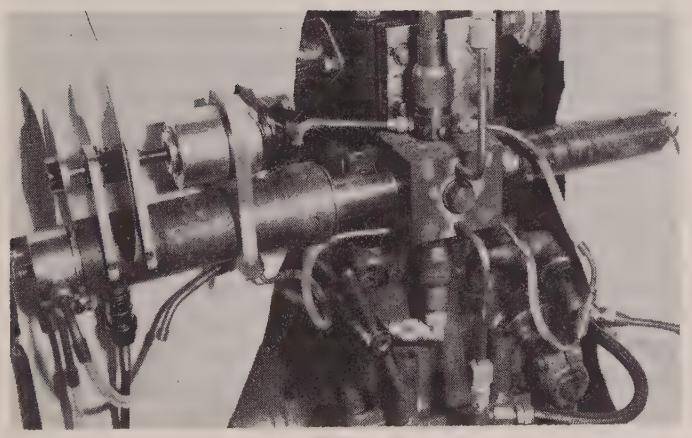

Fig. 16

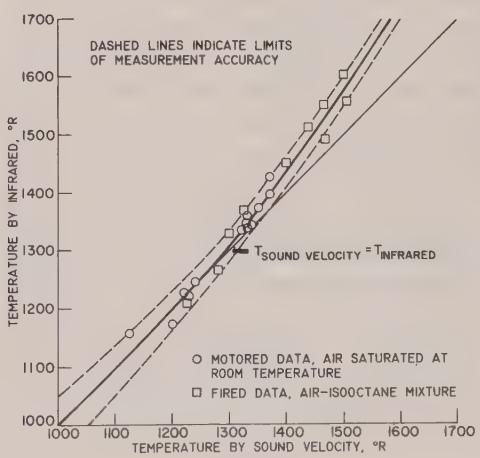

Fig. 17

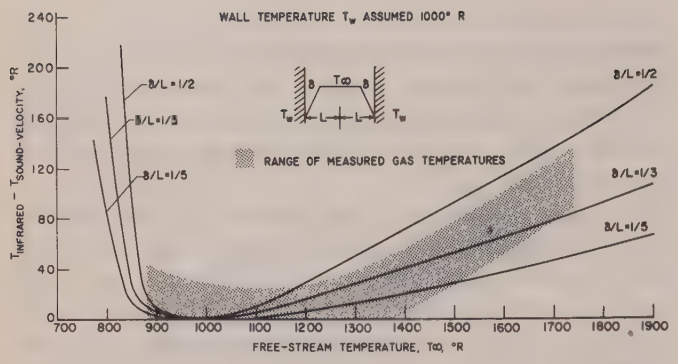

Fig. 18

tive engine data on the ell-head engine used for the development of the iodine-absorption pyrometer (10). Gas temperatures measured by the iodine-absorption pyrometer showed characteristic humping in the earliest data (5); and, despite extensive refinement of the instrument (10) (11), the humping characteristic shown in Fig. 19 persisted. Temperature data by the infrared pyrometer on the same engine operating at identical conditions and using the same optical path had no evidence of the anomalous behavior of the iodine-absorption pyrometer data (Fig. 20).

Subsequent investigations showed no measurable effect of pressure on the absorption pyrometer, or of iodine on the temperature measured by either the absorption pyrometer or the infrared radiation pyrometer. Since the absorption pyrometer itself was operated as close to the ideal as possible, the temperature differences between the two techniques have been postulated to be due to the lack of equipartition of energy of the iodine molecules (10). The infrared pyrometer avoids this problem, since the energy at 2.7 microns appears to be purely thermal in nature.

Effect of Engine Variables

Engine data by the infrared radiation pyrometer were recorded for a variety of engine operating conditions. The variables studied included spark setting, engine speed, cooling-jacket temperature, fuel-air ratio, and octane number. The results are analyzed and compared with previously reported engine data obtained by other methods.

Spark Setting - As the spark timing is retarded, both the residual gas weight and the temperature change. These two changes have opposite tendencies; one tends to increase the mixture temperature while the other tends to decrease it. Fig. 21 shows temperature - crank-angle data for spark settings of 20, 10, and 0 deg crank angle before tdc. There is apparently little resultant effect prior to the passage of the flame front in the open-chambered CFR engine. The ell-head chamber shows a much more pronounced effect of spark advance (Fig. 20). Temperatures measured prior to passage of the flame differed by as much as 150 R. It is obvious that the location of the measuring zone had a large effect on the differences noted between the two sets of data. Velocity-of-sound measurements on the specially pocketed engine showed even more effect, with as much as 250 R difference noted for wide ranges of spark setting (3).

Engine Speed - Engine data by the infrared pyrometer under motored and fired conditions (Figs. 13 and 22) showed an increase in the compression gas temperature with speed. In all of the data shown, the greatest temperature differences caused by the speed of the engine occurred near top dead center, where the effects of heat transfer between the walls and the gas were largest. A similar effect of speed was obtained by the velocity-of-sound instrument on both an open and a pocketed chamber (3). That data differed from the data presented here mostly at the early crank angles of measurement, where the differences in gas temperatures due to speed variations were larger than those indicated by the infrared pyrometer. Gas-temperature - crank-angle data by the iodine-absorption pyrometer were inconclusive when engine speed was varied because of the humping characteristics of the data mentioned earlier (10) (11).

Cooling-Jacket Temperature - There is a very small effect on the compression gas temperatures resulting from changing the cooling-jacket temperature. Fig. 23 shows that a change of 70 R in the cooling-jacket temperature resulted in a gas-temperature difference of about 20 R. Comparative data by the velocity-of-sound instrument showed similar results (3).

Fuel-Air Ratio - The effect that the fuel-air ratio has on the compression gas temperatures in the engine depends on the residual gas and the inner wall temperatures in the cylinder. Since the gas temperature of the burned mixture increases as the fuel-air ratio changes from a rich to stoichiometric mixture ratio, the temperature of the residual gases and the inner wall temperatures will similarly increase, causing the effect on temperatures shown in Fig. 24. The spark advance was the same in all the runs, resulting in different crank angles at which the flame front passed in front of the pyrometer windows. However, since the spark-advance data showed little effect on the compression temperatures, the data in Fig. 24 should not be affected appreciably by an adjustment of the spark advance. Comparable data by the sonic-velocity technique showed similar trends, with maximum temperatures obtained at a stoichiometric mixture ratio (3).

Fuel Octane Number - Fig. 25 shows the effect of octane number on the compression gas temperatures. Several sets of data are shown for both 100 octane (isooctane) and 75 octane (isooctane, n-heptane blend). Comparative curves from Figs. 13b and 24 show the influence of air alone and the variation of fuel-air ratio, respectively. These data differ from those obtained by the iodine-absorption pyrometer in both preliminary (5) and final measurements (10). The infrared pyrometer shows that the use of lower-octane fuel results in higher temperatures, in agreement with early data by the

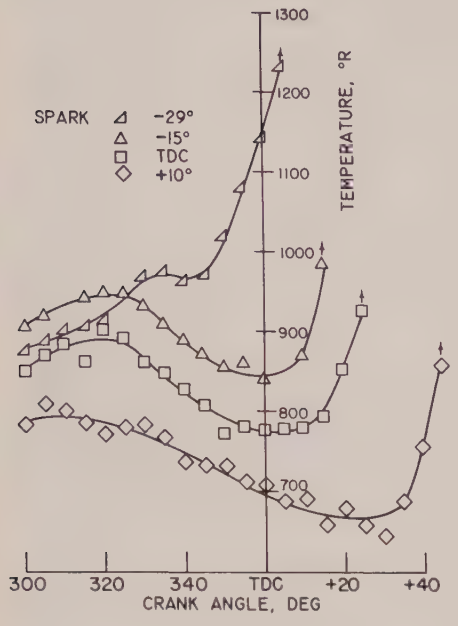

Fig. 19

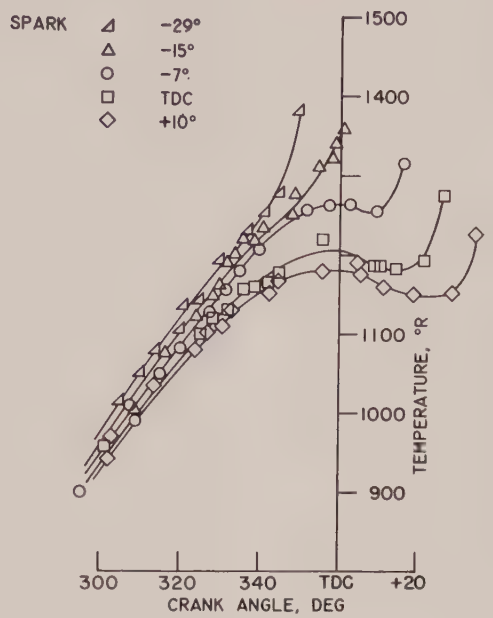

Fig. 20

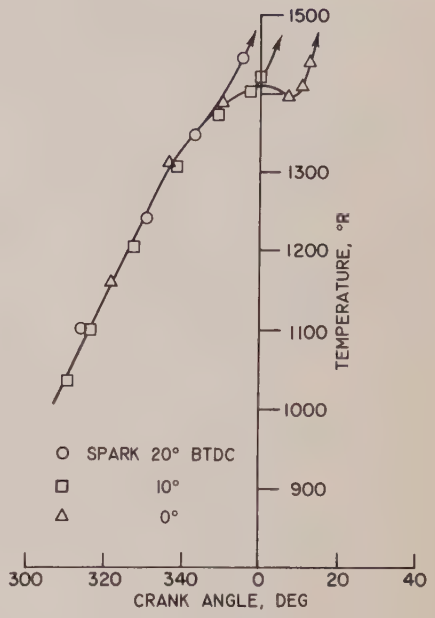

Fig. 21

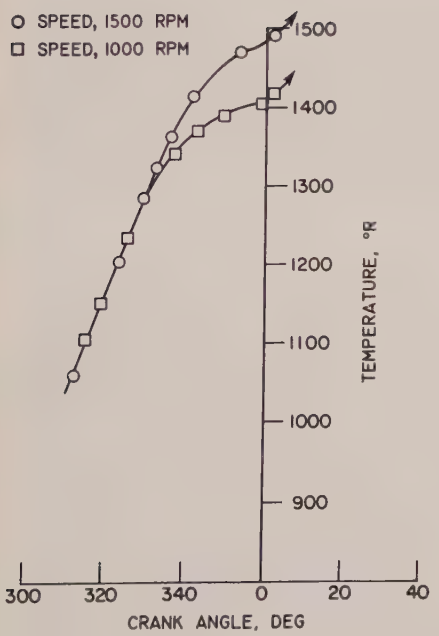

Fig. 22

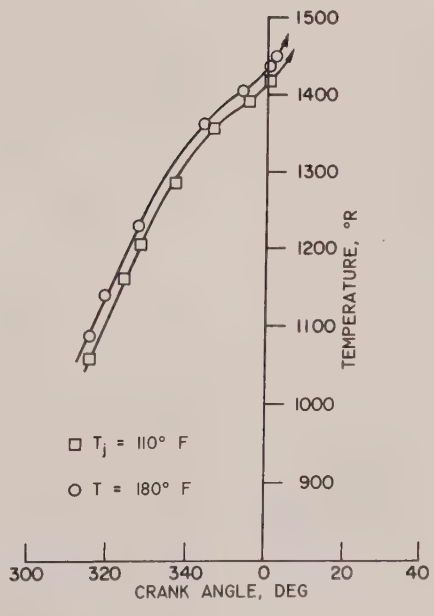

Fig. 23

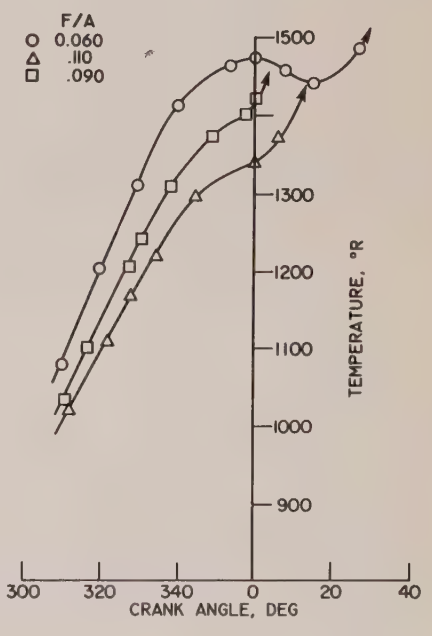

Fig. 24

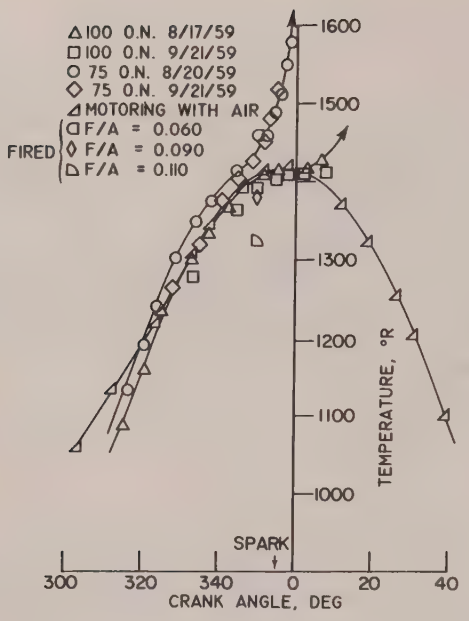

Fig. 25

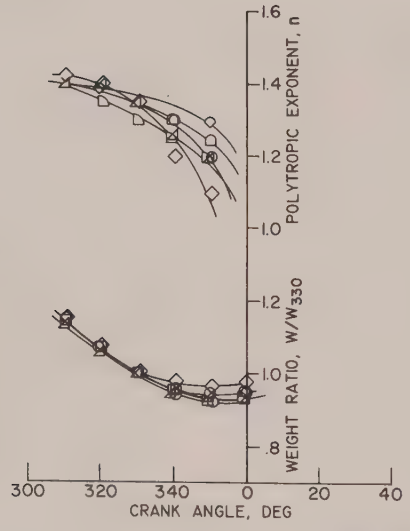

Fig. 26

sonic-velocity instrument at very low compression ratio (5). The iodine-absorption pyrometer, on the other hand, showed that the use of higher-octane fuel resulted in higher compression gas temperatures. Possibly this was due to the shape of the combustion chamber, but since it has not been repeated by the other measurement techniques, this may be an anomalous characteristic of the iodine molecules themselves.

The polytropic exponent n and the weight ratio W/W_{330} were calculated for all of the fired engine data and are presented in Fig. 26. The general trends of the curves showing the polytropic coefficients and weight ratios are similar to those for the motored engine. Again the data show that the apparent mass weight decreases as measured gas temperature increases faster than the mass-average temperature.

Extended Applications

There is a wide range of variables that can be investigated with a temperature-measuring instrument of this kind. However, as with any instrument, its limitations must be known and its results analyzed properly. The gas boundaries are an example of this.

The data presented in the previous section were for the purpose of evaluating the usefulness of the instrument rather than a detailed study of the engine processes. There are many similar areas of investigation in which gas temperature measurements by the infrared pyrometer would be useful. A few of these are

1. The influence of fuel type on gas temperatures.
2. The relation of compression gas temperatures and engine chamber deposits.
3. Combination of techniques for measuring gas temperatures and chamber surface temperatures to determine the total heat transferred through the engine walls as a function of time.
4. The relation of the preflame reactions to the maximum gas temperatures present during compression of the gas mixture.

It is emphasized that the infrared pyrometer is not the only technique that can be used to measure these gas temperatures. As stated before, the selection of the measuring technique will depend on the character of the boundary layer of the gas, the gas volume available, and the kind of measured gas temperature desired.

Conclusions

1. Any technique which is to be used for the measurement of gas temperatures in an engine is influenced in some manner by the boundaries of the gas. For a given technique and an assumed gas temperature profile, the measured gas temperature can be evaluated and compared with other defined temperatures.

2. The infrared pyrometer, utilizing water vapor as the sensing medium and the null method of data recording, is capable of measuring gas temperatures under ideal conditions to within ±5 R as demonstrated by the steady-flow system. The gas temperature of a nonisothermal layer of gas can also be measured, but its meaning is subject to the nature of the boundaries.

3. The reproducibility of the measured gas temperatures by the infrared pyrometer depends on the density of the water vapor in the measuring alone and the overall sensitivity of

the instrument. Water vapor normally present in the intake and clearance gases of the engine are sufficient to give reproducible readings within ±20 R, using the null method of recording data.

4. The infrared pyrometer, when measuring the apparent temperature of a volume of gas in the engine, measures a temperature weighted toward the peak temperature in the gas, whereas the sonic-velocity instrument measures a gas temperature weighted towards that of the mass-average temperature.

5. Comparative engine data using first the iodine-absorption pyrometer and then the infrared pyrometer showed that gas temperatures measured by the former technique had a humped characteristic which was not evident in those measured by the infrared pyrometer. Exhaustive tests of the iodine-absorption pyrometer did not resolve the differences between the comparative gas temperatures. Thus, it was reasoned that the iodine molecules were not in apparent thermal equilibrium with the other gases in the combustion chamber.

6. Engine data obtained by the infrared pyrometer are reproducible within ±20 R and appear to have internal consistency and accuracy when compared with theoretical cycles. Engine data showing the effect of varying selected engine parameters illustrate the applicability of the infrared pyrometer to the measurement of gas temperatures.

Acknowledgement

Special consideration is due John Johnson for his assistance in this project. Comparison of the infrared pyrometer with the iodine-absorption pyrometer and the velocity-of-sound apparatus was made possible by the cooperation of B. K. Ghandhi, J. C. Livengood, and C. F. Taylor. Generous support was provided by the Coordinating Research Council, Inc., Ethyl Research Laboratory, the Wisconsin Alumni Research Foundation, and the Army Ordnance Corps.

Appendix 1 — Symbols

$A_g(\lambda, p, T_g)$ = monochromatic absorptivity of gas at a given pressure and temperature

$A_w(\lambda, T_w)$ = monochromatic absorptivity of an engine window at a given temperature

$a(\lambda, p, T_g)$ = logarithmic decrement of radiation, defined as $(1/L)\ 1n[1 - A_g(\lambda, p, T_g)]$ cm^{-1}

C_1 = first constant in Wien's (and Planck's) radiation formula, $0.599X10^{-12}$ watt cm^2

C_2 = second constant in Wien's (and Planck's) radiation formula, 2.588 cm R

c_p = specific heat of gas at constant pressure

$E_g(\lambda, p, T_g)$ = monochromatic emissivity of gas at a given pressure and temperature

H = enthalpy of gas

$I_b(\lambda, T_b)$ = monochromatic intensity of a black-body source at a given temperature

$I_g(\lambda, T_g)$ = monochromatic intensity of a gas radiating as a black-body at a given temperature

$I_w(\lambda, T_w)$ = monochromatic intensity of an engine window radiating as a black-body at a given temperature

I_1 = intensity of radiation received by detector from radiation source alone

I_2 = intensity of radiation received by detector from radiation source and gas

I_3 = intensity of radiation received by detector from gas alone

L = length of gas path from wall to center of measuring zone

m = mass of gas

p, p_1, p_2 = gas pressure, gas pressure at state 1, and gas pressure at state 2, respectively

T_{AM} = arithmetic mean temperature

T_{IR} = apparent radiant gas temperature measured by infrared pyrometer

T_{MM} = mass mean temperature

T_{SM} = space mean temperature

T_{SV} = apparent gas temperature measured by velocity-of-sound instrument

T_b = temperature of black-body radiation source

T_g, T_{g1}, T_{g2} = gas temperature, gas temperature at state 1, and gas temperature at state 2, respectively

T_w = window temperature

T = free-stream temperature of gas

W = weight

x = incremental distance along axis of gas length

δ = boundary-layer thickness

λ = wavelength of radiation, cm^{-4} or microns

Appendix 2 — Analysis of Infrared Pyrometer

Basic Relations - The radiation from a perfectly radiating solid body can be related to its temperature by the following approximate relation known as Wien's Radiation Law:

$$I_b(\lambda, T_b) = C_1 \lambda^{-5} e^{-C_2/\lambda T_b} \qquad (A1)$$

where the terms are as defined in appendix I.

The temperature error introduced by Eq. (A1) is less than 3 R when applied to the pyrometer. Thus, it is used in place of the more cumbersome but exact equation developed by

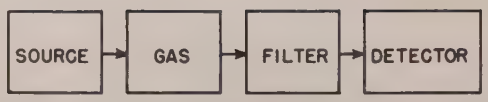

Fig. 27—Radiation source, gas volume, spectral filter and detector arrangement

Planck (7). The radiation from an isothermal volume of gas can be assumed to emit a continuous spectrum at elevated pressure and temperature so that it also can be expressed in the same form:

$$I_g(\lambda, T_g) = E_g(\lambda, p, T_g) C_1 \lambda^{-5} e^{-C_2/\lambda T_b} \quad (A2)$$

where the only difference between equations (A1) and (A2) is in the gas emissivity term, $E_g(\lambda, p, T_g)$. According to Kirchoff there is an exact relation between emission and absorption that exists for monochromatic radiation at constant temperature:

$$E_g(\lambda, p, T_g) = A_g(\lambda, p, T_g) \quad (A3)$$

By proper use of the preceding equations, the gas temperature of a given volume of gas can be determined.

Consider a radiation source, gas volume, spectral filter, and detector arranged as shown in Fig. 27. In the absence of gas, radiation received by the detector from the radiation source is

$$I_1 = I_b(\lambda, T_b) \text{ (Black-Body)} \quad (A4)$$

With the gas present at a given gas temperature, the radiation received by the detector is

$$I_2 = I_b(\lambda, T_b)[1 - A_g(\lambda, p, T_g)] + E_g(\lambda, p, T_g) I_g(\lambda, T_g) \quad (A5)$$

When the radiant intensities I_1 and I_2 become equal, then Eqs. (A4) and (A5) can be equated and written in the form

$$\left.\begin{aligned} &A_g(\lambda, p, T_g) I_b(\lambda, T_b) = E_g(\lambda, p, T_g) I_g(\lambda, T_g) \\ &\text{or} \\ &I_b(\lambda, T_b) = I_g(\lambda, T_g) \\ &\text{or} \\ &T_b = T_g \end{aligned}\right\} \quad (A6)$$

This equality establishes the conditions for the determination of the null gas temperature. With the proper apparatus, a gas-temperature can be found for every given source temperature.

If a chopper is placed between the radiation source and the gas, an additional radiant intensity is received periodically by the detector, that from the gas alone:

$$I_3 = E_g(\lambda, p, T_g) I_g(\lambda, T_g) \quad (A7)$$

Eqs. (A4), (A5), and (A7) can be combined as follows:

$$\text{Ln}\left(\frac{I_1 + I_3 - I_2}{I_3}\right) = \frac{C_2}{\lambda}\left(\frac{1}{T_g} - \frac{1}{T_b}\right) \quad (A8)$$

Eq. (A8) shows that the chopped method of operation should be capable of recording radiation data for a complete gas-temperature - crank-angle diagram in only one cycle of operation. Although it was an attractive means of recording data, the chopped method was found to contain errors when calibrated on the steady-flow system (see text). Thus the null method was used for all of the final comparison engine data.

Effect of Temperature Gradients - Different measuring techniques will not necessarily read the same average temperature of a gas volume in which there are thermal gradients. The average temperature measured by the infrared pyrometer can be calculated by making some simplifying assumptions with regard to the gas:

1. The gas is assumed to have a temperature gradient only along its length.
2. The gas is assumed to be contained on all sides by transparent, nonconducting walls.
3. The emissivity and absorptivity of the gas are considered equal for one wavelength and small temperature differences.
4. An approximate temperature profile is assumed for the gas with a linear temperature gradient at the walls.

The radiant intensity of the radiation entering the gas volume, $I(\lambda, T)$, will be changed by an amount $dI(\lambda, T)$ in passing through a distance dx of the gas. This change in intensity can be expressed in the following form:

$$dI(\lambda, T) = -A_g(\lambda, p, T_g) I(\lambda, T) + E_g(\lambda, p, T_g) I_g(\lambda, T_g) \quad (A9)$$

Replacing the emissivity and absorptivity terms with the logarithmic decrement of radiation $a(\lambda, p, T_g)$ and integrating over the total length of the gas path yields the equation:

$$I(\lambda, T) = e^{-\int_0^L a(\lambda, p, T_g)\, dx} \int_0^L a(\lambda, p, T_g) I_g(\lambda, T_g) \, e^{\int_0^x a(\lambda, p, T_g) dx} \, dx + C e^{-\int_0^L a(\lambda, p, T_g) dx} \quad (A10)$$

When the gas is nonabsorbing and nonemitting ($a(\lambda, p, T_g) = 0$), the constant of the equation C is equal to the blackbody source radiation entering the gas volume. Since the null method of temperature measurement involves matching this radiation with that from the radiation source and gas combined, Eq. (A10) can be written in the form:

$$C_1\lambda^{-5} e^{-C_2/\lambda T} = e^{-a(\lambda, p, T_g)L}\, a(\lambda, p, T_g)$$

$$\int_0^L C_1\lambda^{-5} e^{-C_2/\lambda T_g} e^{\int_0^x a(\lambda, p, T_g)dx}\, dx$$

$$+ C_1^*\lambda^{-5} e^{-C_2/\lambda T_g}\, e^{-a(\lambda, p, T_g)L} \qquad \text{(A11)}$$

Cancelling similar terms, designating the temperature T_{IR}, and setting T_{IR} equal to T_b, the equation for the average temperature measured by the infrared pyrometer is

$$T_{IR} = \frac{1}{-\lambda/C_2 \ln\left\{\frac{a(\lambda, p, T_g)[1 - A_g(\lambda, p, T_g)]}{A_g(\lambda, p, T_g)} \cdot X\right\}} \qquad \text{(A12)}$$

where

$$X = \int_0^L e^{-C_2/\lambda T_g} \cdot e^{a(\lambda, p, T_g)\, x}\, dx \text{ is evaluated}$$

numerically for any given profile of gas temperature along the gas-path length.

The effect of temperature gradients in the gas on the temperature measured by the sonic-velocity instrument has been analyzed elsewhere (4). The equation for the average temperature measured by that method can be written in the form:

$$T_{SV} = \left[\frac{1}{\frac{2\delta}{L(\sqrt{T_\infty}+\sqrt{T_w})} + \left(\frac{L-\delta}{L}\right)\frac{1}{\sqrt{T_\infty}}}\right]^2 \qquad \text{(A13)}$$

Other average temperatures that can be evaluated for a gas volume containing temperature gradients are:

Mass mean temperature:

$$T_{MM} = \int dH \Big/ C_p \int dm \qquad \text{(A14)}$$

Space mean temperature:

$$T_{SM} = 1/L \int_0^L T(x)dx \qquad \text{(A15)}$$

Arithmetic mean temperature:

$$T_{AM} = \frac{T_\infty + T_w}{2} \qquad \text{(A16)}$$

Effect of Intake Gases and Engine Windows - The equations describing the principle of operation of the infrared pyrometer - Eqs. (A1) to (A6) did not include any effect of the engine gases during the intake stroke when the reference level of blackbody source radiation is established. If this radiation is absorbed by more than a negligible amount by the gas during the intake stroke, an error in the measured gas temperatures by the null method will be introduced.

If an absorptivity $A_g(\lambda, p_1, T_{g1})$ is assumed on the intake stroke (state 1), then

$$I_1 = [1 - A_g(\lambda, p_1, T_{g1})]\, I_b(\lambda, T_b) \qquad \text{(A17)}$$

During compression (state 2), when the gas absorption and emission become appreciable quantities, then

$$I_2 = [1 - A_g(\lambda, p_1, T_{g1})]$$

$$[1 - A_g(\lambda, p_2, T_{g2})] I_b(\lambda, T_b) + E_g(\lambda, p_2, T_{g2}) I_g(\lambda, T_{g2}) \qquad \text{(A18)}$$

Since the null point is determined by setting Eqs. (A17) and (A18) equal to each other, the final equation can be reduced to the form:

$$\ln\left[1 - \frac{A_g(\lambda, p_1, T_{g1})}{A_g(\lambda, p_2, T_{g2})}\right] = \frac{C_2}{\lambda}\left[\frac{1}{T_b} - \frac{1}{T_{g2}}\right] \qquad \text{(A19)}$$

The temperature error that occurs when the gas absorption during intake cannot be neglected $[A_g(\lambda, p_1, T_{g1}) \neq 0]$ is

$$T_{error} = T_b - \frac{1}{(1/T_b) - (\lambda/C_2)\ln\left[1 - \frac{A_g(\lambda, p_1, T_{g1})}{A_g(\lambda, p_2, T_{g2})}\right]} \qquad \text{(A20)}$$

Measurements of the gas absorptivity were taken as a function of crank angle on the engine under typical operating conditions, and the ratio $A_g(\lambda, p_1, T_{g1})/A_g(\lambda, p_2, T_{g2})$ was found to vary from 1.0 down to 0.01, resulting in a temperature error as large as 30 R if not corrected.

The engine windows absorb about 10% of the radiation that passes through them when they are clean, and even more when a film of particles collects on their surfaces. Thus their effect must be considered in the final analysis of the instrument.

Fig. 28—Schematic of complete pyrometer

The complete pyrometer can be considered to be made up of a series of radiating and absorbing bodies as shown in Fig. 28. Since radiation and absorption of the window on the pyrometer side of the engine, the lens, the filter, and the detector are constant and do not affect the equality of Eqs. (A4) and (A5), their effect can be excluded from this analysis. The window between the black-body source and the gas does affect the null point and so must be considered.

When the engine windows are cooled by intimate contact with circulating tap water, their radiation can be considered negligible, and the only error is that due to absorption of the black-body source radiation by the window:

$$T_{error} = T_b - \frac{1}{(1/T_b) - (\lambda/C_2)\ln[1 - A_w(\lambda, T_w)]} \quad (A21)$$

If the engine windows are uncooled, they can emit considerable radiation, especially when slightly covered by deposits. An analysis of that effect has shown that the window temperature must be below 1000 R for completely negligible radiation (12).

The effect and magnitude of the preceding errors in gas temperatures measured by the infrared pyrometer can be calculated, but rapid experimental calibration was considered most reliable for determining proper operation of the pyrometer. This was done by mounting a rapid shutoff valve on the intake manifold of the engine. Through proper manipulation of this valve, the separate and combined effects of the intake gases and engine window could be observed on the oscilloscope.

References

1. "Four Proposed Methods of Measuring End-Gas Properties," Rep. No. 277, Coordinating Research Council, Inc., Jan. 1953.

2. J. C. Livengood, T. P. Rona and J. J. Baruch, "Ultrasonic Temperature Measurement in Internal Combustion Engine Chamber," J. Acoustical Soc. Am., Vol. 25-5, Sept. 1954, 824-820.

3. J. C. Livengood, C. F. Taylor, and P. C. Wu, "Measurement of Gas Temperature in an Engine by the Velocity of Sound Method," S. A. E. Trans., Vol. 66, 1958, 683-699.

4. C. F. Taylor and J. C. Livengood, Unpublished Summary Report, Sloan Automotive Laboratory, Massachusetts Institute of Technology, Oct. 1958.

5. S. K. Chen, N. J. Beck, O. A. Uyehara, and P. S. Myers, "Compression and End-Gas Temperatures from Iodine Absorption Spectra," S. A. E. Trans., Vol. 62, 1954, 503-513.

6. D. A. Trayser, "Radiation Measurements with Lead Sulfide Cell Using Spark-Ignited Engine," M. S. Thesis, University of Wisconsin, 1953.

7. M. C. Burrows, "A Fast Infrared Pyrometer for Engine Compression Temperatures," Ph. D. Thesis, University of Wisconsin, 1959.

8. "Specification Sheet on Type 812 Gold-Doped Germanium Infrared Detector," Westinghouse Electric Corp., 1958.

9. H. C. Hottel, G. C. Williams and C. N. Satterfield, "Thermodynamic Charts for Combustion Processes," John Wiley & Sons, Inc., 1949.

10. B. K. Ghandhi, "Evaluation of a Light-Absorption Pyrometer for Nonluminous Engine Gases," Ph. D. Thesis, University of Wisconsin, 1958.

11. P. S. Myers and O. A. Uyehara, Unpublished Interim Reports, Engineering Experiment Station, University of Wisconsin, 1955-1957.

12. J. Johnson, Unpublished Thesis Material, University of Wisconsin, 1960.

End-Gas Temperature-Pressure Histories and Their Relation To Knock

M. E. Gluckstein and C. Walcutt
Ethyl Corp.

EXTENSIVE studies of the autoignition of fuel-air mixtures have been made in the past. Much of this work was done in laboratory reaction vessels at low pressures and temperatures. For the most part, the purpose of that work was to obtain general information about combustion processes (1).*

In 1931 Withrow (2) observed that autoignition occurred in the yet unburned fuel-air mixture in the end zone (end gas) of an internal combustion engine. Since then, a great many researchers, both here and broad, have tried to extend autoignition studies to devices which simulate the conditions that would be expected in the end gas of an engine. The first extensive work of that nature was done by Tyzard and Pye (3); many further references are given in a publication by Taylor et al (4).

In these earlier studies, the general procedure was to rapidly bring a fuel-air mixture to a high pressure and temperature and maintain that state until autoignition occurred. The implicit assumption was that the information obtained would improve understanding of knock in engines. The problem occurred in applying these studies to knock.

There is little doubt that a fuel-air mixtures does autoignite when knock occurs in an engine. But some doubt exists as to whether (1) the pressure rise associated with autoignition generates the sound observed when knock occurs or (2) the sound is caused by a gaseous detonation wave. Those who uphold the detonation wave theory believe that autoignition reactions are too slow to produce the knocking sound (5). Other investigators point out that the rate of energy release during autoignition could be extremely high, provided the reacting gases are of uniform composition (6).

The evidence which supports the necessity of having autoignition as the energy source for knock includes:

1. Fuel ratings have been made in an engine at the limiting compression ratio for continuous, repeated autoignition. These ratings, made without reference to knock intensity, agreed quite well with ratings in a standard engine for a large variety of fuels and additives (7).
2. A correlation between fuel octane number and the delay for autoignition was obtained from data obtained in a rapid-compression machine (8).
3. The major pressure oscillations which occur in a combustion chamber during knock have the same frequency as the oscillations observed outside the engine.

Research at the Massachusetts Institute of Technology on a rapid-compression machine (4) which was sponsored for a number of years by Ethyl Corp., clearly indicated that the thermodynamic state required for autoignition of a given hydrocarbon-air mixture was time dependent. This would imply that the pressure-temperature histories in an engine are the fundamental parameters controlling knock for any given fuel-air mixture. In line with this work, one point of considerable current interest is whether or not the knocking tendency of fuels can be characterized only by the density and temperature in the engine.

The temperature of a medium can be determined from measured values of the speed of sound by well established thermodynamic principles. A practical device to measure the speed of sound of the gases in an engine was developed at the Massachusetts Institute of Technology under the sponsorship of the Coordinating Research Council. The utility

*Numbers in parentheses designate References at end of paper.

Table 1 - Guide Curve Values

	Compression Ratio for Standard Knock			
	Research		Motor	
Fuel	Temp. Engine	Std. Engine	Temp. Engine	Std. Engine
90 PRF	6.70	6.69	7.00	6.76
Isooctane (100 PRF)	8.03	8.02	7.90	8.02
Isooctane + 1 ml TEL	9.15	9.74	8.80	8.89

Table 2 - DIB Knockratings

	Octane Number	
	Temp. Engine	Standard Engine
Research	103	105
Motor	93	89

of such a device for determining fuel-engine relationships in terms of the basic parameters of pressures, temperature, and time at knock-limited conditions was immediately apparent. Therefore, Ethyl Corporation undertook a program to investigate these factors.

Apparatus

The equipment used to determine the temperature of the gases in the combustion chamber is basically similar to that designed and built at MIT. The principle of operation is based on the relationship between temperature and the speed of sound in a gas. Both the theory and practical application of this apparatus to an engine have been extensively covered in previous publications (9,10). Therefore, we will only recount the few minor modifications made in the apparatus.

The cylinder head and block is a 2-piece unit designed by Waukesha Motor Co. for the original CFR engine. This split-head unit has been used to provide an insert between the head and block to hold the sound transducers. The transducers are set at the end of a tapering ellipsoidal pocket, the major axis of which extends radially outward from the main chamber. The spark plug is located at the opposite side of the combustion chamber from the pocket. This combustion chamber geometry is highly satisfactory since it ensures that the sound transducers are located in the end gas.

A special piston with a high crown enables the engine to be operated at 11.0:1 compression ratio. An 18 mm access hole was provided at the end of the pocket for a balanced-pressure-type pickup. Fig. 1 shows the schematic arrangement of these details. Since the pear-shaped combustion chamber is quite unconventional, the shroud on the intake valve was positioned to direct the intake charge into the pocketed area and provide better scavenging.

Another modification was a refinement of the crankangle pulse generator for triggering the delayed-sweep oscilloscope and the barium titanate crystal transmitter. Instead of using conventional breaker points as a pulse trigger, a preset counter and a notched flywheel with photomultiplier pickup are used. With this arrangement, the operator sets the electronic counter to generate a sound pulse at one deg crankangle intervals from 180 deg btc to 180 deg atc. When the pulse from the photomultiplier tube next to the slotted flywheel was used to flash a stroboscope light on the flywheel, it was found that the accuracy of the system was better than 1/4 crankangle deg. A photograph of the apparatus is shown in Fig. 2, and a schematic arrangement in Fig. 3.

Preliminary Investigation

Although this engine has an elongated combustion path, approximately half again as long as the path in a normal engine, the actual time for the flame to traverse the combustion chamber is not significantly different from the time in a standard CFR engine. Also, it was found that the overall operating characteristics of the engine were fairly normal. This conclusion is based on two determinations:

1. Comparison with the Standard Guide Curve data by Motor and Research methods for primary reference fuels (PRF).
2. Ratings obtained for a temperature-sensitive fuel.

Compression ratios for standard knock from the guide cur-

Table 3 - Composition of "Sensitive" (S) and "HOT" (H) Fuels

	Octane Rating		Composition, vol %			
Fuel	Research	Motor	Isooctane	n-Heptane	Diisobutylene	Toluene
98S	98	86.9	43.7	16.0	40.3	0
100S	100	88.3	50.5	11.6	37.9	0
100H	100	89.1	32.5	12.5	0	55.0
104S	104	91.9	60.4	5.3	34.3	0

ves are compared with values obtained in the experimental temperature-measuring engine in Table 1. For the most part, the values are in fairly close agreement.

The performance of this engine using a temperature-sensitive fuel, such as diisobutylene (DIB), is shown in Table 2. As shown, DIB is somewhat less temperature sensitive in the experimental engine than in a standard engine.

This difference in octane numbers obtained for DIB may be due more to modifications which had to be made in the method of measuring knock in this engine than to peculiarities of the combustion chamber. It was observed that the Phillips type pickup caused the knockmeter to show a isooctane. After some study, it was found that pressure oscillations occurred in the combustion chamber at these conditions. The cause of the pressure oscillations was not knock, but a flame-driven organ-pipe oscillation due to the pocket in the combustion chamber. This was reasonably well established by the fact that the frequency of these oscillations could be lowered by increasing the length of the pocket. Because of this situation, further measurements of knock were made by using an SLM pickup (Piezoelectric pickup distributed by Kistler Instrument Co.) and watching the dp/dt signal on the oscilloscope. The onset of knock by this method always corresponded with audible manifestations.

Engine Conditions and Fuels

The normal operating conditions of the engine for this study were 608 ±6 rpm, 15 ±0.5 deg btc ignition, 0.070 ±0.001 fuel-air ratio, 150 ±3 F inlet-mixture temperature, 205 ±5 F water-jacket temperature and 135 ±10 F crankcase-oil temperature. The engine variables investigated were inlet-mixture temperatures of 110 to 400 F, ignition timing of 5 to 25 deg btc, engine speeds of 608 and 1227 rpm, and fuel-air ratios ranging from 0.056 to 0.084. In addition, some runs were made under Motor and Research method conditions. All operation was at wide open throttle (naturally aspirated) with manifold fuel injection. The compression ratio for each fuel and engine condition was adjusted for incipient knock based on the dp/dt trace indicated by an oscilloscope.

The fuels tested included primary reference fuels, both clear and with organometallic additives, ranging in antiknock quality from 60 octane number up to isooctane plus 1.0 ml TEL/gal as 62 Mix. A recently introduced organomanganese antiknock, methylcyclopentadienyl manganese tricarbonyl (AK-33X), was used in some runs both as a primary and supplementary antiknock. "Sensitive" (S) (ternary mixtures of n-heptane, isooctane, and diisobutylene) and "HOT" (H) (ternary mixtures of n-heptane, isooctane, and toluene) fuels also were investigated, as well as 100% dissobutylene. The S and H fuels were used to simulate commercial blends, and were blended to match isooctane at knock-limited conditions in this experimental engine. The compositions of these fuels are shown in Table 3.

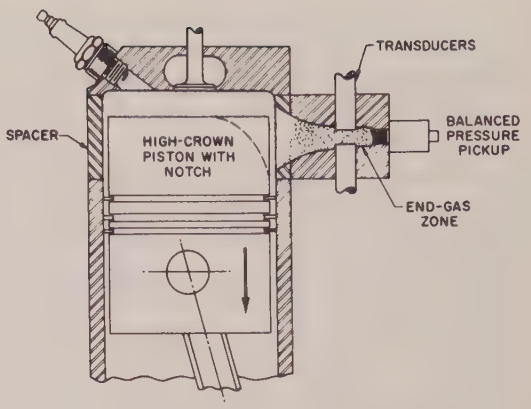

Fig. 1 — Schematic diagram of cylinder head and transducers

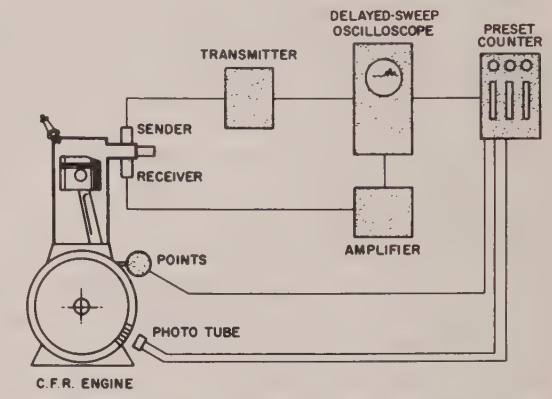

Fig. 2 — Speed-of-sound temperature-measurement apparatus and engine

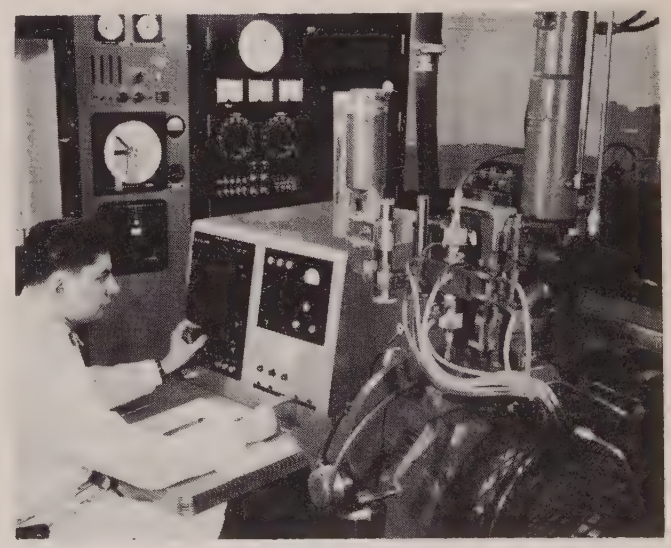

Fig. 3 — Schematic of end-gas temperature measurement equipment

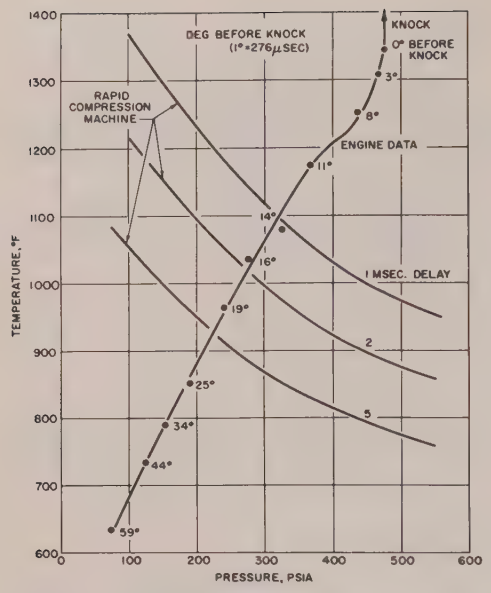

Fig. 4 — Pressure-temperature-time relation for autoignition and knock with isooctane

Data Collection

Before the start of test runs each day, nitrogen, argon, and dry air were introduced into the combustion chamber with the engine at rest. The temperature and pressure were measured by ordinary techniques.

The values of the speed of sound for the three gases at the chamber conditions were obtained from National Bureau of Standards Circular 564, and the transit time for a signal to cross the gap was calculated for each gas from these known values of the speed of sound. The speed-of-sound apparatus was then operated and the total transit time for a signal to pass from the triggering circuit through the electronic circuitry, barium titanate crystals, brass coupling rods, and gas gap was measured.

The difference between the computed gap transit time and the measured total transit time is the instrumental delay, due to electronic delays and acoustic delays in the crystals and coupling rods. The value for the three calibration gases agreed within 0.5%. In the test runs, this instrumental delay was subtracted from the observed time to give the actual transit time for the sound pulse to cross the gas gap.

For each fuel and engine condition, the compression ratio was adjusted for incipient knock. The preset electronic counter was then set to generate a sound pulse across the transducers in the end gas at 40 deg btc, and at frequent crankangle settings thereafter until knock occurred. A determination of temperatures at any earlier time in the engine cycle was considered unnecessary. The delayed-sweep oscilloscope was then set to read the total time for the pulse transit. The time of knock was indicated by an irregular trace on the delayed-sweep oscilloscope.

The pressure was measured at each crankangle position for which a temperature record was obtained. The pressure equipment used was a free-diaphragm, variable-capacity, balanced-pressure unit (11). The movement of the diaphragm of the balanced-pressure unit was displayed along with the time pulse which started the temperature measurement on a second oscilloscope. The operator merely adjusted the pressure behind the diaphragm until the time at which the diaphragm started to move coincided with the timing pulse for temperature measurement. Thus, at the time of temperature measurement, the known pressure behind the diaphragm should just equal the combustion chamber pressure.

A point of some importance, which is considered later, is the significance of the pressure and temperature measurements. The temperature measurement is representative of the gases in the end zone ahead of the flame front. The pressure measurement, however, represents pressure throughout the combustion chamber. Since all pressure disturbances prior to knock are subsonic, it is reasonable to assume that the pressure will be equal at all points in the combustion chamber, within instrumental accuracy.

Temperature Calculation

The procedure used for calculating temperature from the measured speed of sound has been previously reported (12). The equation is:

$$T = \frac{d^2 M}{\gamma t^2 R} \qquad (1)$$

where: T = temperature, R
d = gap distance, ft
M = molecular weight of gases, slugs/lb mole
γ = ratio of specific heats
R = gas constant, ft lb/lb mole, R
t = time, sec

In this equation, the gas constant is known and the gap distance and time are measured values. The molecular weight is assumed to be constant, and is calculated on the basis of fuel-air ratio and an estimation of fraction residuals. It is recognized that precombustion reactions may affect the molecular weight. However, since the total concentration of precombustion products is small (13), the contribution of these products to changes in molecular weight will be negligible. The quantitiative effect of composition errors is discussed in the next section.

For this equation, the ratio of specific heats is computed as a function of temperature from the known fuel-air-exhaust gas composition and the specific heat at constant pressure. Since a final temperature must be assumed for the selection of a value of gamma before the temperature is determined, this problem is solved by an iterative procedure on an electronic computer. After about three iterations, the machine usually will have computed a value for temperature.

Reliability of Data

Unfortunately, a dynamic system of calibration to determine the absolute accuracy of the temperature-measuring equipment would be quite difficult. A static system of calibration would probably be of little value. On the other hand, for this work, knowledge of the accuracy of the instrument is not as important as the precision (reproducibility) of the data. Factors which affect precision are signal pulse timing, pulse duration, pulse detection, gap distance, gas composition, and time delay. The effect of each of these items is discussed in turn.

Signal Pulse Timing - With the photomultiplier tube and the notched flywheel, the reproductibility of the signal pulse timing depends on the optical and mechanical alignment, and electronic circuit stability. Periodic checks showed this system to be reproducible within the combined tolerances of the mechanical and electrical calibration procedures, which was less than 1/4 crankangle deg.

Pulse Duration - The time duration of the pulse across the gap is about 20 microseconds. Since this represents less than 0.1 crankangle at 600 rpm, the temperature change in 20 microseconds should not exceed 4 R. Thus, differences in signal duration in the gap can cause little difficulty.

Pulse Detection - For the equipment used in this work, the error in signal detection on the delayed-sweep oscilloscope was $\pm$0.05 microseconds. For a 20-microsecond signal, this represents an error of $\pm$0.25% in time or not more than 1 R.

Gap Distance - The gap distance for the transducers was during the calibration procedure to ±0.001 in. or a possible error of about ±0.2% in time or not more than 1 R.

Gas Composition - The effect of combustion-gas composition on computed temperatures is shown in Table 4. It is apparent from Table 4 that large changes in end-gas composition have small influence on the computed temperature, and the likelihood of errors exceeding ±15 R due to composition uncertainties is small.

Time Delay - The instrumental delays which must be subtracted from the observed total delay are determined with an accuracy of ±0.25% in time or about 1 R. Any variability in this measurement should be somewhat less than this.

In summary, the total maximum error of temperature measurements should not exceed ±24 deg at 1800 R or about $\pm$1.5%. This is probably equal to or better than the precision of pressure determinations. Undoubtedly, the greatest variability is in the cycle-to-cycle reproducibility within the engine itself rather than in the instrumentation. This engine variability at any condition of engine operation would, of course, cause a variability in pressure and temperature measurements. The total variability of engine and measuring equipment is estimated to be not more than ±2.5%. Successive, replicate runs showed even less variability.

Temperature-Pressure Data

The data gathered in this study are available from the Ethyl Corp. as a separate report (14). The information is presented on 46 curve sheets on which are plotted 114 curves showing the temperature-crankangle and pressure-crankangle relationships for the different fuels and engine operating conditions investigated. Each curve is defined by about 30 data points beginning at 40 deg btc and ending at the time of knock. The presentation to follow is based on these data.

Interpretation of Data - Earlier work at MIT with a rapid-compression machine showed that pressure, temperature, and time were the important basic parameters controlling knock and autoignition. In that work, the combustible mixture was at a reasonably constant thermodynamic state until the start of autoignition. By comparison, the pressure and temperature in an engine are continually changing due to compression of the end gas by the piston and the advancing flame front; therefore, there is no recognizable induction time for reaction.

The relative importance of the pressure and temperature histories can be shown by comparing the autoignition requirements of isooctane as determined in the engine with those observed in the rapid-compression machine. This is shown in Fig. 4. The family of three curves shows the calculated pressures and temperatures required for autoignition of isooctane in the rapid-compression machine at delays of 1, 2, and 5 milliseconds. The pressure-temperature history for an engine cycle is also shown up to the time knock occurred.

For the pressure and temperature at which knock occurs in the engine, the ignition delay in the rapid-compression machine is less than one millisecond. This means that the total effective precombustion reactivity leading to autoignition during the relatively long period of time of end-gas compression is equivalent to the reactivity which would have occurred in a fraction of a millisecond had the charge been compressed quickly to the same pressure and temperature, as in the rapid-compression machine. This can only mean that the contribution to knock by reactions occurring early in the engine cycle must be small in comparison to the con-

Table 4 - Effect of Gas Composition on Temperature

Crankangle Deg	Temperature, R		
	Air + Fuel + Residuals	Air + Fuel (no residuals)	Air as all N_2 + Fuel
-40	1206	1218	1222
-30	1294	1309	--
-20	1370	1384	--
-10 (btc)	1445	1461	--
0 (tdc)	1587	1604	--
+10 (atc)	1764	1784	1789

Table 5 - Final End-Gas Temperature-Pressure Data

Fuel	Rated Octane Number	Compression Ratio	Speed, rpm	Ignition, btc	Inlet-Mixture Temp., F	Fuel-Air Ratio	Final End-Gas Press, psia	Final End-Gas Temp., R	Time of Knock, CA Degrees
60 PRF	60	4.53	613	15	123	0.070	338	1855	+18
60 PRF	60	4.27	613	15	150	0.070	305	1855	+16
60 PRF	60	4.26	611	15	199	0.070	265	1863	+22
75 PRF	75	4.96	614	15	124	0.070	368	1880	+20
75 PRF	75	4.60	612	15	199	0.070	285	1805	+25
75 PRF	75	4.37	609	15	301	0.070	215	1855	+19
75 PRF	75	4.26	607	15	400	0.070	190	1865	+19
80 PRF	80	5.05	615	15	112	0.070	367	1877	+22
80 PRF	80	4.90	612	15	226	0.070	315	1875	+ 8
80 PRF	80	4.27	607	15	403	0.070	222	1877	+17
90 PRF	90	6.13	614	15	102	0.070	435	1790	+21
90 PRF	90	6.05	612	15	151	0.070	395	1830	+21
90 PRF	90	5.94	610	15	224	0.070	365	1795	+17
90 PRF	90	5.40	606	15	400	0.070	283	1810	+18
Isooctane	100	7.40	616	15	117	0.070	480	1855	+15
Isooctane	100	7.20	611	15	226	0.070	480	1865	+ 7
Isooctane	100	6.80	606	15	401	0.070	358	1850	+13
Isooctane + 1 ml TEl/gal*	-	9.20	610	15	116	0.070	687	1835	+ 7
Isooctane + 1 ml TEL/gal	-	8.80	608	15	228	0.070	570	1820	+ 9
Isooctane + 1 ml TEL/gal	-	8.45	605	15	395	0.070	480	1820	+11
Diisobutylene	-	8.75	612	15	108	0.070	712	1805	+ 9
Diisobutylene	-	8.13	607	15	225	0.070	510	1765	+11
Diisobutylene	-	6.80	608	15	395	0.070	410	1828	+14
				Variable Antiknock Additive					
60 PRF	60	4.27	613	15	150	0.070	305	1855	+16
40 PRF + 1.5 ml TEL/gal	60	4.27	613	15	150	0.070	310	2065	+18
71.5 PRF	71.5	4.68	613	15	151	0.070	335	1840	+22
60 PRF + 1.0 ml TEL/gal	71.5	4.68	613	15	150	0.070	342	2000	+20
80 PRF	80	5.05	614	15	150	0.070	372	1840	+16
60 PRF + 1.8 ml TEL/gal	80	5.05	614	15	149	0.070	372	1980	+16
85 PRF	85	5.50	615	15	151	0.070	395	1820	+13
60 PRF +2.0 g Mn/gal**	85	5.50	615	15	151	0.070	395	1905	+16
Isooctane	100	7.25	614	15	150	0.070	525	1830	+15
80 PRF + 3.0 ml TEL/gal + 0.75 g Mn/gal	100	7.25	614	15	150	0.070	525	1920	+14

*TEL as 62 Mix **Mn as AK-33X

continued

Table 5 - continued

Fuel	Rated Octane Number	Compression Ratio	Speed, rpm	Ignition, btc	Inlet-Mixture Temp., F	Fuel-Air Ratio	Final End-Gas Press, psia	Final End-Gas Temp., R	Time of Knock, CA Degrees
Variable Fuel-Air Ratio at 15 btc Ignition									
Isooctane	100	7.15	615	15	151	0.070	473	1870	+ 3
100S	100	7.25	613	15	151	0.070	510	1870	+17
100H	100	7.15	614	15	153	0.070	445	1830	+14
Isooctane	100	7.58	614	15	148	0.084	555	1825	+13
100S	100	7.58	615	15	146	0.084	565	1820	+13
Isooctane	100	8.14	613	15	147	0.056	420	1655	+26
100S	100	8.14	611	15	150	0.056	405	1675	+29
Variable Fuel-Air Ratio at 25 btc Ignition									
Isooctane	100	7.30	612	25	151	0.070	582	1870	+ 3
100S	100	7.30	612	25	150	0.070	583	1870	+ 1
100H	100	7.30	611	25	150	0.070	540	1960	+ 1
Isooctane	100	7.62	612	25	144	0.084	615	1830	+ 1
100S	100	7.62	612	25	150	0.084	620	1850	0
100H	100	7.62	611	25	148	0.084	620	1940	0
Isooctane	100	7.93	611	25	153	0.056	529	1830	+ 6
100S	100	7.93	611	25	156	0.056	528	1850	+ 6
100H	100	7.93	611	25	148	0.056	510	1845	+ 7
Variable Spark Advance at 608 rpm									
Isooctane	100	7.15	615	15	151	0.070	473	1805	+19
100S	100	7.25	613	15	151	0.070	510	1815	+17
100H	100	7.15	614	15	153	0.070	445	1830	+14
Isooctane	100	8.90	614	5	152	0.070	393	1710	+27
100S	100	8.75	614	5	152	0.070	415	1730	+28
100H	100	8.90	613	5	151	0.070	395	1735	+28
Isooctane	100	7.30	612	25	151	0.070	582	1870	+ 3
100S	100	7.30	612	25	150	0.070	583	1870	+ 1
100H	100	7.30	611	25	150	0.070	540	1960	+ 1
Variable Spark Advance at 1227 rpm									
Isooctane	100	9.65	1230	15	150	0.070	535	1810	+18
100S	100	9.65	1231	15	149	0.070	537	1840	+16
100H	100	9.65	1230	15	153	0.070	493	1855	+20
Isooctane	100	10.52	1227	5	152	0.070	495	1660	+27
104S	100	10.52	1226	5	154	0.070	493	1740	+24
Variable Engine Speed at 0.070 F/A and 15 btc Ignition									
Isooctane	100	7.15	615	15	151	0.070	473	1805	+19
100S	100	7.25	613	15	151	0.070	510	1815	+17
100H	100	7.15	614	15	153	0.070	445	1830	+14
Isooctane	100	9.65	1230	15	150	0.070	535	1810	+18
100S	100	9.65	1231	15	149	0.070	537	1840	+16
100H	100	9.65	1230	15	153	0.070	493	1855	+20

continued

Table 5 - continued

Fuel	Rated Octane Number	Compression Ratio	Speed, rpm	Ignition, btc	Inlet-Mixture Temp., F	Fuel-Air Ratio	Final End-Gas Press, psia	Final End-Gas Temp., R	Time of Knock, CA Degrees
Variable Engine Speed at 0.084 F/A and 15 btc Ignition									
Isooctane	100	7.58	614	15	148	0.084	555	1825	+13
100S	100	7.58	615	15	146	0.084	565	1820	+13
Isooctane	100	9.85	1228	15	151	0.084	618	1855	+13
104S	100	9.85	1230	15	150	0.084	645	1880	+13
Variable Engine at 0.056 F/A and 25 btc Ignition									
Isooctane	100	7.93	611	25	153	0.056	529	1830	+ 6
100S	100	7.93	611	25	156	0.056	528	1850	+ 6
100H	100	7.93	611	25	148	0.056	510	1845	+ 7
Isooctane	100	8.62	1223	25	152	0.056	480	1855	+13
104S	100	8.62	1223	25	153	0.056	510	1845	+12
Motor and Research Methods									
Isooctane	100	7.70	613	13	133	0.072	479	1735	+21
Isooctane	100	7.90	906	19	300	0.082	481	1850	+13

tribution of reactions just prior to knock. If this were not the case, it would not be possible to operate modern cars at present compression ratios.

The equations derived for the ignition delay of a fuel-air mixture in the rapid-compression machine show that the delay is an exponential function of reciprocal temperature (8). In a system, such as an engine, where the temperature is continually increasing until knock occurs, it is reasonable to expect progressively more reaction per unit of time during the compression of the end-gas. Some idea of how this might increase during an engine cycle is shown in Fig. 5. For the purpose of this illustration, the relative rate of reaction is equivalent to $1/\tau$, where τ is the ignition delay at any given pressure and temperature.

It is apparent from the curve that most of the preknock reactivity could be expected to take place in the last five crankangle deg before knock. This supports the general concept that, to understand the significance of the pressure-temperature data obtained in an engine, one should be mostly concerned with the state of the gases just before knock.

Based on these condiserations, most of the analyses in this paper are based on the final end-gas pressures and temperatures. Table 5 presents this information along with the fuel, engine operating conditions, and time of knock for each run. The table has been arranged in groups, each of which contains all data covering a variable - either fuel or engine operating condition. In some cases, this has required repetition of data on the table, since some data were used for several correlations.

Fuel-Engine Relationships at Knock-Limited Compression Ratio

The final end-gas pressures and temperatures have been examined to determine the effects produced by the different variables investigated. These variables include engine operating conditions, octane level and precombustion, organometallic antiknock additives, fuel types, Motor and Research methods of knock-rating, fuel sensitivity and engine severity, and time of knock. Each of these items will be considered separately. Also, one other item which seemed appropriate to consider in our analyses is the temperature-density concept of fuel rating.

Engine Operating Conditions - The different engine operating conditions investigated were inlet-mixture temperature, spark advance, engine speed, and fuel-air ratio.

For the study of inlet mixture temperature, the fuels used were primary reference fuels, isooctane plus 1.0 ml TEL, and diisobutylene. The engine was adjusted for knock-limited compression ratios at inlet-mixture temperatures ranging from 110 to 400 F for each fuel. The other engine operating conditions were 15 deg btc ignition, 608 rpm, and 0.070 fuel-air ratio (F/A).

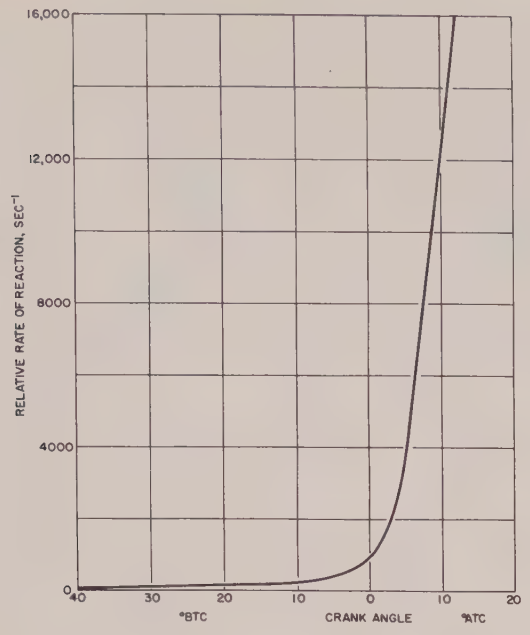

Fig. 5 — Preknock reaction rate history for isooctane

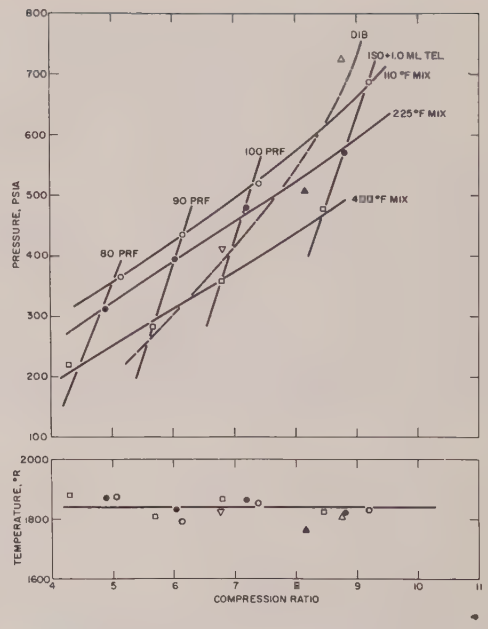

Fig. 6 — Fuel-engine relationships as a function of end-gas final pressure and temperature

The effects of engine and fuel variables on final end-gas temperature and pressure are shown in Fig. 6. In this figure, compression ratio is plotted against final pressure in the upper part and against final end-gas temperature in the lower part. Separate lines pass through the data points for all primary fuels at each inlet-mixture temperature. Similarly, separate lines pass through the data points for each fuel at different inlet-mixture temperatures. The pressure data lines are separate and distinct, but all lines for the temperature data merge into one within the experimental variability. In other words, at knock-limited compression conditions, all fuels knock at the same final end-gas temperature over a wide range of inlet-mixture temperatures. The major distinction between the fuels and engine operating conditions lies in the pressure values.

Using a special compression ignition engine, Levedahl (15) found that hot flames first appeared (autoignition) in the temperature range of 1560 ±50 R for all aliphatic fuels studied. It is believed, however, that the relative contancy of temperature is only a matter of circumstances relating to engine operation and fuel behavior characteristics. Fuel behavior is discussed in a later section dealing with precombustion.

Engine operation relates to the manner in which knock-ratings are made in a variable-compression-ratio engine. If the inlet mixture is heated, the engine will knock more. To reduce knock, the compression ratio is lowered. This means that the higher inlet mixture temperature, and its effect in producing a higher final end-gas temperature, is compensated by a reduction in compression ratio. The pressure, on the other hand, must decrease due to the decrease in compression ratio.

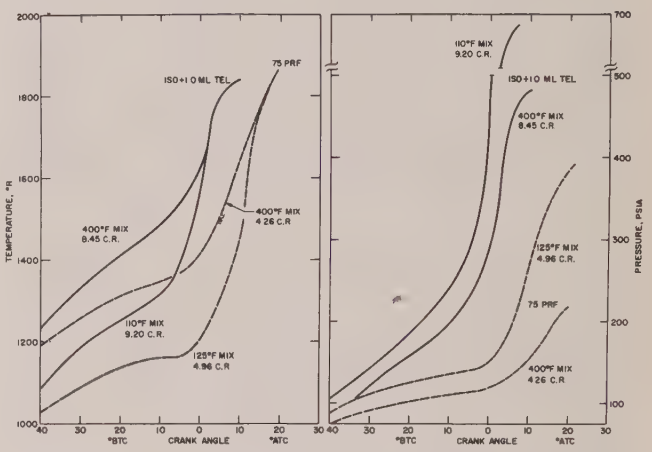

Fig. 7 — Effect of octane number of prf on end-gas temperature and pressure

As an example of the constancy of temperature, the pressure-crankangle and temperature-crankangle relationships for 75-O.N. PRF and isooctane + 1.0 ml TEL at low (nominal 120 F) and high (400 F) inlet-mixture temperatures are shown in Fig. 7. Before top center, the pressures and temperatures for the 75 PRF are considerably lower for a given inlet-mixture temperature than for isooctane + 1.0 ml TEL. This is to be expected, since the knock-limited compression ratio for the 75 PRF is much lower. After top center, the gas temperature for the lower octane fuel at both inlet-mixture continues to rise until the final end-gas temperature before knock is about the same for both fuels.

It is not that the rate of temperature rise is appreciably

greater with 75 PRF but that the temperature rise with the higher octane fuel was terminated by knock about 10 deg sooner in the engine cycle. A point of some interest is that, although the final end-gas temperatures are about the same for both fuels at both inlet-mixture temperatures, the maximum difference is 550 R at 5 deg btc.

The difference in pressure between these two fuels at a given inlet-mixture temperature increases throughout the engine cycle. At the time of knock, the maximum pressure difference amounts to 500 psi, in contrast to a negligible difference in the final end-gas temperature. The differences in pressure are in accord with the differences one would expect from the differences in knock-limited compression ratios required.

Based on the premise that pressure, temperature, and ignition delay are the important factors controlling knock, a higher inlet-mixture temperature must require a longer ignition delay since the final cylinder pressure is lower with no change in final end-gas temperature. This is reasonable since the rate of change in pressure and temperature tend to decrease with increased inlet-mixture temperature. Since knock was held constant in this study, the only requirement on the delay is that it be of sufficient duration to allow all but an end fraction of the fuel to be consumed by normal combustion before autoignition occurs. Too long or too short a delay would mean either too little or too much knock. For each operating condition, the pressure-temperature history must be adjusted by varying compression ratio to produce the correct delay, in order to maintain a constant knock intensity.

Fig. 6 shows that, in the case of DIB, a much larger reduction in pressure is required to maintain the same knock intensity when inlet-mixture temperature is raised from 110 to 400 F. This is also reflected by a much larger change in compression ratio for DIB. It is this greater required change in compression ratio for DIB that causes its octane value to change from 92 to 104 in this engine when the inlet-mixture temperature is lowered from 400 to 110 F.

To study the effect of spark advance, three fuels were used: isooctane and S and H fuels blended to 100 octane number. The pressure-crankangle and temperature-crankangle relationships at spark advances of 5, 15, and 25 deg btc are shown on Fig. 8 for 608 rpm, 150 F inlet-mixture temperature, and 0.070 fuel-air ratio. The curves for the three fuels are nearly identical, as shown by the shaded bands which encompass the corresponding data for the three fuels. The lowest compression ratio and the lowest pressure and temtemperature before top center occur with the 15 deg btc spark advance. After top center, however, the pressures and temperatures at any given crankangle become higher as the spark is advanced from 5 deg btc.

The effect of spark advance on final end-gas temperatures is shown in Fig. 9 at both 608 and 1227 rpm. A nearly linear relationship exists between increase in final end-gas temperature and spark advance. A 20-deg increase in spark advance raises the final end-gas temperature by 180 R.

The same three fuels: isooctane and S and H fuels blended to 100 octane number - were used to study the effects of engine speed. The pressure-crankangle and temperature-crankangle relationships at engine speeds of 608 and 1227 rpm are shown in Fig. 10 for 15 deg btc ignition timing, 150 F inlet-mixture temperature, and 0.070 fuel-air ratio. Again, the curves for the three fuels are practically identical as shown by the shaded bands which include the corresponding data points. A greater knock-limited compression ratio is required at 1227 rpm, and this is reflected in appreciably greater pressure and temperatures before top center. Later in the cycle, the pressures and temperatures become more nearly equal. If time is measured on a crankangle basis, the rates of pressures and temperature rise following ignition are greater at the lower speed, particularly the rate of pressure rise.

The effect of engine speed on final end-gas temperatures for all engine operating conditions investigated is shown in Fig. 11. It is apparent that for the small range investigated, engine speed has a negligible effect on final end-gas pressures and temperatures.

The effect of fuel-air ratio was investigated using the same three fuels. The pressure-crankangle and temperature-crankangle relationships at fuel-air ratios of 0.056, 0.070 and 0.084 are shown in Fig. 12 for 608 rpm, 25 deg btc ignition timing, and 150 F inlet-mixture temperature. The lowest knock-limited compression ratio occurred at 0.070 fuel-air ratio, and resulted in lower pressures and temperatures before top center. After top center, however, the pressures and temperatures for the richer mixtures rose more rapidly. This is undoubtedly caused by the greater energy available in the richer mixtures. Increasing the fuel-air ratio appreciably above the chemically correct requirements caused a negligible increase in pressure and temperature. This is further indicated by Fig. 13 which shows the effect of fuel-air ratio on final end-gas temperatures at different speeds and spark advances. As shown, changing the fuel-air ratio from 0.056 to 0.070 can cause the final end-gas temperature to increase by about 150 R. Further enrichment has little additional effect.

The reason for the changes in final end-gas pressures and temperatures at knock-limited compression ratio for changes in engine operating conditions can be understood on the basis of the factors controlling ignition delay. In general, it was observed that a change in engine operation which causes a higher rate of pressure or temperature rise just before knock, allows the final end-gas pressure or temperature, or both, to reach higher values. This is in agreement with the basic ignition-delay concept, that a higher pressure or temperature must result in a shorter delay for knock. When the rates of pressure and temperature rise are higher, the time to reach the pressure and temperature obtained at a lower rate must be shorter. If the engine was knock-limited at the lower rates, then the fuel could not knock at the higher rate for the same final pressure and temperature as at the lower rate,

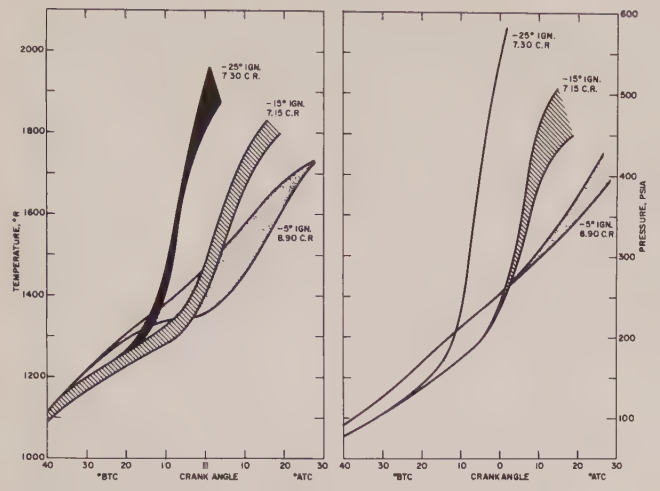

Fig. 8 — Effect of ignition timing on end-gas temperature and pressure

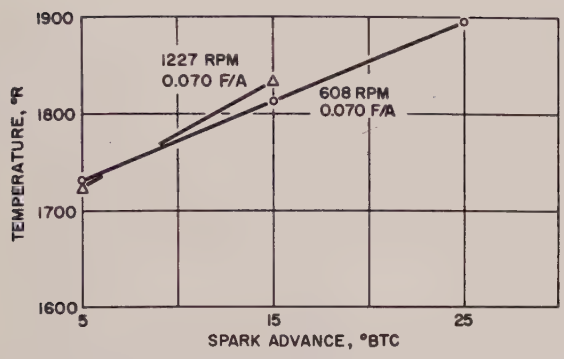

Fig. 9 — Effect of spark advance on final end-gas temperature isooctane at knock limited compression ratios

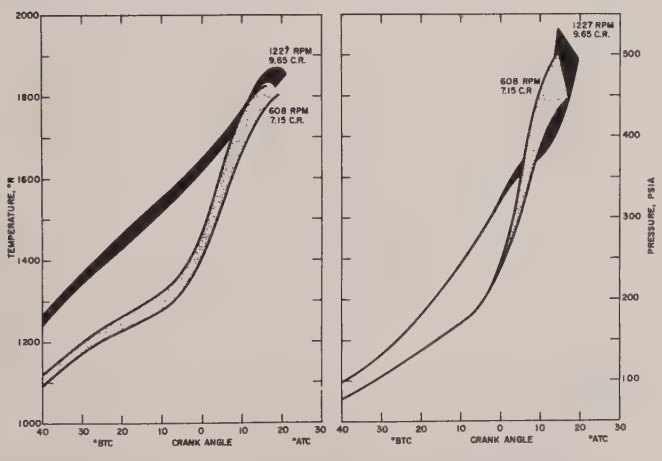

Fig. 10 — Effect of engine speed on end-gas temperature and pressure, —15 deg spark, 0.070 F/A, 150 F Mix. T, isooctane, 100 S, 100 H

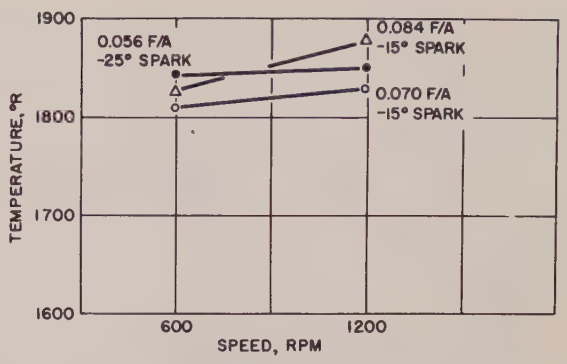

Fig. 11 — Effect of engine speed on final end-gas temperature isooctane at knock limited compression ratios

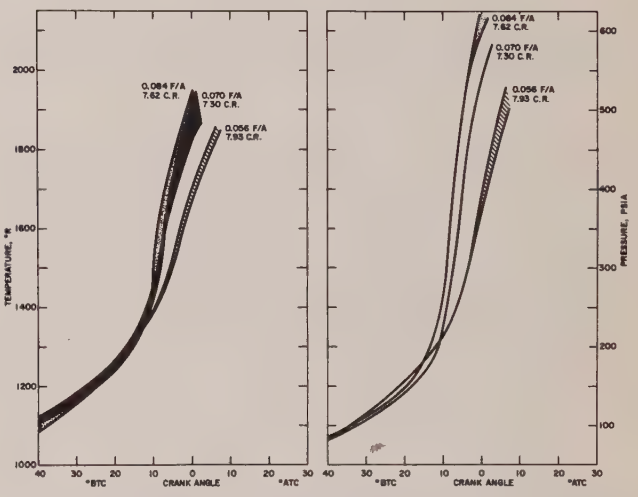

Fig. 12 — Effect of F/A on end-gas temperature and pressure, 608 rpm, —25 deg spark, 150 F Mix. T, isoctane, 100 S, 100H

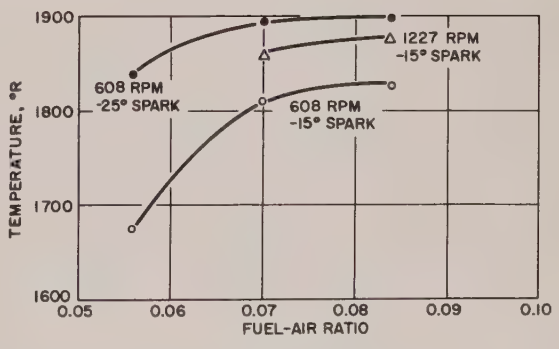

Fig. 13 — Effect of fuel-air ratio on final end-gas temperature isooctane at knock limited compression ratios

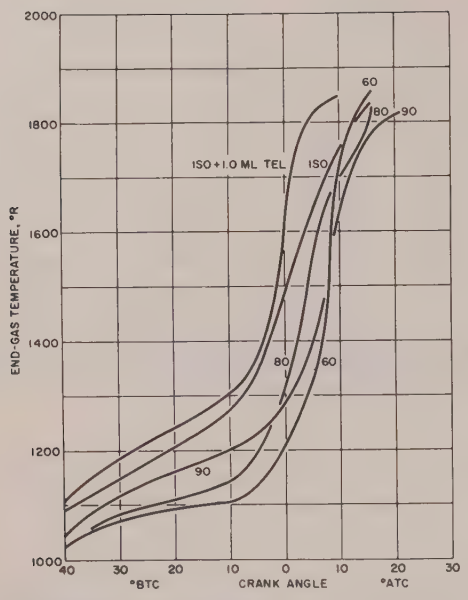

Fig. 14 — Precombustion reactivity in a fired engine, —15 deg spark, 150 F Mix. Temp, 0.070 F/A

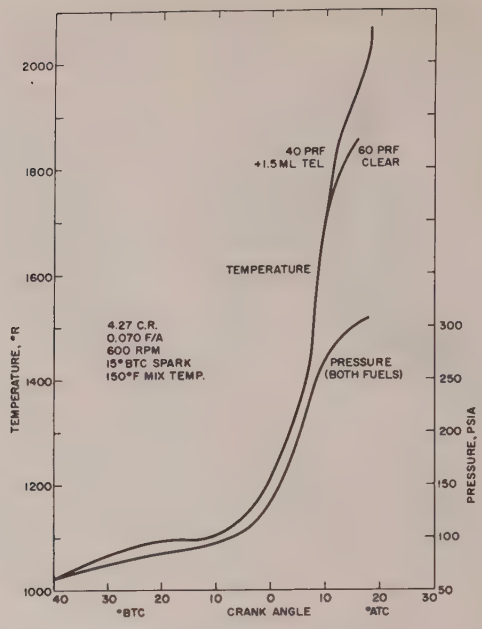

Fig. 15 — Temperature and pressure history for 40 prf +1.5 ML TEL

since the elapsed time would be too short. In other words, the pressure and temperature at the higher rate must continue to rise until the proper combination of pressure, temperature, and ignition delay are obtained for knock to occur.

Octane Level and Precombustion - The fuels of different octane level investigated were the primary reference fuels and isooctane + 1.0 ml TEL. All runs were made at 15 deg btc ignition timing, 608 rpm, 150 F inlet-mixture temperature, and 0.070 fuel-air ratio. The temperature-crankangle relationships obtained are shown in Fig. 14. Before ignition, the lower octane fuels, which have lower knock-limited compression ratios, have proportionately lower temperatures. As combustion proceeds, however, the lower octane fuels tend to have a greater rate of temperature rise and attain the same final temperatures reached by the higher octane fuels. Obviously, there must be some explanation for this phenomenon.

It is generally known that the heat released by precombustion in a motored engine increases as fuel octane number decreases, particularly for a given hydrocarbon series (16). The same situation might be expected in a fired engine, although the existence of cool flames and other precombustion reactions in this engine has received limited study (10). The data obtained in this study, as shown in Fig. 14, indicate that precombustion reactivity is probably the cause of the unusual temperature rises observed. It necessarily follows that this reactivity must occur only in the end-gas, since the rest of the charge has already been consumed by the flame front. That is why it is important to have the temperature-measuring apparatus in this zone of the combustion chamber.

Pressure records in a fired engine, however, show no evidence of precombustion reactivity. The reason for this is that the amount of reacting gas just before knock is very small. Since the pressure pickup can only detect pressure changes throughout the combustion chamber, this small energy release is incapable of changing pressure appreciably.

Hence, precombustion reactivity is another reason for the constancy of final end-gas temperature with change in fuel-octane level, while pressure changes occur in an expected manner.

Organometallic Antiknock Additives - The additives used in this study were TEL as 62 Mix, manganese as AK-33X, and AK-33X as a supplement to TEL. All runs were made at 15 deg btc ignition timing, 608 rpm, 0.070 fuel-air ratio, and 150 F inlet-mixture temperature. Fig. 15 shows the pressure-crankangle and temperature-crankangle relationships for clear 60 PRF and 40 PRF containing 1.5 ml TEL/gal to boost it to 60 octane number. There is no difference in the temperature-crankangle relationship for the two fuels until about 25 deg after ignition. At that time, higher temperatures are obtained for the fuel containing TEL. This cannot be attributed to some engine condition since conditions were identical for both fuels.

Prior studies in a motored engine have shown that, for fuels of the same octane level, a leaded fuel will develop more heat of precombustion when the engine is operated at its autoignition-limited compression ratio (16). The higher temperatures observed with leaded fuels in a spark-ignited engine are, again, believed to be due to the increased precombustion. It is known that TEL does not cause greater precombustion reactivity; it merely allows the precombustion reactions of the base fuel to proceed further at the higher knock-limited compression ratio permitted when TEL is pres-

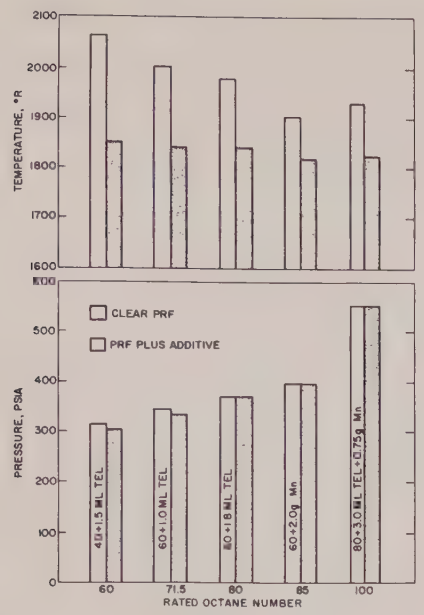

Fig. 16 — Effect of organometallic additives on final end-gas temperature and pressure of prf

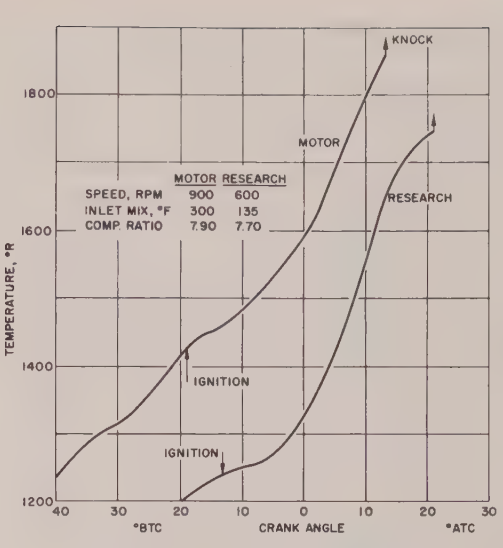

Fig. 17 — End-gas temperature histories for isooctane

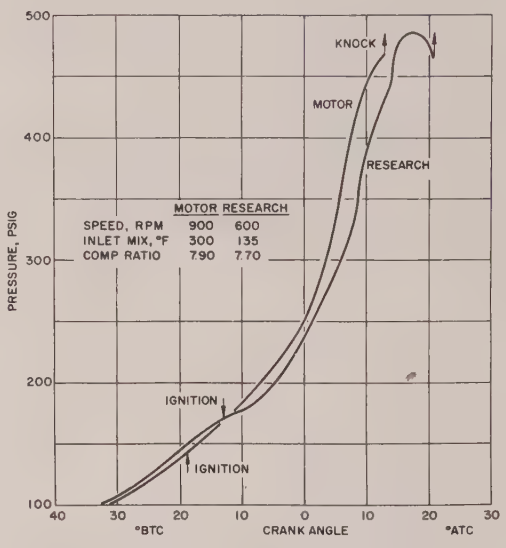

Fig. 18 — Cylinder gas pressure histories for isooctane

ent. This is further evidence that knock and the extent of exothermic precombustion reactivity are not directly interrelated (17).

TEL, AK-33X, or AK-33X as a supplement to TEL all have the same effect of allowing higher final end-gas temperatures before knock will occur. This is shown by the bar chart on Fig. 16. It is interesting to note that the addition or organometallic additives allows no change in final end-gas pressure. The reason for this is the same as stated for the precombustion in the case of the primary reference fuels: the heat release in the end-gas zone is too small to affect the overall cylinder pressure. The effect of additives on increasing the final end-gas temperature tends to decrease as the octane number of the base fuel is raised, as shown in Fig. 16. This occurs regardless of whether TEL and/or AK-33X is added.

Fuel Types - Since only a few fuel types were studied in this investigation, it is not possible to draw broad conclusions regarding their effect on end-gas pressures and temperatures. If we are allowed to say that isooctane is a typical paraffin, S fuels are typical of olefins, and H fuels are typical of aromatics, then, at the same octane level, fuel type has no effect on pressure-crankangle and temperature-crankangle relationships. This is illustrated in Figs. 8, 10, and 12 for isooctane and the S and H fuels at various engine operating conditions.

Motor and Research Methods - Because of the broad general interest in motor and research methods of knockrating and because these engine methods are used to classify fuels by sensitivity, the desirability of investigating these procedures was evident. Since knock is presumably a function of pressure, temperature, and reaction time, an investigation of pressure-crankangle and temperature-crankangle data should show the fundamental differences between these methods. It is recognized, of course, that the engine used in this study is not a typical CFR engine. However, its performance in terms of guide curve values and the knockrating of various fuels indicated that this special engine is reasonably close to a conventional engine in performance. The pressure-crankangle and temperature-crankangle relationships obtained by motor and research method procedures for isooctane are shown in Figs. 17 and 18. It is apparent that the pressure paths and the final pressures are about the same by the two methods. However, the temperature paths and final end-gas temperatures are appreciably different. The major effects of the motor method are to produce higher

temperatures earlier in the cycle, higher temperatures before knock occurs, and knock earlier in the cycle. The research method engine apparently takes more time to reach knock because of its more retarded ignition and lower speed, but this is compensated for by the higher temperatures of the motor method.

The pressure and temperature histories which occur for motor and research methods differ from those obtained when the inlet-mixture temperature alone is varied, and can be explained. Based on the pressure, temperature, and time factors for knock, an increase in inlet-mixture temperature, as in going from the research method to the motor method, should cause an increase in final end-gas temperature. This should reduce ignition delay and cause the knock to increase. If the necessary changes in engine speed and spark advance in going from the research method to the motor method are now made as well, the available time delay for knock is reduced. Since practically no change in compression is required, as shown by Guide Curve values, there is no change in final cylinder pressure. This means, then, that the decrease in ignition delay due to an increase in inlet mixture temperature does not cause an increase in knock. Rather, at the new operating condition, only a shorter delay is required to keep the knock at the same intensity.

Fuel Sensitivity and Engine Severity - Previous studies in the rapid-compression machine (8) showed that the ignition-delay equations for diisobutylene and isooctane with stoichiometric mixtures of fuel and air are:

Diisobutylene:

$$\log \tau = -3.734 - 0.944 \log P + 4975/T \qquad (2)$$

Isooctane:

$$\log \tau = -3.028 - 1.490 \log P + 5837/T \qquad (3)$$

where: τ = ignition delay for autoignition, sec
P = pressure of fuel-air mixture, psia
T = temperature of fuel-air mixture, R

These equations indicate that an increase in either end-gas pressure or temperature will cause a greater decrease in ignition delay for isooctane than for DIB. Conversely, a decrease in pressure or temperature will cause the ignition delay to increase more for isooctane than DIB. From this it can be inferred that increases in either end-gas pressure or temperature will cause DIB to appreciate relative to issoctane, or to depreciate with a reduction in either pressure or temperature.

In applying this ignition-delay data to engines, one must consider the change in ignition delay with change in operating conditions. Two fuels will presumably have the same delay at any operating condition when they knock alike. It, therefore, follows, that the same change in delay would be required when changing operating condition and maintaining constant knock level.

When the inlet-mixture temperature alone was increased, the final end-gas temperature remained constant but the final cylinder pressure decreased. Examination of Eqs. 2 and 3 for DIB and isooctane shows that the decrease in pressure under these conditions will cause the ignition delay for DIB to increase less than the delay for isooctane. Thus, DIB depreciates relative to isooctane which was found experimentally. This was also true in a motored engine (8). The fact that DIB loses antiknock value relative to a primary reference fuel as engine conditions are made more severe means, in the usual sense of the word, that DIB is a sensitive fuel.

When changing conditions from research to motor method, the end-gas temperature increased but the pressure remained constant. From Eqs. 2 and 3 it can be seen that the ignition delay decreases less for DIB than for isooctane. This is inconsistent with the experimental evidence that DIB depreciates relative to isooctane when changing from research to motor method.

As yet, this inconsistency has not been fully resolved, but it is believed that a number of factors may be responsible for the anomaly. One is the apparent high precombustion reactivity of isooctane by the research method, as shown by the decrease in pressure prior to knock while the temperature is still ring rapidly. Another is the fact that the simulated motor method engine operates considerably richer than research engine. The ignition delay data used in this study, as stated previously, were for a stoichiometric mixture only.

The data presented in this paper on the effect of different engine operating conditions on final end-gas pressures and temperatures can now be analyzed for the effect of these conditions on engine severity.* For the purposes of this analysis, DIB and isooctane will be used, and the fuels will be considered as having equal knockrating at some given set of engine conditions.

Increasing the compression ratio will cause both the end-gas pressure and temperature to increase. Eqs. 2 and 3 for DIB and isooctane show that such changes in pressure and temperature will decrease the ignition delay, and that the decrease for isooctane will be greater than for DIB. In other words, increasing the compression ratio makes the engine milder, provided no other engine operating condition is changed as well.

For the engine variables studied, compression ratio was always adjusted to maintain a constant knock level. When the spark was advanced and the compression ratio properly adjusted, the final end-gas temperature and pressure increased. This occurred because the more rapid rates of pressure and temperature rise associated with increased spark advance necessitates a much shorter ignition delay. Increasing spark advance, like increasing compression ratio, should

*An engine which gives a low rating to a sensitive fuel is a "severe" engine.

make an engine milder.

Increasing the inlet-mixture temperature at knock-limited compression ratio caused the final cylinder pressure to decrease and the final end-gas temperature to remain substantially constant. This means a smaller relative increase in ignition delay for DIB than for isooctane or that DIB depreciates relative to isooctane and the engine becomes more severe.

At fuel-air ratios richer than stoichiometric, there is no appreciable change in either final end-gas pressure or temperature when the fuel-air ratio is changed. Thus, changes in fuel-air ratio at rich operating conditions should cause no change in engine severity. On the other hand, if the fuel-air ratio is made leaner than stoichiometric, the final end-gas temperature and pressure decrease. This implies a relatively longer delay for isooctane than DIB and the engine should become more severe.

Increasing the engine speed resulted in slightly higher end-gas temperature and generally higher pressure at knock-limited compression ratio for the small range of speeds investigated. With the data available, it would be expected that increasing engine speed would reduce engine severity.

Although no pressure-temperature data were obtained during part-throttle operation, it should be relatively easy to deduce what would happen under part-throttle operation. For this condition, the final cylinder pressure would certainly decrease. Then, if the air-fuel ratio was made lean, as occurs during part-throttle operation, the final end-gas temperature should decrease. This would cause the engine to become more severe as the throttle is closed.

All these deductions regarding the influence of different operating conditions on engine severity are based on adjustment of knock-limited compression ratio. Since compression ratio affects engine severity, different results might be obtained had the knock-limiting condition been obtained by adjusting some other engine parameter than compression ratio.

The deductions made with regard to engine severity in this paper can be compared with experimental information obtained by knock-rating fuels (18). This comparison is shown in Table 6.

Table 6 - Influence of Engine Conditions on Severity

Engine Variable	Severity Effect: Deduced	Severity Effect: Experimental
Compression ratio increase	milder	slightly milder
Spark advance increase*	milder	more severe
Mixture temperature increase*	more severe	more severe
Fuel-air ratio* going richer than stoichiometric	no effect	-
Fuel-air ratio* going leaner than stoichiometric	more severe	-
Speed increase*	slightly milder	more severe
Increased throttling*	more severe	more severe

*Variable knock-limited compression ratio

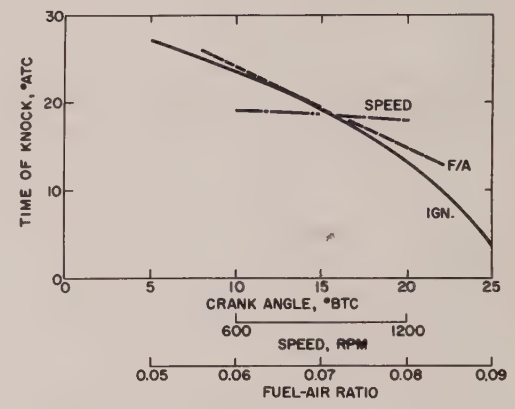

Fig. 19 — Effect of engine variables on time of knock

It is apparent that the agreement between the experimental multicylinder engine data and that obtained by deduction based on this single cylinder study is reasonably good. This is further support for the usefulness and validity of the basic ignition-delay concept for increasing the understanding of fuel-engine relationships at knock-limited compression ratios.

Time of Knock - The time of knock for all fuels and engine conditions investigated is shown in Table 5. These data indicate that the time of knock is about 20 deg atc for variable inlet-mixture temperatures, for clear and additive fuels of the same octane number, and for octane number levels from 60 PRF to 90 PRF. With isooctane and isooctane plus 1.0 ml TEL, the time of knock advances. The change is about 5 deg, on the average, for isooctane, with an additional 5 deg advance for isooctane plus 1.0 ml of TEL. This may account for some of the difficulty in rating fuels at 100 octane number and above.

Some engine conditions, such as spark advance, engine speed, and fuel-air ratio, seem to affect the time of knock. Fig. 19 shows the effects of these three variables when isooctane is used. These effects are not particularly different for the S and H fuels. A greater spark advance or enrichment of the fuel-air ratio definitely makes knock occur earlier in the cycle, while increasing engine speed has little effect on the time of knock.

Temperature-Density Concept - Some years ago Rothrock (19) proposed that the knocking tendency of any particular fuel

could be characterized by the relationship between end-gas temperature and density. The idea was that one would need only to obtain a reference-fuel framework and then determine the octane value of unknown fuels by their position on this framework. His analysis was based on computed values for the end-gas state. Now that some actual measurements of the end-gas pressure and temperature are available, it should be possible to test this concept. From thermodynamic considerations, specifying pressure and temperature is equivalent to specifying density and temperature. Since Rothrock used density and temperature in his correlations, we converted our data to his units by means of the ideal gas law:

$$\frac{P}{\rho} = \frac{RT}{M} \tag{4}$$

where:

P = pressure
ρ = density
T = temperature
R = universal gas constant
M = molecular weight

Then

$$\rho = \frac{PM}{RT} \tag{5}$$

Since

R/M = K, a constant, the equation becomes

$$K\rho = \frac{P}{T} \tag{6}$$

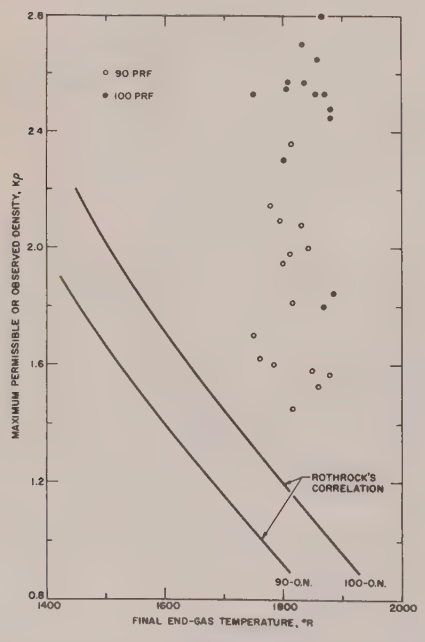

Fig. 20 — Comparison of temperature-density correlations

Fig. 20 is a plot of our temperature-density data for 90 PRF and 100 PRF at different inlet-mixture temperatures and the computed relationships obtained by Rothrock for these same fuels. As would be expected, the correlation is very poor, since our temperatures are relatively constant. Also, it is impossible to distinguish one fuel from another on the basis of temperature-density values.

As a further check on Rothrock's hypothesis, his equations were used for the computation of end-gas temperature and density with our data. Then these computed values were compared with those actually observed. This comparison is shown in Fig. 21 for all primary reference fuels used, as well as all fuel types, at engine conditions of 15 deg btc ignition timing, 608 rpm, and 0.070 fuel-air ratio. Again, there is no correlation between computed and observed values.

As a simplification of calculating the end-gas state, it has been suggested that merely compression temperature and density be used (20). The conjecture is that these variables should have a definite relationship to end-gas conditions. To investigate this, both compression and end-gas temperature were measured. The compression temperature was obtained by momentarily flicking off the ignition and recording the necessary data. By trial-and-error presetting of the instrumentation it was possible to record this information in the first one or two cycles after the ignition was turned off. The results are shown in Fig. 22. It is apparent that the suggested correlation between end-gas temperature and compression temperature was not obtained.

We recognize that our conditions differ appreciably from Rothrock's. However, since his proposed correlation was to have general applicability, regardless of conditions, its failure to hold in any one condition renders the concept unsuitable.

In spite of the invalidity of the extension of Rothrock's proposal to compression temperatures, it is to be recognized that a knockrating procedure based on computed values from

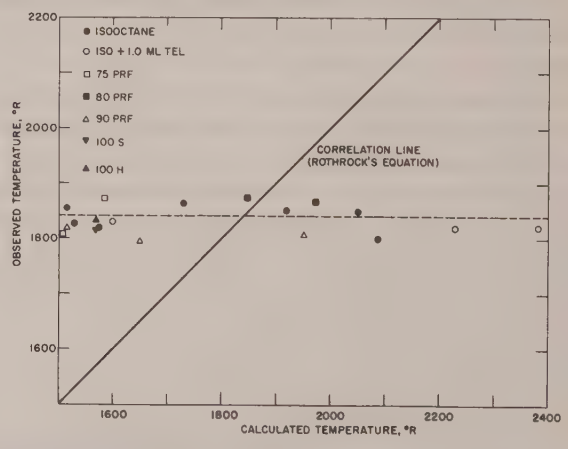

Fig. 21 — Comparison of observed end-gas temperature with calculated values, 608 rpm, —15 deg ignition, 0.070F/A, Mix. Temp. variable

3. The final cylinder pressures vary widely in a manner which is to be expected by the change in compression ratio required to provide knock-limited performance.

4. At our standard engine operating conditions with knock-limited compression ratio, the final end-gas temperature is 1840 ±40 R for a wide selection of primary reference fuels as well as diisobutylene and two blends representative of olefinic and aromatic types; this was also true when inlet-mixture temperature was varied. At other operating conditions, the final end-gas temperature varied over a range of 350 R; at any one condition of operation, however, the fuel effect was still ±40 R.

5. The essentially unchanged final end-gas tempera- engine measurements may still provide useful results. This method, however, would provide another means of evaluating knock in terms of engine parameters.

Conclusions

From this study, in which the same knock level was maintained by adjusting the compression ratio for all fuels and engine conditions investigated, the following conclusions are made:

1. The velocity-of-sound equipment used in this laboratory for determining the temperature of the unburned fuel-air mixture gave highly satisfactory performance with a minimum of care and service. It is estimated that the precision of the apparatus in determining the temperature of the gases in the end zone of an engine is ±1.5%. Since the apparatus, as used, indicated the average value for a number of engine cycles, it is expected that cycle-to-cycle variability would reduce the precision to about ±2.5%.

2. Because of exponentially increasing reactivity with temperature rise, it is to be expected that the major portions of the reactions leading to knock in an engine occur immediately prior to the time of knock. It is believed that this characteristic of the fuel-engine relationship is what makes it possible to operate engines at today's high compression ratios.

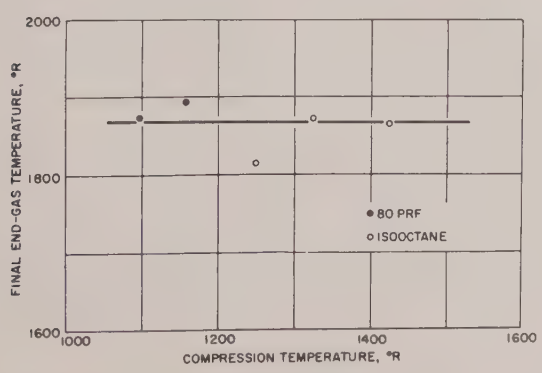

Fig. 22 — Compression temperature versus final end-gas temperature

ture for different fuels under fixed engine conditions is attributed to the increased precombustion reactivity which occurs as the octane number is lowered. We believe that the increased heat released by precombustion tends to compensate for the lower knock-limited compression ratio as the octane number is reduced.

6. Increasing engine speed, advancing ignition timing, or increasing fuel-air ratio from lean to stoichiometric cause higher final end-gas temperatures. Large changes in inlet-mixture temperature had no effect on final end-gas temperature.

7. The addition of organometallic additives, such as TEL and/or AK-33X, to improve fuel antiknock quality causes the final end-gas temperature to increase 50 to 150 R above the value for clear primary reference fuels of matching octane number. The size of the increase is somewhat greater with lower octane fuels, which develop more precombustion reactivity before knock. It is believed that the increased heat release with the additive occurs because the additive merely allows the inherent reactivity of the lower octane base fuel to proceed further before knock occurs. This is added support for the argument that the extent of exothermic precombustion reactivity, in itself, does not control knock.

8. Different clear fuels in the 100 octane number range have the same pressure crankangle and temperature-crankangle relationships before knock occurs for any given set of knock-limited parameters.

9. Based on the modified engine used in this study, the major distinction between the Motor and Research methods of knockrating fuels is that the Motor method stresses the temperature sensitivity of the fuel while the Research method stresses the time for reactions leading to knock. The pressure histories in the two engines are very similar.

10. The characterization of fuel-engine relationships on the basis of relationships between end-gas temperature and density or between compression temperature and density lacks experimental confirmation.

11. The study of the autoignition of fuel-air mixtures in an apparatus which permits the determination of ignition delay under controlled conditions can be useful in understanding the complexities of knock in an engine.

12. Fuel sensitivity and engine severity can be understood on the basis of final end-gas temperatures and pressures and the basic ignition-delay characteristics of fuels. It was reasoned that increases in compression ratio, spark advance, and engine speed will make an engine milder. Higher inlet-mixture temperature, more throttling, and leaner fuel-air ratio than the chemically correct requirement will make the engine more severe.

13. The time at which knock occurs comes earlier in the cycle for clear or leaded isooctane than for lower octane primary reference fuels. This may be related to the difficulty in rating fuels in the high-octane range. Increasing spark advance or enrichening the fuel-air ratio tend to make knock occur earlier in the engine cycle.

References

1. T. A. Townend and E. A. C. Chamberlain, "The Influence of Pressure on the Spontaneous Ignition of Inflammable Gas Mixtures," Proc. Roy Soc., 154A, (1936), 95-112.

2. L. Withrow and T. A. Boyd, "Photographic Flame Studies in the Gasoline Engine," Ind. Engr. Chem., 23, (1931), 539-547.

3. H. T. Tizard and D. R. Pye, "Experiments on the Ignition of Gases by Sudden Compression," Phil. Mag., 44, Series 6, No. 259, (1922), 79.

4. C. F. Taylor, E. S. Taylor, J. C. Livengood, W. A. Russell and W. A. Leary, "The Ignition of Fuels by Rapid Compression," SAE Quart. Trans., 4, (1950), 232-270.

5. C. D. Miller, "A Study by High Speed Photography of Combustion and Knock in a Spark-Ignition Engine," SAE Quart. Trans., 1, (1947), 98-143.

6. G. A. Ball, "Photographic Studies of Cool Flames and Knock in an Engine," Fifth Symposium on Combustion, Reinhold Publishing Corp., (1955), 366-372.

7. C. Walcutt, Discussion of Paper by D. L. Pastell, SAE Quart. Trans., 4, (1950), 584-585.

8. E. B. Rifkin and C. Walcutt, "A Basis for Understanding Antiknock Action," SAE Trans. 65, (1957), 552-566.

9. J. C. Livengood, T. P. Rona and J. J. Baruch, "Ultrasonic Temperature Measurements in Internal Combustion Engine Chamber," J. Acoustical Society of America, 25, (1954), 824.

10. J. C. Livengood, C. F. Taylor and P. C. Wu, "Measurement of Gas Temperature in an Engine by the Velocity of Sound Method," SAE Trans., 66, (1958), 683-699.

11. J. D. McCullough, "Engine Cylinder Pressure Measurement." SAE Trans. 61, (1953), 557-567.

12. M. E. Gluckstein, Discussion of paper by Livengood et. al., SAE Trans. 66, (1958), 699.

13. B. Lewis and G. von Elbe, "Combustion, Flames and Explosions of Gases," 154ff, New York: Academic Press, (1951).

14. Ethyl Corp., Report No. 60-4A.

15. W. J. Levedahl and C. R. Yokley, "New Data on Automotive Combustion," NBS Tech. News Bull., 37, No. 8, (1953), 113-115.

16. C. Walcutt and E. B. Rifkin, "Precombustion Reactions in an Engine," Ind. and Engr. Chem., 43, (1951), 2844-2849.

17. E. B. Rifkin, C. Walcutt and G. W. Betker, Jr., "Early Combustion Reactions in Engine Operation," SAE Quart. Trans. 6, (1952), 472-487.

18. R. V. Kerley and K. W. Thurston, "The Knocking Behavior of Fuels and Engines," SAE Trans., 64, (1956), 554-569.

19. R. A. Rothrock, "Fuel Rating - Its Relation to Engine Performance," SAE Trans., 36, (1941), 51-65.

20. E. M. Barber, L. E. Endsley, Jr., and T. H. Randall, "Some Characteristics of Combustion in the ASTM-CFR Knock-Test Engine," API Division of Refining, 27 (III), (1947), 103-115.

Discussion

Concerning Data Reliability and Future Work

A. R. Rogowski
Massachusetts Institute of Technology

AS THE speed-of-sound technique for measuring instantaneous gas temperatures in engine cylinders was originally developed by the Sloan Laboratory Staff at MIT, it is particularly gratifying to see this new research method used so successfully by Gluckstein and Walcutt in their study of end-gas relationships.

The section of this paper which deals with Data Reliability should do much to instill confidence in this method in the minds of other workers in the field and spread the use of this effective tool. We at MIT have also been quite satisfied with the reliability of data obtained with this equipment. One factor which must be considered is the possibility of heat transfer between the transducer bars and the gases in the gap. It appears that gaps of less than 1/2 in. in length may lead to appreciable errors.

The rapid rise in end-gas temperatures, shown in the paper, points up the importance of making certain that the gas being measured in the transducer gap is actually the end-gas. This is one of the problems when the transducer bars are used at right angles in a conventionally shaped chamber. From the standpoint of combustion research, it is also evident that the usual fuel-air cycle calculations of end-gas temperatures where the effects of pre-knock reactions are ignored, are not necessarily accurate.

With regard to future work, I would like to see the effect of fuel-air ratio on end-gas temperature (Fig. 13) extended to richer mixtures to see if the longer burning time would reduce the allowable temperature, as it seems to do for the lean mixtures. It would also be interesting to use inlet pressure as a variable in place of compression ratio. This would eliminate the effect of changes in combustion chamber geometry from one run to another. The effect of engine speed and fuel-air ratio (Figs. 10 and 12) would be even more interesting if rerun with ignition timing set at each point to the value which would have given best power with a non-detonating fuel. The pressure-time histories would then be more nearly the same and the temperatures of Fig. 13 would probably be nearly constant.

One of the uses of new methods is the checking of old the-

ories which may have been used too long. In the case of the temperature-density theory, the authors have demonstrated that its further use would be of little service to combustion research.

Final and Early Knocking

J. C. Livengood
Joseph Kaye & Co., Inc.

IN DISCUSSING the results and conclusions of this paper, I wish first to agree with the authors' belief that "...the relative constancy of (the end-gas) temperature is only a matter of circumstances relating to engine operation and fuel behavior characteristics."

That the final (knocking) temperatures and pressures of the end-gas in a given fuel-air mixture depend upon their histories is shown conclusively in Ref. (B).* The range of pressures for the occurrence of knock reported therein, ranged from 150 to 495 psia and the temperatures, ranged from 1390 to 1900 deg R in the various experiments. The experiments in Ref. (B) were not performed at threshold knock, as were those in the present paper. With this limitation removed, it is possible to study the knock reaction over a wide area of the "map" as represented in Fig. 4.

I also agree with the general observation that, "...the contribution to knock by reactions occurring early in the engine cycle must be small in comparison to the contributions of reactions just prior to knock."

However, this does not mean that the reactions which occur early in the knock process are unimportant. Perhaps the greatest difficulty which may arise from attaching too much emphasis to the peak end-gas temperature, involves the preknock reactions of mixtures of compounds having greatly dissimilar chemical reactivity. In some of these cases there is evidence that the preknock reaction products from the different compounds interact, so that, for example, a mixture of a with b may have a knock resistance higher than either a or b. This is known as synergism (C).

This same problem applies to the behavior of additives. An extreme example can be cited from the behavior of certain fuels in the MIT Rapid Compression Machine, where the addition of 6 ml/gal of TEL produced no effect on ignition delay. In the engine, however, with the same peak end-gas temperature and pressure, there was a marked reduction or elimination of knock. This difference in the effect of TEL in the compression machine and in the engine can be explained on the basis of the TEL decomposition reaction during the entire pressure-temperature-time history of the charge (D). It cannot be rationalized on the basis of the peak temperature and peak pressure alone.

With regard to the Rothrock Temperature-Density correlation, there are two benefits which we now have, but which Rothrock did not:

1. We have gross reaction-rate data from compression machines, motored engines and now finally from firing engines.
2. We can now measure, with nearly satisfactory accuracy, the actual temperatures in the cycle.

With these tools it is possible to evaluate properly the time effects which are so important. I am reminded of a remark made once by A. R. Ubbelohde to the effect that the science of combustion kinetics is laboring under a burden of too many theories and a paucity of experimental methods. It is encouraging to see that the authors are beginning to put things into balance.

References

A. Alden H. Ryan, "Advanced Energy Sources and Conversion Techniques," Dept. Comm. OTS No. P. B. 151461.

B. J. C. Livengood and P. C. Wu, "Correlation of Autoignition Phenomena in Internal Combustion Engines and Rapid Compression Machines" Fifth Symposium (International) on Combustion, Reinhold, N. Y., 1955.

C. Anon. "The Synthesis, Purification and Properties of Hydrocarbons on low Molecular Weight," 18th Ann. Rep., Amer. Petr. Inst., Res. Proj. 45, June 1956.

D. E. B. Rifkin, "The Role of Physical Factors in Knock" Presented at the 23rd Midyear Mtg. Div. of Ref. Amer. Petr. Inst., May 12, 1958.

Calculated Compression Temperature-Density Relationships — Valid or Invalid?

B. R. Siegel, and
A. V. Mrstik
Sinclair Research Laboratories, Inc.

THIS PAPER REPRESENTS a significant advance in the field of establishing end-gas conditions at the time of knock. However, we challenge the generalization drawn by the authors that the characterization of fuel-engine relationships on the basis of the relationship between compression temperature and density lacks experimental confirmation. At least one prepared discussion of this paper also questioned the application of the temperature-density relationship in anti-knock studies. We hold to the substantiated belief that calculated compression temperature-density relationships are applicable as a very useful tool in relating fuel and engine performance.

First, let us look at two examples demonstrating the validity of the concept. The first example will demonstrate

*Letters in parentheses designate References.

Table A - Results of Tests Evaluating Fuel Anti-knock Quality

Engine Speed rpm	Comp. Ratio	Mixture Temp. F	Calculated Comp. Temperature, R	Knock Limited Pressure: Manifold Air Press., "Hg.	Knock Limited Pressure: Comp. Dens. lb/FT^3
1000	4:1	300	1207	60.6	0.346
1000	6:1	200	1200	36.4	0.349
1000	10:1	100	1207	20.2	0.351

Table B - Results of Test Relating Fuel Performance to Engine Performance

Reference Fuel System	Fuel Required for Trace Knock
Iso-octane - n-Heptane	94% Isooctane, 6% n-Heptane
Toluene - n-Heptane	77% Toluene, 23% n-Heptane
80 Octane Primary Ref. Fuel - TEL	80 Octane PRF + 1.65 ml/gas TEL
Prem. gaso. blend - reg. gaso. blend	90% regular - 10% premium

Table C - Test Results with Limiting Fuels Run in Single-Cylinder Engine

	94% Isooctane 6% n-Heptane	77% Toluene 23% n-Heptane	80 Oct. PRF +1.65 ml/gal TEL	90% regular 10% premium
Engine Speed, rpm	1800	1800	1800	1800
Comp. Ratio	6.1	6.1	6.1	6.1
Mixture Temp. F	100	100	100	100
Calc. Comp. Temp., R	1024	1024	1024	1024
Knock limited pressure				
Manifold Air Pres., "Hg.	32.0	31.5	32.0	32.5
Calc. Comp. Density, lb/Ft^3	0.345	0.339	0.345	0.351

the utility of the concept in evaluating fuel anti-knock quality. Isooctane was run in a single-cylinder engine at a variety of conditions using peak power spark advance. In these tests, the mixture temperature and compression ratio were mutually adjusted to give the same calculated compression temperature. The manifold pressure was then varied to determine the level at which trace knock occurred. Table A shows the results which were obtained.

The excellent agreement between the permissable calculated compression densities for a given calculated compression temperature, regardless of how widely the operating conditions were varied, indicates that these two variables properly describe the temperature, time and pressure environment of the fuel. This type of data has been obtained on scores of fuels.

The second example illustrates that fuel performance can readily be related to engine performance by means of the compression temperature, compression density concept. In these tests, the octane requirement of a modern multi-cylinder engine operating at wide-open throttle at 2000 rpm was obtained with four different reference fuel systems with the results shown in Table B.

Since the fuels shown in the table just knocked in the engine, and since they were subjected to a common environment, it necessarily follows that they must have had a common knock-limited compression temperature if the temperature-density concept is to be considered valid. To check the validity of this concept, these limiting fuels were run in the ASTM single-cylinder engine, and the knock-limited compression density was determined for each fuel at maximum power spark advance with the results shown in Table C.

After considering the accuracy of requirement data on

multi-cylinder engines, it is noted that all fuels had, for all practical purposes, the same knock-limited compression density at a common compressure temperature. This demonstrates the utility of this technique for properly describing the severity or combustion environment of a given engine, and for predicting the behavior of any fuel in that engine if its performance at a 1024 R compression temperature has been established in the single-cylinder engine.

Having demonstrated the validity of the compression density-compression temperature technique for relating fuel performance to engine requirements, the question arises as to why the authors obtained what they consider contradictory data. In reviewing the paper, several inconsistencies are apparent. First, the MIT rapid compression machine data, Fig. 4, show there is indeed a relationship between end-gas temperature and pressure for a given time delay to knock. Fig. 20, however, based on end-gas temperature and pressure measurements in an engine would indicate that knock is caused by temperature and is independent of pressure.

A possible explanation for the discrepancy is that the combustion environment in comparative tests was not uniform, and that the effective temperature-time-pressure history was coincidentally varied so that regardless of the end-gas pressure, knock always happened to occur at the same temperature. Development of the temperature-density concept for evaluating anti-knock performance utilizes comparisons made at peak spark advance. In examining the authors' data, it is noted that essentially all the work was done at a fixed spark advance regardless of the operating conditions used. Consequently, in many cases the engine desired a considerably different spark advance than it received. The paper shows that the end-gas temperature varies considerably with spark advance, and suggests that the constant spark advance may have been partially responsible for the peculiar end-gas temperature and density relationships noted. The absence of air-consumption data in the paper and data addendum makes it impossible to reanalyze the data in accordance with current analytical practices to establish whether this is the true explanation. If a more comprehensive series of tests had been run, devoid of the confusion of improper spark advance, and utilizing the one independent variable available to the motorist, manifold air-pressure, the end-gas temperature for knock might not have been constant.

On the other hand, it is undoubtedly true that there is a given end-gas temperature at which all fuels will auto-ignite. For example, our work with commercial-type fuels covering a significant range of octane numbers indicates that at a calculated compression temperature of about 1428 R all these fuels will auto-ignite at any compression density.

In summary, comprehensive work carried out during the past several years appears completely to validate the use of calculated compression temperature and density for describing anti-knock quality. The concept, as now developed, has significantly progressed the science of relating fuel anti-knock performance to engine anti-knock requirements. Drawing a generalized contrary conclusion on the basis of the rather limited measured end-gas temperature data available would appear to be premature. We would encourage the authors to continue their temperature-measurement studies to clarify the relationship of the engine variables which affect the combustion environment of fuels in engines.

Ignition Delay Period

D. R. Diggs
E. I. Du Pont de Nemours & Co.

DEVELOPMENT of practical methods for the measurement of gas temperatures in an operating engine has made possible real advancements in our knowledge of engine thermodynamics. The authors have provided a wealth of new data, particularly related to conditions at the time of knock, which supplement the information on normal combustion previously reported by Livengood (A).

Since end-gas temperatures at knock-limited conditions can now be measured and end-gas pressures can also be measured, it is only necessary to determine a meaningful value for the ignition delay to have an absolute definition of the fundamental variables: temperature, pressure, and time-controlling knock. The authors' paper contains a great deal of helpful data on knock-limited end-gas temperatures and pressures but more information on ignition delay is still needed. The importance of the time concept is shown by the authors' demonstration that Rothrock's temperature-density concept of knock is not confirmed experimentally. The failure of this concept to consider the time factor is very likely a major reason for its inadequacy. As the authors point out, it is difficult to understand knock-limited fuel-engine relationships without the help of basic ignition delay information. The question is then how to obtain this information.

In trying to assign a value to the ignition delay, the problem is to define the beginning of the delay period. It can be reasonably assumed that the delay period ends at the time knock occurs and this can be easily determined. Broadly, the beginning of the delay might be defined as the time at which the state of the end-gas first deviates from that which would exist if there were no fuel present. However, there is no convenient way of determining when this occurs. It may be marked only by chemical changes which have no immediate physical manifestation. The earliest event in the combustion process which lends itself readily to measurement is ignition. Recognizing that there is no reason why the ignition delay period of the end gas should not begin before ignition but also recognizing that it must begin no later than ignition (if for no other reason than that radiation from the flame would alter the state of the end-gas), some of the authors' data have been used to examine the relation between the state of the end-gas and an ignition delay, arbitrarily

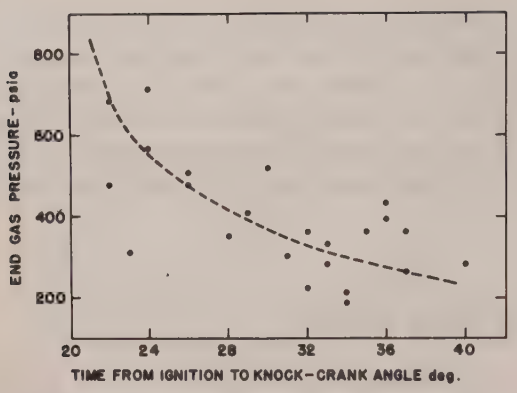

Fig. A — Ignition delay of various fuels at several Mix. Temp. with constant end-gas temperature

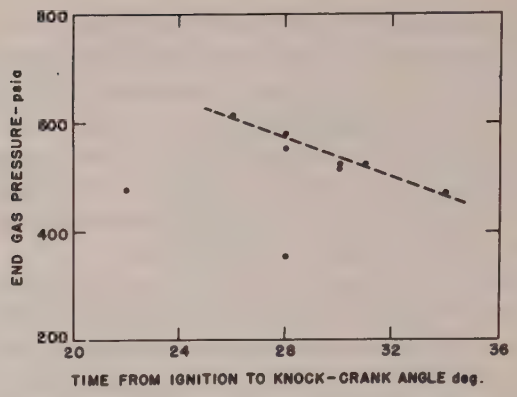

Fig. B — Ignition delay of isooctane at several engine operating conditions with constant end-gas temperature

defined as the time between ignition and knock. The purpose of this definition is merely to establish some quantity which can be used to test the importance of the time factor.

Since pressure, temperature, and time are all variable, it is convenient to hold one constant while examining the relation between the other two. Therefore, experiments which resulted in an essentially constant end-gas temperature were selected. The data from these experiments, which were conducted with different fuels and different mixture temperatures, are given in the first section of Table 5. The engine speed, ignition timing, and fuel-air ratio were constant. Fig. A shows that, although there is considerable scatter of the data, the higher the knock-limited end-gas pressure (at constant temperature)the shorter the arbitrarily defined ignition delay. This is in accord with theory. Furthermore, an exponential relation between pressure and time fits the data of Fig. A reasonably well. This type of relation has been found previously in rapid compression machine studies.

The scatter of data in Fig. A is not unexpected because it includes observations on different fuels at different mixture temperatures. These factors would certainly influence the form of the relation between pressure and ignition delay. A more precise demonstration of the importance of the time factor is obtained by examining the experiments with a single fuel. Fig. B is a plot of all the data reported by the authors for isooctane when the engine speed and end-gas temperature were reasonably constant. Fuel-air ratio and ignition timing were varied. It is quite apparent that the relation between pressure and time is real. There are two data points, however, which are quite far removed from the correlation line. These data were obtained at mixture temperatures considerably above the nearly constant temperature at which all the other data shown were obtained. It seems reasonable that at higher mixture temperatures the ignition delay period would begin sooner and might in fact start before spark ignition. This, of course, would not be considered in measuring the delay from the time of ignition. Note that longer real delays at these two conditions would move the points in the direction of the correlation line.

To test the relevancy of the arbitrarily defined ignition delay further, the data at two different engine speeds were examined. Relatively small changes in the number of crank-angle degrees from ignition to knock accompanied a change in engine speed from 600 rpm to 1200 rpm. There was generally a small increase in the knock-limited pressure at nearly constant end-gas temperature at the higher speed. Considering, however, that the absolute delay period was halved at the higher speed, much larger increases in knock-limited pressure might have been expected. Perhaps this is only a reflection of the inadequacy of the ignition time as a measure of the start of delay.

From the foregoing it is apparent that increased understanding of knock-limited fuel-engine relationships would be possible if accurate information on the ignition delay in the end-gas were available. Although data of the type obtained by the authors can be manipulated to show the importance of the delay concept, fundamental methods for determining the real value of the delay are needed. Perhaps this could be accomplished by measuring the end-gas state throughout the cycle in the absence of combustion and comparing it to the state existing with combustion to find the start of the delay period. The authors' measurement of compression temperatures suggest that this approach might be feasible, or data might be obtained with various proportions of oxygen and nitrogen in the charge so that the start of the delay period might be determined.

The difficulty of using the temperature-pressure-time history of the end-gas to formulate an absolute system of knock-rating is well illustrated by the authors' data on fuels of the same octane number achieved by blending or by use of an antiknock additive. Here quite substantial differences in the end-gas temperature exist with the same end-gas pressure and time of knock. Compare the data for 60 ON primary reference fuel and 40 ON primary reference fuel plus 1.5 ml TEL/gas (which rates 60 ON) for example. The differences in temperature are ascribed by the authors to greater precombustion activity of the lower octane number fuels and

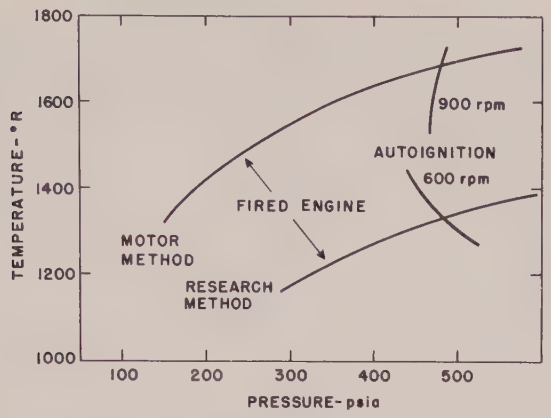

Fig. C — End-gas temperature-pressure history of isooctane under knock-rating conditions

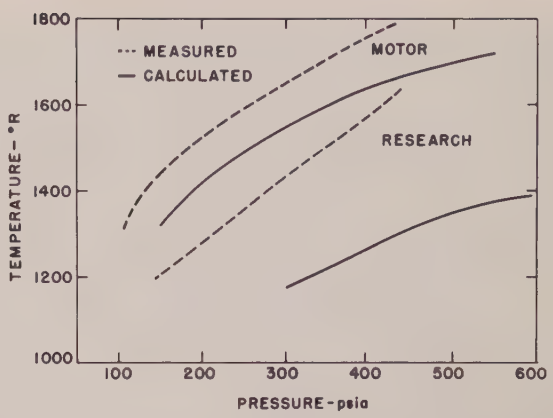

Fig. D — Comparison of calculated and measured end-gas temperature-pressure histories of isoctane under knock-rating conditions.

this is entirely reasonable. It is somewhat surprising, however, that no manifestation of this difference is apparent until about 25 crankangle deg after ignition (Fig. 15). It might be expected to occur earlier even though, as the authors have said, the major portion of precombustion activity occurs just prior to knock. However, the complete history is shown only for the 60 octane number fuels, Fig. 15. Was the same type of history, with the precombustion activity manifesting itself late in the cycle, observed with the higher octane level fuels?

As the authors point out, their analyses are based on one particular way of achieving knock-limited conditions. It is interesting to speculate what might happen if data were obtained at varying manifold air pressures and constant mixture temperature. At high manifold pressures low compression ratios would suffice for knock and vice versa. It might be argued that end-gas pressures would then be nearly constant and end-gas temperatures vary in the same way that pressures varied at nearly constant temperature when inlet mixture temperature was changed in the authors' studies. It is hoped that data of this type will one day be available. Also, what might happen if the compression ratio were held constant and the manifold air pressure raised to produce knock?

Now that methods are available to measure end-gas temperature it is instructive to examine previous data based on calculated end-gas temperatures. Fig. C is taken from an SAE paper by Corzilius, Diggs, and Pastell (B). It shows the end-gas history of isooctane under research and motor method octane rating conditions. The curves were developed from measured pressures and calculated temperatures assuming isentropic compression of the end-gas. Also shown are the autoignition limits of isooctane determined in a motored engine operated at speeds corresponding to those of the research and motor method. At the time that work was done it was postulated that the intersection of the autoignition limit curves and the fired engine curves would define the end-gas state at which isooctane would be knock-rated by the respective methods. The time factor was accounted for by defining the curves at the appropriate speeds. Notice that according to Fig. C isooctane should knock at the same end-gas pressure in both methods and this value should be about 480 psia. These suppositions are quite nicely supported by Fig. 18.

The suppositions with respect to end-gas temperature are not nearly as good although the difference between the actual value, Fig. 17, and the calculated value is only 150 R in the case of the motor method. It is considerably greater under research method conditions. Since the temperature calculations do not take into account any heat liberated by precombustion reactions, it might be expected that they would be in the greatest error in the case of the research method where more time is available for precombustion activity. The difference between calculated and measured end-gas histories is shown in Fig. D. The measured values were obtained by cross-plotting the data from Fig. 17 and 18.

The authors have shown how information on end-gas pressures and temperatures can be used to further our understanding of fuel-engine relationships. It is to be hoped that they, as well as others, will continue to use the technique discussed in the paper to develop still more knowledge of end-gas thermodynamics.

References

A. J. C. Livengood, C. F. Taylor and P. C. Wu, "Measurement of Gas Temperature in an Engine by the Velocity of Sound Method, SAE Trans. Vol. 66, (1958), 683.

B. M. W. Corzilius, D. R. Diggs, and D. L. Pastell, "Some Factors Affecting Precombustion Reactions in Engines", SAE Trans. Vol. 61, (1953), 386.

Authors' Closure to Discussion

FIRST, we would like to thank Messrs. Livengood, Rogowski, and Diggs for their efforts in preparing discussions of our pa-

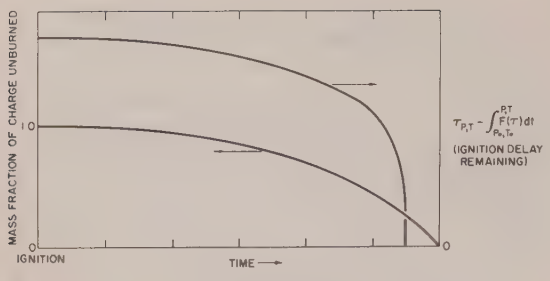

Fig. E — Ignition delay in engine

per and for their many kind words.

Apparently the one factor causing the greatest concern is the evaluation of the time element in knock. Livengood's approach requires that knock should occur when the integral of reciprocal ignition delay with respect to time is equal to unity. This presumes that the reactions leading to knock are of zero order, or dependent on time alone and independent of concentration of reactive species. Although this model has led to useful results in a rapid-compression machine, it is inconsistent with established combustion and chain-branching mechanisms. We have not found it to be generally applicable.

Diggs questions whether some method might be developed that would indicate the time of initiation of reactions leading to knock. His figures showing that the time between spark ignition and knock increases as end-gas pressure decreases at a fixed end-gas temperature are most interesting. We believe, however, that no significance can be placed on the time of ignition as the time of initiation for preknock reactivity, since a similar relationship would have been obtained had any other starting time been used. Although these plots do not show the time at which knock reactions start, they do give very nice additional evidence in support of the time factor in engine knock.

We agree with Diggs that the onset of reactions leading to knock may have no outward physical manifestations. Evidence of the thermoneutral reactions leading to knock is shown by some of our previous work. (A) In that study, we compressed a fuel-air mixture in a motored engine and then fed the exhaust products into a spark-ignited rating engine. The results obtained show that although exothermic reactivity did not begin to occur in the motored engine until compression ratio reached about 12.3:1, sufficient thermoneutral reactivity was occurring at about 11.6:1 to cause a sharp decrease in fuel antiknock quality.

The major obstacle to the determination of the significant ignition delay in an engine is the proper formulation of the mathematical law for integration of delay under changing end-gas state. Clearly, the exponential term in the delay equations does not permit a zero delay. However, physically, the integrated delay must go to zero if knock is to occur. In addition, when the delay goes to zero, there must be a finite quantity of end-gas remaining. This is shown schematically in Fig. E which plots mass-fraction end-gas and the difference between the delay at a given instant in the engine cycle and the total integrated delay up to that instant against cycle time. By formulating the delay in this manner, a zero delay may be obtained even with an exponential equation. The instantaneous delay could be computed from information such as obtained in the rapid-compression machine. However, there is no way known, as yet, to determine the integrated delay. Thus, a complete solution to the problem of knock as outlined in Fig. E is not possible at the present time. It is for this reason that we believe knock ratings will necessarily have to continue to be made in conventional engine apparatus.

Comment was made that we showed the complete history for only 60 ON primary reference fuel and the matching 40 ON primary reference fuel plus 1.5 ml TEL/gal. Similar data are presented in an addendum to this paper for other additive fuels.

Many competent workers have endeavored to calculate the end-gas temperatures in an engine. It is not likely that, even with the most sophisticated procedures, calculations can be made with suitable precision for use in understanding knock reactions. The main difficulty lies in the absence of a priori data on the mass and volumetric burning rates and the energy liberated by precombustion reactivity. Ordinary thermodynamic calculations based on polytropic compression are unsatisfactory, since compression of the end-gas by the flame front differes from compression by an ordinary piston in that the mass of the compressed medium varies in an unknown manner. The polytropic law is devised for a closed or steady-state system. There appears to be no alternative to direct temperature measurement.

As suggested, we have speculated that it should be possible to operate an engine with variable manifold pressure and adjust the compression ratio for constant knock at a fixed inlet-mixture temperature. This should allow the final end-gas pressure to remain constant while the end-gas temperature is varied. There are undoubtedly many experiments that still need to be done. The work we have presented here is only a small start in a direction that we hope will help to clarify the whole knock problem.

We are grateful to Messrs. Mrstik and Siegel for their prepared discussion of our paper. We regret that they feel our findings are contradictory to their experiences. In our studies, we were attempting to make measurements of the physical state of the end-gas and correlate the evidence thus obtained. We found, unfortunately, that a correlation between end-gas temperature and density, as proposed by Rothrock, was not indicated. This, as stated in the paper, does not mean that correlations based on engine parameters are not useful.

We would like to emphasize that we believe the factors controlling knock for a given fuel-air mixture are end-gas pressure and temperature and the ignition delay. Unfortunately, we know of no way to measure ignition delay in

an engine. Therefore, it was necessary to interpret the engine data with the help of results from the rapid-compression machine. Fig. 4 shows the nature of this correlation. In Fig. 20, which is purely engine data (Rothrock's and our own), the element of time is completely absent. It was found for the particular tests we ran that knock is highly pressure sensitive (or density sensitive) with a relatively constant end-gas temperature. We had expected that the pattern of plotted points would fall along lines similar to those found by Rothrock. Since this is not the case, we can only conclude that the time element, which is not shown in Fig. 20, must be the controlling factor. The implication would be that the points near the top of Fig. 20 correspond to a much shorter ignition delay than those nearer the bottom.

We have assumed that, for a basic concept to be valid, it must be operative at all engine conditions that bring on knock. Since a few engine operating conditions were found where the basic concept did not work we saw no great use in examining all other conditions where different results might be obtained. It should be emphasized that we do not believe the end-gas temperature is constant for all engine operating conditions. Our work with a number of engine parameters, as discussed in the paper, shows that this is not the case. We stated that the relative constancy of temperature in some of our results was only a matter of circumstances arising from the engine operating conditions employed.

In our original engine records very much more data were recorded than was possible to put into our paper. Because of brevity, there is always some question of what data to include in the text. However, we will be glad to furnish interested parties information on fuel and air consumption, or manifold pressure.

Reference

A. C. Walcutt, J. M. Mason and E. B. Rifkin, "Effect of Preflame Oxidation Reactions on Engine Knock," Ind. Eng. Chem. 46, (1954), 1029-1034.

Effect of Material and Processing Variables on Residual Stress in

E. T. Bergquist
Western Gear Corp.

S. M. Lenhoff
U. S. Army Ordnance

COMPONENT PARTS of machinery used in all phases of industry are being required to carry higher unit loads for longer periods of time. This is done at the same time that design requirements demand overall lighter-weight machinery.

Assuming the above to be true, all that seems necessary would be to find the optimum processing technique for a given material which would result in a relatively high amount of residual compressive stress. While this can often be done with simple shapes, a more difficult problem is encountered when dealing with parts of complex geometry, such as gears.

Since the final drive gearing on Army Ordnance Tanks and other tracked vehicles are among the most highly stressed gears in use at the present time, it was felt that if manufacturing methods which would produce residual compressive stresses could be developed, increased performance of the gears would probably result.

Discussion

An investigation was begun in 1956* to compare residual stresses resulting from different combinations of materials and heat treatment. The hardenability and chemical analyses of the materials used in this investigation are shown

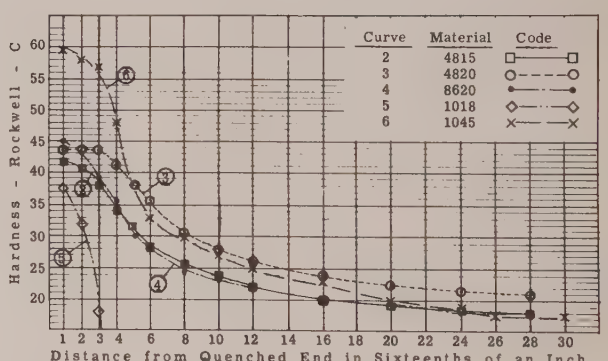

CHEMICAL ANALYSIS

Type of Steel	4815	4820	8620	1018	1045
Heat Number	21992	48796	46574	728011	837686
C	0.12	0.18	0.20	0.17	0.48
Mn	0.52	0.55	0.74	0.80	0.80
P	.011	.015	.023	.008	.013
S	.017	.020	.023	.030	.029
Si	0.31	0.26	0.25		
Cr	-	-	0.54		-
Ni	3.30	3.36	0.50		-
Mo	-	-	0.20		

Fig. 1 — Jominy hardenability curves and chemical analysis

*The work described in this paper was conducted at Western Gear Corp., Lynwood, Calif., under contract to Pacific Car and Foundry Co., Renton, Wash., and under the direction of Ordnance Tank-Automotive Command, Centerline, Mich.

Carburized and Induction-Hardened Gears

Table 1 - Gas Carburized Samples

Material	4820		4815		8620	
Effective Case Depth (Notes 1 & 2)	Shallow	Deep	Shallow	Deep	Shallow	Deep
Quench Method						
Agitated Oil Direct Quench	X	X	X	X	X	X
Direct Brine Quench	X	X	X	X	X	X
Martemper	X	X	X	X	X	X
Double Quench in Agitated Oil	X	X	X	X	X	X
Slow Cool, Reheat, Agitated Oil Quench	X	X	X	X	X	X
Slow Cool, Reheat Brine Quench	X	X	X	X	X	X

in Fig. 1.

Of the steels shown in Fig. 1, 4815 and 4820 are those normally utilized in Ordnance Final Drive Gearing. The other materials were chosen in order to evaluate the potential of processing leaner alloy steels to obtain residual compression in the gear tooth surfaces.

The scope of the investigation is shown in Tables 1-4. For each X mark shown, a minimum of four samples were processed. The "shallow" and "deep" under each material indicates "effective case depth" (RC 50 minimum). This was checked on a cross-section of the tooth at the start of active tooth profile. The case carbon content of all carburized samples was maintained at approximately eutectoid composition.

In Table 1 it can be seen that for any given case depth, six different methods of quenching were tried on any given material. A minimum of 144 samples were processed by gas carburizing, using the quenching methods indicated. The pack carburized samples were investigated to determine if the method of carburizing had an effect on the residual stresses obtained. The quench method used for the pack carburized samples was the method which resulted in the highest residual compressive stress obtained in the gas carburized samples.

Table 3 lists the steels and processes utilized in the induction-hardening phase. The "deep" case depth denoted for the 1045 steel was obtained by induction-hardening a previously quenched and tempered structure. The carburizing grades shown were initially carburized and then either slow-cooled and induction-hardened, or else quenched and tempered and induction-hardened as indicated. In each case every effort was made to have the final effective case depth in the range of 0.070 to 0.090 in.

The final phase (Table 4) of this investigation was included to evaluate the effect of varying amounts of retained

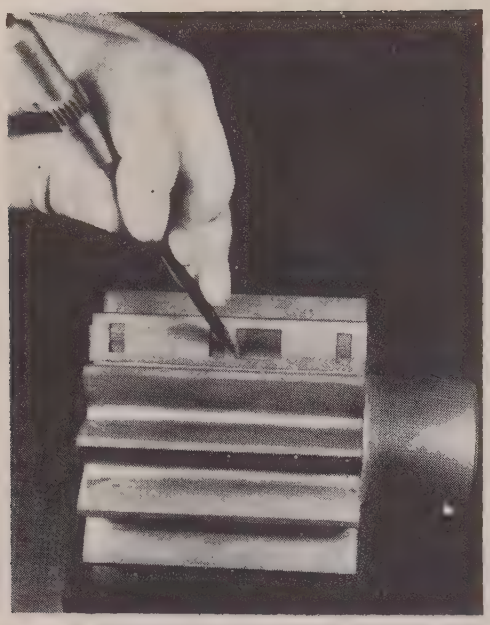

Fig. 2 — Scribing gage location with template guide

Table 2 - Pack Carburized Samples

Material	4820		4815		8620	
Case Depth	Shallow	Deep	Shallow	Deep	Shallow	Deep
Quench Method						
Best	X	X	X	X	X	X
Worst	X	X	X	X	X	X

Note:
Quench Method to be established from results of Table 1.

austenite on residual stress. Samples of 4820 steel were gas carburized and quenched by the "best" method of Table 1 and subjected to the indicated period of time at -100F. All times shown at -100F are total time of immersion in a bath of Methanol and dry ice. As can be noted, half of these samples were subsequently drawn at 325F.

The sample used in this investigation is shown in Fig. 2. All samples were gears with a 3-1/2 in. face width, approximately 4 in. in diameter, 14 teeth, 4 diametral pitch size of gear teeth, and a 25 deg pressure angle. The hub extension on the sample, which was 2 in. in diameter and 1-1/2 in. long, was used for determination of case carbon content and for metallurgical investigations. All of the sample gears were manufactured using identical manufacturing techniques. The various materials were normalized, rough-turned, rough-hobbed, given a thorough stress relief, and then finish-hobbed and shaved to the final gear dimensions. Complete inspection records were kept as to tooth dimensions and sizes during all final stages of processing. After final heat treatment and final inspection had been com- After final heat treatment and final inspection had been completed, three teeth of the sample were marked. These teeth were equally spaced around the sample. The three teeth were then fitted with a template and locations for strain gages were scribed. This insured that the strain-gage locations on the teeth would be the same with respect to the ends, tips, and roots of the teeth for all samples.

After locating the areas for strain-gage attachment, the parts were thoroughly cleaned. It was found during this investigation that if extreme care in cleaning the samples was not exercised, improper strain-gage readings resulted. All gages were attached with Duco cement and thoroughly dried. Gages were attached to both sides of the selected gear teeth. A special waterproofing wax was applied over the strain gages to protect them during subsequent parting-out of the specimen used for analysis.

Caution had to be exercised in taking the actual strain-gage readings. It was found that the location of attachment of the leads from the strain gage to the lead wires going to the strain recorder made a definite difference in the values of the strain reading. Therefore, the individual lead wires from the strain gage were bent and immersed in a mercury cup for contact. Fig. 3 shows the lead wires being bent to the exact length for immersion in the mercury cup. Fig. 4 shows the initial or zero strain-gage readings being taken. As can be seen in Fig. 4, both horizontal and vertical strain gages were used. A total of 12 strain gages, one vertical and one horizontal on each side of the three selected teeth, were used in the analysis of each sample gear.

Fig. 5 shows the tooth being parted from the sample. A positioning fixture was used to insure that all parting-out cuts were made in an identical fashion, so that if any stresses

Fig. 3 — Bending gage lead wires uniformly with gage

were introduced during this operation they would be the same on a comparative basis for all samples. A copious amount of coolant was used to avoid overheating and burning of the specimen.

Fig. 6 shows a breakdown of the sample to its final size, denoting the way the sample was cut and then dissected down to the final specimen. A cross-section of the tooth shown at the left of Fig. 6 was parted 1/2 in. in from the end of the tooth, and was used for case depth determinations. The specimen plug used for carbon analysis is shown near the center of Fig. 6. This specimen plug was parted from the test pinion after removal of the tooth used for analysis. The actual sequence of taking strain-gage readings, was as follows:

Initial strain-gage readings were taken after heat treatment and dimensional inspection to establish "zero conditions" on the intact gear. Subsequent strain-gage readings were taken both after parting of the tooth from the sample pinion, and also after specimen sizing. The difference between the zero reading and the specimen-sizing reading was denoted as S_t. This value included two factors:

1. Change in length.
2. Change in curvature.

At this point the strain gage was removed and dissection begun to determine subsurface stresses. During this dissection process, curvature readings were taken after each removal of 0.001 in. increments of material until the specimen was reduced to approximately 0.030 in. thickness.

The curvature changes obtained during the dissection process were then converted to stress data by use of the "beam dissection method" of calculation. A typical curve of the subsurface stress gradient is shown in Fig. 7 as the dotted line labeled "uncorrected" curve. The straight line shown as "correction factor" was established from the S_t value, incorporating the change in length and change in curvature prior to dissection as mentioned above. The algebraic addition of the "correction factor" to the "uncorrected" curve then gave the final solid line labeled "corrected curve" shown in Fig. 7.

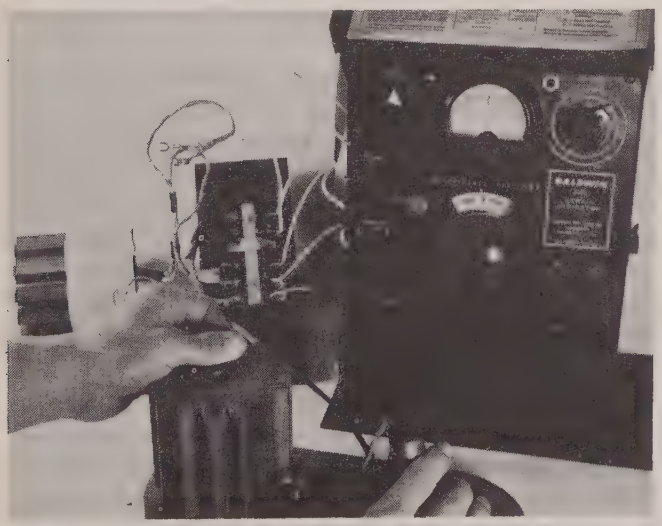

Fig. 4 — Using mercury cup connector for first (zero) strain gage reading

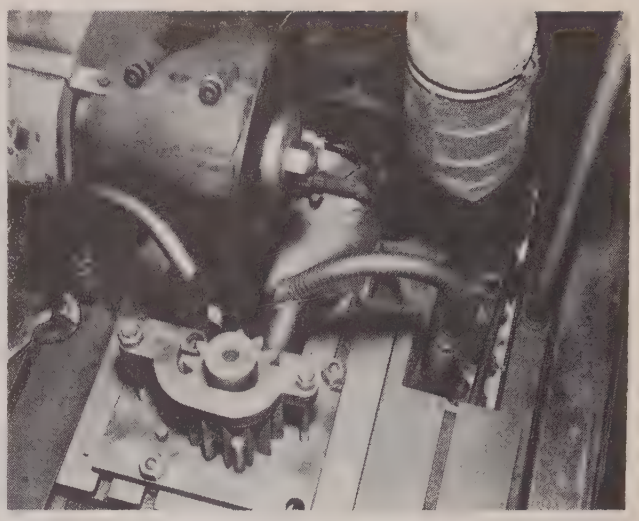

Fig. 5 — Parting tooth

Table 3 - Induction Hardening

Material	1045		1018		4815	8620
Case Depth	Deep	Deep	Deep	Deep	Deep	Deep
Quench Method	X[1]	X[2]	X[3]	X[2]	X[3]	X[2]

Note:

1. Quench and tempered at 1000 F prior to induction Hardening.
2. Carburized, Quench and tempered at 1000 F prior to Induction Hardening.
3. Carburized, slow cooled and Induction Hardened.

A previous study conducted in 1954, in which 90 samples were stress-analyzed by the beam-dissection method, established the fact that the final or "corrected" residual stress at the surface (Sf) was normally within ±10,000 psi and at most, in rare cases, within ±20,000 psi of the S_t value. Preliminary tests, which were run at the beginning of the 1956 investigation, reconfirmed that the S_t value was still the dominating factor of surface stress. In view of this and the basic fact that the majority of gear failures encountered normally originate at the surface, it was felt that the objectives of the program could be attained by utilizing the S_t values as a measure of residual stress for 90% of the total samples. The remaining 10%, plus those of the original 90% which displayed high compressive values of S_t, were completely dissected. This was considered advantageous in that it allowed a greater number of material and processing variables to be evaluated.

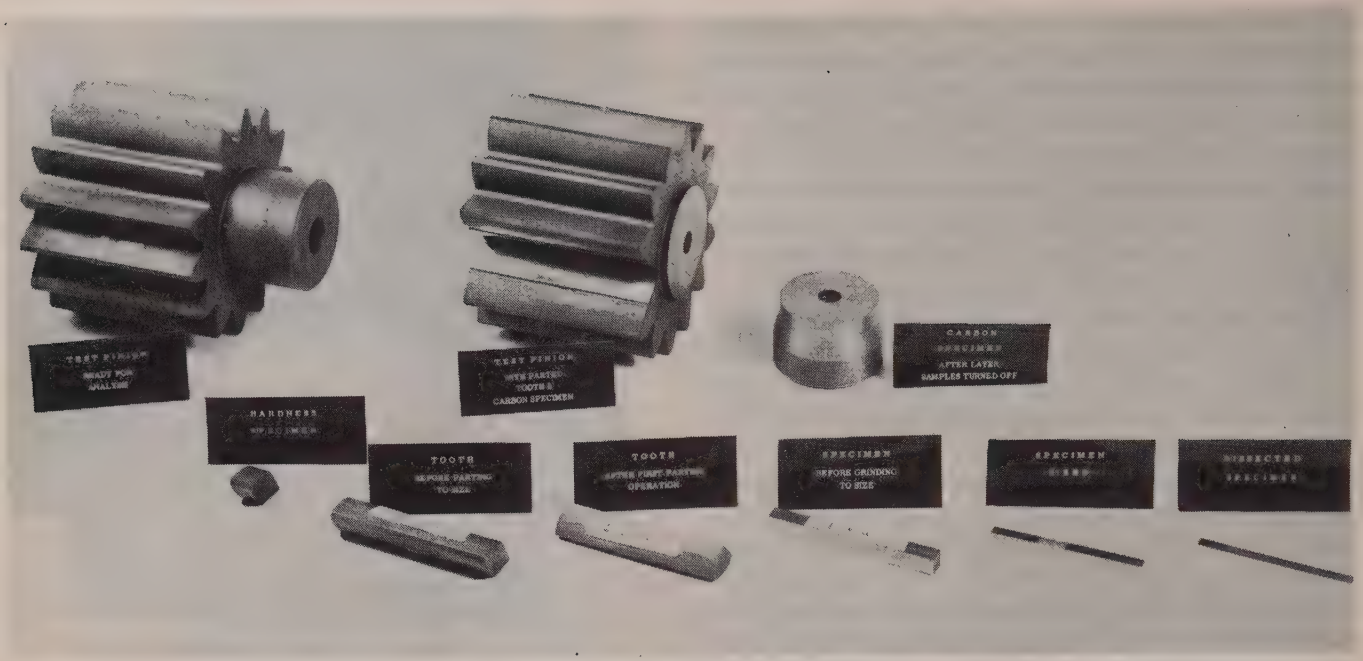

Fig. 6 — Operational requirements for analysis

Table 4 - Sub-Zero Treatment (Retained Austenite)

Time at - 100 F (Minutes)	0		2		30	
Draw at 325 F	Yes	No	Yes	No	Yes	No
Specimen	X	X	X	X	X	X

Material AISI 4820 steel carburized 0.070 in. /0.090 in. deep. Carbon 1.00%

Direct Quench by best method as determined by Table 1.

Notes

1. Shallow effective case depth - 0.040/0.060
2. Deep effective case depth - 0.070/0.090
3. Case carbon range - 48XX - Eutectoid composition ± 0.08% carbon
   - 86XX - Eutectoid composition ± 0.08% carbon

Results of Investigation

Gas Carburized Samples - Table 5 shows the average S_t value obtained on any given set of samples. The numbers shown in their respective locations of case depth, material and quench method, indicate the average S_t value (in 1000 psi) obtained on samples processed. Negative values indicate residual compressive stress. It can be seen that no material or quench method gives consistently outstanding results. The 8620 material processed by slow cooling, reheating, and quenching into agitated brine gave the highest S_t values (42,700 psi average) for the gas carburized samples.

In view of the fact that a 0.070 - 0.090 in. case depth on the slow-cooled, reheated, and brime-quenched 8620 gave the best results, it was decided to run additional samples with a deeper case (0.100 in.) to ascertain whether higher compression might be attained. It can be seen that the residual compressive stress dropped to a value of 22,000 psi. Similar tests (results of which are not included) were run on other steels within this group. The results indicate that there seems to be an optimum depth, in terms of residual stress, for any given material and processing for this gear geometry.

It was felt that definitive trends might be established by re-evaluating the results of Table 5A. Accordingly, all S_t results of samples of one particular material which were gas carburized, regardless of the quenching method, were grouped together. The materials were then analyzed on the basis of the highest S_t value. As can be seen in Fig. 8, the average results for the 8620 material is slightly superior to the other two materials tested. The difference, however, is not very great. In this same figure are shown the average S_t values of all shallow- and deep-case samples irrespective of materials; and here again the difference between shallow-case and deep-case samples is considered to be negligible. Based on any single sample the highest S_t value was found for the deep-case sample and was approximately 44,000 psi. The highest shallow-case sample had an S_t value of approximately 26,000 psi. The single line extending from the sol-

Table 5 - Average Values of S_t in 1000 psi
(each value is average of two results with exceptions noted below)

A. Gas Carburized Samples

Material	4820		4815		8620	
Quench Method Eff Case	Shallow	Deep	Shallow	Deep	Shallow	Deep
Agit'd Oil Direct Q	- 3.59	- 8.01	- 7.93	- 9.13	- 2.83	-12.75
Direct Brine Q	-13.85	-16.62	-14.58	-13.56*	-13.21	-26.30
Martemper	-18.39	-26.23	-18.65	- 3.77	-10.26	- 5.99
Dbl. Q in Agit'd Oil	-11.40	-28.50	-16.00	- 2.51	-16.17	- 8.38
Sl. Cool, Reh't, Agit'd Oil	- 7.06	-21.83	- 8.43	- 1.02	-25.80	-16.32
Sl. Cool, Reh't Brine Q	-11.87	-20.83	-17.50	- 6.72*	-16.63	-42.70
	Deeper Case (0.100 in) Sl Cool, Reh't Brine Q					-22.00

B. Pack Carburized Samples

Material	4820		4815		8620	
Eff. Case Depth	Shallow	Deep	Shallow	Deep	Shallow	Deep
Sl. Cool, Reh't, Brine Q	-11.85	- 3.65	-13.78	-11.47	-13.11	- 6.11

C. Induction Hardening

Material	1045	1018		4815		8620
Case Depth	Deep	Deep	Deep	Deep	Deep	Deep
Quench Method	X^1	X^2	X^3	X^2	X^3	X^2
Specimen	-17.95*	- 5.15	-20.53	-18.64	- 7.54	-19.35

Note: 1. Quench and Tempered at 1000 F prior to Induction Hardening.
2. Carburized, Quench and Tempered at 1000 F prior to Induction Hardening.
3. Carburized, Slow Cooled and Induction Hardened.

D. Sub-Zero Treatment (Retained Austenite)
4820 Material Deep Case (Direct Brine Quench)

TIME AT - 100 F (Minutes)	0		2		30	
Draw at 325 F	Yes	No	Yes	No	Yes	No
Specimen	- 9.05	-18.87	-11.72	-16.95	- 6.77	-26.00

Note: *Indicates values average from four (4) results
Negative values indicate compression

id average bar denotes the highest S_t value obtained for that particular material which was gas carburized.

No logical explanation can be given why the 4820 and 8620 material had higher S_t values in the deep case, and the 4815 material showed the highest S_t value for the shallow-case depths. We cannot explain this on the basis of differences in hardenability since the hardenability curves of the 4815 and 8620 materials were almost identical.

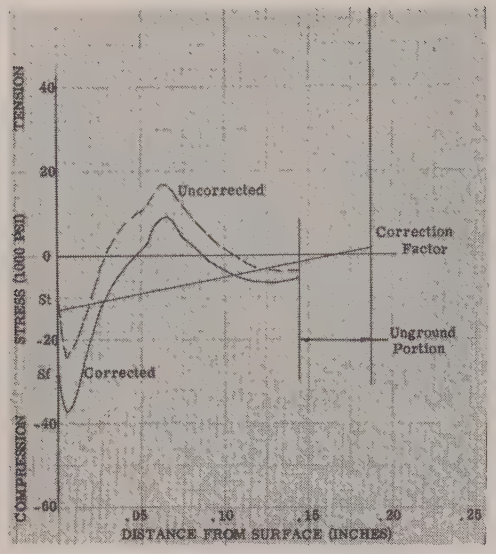

Fig. 7 — Typical stress gradient curve for carburized gear

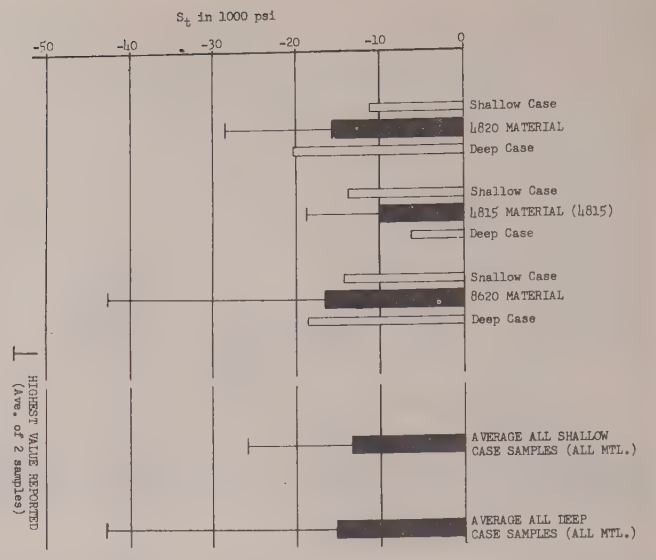

Fig. 8 — Average values by material, all quenches combined (Table 1 — gas carburized)

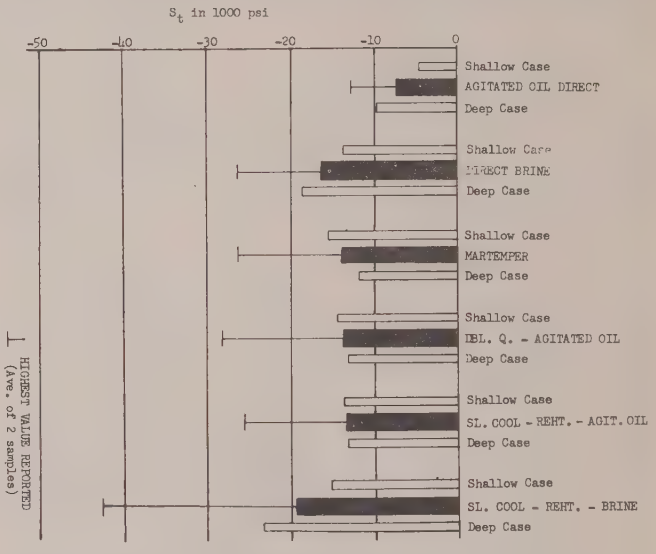

Fig. 9 — Average values by quench method, all material combined (Table 1 — gas carburized)

In Fig. 9 the quench methods are evaluated and the material is disregarded. As can be seen, the slow-cooled, reheated, and brine-quenched samples resulted in the highest average S_t values. The average value is shown as the black bar of any given method of quenching. The highest S_t values obtained by that quench method is shown by the single line extending from the average bar values. Here again, note that the slow-cooled, reheated, and brine-quenched samples resulted in an S_t value of approximately 43,000 psi, which is considerably higher than any of the S_t values obtained for any other method of quenching. Quenching directly into agitated oil (which is customary practice on the part of many concerns) resulted in the lowest S_t value.

Pack Carburizing - From the quench methods, shown in Table 2, used in pack carburizing, it can be readily seen that the optimum process varied for the steel and case depth utilized. It was, therefore, decided to take the method resulting in the highest S_t value (slow-cool, reheat, and brine-quench) and use the same procedure for all samples in the pack-carburizing phase of the investigation. Table 5B lists the values of S_t for the samples processed by pack carburizing. As can be seen from this table no exceptionally high S_t values were obtained. In comparing these values with the S_t values obtained from gas carburizing, two major points of interest were found. First, the shallow-case depth pack carburized samples showed comparable S_t values to those which had been gas carburized and identically quenched; whereas the pack carburized specimens having a deep case showed much lower values (with the exception of 4815 steel) than did the comparable gas-carburized specimens. Second, in all instances, the best results were obtained in the pack-carburized samples with the shallow-case depth. It is interesting to note that a comparison of S_t values for shallow-case depth of all pack-carburized materials shows them to be almost identical.

Induction-Hardened - The materials which were induction-hardened resulted in S_t values ranging from 20,500 to 5,150 psi (Table 5C). As mentioned previously, all samples that were carburized prior to induction-hardening were given sufficient time in the carburizing media to assure that a "deep" carburized case was obtained. Here again, no exceptionally high S_t values were found. A comparison of 1018 and 4815 materials, with varying pretreatments, indicated a definite lack of trend to indicate an optimum heat treatment prior to induction hardening.

Subzero Treatments - Table 5D lists the S_t values for the subzero treatment of the 4820 material. In all cases the samples were quenched from the carburizing temperature into a 10% brine bath maintained at 50F. Microexamination of the quenched samples showed appreciable amounts

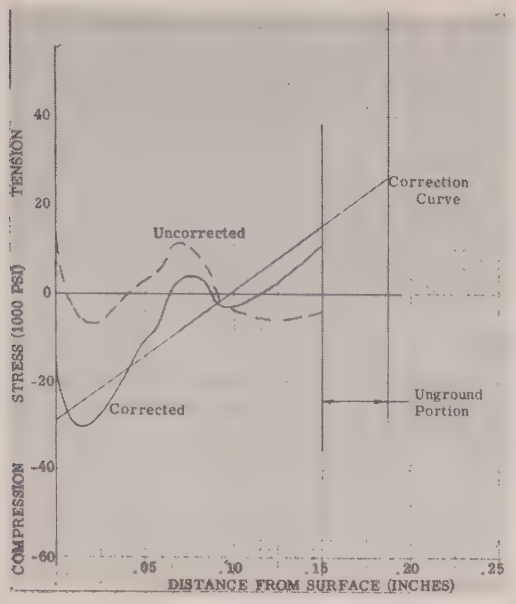

Fig. 10 — Stress gradient of specimen 3CAA (4820 material, deep case, martempered)

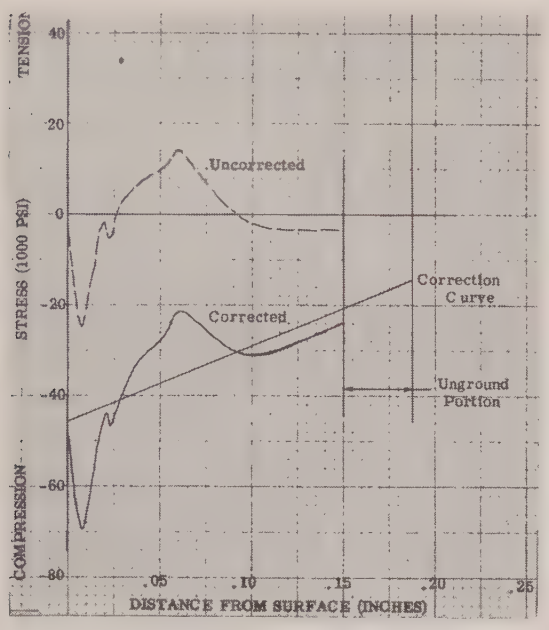

Fig. 11 — Stress gradient of specimen 4FAA (8620 material, deep case, slow cooled, reheat, brine quenched)

of retained austentite and a surface hardness equivalent to 56 RC. It may be noted that the S_t value of the brine-quenched sample which had not been drawn was increased from approximately 19,000 psi to 26,000 psi after a 30-minute subzero treatment. The surface hardness at this time was 66 RC. A comparison at equivalent subzero times of those

*Numbers in parentheses designate References at end of paper.

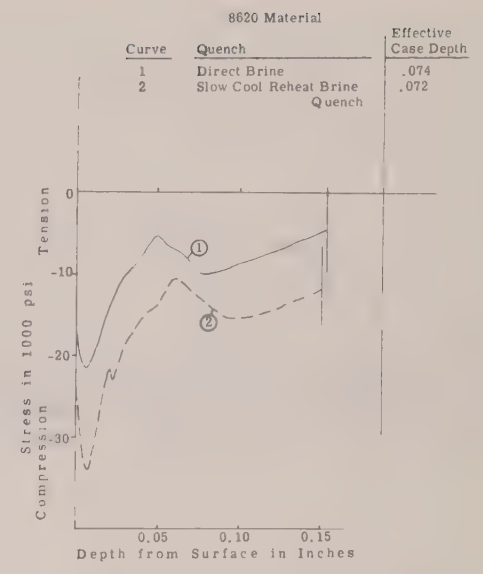

Fig. 12 — Residual stress gradients, gas carburized pinions

specimens which were not drawn to those drawn at 325F shows that in each case there was a marked reduction in the S_t value. In view of the fact that it is a common practice to temper after a subzero treatment, these reductions in residual compression merit further consideration of this tempering practice.

Completely Dissected Specimens - The completely dissected specimens gave corrected curves which showed extremely close correlation between S_f and S_t, thus confirming the original assumption that a restricted analysis was adequate to obtain the objective of the program of determining surface stresses. In conformation of this, as well as to show subsurface residual stress distribution, Figs. 10 and 11 are shown. In addition to the correlation between S_f and S_t there is another factor which is noteworthy. In both figures, the location of maximum residual compressive stress is not at the surface, but rather at a distance of 0.012 in. below the surface. Subsurface stress reversals have also been noted by other investigators in the field (1)*

To show the effect of quench variables, sample pinions of 8620 material were carburized in the same furnace load, and quenched as shown in Fig. 13. It can be seen that the reheated sample developed an overall higher residual compressive stress. Note how closely the shape of the two curves are in agreement.

Summary

The original objective of this work was to correlate residual stresses with existing industrial heat-treating practices for various commercial steels for the ultimate improvement of tank and other tracked vehicle final-drive assemblies by using optimum processes. After selecting the areas

for investigation the specific purposes were:

1. To compare residual stresses resulting from the different combinations of materials and heat-treating methods.

2. To discover the combination of material and heat-treat method resulting in the most favorable residual stress pattern.

3. To determine whether the parting-out stress (S_t) correction factor is a major determing factor of surface stress.

In the pursuance of this work, over 300 sample pinions of different materials were processed. The results of the analysis showed that optimum residual compressive stress (S_t value = 42,700 psi compression) was attained by gas-carburizing, slow-cooling, reheating, and brine-quenching 8620 steel. However, the S_t value obtained with this steel and processing method was not particularly outstanding over some of the other samples treated. Considering the program as a whole, the maximum difference between the highest and lowest S_t value was approximately 42,000 psi. In conclusion, it is obvious that the relationship and understanding of the role of residual stresses to gearing can be considered as an art rather than a science. The benefits of further understanding and control of these stresses are certainly worthy of the efforts which will be necessary to achieve them.

Reference

1. "Fatigue Durability of Carburized Steel," General Motors Corp., Pub. by ASM, 1957.

The Film Vaporization Combustor

A. W. Hussmann
Pennsylvania State University

G. W. Maybach
Maybach-Motorenbau

COMBUSTORS for gas turbine engines, especially for aircraft application, have been developed to a high degree of thermal efficiency and to a high rate of heat release per unit combustion-chamber volume and per unit pressure. However, the occurrence of carbon deposits and smoke still presents a formidable problem. Carbon deposits and smoke have no immediate effect on the thermal efficiency of a combustor; they are undesirable for the reason of operational reliability.

The formation of smoke and soot is a consequence of the mixture formation and the reaction kinetic processes during the combustion. These problems are similar in gas turbines and in diesel engines.

Mixture Formation and Combustion

In reciprocating as well as in continuous-flow internal combustion engines operating on liquid hydrocarbon fuels, two methods are being applied to prepare the liquid fuel with the air-oxygen to form a combustible mixture: the carburetion or prevaporization method, and the atomization method. Each of these methods results in a different combustion mechanism. The prevaporized or carbureted mixture, in which the fuel vapor and the air-oxygen are in intimate contact prior to the oxidation, renders a premixed flame comparable to that of a Bunsen burner (spark ignition engines, vaporizer-combustors). The mixture consisting of air and atomized fuel droplets results in a typical diffusion flame (conventional diesel engines, atomizer combustors).

The two combustion mechanisms differ considerably from each other in several respects; however, most important for the present study is the fact that the premixed flame is essentially free from the formation of solid carbon particles as intermediate combustion products, whereas the diffusion flame produces a considerable amount of carbon in the intermediate stages of its combustion process. In spite of the considerable carbon formation during the intermediate combustion stages, a diffusion flame does not necessarily smoke or form carbon deposits. If the combustion zone of the diffusion flame is sufficiently large and hot, and if sufficient oxygen is available, the solid carbon of the intermediate stages can be burned completely, resulting in an entirely smokeless and deposit-free flame. However, if the combustion region in a diffusion flame becomes quenched, or if insufficient oxygen is available to oxidize the solid carbon particles, severe smoke and carbon deposits are very likely, depending on the fuel.

The ideal mixture formation is the intimate molecular

mixing of hydrocarbon molecules with the oxygen molecules of the combustion air. This can obviously be done only in the vapor phase. Just to illustrate how poorly we approach the ideal even with the finest fuel atomization: A droplet of 50 micron diameter still contains about 2×10^{14} molecules of fuel of a molecular weight 196 (for example, $C_{12}H_{26}$). For a 100-hp gas turbine with a fuel input of 14.6×10^{-3} lb/sec and a dwell time of a droplet of 3×10^{-3} sec we would have 3×10^5 droplets simultaneously in the combustor. Each droplet, however, still contains 2×10^{14} molecules, that is, the ideal "atomization" should have been 10^9 times better than it was.

The further preparation of the mixture must now be done by molecular diffusion around every vaporizing droplet. This takes place under simultaneous combustion in the droplet envelope, subjecting part of the forming vapors to excessive temperatures. The consequences are cracking and slowed-down reaction rates, leading to the yellow luminescence and finally soot formation of diffusion flames, if the time necessary for the slow reaction cannot be made available. Precisely, this action takes place in a diesel engine when the combustion extends into the expansion stroke, and in the gas turbine combustor when the slow burning droplet enters the mixing zone with the secondary air, quenching the reaction. The same phenomenon produces the lamp black in the classical example of a diffusion flame, the wick lamp, when the flame is quenched by a cool surface.

Prevaporization and mixing of fuel vapors and air as in the Bunsen burner then seems to be the answer. Such a premixed flame will burn with a pale blue flame because of the absence of cracking and of incandescent carbon particles. However, prevaporization alone does not avoid cracking, yellow flame, and soot formation. If the fuel vapors are subjected to high temperatures in the absence of sufficient oxygen, the same cracking process takes place as in the vapor cloud around a burning droplet, resulting in yellow flames and, eventually, soot. Another element has to be added to the mixture formation process: Fuel vapors and air must be mixed and kept below the cracking temperature before the mixture enters the combustion zone.

Concept of Film Vaporization

The reasoning in the preceding chapter has led Meurer(1)* to his invention of the M-system for diesel engines (Fig. 1). In contrast to conventional diesel combustion of atomized fuel, Meurer does not atomize the fuel but spreads it as film on the relatively cool wall of the combustion chamber. A vigorous air swirl with a peripheral velocity in the direction of the fuel jet helps to centrifuge the fuel against the wall and to spread it as film. However, the fuel issuing from a high pressure injector does not reach the wall in an entirely solid jet. A small part is unavoidably atomized. The larger droplets are centrifuged against the wall in a short trajectory while the smaller droplets travel a longer distance with the air. During that time they evaporate partly and, after the ignition delay period, ignite. Since most of the fuel is on the wall, the resulting initial pressure rise is small. The burning droplets are carried around by the air, igniting the vapor-air mixture forming off the wall before the self-ignition temperature is reached and before the fuel can crack. The total reaction is now accelerating without getting out of control, with more and more heat available for evaporation. In the strong centrifugal field of the swirl, the lighter combustion products move inwards while the fresh air moves outwards to sustain combustion in the vapors forming off the wall. Recent investigations using high-speed pictures show very clearly the strong inward radial velocity component produced by combustion in a swirl (2, 3, 4).

The consequent application of the film vaporization principle has been very successful in diesel engines. The same principle should be applicable also to gas turbine combustors. The present study is an attempt to do this.

In transposing the M-system for diesel engines into a gas turbine combustor we retained the following elements (Fig. 2):

1. The fuel is spread as a film on the wall of a "vaporizer tube."
2. Primary air is flowing through this tube with a vigorous air swirl.

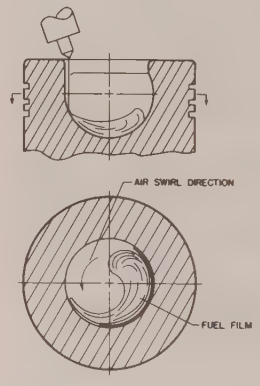

Fig. 1—M system for diesel engines

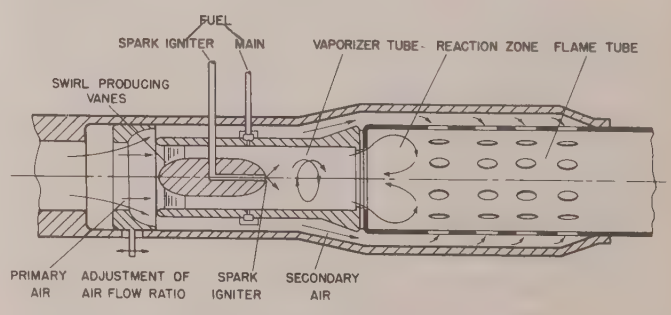

Fig. 2—Schematic diagram of film vaporization combustor

Numbers in parentheses designate references at end of paper.

3. The walls of the tube are kept relatively cool and the heat of evaporation is taken largely from the combustion itself by means of recirculating combustion products in the core of the air swirl.

Fig. 2 shows schematically such an arrangement. A portion of the air from the compressor flows as a secondary stream around the vaporizer tube and mixes later in the flame tube with the combustion products. Another part, the primary air, flows through swirl producing vanes and the vaporizer tube into the flame tube. The fuel is introduced under low pressure through a multitude of radial holes into the vaporizer tube and is spread onto the inner surface of that tube by means of the air swirl. The wall separating the primary-air duct from the secondary-air duct is cooled by secondary air on the outside and shielded against conductive heat transfer from the adjoining reaction zone.

At the end of the vaporizer tube the air swirl expands into the reaction zone where the flame stabilizes, and further into the flame tube. The vortex-type flow of the primary air produces a low pressure region in the core of the vortex, leading to a strong recirculating flow of hot combustion products back into the vaporizer tube. While being recirculated the hot combustion products mix with the primary air and increase its temperature. The heat necessary for the vaporization of the liquid fuel is transferred from the primary-air swirl to the liquid film by turbulent convection. Immediately upon its formation, the fuel vapor diffuses into the primary-air swirl by convective mixing, thus ensuring that the fuel vapor-air mixture leaving the vaporization zone and entering the reaction section is a thoroughly premixed combustible mixture.

The inherent advantage of prevaporizing the fuel from a film rather than from droplets lies in the fact that a comparatively large relative velocity between the fuel and the primary air can be maintained when the fuel is spread as film. If the fuel is atomized, an initial relative velocity between the fuel droplets and the air will very quickly diminish to a negligible value because of the large drag of the droplets, and the droplets will float in the air with a velocity approximately equal to the air velocity, that is, without relative velocity. A large relative velocity between the fuel and the air increases the heat-transfer and mass-transfer coefficients at the liquid-gaseous interface, and increases the rate of mixing of the fuel vapors and the air, thereby reducing the length required for the vaporization section and for the entire combustor.

A further and most important advantage of film vaporization is the fact that the fuel and fuel vapors can be kept below the cracking temperature during the mixing process.

Specific Problems of Film Vaporization

In designing a research prototype combustor working on the above described principles, several problem areas had to be investigated:

1. The attachment of liquid films onto the inside wall surfaces of circular ducts in the presence of high-velocity gas streams flowing through the ducts.
2. The spread of such films.
3. The stability behavior of such films.
4. The problem of simultaneous heat transfer and mass transfer between a high-temperature, high-velocity gas stream and the liquid film.
5. The recirculation flow of hot combustion products from the reaction zone upstream into the vaporization section, and the ensuing problem of flame stability.

Each of these problems has been extensively treated in a previous report (6). In the present report only the main results are presented.

Film Attachment - Initial investigations of the possibilities of attaching liquid films onto the inside wall surfaces of a duct in the presence of high-velocity gas streams flowing through the duct, were conducted in a model. This model permitted the insertion of various injection devices such as slots, screens, and single-hole nozzles inclined at different angles toward the duct wall surface. The duct cross-section in the test section of the model was a flat square. The airflow in the test section was fully developed turbulent.

These initial experiments proved that the simplest and most effective method of attaching liquid films is by introducing the liquid through holes drilled through the duct wall perpendicularly to the surface. The film then becomes attached by the action of the high-velocity gas stream. For the present study, therefore, the utilization of more complex fuel injection devices for the film vaporization combustor, such as porous walls, circumferential slots, or inclined holes shielded by splash rings or unshielded, was not considered further.

Fig. 3 shows in three successive pictures, from left to right, the attachment process of a liquid jet entering perpendicularly into a gas stream of linear velocity profile when, at otherwise constant conditions, the liquid flow rate through the injection hole is reduced.

The liquid jet enters the gas stream perpendicularly, becomes deflected in the direction of the gas stream by the action of the radially increasing gas velocity, and reaches asymptotically the maximum penetration distance y_{max}. For a reduced liquid flow rate, at otherwise constant conditions, the maximum penetration distance decreases and the base of the jet in the immediate vicinity of the wall increases in diameter. With a further minute reduction of the liquid flow rate, the action of the gas flow causes the thickened base of the jet to be swept downstream, thus attaching the jet to the wall surface.

A criterion to express the conditions at which film attachment can be obtained was found (2) to consist of a relationship between the maximum penetration distance of the liquid jet (that is, the potential maximum penetration dis-

tance) and the gas stream Reynolds number based on the jet diameter (that is, the injection hole diameter) and the gas flow velocity at the wall. The criterion was found to be independent of surface tension forces or interfacial tension forces between liquid, gas and wall surface, independent of gravitational forces, and independent of the duct geometry.

The experimentally established criterion for film attachment is expressed in Fig. 4. The ordinate is chosen to be the dimensionless critical maximum penetration distance for film attachment, and the abscissa is the Reynolds number of the gas stream (based on the injection hole diameter and gas velocity at the wall). The critical penetration distance is the maximum distance at which incipient film attachment can still be obtained.

The curve in Fig. 4 drawn through the average of several plotted test data reveals clearly the trend of the film attachment mechanism. The test data were obtained for several different injection hole diameters, various liquids, various liquid supply rates, and various gas stream velocities and geometries. The critical maximum penetration distance for a liquid jet to become attached to the wall surface approaches a minimum value of $y_{crit}/d = 0.50$ for increasing gas Reynolds numbers. For this value the jet must necessarily touch the wall surface right at the orifice; that is, the jet remains attached. If the maximum penetration distance of the jet exceeds one-half of the injection hole diameter, the conditions at which, for smaller gas Reynolds numbers, film attachment can still be expected can be obtained from Fig. 4.

If a liquid film is to be attached from radial injection holes to the wall surface of a circular duct, and if the flow pattern of the high-velocity air is a swirl, a liquid film can still be produced although the liquid jet may be detached. In this case, the film spreading mechanism is based on the centrifugal force acting upon the liquid which is forced to flow in a curved path. In a straight air flow, the liquid jet propagates in a plane that contains the center axis of the duct; in a swirling air flow, the liquid jet becomes deflected from that plane and is centrifuged back to the wall surface of the duct.

Film Spread - A coherent and homogeneous spread of the liquid film is important for making economical use of the available vaporization surface.

Our experiments revealed that the spreading of a liquid film from holes positioned perpendicularly to the surface onto which the film is to be spread depends on two factors: the surface tension coefficient of the liquid, and the method of film attachment.

The effect of the surface tension forces is such that if the difference of the surface tensions of the solid and the liquid is equal to or larger than the interfacial tension between the solid and the liquid, the contact angle vanishes and the liquid spreads nearly infinitely as a film. Jet fuel and most other petroleum oils satisfy this condition for film spread for most clean metallic surfaces. However, the surface tension coefficient of water, for instance, combined with the interfacial tension between the solid and the water, is so much larger that the contact angle normally assumes a finite value and no film is spread, unless mechanical means are applied.

The other factor influencing film spread is the method of attachment, that is, whether the film is attached by a straight gas (air) flow or a swirling gas flow. Our experiments proved that attachment by means of a swirling airflow has a generally superior effect on the film spread of the liquid of high surface tension. However, the liquid injection holes can be designed so that within a certain range airflow as by a swirling airflow. In order to make use of this effect for liquids of high surface tension coefficient, the injection holes have to be placed so closely that the liquid streaks spreading from the injection holes, contact each other, thus forming a continuously spread film surface.

Film Stability - When liquid films are exposed to high-velocity gas flows, surface disturbances of a wavelength of approximately 10 times the film thickness were observed for all liquid flow rates by several investigators (7, 8). The scale of these disturbances was found to decrease with increasing gas Reynolds number. Relatively smooth and stable film surfaces are obtained only when the film thickness, and consequently the liquid flow rate, does not exceed a certain critical value. If the thickness is greater than this critical value, severe disturbances develop over the entire film surface, with the effect that some of the liquid becomes directly entrained by the gas flow in form of droplets. The incipient point for film disturbance is independent of the gas flow Reynolds number or the mass rate of flow of the gas.

For liquid films in the presence of straight, concurrent gas flows, at least two stability criteria exist (7, 8). An entirely different behavior of the stability of liquid films, however, was observed in our experiments when the films were applied with the aid of swirling high-velocity gas flows.

At swirling airflows and liquid flow rates corresponding to thin films, the film surfaces did not behave differently from corresponding experiments with straight airflows. For increased liquid flow rates, however, although the film surface was covered with severe disturbances, the liquid droplets that eventually separated from the film surface were immediately centrifuged back to the film surface. This centrifuging effect on the droplets is due to the motion with a peripheral component which the swirling airflow imparts to the droplets as they separate from the film surface.

The presence of swirling gas flows produces films that are stable over the entire range of film thicknesses, irrespective of the intensity of disturbances on the film surface. If, however, the films are applied by means of straight air flows, a film stability criterion (as given in Ref. 7 or 8) must be observed in order to avoid instabilities.

Film Vaporization - The heat for evaporation of the liquid fuel film is taken from the vaporizer tube wall as well

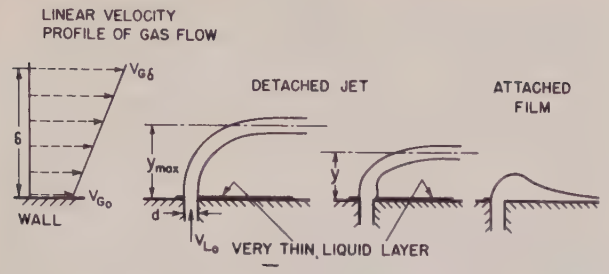

Fig. 3—Attachment process of liquid film in 3 successive steps for decreasing liquid flow rate at otherwise constant conditions

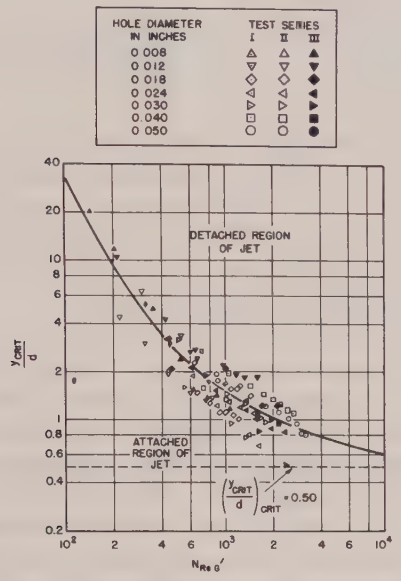

Fig. 4—Dimensionless plot of film attachment criterion

as from the air mixed with recirculated combustion products.

The influence of the wall temperature on the evaporation rate of a fuel film has not been adequately studied. Tamura and Tanasawa (9) have investigated the evaporation of a droplet on a heated quartz plate. Fig. 6 shows their result with kerosene. Plotted are the time for complete evaporation against the wall temperature. As expected, the time decreases at first with increasing temperature until it reaches a minimum. If the wall temperature is further increased, the time needed for complete evaporation rises again to a duration much greater than that which was needed at the lower temperature. The reason is, of course, the well known Leidenfrost phenomenon, insolating the liquid drop from the hot surface by a vapor cloud. It is most likely that for film vaporization in a strong swirling flow similar curves would be obtained but that the critical temperatures for highest vaporization rates would be considerably higher. The insulating effect of the Leidenfrost phenomenon would partly be balanced by a strong centrifugal field.

We learn from these tests that it would be advantageous to keep the wall temperatures slightly above the vaporization temperature of the main fuel fraction. Higher temperatures not only slow down the rate of evaporation but may lead to partial cracking of overheated fuel vapors and, consequently, slowed reaction rates for the later combustion.

In addition to the heat input from the wall, the heat- and mass-transfer between the fuel film and the air govern the evaporation rates. Several theoretical and semi-empirical methods exist for calculating vaporization rates from liquid films spread on the inside wall surfaces of ducts when the high-temperature and high-velocity air flows inside the ducts are fully developed turbulent and straight flows (6). As yet, no effective theory has been developed that would permit the prediction of film vaporization rates for the case of gas flows different from fully developed straight turbulent flows, such as swirling gas flows. Since the swirling gas flow is of special interest to the film vaporization combustion principle, a semi-empirical method was, therefore, developed to account for the effects of the swirling gas flow on the film vaporization process (6).

Kinney et al. (8) proved experimentally that the well-known dimensionless equation for heat transfer under conditions of forced convection:

$$N_{Nu} = a(N_{ReG})^m(N_{PrG})^n \qquad (1)$$

is applicable also to superimposed heat and mass transfer between a fully developed turbulent high-temperature airflow and a stationary, stable liquid film. The exponents were found to be m = 1; n = 0; and the proportionality factor was found to be constant over a large range of Reynolds numbers.

$$N_{Nu} = b\,(N_{ReG})$$

or:

$$\frac{\alpha D}{K_G} = bN_{ReG} \qquad (2)$$

Equating the enthalpy increase Δh of the evaporated fuel from the state of injection through evaporation to the heat transfer:

$$m_f \Delta h = \alpha\, \Delta T \pi\, DL \qquad (3)$$

and introducing α from the above general relation between the Nusselt and Reynolds number leads to:

$$\frac{\dot{m}_f}{\pi D} = b \cdot \frac{LK_G(T_G - T_s)}{D\Delta h} \cdot N_{ReG} \qquad (4)$$

A generalized plot of the vaporization rate per unit periphery according to the above equation showed a straight-line relation for smaller flow rates. For larger liquid flow rates (thick liquid films) the plot departed from the straight line which was explained by Kinney et al. to be due to the increasing film instability for increased flow rates causing liquid entrainment by the airflow.

The semi-empirical method of Kinney et al. was found to be very suitable to an extension to swirling gas flows inside circular ducts. For the extension the assumption was retained that heat transfer is the process controlling mass transfer from the liquid film. In order to account for the swirling gas motion, however, the Nusselt number and the Reynolds number of Eq. 4 have to be modified.

The characteristic velocity entering the Reynolds number is generally represented by the average bulk velocity or the undisturbed velocity. For swirling gas flows inside a circular duct, however, the definition of an average axial velocity has little meaning except for determination of the axial through-flow. Therefore, the absolute gas velocity near the wall surface V_{Go} was chosen to represent the characteristic velocity for the evaporation rate in swirling gas flows inside circular ducts.

Eq. 4 can now be written:

$$\frac{\dot{m}_f}{\pi D} = 3.8 \times 10^{-3} \frac{\rho_G K_G (T_G - T_S) V_{Go} L}{\mu_G \Delta h} \qquad (5)$$

$$y = c \cdot x$$

The constant in the equation was determined by introducing the velocity near the wall instead of the bulk velocity. The ratio of these velocities was found experimentally by mapping the velocity profiles for the 1.75 in. diameter vaporization tube and for Reynolds numbers between 4×10^4 and 16×10^4. Fig. 6 shows a plot of Eq. 5 in curve A. For higher vaporization rates (liquid flow rates) the curve B rather than the straight-line extension would hold for straight flow, indicating the influence of the film instability and entrainment of liquid. Since the film for swirling gas flows is stable up to much higher gas and liquid flow rates, the dashed extension of the straight-line relation (curve A) may be considered as a conservative estimate for the vaporization rate under swirling flow. Actually, film disturbances, entrainment, and centrifuging back to the wall of entrained particles, will increase the vaporization rates beyond that indicated by curve A.

Recirculation of Combustion Products - There are two principal types of recirculation which are used in combustion chambers to transport combustion products behind the flame front: the macroscopic or large scale recirculation and the microscopic or small scale recirculation. The objective of recirculating a part of the combustion products is to render stable flames which, in a given space, burn all of the fuel admitted to the combustion chamber.

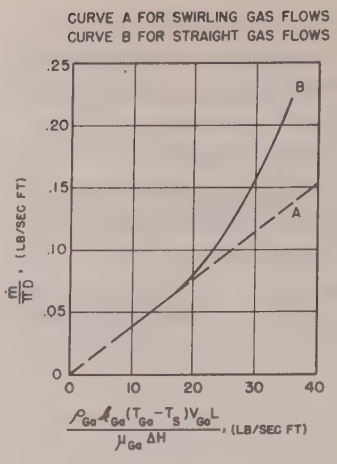

Fig. 6—Generalized plot for film vaporization rates

Large scale recirculation is a reverse flow induced by pressure differences as a secondary flow. Unlike microscopic recirculation, which is essentially a local region of turbulence induced by flow separation, large scale recirculation is a reverse flow that can be utilized to transport hot combustion products over a relatively large distance behind the flame front, into the region of the primary airflow.

Various experimental arrangements of the vaporization and reaction sections of the film vaporization combustor were investigated in isothermal flow tests and in actual combustion tests (6) for their ability to produce a sufficient amount of large and small scale recirculation at minimum pressure losses. In order to determine quantitatively the rates of the recirculation flows, a special probe was devised to measure velocity patterns in swirling flows inside circular ducts. Examples are to be discussed later.

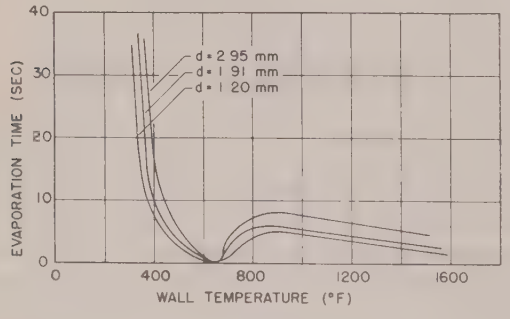

Fig. 5—Evaporation time of a lens-shaped drop of kerosene on a heated surface (test by Tamura and Tanasawa)

Prototype Combustor

Design of Prototype - Details of the principle, and the final design of the research prototype combustor incorporating the film vaporization principle are the direct result of theoretical and experimental investigations on the mixture formation mechanism, and of qualitative combustion experiments with different intermediate design arrangements of the combustor (6).

Fig. 7 shows a longitudinal section through the combustor. This prototype was built as a versatile experimental tool to allow for exchangeability of individual components. For this reason heavy wall thicknesses, thick flanges, and other relatively heavy elements were used at locations where, in a production prototype, thin walls and welded connections would be more appropriate.

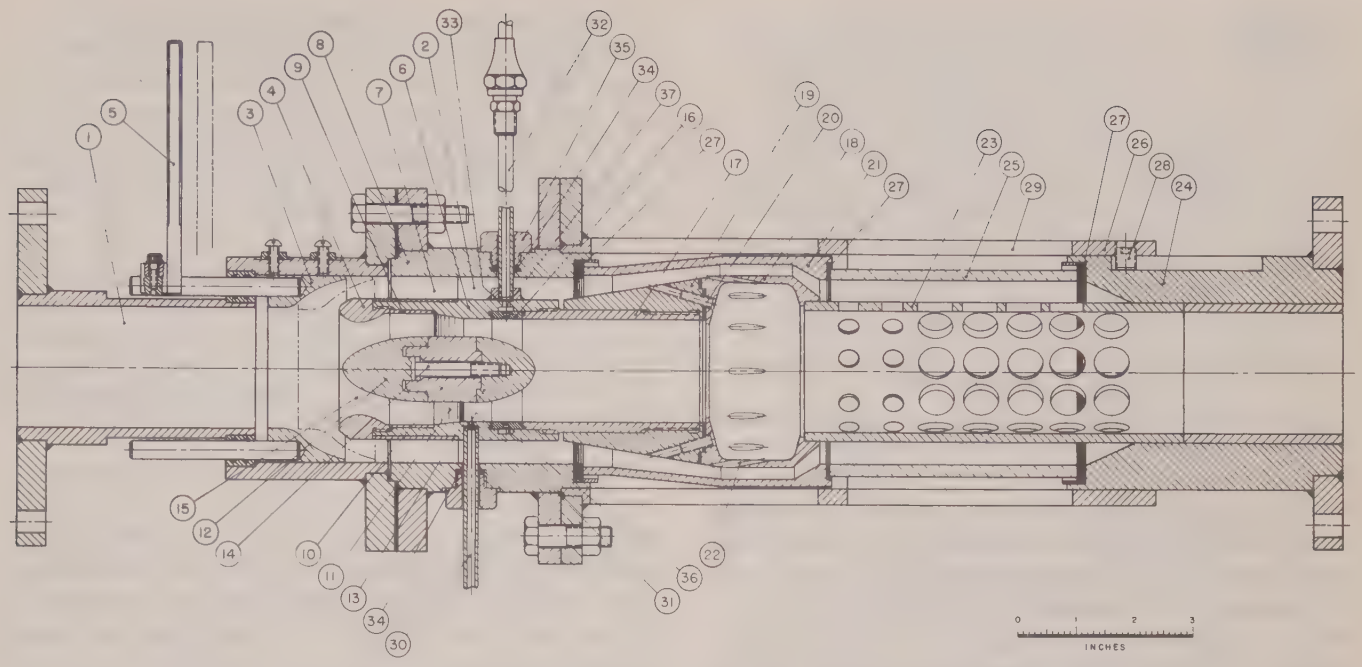

Fig. 7—Longitudinal section through film vaporization research prototype combustor

The air enters the combustor from the left through the air intake duct assembly (1) and is divided, as in conventional combustors, into a primary (combustion) and a secondary (dilution) airflow.

The air duct separation tube (6) separates the primary and the secondary airflows, contains the low-pressure fuel injection arrangement, and the vaporization tube, and supports the cool end of the combustion section.

The primary air enters the primary-air duct (15) as a turbulent, axially directed flow. In the stationary swirl-generating nozzle (11), the primary air is set into turbulent swirling motion.

The fuel is introduced under low pressure through 32 radial holes of 1/64 in. diameter, equally spaced about the central inside perimeter of the fuel injection ring (16). The fuel film is attached to the wall surface by the action of the high-velocity primary airflow.

Because of secondary flow effects in the swirling primary air, augmented by the sudden area increase at the downstream end of the vaporization tube, hot combustion products from the flame zone in the reaction chamber recirculate effectively through the core of the primary-air swirl. These recirculated combustion products mix with the primary air, increasing its temperature by turbulent convection.

The fuel film which is continuously spread over the inside surface of the vaporization tube, is evaporated by heat transfer from the wall and mainly by convective heat transfer from the primary air. Immediately upon formation, the fuel vapor is picked up by the primary air, and intimately mixed with the combustion air by the action of turbulent convection. At the downstream end of the vaporization tube, the swirling flow, then consisting of a thoroughly premixed combustible air-fuel vapor mixture, expands into the actual reaction chamber (18), where it forms a torus shaped swirl, superimposed to the main swirl.

When the swirling flow of the combustible mixture passes the circular turbulence-generating shoulder, the flow separates at its outer boundary and becomes enveloped by a turbulence sheet. In the reaction chamber, the swirl, enveloped by a sheet of microscopic recirculation, and the large scale recirculation induced by secondary flow represent an effective means to stabilize the flame in the reaction chamber without causing an excessive pressure drop across the combustion chamber.

For visual observation of the flame front in the reaction chamber and the flame tube, a heat-resistant Vycor glass tube (25) of 3-1/2 in. OD and 3/32 in. wall thickness is arranged between the secondary-air duct shrouding and the flame tube housing.

The research prototype combustor is started by introducing propane gas into the primary-air passage. For the re-

Fig. 8—Installation of combustion chamber for combustion tests

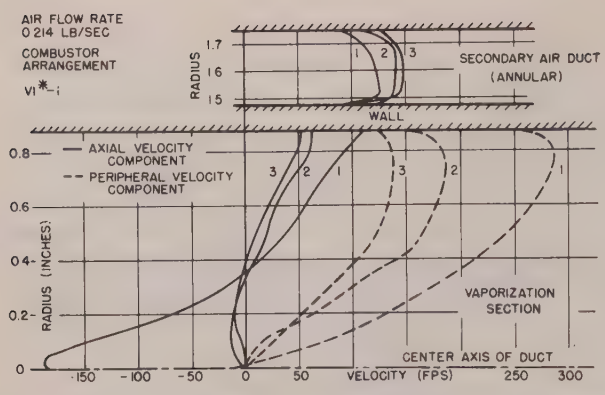

Fig. 9—Velocity distributions in combustor for isothermal flow conditions at 3 different lever settings (70 deg swirl nozzle)

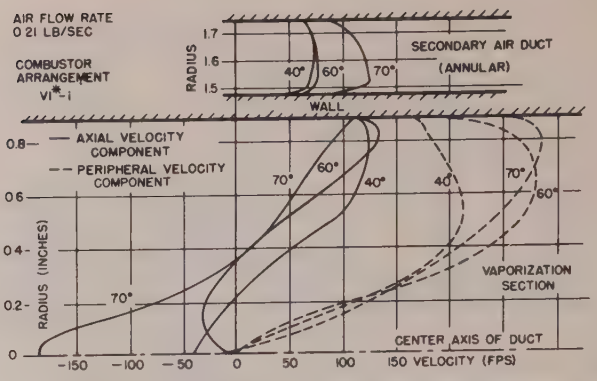

Fig. 10—Velocity distributions in combustor for isothermal flow conditions at lever setting 1 for 40, 60, and 70 deg swirl generating nozzles

search prototype this external starting arrangement was preferred, since an integral starting arrangement would have complicated the design of the prototype unnecessarily without offering the advantage of yielding additional information. An integral starting arrangement, consisting, for instance, of a torch igniter can easily be mounted into the hub of the stationary swirl-generating nozzle, with the discharge nozzle of the torch igniter pointing in downstream direction at the position of the short tail cone, as indicated in Fig. 2.

The temperature of the combustion products which recirculate through the core of the primary air swirl in the vaporization section ranges between 2000-3000 F. In order to prevent re-entrainment of droplets and the exposure of concentrated fuel vapors around the droplets to this high-temperature reverse flow, the liquid fuel jets leaving the injection holes of the fuel induction ring should be attached to the vaporization surface at all times and for all operating conditions. This requirement is satisfied with the film attachment criterion (Fig. 4) observed for maximum fuel flow and richest overall air-fuel ratio.

The choice of the overall dimensions of the research prototype was subject to the following two requirements: (1) to keep the velocity of the air approaching the combustor within the limits of that for conventional (full scale) combustors, and (2) to ensure a versatile design with readily exchangeable parts without increasing the diameter of the combustor much beyond the diameter of its entrance section. The length of the combustor, that is, the length of the vaporization section, was calculated for given primary air and recirculation conditions from Eq. 5.

A photograph of the combustor assembly is shown in Fig. 8.

Flow Patterns Inside Combustor - Local velocity measurements inside the research prototype combustor were made for isothermal and adiabatic flows at atmospheric conditions. The procedure by which the velocities were mapped is described in detail by Maybach (6).

Fig. 9 shows a typical series of velocity distributions measured in the vaporization and the secondary-air sections of the combustor, approximately 0.5 in. upstream of the turbulence-generating shoulder. The combustor arrangement (VI*-i) is the same as shown in Fig. 7. The primary-air swirl was produced by a 70-deg swirl generating nozzle and the measurements were taken for three different lever settings of the restriction ring, at otherwise unchanged conditions. At lever position 0, the ring restricts the entrance to the secondary-air duct the most; at position 10, the least.

Whereas with increasing lever position (that is, decreasing restriction of the secondary air duct entrance section) the weight ratio of secondary air to primary air increases, the weight percentage of reverse flow decreases. The stronger peripheral velocity gradients in the vaporization section induce evidently a stronger secondary flow, thus enhancing a macroscopic recirculation flow through the core of the primary-air swirl. This effect becomes weaker and less consistent with decreasing strength of the primary-air swirl.

Fig. 10 shows velocity profiles for different swirl nozzles in the same combustor arrangement, at constant lever setting (position 1), and at the same constant total airflow rate. With a 40-deg swirl nozzle, the ratio of secondary air to primary air was unrealistically low (= 0.892). For the 60-deg nozzle, this ratio was still low (= 1.18); whereas for the 70-deg nozzle the ratio amounted to = 3.15. The rate of large scale recirculation, which was 22.8% of the primary airflow for the 70-deg swirl nozzle, reduced to 3.5% for the 60-deg nozzle, and to 1.2% for the 40-deg swirl nozzle.

It can be seen in Fig. 10 that the peripheral velocity of the 40-deg swirl close to the wall approaches very nearly the condition of constant angular momentum. At the same time, the axial velocity distribution remains nearly constant, and also the flow angle distribution, both being the characteristics of a free vortex flow pattern, causing very little secondary flow. More toward the core of the flow, the free vortex of the 40-deg swirl becomes disturbed and the flow pattern approaches that of a solid-body rotation accompanied by some macroscopic flow recirculation in axial direction.

In the case of the 60-deg swirl, the transition from the free vortex to the solid body rotation begins somewhat closer to the wall surface, and the free vortex is less pronounced. For the 70-deg swirl nozzle, the free vortex cannot form at all and a flow pattern similar to the solid-body rotation begins already in the boundary layer, and the axial velocity component decreases immediately from the wall toward the center, indicating a strong reverse flow as a consequence of the increased secondary flow effect. From these measurements, it is concluded that in order to obtain the desired rate of macroscopic recirculation through the core of the primary-air swirl, the swirl must be generated such that the formation of a free vortex is prevented.

There is a decisive difference in the recirculation behavior of straight and swirling flows. Fig. 11 shows schematically the contour of the vaporization section and the reaction section of the combustor. A straight flow separates as it passes the turbulence-generating shoulder, the separated eddies collect in the widened section of the reaction chamber into the flame tube without being much affected by the "dead-water" eddies.

A swirling flow in the same arrangement evidently expands into the widened section of the reaction chamber, enveloped by a separated sheet of turbulence. Because of the superimposed secondary flow effects a portion of the turbulence sheet and of the swirling flow becomes recirculated from the reaction chamber through the core of the swirling flow.

Both the straight and the swirling flow in the arrangement shown induce microscopic and large scale recirculation. However, only the superimposed recirculation caused by the swirling flow can be successfully employed to simultaneously stabilize the flame in the reaction chamber and to preheat the primary air in the evaporization section.

It is recognized that the recirculation rates measured in the research prototype combustor for isothermal and adiabatic flow conditions will be appreciably affected by the presence of a flame front in actual operating conditions. The recirculation rates, therefore, must be evaluated as relative rather than as absolute rates.

Test Results

Several designs, differing in details from that shown in Fig. 7, have been tested. Most of the test work, however, has been carried out on a combustor arrangement very similar to that in Fig. 7. The emphasis in all tests was on investigating the principle of film vaporization rather than on developing detail features.

The fuel used for most tests was a JP-4 jet engine fuel of the specification Mil-5-5624 D. Limited testing has been done with a commercial diesel fuel No. 1, a 100% catalytically cracked diesel fuel No. 2, and a commercial burner fuel oil No. 2.

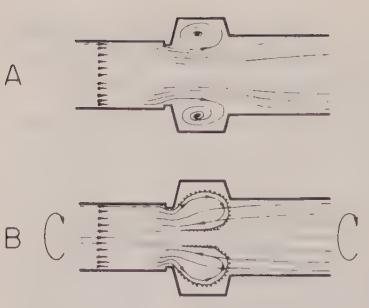

Fig. 11—Separation and recirculation flow patterns in (A) straight flow, and (B) swirling flow

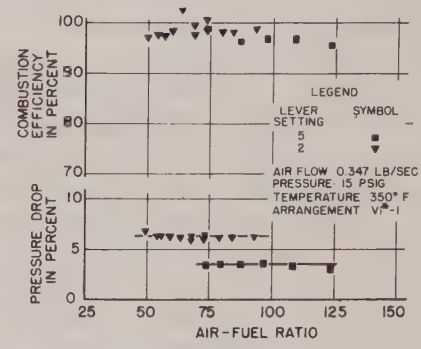

Fig. 12—Performance characteristics of research prototype combustor for 2 different lever settings (70 deg swirl nozzle)

The aim was to achieve smokeless blue flame combustion. We were able to obtain blue flame combustion over a wide range of air-fuel ratios, combustor pressures and fuels. There is no doubt that with further development almost all of the present limits can be extended.

Fig. 12 shows as an example typical characteristics for two different lever settings of the restriction ring (3) of Fig. 7. The test conditions simulate subsonic flight of 35,000-ft altitude with a compressor ratio of 6.5/1.

Combustion Efficiency - The combustion efficiencies measured were satisfactorily close to 100%. The scatter of the combustion efficiency data can be explained as caused by inaccuracies in the airflow and fuel flow measurements; it was exceedingly difficult to keep airflow and fuel flow accurately constant during the tests. The characteristic of the combustion efficiency data is typical for good prevaporization combustors. Contrary to prevaporization combustors, in atomization combustors the efficiency drops off at higher and at lower air-fuel ratios, owing to unsatisfactory spray distribution in off-design conditions.

Pressure Drop - The pressure drop Δp, conventionally expressed as the ratio of the total pressure drop across the combustor divided by the total pressure in the combustor entrance section, proved to be approximately of the same order of magnitude as that of conventional aircraft gas turbine combustors. Fig. 12, for instance, shows the pressure drop data for two different positions of the restriction ring. In the lean range of operation, the ratio of secondary air to primary air can be increased and the secondary-air duct is consequently less restricted, causing a lower pressure drop.

Flame Stability - Fig. 13 is a typical plot of the flame stability data for the film vaporization research prototype combustor. The combustor arrangement was the same as that shown in Fig. 7 with the 70 deg swirl-generating nozzle, for which the operational characteristics are plotted in Fig. 12.

The rich limit was determined by the appearance of incipient luminescent streaks in the otherwise pale blue flame. The lean limit was determined by the observation of incipient instabilities leading to blowout of the flame. The 100% airflow rate was 0.410 lb/sec determined by the capacity limit of the shop air supply system.

Flame stability tests were performed also for the same combustor arrangement and the 60 deg and 40 deg swirl-generating nozzle. The results of these tests, however, proved to be inferior because of the reduced macroscopic recirculation rates in the less strong primary-air swirls. Tests with a combustor arrangement without air admission (holes 22 in Fig. 7) to the reaction chamber, with lengthened vaporization tube, and with the 70 deg swirl nozzle, extended the lean limit, especially in the lower air flow rate range, to air-fuel ratios close to 300.

Specific Heat Release - The heat output of the prototype combustor at a total air-fuel ratio of 50 and at conditions equal to those reported in Fig. 12, is 10×16^6 Btu/ft^3 hr atm, if the volumes of the entire vaporization zone, the entire reaction chamber, and the entire flame tube are considered. Actually, however, because only a small part of the flame tube contributes to the actual space in which the reaction proceeds, a value of 15×10^6 Btu/ft^3 hr atm is a more realistic figure in characterizing the combustor. This latter value still does not mark the maximum specific heat release rate for the prototype, since the airflow was limited by the capacity of the shop air supply system rather than by the stability limits of the combustor.

Influence of Fuel on Blue-Flame Combustion - In addition to tests with JP-4 fuel, a few check tests have been made with other fuels. A regular JP-5 fuel and JP-5 fuel with 65.7% aromatics have been tested. The blue flame limits were about the same as for the JP-4 fuel.

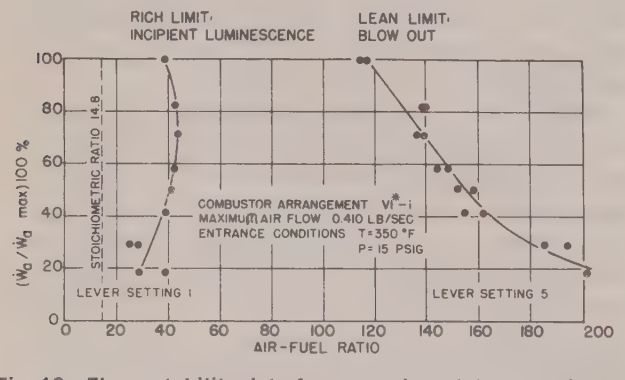

Fig. 13—Flame stability data for research prototype combustor (70 deg swirl nozzle)

A 100% catalytically cracked diesel fuel was tested having the specifications shown in Table 1.

Without any modifications to the combustor, blue flame combustion could be maintained for air-fuel ratios between 42 and 67 for combustor inlet pressures of 30 psia and for air-fuel ratios between 50 and 75 for pressures of 40 psia. The airflow at these tests was 0.240 lb/sec and the inlet temperature 345 F. The lower air-fuel ratio limits indicate the point of incipient luminescence or of exhaust temperatures becoming too high for our laboratory equipment.

With a view of exploring the possibilities of the film vaporization combustor as a burner with low back pressure, some check tests were run with the lowest pressure obtainable on our test bench. For a flow of 0.158 lb/sec the lowest combustor pressure was 16.2 psia with an entrance temperature of 70-80 F. Blue flame combustion with JP-4 could be obtained for air-fuel ratios of 43-77. If either the primary air or the vaporizer tube would be preheated, the lean limit could be extended considerably.

Household heating fuel No. 2 and a commercial diesel fuel No. 1 could not be operated with blue flames for cold air conditions. However, heating up the air to an entrance temperature of 325 F restored blue-flame conditions for air-fuel ratios between 42 and 100.

If a film-vaporization burner were to be designed for lower volatility fuels and cold air, the vaporizer tube should be kept close to the temperature for minimum vaporization time as indicated in Fig. 5. Preheating the primary air and effective recirculation of combustion products with the vaporizer section would further extend the limits of operation.

Carbon Deposits and Smoke - As long as the combustor was operated under blue flame conditions, no smoke or deposits were found after as long as 20 hr operation.

Extended tests were run with the 100% catalytically cracked fuel at high combustor pressure (58 psia) and at rich air-fuel ratios (exhaust temperatures around 1500 F). The flame color was bright yellow under these conditions. The smoke was still very light. Measured with a Von-Brand smoke

Table 1 - Specifications of 100% Catalytically Cracked Diesel Fuel Test

Specific gravity at 60 F	0.876
Viscosity, kinematic, cs at 100 F	2.81
Aromatics, % vol	26.5
Naphthalenes, % weight	22.3
Olefins, % (calculated)	13.5
Heat of Combustion, gross Btu/lb	19,150
Distillation, deg F	
Ibp	396
50%	523
90%	592
End Point	649

meter with the lowest tape speed (2 in./min) and the highest pressure across the filter (5 in. Hg), the smoke reading was less than No. 1 on the Bacharach smoke scale (that is, less than 10% light absorption if the light absorption of the clean filter paper is called 0%. Examination of the combustor after 8 hr running showed only slight deposits of the nature of a soft soot layer.

Deposits at the end of the vaporization tube have been observed when the vaporization tube wall temperature was too high, as would be the case in the prototype design without insulation between the reaction zone structure and the vaporizer tube. In such cases the flame would always have at least yellow streaks.

An interesting observation should be noted here: If the recirculation of combustion products was increased beyond a critical limit, the flame would become strongly luminescent. The fuel vapors, subjected to the high temperature of the recirculating gases are obviously undergoing a cracking process which slows down the rate of the combustion reaction.

Summary and Conclusions

The present study has shown that the principles of the M-system for diesel engines are applicable to constant pressure burners. The fuel is applied as a film by a very simple fuel induction system. The film is formed on a vaporizer surface at the inside of a tube through which the primary airflows with a vigorous air swirl.

The problems of film-formation, -spread, -stability and -vaporization have been studied and satisfactory solutions have been found. With the proper vaporizer wall temperature, air temperature, and recirculation rate, blue flame combustion could be obtained over a wide range of air-fuel ratios and for various fuels including diesel fuels with high percentages of aromatics.

As long as blue-flame combustion was maintained, absolutely no smoke or deposits were formed. Under conditions of yellow-flame combustion (high-aromatic fuel, rich mixture, high combustor pressure) the smoke was still very light and deposits were of the nature of a soft, easily removeable soot.

The heat release rates of the prototype combustor were found to be comparable to those of modern gas turbine combustors. Because of the nature of premixed flame combustion, the flame tube can be extremely small, so that the space requirements including the vaporizer sections are still low.

The pressure drop across the combustor is in line with that of atomizer type combustors.

Many problems, as for example response rates, stability in transient conditions, and others still remain and can be solved only by further studies and development of a production prototype combustor.

Nomenclature

α = Heat transfer coefficient, Btu/ft^2 sec F
a = Constant
b = Constant
c = Constant
D = Duct dia., ft
d = Liquid jet dia., ft
ϵ = Ratio of secondary to primary air
Δh = Change in enthalpy from injection condition through vaporization, Btu/lb
k_G = Average heat conductivity of bulk of gas, Btu/ft sec F
L = Length of liquid film, ft
m = Constant exponent
m_f = Weight rate of film vaporization, lb/sec
u_g = Average gas viscosity, lb sec/ft^2
n = Constant exponent
N_{Nu} = Nusselt number
N_{Pr} = Prandtl number
N_{ReG} = Reynolds number
Δp = Pressure drop across combustor, lb/ft^2
δ_G = Density of gas, lb/sec^2/ft^4
T_G = Temperature of gas near wall, R
T_s = Temperature of film surface, R
V_{Go} = Gas velocity near wall, ft/sec
y_{crit} = Maximum penetration distance of jet for film attachment, ft

Acknowledgments

The work here reported was done in the Department of Mechanical Engineering of The Pennsylvania State University and was sponsored by the Office of Naval Research under Contract No. NR 656 (13). Task Order No. NR 097-341.

References

1. J. S. Meurer, "Evaluation of Reaction Kinetics Eliminates Diesel Knock," SAE Transactions, Vol. 64, 1956.

2. A. Pischinger and F. Pischinger, "Der Einfluss der Wand bei der Verbrennung eines Brennstoffstrahles in einem Luftwirbel," MTZ, Vol. 20, 1959.

3. F. Nagao and H. Kakimoto, "Kraftstoffeinspritzung und Verbrennung in der Wirbelkammer des Dieselmotors," MTZ. Vol. 20, No. 6 and 8, 1959.

4. H. Kakimoto, "Swirl and Combustion in Divided Combustion Type Diesel Engines," Doctoral Thesis, Kyoto University, Kyoto, Japan, 1960.

5. F. Kahoun, "Spray Dispersion in a Centrifugal Flow Field," M. S. Thesis, Pennsylvania State University, 1960.

6. G. W. Maybach, "The Film Vaporization Combustor for Gas Turbine Engines, Theoretical and Experimental In-

vestigations," Pennsylvania State University, College of Engineering and Architecture, Engineering Research Bulletin B-75, 1959.

7. E. L. Knuth, "The Mechanics of Film Cooling," Jet Propulsion, Vol. 24 and 25, 1954, 1955.

8. G. R. Kinney, et al, "Internal Liquid Film Cooling Experiments with Air Stream Temperatures to 2000 F in Two and Four Inch Diameter Horizontal Tubes," NACA Report 1087, 1952.

9. Z. Tamura and Y. Tanasawa, "Evaporation and Combustion of a Drop Contacting a Hot Surface," Seventh International Symposium on Combustion, Butterworths Scientific Publications, London, 1959, 509-522.

Discussion

Conditions of Smokeless Combustion

P. H. Schweitzer
Schweitzer & Hussmann
Engineering Office

IT IS A widely held belief that the cause of smoke is shortage of oxygen during combustion. This writer himself expounded this theory in his paper to the SAE, "Must Diesel Engines Smoke?" (SAE Quarterly Trans. July, 1947), when he wrote: Overrich or locally overrich mixture -- where fuel is burned in the presence of less than the stoichimetric amount of air--produces smoke irrespective of operating conditions. I regret now having said that.

The statement is without theoretical foundation. Complete combustion is not a necessary condition for smokeless combustion. A hydrocarbon consisting of seven weights of carbon to each weight of hydrogen may burn smokelessly into H_2O and CO with only 65% of the stoichiometric air needed for complete combustion. This means the air-fuel mixture could be 53% rich and still produce no smoke.

It is also known to chemists that the combustion of methyl alcohol (CH_3OH) and of formaldehyde (CH_2O) is never accompanied by smoke no matter how rich the fuel-air mixture is.

On the other hand, the presence of an adequate amount of oxygen, as exists in a homogenious lean mixture, does not assure smokeless combustion. The exhaust of a diesel engine with 50% or more excess air is often smoky. The exhaust of gas turbine with more than 200% excess air also is sometimes smoky. We can't blame a shortage of oxygen for this.

The combustion theory, by which carbon is formed, is less new to chemists than to engineers. When hydrocarbon burns, two chemical processes are taking place side by side; oxidation on one hand and pyrolysis or thermal decomposition, commonly called cracking, on the other hand. When exposed to high temperature and pressure the molecules break into atoms.

If combustion were merely an oxidation reaction, no smoke or soot - both an agglomeration of solid carbon particles - would ever appear. Cracking is responsible for smoke formation. When heavy carbon atoms crack, carbon usually appears in the flame, instantly recognizable by the brilliant yellow color. The incandescent carbon particles which give the flame its brilliance are of a solid state. A "premixed" flame, even if the mixture is 30 or 40% rich, contains no solid carbon and is pale blue. A blue flame never produces smoke. A yellow flame often does. If enough oxygen is present the carbon particles may be consumed by the flame before any part of it is released as smoke. This is where excess air comes in handy. But in the absence of cracking, carbon would not even form and the best way to avoid smoke is to avoid thermal decomposition of the fuel during the combustion process.

Thermal decomposition is promoted by high pressure and temperature. This can be spectacularly demonstrated by two simple experiments.

Put an inadequate size chimney on a kerosene wick lamp so as to make it smoke slightly. Place a bell jar over the smoking lamp. Evacuate the air from the bell jar. At one point the lamp will quit smoking. If you continue evacuation, the flame will, of course go out. While the bell jar was evacuated, oxygen was removed. But at the same time the pressure was lowered. With lower pressure the cracking ceased and the smoke vanished in spite of the growing oxygen deficiency.

From this it appears that the best way to prevent smoke is to make it impossible for the fuel molecules to crack. Since most fuels cannot be kept from cracking when exposed to high temperature, the next best thing is to oxidize the carbon molecules before much of it has a chance to crack. Oxidation requires a molecular contact between oxygen and carbon molecules. Atomization alone will not accomplish this. Even the finest droplets of 10 micron diameter contain more than 10^{13} molecules. Only a small portion of these molecules are on the surface of the droplets, the rest depend upon evaporation, and diffusion for access of oxygen. This takes time and during this time the cracking process proceeds inexorably.

The right thing therefore is to vaporize the fuel at a relatively low temperature. Oxidation then can proceed promptly and most of it completed before cracking can do much damage. For oxidation, of course, the presence of an adequate amount of oxygen adjacent to the fuel molecules is essential.

It is obvious that by discouraging cracking we discourage smoke formation. Dr. Meurer* accomplishes this in a diesel combustion chamber of the M system by vaporizing the fuel before it is mixed with air. Drs. Hussmann and Maybach did the same thing in a gas turbine combustor. In either case the temperature of the fuel is kept low before combustion to discourage thermal decomposition.

---

* J. S. Meurer, SAE Transactions, (1956), 250.

Radioisotopes Broaden The Approach To Machining Studies

Marko Paliobagis, and E. J. Krabacher
Cincinnati Milling Machine Co.

THE INTRODUCTION of radioisotopes to industry has made availabale a new research tool which has made it possible to broaden the approach to machining studies. The use of radioisotopes in the form of radioactive cutting tools which have been rendered radioactive by neutron bombardment in an atomic reactor has made it possible to extend our knowledge of the tool wear process. The necessity for a thorough understanding of this process has become increasingly important with recent advances in metal working requirements.

In the ten year period since the introduction of the radioactive tool wear test method (Fig. 1) for evaluating and studying the mechanism of the wear of cutting tools, American industry has entered an era in which the exotic materials of ten years ago have become the materials of nuclear reactors, satellites and rockets of today, an era in which the introduction of the high strength thermal resistant alloys has caused industry to revert to the cutting speeds and feeds of the earlier thirties, an era in which the total machining costs to American industry is in excess of ten billion dollars annually (1)*. In order to cope with these problems of new materials and increasing machining costs, a clear understanding of the mechanism of tool wear and methods for reducing it must be developed.

The importance of tool wear can best be understood when one considers the ways and means available for reducing machining costs. These costs are made up essentially of two parts:

1. The cost of cutting, which is the labor and overhead on the machine tool.

2. The cost of preparation of the cutter, which is the labor and overhead involved in resharpening.

In the case of throwaway carbide tooling, the latter cost is very greatly reduced.

Normally, there are two ways in which machining costs can be reduced. If the cutting speeds and feed rates can be increased, the number of parts produced per unit time will increase proportionately, hence the cost per part will decrease. If the life of the tool can be increased by some means when machining at a given condition, then the tool preparation cost per unit part will also decrease. Either of these methods will reduce machining costs -- but both depend on tool wear.

Since the cutting phenomena is a complicated physical process, the accurate measurement of tool wear becomes a difficult problem. Essentially, three conventional methods are available for measuring tool wear:

1. Measurement of the linear dimensions of the worn areas of the cutting surfaces of the tool (such as measurement of the wear land on the flank).

2. Geometrical determination of the worn areas or volumes.

3. Determination of the weight of the worn volumes.

The most generally used method of tool life end point determination is by optical measurement of the linear dimen-

Fig. 1 — View of radioisotope laboratory

*Numbers in parenthesis designate references at the end of the paper

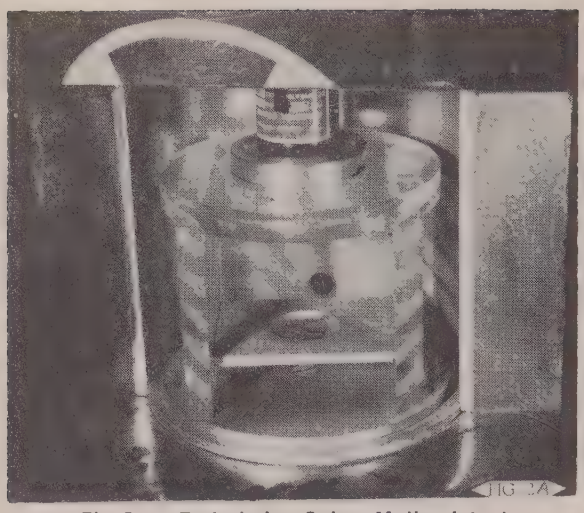

Fig. 2a — End window Geiger-Muller detector

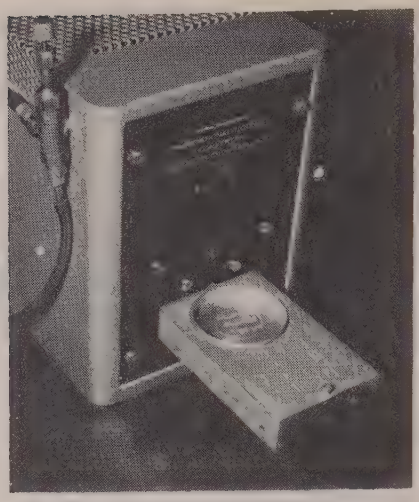

Fig. 2b — Gas flow detector

sions, i.e. measurement of the wear land on the tool flank. The relationship between flank wear and cutting time is observed until complete failure of the tool occurs or until a predetermined amount of flank wear is reached. While a plot of the flank wear versus cutting time can, in many cases, give a linear relationship and a measure of tool wear, the experimental scatter in the data, especially if the cascading type of wear is present, makes it difficult to predict tool life accurately. Uncertainty of tool wear based on the above tool life end point criteria commonly varies by as much as $\pm$ 30%.

The determination of tool wear by measuring the volume or weight changes of the cutting tool would be a better method. However, in view of the fact that the loss of volume or weight of the tool during the wear process is an extremely small quantity, in most cases, as compared to the total volume or weight of the tool, the uncertainties of measurement due to build-up (i.e. particles of built-up edge, and other foreign material remaining attached to the tool) are often of the same order of magnitude as the quantities being measured themselves.

The principal deficiencies of the methods listed above are:

1. The comparatively low precision of measurement.
2. The expenditure of large amounts of labor, time and material.

With the introduction of the radioactive tool wear method by M.E. Merchant (2, 3) in 1950, and B. Colding and L. G. Erwall (4) in 1951, a method became available for accurately and rapidly evaluating tool wear. Not only has it proven to be an accurate and rapid method, it offers a technique for investigating the actual mechanism of tool wear. Essentially, in this method one determines the amount of tool material worn from a cutting tool during a brief period of cutting. By machining with a radioactive cutting tool and then measuring the activity of the wear products on the chips, a quantitative measure of tool wear can be obtained. Since the amount of radioactivity present on the chips is directly proportional to the quantity of metal worn from the tool during the cutting operation, this radioactivity indicates directly the rate of tool wear. Therefore, if the radioactivity of chip samples obtained under different machining conditions are compared, then the relative tool wear or tool life for these different conditions can be determined.

The sensitivity of the radioactive method is related to the ability of detecting and accurately measuring extremely minute amounts of radioactivity. As an example, for a cutting tool with a specific activity of 1 millicure/gr (2.2×10^9 disintegrations per minute), wear products of the magnitude of 10^{-10} gr can be easily determined.

The accuracy of the radioactive method is due to the fact that all test cuts of a particular evaluation are made with the same cutting edge under otherwise identical conditions. Further, the duration of each test cut is quite brief, thus excluding abrupt changes in the cutting process. Finally, a fairly large number of test cuts can be made in a short period of time, and since each test cut constitutes a tool wear determination, an average tool wear value can be obtained.

Radioactive Tool Wear Procedures

There are a number of methods by which the cutting tool can be made radioactive. Of the methods available, by far the simplest and the one almost universally used, is the thermal neutron irradiation process. In this method, the tools are prepared ahead of time in the normal manner and then sent to an authorized facility for irradiation. E.I. Goodman (5) has developed the following technique for preparing radioactive tools: Pure tungsten powder is thermal neutron irradiated, producing W-185 and W-187 activity is permitted to die out (24 hr half-life) and then the W-185 is mixed in a carbide formula and sintered into finished cutting tools.

The choice of the radioisotope to be used in the cutting tool depends on a number of factors:

1. The chemical composition of the tool material.
2. The half-life of the available isotopes.

3. The method to be used to detect the activity.
4. The specific activity of the tool.

Essentially all high speed steel and carbide tool materials contain either chromium, cobalt, tantalum or tungsten, or a combinations of these elements. Since these elements can readily be made radioactive by thermal neutron irradiation, the activation of tool materials becomes a simple matter. The radioisotopes formed are Cr-51, Co-60, Ta-182, W-185 and W-187.

The half-life of the radioisotope is an important consideration, since it determines the length of time that will be available for carrying out the tests. If one uses the W-185 isotope (as have B. Colding and L. G. Erwall (5), B. Colding (6) and M. C. Shaw, et al (7)), which has a half-life of 24 hr, the total useful time for carrying out the tests is about 5 days. Additionally, since the activity of the tool is decreasing rapidly, a correction factor for the decay constant must be applied to the counting data. The use of the relatively long half-life radioisotopes, such as Co-60 (5.24 years), Ta-182 (112 days) or W-187 (74 days), overcomes the problems encountered with the use of W-185 but introduces the minor problem of disposing of the cutting tools and chips after the tests have been completed. Users of the radioactive tool wear test method are divided about equally between the use of short and long half-life isotopes.

The method or methods to be used in detecting the radioactivity must be considered since the instrumentational techniques depend on the type of radiation emitted by the various radioisotopes. If beta radiation is used for indicating the radioactivity present on the chips, it is necessary to flatten and arrange them in a standard pattern for measurement with a beta detector, normally an end-window Geiger-Muller tube or a gas flow counter. Fig. 2a shows a set-up for beta counting with a Geiger-Muller tube and Fig. 2b with a gas flow counter. The efficiency of detection with the Geiger-Muller tube is about 10% and approximately 50% for the gas flow counter. If gamma radiation is used for the detection of the radioactivity, it is not necessary to flatten the chip because of the penetrating power of gamma rays. The chips are placed in a container and placed "on" or "in" a well of a scintillation counter. Fig. 3 shows a well-type scintillation counter. The efficiency of this counter is 24%. As will be seen later, it is advantageous to be able to measure both the beta and gamma radiation of the wear products on the chips.

The specific Activity (i. e. millicuries or microcuries per gr of tool material) is determined, to a large extent, by the method or methods used in detecting the radioactivity of the wear products on the chips. In the early days of the radioactive tool wear test method, when the only available means for measuring the gamma activity was the Geiger-Muller tube, specific activities of 6-60 millicuries per gr of tool material were common. The need for such relatively high activities was necessary, because of the very low efficiency of gamma detection by Geiger-Muller tubes (0.1%). With the advent of scintillation counting techniques, however, it has been possible to greatly reduce the specific activity of the tool and still, in fact, obtain much higher chip counting rates. At the present time, tools with a specific activity of 500-600 micro-curies (1-10 - 1/100 of the former values) per gr of tool material can be used.

Table 1 - Effective Radioisotopes

Isotope	Half-Life	β - Energy M.E.V.	γ - Energy M.E.V.
Cr - 51	28 days		0.3
Co - 60	5.2 years	0.3	1.2, 1.3
Ta - 182	112 days	0.5	0.07, 1.1
W - 185	74 days	0.4	None
W - 187	24 hours	.6, 1.3	Many

Table 1 lists the physical characteristics of the effective radioisotopes used in the radioactive tool wear method.

When gamma radiation is used for the detection of the radioactivity of the wear products on the chips, a measure of the total or gross wear of the tool is obtained. However, if the radioisotope is also a beta emitter, it is possible to measure the flank and face wear of the cutting tool independently. During the process of cutting, most of the tool wear products remain attached either to the side of the chip which moves across the rake face of the tool, or to the newly developed surface. In Fig. 4 the wear products that come from the rake face of the tool become attached to the surface A of the chip, while the wear products that leave the flank side of the tool remain attached to side B. In making a second cut, it is evident that the chip produced will have tool wear products attached to both sides of the chip, side A the rake wear products, and side B the flank wear products. The relative amounts of flank and rake wear can be determined by beta counting the respective sides of the chips. Since beta rays have low penetrating power, the rays coming from the chip side opposite the detector are stopped by

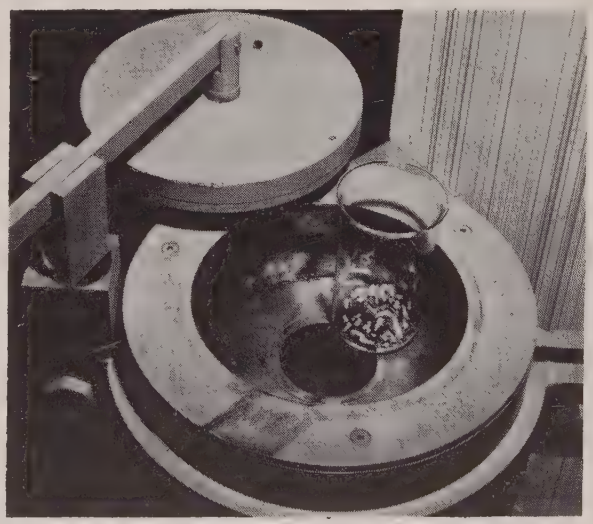

Fig. 3 — Well type scintillation detector

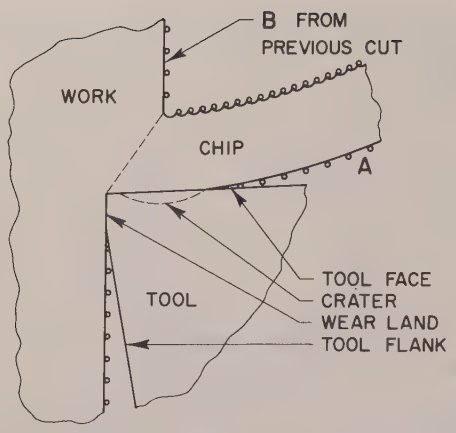

Fig. 4 — Transfer of wear products to flank and face sides of a chip

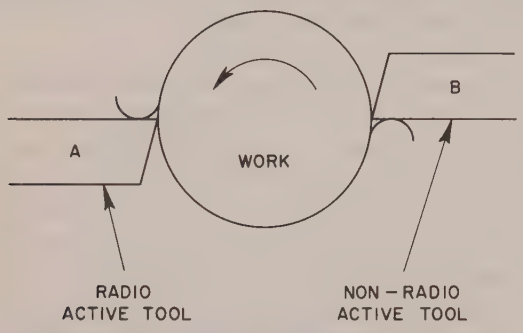

Fig. 5 — Method of hake for determining tool flank and tool face wear by gamma detection

the chip thickness and are not measured.

O. Hake (8) has developed a method for differentiating flank and rake wear by means of gamma detection. Fig. 5 shows schematically the procedure used. Two cutting tools A and B, with only tool A being radioactive, are used simultaneously. They are set at 180 deg with respect to each other in making a test cut. The chips cut with the radioactive tool have radioactive wear products which come from the rake side, while the chips cut with the non-radioactive tool have radioactive wear products which come from the flank side. By gamma counting the separate chips, a measure of the flank and rake wear of the tool is obtained.

Comparison of Radioactive and Conventional Tool Wear Methods

In order to be of real value to metal cutting research, the radioactive tool wear method must more readily yield results which are equivalent to and more accurate than those obtainable by conventional means. The data to be presented below are given to establish the validity and applicability of the radioactive tool wear test method and to compare the results obtained by this method with those obtained by conventional tool-life testing.

The result of a series of test cuts taken on AISI 8650 is shown in Fig. 6. The accumulated radioactivity, which is proportional to the amount of tool wear, is plotted against

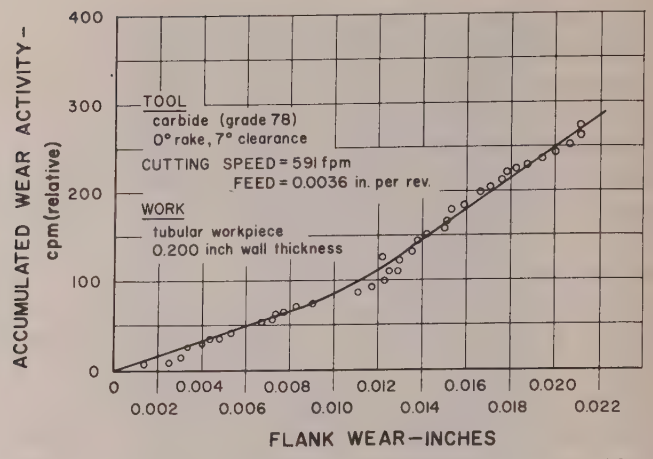

Fig. 6 — Accumulated activity of wear products on the chip's versus optical flank wear

the optical flank wear. It is evident from this figure that the accumulated gross wear (gamma counting) does correlate with the optical flank wear measurements. B. Colding (8, 9) has shown that the integrated rake wear, flank wear and total wear when plotted against time gave linear relationships. E. E. Nadeinskaya (10) has also shown, in his work with different grades of carbide tool materials, a relationship between the accumulated activity and cutting time. In addition, he reports that the tool life data as determined by the radioactive tool wear method agrees closely with tool-life data obtained by conventional flank wear measurements. H. Opitz and O. Hake (11) have also shown, in their work with the double tool method, a linear relationship between integrated flank and rake wear and cutting time.

In order to completely establish the unit relationship between the radioactive tool wear test method and the conventional flank wear method, a series of tests has recently been completed, in which the two methods were compared directly. The radioactive tool wear test data were obtained in the following manner: A series of 10 consecutive test cuts (each test cut constituting a tool wear determination) were made at each of the two test conditions and were evaluated on the same cutting edge. The duration of each test cut was so chosen as to yield at least 20 gr of chips. If less than 20 gr of chips had been cut, in these particular tests, the effect of the entering and leaving of the cutting tool from the work material would have affected the results. Since there is the possibility of a "cross" or "conditioning" effect (i. e. the conditioning of the cutting edge when machining under test conditions A can influence the results when machining under test conditions B.) it is necessary to run the tool "in" at each test condition. This running "in" period consists of making one cut of a duration equal to ten test cuts. The chip samples obtained after this running "in" period are then weighed and the gamma counted and the quantity, counts per minute per gr of chip, which is a measure of the rate of wear of the tool is formed for each test cut. The average wear rate value is formed for each test

condition and the ratio of these two represents the relative tool life. The conventional optical flank wear tests were carried out in the normal manner, with 0.030 in. flank wear as the criteria for tool life end point. The results of the comparison between the two methods are given in Table 2.

The actual tool life values in minutes for 0.030 in. optical flank wear, the relative (ratio) tool life for each evaluation as determined from the conventional tests, and the relative tool life as determined by the radioactive method are given in the table. Examination of these data clearly indicates the unit relationship between the two methods of evaluating tool wear. Further, it has been established that the radioactive method is superior to the conventional method in terms of reproducibility. It is also quite evident that the radioactive method is much more rapid than the conventional method. The total time required for the radioactive tests was 3-1/2 work days as compared to 21 days for the conventional tests.

In all of the discussions so far, it has been assumed that all or nearly all of the wear products remain attached to the chips during the cutting operation with a negligible amount of wear products going into the environment, i.e into the cutting fluid if a cutting fluid is used, or into the surrounding air if the cutting is performed dry. In the machining of steels and cast iron this assumption has been borne out by numerous measurements. When machining with a cutting fluid it was established that 90% or more of the tool wear products remain attached to the chips. B. Colding has also shown that in dry cutting the vast majority of the wear products remain attached to the chips. In a recent study of the machinability characteristics of a number of aluminum alloys, it has been found that the percentage attachment of the wear products to the aluminum chips is quite different from steel chips. In the case of these aluminum alloys, the amount of tool wear products remaining attached to the chips varied between 41% for one alloy to 86% for another alloy. Thus, in this investigation it would not have been valid to neglect this factor. It was, therefore, necessary to correct the wear rate data obtained by counting the wear products on the chips by the amount of wear products present in the cutting fluid. The amount in the cutting fluid was determined by collecting and counting the radioactivity present in the fluid. That the percentage of wear products remaining attached to the chips can vary significantly, does not, however, invalidate the radioactive tool wear method in any way, since in most cases it is a simple matter to account for this factor.

The weight of evidence above makes it clearly evident that the radioactive tool wear method is indeed a rapid and accurate method for determining tool wear and yields results which are commensurate with those obtained by conventional methods.

Typical Results

In the last ten years since the introduction of the radioactive tool wear method, The Cincinnati Milling Machine Co. has been using this method on a routine basis for evaluation of the effects of the numerous machining parameters as related to tool wear. In this time more than 600 tool wear evaluations, representing more than 6000 individual tool wear tests, have been completed. These tests have covered nearly all phases influencing tool wear, such as cutting speed, feed rate, work material, tool material, cutting fluid, tool geometry, method of tool preparation, and effect of vibration and rigidity. The results of typical applications of the radioactive tool wear method will be discussed to illustrate the effectiveness and usefulness of the method.

Table 2 - Comparison of Conventional and Radioactive Methods of Tool Life Determination

Conditions Conditions Evaluated	Tool Life for 0.030 Flank Wear Min.	Relative Tool Life from Flank Wear Tests	Relative Tool Life as Determined by Radioactive Method
AISI 1117 and AISI 1018	970 1510	0.64	0.96 ±0.08*
AISI81B45 and AISI 1117	450 1510	0.12	0.12 ±0.01
Emulsion Type Cutting Fluid and water	470 345	1.33	1.78 ±0.08
Cut Speed .50 fpm and 100 fpm	345 41	3.43	3.10 ±0.16

*Uncertainties are based on 90% statistical confidence limits.

Table 3 shows the results of the aluminum alloy evaluation mentioned earlier. The information required in this evaluation was a determination of the relative machinability of an experimental high silicon content aluminum alloy as compared to a number of commercial aluminum alloys. The data have been standardized for a relative machinability index of 100% for the 355 alloy. It is interesting to note the relatively large variation in the machinability index of the various commercial alloys, from 100% for the 355 alloy to 54% for the 356 alloy. The low index for the high silicon content experimental alloy, 30%, is attributed to the abrasive action of the silicon on the cutting tool. It is important to mention that if these tests had been performed by the conventional flank wear measurement method, at least six weeks would have been required with the expendi-

Table 3 - Relative Tool Life of a Number of Aluminum Alloys

Aluminum Alloy	Relative Tool Life	% of Wear Products Remaining Attached to the Chips
355	100%	74%
355S*	62%	75%
356	54%	41%
356S*	80%	68%
High silicon alloy	30%	86%

*Solution treated and aged.

Table 4 - Effect of Rigidity on Tool Life

Test Conditions	
Work Material	AISI 81B45
Cut Speed	50 fpm
Feed	0.008 in. rev.
Tool	H.S.S., Orthogonal cut +10 rake, 7 deg clearance

Results: Optical Flank Wear on the Tool	Relative Tool Life Least Rigid Tool Holder / Most Rigid Tool Holder
0.004	1.38 ±0.09
0.010	1.93 ±0.13
0.017	1.52 ±0.12
0.022	0.87 ±0.10

Integrated Value 0 - 0.030 Flank Wear 1.35

ture of a vast amount of metal as well. The radioactive method required five days and 20 lb of metal.

Aside from the routine evaluation of work materials and cutting fluids, the radioactive tool wear method has been used as a research tool for investigating numerous other areas of metal cutting research. One of these has been to obtain definite information regarding the influence of vibration and rigidity on tool wear. While it has been known in a general way for many years that vibrations and rigidity can be an important consideration in the life of a cutting tool, quantitative information has not been available to pinpoint the actual magnitude of this effect. In this investigation the radioactive method provided a means for accurately and rapidly exploring a large domain of machining conditions. Two tool holders of widely different rigidity characteristics were employed. Tool holder A, the most rigid one, had a static "stiffness" of 1.8×10^6 lb/in. and a corresponding natural vibrational frequency of 28,000 cycles per second, while tool holder B, the least rigid, a "stiffness" of 8.5×10^4 lb/-

Table 5 - Effect of Rigidity on Tool Life

Test Conditions	
Work Material	AISI 81B45
Cut Speed	100 fpm
Feed	0.004 in. rev.
Tool	H.S.S., Orthogonal cut + 10 rake, 7 deg clearance

Results: Optical Flank Wear on the Tool	Relative Tool Life Least Rigid Tool Holder / Most Rigid Tool Holder
0.006	2.02 ±0.26
0.013	1.25 ±0.08
0.022	2.81 ±0.32

Integrated Value 0 - 0.030 Flank Wear 1.81

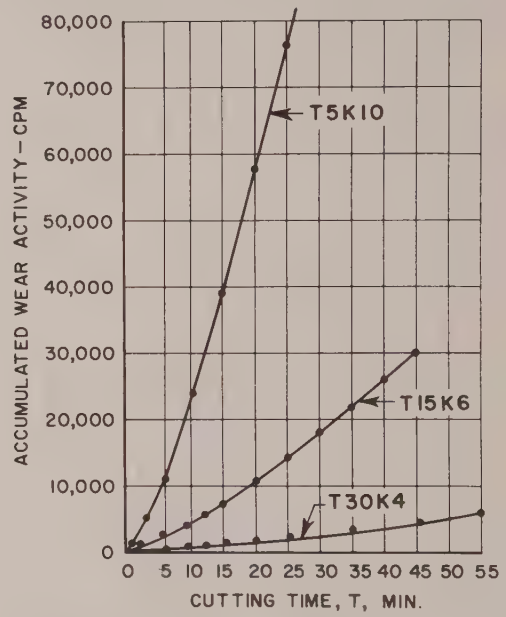

Fig. 7 — Wear characteristics of three grades of carbide tool materials

in. and a natural vibrational frequency of 3700 cycles per second. Results obtained at two different test conditions with these two tool holders are given in Tables 4 and 5.

It is evident from these results that not only does rigidity materially affect tool wear, but that the effect of rigidity on wear rate is also a function of the amount of optical flank wear present on the tool when each evaluation was made. The effect of rigidity on overall tool life can be obtained by integrating these values between the limits of flank wear 0-0.030 in. For the conditions in Table 4 the overall tool life was reduced by 35% and for conditions in Table 5 by 81%.

E. B. Nadeinskaya (10) has used the radioactive tool wear

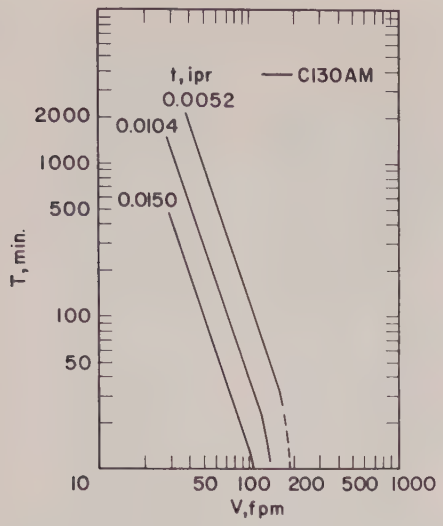

Fig. 8 — Tool life versus cutting speed — C 130 titanium

method to investigate the wear resistance characteristics of a number of grades of carbide cutting tools. Fig. 7 shows the results of the effect of cutting speed on the gross wear of three grades of carbide tool materials. The relative tool lives of three grades were found to be in the proportion of T5K10/T15K6/T30K, 1/7.5/26. In the same paper, Nadeinskaya reports on the optimization of the wear characteristics of a high-speed steel tool material as related to five different conditions of the tool, namely, normal heat treatment, cyaniding, and three different variations of sulfurization. The results of the radioactive tests permit him to find the zone of minimum wear and establish the fact that the best results were secured by cyaniding and normal heat treatment. Sulfurization did not reduce the wear of the tool.

M. C. Shaw, P. A. Smith, B. Colding and N. H. Cook (7) in their work on the machining of titanium used the radioactive tool wear method to extend tool life data obtained by the conventional flank wear method, i.e. a minimum number of conventional tool life tests were made in order to establish the basis of absolute wear, tool life in minutes, with the rest of the data necessary for the Taylor curves being secured by the radioactive tool wear method. Fig. 8 shows the tool life (0.030 in. flank wear) versus cutting speed for titanium alloy C 130 AM as obtained by the radioactive method.

While the application of the radioactive tool wear method has been limited almost exclusively to turning operations, some work has been done in milling. Fig. 9 shows the milling setup used in these studies. Fig. 10 shows a plot of the accumulated activity of the wear products on the chip versus the weight of metal removed.

There, as in most of the lathe tests, a linear relationship exists between wear and the amount of metal cut. Fig. 11 gives the results of a series of tests of the relative tool life of a milling cutter when the cutting speed is varied. The results obtained in this test coincide with those that are known to exist between cut speed and tool life as obtained

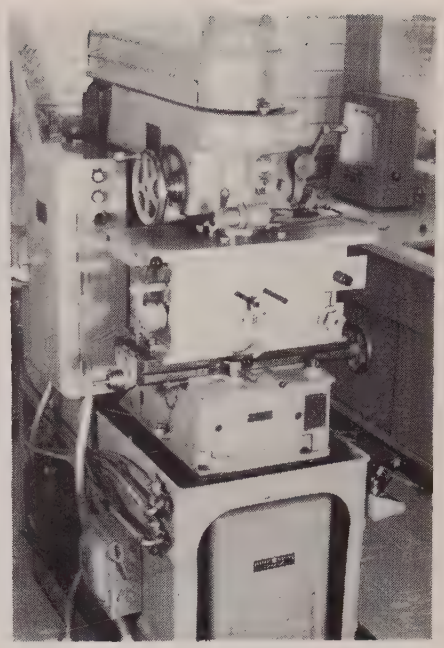

Fig. 9 — Milling setup for radioactive testing

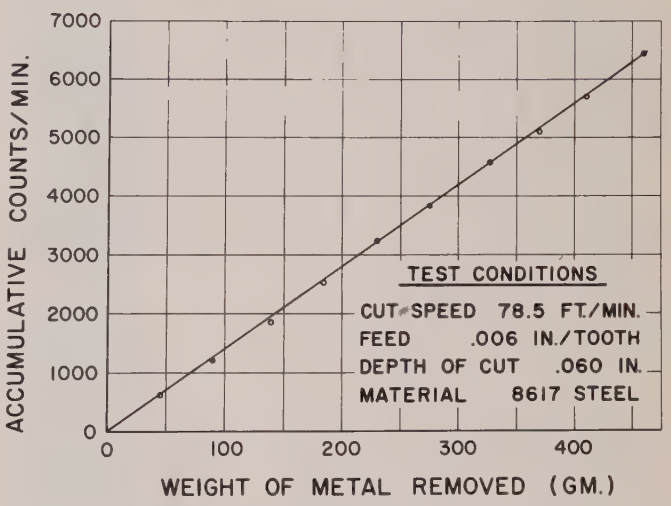

Fig. 10 — Accumulated activity of wear products on the chip's versus weight of metal removed — face milling

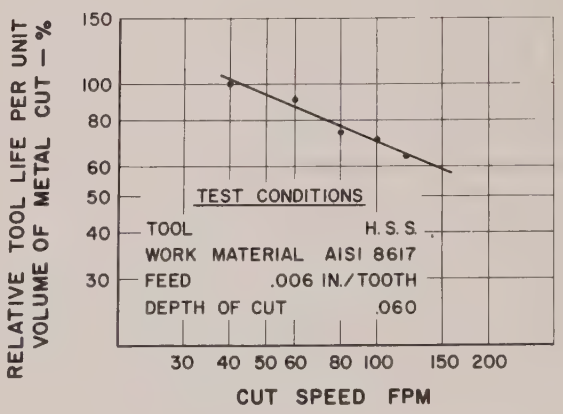

Fig. 11 — Tool life versus cut speed — face milling

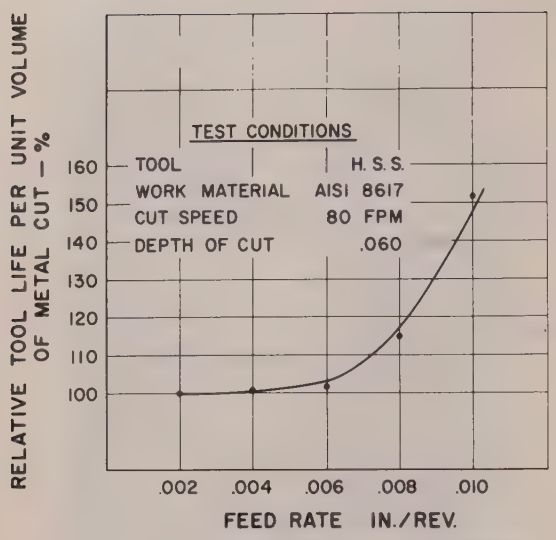

Fig. 12 — Tool life versus feed rate — face milling

by the conventional method. Fig. 12 shows the results when the cutting speed is held constant and the feed rate is varied. Here again, the results obtained in this test coincide with those that are known to exist between cut speed and tool life as obtained by the conventional method. Fig. 12 shows the results when the cutting speed is held constant and the feed rate is varied. Here again, the results agree closely with the known relationship between feed and tool life.

As in turning operations, the question arose as to the amounts of tool wear products that remain attached to the chips, that pass into the environment, and that remain attached to the milled surface. The latter amount would be due to the rubbing action of the tool on the freshly cut surface of the workpiece. This quantity was determined by first cutting with a radioactive cutting tool and then making a second cut with a non-radioactive cutting tool. By comparing the activities of the two chip samples, the second sample giving the amount of wear products left on the surface on the milled workpiece by the radioactive tool, the percentage remaining attached to the milled workpiece was determined. It was found that only 1.5% of the total wear products remain attached to the workpiece. The amount going into the cutting fluid was very minute. In fact only an upper limit can be assigned because no measurable amounts have been found in the cutting fluids. Based on counting statistics, a value of about 1/2% can be assigned. Thus, it can be seen that, as in turning, the vast majority of the wear products remain attached to the chips.

Special Studies with Radioactive Tools

Use of radioisotopes in the form of radioactive cutting tools has provided the opportunity for the development of techniques useful in investigating the nature and mechanism of tool wear. By means of autoradiographs it is possible to detect and measure the nature and distribution of individual wear particles. An autoradiograph can be obtained by placing a chip cut with a radioactive tool in contact with photographic film and allowing the radiation emitted by the wear particles to expose the film. In preparing the chips for autoradiographing, a number of precautions have to be taken. Since most chips are not flat enough for autoradiographing directly, it is necessary to carefully anneal the chip in a vacuum furnace prior to flattening, in order to prevent the formation of an oxide film which can disturb the wear particles on the chips. Chips must be handled with care since some of the wear particles can easily be detached. Fig. 13 shows autoradiographs of the face and flank side of lathe chips for two work materials, AISI 1018 and AISI 81B45 and four different feed rates. Visual examination of these autoradiographs will disclose a number of interesting facts which have heretofore not been known and in all probability could not have been disclosed by any other means. For AISI 1018 it can be seen that the concentration of wear particles per unit area decreases rapidly with increasing feed, while the physical size of the wear particles increases. At the 0.0015 feed rate the wear particles must be extremely small and densely distributed in order to give such a uniform exposure of the photographic film. At the 0.004 feed the wear particles have become discrete and are much larger in size. The AISI 81B45 has the same trends; density of wear particles decreases with feed, while the size of the wear particles increases. However, the absolute magnitude of the concentration and physical size of the wear particles are quite different. While it is not possible to give a complete interpretation of these autoradiographs, it is clearly evident that the use of such techniques can shed much needed information on the nature and mechanism of tool wear.

The application of autoradiographic techniques to the study of milling chips has yielded interesting information on the role of the built-up edge as related to rool wear. Fig. 14 shows an optical photograph and an autoradiograph of the face side of the same milling chip. At the left is that portion of the chip that was formed when the cutter first entered the work material. It is immediately apparent that the high concentration of wear particles is the result of impact as the tool enters the workpiece. This effect of impact can also be seen in the autoradiograph of the workpiece surface (Fig. 15). The top of Fig. 15 shows the high concentration of wear particles that results each time the cutter enters the workpiece. As the cutter continues through the workpieve, the wear particles become less densely and more uniformly distributed. On the right hand side of the chip autoradiograph, there is also an area of high concentration of wear particles. This high concentration results from the presence of the built-up edge on the tool, for as the tool leaves the workpiece the built-up edge remains with the chip, but in being removed from the tool it "plucks" material from the tool. This "plucking" of the tool as the built-up edge is sloughed off, can also occur during any stage of the cut. Fig. 16 shows this sloughing of the built-up edge along the whole length of the chip. Thus, the importance of the presence of

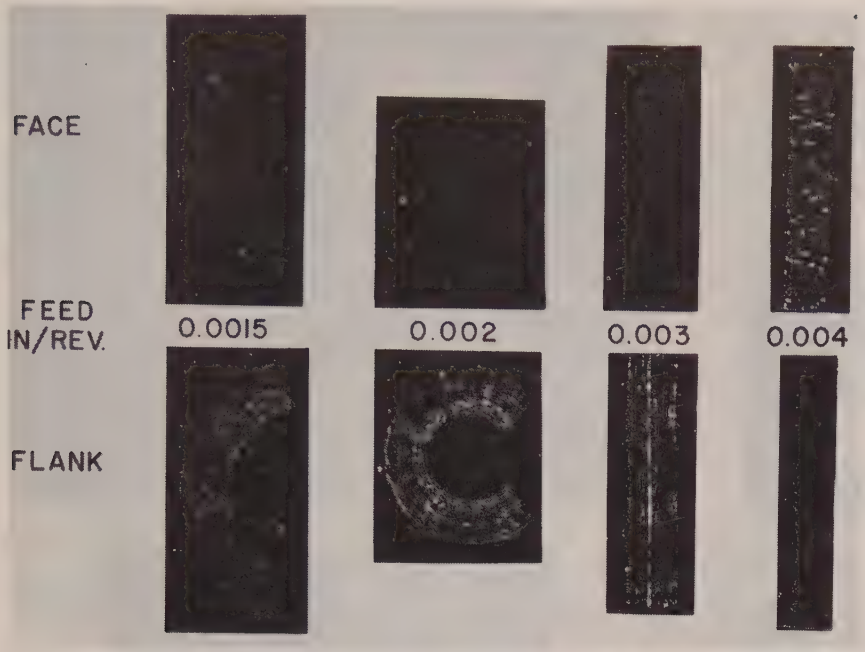

Fig. 13a — Lathe chips autoradiographs for 1018 work material, 30 cut speed.

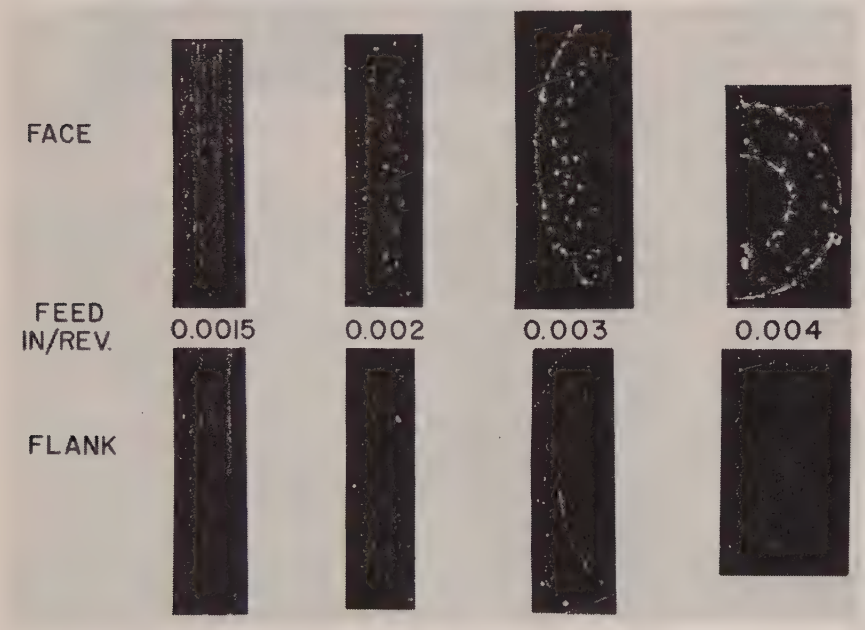

Fig. 13b — Lathe chips autoradiographs for 81B45 work material, 30 cut speed.

the built-up edge can be appreciated. If this "plucking" of the tool material by the sloughing built-up edge can be reduced or eliminated, the wear of the cutting tool can be decreased and its life increased.

In their study of the transfer of work material to a cutting tool, I. Finne and E. Rabinowicz (11) used a variation of the radioactive tool wear method. In place of radioactive tools, they used ordinary tools to cut a radioactive work material, copper. The amount of transfer was determined by making quantitative autoradiographs of the cutting tools. They found that the amount of metal transfer to the cutting face was of the same order of magnitude as would be produced in a sliding experiment under similar condition. The use of lubricants was found to reduce drastically the amount of metal transfer.

Summary

The use of radioisotopes in the form of irradiated cutting tools has proven to be a very powerful tool for investigating the problems of tool wear as influenced by the numerous machining parameters. It not only provides a method for rapidly and accurately evaluating these parameters, but offers a means for studying the actual mechanism of tool wear as well. Much of the information now available was unattainable by more conventional tenchiques. While the radioactive tool wear method does have some distinct advantages over the conventional methods of obtaining tool wear information, and for investigating the mechanism of tool wear,

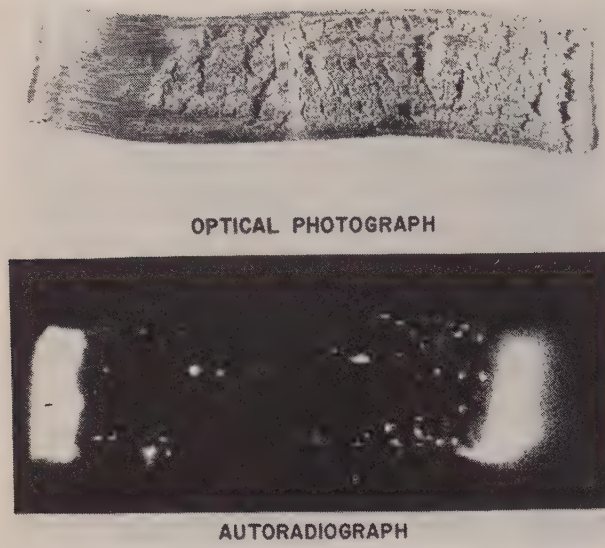

Fig. 14 — Optical photograph and autoradiograph of face side of milling chip

it does not replace or supercede the conventional methods, as much information can be obtained by the conventional methods. Combined use of the two methods will go a long way in solving the practical problems associated with the cutting process and shed more light on the mechanism of tool wear.

Acknowledgements

The authors wish to acknowledge the contributions of: Dr. M. E. Merchant for his interest and guidance in the research reported here; Mr. J. L. Neu and Mr. J. C. Hawlik for the development of autoradiographic techniques and the application of these to turning and milling research; Mrs. Dorothy Massie for carrying out the experimental test cuts; and Mrs. Connie Chaney for the preparation of the technical illustrations. Appreciation is also expressed to Miss Helen Conner for her preparation of the manuscript.

References

1. Hans Ernst, "Economics of Machining," Report from Cincinnati Milling, Vol. 13, No. 1, (1956), 12-15.

2. M. Eugene Merchant, Hans Ernst and E. J. Krabacher, "Radioactive Cutting Tools for Rapid Tool Life Testing," Trans. ASME, Vol. 75, (1953), 549-559.

3. M. Eugene Merchant and E. J. Krabacher, "Radioactive Tracers for Rapid Measurement of Cutting Tool Life," J. A. P., Vol. 22, No. 12, (Dec. 1951), 1507-1508.

4. B. Colding and L. G. Erwall, "Wear Studies of Irradiated Carbide Cutting Tools," Nucleonics, Vol. 11, No. 2 (Feb. 1953), 46-49.

5. E. I. Goodman and I. J. Gruverman, "Tool Wear Measurement Using Beta Emitting Tungsten-185," Third Industrial Nuclear Technology Conference, Chicago, Ill. Sept. 22-24, 1959.

6. B. Colding, "Testing of Machinability by Radioactive Methods," MSc., Thesis M. I. T., 1956.

Fig. 15 — Autoradiograph of workpiece surface

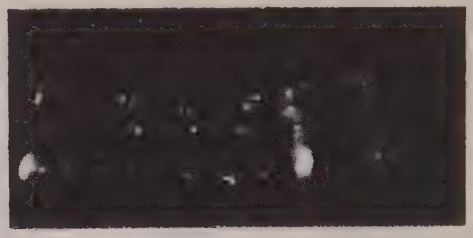

Fig. 16 — Autoradiograph of milling chip showing sloughing of built-up edge

7. M. C. Shaw, et al, "Machining Titanium II," A Report Prepared for the United States Air Force, Wright-Patterson Air Force Base, Dayton, Ohio, Under Contract No. AF33(600)-31636.

8. O. Hake and H. Opitz, "Wear Analysis of Hard Metal Turning Tools by Means of Radioisotopes," Microtecnic, Vol. X, No. 1.

9. B. Colding, "A Wear Relationship for Turning, Milling and Grinding - Machining Economics," Doctors Dissertation, Royal Institute of Technology, Stockholm, Sweden, 1959.

10. E. P. Nadeinskaya, "Use of Radioactive Isotope in Investigating Cutting Tool Wear," Conference of the Academy of Sciences of the U. S. S. R. on the Peaceful Uses of Atomic Energy, July 1-5, 1955, Session of the Division of Technical Science, 85-95.

11. O. Hake, "Zerspanungsuntersuchungen mit verschiedenen Prüfrerfahren," Forschungsbericht "Zerspanug" II, Nr. 63, (Aug. 7, 1956), 950-953.

12. I. Finnie and E. Rabionowicz, " A Radioactive Study of the Metal Cutting Process," Lubrication Engineering, (January-February, 1956), 29-31.

References Not Cited

13. "Radioisotopes: New Tool for Industry," The Iron Age, (Oct. 23, 1952).

14. E. Petrozzi, "Absolute Measurement of Tool Wear," Nucleonics, Vol. 14, No. 11, (Nov. 1956).

(continued on page 613)

Recent Developments in Cam Design

J. H. Nourse
Engineering Consultant

R. C. Dennis
Atomic Power Development Associates

W. M. Wood
Associated Spring Corp.

THE MATHEMATICS of the optimized cam design method is based upon the "polydyne" analysis where in the differential equations of motion connecting the desired valve motion with cam displacement are solved by means of polynomial equations. A certain familiarity on the part of the reader with the "polydyne method of cam design" has had to be assumed—partly in the interests of brevity and partly because, in the opinion of the authors, the presentations given in the original work (1)* could not be improved. This paper, therefore; while quoting freely from the original work, discusses primarily additions and modifications to the polydyne method of cam design.

This paper is divided into three sections:

1. A Statement of the Cam Design Problem - wherein the cam design goals and limitations are discussed. It is shown that in overhead-valve (pushrod) engines, five basic interdependent variables are involved in any particular cam design. These are

a. Valve event length.

b. Valve lift.

c. Range of engine speeds.

d. Valve train natural resonant frequency (fundamental mode).

e. Force-stress limits in the valve train.

Of five, only three may be chosen independently. This is done as follows:

a. The valve event length is chosen based on gas dynamics considerations.

b. The range of engine speeds is fixed (with, in particular, the maximum and engine design speed) from measured values of the valve train resonant frequency—based on an empirical design equation.

c. The valve lift is then determined (in a series of ordered steps) based on an arbitrary design choice for the maximum allowable force-stress limits in the valve train system.

By means of a digital computer program a valve lift is determined which maximizes the area under the valve lift diagram.

Finally, it is shown that the design problem is similarly solved for the overhead cam engine except that the valve train resonant frequency is not a limiting factor. For this engine type, the engine speeds are chosen from either gas dynamics or force-stress limits considerations. In general, this section of the paper defines the optimal cam design problem.

2. A summary-extract of the polydyne method for cam design - by means of a flow chart, a general perspective of

*Numbers in parentheses designate References at end of paper.

the mathematical steps involved in a polydyne solution is given which, with an optimum solution considered, leads to the overall desirability of electronic computer programming. In general, this part of the paper provides a digested review of the mathematical means for problem accomplishment.

3. Discussion of the computer work and how the desired boundary conditions in an optimal cam profile design solution are achieved - in addition, an analytical method for selecting the valve spring design which matches the particular dynamics of the cam profile is discussed. When complemented by the original polydyne method text, this section states how the optimal cam design problem solution may be accomplished.

Statement of Cam Design Problem

In the beginning one might regard the automotive engine type cam as not more than a smooth lump on an otherwise round metal shaft. The cam function is to drive the valve train in such a way as to open, then close, the valve as rapidly as possible with an overall valve event of predetermined duration. A vast quantity of engine design and development experience has shown, however, that a precise and carefully controlled profile for the cam is of vital importance to the successful performance of the engine. An extensive literature has evolved to provide the engine designer with an analytical solution to the cam design problem, and yet, to a large extent, the methods actually employed in the industry remain trial-and-error, expensive procedures. This is partly because the analytical methods of cam design are technically involved, and because the basic problem objectives and limitations have not been sufficiently well defined to permit a successful analytical solution with a high degree of certainty. Both the goals and the limitations in the analytical definition of the design of an optimum cam profile will be critcally considered here.

The objective of the cam design procedures is to obtain the most effective valve-lift diagram possible with a given valve train system considering the practical limits imposed upon the design by

1. The prescribed limits on valve event.
2. The maximum allowable loads and stresses permissible in the valve train.
3. The elastic characteristics of the valve train.
4. The practical limits imposed by production cam manufacturing accuracy.

Restated, the design objective is to approach as nearly as possible (from the conservative side) the "optimum" cam profile for any particular engine.

This work was begun some years ago. The initial step was a literature survey and review which included, we believe, nearly every paper (English language) published on the subject of engine cam design. The more important of these were studied in detail. This paper, therefore, is presented as having been built upon the original concepts and contributions of many other engineers whose work preceded our own. Our effort has been one of organization and arrangement; and while it is hoped that we may have contributed an ideal here and there, mainly, this work was begun from an established foundation.

Most important (as a foundation to this paper) has been a remarkably fine series of papers offered to the engine design and manufacturing industry some years ago by the Valve Division of Thompson Products, Inc. (now Thompson-Ramo Wooldridge). These papers have earned an established and respected place in cam design literature. Ref. (1) which was based upon work by Dr. W. M. Dudley, defines and presents a method for cam design that provides for the elastic deflections in the valve train system during engine operation. This method is called the polydyne method of cam design. We believe their study (in the original form) to be of fundamental importance to the subject of valve train design as well as cam design.

In all respects, the engine is an elastic system. The valve timing and event lengths control the fluid flow of gases having inertial and compressible properties. The fixing of these values for a cam design in any given engine system depends, therefore, upon the general subject of gas dynamics. In addition, there is inherent to the design of the engine elastic system the problem of the inertial dynamics of the mechanical components. In particular, a consideration for the dynamic deflections in the valve train linkage and support points is vital to the design of the cam contour. This fact becomes more important as the valve loads increase with higher design engine speeds, and again, as the valve train stiffness-to-mass ratios decrease with the design effort toward lighter engine weights. It has been aptly stated (1) that "The actuating forces in the valve train at high (engine) speeds in combination with inherent (valve train) flexibility result in a valve motion that bears no simple relationship to cam contour."

Simply given, the considerations for the gas dynamics and inertial dynamics in the engine have caused the cam lobe shape to modify from what could previously be regarded as not more than a smooth lump on a round metal shaft to a precise and carefully controlled contour.

GENERAL OBJECTIVES - A qualitative statement of the cam design problem can be given as follows: Based upon a given, desired engine performance (that is, specific torque and horsepower characteristics diagrams), and a particular valve train configuration, how may the optimum cam lobe contour be selected through ordered analytical steps from among the infinite number of possible contours available? The "optimum" cam lobe contour is defined as that contour which most nearly obtains the engine performance objectives while taking account of the limitations imposed upon the design by the elastic characteristics of the engine system.

The single, most important rule for obtaining a successful cam profile is that of starting the design with objectives which are both reasonable and compatible with the design limiting criteria. Engine design performance objectives will seek to specify (cam design) values for:

1. Valve event (and timing).
2. Valve lift.

(Both controlled over a specified range of engine speeds up to some maximum speed.)

The limitation to the accomplishment of any arbitrary set of such goals will be fixed by certain physical characteristics in the valve train. These may be broadly divided into two classifications:

1. Valve train dynamics limits—where, in overhead-valve (push-rod) systems, the fundamental natural resonant frequency of the valve train will normally limit the practical maximum engine operating speeds.

2. Force-stress limits—wherein the valve train interface designs, including metallurgy and lubrication, will fix the maximum allowable forces and bearing stresses. These limits will normally establish the maximum allowable accelerations in cam designs for either overhead-cam or overhead-valve engines.

The important point to this generalized discussion is that we seek a particular valve motion to obtain a desired engine performance. From the cam profile design point of view, the valve train system characteristics limit the performance that can be realized. The relationship between the parameters affecting design goals as opposed to systems limitations are both numerous and subtle. If the cam profile is to be optimized, these parameters must be defined quantitatively. It is necessary to examine the solution boundary conditions to determine which must be considered rigid, and which may be adjusted in favor of some other more desirable requirement. In this engineering problem, as in most, the final solution is the result of compromise. We seek the optimum compromise.

SPECIFIC DESIGN GOALS - Consider first, the specific values of valve event length, valve lift and operating range of engine speeds as these relate to the gas dynamics problem of engine design performance.

Valve Event Length - In the context of this problem, the subject of gas dynamics relates the particular configuration of the engine gas flow passages (with valve timing and event lengths) to the desired characteristics of engine performance. While this is a vitally important problem, there exists no analytical method for choosing optimum valve event and timing values expressed as a function of engine manifold geometry for engine torque and horsepower performance characteristics. Fortunately, there does exist an extensive practical experience which allows near optimum values to be chosen empirically. These, normally, are then varied in a few carefully chosen trials to maximize a desired performance result. Such trials require a limited number of cam designs, but it is important to recognize that the valve event lengths and timing must be rigidly determined in each trial as well as in the final choice of such values. For the optimum cam design the valve event length, having been selected, becomes invarient.

Valve Lift - While it is customary (with engine cam design methodology) to consider the valve lift as a rigid design specification, it will be shown that there are important advantages which will accrue to the cam profile (and to the engine performance) if the design value of the valve lift is not rigidly prescribed. It is suggested that the optimum cam design specification should state, instead, a minimum and maximum acceptable valve lift limit. The design goal then will be to achieve the maximum lift obtainable within the specified tolerance.

The valve lift required to produce an annular valve-open area just larger than the port area at the valve seat is a lift equal to 25% of the valve seat diameter (2). The design value for the valve lift is, therefore, normally fixed at this level. Two ideas are necessary to explain why this value should not be considered a rigid specification.

First, consider the parameter used to evaluate and maximize the "engine breathing," the area under the valve-lift diagram. While it is true that area added to the diagram above the normal (25% of valve seat diameter) valve lift level is relatively ineffective, there is a significant gain in area below this level associated with a higher valve lift. (See Fig. 1.) The gas dynamics of the flow through both intake and exhaust valves has been studied. These considerations show that a true evaluation factor for the relative effectiveness of the areas under the valve-lift diagram would be quite complex but that, however this may be done, a practical and simple maximizing of the area achieves the desired effectiveness evaluation result. The important point is that higher valve lifts improve the effective breathing of the engine and also that this effectiveness can be evaluated from the valve lift diagram area even though the gain in effectiveness with area is not linear.

Second, as will be shown later, the design values for valve event, valve lift, engine design speed, valve train resonant frequency, and the maximum allowable interface bearing stress are interdependent quantities in any particular cam

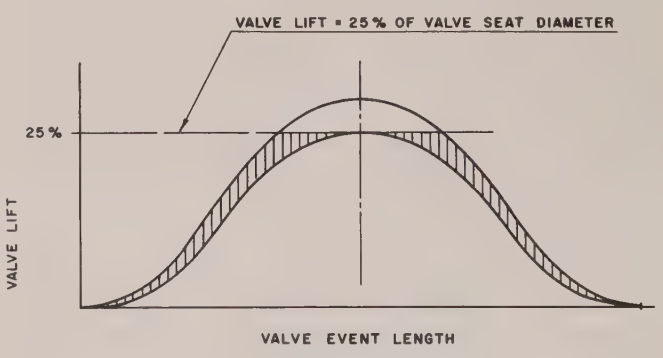

Fig. 1 — Gain in effective valve lift diagram area with optimized lift

design. The maximum possible valve lift attainable (assuming there is not a clearance problem) will, in general, increase with a longer valve event, increase with a higher valve train resonant frequency, and also increase with a higher allowable stress, but will decrease with a higher engine design speed. The interdependency of these factors is such that it can, and occasionally does, happen that the specified value for valve lift cannot be obtained without exceeding one or more of the limiting factors. An important part of the cam design problem is the discovery of this fact; but equally important is the discovery that a greater valve lift is available to a given design. For example, it is usual to gain between 5% and 10% in valve lift area by optimizing the valve lift. In a recent cam solution, an improvement in engine peak horsepower performance of 16% was obtained from this single consideration.

Engine Speed Range - The third (and last) cam design factor involved with gas dynamics is the range of engine design operating speeds. While torque performance depends upon an accurate valve timing and control related to single units (cylinder volumes) of fuel-air mixture in each cylinder, the horsepower performance is related to the rate at which successive units of mixture can be effectively processed. That is, power performance is closely identified with engine speed. Since accurate valve control over a range of engine speeds depends upon the valve train resonant frequency more than any other single factor, from the point of view of the cam design, the power performance, the range of engine operating speeds in general, and the maximum engine operating speed in particular, depend primarily upon the stiffness and mass (that is, the resonant frequency) of the valve train.

Earlier in this discussion, the limiting factors in a cam design were broadly classified into two parts: the valve train dynamics and force-stress limits. The importance of the valve train resonant frequency parameter can best be appreciated by comparing the difference in the range of engine speed performance between the overhead-valve (pushrod) and the overhead-cam type engines. The pushrod engine will normally have a valve train resonant frequency of 30,000 to 50,000 cpm; the corresponding maximum engine speeds will be between 4000 and 6000 rpm. These ranges assume that the valve spring load at the cam will be sufficiently low so that excessive bearing stresses will not occur at engine crank and idle speeds with normal production materials and lubrication. In the overhead-valve engine, the valve train resonant frequency will design the maximum engine speed; the force-stress limits will design the maximum allowable cam profile accelerations.

The overhead-cam engine will normally have a valve train resonant frequency of 200,000 to 500,000 cpm and a maximum engine speed of 6000 to 8000 rpm. On the basis of valve train frequency, the engine speed would not become important below about 12,000 rpm; the force-stress limits are the controlling factor in the overhead-cam engine cam design.

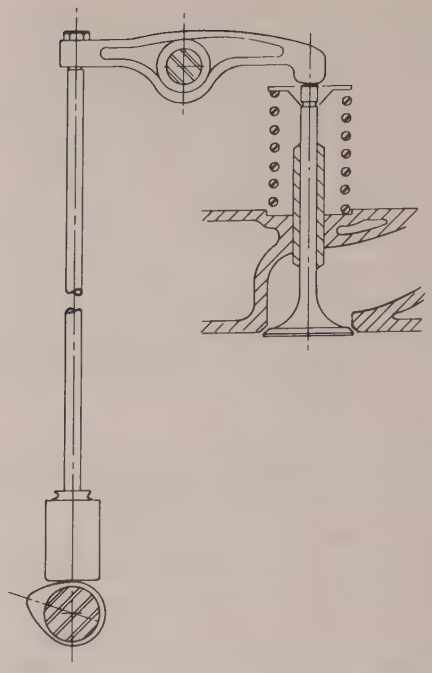

Fig. 2 — Overhead (pushrod) valve train

Consider the general arrangement of a typical overhead-valve (pushrod) gear design (see Fig. 2.), and retain in mind that the specific function of the gear is to control precisely the motion of the end element (valve) at engine speed. As the tappet moves up the cam opening ramp, first any clearance, then the static and dynamic deflections in the valve train, are taken up in such a way that, ideally, the valve will just lift from the valve seat as the tappet reaches the top of the ramp. At this moment, then, the valve train has experienced some compression and has stored an amount of elastic energy. In the first few degrees of the cam opening event, much larger acceleration forces are applied by the cam to the valve train to accelerate the valve. Further valve train compression takes place, and thus still more potential elastic energy is stored in the valve train system. If at this further moment the accelerations imparted by the cam continue, the system will rebound with the potential energy of compression exchanged for kinetic energy in the end (valve) element. The effect at the valve is to induce suddenly a much higher acceleration than that given by the cam. The elapsed time required for this rebound to occur is precisely related to the natural resonant frequency of the valve train system, and it is important to note that this interval is wholly independent of engine speed.

In the "polydyne" system of cam design, the acceleration forces applied to the valve train system at the cam are adjusted in such a way (that is, in the right amount and at the right time) so as to just relieve and compensate for this release of potential compression energy. By this means, the valve acceleration diagram is properly controlled; while the cam acceleration diagram shows a pronounced dip. (See

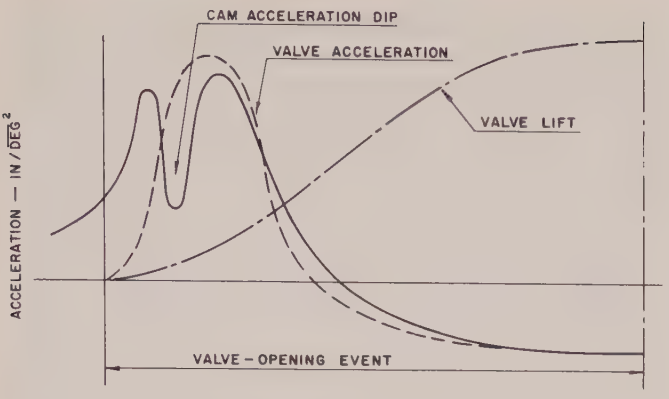

Fig. 3 — Acceleration diagram showing cam dip

Fig. 3.) Because, however, the elapsed time for valve train compression and rebound depends directly upon valve train frequency and is independent of engine speed, the compensation in the cam profile can be exactly positioned for only one engine speed—this will be the engine design speed.

Summarizing, the optimum cam design goal for engine speed range will be fixed by a consideration of the vale train resonant frequency in overhead-valve engines—and by a consideration for gas dynamics and force-stress limits in overhead-cam engines.

DESIGN LIMITATIONS - Valve Train Dynamics - Every real physical system has an infinite number of degrees of freedom—that is, each particle of mass within the system is able to deflect and vibrate along three perpendicular axes as well as rotate about each one. Also, any real system is non-linear in the sense that a particle of mass after displacement does not experience a restoring force exactly proportional to the amount of such displacement. Elastic systems made from metal are, however, very nearly linear—and further, most valve train systems can be reduced or idealized to one having a single degree-of-freedom. These two simplifying factors enable the engineer-mathematician to handle cam design problems as these relate to the inertial dynamics of valve train systems. The idealized single degree-of-freedom valve train of the typical overhead-valve engine will appear as in Fig. 4, the overhead-cam engine as in Fig. 5.

That any particular valve train system is a near approximation to a single degree-of-freedom system cannot be safely assumed in practice. It is very desirable to check this point prior to the start of any particular cam design. During the single degree-of-freedom check, several important pieces of information are gained; one way to accomplish this step will be explained later in this paper.

Valve train systems which respond as having a single degree-of-freedom, and which also are driven by a cam profile wherein the correction for valve train compression has been properly made for a particular engine speed will show vibration amplitudes at the end element plotted as a func-

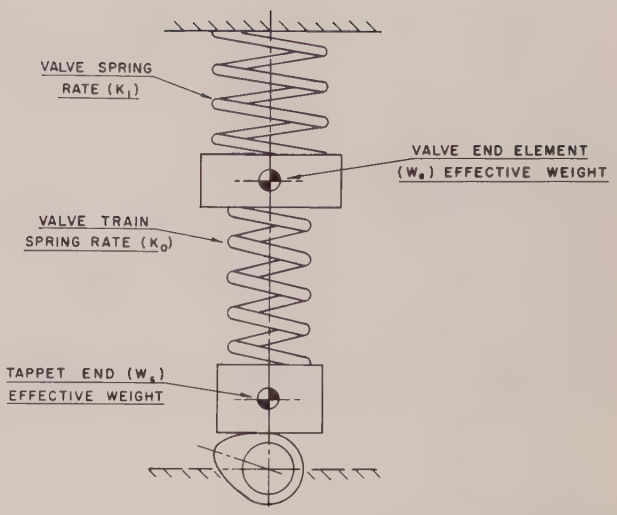

Fig. 4 — Idealized (S.D.F.) overhead (pushrod) valve train

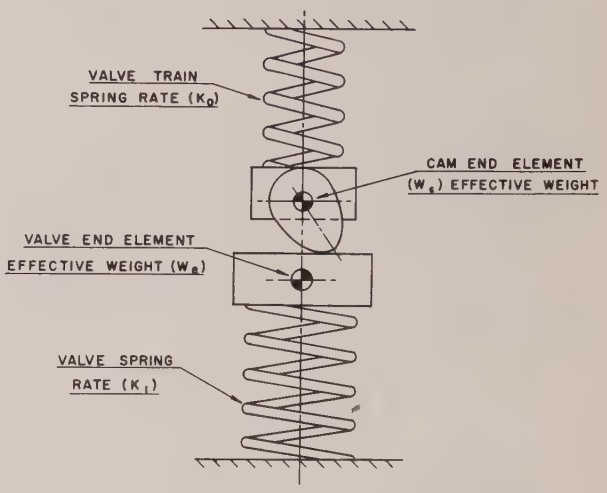

Fig. 5 — Idealized (S.D.F.) overhead cam valve train

tion of engine speed similar to that given in Fig. 6. Ideally, the vibration of the end element will become zero at design speed, will have a maximum amplitude at about 70% design speed, and will have an equal amplitude again at 110% design speed. At engine speeds above 110% design speed, the amplitude increases very rapidly. The kind of response shown is characteristic of the single degree-of-freedom system, but the degree of response is a function of the valve train resonant frequency so that for systems which are in all other respects (mathematically) equal, the plot will look like that shown in Fig. 7. By continuing along this line of investigation, it is found that the engine design speed can be adjusted for each system having a different valve train resonant frequency, as shown in Fig. 8. This figure shows that (theoretically) the design engine speed can be adjusted for each system such that the maximum vibration amplitudes will be an equal and predetermined amount. It is also shown that for a limited and controlled level of vibration

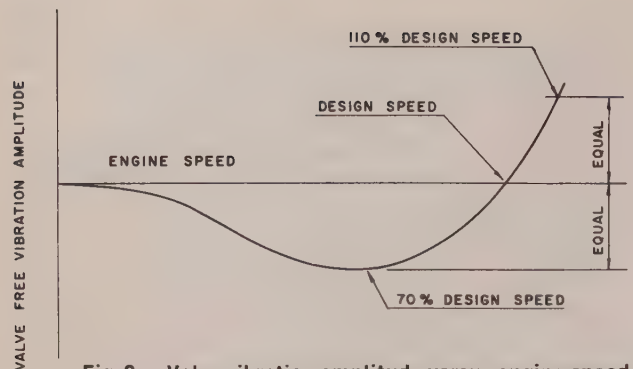

Fig. 6 — Valve vibration amplitude versus engine speed

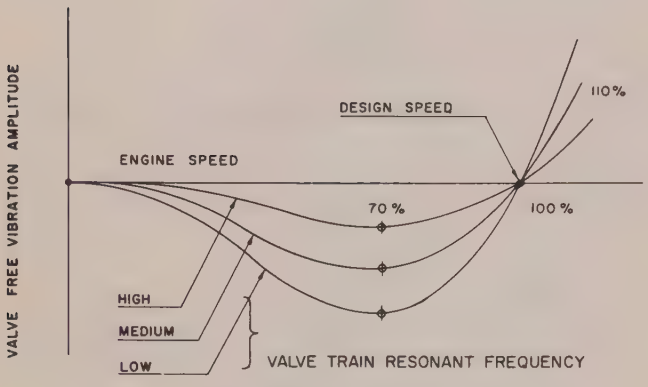

Fig. 7 — Effect of valve train resonant frequency

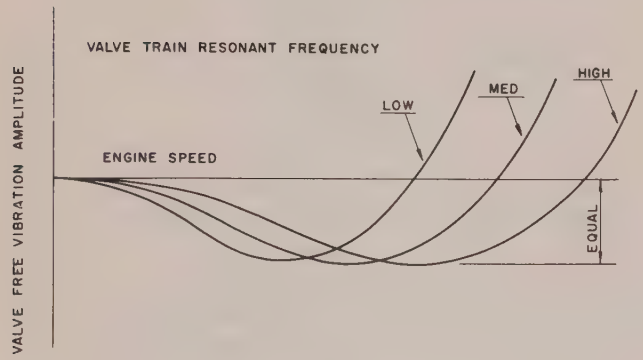

Fig. 8 — Effect of engine design speed

amplitude in any system, the engine design speed must be fixed as a function of the system's valve train resonant frequency.

The valve spring force can be adjusted to retain the valve train parts under some compression in the presence of vibration amplitudes of limited magnitude. As the amplitudes are permitted to become greater by extending the engine design speed for any given level of valve train resonant frequency, corresponding increases in valve spring loads are required, but these very rapidly produce excessive bearing pressures near the location of minimum instantaneous radius of curvature along the cam profile. Nevertheless, the dynamic considerations introduced up to this point suggest that at engine design speed, the vibration amplitude level will be zero; that if the cam acceleration profile and systems response avoids an excessive amplitude at 70% engine design speed, the response at 100% design speed must be controlled. Unfortunately, in practice, this conclusion turns out to be true only with some additional qualification; consider the following concept of command and response.

Command and Response - This concept in the valve train dynamics deals with the time required for a given command signal imparted by the cam to travel the length of the valve train and be received for response by the end (valve) element. A cam acceleration force imparted to the tappet moves through the tappet and pushrod as a compression wave—the bridge across the rocker arm to the valve is partly a shear wave and partly a longitudinal wave. Each type of wave moves at a characteristic (and nearly invarient) velocity. The compression wave velocity is about 15000 fps; the other types are less than 1/10 of that amount.

At an engine speed of 4000 rpm, the corresponding cam angular velocity is 12000 deg per sec. If the valve train path length is in the order of 15 to 18 in., the cam will have advanced between 2 and 4 deg during the command-response time interval. At this later moment, the cam will normally be generating a completely different signal than the one received by the end element. The effect is similar to that of dumping packages ever more rapidly upon a conveyor system of constant velocity. At some characteristic engine speed and cam angular velocity, the valve train command-response system becomes disorganized. In the technical sense, while it retains its linearity, it ceases to respond as a system having a single degree-of-freedom. Each of the several parts begin to respond out of phase with the others and the motion of the (valve) end element becomes uncontrolled.

It is technically not possible, of course, to devise a cam of fixed profile able to control a system having more than a single degree-of-freedom. A careful evaluation of this

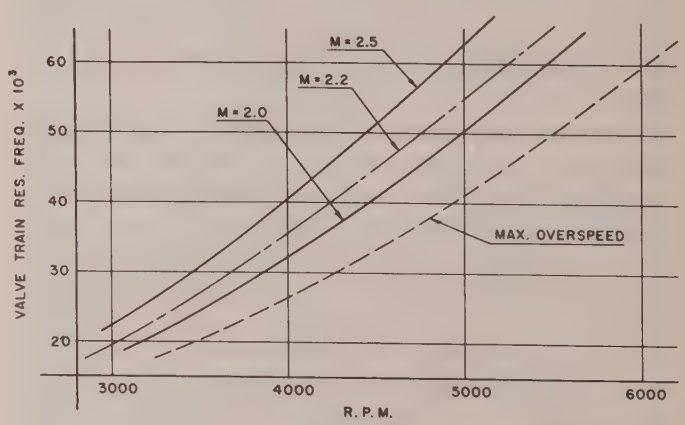

Fig. 9 — Engine design speed versus valve train research frequency for overhead valve (pushrod) engines

phenomenon shows, however, that the command and response problem is related directly to the length and complexity of the valve train and is, incidentally therefore, the central reason for the superiority of the overhead-cam system over the pushrod engine design. From these considerations, it follows that command-response problems are an indirect function of the valve train resonant frequency.

Engine Design Speed Chart for Overhead Valve Train Systems - Based upon the foregoing valve train dynamics, single degree-of-freedom and command-response limitations, an empirical design chart showing engine design speed as a function of valve train resonant frequency is given (see Fig. 9) for overhead-valve engine systems of average automotive size. The chart is based upon the equation

$$E.D.S. = \sqrt{\frac{f_n}{m \times 10^{-3}}} \qquad (1)$$

where,

f_n = valve train resonant frequency, cpm

m = empirical constant, nominal value (2.2) and where $2.0 \geq m \geq 2.5$

It is to be specifically noted that the nominal value (2.2) of the constant (m) applies to systems of average length, complexity and weight—held in compression by low valve spring forces such that excessive bearing stresses do not occur at engine crank and idle speeds with materials and lubrication in average production use. The range of values for (m) will then be from

m = 2.0 for systems which are short, light and simple;

m = 2.2 nominal value, average;

m = 2.5 for systems somewhat longer, heavier or more complex than average.

In all systems, the engine design speeds can be increased from 10 to 20% by the use of high-load valve springs—but with the attendant bearing stress problems that such spring loads produce.

Based on the engine speed design chart, an average valve train design having a single degree-of-freedom response and a resonant frequency of 40,000 cpm should be designed for an engine speed of 4300 rpm. The maximum overspeed with good valve control throughout the entire range of engine speeds should be 4700 rpm; that is, 0 to 110% design speed.

Force-Stress Limits - In the valve train system, the forces are a function of.

1. The equivalent mass-weight of the parts--inertia load
2. The magnitude of the accelerations--inertia load
3. Valve-spring loads

The stresses (bearing) are a function of

1. The interface materials properties.
2. Type of surface lubrication.
3. Size of contact area (force per unit area).
4. Shape of contact area (force per unit area).

The cam profile design has a major influence on the acceleration and spring forces and also the bearing stress at the cam to tappet interface through control over the size and shape of that contact surface area. In particular, with the effective mass of the valve train system known, the inertia loads at the cam face may be determined from the accelerations. The sum of the inertial and spring forces will determine the total force acting at the cam to tappet interface. By this means a plot can be made of the total load as a function of position along the cam profile and also as a function of engine speed. (This will be discussed more completely later in the paper.) The cam profile accelerations at any point also determine the cam face radius of curvature at that point. Based on these determinations and the fixed design characteristics of the system, the instantaneous bearing stress for all points along the cam profile can be determined as a function of engine speed. An arbitrary design stress limit can be chosen; normally, for materials and lubrication properties in average production use. This will be at most about 150,000 psi, (2) although this limit can be adjusted to fit the particular design circumstance. Now, finally, the quantitative cam design problem is to determine that profile which maximizes the area under the valve-lift curve by allowing the stress levels to approach very closely but not exceed fixed design stress limits.

Design Limitations in Overhead-Cam Systems - Since overhead-cam engine systems have inherently very high valve train resonant frequency rates, this parameter is not a design limitation in the optimum cam profile design problem. Thus, the original list of five interdependent quantities is reduced to four:

1. Valve event length.
2. Valve lift.
3. Engine speed range (maximum fixed).
4. Force-stress limits.

Of these, any three may be fixed as design criteria with the fourth determined by the design solution. The normal cam design practice is to specify all four values, but it will be appreciated that if, for example, maximum engine speed and force-stress limits are fixed, the maximum available valve lift will increase as the valve event length becomes longer. For the optimum cam profile, therefore, (as in overhead-valve systems), it is recommended that a range of acceptable valve lift values be provided as a specification. The optimum solution will then seek the maximum valve lift (and valve-lift diagram area) available to the system within the specified tolerances.

Cam Accuracy - The required accuracy necessary for the cam profile to obtain good valve train dynamics has been studied by others; the results given by Rothbart (3) have (essentially) been verified in our computer programmed vibrational analysis studies. These results show that cam profile tolerances should be in the order of ±0.00020 in. for point to point consecutive degree positions on the profile with the tolerance at 180 deg positions in the order of ±0.0020 in.,

although this latter tolerance is difficult to establish with certainty. The very close tolerances appear to be justified only on the opening and closing cam flanks in the areas of high positive acceleration, especially in the region provided for valve train compression compensation.

The accumulative effect of round-off error in the design computations is evaluated in terms of the foregoing manufacturing tolerances. Our practice is to use eight significant digits with a cam profile specification of five significant figures.

OPTIMUM DESIGN SPECIFICATIONS - A quantitative definition and specification for the design of an optimized cam profile evolves from a revised statement of the design objectives as follows:

The "optimum" cam profile is that profile which provides an accurate control of the valve dynamics over a specified range of engine speeds, and which also maximizes the area under the valve lift diagram for a specified valve event length. This statement assumes that the engine speed range is chosen with due regard for the particular valve train length, complexity and natural resonant frequency; that the valve lift may be maximized based on the force-stress limits of the valve train system—or if preassigned, the valve lift is an attainable value within such limits.

The quantitative specifications are given, as follows:

Design Engine Performance and Selected Design Goals

1. Desired general engine performance characteristics
   a. Maximum horsepower at engine rpm..... ( )
   b. Maximum torque at engine rpm ..... ( )
   c. Engine idle rpm ..... ( )
2. Engine design speed—rpm
   a. Maximum normal operating speed ..... ( )
   b. Maximum overspeed..... ( )
3. Valve event length (timing)—degrees of crank angle
   a. Intake event ..... ( )
   b. Exhaust event ..... ( )
4. Valve lift at engine design speed Min. Nom. Max.
   a. Intake ..... ( ) ( ) ( )
   b. Exhaust ..... ( ) ( ) ( )
5. Cam ramp design
   a. Opening ramp design type ..... ( )
   b. Closing ramp design type ..... ( )
   c. Design valve seating velocity
      (1) Intake ..... ( )
      (2) Exhaust ..... ( )
   d. Mechanical valve lash
      (1) Intake (a) Engine hot ..... ( )
          (b) Engine cold ..... ( )
      (2) Exhaust (a) Engine hot ..... ( )
          (b) Engine cold ..... ( )

Valve Train Characteristics and Design Limitations

6. Section drawing of the valve train system and an engineering print of each valve train part.

7. List and actual piece for every moving part in both intake and exhaust valve train systems for weights (correct to four decimal places) and effective inertia calculations. Note any special conditions that may modify the weights on installation; that is, pushrod filled with oil, etc.

8. Valve train spring rates—measured data, at least one hysteresis loop for each valve in the engine. Data to be obtained in accord with recommended procedure (1).

9. Valve train resonant frequency—measured data, at least one decay trace for each valve in the engine. Data to be obtained in accord with recommended procedure (Final section of this paper).

10. Ratio of engine to camshaft speed ..... ( )
11. Cam base circle radius
    a. Nominal design value..... ( )
    b. Maximum cam clearance radius
12. Cam to valve motion, rocker arm ratio
    a. Intake—nominal design value..... ( )
    b. Exhaust—nominal design value..... ( )
    c. Measured data—valve lift given as a function of cam rotation.
13. Tappet (make—kind)
    a. Mechanical—see valve lash data
    b. Hydraulic—give leak-down rate for given load and oil viscosity at temperature ..... ( )
    c. Cam contact surface, spherical radius ..... ( )
14. Design bearing stresses—maximum allowable
    a. At rocker arm to valve stem interface ..... ( )
    b. At pushrod to rocker arm ..... ( )
    c. At pushrod to tappet ..... ( )
    d. At tappet to cam interface ..... ( )

An Extract from Polydyne Method of Cam Design

This section of the paper discusses briefly, "The Polydyne Method of Cam Design," as presented to the industry by Thompson Products, Inc. (4). The name "polydyne" is a neologism derived from 'polynomial,' the type of equations used to solve the differential equations of the design method, and 'dynamics,' the general study of masses in motion. Since a compensation in the cam acceleration profile for the dynamic deflections in the valve train is a major requirement to a successful cam design, and since also our work (Final section of this paper) has been based upon the "polydyne" equations, a review is necessary to an understanding of the present paper. This section, then, by means of a flow chart, provides a general view—an overall perspective of the mathematical steps involved in a polydyne solution.

Nomenclature

S.D.F. = single degree-of-freedom
E.D.S. = engine design speed ..... rpm
N = camshaft design speed ..... rpm
f_n = valve train resonant frequency ..... cpm
w_t = actual weight of the valve train parts ... lb

w_e = effective weight of the valve train acting at valve ..... lb
w_c = effective weight of the valve train acting at the cam ..... lb
k_o = valve train spring rate ..... lb/in.
k_1 = valve spring rate ..... lb/in.
h_r = ramp height ..... in.
ρ = 1 + static deflection in valve train/y (x)
ϕ = dynamic deflection in the valve train/y" (x)
x = Θ/D—any particular position along the valve event, $0 \leq x \leq 1$.
Θ = part of event length measured from valve lift (max) toward ramp ..... deg
D = total event length from valve lift (max) to ramp ..... deg
y(x) = valve lift an any point ..... in.
y(0) = valve lift at x = 0 ..... in.
y(1) = valve lift at x = 1 ..... in.
y' (0) = valve velocity at x = 0 .....in/deg
y''(0) = valve acceleration at x = 0 ..... in/deg^2
$y_o(x)$ = equivalent cam lift at any point ..... in
$y_o(0)$ = equivalent cam lift at x = 0 ..... in.
$y_o'(0)$ = equivalent cam velocity at in/deg
$y_o''(1)$ = equivalent cam acceleration at x = 1 in/deg^2
$z_o(x)$ = actual cam lift at any point ..... in.
$z_o(x)$ = y_o/R_1
R_1 = rocker arm ratio (normally a constant, but may be variable)

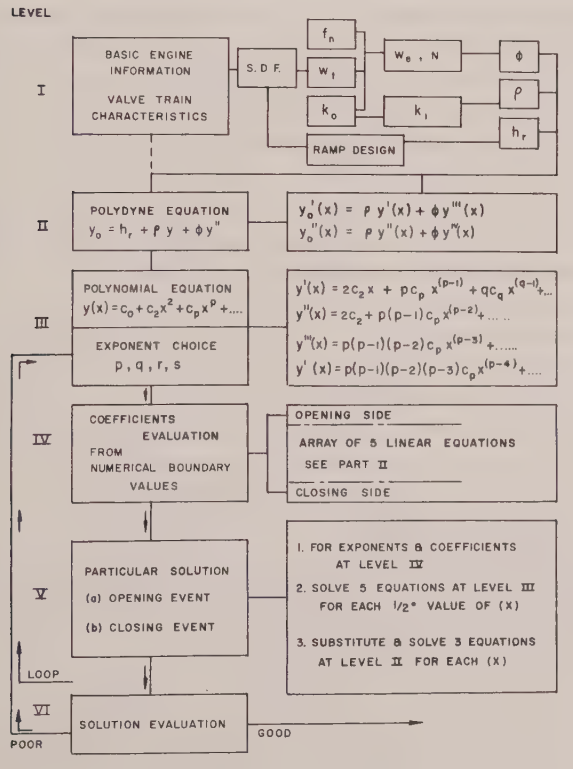

Fig. 10 — Polydyne method of cam design — flow chart

FLOW CHART (FIG. 10) DISCUSSION - First Level - The first box at the top left of Fig. 10 represents basic engine information necessary to fit a polydyne design to the individual valve train characteristics of a particular engine. To the right and center is a second box marked (S. D. F.). While not stated in precisely these terms in the original paper, the polydyne equations depend upon the validity of a reduction of the distributed mass valve train system to one having a single degree-of-freedom (see Figs. 4 and 5). Notice the lumped mass representing the end (valve) element of the valve train marked (w_e), the lumped mass representing the tappet end of the valve train (w_c), the very stiff spring representing the elastic characteristics of the valve train system (k_o), and finally, the valve spring (k_1) which holds the system in contact. The idealized system does not have a rocker arm to multiply the motion between the tappet and the valve; in the polydyne cam, this larger resulting cam displacement is called the equivalent camllift (y_o) and in a later step, the actual cam lift (z_o) is found by dividing (y_o) by the rocker arm ratio (R_1). To the right at the top level of the flow chart is a series of boxes, all of which represent information gathering and processing steps. In our work, the valve train spring rates (k_o), the weight of the individual valve train parts (w_t), and the ramps are designed about as suggested in the original text.[1] We have, however, added a direct measurement of the valve train natural resonant frequency (f_n). This measurement provides

1. A direct check on the single degree-of-freedom validity for the system.
2. A direct calculation for (w_e), the equivalent weight of the valve train acting at the valve end.

(The details of this latter step are given in the final part of this paper.)

Based on the measured value of (f_n), the design speed of the engine can be found from the design chart given in the first part of this paper (Fig. 9), and the corresponding design speed of the camshaft (N) can be determined. Notice that if at this point in the calculations, the design speed is lower than considered satisfactory, immediate steps can be taken to improve the stiffness-to-mass ratio of the valve train before continuing with the cam design. At the extreme right at the first level in the flow chart are shown the values of certain constants. These are calculated exactly as suggested in the original polydyne text.

Second Level - At the second level in the flow chart on the left is given the basic polydyne (differential) equation. It states that the equivalent cam lift (y_o) at any local point along the valve event is equal to the sum of three terms:

1. The ramp height (h_r).
2. Plus the (local) valve lift (y) multiplied by an allowance for the static deflection (ρ).
3. Plus the (local) dynamic deflection in the valve train ($\phi y''$).

The derivation of this equation must be studied in the ori-

ginal text to be understood and fully appreciated.

At the right on the second level are shown the first and second differentiations of the basic differential polydyne equation. These provide expressions for the equivalent cam velocity (y_o'), and the equivalent cam acceleration (y_o''). Notice that the equivalent cam velocity depends upon the valve velocity and also the valve time rate of change of acceleration called "jerk;" that the equivalent cam acceleration depends upon the valve acceleration (y'') and also the valve time rate of change of jerk, (y''''). Finally, it is especially important to notice that the time factor in these equations is measured in terms of angular displacement (Θ) so that all the derivatives shown are taken with respect to (Θ) providing the dimensions of inches per degree for velocity and inches per degree (2) for acceleration, etc.

Third Level - At the third level in the flow chart on the left is shown the general polynomial equation for an assumed valve displacement (y) given as a function of an (x) displacement position. At this particular location on the flow chart, the mechanics of the cam profile solution is divided into two parts (although these are not necessarily equal parts). In the first operational sequence, the opening side of the cam profile is solved starting from the mid-position at valve maximum lift corresponding to ($x = 0$); i.e., [y (0)], and moving forward toward the juncture with the opening ramp at ($x = 1$); i.e., [y(1)]. In a second sequence, the closing side is solved starting again from the mid-position [y(0)] and moving rearward to the juncture with the closing ramp. The general polynomial equation has six terms which were cleverly contrived in the original work to be the least number necessary to satisfy the boundary conditions for any particular solution. The exponents p, q, r, and s are even positive integers such that $8 \leq p < q < r < s \leq 50$. The (C's) are constant coefficients so chosen that (y) and certain of its derivatives satisfy the prescribed boundary conditions at each end of the event. The restrictions on the exponents (p, q, r, s) have been evolved from experience, and while these restrictions may seem severe, there are more than 7300 permissible combinations of exponent values. A procedure is outlined in this paper to search this seemingly vast array for an optimal solution with a minimum number of trials.

At the third level of the flow chart on the right is shown the first four differentiations of the general polynominal. Notice that (in general form) these are the values of the valve lift derivatives required to solve (by direct substitution) the cam profile equations given at the second level.

Fourth Level - At the fourth level in the flow chart on the left is shown the evaluation of the coefficients (C's) which satisfy the particular boundary values. Small differences exist in the procedures involved between the opening side and closing side solution as shown in the chart at the fourth level to the right.

Considering first the opening side at the point ($x = 0$), and considering also the shape and position of the desired valve displacement, velocity and acceleration curves, the values for

$$y'(0) = y'''(0) = y''''(0) = 0 \qquad (2)$$

and hence, from the equations at the third level,

$$y''(0) = 2C^2 \qquad (3)$$

An opening ramp had been designed as noted in the chart on the right at the first level. From this design, specific values for the equivalent cam displacement, velocity and acceleration are established at ($x = 1$). That is,

$$\left.\begin{aligned} y_o(1) &= \\ y_o'(1) &= \\ y_o''(1) &= \end{aligned}\right\} \text{ Specific numerical values from the opening ramp design} \qquad (4)$$

It is also desired that the valve displacement, velocity and acceleration at ($x = 1$) be zero, that is,

$$y(1) = y'(1) = y''(1) = 0 \qquad (5)$$

From the equations on the right at the second level,

$$\begin{aligned} y_o(1) &= h_r \\ y_o'(1) &= \phi y'''(1) \quad [\text{since } y'(1) = 0, \text{ see above}] \\ y_o''(1) &= \phi y''''(1) \quad [\text{since } y''(1) = 0, \text{ see above}] \end{aligned} \qquad (6)$$

Since by definition,

$$x = \frac{\theta}{D} \qquad (7)$$

and therefore, in general,

$$\frac{d^n y}{d\theta^n} = \frac{1}{D^n}\frac{d^n y}{dx^n} \qquad (8)$$

hence,

$$y'''(1) = \frac{y_o'(1)}{\phi}(D)^3$$

$$y''''(1) = \frac{y_o''(1)}{\phi}(D)^4 \qquad (9)$$

Based upon the foregoing and by direct substitution into the equations at the third level, an array of five arithmetic linear equations for the evaluation of the coefficients can be written as follows

$$C_2 + C_p + C_q + C_r + C_s = -y(0)_{max} \qquad (10)$$

$$2C_2 + pC_p + qC_q + rC_r + sC_s = 0 \qquad (11)$$

$$2C_2 + p(p-1)C_p + q(q-1)C_q + r(r-1)C_r + s(s-1)C_s = 0 \quad (12)$$

$$p(p-1)(p-2)C_p + q(q-1)(q-2)C_q + r(r-1)(r-2)C_r + s(s-1)(s-2)C_s = \frac{y_o'(1)}{\phi}(D)^3 \quad (13)$$

$$p(p-1)(p-2)(p-3)C_p + q(q-1)(q-2)(q-3)C_q + r(r-1)(r-2)(r-3)C_r + s(s-1)(s-2)(s-3)C_s = \frac{y_o''(1)}{\phi}(D)^4 \quad (14)$$

Notice that in every case the right hand term of the foregoing set of equations is determinable from know properties of the ramp at (x = 1) and/or the main event at (x = 0). Notice also that based on a particular choice of exponents (p, q, r and s), the five equations are linear in the five unknowns C_2, C_p, C_q, C_r and C_s. The concluding step at this fourth levelis to choose values for the exponents and solve the foregoing array of linear equations for the corresponding particular values of the coefficients.

The closing event solution is handled somewhat differently in that one additional boundary value must be added as (x = 0) as derived from the opening solution. Specifically, it is necessary that

$$y''(0) = \text{the value found from the opening event solution} = 2C_2/(D)^2 \quad (15)$$

This added restriction reduces the array of five simultaneous linear equations to an array having only four unknown coefficients—a problem which admits of no direct solution. The procedure used to overcome this difficulty is to consider y(0) as an unknown (even though, in point of fact, the value is known and must match the opening event). Then, for a given choice of exponents, the array of equations is solved for the remaining unknown coefficients with, in particular, a value for y (0). In general, the value thus found will not match the required value from the opening event—whereupon, successive trial values of exponents must be chosen and the array of equations resolved until matching values for y (0) are found. We have defined a tolerance on the match at this point of y (0) of ±0.00010 in. and the procedure is continued until some reasonable number of exponent combinations are found which both satisfy the tolerance, and also broadly cover the whole spectrum of possible polydyne solutions. In a later step, and after the particular solution is found which has been evaluated as the best of those available, the closing event is recalculated in the manner of an opening event. A perfect match for y(0) between the opening and closing events is thus assured.

Fifth Level - At the fifth level of the flow diagram, a particular solution for either an opening event cam profile—or later, a closing event profile—is obtained. Based upon a particular choice of exponents and the corresponding coefficients calculated at the fourth level of the flow diagram, a direct substitution of values can be made in the array of polynomial equations at the right at the third level. In turn, and for each desired value of (x) [in our work, each 1/2 deg position is solved for the length of the event], values for y, y', y'', y''', and y'''' are calculated. These numerical values are then substituted into the differential polydyne equations shown at the right at the second level. In this manner, the equivalent cam displacement, velocity and acceleration are calculated for each 1/2 deg position throughout the event. Roughly 10,000 arithmetic calculations are required to complete the fifth level information—with each arithmetic operation performed with a minimum of six numerical digits to obtain the required accuracy.

Sixth Level - The sixth level of the flow diagram consists of the operations associated with particular solution evaluations. This subject is to be discussed fully later in this paper but, in general, these evaluations consists of a check for agreement with the required boundary conditions. Then by means of a graphed presentation of the equivalent cam acceleration profile, the behavior of this important parameter is observed. It is necessary that the slope of (y_o'') profile meet six evaluation criteria through the event. Maximum values for the loads, stresses, instantaneous radius of curvature, and eccentricity are observed in addition. It is most improbable that the first choice of exponents made at the third level of the flow chart will provide an optimum or even an acceptable solution at this sixth level. Whereupon, a new choice of exponents must be made and a new solution obtained starting again from the third level. This loop of flow chart operations between the third through sixth level is required until an optimum solution has been determined; the whole operation is then repeated (starting fromthe third level) for the design of the closing event.

The normal optimized opening event requires between 10 and 15 trials followed by about five trials for the closing event solution. Taken altogether, roughly 150,000 to 200,000 arithmetic calculations are required; by desk calculator methods, this would take about 75 man-months of applied effort. Obviously, electronic computer programming is necessary to make the procedure practical. With an IBM 650 computer suitably programmed, each solution is obtained in about 10 minutes; the optimized final solution requires about 3 hr. With an IBM 704 computer, the whole operation may be accomplished in about 20 minutes of computer time.

Modifications to Polydyne Cam Design Procedures with Computer Programming for Optimized Solutions

The arithmetic task of the optimum cam design solution is prohibitively great without electronic computer methods and techniques. With the computer, tactical methods are

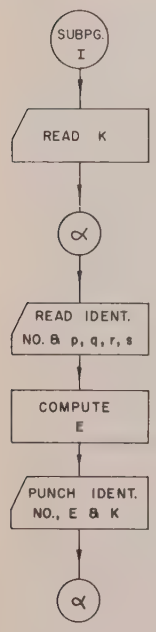

Fig. 11 — Subprogram I

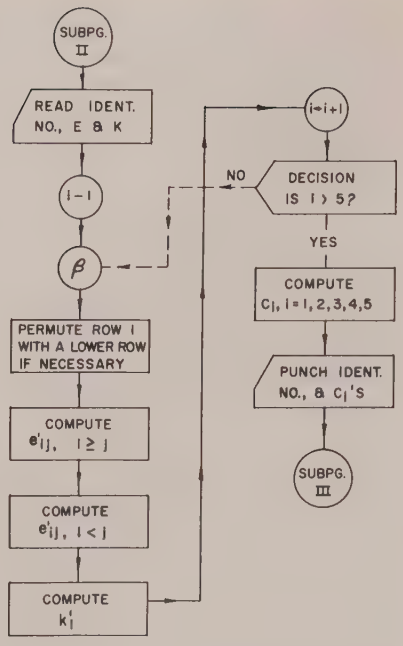

Fig. 12 — Subprogram II

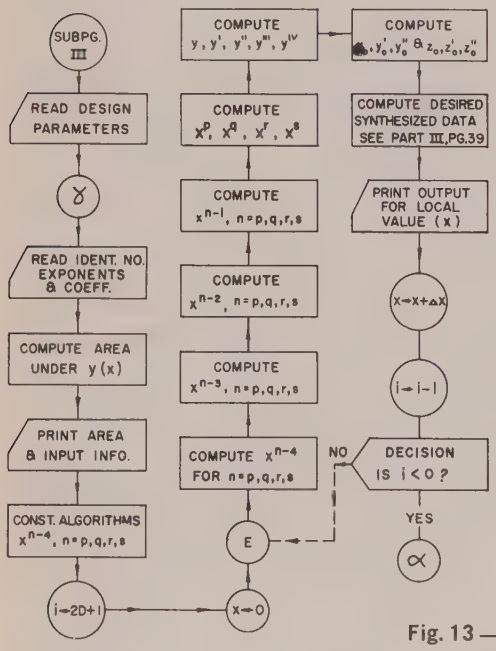

Fig. 13 — Subprogram III

required to thread the way from a beginning to the final solution in a least number of successive exponent trials. Careful programming is necessary to minimize the run time and also retain solution accuracy. The program described below has been divided into three sub-program parts herein referred to as Subprograms (Subpg.) I, II and III. This separation was deemed advisable during the development and investigation for the methods of optimizing the solution. While the entire problem is presently being reprogrammed as a single code for the IBM 704, a discussion of the original 3-part IBM 650 program is considered pedagogically more desirable.

COMPUTER METHODS FOR CAM DESIGN - The Computer Program - The logical flow charts of these programs are shown in Figs. 11-13. The output of Subpg. I serves as input to Subpg. II; the output of Subpg. II is used as input for Subpg. III. Each part is designed so as to solve serially the pertinent part of any number of problems, the process being repeated until the supply of input data is exhausted. The use of these programs for closing event design as opposed to opening event design differs solely in the form of the input to Subpg. I and III.

As previously shown, the values of the coefficients of the polynomial representation of valve lift are obtained by solving a system of five simultaneous linear algebraic equations. This system of equations can be represented in matrix notation as

$$E_c = k \qquad (16)$$

where (E) is a five by five matrix, and (c) and (k) are column vectors of length five.

For the opening event design problem, (E) is

1	1	1	1	1
2	p	q	r	s
2	p(p - 1)	q(q - 1)	.	.
0	p(p - 1)(p - 2)	.	.	.
0	p(p - 1)(p - 2)(p - 3)	.	.	.

(C) is the solution vector whose components are C_2, C_p, C_q, C_r and C_s; while (k) is the column vector.

$$\begin{matrix} -y_{max} \\ 0 \\ 0 \\ D^3y_o'(1)\ \phi \\ D^4y_o''(1)\ \phi \end{matrix}$$

For the closing event design problem the matrix (E) is the same as for the opening event problem except the elements of the first column are all zero except the first which is unchanged; i.e., one. The components of (C) are C_0, C_p, C_q and C_s, while (k) is the column vector.

$$\begin{matrix} -M/2 \\ -M \\ -M \\ D^3y_o'(1)\ \phi \\ D^4y_o''(1)\ \phi \end{matrix}$$

Where,

$$M = \left(\frac{\text{length of closing event}}{\text{length of opening event}}\right)^2$$

(C_2 of the matching opening event) (17)

and of course D, $y_o'(1)$, and $y_o''(1)$ pertain to the closing event.

The input to Subpg. I consists of first, the components

of (k), followed by one card for each problem requested containing the values of p, q, r and s and a problem identification number. This program computes the elements of the matrix (E) and punches out a set of cards for each problem containing the identification number and the elements of (E) and (k). These output cards form the input to Subgp. II.

Subpg. II solves the set of equations, $Ec = k$, for each problem. The method known as Crout's Reduction is used with some modification. This procedure is well adapted for machine computation.

Let (M) be the augmented five by six matrix formed by adjoining (k) to the right of (E) so as to form a sixth column. Let the elements of (E) and (k) be denoted as (e_{ij}) and (k_i), respectively; (i) denoting the (i^{th}) row and (j) the (j^{th}) column; i.e., (M) is

$$\begin{matrix} e_{11} & e_{12} & e_{13} & e_{14} & e_{15} & k_1 \\ e_{21} & e_{22} & . & . & e_{25} & k_2 \\ . & . & . & . & . & \\ e_{51} & e_{52} & . & . & e_{55} & k_5 \end{matrix}$$

Crout's Reduction consists of computing a new five by six matrix, (M'), as follows. The elements of the first column of (M') are the same as those of (M). The remaining elements of the first row, i.e., those to the right of the first element are formed by dividing the corresponding element of (M) by (e_{11}). Next, the following procedure is repeated, in turn, for each 1 = 2, 3, 4, 5. Thus,

$$e'_{ij} = e_{ij} - \sum_{n=1}^{j-1} e'_{in}\, e'_{nj} \qquad (i \geq j) \qquad (18)$$

$$e'_{ij} = \frac{1}{e'_{ij}} \left[e_{ij} - \sum_{n=1}^{i-1} e'_{in}\, e'_{nj} \right] \qquad (i < j) \qquad (19)$$

$$k'_i = \frac{1}{e'_{ii}} \left[k_i - \sum_{n=1}^{i-1} e'_{in}\, k'_n \right] \qquad (20)$$

Finally the solution vector, (c), is obtained as follows:

$$c_5 = k'_5 \qquad (21)$$

and

$$c_i = k'_i - \sum_{n=i+1}^{5} e'_{in}\, c_n \qquad (22)$$

where for clarity we denote the (i^{th}) element of (c) as (c_i).

These calculations, as almost all performed by the computer, retain eight significant digit accuracy. To insure that round-off error (the error introduced by rounding intermediate results to eight digits) is minimized, a modification of the above procedure has been employed. If at any stage of the reduction, the diagonal element [i.e., (e'_{ii}) for the current value of (i)] is significantly smaller than any of the elements which lie to its right in the same row, the round-off error is apt to be excessive. Hence, before beginning each stage of the reduction, the program is designed to check for this condition. If the current row is ill-conditioned, this row is interchanged with some lower row which is not.

The output of Subpg. II for each problem consists of a single card containing an identification number and the values of the coefficients. This card together with one more containing the values of the exponents p, q, r and s form the input to Subpg. III for each problem.

When these codes are used to design the closing event, the output of Subpg. II contains, in particular, the value of the maximum lift achieved by a particular selection of values for p, q, r and s such that the value of y''(0) matches that of the opening event. The strategy employed by the designer is to discover those combinations of values of p, q, r and s for which the maximum lift obtained is sufficiently close to the maximum lift specified in the opening event. Hence, Subpgs. I and II are repeated until such combinations are found. Subpg. III is then performed for these combinations so that a final choice may be made based on the dynamic performance of such cams.

The on-line printer attached to the IBM 650 is set up to print ten numbers per line. For this reason, Subpg. III has been programmed so that in addition to (x), nine parameters may be selected as output. (See next discussion.) After this selection has been made, the designer prepares several additional input cards which contain the values of each of the design parameters. These cards are read first by Subpg. III. Following this, Subpg. III reads the two input cards describing the first problem to be solved.

At this point the code computes the area under the valve-lift curve and prints out this value together with the input data. Following this, the code computes and prints out for successive values of (x), corresponding to each 1/2 deg position in the event, the value of each of the nine preselected parameters.

To obtain these values, for any particular (x), the code must first compute the value of (y) and its first four derivatives. The evaluation of these functions involves the computation of several terms involving (x) raised to some large power. To minimize the computer running time, special purpose algorithms are constructed at this point for the specific values of p, q, r and s selected.

Next a counter is reset to 2D + 1, the total number of (x) values to be considered; then (x) is reset to zero and the computation begins.

Following the evaluation of the required powers of (x), the values of (y) and its derivatives are obtained. Then y_o, y_o', y_o'' and z_o, and z_o', z_o'' are computed. At this point all of the information necessary to compute the synthetic

output parameters has been derived. These parameters are now computed and printed out.

Now the value of (x) is increased an amount (dx) corresponding to 1/2 deg, and the above mentioned counter is reduced by one. If the new setting of the counter is negative, then all values of (x) to be computed have been obtained and the program reads the input data for the next problem. If the counter is non-negative, the program is instructed to reenter the calculation at the point labeled (E) in the flow sheet shown in Fig. 13, and the computations continue until all the machine instructions have been completed.

During the print out of the parameters representing any particular solution, the designer will apply the evaluation criteria to that solution and elect at any point to continue, or to modify the input data, or to discontinue any further work based on an achievement of the desired problem objectives.

Computer Output - Any nine parameters may be selected for output from the on-line printer attached to the IBM from among the following:

Basic Machine Data

1. y = valve, lift (displacement) — in.
2. y' = valve, velocity — in./deg
*3. y'' = valve, acceleration — in./deg^2
4. y''' = valve, jerk — in./deg^3
5. y'''' = valve, jerk rate of change — in./deg^4
6. y_o = equivalent cam, lift (displacement) — in.
7. y_o' = equivalent cam, velocity ..... in./deg
*8. y_o'' = equivalent cam, acceleration ..... in./deg^2

Synthesized Data

*9. $z_o = y_o/R_1$ = actual cam lift ..... in.
10. $z_o' = y_o'/R_1$ = actual cam velocity ..... in./deg
11. $z_o'' = y_o''/R_1$ = actual cam acceleration ... in./deg^2
*12. $R_c = R_b + z_o + 3283\,z_o''$ = cam face instantaneous radius of curvature ..... in.
*13. $e = 57.3\,z_o'$ = eccentricity ..... in.
*14. S = (preload) + $k_1 y$ = spring load at valve — lb
*15. L_v = inertia load of the valve train acting at the valve at 115% design speed
$= 0.123 w_e N^2 y'' + 0.123 w_c^2 z_o'')/R_1$ ..... lb
*16. L_c = inertia load of the valve train plus the valve spring load acting at the cam face at 115% design speed
$= 0.123 w_c N^2 z_o'' + R_1(0.123 w_e N^2 y'' + S)$... lb
*17. $S_b = (z_o + R_b + e)/57.3$ = scrub velocity (tappet to cam face) ..... in./deg
18. R_1 = constant or variable

Of the foregoing, parameters marked * are normally printed in the initial run and used for the solution evaluation. The remaining parameters are printed later to complete the data for only the final selected solutions. The new code for the IBM 704 provides, in addition, a calculation for the Hertz stress at the cam to tappet interface. Typical computer run print-out solutions are shown in Figs. 14 and 15.

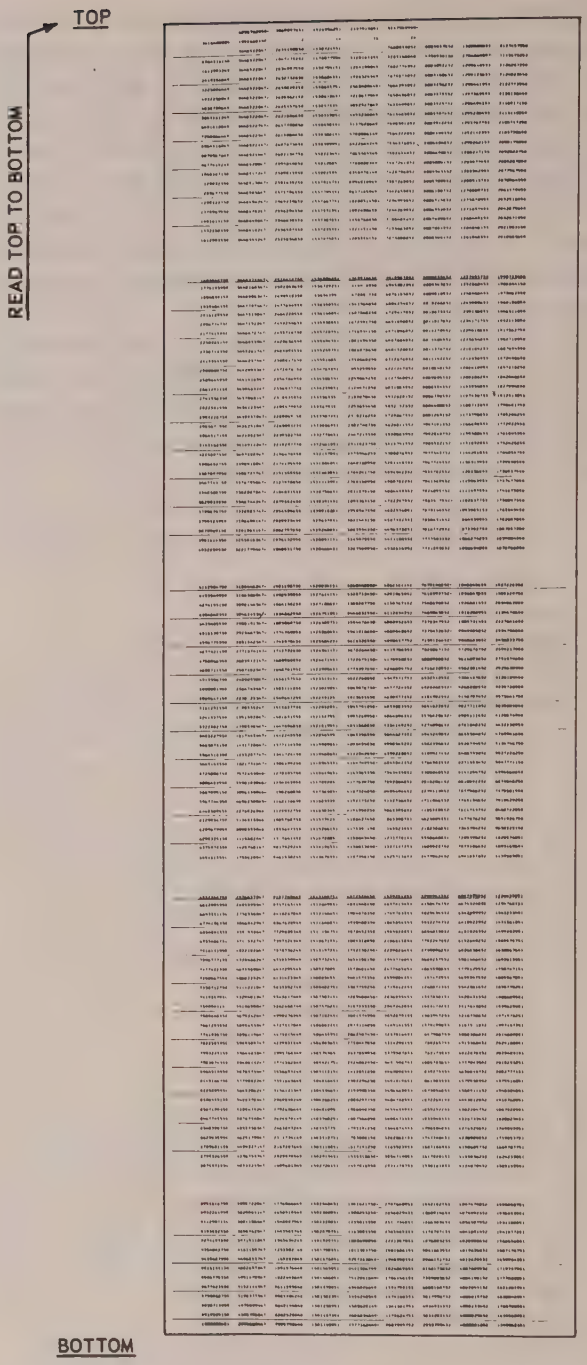

Fig. 14 — Typical computer print-out for cam design solution

The parameter (R_1), the rocker arm ratio, is normally treated as a constant, but caution is advised since this may not be valid with certain valve train geometries. Where the variation in (R_1) with (y) produces a difference greater than (±0.00005) at the cam, an equation giving

$$R_1 = f(y) \qquad (23)$$

is determined for the particular geometry of the valve train system and applied as a variable (R_1) to the calculations.

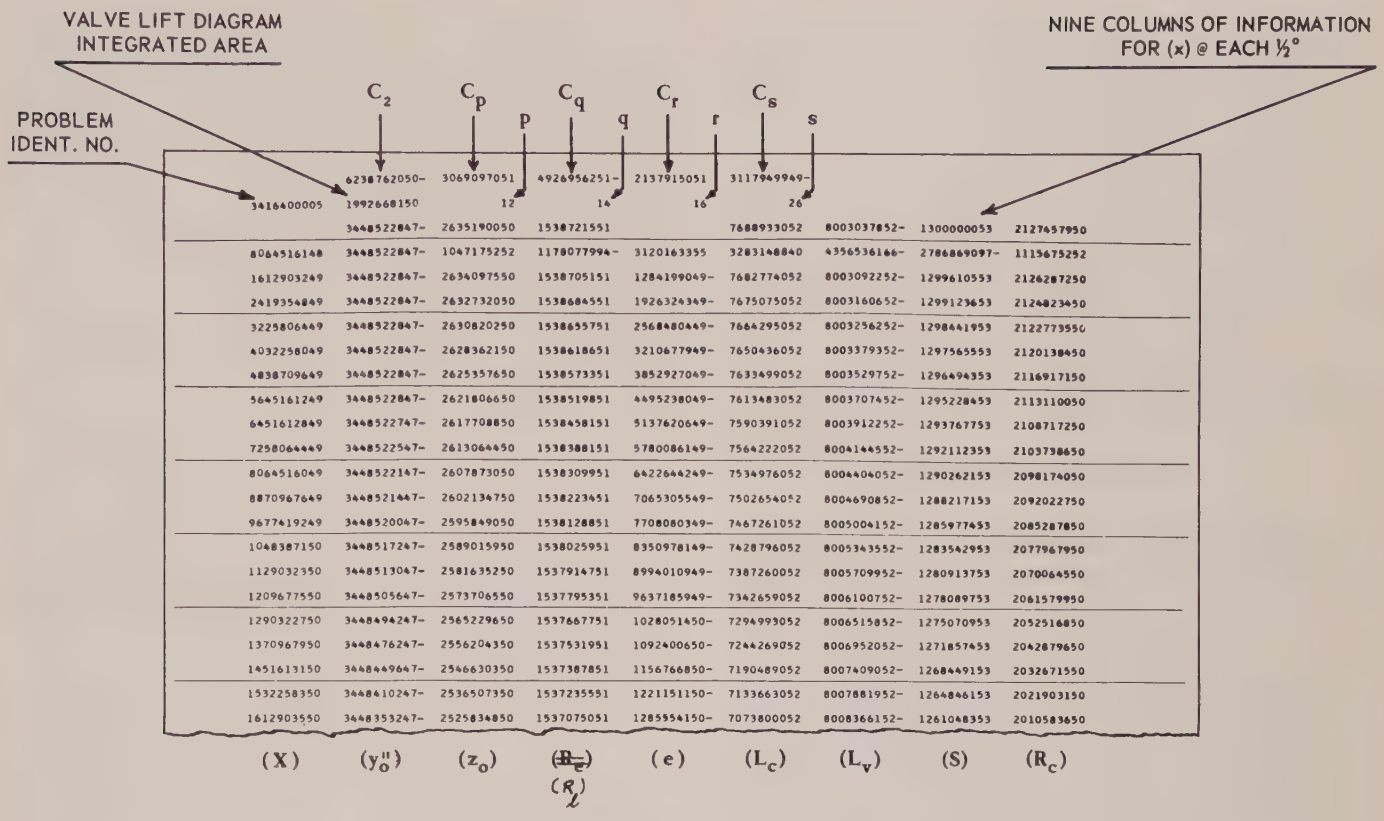
VALVE LIFT DIAGRAM INTEGRATED AREA
NINE COLUMNS OF INFORMATION FOR (x) @ EACH ½°
PROBLEM IDENT. NO.
C2 Cp Cq Cr Cs
p q r s
(X) (y0'') (z0) (Re/Rl) (e) (Lc) (Lv) (S) (Rc)

	62387620 50-	3069097051	4926956251-	2137915051	3117949949-			
	12		14	16	26			
3416400005	1992668150							
	3448522847-	26351900 50	1538721551		7688933052	8003037852-	1300000053	2127457950
806451614 8	3448522847-	1047175252	1178077994-	3120163355	3283148840	4356536166-	2786869097-	1115675252
1612903249	3448522847-	2634097550	1538705151	1284199049-	7682774052	8003092252-	1299610553	2126287250
2419354849	3448522847-	2632732050	1538684551	1926324349-	7675075052	8003160652-	1299123653	2124823450
3225806449	3448522847-	2630820250	1538655751	2568480449-	7664295052	8003256252-	1298441953	2122779550
4032258049	3448522847-	2628362150	1538618651	3210677949-	7650436052	8003379352-	1297565553	2120138450
4838709649	3448522847-	2625357650	1538573351	3852927049-	7633499052	8003529752-	1296494353	2116917150
5645161249	3448522847-	2621806650	1538519851	4495238049-	7613483052	8003707452-	1295228453	2113110050
6451612849	3448522747-	2617708850	1538458151	5137620649-	7590391052	8003912252-	1293767753	2108717250
7258064449	3448522547-	2613064450	1538388151	5780086149-	7564222052	8004144552-	1292112353	2103738650
8064516049	3448522147-	2607873050	1538309951	6422644249-	7534976052	8004404052-	1290262153	2098174050
8870967649	3448521447-	2602134750	1538223451	7065305549-	7502654052	8004690852-	1288217153	2092022750
9677419249	3448520047-	2595849050	1538128851	7708080349-	7467261052	8005004152-	1285977453	2085287850
1048387150	3448517247-	2589015950	1538025951	8350978149-	7428796052	8005343552-	1283542953	2077967950
1129032350	3448513047-	2581635250	1537914751	8994010949-	7387260052	8005709952-	1280913753	2070064550
1209677550	3448505647-	2573706550	1537795351	9637185949-	7342659052	8006100752-	1278089753	2061579950
1290322750	3448494247-	2565229650	1537667751	1028051450-	7294993052	8006515852-	1275070953	2052516850
1370967950	3448476247-	2556204350	1537531951	1092400650-	7244269052	8006952052-	1271857453	2042879650
1451613150	3448449647-	2546630350	1537387851	1156766850-	7190489052	8007409052-	1268449153	2032671550
1532258350	3448410247-	2536507350	1537235551	1221151150-	7133663052	8007881952-	1264846153	2021903150
1612903550	3448353247-	2525834850	1537075051	1285554150-	7073800052	8008366152-	1261048353	2010583650

Fig. 15 — Detail of computer print-out for cam design solution

Solution Evaluation - Particular solutions are evaluated by means of the following criteria with successive exponent trials and boundary value changes (i.e., valve lift) until an optimum solution as previously defined has been obtained.

1. The numerical values for the particular solution boundary conditions are compared with the design values as a final check against the proper operation of the machine program.

2. Then the print-out area under the valve-lift diagram is noted—to achieve in successive solutions a maximum value.

3. Next the equivalent cam acceleration diagram (y_o'') is plotted (during the print-out operation) and will have the general form shown in Fig. 16.

a. The form should be such that at (A) the acceleration diagram provides a continuous ramp juncture as shown in Fig. 17. A frequent fault is a sharp drop as shown in the figure by the dotted line. It should be appreciated that while the magnitude of the acceleration is proportional to the force applied to the valve train system, the slope of the acceleration diagram is proportional to the rate at which the force is applied. Any sharp application of force is equivalent to a hammer blow and is to be avoided especially at the beginning of the valve event. For this reason discontinuities in the acceleration diagram are avoided and special precautions are taken in the opening ramp design, as well as the ram p to main event juncture, to accomplish this result.

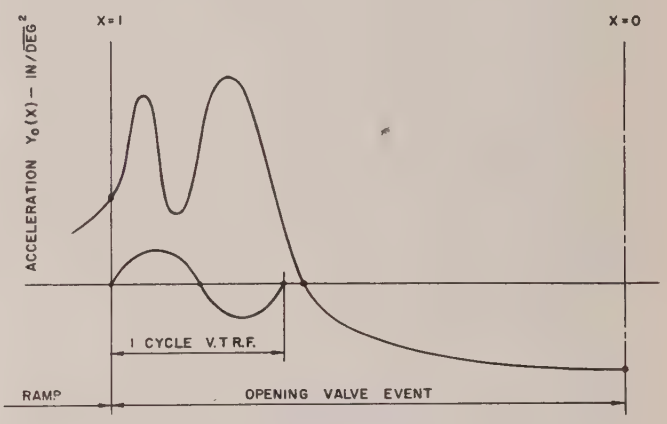

Fig. 16 — Ideal cam acceleration diagram

b. The first maximum point marked (B) should not be higher than that shown at (D) and preferably should be somewhat lower, a frequent fault will show (B) higher (often very much higher) than (D).

c. The valve train compression compensation dip shown at (C) should not be permitted to become negative as this would correspond with a zero inertial loading of the valve train.

d. The second maximum point shown at (B) corresponds with the maximum positive acceleration at the cam face and is used in the evaluation as a general guide to limit the surface stress. The actual maximum cam face surface stress

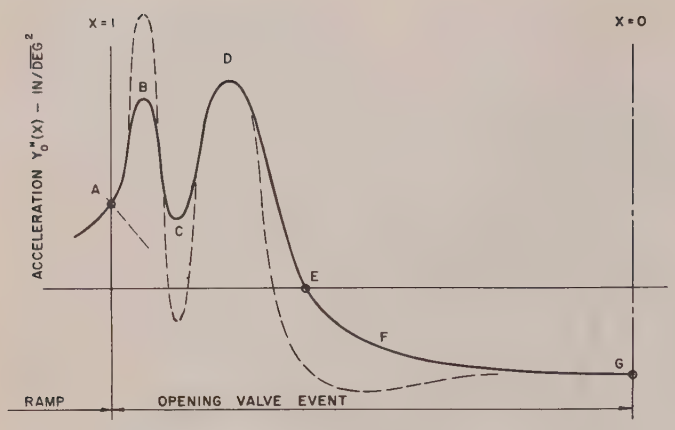

Fig. 17 — Typical faults cam acceleration diagram

will be found on later analysis to occur between points (C) and (D) with maximum engine speed, or near (F) for engine crank and idle speeds.

e. The width of the positive acceleration pusle (AE) should be about equal to (but not less than) the length of one cycle (the period) of the valve train resonant frequency (5). This assures a positive compression loading through the valve train rebound, which appears to be particularly helpful at engine speeds just below and, again, above design speed.

f. The form of the cam acceleration diagram should decrease from (E) to (G) gradually, a common fault is shown in the figure by the dotted line where in the region of (F) the diagram has a lesser value than at (G). The region (F) is the most critical for the dependence of the valve train upon the valve spring to maintain compression; a dip at this point in the diagram requires a higher valve spring load than would be otherwise necessary. It also happens that in this same region, the cam face instantaneous radius of curvature (R_C) will be a minimum and excessive valve spring loads must be avoided to control the cam face bearing stress at engine crank and idle speeds.

g. The maximum negative value of (y_0'') shown at (G) will normally be about 1/3 the maximum positive value shown at (D). Of course, the area under the positive portion of the diagram must be exactly equal to the area under negative portion of the diagram, but this is automatically taken care of by the original boundary conditions in the machine program.

4. The inertial load of the valve train at the valve (L_V) is computed for 115% engine design speed. Since the inertial loads are proportional to the square of the engine speed, this inertial load will be 32% greater than at design speed. In a later step, it will be shown that the valve spring loads must be carefully matched to the dynamics of the cam acceleration profile. At this stage, however, the machine will be printing values for the loads produced by an assumed valve spring. The evaluation at this point will be to compare the spring load against the inertia loads to see that such loads are at least nearly in agreement in the region of (F) on the diagram.

5. The inertia load of the valve train at the valve face (L_C) has also been computed for 115% engine design speed. These values with the corresponding values of the instantaneous radius of curvature (R_C) provide the data required to find the cam face surface bearing stress. The (y_0'') maximum accleration value shown at (D) is adjusted to be just less than the load required to produce the allowable limiting surface stress in the critical region between (C) and (D), or alternately, to control the acceleration magnitudes in the region of (F) which will be critical with the valve spring load at engine crank and idle speeds.

6. The eccentricity (e) is checked to be less than the maximum allowable value as shown by the cam design specifications. Any necessary changes are normally made to the tappet diameter, although the eccentricity can be decreased by a reduction in the cam face velocity, which, in turn, will be reduced with lower values of cam acceleration.

Exponent Manipulation - Recall the form of the general polynomial equation

$$y(x) = C_0x^2 + C_px^p + C_qx^q + C_rx^r + C_sx^s$$

wherein the exponents p, q, r and s may have values such that $8 \leq p < q < r < s \leq 50$. The task is to choose (in the least number of trials and with a given set of problem boundary values) that combination of exponents which satisfy the evaluation criteria. For optimizing the valve lift, a first solution is obtained with the minimum acceptable value of valve lift. Then, with these exponents known, the valve lift boundary value is increased in discrete steps with modifications to the exponents as required until the limiting (optimum) value has been found.

The exponent investigation begins by evaluating an array of solutions which cover in large steps the whole spectrum of possible polydne solutions. The choice of exponents is mapped as shown in Fig. 18. The resulting general effect of such solutions on the valve acceleration diagram is shown

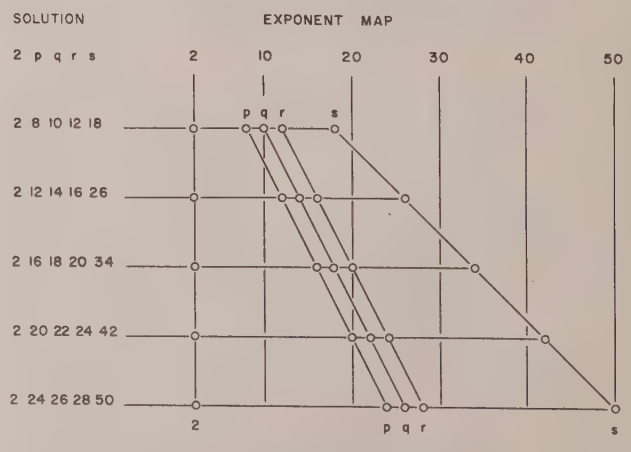

Fig. 18 — First exponent mapping

in Ref. (1).

The equivalent cam acceleration diagrams [$y_0''(x)$] may also be drawn. The forms will depend upon the boundary values for the particular problem, but it will be found that some adjacent solutions will approximately bracket the desired result.

A second possible exponent mapping is shown in Fig. 19.

Study of the trends in the solutions associated with each of these exponent mappings provides the following guide to exponent selection:

1. The magnitude (or height) of the positive acceleration pulse increases with higher valued exponents, in particular exponents (r) and (s).

2. The width of the positive acceleration pulse increases with lower valued exponents, in particular exponents (p) and (q).

Therefore, having bracketed a desired solution with an exponent array as in Fig. 18, local control of the acceleration diagram form is obtained by exponent distribution acceleration diagram form is obtained by exponent distribution according to the guide rules above. A typical successive solution network taken from a recent cam design problem is given below. The pattern was fixed in advance of the computer run and decisions on the direction to be taken on each branch made as the solution results progressed.

o = over
u = under

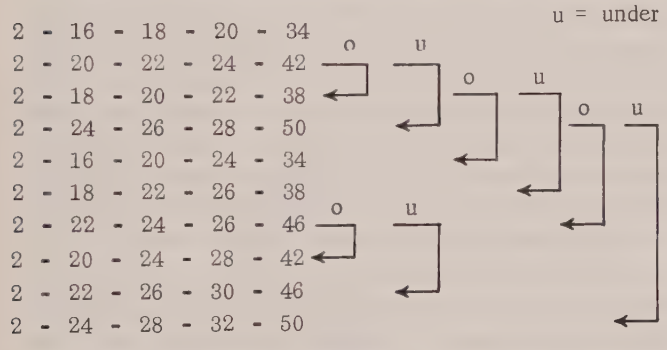

It will be appreciated that with respect to the problem of exponent choice and manipulation there is a certain facility which may be gained only through experience. Such experience, however, will serve mainly to decrease the number of trials necessary to obtain a desired result.

Summarizing at this point, it can be stated that

1. The arithmetic task of the optimized cam design solution is sufficiently great that computer methods are a practical necessity.

2. The properly designed computer program must

a. Minimize the individual problem solution run time.

b. Maintain problem accuracy.

c. Allow an operational flexibility such that the designer may move quickly along the main theme toward the problem objectives. His task will then consist of trial choices for exponents with boundary conditions evaluated in terms of the effect upon the problem limitations; namely, valve train dynamics and bearing stresses.

3. The optimized problem solution is found by seeking first the correct combination of exponents for the given boundary conditions which include the minimum acceptable value for valve lift. In successive steps the valve lift is gradually increased with exponent modifications as required until the specified problem limitations have been reached.

RESONANT FREQUENCY MEASUREMENTS - For reasons discussed earlier in this paper, a resonant frequency measurement for each valve train in an overhead-valve type engine is most desirable before starting cam design computations. Such measurements secure the following:

1. A test for the validity of the single degree-of-freedom assumption necessary to the basic requirements of the differential equations used in cam design.

2. A test for the uniformity of vibrational response characteristics in a set of valve trains for a given engine.

3. A basis for fixing the maximum allowable design speed in overhead valve type engines.

4. A direct calculation for the valve train equivalent weight (w_e) acting at the (valve) end element.

One of several possible physical arrangements for making such measurements is shown in Ref. (6). Briefly, the permanent magnet element of a small and lightweight linear velocity transducer is firmly attached to the valve stem with the shielded cylindrical coil assembly rigidly attached to some non-moving part and in proper position relative to the magnet above the valve. The cam is rotated to a position which lifts the valve free from the valve seat; the valve train is then unrestrained at the (valve) end element. The valve is caused to vibrate by a light, sharp tap applied to the valve in line with, and in the direction of the valve stem. The electrical linear velocity signal generated in the transducer by the vibratory motion is fed into a differentiating circuit which then provides an electrical signal proportional to the valve accelerations. This signal, in turn, is fed to some type of recorder. For the recorder, an oscilloscope with a camera attachment or a moving paper type instrument may be used. In either recorder, a trace showing acceleration

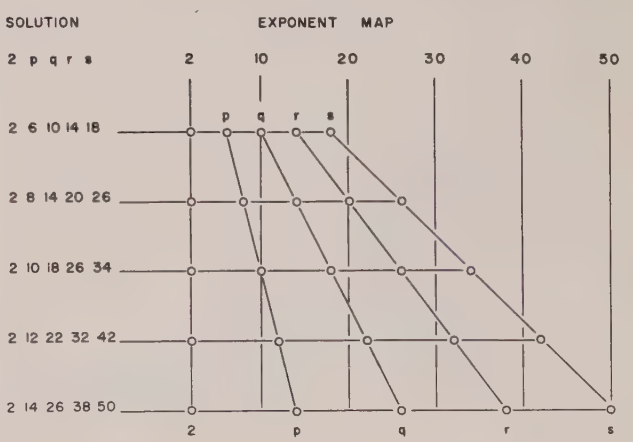

Fig. 19 — Second exponent mapping

amplitude versus time is obtained. For the proposed cam design, at least one good trace for each valve train in the engine is required. The recorded trace should appear about as shown in Fig. 20.

The test for the validity of the single degree-of-freedom assumption is made by observing the smooth sinusoidal shape for the trace. The frequency in cycles per minute is found from the time for one cycle, or better, from the average time per cycle measured over a number of cycles. The direct calculation for the valve train equivalent weight acting at the valve (w_e) is obtained from the equation

$$w_e = k_o \left[\frac{188}{f_n}\right]^2 \qquad (24)$$

where,

k_o = the valve train spring rate (lb/in.) as measured in a previous step

f_n = valve train resonant frequency (cpm)

THE VALVE SPRING DESIGN RELATED TO CAM PROFILE DYNAMICS - The single most important fact about the valve spring as related to the cam profile is that both are integral, interdependent designs; the valve spring design and the cam design should be a matched pair. The valve spring design should begin from those considerations which give dimensions to the cylindrical space provided in the valve train for the spring. Since starting from this point would involve a considerable discussion length, it is planned for another paper. These paragraphs on the valve spring design are concerned with only that part of the problem which affects directly the cam profile dynamics.

At the inception of the cam design problem, the designer found it neces ry to assume (sse Ref. 1) a valve spring preload and spring rate. At this later time, the cam design will have been substantially completed; and the present task is to choose the valve spring characteristics which particularly match the requirements of the valve train system and cam profile dynamics. As a starting point, the designer will know the particular dimensions of the cylindrical space provided for the spring. Also, he will have determined a value for the valve lift and will know the dynamic characteristics of the new cam profile.

Factors for a Good Valve Spring Performance - A valve spring design is to be found such that

1. The spring will have good dynamics free from surge and coil clash, will follow the valve motion throughout the engine speed range, and will continue to do so for the expected engine life. The spring will resist any tendency to lose loads during operation, particularly as this may be caused by excessive heat or stress.

2. The spring loads and rates will match the cam dynamics such that valve train compression will be maintained at the highest engine operating speed without causing excessive bearing stresses at the cam to tappet interface during engine crank and idle speeds.

Valve Spring Loads and Rates Matched to Cam Profile Dynamics - The match of the valve spring final design loads and rates to the particular requirements of a given cam profile dynamics is accomplished in three graphical steps, as shown in Fig. 21.

1. The computer output parameter (L_V) is plotted for the region of negative cam profile acceleration. Recall that (L_V) is given in pounds and is the inertia load at the valve for the valve train at 115% engine design speed. The final design valve spring forces at the valve (S) must be just larger than (L_V) for all values of (x); that is $S \geq L_V$ for $0 \leq x \leq 1$.

2. A second parameter (L_S) is plotted for the same region of the cam profile. (L_S) is the load in pounds applied to the valve train at the valve end required to produce the limiting (prescribed) value of bearing stress at the cam to tappet interface; this load will vary along the profile with (R_C). The final design spring forces must be just less than (L_S) for all values of (x); i.e., $S \leq L_S$ for $0 \leq x \leq 1$.

3. Consider the plotted values of (L_V) and (L_S) in Fig. 21. Based on a controlled (dynamics) cam design profile, there will be a carefully designed gap (space) between these two curves. The desired spring loads and rates can be chosen such that (S) will be somewhat greater than (L_V) but less than (L_S); i.e., $L_V \leq S \leq L_S$ for $0 \leq x \leq 1$.

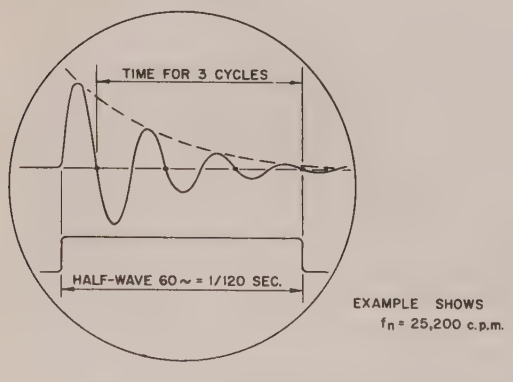

Fig. 20 — Valve train resonant frequency measurement

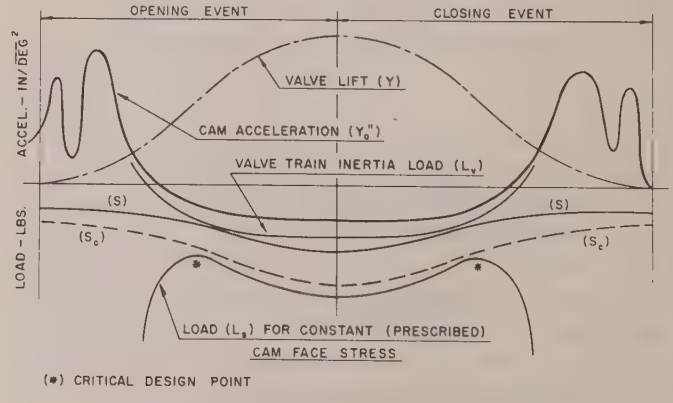

Fig. 21 — Valve spring load and rate design

Two areas of the cam profile are subject to the limiting bearing stress criteria. The first of these is located between (C) and (D) shown in Fig. 17 and is associated with the maximum allowable positive cam accelerations in the cam profile. The evaluation involves the parameters (L_V) and an assumed (S) as previously discussed. This point is relatively insensitive to small changes in spring loads by reason of the large radius of curvature (R_C) in this region of the profile. The second critical stress bearing area is in the region of (F), Fig. 17, and also * Fig. 21; this location is highly sensitive to small changes in the spring design load due to minimum values of (R_C). Ideally, the bearing stresses would be limited to about 150,000 psi at both locations. Since, however, the stress limitation in the area of (F) occurs only at engine start and idle, the stress levels at this location can be raised somewhat where the engine is designed to operate at speed for most of the working life.

Equations and Experience Factors for a Good Valve Spring Design - After the valve spring maximum loads (P) and spring rates (k_1) have been fixed in accord with the procedures outlined above, a good spring design performance can be achieved by means of the equations[6] and experience factors given as follows:

Equations

1. Relationship of spring rate (k_1) to wire diameter (d), mean spring diameter (D) and active coils (N).

$$k_1 = \frac{Gd^4}{8D^3 N} \qquad G = \text{Torsional Modulus} \qquad (25)$$

$$= 11.5 \times 10^6 \text{ for steel spring wire}$$

2. Relationship of load (P) to stress (S), wire diameter and mean diameter, (K) Wahl correction factor:

$$S = \frac{8PD}{\pi d^3} (K) \qquad (26)$$

3. Relationship of spring natural frequency (f_s) to wire diameter, mean diameter and active coils:

$$f_s = \frac{826,500\ d}{ND^2} \qquad (27)$$

Experience Factors

1. The spring should have a height to outside diameter ratio of between $1\frac{1}{2}$:1 and 1:1. This is necessary to reduce the side thrust of the valve on the guide by allowing the spring to become square under load.

2. The difference between the spring solid height and valve open height should be at least 1/2 a wire diameter to avoid coil clash and noisy operation.

3. It is best to design springs ending on the 1/4 to 3/4 coil. This factor also tends to give a spring which is more square under load.

4. Allow one dead coil at each end of the spring for squaring the spring ends.

Based on the foregoing,

$$\text{Spring valve open height} = (N + 2\tfrac{1}{2})\ d \qquad (28)$$

where,

N = $1\frac{1}{2}$, $2\frac{1}{2}$, $3\frac{1}{2}$ --- etc.

Spring outside diameter = (D + d)

5. The limiting valve open wire stress should be about 95000 psi. This will insure an infinite life and reduce the tendency to lose load during operation.

6. The choice of spring materials is based primarily upon maximum operating temperature conditions.

7. The natural resonant frequency of the spring (f_s = cpm) should be designed to be at least 13 times the maximum camshaft speed.

8. The ideal ratio of spring mean diameter (D) to wire diameter (d) is between 7 and 8. This leads to a "Wahl Correction Factor" (K) of 1.19. (K) is used in all spring design stress calculations to include the additional stress caused by the curvature of the wire and shear load.

The simultaneous solution of the spring design equations can be achieved in a series of ordered steps for the conditions imposed by the experience factors and the requirements of the cam profile. This solution yields an optimum match between the valve spring and cam profile design.

Special Valve Spring Design Devices and Techniques - The valve spring design derived by means of the foregoing analysis will have constant pitch coils and will be a constant rate spring of very high natural frequency. The design depends, in part, upon having selected the proper cylindrical space for the spring in the original engine design layout work. Where these space dimensions are only modestly different from optimum, certain devices in the spring design can be used.

1. Dual inner and outer springs—By distributing the required load between two springs, somewhat less volume is needed for a given spring performance. Also, in the event of a spring failure, extensive engine damage is avoided. The disadvantage is that, in general, neither spring will have optimum frequency characteristics.

2. Variable pitch, "basketed coil," valve springs wherein the space between the active coils is graduated produce a variable rate and resonant frequency—also, variable diameter wherein a taper in the outside diameter of the coils is used to produce a spring of variable rate and resonant frequency.

3. Mechanical friction dampers—The usual design consists of helically coiled spring strips forced into the inside diameter of the spring.

In general, these devices are employed to overcome certain deficiencies in the overall valve train design usually

brought about by either a valve train natural resonant frequency which is too low for the desired maximum engine operating speeds or a mismatch between the cam profile and valve spring designs.

THE PHOTOMETRIC ANALYSIS OF VALVE MOTIONS - The photometric analysis of the valve motion is a means for determining with reasonable accuracy the dynamic performance of the dam profile in terms of the control actually obtained over the valve displacement, velocity and acceleration through the range of engine speeds. The analysis consists of two parts:

1. By means of high-speed motion pictures, data is taken so that the valve-lift diagram is defined for each engine speed of interest to the analysis.

2. The data is processed—again, by means of a special computer program—with a valve acceleration diagram as the final result. This diagram may then be compared directly with the original cam design data.

It may also be of interest that the same special computer program is used to determine the acceleration profile of the prototype master cam as manufactured from the design drawings and may also be used to analyze the acceleration profile of any arbitrary cam of interest.

Cinemaphotographic Data Recording - The high-speed photographic recording is done with standard Wollensak Fastax 16 mm high-speed equipment. Normally, telephoto lenses mounted on extension tubes are used to secure maximum image size at the film plane. By proper coordination of the many photographic factors involved, resolution limits in the order of 60 lines per millimeter are obtained. The camera is mounted in such a way as to view the valve stem to rocker arm interface; the finish grind marks on the valve stem can frequently be distinguished in pictures taken with the engine running at 5000 rpm and the camera nominal framing rate fixed at 5000 frames per sec. The object to image ratio is nearly 1:1 and with this image projected on a screen with a projection size of 3 x 4 ft, the overall accuracy of the data is such that valve displacements are determined within a tolerance of ±0.0010 in. A frame by frame measurement of the valve motion obtains a table of values which define the valve displacement diagram.

Data Processing - The data processing technique is to consider any three consecutive points on the valve-lift diagram (or cam-lift profile diagram) and fit a curve described by a second degree equation through these points. Considering next the region of the curve near the midpoint of this original set, the local area of the equation may be differentiated once for velocity and, again, for the acceleration. In a continuing step, the set of three points are advanced one interval, and the process repeated. By means of curve fitting, the true displacement velocity and acceleration diagrams are approximated much more closely than is the case with straight-line averaging. It will be recalled that in this latter (usual practice) technique, point-to-point difference provide average velocities over each interval and plotted, give the velocity profile. In a second step, differences between consecutive points in the velocity profile are found. These differences provide an acceleration curve wherein the averaging effects have been compounded. This method, therefore, is relatively inaccurate and insensitive to small changes in the true acceleration profile.

In the curve fitting technique for data processing, the arithmetic task is relatively great. Therefore, a computer program has been designed which is able to read the consecutive valve-lift diagram points from a table of values, process the data by curve fitting, and provide accurate and sensitive values for the corresponding velocity and acceleration profiles. The whole task is completed in a few minutes of computer run time.

Summary and Conclusions

A Statement of the Cam Design Problem

1. Recent analytical methods for the design of the cam profile as related to the control of valve train dynamics are extended in this paper to obtain optimum engine breathing with also a control over the cam face bearing stresses.

2. The engine is in all respects to be regarded as an elastic system. The cam design goals are a function of the gas dynamics of the system which specify valve event (and timing), valve lift and range of engine operating speeds. The cam design limitations are a function of the valve train dynamics limits and systems force-stress limits.

3. The analytical procedures for cam design (herein described) seek an "optimum" design solution through a series of carefully ordered steps. The optimum cam profile is defined as that profile which provides an accurate control of the valve dynamics over a specified range of engine operating speeds, and which also maximizes the area under the valve lift diagram for a specified valve event length.

4. The major cam design parameters are shown to be five in number: valve event length, valve lift, engine speed range, valve train resonant frequency and force-stress limits; of which only three may be chosen independently.

5. In overhead valve (pushrod) engines the optimum profile may be derived if the engine speed is fixed as a function of the valve train resonant frequency (a design chart is given), the valve event length and force-stress limits are arbitrarily specified and the valve lift is maximized as part of the cam design solution.

6. In overhead cam (non-pushrod) engines, the valve train resonant frequency does not directly define the engine speeds and, therefore, the engine speed may be chosen based on gas dynamics considerations. In this manner, the five interdependent variables are reduced to three as before, with the problem solution obtained as in pushrod engine design procedures.

7. The first part of the paper concludes with a quanti-

tative definition for an optimum cam profile with a cam design specification chart.

An Extract from the Polydyne Method of Cam Design

1. This section, by means of a flow chart, provides a general view - an overall perspective of the mathematical steps involved in a polydyne solution.

2. It is stated that in an optimized cam design solution about 150,000 to 200,000 arithmetic calculations are required; by desk calculator methods these would take about 75 man months. It is thus concluded that electronic computer programming is necessary. The IBM 650 computer requires 3 hr; the IBM 704 computer, about 20 minutes run time to obtain an optimized cam design solution.

Modifications to the Polydyne Cam Design Procedures with Computer Programming for Optimized Solutions

1. It is stated that with electronic computer techniques, tactical methods are required to thread the way from a beginning to a final solution in a least number of trials. Careful programming is necessary to minimize run time and also retain solution accuracy.

2. The main elements of the IBM 650 computer program and design methods are given.

3. The computer basic machine data and synethesized output parameters are listed and summarized.

4. A detailed description of the method of solutions evaluation is given and shown to depend primarily upon the synthetic output parameters given by the machine program. Of the evaluation parameters, the cam acceleration diagram is the most important.

5. The method of exponent manipulation in the machine program to achieve the optimum cam design profile is detailed.

6. The importance of the valve train resonant frequency design parameter had been established in the first part of the paper. In this section, a method for the measurement and evaluation of this factor was given.

7. It was stated that the most important fact about the valve spring as related to the cam profile is that both are interdependent designs. An analytical method for matching the valve spring rate and maximum load to the dynamics of the cam profile was given. The method of simultaneous solution of three equations conditioned by experience factors for an optimum spring design was deferred, because of length, to another paper.

8. A description of a method used for the photometric analysis of valve motions was given.

It is an overall conclusion of this paper that a quantitative definition for an optimum cam profile design can be made so that an ordered analytical solution is possible; that analytical cam design procedures can be rapid, successful, and inexpensive as compared with trial-and-error procedures which are inherently slow and expensive; that the analytical cam design procedures, because of the great arithmetic task involved, become practical through the use of electronic computer techniques.

Acknowledgment

The authors wish to express their appreciation to Mr. G. C. Harbert, formerly chief engineer of Willys Motors, Inc., for his patience, understanding and foresight; his confidence extending over years made possible the study which permitted, finally, the preparation of the present paper.

The authors also wish to thank Mr. J. V. Doe, Mr. D. B. Hammond, Mr. G. E. Henry and Mr. K. Matthews, all of Willys Motors, Inc. for their vital support. Special mention is made of Mr. M. Ordorica and Mr. A. C. Sampietro—esteemed automotive consultant—for their valuable criticisms of the original manuscript.

Selected References

1. T.R. Thoren, H. H. Engemann and D. A. Stoddart, "Cam Design as Related to Valve Train Dynamics," SAE Transactions, Vol. 6, No. 1, January, 1952.

2. Max J. Tauschek, "Valve Train Engineering—Fundamentals for the Engine Designer," SAE Milwaukee Section Lecture Series, February, 1958.

3. Harold A. Rothbart, "Cams—Design, Dynamics and Accuracy," John Wiley & Sons, Inc., 1956.

4. "The Polydyne Method of Cam Design," SAE Transactions, Vol. 6, No. 1, January, 1952.

5. R. A. Roggenbuck, "Designing the Cam Profile for Low Vibration at High (Engine) Speeds," SAE Transactions, Vol. 61, 1953, 701-705.

6. M. C. Turkish, "Relationship of Valve-Spring Design to Valve Gear Dynamics and Hydraulic Lifter Pump-up," SAE Transactions, Vol. 61, 1953, 706-714.

7. "Handbook of Mechanical Spring Design," published and distributed by Associated Spring Corp., Bristol, Conn., 1958.

Discussion

Production Design Considerations

Phillip A. Martel
Ford Motor Co.

THIS PAPER SHOULD serve as an invaluable reference source for cam design research and should provide a useful tool for determining the best cam design approach. Of particular interest to the writer were certain aspects in the polynomial approach outlined in the paper. Since our own experiences and those of our English counterparts appear to follow the same pattern, it seems appropriate to discuss the results of our studies with the polydyne method as they apply to the automotive industry or, more specifically, as to how this data can be utilized in practical engineering for production.

Noise

In addition to the performance and durability objectives discussed in this paper, we must obtain an acceptable valve train noise level with the engine installed in a vehicle. To go a step further, our design objective allows any noise in the valve train that is not heard by the occupants of the car. This is more logical than humorous, since valve noises are particularly distracting and obnoxious to the average person because of the frequency range involved. Experiments indicate that while the design speed noise level is significantly reduced by the polydyne system, this is not true at all lower speeds. It appears that the kink produced in the cam acceleration trace, which is required to tune the system at design speed, causes a disturbance particularly apparent at lower engine speeds.

Fig. A shows a comparison of the general dynamometer noise characteristics observed from both average polydyne cam and normal cam arrived at by the "experience" method. It will be noted that the polydyne cam, in general, has a lower and more uniform noise level, while the "experience" cam has more sharply defined and higher peaks in the area of design speed. When we compare these cams as installed in a passenger car, we find that high speed noise level is obscured by other noises present at the car speeds associated with high engine speed.

Fig. B has been plotted to show the general characteristics of the two types of cams with regard to sound level in the front seat of the car when running under steady speed conditions. It may be pointed out that in accelerating from a standing start, the curve for engine speeds and related valve train noise will shift to the left from the position illustrated on this diagram. The higher noise levels of the experience cams will not be objectionable normally, because of the sharpness of the sound peaks and the rapidity with which the engine passes through them.

The noise scale has been purposely omitted from Fig. B because of the many variables which influence the absolute units, such as firewall insulation, interior car acoustics, type of pavement, body styling, fan drive ratio and type. It is possible that in some particular car, using a given polydyne profile, the general "hash" noise might not be objectionable.

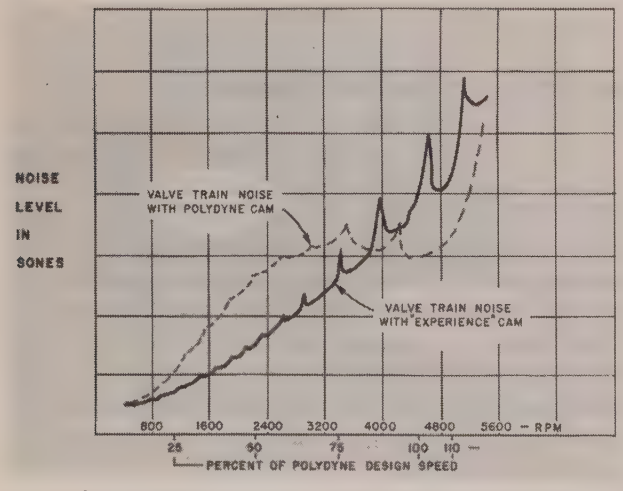
NOISE LEVEL IN SONES
VALVE TRAIN NOISE WITH POLYDYNE CAM
VALVE TRAIN NOISE WITH "EXPERIENCE" CAM
800 1600 2400 3200 4000 4800 5600 — RPM
25 50 75 100 110 —
PERCENT OF POLYDYNE DESIGN SPEED

Fig. A — Noise level on dynamometer comparison

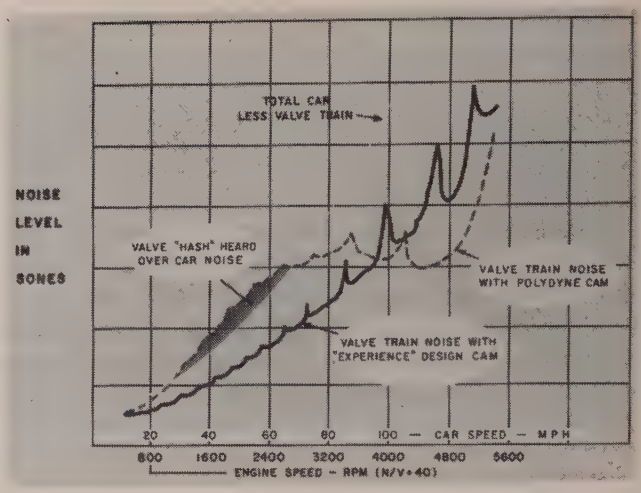
NOISE LEVEL IN SONES
TOTAL CAR
LESS VALVE TRAIN
VALVE "HASH" HEARD OVER CAR NOISE
VALVE TRAIN NOISE WITH POLYDYNE CAM
VALVE TRAIN NOISE WITH "EXPERIENCE" DESIGN CAM
20 40 60 80 100 — CAR SPEED — M P H
800 1600 2400 3200 4000 4800 5600
ENGINE SPEED — RPM (N/V=40)

Fig. B — Noise level in front seat of car

Another factor contributing to valve train noise is the rapid rate of increase in cam acceleration which occurs before the valve has opened. This condition is most severe when attempting to obtain maximum breathing in the polydyne approach to improve performance. No mention has been made in the paper regarding steps taken to include the deflection on the exhaust valve system due to gas pressure forces. These gas loads add to the inertia due to mass just prior to valve opening. After the valve opens, the affect of this gas force soon becomes negligible, thus causing valve jump to occur.

Event

The use of the term "event", while necessary in any cam lobe discussion, can be misleading. Depending upon the exponents selected, the valve lift curve may vary quite markedly as it leaves the ramp and affect top overlap, idle, and low-speed performance. Fig. C is a plot of the top overlap of two polydyne cams with the same event and maximum valve lift. Experience shows that the top overlap would have to be reduced on the rapid opening and closing cam. This comment is made, since in designing a cam on the computer, the original event may be altogether different than the concept of event as applied to an experience design. Many instances have been noted over the years wherein an additional 4 or more deg could be added to the event. This allowed the use of a more gentle acceleration rate which helped reduce valve "hash" in the car.

The authors state that this program will result in an opti-

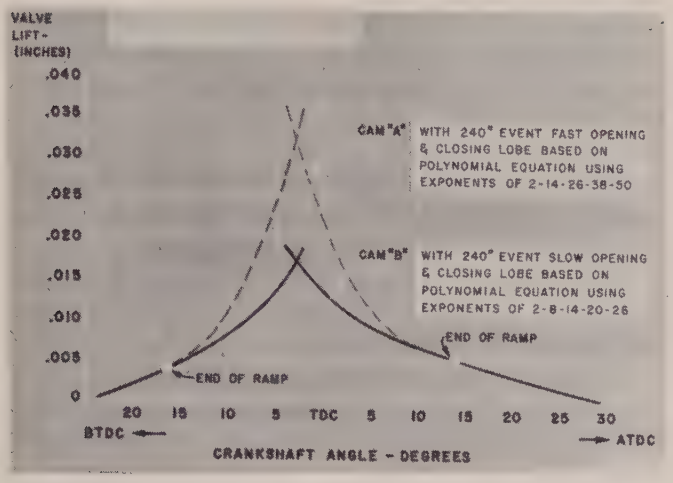
VALVE LIFT - (INCHES)
.040
.035
.030
.025
.020
.015
.010
.005
0
CAM "A" WITH 240° EVENT FAST OPENING & CLOSING LOBE BASED ON POLYNOMIAL EQUATION USING EXPONENTS OF 2-14-26-38-50
CAM "B" WITH 240° EVENT SLOW OPENING & CLOSING LOBE BASED ON POLYNOMIAL EQUATION USING EXPONENTS OF 2-8-14-20-26
END OF RAMP
END OF RAMP
20 15 10 5 TDC 5 10 15 20 25 30
BTDC
ATDC
CRANKSHAFT ANGLE - DEGREES

Fig. C — Comparison of top overlap

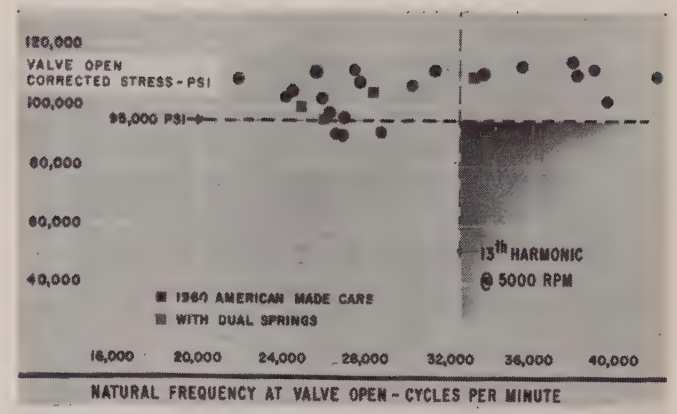

Fig. D — Valve spring stress versus natural frequency

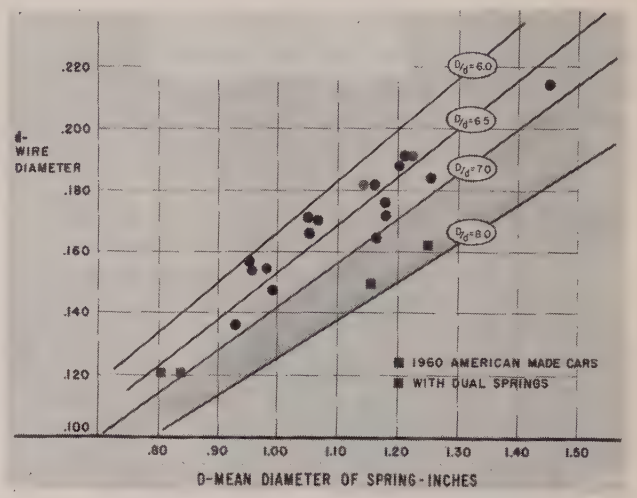

Fig. E — Wire diameter versus mean diameter

mum design for breathing under the conditions given. What precepts dictate the choice of the exponent pattern to be used? Should it be concluded that only one cam profile will result from the use of this polydyne program, or is it possible to select a slightly different pattern and optimize on a different profile?

Valve lift is normally governed by valve space considerations rather than cam or engine speed limitations. Variable valve lift usually is sacrificed for one or more of the following considerations:

1. Proper guide length.
2. Minimum valve overhang.
3. Maximum space for insertion of oil seal.
4. Valve spring stress range.
5. Interference of spring retainer to rocker arm.
6. Undesirability of notches in piston to clear the valves.
7. Rocker cover clearance to chassis components.

Valve and port sizes can usually accomplish the same result as additional lift, and do so with better durability prospects.

Valve Spring

The first point of interest regarding valve springs is that no mention was made of integrating harmonic spring load analysis into the program. Even when using springs which possess a high natural frequency, surge is noted at some critical speeds, which results in reduced spring load available to keep the train in contact. Adding this complexity to the computer program is easier said than done.

The general rules laid down for good spring design agree substantially with current practice except for some conservatism regarding stress level and diameter ratios. A plot of stress versus natural frequency for the majority of the valve springs used on 1960 model American built cars is shown in Fig. D. The vacant shaded quadrant on the lower right is the area recommended by the authors. Similarly, when plotting wire diameter versus mean diameter (Fig. E) for the industry, it will be noted that the bulk is grouped around a ratio of 6.5 instead of the recommended 7 to 8 ratio.

An attempt was made to show the difference between average practice and the recommendations made in this paper. The following valve spring requirements represent an average for American passenger cars being produced in 1960.

1. Valve lift ..... 0.390.
2. Valve closed load ..... 80 lb.
3. Valve open load..... 175 lb.

Fig. F shows the relationship of natural frequency, stress, and wire size for different diameter ratios on a constant rate spring. The spring designed for condition "A", using present industry practice, would weight approximately 0.143 lb. The spring designed for condition "B", while undoubtedly better considering stress and stability only, would weigh approximately 0.184 lb. In addition, this spring is 1.75 in. outside diameter as opposed to 1.38 in. outside diameter for spring "A". This increase in outside diameter would very likely require an increase of 15% on the length of the long side of the rocker arm which "snowballs" the polar moment, if rigidity is maintained. In addition, the weight of

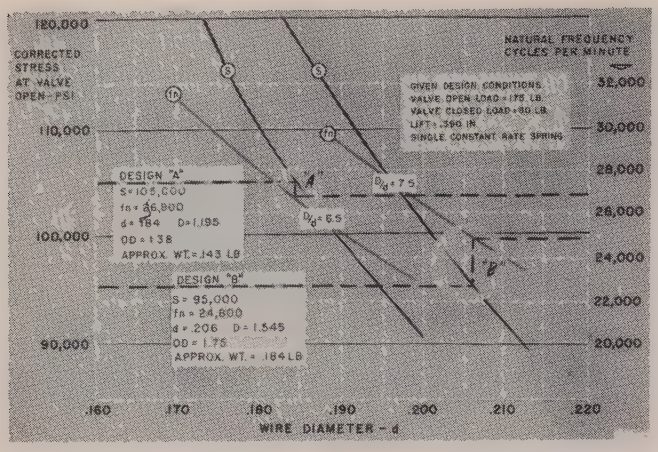

Fig. F — Spring comparison

the larger spring retainer and 29% heavier spring increase the inertia forces. It appears that the limits are so safe that production engines cannot afford to use them for the reasons shown.

"Experience" Cam Design

Let us briefly explore current methods used to design successful valve mechanisms using "trial and error, expensive procedures." It must be agreed that valve mechanism design is a trial and error procedure. However, the bulk of the trial and error is not normally devoted to the design of the cam profile, but rather to the multitude of other variables relating to performance, durability and noise.

In the design of a new engine, every attempt is made to secure maximum valve train rigidity consistent with the overall design objectives. By this, we mean short pushrods, rigid rocker and support geometry, lightweight parts with efficient stress distribution, large cam bearing diameters to provide stiffness and allow adequate base circle radius, maximum lift consistent with design limitations previously outlined, and sufficient space so that a satisfactory valve spring can be designed. After this initial design stage, only minor changes in stiffness or valve lift are possible without jeopardizing program timing.

The original cam profile, event and timing are then selected on the basis of experience and program objectives. Detail drawings are not yet available from which to calculate or even estimate the natural frequency of the valve train since the camshaft casting requires more lead time than the balance of the small parts in the train. This original cam will not likely be used in production; but it must be close enough to a production version, so that testing on the first engines is not delayed.

Other phases of the initial calculations include the design of a vlave spring to provide the required toss or pump-up speed.. Harmonic analysis, based on the cam profile previously designed, is used in this calculation. The tappet-to-cam (Hertz) stress is determined for nomial and limit stack conditions to ascertain whether cam lobe offset and lobe width are ideal.

After initial dynamometer and mechanical prototype car tests have been run, the test data is reviewed and a second camshaft is designed. This is based on:

1. Revisions desired in shape of torque curve.
2. Deviation from expected toss or pump-up speed.
3. Ramp adequacy for temperature and dynamic conditions encountered in car operations.
4. Noise characteristics observed on car testing.

At this stage in engine development, it is normal to try various combinations of valve spring features to minimize objectionable noise and/or surge conditions throughout the operational speed range.

Summary

The idea of having the cam profile compensate for the flexibility of the overhead valve system is an important goal. In my opinion, designing by formula, polynomial or other, impedes design flexibility of applying knowledge obtained through years of experience. Utopia in cam design would allow feeding the desired valve acceleration characteristics into the input of the computer and having the output for cam acceleration contain the best compromise for the total speed range. We are continuing studies to develop and evaluate various formulae and computer programs. However, until further progress is made in this direction, we believe that the "experience" method provides the most practical course to follow.

Control of Vibration Amplitude

Richard S. Johnson
International Harvester Co.

THERE ARE MANY points in this paper which might be questioned or discussed, but it is surprising how many of these can be related to a single subject, the control of vibration amplitude. Despite the references to vibration which are sprinkled through the paper, I do not believe that the authors have emphasized its importance sufficiently. The "polydyne" system is designed to eliminate valve mismotion due to train vibration at the design speed by exactly compensating the cam profile for train deflections. This technique apparently works at design speed, but unfortunately it does not automatically give adequate valve train control at other speeds.

The authors review the fact that vibration reaches a maximum at 70% of the design speed and has an approximately equal value at 110% of design speed after which it increases indefinitely. Actually, these figures are from a curve con-

necting the high points of a series of vibration amplitude loops representing orders of resonance between speed and natural frequency. The authors recognize the importance and then fix the valve train design speed as a dependent function. The maximum permissible over-speed condition would be limited to 110% of the design speed. It has been further suggested that if these speeds are not sufficiently high for the desired engine operation we should stiffen the valve train or make it lighter so that the procedure can be used. Unfortunately, it is not always possible to make such changes. What can we do in this case? Possibly we can limit the magnitude of the vibration at whatever speed it may occur.

To compute contact stresses, acceleration loads are considered against the cam; and to compute separation speeds, we consider deceleration loads against the valve spring. Vibration forces affect both of these results, and it is only when vibration forces are added to the stress calculations and to the separation speed calculations that the true importance of vibration control becomes apparent.

Minimizing the vibration amplitude and the vibration forces at off-design speeds can affect the choice of almost all the design variables. There are no good substitutes for high rigidity and low weight, but if we must substitute, there are several areas which can be considered. Valve event duration and valve lift have been mentioned. Possibly a less well understood influence is the establishment of the boundary conditions of the differential equations. A smooth transition from the ramp is necessary, and for most designs there is an optimum ramp velocity which produces the least vibration. Perhaps the largest influence outside weight and rigidity is the selection of the power series. This can have a very significant influence on off-design speed vibration. A considerable portion of our computer work using an IBM 705 has been to find the trends of vibration amplitude with each of the design variables.

Next I'd like to mention two specific points. One is a defense of what the paper refers to as "normal practice..." which "...does not ordinarily achieve an optimum result."

The authors want to specify the maximum operating speed and then find the highest permissible valve lift. We have used this procedure but find that it is sometimes better to use the old outdated "normal practice." For example, let's put a fairly large engine in a highway truck and limit the maximum engine power with a governor, hook on a loaded trailer and start the whole thing down the side of a mountain. (Let's add the requirement that we stay on the road). Under these conditions during which the engine functions as a retarder with the transmission in one of the lower gears, there is a great need for over-speed capacity but no need at all for optimized valve lift since the governor has closed the throttle. It's better in this case to specify an acceptable range of air flow capacity..." and seek the maximum engine speed within the limits of good valve control."

The other point is the specification in the second part of the paper that the exponents, p, q, r and s be even positive integers such that p is equal to or more than 8 and s is equal to or less than 50. Why and why 50? The engine series most recently put in production by the Motor Truck Division of International Harvester uses a polydyne camshaft for which the first exponent after the square is 6. We're not sure how the authors feel. Fig. 19 shows a 2-6-10 and so on series. Also, in a special experimental design we found it necessary to use 66 for the last term exponent to obtain the required result. For that matter if we consider profiles from the maximum lift downwards, why should we exclude the odd powers? Are there any real reasons for these limitations or are they just for convenience to limit the field of choice?

Success of Polydyne Method?

F. G. Butler
General Motors Corp.

SINCE THE AUTHORS have not given any examples or results of their work with the polydyne method, it is difficult to determine what success they have had with the method. It must be assumed, therefore, that satisfactory results have been obtained with the procedures outlined.

During 1951 and 1952, Oldsmobile Engineering carried on an extensive experimental investigation of the polydyne method of design and resulting cams and valve motions. During this time, several different designs were made and tested in engines. The investigations indicated the polydyne method was in need of a great amount of further development. Dynamic distress resulting in excessive noise was encountered in mid-range engine speeds. Oldsmobile discontinued further work with this procedure to await more study and refinement at a later date.

The authors have made modifications to the polydyne approach, introducing new design parameters. However, I can not conclude from this paper that they have the answer to the cam design problem because no data concerning actual engine tests are given. The reason I question the present work is not due to the original concept nor to the authors subsequent efforts but primarily because a very complex mechanical system has been over-simplified for purposes of analysis. This over-simplification consists of reducing a multi-mass variable stiffness system with indeterminate dampening to an equivalent dynamic single mass mathematical model with constant stiffness and no dampening. Until procedures are developed to comprehend a greater number of these variables such as variable multi-mass, variable stiffness, and multi-dampened systems as encountered in the modern high performance automotive engine.

I am not here to merely criticize Mr. Nourse and his coauthors, but I hope to challenge them to a continuing effort in this field along the course they have undertaken.

Recalling the diagrams of the valve and cam accelera-

tion curves shown in this paper, I do not believe that all of the valve train components will adjust to the extreme changes in force as shown in the positive portions of the cam acceleration curves. To get equivalent areas under acceleration curves as are now found in most cam profiles, it would be necessary to have higher positive acceleration values not once but twice during any opening or closing cycle. This indicates more detrimental inertia forces in a given system. One may not be concerned with the area under an acceleration curve, but (recalling some of our fundamental mechanics) area under such a curve is defined as work done. Therefore, why not take advantage of this and put it to its fullest use. In this paper, the authors state that the important part of the valve lift is that which comes before the port acts as the breathing restriction. In this tenor, it almost becomes mandatory to take full advantage of every potential contained in any given system. In the flanks of the cam, we therefore utilize maximum area under the acceleration curve. This results in greater velocity with higher values of lift at any cam angle. This approach does present some difficulties. For example, it is not generally considered good practice to have greater values of negative acceleration farther away from the maximum cam lift point than the value at this point. As discussed in this paper, this is an undesirable characteristic, but where in Engineering have we found an ideal uncompromised system? Use of a design of this type, containing the so-called detrimental negative acceleration characteristics, does permit the designer to develop cams that take full advantage of that area under the flank lift curve for engine breathing without increasing the maximum valve lift over the limits defined by the valve spring solid height. This is relatively simple to explain without diagrams. Recall again the acceleration curve and the centroids of both the positive and negative parts as seen along the time axis and make a summation of moments about the maximum lift point; and we have determined maximum lift. With this in mind, it can be readily understood that maximum lift may be minimized by the proper application of the so-called detrimental acceleration curve.

Oldsmobile engineers have designed and developed many different types of cams to satisfy many variable conditions, but as yet, we have not found a fool-proof purely mathematical method of design that will satisfy the conditions prescribed by engine requirements.

I wish to compliment Mr. Nourse, Mr. Dennis and Mr. Wood on their recent spring designs, photo-metric analysis and data processing procedures. We have used high speed photographic analysis for a number of years (having been first introduced to the procedure by H. H. Engemann) and we have found this to be one of the most valuable tools for critical, analytical evaluation of valve train dynamics. I only wish the authors had seen fit to describe these procedures more fully to awaken the interest of those who are uninitiated in this art.

Acknowledgment

I wish to pay tribute to two excellent scientist-engineers, Dr. W. M. Dudley and H. H. Engemann who laid the foundation for the challenging concept contained in the polydyne method of cam design.

I also wish to acknowledge the cooperation and aid of two Thompson Products' engineers D. A. Stoddart and H. H. Engemann, who worked with Oldsmobile during their experimental investigation of 1951-1952.

Force-Stress Limits in Valve Train

Max J. Tauschek
Thompson-Ramo-Wooldridge, Inc.

IF THERE IS one particularly significant contribution in the authors' paper that overshadows all else, it is their recognition of the importance of the force-stress limits in the valve train. These force-stress limits have increasingly, in the past few years, limited the performance of valve trains, not only at a tappet-cam interface but particularly at the rocker arm-valve tip contact area.

Approximately 10 to 15 years ago, the predominate valve train problem was lack of control of the valve train dynamics causing erratic valve motion and bounce which in turn, caused high seating velocity and valve breakage. The polydyne-cam design work was undertaken by the Thompson Products, Valve Division in order to afford a means of controlling valve train motion. The polydyne method, properly applied, accomplishes this objective. The method requires, however, that the valve lift curve be assumed as the first step in the solution. This assumption is made without any knowledge of the loads or other limits imposed on the valve train. Yet, an appropriate polydyne solution can be achieved for any arbitrary valve lift curve. It is possible and quite frequently happens, that the assumed valve lift and acceleration produces loads far exceeding allowable limits. It is, therefore, gratifying that the authors have extended the polydyne solutions, not only to consider such loads but also to provide means of optimizing the valve lift curve so as to take full advantage of permissible stresses in the valve train.

The polydyne method has not been universally accepted, partly because of its mathematical complexity and partly because of assumptions which, although they impair its accuracy, are necessary to permit the equations to be solved at all. The advent of high speed digital computers obviates the first difficulty. The refinements added by the authors, particularly their recognition that the polydyne method will not apply to systems having multiple degrees-of-freedom and their technique for determining the equivalent weight of the valve train by deduction from its resonant frequency, improve the accuracy and extend the usefulness of this method.

The authors stress that the polydyne technique applies only

to systems which vibrate roughly sinusoidally. This raises a question concerning their approach to systems exceeding a single degree-of-freedom. Is it possible to constrain such systems to one-degree-of-freedom and if so, what is the means for accomplishing this end?

Again the authors stress the importance of high resonant frequency in determining the engine design speed. The authors' equation for determining engine design speed is empirical and the cam would require less compensation if the maximum engine operating speed were a smaller fraction of the valve train resonant frequency. The importance of maintaining high stiffness and low weight in the valve train is self-evident, yet it has been our experience that factors such as cam shaft bearing spacing, or cantilevered rocker arms which contribute to the elasticity of the system, are not generally appreciated. Therefore, are there not instances where it is more practical to attempt to increase the resonant frequency of the valve train instead of or prior to compensating the cam? If so, are there particularly effective techniques that the authors have discovered for reducing the effective weight or increasing the stiffness of the valve train?

Authors' Closure to Discussion

THE AUTHORS sincerely appreciate the time each of the discussers has taken to prepare critical reviews to this paper. We have been reminded rather forcibly, however, of the story about the seven blind men who went to see the elephant. It will be recalled that one blind man had touched the elephant's side and so decided the elephant was like a wall; another, having found the tail, decided the elephant was not at all like a wall but like a rope; a third, having found the elephant's leg, knew immediately that both the others had been wrong—the elephant was, in fact, much like a tree, and so on. In these discussions, one has looked at the cam design elephant as "noise," another has looked at "vibration," and still another finds the cam problem too complicated for an analytical solution by any means. We suspect that each of us is partly right and that the truth of the matter may be somewhere between.

There is one impression, however, which demands an immediate reply. Several reviews have implied that there is a fundamental difference to be appreciated between the "analytical" cam design method as compared with the "experience" method and that the experience method is much to be preferred. In our view this is a twisting of words which is fallacious, to say the least. Surely it is necessary to begin from the premise that in any problem, the analytical method must depend heavily upon experience to be successful—must be generated directly from it. In cam design the analytical method should contain not only cam experience but also all that can be gained from mechanics, the methods of machine and shock and vibration problem solving, as well as experience in numerical analysis where this can be applied effectively. To set the words "analytical" and "experience" into opposition is deplorable; the fundamental issue is to make experience the servant—not the master.

REPLY TO PHILLIP A. MARTEL - Noise—We agree that "noise" is an important part of the cam design problem but disagree with the conclusion that valve train noise at intermediate engine speeds is inherent to a cam designed by the methods outlined in the paper. Valve train noise derives primarily from valve train separation (valve lofting and/or bounce) and valve spring coil clash. The solution to both problems depends upon good valve motion control over the entire range of engine speeds. It is important that any discontinuity in the cam acceleration diagram be avoided—particularly at the ramp to main event juncture. This point was stressed in our paper under "Solution Evaluation," item 3a; we thought this to be one of the important modifications to the original polydyne method.

Cam displacement and valve displacement occur on opposite ends of an elastic linkage. Both displacements with all higher derivatives through at least the fourth derivative (the time rate of change of jerk) must be controlled as a necessary (not to be interpreted as a sufficient) condition for superior cam design performance. Our experience has been that when the time rate of change of acceleration diagram at the cam surface is controlled very carefully—especially at the ramp to main event juncture—the noise as a problem disappears over the entire range of engine speeds.

Event—It is agreed that the design method will affect both event length and top overlap valve timing specifications. Where this is accomplished with good valve control, the effect of sharpening the precise moment at which the valve is opened is a great advantage rather than disadvantage to the engine performance. The low ramp velocities (suggested in the discussion) lead to wider variation in valve timing.

Valve Spring Design—The discussion point made with regard to the relative weight (and therefore cost) of two valve springs, one of which represents "general practice" and the other the more "conservative" design, is well taken. We would agree that in a comparison made on the basis of equal spring preload and rate, the more conservative design would result in a somewhat greater initial cost.

Our basic argument is, however, that the modified polydyne cam provides for the accurate control of the second through fourth derivatives of the valve motion and that this control avoids to some very high degree the valve spring surge excitation forces. For this reason the valve spring can be designed with a significantly lower valve open load. Less valve spring energy storage capacity per cycle is required.

The energy capacity of a valve spring is primarily a function of the weight as is also the cost. Our experience has been that the cam design and valve spring design can be replaced as a matched pair in any existing normal valve train

system; when this is done, the new valve spring is lighter in weight, costs less, and follows the "conservative" design with all the attendant advantages therefrom.

"Experience" Cam Design—The discussion states that "the bulk of the trial and error is not normally devoted to the design of the cam profile but rather to the multitude of other variables relating to performance, durability and noise." Our position is that the performance, durability and noise problems are precisely an important and integral part of the cam profile design problem, that the "trial and error bulk" can be greatly reduced through critically evaluated analytical design procedures.

REPLY TO RICHARD S. JOHNSON—Vibration—If we have failed to emphasize the importance of vibration sufficiently, the only defense that can be offered is that the broad scope of this paper has forced us to be rather terse. The primary motivation of the "polydyne" method concerns vibration and its compensation. Hopefully, we shall find the opportunity at a future date to present a summary of our investigations in this area. Two conclusions from that work can be given here, however, that may be pertinent.

1. Considering the simplest possible vibration system (that is, the single deg-of-freedom system) there is no cam having a fixed profile which can compensate for the valve vibration at more than one engine speed. This statement is true in the theoretical sense and independent of the design method. In that same sense, there is no cam of fixed profile able to compensate a system of more than a single deg-of-freedom at any engine speed (see paper, last paragraph of Command and Response). In the practical sense, however, there are a large number of cams having a fixed profile which can compensate the system adequately well over a limited range of engine speeds. [The analytical method for finding the optimum profile from among these is, of course, the subject of our paper.]

2. For the "polydyne" cam, it can be shown that the valve vibration amplitude varies in accord with the following expression:

$$\text{Valve Vibration Amplitude} = M\left(\frac{\text{E. D. S.}}{f_n}\right)^4 x^2 (x^2 - 1).$$

where:

- M = the maximum value of the time rate of change of valve "jerk" (y'''') at design speed—in/deg^4
- E. D. S. = engine design speed—deg/sec
- f_n = valve train natural resonant frequency—cycles/sec
- x = the ratio of engine speed to design speed

We have found the foregoing relationship very useful.

Specification of Exponents—In regard to the choice of suitable polynomials, the restrictions specified on exponents were not meant to be "iron-clad;" we also have found exceptions. [One cam now in production is designed with the exponents 2 - 12 - 20 - 46 - 66; the valve train spring rate is 385,000 lb per in.—the engine, overhead cam.] In general, it was thought that the initial explorations should be confined by the guidelines given in the paper, that the majority of final solutions would be in this area.

It is reasonable to suppose that there exists other general classes of equations (Legendre polynomials, for example) which could be used to describe the displacements and derivatives in analytic functional form. The important advantage sought would be easier computation with round-off error.

REPLY TO F.G. BUTLER—Perhaps a criticism of our paper for the lack of specific examples and results obtained may be justified, although we thought that the scope and complexity of the material was such as to preclude an even greater length. It is our intention to prepare this subject for another SAE paper at some early future date. The fact is that this analytic method for cam design succeeds very well—a fact we would be delighted to discuss and demonstrate to anyone having a sufficient interest.

REPLY TO MAX J. TAUSCHEK—The authors of this paper are especially appreciative of the particularly perspicacious criticisms brought out by this discussion.

With respect to the question concerning single deg-of-freedom systems, it should be observed (as noted above) that theoretically there is no fixed cam profile which will compensate the end (valve) element for two (or more) deg of freedom at any engine speed—much less over a range of engine speeds. From a practical viewpoint, the question becomes one of degree rather than kind. If, for example, the system happens to display 2 deg where the first is a low natural resonance (20,000 cpm) and the second is high (200,000 cpm), then we would presently believe good success could be obtained by designing for the lower resonance while ignoring the higher provided that the acceleration forces are sufficiently limited. There is a great deal to be said on this subject having to do with the actual valve train compression deflections under acceleration forces as these relate to the cam profile accuracy required for good valve control performance. We have studied the theoretical part of this problem and believe the design can be handled within certain limitations on engine speed range and the ratios of first to second resonant frequencies.

In reference to the statement about the great importance of maintaining high stiffness with low weight in the valve train as well as stiffness at the rocker arm support points and camshaft bearings, we agree most forcibly. Just as suggested, there are instances where the desired engine performance is found incompatible with the cam design specification after the valve train parts weights and stiffness have been measured. In this case, the most prudent course of action is to improve the valve train design or modify the performance objectives. Very often the improvement must

be directed toward the valve train support system including, on occasion, the torsional rigidity of the camshaft.

General Comments

It should be appreciated that the status of the modified polydyne cam design method reported upon in this paper (dated June, 1960) corresponds with the state of development as of the year 1959—except that the computer programs for the IBM 650 had been reprogrammed into Fortran notation for the IBM 704. These changes brought about a number of refinements and sophistications in the method which, it was thought, was best left to the discussions of some future paper. The present status of the method (June, 1961) provides, for example:

1. A special exponent scanning program—which examines the critical values of certain design parameters and allows high speed resolution of the optimum exponent choices.

2. The Hertz bearing stress is programmed for a rapid evaluation of the contact stress at any critical valve train interface.

3. The paper provides certain kinematic equations which are identified with the flat-faced cam follower. We have programmed the kinematic equations of motion for the translated roll follower with also equations for the pivoted roll follower.

4. A compensation in the cam design for the valve train deflections due to gas pressure loads on the exhaust valve face has been pointed out as a special problem in several of the reviews. This compensation is particularly important and necessary for engines which are supercharged or for engines which have a low natural resonant frequency valve train. A special difficulty with this problem is that the gas pressure load decreases as a cubic function of time and reaches zero, normally, at about 1/2 to 2/3 of the cam opening side half event. The present modified polydyne cam design method has obtained the necessary changes in the differential equations and solution boundary conditions with the corresponding changes to the computer programs required for the gas load problem solution.

—continued from page 584, M. PALIOBAGIS and E.J. KRABACHER

15. M. Eugene Merchant, Hans Ernst and E.J. Krabacher, "Tool Wear Tests Speeded, "Nucleonics, Vol. 14, No. 5, (May, 1956), 54-57.

16. "Use of Radio-Active Tracers for Investigating Cutting Tool Wear," Machinery, Vol. 88, (April 20, 1956).

17. E. I. Goodman, "How Cutting Tool Wear is Determined by Radioactivity," Carbide Engineering, (January, 1958), 11-14.

18. F. Daasch, S. Ersler and W. D. McHenry, "Machining Studies by Radioactive Methods," U. S. Dept. of Commerce PB111473.

19. O. Hake, "Die Radioaktive Verschleibmessung in der Zerspanung," Grundlagenuntersuchungen bei der Zerspanung, Nr. 11, (Feb. 7, 1958), 385-394.

20. B. Colding and L. G. Erwall, "Accuracy and Applicability of Radioactive Studies of Carbide Cutting Tool Life," Radioisotope Conference (Eng.) 1954, Vol. II, 181-187.

21. Robert Hook, "Radio-Isotopes Measure Tool Wear in Metal Cutting," Machinery, (U.S.) Vol. 62, No. 3, (Nov. 1955), 141-145.

22. F. J. Daasch, "Machinability Testing and the use of the Radiometric Method," Proceedings of Industrial Technology Conference on Metals Processing, U.S. Dept of Commerce, PB 151208, (Oct. 16-18, 1957), pp. E1-1-10.

23. "Radioactive Tracers Assist Cutting Oil Research," Scientific Lubrication, (April, 1956).

Theoretical Prediction of the

THE EFFECT OF TRACTION on cornering force is one of the major factors affecting handling of an automobile. The basic difference between the handling characteristics of front wheel drive and rear wheel drive vehicles is determined almost exclusively by the interaction between traction and cornering force. The amount of "understeer" or "oversteer" which has to be "built-in" the vehicle to achieve satisfactory handling characteristics is governed to a great extent by the effect of power application on cornering force.

Very little experimental work has been performed in this special field. Previous investigations were limited exclusively to tire testing on drums. To the best of our knowledge, no attempts have been made to explain this phenomenon theoretically. Tire theories developed in the past were concerned primarily with the study of lateral tire force and aligning torque and did not explain the phenomenon of interaction between traction and cornering force.

The theory presented in this paper undertakes to explain the effect of traction on cornering force by using a new concept of "spring interaction." This theory has been substantiated by tire road tests. Very good correlation was found between calculated and test data. As a result of this study, the major factors determining the effect of power application on cornering force were established.

These factors are:

1. Reduction of overall lateral stiffness of a tire.
2. Reduction of effective lateral coefficient of friction.

Since the effect of tractive power application on cornering force cannot be separated from the effect of vertical load, the latter is also included in the discussion. Application of the tire theory presented in this paper to the evaluation of vehicle handling is reviewed following an explanation of the theoretical concepts.

Basic Nature of Pneumatic Tire

The pneumatic tire is in many respects very similar to the muscles of animals in function, structure, and basic characteristics. Both tires and muscles are elastic, deflecting in the act of transmitting forces; both are strongly nonlinear in their responses to external stimuli; both are greatly influenced by temperature changes. It is rather a strange coincidence that the inventor of the pneumatic tire, John Dunlop, was a veterinarian.

This similarity is mentioned here only as a scientific oddity. To pursue the analogy in the hope of clarifying our understanding of tire behavior would obviously be fruitless; it would likely produce more confusion than enlightenment. A much better analytical approach is to consider the tire as a three-dimensional spring system, which transmits forces in the vertical, lateral, and longitudinal directions. The pneumatic tire is not an air spring. The elastic properties of a pneumatic tire are determined almost exclusively by deformations of the carcass and the tread. The principal function of the compressed air in the tire is to preload the carcass and therefore to predetermine the range of utilization of the basic characteristics of the tire. A load increase in an air spring results in an increase of pressure, but in a pneumatic tire it results in an increase of the tire contact area with virtually no pressure change.

By defining a tire as a spring, we can adopt the general term "spring rate" or "spring constant" to describe its force-deflection characteristics. In automotive practice, we use tire rate expressed in lb/in. only in a sense of vertical tire rate. In this case, we define the rate as a ratio of vertical load to deflection. However, in describing the same relationship in the case of lateral force, we use terms such as

Effect of Traction on Cornering Force

slip angle in degrees and cornering power in lb/deg, instead of lateral deflection in inches and lateral rate in lb/in. Tire deflection as a result of longitudinal forces is usually expressed by the wheel slip in per cent and the term representing longitudinal tire rate does not exist at all. The lack of a common terminology as applied to the pneumatic tire is one of the obstacles in the way of understanding the nature of a tire.

Model of Pneumatic Tire and Interaction Effects

The general model of a pneumatic tire can be considered as a three-dimensional springing and damping system. In the first approximation, for purposes of simplification, we ignore the damping properties of a tire and limit ourselves to a description of its springing characteristics. Then the model of a tire can be constructed from three groups of elementary springs (Fig. 1). The axes of symmetry of these springs are located as follows:

1. In the plane of the wheel concentrically with the wheel rim.
2. Perpendicular to the plane of the wheel.
3. In the plane of the wheel radially to its center.

For a sufficiently small element of a tire, the curvature of the axis of the elementary spring from the first group can be neglected. Then each tire element will consist of three elementary springs whose axes of symmetry are perpendicular to each other. Let us denote the axes of these elementary springs as X, Y, and Z and their basic spring constants or rates as C_{xo}, C_{yo}, and C_{zo}, respectively. These basic spring rates express longitudinal, lateral, and vertical load-deflection characteristics. The basic spring rate is defined as the load-deflection ratio derived from each of these elementary springs independently. This independent operation of each elementary spring is possible only when one spring is completely separated from the others. However, under actual conditions these three elementary springs which comprise the tire element are connected together in one single unit. This connection results in interaction effects, which play a very significant role in tire mechanics and can be considered a major factor affecting car handling. The "interaction effect" is defined as a change of rate in one elementary spring, due to forces acting on the other elementary springs within the same element of a tire. When a tire element is subjected to forces acting simultaneously along two or all three axes, the spring rates along each of the axes vary. The change of spring rates under the circumstances described above can be illustrated on the model of the tire element shown in Fig. 2.

This model is constructed from three coil springs. The axes of symmetry of these springs are perpendicular to each other. When no load is applied to any one of them, then the rates of these individual springs remain constant. These rates constitute the basic spring constants C_{xo}, C_{yo}, and C_{zo}. The springs are connected together in one unit. Outer ends of each spring are attached to universal joints, of which one is stationary and the other can slide in a frictionless guide whose center line coincides with the undistorted spring axis. Load-deflection characteristics of each spring can be ascertained by applying load to the spring through the movable universal joint and measuring displacement of the latter. Let us identify the springs situated along x, y, and z

Walter Bergman
Ford Motor Co.

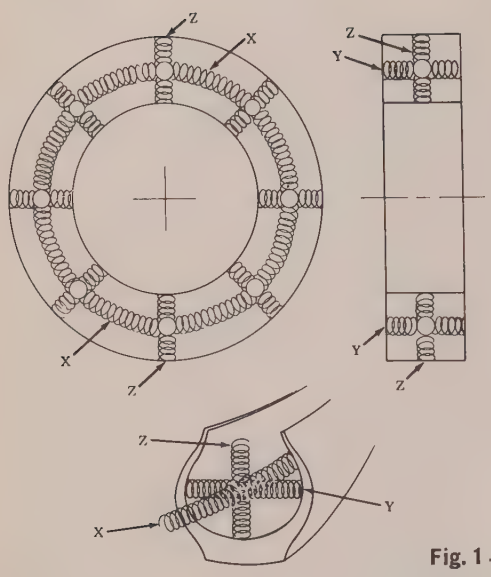

Fig. 1 — Model of a tire

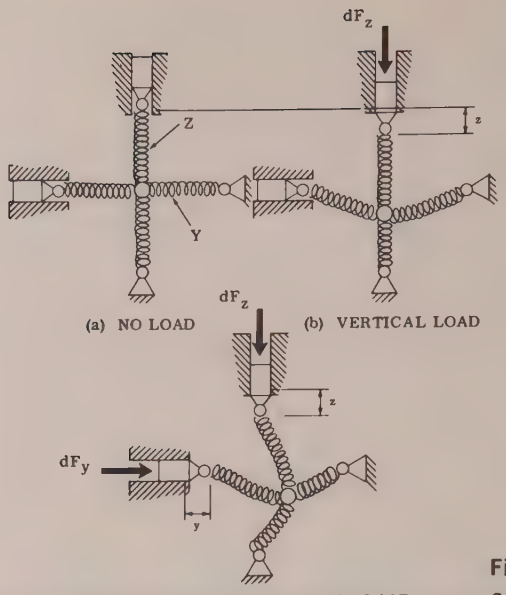

Fig. 2 — Model of a tire element

axis as "X," "Y," and "Z," respectively. If we measure load-deflection characteristics of the spring "Y" and at the same time apply a progressively increasing load to the spring "Z," we will find that the rate of the spring "Y" shows a decrease with an increase of the load acting on spring "Z." Conversely, the rate of the spring "Z" also decreases as the load acting on spring "Y" increases. This phenomenon can be explained by the fact that the load increase on the "Z" spring produces bending of the axis of the "Y" spring, which results in a rate decrease of the latter. If three progressively increasing forces, dF_X, dF_Y, dF_Z act on elementary springs "X," "Y," and "Z," each of these springs will experience a reduction of its respective rate due to the increase in forces applied to the other two springs. The force dF_X will produce bending of the axes of the springs "Y" and "Z" and therefore will cause reduction of their rates. Similarly, forces dF_Y and dF_Z will cause rate reductions in the springs "X"-"Z" and "X"-"Y," respectively.

Let us define this phenomenon of spring rate reduction, due to an increased load applied to another spring of the same spring system, as a primary rate reduction effect. This will distinguish it from the secondary effect described below.

The secondary rate reduction effect in a three-dimensional spring system can be defined as a rate reduction of a spring with an increase of load acting on it, when the loads applied to another spring of the system are constant. Let us apply progressively increasing load to the spring "Z" while maintaining constant loads acting on the spring "X" and "Y". From the previous discussion, an increase of load applied to the spring "Z" will cause, as a primary effect, rate reduction of the springs X and Y. As a result of rate reductions in the springs X and Y, constant loads applied to them will increase their deflections. Since all three springs are connected together in one unit, an increase in the deflections of springs "X" and "Y" will cause increased bending of the axis of the spring "Z" and therefore reduce its rate. Rate reduction effects under various conditions are expressed by linear equations which are shown in the Appendix.

Vertical Tire Characteristics

Vertical tire characteristics are determined mainly by properties of the elementary springs "Z" located radially in the plane of the wheel. By applying a vertical load to the wheel we produce deflections of the elementary springs "Z" which are in contact with the road surface and also we increase the number of these springs engaged in contact with the road surface. Therefore, application of vertical load results not only in deflections of elementary springs "Z" but also in and increase of the contact area.

Since the surface of an unloaded tire is one of double curvature, it contracts within its contact area as a result of flattening due to load application. The tire has a curved profile in the side elevation as well as in the front view (tread radius), therefore compression takes place in both directions. Compression of the tire surface has been demonstrated by a rather simple test described by Schuster and Weichsler (1).* The test was conducted by rolling a tire over a paper strip which had a grid chalked on its surface. These chalk lines were thus transferred to the tire surface. The resulting grid squares on the tire surface were larger than the original squares drawn on the paper. This proves that compression takes place within the tire contact area.

Compression of the tire surface within the contact area

*Numbers in parentheses designate References at end of paper.

also can be demonstrated directly by observing the contact area from underneath the tire through a glass plate while a load is applied. Deformation of the tire surface within the contact area naturally implies stresses. Martin (2) actually measured stress distribution within the contact area and found that stresses are directed toward its center. In applying the concept of interaction developed in the preceding section of this paper, it would appear that these stresses produce bending of the vertical springs, thus reducing tire rate.

Compression of the tire surface can be explained simply. The projected contact area becomes the chord of the undeflected arc-shaped surface of the tire. Since a chord is always shorter than its arc, the surface must compress in order to comply with these new conditions.

Heldt (3) found that the actual size of the contact area is smaller than that which would be calculated subject to the assumption that area is directly proportional to deflection and load; he attributes this to the fact that when a tire deflects under load, not only is its surface flattened out within the contact area, but also its side walls bend additionally, thus contributing to total deflection. Therefore, as a result of compression of the tire contact area and bending of the side walls, the actual length and width of the contact area are smaller than those which would be calculated simply as lengths of the chords plotted to the original undeformed major radius of the tire and to the tread radius.

Let us define the ratio of actual length and width of the tire contact area to the respective chord lengths as a deformation coefficient. Then the length and width of the contact area can be expressed as a product of a chord length and this deformation coefficient. The height of this corrected chord length represents vertical tire deflection. The size of the contact area was determined by assuming a rectangular shape for the contact area. This assumption is justified for passenger-car tires, since it is in good agreement with the actual shape of the tire imprint obtained from test, as shown in Fig. 3. Based on findings of Martin (2), parabolic pressure distribution was assumed across the length of the contact area.

According to the concept of interaction developed in this paper, the lateral and longitudinal stresses acting at the tire contact area produce a decrease of vertical unit rate (rate of elementary "Z" springs). Since these stresses originate with the vertical load and show an increase with an increase of vertical load, we can conclude that increased vertical load causes a decrease of vertical unit rate. By using the assumptions outlined, above, mathematical equations showing the relationship between vertical load and tire deflection were developed. These are Eq. (9) and (10) in the Appendix.

If the vertical unit rate were constant, tire deflection determined from these equations would increase less than linearly with an increase of load (Fig. 4a). However, since the actual vertical unit rate decreases with an increase of load and thus conteracts nonlinearity of the basic trend, the resultant tire load deflection curve shows an approximately linear character (Fig. 4b) almost within the whole range of deflections, except in the region of very small deflection values.

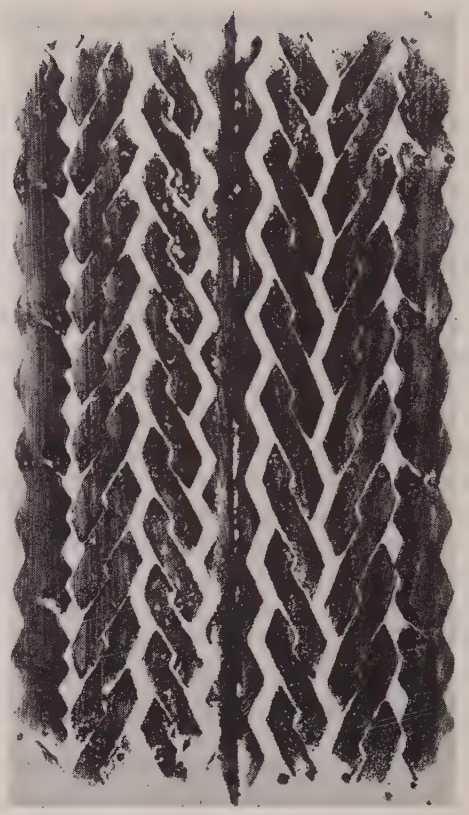

Fig. 3 — Imprint of a tire contact area for 6:70-15 tire 24-psi, 1065-lb load

The calculated tire load-deflection curve agrees closely with the test results, thus confirming our assumption of linear unit rate reduction with an increase of load.

Vertical tire rate is usually determined by loading the tire under static conditions within rather narrow limits of load variations below and above the rated load. The results of these tests indicate that the tire rate for all practical purposes is constant within the load limits used during the test. The fact that the extended test curve does not meet the origin of the coordinate system proves that this approximate linearity ends at small tire deflections.

According to the spring interaction concept, traction force and cornering force will produce an additional reduction of the vertical unit rate. The mechanism of lateral unit rate reduction, which is discussed in the next section, is similar to that of vertical unit rate reduction. Therefore, we might expect larger tire deflections due to lateral weight transfer in cornering than those due to the same weight transfer in static test. Power application should result in even greater discrepancies between static and dynamic value of tire rates. These predictions are based exclusively on the spring in-

teraction concept and have not yet been substantiated by tests.

Lateral Tire Characteristics

Definitions - Lateral tire characteristics can be described in our model by the springing properties of the second group of elementary springs "Y" with the axis of symmetry located perpendicular to the plane of the wheel. One could imagine these lateral springs not separated from each other but rather connected together with some kind of band or string. Therefore, a lateral force applied to the tire within the contact area produces deflection of these elementary springs, not only within the contact area, but also beyond it (Fig. 5). This phenomenon was observed experimentally by photographing the lateral distortion of a tire operating under a slip angle (4). Considering the significance of the existence of deformation zones beyond the limits of the contact area, let us identify these zones as elastic lead and elastic trail. Elastic lead is defined as the length of the deformation region forward of the contact area. Conversely, elastic trail constitutes the length of the deformation zone behind the area of contact.

Lateral tire forces are determined by lateral tire deformations. Considering that tire deformations extend beyond the region of the contact area, we conclude that the elastic forces acting on the wheel rim have their source not only within the contact area, but also beyond it. Deformations of a tire are distributed unsymmetrically with respect to the wheel axis. Deformations in the aft region are greater than those in the forward region. We assume that the distribution of lateral elastic forces acting on the wheel rim is proportional to the lateral deformations of a tire. Therefore, if we replace the distributed elastic forces by a concentrated

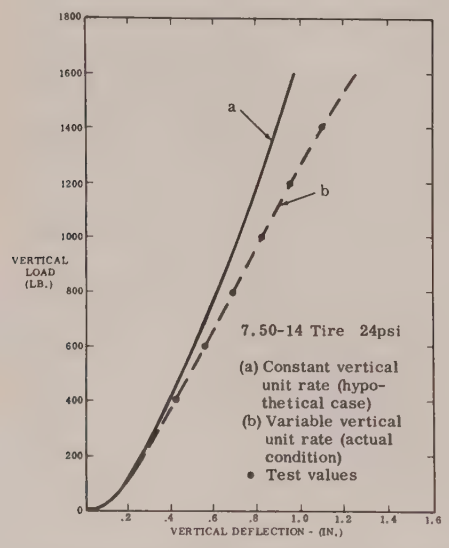

Fig. 4 — Vertical load versus tire deflection — calculated and tested values

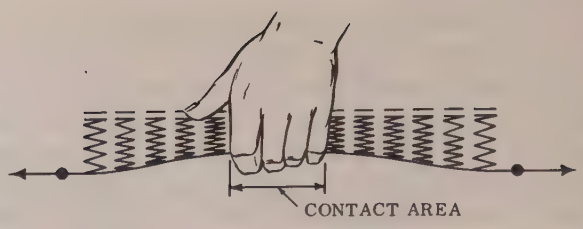

Fig. 5 — Illustration of lateral elasticity of the pneumatic tire

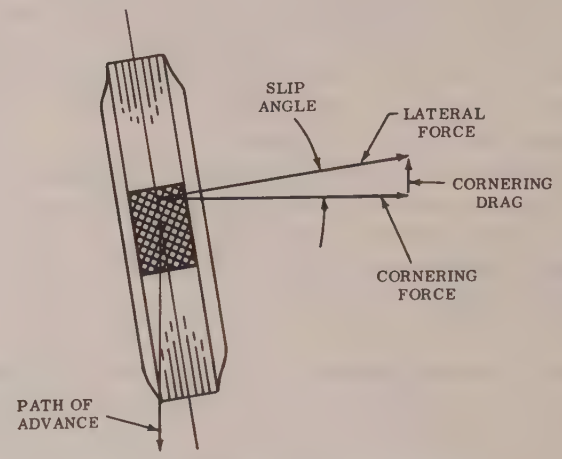

Fig. 6 — Components of lateral tire force

one, the point of application of the latter will be located behind the wheel axis. The horizontal distance between the point of application of this force and the wheel axis constitutes the moment arm of this lateral tire force. In tire terminology, this moment arm is known as pneumatic trail.

The reaction caused by the lateral elastic force acting on the wheel rim is a lateral force acting between the tire and the road surface. This lateral reaction is confined within the contact area and is limited by the friction between the tire and road surface. The lateral force acting between the tire and road is that part of the total available friction force, at the tire contact area, which is utilized as the reaction to the elastic force. In tire mechanics we usually define lateral force as a lateral force acting between the tire and the road surface.

The moment produced by lateral tire force about the vertical axis through the center of the wheel is called aligning torque. Aligning torque also can be defined as a product of the lateral tire force and the pneumatic trail. The lateral tire force acts perpendicular to the plane of the wheel and can be resolved into two components: cornering force and cornering drag (Fig. 6). Cornering force is defined as a component of the lateral tire force acting perpendicular to the direction of motion. Cornering drag constitutes a component of the lateral tire force in the direction of motion. The cornering drag is additive to rolling resistance of a tire.

The angle between the direction of motion and the plane of the wheel is defined as slip angle. Slip angle represents a convenient measure of lateral tire deflection. The term

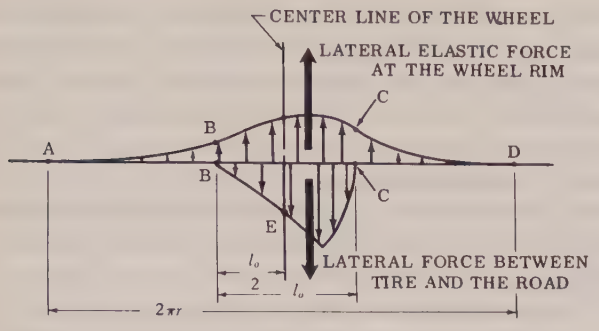

Fig. 7 — Free body diagram of developed circumference of a tire

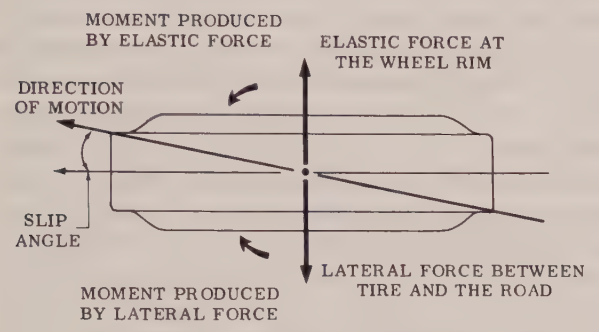
MOMENT PRODUCED BY ELASTIC FORCE
ELASTIC FORCE AT THE WHEEL RIM
DIRECTION OF MOTION
SLIP ANGLE
LATERAL FORCE BETWEEN TIRE AND THE ROAD
MOMENT PRODUCED BY LATERAL FORCE

Fig. 8 — Simplified free body diagram of a tire

"slip angle" is rather a paradox, because this angle can be produced only when no slip or sliding between tire and the ground takes place. The process of producing the slip angle can be described as follows:

When a tire element touches the ground, friction causes it to travel in the direction of motion; however, the upper part of this element, being attached to the rim, continues to move in the plane of the wheel. Therefore, each element will deflect laterally and this deflection will progressively increase from the front toward the rear of the contact area. Assuming that the lateral rate of all elements is constant, we conclude that the deflection of each element will produce a force proportional to its deflection. Therefore, the progressively increasing deflection of the tire elements along the contact area will result in progressively increasing force. When the lateral force at the tire element reaches the value of friction force, the tire element breaks loose and slides laterally toward its initial undistorted position.

The free body diagram of the developed circumference of the laterally deformed tire is shown in Fig. 7. Area A B C D represents the lateral elastic force acting at the wheel rim and the area bounded by the curve B E C represents lateral tire force between the tire and the road surface. The lateral elastic force is equal to lateral tire force between the tire and ground. Therefore, areas shown in Fig. 7 are also equal to each other. By substituting single forces for the distributed forces, we have to apply these forces at the c.g. of the areas bounded by the curves A B C D and B E C.

Elastic force and lateral force at the contact area produce the same moment about the vertical axis through the geometrical center of the wheel. Therefore, c.g.'s of the areas bounded by the curves A B C D and B E C are located at the same distance behind the center line of a wheel. Then the free body diagram of the tire can be represented simply by single forces applied at the center of the wheel perpendicular to the wheel plane, combined with moments about the vertical axis through the wheel center (Fig. 8).

Review of Existing Tire Theories - Tire theories developed in the past can be broken down into two major categories. One group is based on study of lateral elastic forces around the whole circumference of the tire. The other is concerned with lateral force between the tire and the road surface. Von Schlippe's (5) and Fiala's (6) theories can be considered typical representatives of these two categories. Von Schlippe's theory was based on an assumption of linear path of travel of the tire element within the whole length of the contact area. Deformations of a tire outside the area of contact were described by an "e" function. Lateral tire force was expressed in terms of lateral tire deflections and other parameters. Difficulties associated with measurement of lateral tire defelction limit the practical application of Von Schlippe's (5) theory. Furthermore, assumption of linear deformation within the whole length of the contact area is valid only for uniform pressure distribution and small values of slip angles.

Fiala (6) determines lateral force from deformation of the tread relative to the deformed carcass. He assumes that lateral displacement of the tread in relation to the carcass takes place only within the contact area. We believe that this assumption can be justified only in the case when the tread is divided into a series of separate lugs. On modern tires, the tread forms a continuous band and its deformation cannot be confined within the contact area. As a result of this assumption, the values of aligning torque calculated from Fiala's equations are lower than those obtained from tests. In spite of limitations discussed above, the theories of Fiala (6) and Von Schlippe (5) can be considered as the most fundamental and significant works in the field of tire mechanics.

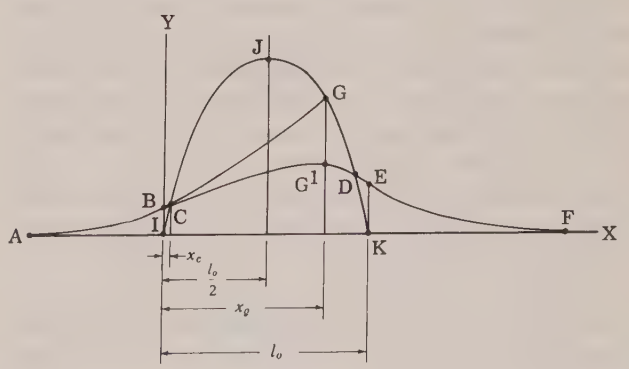

Fig. 9 — Lateral force diagrams superimposed on friction force diagram

New Tire Theory - Due to the immense complexity of tire mechanics, it is very difficult, if not impossible, to develop mathematical equations describing lateral tire force and aligning torque without using a number of simplifying assumptions.

Before discussing the present theory and the assumptions on which it was developed, let us attempt to describe actual lateral tire characteristics as we see them. Fig. 9 shows the lateral elastic force diagram ABCG'DEF superimposed by the curves CG and ICJGDK, representing lateral force intensity between tire and ground and friction force intensity, respectively. The lateral elastic force diagram can be broken down into three regions, one which lies within the limits of the contact area and two which are outside of it.

Extensive experimental study of lateral tire force between the tire and ground was conducted by Gough (7, 8) and Cooper (9). These authors measured distribution of lateral tire force and lateral deformations across the length of the contact area with a specially designed apparatus.

Lateral deformations along the circumference of a tire were studied experimentally by Huber (4) by painting reference lines on the tread of a tire and photographing their lateral distortions. Observations of these distorted lines in the regions outside the contact area show that these lines can be considered as exponential curves. This confirms the validity of Von Schlippe's (5) approach in the regions outside of the contact area. Therefore, curves AB and EF in the outside regions of the elastic force diagram can be expressed by an "e" function.

The region within the contact area can be divided into regions of adhesion and sliding. It is generally accepted that sliding occurs in the rear part of the contact area. It starts at the point G, where intensity of lateral force between tire and ground reaches the value of friction force intensity. However, we believe that sliding also takes place in the front region of the contact area. The sliding in the front part of the contact area is due to the fact that within the region between points B and C the intensity of elastic force exceeds that of the friction force. Within this region, the tire element is subjected to forces transmitted to it from the adhesion zone and also to progressively increasing friction force. This results in rather complex motion of the tire element which is neither exponential nor linear. The adhesion starts first at the point C where intensity of friction forces reaches the intensity of elastic force. Therefore, on our diagram shown on Fig. 9 the length of adhesion region can be expressed as a difference $X_g - X_c$. Linearity of the path of travel of a tire element ends at the point G^1 and not at the point of intersection of the elastic force curve with the friction force curve (Point D).

The above discussion assumes parabolic pressure distribution across the length of the contact area. The validity of this assumption has been confirmed by experimental findings of Martin (2).

Due to nonuniform distribution of lateral forces between the tire and the ground, deformations of the tire within the elastic trail regions are greater than those in the elastic lead regions. This results in a larger component of elastic force produced by deformations in the elastic trail region, which in turn results in an increase of aligning torque. The component of aligning torque produced by the unequal elastic force components in the regions outside the contact area is additive to the torque resulting from unequal deformation distribution within the contact area.

This explains why the values of aligning torque obtained from tests are higher than those calculated from deformation of the tread within the contact area.

Present theory determined the lateral force as being an elastic force acting on the wheel rim. Since it is very difficult to express this force mathematically, we substitute for it another force which has the same magnitude and produces the same moment about the vertical axis through the center of the wheel as the actual elastic force. However, the distribution of this substitute force is greatly simplified, compared to that of actual elastic forces. In the discussion below, we will refer to this substitute force as a lateral force. The moment produced by this force about the vertical axis through the center of the wheel will be referred to as an aligning torque. Intensity of the lateral force is derived from deformation of the tire, assuming linearity between force intensity and corresponding deflection. Deformation of the tire is the lateral displacement of the center of tire tread with respect to the center line of the rim. Tread is treated as a part of a carcass. Therefore, relative deflection of the tread with respect to the carcass is not considered. The assumption is made that a tire element first starts to deflect laterally at the point of entry into the area of contact. Accordingly, elastic lead is omitted in this simplified representation of lateral force. Furthermore, it is assumed that lateral deflection of the tire element increases linearly during its motion from the front toward the rear until lateral force intensity reaches the value of friction force intensity. At this point, which is defined as the breakaway point, the tire element starts to break loose and slide back toward its original undisplaced position. The distance measured along the center line of the rim, between the breakaway point and the front end of the tire contact area, is defined as the length of the adhesion region. Within this adhesion region, the tire element describes a linear path which is parallel to the velocity vector of the wheel. Therefore, the angle between the path described by the tire element and the wheel is the slip angle. Assumption of linearity of the path described by the tire element can be justified only when the radius of curvature described by the wheel is considerably larger than the length of the contact area. It is assumed that a tire element returns to its initial position at the center line of the undistorted tread, not at the rear end of the contact area, but some distance behind it. The distance between the rear end of the contact area and return point, measured along the wheel rim, constitutes the length of the elastic trail region.

We assume a linear path of travel of the tire element within the elastic trail region and also in the adjacent rear portion of the contact area, where lateral force intensity exceeds friction force intensity.

The friction force intensity is determined by assuming parabolic pressure distribution along the length of the contact area and constant pressure distribution across its width.

Lateral force Diagram a, constructed subject to the assumptions discussed above, is shown in Fig. 10. This diagram is superimposed on friction force Diagram b. Both diagrams are plotted in the XY coordinate system whose origin is chosen to be at the front end of the contact area on the center line of the wheel rim. The Y axis is chosen to be parallel to the axis of wheel rotation and, consequently, the X axis is parallel to the plane of the wheel. Symbols shown on the diagram are explained in Table 1.

The ratio of length of effective area of application of lateral force to length of the contact area is defined as the elastic trail coefficient. This coefficient is determined experimentally from actual measurement of aligning torque value in the same way that unit rate is obtained from the experimentally obtained value of lateral force. Measurement of aligning torque and lateral force will enable us to calculate the values of elastic trail coefficient and lateral unit rate from tire equations. (See Eq. (34)and (35) in the Appendix.) Assumptions made previously of proportionality between force intensity and lateral tire deflection allow us to represent lateral deformation of the tire by a diagram shown in Fig. 11, which is similar to the force diagram shown in Fig. 10 above. Angles α and β, shown on the lateral deflection diagram on Fig. 11, are slip angle and elastic trail angle, respectively. Elastic trail angle is defined as an angle between the plane of the wheel and the deformed center line of the tread, within the elastic trail region and the adjacent part of the contact area.

The equation of lateral tire force (Eq. 34) was derived by integrating the area FAE shown on Fig. 10.

The mathematical expression of aligning torque (Eq. 35) was obtained by taking moments of the area FAE about the center of the contact area. Here we assume that the center of the contact area coincides with the center line of the wheel axis.

Effect of Camber Thrust on Lateral Tire Force - Camber thrust is defined as a horizontal lateral force between the tire and road, produced due to an angle between the plane of the wheel and the vertical (Fig. 12). This angle is called the dynamic camber angle, to distinguish it from static camber used in automotive design practice. Camber thrust always acts in the direction in which the top of the wheel leans. Since in most modern cars the wheels lean toward the outside of a turn, camber thrust opposes lateral tire force, thus reducing the latter. The value of camber thrust can be computed from Eq. (46), shown in the Appendix.

We consider the dynamic camber angle as being positive when the wheel leans in the same direction in which it turns. Therefore, positive dynamic camber angle produces positive camber thrust, which is additive to the lateral force. Negative dynamic camber angle produces negative camber thrust, which opposes the lateral tire force.

Camber thrust also affects the effective coefficient of friction between the tire and road surface which can be util-

Table 1 - Symbols Used in Fig. 10

F	Front end of contact area
R	Rear end of contact area
A	Breakaway point
E	Rear end of elastic trail region
X_a	Length of adhesion region
l_o	Length of contact area
l_1	Effective length of application of lateral tire force

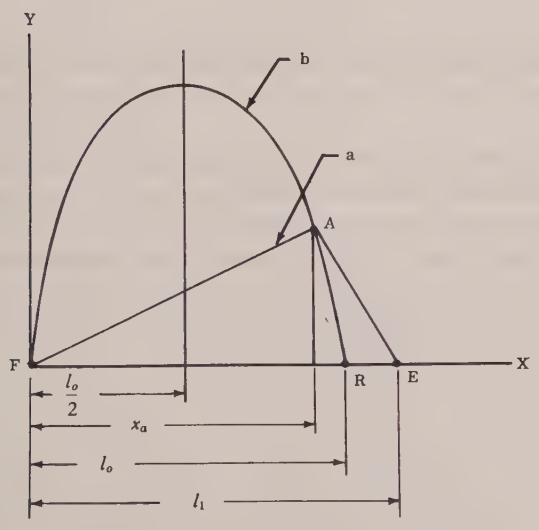

Fig. 10 — Simplified lateral force diagram superimposed on friction force diagram

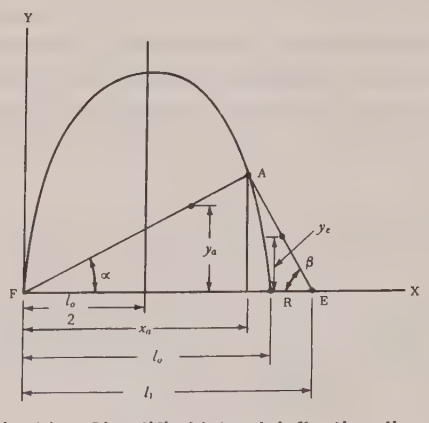

Fig. 11 — Simplified lateral deflection diagram

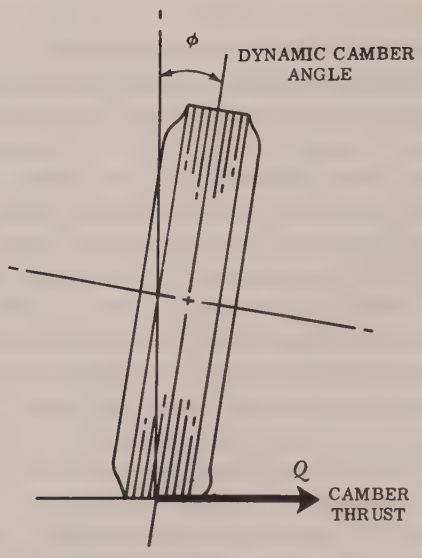

Fig. 12 — Camber thrust

ized by the lateral tire force produced by slip angle. The static coefficient of friction between the tire and the road surface is defined as the ratio of a maximum resultant horizontal force between the tire and road surface to the vertical wheel load. When the noncambered wheel rolls under slip angle and only lateral force produced by the slip angle acts upon it in the horizontal plane, the effective coefficient of friction available for this force is equal to the static coefficient of friction. We ignore the force resulting from tire rolling resistance as being small and also do not consider sliding in certain parts of the contact area.

In the case of a cambered wheel subject to a slip angle, only a part of the static coefficient of friction can be utilized by the lateral tire force produced by slip angle, if camber thrust and this lateral force are acting in the same direction. The effective coefficient of friction will be equal to the difference between the static coefficient of friction and the ratio of camber thrust to vertical wheel load. Therefore, camber thrust, when acting in the same direction as the lateral force produced by slip angle, reduces the effective coefficient of friction available for the latter force.

In the case when camber thrust acts in an opposite direction to lateral force due to slip angle, it increases the effective coefficient of friction available for the latter force.

The effective coefficient of friction then becomes equal to the sum of the static coefficient of friction and the ratio of camber thrust to vertical wheel load.

Effect of Traction on Cornering Force

Forces Acting on a Tire - In the general case, when power is applied to a cambered tire subject to a slip angle, the following forces are acting on the tire:

1. Effective tractive effort.

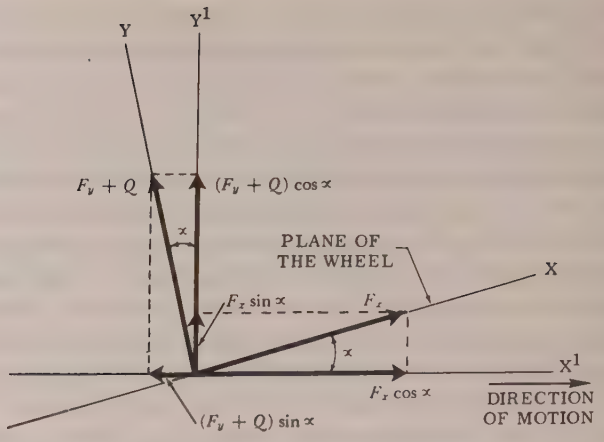

Fig. 13 — Resultant cornering and traction forces acting at the tire contact area

2. Lateral tire force due to slip angle.
3. Camber thrust.
4. Vertical load.

Effective tractive effort is defined as the resultant longitudinal force between the tire and road acting in the plane of the wheel. The effective tractive effort is equal to tractive effort less rolling resistance and power transmission losses in a tire. The tractive effort is determined as the ratio of wheel torque to axle height. Rolling resistance is defined as a horizontal longitudinal force resulting from hysteresis losses in a free-rolling tire. Rolling resistance acts in the plane of the wheel in a direction opposite to the wheel motion.

Power transmission losses (10) are defined as additional hysteresis losses in a tire caused by deformation of the tire due to transmission of a torque through the tire. Therefore, these losses are equal to the difference between the tractive effort produced by the applied wheel torque required to propel the tire and the horizontal force necessary to tow the tire.

Let us define cornering force as a component of the resultant horizontal force between the tire and road surface, acting in the direction perpendicular to direction of wheel travel.

Traction force is defined as a component of the resultant horizontal force between the tire and road surface acting in the direction of wheel motion.

Then traction force and cornering force can be determined simply by resolving effective tractive effort and lateral tire forces into components acting in the direction of motion and perpendicular to it (Fig. 13).

$$F_x^1 = F_x \cos\alpha - (F_y + Q)\sin\alpha$$

$$F_y^1 = (F_y + Q)\cos\alpha + F_x \sin\alpha \qquad (1)$$

where:

$F_x{}^1$ = Traction force
F_y1 = Cornering force
F_x = Effective tractive effort
F_y = Lateral tire force due to slip angle
Q = Camber thrust
α = Slip angle

The component of the effective tractive effort $F_X \sin \alpha$ acts in the direction of cornering force and thus assists the latter. However, the effect of this factor is small compared to the effects of other factors which produce reduction of cornering force due to power application. Therefore, the final effect of power application on cornering force results in reduction of the latter. The major factors reducing lateral force and consequently cornering force are:

1. Reduction of overall lateral tire stiffness due to reduction of lateral unit rate resulting from power application.
2. Reduction of effective lateral coefficient of friction due to power application.

Reduction of Overall Lateral Tire Stiffness Due to Power Application - According to the concept of spring interaction presented in this paper, we find that longitudinal tire force, resulting from power application, produces bending of lateral elementary springs in our tire model. The reduction of lateral unit rate due to power application is assumed to be equal to the product of the effective tractive effort and the lateral bending coefficient. The lateral bending coefficient is defined as an increment of the lateral unit rate reduction produced by a force equal to 1 lb. Since the tire is also subject to vertical load, we might expect an additional reduction of lateral unit rate due to this load. The reduction of lateral unit rate due to vertical load is equal to a product of vertical load and the lateral bending coefficient.

The values of lateral bending coefficients depend on the direction in which force is applied. Therefore, their values for longitudinal forces differ from those for vertical loads. The values of lateral bending coefficients are determined by internal tire design factors and inflation pressure. They are lower for a tire with a stiff carcass and high inflation pressure than for a soft tire with low inflation pressure.

For a given tire, lateral unit rate decreases linearly with an increase of forces acting on it. Therefore, power applied to a tire operating at a slip angle produces a reduction of lateral unit rate, which in turn results in a reduction of the overall lateral stiffness of a tire. When a power application also produces an increase of vertical load, an additional decrease of lateral stiffness of a tire will result.

Reduction of overall lateral tire stiffness produces a reduction of lateral tire force. The lateral tire force is a major component of cornering force. Therefore, reduction of the former results in a decrease of the latter.

Reduction of Effective Lateral Coefficient of Friction Due to Power Application - When power is applied to a tire operating under a slip angle, in the limiting case the resultant of the effective tractive effort and lateral tire force will reach the value of friction force (Fig. 14). Under this condition, lateral tire force and effective tractive effort can be treated as lateral and longitudinal components of the friction force. Therefore, only the lateral component of the friction force and not the whole friction force will limit the lateral tire force. Since it is more convenient to deal with nondimensional coefficients instead of forces, we introduce lateral and longitudinal components of coefficient of friction. The lateral component of coefficient of friction is defined as the ratio of lateral component of friction force to the vertical load. This lateral component of coefficient of friction can also be called effective lateral coeffieicnt of friction. In the case of power application, the maximum lateral force which could be developed at the tire contact area is determined by the effective lateral coefficient of friction and not by the static coefficient of friction. The effective lateral coefficient of friction can be expressed as follows:

where:

$$\mu_y = \sqrt{\mu^2 - \mu_x{}^2} \qquad (2)$$

where:

μ = Static coefficient of friction
μ_X = Effective tractive coefficient

The effective tractive coefficient is defined as the ratio of effective tractive effort to vertical wheel load. The lateral tire force reduces with a decrease in the effective lateral coefficient of friction. Since this coefficient decreases with an increase of effective tractive effort or a decrease of vertical wheel load, corresponding change of these factors will result in a decrease of lateral tire force. It is not difficult to see that the reduction of lateral tire force due to power application is greater at lower values of static coefficient of friction and lower values of vertical wheel loads. Since the lateral tire force is a major component of cornering force, reduction of the former produces a decrease of the latter. Therefore, power application, causing a decrease of effective lateral coefficient of friction, reduces cornering force and thus affects car handling.

Effect of Power Application on Elastic Trail - The effective tractive effort resulting from power application produces deflection of the tire elements in a longitudinal direction. On our tire model, it results in deflection of the longitudinal elementary springs "X." This produces compression of the tire surface within the contact area and in the adjacent forward region. Deflection of the tire elements progressively increases from the front to the rear end of the contact area, causing tension in the region behind the contact area.

An increase of tension in the region behind the contact area results in an elongation of the elastic trail and consequently in an increase of aligning torque and lateral tire

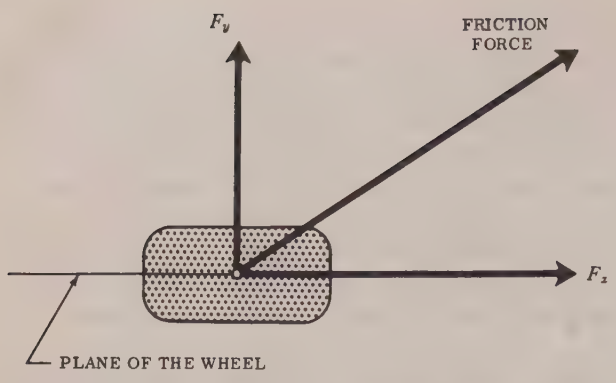

Fig. 14 — Horizontal forces at the tire contact area at skid point

force (11, 12). We assume that the elastic trail coefficient increases linearly with the tractive coefficient. Increased elastic trail, with increased traction, produces increased lateral force and increased aligning torque. Increased lateral force due to an increase in elastic trail is insignificant. It cannot offset a decreased lateral force which is caused by a decrease in the basic lateral unit rate and by a reduction of the effective lateral coefficient of friction. However, an increase of elastic trail is large enough not only to offset the decrease of aligning torque due to reduction of lateral force, but even to produce a slight increase of aligning torque at moderate values of tractive force. This peculiar effect of traction on lateral force has an important implication for front wheel drive vehicles. Moderate power application in cornering produces an increase of aligning torque and decrease of lateral force.

Theoretical Prediction of Lateral Tire Characteristics Under Power Application

To illustrate theories presented in this paper, calculated values of lateral tire forces are plotted against effective tractive effort in Fig. 15 for slip angles of 1-6 deg. Calculations were performed for a 7.50 x 14 tire, 1120 lb vertical wheel load, 1.18 static coefficient of friction (13), and zero dynamic camber angle. The lateral force curves show almost linear decrease at small slip angles. At extreme power application under conditions approaching skidding, lateral tire forces show a pronounced decrease at a progressively increasing rate. The nonlinear reduction of effective lateral coefficient of friction mainly contributes to this rapid decrease of lateral tire force. However, a gradual decrease of lateral force at lower values of effective tractive effort is caused chiefly by reduction of overall lateral tire stiffness, due to decreased lateral unit rate. At larger slip angles, the reduction of effective lateral coefficient comes into effect at lower values of effective tractive effort than is the case at small slip angles.

This causes an increasing nonlinearity of the curves with increasing slip angles. Calculated curves of lateral tire force

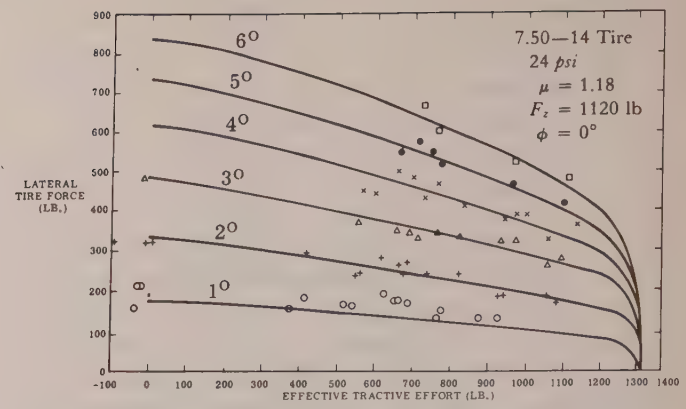

Fig. 15 — Lateral tire force versus effective tractive effort at various slip angles — tested and calculated values

versus effective tractive effort, shown in Fig. 15, are superimposed on values of lateral tire force obtained from road tests. These road tests are discussed in a separate paper by C. A. Freeman (13). Calculated values of lateral tire force exhibit very good correlation with the test data.

To obtain the relationship between cornering force and traction force, their values were computed from lateral force and effective tractive effort. Equations previously shown in the text were used for these computations.

A family of curves showing cornering force versus traction force for slip angles of 1-6 deg was plotted from calculated values (Fig. 16). These curves are basically similar to those shown on Fig. 15. However, the rate of decrease of cornering force with an increase of traction force is less than that of lateral tire force shown in Fig. 15. This reduction in the rate of decrease of cornering force is caused by the component of the effective tractive effort acting in the direction of the cornering force. At extreme power application near the skid point, cornering force shows a more abrupt decrease than lateral tire force. Calculated cornering force versus traction force curves, shown on Fig. 16, shows a trend basically similar to the test data published by Huber and Dietz (14) and Buck (15).

When power is applied to a vehicle negotiating a turn, the vertical loads on outer and inner wheels are different. However, both wheels transmit the same torque. Therefore, it is of a practical interest to see how the effect of power application on lateral tire force varies at different loads. Fig. 17 shows curves of lateral tire force versus effective tractive effort plotted from values which were calculated for two different wheel loads, 1400 and 600 lb. This curve indicates that the wheel load is a major factor limiting power application. The effect of decreasing wheel load is as follows:

1. It reduces the ultimate value of effective tractive effort at which a tire starts to skid.

2. It produces more rapid decrease of lateral tire force at low effective tractive efforts.

Therefore, if both tires are connected together through a normal differential and they transmit the same torque lateral tire force is more greatly reduced on the wheel with

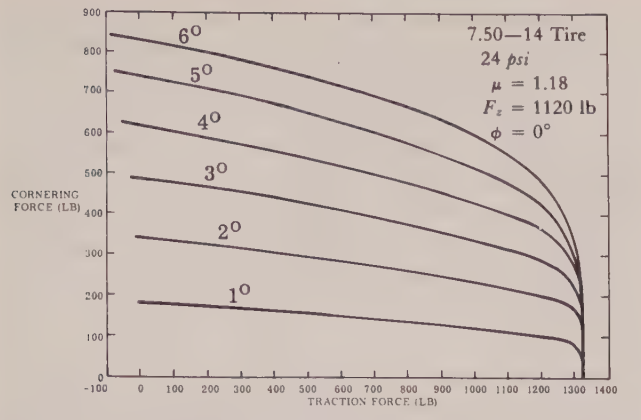

Fig. 16 — Cornering force versus traction force at various slip angles — calculated values

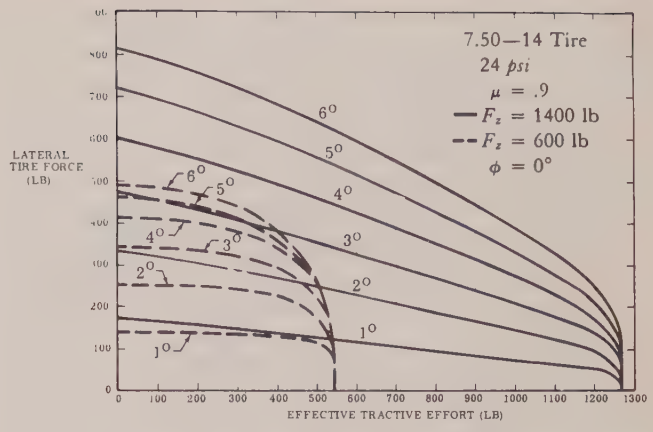

Fig. 17 — Lateral tire force versus effective tractive effort. Families of curves for various slip angles at 1400- and 600-lb vertical wheel load — calculated values

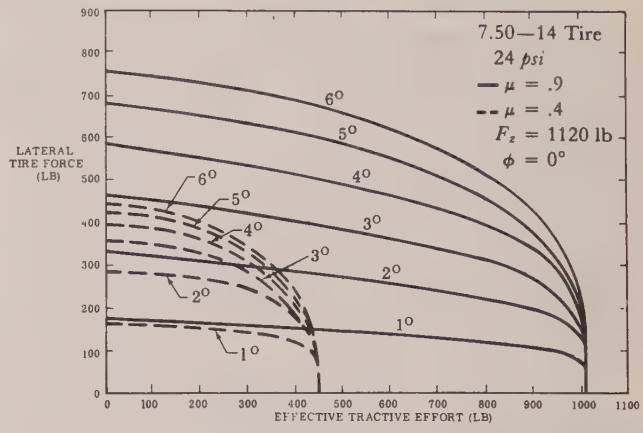

Fig. 18 — Lateral tire force versus effective tractive effort. Families of curves at various slip angles at static coefficient of friction of 0.9 and 0.4 — calculated values

lighter load than on the wheel with the heavier load. The static coefficient of friction has an effect on the relationship between lateral tire force and effective tractive effort very similar to the effect in the case of vertical wheel loads. Curves of lateral tire force versus effective tractive effort, shown on Fig. 18, illustrates this effect. These curves are plotted from calculated values for coefficient of friction of 0.9 and 0.4, which corresponds to dry and wet road surfaces. These curves illustrate that the effect of power application on wet roads is more pronounced than on dry roads.

To illustrate the effect of power application on lateral tire force on tires which have dynamic camber, lateral tire force values are computed for +4 and -4 deg dynamic camber angle. These curves are shown in Fig. 19. They indicate that dynamic camber merely shifts the curve but does not change the basic trend. Calculated values of aligning torque are plotted against effective tractive effort on Fig. 20. Curves on Fig. 20 show a slight increase of aligning torque with a moderate increase of tractive effort, which confirms experimental findings of Joy and Hartley (11, 12) and Bull (16). Implications of the increase of aligning torque due to power application have been discussed previously in the text.

Reduction of the static coefficient of friction has a rather peculiar effect on aligning torque. It produces not only an overall reduction of aligning torque values with moderate power applications, but also reverses the relationship between aligning torque and slip angle.

At a high value of static coefficient of friction (μ = 1.18), aligning torque increases with increasing slip angles, within the range of calculated values up to 6 deg. However, in reducing the static coefficient of friction to 0.4 we find that aligning torque increases with increasing slip angles only up to 2 deg, and then starts to decrease with any further increase of the slip angle. At extreme power application with a tire operating at larger slip angles on a slippery road, the aligning torque even reaches negative values (Fig. 21). Experience has shown that negative values of aligning torque can also be obtained without power application at large slip angles.

Effect of Power Application on Vehicle Handling

The results of theoretical and experimental study of the effects of traction on cornering force are important in enabling us to predict the effects of power application on vehicle handling. The findings of this study also enable us to explain the basic difference between the handling characteristics of front wheel drive and rear wheel drive vehicles.

Power application on a rear wheel drive automobile negotiating a corner results momentarily in a reduction of cornering forces at the rear tires. Since cornering forces at the front tires are momentarily unchanged, reduction of the rear cornering force will produce a yawing moment tending to turn the vehicle into the turn. This well-known phenomenon is sensed by a driver as a breaking loose of the rear of the car and is defined as oversteer. The vehicle can be held on the road either by applying a steering correction (steering out of the turn) or by releasing the accelerator. By releasing the accelerator, we cease the power application; this results in increased cornering forces at the rear tires. When

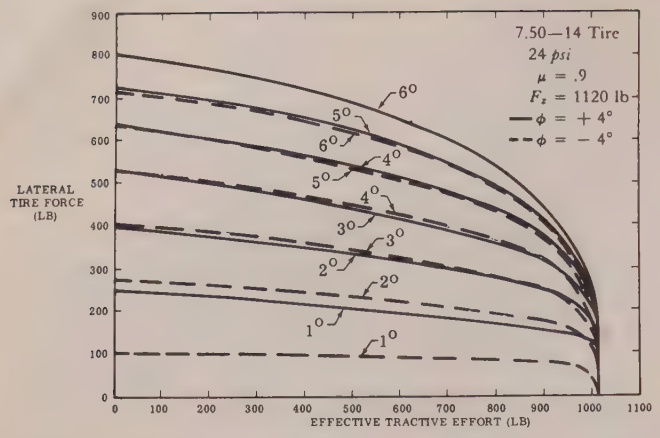

Fig. 19 — Lateral tire force versus effective tractive. Families of curves for various slip angles at +4 and —4 degree dynamic camber angle — calculated values

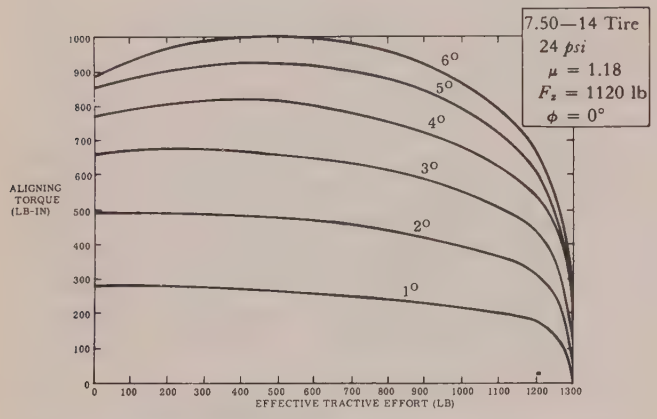

Fig. 20 — Aligning torque versus effective tractive effort at various slip angles — calculated values

the cornering forces at the rear tires reach their initial values, the condition of dynamic equilibrium is restored and the vehicle resumes its original motion.

By applying power on the front wheel drive vehicle in cornering, we momentarily reduce the cornering force at the front tires. This produces a yawing moment which tends to turn the vehicle out of the curve. This phenomenon is known as understeer. A steering correction toward the inside of the turn is necessary to keep the vehicle on the road. As a result of this steering correction, we increase the slip angle on the front tires, thus increasing the front cornering force and restoring the condition of dynamic equilibrium. Now let us suddenly cease to apply power; this will result in a momentary increase of cornering force at the front, which will produce a yawing moment tending to turn the vehicle into the turn. This oversteering effect caused by the cutting off of the power in a front wheel drive vehicle is familiar to front wheel drive automobile owners.

Now let us evaluate the effects of power application on car handling in more detail by applying the tire theory described in this paper. First of all, in the case of a vehicle

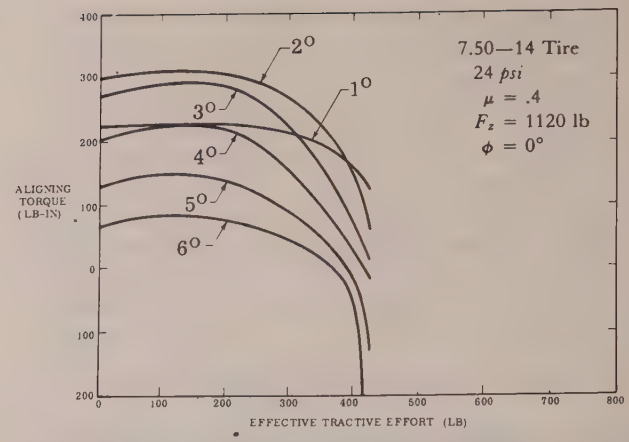

Fig. 21 — Aligning torque versus effective tractive effort at various slip angles — calculated values

negotiating a corner, we cannot isolate the effect of power application on cornering force from other important factors. These factors are:

1. Change of vertical wheel load due to lateral and fore and aft weight transfer.
2. Change of camber thrust due to change of camber angle.

Therefore, all these effects have to be considered simultaneously. By applying power to an automobile negotiating a corner, we increase its speed, which results in forward acceleration and in an increase of lateral acceleration. This will cause an increase of total vertical load on the rear axle and also an increase of lateral weight transfer. Since the axle torque is equally distributed between both wheels, in the case of the car equipped with a standard differential, the vertical load at the inner wheel will determine the effective lateral coefficient of friction and thus control the breakaway condition.

On a rear wheel drive vehicle, the weight transfer due to acceleration opposes lateral weight transfer on the rear inner wheel. This increases the value of effective lateral coefficient of friction, thus improving the ultimate cornering ability of the rear wheel drive vehicle. The combined effect of power application and change of wheel load on ultimate cornering ability of a tire depends on the value of static coefficient of friction between tire and road surface. This effect is much more pronounced on slippery roads with low static coefficient of friction than on dry pavements.

On the vehicle equipped with a conventional solid rear axle, an additional lateral weight transfer takes place due to the driveshaft torque. The effect of driveshaft torque results in a load increase at the left rear wheel and load decrease at the right rear wheel. Therefore, in a left turn the load increase at the left rear wheel due to driveshaft torque opposes lateral weight transfer due to inertia forces and thus improves ultimate cornering ability. Since in a right turn the effect of driveshaft torque is opposite to that in a left turn, we conclude that the rear wheel drive vehicle equip-

ped with a solid rear axle has better ultimate cornering ability in a left turn than in a right turn.

The effect of power application results not only in reduction of effective lateral coefficient of friction, but also in reduction of lateral unit rate of the tire. This latter effect reduces the overall lateral stiffness of a tire and results in a decrease of cornering force with power on.

At small values of slip angle with moderate traction application, the reduction of lateral unit rate is a major factor determining the decrease of cornering force with power on. However, for larger slip angles with fairly extreme power application, the reduction of effective lateral friction coefficient is a major factor and produces a very rapid decrease of cornering force. The rate of this decrease progressively increases near the breakaway stage.

The effect of vertical load on lateral unit rate results in nonlinear relationship between the lateral tire force and the vertical wheel load (Fig. 22). Nonlinearity between lateral tire force and vertical load is a major factor which causes a "front heavy" vehicle to understeer and a "rear heavy" vehicle to oversteer. This nonlinearity also results in a decrease of the sum of cornering forces on outer and inner tires due to lateral weight transfer in roll. Therefore, this nonlinearity between lateral tire force and vertical load explains the understeering effect produced by increasing the lateral weight transfer in roll. It also explains the understeering effect produced by increasing the lateral weight transfer in roll on the front by means of a stabilizer bar. The oversteering effect achieved by increasing roll rate at the rear and thus increasing lateral weight transfer on the rear, is also caused by this nonlinearity. Therefore, by applying power we reduce cornering force, not only due to an increase of traction, but also due to an increase of lateral weight transfer. To compensate for this reduction of cornering force due to power application, it is desirable to decrease the lateral weight transfer in roll on the driving tires. This can be done by changing the distribution of overall roll rate between driving and nondriving wheels.

The amount of reduction of cornering force due to reduction of lateral tire rate, as a result of power application and lateral weight transfer, depends on the tire size, rim size, inflation pressure, and certain tire design factors such as cord angle and width-to-height ratio. For a given vehicle, the reduction of cornering force resulting from power application and lateral weight transfer is reduced as tire size is increased. An increase of rim size, decrease of cord angle, an increase of width to height ratio, or an increase of inflation pressure also reduces the amount of change of lateral tire force caused by the change from power off to power on.

Power application on the front wheel drive automobile results in reduction of lateral force on the driving tires. Reduction of lateral tire force in this case produces an understeering effect.

The final effect of power application on handling of the front wheel drive vehicle depends on fore and aft weight transfer, lateral weight transfer and dynamic camber. The fore and aft weight transfer due to acceleration on the front wheel drive vehicle decreases the load on the front tires. This decrease of load is additive to the decrease of load on the inner tire due to lateral weight transfer. Therefore, weight transfer reduces the value of effective lateral friction coefficient on the front inner tire. This promotes breakaway of the front inner tire and, therefore, adversely, affects the ultimate cornering ability of the vehicle. To counteract this, the lateral weight transfer at the front tires should be reduced relative to that at the rear.

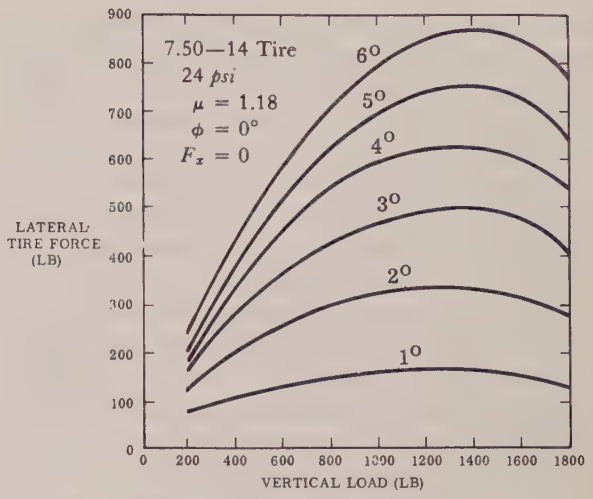

Fig. 22 — Lateral tire force versus vertical load at various slip angles — calculated values

Dynamic camber in most modern passenger cars is such that the front wheels lean toward the outside of a turn. Therefore, the resulting camber thrust opposes the lateral tire force, which results in an additional understeering effect. Camber thrust reduces lateral tire force and at the same time increases effective lateral coefficient of friction. Therefore, camber thrust does not reduce ultimate cornering ability. Camber thrust produces less abrupt reduction of lateral tire force near the breakaway point. Hence, camber thrust gives more warning to the driver before the breakaway point is reached.

The effective tractive effort at the front wheels produces a lateral force component which acts perpendicular to the longitudinal axis of the vehicle. This component of the effective tractive effort results in a yawing moment about the vertical axis through the c.g. of the vehicle. The yawing moment tends to turn the vehicle inside the turn. This tends to counteract the reduction of yawing moment which is caused by reduction of cornering force due to power application. Therefore, this lateral component of effective tractive effort improves handling of the vehicle. Since the lateral component of the effective tractive effort increases with an increase of steer angle (the angle between the plane of the wheel and the longitudinal axis of the vehicle), this force

component produces more assistance for cornering in turns of small radius than in turns of large radius. This explains the fact that the front wheel drive vehicle can reach higher ultimate values of lateral acceleration in small radius turns than in large radius turns (17).

The lateral component of the effective tractive effort is particularly effective on slippery roads. This contributes to superiority in handling of front wheel drive vehicles compared to rear wheel drive vehicles on slippery roads.

As mentioned previously, cutting off power on a front wheel drive vehicle in a turn results in an oversteering effect, caused by an increase of cornering forces on both driving tires. However, in most cases, the reduction of cornering force at the inner tire is greater than that on the outer tire. This is caused mainly by an inefficient distribution of cornering forces between inner and outer tires. Inefficient distribution of cornering forces results from the fact that the inner tire usually operates at a larger slip angle than the outer tire. Since the inner tire operates at reduced vertical load due to lateral weight transfer, the percentage utilization of cornering component of the friction force at the inner tire is much higher than that at the outer tire (18). Therefore, the inner tire approaches skid conditions much sooner than the outer tire. This produces a considerable reduction of cornering force at the inner tire. At the same time, the percentage utilization of the cornering component of the friction force at the outer tire remains essentially smaller than that at the inner tire. Consequently, the inner tire is the principal contributor to the total reduction of cornering force at the front wheels with power applied. In order to decrease the undesirable oversteering effect resulting from an increase of cornering force by changing from power on to power off, the cornering forces between outer and inner tires need to be distributed in proportion to their respective cornering components of the friction forces. If cornering components of the friction forces of both tires are utilized equally, a significant reduction of cornering force will occur only in extremely severe cornering, when both tires are approaching skid conditions. Therefore, in most driving situations, neither of the tires will reach a critical condition and the drop in cornering force due to power application will be substantially reduced.

The driver's "feel" of the steering wheel is also an important factor in vehicle handling. This "feel" is produced mainly by steering effort whose major source is aligning torque. Aligning torque increases with increasing slip angle, reaches a maximum at a certain value of slip angle, and then starts to decrease with a further increase of slip angle. The value of slip angle at which aligning torque reaches its maximum reduces with a decrease of static coefficient of friction. Therefore, in driving on a dry concrete road, aligning torque increases within the normal operating range of slip angles, 1-6 deg. Hence, negotiating a given radius curve on a dry pavement at a lower speed requires less steering effort than the same cornering maneuver at higher speed. By repeating the same cornering maneuver on slippery pavement, we find a reverse trend -- that is, less steering effort at higher speeds than at lower speeds. A moderate power application on a front wheel drive vehicle while negotiating a corner results in a slight increase of aligning torque, provided the slip angle remains constant. A severe power application produces rapid decrease of aligning torque. In driving on slippery roads, negative values of aligning torque can be reached with large slip angles. Application of power to the front wheels aggrevates this tendency.

Conclusions

1. A tire is a three-dimensional spring.
2. A mathematical model of a tire element can consist of three springs connected together. The axes of symmetry of these springs are mutually perpendicular.
3. Forces applied to any one of the springs comprising a tire element produces bending of the other two related springs and this results in a decrease of their respective rates. This phenomenon is called "interaction effect."
4. "Interaction effect" is a major factor which counteracts nonlinear tire characteristics and so produces approximately linear relationship between vertical load and deflection within a limited range of applied loads.
5. "Interaction effect" causes a reduction of overall lateral stiffness of a tire with an increase of vertical load.
6. "Interaction effect" is one of the two major factors which reduce lateral tire force when power is applied.
7. The effective lateral coefficient of friction is reduced with increasing applied power and also with decreasing vertical load. This is the other major factor which reduces lateral tire force when power is applied.
8. Lateral tire characteristics are described by lateral tire force and aligning torque. Lateral tire force is derived from deformations of a tire both inside and outside the contact area.
9. Camber thrust acting in the direction of lateral tire force has two opposite effects: it is additive to lateral tire force but reduces the value of the latter due to reduction of the effective lateral coefficient of friction.
10. Cornering force and traction force are composed of components of lateral tire force, camber thrust, and effective tractive effort acting respectively perpendicular and parallel to the direction of motion.
11. Moderate power application increases elastic trail and aligning torque. Aligning torque decreases with severe power application.
12. The effect of power application on cornering force has important implications in car handling. It produces an oversteering effect on rear wheel drive vehicles and an understeering effect on front wheel drive vehicles.
13. The oversteering tendency of the front wheel drive automobile evident in changing from power on to power off is also caused by the effect of power application on corner-

ing force.

14. The theory developed in this paper can be applied to predict the effect of traction on cornering force. Calculated values of lateral tire force during power application show very good correlation with values obtained from tests.

The mathematical part of this paper is separated from the text and is placed in the Appendix in order to relieve the reader from the details involved in derivation of tire equations.

Equations (34) and (35) are the principal tire equations which describe lateral tire force and aligning torque as functions of slip angle, vertical tire load, effective tractive effort, coefficient of friction, and camber angle. These equations are supplemented by various auxiliary equations. The application of tire theory for the mathematical prediction of handling characteristics of a vehicle in the design stage is beyond the scope of this paper.

Tire equations have been programmed on an IBM 650 computer and provisions were made for plotting tire curves on an XY plotter. A separate computer program has been developed for calculation of tire constants from the test data. These tire constants are used as an input in car handling equations, thus describing the effect of a tire on vehicle behavior.

Appendix

List of Symbols

l_o = Length of contact area (in.)
l_1 = Length of effective area of application of lateral force (in.)
s = Width of the contact area (in.)
s_{max} = Maximum width of contact area (in.)
r = Tire static radius without load (in.)
r_w = Tire rolling radius under load (in.)
r_1 = Tread radius (in.)
x_a = Length of the adhesion region (in.)
x_b = Distance between front end of contact area and point of intersection of elastic trail line with lateral deflection curve produced by friction (in.)
x_o = Distance between front end of contact area and point at which elastic trail line becomes tangent to deflection curve produced by friction (in.)
y = Lateral tire deflection at any point within or outside contact area (in.)
y_f = Lateral deflection of tire element produced by friction at any point within contact area (in.)
y_a = Lateral deflection of tire element at any point within adhesion region (in.)
y_e = Lateral deflection of tire element at any point outside adhesion region (in.)
y_c = Lateral deflection of element due to camber (in.)
Z_{max} = Vertical deflection of tire, measured at center of contact area (in.)
α = Slip angle (radians)
β = Elastic trail angle (radians)
ϕ = Dynamic camber angle (radians)
c_y = Lateral unit rate (lb/in./sq in. = lb/cu in.)
c_z = Vertical unit rate (lb/cu in.)
c_{yo} = Basic lateral unit rate (lb/cu in.)
c_{zo} = Basic vertical unit rate (lb/cu in.)
ζ_{yx} = Lateral bending stiffness coefficient in the longitudinal direction (in.$^{-3}$)
ζ_{yz} = Lateral bending stiffness coefficient in the vertical direction (in.$^{-3}$)
ζ_{zz} = Vertical bending stiffness coefficient in the vertical direction (in.$^{-3}$)
ϵ = Elastic trail coefficient (nondimensional)
ϵ_o = Basic elastic trail coefficient (nondimensional)
ϵ_x = Elastic trail tractive coefficient (nondimensional)
k = Deformation coefficient (nondimensional)
μ = Static coefficient of friction between tire and road surface (nondimensional)
$\mu_y{}^1$ = Effective lateral coefficient of friction (including effect of camber)(nondimensional)
μ_y = Effective lateral coefficient of friction (excluding effect of camber) (nondimensional)
μ_x = Effective tractive coefficient (nondimensional)
p = Pressure between tire and road surface (lb/sq in.)
p_{max} = Maximum pressure between tire and the road surface (lb/sq in.)
F_x = Effective tractive effort (lb)
F_y = Lateral tire force due to slip angle (lb)
F_z = Vertical tire load (lb)
$F_x{}^1$ = Traction force (lb)
$F_y{}^1$ = Cornering force (lb)
Q = Camber thrust (lb)
M = Aligning torque (lb-in.)

Vertical Tire Characteristics - The length and width of the contact area are expressed by chord equations corrected by an empirical deformation coefficient.

$$l_o = 2k\sqrt{2rz_{max} - z^2_{max}} \tag{1}$$

$$s = 2k\sqrt{2r_1z_{max} - z^2_{max}} \tag{2}$$

Simplifying Eqs. (1) and (2) by omitting a second order term z^2_{max} we obtain

$$l_o = 2k\sqrt{2rz_{max}} \tag{1a}$$

$$s = 2k\sqrt{2r_1z_{max}} \tag{2a}$$

Since the value of s is limited by the actual width of the tread, Eq. (2a) can be used only when

$$s < s_{max}$$

The vertical load acting on a tire is

$$F_z = s \int_0^{l_o} p\,dx \qquad (3)$$

Assuming parabolic pressure distribution across the length of the contact area and equal pressure across its width, the pressure at any point of the contact area becomes

$$p = 4 \frac{p_{max}}{l_o} \left(1 - \frac{x}{l_o}\right) x \qquad (4)$$

Equation (4) assumes the coordinate origin to be at the forward end of the contact area.

Substituting (4) into (3) and integrating the latter, we have

$$F_z = \frac{p_{max}}{1.5} l_o s \qquad (5)$$

where:

$$p_{max} = c_z z_{max} \qquad (6)$$

Substituting (6) into (5), we have

$$F_z = \frac{c_z z_{max} l_o s}{1.5} \qquad (7)$$

where:

$$c_z = c_{zo} - \zeta_{zz} F_z \qquad (8)$$

Substituting (1a) and (2a) into (7) and solving the latter equation for z_{max} we have

$$z_{max} = \frac{1}{4k} \sqrt{\frac{3F_z}{c_z \sqrt{r r_1}}} \qquad (9)$$

Equation (9) is valid when

$$s < s_{max}$$

When $s > s_{max}$,
set $s = s_{max}$
and use equation (10) below

$$z_{max} = \frac{1}{2} \left(\frac{1.5\, F_z}{c_z\, s_{max}\, k\, \sqrt{r}} \right)^{2/3} \qquad (10)$$

Lateral Tire Characteristics - From Fig. 11, the lateral deflection of a tire element at any point within the region of adhesion can be expressed as:

$$y_a = x \tan \alpha \qquad (11)$$

Since α is small,

$$\tan \alpha \approx \alpha$$

and

$$y_a = x\, \alpha \qquad (11a)$$

The lateral deflection of a tire element in the elastic region beyond the breakaway point where

$$y_e > y_f$$

becomes

$$y_e = (l_1 - x) \tan \beta \qquad (12)$$

where

$$l_1 = \epsilon l_0 \qquad (12a)$$

$$\tan \beta = \frac{x_a\, \alpha}{l_1 - x_a} \qquad (13)$$

Substituting (13) into (12) we have

$$y_e = \frac{x_a\, \alpha\, (l_1 - x)}{l_1 - x_a} \qquad (14)$$

The lateral tire deflection produced by friction force can be expressed as:

$$y_f = \frac{\mu_y l p}{c_y} \qquad (15)$$

Substituting (4) into (15) we have

$$y_f = \frac{4 \mu_y l p_{max}}{c_y l_o} \left(1 - \frac{x}{l_o}\right) x \qquad (16)$$

In the case where

$$x_a = x_o \qquad \text{(See Fig. 23)}$$

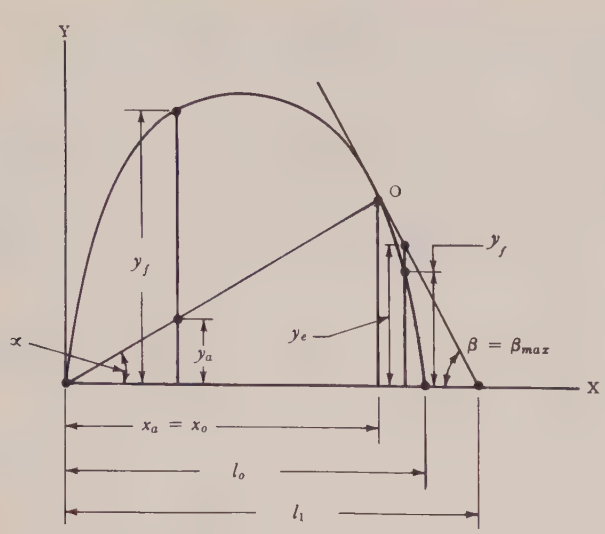

Fig. 23 — Lateral deflection diagram. Condition $X_a = X_o$

then at the point O

$$y_e = y_f$$

and

$$\frac{dy_e}{dx} = \frac{dy_f}{dx}$$

By setting $x = x_o$ in Eqs. (14) and (16) and equating them we have

$$\frac{x_a \alpha}{l_1 - x_a}(l_1 - x_o) = \frac{4\mu_y{}^1 p_{max}}{c_y l_o}\left(1 - \frac{x_o}{l_o}\right)x_o \qquad (17)$$

Differentiating Eqs. (14) and (16) setting $x = x_o$ in derivatives and equating them, we obtain

$$-\frac{x_a \alpha}{l_1 - x_a} = \frac{4\mu_y{}^1 p_{max}}{c_y l_o}\left(1 - \frac{2x_o}{l_o}\right) \qquad (18)$$

Substituting (18) into (17) we have

$$-(l_1 - x_o)\frac{4\mu_y{}^1 p_{max}}{c_y l_o}\left(1 - \frac{2x_o}{l_o}\right) = \frac{4\mu_y{}^1 p_{max}}{c_y l_o}\left(1 - \frac{x_o}{l_o}\right)x_o \qquad (19)$$

from which is derived the following equation:

$$x_o = l_1 \pm \sqrt{l_1{}^2 - l_1 l_o} \qquad (20)$$

Then, since

$$x_o < l_1$$

$$x_o = l_1 - \sqrt{l_1{}^2 - l_1 l_o} \qquad (21)$$

Substituting (12a) into (21) we have

$$x_o = l_o\left(\epsilon - \sqrt{\epsilon(\epsilon - 1)}\right) \qquad (22)$$

At the breakaway point, when $x = x_a$, the intensity of lateral force reaches the value of friction force. Therefore, deflections produced by each of these forces will be also equal to each other.

$$y_a = y_f$$

By substituting expressions for these deflections from Eqs. (11a) and (16) we have

$$x_a \alpha = \frac{4\mu_y{}^1 p_{max}}{c_y l_o}\left(1 - \frac{x_a}{l_o}\right)x_a$$

Solving this equation for x_a we have

$$x_a = l_o\left(1 - \frac{\alpha c_y l_o}{4\mu_y{}^1 p_{max}}\right) \qquad (23)$$

Lateral force F_y and aligning torque M produced by lateral tire deflection y can be determined by integrating the following general equations:

$$dF_y = c_y s\, y dx \qquad (24)$$

$$dM = c_y s\, y\left(x - \frac{l_o}{2}\right)dx \qquad (25)$$

In the case shown in Fig. 24, where

$$x_a > x_o$$

we integrate Eqs. (24) and (25) within the length of the ef-

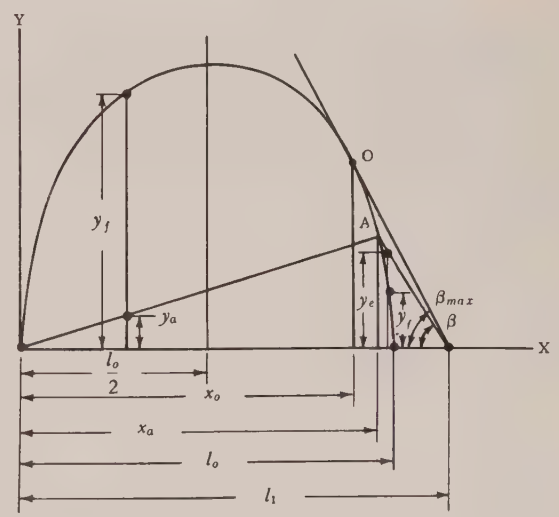

Fig. 24 — Lateral deflection diagram. Condition $X_a > X_o$

fective area of application of lateral force by breaking this area into two major parts:

1. Region of adhesion.
2. Sliding and elastic trail region.

$$F_y = c_{ys} \int_0^{x_a} y_a dx + c_{ys} \int_{x_a}^{l_1} y_e dx \qquad (26)$$

$$M = c_{ys} \int_0^{x_a} \left(x - \frac{l_o}{2}\right) y_a dx + c_{ys} \int_{x_a}^{l_1} \left(x - \frac{l_o}{2}\right) y_e dx \qquad (27)$$

Substituting expressions for y_a and y_e (Eqs. (11a) and (14) into Eqs. (26) and (27) we have

$$F_y = c_{ys} \int_0^{x_a} \alpha\, x dx + c_{ys} \int_{x_a}^{l_1} \frac{x_a \alpha (l_1 - x)}{l_1 - x_a} dx \qquad (28)$$

$$M = c_{ys} \int_0^{x_a} \left(x - \frac{l_o}{2}\right) \alpha\, x dx + c_{ys} \int_{x_a}^{l_1} \frac{x_a \alpha (l_1 - x)}{l_1 - x_a} \left(x - \frac{l_o}{2}\right) dx \qquad (29)$$

After integration

$$F_y = \frac{1}{2} c_y l_1 s x_a \alpha \qquad (30)$$

$$M = \frac{1}{12} c_y l_1 s x_a \alpha (2l_1 - 3l_o + 2x_a) \qquad (31)$$

The case shown in Fig. 25 represents the condition

$$x_a < x_o$$

To obtain expression for lateral force and aligning torque, we have integrated Eqs. (24) and (25) within the length of effective area of application of lateral force. In this case, the sliding region of the contact area has to be divided into two parts:

1. Region.

$$x_a \leq x \leq x_b$$

where:

$$y_e \leq y_f$$

2. Region.

$$l_o \geq x \geq x_b$$

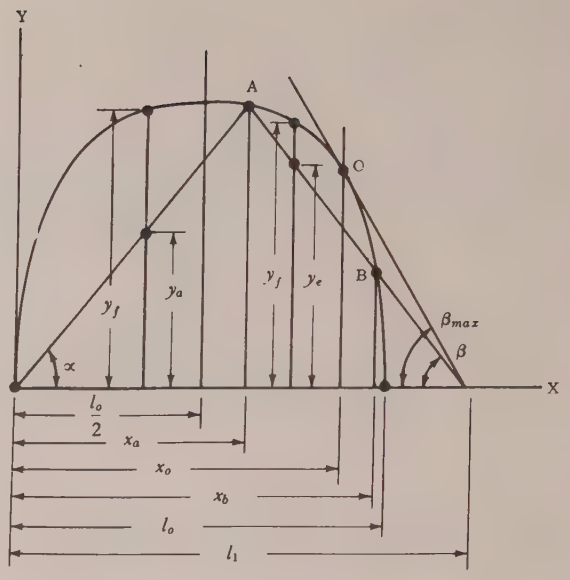

Fig. 25 — Lateral deflection diagram. Condition $X_a < X_o$

where:

$$y_e \geq y_f$$

Therefore, Eq. (14) is applicable only to the rear part of sliding region and not to the whole length of the sliding area, as it was in the first case. Consequently, only the rear portion of the sliding region where $l_o \geq x \geq x_b$ can be combined with the elastic trail area for the purpose of integration. However, part of the sliding region adjacent to the breakaway point (A) has to be integrated separately.

Therefore, Eqs. (24) and (25) can be integrated as follows:

$$F_y = c_{ys} \int_0^{x_a} y_a dx + c_{ys} \int_{x_a}^{x_b} y_f dx + c_{ys} \int_{x_b}^{l_1} y_e dx \qquad (32)$$

$$M = c_{ys} \int_0^{x_a} \left(x - \frac{l_o}{2}\right) y_a dx + c_{ys} \int_{x_a}^{x_b} \left(x - \frac{l_o}{2}\right) y_f dx + c_{ys} \int_{x_b}^{l_1} \left(x - \frac{l_o}{2}\right) y_e dx \qquad (33)$$

And after rearranging terms:

$$F_y = c_{ys} \int_0^{x_a} y_a dx + c_{ys} \int_{x_a}^{l_1} y_e dx + c_{ys} \int_{x_a}^{x_b} (y_f - y_e)\, dx \qquad (32a)$$

$$M = c_{ys} \int_0^{x_a} \left(x - \frac{l_o}{2}\right) y_a dx + c_{ys} \int_{x_a}^{l_1} \left(x - \frac{l_o}{2}\right) y_e dx$$

$$+ c_y{}^s \int_{x_a}^{x_b} (y_f - y_e)\left(x - \frac{l_o}{2}\right) dx \qquad (33a)$$

The first two terms in Eqs. (32a) and (33a) are the same as those in Eqs. (26) and (27). The third term in Eqs. (32a) and (33a) become zero when $x_a = x_b$ and these equations become identical with Eqs. (26) and (27).

After integration:

$$F_y = \frac{1}{2} c_y l_1{}^s x_a \alpha + \frac{4\mu_y{}^1 p_{max}{}^s}{l_o}(x_b - x_a)\left(\frac{x_b + x_a}{2} - \frac{x_b{}^2 + x_b x_a + x_a{}^2}{3l_o}\right) - \frac{c_y{}^s x_a \alpha (x_b - x_a)}{(l_1 - x_a)}\left(l_1 - \frac{x_b + x_a}{2}\right) \qquad (34)$$

$$M = \frac{1}{12} c_y l_1{}^s x_a \alpha (2l_1 - 3l_o + 2x_a) + \frac{\mu_y{}^1 p_{max}{}^s}{l_o{}^2}(x_b - x_a)\left[2l_o (x_b{}^2 + x_b x_a + x_a{}^2) - (x_b + x_a)(x_b{}^2 + x_a{}^2 + l_o{}^2)\right] - \frac{c_y{}^s x_a \alpha (x_b - x_a)}{12 (l_1 - x_a)}\left[(x_b + x_a)(6l_1 + 3l_o) - 4 (x_b{}^2 + x_b x_a + x_a{}^2) - 6l_o l_1\right] \qquad (35)$$

The limit of integration x_b can be determined from the condition

$$y_f = y_e$$

when $x = x_b$.

Then by substituting $x = x_b$ in Eqs. (16) and (14) and equating them we have

$$\frac{4\mu_y{}^1 p_{max}}{c_y l_o}\left(1 - \frac{x_b}{l_o}\right) x_b = \frac{x_a \alpha (l_1 - x_b)}{l_1 - x_a} \qquad (36)$$

Rearranging terms in the above equation, we obtain

$$\frac{4\mu_y{}^1 p_{max}{}^s}{l_o{}^2} x_b{}^2 - \left(\frac{4\mu_y{}^1 p_{max}{}^s}{l_o} + \frac{c_y{}^s x_a \alpha}{l_1 - x_a}\right) x_b + \frac{c_y l_1{}^s x_a \alpha}{l_1 - x_a} = 0 \qquad (37)$$

set

$$a = \frac{4\mu_y{}^1 p_{max}{}^s}{l_o} \qquad (38)$$

$$b = \frac{c_y l_1{}^s x_a \alpha}{l_1 - x_a} \qquad (39)$$

Substituting Eqs. (38) and (39) into equation (37) and solving the latter we have

$$x_b = \left[\left(a + \frac{b}{l_1}\right) \pm \sqrt{\left(a + \frac{b}{l_1}\right)^2 - \frac{4ab}{l_o}}\right] \frac{l_o}{2a} \qquad (40)$$

Since $x_b > x_a$

$$x_b = \left[\left(a + \frac{b}{l_1}\right) - \sqrt{\left(a + \frac{b}{l_1}\right)^2 - \frac{4ab}{l_o}}\right] \frac{l_o}{2a} \qquad (41)$$

The values of $\mu_y{}^1$, c_y, and ϵ used in Eqs. (34) and (35) are expressed by the following equations:

$$\mu_y{}^1 = \sqrt{\mu^2 - \mu_x{}^2} - \frac{Q}{F_z} \qquad (42)$$

$$c_y = c_{yo} - (\zeta_{yx} F_x + \zeta_{yz} F_z) \qquad (43)$$

Note: Secondary spring rate reduction effect is neglected in Eq. (43) because of its relative insignificance.

$$\epsilon = \epsilon_o + \epsilon_x \mu_x \qquad (44)$$

where:

$$\mu_x = F_x / F_z \qquad (45)$$

and

$$Q = \frac{\phi c_y{}^s l_o{}^3}{12 r_w} \qquad (46)$$

We treat Q as a separate force which is additive to F_y. However, we do consider the effect of Q on $\mu_y{}^1$, which latter affects F_y.

Equation (46) was obtained from integration of

$$Q = \int_o^{l_o} c_y{}^s y_c dx$$

where y_c is expressed by using Fiala's (6) equation:

$$y_c = \frac{\phi l_o{}^2 x}{2 r_w l_o}\left(1 - \frac{x}{l_o}\right)$$

Symbols in Fiala's original equation are replaced by new symbols when used in this paper.

Table 2 - Parameters of Firestone Tire

c_{zo} = 72.388 lb/cu in.	r = 13.6 in.
c_{yo} = 128.33 lb/cu in.	r_1 = 10.2 in.
ζ_{zz} = 0.016 in^{-3}	s_{max} = 4.27 in.
ζ_{yz} = 0.0512 in^{-3}	ϵ_o = 1.15 (nondim.)
ζ_{yx} = 0.0357 in^{-3}	ϵ_x = 0.20 (nondim.)
k = 0.7737 (nondim.)	

In the case when

$$Q = 0$$

and

$$F_x = 0$$

Eqs. (42), (43), and (44) become

$$\mu_y{}^1 = \mu \tag{42a}$$

$$c_y = c_{yo} - \zeta_{yz} F_z \tag{43a}$$

$$\epsilon = \epsilon_o \tag{44a}$$

Tire Parameters Values - The parameters of 7.50 - 14 Firestone tire used for calculations of the tire characteristics shown in this paper are listed in Table 2.

Acknowledgements

The author is greatly indebted to Mr. J. G. McQuaid for invaluable technical assistance, practical guidance and encouragement throughout the planning, execution and reporting of the project of which this paper describes an important phase.

The author also wishes to thank personnel of the Ford Vehicle Testing Laboratories, Testing Operations Office for developing instrumentation, conducting tire testing, and supplying the test data necessary to verify the author's tire theory.

Further acknowledgement of the development of a tire test rig and supplying of tire data is made to Firestone Tire & Rubber Co. Acknowledgment is also made to various associates in the Ford Engineering organization, for interest in the project, helpful discussions during the work and assistance in preparation of the paper.

References

1. R. Schuster and P. Weichsler, "Der Kraftschluss Zwischen Rad und Fahrbahn," ATZ (1935), 499-504.

2. Herbert Martin, "Druckverteilung in der Berührungsfläche zwischen Reifen und Fahrbahn," Kraftfahrtechnische Forschungsarbeiten des VDI, Heft 2 (1936).

3. P. M. Heldt, "Ground-Contact Area of tires varies directly with Defelction," Automotive Industries, 128 (July, 1932), 100-113.

4. L. Huber, "Die Fahrtrichtungsstabilität des Schnellfahrenden Kraftwagens," Deutsch Kraftfahrtforschung, Heft 44 (1940), 23.

5. B. Von Schlippe and R. Dietrich, "Shimmying of a Pneumatic Wheel," Bericht 140 der Lilienthal - Gesellschaft (1941), 35-45.

6. E. Fiala, "Seitenkräfte am rollenden Luftreifen," Z. VDI (October, 1954), 973-979.

7. V. E. Gough, "Practical Tyre Research," SAE Trans., Vol. 64 (1956), 310-318.

8. V. E. Gough, "Tyre to Ground Contact Stresses," Wear, Vol. 2 (1958/59), 107-126.

9. D. H. Cooper, "Lateral Forces on Tyres," Automobile Eng. (1958), 524-527.

10. K. A. Stonex, "Passenger Car, Wind and Rolling Resistance," SAE Preprint, March 10, 1949.

11. T. J. P. Joy, D. C. Hartley, and D. M. Turner, "Tires for High Performance Cars," SAE Trans., Vol. 64 (1956), 319-333.

12. T. J. P. Joy, D. C. Hartley, "Tyre Characteristics as Applicable to Vehicle Stability Problems," Proc. Inst. Mech. Engg. (1953/1954), 113-133.

13. C. A. Freeman, "Experimental Determination of the Effect of Traction on Cornering Force" Paper to be presented at the SAE Summer Meeting, 1960.

14. L. Huber and O. Dietz, "Die Seitenführungskraft des gummibereiften Rades bei Antrieb und Bremsung," Deutsche Kraftfahrtforschung Technischer Forschungsbericht Zwischenbericht No. 100, 1941.

15. W. Buck, "Faktoren zur Beeinflussung der Strassenlage," Motor Revue (1957), 84-96.

16. A. W. Bull, "Tire Behavior in Steering," SAE Jour., Vol. 45, No. 2 (August, 1939), 344-350.

17. O. Dietz and R. Harling, "Die Fahrlage des Kraftwagens in der Kurve," Deutsche Kraftfahrtforschung, Heft 44 (1940).

18. E. Fiala, "Kraftkorrigierte Lenkgeometrie Lenkgeometrie unter Berücksichtigung des Schräglaufwinkels," ATZ, (February, 1959), 29-32.

Interactive Effects of Various Spring Rates and Reduction of Lateral Tire Force as a Function of Power Application

Prof. S. K. Clark
University of Michigan

MR. BERGMAN IS to be congratulated on such a thorough and complete discussion of the many factors which influence the development of cornering forces during slip of a tire. An anaylsis such as this is particularly valuable since it allows a broad, overall view of the phenomenon to be obtained. In contrast to this approach, any exact treatment of tire be-

havior becomes so complicated, due to the very nature of the problem, that one very soon loses sight of the forest for the trees. For this reason, papers such as this are helpful, even necessary, to the tire and vehicle designer.

One question which appears to merit some discussion is that of the interactive effects of the various spring rates. In Mr. Bergman's paper, it is stated that the general effect of traction is to reduce lateral spring rates. It would be helpful to know the origin of such a reduction. One possible mode of interactive effects arises due to additional stresses caused in a tire by the application of traction or braking. Due to the severely nonlinear stress-strain curves of tire materials, these stresses may cause a movement along the stress-strain curve to some new position which, due to the nonlinearity, may now have a new slope or effective modulus. Another mechanism which may come into play here is the actual geometric deformation of the tire itself under the effect of traction, and in this case, lateral deformations of the tire would then take place on a structure geometrically different from one free of traction.

It would appear that considerably more real significance could be attached to these interactive effects if one were able to attribute them to such real physical facts as mentioned. I do not know of any information concerning the stiffening or softening of a tire due to changes in its shape brought about by the application of traction forces, and I wonder if Mr. Bergman has any data of this kind which could be made public.

It would also appear to this reviewer that it is by no means self-evident that softening of the tire in the lateral direction accompanies traction or braking, and so it would be very helpful to have the author comment on the possibility of stiffening of the tire under these conditions.

Another question which this reviewer would like to see clarified is that of the degree of the reduction of lateral tire force as a function of power application. It is stated that this reduction is greater at lower values of static coefficient of friction and at lower values of vertical wheel load. Since the effect in question appears to be a purely geometric one involving the basic stiffness of the tire and the direction of the total friction vector, then it is not clear how friction coefficient and vertical wheel load enter into the problem.

As a last comment, it would be interesting if some statement could be made as to the general situation which would prevail at very low tire deflections, where the low deflection relationship is not linear.

Author's Closure to Discussion

I am in full agreement with Prof. Clark's interpretation of the physical nature of the "interaction effect" and believe that both factors pointed out by him are of great importance.

The conclusion that tire stiffness decreases with the application of traction was reached from test results referred to in the References. The assumption of linear reduction of lateral unit rate with an increasing power application shows good agreement with test data and therefore can be justified. The phenomenon was explained by bending of the springs used in the tire model. However, this artificial model merely illustrates the phenomenon and does not necessarily explain its true physical nature. The writer has no data pertaining to physical changes in the material of a tire during application of traction.

Tests described in References 14 and 16 indicate the possibility of a relatively insignificant stiffening of the tire as a result of light braking application; a further increase of braking results in softening of a tire.

As stated in the paper, two major factors determine reduction of lateral tire force with power application: interaction effect and effective lateral coefficient of friction. Since the second factor reduces with a decrease of static coefficient of friction and a decrease of vertical wheel load, power application results in greater reduction of lateral tire force at lower values of static coefficient of friction and lower values of vertical wheel load.

The last question brought up by Prof. Clark, regarding "the general situation prevailing at very low tire deflection" is not quite clear. Presumably, he is interested in the actual relationship between lateral tire force and later deflection. No attempts have been made to develop this relationship in the paper, either for small or large deflection values. Lateral tire force was expressed as function of slip angle, rather than of lateral tire deflection.

Quantitative Determination of Lateral Tire Force

M. G. Anderson
Goodyear Tire & Rubber Co.

THE PLOTTED RESULTS of calculated lateral force, presented by Mr. Bergman, show excellent correlation with the actual test measurements. We have done some measurements of lateral stiffness characteristics by applying lateral force to the rear axle of a car with one rear wheel mounted on a frictionless support, so that all of the lateral force applied was counteracted by the lateral stiffness of only one rear tire. It was found that the lateral displacement of the rear car axle was due to the accumulation of deflections consisting not only of the tire, but also to an appreciable extent the axle and wheel. A 300-lb lateral force applied to the car axle rear shaft created a 0.510 lateral displacement at the axle; however, the roll of the tire itself accounted for only 0.345 in. of the displacement (Fig. A).

On a percentage basis, the lateral displacement of the axle was due to distortions shown in Table A.

When measuring the steer effects of tire lateral stiffness, it is necessary to consider the axle and wheel distortions, because the tire may account for only 67% of the lateral displacement of the car axle.

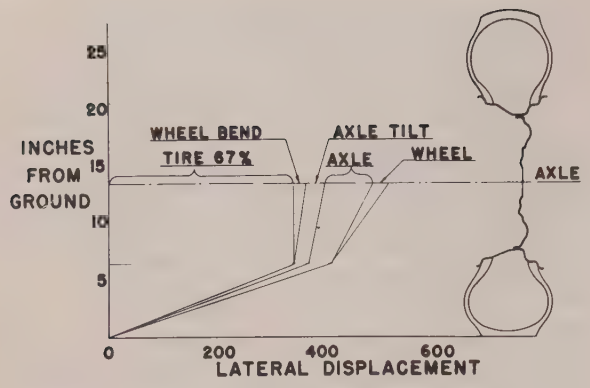

Fig. A — Lateral displacement — 300-lb lateral force

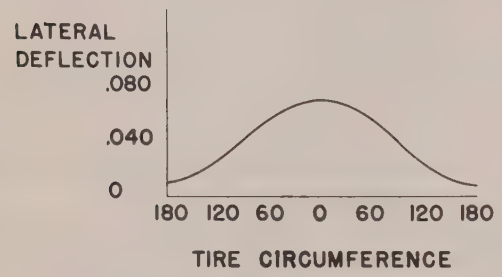

Fig. B — Tire lateral deflection — 300-lb side force

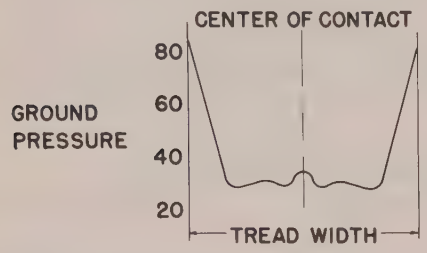

Fig. C — Ground contact pressure

Table A-Distortions Causing Lateral Displacement of Axle

	%
Tire lateral roll	67
Axle shaft bend	18
Axle housing tilt	7
Wheel bend	3
Wheel umbrella-type distortion	5
	100

When a lateral force is applied to a tire at the ground contact area, it is common knowledge that a sidewise roll is created. Our tests have shown that this sidewise roll extends completely around the tire and that the top half of the tire rolls in the same direction as the bottom half. In other words, the distortion is umbrella type. The actual displacement of the top of the tire is approximately one-third that at the contact area (Fig. B).

When a tire is subjected to a lateral force, the tread centerline is displaced sidewise with respect to the wheel centerline throughout the entire circumference of the tire, and the amount of displacement at the top is approximately one-third that which occurs at the ground contact region.

When working with conventional bias angle tires, we are inclined to think of lateral tire stiffness and cornering power as closely related characteristics. While they may be closely related, they are however, not the same. The difference between lateral stiffness and cornering power may be illustrated by comparing the belted-type radial ply tire (such as the Michelin"X") with a standard bias angle tire.

A radial ply belted tire has approximately twice the cornering power of a conventional tire but, at the same time, has much lower lateral spring rate.

Here we have a case of a tire with low lateral spring rate and a high cornering power. Cornering power seems to be related to the resistance of the tread band of the tire to lateral bending. For bias angle tires, cord angle changes which create higher lateral spring rates also usually add to the lateral bending stiffness of the tread band.

Lateral spring rate of a tire has an effect on the steering qualities of a tire, because it causes a time lag between the creation of the slip angle and the generation of cornering force. This time delay or slowness of response of steering is a deficiency of control which is sometimes put in the general class of instability. This slowness of steering response is particularly noticeable in belted tires, and it takes some time for a driver to get used to it. However, once they do get started around a corner, they do have good cornering characteristics.

In regard to tire ground contact pressures (Fig. C), reference is made to a report by Herbert Martin in 1936. At that time, tires were generally made with comparatively round treads and the road contact areas had the shape of long ovals. On these tires, the ground pressure across the width of the contact area was approximately uniform. However, this does not hold true on present-day tires, which have much flatter tread radii. I agree that the contact print of modern tires is rectangular as Mr. Bergman describes them, but on such tires the ground pressure at the shoulder is more than twice that at the center of the tread. This is true for a static deflection. If a lateral force is applied, the ground pressure will be increased on one shoulder and reduced on the other shoulder, but still it will not be uniform throughout the width of ground contact.

Mr. Bergman's paper has done much to explain the steering characteristics of front wheel drive cars, and I am sure that those who have carefully studied his analysis now have a better understanding of the influence of tire mechanics on car performance. Mr. Bergman has made a considerable contribution to the present knowledge of tire mathematics.

Author's Closure to Discussion

The analysis presented in the paper was concerned with quantitive determination of lateral tire force under various operating conditions: slip angle, traction, vertical load, and camber.

No attempt has been made to predict quantitatively actual values of lateral tire deflection or of lateral displacements of the car axle. The expression for relative lateral deflection of a tire was used merely for derivation of the final lateral force equation, rather than for determining the actual lateral deflection.

The lateral properties of a tire were described by a parameter, lateral unit rate, which was calculated from the lateral force equation for the given test value of lateral tire force at the given value of slip angle. Therefore, lateral unit rate expresses rather the cornering power of the tire than its actual lateral stiffness.

The writer fully agrees with Mr. Anderson that if one is interested in actual lateral displacement of the axle, all deformations listed by him should be considered.

It is also acknowledged that pressure distribution across the width of the contact area is nonuniform; however, the simplifying assumption of uniform distribution was necessary in order to enable us to treat this very complex problem mathematically.

Standardization of Terms

W. C. Johnson
Goodyear Tire & Rubber Co.

IT HAS BEEN MENTIONED by Mr. Charles A. Freeman of Ford Motor Co. that test data has resulted in about 0.10 in. treadwear. To the tire industry this is a relatively large amount and suggests that, unless the tires are reversed frequently, this wear will be one directional. A tire when cornered in one direction, tends to reduce its ability to generate as high side force for the same angle as wear develops and, if the wear is appreciable, as it apparently is in this case, may adversely affect the test data. As mentioned in, the agreement which was attained with the calculations of Mr. Bergman does support both the experiment and the calculations as being reasonably accurate.

I would like to point out a question in terminology. In both papers the side force on the tire perpendicular to its plane of rotation has been called "lateral tire force", whereas the component normal to the longitudinal axis of the car is called "cornering force". There exists an SAE definition of cornering force under the subject of "Ride and Vibration Terminology" as follows:

7.52 Cornering force is the force at the road surface, normal to the wheel plane, exerted by the road on a wheel rolling at zero camber and at a given slip angle.

There is no question in either of these papers as to what is meant, but it does seem that further consideration should be given to standardize these terms.

Author's Closure to Discussion

ALTHOUGH MR. JOHNSON'S discussion was addressed to Mr. Freeman, two points brought out therein concern the theoretical paper and are therefore answered by the author.

We fully agree with Mr. Johnson that lateral tire characteristics are affected by tire wear. However, since the values of lateral bending stiffness coefficients employed in calculations were determined experimentally, the effect of tire wear is assimilated in both test and computed values.

The statement made by Mr. Johnson that "the component normal to the longitudinal axis of the car is called 'cornering force' does not agree with the definition of cornering force given in the author's paper. Cornering force is defined by the author as a component of the lateral tire force acting perpendicular to the direction of motion. On a vehicle negotiating a corner, the direction of wheel motion does not coincide with the longitudinal axis of the vehicle. An angle exist between the direction of motion of the wheel and the vehicle's longitudianl axis. This angle is the sum of an angle between the velocity vector at the CG of the vehicle and the longitudinal axis plus an additional angle resulting from the lateral velocity component due to the vehicle's yawing velocity.

It is true that the author's definition of cornering force does not agree with the SAE definition, but it is the one used in tire publications and was considered preferable.

Validity of Simplifying Assumptions

S. A. Lippmann
United States Rubber Co.

MR. BERGMAN HAS undertaken the analysis of a complex subject and, much to his credit, the development is extremely lucid. The nature of the task appears quite imposing when one considers the number of interrelationships discussed in the paper. Let us for the moment take a simplified view of the task Mr. Bergman tackled, in order to treat the problem in more general terms.

As the paper shows, when a tire develops steering forces, there are distortions in the contact region, because friction tends to hold the tread to the pavement. The tread moves further out of the plane of the tire as it progresses through the contact region. Usually, there is slipping against the road at the end of contact and the tread tends to return to the plane of the tire. If friction is insufficient, slippage may occur well before the end of contact. The shorter the region of adhesion between the tire and the road, the smaller will be the lateral deflection and the thrust. Since forces in the rear half of the contact region are diminished, there is a reduction in the self-aligning torque for shorter contact areas. The paper also shows that the available friction forces

can be exceeded by a combination of elastic forces and tractive forces. The concepts just outlined are entirely in accord with our experience at U. S. Rubber and, as far as we know, are generally accepted.

From these ideas, one might readily deduce the essential conclusions of the paper, although this is not outlined here. The conclusions are as follows:

1. The cornering force should decrease with increasing tractive demand.
2. The greater the steering angle, the greater is the effect of the tractive force in reducing the cornering force.
3. There are conditions for which the cornering force might be expected to drop to almost zero.
4. Variation of the self-aligning torque should exhibit dependencies similar to that of the cornering force.

Mr. Bergman undoubtedly realized that the phenomena covered in the paper are dominated by these few concepts. The goal, however, is to provide quantitative predictions from the theoretical considerations. The paper calls upon many experimental and theoretical relationships to support the analysis. It unfortunately is the nature of the problem that inappropriate assumptions may be balanced against each other through the choice of coefficients. Since the form of the results are set by the assumptions already noted, the choice of many subsidiary relationships is not necessarily validated by the agreement of the data and theoretical curves. However, if Mr. Bergman had extended his analysis to dynamic steering rather than to steady-state steering, he might have found some of his assumptions inadequate. I would like to indicate a few of our findings that bear on this point.

It has become common practive in the literature to assume a certain rule for the lateral displacement of an element of tread on high-frictional surface. The lateral displacement is taken as the product of the slip angle (in radians) and the distance from the entering edge of the contact patch. This concept is contained in Eq. (11a) of the paper. Experiments with cathetometers and photoelectric devices show that this is the case only for a particular instant during dynamic steering. It certainly is not the case during steady-state. Although the distortion of the contact region tends to follow that of the steering angle, from the moment of instantaneous steering onward, the lateral distortion of the tire increases progressively. The lateral distortion grows asymptotically to a value determined by the construction of the tire and operating conditions.

Let me quote data for a 6.40-15 tire. This is an odd size to discuss these days, but it was current in 1950 when we were studying some dynamic effects. At approximately normal conditions, the tire developed a tread length of 5.3 in. At 1, 2, and 3 deg of slip angle, the maximum lateral displacements in the contact region were respectively 0.17, 0.34, and 0.51 in. According to Eq. (11 a), the calculated lateral deflections could not exceed 0.0992, 0.184, and 0.276 in. Hence, the theory is in error by about 100%. Other deflections of the tire, other operating conditions, other sizes, and other constructions of the tire show large discrepancies with the theory.

The author has treated the tire as though it were a series of adjoining springs. Implicit in this analysis is another assumption -- that the tire has a zero shear modulus in the plane of the tread. Should this shear modulus not be zero, there would be a transfer of stress from one section to the adjoining sections. In the absence of this shear modulus, we are led to Eq. (26). This equation states that each laterally displaced section acts on the rim with an element of lateral force porportional to the degree of lateral displacement. Tires do have a large shear modulus in the plane of the tread, and it is therefore possible for the centrally located regions of the contact area to contribute relatively little to the lateral force. We are aware of static tests that support the contention of Eq. (26), but have reason to doubt the validity in dynamic tests.

The choice of model underlying Eq. (26) leads to a further compensating assumption, that the lateral spring rate of each differential section decreases as the vertical deflection grows. Here, again, I would like to refer to the 6.40-15 tire of 1950. Let us consider the overall spring rate of the tire in lateral deflection. The steered tire was running at equilibrium against a road surface; the force at the axle is measured by stress gages and the lateral displacement of the contact area is measured eptically. The lateral spring rate is approximately independent of the lateral distortion over the usual range of slip angles. As the vertical deflection was changed progressively from 0.30 to 1.25 in., the lateral spring rate changed linearly from 610 lb/in. to 570 lb/in. This is merely a 7% variation, and is consistent with what one would expect from a high shear modulus in the plane of the tread.

The assumption of zero shear modulus implicit in Eq. 26, however, leads to the requirement that as the contact length increased with the deflection, the unit spring rate varied greatly. In this case, the spring rate for the differential elements would have to vary from 156 to 81 lb/sq in. as the deflection changed from 0.30 to 1.25 in. As we all know, this lateral spring is not really a coil of wire. The effect of a lateral spring comes about from the action of the air pressure within the tire on the doubly curved surfaces. These large changes in unit spring rates do not seem entirely reasonable from measurements of curvature changes and surface inclinations.

This leads to another point, and this is intended as a criticism of the general tendency in the literature rather than of this paper. The tire is too often treated as a group of simple springs. It should be emphasized that the tire develops most gross forces because its contours become unsymmetrical as a result of some kind of distortion. The air pressure acts on these unsymmetrical surfaces and produces unsymmetrical tensions in the load-bearing members (cords). The orientation of these load-bearing members, as well as

their tensions, are unsymmetrical; as a consequence, the tire develops a net reaction.

I would like to reiterate my belief that as we understand it, the paper contains the essential characteristics of the phenomenon it is intended to analyze. There are, however, several assumptions of a subsidiary nature whose validity I have questioned.

Before closing, I should like to mention two of the implications of the curves. The range of tractive efforts covered in the study is extremely great. Presumably, these tests account for certain kinds of emergency conditions. It would be of interest to treat the more prevalent condition of emergency -- that of braking traction. We also wish to point out that additional steering easily compensates for the decrease due to traction. At 3 deg slip angle, for instance, the effect of 1000 lb of tractive effort is compensated for by increasing the slip angle to 5 deg. 1000 lb amounts to accelerations of about 1 g. Maximum demands are likely not to exceed 0.4 g and this requires a change in slip angle from 3 to 3.5 deg.

Author's Closure to Discussion

It is not immediately evident how the four conclusions enumerated by Mr. Lippmann could be derived from the "simplified view" he outlines, although the first three follow readily enough when one employes the concepts of interaction effect and effective lateral coefficient of friction developed in the paper. Conclusion 4, however, is not in agreement with the tire theory developed in the paper; aligning torque responds to moderate power application quite differently than does cornering force, at slip angles of 3 deg or more, because of the influence of changes in elastic trail as explained in the paper and illustrated by comparing Figs. 15 and 20.

Possibly because of confusion in terminology, the author is unable to agree with Mr. Lippmann's statement that "the paper also shows that the available friction forces can be exceeded by a combination of elastic forces and traction forces."

Mr. Lipmann's criticism of several of the simplifying assumptions used in the paper would be perfectly valid, if the author's theory were intended to describe the actual tire mechanism and its internal stresses and strains. But it should be emphasized that his sole purpose was to find, as a free body substitute for the exceedingly complex mechanism of the real tire, a mathematically tractable model which would produce comparable and computable end results in terms of forces at the wheel rim and at the road surfaces. Its internal behavior is described mathematically only as a means of computing its external responses, not to describe, for example, actual lateral deflections in a real tire.

A case in point is Eq. (11-a), which was used for the sole purpose of deriving the lateral tire force and aligning torque Eq. (34) and (35). However, even if Eq. (11a) were to be used to compute internal deflections, it should be noted that this equation neglects elastic lead; it determines lateral displacement of a tire element only in relation to its initial position at the forward end of the contact area. Since deformation also occurs forward of the contact area, the initial position is already subject to a displacement which should be added to the value calculated from Eq. (11a), in order to arrive at the absolute value of lateral deflection. This may explain the 100% disagreement between calculated and measured values quoted by Mr. Lippmann.

Two other assumptions questioned by Mr. Lippmann are those of a linear path of the tire element within the adhesion region, and of proportionality between lateral force intensity and deflection. Both these assumptions are fundamental in tire theory, both are generally accepted in tire literature, and computed values of lateral tire force and aligning torque based on them agree very well with test values. They may not hold true for each individual tire element but, in their overall effect on resultant external tire forces, they seem to be fully justified.

In discussing the implications of Eq. 26, Mr. Lippmann apparently questions what he calls a compensating assumption: namely, the reduction of lateral unit rate with an increasing vertical load. This is the interaction effect which is a key element of the author's tire theory. However, in the numerical example he uses to illustrate apparent discrepancies between theoretical and test values, Mr. Lippmann compares experimental lateral tire rates with theoretical lateral unit rates: these two rates are actually quite different. As vertical load increases, the lateral tire rate reduces much less rapidly than does the lateral unit rate, because the number of Y-spring elements influencing the lateral tire rate increases at the same time, thus tending to compensate for the unit rate reduction of each element.

Quantitatively, the assumption in question apparently leads to good correlation between the external force output of the artificial model and that of real tires.

Theoretical Assumption Versus Current Tire Experience

R. P. Powers
Firestone Tire & Rubber Co.

MR. BERGMAN HAS made some interesting observations and explanations which will be of much value. By comparing a tire with an assembly of springs and using some basic assumptions along with available factual data, he has been able to predict certain tire performance characteristics which up to now have not been available in mathematical form.

This paper is particulary interesting to tire engineers, because in developing his theory as to how tires effect the vehicle, Mr. Bergman has actually gone "inside the tire." This is a field which tire engineers in the past, particularly in this country, have minimized in their technical papers.

Those which have been published usually refer to test data, or some general tire property, or perhaps to a controversial program of the moment. Competitive reasons may be partially responsible for avoiding this theoretical phase, but I believe the more significant reason is that tire development has necessarily depended upon much "cut and try" engineering. The practice has been to theorize initially and privately, and then test if for the final evaluation.

In reviewing Mr. Bergman's paper, we find that our theories generally agree with his. However, some of his assumptions, as he probably realizes, do not reflect current tire experience. Along that line, the following comments are offered, to which perhaps Mr. Bergman may wish to reply:

1. Tire contour or tread radius has a significant effect on vertical deflection and on pressure distribution in the contact area: the flatter the contour the smaller the tire deflection; and the unit loading, instead of being parabolic, is likely to be high under the tread shoulders and low in the center.

2. The footprint or pad of a free-rolling tire is not usually centered under the axle, but is slightly behind it. Braking torque moves it back further while driving torque may actually put it ahead of the axle.

3. Tread movement with respect to the body of a tire may be quite substantial, depending upon how the elements are tied together. Whether this has significant effect on the proposed formulas is yet to be determined.

In the way of further substantiating Mr. Bergman's analyses, it can be shown that moderate torque application results in a slight increase in tire deflection, as would be expected in an interconnected spring assembly such as Mr. Bergman describes. Also, recent measurements of cornering force and self-aligning torque during brake application show a slight reduction in the lateral force and a considerable increase in alignment torque.

Although tire development is still very much based on experience, I wish to point out that strain gages and load cells, along with oscilloscopes, XY plotters, and oscillographs are being successfully used in tire work just as they are in more scientific fields. As a result, new, more realistic data is constantly being obtained, some of which can be expected to conflict with what was available before. For example, measurement of vertical, lateral, and longitudinal forces acting on the tread elements is being undertaken with the help of electronic equipment, and data of this nature may help to clear up some of the unknowns existing. Although presently workable with 0-deg slip angles, we hope later to obtain measurements during cornering.

Author's Closure to Discussion

The reply to comments presented by Mr. Powers follow the order set by him:

1. The effect of tread radius on vertical deflection was expressed in Eq. (9). Equation (6) describes the pressure at the contact area in terms of vertical deflection and includes the effect of tread radius. For purposes of simplification, uniform pressure distribution was assumed across the width of the contact area, instead of the nonuniform pressure distribution which actually exists.

2. Fore and aft motion of a tire contact area relative to the wheel center line results from deformation of the X-springs in the tire model due to application of forces acting in the longitudinal direction. The effect of this deformation on lateral tire force was explained by the concept of "interaction effect" and was incorporated in tire equations. However, this deformation was not expressed quantitively, due to lack of necessary experimental data. Therefore, aligning torque was calculated by taking moments about the center of the contact area.

3. Deflection of the tread in relation to the carcass was not treated mathematically. However, the effect of tread deformation was incorporated in the empirically determined coefficients used in equations of lateral tire force and aligning torque. The tread deformation has a definite effect on lateral tire characteristics. An increase of tread deformation results in a decrease of lateral unit rate.

The simplifications discussed above were necessary in order to enable the tire to be treated mathematically. The actual tire mechanism is extremely complex and it is practically impossible to deal with it mathematically without using simplifying assumptions. Simplification is justified by the good correlation found between calculated and test values.

The Rotating Combustion Engine

Roy T. Hurley *

and M. Bentele
Curtiss-Wright Corp.

ALMOST AS SOON as inventors and engineers made a successful steam engine in the 18th Century, they were working on rotary engines. However, the reciprocating principle was more obvious and posed less problems for the operating cycle and the sealing of high pressure and was, therefore, predominant for almost two centuries. The first applications of the rotary principle can be traced back to James Watt and his co-worker, Murdock, the latter having reportedly made a steam expansion engine similar to an ordinary gear pump, but with wooden bars as sealing elements. Murdock's engine delivered half a horsepower and was used by him to drive a lathe in his workshop. Other famous engineers worked on rotary engines, for example, James Ericson, the builder of the first armored steel vessel, the "Monitor"; Westinghouse; de Laval; and Parsons. None of their designs, however, were successful. Other rotary machines, such as compressors and pumps, have less stringent requirements for the cycle and the seals than engines. Therefore, quite a number of designs using the rotary principles were put into practice and became commercial successes. That many people were also working on rotary engines is best shown by the fact that hundreds of patents were granted which display a multitude of configurations and designs.

A number of patents to an American inventor, J. F. Cooley (and the Cooley Epicycloidal Engine Co.) in the first decade of this century, and patents to a French inventor, Sensaud de Lavaud, shortly before World War II, show interesting examples of such engines. However no reliable test data were ever made available. This can only mean one of two things:

1. The designs were not even capable of short test runs.
2. The test results were so disappointing that publishing them was not warranted.

An English book on the history of rotary engines and pumps, published in 1939, gave no hope for a successful realization of a rotary engine.

In 1926, the German engineer, Felix Wankel, showed interest in rotary engines and started to study and investigate them systematically. He established an institute where he also designed and built test rigs for the evaluation of sealing elements. As an intermediate result of his research on seals, he developed a sealing arrangement for a rotary disc valve for a reciprocating engine which was successfully operated and tested as a liquid-cooled high performance aircraft engine.

In 1951, he was able to reopen his Research Institute with the financial assistance of three German concerns. He then investigated known and new rotary machines. This study led him to the conclusion that three main problems had prevented the rotating engine from achieving success so far:

1. The multiplicity of possibilities of arrangements and cycles for rotary engines which almost overwhelmed the inventors.
2. The problem of sealing high pressure chambers. This involved not the simple task of sealing a circular cylinder (like the pistion ring in reciprocating engines), but the more complex problem of sealing in several planes, with the sealing of corners as the most difficult.
3. The problem of developing a proper thermodynamic and gas cycle with adequate port areas and timing of events.

Wankel Engine Principle

The combination of a suitable geometric and kinematic arrangement which offered good sealing possibilities, and

* Formerly of Curtiss-Wright Corp.

could incorporate an efficient cycle within one engine, had to be found. Wankel eventually arrived at two rotating combustion engine configurations which appeared superior and were subsequently built and operated satisfactorily.

In both configurations, the engine has two main components, an outer rotor having a cavity within which an inner rotor is relatively rotable. In practice, the outer rotor preferably consists of a center housing and two attached parallel side housings. The two rotors have spaced but parallel axes. The inner surface of the center housing is an epitrochoid while the outer surface of the inner rotar approximates the inner envelope of this epitrochoid during their relative rotation. The apexes of the inner rotor are in contact with the epitrochoid at all times which simplifies their sealing. The two rotors are rotated in the same direction about their respective axis at a speed ratio of the outer rotor to the inner rotor of n + 1/n when n is equal to the number of lobes of the epitrochoid. The speed ratio particularly suitable for an efficient and still simple cycle is 3/2. This geometry is shown in Fig. 1.

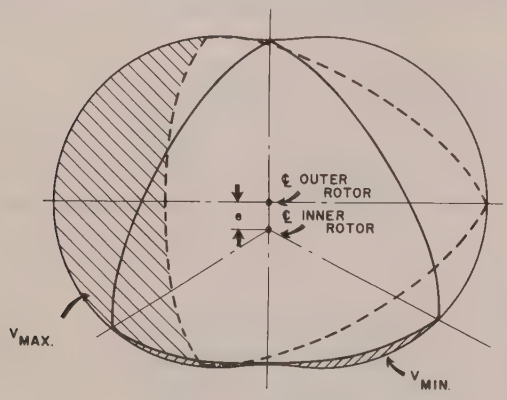

Fig. 1 — Engine geometry

Two positions of the rotor are depicted which give the maximum volume of a working chamber (at bdc) and the minimum volume (at tdc). The difference between these volumes, of course, constitutes the displacement of the engine and their ratio the theoretical compression ratio. The volume change with rotation is sinusoidal. A cutout in the inner rotor provides the actual desired compression ratio and a gas transfer passage at tdc. In one configuration, both rotors rotate at this speed ratio while in the other configuration, the outer rotor is stationary and the inner rotor has a planetary motion about the axis of the outer rotor. The relative motion of the two rotors is, however, the same in both cases and will be demonstrated later on. The configuration in which both rotors rotate (which will be refered to as the "dual rotation" type) has advantages from the standpoint of the seal operation and since Wankel was very much concerned with the sealing problem, this was the configuration on which his first engine was based. It was designed by him

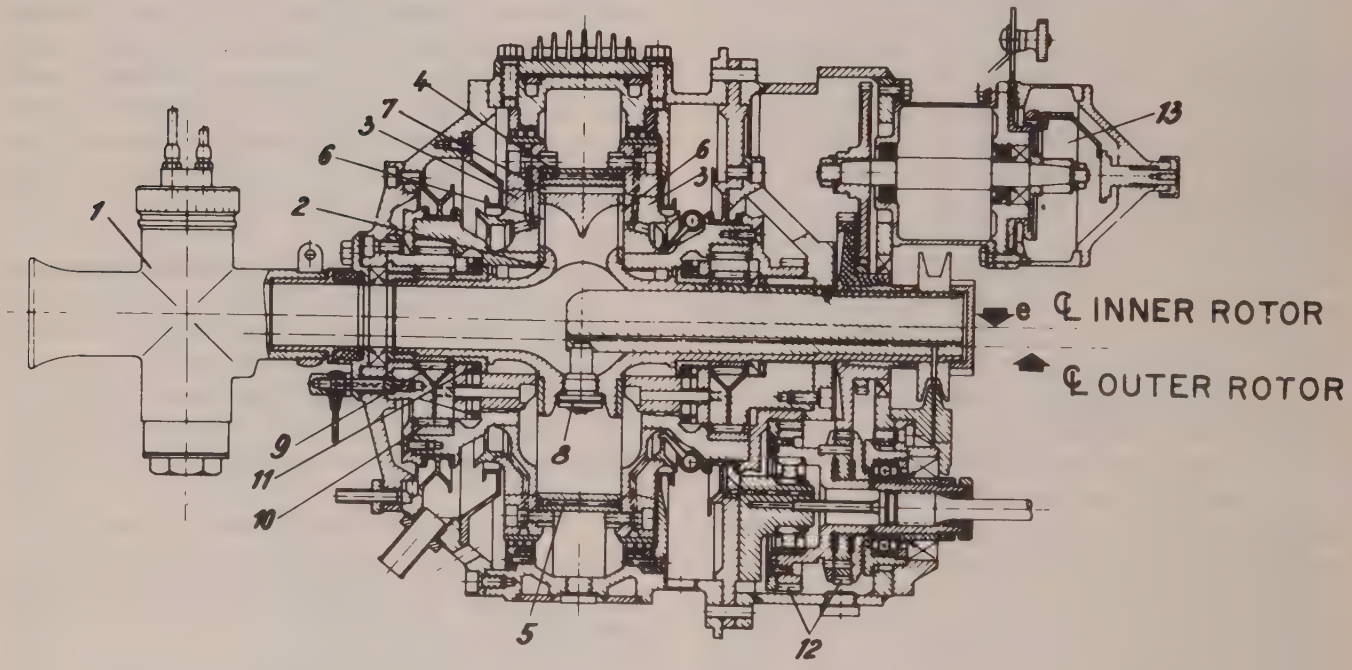

1. Carburetor.
2. Inner Rotor.
3. Outer Rotor - Side Housings.
4. Outer Rotor - Center Housing.
5. Cooling Channels.
6. Sealing Side Plates.
7. Apex Seals.
8. Spark Plug.
9. Bearing for Inner Rotor.
10. Bearing for Outer Rotor.
11. Low Pressure Gas Seals.
12. Gears for Outer and Inner Rotor.
13. Breaker.
14. Output Shaft.

Fig. 2 — Longitudal section of first experimental rotating combustion engine with dual rotation (NSU-Wankel)

and his associate, engineer Ernst Hoeppner.

NSU-Wankel Experimental Engines

The longitudinal section of this engine (Fig. 2) depicts the inner rotor and the outer rotor whose parallel axes are at a distance e and which rotate in the same direction with a speed ratio of 2/3. The engine, therefore, is fully balanced and does not have any mechanical vibration. The outer and inner rotor are connected by gears which guarantee exact positioning of the two rotors but do not transmit the engine torque. The air fuel mixture enters the chambers through the carburetor, the hollow shaft of the inner rotor, intake ports in the inner rotor and cutouts in the side housings of the outer rotor. The inner rotor contains three spark plugs, one for each chamber, which are supplied by a breaker shown on the right. Both the inner and the outer rotor are supported by needle bearings. The outer rotor and, at a later stage of development, the inner rotor as well, are water cooled. This dual rotation engine and its gear arrangement and water cooling make for a rather complex design and intake system but it served its purpose in supplying basic information on the thermodynamic and gas cycle and the performance of the engine.

Fig. 3 shows the actual engine partly disassembled, the inner rotor, one of its spark plugs and intake ports, the outer rotor with the cutouts in the side housing, and the trochoidal shape of the center housing, the cooling channels in the center housing, and the stationary engine housing with exhaust outlets. The engine exhaust emerging from the single exhaust port in the outer rotor is collected in an annular passage between the outer rotor and the engine housing and leaves through these stationary outlets.

Fig. 3 — First experimental engine, partly disassembled. Inner rotor with spark plug and intake ports, side housings of outer rotor with cutouts, outer rotor center housing showing trochoid, engine housing with exhaust outlets

Fig. 4 — Inner rotor partly disassembled showing seal side plates with strip seals, apex seals, and corner pins

Fig. 4 shows the inner rotor partly disassembled, the sealing plates with sealing strips, the apex seals which are made in five pieces for good sealing of the corners, and the pin which provides sealing between the sealing strips, the apex seals, and the side housings of the outer rotor.

Under Dr. W. Froede's direction, this engine was built and tested by NSU and eventually developed 28.4 hp at 17,000 rpm of the outer rotor (11,300 rpm of the inner rotor) which is equivalent to 1.23 hp per cu. in. displacement.

A single rotation engine of the same displacement was subsequently designed. It was much smaller and simpler than the dual rotation engine although its sealing elements were essentially the same.

At this point in the development, Curtiss-Wright became interested in this type of engine because it showed promising capabilities with respect to simplicity and costs, complete freedom of mechanical vibration, small bulk and weight, elimination of speedrestricting valve gear mechanisms, and an efficient operating cycle. Curtiss-Wright made a license and engineering assistance agreement with NSU and Wankel. The company concentrated on a bigger engine, eight times the size of the two German experimental engines, and has designed, built and tested nine experimental engines of the single rotation type with 60 cu in. displacement.

Curtiss-Wright Engines

Fig. 5 shows the components of this experimental engine. Fig. 6 shows the engine assembled and Fig. 7-11 show the cycle sequence:

1. Fuel-Air Intake.
2. Fuel-Air Compression.
3. Fuel-Air Ignition and Combustion.

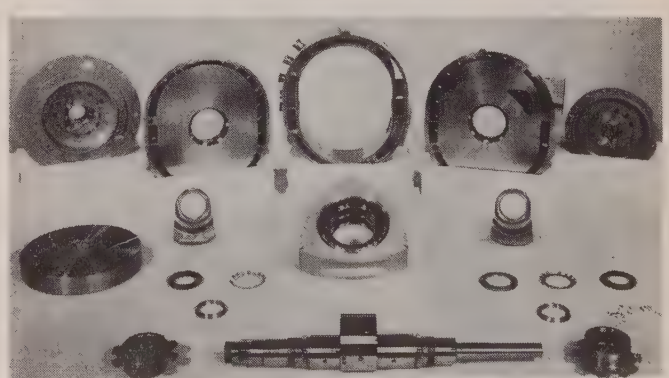

Fig. 5 — Components of first Curtiss-Wright rotating combustion experimental engine

4. Power Phase.
5. Exhaust.

In the design, ample margins were provided for the crankshaft, the bearings, and the cooling of the rotor and the housings. No major failure occured during hundreds of hours of performance and durability testing.

The sealing system was copied from the small engines. Whereas the bigger engine gave advantages in some respects: many of the sealing components were not durable enough and a more rugged system was worked out and incorporated in the rotor. This seal arrangement proved more durable and tighter.

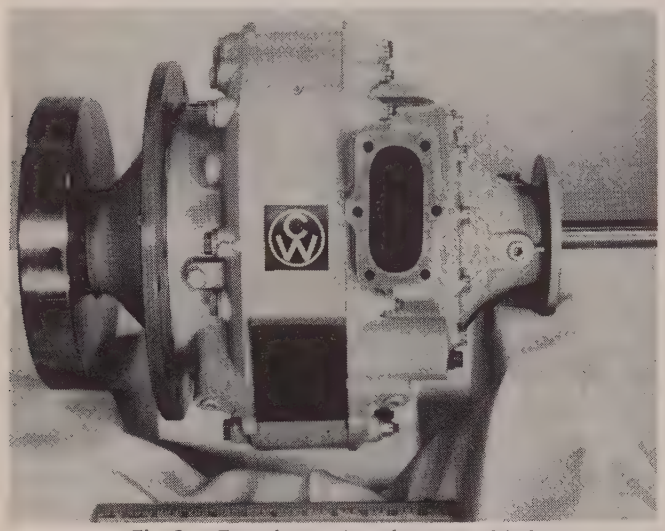

Fig. 6 — Experimental engine assembled

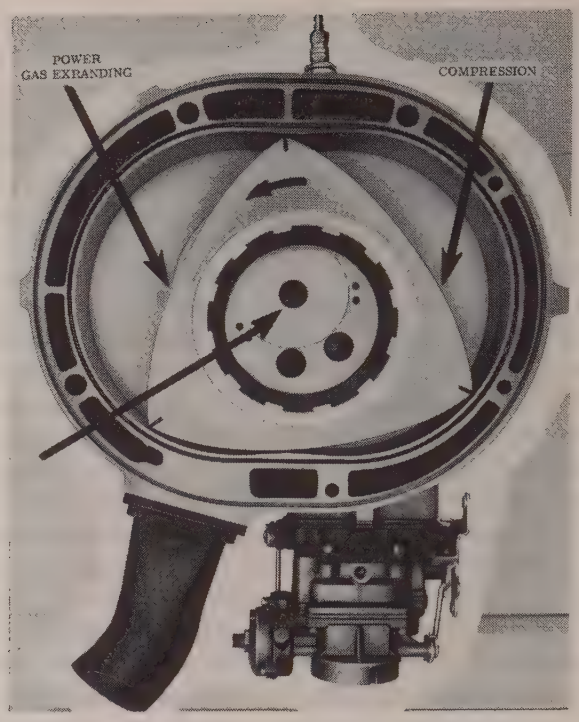

Fig. 8 — Fuel-air compression

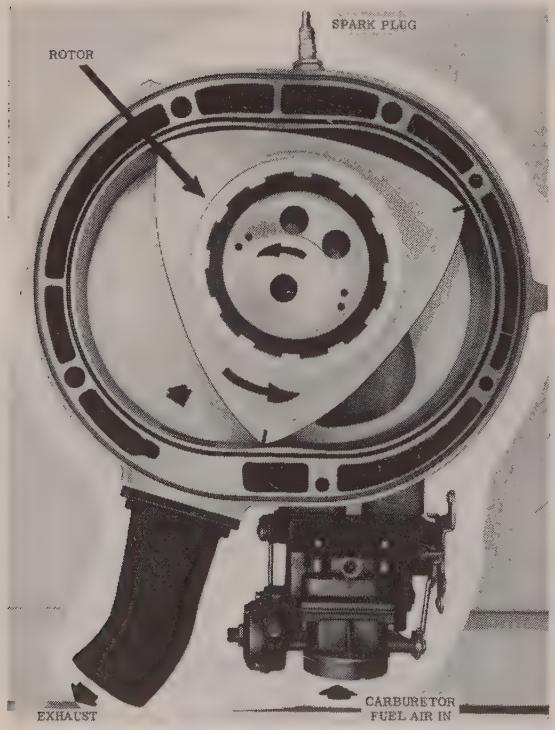

Fig. 7 — Fuel-air intake

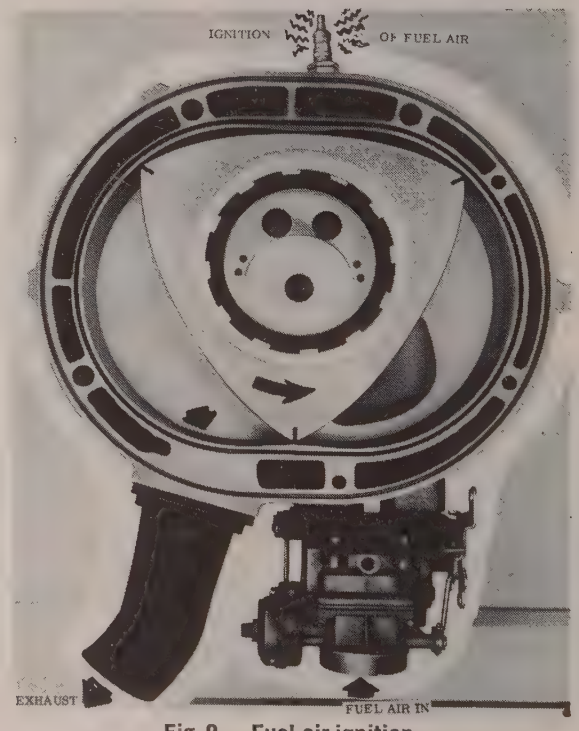

Fig. 9 — Fuel-air ignition

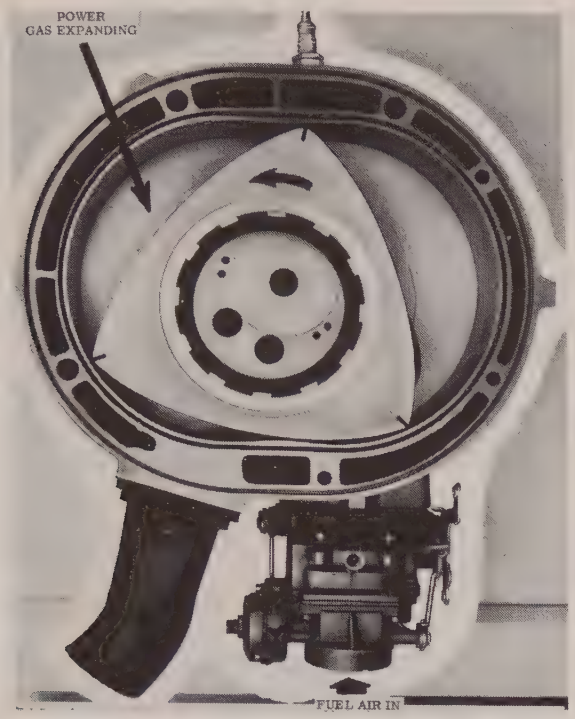

Fig. 10 — Power stroke — gas expanding — intake opening — exhaust closing

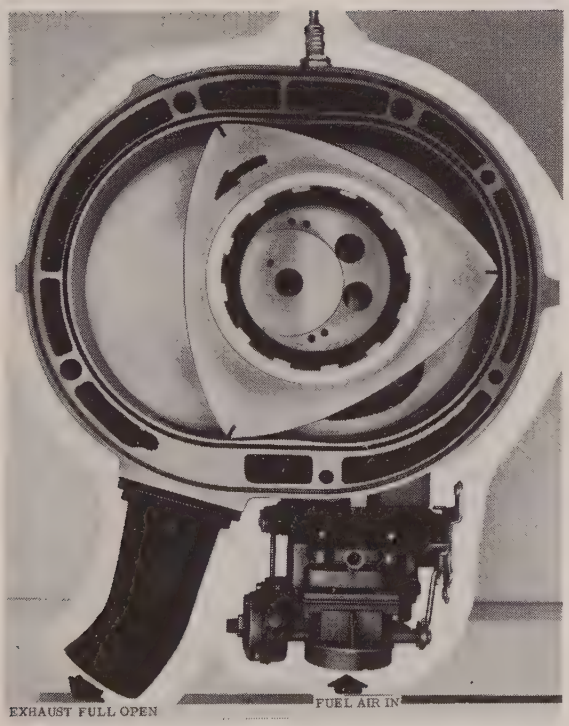

Fig. 11 — Exhaust

Fig. 12 compares the cycle of a single unit rotating combustion engine with a single cylinder 4-stroke cycle reciprocating engine. Plotted are chamber pressures versus crank angle covering four revolutions of the crankshaft for each engine. The diagram shows that during these four revolutions, the reciprocating engine, of course, has two power sequences, whereas the rotating combustion engine has four. This being significant in itself, the diagram also shows that each power sequence of the rotating combustion engine covers a wider crank angle than reciprocating engine, the ratio being 3/2.

Consistent with this are, also, the intake and exhaust flow, both of which have shorter dwell periods for the rotating combustion engine, thus reducing intake and exhaust losses and providing a smoother operation for single and

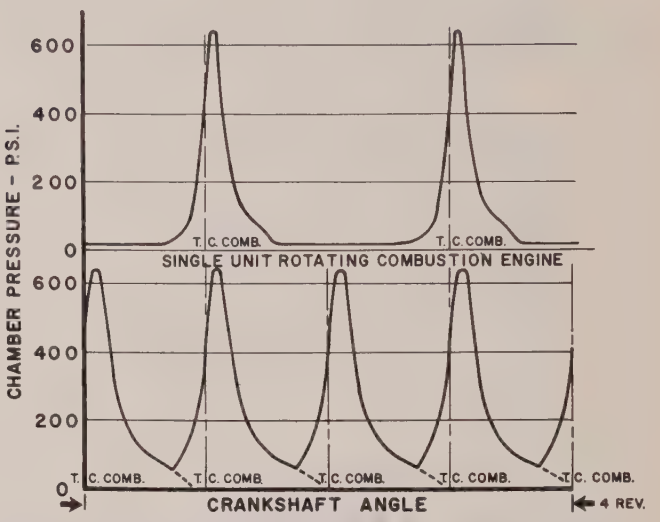

Fig. 12 — Chamber pressure versus crank angle, single cylinder 4-stroke cycle reciprocating engine

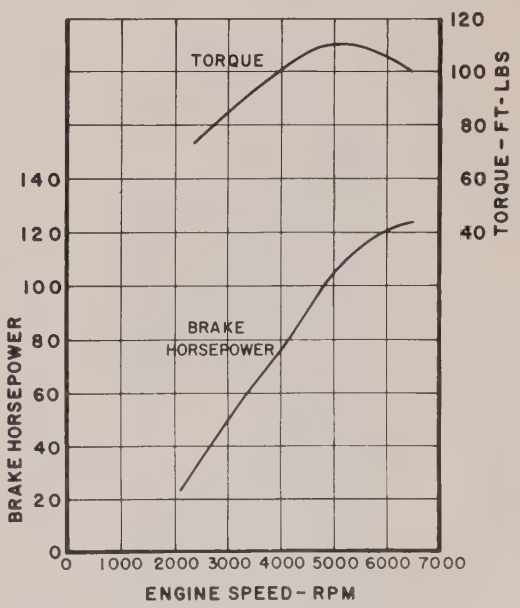

Fig. 13 — IRC 6 test performance, full throttle, peripheral intake port

multi-power section engines. A multi-unit engine has been built by stacking power sections with an integral crankshaft.

Curtiss-Wright designated this engine as the "Rotating Combustion Engine".

Test Results

Fig. 13 shows the full throttle performance of the engine equipped with a side port intake. This engine develops 100 hp at 5500 rpm which is equivalent to 1.67 hp per cu in. displacement. The output curve further shows that the port areas are not limiting factors. The torque curve is flat over a wide speed range from about 2000 - 6000 rpm. At the lowest speeds, the torque drops somewhat but can be modified by other porting as will be shown later, or by further development of the engine. In the initial development stages, attention has not been directed toward the low speed torque end. However, test experience with porting configurations and satisfactory starting at very low speeds has indicated that improved performance in this regime can certainly be obtained if required for certain uses. The specific fuel consumption is also flat over a broad speed range and shows a minimum consumption of 0.47-lbs/hp/hr.

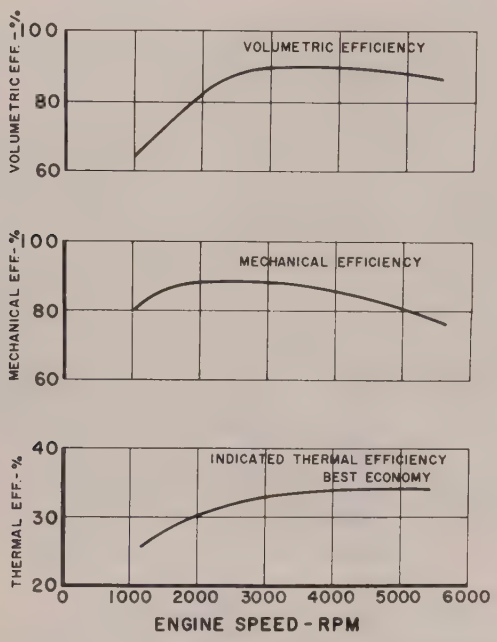

Fig. 14 — IRC 6 test performance, full throttle, side intake port

Fig. 14 shows the volumetric, mechanical and indicated thermal efficiencies. Consistent with the torque characteristic, the volumetric efficiency is high over a wide speed range and reaches, with a side port intake, values of 90% and more. The mechanical efficiency also reaches almost 90% at the lowest speeds, indicating that the mechanical friction of the engine is low. The mechanical efficiency drops at higher speeds, but this is expected to be improved with further developemnt. It should be noted that at 100 hp, the mechanical efficiency still is approximately 80%. The indicated thermal efficiency for best economy reaches 34% over a wide speed range.

Fig. 15 shows the performance of the same engine but equipped with a peripheral intake port. This port further reduces the intake losses and results in correspondingly higher airflow and output. The engine delivers 124 hp at 6500 rpm, equivalent to 2.05 hp per cu in., and again shows promise of further output increase with speed and some development. In the meantine, speeds up to 8000 rpm have been successfully run.

The volumetric efficiency and airflow in Fig. 16 show the high-speed characteristic of this engine, with volumetric

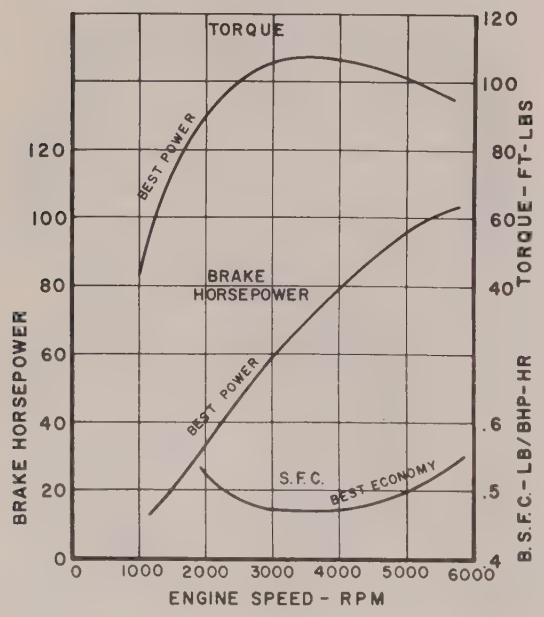

Fig. 15 — IRC 6 test performance, full throttle, side intake port

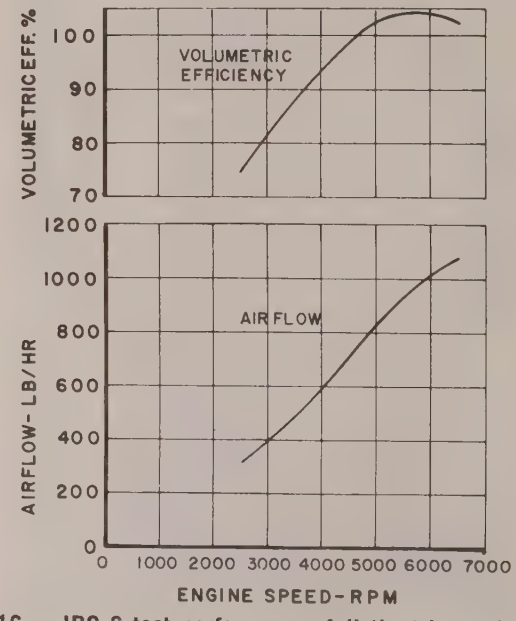

Fig. 16 — IRC 6 test performance, full throttle, peripheral intake port

efficiencies exceeding 100% and a steadily increasing airflow with speed reaching almost 1100-lbs/hr at 6500 rpm. At the present time, the peripheral port engine is slightly inferior with regard to air utilization as compared to the side port engine. This fact is reflected in a somewhat higher specific fuel consumption. This peripheral port configuration provides good breathing capacity and will eventually exceed the side port performance.

Fig. 17 demonstrates that the engine speed-torque characteristic can be considerably varied and adjusted to different applications by port area and timing. Whereas the "large port" designated engine shows a peak torque of 95-ft/lbs at 6000 rpm, the "small port" engine delivered--consistent with the airflow characteristic--105-ft/lbs at 4000 rpm.

Fig. 18 demonstrates the power and fuel consumption as a function of the fuel/air ratio for full throttle constant speed. The values of 0.061 fuel/air ratio for best economy and 0.073 for best power show good combustion characteristics in the engine.

Having reached the performance figures just discussed, various engines were submitted to endurance tests. At full throttle and speed, the engine characteristics were consistent during 100 hrs of operation. This same consistency was achieved during cyclic endurance tests consisting of alternate periods of full throttle and full speed, part throttle and full speed, part throttle and reduced speed, and idle.

Appendix

Cooling - Liquid cooling has been used for both the housing and the rotor. The former is water cooled and the latter is cooled by lubricating oil pumped through the main shaft.

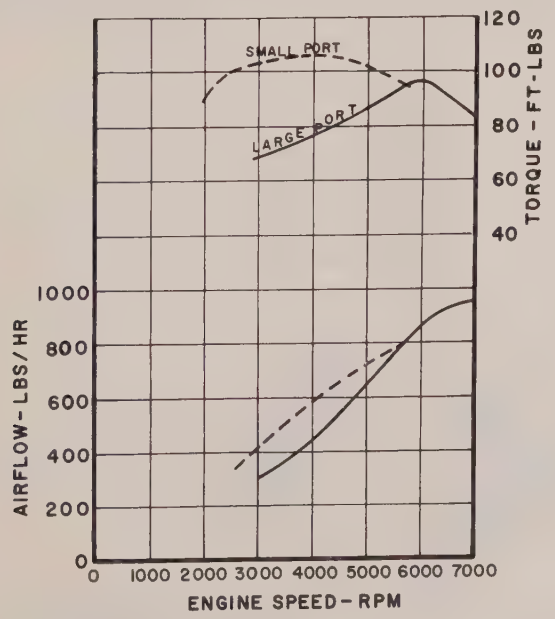

Fig. 17 — IRC 6 test performance, full throttle, small versus large side intake port

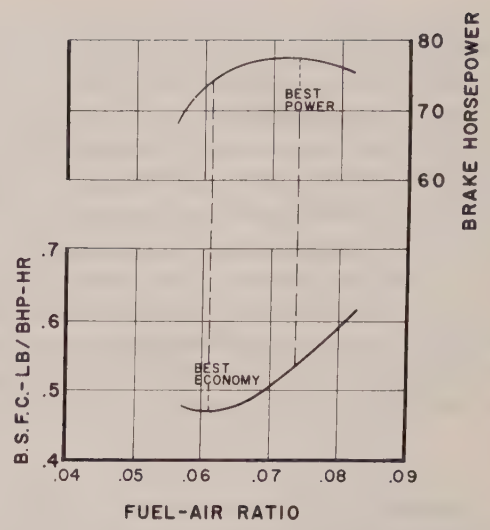

Fig. 18 — IRC 6 test performance, mixture characteristics, 4000 rpm — full throttle

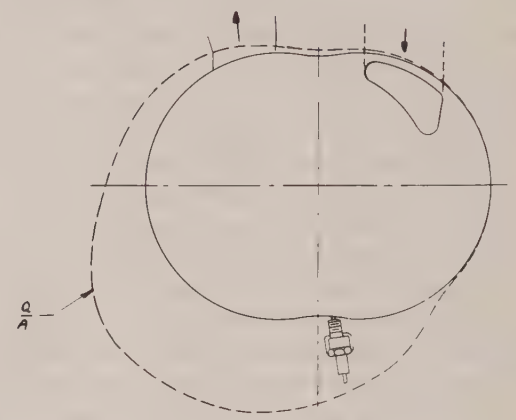

Fig. 19 — Plot of heat input per unit of gas-exposed area

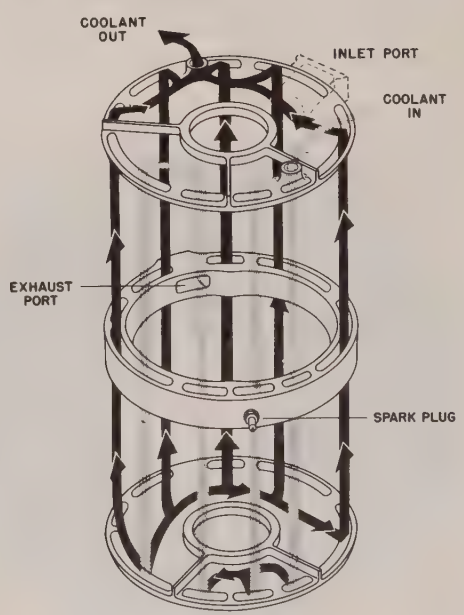

Fig. 20 — Schematic of housing cooling system

1. Housings. The rotating combustion engine, unlike a conventional reciprocating engine, always exposes the same stationary housing locations to the same portion of the cycle; the variation of heat input per unit of gas-exposed area along the trochoid periphery is hown in Fig. 19. To match this distribution, the housing cooling was designed as a multipass forced-flow system, as schematically illustrated in Fig. 20. The cooling liquid flows back and forth through the rotor housing and between the end housing walls. The rotor housing flow passages are parallel to the engine axis; the internal ribbing of the end housings redirects the flow, as shown in Fig. 21, where the trochoidal rotor housing is in position and the wear face of the end housing has been removed.

The flow area and wetted perimeter, and thus the hydraulic diameter, vary from pass to pass, and are adjusted to match the combustion cycle heat input variation. For example, in hot regions of the engine, the flow velocity is high; the amount of heat transfer surface, accomplished by additional ribbing, is large; and the ratio of the total flow area to the total wetted perimeter per pass is small. This series forced-flow configuration permits balanced cooling with large, clog-free, easy to manufacture passages, and avoids vapor accumulation. Furthermore, the large passages permit a cooled wet-bolt application.

This system minimizes temperature variations of the housings. Thermal distortions are further restrained because of the type of structure employed: the outer walls of the housings run cold and maintain the designed shapes while permitting uniformly thin heat transfer walls. The locations of maximum heat input correspond to the locations of maximum stress, so that the addition of ribs, to improve heat transfer, serves to accommodate structural needs as well.

2. Rotor. The rotor is made from an aluminum forging, which offers the benefits of lightweight and high thermal conductivity, but requires adequate cooling.

One of the most successful aluminum rotor designs is cooled by forced circulation of oil from the engine lubrication system. The cooling circuit is schematically illustrated in Fig. 22. Oil is supplied from the hollow shaft, through radial feed holes in the eccentric, and then to the rotor bearing central annulus. The oil then divides, one part to lubricate the bearing and the other to cool the rotor.

Integral fins in each rotor lobe provide adequate cooling surface and a small hydraulic diameter. A recess at each end of these finned passes acts as a manifold for distribution of the oil.

The oil from the rotor exit, after passing the bearing end annulus, is discharged from timed shaft eccentric passages directly into the housing drain annulus.

The oil entering temperature, temperature rise, and period of contact with the metal are controlled to avoid coking or other lubricant deterioration. To date, we have had no evidence of adverse effects in this regard. While the oil flow of this design is continuous, the velocity varies as a function of the system dynamics: shaft and rotor inertia pumping superpose a roughly sinusoidal pressure increment onto the oil supply pressure. The cooling oil is metered at the exit; in this way, the rotor cavities are maintained full.

Whereas this aluminum rotor was designed and proved suitable for high-performance, high-speed operation a nodular cast iron rotor has performed satisfactorily for less stringent conditions in this respect. This was achieved with a simpler cooling system and even with no internal oil cooling at all.

Ignition - Initial engine tests used automotive ignition systems and spark plugs of a normal automotive heat range. With increase in power and speed, it was found necessary to use a spark plug of very cold design for plug durability, and some plug fouling was then encountered. An auxiliary air gap at the spark plug reduced the fouling somewhat, but the periods between plug changes due to fouling and gap erosion

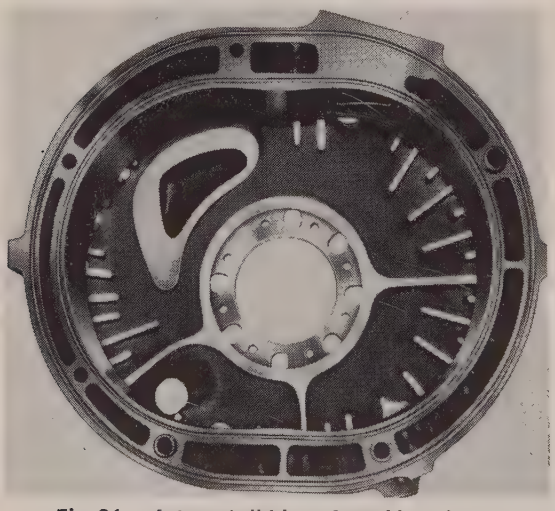

Fig. 21 — Internal ribbing of end housings

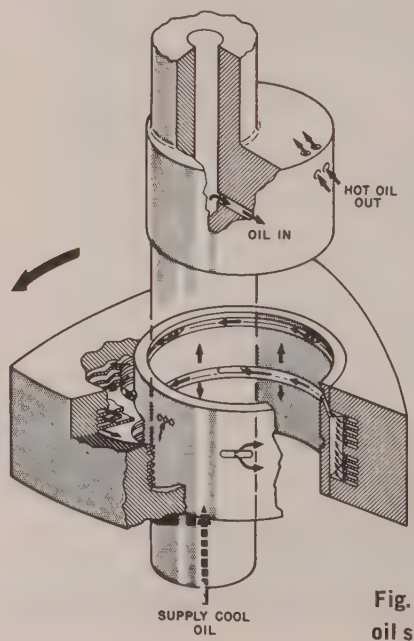

Fig. 22 — Rotor cooling oil schematic

were still not acceptable.

A Curtiss-Wright designed condensor discharge system, which produced a voltage rise rate four times that of an automotive system, reduced gap erosion and sensitivity to fouling deposits considerably. The plug change periods were increased four to ten times. With a still higher voltage rise rate, full power tests for 150 hr, cyclic endurance tests for 75 hr, and numerous general development tests with no cases of plug fouling and a very low gap erosion rate were accomplished.

The basic system is outlined in Fig. 23. A transistorized power supply charges the condensor. When the engine driven maker closes, the condensor discharges to ground, causing a surge of current through the coil primary. This surge generates a secondary voltage to fire the spark plug.

The coil is small and is designed to provide an adequate firing voltage even when loaded with a fouled spark plug.

The usual breaker system is modified to a maker and, at the same time, the dwell is much shorter to conserve dc power. Due to the high voltage that is being switched, the quality of the contact surfaces need not be high to generate a reliable spark.

A standard distributor unit has been satisfactorily run for some 800 hr at 10,000 sparks per min. Timing drifted about 2 deg in the first 400 hr and about 1 deg in the last 400 hr. Point gap decreased about 4/1000 in. from the nominal 17 setting. Spark voltage was normal during this period and there was no tendency for the points to weld and stick.

Fig. 24 shows the plug voltage required by a large, conventional V-8 engine versus the requirement of the 1RC6 type in terms of sparks per minute. The rotating combustion engine requires a lower voltage over the operating speed range.

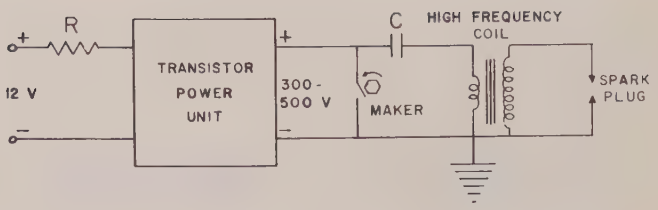

Fig. 23 — Basic system outline

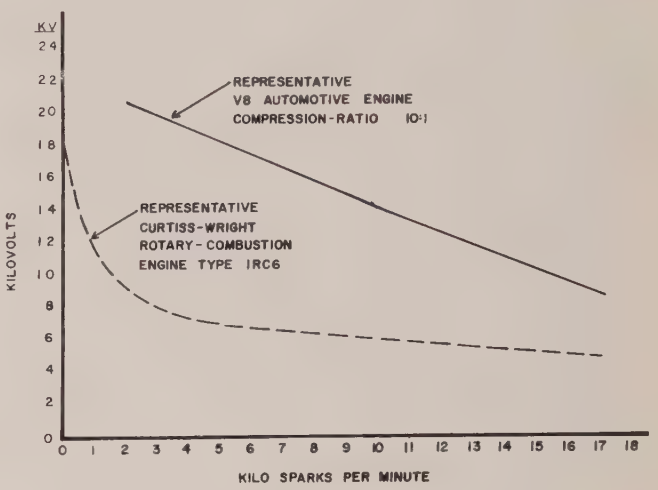

Fig. 24 — Engine ignition voltage requirements

Strength of Materials After Severe and Complex Thermal Histories

D. M. Badger and C. D. Brownfield
Northrop Corp.

ACCURATE METHODS are needed for predicting the effect of severe thermal environments on the strength of flight vehicle materials. Most metallic materials for such applications derive a large part of their strength from a hardening treatment. The hardening mechanism becomes unstable at high temperatures and progressive changes occur which cause softening and strength reduction. Addition of stress during elevated temperature exposure can have an accelerating effect on this strength reduction. These permanent changes are additive to the recoverable losses in strength which all metals show with increasing temperature. If the effects of these variables on materials can be predicted for complex environments the useful temperature range can be extended.

This paper presents an approach for predicting cumulative losses in short time strength of many materials as a result of exposure to complex thermal and stress histories. This approach is based on rate process theory.

Background

Many time and temperature dependent metallurgical processes occur in good agreement with the rate process equation:

$$r = Ae^{-Q/RT} \quad (1)$$

where:

- r = reaction rate
- A = constant
- Q = activation energy for the process
- R = gas constant
- T = absolute temperature

A very useful time-temperature parameter has been derived from this basic equation. It is:

$$\theta = T(C + \log t) \quad (2)$$

where:

- θ is used to identify the parameter
- C = a constant which varies with the material and process
- T = absolute temperature
- t = time

The units for temperature and time are selected as deg R and hr, respectively, for use in this paper.

This expression was used first by Holloman and Jaffee to relate time and temperature for a given final hardness in the tempering of steel, (1)* and later by Larson and Miller in the creep and rupture of aluminum alloys (2).

In 1956, Fortney and Avery, working under Air Force sponsorship at Northrop Corp., Norair Division, found that the same expression could be used to relate time and temperature in the over-aging of 2024-T3 and 7075-T6 aluminum alloys (3). They extended the use beyond simple exposures, however, to include complex exposures having up to four temperature steps.

The value of such a development is apparent. It made determination of the effect of complex thermal exposures on material strength possible without performing a test program for each design situation. Fortney and Avery carried their work through the development of generalized design curves covering the tensile properties of the alloys studied.

Further progress has been made since this initial investigation. A more detailed investigation has been made of the 7075-T6 alloy covering more complex exposures; strengths in compression, bearing, and shear; and the effects of adding stress to the exposure environment (4). Techniques in applying this approach to other alloys (PH15-7Mo, AISI Type 301 Extra Hard Stainless and Rene' 41) are currently under development (7).

The 7075-T6 alloy is discussed in detail in this paper since this was the study material on which the methods of analysis were developed and therefore on which the most complete data have been obtained.

Thermal Exposure Effects

Aluminum alloy 7075 reaches its maximum strength "T6"

*Numbers in parentheses designate References at end of paper.

condition through a heat-treat procedure which results in a controlled degree of precipitation or aging. Further precipitation results in a lessening of strength and is termed "over-aging." The precipitation reaction is time and temperature dependent, occurring more rapidly as temperature is increased. At least two different time-temperature conditions could therefore give the same degree of over-aging and result in the same final strength.

If this reaction were to follow the rate process equation there would theoretically be an infinite number of combinations of time and temperature for any given degree of over-aging, or for any given value of T(C + log t).

Studies have shown that within practical limits this is the case for aluminum alloys 7075-T6 and 2024-T3, and many other hardened materials in which similar reactions occur. The agreement obtained from test data on the ultimate strength of 7075-T6 is shown in Fig. 1 reproduced from Ref. (4). Strength values at room temperature and at 300 F after prior exposure to various combinations of time and temperature are plotted against the exposure parameter T(C + log t) using a value of C = 17. Good agreement with the exposure parameter is indicated for exposure conditions ranging from 1 to 100 hr in duration. Data developed by Fortney and Avery on this alloy and also on 2024-T3 were in good agreement with the exposure parameter (although with different values of C) for exposure times which ranged from 0.1 to 1000 hr (3).

If this agreement persists unaffected by variable or intermittent temperature conditions, then this parameter provides a useful method for assessing the cumulative effects of complex thermal exposures. The results of a series of complex exposure tests on 7075-T6 are shown plotted against the same exposure parameter in Fig. 2. These data include tests on specimens exposed to two, three, four, or ten increments of differing temperature-time conditions; some sequences had single direction temperature trends, increasing or decreasing, others had well-mixed exposure conditions. The single exposure curve of Fig. 1 is reproduced here to show the agreement obtained.

The values of the exposure parameter for each complex exposure condition were obtained in the following way:

1. Each increment of exposure was converted into a value of the exposure parameter θ.
2. The incremental θ values were then converted into equivalent values of time at a chosen reference temperature T_{ref}.
3. The values of equivalent time were added to find the total equivalent time at T_{ref} for the entire exposure spectrum, as shown in Table 1.
4. The exposure parameter value, θ_{total}, for the complex exposure condition was then computed from T_{ref} and the total equivalent time value.

Correlation in these two cases (Figs. 1 and 2) demonstrates that overaging of 7075-T6 follows the rate process equation whether the thermal exposure is simple or complex with up to 10 exposure steps. Similar correlation was also demonstrated on 2024-T3 by Fortney and Avery, for up to 4 temperature-time increments. It is reasonable to expect that these materials will continue to demonstrate such agreement for even more complex cases than those tested provid-

Table 1 - Total Equivalent Time at T_{ref} for Entire Exposure Spectrum

Given Spectrum	$\theta = T(17 + \log t)$	Equiv. Time at T_{ref}
T_1, t_1	θ_1	Equiv. t_1
T_2, t_2	θ_2	Equiv. t_2
T_3, t_3	θ_3	Equiv. t_3
.	.	.
.	.	.
	$\sum t_i$ =	Total Equiv. Time at T_{ref}

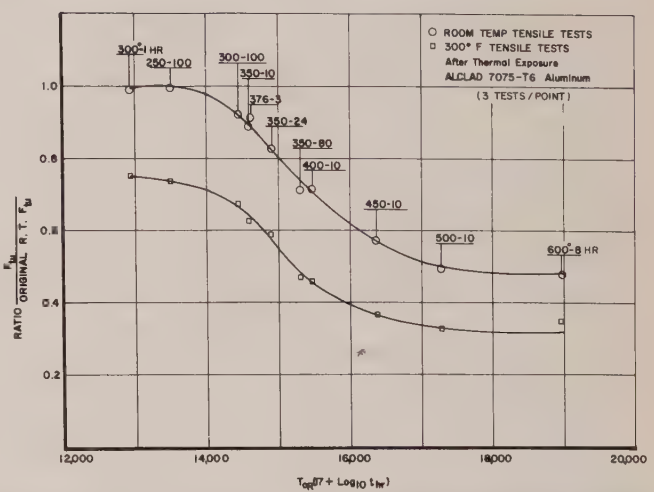

Fig. 1 — Tensile strength of 7075-T6 versus exposure parameter — single exposure (4)

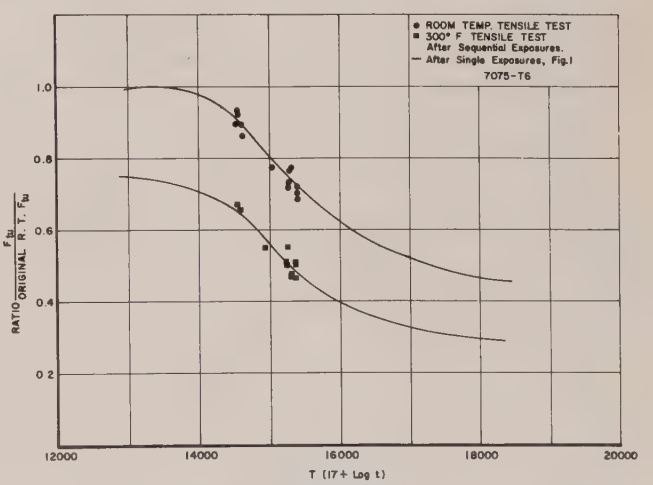

Fig. 2 — Tensile strength after complex exposures compared with strength after single exposures (4)

ed that the effects of transition between temperature levels are negligible or are properly accounted for. However, continuing agreement for very large numbers of temperature changes remains to be demonstrated.

An area of special interest in these studies is that of variation in the best value for the constant C in the expression T(C + log t). Among the various alloys studied values of C as low as 14 and as high as 40 have been found. According to the rate process basis for this expression, a change in C value should indicate a change in the activation energy for the controlling process. It is known that a change in chemistry can result in such a change in activation energy and this is probably the most important source of variation in C. In tests on two different lots of 7075-T6, values of C of 14 (approximately) and 17 gave the best agreement. This seems to indicate that very slight changes in chemistry can cause a change in the activation energy. Finally in some alloys the best value for the constant C apparently increases between the moderate and the severe (higher temperature) regions of thermal exposure. Further study is needed in these latter two areas.

The basic rate process approach to strength deterioration has been applied with fair to very good success to the following aluminum alloys: 2024-T3, 2024-T86, 2014-T6, X2020, 2618-T61, 7075-T6 and 7079-T6. It has also been successfully applied to the heat-treatment of titanium alloys (9). It has already been noted that the tempering of martensitic steel is in accord with the rate-process approach. Recent studies at Norair have indicated similar agreement for two stainless steels, AISI Type 301, Extra hard and PH15-7Mo, but some difficulties with the superalloy Rene' 41.

Characteristic Strength Changes

Practical design situations frequently require other types of strength data than ultimate tensile strength; such as yield strength in tension or compression, and strength in shear and bearing. Fortunately, there is ample justification for extending the above approaches to other mechanical strength properties. The agreement of data on tensile strength after

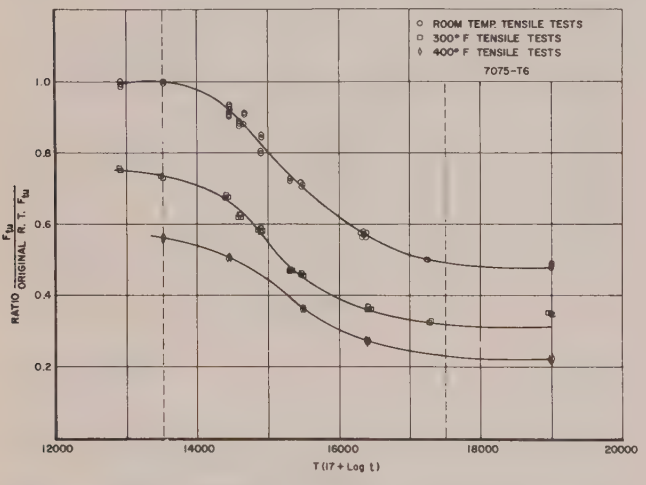

Fig. 3 — Tensile ultimate strength variation with thermal exposure (4)

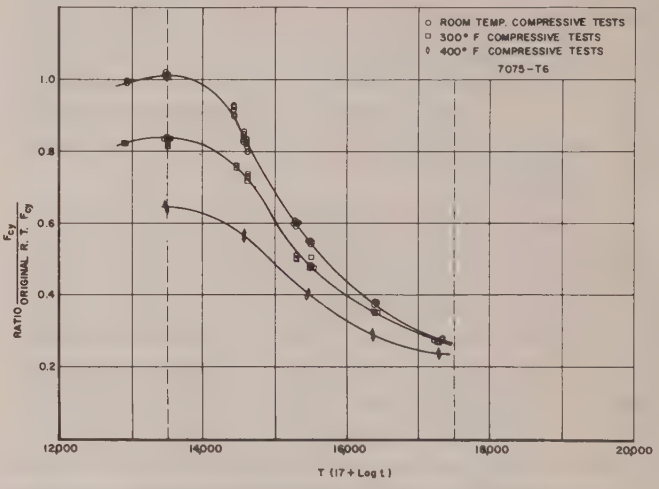
ROOM TEMP. COMPRESSIVE TESTS
300° F COMPRESSIVE TESTS
400° F COMPRESSIVE TESTS
7075-T6
RATIO $\frac{F_{cy}}{\text{ORIGINAL R. T. } F_{cy}}$
T (17 + Log t)

Fig. 5 — Compressive yield strength variation with thermal exposure (4)

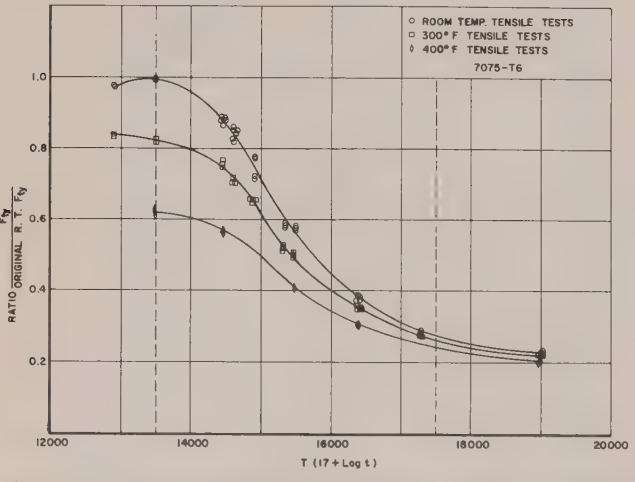

Fig. 4 — Tensile yield strength variation with thermal exposure (4)

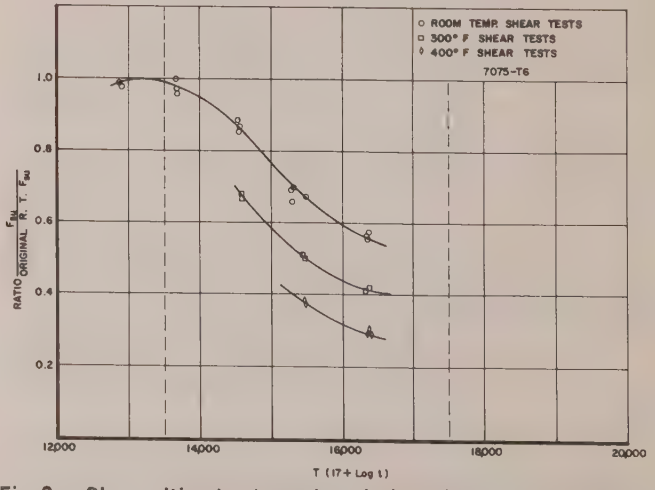

Fig. 6 — Shear ultimate strength variation with thermal exposure (6)

exposure with a time-temperature relating expression is actually an indication of similar agreement on the part of the basic metallurgical process. This basic process is thus a tie which relates the characteristic changes with exposure of all mechanical properties on which it has any effect.

This concept has been borne out in tests conducted on 7075-T6 in tension, compression, bearing and shear after various exposure conditions (4). The results of these tests are shown plotted against the exposure parameter $T(17 + \log t)$ in Figs. 3-7, wherein each data point plotted represents a single test result. It is apparent that this expression relates exposure time and temperature for all five types of strength at all test temperatures equally well. To further illustrate the similar characteristics in these curves, vertical (dashed) guide lines have been drawn at key exposure values. Agreement can be seen in the degree of exposure at which strength loss begins to occur and again in the degree of exposure at which the process is essentially complete. Furthermore, the same general shape of transition curve can be noted in all cases, although the range of total strength change does differ.

Further comparison of the various transition curve characteristics can be accomplished by relating the strength at any degree of exposure to the interval between the initial strength and the annealed strength. This approach is illustrated in Fig. 8. Here the ratio of the remaining strength increment (above annealed strength) to the total strength range expresses the position of the strength-after-exposure value in the range of possible values. This ratio has been called the Strength Deterioration Factor and is written:

$$D = \left. \frac{F_\theta - F_a}{F_o - F_a} \right|_{T_{test}} \qquad (3)$$

where:

F_θ = strength after exposure θ

F_o = initial strength

F_a = annealed strength

T_{test} = temperature of testing for all values

Two reference values of strength are needed to use this relationship, F_o and F_a, and these are needed for each type of strength and for all temperatures under consideration. For the 7075-T6 previously discussed, the needed reference values are shown in Figs. 9-13. The F_o values in each case

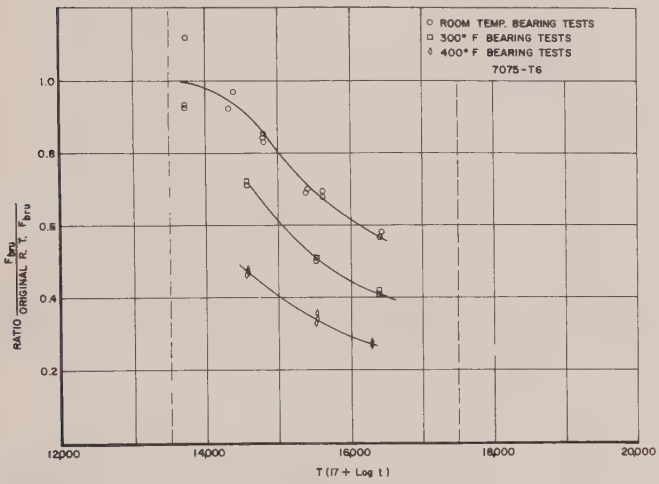

Fig. 7 — Bearing ultimate strength variation with thermal exposure (7)

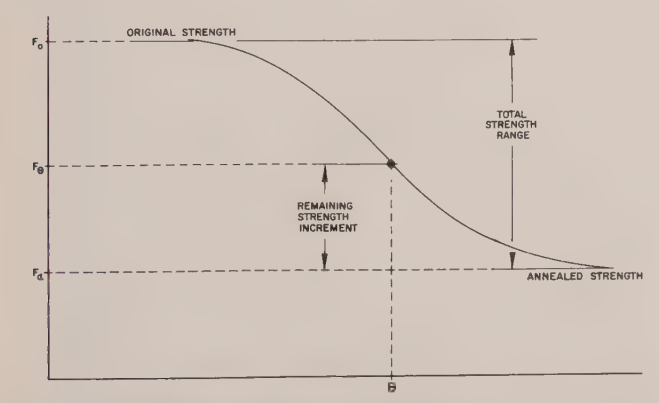

Fig. 8 — Strength after exposure as related to total strength range

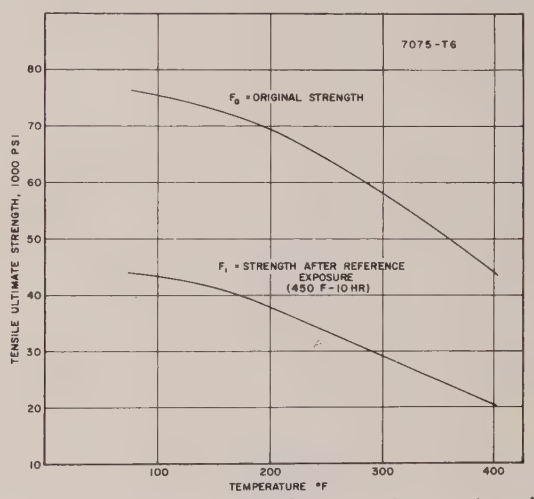

Fig. 9 — Tensile ultimate strength versus temperature before and after a reference exposure (4)

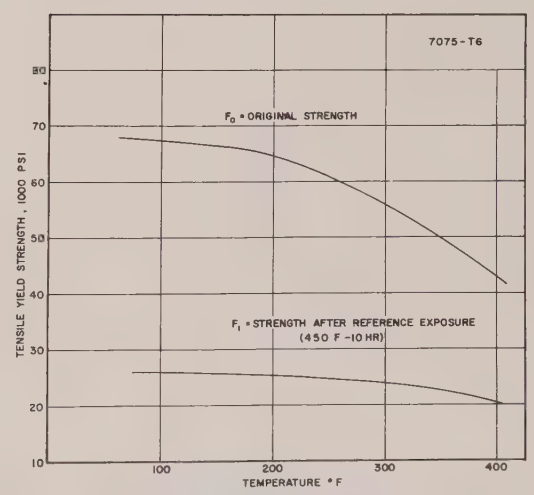

Fig. 10 — Tensile yield strength versus temperature before and after a reference exposure (4)

are strength at temperature after no exposure, and the F_1 values are strength at temperature after a reference exposure of $\theta = 16,380$ (450 F for 10 hr). Use of F_1 (nearly annealed) values instead of F_a (fully annealed) values is a matter of convenience and avoidance of scatter found in the fully annealed test values; this introduces negative values of the D factor but does not change the concept.

Comparison of all the 7075-T6 data of Figs. 3-7 on this basis is accomplished in Figs. 14 and 15. In Fig. 14 tension ultimate, tension yield, and compression yield strengths at room temperature 200 F, 300 F, and 400 F after single and multiple exposures are found to correlate together closely enough to be represented by a single curve.

In Fig. 15, shear ultimate and bearing ultimate strengths are compared to the single curve from Fig. 14. The same trends of the data are evident as before, although there is a tendency for the shear strength data to fall slightly below the curve and the bearing strength data to fall above.

The general correlation achieved provides the basis for procedures for prediction of strength of 7075-T6. Given a complex thermal exposure history, the first step is to find the total exposure, θ, by methods previously described. Next, the strength deterioration factor D is found either from the curve of Fig. 14 or from the empirical expression for this curve:

$$D = \frac{34.80}{(\theta \times 10^{-3} - 12.92)^4 + 28.95} - .202 \qquad (4)$$

$$(13,000 < \theta < 16,380)$$

Once D is known, the reference strength values for the type of strength and the temperature desired are chosen from Figs. 9-13. Finally, the desired strength is found from the following relationship:

$$F_\theta = DF_o + (1 - D) F_1 \Big|_{T_{test}} \qquad (5)$$

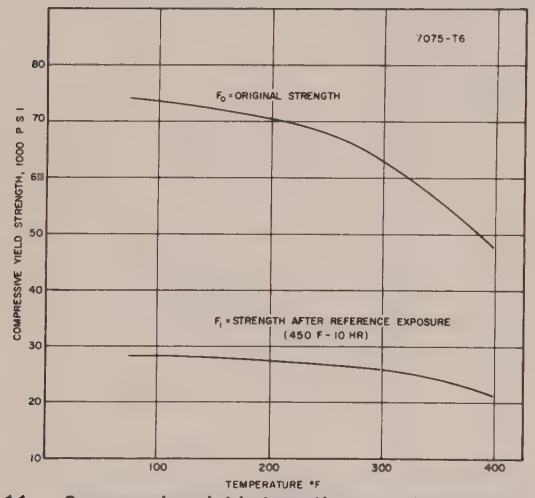
7075-T6
F_o = ORIGINAL STRENGTH
F_1 = STRENGTH AFTER REFERENCE EXPOSURE (450 F - 10 HR)
COMPRESSIVE YIELD STRENGTH, 1000 P S I
TEMPERATURE °F

Fig. 11 — Compressive yield strength versus temperature before and after a reference temperature (4)

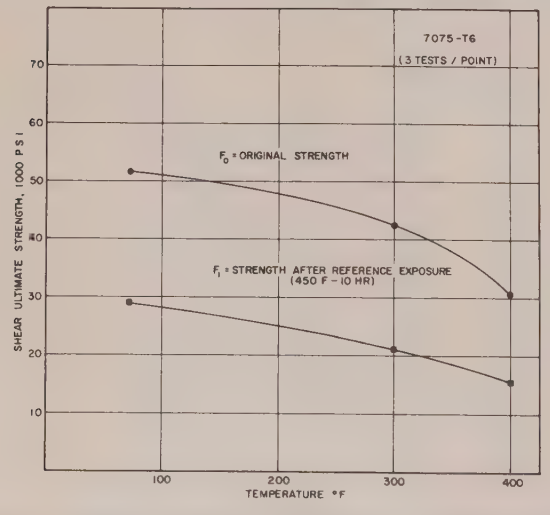
7075-T6
(3 TESTS / POINT)
F_o = ORIGINAL STRENGTH
F_1 = STRENGTH AFTER REFERENCE EXPOSURE (450 F - 10 HR)
SHEAR ULTIMATE STRENGTH, 1000 P S I
TEMPERATURE °F

Fig. 12 — Shear ultimate strength versus temperature before and after a reference exposure (6)

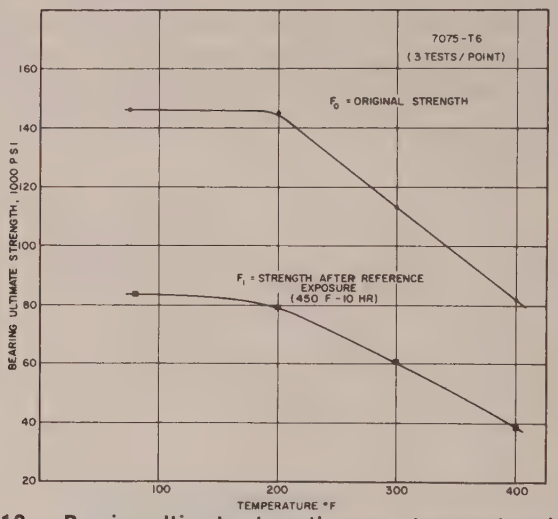
7075-T6
(3 TESTS / POINT)
F_o = ORIGINAL STRENGTH
F_1 = STRENGTH AFTER REFERENCE EXPOSURE (450 F - 10 HR)
BEARING ULTIMATE STRENGTH, 1000 P S I
TEMPERATURE °F

Fig. 13 — Bearing ultimate strength versus temperature before and after a reference exposure (7)

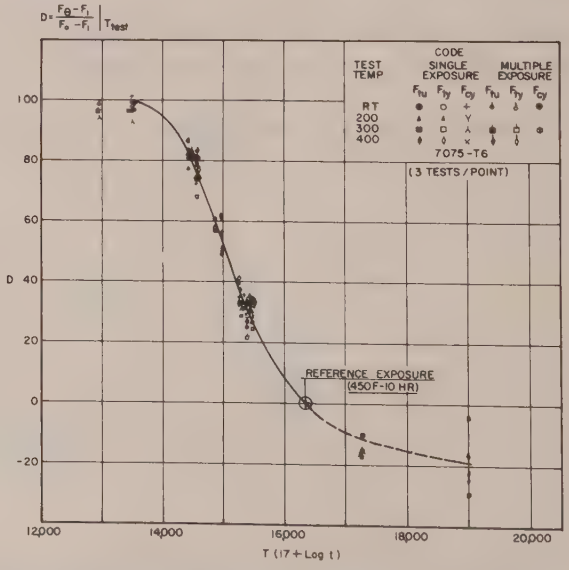

Fig. 14 — Tensile and compressive strength deterioration with thermal exposure for all conditions tested (4)

derived from Eq. (3).

This success with 7075-T6 graphically demonstrates the value of both the rate process approach to the problem of material over-aging and the hypothesis that all types of strength symptomatically reflect the same basic change in the material and hence tend to exhibit similarities in characteristics.

It should be noted, however, that there is no firm basis for expecting all mechanical properties to fall exactly on the same "D" curve. Ductility for instance, would have to follow an entirely different shape of curve, increasing in some fashion with increasing exposure. Similarly, any mechanical property affected by ductility such as notched tensile strength or tear resistance, should also be influenced in this direction. Thus, the tendencies for the shear data in Fig. 15 to fall slightly below and bearing above the curve probably represent real differences in the curve shapes. Tensile yield and ultimate strength values may also follow distinct paths which differ too slightly to be noticed in Fig. 14.

Other alloys may be expected to follow more complex behavior patterns. Fig. 16 shows the relative shapes of 2024-T3 tensile yield and ultimate strengths. It is obvious that this material would not submit to as simple a normalization process as 7075-T6.

Nevertheless, useful characteristic strength changes can be found for 2024-T3. It is apparent that peak strengths, minimum strengths, increasing strength ranges and decreasing strength ranges occur at the same degree of exposure for both ultimate and yield strength. These similarities should hold approximately true for all strength properties, since all reflect in some symptomatic way the same basic metallurgical change.

The concept of characteristic strength changes provides a useful means of comparing the several types of strength. In some cases it may facilitate definition of a variety of strength characteristics with a minimum of test data.

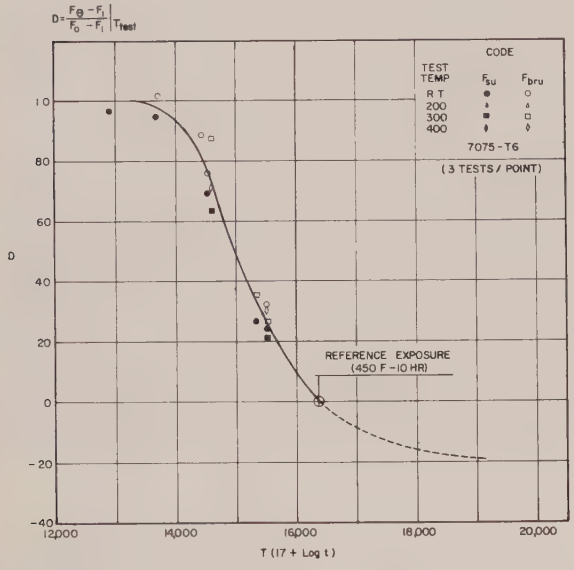

Fig. 15 — Shear and bearing strength deterioration with thermal exposure for all conditions tested (6, 7)

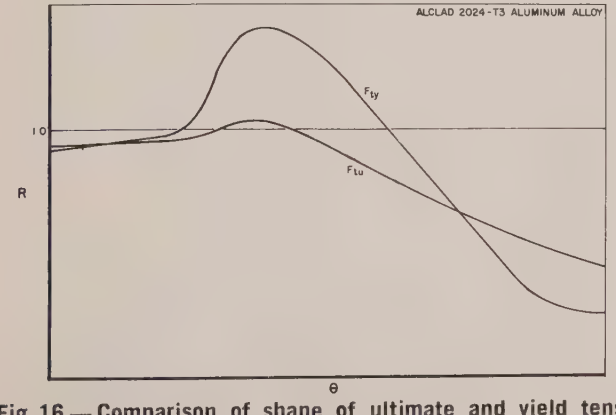

Fig. 16 — Comparison of shape of ultimate and yield tensile strength curves for 2024-T3 after exposure (3)

Effects of Stress During Exposure

Periods of stress are a basic part of the exposure environment of high strength structural materials, raising questions as to the possibility of further accelerating the reduction of strength during exposure. Studies on 7075-T6 proved that exposure-stress sufficient to produce inelastic strain does indeed have a detrimental effect on residual strength after exposure (4).

In this alloy the effect is small for practical degrees of strain. This effect correlates very well with the amount of inelastic strain accumulated; it also correlates well with the exposure parameter found suitable for unstressed exposures. These relationships are shown in Fig. 17.

In Fig. 17, tensile ultimate, tensile yield and compressive yield strength after stressed exposure resulting in 0.2% and 1.0% accumulated inelastic strain are compared with the unstressed strength deterioration curve from Fig. 14. The development of these curves is shown in Ref. 4.

The manner of using these curves to evaluate strength aft-

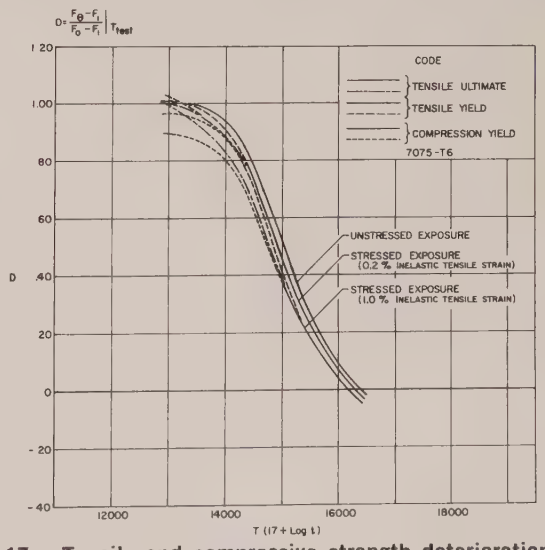

Fig. 17 — Tensile and compressive strength deterioration after (tensile) stressed exposures (4)

er stressed exposure is similar to that discussed for Fig. 14 provided that the degree of inelastic strain is known. For designs in which strength at the end of the exposure life is critical the maximum permissible inelastic strain is frequently 0.2%. For such cases the effect of stress during exposure is small and can be simply accounted for by using the 0.2% exposure curve for all situations, rather than attempting to determine an exact value of accumulated strain between zero and 0.2%.

The stressed exposure curves of Fig. 17 may be considered accurate for cases where the straining either occurs early in the exposure period or is reasonably distributed throughout this period. Check tests have indicated that they are also sufficiently accurate for straining prior to exposure such as might occur during manufacturing where limited forming may be done in the T-6 condition. Other tests have shown that strain which accumulates very late in the exposure history will have less effect in reducing final strength than strain accumulated early or throughout the exposure.

It can be seen that the largest effect of inelastic strain during exposure occurs at the lowest exposure values. In this region the Bauschinger effect is evident in that prior straining causes an increase in yield strength for restressing in the same direction and a decrease in yield strength for the opposite direction of stressing. This should be borne in mind in using these curves for cases where exposure stresses in one direction may be followed by critical stressing in the opposite direction; for such cases the lowest curve in Fig. 17 (F_{cy} curve) for the given degree of strain should be used. This approach has been confirmed by check tests for compressive stressed exposure followed by testing in compression.

The degree of influence of inelastic strain on the final strength of thermally exposed materials may be greater for some other alloys as has been indicated in the work of Gluck, et. al. (8) This should be evaluated when important.

Use of Hardness Testing

The above concepts can greatly reduce the testing required to define the thermal exposure characteristics of new alloys. Test effort can be further minimized in a rate process oriented investigation if test conditions are selected strategically. This requires some prior knowledge of the material exposure characteristics.

Hardness measurement provides an attractive means of obtaining this type of information, since hardness tests and test specimen are simple. It has been found that within a given lot of an alloy, hardness is a good indicator of the trends (though not the magnitudes) of strength with exposure severity. In addition, hardness depends upon much the same basic material properties as do other mechanical strength properties and shows similar agreement with the exposure parameter. Hardness data for 7075-T6 at room temperature after exposure are shown in Fig. 18 plotted against the exposure parameter used earlier for strength. Good correlation is indicated. Thus, hardness measurements can be used to indicate the exposure region in which material strength declines, to give a first check on material agreement with a thermal exposure parameter, and to find an approximate value of C for the parameter.

Hardness testing has been used effectively in this way in the current studies of AISI Type 301 and PHIS-7 Mo Stainless Steels and René 41. Fig. 19 shows the hardness of 301 extra hard stainless from such exploratory tests.

Summary

The rate process relationship in the form of parameter T(C + log t) is a valuable tool for assessing the cumulative effects of variable thermal exposure on the remaining strength of metallic materials. This tool has been successfully applied to precipitation hardened aluminum alloys and is demonstrated in this paper to apply quite well to 7075-T6 alloy.

Strength changes in tension, compression, bearing and shear are all related to the same basic metallurgical changes

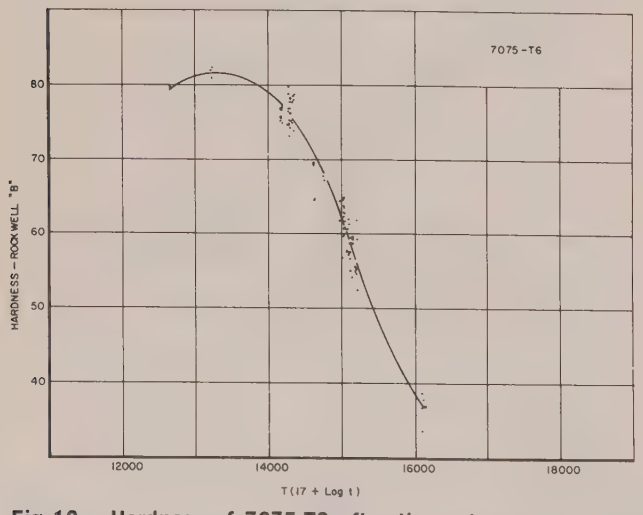

Fig. 18 — Hardness of 7075-T6 after thermal exposure, versus exposure parameter (40)

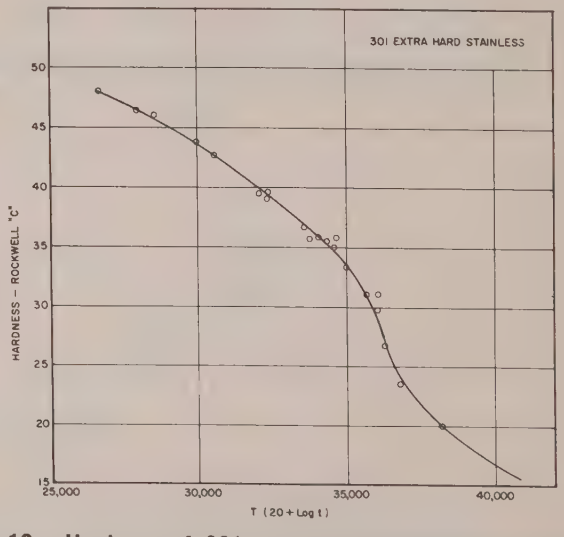

Fig. 19 — Hardness of 301 extra hard stainless after thermal exposure (4)

occurring during thermal exposure and exhibit similar characteristics, and a concept of characteristic change was found useful in relating the changes in these properties. The effects of exposure stress on the remaining strength of 7075-T6 were found to be significant but small and were found to correlate well with the amount of inelastic strain accumulated during exposure. Hardness testing was found to be useful for conducting exploratory studies.

There is evidence to indicate that the rate process relationship describes reasonably well the behavior of a large number of hardened alloys during thermal exposure.

Acknowledgement

Much of the work on which this paper is based was performed under sponsorship of the Air Force Aeronautical System Division (formerly Wright Air Development Division) with Mr. R. F. Klinger of Materials Central acting as Project Engineer.

References

1. J. H. Hollomon and L. D. Jaffe, "Time-Temperature Relations in Tempering Steel." Transactions, American Institute of Mining and Metallurgical Engineers, Iron and Steel Division, Vol. 162, 1945, 223.

2. F. R. Larson, and James Miller, "A Time-Temperature Relationship for Rupture and Creep Stresses." Transactions of the ASME, July 1952, 765.

3. R. E. Fortney and C. H. Avery, "Effects of Temperature-Time-Stress Histories on the Mechanical Properties of Aircraft Structural Metallic Materials, Part I Temperature-Time Studies of 2024-T3 and 7075-T6 Alclad Sheet." WADC Technical Report 56-585, Part I, December 1956.

4. C. D. Brownfield, and D. M. Badger, "Effects of Temperature-Time-Stress Histories on the Mechanical Properties of Aircraft Structural Metallic Materials, Part II Stressed Exposure of 7075-T6." WADC Technical Report 56-585, Part II, September 1959.

5. Northrop Corp., Norair Division, "Effects of Temperature-Time-Stress Histories on the Mechanical Properties of Aircraft Structural Materials," Bi-Monthly Progress Report No. 8, under WADD Contract AF 33(616)-5769, 15 May 1960. (Northrop Norair Report No. NOR-60-150.)

6. Northrop Corp., Norair Division, "Effects of Temperature-Time-Stress Histories on the Mechanical Properties of Aircraft Structural Materials," Bi-Monthly Progress Report No. 9, under WADD Constract AF33(616)-5769, 15 July 1960. (Northrop Norair Report No. NOR-60-240.)

7. To be published as ASD (formerly WADD) Technical Report 61-194 Part I, final report on Contract AF33(616)-5769.

8. J. V. Gluck, H. R. Voorhees, and J. W. Freeman, "Effect of Prior Creep on Mechanical Properties of Aircraft Structural Materials." University of Michigan: WADC Technical Report 57-150, Parts I, II and III, January 1957 to May 1958.

9. N. M. Erkun, "The Application of Rate Process Theory to the Heat Treatment of Titanium Alloys." Transactions, American Society for Metals, Vol. 51, 1959, 787.

Ride Requirements

R. Schilling
Chevrolet Motor Division, General Motors Corp.

THE "RIDE" of a car is the total of all the motions and oscillations below the audibility limit which the passengers of a car experience. We are interested in ride because it determines "Riding Comfort."

The ride problem is usually subdivided into the three areas: basic ride is the body motion of the spring mass; wheelhop and shake have to do with the oscillations of the unsprung masses and the related deformations of the car structure; harshness and noise belong to the higher frequency ranges. We shall here restrict ourselves to a consideration of basic ride only.

Although road waves nearly always show complex contours and although the ride is not a linear process, the basic problems of ride can be seen by studying the motion of a car over a single sinusoidal road wave. This is illustrated by Fig. 1. It shows a road wave with displacement:

$$y = \frac{y_o}{2} \times \left[1 - \cos \frac{2\pi v t}{L}\right] \qquad (1)$$

where:

- y = Height of wave above original level
- y_o = Maximum height of wave
- v = Car speed
- L = Length of wave
- t = Variable time

Although there is only one wave, we can define a frequency as the inverse of the wave length and get:

$$\text{Wave Frequency } \nu = \frac{V}{L} \qquad (2)$$

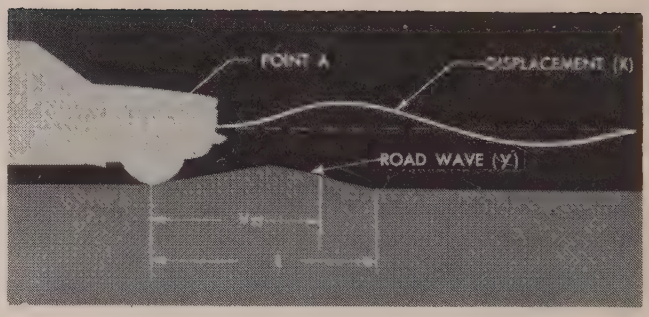

Fig. 1—Motion of a single point over a single road wave

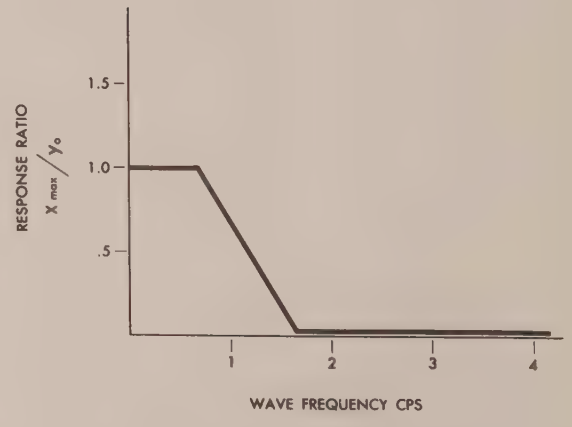

Fig. 2—Ideal response on small waves

To start with the simplest problem we shall follow only the displacement X of point "A" of the car located exactly above the tire and consider it as a single degree of freedom. This is shown as the upper curve.

The first question is this: What should the displacement X be on an ideal suspension if the road wave is given by its amplitude y_o and the length L? At first sight it seems obvious to require X = 0, but this is the wrong answer.

When the road level and road grade change and also on very long waves, the car must follow the road contour statically. If we plot in Fig. 2 the required response ratio X_{max}/y_o as ordinate and the wave frequency ν as abscissa, we must require a response of 1.0 between frequency zero and approximately 0.75 cps. This limiting frequency is not definitely set by any law of dynamics, but depends on how roads and driveways are built and how people expect cars to behave. For instance when approaching a ramp, a driver will slow down to a certain speed because he knows that a car responds just so fast to the new grade. If the car takes a longer time, it will strike through severely. Similarly with long high waves: if the car reacts slower than the driver expects, there will be a severe jolt and at high speeds there may be trouble in controlling the car. The improvement of highway contours is reducing the difficulties of striking through; and ultimately this static response limit may be set only by ramps and driveway approaches.

At high frequencies we will certainly want zero response, and in between there must be a gradual transition as shown in Fig. 2. However, there is another limitation due to the finite ride clearance "C" which exists on every real suspension. If the wave height equals the ride clearance ($y_o/c = 1$) the ride amplitude X can remain zero. But if y is larger than c, then the car must be lifted over the wave so that:

$$X_{max} \geq (y_o - c) \qquad (3)$$

Adding this requirement to the plot of Fig. 2 we get Fig. 3, showing increased amplitudes for various values of y_o/c.

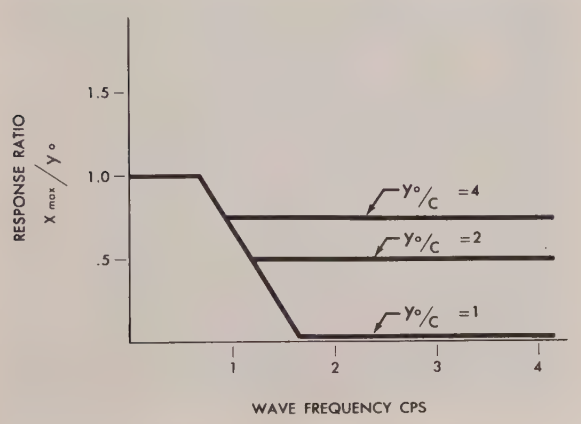

Fig. 3—Ideal response on large waves

It seems rather paradoxical to require higher response ratios for higher waves, especially at high frequencies where the resulting accelerations will be large, but that is the inherent consequence of the limited ride clearance. Hence, high-speed, off-the-road vehicles need exceptionally large ride clearance.

Actually, Fig. 3 shows only a minimum value for the displacement which is possible if X remains in phase with y. When X lags in phase as shown in Fig. 1, the amplitude ratio X_{max}/y_o will have to be even larger, but vertical acceleration can be decreased by this lag. Hence, for the condition where y_o is larger than c, Fig. 3 shows only the minimum but not the optimum amplitudes. But it is quite clear that in order to lift the car over such a wave with the minimum acceleration no mechanism built into the suspension can adjust the lifting to the proper acceleration, unless all waves indicate in their first few inches just how high the crest will be. Since the road waves are not sinusoidal or of any other regular contour, even the "ideal" suspension cannot adjust its lift unless it has advance information on the maximum wave height. It would need a radar set to measure the road surface ahead and a computer to prescribe the lift curve for maximum riding comfort.

A less "intelligent" suspension will have to start lifting the car before the ride clearance is used up, even if the wave height y_o should turn out to be less than the ride clearance. This means that the zero amplitude in the curve $y_o c = 1$ cannot be maintained when y_o exceeds a substantial fraction of c, such as 60 or 70%. With practical car dimensions, this is the case on a large portion of our road mileage. The most serious problem of suspension design, even for an "ideal" mechanism, is hence not how to obtain zero lift and zero acceleration, but how to manage the car motion when it is being lifted by a road curve.

Fig. 4 compares this "ideal" diagram with the "actual" performance of a modern suspension. This mechanism, consisting of spring, damper, and mass has the properties of a damped vibrating system and even on a single wave will show a response factor X_{max}/y_o of approximately 1.5 at the resonance frequency. It meets the static requirement satisfactorily but shows, besides the undesirable resonance, large finite amplitudes at all higher frequencies where we would like to see a zero response. On a wavy road the motions will be many times larger than for the ideal. The diagram shows only the action on road waves considerably smaller than ride clearance; on the higher waves the comparison will look no better, but remains uncertain unless the ideal suspension is completely specified for this condition.

How much can we improve the conventional suspension without introducing new elements? The first and obvious measure is to drop the spring rate. The effect is demonstrated in Fig. 5. Here we compare the previous "ideal" and

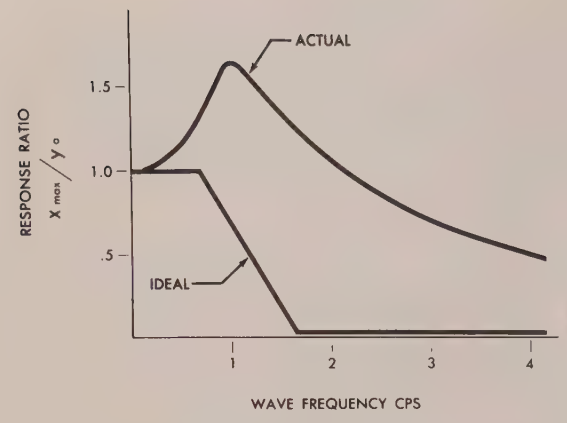

Fig. 4—Comparison of ideal and actual response

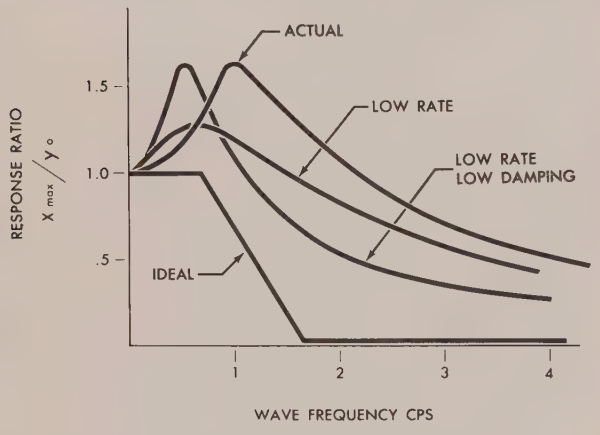

Fig. 5—Improvement in response by low rate and low damping

"actual" suspension to a "low rate" design, where spring rate has been decreased to 25% so that the frequency drops to 50%; the damping is maintained unchanged and consequently the amplitudes at resonance are reduced materially, but at high frequencies the "low rate" curve approaches the "actual" curve again. This is, of course, a great improvement, but at the sacrifice of static response in the range of 0.25-0.75 cps. If this arrangement will be acceptable depends entirely on the road conditions in which it is to be used.

When the damping forces are reduced in the same ratio as the spring rate, the "low rate" curve will change to the curve marked: "low rate, low damping". Here the resonance amplitude is again increased and is the same as for "actual", but at higher frequency the amplitudes are further reduced. Although this diagram cannot show it, "low rate, low damping" will be found to be far better for riding comfort all around than "low rate", since accelerations and rates of change of acceleration are much lower. But it has one serious shortcoming; the static response is even worse than "low rate" because of more phase lag with respect to the road wave.

If we want to understand the effect of damping, we must take a detailed look at the forces and motions between car and road. From practical experience we know very well that spring rates alone do not make riding comfort; shock absorber design and adjustment is extremely important. We also know from direct experience that these damping forces must be strongly nonlinear so that an approximate analysis using linear damping will miss the features that are important to riding comfort.

Let us go back to a diagram like Fig. 1, but follow the events in more detail. This is shown in Fig. 6. At the top are shown the displacements, y of the road wave and X of the single point of the sprung mass. They are plotted as functions of distance or, since we assume constant car speed, also as a function of time.

From point 0 to point 1 the displacement y increases faster than X, hence the clearance decreases; this is the first compression stroke. From 1 to 2 the clearance increases; this is the first rebound stroke, although in the case shown here, the displacement X decreases during the latter part of this stroke. From 2 to 3 the clearance decreases again, it is the second compression stroke. From 3 to 4 we see the second rebound stroke; beyond this point it is not necessary to follow the motions since the amplitude X becomes fairly small.

The lower part of the diagram shows the forces between road and sprung mass. There is first the excess spring force. It is almost proportional to relative displacement for small displacements as encountered on the boulevard ride. The second force is the damping force which is produced by the shock absorber and any other source of hysteresis, such as friction or dynamic damping in rubber bushings. This is definitely not linear and is altogether different in rebound than in compression.

During the first compression stroke the excess spring force and the damping force both are directed upward while the displacement X is increasing. In this period then the damp-

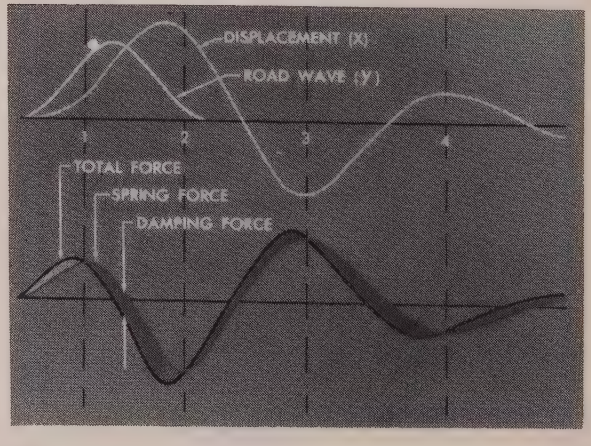

Fig. 6—Computed displacements and forces on single wave (1940 model)

ing force increases the upward acceleration. This improves the static response, but on the other hand, at all higher frequencies it introduces undesirably high accelerations. During the first rebound stroke the damping force at first tends to damp the motion while X is still increasing, but it may cause a rapid change of acceleration or jerk and must therefore be limited in magnitude on short and high waves. During the second part of this stroke, where X decreases, the damping force adds to the downward acceleration and increases the kinetic energy of the sprung mass.

During the second compression stroke the damping force absorbs energy. Since it is not in phase with the spring force, it increases the acceleration little or not at all; it is wholly beneficial. The same is true on the second rebound stroke.

We see than that from the standpoint of riding comfort the damping requirements vary greatly for the different strokes. Generally, damping is completely undesirable in the first compression stroke, and should be limited also during the first rebound stroke. However, we must use all the damping compatible with comfort in the first rebound in order to stop the motion of the unsprung mass before the car meets the next road wave.

As long as we use shock absorbers that cannot distinguish the first compression and rebound from the second, we are forced to compromise seriously and cannot establish damping specifications from general considerations. Only the fact that our shock absorber designers have given us a mechanism that permits quick changes enables us to find good ride calibrations by trial and error.

The displacements and forces shown in Fig. 6 were computed for the mass, spring and damping characteristic of a 1940 model car. Fig. 7 repeats the corresponding information for a 1960 model car. A comparison of the two shows how our idea of riding comfort has changed.

During the first compression stroke, the 1960 car shows much less damping. On the 1940 model, the impulse (force x time) as indicated by the area under the force curves is about the same for the spring force and the damping force. On the 1960 car, the damping force contributes less than half that of the spring force. Again, during the first rebound stroke on the 1940 car the damping is larger compared to the spring force.

The effects can be seen in the displacement curves. Although both overshoot the road wave amplitude by about the same amount, the 1940 compression displacement at point 3 in less than a third of that at maximum rise; the 1960 curve shows still almost 70% of the maximum rise at point 3. Correspondingly, the forces at points 3 and 4 are much larger in 1960 than in 1940. The 1960 car then has obtained lesser accelerations and especially lower rates of a change of acceleration during the first compression and first rebound strokes, but it has had to accept a longer persistance of motion and hence higher accelerations in the second compression and rebound strokes.

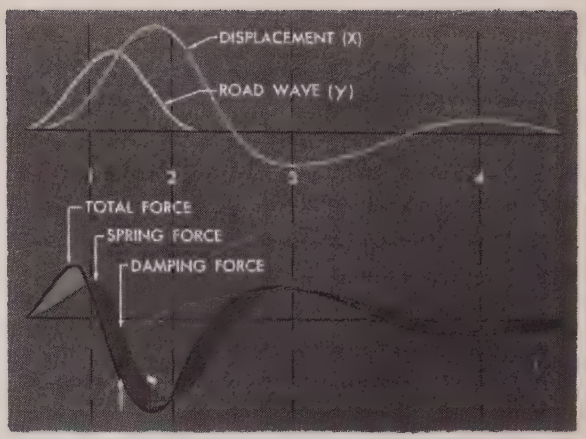

Fig. 7—Computed displacements and forces on single wave (1960 model)

These diagrams of Figs. 6 and 7 do not tell the whole story; there are additional difficulties due to superposition of waves and especially because we must also damp the wheelhop. But even these simple considerations show that more refined control of damping force can make more improvement in riding comfort than is obtainable from lower ride rates. Inertia controlled shock absorbers have been tried and showed some promise in this direction, but they were on the whole unsatisfactory because they used mechanical and hydraulic elements that were not adequate. With today's and tomorrow's electronic and hydraulic components we should be able to do a far better job in analysing the requirements and in buliding a superior mechanism.

So far, we have considered only a model with a single degree of freedom. Actually, the car moves in three degrees of freedom: bounce, pitch, and roll. However, I believe that the implications of these features are much better understood than the problem of damping. Various designers and inventors have demonstrated what gains can be had by proportioning front and rear rates or interconnecting them as well as by using extremely low rates.

The reason that such arrangements have not been commercially successful seems to be that they do not make a significant change in total riding comfort, even while they improve the basic ride. The situation seems to be similar to that in acoustics. If a certain noise level is produced by two or more sources of approximately equal intensity, the reduction or even suppression of a single source makes only a minor difference in the total noise level.

Similarly, the discomfort caused by shake and harshness on our present cars is equal to that due to basic ride motion, so that a major improvement in basic ride has only a minor effect on total riding comfort.

All this means that the problems of shake and harshness are extremely important from the standpoint of riding comfort, and they must receive at least as much engineering effort as the basic ride.

Case Hardenability of SAE 4028, 8620, 4620 and 4815 Steels

J. A. Halgren and E. A. Solecki
International Harvester Co.

THIS PAPER reports the results of case hardenability studies on four carburizing grades of SAE steels: 4028H, 8620H, 4620H, and 4815H. These studies, which attempted to include data for both high and low side chemistries of each grade, represent a cooperative effort of members of Division 33 - Gear Metallurgy - of the Iron and Steel Technical Committee of SAE

The basic need for information of this type was expressed when Division 33 was organized in 1955. Literature on carburizing steels has been predominantly concerned with the effect of carburizing time, carburizing temperature, carbon penetration and alloying elements[1, 2, 3]*. While standard hardenability band steels of carburizing grades have been agreed upon by both consumers and producers, published information has been primarily limited to the hardenability of the core material. Most data which have been presented upon the case hardenability of these steels have been fairly recent in origin. The literature has been scant but does indicate that an interest exists outside of Division 33 in the field of case hardenability.

Jominy and Boegehold[4] developed the end quench bar originally as a means for measuring the case hardenability of carburized steels. Their classic paper included case hardenability studies of twelve grades of SAE steels, made both at the surface and at 0.015 in. below the surface. It also contained data on the effect of double quenching practice upon case hardenability and on the spread in case hardenability of 12 production heats of SAE 4620 steel.

Kayser, Thomson, and Boegehold[5] proposed the use of a trapezoidal end quench bar for determining hardenability of carburized steels. They evaluated the trapezoidal bar and showed it to be a reliable means for determining case hardenability. Their paper presented data for seven carburizing steels, three of which are covered in this investigation.

Meyer[6] conducted end quench tests to determine the case and core hardenability of 11 American and German steels and of 12 experimental steels. The 11 commercial steels included the four grades of carburizing steels which Division 33 selected for its investigation, but no attempt was made to include heats representing both minimum and maximum chemistries for each grade. His case hardenability studies were made at carbon levels of 1.10, 1.00, and 0.90%, and his results were plotted on standard end quench charts.

Gurley and Hannewald[7] proposed the use of isohardness diagrams for illustrating the relationship between speed of quench, carbon content, and hardness in carburized parts. They studied the case hardenability of SAE 4028 steel similar in composition to the low chemistry SAE 4028H steel which Division 33 investigated. They cited several advantages for presentation of case hardenability data in the form of isohardness diagrams, in which preselected levels of hardness are plotted in relation to carbon content and J-position on the end quench bar. The advantages of their proposed method warrant its use in this paper.

Ruffle[8] used isohardness diagrams to report his investigations on case hardenability of 14 British and three American steels. His paper included end quench hardenability data at various carbon levels. Two heats of SAE 4620 and one heat of SAE 8620 were studied.

The interest of members of Division 33 in this subject encompassed not only the relationship between the case hardenabilities of standard H steels but also the range of case hardenability which can be expected in any one grade of steel when its chemical composition and core hardenability vary from the top side to the bottom side of its specified band. It was felt that this information would be valuable both to the manufacturer of carburized parts and to the materials engineer who selects carburizing steels and designates hardness requirements for these parts.

Members of Division 33 also felt that this investigation would produce useful information on the effect of chemical composition, direct quench practice versus reheat practice, and hardness measurement procedures upon case hardenability. It was hoped that it might lead to the adoption of a standard procedure for measuring and reporting the case hardenability of carburizing grades of SAE steels.

Selection of Carburizing Steels

The selection of the four grades of carburizing steels which were used in these studies was made by members of Division 33. The use of commercial heats was deemed to be more practical for the intended purpose than the use of

* Numbers in parentheses designate References at end of paper.

experimental heats. In order to aid the selection process criteria of alloy content were applied. High hardenability heats were chosen on the basis of alloying elements being in the upper third of the specified chemical ranges for H steels. Low hardenability heats were chosen on the basis of alloying elements being in the lower third of the specified chemical limits. All heats were examined for grain size, chemistry, core hardenability, and soundness before being approved for the case hardenability studies.

Table 1 contains the McQuaid-Ehn grain size and chemistry of all eight heats of steel, together with the specified analyses for H steels. The major variable in alloy composition is nickel, which is present from residual amounts in SAE 4028H steel up to 3.8% in SAE 4815H steel.

Core Hardenability

SAE standard end quench procedure, except as noted, was used upon duplicate bars of all eight heats of steel. One pair was austenitized at 1700 F for 20 min at temperature before quenching. The other pair was austenitized for 40 min at temperature (instead of 20 min) at the following temperatures before quenching

SAE 4028H steel -- 1525 F
SAE 8620H steel -- 1550 F
SAE 4620H steel -- 1525 F
SAE 4815H steel -- 1500 F

The first pair of bars represented direct quench practice from the carburizing temperature, and the second pair represented reheat and quench practice.

Figs. 1 - 4 show the core hardenabilities of the 4 grades of steel in relation to their respective hardenability limits.

Selection of Method

Two types of specimens for measuring case hardenability were considered: the trapezoidal bar and the standard end quench bar. Upon recommendations of ISTC Division 5 -

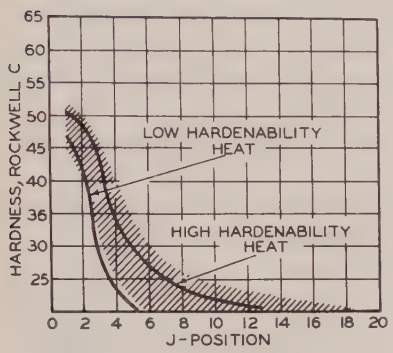

Fig. 1—Core hardenability of SAE 4028H versus standard SAE 4028H steel hardenability band

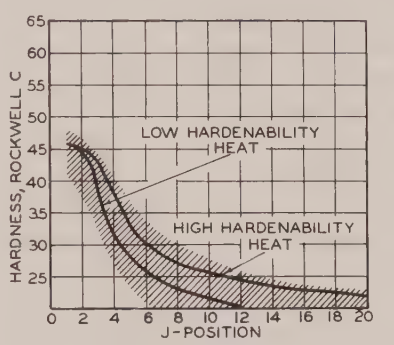

Fig. 2—Core hardenability of SAE 8620H versus standard SAE 8620H steel hardenability band

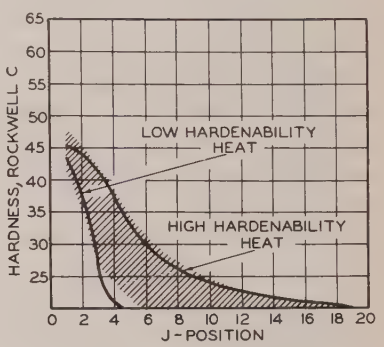

Fig. 3—Core hardenability of SAE 4620H versus standard SAE 4620H steel hardenability band

Table 1 - McQuaid-Ehn Grain Size and Chemical Composition of Steels Selected for Case Hardenability Studies

Steel Grade	Chemistry	Chemical Composition, % C	Mn	Si	Ni	Cr	Mo	S	P	Grain Size
4028H	Low	0.27	0.82	0.22	0.02	0.07	0.23	0.045	0.018	7-8
	High	0.31	0.85	0.32	0.17	0.28	0.24	0.044	0.016	7-8
Specified	Min	0.24	0.60	0.20	0.25	0.20	0.20			
	Max	0.30	1.00	0.35	max	max	0.30			Fine
8620G	Low	0.20	0.70	0.24	0.50	0.45	0.18	0.020	0.032	7-8
	High	0.20	0.84	0.28	0.70	0.56	0.26	0.014	0.035	8
Specified	Min	0.17	0.60	0.20	0.35	0.35	0.15			
	Max	0.23	0.95	0.35	0.75	0.65	0.25			Fine
4620H	Low	0.18	0.46	0.28	1.68	0.03	0.21	0.030	0.011	7-8
	High	0.20	0.64	0.29	1.93	0.21	0.31	0.023	0.010	6-7
Specified	Min	0.17	0.35	0.20	1.55	0.20	0.20			
	Max	0.23	0.75	0.35	2.00	max	0.30			Fine
4815H	Low	0.16	0.39	0.22	3.3	0.10	0.19	0.020	0.010	6-8
	High	0.18	0.54	0.34	3.8	0.23	0.27	0.007	0.008	6-8
Specified	Min	0.12	0.30	0.20	3.2	0.20	0.20			
	Max	0.18	0.70	0.35	3.8	max	0.30			Fine

Method of Determining Hardenability - the end quench bar was selected. Either type of specimen, however, was adjudged to be satisfactory for use. ISTC Division 5 suggested that either Superficial Rockwell or Tukon hardness procedures be used because of the presence of hardness gradients in carburized cases. Division 33 decided to specify Rockwell A procedures for all carbon levels, with either Rockwell 15N or Vickers 10 kg at several carbon levels selected at the option of the cooperating laboratory performing the tests. Two cooperating laboratories made Rockwell 15N readings, and two made Vickers 10 kg readings alternately with Rockwell A readings at 1/16 in. intervals at carbon levels of 1.00, 0.80, 0.60, and 0.40%. Only Rockwell A procedures were used at the other carbon levels of 1.10, 0.90, 0.70, 0.50, and 0.30%.

Preparation of Specimens

Two bars, 1-1/4 in. in diameter by 6 ft long, were forged from each billet of steel. The remaining billet section (1500 lb) of each heat has been retained for possible future use. The forged bars were normalized at 1700 F for 1 hr at temperature. One bar has been set aside for possible future use. The other was sectioned consecutively into four 6-3/16 in. lengths for carbon gradient bars, four 5 in. lengths for case hardenability bars, and four 5 in. lengths for standard end quench bars. Four carbon gradient bars, 1 in. round by 6 in. long, and eight case and core hardenability bars, 1 in. round by 4 in. long, were prepared to 0.002 in. tolerance on diameter. The case hardenability bars had a pair of preground flats for surface hardness readings after they were carburized and quenched.

Heat Treatment

Carburizing Procedure - On successive days two hardenability bars with preground flats and two carbon gradient bars of the same heat of steel were packed in solid carburizing compound inside a covered alloy carburizing box of 6 x 7 x 8-1/2 in. inside dimensions. The ends of the hardenability bars were not protected from carburization. At least 1/2 in. of compound surrounded each test bar. All carburizing was done with new compound from the same batch of the following approximate composition:

Charcoal	- 50%	Sodium Carbonate	- 3%
Coke	- 30%	Calcium Carbonate	- 3%
Barium Carbonate	- 12%	Molasses Binder	- 2%

The lids were sealed with high-temperature cement, and the carburizing boxes were placed in a furnace at 800 F, heated with the furnace to 1700 F, held at 1700 F for 18 hr, and then removed from the furnace.

Direct Quench Practice - One hardenability bar was immediately removed and end quenched for 10 min. At the same time its accompanying carbon gradient bar was removed and placed in loose hydrated lime to cool.

Reheat and Quench Practice - Immediately after the first pair of test bars was removed, the second pair was removed and allowed to air cool to room temperature. After careful removal of any slight oxide coating which developed, the hardenability bar and the carbon gradient bar were reheated for 40 min at the reheat temperature previously given under "Core Hardenability."

Furnace atmosphere conditions during the reheat period varied as follows:

4028H - gas carburizing atmosphere, carbon potential 1.15%

8620H - gas carburizing atmosphere, carbon potential 1.15%

4620H - manually controlled gas carburizing atmosphere

4815H - graphite lined alloy box

After being at heat for 40 min, the case hardenability bar was removed from the furnace and end quenched for 10 min. At the same time the carbon gradient bar was removed and placed in loose hydrated lime to cool.

Determination of Carbon Gradient

After removal of any surface oxide by light vapor blasting, carbon gradients were determined by duplicate analysis of turnings machined from the carbon gradient bars in radial increments of 0.005 in. to a depth of 0.020 in. below the surface and in increments of 0.010 in. to a depth of 0.120 in. below the surface. (Several laboratories used smaller increments to a depth of 0.010 in. below the surface.) The average carbon content for each increment on each bar was plotted against its average depth below the surface in order to determine the depths corresponding to carbon levels of 1.10, 1.00, 0.90, 0.80, 0.70, 0.60, 0.50, 0.40, and 0.30% in each bar.

The average carbon gradients for the high hardenability heats of all steels are plotted in Fig. 5 (Data taken from the samples which accompanied the direct quench bars). The minimum and maximum spreads encountered in the carbon gradient determinations between duplicate specimens of any steel are plotted in Figs. 6-7.

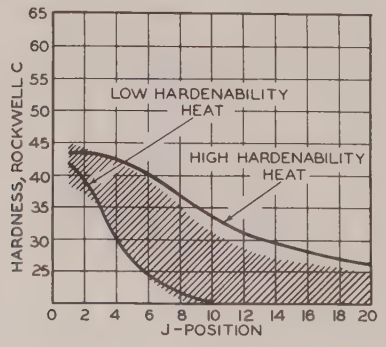

Fig. 4—Core hardenability of SAE 4815H steel versus standard SAE 4815H hardenability band

Determination of Hardness

Surface hardness readings on the preground flats were made but are not included in this report because of the vari-

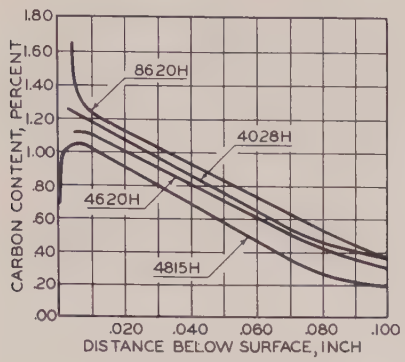

Fig. 5—Average carbon gradient curves for high hardenability heats of steel, carburized at 1700 F

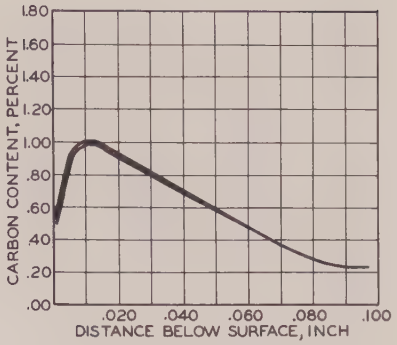

Fig. 6—Minimum spread between two duplicate carbon gradient bars; curves are for SAE 4815H, high hardenability heat

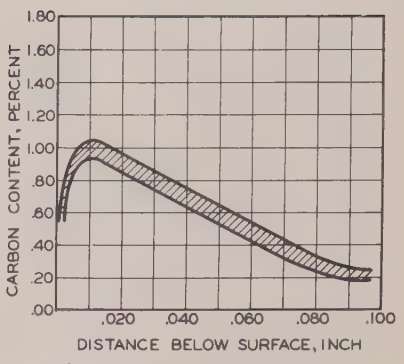

Fig. 7—Max spread between two duplicate carbon gradient bars; curves are for SAE 4815H, low hardenability heat

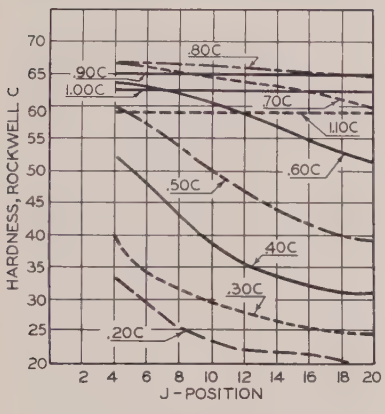

Fig. 8—Carburized end quench hardenability of SAE 4620H steel, high hardenability direct quench. Curves are for 0.20 to 1.10% carbon

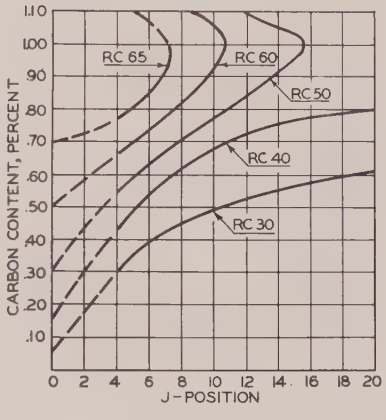

Fig. 9—Isohardness diagram for carburized SAE 4028H steel, high hardenability direct quench

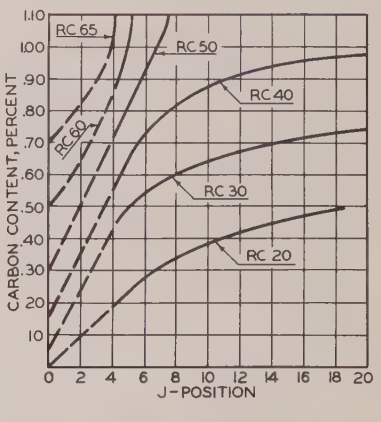

Fig. 10—Isohardness diagram for carburized SAE 4028H steel, low hardenability, direct quench

ation in surface carbon content from one sample to another and from one laboratory to another. Either surface decarburization or recarburization to a higher carbon level were present in varying degrees, depending upon procedures used by the cooperating laboratories in removal of samples from the carburizing box and upon reheat procedures and atmosphere. It was concluded that these variations in surface carbon produced negligible influence upon case hardenability studies conducted below the surface.

Additional flats were carefully ground on each hardenability bar to preselected carbon levels, starting at 1.10% carbon, except in the SAE 4815H steels, whose surface carbon content necessitated grinding of the initial flat to a 1.00 % carbon level. A minimum of 0.020 in. and 0.030 in. was ground off each flat on the SAE 8620H steel direct quench and reheat and quench hardenability bars respectively, before readings were taken at another lower carbon level on the same flat location. A minimum of 0.050 in. was ground off each flat on the other three grades of steels before hardness readings were made at a lower carbon level on the same flat location.

Rockwell A hardness impressions were made alternately with Rockwell 15N impressions at 1/16 in. intervals on SAE steels 8620H and 4815H: and with Vickers 10 kg at 1/16 in. intervals on steels 4028H and 4620H at the 1.00, 0.80, 0.60, and 0.40% carbon levels. Only Rockwell A impressions were made at other carbon levels.

Case hardenability at the many carbon levels studied can be a rather unwieldy subject if the data are handled in the manner customary for end quench tests. The isohardness diagram contains information in a form which facilitates analyses of the case hardenability data obtained. Fig. 8 shows case hardenability data presented in a standard end quench diagram. The inclusion of 10 curves in the diagram, one for each carbon level, adds to confusion and presents a complex diagram for comparative analysis. The corresponding isohardness diagram, shown in Fig. 13, at first glance may seem complex, but study of it clearly brings out the variables involved and their relationship to each other. The isohardness diagram is an expedient means of presenting case hardenability data.

The results of all case hardenability data, obtained with Rockwell A procedures and averaged for duplicate specimens, are presented graphically in the form of isohardness diagrams. Below the J4 position on the diagrams solid lines are not used because the quenched end of the hardenability

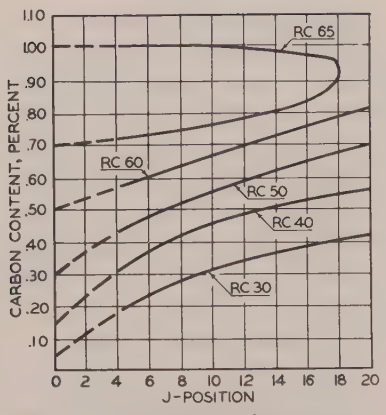

Fig. 11—Isohardness diagram for carburized SAE 8620H steel, high hardenability, direct quench

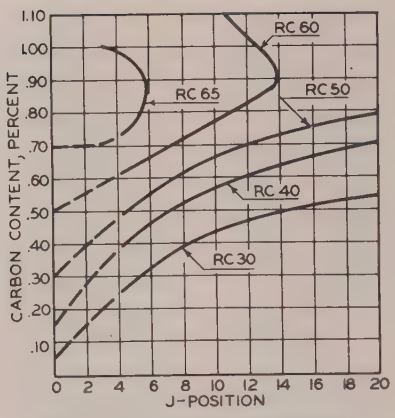

Fig. 12—Isohardness diagram for carburized SAE 8620H steel, low hardenability, direct quench

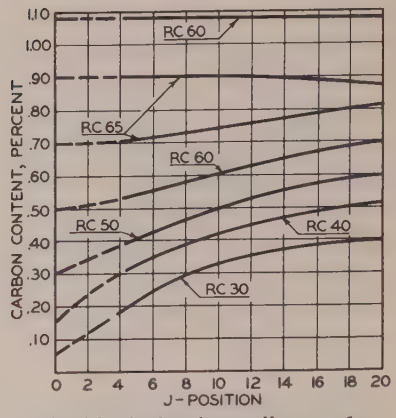

Fig. 13—Isohardness diagram for carburized SAE 4620H steel, high hardenability, direct quench

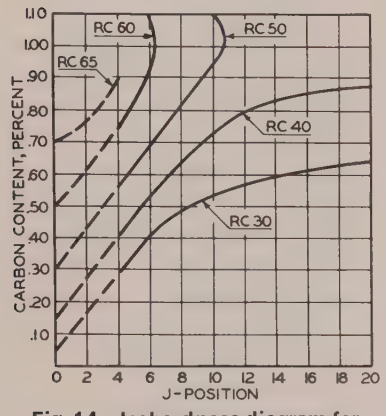

Fig. 14—Isohardness diagram for carburized SAE 4620H steel, low hardenability, direct quench

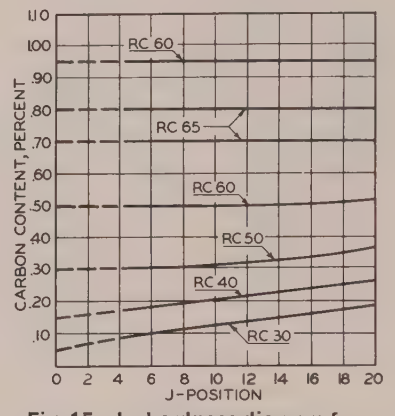

Fig. 15—Isohardness diagram for carburized SAE 4815H steel, high hardenability, direct quench

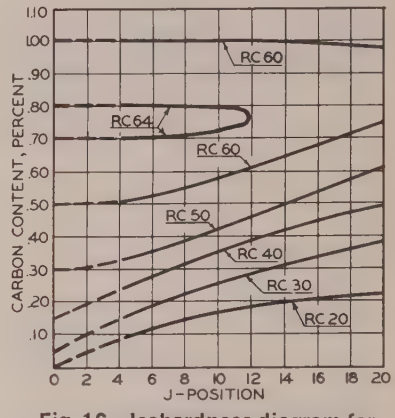

Fig. 16—Isohardness diagram for carburized SAE 4815H steel, low hardenability, direct quench

bar was not protected against carburization and hence the carbon gradient near the quenched end differed from that in the balance of the bar.

Figs. 9-16 show the case hardenability results obtained upon the direct quench bars of all steels. Ninety four per cent of the plotted points which were derived from the original hardenability data fall directly on or within 0.01% carbon of being on the curves shown. The maximum deviation of the remaining plotted points from these curves does not exceed 0.03% carbon. Data at the 0.60% carbon level for one of the SAE 8620H bars were discarded because they were inconsistent with all other results. No reason for this behavior was found despite a thorough metallurgical check. The curves are not extended beyond the J20 position because Division 33 members felt that there would be limited use for such information in their activities.

Figs 17-24 show corresponding isohardness diagrams for the reheat and quench bars.

Fig. 25 shows typical variations between end quench curves obtained from Rockwell A procedures and Rockwell 15N or Vickers 10 kg procedures at several carbon levels.

Discussion

Chemical Composition - Examination of the chemical composition of the eight heats of steel used in this study of case hardenability (Table 1) shows that all of them meet the prescribed requirements for alloy content, with low hardenability heats falling in the lower one-third of their respective range for chemistry, and high hardenability heats, in the upper one-third of their range. Carbon content is not being considered at this time.

SAE 4028H Steel - The low hardenability heat of SAE 4028H is considered to be a borderline heat with respect to composition. Its manganese content is 0.09% above the one-third limit, and its other alloying elements which affect hardenability are exactly at the one-third limit.

The high hardenability heat of SAE 4028H would also be considered to be a borderline heat -- perhaps even below borderline because of its low molybdenum content -- if its residual chromium content did not exceed the maximum limit by 0.08%. This high residual chromium content tends to place it close to the two-thirds point of the analysis range.

SAE 8620H Steel - The low hardenability heat is considered to be a borderline heat, with all alloying elements being very close to the one-third point of the range. The high hardenability heat falls somewhat above the two-thirds point in the chemistry range for SAE 8620H steel, thus being well within the desired upper one-third range in composition.

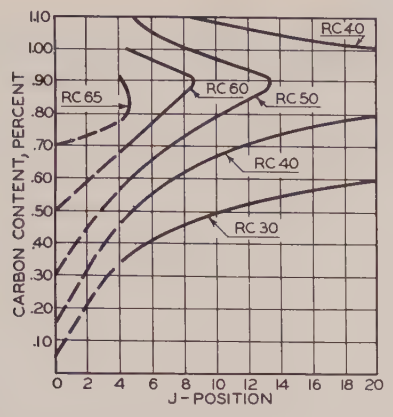

Fig. 17 — Isohardness diagram for carburized SAE 4028H steel, high hardenability, reheated and quenched

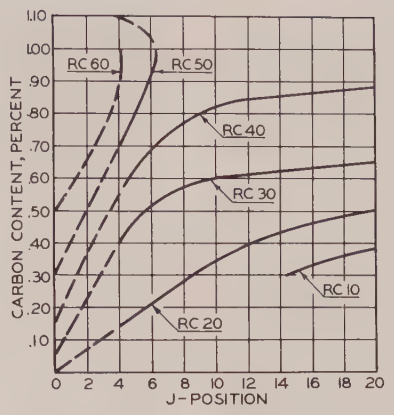

Fig. 18—Isohardness diagram for carburized SAE 4028H steel, low hardenability, reheated and quenched

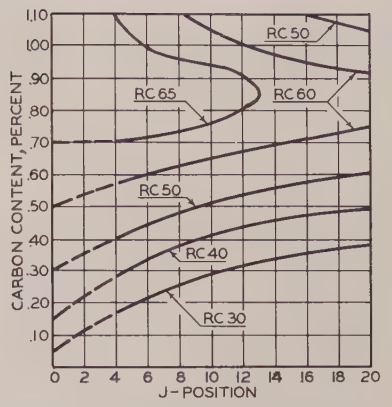

Fig. 19—Isohardness diagram for carburized SAE 8620H steel, high hardenability, reheated and quenched

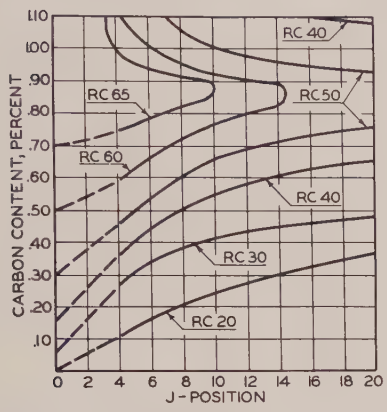

Fig. 20—Isohardness diagram for carburized SAE 8620H steel, low hardenability, reheated and quenched

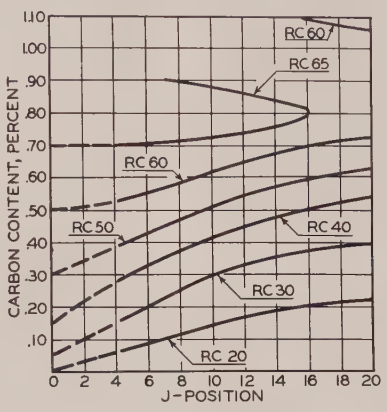

Fig. 21—Isohardness diagram for carburized SAE 4620H steel, high hardenability, reheated and quenched

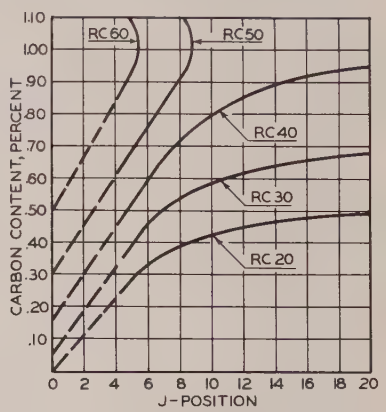

Fig. 22—Isohardness diagram for carburized SAE 4620H steel, low hardenability, reheated and quenched

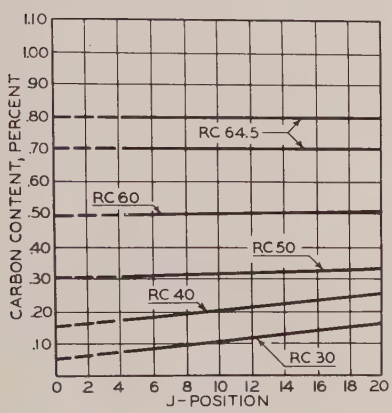

Fig. 23—Isohardness diagram for carburized SAE 4815H steel, high hardenability, reheated and quenched

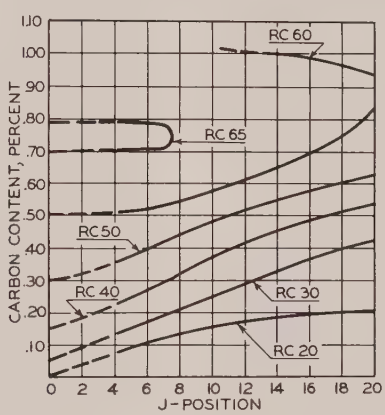

Fig. 24—Isohardness diagram for carburized SAE 4815H steel, low hardenability, reheated and quenched

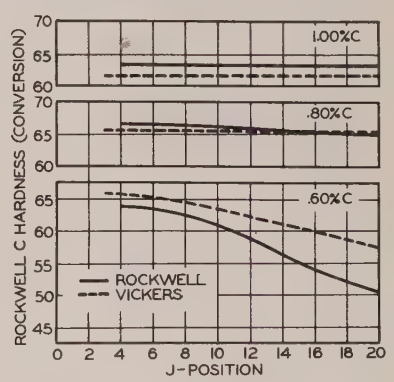

Fig. 25—Differences in case hardenability at 3 carbon levels caused by using different methods in determining hardness. Data are for Rockwell A and Vickers 10KG for SAE 4620H, high hardenability, direct quenched

SAE 4820H Steel - The alloy content of the low hardenability heat places it somewhat below the one-third point in the specified range for SAE 4620 steel. The high hardenability heat is considered to be almost a maximum analysis heat. Since its manganese and silicon contents are at the two-thirds point, it falls just below a maximum analysis heat.

SAE 4815H Steel - Except for its manganese content being near the one-third point and its residual chromium content being one-half of the maximum permissible, the low hardenability heat of this steel tends to approach a minimum analysis heat.

The high hardenability heat of SAE 4815H is somewhat below a maximum analysis heat. Its molybdenum and man-

ganese contents are at the two-thirds points, but its residual chromium content exceeds the specified maximum of 0.03%.

CORE HARDENABILITY - Core hardenability data in Figs. 1-4 are plotted only for the 1700 F austenitizing temperature. The core hardenabilities of end quench bars which were quenched from the reheat temperatures are almost identical to the data plotted.

SAE 4028H Steel - The core hardenability of the low hardenability heat (Fig. 1) is considered to be in good agreement with minimum H-band requirements, even though its alloy content and its carbon content correspond to that of a one-third analysis heat.

The high hardenability heat of SAE 4028H steel has a core hardenability fairly close to the 2/3 point. Its core hardenability is in agreement with its alloy content.

SAE 8620H Steel - The core hardenabilities of the low and the high hardenability heats approximate the one-third point and two-thirds point respectively of the H-band for SAE 8620H steel (Fig. 2). Agreement between core hardenability and alloy content is considered to be good.

SAE 4620H Steel - The core hardenabilities of the low and high hardenability heats of SAE 4620H steel approach their respective H-band limits (Fig. 3). Substantial agreement between core hardenability and alloy content is apparent in both steels, although the alloy content of the low-side heat would tend to indicate a slightly higher core hardenability.

SAE 4815H Steel - The low hardenability heat has a core hardenability which corresponds to the minimum of the H-band for SAE 4815H steel (Fig. 4). Its alloy content also classified it to be almost a minimum analysis heat.

The high hardenability heat exceeds the maximum of the H-band in core hardenability, even though its alloy content indicated it to be just below a maximum analysis heat.

Effect of Alloy Content - In order to appreciate the role of the alloying elements in case hardenability, it would be desirable to eliminate or minimize the effect of carbon content upon core hardenability, so that the major effect which is being studied is that of the alloy content itself. Various investigators[9, 10] have developed hardenability factors for alloying elements, but for the purposes of this discussion an approximation of the effect of alloying elements upon core hardenability within a given series of steels can be obtained if this series is available in several ranges of carbon. The SAE 8600 H-band series meets these requirements. This approximation then relates the spread in core hardenability which is present in SAE 8600 H-band steels at a single carbon level.

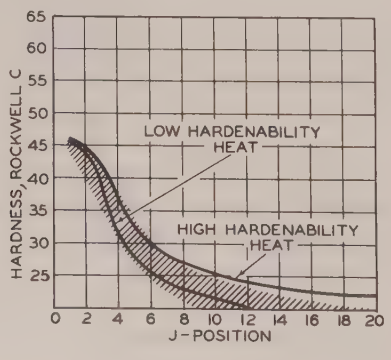

Fig. 26—Core hardenability of SAE 8620H steel versus derived "standard SAE 8620H hardenability band for a constant 0.20% carbon content"

It is realized that this approximation is subject to many criticisms. One is the different percentages of elements that can be present within one steel and that can affect its hardenability. The limits of the hardenability bands are not solely determined by the carbon content but represent a combined effect of carbon content and alloy content upon hardenability. At the quenched end the hardenability band is vertically spread out, partly because the top or bottom limit for carbon which defines this region is subject to allowable variations for check analysis. Nevertheless, the introduction of this concept of analyzing the core hardenability of a steel with respect to minimum and maximum hardenability bands projected for a steel of the same carbon content does offer further insight into the problem of correlating case and core hardenabilities.

In Fig. 26 the core hardenabilities of the low and high hardenability heats of SAE 8620H steel, each of which analyzed 0.20% carbon, are compared with derived minimum and maximum core hardenabilities of SAE 8600H steels having 0.20% carbon. This latter hardenability band is seen to be much narrower than the actual H-band for SAE 8620H steel. It reflects to a greater degree the combined effect of the alloying elements upon the core hardenability. The high hardenability heat, which previously was analyzed as just meeting the minimum requirements set up by Division 33 for core hardenability is now almost coincident with the maximum of this derived hardenability band. The low hardenability heat approaches the minimum of this band at quenching speeds equivalent to the J4 to J7 position but deviates toward the high end at both slower and faster quenching speeds.

It is apparent that core hardenability of a given steel per se should not necessarily agree with case hardenability. Hence, the decision of SAE Division 33 to use alloy content as the main criterion for selecting these steels was sound. Limitations of time did not permit the selection of absolute minimum and maximum analyses heats in all grades. This factor must be considered, therefore, in arriving at conclusions in the case hardenability studies.

Carbon Gradient - The data in Fig. 5 tend to agree quite well with previous information upon surface carbon levels and carbon penetration reached in steels having varying alloy content, particularly nickel and chromium, when subjected to the same carbon potential. Chromium accelerates penetration and increases surface carbon content. Increasing nickel content slows down penetration and decreases surface carbon content. The variation in carbon content in the vicinity of the surface is considered to be too large to use surface hardness readings for comparing the characteristics of these steels in the case carburized condition.

The range in results between duplicate samples of carbon gradient bars, shown in Figs. 6-7, substantiates the need

for precautions voiced by ISTC Division 5 in identifying accurately the depth below the surface at which desired carbon levels are located. Deviations as high as 0.18% carbon occur between duplicate samples at a given depth below the surface. The normal deviation, however, is considerably less than this.

Case Hardenability

Use of Isohardness Diagrams - The isohardness diagrams for all steels (Figs. 9-24), both low and high hardenability, have one definite characteristic in common. The left end of each isohardness curve slopes toward the average carbon content (at the quenched end) which will harden to this same hardness with a perfect quench (99.9% martensite)[11]. The developed isohardness curves are extended as dotted lines below the J4 position in order to illustrate this characteristic.

This apparent correlation between the constructed isohardness curves and the empirically determined carbon contents having equivalent hardnesses with a perfect quench lends support to the accuracy and consistency of the experimental data.

The extension of the isohardness lines to the J-0 position appears to be valid and to permit determination of case hardenability at positions below J4 on the hardenability bar, even if direct data could not be made because of varying carbon gradients in this area of the bar.

The ease of interpretation of case hardenability from isohardness diagrams is brought out in Figs 9-24. It is obvious that a steel which will harden uniformly to a stated hardness level across the length of the hardenability bar will possess greater hardenability than one whose isohardness curve slopes rapidly upward. The slope of the isohardness curve, therefore, is a measure of the hardenability of the steel. Steels with steep isohardness curves have low hardenability. Those whose isohardness curves have low slopes have high hardenability.

Since engineers and production metallurgists are generally interested in actual hardness attained in carburized cases, the isohardness method of data presentation can be a considerable help to them. These diagrams can yield information on the following types of questions:

1. What surface carbon content will result in maximum surface hardness for each grade of steel at various speeds of quench?

2. What carbon gradient is necessary to obtain a desired hardness gradient in a given grade of steel and stated quench? How is this gradient affected by top and bottom side chemistry heats?

3. What is the effect of reheat and quench practice compared to direct quench practice for different grades of steel?

4. What steel should be selected to obtain a desired hardness gradient with a given carbon gradient and stated quench?

5. How deep must a carburized case be to attain a minimum effective case depth (measured to RC 50) with a given speed of quench and grade of steel?

6. What is the effect of alloy content on case hardenability?

7. Is the case hardenability of a steel related to its core hardenability?

8. What range of case hardenability can be expected in one grade of steel when its alloy content faries from minimum to maximum?

Effect of Hardness Procedure - At carbon levels above 0.70%, approximately, higher RC hardness is indicated for data obtained with Rockwell A procedures than with Rockwell 15N or Vickers 10 kg procedures. Below 0.70% carbon the situation is reversed; RC conversions from Rockwell A readings are lower than those from Rockwell 15N or Vickers 10 kg readings. The maximum spread in RC hardness at any carbon level for different hardness procedures is approximately 7 RC. Typical comparisons between Rockwell A and Vickers 10 kg procedures are shown in Fig. 25.

The differences in converted hardness at these carbon levels are associated with the relative depths of impression made by the respective hardness procedures and with the character of the hardness gradient below the surface. Because of their very shallow impressions microhardness procedures would tend to be superior to any of the hardness procedures used in this investigation, insofar as measurement of actual surface hardness for a given carbon content is concerned. The authors feel that any advantage gained by such procedures, however, is offset by the greater variation in hardness obtained with them on heterogeneous structures and by the greater difficulties inherent with these procedures in obtaining samples suitable for test purposes.

The above remarks pertain only to hardness grdient conditions of the type associated with relatively deep carburized cases. They do not apply to shallow carburized cases or to other shaped hardenability bars, such as the trapezoidal bar.

The use of Vickers 10 kg or Rockwell 15N tends to shift the isohardness curves slightly downward at carbon levels below approximately 0.70%. At higher carbon levels the isohardness curves are also shifted downward somewhat. The net result, therefore, would be to indicate slightly greater hardenability at hypoeutectoid levels and less hardenability at hypereutectoid levels.

Effect of Steel Grade - If the core hardenabilities of the eight heats of steel are adjusted to a common carbon content, their case hardenabilities appear to be directly related to their respective "isocarbon" core hardenabilities. In other words, the case hardenabilities of SAE steels in the 4000H, 8600H, 4600H, and 4800H grades appear to de directly related to their core hardenabilities when their core hardenabilities are measured at a common carbon level, for example, 0.20% carbon.

In ascending order the case hardenability rating of these four grades of steel is: SAE 4000H, SAE 4600H, SAE 8600H, SAE 4800H.

This rating takes into consideration the fact that the high hardenability heat of SAE 4620H steel is nearly a maximum analysis heat, while the high hardenability heat of SAE 8620H steel is only somewhat more than a two-thirds analysis heat. The actual difference in hardenability of the high hardenability heats of these two steels is relatively small.

Changes in alloy content (including residual alloys) from the top to the bottom of the range have a significant effect upon case hardenability. Less effect is apparent for the higher hardenability grades than the lower hardenability grades.

Effect of Reheat and Quench Practice - The general effect of the particular reheat and quench practice which was used on the four grades of SAE steels is to reduce their case hardenabilities slightly. This effect is particularly noticeable in the hypereutectoid regions of the case of the SAE 8600 grade and is apparently associated with the resistance of chromium carbides to go into solution during reheating cycles. Because of changes in retained austenite content, the higher nickel SAE grades 4600H and 4800H tend to show slightly greater hardness at carbon levels above 0.70% when given a reheat and quench as compared to a direct quench. The case hardenability of the SAE 4800H grade of steel appears to be least affected at all carbon levels.

Comparison with Published Data on Trapezoidal Bar Method - Case hardenability data which was reported by Kayser, et al, with a trapezoidal bar on SAE 8620, 4620, and 4815 steels can be compared only in a general way with the end quench data presented in this paper, since variations in hardness procedures, steel compositions, and hardenability methods are present.

1. SAE 8620H Steel

The chromium, manganese and silicon contents of Kayser's heat of SAE 8620 steel correspond closely to those of the high hardenability heat studied by Division 33. The nickel and molybdenum contents compare favorably with those of the low hardenability heat. Hence, Kayser's heat is lower in alloy content than the high hardenability heat studied by Division 33. The core hardenability of Kayser's heat of SAE 8620 steel checks very closely to that of the high hardenability heat.

The trapezoidal specimen indicates a slightly greater case hardenability for Kayser's heat of SAE 8620 steel than was obtained with the end quench bar by Division 33. The difference is diminished when the trapezoidal results are compared with Rockwell 15N results, instead of Rockwell A results, on the end quench bar. The results would be still closer together if the slight difference in cooling rate between the two specimens, reported by Jatczak and Christenson in a discussion of the paper by Kayser, is leveled.

At the higher carbon levels in both types of specimens converted RC hardnesses are similar for the Vickers 10 kg procedure used by Division 33 and the Vickers 3 kg procedure used by Kayser. Rockwell A procedures of Division 33 indicated 5 points greater hardness at 0.90% carbon than the Vickers 10 kg and Vickers 3 kg procedures.

2. SAE 4620H Steel

The Kayser heat is comparable to the high hardenability heat of Division 33 in chromium, nickel, and silicon contents and falls midway between the high and low hardenability heats in manganese and molybdenum contents. Its alloy content, therefore, falls somewhat below that of the high hardenability heat. Its core hardenability, however, after adjusting for carbon content, is estimated to be very slightly greater than that of the high hardenability heat of Division 33.

The trapezoidal case hardenability of the Kayser heat of SAE 4620 is indicated to be somewhat greater than the end quench case hardenability of the Division 33 heat. Again, part of this discrepancy is removed when the trapezoidal results are compared with Vickers 10 kg hardness conversions on the Division 33 end quench bars. A still closer correspondence is indicated if the difference in cooling rate between the trapezoidal and end quench bars is considered.

An appreciable discrepancy in hardness is indicated at the higher carbon levels between the several hardness procedures which were used. The Kayser data, taken with Vickers 3 kg measurements, convert to 57 RC at a carbon level of 0.90%. The Division 33 data, taken with Rockwell A procedures, convert to 65 RC at this same carbon level. The same data, taken with Vickers 10 kg procedures, indicate a converted hardness of approximately 63 RC at 0.90% carbon.

3. SAE 4815H Steel

The chemical composition of Kayser's heat of SAE 4815 steel falls slightly below that of the high hardenability heat of Division 33 in alloy content. Their core hardenabilities, adjusted for carbon content, are estimated to be quite close together.

At carbon contents of 0.60% and lower, the trapezoidal and end quench case hardenabilities of these steels are almost identical. Variations in hardenability due to hardness procedures are negligible. Variations in converted RC hardness at 0.80% carbon are appreciable, however, falling from 65 to 63 to 60 for Rockwell A, Vickers 10 kg, and Vickers 3 kg procedures, respectively.

The maximum hardness which Kayser reported for SAE 4815 and 4620 steels was approximately 63 RC (converted from Vickers 3 kg) and occurred at some carbon levels within the range of 0.50% to 0.80%. Since hardnesses of 65 RC and above were obtained on these steels within this same carbon range by use of Rockwell A, Rockwell 15N and Vickers 10 kg procedures in the present investigation, there appears to be a slight discrepancy in maximum obtainable hardness which should be resolved.

Standard Method for Measuring Case Hardenability - The results of this and previous studies indicate that reliable case hardenability data can be obtained from either the trapezoidal bar method or the end quench method.

Information from both methods is affected by the hardness procedure which is used. Hardness procedures for the end quench bar should preferably be those which utilize in-

dentor loads of 15 kg or less. Even with loads of 15 and 10 kg, and with the particular carbon gradients present in the end quench bars, sharp hardness gradients have a slight effect upon converted hardness readings. Use of indentor loads of less than 10 kg require greater care in surface preparation and finer surface finishes.

Despite certain advantages which the trapezoidal method possesses, the authors feel that the use of a standard end quench bar is preferable for case hardenability studies by most laboratories. The trapezoidal method requires the use of microhardness instruments, extreme care in preparation of surface finishes, and an impervious copper plate on the parallel sides of the bar. The cooling rate of the trapezoidal bar is somewhat different from that of the end quench bar.

The authors recommend, therefore, that the end quench bar be used for any further case hardenability studies by Division 33. The only variation from the procedures which were used in the current study is that Rockwell 15N or Vickers 10 kg procedures should be used for all hardness determinations.

Since the isohardness diagrams which are included in this study are based upon Rockwell A procedures, and hence indicate a somewhat different picture of the case hardenabilities of these four grades of steel than would be obtained by Rockwell 15N or Vickers 10 kg procedures, the authors recommend that the bars from this study be checked at all carbon levels by Rockwell 15N or Vickers 10 kg procedures and that the results be published in a subsequent paper.

Summary

The case hardenabilities of SAE steels 4028H, 4620H, 8620H, and 4815H appear to be directly related to the core hardenabilities of these grades, adjusted to a common carbon level.

The case hardenability rating of these SAE grades of steel in ascending order is 4000, 4600, 8600, and 4800.

As the case hardenability rating increases, the variation in case hardenability of steels from their minimum to their maximum chemistry range appears to decrease.

Reheat and quench practice tends to lower the case hardenabilities of all grades of steel slightly. The SAE 8600 grade, which contains chromium, is affected most, particularly in the hypereutectoid region. The relative case hardenability rating of the four grades of steel is not appreciably changed by reheat and quench practice.

The end quench bar is recommended for case hardenability studies. Rockwell 15N or Vickers 10 kg procedures should be used for measuring hardness. Since the isohardness diagrams in this paper are derived from Rockwell A procedures, and are affected by the errors introduced by the use of these procedures on surfaces with hardness gradients, the present end quench bars should be rechecked by Rockwell 15N or Vickers 10 kg procedures and new isohardness diagrams should be presented in a subsequent paper.

Acknowledgments

The authors wish to thank the members of ISTC Division 33, Gear Metallurgy, for the opportunity to prepare this report from the data compiled during this cooperative investigation of case hardenability. Special acknowledgment is due to the following members and their companies for conducting the laboratory work necessary for this investigation:

H. J. Bates - Fairfield Mfg. Co.
W. E. Frank - Caterpillar Tractor Co.
H. H. Zurburg - Chrysler Corp.
R. F. Thomson - General Motors Corp.
D. V. Doane - Climax Molybdenum Co.
R. B. Kropf - International Nickel Co.

Our appreciation and thanks are also extended to members of ISTC Panel A for their assistance in the procurement of the steels which were studied for case hardenability and to J. A. Zerkel and the Milwaukee Forge and Machine Co. for their assistance in the investigation. E. S. Rowland and the Timken Roller Bearing Co. deserve special mention for melting several commercial heats of steel with alloy composition in the desired ranges for these studies.

References

1. F. E. Harris, "Case Depth," Metal Progress, Vol. 44 (August, 1943), 265-272.

2. J. K. Stanley, "Steel Carburization and Decarburization, a Theoretical Analysis, "The Iron Age (Feb. 4, 1943), 49-55.

3. A. G. Guy, "Predicting Carbon Penetration Curves in Carburizing," The Iron Age, Vol. 163 (Jan. 27, 1949), 74-76.

4. W. E. Jominy and A. L. Boegehold, "Hardenability Test for Carburizing Steel," Transactions of American Sosiety for Metals, Vol. 26 (1938), 574-606.

5. F. X. Kayser, R. F. Thomson and A. L. Boegehold, "End Quench Test for Determining the Hardenability of Carburized Steels," Trans. A. S. M., Vol. 45 (1953), 1056-1070.

6. H. U. Meyer, "Influence of Alloying Elements on Case Hardenability of Carburizing Steels," Stahl und Eisen, Vol. 76, No. 2 (1956), 67-78. (Henry Brutcher Translation No. 3787).

7. A. E. Gurley and C. R. Hannewald, "Development and Application of Isohardness Diagram," Metal Treating, Vol. 7, No. 3 (May-June, 1956), 2-6, 32, 33.

8. T. W. Ruffle, "Gas Carburizing and Case Hardenability, Some Basic Data," Metal Treatment and Drop Forging, Vol. 25, No. 158 (November, 1958), 475-481.

9. M. A. Grossman, "Hardenability Calculated from Chemical Composition, "Transactions, AIME Vol. 150 (1942), 22.

10. I. R. Kramer, R. H. Hafner and S. L. Toleman, "Effect of Sixteen Alloying Elements on Hardenability of Steel," Transactions, AIME, Vol. 158 (1944), 138.

11. J. M. Hodge and M. A. Orehoski, "Relationship Be-

tween Hardenability and Percentage of Martensite in Some Low Alloy Steels," Transactions, AIME, Vol. 167 (1946), 627-638.

Discussion

Calculated and Measured Hardenability Values

E. S. Rowland and C. F. Jatczak
Timken Roller Bearing Co.

THE SUBJECT of case hardenability of carburizing steels is one which is very often slighted or ignored, and it is heartening to find that this problem has received such attention by the Gear Metallurgy Division of the Iron and Steel Technical Committee.

In two recent papers*, one of the present discussors and others in our laboratory have devised procedures for the estimation of case hardenability from chemical composition. Since we were curious as to how well the calculated and measured hardenability values would compare under the different conditions of carbon level and hardening temperature, we computed the hardenability values for 4028, 8620 and 4620 as shown in Tables A-C, respectively. The 4815 steel, has a composition beyond the limits of our calculation procedure.

Table A indicates that the comparison between measured and calculated hardenability at three carbon levels and both hardening temperatures is quite good for both the low and

*C. F. Jatczak and R. W. Devine, Jr., "Calculation of Hardenability in High Carbon Alloy Steels," Transactions ASTM, Vol. 47 (1955), 748-768.

C. F. Jatczak and D. J. Girardi, "Multiplying Factors for Calculation of Hardenability of Hypereutectoid Steels Hardened from 1700 F," Transactions American Society for Metals, Vol. 51 (1959), 335-352.

Table A - Comparison of Calculated and Division 33 Measured Case Hardenability Data for Type 4028

		Case Hardenability at Indicated Case Carbon Level								
		1.10% Carbon			1.00% Carbon			0.90% Carbon		
	Hardening Temp F	Calculated Di, In.	Calculated J-60 Dist. (16's)	Measured J-60 Dist. (16's)	Calculated Di, In.	Calculated J-60 Dist. (16's)	Measured J-60 Dist. (16's)	Calculated Di, In.	Calculated J-60 Dist. (16's)	Measured J-60 Dist. (16's)
Low Chemistry	1700	2.22	4.8	5.0	2.37	5.3	5.1	2.37	5.3	4.5
High Chemistry	1700	3.52	10.8	9.0	3.82	11.8	10.8	3.82	11.8	9.8
Low Chemistry	1525	1.38	2.8	2.8*	1.53	3.3	4.0	1.89	4.2	4.0
High Chemistry	1525	2.00	4.5	-	2.22	4.8	4.8	2.89	7.7	8.4

*Estimated from extrapolation of data in Fig. 18.

Table B - Comparison of Calculated and Division 33 Measured Case Hardenability Data for Type 8620

		Case Hardenability at Indicated Case Carbon Level								
		1.10% Carbon			1.00% Carbon			0.90% Carbon		
	Hardening Temp F	Calculated Di, In.	Calculated J-60 Dist. (16's)	Measured J-60 Dist. (16's)	Calculated Di, In.	Calculated J-60 Dist. (16's)	Measured J-60 Dist. (16's)	Calculated Di, In.	Calculated J-60 Dist. (16's)	Measured J-60 Dist. (16's)
Low Chemistry	1700	3.93	12.7	11.0	4.22	14.0	13.0	4.22	14.0	14.0
High Chemistry	1700	6.15	29.0	--	6.55	34.0	34.0*	6.55	34.0	34.0*
Low Chemistry	1525	2.00	4.4	--	2.22	4.8	--	2.86	7.5	--
	1550	--	--	4.5	--	--	6.2	--	--	12.5
	1575	2.24	4.9	--	2.89	7.7	--	3.82	12.5	--
High Chemistry	1525	2.58	6.5	--	2.86	7.6	--	3.56	11.0	--
	1550	--	--	8.3	--	--	12.0	--	--	22.0
	1575	3.08	8.8	--	3.96	12.8	--	5.38	22.0	--

*Estimated from extrapolation of data in Fig. 11.

high chemistry heats. The same is true in Table B for 8620 steel if one is content to interpolate the computed hardenability for 1550 F hardening temperature from calculated values at 1525 F hardening temperatures. It would appear that the computed values for a 1575 F hardening temperature agree more closely with the values measured at 1550 F than the mean of the computed values from the two hardening temperatures.

Table C discloses the only serious divergence between calculated and measured hardenability values. This relates to the low chemistry heat of 4620 when direct quenched from 1700 F. In this case, the calculated hardenability is almost twice the measured value at all three carbon levels. This same heat, when hardened from 1525 F, gave excellent agreement between calculated and measured values except at the 0.90 carbon level where the agreement leaves something to be desired. The high chemistry heat is in quite good agreement.

Considerable case hardenability testing has been done on 4620 steel and we have yet to see a heat with as low a measured hardenability as the low chemistry heat quenched from 1700 F. We have no criticism of the committee's hardenability testing procedure, and, in fact, recommend it. We might suggest, however, that the committee consider retesting this one heat to be sure that some error in carbon level did not occur to alter the results.

We would also like to comment on the authors' recommendation that Rockwell 15N or Vickers hardness measurements be used rather than Rockwell A in determining hardnesses on the carburized end quenched bar. We do not concur in this recommendation and believe that for practical case hardenability testing the Rockwell A measurement is superior for the following reasons:

1. That Rockwell A values are much less sensitive to sample grinding and surface preparation techniques than the other two methods.

2. We believe the effect of penetration on the hardness results in the case of the Rockwell A method has been overplayed. At a Rockwell A 85 hardness level (RC 66), the indentor penetrates to a depth of 0.001 in. At Rockwell A 76 (RC 50) the penetration depth is only 0.0015 in. If a carbon penetration curve of sufficiently gentle slope to provide a fall of only 0.01% carbon per 0.001 in. depth is used, the effect of penetration covers only about 0.02% in carbon below the surface of measurement. This is about the precision of measurement of the carbon level itself and we do not believe it seriously affects the results.

3. The Vickers method suffers from the need of measuring the length of the indentation optically with consequent disagreement among observers, while both the Vickers and Rockwell 15N procedures introduce uncertainties because of micro segregation in the material itself.

4. Finally, not every laboratory has superficial Rockwell or Vickers equipment available and the cost of the test by these methods if necessarily higher.

For these reasons, we believe the committee should wait for the balance of the recommended data before reaching a final decision on this point.

Iso-Hardness Presentation and Spread of Hardenability

D. V. Doane
Climax Molybdenum Co. of Michigan

THE AUTHORS are to be commended for their clear summary of the large volume of data obtained by the cooperating laboratories. Their use of the isohardness charts clarified the presentation of the case hardenability at all carbon levels. The extrapolations to the J-O positions at the lower carbon levels, using the ideal quenched hardness values, appear to be valid, and add considerably to the experimental data.

There are two possible limitations to the isohardness presentation:

1. Data at a relatively large number of carbon levels are necessary to construct such curves. For many applications it may be feasible to limit case hardenability tests to a few carbon levels.

Table C - Comparison of Calculated and Division 33 Measured Case Hardenability Data for Type 4620

		Case Hardenability at Indicated Case Carbon Level								
		1.10% Carbon			1.00% Carbon			0.90% Carbon		
	Hardening Temp F	Calculated Di, In.	Calculated J-60 Dist. (16's)	Measured J-60 Dist. (16's)	Calculated Di, In.	Calculated J-60 Dist. (16's)	Measured J-60 Dist. (16's)	Calculated Di, In.	Calculated J-60 Dist. (16's)	Measured J-60 Dist. (16's)
Low Chemistry	1700	3.34	10.0	6.0	3.56	11.0	6.5	3.56	11.0	6.0
High Chemistry	1700	6.25	30.0	--	6.70	35.0	36.0*	6.70	35.0	36.0*
Low Chemistry	1525	2.18	5.0	5.0	2.45	5.8	5.5	3.07	8.5	4.8
High Chemistry	1525	4.92	18.2	16.0	5.48	23.5	26.0*	6.90	38.0	--

*Estimated from extrapolation of data in Fig. 13 and 21.

Table D - Calculation of Minimum and Maximum Case Hardenability

Using multiplying factors from Jatczak and Girardi, ASM Vol. 51, 1959, p 335ff. Data are for bars direct quenched from 1700 F, (D_I = 1.42 for base) and are presented for 1% carbon levels only.

Steel	Calc. D_I	Av. D_I	D_I max -D_I min	J Distance to RC 60 Calculated	J Distance to RC 60 Measured
4028 H					
Low	2.52	3.28	1.52	6	5
High	4.04			13	10.5
SAE min	2.21	3.84	3.25		
SAE max	5.46				
4620 H					
Low	3.75	5.48	3.45	12	6.5
High	7.20			42	>20
SAE min	3.52	5.55	4.06		
SAE max	7.58				
8620 H					
Low	4.24	5.98	2.48	14	14
High	6.72			36	>20
SAE min	3.78	6.05	4.54		
SAE max	8.32				
4815 H					
SAE min	(4.36)	8.31	6.89		
SAE max	(11.25)				

SAE 4815 H values for calc. D_I are estimates, since factors for high Ni contents are extrapolated.

2. The "spread" or range of hardenability for a given composition range is somewhat difficult to present on a single iso-hardness curve. However, by limiting the presentation to one, or possibly two hardness values, hardenability ranges could be shown.

The writer would like to comment further on the "spread" in case hardenability data obtained in this investigation of high and low chemistry heats of four commonly used alloy carburizing steels, in the hope that emphasizing this factor will stimulate further studies of case hardenability and will ultimately result in the establishment of case hardenability specifications for carburizing steels. In his discussion, Dr. Rowland presented calculated hardenability data for the steels studied in the paper, expressed the results in terms of distance to RC 60, and compared the calculated and measured hardenability data on this basis. The writer performed similar calculations for the 1% carbon levels of direct quenched steels, which are summarized in the following table. Calculations were also performed for the minimum and maximum chemical analysis shown in the SAE H-band chemical composition tables for the steels studied in the paper (Table D).

The writer wished to point out that the hardenability spread (D_I max - D_I min) obtained in the case hardenability investigation reported by the authors is not as great as one might expect if actual extremes of analysis were encountered (although SAE Division 33 certainly tried hard to obtain commercial heats exhibiting extremes in chemical composition). The hardenability spread calculated for the extremes of each SAE H-band chemical composition range is substantially greater than for the low and high heats investigated. If it is desirable to control case hardenability to a narrower range, it is obviously necessary to place narrower limits on chemical composition, or at least establish some minimum case hardenability requirement.

The authors concluded that "as the case hardenability rating increases, the variation in case hardenability of steels from their minimum to their maximum chemistry range appears to decrease." If this observation is restricted to the hardenability expressed as distance to RC 60 at 1% carbon, as in the above table, it is difficult to confirm. The calculated spread (D_I max - D_I min) apparently increases with increasing average D_I.

Earlier Investigation of Case Hardenability Characteristics

A. E. Gurley, and
D. W. Trinklein
Chrysler Corp.

WE WISH to commend Division 33 for focusing attention to on this particular phase of gear metallurgy. Knowledge of

how a particular steel behaves with respect to carbon addition and quenching behavior is considered pertinent in order to produce a gear with optimum metallurgical qualities. Without this knowledge it is impossible to consistently produce well balanced gears from the standpoint of case and core relationship. Stress relationship between case and core is established during the quench and is governed by original hardenability of material used and hardness gradient of the case. These facts have been pointed out by the authors of this paper.

The primary function of carburizing is to produce a hardened case in the broad sense. However, it is emphasized in this paper that this hardened case has to be controlled and fall within a desired pattern. The use of the isohardness line for evaluating, predicting and controlling the case characteristics as used in this paper is in line with the intent and thinking of the authors. This device has been used by us for the past 10 years in improving the quality of gears by imposing control measures during carburizing as well as an aid in the selection of hardenability range for each gear application.

Our original investigation of case hardenability characteristics was conducted on the identical steels which were reported in this paper. Some differences were noted in the carbon concentration at which the isohardness lines peaked. In our findings the carbon level which was the most effective from the standpoint of hardenability more closely approached the eutectoid composition.

For AISI 4028 steel it was found that the 0.85% carbon level produced the maximum hardness with the slowest cooling rate. This was found to be true for both high and low hardenability heats. With increased hardenability the highest isohardness line peaked at a greater J position; however, the peak occurred at the same carbon level.

The peak effect of carbon on AISI 8620 was found at approximately 0.83% carbon and on AISI 4620 at about 0.87% carbon. Additional carbon above this amount was found to do nothing for the steels from the hardenability standpoint, but rather it rapidly increased the formation of austenite. The maximum carbon effect on AISI 4815 was identical with that found by the authors at 0.75% carbon. Hardness dropped very rapidly on this alloy with increased carbon above 0.80%.

The reason for the difference noted between this paper and our findings are not known. After considerable preliminary tests prior to our final investigation, we concluded that the most accurate results were obtained by directly quenching the concentration bars and then tempering at a high temperature. This prevented any carbon migration which might occur on reheating above the critical temperature. Also, we found it extremely important that the bars were perfectly straight. We believe Rockwell 15N or 10 kg Vickers are the best for accurate hardness values.

In this paper the case hardenability characteristics of AISI 8620 are rated higher than those of AISI 4620 based on single high hardenability heats of these two steels. We feel that these data are not complete enough at this time to draw this conclusion without addition supporting data. Some doubt arises when considering the information presented on the low hardenability heats of these two steels. It is noted on the isohardness diagrams that for the 0.50% carbon level, 50 RC is obtained at the J3 position on AISI 4620 and the J4.5 position on the AISI 8620 steels. This indicates that the case hardenabilities for these two heats are quite similar. However, the low hardenability heat of AISI 8620 used almost approaches the mid-range of the AISI 8620 hardenability band (J4-32 RC), while the low hardenability heat of AISI 4620 is lower than the bottom limits of the hardenability band established for AISI 4620 (J4-21 RC). Had a heat of AISI 8620 been used which more closely approached the lower part of the band, it is quite conceivable that the case hardenability of AISI 4620 would have been the higher.

In reference to Fig. 26 the text states that "The low hardenability heat approaches the minimum of this band at quenching speeds equivalent to the J4 to J7 position, but deviates toward the high end at both slower and faster quenching speeds." We feel this should be modified to read "J4 to J6 positions" as the hardenability curve definitely begins to deviate from the low range after J6.

Carbon Distribution

A. J. Miller, and
D. L. Pasquine
International Nickel Co., Inc.

THE MEMBERS of Division 32-Gear Metallurgy of the ISTC of SAE and the authors are to be congratulated for this contribution to a better understanding of the factors which influence the hardenability of carburized steels. The choice of steels was particularly good because it covers a wide range of hardenability. The isohardness diagrams, illustrating the change in hardenability with carbon content, contribute greatly to the usefulness of the paper.

It was gratifying to see that the reported core and case hardenabilities are in the same order as the published core hardenability limits of the H-steels (American Iron and Steel Institute, July, 1958) and in agreement with some results obobtained at our laboratory a few years ago. The fact that all these sources place the near-equal hardenabilities of the SAE 8620H and 4620H steels in the same order attests to the good quality of the work performed by the laboratories cooperating with Division 33.

The carbon distribution curves are of particular interest to us because they are in agreement with our study of carburized 9% nickel steel. Using a high potency carburizer, of the same composition as that used in the present work, we developed a max carbon content of only 0.88% in the 9% nickel steel. This value falls on a linear extension of the max carbon versus per cent nickel relationship for the 3 steels, SAE 4028, 4620 and 4815, of the present paper (Fig. A). The fourth Division 33 steel, SAE 8620, has high max

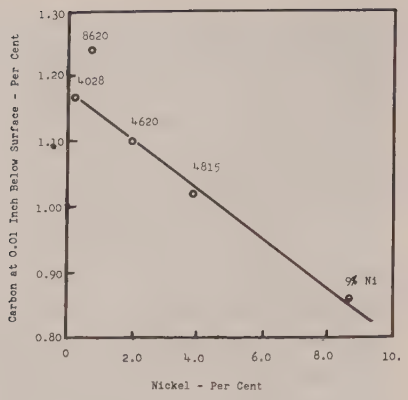

Fig. A—Maximum carbon in carburized nickel—containing SAE steels

carbon because of its chromium content, as stated by the authors.

The carbon gradient for each steel is essentially a straight line except at the surface and near the core (Fig. 5). The slope of this gradient is about 0.01% carbon per 0.001 in. Max surface carbon content is highest for the 8620 steel which is followed in order by the 4028, 4620 and 4815. This order is correctly attributed to the difference in nickel content of the steels, as stated by the authors, that is, the higher the percentage of nickel the lower the surface carbon. However, the conclusion by the authors that increasing nickel content slows down the rate of carbon penetration is open to question and in disagreement with published case depth and carbon diffusion studies.* Their data, we believe, do not show differences in the diffusion rate of carbon in these steels but, rather, indicate the differences between max and core carbon contents. The max depth of carbon penetration for the 4815 steel was about 0.120-0.130 in. which is approximately the same for all the steels studied.

Authors' Closure To Discussion

WE ARE indebted to Dr. Rowland and Mr. Jatczak for their comparison between calculated and measured case hardenabilities. The agreement which they show is gratifying and attests the quality of the previous investigations by Jatczak, Devine, and Girardi on calculated hardenability factors as well as the quality of the studies made by cooperating laboratories in this SAE Division 33 program. It also serves to substantiate our conclusion that case hardenability appears to be directly related to core hardenability, adjusted to a common carbon level. We cannot explain the difference between calculated and measured hardenability of the SAE 4620-H low chemistry heat of steel in the direct quench condition. Perhaps further investigation might lead to an answer to this discrepancy.

We do not agree with Rowland and Jatczak's remarks upon the effect of indentor penetration upon hardness. We believe that hardness values are affected by any variation in material hardness to a much greater depth than that of the indentor penetration.

Mr. Doane's comments concerning possible limitations of the isohardness presentation are well taken. The advantages of this type of presentation appear to greatly outweigh these limitations. As an example, the specification of "effective case depth to a given hardness level" can be handled conveniently with isohardness charts but is difficult or impossible to handle with the usual hardenability data obtained at a few high carbon levels.

Doane also notes that the spread in case hardenability between extreme high and low chemistry heats of steel will be larger than the spread found in the present study. Since SAE H-band steels are limited in composition range by core hardenability requirements, we do not believe that it is proper to use actual extremes in permissible analysis range of each element in calculating spread in hardenability for any grade of steel. It would seem that the extreme spread would be reached between (1) a steel having minimum core hardenability requirements but maximum carbon content and (2) a steel having maximum core hardenability requirements but minimum carbon content.

Our conclusion regarding variation in case hardenability from minimum to maximum chemistry range in the 4 grades of steel that were studied was based upon the use of the slope of the isohardness curves as a measure of hardenability. The numerical difference between the slopes of the isohardness curves for low and high side heats of each steel grade appears to decrease in the order given in the paper.

We agree with Mr. Miller and Mr. Pasquine that the rate of carbon penetration or diffusion is not affected by alloy content within the ranges studied. Our statement concerned the effect of these elements upon carbon penetration and not upon rate of carbon penetration. We should have been less ambiguous. Miller and Pasquine correctly ascribe the difference in carbon content at given distances below the surface to the effect of core carbon content and surface carbon content in these steels.

We have not attempted to resolve the discrepancy noted by Mr. Curley and Mr. Trinklein between the carbon levels at which they noted case hardenability to peak and those at which the SAE Division 33 investigation yielded peak effect. Only a small part of this discrepancy appears to be associated with the difference in hardness procedures used.

On the basis of single heat tests we agree that the relative case hardenability rating of SAE 8620-H steel and SAE 4620-H steel is open to question. Our conclusion appears to follow, however, from the fact that the core hardenability of SAE 8620-H steel slightly exceeds that of SAE 4620-H steel and from our conclusion that case hardenability appears to be directly related to core hardenability in these steels.

*F. E. Harris, "'Case Depth' - an Attempt at Practical Definition," Metal Progress, Vol. 44 (1943).

Cyril Wells and Robert F. Mehl, "Rate of Diffusion of Carbon in Austenite in Plain Carbon, in Nickel and in Manganese Steels," Trans. AIME, Vol. 140 (1940).

Index—Vol. 69, 1961

AGNEW, J. T.
Discussion of "End-Gas Temperature Measurement by Two-Wavelength Infrared Radiation Method" by W. G. Agnew 513
AGNEW, W. G.
End-Gas Temperature Measurement By A Two-Wavelength Infrared Radiation Method..... 495
AIR TRANSPORT
Applications of the Army-Navy Instrumentation Program to Transport Aircraft—A. M. Mayo and H. L. Wolbers 54
AIRCRAFT DESIGN
Mach 3 Wing Structures Stiffened Skin Versus Sandwich—Jack C. Joanides, Stanley C. Mellin and Leslie M. Lackman 167
ANDERSON, GUVEREN M.
Snap 2—A Reactor Powered Turboelectric Generator for Space Vehicles 390
ANDERSON, M. G.
Discussion of "Theoretical Prediction of Effect of Traction on Cornering Force," by W. Bergman... 635
APPS, DAVID C.
Discussion of "Cures for Powerplant Bending Noise Problems" by R. H. Bollinger and J. H. Ruhl..... 85
ASHURKOFF, PETER
Discussion of "Fuel Injection and Positive Ignition, Basis for Improved Efficiency and Economy" by C. W. Davis, E. M. Barber, and E. Mitchell..... 133
BADGER, D. M.
Strength Prediction After Severe and Complex Thermal Histories 650
BAIER, WILLIAM H.
Vehicle Steering Fundamentals 256
BARBER, E. M.
Fuel Injection and Positive Ignition, A Basis for Improved Efficiency and Economy..... 120
BAUMONT, M. P.
From 4 Plies to a Single Ply in Steel-Cord Casing Tires 238
BECK, N. J.
Discussion of "Piston Rings for Transportation Diesels" by G. F. Hyde, F. A. Robbins, and P. R. Shepler 307
BEGEMAN, C. R.
Discussion of "Metallic Tracer Method for Determining Lubricant in Engine Exhaust" by F. R. Bryan, J. C. Neerman, and J. E. Hinsch..... 210
Discussion of "Radioactive Tracer Study of Lubricating Oil Consumption" by E. S. Starkman..... 95
BENNETHUM, JAMES E.
Unsteady Heat Transfer in Engines..... 461
BENNETT, P. A.
An Engine Test For Predicting the Performance of Engine Lubricants in Most Severe Passenger Car Service 416
Discussion of "Metallic Tracer Method for Determining Lubricant in Engine Exhaust" by F. R. Bryan, J. C. Neerman, and J. E. Hinsch..... 307
Discussion of "Radioactive Tracer Study of Lubricating Oil Consumption" by E. S. Starkman..... 95
BENTELE, M.
Curtiss-Wright's Development on Rotating Combustion Engines 194
Rotating Combustion Engine 641
BERGMAN, WALTER
Theoretical Prediction of the Effect of Traction on Cornering Force 614
BERGQUIST, E. T.
The Effect of Material and Processing Variables on Residual Stresses in Carburized and Induction-Hardened Gears 554
BOLLINGER, R. H.
Cures for Powerplant Bending Noise Problems..... 77
BOWDITCH, F. W.
A Consideration of the Deposit Ignition Mechanism.. 435
A New Tool for Combustion Research..... 17
BRABETZ, J. C.
Discussion of "Radioactive Tracer Study of Lubricating Oil Consumption" by E. S. Starkman..... 97
BRENNEKE, A. M.
Discussion of "Radioactive Tracer Study of Lubricating Oil Consumption" by E. S. Starkman..... 97
BRITISH PETROLEUM RESEARCH CORP.
Discussion of "Metallic Tracer Method for Determining Lubricant in Engine Exhaust" by F. R. Bryan, J. C. Neerman, and J. E. Hinsch..... 209
BROWNFIELD, C. D.
Strength Prediction After Severe and Complex Thermal Histories 650
BRYAN, F. R.
Metallic Tracer Method for Determining Lubricant in Engine Exhaust..... 204
BURROWS, M. C.
The Measurement of Unburned-Gas Temperatures in an Engine by an Infrared Radiation Pyrometer 514
BUTLER, F. G.
Discussion of "Recent Developments in Cam Design" by J. H. Nourse, R. C. Dennis, and W. M. Wood.. 609
CALLAGHAN, EDMUND E.
Discussion of "Bypass Engine Noise" by F. B. Greatrex 323
CLARK, S. K.
Discussion of "Theoretical Prediction of Effect of Traction on Cornering Force" by W. Bergman.... 634
CLEVELAND, A. E.
Discussion of "Fuel Injection and Positive Ignition, Basis for Improved Efficiency and Economy" by C. W. Davis, E. M. Barber, and E. Mitchell..... 132
COIT, R. A.
Discussion of "Radioactive Tracer Study of Lubricating Oil Consumption" by E. S. Starkman..... 99
COMBUSTION, ABNORMAL—OTTO CYCLE ENGINE
A Consideration of the Deposit Ignition Mechanism—F. W. Bowditch and T. C. Yu..... 435
Concurrent Pyrolytic and Oxidative Reaction Mechanisms in Precombustion of Hydrocarbons—C. E. Welling, G. C. Hall and J. S. Stepanski..... 448
COMBUSTION, KNOCKING—OTTO CYCLE ENGINE
End-Gas Temperature-Pressure Histories and Their Relation to Knock—M. E. Gluckstein, C. Walcutt 529
End-Gas Temperature Measurement by a Two-Wavelength Infrared Radiation Method—W. G. Agnew 495
The Antiknock Behavior of the Alkyl Lead Compounds, H. E. Hesselberg and J. R. Howard..... 5
CONSTRUCTION AND INDUSTRIAL EQUIPMENT
Aircooling Versus Water-Cooling in Agricultural and Construction Equipment—H. H. Haas..... 402
CORROSION
Corrosion Resistance of Aluminum Automobile Engine Components—Allen M. Montgomery..... 24
CROOKS, RONALD D.
The Performance of Springs at Temperatures Above 900F 325
CULLEN, ORVILLE E.
Practical Application of High Temperature Gas Carburizing 250
DAVIS, C. W.
Fuel Injection and Positive Ignition, A Basis for Improved Efficiency and Economy..... 120
DENNIS, R. C.
Recent Developments in Cam Design..... 585
DIGGS, D. R.
Discussion of "End-Gas Temperature-Pressure Histories and Their Relation to Knock" by M. E. Gluckstein, and C. Walcutt..... 549
DIRECT CONVERSION TO ELECTRICITY
A Nitrosyl Chloride Solar Regenerative Fuel Cell System—W. E. McKee, J. D. Margerum, E. Findl and W. B. Lee 64
DOANE, D. V.
Discussion of "Case Hardenability of SAE 4028, 8620, 4620, and 4815 Steels" by J. A. Halgren and E. A. Solecki 673
ELTINGE, LAMONT
Discussion of "Unsteady Heat Transfer in Engines" by V. D. Overbye, J. E. Bennethum, O. A. Uyehara, and P. S. Myers 493

ENGINE COOLING
Aircooling Versus Water-Cooling in Agricultural and Construction Equipment—H. Haas 402
ENGINES, DIESEL
Stress Analysis of Aluminum V-8 Diesel Cylinder Block—H. W. Van Camp 212
ENGINES, GENERAL
Curtiss-Wright's Development on Rotating Combustion Engines—M. Bentele 194
The NSU-Wankel Rotating Combustion Engine—Dr. Walter G. Froede 179
Unsteady Heat Transfer in Engines—Vern D. Overbye, James E. Bennethum, O. A. Uyehara & P. S. Meyers 461
Rotating Combustion Engine—Roy T. Hurley and M. Bentele 641
ENGINES, JET & TURBINE, GROUND VEHICLE
The Film Vaporization Combustor—A. W. Hussmann and G. W. Maybach 563
An Advanced Automotive Gas Turbine Engine Concept—I. M. Swatman and D. A. Malohn 219
ENGINES, MEDIUM DUTY GASOLINE
A New Tool for Combustion Research—Fred W. Bowditch 17
Corrosion Resistance of Aluminum Automobile Engine Components—Allen M. Montgomery 24
ENGINE NOISE JET
By-Pass Engine Noise—F. B. Greatrex 312
ENGINES, SMALL GASOLINE
Vibration and Noise Control of Outboard Motors and Other Products— James W. Mohr 228
EXHAUST SYSTEMS AND GASES
Metallic Tracer Method for Determining Lubricant in Engine Exhaust—F. R. Bryan, J. C. Neerman and J. E. Hinsch 204
FEDDERSEN, E. W.
Production Application of High Energy Rate 361
FINDL, E.
A Nitrosyl Chloride Solar Regenerative Fuel Cell System 64
FROEDE, DR. WALTER G.
The NSU-Wankel Rotating Combustion Engine 179
FULLER, L. E.
Mating Materials in Unlubricated, High Load, Low Speed, Wear Tests at High Temperature in Air.. 148
FUEL INJECTION
Fuel Injection and Positive Ignition, A Basis for Improved Efficiency and Economy—C. W. Davis, E. M. Barber and Edward Mitchell 120
GAY, ERROL S.
Discussion of "Fuel Injection and Positive Ignition, Basis for Improved Efficiency and Economy" by C. W. Davis, E. M. Barber, and E. Mitchell 132
GEARS
"Case Crushing" of Carburized and Hardened Gears —R. Pedersen and S. L. Rice 370
The Effect of Material and Processing Variables on Residual Stresses in Carburized and Induction-Hardened Gears—E. T. Bergquist and S. M. Lenhoff 554
GLUCKSTEIN, M. E.
End-Gas Temperature-Pressure Histories and their Relation to Knock 529
GRAHAM, J. D.
Discussion of "Case Crushing of Carburized and Hardened Gears" by R. Pedersen and S. L. Rice 377
GREATREX, F. B.
By-Pass Engine Noise 312
GUINN, V. P.
Discussion of "Radioactive Tracer Study of Lubricating Oil Consumption" by E. S. Starkman 99
GURLEY, A. E.
Discussion of "Case Hardenability of SAE 4028, 8620, 4620, and 4815 Steels" by J. A. Halgren and E. A. Solecki 674
HAAS, H. H.
Aircooling Versus Water-Cooling in Agricultural and Construction Equipment 402
HAAS, LOWELL E.
Discussion of "Vibration and Noise Control of Outboard Motors and Other Products by J. W. Mohr.. 236
HALGREN, J. A.
Case Hardenability of SAE 4028, 8620, 4620 and 4815 Steels 662
HALL, G. C.
Concurrent Pyrolytic and Oxidative Reaction Mechanisms in Precombustion of Hydrocarbons 448
HAMBURGER, W. J.
Cord Fatigue in Fleet Tested Tires 158
HANYSZ, E. A.
Automatic Highway and Driver Aid Developments.. 31
HEATON, DONALD H.
U. S. Lunar Travel Program 101
HESSELBERG, H. E.
The Antiknock Behavior of the Alkyl Lead Compounds 5
HINSCH, J. E.
Metallic Tracer Method for Determining Lubricant in Engine Exhaust 204
HOWARD, J. R.
The Antiknock Behavior of the Alkyl Lead Compounds 5
HUBER, PAUL
Discussion of "NSU-Wankel Rotating Combustion Engine" by W. G. Froede and "Curtiss-Wright's Development on Rotating Combustion Engines" by M. Bentele 200
HURLEY, ROY T.
Rotating Combustion Engine 641
HUSSMANN, A. W.
The Film Vaporization Combustor 563
HYDE, GLENN F.
Piston Rings for Transportation Diesels 283
INSTRUMENTATION
Applications of the Army-Navy Instrumentation Program to Transport Aircraft—A. M. Mayo and H. L. Wolbers 54
JATCZAK, C. F.
Discussion of "Case Hardenability of SAE 4028, 8620, 4620, and 4815 Steels" by J. A. Halgren and E. A. Solecki 672
JENSEN, J. K.
Discussion of "Fuel Injection and Positive Ignition, A Basis for Improved Efficiency and Economy" by C. W. Davis, E. M. Barber, and E. Mitchell 131
JOANIDES, JACK C.
Mach 3 Wing Structures Stiffened Skin Versus Sandwich 167
JOHNSON, RICHARD S.
Discussion of "Recent Developments in Cam Design" by J. H. Nourse, R. C. Dennis, and W. M. Wood.. 608
JOHNSON, W. C.
Discussion of "Theoretical Prediction of Effect of Traction on Cornering Force" by W. Bergman 637
JOHNSON, WILLIAM R.
The Performance of Springs at Temperatures Above 900 F 325
KASH, S. W.
Plasma Propulsion 346
KENYON, WILLIAM S.
Discussion of "Piston Rings for Transportation Diesels" by G. F. Hyde, F. A. Robbins, and P. R. Shepler 308
KLEIN, W. G.
Cord Fatigue in Fleet Tested Tires 158
KOHR, ROBERT H.
Analysis and Simulation of Automobile Ride 110
KRABACHER E. J.
Radioisotopes Broaden the Approach to Machining Studies 575
KUNC, J. F.
Discussion of "Concurrent Pyrolytic and Oxidative Reaction Mechanisms in Precombustion of Hydrocarbons" by C. E. Welling, G. C. Hall, and J. S. Stepanski 458
LABORATORY EQUIPMENT AND FACILITIES
A New Tool for Combustion Research—Fred W. Bowditch 17
The Measurement of Unburned-Gas Temperatures in an Engine by an Infrared Radiation Pyrometer—M. C. Burrows, S. Shimizu, P. S. Meyers and O. A. Uyehara 514
LEE, W. B.
A Nitrosyl Chloride Solar Regenerative Fuel Cell System 64

LACKMAN, LESLIE M.
Mach 3 Wing Structures Stiffened Skin Versus Sandwich 167
LENHOFF, S. M.
The Effect of Material and Processing Variables on Residual Stresses in Carburized and Induction-Hardened Gears 554
LIPPMANN, S. A.
Discussion of "Theoretical Prediction of Effect of Traction on Cornering Force" by W. Bergman.... 637
LIVENGOOD, J. C.
Discussion of "End-Gas Temperature-Pressure Histories and Their Relation to Knock" by M. E. Gluckstein and C. Walcutt..... 547
LUBRICANTS AND LUBRICATION—CRANKCASE
An Engine Test for Predicting the Performance of Engine Lubricants in Most Severe Passenger Car Service—P. A. Bennett, G. K. Malone, and C. K. Murphy 416
A Radioactive Tracer Study of Lubricating Oil Consumption—E. S. Starkman 86
LUNSFORD, DALLAS
Discussion of "Piston Rings for Transportation Diesels" by G. F. Hyde, F. A. Robbins, and P. R. Shepler 309
MACKAY, D. B.
Secondary Power Systems for Space Vehicles 331
MALO, ALGER F.
Discussion of "Automatic Highway and Driver Aid Developments" by H. M. Morrison, A. F. Welch, and E. A. Hanysz 49
MALOHN, D. A.
An Advanced Automotive Gas Turbine Engine Concept 219
MALONE, G. K.
An Engine Test for Predicting the Performance of Engine Lubricants in Most Severe Passenger Car Service 416
MARGERUM, J. D.
A Nitrosyl Chloride Solar Regenerative Fuel Cell System 64
MARTEL, PHILLIP A.
Discussion of "Recent Developments in Cam Design" by J. H. Nourse, R. C. Dennis, and W. M. Wood.. 605
MAYBACH G. W.
The Film Vaporization Combustor 563
MAYO, A. M.
Applications of the Army-Navy Instrumentation Program to Transport Aircraft 54
MC KEE, W. E.
A Nitrosyl Chloride Solar Regenerative Fuel Cell System 64
MC REYNOLDS, L. A.
Discussion of "Radioactive Tracer Study of Lubricating Oil Consumption" by E. S. Starkman..... 98
MEILE, CARL H.
Discussion of "NSU-Wankel Rotating Combustion Engine" by W. G. Froede and "Curtiss-Wright's Development on Rotating Combustion Engines" by M. Bentele 202
MELLIN, STANLEY C.
Mach 3 Wing Structures Stiffened Skin Versus Sandwich 167
MERRITT, H. E.
Discussion of "Case Crushing of Carburized and Hardened Gears" by R. Pedersen and S. L. Rice.. 376
Discussion of "Fatigue, Impact, and Tensile Properties of High Strength Leaded and Nonleaded SAE 4140 Steel" by William Simon..... 76
METALS, FERROUS
Case Hardenability of SAE 4028, 8620, 4620 and 4815 Steels—J. A. Halgren and E. A. Solecki 662
Fatigue, Impact, and Tensile Properties of High Strength Leaded and Nonleaded SAE 4140 Steel —William Simon 69
Mach 3 Wing Structures Stiffened Skin Versus Sandwich—Jack C. Joanides, Stanley C. Mellin and Leslie M. Lackman 167
Mating Materials in Unlubricated, High Load, Low Speed, Wear Tests at High Temperature in Air, L. E. Fuller 148
Practical Application of High Temperature Gas Carburizing—Orville E. Cullen 250
Strength Prediction After Severe and Complex Thermal Histories—D. M. Badger and C. D. Brownfield 650
The Performance of Springs at Temperatures Above 900 F—William R. Johnson and Ronald D. Crooks 325
METALS, NONFERROUS
Mach 3 Wing Structures Stiffened Skin Versus Sandwich—Jack C. Joanides, Stanley C. Mellin and Leslie M. Lackman 167
Mating Materials in Unlubricated, High Load, Low Speed, Wear Tests at High Temperature in Air—L. E. Fuller 148
Stress Analysis of Aluminum V-8 Diesel Cylinder Block—H. W. Van Camp 212
MILKA, H. S.
Discussion of "Automatic Highway and Driver Aid Developments" by H. M. Morrison, A. F. Welch, and E. A. Hanysz 52
MILLER, A. J.
Discussion of "Case Hardenability of SAE 4028, 8620, 4620, 4815 Steels" by J. A. Halgren and E. A. Solecki 673
MITCHELL, EDWARD
Fuel Injection and Positive Ignition, A Basis for Improved Efficiency and Economy 120
MOHR, JAMES W.
Vibration and Noise Control of Outboard Motors and Other Products 228
MONTGOMERY, ALLEN M.
Corrosion Resistance of Aluminum Automobile Engine Components 24
MORRISON, H. M.
Automatic Highway and Driver Aid Developments.. 31
MURPHY, C. K.
An Engine Test for Predicting the Performance of Engine Lubricants in Most Severe Passenger Car Service 416
MYERS, P. S.
The Measurement of Unburned-Gas Temperatures in an Engine by an Infrared Radiation Pyrometer.. 514
Unsteady Heat Transfer in Engines 461
MRSTIK, A. V.
Discussion of "End-Gas Temperature-Pressure Histories and Their Relation to Knock" by M. E. Gluckstein and C. Walcutt..... 547
NEERMAN, J. C.
Metallic Tracer Method for Determining Lubricant in Engine Exhaust 204
NOURSE, J. H.
Recent Developments in Cam Design 585
OVERBYE, VERN D.
Unsteady Heat Transfer in Engines 461
PAHNKE, A. J.
Discussion of "Consideration of Deposit Ignition Mechanism" by F. W. Bowditch and T. C. Yu..... 445
PALIOBAGIS, MARKO
Radioisotopes Broaden the Approach to Machining Studies 575
PASQUINE, D. L.
Discussion of "Case Hardenability of SAE 4028, 8620, 4620, and 4815 Steels" by J. A. Halgren and E. A. Solecki 673
PASSENGER CAR DESIGN AND PERFORMANCE
Computer Predicts Car Acceleration—Henry L. Setz 351
Handling Requirements—O. J. Winkelmann..... 381
PEDERSEN, R.
"Case Crushing" of Carburized and Hardened Gears 370
PISTONS AND RINGS
Piston Rings for Transportation Diesels—Glenn F. Hyde, Fred A. Robbins and Paul R. Shepler 283
PLATT, M. M.
Cord Fatigue in Fleet Tested Tires 158
POWERS, R. P.
Discussion of "Theoretical Prediction of Effect of Traction on Cornering Force" by W. Bergman .. 639
PRODUCTION—METHODS
Production Application of High Energy Rate— E. W. Feddersen 361
Radioisotopes Broaden the Approach to Machining Studies—Marko Paliobagis and E. J. Krabacher.. 575
RAILROADS
Crank-Piston Gas-Generator Locomotives—L. H. Tengner 135

RICE, S. L.
"Case Crushing" of Carburized and Hardened Gears 370
ROADS AND STREETS
Automatic Highway and Driver Aid Developments—H. M. Morrison, A. F. Welch, and E. A. Hanysz.. 31
Scientific Highway Design for Safer Motoring—K. A. Stonex 269
ROBBINS, FRED A.
Piston Rings for Transportation Diesels 283
ROBLEE, H. S.
Discussion of "Concurrent Pyrolytic and Oxidative Reaction Mechanisms in Precombustion of Hydrocarbons" by C. E. Welling, G. C. Hall, and J. S. Stepanski 458
ROENSCH, M. M.
Discussion of "Radioactive Tracer Study of Lubricating Oil Consumption" by E. S. Starkman..... 97
ROGOWSKI, A. R.
Discussion of "End-Gas Temperature-Pressure Histories and Their Relation to Knock" by M. E. Gluckstein and C. Walcutt..... 54
ROWLAND, E. S.
Discussion of "Case Hardenability of SAE 4028, 8620, 4620, and 4815 Steels" by J. A. Halgren and E. A. Solecki 672
RUHL, J. H.
Cures for Powerplant Bending Noise Problems 77
RYASON, P. R.
Discussion of "Concurrent Pyrolytic and Oxidative Reaction Mechanism in Precombustion of Hydrocarbons" by C. E. Welling, G. C. Hall, and J. S. Stepanski 459
SCHILLING, R.
Ride Requirements 658
SCHWEITZER, P. H.
Discussion of "Film Vaporization Combustor" by A. W. Hussmann and G. W. Maybach 574
SETZ, HENRY L.
Computer Predicts Car Acceleration 351
SHEPLER, PAUL R.
Piston Rings for Transportation Diesels 283
SHIMIZU, S.
The Measurement of Unburned-Gas Temperatures in an Engine by an Infrared Radiation Pyrometer .. 514
SIEGEL, B. R.
Discussion of "End-Gas Temperature-Pressure Histories and Their Relation to Knock" by M. E. Gluckstein and C. Walcutt..... 54
SIMON, WILLIAM
Fatigue, Impact, and Tensile Properties of High Strength Leaded and Nonleaded SAE 4140 Steel... 69
SKINNER, DOUGLAS J.
Discussion of "Vibration and Noise Control of Outboard Motors and Other Products" by J. W. Mohr. 237
SOLECKI, E. A.
Case Hardenability of SAE 4028, 8620, 4620 and 4815 Steels 662
SOLTAU, JOHN P.
Discussion of "NSU-Wankel Rotating Combustion Engine" by W. G. Froede and "Curtiss-Wright's Development on Rotating Combustion Engines" by M. Bentele 202
SPACE VEHICLES AND SATELLITES
Plasma Propulsion ..... 34€
Secondary Power Systems for Space Vehicles—D. B. Mackay 331
SNAP 2—A Reactor Powered Turboelectric Generator for Space Vehicles—Guveren M. Anderson 390
U. S. Lunar Travel Program—Donald H. Heaton.... 101
SPARKS, CECIL R.
Discussion of "Vibration and Noise Control of Outboard Motors and Other Products" by J. W. Mohr 237
STARKMAN, E. S.
A Radioactive Tracer Study of Lubricating Oil Consumption 86
STEERING
Vehicle Steering Fundamentals—Baier..... 256
STEPANSKI, J. S.
Concurrent Pyrolytic and Oxidative Reaction Mechanisms in Precombustion of Hydrocarbons 448
STONEX, K. A.
Scientific Highway Design for Safer Motoring 269
SWATMAN, I. M.
An Advanced Automotive Gas Turbine Engine Concept 219
SUSPENSION SYSTEMS
Ride Requirements—R. Schilling 658
The Performance of Springs at Temperatures Above 900F—William R. Johnson and Ronald D. Crooks. 325
TAUSCHEK, MAX J.
Discussion of "Recent Developments in Cam Design by J. H. Nourse, R. C. Dennis, and W. M. Wood.... 610
TENGNER, L. H.
Crank-Piston Gas-Generator Locomotives 135
TETER, ROBERT K.
Discussion of "Vibration and Noise Control of Outboard Motors and Other Products" by J. W. Mohr 235
TIRES, PASSENGER CAR
Cord Fatigue in Fleet Tested Tires—W. G. Klein, M. M. Platt and W. J. Hamburger 158
Theoretical Prediction of the Effect of Traction on Cornering Force—Walter Bergman 614
TIRES, TRUCK AND HEAVY DUTY EQUIPMENT
From 4 Plies to a Single Ply in Steel-Cord Casing Tires—M. P. Baumont 238
TRINKLEIN, D. W.
Discussion of "Case Hardenability of SAE 4028, 8620, 4620, and 4815 Steels" by J. A. Halgren and E. A. Solecki 674
TURUNEN, W. A.
Discussion of "Advanced Automotive Gas Turbine Engine Concept" by I. M. Swatman and D. A. Malohn 227
UYEHARA, O. A.
The Measurement of Unburned-Gas Temperatures in an Engine by an Infrared Radiation Pyrometer ... 514
Unsteady Heat Transfer in Engines 461
VALVES & VALVE MECHANISMS
Recent Developments in Cam Design—J. H. Nourse, R. C. Dennis and W. M. Wood 585
VAN CAMP, H. W.
Stress Analysis of Aluminum V-8 Diesel Cylinder Block 212
VERSACE, JOHN
Dicussion of "Automatic Highway and Driver Aid Developments" by H. M. Morrison, A. F. Welch, and E. A. Hanysz 51
VIBRATION
Analysis and Simulation of Automobile Ride—Robert H. Kohr 110
Cures for Powerplant Bending Noise Problems — R. H. Bollinger and J. H. Ruhl 77
Vibration and Noise Control of Outboard Motors and Other Products—James W. Mohr 228
VON DER NUELL, W. T.
Discussion of "Advanced Automotive Gas Turbine Engine Concept" by I. M. Swatman and D. A. Malohn 227
WAGNER, T. O.
Discussion of "Unsteady Heat Transfer in Engines" by V. D. Overbye, J. E. Bennethum, O. A. Uyehara and P. S. Myers..... 493
WALCUTT, C.
Discussion of "Concurrent Pyrolytic and Oxidative Reaction Mechanisms in Precombustion of Hydrocarbons" by C. E. Welling, G. C. Hall, and J. S. Stepanski 459
End-Gas Temperature-Pressure Histories and their Relation to Knock..... 529
WELCH, A. F.
Automatic Highway and Driver Aid Developments... 31
WELLING, C. E.
Concurrent Pyrolytic and Oxidative Reaction Mechanisms in Precombustion of Hydrocarbons..... 448
WINKELMANN, O. J.
Handling Requirements..... 381
WOLBERS, H. L.
Applications of the Army-Navy Instrumentation Program to Transport Aircraft..... 54
WOOD, HOMER J.
Discussion of "Secondary Power Systems for Space Vehicles" by D. B. Mackay..... 344
WOOD, W. M.
Recent Developments in Cam Design..... 585
YU, T. C.
A Consideration of the Deposit Ignition Mechanism.. 435

DATE DUE

GAYLORD			PRINTED IN U. S. A.